

FINAL TECHNICAL REPORT

**"Interpretation of Plasma Diagnostics Package Results
in Terms of Large Space Structure Plasma Interactions"**

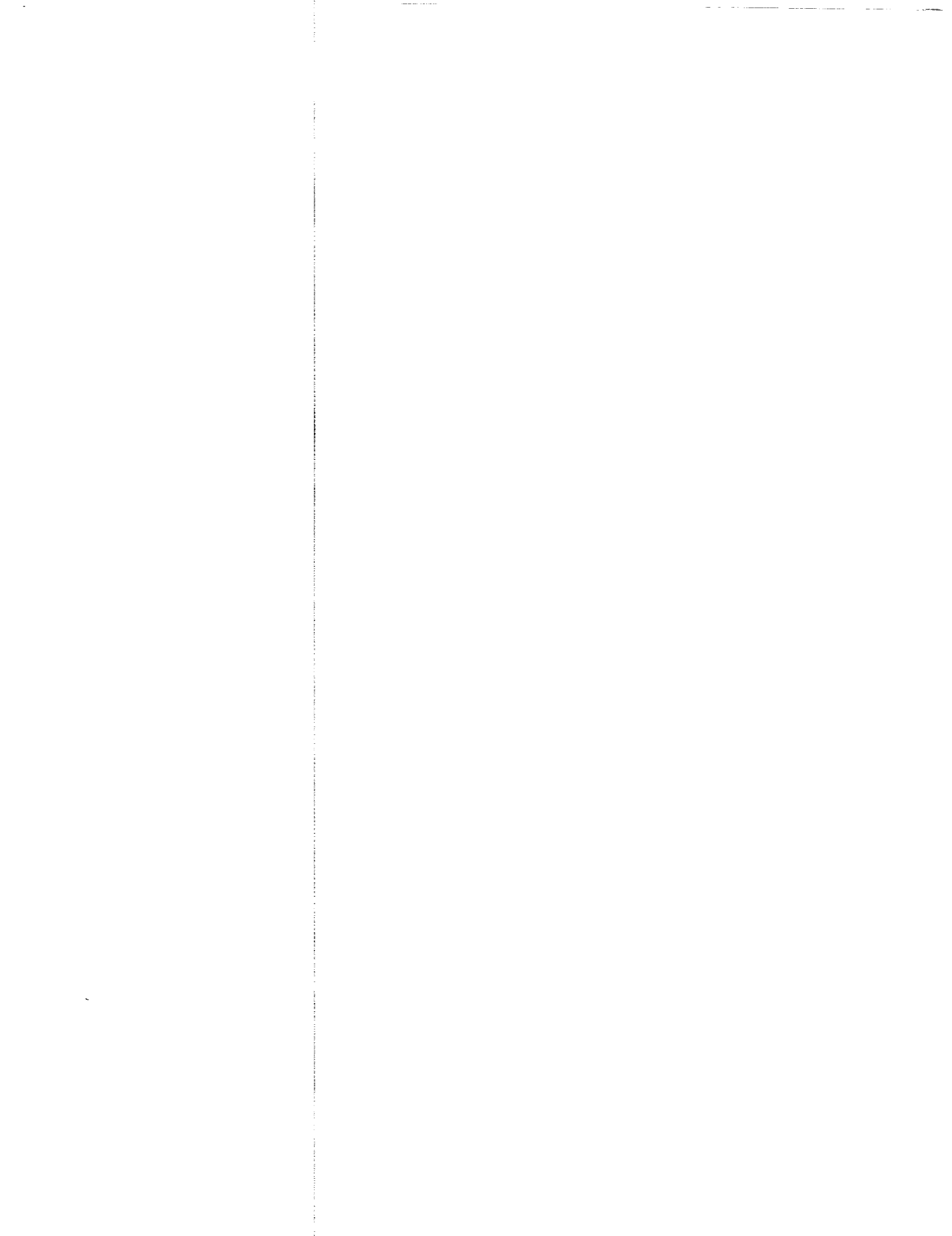
NASA Lewis Research Center Grant NAG 3-449

10 July 1983 through 1 August 1991

August 1991

Principal Investigator: William S. Kurth

**The University of Iowa
Department of Physics and Astronomy
Iowa City, IA 52242**



FINAL TECHNICAL REPORT

1. General

- 1.1 Date of Report : 1 August 1991
- 1.2 Period Covered : 10 July 1983 through
1 August 1991
- 1.3 Title of Grant : Interpretation of
Plasma Diagnostics
Package Results in
Terms of Large Space
Structure Plasma
Interactions
- 1.4 Principal Investigator : William S. Kurth
- 1.5 Grant Number : NAG 3-449
- 1.6 Grantee's Institution : The University of Iowa
Department of Physics
and Astronomy
Iowa City, IA 52242
- 1.7 Signature : Prepared by:



Jolene S. Pickett

Submitted by:



William S. Kurth



2. Introduction

The Plasma Diagnostics Package (PDP) is a spacecraft which was designed and built at The University of Iowa and which contained several scientific instruments. These instruments were used for measuring shuttle orbiter environmental parameters--temperature, pressure and potential--and plasma parameters--electric and magnetic fields; electron density, irregularity spectra and temperature; ion composition, density, temperature, energy distribution and beam direction; electrostatic and electromagnetic plasma wave spectra; and energy and pitch angle distribution of energetic ions and electrons. The PDP has flown on two space shuttle flights to date.

The first flight of the PDP took place from March 22, 1982 to March 27, 1982 on shuttle mission STS-3. The PDP was a part of the NASA/Office of Space Science payload (OSS-1), which contained instruments for conducting experiments in the disciplines of astronomy, space plasma physics and life science. Approximately 40 hours of data were obtained from the PDP's pallet location and 15 hours from the 50-foot Remote Manipulator System (RMS). During OSS-1 Iowa coordinated several joint experiments with the Stanford University/Utah State University Vehicle Charging and Potential (VCAP) Experiment, particularly during operations of the 1 keV, 50 ma Fast Pulse Electron Generator (FPEG).

The second PDP flight took place from July 29, 1985 to August 6, 1985 on shuttle mission STS/51F. On this flight the PDP was a part of Spacelab 2, a laboratory designed for conducting research in the areas of Solar, Atmospheric and Plasma Physics; High-Energy Astrophysics; Infrared Astronomy; Technology; and Life Sciences. During Spacelab 2 the PDP obtained about 70 hours of data from its pallet location and 65 hours from the RMS. In addition, 6 hours of data were obtained while the PDP was a free-flying satellite out to a distance of almost 500 m from the shuttle orbiter. As on OSS-1, joint experiments were conducted with the VCAP experiment.



The interpretation of both the OSS-1 and Spacelab 2 PDP results in terms of large space structure plasma interactions was the focus of the work performed under the subject grant.

3. Summary of Research Results

A brief summary of some of the major results of the research conducted under this grant is contained below.

3.1 Spacelab 2 Review Paper

A PDP review paper describing the PDP spacecraft, its instrumentation, and its operation on Spacelab 2 was written by W. S. Kurth, the Principal Investigator under this grant, and L. A. Frank in 1988. This paper also contains a summary of the scientific results up to the time at which it was written. The citation for this paper and a copy of the paper itself can be found later in this report.

3.2 Wake Studies

A study of the orbiter's wake was first completed using OSS-1 Langmuir probe data. For the near wake deep density depletions were seen accompanied by sharp increases in temperature with the regions showing the strongest gradients often being characterized by intense plasma turbulence. These same results for the near wake were obtained using data from the Langmuir Probe on Spacelab 2. Here, the key result was a smooth, well-defined structure in density which was highlighted at the boundaries with sharply elevated temperatures. The structure showed asymmetries which were probably due to the effects of the terrestrial magnetic field imposed at various angles with respect to the velocity vector. Other variations observed appear to be related to the large outgassing rate of the orbiter; at times the wake was dominated by contaminant ions. For the far wake, $d > \text{about } 30 \text{ m}$, the density depletion effects were small and lacked the large-scale turbulence one might expect far downstream from the orbiter. Of particular



significance was a slight density enhancement 100 m downstream of the orbiter directly on wake axis, which may be indicative of crossing streams of ions. The Spacelab 2 wake results were compared to the POLAR wake model with favorable results. For $d > 30$ m the agreement is very good. For $d < 30$ m the model underestimates the density by as much as an order of magnitude. It was concluded that outgassing from the orbiter can be a substantial contributor to the wake density in the near zone of the orbiter.

3.3 Chemical Releases

Chemical releases associated with the normal maintenance and operation of the shuttle, i.e., water dumps, flash evaporator operations, and thruster firings, were first studied on OSS-1. Associated with all of the releases were enhanced levels of electrostatic noise primarily below the lower hybrid resonance frequency and the detection of energetic ions, up to several hundred eV. It is thought that the newly created ions (formed by the ionization of neutral contaminants of the orbiter) are picked-up by the motion of the magnetic field past the craft and form a ring distribution that is unstable to lower hybrid resonance waves. The anisotropic distribution of these picked-up ions may explain why plasma wave observations show an intense band of electrostatic turbulence associated with various types of gas releases from the orbiter. The frequency range of these waves is below about 10 kHz and the region of greatest intensity is downstream from the orbiter. The topic of picked up ions will be discussed in more detail in Section 3.4.

Water dumps were looked at more closely using Spacelab 2 Langmuir Probe data. It was found that a strong increase in the level of turbulence near the orbiter is seen during the water dump. The spectrum of the fluctuations peaks at the lowest frequencies measured (a few Hertz) and extends up to a few kilohertz, near



the lower hybrid frequency. Two possible mechanisms for producing this turbulence are the ion-plasma instability and the Ott-Farley instability.

A study of the effect of thruster firings on spacecraft potential has not been completed as yet. However, it is known that thruster firings generally tend to drive the potential more negative although a few events have caused the opposite effect. In particular, it is noted that thruster firings which took place during FPEG sequences, which produce a more positive spacecraft potential, often tend to drive the potential even more positive.

3.4 Contamination Cloud

Observations by the Lepedea, pressure gauge, ion mass spectrometer, and retarding potential analyzer on both PDP flights indicate that the orbiter is accompanied in orbit by an extensive gas cloud composed of orbiter contaminants, primarily water. As mentioned in Section 3.3 these water molecules are ionized in the gas cloud around the orbiter, picked up by the magnetic field sweeping through the cloud at about 8 km/s, and thus are given a highly anisotropic distribution known as a ring distribution. Lepedea measurements indicate a neutral water production rate of the order of 10^{22} s^{-1} from the orbiter (or about 200 kg) over an eight day mission. Most of the pick-up occurs within a sphere of about 100 m radius, but with the primary pick-up occurring in the region downstream from the orbiter. Measurements at a distance of 200 m give pick-up ion densities of about 200 cm^{-3} upstream and, as high as 10^4 cm^{-3} downstream from the orbiter. The ring distribution is unstable to plasma waves and could be responsible for the production of the broadband electrostatic waves observed in the vicinity of the orbiter on both flights. This noise typically extends with a relatively flat spectrum from a few Hz to 20 or 30 kHz. The broadband electric field strength is about 10



mV/m. The noise is generally strongest in the region downstream of the orbiter, although high intensities are also observed near magnetic conjunctions.

Another strong indication that the waves are driven by the water pick-up ions is that "mushroom" spectral features have been identified in the plasma wave data. The top of a mushroom feature is formed by a band of lower hybrid frequency waves, while the base of the mushroom is formed by low frequency waves whose frequency bandwidth increases to meet the lower hybrid frequency band at the apex of the mushroom. These mushroom spectral features are centered near times when the orbiter's velocity relative to the ionospheric plasma is perpendicular to the ionospheric magnetic field and when the PDP is downstream from the orbiter. More nearly parallel flows are characterized by low wave levels. The near zone waves (within about 10 m of the orbiter while the PDP was on the RMS) were also studied. As in the case of the far zone, these waves show a pronounced amplitude and frequency variation depending on the ratio of the orbiter's velocity parallel to B , to its velocity relative to the ionospheric plasma. When this quantity is near its maximum, very low wave levels and small frequency extents are observed; whereas when this quantity is near zero, the highest wave levels and extents in frequency are observed. This implies that the waves are plausibly driven by water pick-up ions and that nonlinear effects may be important in understanding the evolution of the waves.

Antenna interference patterns in wideband spectra have provided a new method of determining the wavelength and direction of propagation of short wavelength electrostatic waves. Two distinct patterns have been identified: one is produced by zero frequency emissions, the other is associated with lower hybrid waves. Both types of waves are believed to be produced by the pick-up ions associated with charge exchange ionization of the neutral gas cloud around the orbiter. In another study it is argued that the newly ionized water ions may be



represented as a ring-beam distribution to a first approximation. Using plasma parameters from various PDP instruments, a dispersion equation was derived for electrostatic waves in this magnetized plasma.

It also appears in some cases that the contamination cloud can screen the orbiter from the usual motional $\mathbf{V} \times \mathbf{B}$ electric field by a system of currents associated with the contaminant ions. The currents are driven by the motional electric field which displaces the ions created in charge exchange reactions with the ambient O^+ ions. The pick-up current, which screens the motional field is closed by field-aligned currents which are carried by a propagating Alfvén wave.

3.5 Electron Beam Studies

During the time that the PDP was a free-flying satellite on Spacelab 2, the electron generator (FPEG) was used to produce a 1-keV electron beam. The primary electron beam was not observed because the orbiter could not attain the accuracy necessary to put the FPEG and PDP on the same magnetic field lines. However, when the PDP was on field lines which were directly downstream from the orbiter/beam field line by as much as 150 m, a sheet of electrons scattered by the injected beam formed in the wake of the shuttle were observed. The electron distribution function of the electrons in this sheet is generally field aligned and forms a secondary electron beam. Coincidentally, with the observations of the electron beam were observations of intense broadband electrostatic waves at frequencies up to about 10 kHz. These intense waves were detected close to the magnetic field line threading the beam generator and a thin, magnetically-aligned sheet in the wake of the orbiter. The thickness of this sheet of returning electrons was about 20 m. Numerical simulations show that electrons can be accelerated in the direction opposite of the beam velocity as a result of wave-particle interactions. The simulations also show that the relative drift of the electrons and



ambient ions can drive the ion acoustic instability. The ion distribution suggests a spacecraft charge of about 5 to 10 v. The electric field probe observed significant effects only when the PDP was directly downstream from the beam. Within 40 m of the beam, the observations suggest the energetic electrons are more or less isotropic. However, in the region from 80 to 170 m downstream, the signal can be explained if the energetic electrons are primarily returning back down the field line.

In yet another study involving DC electron beams emitted from the FPEG on Spacelab 2, antenna interference patterns which were seen in wideband spectrograms at frequencies from 0-30 kHz were analyzed to determine wave direction, wavelength, the dispersion relation, and the location of the source region of these short wavelength waves. The observed waves associated with the FPEG events have a linear dispersion relation very similar to that of ion acoustic waves. The waves were confirmed to be oblique ion acoustic waves which are generated by the returning background electrons.

Another study of the interaction of an electron beam with the ionospheric plasma involved the analysis of whistler-mode waves known as VLF hiss generated by the electron beam. By comparing the emissivity of the beam to various theories for the wave generation, the conclusion was reached that the generation mechanism is a coherent Cerenkov process and, in turn, implies that bunching of the electrons in the beam must be occurring. An expression was then derived that describes the coherent Cerenkov radiated power from a group of test particles in a plasma medium moving parallel to a magnetic field. A detailed model of the coherent Cerenkov emission process from the beam was developed.



4. Publications and Oral Presentations

4.1 List of Publications

Listed below are the scientific papers that have been published which are applicable to the subject grant during the period for which the grant was in force. All of these papers present or reference PDP data taken during the OSS-1 or Spacelab 2 flights. Copies of these publications are included at the end of this report.

PUBLICATIONS:

1. Interaction of the Space Shuttle Orbiter With the Ionospheric Plasma
G. B. Murphy, S. D. Shawhan, L. A. Frank, N. D'Angelo, D. A. Gurnett, J. B. Grebowsky, D. L. Reasoner, and N. Stone
17th Symposium on Spacecraft-Plasma Interactions and Their Influence on Field and Particle Measurements, Noodwijk, Netherlands, Proceedings, September 1983.
2. Suprathermal Plasma Observed on the STS-3 Mission by the Plasma Diagnostics Package
W. Paterson, L. A. Frank, H. Owens, J. S. Pickett, G. B. Murphy, and S. D. Shawhan
USAF/NASA Spacecraft Environmental Interactions Technology Conference, U.S. Air Force Academy, Colorado Springs, CO, Proceedings, 4-6 Oct. 1983.
3. Electron and Ion Density Depletions Measured in the STS-3 Orbiter Wake
G. B. Murphy, J. Pickett, W. J. Raitt, and S. D. Shawhan
USAF/NASA Spacecraft Environmental Interactions Technology Conference, U.S. Air Force Academy, Colorado Springs, CO, Proceedings, 4-6 Oct. 1983.
4. Effects of Chemical Releases by the STS-3 Orbiter on the Ionosphere
J. S. Pickett, G. B. Murphy, W. S. Kurth, C. K. Goertz, and S. D. Shawhan
J. Geophys. Res., **90**, 3487, 1985.
- *5. Measurements of Plasma Parameters in the Vicinity of the Space Shuttle
G. Murphy, J. Pickett, N. D'Angelo, and W. S. Kurth
Planet. Space Sci., **34**, 993, 1986.
6. A Review of the Findings of the Plasma Diagnostics Package and Associated Laboratory Experiments: Implications of Large Body/Plasma Interactions for Future Space Technology
G. B. Murphy and D. E. Lonngren
Workshop on Space Technology Plasma Issues in 2001, Jet Propulsion Laboratory, Pasadena, CA Proceedings, 24-26 Sept. 1986.

*Publications in refereed journals.



- *7. Plasma Wave Turbulence Around the Shuttle: Results from the Spacelab-2 Flight
D. A. Gurnett, W. S. Kurth, J. T. Steinberg, and S. D. Shawhan
Geophys. Res. Lett., 15, 760-763, 1988.
- *8. Exposed High-Voltage Source Effect on the Potential of an Ionospheric Satellite
A. C. Tribble, N. D'Angelo, G. B. Murphy, J. S. Pickett, and J. T. Steinberg
J. of Spacecraft and Rockets, 25, 64-69, 1988.
- *9. The Plasma Wake of the Shuttle Orbiter
G. B. Murphy, D. L. Reasoner, A. Tribble, N. D'Angelo, J. S. Pickett, and W. S. Kurth
J. Geophys. Res., 94, 6866-6872, 1989.
- *10. Gaseous Environment of the Shuttle Early in the Spacelab 2 Mission
J. S. Pickett, G. B. Murphy and W. S. Kurth
J. of Spacecraft and Rockets, 25, 169-174, 1988.
- *11. Hot Ion Plasmas from the Cloud of Neutral Gases Surrounding the Space Shuttle
W. R. Paterson and L. A. Frank
J. Geophys. Res., 94, 3721-3727, 1989.
- *12. Double-Probe Potential Measurements Near the Spacelab 2 Electron Beam
J. T. Steinberg, D. A. Gurnett, P. M. Banks, and W. J. Raitt
J. Geophys. Res., 93, 10,001-10,010, 1988.
- *13. The POLAR Code Wake Model: Comparison With In-Situ Observations
G. Murphy and I. Katz
J. Geophys. Res., 94, 9065-9070, 1989.
- *14. Coherent Cerenkov Radiation from the Spacelab 2 Electron Beam
W. M. Farrell, D. A. Gurnett, and C. K. Goertz
J. Geophys. Res., 94, 443-452, 1989.
- 15. Contaminant Ions and Waves in the Space Station Environment
G. B. Murphy
Proceedings of the Space Station Contamination Workshop, Hilton Head Island, South Carolina, 29-30 October, 1987, NASA Conference Publication 3002.
- *16. The Spacelab 2 Plasma Diagnostics Package
W. S. Kurth and L. A. Frank
J. Spacecraft and Rockets, 27, 70-75, 1990.
- *17. Plasma Density, Temperature, and Turbulence in the Wake of the Shuttle Orbiter
A. C. Tribble, J. S. Pickett, N. D'Angelo, and G. B. Murphy
Planet. Space Sci., 37, 1001-1010, 1989.
- *18. The Coherent Cerenkov Radiated Power from a Group of Field-Aligned Test Particles in a Magnetoplasma
W. M. Farrell, and C. K. Goertz
Planetary Space Sci., 38, 373-381, 1990.

*Publications in refereed journals.



- *19. **Electron Velocity Distribution and Plasma Waves Associated with the Injection of an Electron Beam into the Ionosphere**
L. A. Frank, W. R. Paterson, M. Ashour-Abdalla, D. Schriver, W. S. Kurth, D. A. Gurnett, N. Omid, P. M. Banks, R. I. Bush, and W. J. Raitt
J. Geophys. Res., 94, 6995-7001, 1989.
- *20. **Plasma Density Fluctuations Observed During Space Shuttle Orbiter Water Releases**
J. S. Pickett, N. D'Angelo, W. S. Kurth
J. Geophys. Res., 94, 12,081-12,086, 1989.
- *21. **Spacelab 2 Electron Beam Wave Stimulation: Studies of Important Parameters**
G. D. Reeves, P. M. Banks, T. Neubert, K. J. Harker, D. A. Gurnett, and W. J. Raitt
J. Geophys. Res., 95, 10,655-10,670, 1990.
- *22. **Comments on 'Pulsed Electron Beam Emission in Space' By Neubert et al. [1988]**
W. M. Farrell
J. Geomag. & Geoelec., 42, 57-62, 1990.
- *23. **Transition from Ring to Beam Arc Distributions of Water Ions near the Space Shuttle Orbiter**
I. H. Cairns
J. of Geophys. Res., 95, 15,167-15,173, 1990.
- *24. **Control of Plasma Waves Associated with the Space Shuttle by the Angle Between the Orbiter's Velocity Vector and the Magnetic Field**
I. H. Cairns and D. A. Gurnett
J. Geophys. Res., 96, 7591-7601, 1991.
- *25. **Plasma Waves Observed in the Near Vicinity of the Space Shuttle**
I. H. Cairns and D. A. Gurnett
J. Geophys. Res., in press, 1991.
26. **Plasma Waves Associated with the Space Shuttle**
I. H. Cairns and D. A. Gurnett
Proceedings of the Joint Varena-Abastumani-ESA-Nagoya-Potsdam Workshop on Plasma Astrophysics, Tbilisi, Georgia, USSR, June 4-12, 1990, ESA SP-311, 87, 1990.
- *27. **Interference Patterns in Wideband Spectra in the Spacelab-2 Plasma Wave Data: Ion Acoustic Waves Generated by the Electron Beam**
W. Feng, D. A. Gurnett and I. H. Cairns
J. Geophys. Res., in preparation, 1991.
- *28. **Spacelab 2 Potential Measurements Around the Shuttle Orbiter**
J. S. Pickett and W. S. Kurth
Planet. Space Sci., in preparation, 1991.
- *29. **Electrostatic Waves Associated with the Spacelab 2 Electron Beam**
W. S. Kurth, D. A. Gurnett, L. A. Frank, W. R. Paterson, M. Ashour-Abdalla, D. Schriver, P. M. Banks, R. I. Bush, and W. J. Raitt
Geophys. Res. Lett., in preparation, 1991.



4.2 List of Thesis Projects

The following thesis projects, which primarily present, analyze and discuss PDP/Spacelab 2 data, were made possible, in part, due to the support of the subject grant. Copies of these theses are included at the end of this report. Additional copies may be obtained from University Microfiche International, 300 N. Zeeb Road, Ann Arbor, MI 48106, Telephone 800-521-0600.

THESIS:

1. Plasma Parameters in the Vicinity of the Shuttle Orbiter
A. C. Tribble
M.S. Thesis, The University of Iowa, Iowa City, IA May 1986.
2. An Analysis of Whistler-Mode Radiation from the Spacelab-2 Electron Beam
W. M. Farrell
Ph.D. Thesis, The University of Iowa, Iowa City, IA, July 1987.
3. Ion Plasmas in the Vicinity of the Orbiter: Observations and Modeling
W. R. Paterson
M.S. Thesis, The University of Iowa, Iowa City, IA, July 1987.
4. The Large Scale Wake Structure of the Shuttle Orbiter: Plasma Density, Temperature, and Turbulance
A. C. Tribble
Ph.D. Thesis, The University of Iowa, Iowa City, IA, May 1988.
5. Quasi-Static Electric Field Measurements Made with the Plasma Diagnostics Package in Free Flight During Spacelab-2
J. T. Steinberg
Ph.D. Thesis, The University of Iowa, Iowa City, IA, May 1988.

4.3 List of Oral Presentations

During the period of this grant several opportunities were available, which Iowa took advantage of, to present the results of the research performed under this grant. These presentations served two very valuable purposes: (a) informed the scientific community of new and worthwhile results, and (b) obtained feedback from them on possible future directions for this research. A list of the oral presentations which were made and which deal with the subject matter of this grant is given below.



Oral Presentations:

1. **The Large Scale Wake Structure of the Shuttle Orbiter**
G. B. Murphy, I. Katz, D. L. Reasoner, N. D'Angelo, J. S. Pickett, and W. S. Kurth
Presented at the 1986 Fall American Geophysical Union Meeting, San Francisco, California, December 8-12, 1986.
2. **The Effect of the Earth's Magnetic Field on Plasma Turbulence Near the Shuttle Orbiter**
A. C. Tribble, N. D'Angelo, G. B. Murphy, and J. S. Pickett
Presented at the 1986 Fall American Geophysical Union Meeting, San Francisco, California, December 8-12, 1986.
3. **Electric Field Measurements Near the Space Shuttle at Times of Shuttle Thruster Operation**
J. T. Steinberg, and D. A. Gurnett
presented at the 1987 Spring American Geophysical Union Meeting, Baltimore, Maryland, May 18-22, 1987.
4. **Effect of an Exposed High-Voltage Source on the Potential of an Ionospheric Satellite Released from the Shuttle Orbiter**
A. C. Tribble, N. D'Angelo, G. B. Murphy, J. S. Pickett, and J. T. Steinberg
Presented at the 1987 Spring American Geophysical Union Meeting, Baltimore, Maryland, May 18-22, 1987.
5. **Shuttle/Plasma Interactions and Subsattelites**
G. B. Murphy
Presented at the Space Physics Briefing for Astronaut Corps, Johnson Space Center, Houston, Texas, September 9, 1987.
6. **The Secondary Electron Beams and Plasma Waves Associated with Electron Beam Injection in Space**
L. A. Frank, D. A. Gurnett, M. Ashour-Abdalla, W. R. Paterson, W. S. Kurth, N. Omid, P. M. Banks and W. J. Raitt
Presented at Twenty-Ninth Annual Meeting, American Physical Society, Division of Plasma Physics, Princeton, New Jersey, November 2-6, 1987.
7. **The Plasma Wake of the Shuttle Orbiter**
G. B. Murphy
Presented (invited) as a seminar at Jet Propulsion Laboratory, Pasadena, California, November 12, 1987.
8. **A Comparison of the Plasma Wake of the Shuttle Orbiter to the Wake of a Smaller Ionospheric Satellite**
A. Tribble, N. D'Angelo, and G. Murphy
Presented at the 1987 Fall American Geophysical Union Meeting, San Francisco, California, December 6-11, 1987.
9. **Observations and Modeling of Ion Pickup in the Vicinity of the Orbiter**
W. R. Paterson, and L. A. Frank
Presented at the 1987 Fall American Geophysical Union Meeting, San Francisco, California, December 6-11, 1987.



10. **Coherent Cerenkov Radiation from the Spacelab-2 Electron Beam**
W. M. Farrell, D. A. Gurnett and C. K. Goertz
Presented at the 1987 Fall American Geophysical Union Meeting, San Francisco, California, December 6-11, 1987.
11. **Plasma Observations in the Vicinity of the Shuttle**
L. A. Frank, W. R. Paterson, P. M. Banks, R. I. Bush, and W. J. Raitt
Presented at the 1988 National Radio Science Meeting, International Union of Radio Science, Boulder, Colorado, January 5-8, 1988.
12. **Coherent Cerenkov Radiation from the Spacelab-2 Electron Beam**
W. M. Farrell, D. A. Gurnett, and C. K. Goertz
Presented at the 1988 National Radio Science Meeting, International Union of Radio Science, Boulder, Colorado, January 5-8, 1988.
13. **Quasi-Static Electric Field Measurements Near the Space Shuttle at Times of Shuttle Thruster Operation**
J. T. Steinberg, D. A. Gurnett, and C. K. Goertz
Presented at the 1988 National Radio Science Meeting, International Union of Radio Science, Boulder, Colorado, January 5-8, 1988.
14. **Electron Distributions Observed from Electron Beam Injections During the Spacelab-2 Mission**
W. R. Paterson, L. A. Frank, M. Ashour-Abdalla, D. Schriver, N. Omid, P. M. Banks, and W. J. Raitt
Presented at the 1988 Spring American Geophysical Union Meeting, Baltimore, Maryland, May 16-20, 1988.
15. **Electrostatic Waves Associated with the Spacelab 2 Electron Beam**
W. S. Kurth, D. A. Gurnett, L. A. Frank, W. R. Paterson, M. Ashour-Abdalla, D. Schriver, P. M. Banks, R. I. Bush, and W. J. Raitt
Presented at the 1989 Spring American Geophysical Union Meeting, Baltimore, Maryland, May 7-12, 1989.
16. **On the Broadband Electrostatic Waves Associated with the Shuttle**
I. H. Cairns and D. A. Gurnett
Presented at the 1989 Spring American Geophysical Union Meeting, Baltimore, Maryland, May 7-12, 1989.
17. **An Analysis of Antenna Interference Patterns in Wideband Spectrums from the Spacelab-2 Mission**
W. Feng, I. H. Cairns, and D. A. Gurnett
Presented at the 1989 Cambridge Workshop in Theoretical Geoplasma Research, Wave-Particle Interaction Phenomena in Geoplasmas, Cambridge, MA, June 12-16, 1989.
18. **Injection of an Electron Beam into the Ionosphere: Electron Velocity Distributions and Plasma Waves in the Wake of the Beam**
L. A. Frank, W. R. Paterson, M. Ashour-Abdalla, D. Schriver, W. S. Kurth, D. A. Gurnett, P. M. Banks, R. I. Bush, and W. J. Raitt
Presented at the Thirty-first Annual Meeting of The American Physical Society, Division of Plasma Physics, in Anaheim, CA, November 13-17, 1989.



19. **On Broadband Electrostatic Waves Associated with the Space Shuttle**
Iver H. Cairns and Donald A. Gurnett
Presented at the 1989 Fall American Geophysical Union Meeting, San Francisco, CA, December 4-8, 1989.
20. **Control of Plasma Waves Associated with the Space Shuttle by the Angle Between the Orbiter's Velocity Vector and the Magnetic Field**
Iver H. Cairns and Donald A. Gurnett
Presented at the 1990 Spring American Geophysical Union Meeting, Baltimore, MD, May 29 - June 1, 1990.
21. **Plasma Waves Associated With the Space Shuttle**
I. H. Cairns and D. A. Gurnett
Presented at the Varena-Abastumani-Nagoya Workshop on Plasma Astrophysics, Tbilisi, Soviet Republic of Georgia, USSR, June 3-15, 1990.
22. **Interference Patterns in Wideband Spectra in the Spacelab-2 Plasma Wave Data: Ion Acoustic Waves Generated by the Electron Beam**
W. Feng, D. A. Gurnett, and I. H. Cairns
Presented at the Fall American Geophysical Union Meeting, in San Francisco, CA, December 3-7, 1990.
23. **Interference Patterns in Wideband Spectra From the Spacelab-2 Plasma Wave Data: Lower Hybrid Waves Associated With Shuttle Thruster Firings**
W. Feng, D. A. Gurnett, and I. H. Cairns
Presented at the Spring American Geophysical Union Meeting, in Baltimore, MD, May 28-June 1, 1991.

3.4 Publications

The remainder of this Final Technical Report is devoted to presenting copies of the publications listed in Subsection 4.1 and the thesis projects listed in Section 4.2. These papers and theses are included in the same order as that given in the list.



INTERACTION OF THE SPACE SHUTTLE ORBITER WITH THE IONOSPHERIC PLASMA

G B Murphy, S D Shawhan, L A Frank,
N D'Angelo & D A GurnettDepartment of Physics and Astronomy
University of Iowa, USA

J M Grebowsky

NASA GSFC
Greenbelt, MD, USA

D L Reasoner & N Stone

NASA, MSFC
Huntsville, AL, USA

ABSTRACT

The Plasma Diagnostics Package (PDP), which flew as part of the NASA Office of Space Science (OSS-1) payload on STS-3 consisted of an instrument complement capable of characterizing the plasma environment in and around the Space Shuttle Orbiter. These measurements coupled with those made by the Vehicle Charging and Potential (VCAP) experiment also on OSS-1, as well as diagnostics from subsequent flights, provide insight into the effects a large vehicle such as the Orbiter has on the ionospheric plasma. Modification of the environment by contamination such as Orbiter outgassing, thruster operation and water dumps results in altered neutral pressure, modified plasma density and an altered chemical composition. The physical size and velocity of the Orbiter vehicle produces a plasma wake, generates electric fields, results in surface effects and generates broadband electrostatic noise.

Keywords: Large Vehicle Interaction, Wake, Ionospheric Plasma, Shuttle Environment

1. INTRODUCTION

1.1 Background

Until the flight of STS-3 in March 1982 little opportunity was available to study the interactions of a vehicle whose scale was large compared to an ion gyroradius and that was moving at a high velocity with respect to a relatively dense and cool plasma. Table 1 summarizes the plasma parameters in the F2 ionosphere and includes Orbiter parameters of interest.

Extensive theoretical work has been done on the problem of plasma wakes. Stone (Ref. 1) provides an excellent summary of this research and more recently Samir et al (Ref. 2) have studied the expansion of a plasma into a vacuum and discussed such phenomena as ion streams, rarefaction waves, and plasma instabilities and suggest appropriate in situ measurements on the space shuttle.

1.2 Instrumentation

Instruments aboard the Plasma Diagnostics Package (PDP) were designed to measure thermal particle densities and temperatures, energetic particle distribution functions, electric and magnetic

Table 1.

Plasma Parameters	
Ambient Density	$n_e \approx 10^5 - 10^6 \text{ cm}^{-3}$
Ambient Temperature	$T_e \approx 1200^\circ - 2400^\circ \text{K}$
Electron Gyroradius	4.3 cm
Ion Gyroradius	$\sim 4\text{m} (O^+)$
Ion Thermal Speed	1.3 km/sec
Orbiter Parameters	
Vorb = 7.8 km/sec	Surface Area:
	Insulator $\sim 1400\text{m}^2$
Mach # 5-8	Conductor $\sim 60\text{m}^2$
Characteristic Length	37m long, 24m wingspan

fields, and electrostatic and electromagnetic waves. Table 2 lists the complement of instruments aboard this experiment and the parameters they measure. The PDP was designed both for on pallet measurements and as an RMS (Remote Manipulator System) probe. The PDP was lifted out of the bay with the RMS and maneuvered around the Orbiter in sequences designed to measure the electric and magnetic fields, electrostatic and electromagnetic waves as well as the thermal and energetic particle environment.

Other investigations of interest to this discussion that were part of the OSS-1 payload were the VCAP (Vehicle Charging and Potential) experiment and the FPEG (Fast Pulse Electron Gun). (For a complete description of the OSS-1 experiment complement see Neupert et al Ref. 3). The VCAP investigation consisted of charge and current probes (primarily for measuring vehicle capacitance with respect to the plasma), a Langmuir Probe (LP) for measurement of electron density and temperature and a Spherical Retarding Potential Analyzer (SRPA) for ion density and temperature.

1.3 The STS-3 Mission

Since STS-3 was still a flight test mission, the payload had a low priority for selection of flight attitude and the one chosen as a compromise for the payload/orbiter objectives lead to difficulties in sorting out day/night and ram/wake

Table 2.

●	LOW ENERGY PROTON AND ELECTRON DIFFERENTIAL ENERGY ANALYZER (LEPEDEA)
-	Nonthermal Electron and Ion Energy Spectra and Pitch Angle Distributions for Particle Energies between 2 eV and 50 keV
●	AC MAGNETIC WAVE SEARCHCOIL SENSOR
-	Magnetic Fields with a Frequency Range of 30 Hz to 178 kHz
●	TOTAL ENERGETIC ELECTRON FLUXMETER
-	Electron Flux $10^6 - 10^{14}$ Electrons/cm ² Sec
●	AC ELECTRIC AND ELECTROSTATIC WAVE ANALYZERS
-	Spectra with a Frequency Range of 30 Hz to 800 MHz
-	Electric Field Strength at S-Band, 2.2 GHz
●	DC ELECTROSTATIC DOUBLE PROBE WITH SPHERICAL SENSORS
-	Electric Fields in one axis from 4 mV/m to 4 V/m
●	DC TRIAXIAL FLUXGATE MAGNETOMETER
-	Magnetic Fields from 12 Milligauss to 1.5 Gauss
●	LANGMUIR PROBE
-	Thermal Electron Densities between 10^3 and 10^7 cm ⁻³
-	Density Irregularities with Frequencies of .5 Hz to 178 kHz.
●	RETARDING POTENTIAL ANALYZER/DIFFERENTIAL ION FLUX PROBE
-	Ion Number Density from 10^2 to 10^7 cm ⁻³
-	Energy Distribution Function below 6 eV
-	Directed Ion Velocities up to 15 km/sec
●	ION MASS SPECTROMETER
-	Mass Ranges of 1 to 64 Atomic Mass Units
-	Ion Densities from 20 to 2×10^7 Ions cm ⁻³
●	PRESSURE GAUGE
-	Ambient Pressure from 10^{-3} to 10^{-7} Torr

effects. The attitude of the Orbiter for all of the PDP data presented here is referred to as Nose-To-Sun (NTS) with a 2x orb rate roll (see Figure 1). This attitude results in a cyclic ram/wake cycle for instruments in the payload bay such that maximum ram occurs around ascending node and maximum wake at descending node.

Effects of the Space Shuttle Orbiter on the ionospheric plasma will be discussed in two parts. The

first is induced contamination which will be treated only briefly and the second are effects induced by the vehicle's size, velocity and electrical properties.

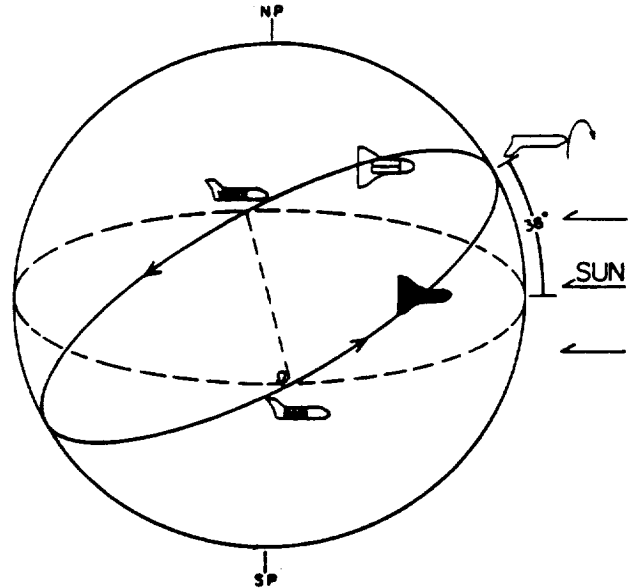


Figure 1. STS-3 Orbit Attitude

2. INTERACTION VIA CONTAMINATION

Electromagnetically, the Orbiter is relatively clean. Shawhan and Murphy (Ref. 4) indicated that both transmitters and unintentional interference are well below Interface Control Document specs. The predominant noise turned out to be the ubiquitous broad band electrostatic noise which will be discussed in the next section.

The principle form of modification via contamination takes the form of chemical releases. These chemicals; water, nitrogen, hydrogen and traces of other heavier molecules, enter the ionosphere as a result of Orbiter outgassing, thruster firings, and water dumps. In a discussion of the pressure environment, Shawhan and Murphy (Ref. 5) pointed to high payload bay outgassing rates that bring neutral pressure to 4×10^{-5} torr when the doors are closed in orbit. The gas cloud did not decrease significantly as the mission progressed evidenced by enhanced pressures when the payload bay was turned "Top-To-Sun" on the sixth day of the mission.

A Bennett Ion Mass Spectrometer utilizing retarding potentials was capable of separating the ambient ionospheric ions from those released by the Orbiter. Results reported by Grebowsky et al (Ref. 6) indicate that the expected O^+ ion is predominant, but that there is a significant amount of H_2O^+ , NO^+ and CO_2^+ . Narcisi et al (Ref. 7) on a subsequent shuttle flight, confirm the presence of high concentrations of H_2O^+ and noted that at times over one-half of the ambient O^+ has been converted to H_2O^+ by a reaction with water vapor in the Orbiter vicinity.

This molecular contamination is accentuated by thruster operation. The dominant neutral species

released by the N_2O_4 /hydrazine attitude control thrusters is H_2O (32% mole fraction), N_2 (31%) and H_2 (17%). These neutrals act to deplete the surrounding plasma by means of recombination reactions. Narcisi et al, reported an order of magnitude decrease in ambient O^+ density when thrusters are fired. In a detailed report summarizing the observed effects of thrusters on the local plasma Murphy et al (Ref. 8) pointed to plasma turbulence, momentary increases in pressure and electron density as well as enhancement of broadband electrostatic noise that were associated with thruster events. Abrupt shifts in spacecraft potential were also noted with the admonition that events were extremely variable and depended on Orbiter orientation as well as the location of the thruster with respect to the sensor.

3. INTERACTIONS RESULTING FROM VEHICLE MOTION

3.1 The Plasma Wake

As can be seen in Table 1, the size and speed of the Orbiter enables it to produce a significant plasma wake. Several investigators have measured ion and electron energies and densities in this wake. Raitt and Siskind (Ref. 9) reported four orders of magnitude decreases in the electron density in the near wake and noted elevated temperatures of $> 4000^{\circ}K$. They had difficulty in getting reliable temperature measurements because of the severe plasma turbulence present near the Orbiter which had not been seen on small spacecraft. Data reduction for the PDP Langmuir Probe is still in a preliminary state, but comparisons with Raitt's data (Ref. 9) from the VCAP investigation has provided a cross calibration point and qualitative agreement

is good. Figure 2 shows the measured electron density as a function of attack angle from the PDP data. An angle of 0° corresponds to ram condition (payload bay pointing into velocity vector) and 180° is wake condition. Since these data have an absolute scale that is uncertain by a factor of 2 to 5, they are primarily noteworthy in that the 4 orders of magnitude depletions are also evident. Measurements made by the PDP on the RMS arm at distances 5 to 10 meters from the payload bay show depletions which are narrower in spatial extent and of only 2 to 3 orders of magnitude. Since maximum ram occurs at approximately sunrise and maximum wake at sunset, the correction for day/night density differences is unnecessary to first order.

Stone et al (Ref. 10) reported differential ion flow measurements made with the PDP while on the RMS. Ion streams up to 40° from the angle of attack and with 10% of the full ram current density were observed. These secondary streams had not been previously observed and are as yet unexplained.

4. VEHICLE CHARGING AND ASSOCIATED ELECTRIC FIELDS

Several experimentors have measured vehicle potential at F2 region altitudes and low inclination orbits. Shawhan and Murphy (Ref. 5) measured the potential of two spherical floating probes with respect to the Orbiter chassis and reported potentials of several volts with no electron gun operation. Murphy et al (Ref. 8) observed a dramatic shift in this vehicle potential accompanied by rapid changes in the electric field when thrusters fire.

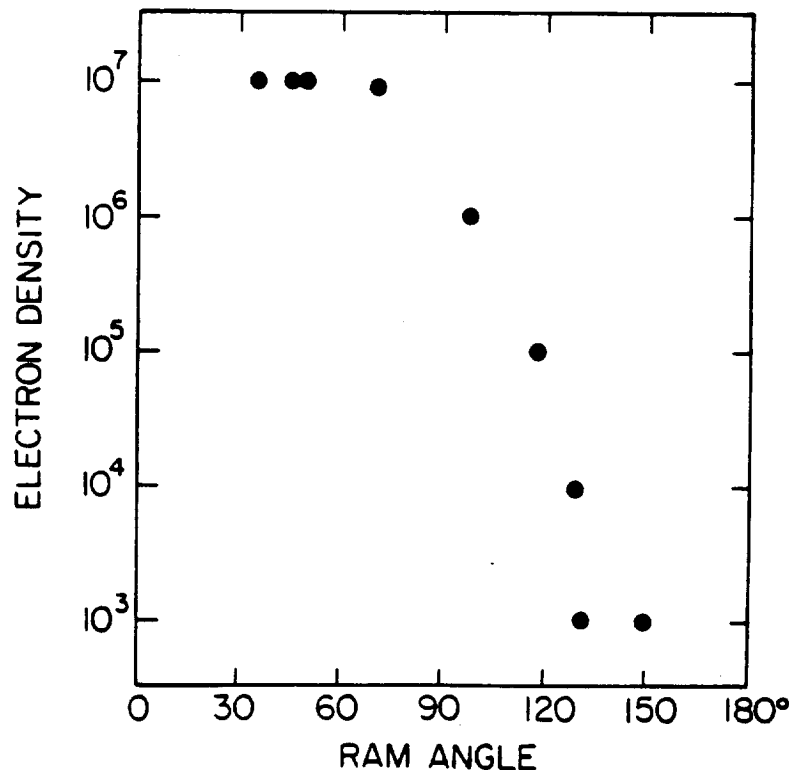


Figure 2.

Both Kaitt and Siskind (Ref. 9) and Shawhan and Murphy (Ref. 5) reported the potentials measured by their plasma probes are consistent with $V \times B \cdot L$ charging effects where L is the distance between the main engine nozzles (the principle exposed conducting surface) and the probes. Any passive charging due to energetic electrons or similar sources appeared to be negligible and was a minor perturbation to the overall $V \times B$ effect.

5. OPTICAL EMISSIONS

One of the surprises of the STS-3, was the discovery by Banks et al (Ref. 11) of the presence of a glow near the ram surface of the vehicle. This glow, which may be due to a chemical reaction near the surface of the vehicle, has a brightness of 10K Rayleighs or greater. The precise brightness depends on the wavelength of the emission. This glow is not entirely unprecedented and has been reported from Atmospheric Explorer (AE) observations at low altitude. Yee and Abreu (Ref. 12) in a detailed study attributed the AE results to an interaction of atomic oxygen with the vehicle surface.

Papadopoulos (Ref. 13) speculated that the shuttle glow was a critical ionization phenomena and proposed a series of measurements to determine if the shuttle behaves like an artificial comet.

PDP observations on STS-3 indicated a surface pressure enhancement on the ram side of the vehicle as great as a factor of 200 over ambient (Ref. 5). These enhanced pressures would be consistent with chemical interaction on or near the vehicle surface since they are 2 to 5 times greater than pressure enhancements in the normal supersonic shock front.

Recent flights of hand-held spectrometers should lead to confirmation of the Yee and Abreu, or Papadopoulos explanation or perhaps to a new theory. The glow seems most pronounced at lower altitudes and Banks et al (Ref. 11) also report that the glow is enhanced during and for a brief period following thruster operations.

6. ELECTROSTATIC NOISE

The most intense emission observed at any frequency by the PDP plasma wave receivers has been called Broadband Orbiter Generated Electro Static (BOGES) noise. The characteristics of this noise as briefly reported by Shawhan and Murphy (Ref. 4) are summarized in Table 3. The Table has been divided into two columns designated "above and "below" the presumed Lower Hybrid Resonance (LHR) frequency. The marked difference in degree of polarization of these electrostatic waves is illustrated in Figure 3. Note the sharp peaks in emissions above LHR at oblique angles to the magnetic field. The lower frequency waves show virtually no polarization. These observations were made while the PDP was being maneuvered on the RMS arm and were well out of the payload bay. At no time did the RMS move the PDP far enough from the Orbiter to see a noticeable decrease in the intensity of this noise. Figure 4 illustrates that BOGES noise is relatively intense anytime the PDP is out of the deep wake and the small variations seen are believed to be local geometry effects not related to the plasma density as measured at the PDP. Note also the data in Figure 4 indicate that high frequencies disappear first and reappear last as the PDP passes through the wake condition. This is generally true for all cases although there is considerable variability from orbit to orbit on the details. For example, if spectrograms like Figure 4 taken 12 hours apart are compared, there are considerable differences in the details of the behavior close to maximum wake. The only difference in these cases is the magnetic field direction at that point in the orbit which infers that the generation or propagation of these waves depends on the magnetic field between the source of the emission and the detector. Another characteristic of this noise is that it is well correlated with $\Delta N/N$ turbulence as measured with the PDP Langmuir Probe. Peak $\Delta N/N$ values of 1-3% are observed when the noise is most intense. This turbulence and associated noise is increased by thruster operations and water dumps.

Waves of a similar nature near and below the LHR frequency have been reported by Koskinen et al (Ref. 14) on the Swedish S29 Barium-GEOS Sounding Rocket.

Table 3

<ol style="list-style-type: none"> 1. Broadband: approximately 30 Hz to 200 kHz with 50 to 70 dB variation over orbit 2. Peak spectral density occurs at 100-300 Hz and is approximately 80 dB $\mu\text{V}/\text{M}/(\text{Hz})^{1/2}$ 3. Well correlated with plasma turbulence as measured by $\Delta N/N$ spectrum 4. Has distinctly different character above and below LHR 	
<u>Below LHR:</u>	<u>Above LHR:</u>
<ul style="list-style-type: none"> - Noise present for virtually whole orbit but modulated by attitude and B-field orientation of orbiter - No evidence of significant polarization - Seems to disappear completely only when PDP is in orbiter wake - Primarily electrostatic 	<ul style="list-style-type: none"> - Evidence of increasing polarization at higher frequencies - Peak intensities occur when E-field sensor axis is 30-45 degrees from B-field alignment - E-field intensity as high as .01 V/m at 100 kHz observed

ELECTROSTATIC NOISE POLARIZATION

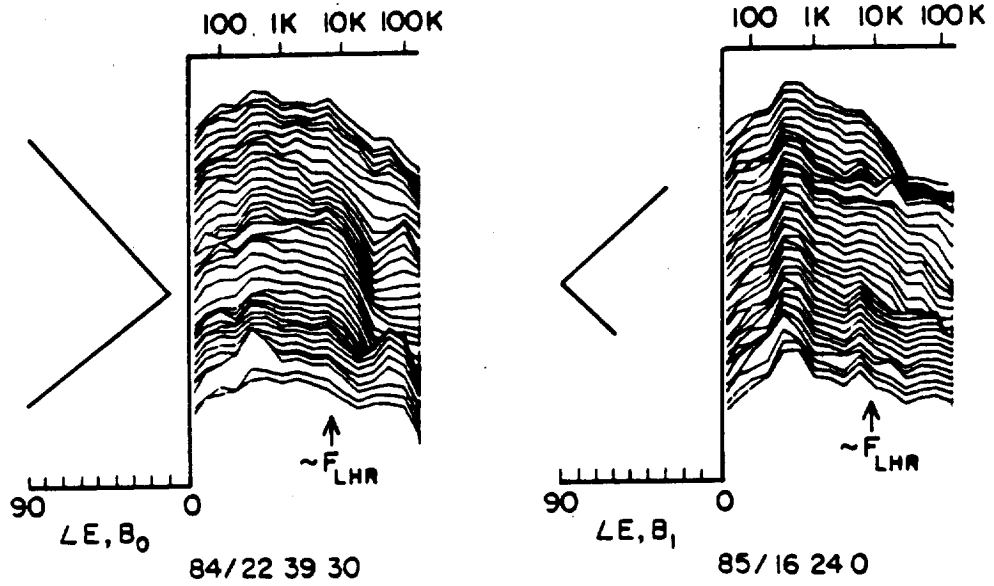


Figure 3

ES NOISE SPECTRUM AS FUNCTION OF TIME

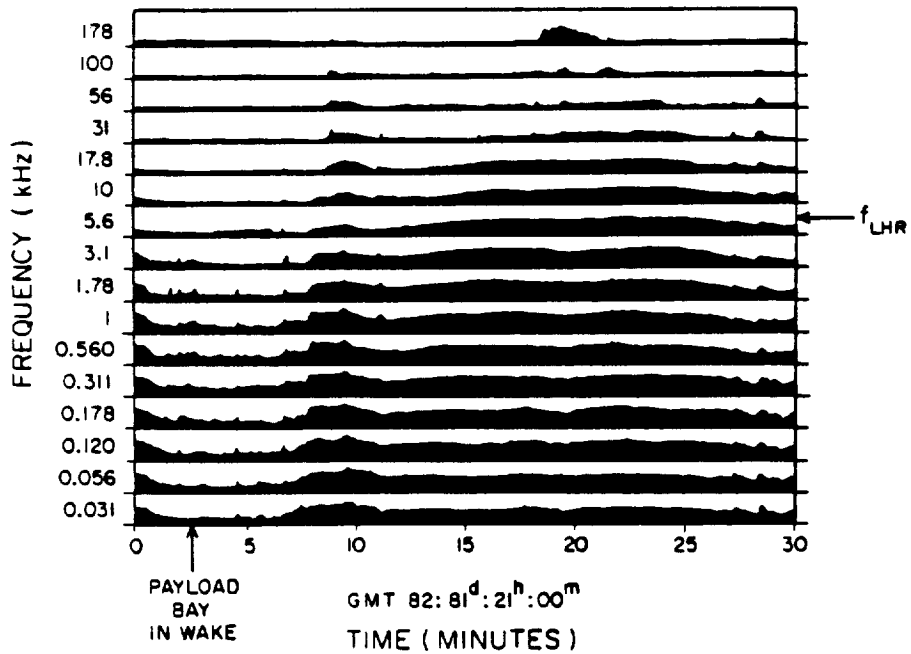


Figure 4

Several explanations are available (Ref. 14) for the phenomenon observed on this and other rocket flights, but they do not adequately explain all characteristics of the BOGES noise observed on the STS Orbiter. Kintner et al (Ref. 15) described ion acoustic noise during a chemical release which they attributed to ion-ion streaming between Cs^+ and ambient ions. Considering the observation of ion streams by Stone (Ref. 10) this may be a candidate for explaining the Shuttle induced noise. It is important to note that neither of these observations have a spectrum quite like the BOGES noise observed on STS-3. Much theoretical work is being done at present dealing with this problem. Papadopoulos (Ref. 16) is working to explain the noise spectrum by a critical ionization velocity phenomena driven by plasma instabilities. Initial agreement looks good and results will soon be published. Parrish et al (Ref. 17) have taken another approach seeking to use strong turbulence theory to produce hydrodynamic or ion acoustic waves. Present observational data may not be sufficient to choose the correct theory but additional experimentation on Spacelab-2 should lead to a better understanding of this phenomena.

7. SUMMARY

The flight of the Shuttle Orbiter through the ionosphere has proved to be an interesting plasma physics experiment. Discovery of the vehicle glow, secondary ion streams, BOGES noise and other associated phenomena are leading to an increased understanding of the F2 ionospheric physics and chemistry. The flights of Spacelab-1 (1983) and Spacelab-2 (1985) carry plasma diagnostics as well as electron and ion guns to stimulate plasma interactions and study Orbiter charging. Further theoretical work on the instabilities creating BOGES noise and the physics of the Orbiter wake will provide further guidance for the experiments on these missions and ultimately for a Space Plasma Lab mission in the 1987 time frame.

8. REFERENCES

1. Stone N H 1981, The aerodynamics of bodies in a rarefied ionized gas with applications to spacecraft environmental dynamics, NASA Technical Paper 1933, November.
2. Samir U et al 1983, The expansion of a plasma into a vacuum--basic phenomena and processes and applications to space plasma physics, submitted to Reviews of Geophysics and Space Physics, NASA MSFC-Space Science Lab Preprint #83-102.
3. Neupert W M 1982, OSS-1 a pathfinder mission for space science on shuttle, 21st Aerospace Science Meeting, AIAA Paper 83-0249.
4. Shawhan S D et al 1983, Measurements of STS-3 electromagnetic interference by the OSS-1 plasma diagnostics package, submitted for publication J. Spacecraft & Rockets, special STS-3/OSS-1 issue.
5. Shawhan S D & Murphy G B 1983, Plasma diagnostics package assessment of the STS-3 orbiter plasma environment, submitted for publication J. Spacecraft & Rockets, special STS-3/OSS-1 issue.
6. Grebowsky J M et al 1983, Measured thermal ion environment of STS-3, Fall 1983 AIAA Meeting on Shuttle Environment, AIAA-83-2597-CP.
7. Narcisi R et al 1983, Gaseous and plasma environment around the space shuttle, Fall 1983 AIAA Meeting on Shuttle Environment AIAA-83-2659-CP.
8. Murphy G B et al 1983, Perturbations to the plasma environment induced by orbiter's maneuvering thrusters, Fall 1983 AIAA Meeting on Shuttle Environment, AIAA 83-2599-CP.
9. Raitt W J et al 1983, Measurements of the thermal plasma environment of the space shuttle, submitted to Planet Space Sci., August 1983.
10. Stone N H et al 1983, Multiple ion streams in the near vicinity of the space shuttle, submitted to Geophys. Res. Lett.
11. Banks P M et al 1983, Observations of optical emissions from STS-3, Geophys. Res. Lett., February 1983.
12. Yee J H & Abreu V J 1982, Contamination observed with the atmospheric explorer satellite, Proc. SPIE.
13. Papadopoulos K & Ko K 1983, Electron energization and optical emissions in the space shuttle, Geophys. Res. Lett., submitted for publication.
14. Koskinen E J et al 1983, An observation of LHR noise with banded structure by the sounding rocket S29 Barium-Geos, J. Geophys. Res., Vol. 88, p. 4131-4136, May 1983.
15. Kintner et al 1980, The observation and production of ion acoustic waves during the trigger experiment, J. Geophys. Res., Vol. 85, #A10 p. 5071-5077, October 1, 1980.
16. Papadopoulos K 1983, Shuttle glow (the plasma alternative), SAI Report 84-147-WA.
17. Parrish J 1983, Private Communication, September 1983.

From: Proceedings of the USAF/NASA Spacecraft Environmental Interactions
Technology Conference, U. S. Air Force Academy, Colorado Springs,
CO, Oct. 4-6, 1983.

SUPRATHERMAL PLASMA OBSERVED ON THE STS-3 MISSION BY THE
PLASMA DIAGNOSTICS PACKAGE*

W. Paterson, L. A. Frank, H. Owens,
J. S. Pickett, and G. B. Murphy
University of Iowa

S. D. Shawhan
NASA Headquarters

INTRODUCTION

Artificially produced electron beams have been used extensively during the past decade as a means of probing the magnetosphere (ref. 1), and more recently as a means of actively controlling spacecraft potential (ref. 2). Experimentation in these areas has proven valuable, yet at times confusing, due to the interaction of the electron beam with the ambient plasma. The OSS-1/STS-3 Mission in March 1982 provided a unique opportunity to study beam-plasma interactions at an altitude of 240 km. On board for this mission was a Fast Pulse Electron Generator (FPEG), which served as part of Utah State University's Vehicle Charging and Potential experiment. Measurements made by the Plasma Diagnostics Package (PDP) while extended on the Orbiter RMS show modifications of the ion and electron energy distributions during electron beam injection.

In this paper, some of the observations made by charged particle detectors are discussed and related to measurements of Orbiter potential. The paper is divided into three sections. A brief description of several of the PDP instruments appears first, followed by a section describing the joint PDP/FPEG experiment. The third section consists of observations made during electron beam injection.

INSTRUMENTATION

The PDP carries a wide range of instruments for the measurement of pressure, waves, fields, and particles. A discussion of these instruments and some of the preliminary results of the mission can be found in Shawhan et al. (ref. 3). Of interest for this discussion are the charged particle detectors, and to a lesser extent, instruments used to measure electric potential and the geomagnetic field in the vicinity of the Orbiter.

The Low Energy Proton and Electron Differential Energy Analyzer (LEPEDEA) is a curved plate detector capable of detecting ions and electrons with energies between 2 eV and 36 keV. It is nearly identical to instruments flown on ISEE-1 and ISEE-2. The energy resolution of LEPEDEA is $\Delta E/E = 0.16$, and 1.6 sec. is required for a complete energy scan. The LEPEDEA fields of view are shown in figure 1. The seven detectors are sampled simultaneously and together have a field of view of 6 degrees by 162 degrees.

*This work is supported by NASA/Lewis Research Grant No. NAG3-449

An electron fluxmeter is also included in the PDP for detection of electrons. This instrument samples the electron flux independent of energy ten times per second. The fluxmeter is directed opposite to the LEPEDEA. It has a wide field of view with low angular resolution.

Electric fields were measured by two 20 cm spherical probes separated by 1.6m. The average potential between these spheres was measured relative to Orbiter ground with a range of ± 8.2 v. When the PDP was extended on the RMS, this potential was a measure of the plasma potential in the vicinity of the PDP.

A triaxial fluxgate magnetometer was used to measure magnetic fields. The magnetometer sampled the magnetic field 10 times each second, along each of its 3 axes with a resolution of ± 12 mgauss.

THE JOINT PDP/FPEG EXPERIMENT

Joint operations between the PDP and the FPEG were conducted while the Orbiter was in a nose-to-sun attitude with a roll rate of twice per orbit (see figure 2). For the experiment discussed in this paper, the FPEG emitted a 50-mA, 1-keV, unmodulated electron beam. A total of eleven emissions occurred under both daytime and nighttime conditions and at various injection pitch angles with each emission approximately fifteen minutes in duration. During these injections, the PDP was deployed on the Orbiter RMS and moved about the Orbiter in an effort to locate the beam.

The primary instrument for location of the beam was an electron fluxmeter located on the opposite side of the PDP from the LEPEDEA. During the search for the beam, the fluxmeter was pointed downward toward the FPEG aperture in the Orbiter bay which left the LEPEDEA looking away from the electron beam. Because of this orientation, the LEPEDEA did not detect primary beam electrons. At times, however, the PDP was rotated through 90 degrees about its spin axis (see figure 1) which allowed the LEPEDEA to view a range of particle pitch angles including primary particles.

OBSERVATIONS

Because of changing Orbiter attitude (twice per orbit roll rate) and variations in the geomagnetic field over the course of an orbit, a wide range of injection pitch angles were observed. Calculations by J. Sojka of Utah State University show that for injection pitch angles greater than about 60 degrees (depending on the precise beam-orbiter orientation), the beam intercepted the Orbiter surface. At angles less than this the beam escaped. Qualitative analysis of charged particle and potential measurements made by the PDP support this analysis.

Ambient electrons (photoelectrons) were detected with energies up to about 80 eV during the day and 10 eV at night, while ions were seen at energies principally below 10 eV during both day and night. During beam injection at angles less than 30 degrees, intense fluxes of electrons were detected at energies up to the primary beam energy of 1 keV. Virtually no ions were seen at these times. Enhanced electron fluxes were observed at all points accessible to the PDP. However, due to the limited reach of the RMS, no measurements were made at distances greater

than 7m from the beam. For beam injection, at angles greater than 60 degrees, the measured ion and electron fluxes often resembled the flux seen with the beam off.

Measurements of Orbiter potential during small angle injection also differed from the ambient case. When the beam was off, the Orbiter potential relative to the nearby plasma remained $< \pm 8.2\text{v}$ consistent with $V \times B \cdot L$ (ref. 3). When the beam was injected at less than 30 degrees, the potential was offscale and positive, and dropped below the maximum measurable value of 8.2v only at the maximum distance from the beam of 7m. Potentials during large angle injections were generally nearer to those measured with the beam off.

The observations tend to support the claim that the beam did escape from the near vicinity of the Orbiter for small angle injection, but did not at larger angles. The enhanced electron flux and elevated potential associated with small angle injection may be due to escape of the beam. If this is so, the large angle conditions which were so similar to ambient conditions could be due to the electron beam impacting the Orbiter rather than escaping. In this case, almost all of the beam current is collected so that the disturbance is localized and the Orbiter does not need to charge.

Figure 3 shows the measured flux during one of these rotations which took place at a distance of 7m from the center of the beam. Since this distance is roughly twice the gyroradius of a 1 keV electron travelling perpendicular to the magnetic field, these measurements must be of electrons outside of the primary beam. The angles shown in figure 3 are the pitch angles of electrons as they were detected by the LEPEDA. Angles greater than 90 degrees correspond to electrons travelling down the field lines from the direction in which the beam was injected. Angles less than 90 degrees indicate electrons moving up the field in the same direction as the outgoing beam. Although pitch angles less than 30 degrees and greater than 140 degrees were not sampled, this figure seems to show a net return of electrons along the field lines from the direction in which the beam was injected indicating that more current returns from the upper hemisphere during upwards injection than from the lower.

Based on this preliminary analysis of measurements made during electron beam emission, it appears that the electron beam did escape from the Orbiter. These escapes induced positive Orbiter potentials, and were associated with enhanced fluxes of electrons. During escape of the beam, there is evidence that there was a net flow of electrons along the magnetic field from the direction in which the beam was injected.

REFERENCES

1. Winckler, J. R.: The Applications of Artificial Electron Beams to Magnetospheric Research. Rev. Geophys. Space Phys., 18, 659, 1980.
2. Pedersen, A.: Plasma Diagnostics by Electron Guns and Electric Field Probes on ISEE-1. Artificial Particle Beams in Space Plasma Studies, (B. Grandal, ed.), Plenum Press, New York.
3. Shawhan, S. D.; Murphy, G. B.; and Pickett, J. S.: Plasma Diagnostics Package Initial Assessment of the Shuttle Orbiter Plasma Environment. Accepted J. of Spacecraft and Rockets, 1983.

LEPEDEA FIELDS-OF-VIEW

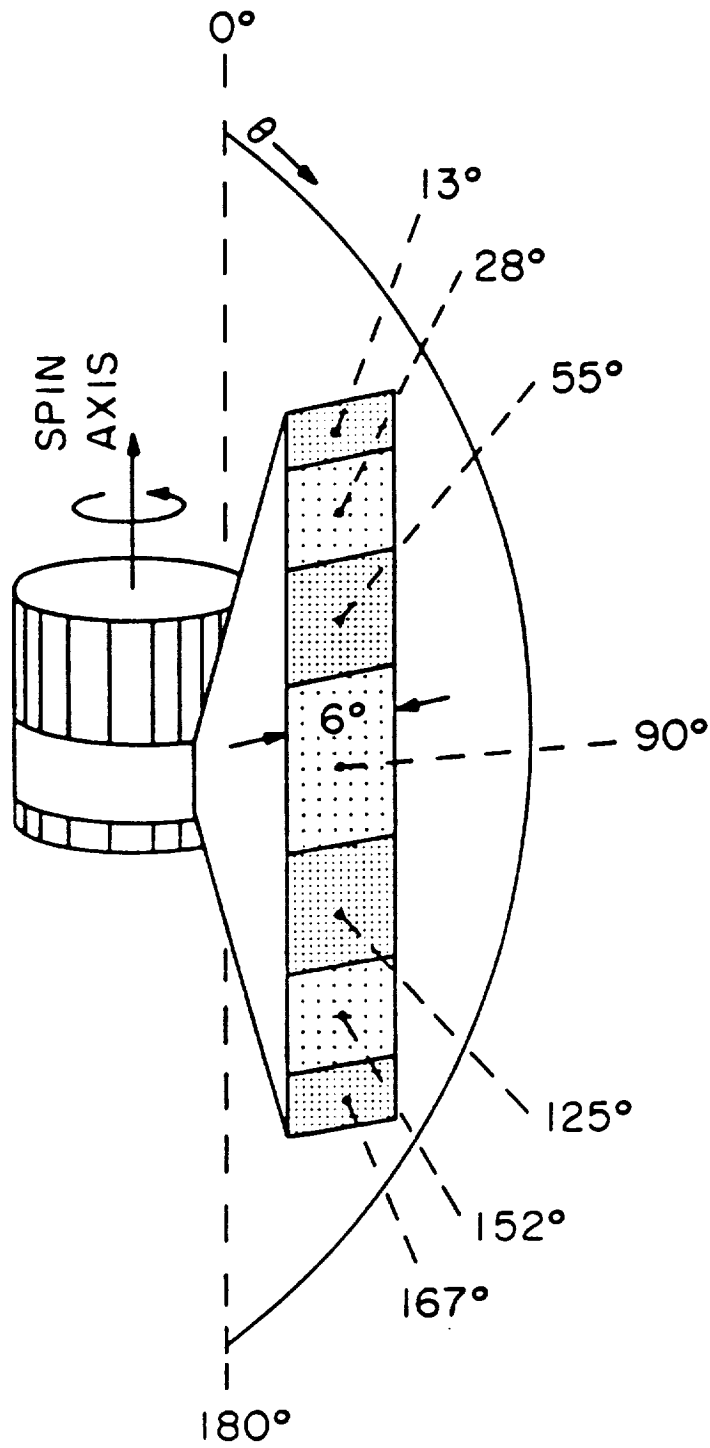
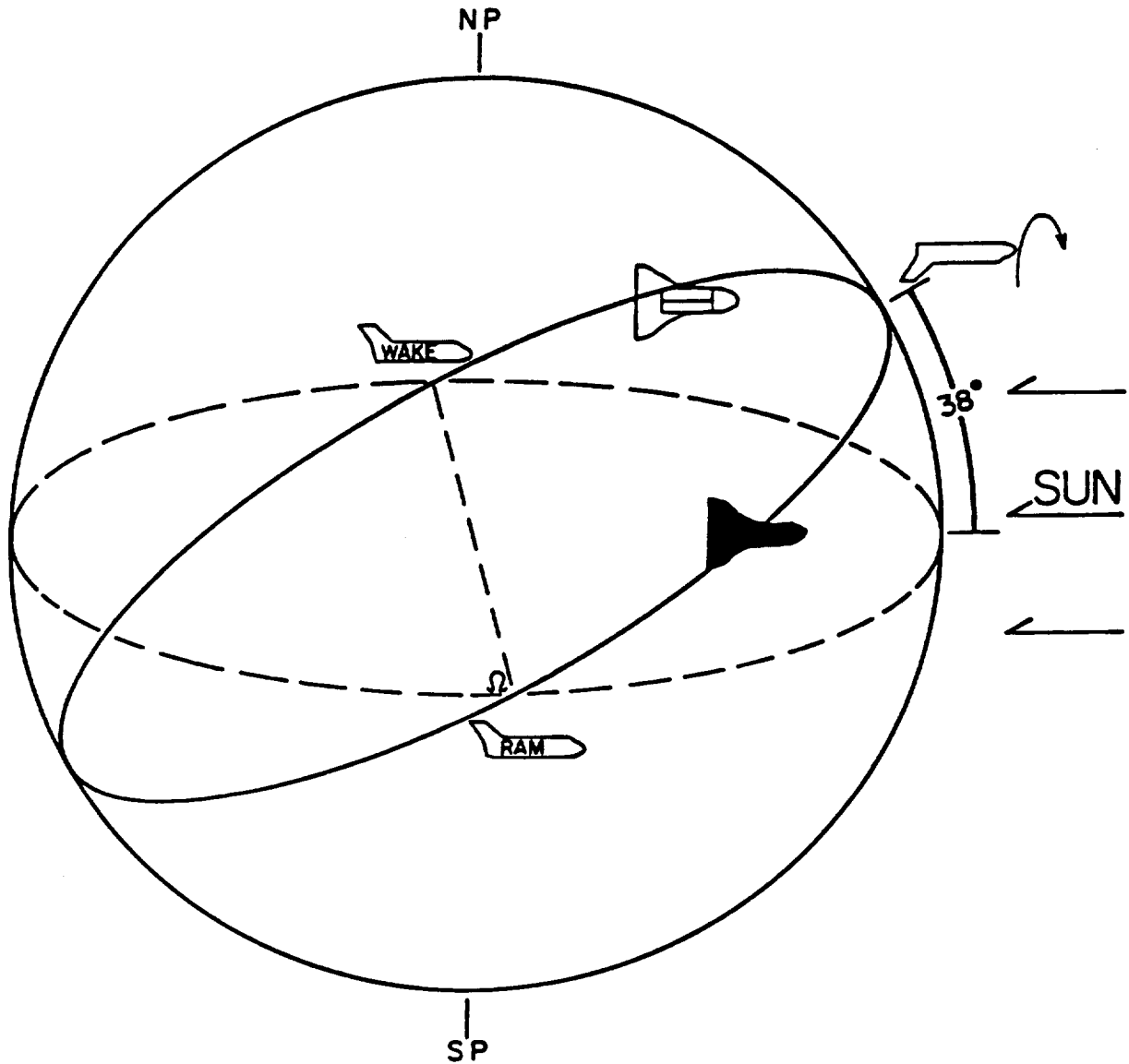


Figure 1

STS-3 ORBIT ATTITUDE
MARCH 24, 1982



NOSE TO SUN 2x ORB RATE ROLL

Figure 2

Electron flux 7m from the beam ($2 \text{ eV} < E < 36 \text{ keV}$).

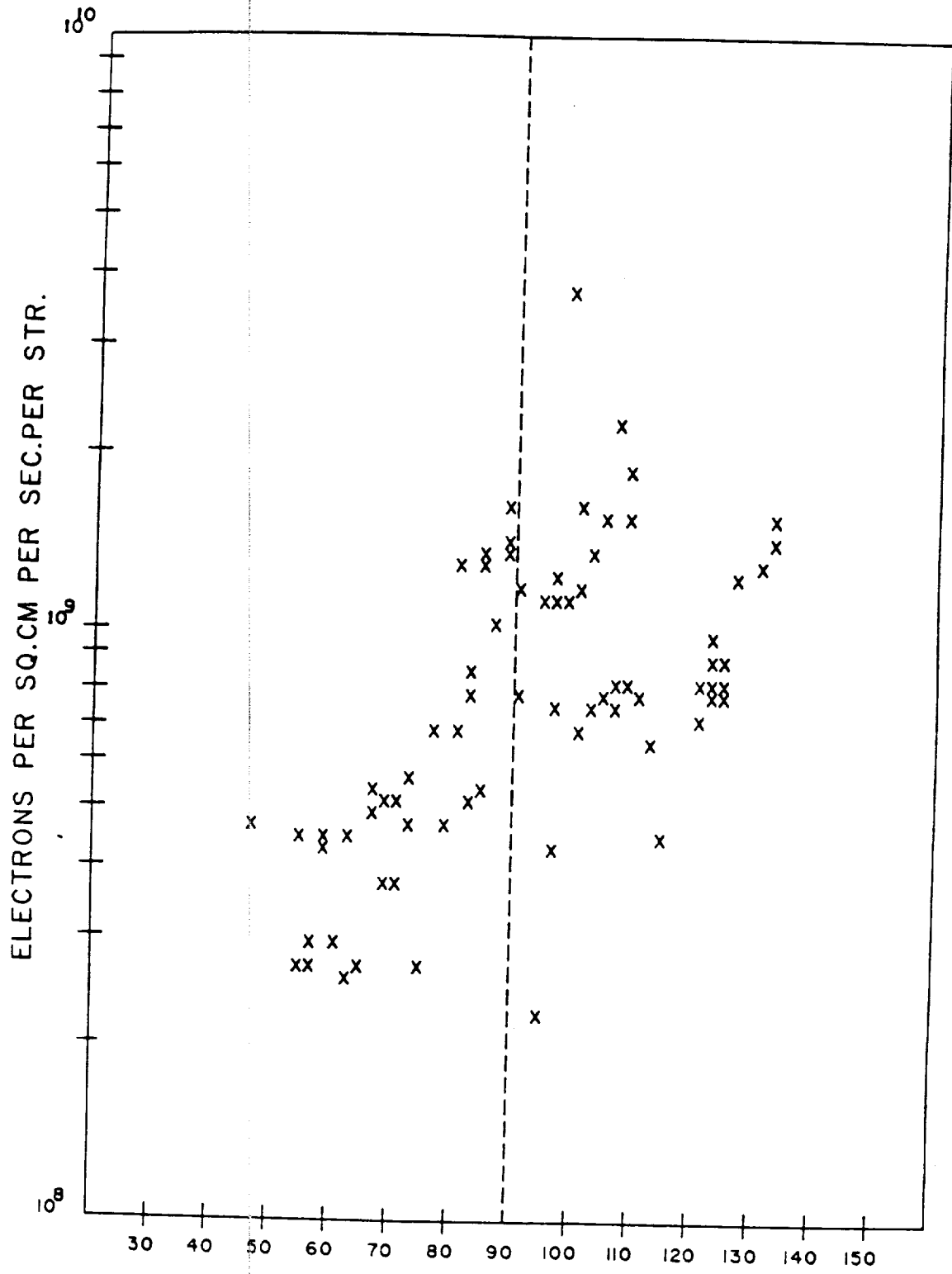


Figure 3

From: Proceedings of the USAF/NASA Spacecraft Environmental Interactions
Technology Conference, U. S. Air Force Academy, Colorado Springs,
CO, Oct. 4-6, 1983.

ELECTRON AND ION DENSITY DEPLETIONS MEASURED IN THE STS-3 ORBITER WAKE*

G. B. Murphy and J. S. Pickett
University of Iowa

W. S. Raitt
Utah State University

S. D. Shawhan
NASA Headquarters

INTRODUCTION

The third Space Shuttle flight on Columbia carried instrumentation to measure thermal plasma density and temperature. Two separate investigations, the Plasma Diagnostics Package (PDP) and the Vehicle Charging and Potential Experiment (VCAP), carried a Langmuir Probe, and the VCAP also included a Spherical Retarding Potential Analyzer (SRPA). The Langmuir Probe on the PDP made measurements while the PDP was attached to the pallet in the Orbiter bay and while the PDP was articulated by the RMS. Only those measurements made while the PDP is in the payload bay are discussed here since the VCAP instrumentation remains in the payload bay at all times and the two measurements are compared.

Figure 1 illustrates the location of the PDP and VCAP instrumentation on the science payload pallet.

The principle thrust of this paper is to discuss the wake behind a large structure (in this case the Space Shuttle Orbiter) flying through the ionospheric plasma. Much theoretical work has been done regarding plasma wakes (ref. 1) and to a certain extent laboratory plasmas have provided an experimental and measurement basis set for this theory. The instrumentation on this mission gives the first data taken with a large vehicle in the ionospheric laboratory.

First, the PDP Langmuir Probe and its data set will be presented, then the VCAP Langmuir Probe and SRPA with associated data. A discussion of agreement between the two data sets is then followed by some other PDP data which infers an even lower wake density.

Lastly, conclusions, caveats and a description of future work which will further advance the measurement techniques and data set are put forth.

PDP LANGMUIR PROBE RESULTS

The PDP Langmuir Probe is a 6 cm diameter gold-plated sphere which is operated in two modes, the $\Delta N/N$ mode and the swept mode. The swept mode which is of concern

*This work is supported by NASA/Lewis Research Grant No. NAG3-449

The science pallet configuration on STS-3 showing the location of the instrumentation in question.

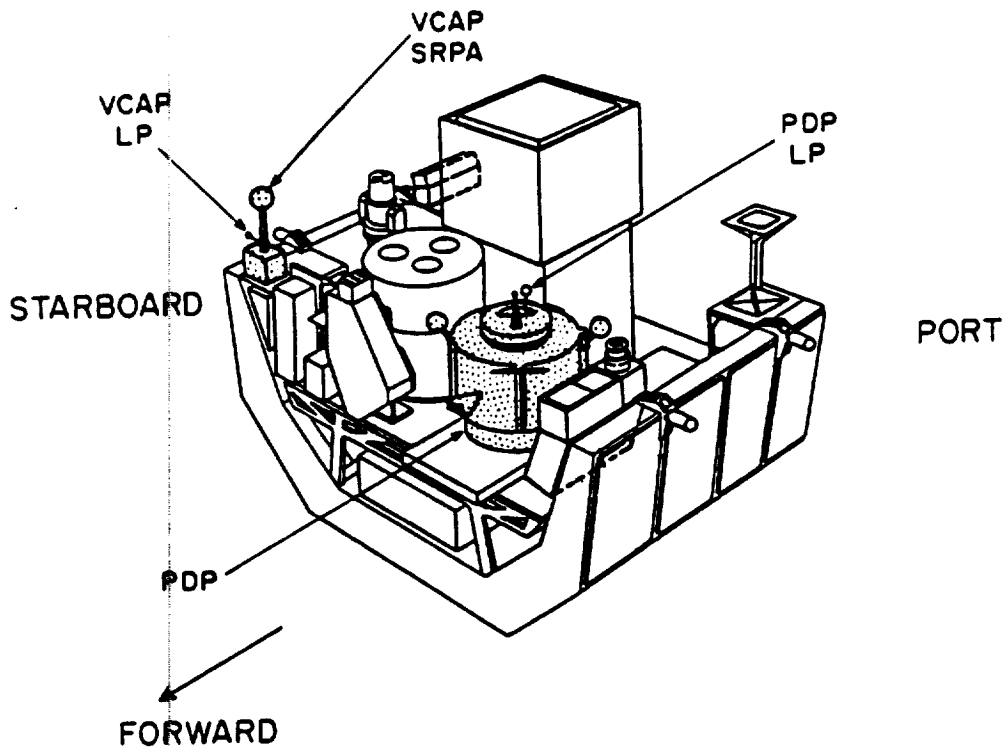


Figure 1

here is a 120 step voltage sweep which lasts 1.2 seconds and is executed 5 times per minute. The nominal density range of the probe is approximately 5×10^2 to $5 \times 10^6/\text{cm}^3$, the precise sensitivity depending on temperature. Operating in this mode, the Langmuir Probe has a current voltage characteristic whose slope is proportional to $1/T_e$ and which has a "knee" in the curve proportional to N_e .

There are two limitations to the PDP Langmuir Probe measurements. The first occurs when the plasma is too dense to really see the entire knee of the curve resulting in instrument saturation and an underestimate of density. The second occurs when the plasma temperature is too high and density too low to get a reliable slope resulting in only an upper bound on density and lower bound on temperature.

Figure 2 illustrates the electron density and temperature for one orbit as a function of vehicle attitude. (The data is repeated for a second orbit to provide clarity for the graph and illustrate a periodicity which is real). The vehicle attitude is described by θ_1 and θ_2 which are illustrated at the top of the figure. Maximum wake occurs when the vehicle flies tail first with the plasma ramming into the Orbiter belly (e.g. GMT 83:20:48). At this point in time, the vehicle is flying a nose-to-sun attitude with a 2 times orbit roll. (See figure 2 in the paper "Suprathermal Plasma Observed on the STS-3 Mission by the Plasma Diagnostics

Package, by Paterson et al. (ref. 2) in this issue for a description of this attitude.) This results in a once per orbit ram/wake cycle which is evident in figure 2 by the e^- density and neutral density (pressure) measurements.

Several important observations summarize figure 2:

1. Although density is near ambient while the payload bay is neither pointing directly into the velocity vector or into the wake, there is evidence that the density may be 2 to 10 times ambient when the bay points close to the velocity vector. The probe saturates making reliable measurement above 2×10^6 difficult. The region cross hatched in figure 2 is where this higher density regime is encountered.
2. Density decreases rapidly as the Orbiter rolls into wake condition.
3. The minimum reliable measurement of density with the PDP probe is approximately $5 \times 10^2 / \text{cm}^3$. At least another order of magnitude decrease is required to pull the sweep totally offscale which is subsequently observed to happen. The sweep remains offscale for approximately 25 minutes centered around 83:20:48.
4. During all non-wake conditions, the temperature remains relatively constant at about $1000^\circ (\pm 30\%)$.
5. Temperature rises rapidly as density decreases.
6. The highest reliable temperatures occur at 6000°K . However, the trend continues suggesting temperatures in excess of 7000°K in the deep wake.

It is also worthwhile to note that in near ram condition the neutral density (pressure) was almost two orders of magnitude above ambient ionospheric conditions and fell below 10^{-7} torr (the instrument sensitivity limit) during wake conditions.

THE VCAP LANGMUIR PROBE AND SRPA

Data on the characteristics of the ambient thermal plasma are extracted from the probes using a technique similar to that described by Raitt et al. (ref. 3). This AC technique employed for the probes enables direct measurement of the second derivative of the SRPA current-voltage characteristic and the first derivative of the LP current-voltage characteristic.

The SRPA signal is obtained by adding two sinusoidal AC signals (at 8.5 kHz and 10.7 kHz) to a sawtooth sweep voltage. The probe current is passed through a narrow band amplifier that selects the difference frequency of 2.2 kHz, which is a measure of the non-linearity of the probe current-voltage characteristic, and results in a signal proportional to the second derivative of the current-voltage characteristic. Two ac current ranges are available: one from -76 dB to -24 dB and the other from -40 dB to 0 dB relative to 10^{-7} amp rms. Each successive sweep of the probe alternates between the two ranges. Since the sweep period is 17 seconds the complete dynamic range is covered each 34 seconds.

Summary of PDP Langmuir Probe electron density and temperature as function of vehicle attitude. Neutral pressure measurements are included for reference. The cross-hatched areas are where the probe sweep saturates and the routine used to calculate N_e under-estimates density by as much as an order of magnitude.

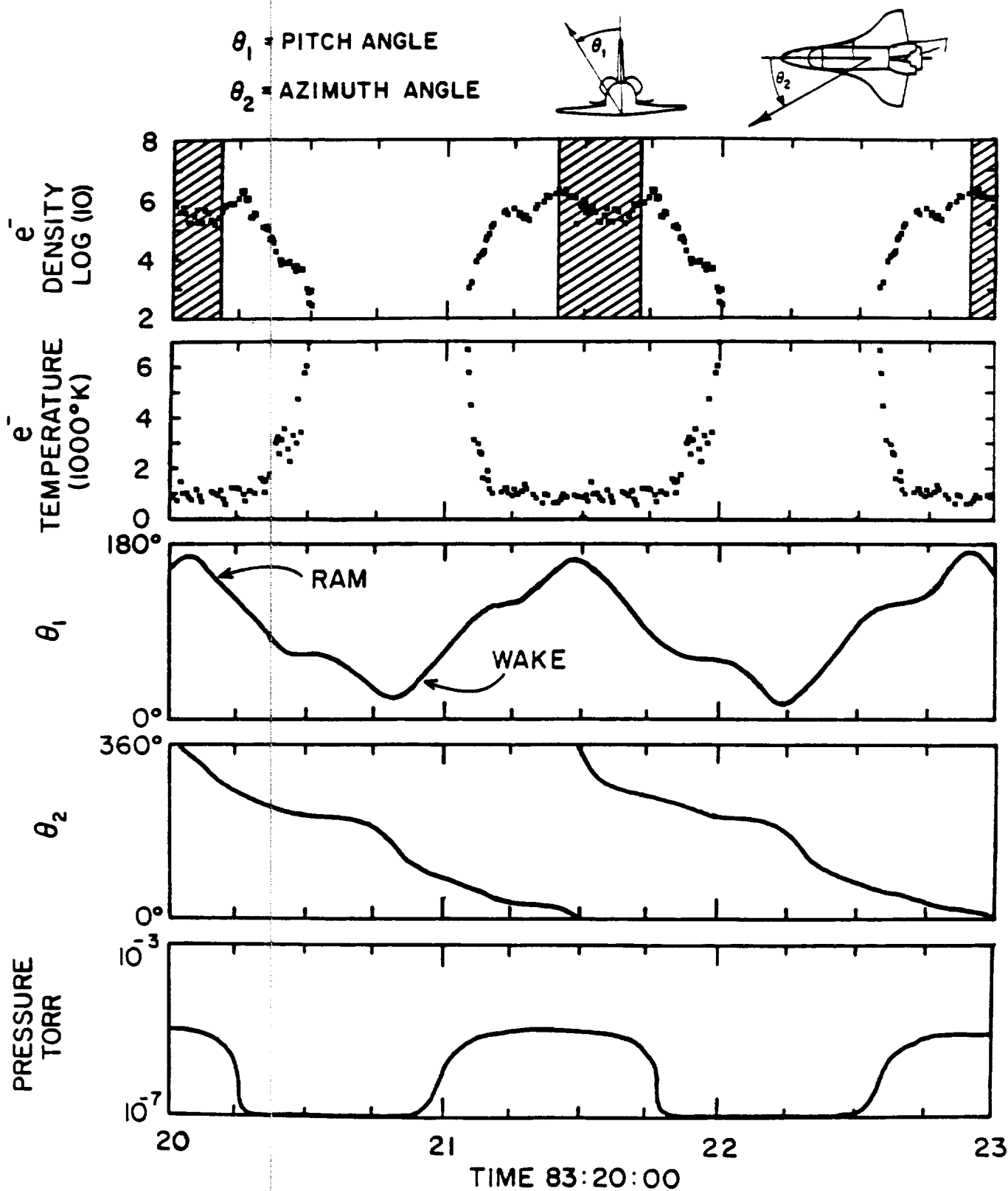


Figure 2

The LP has only one AC signal (at 3.2 kHz) added to the sweep voltage. The amplitude of the alternating component of the probe current derived by using a narrow band amplifier tuned to 3.2 kHz enables the first derivative of the current voltage characteristic to be measured directly. A single dynamic current range, from -80 dB to +10 dB relative to 10^{-6} amp rms, is used for all sweeps. The range of the sawtooth voltage is from -2 V to +3 V, the period and phase of the sweep being synchronized to the SRPA sweep.

Figure 3 illustrates data taken under similar conditions as that taken by the PDP, although at a different time. In this case the vehicle attitude is different, but the same angles are used to characterize the direction of the velocity vector. The addition of the dark bar on this figure serves to show when day and night occur during the orbit.

The results of the Langmuir Probe (dotted line) and SRPA (solid line) generally confirm results of the PDP Langmuir Probe. VCAP Langmuir Probe temperatures are not plotted, but the following results are notable:

1. Close to ambient (1000°K) ionospheric temperatures are measured during non-wake condition.
2. As the Orbiter rolls into wake, a turbulence at all frequencies adds noise to the 3.2 kHz LP first derivative, but measurements indicate an increase in temperature to beyond 4000°K .

VCAP LP densities indicate the following:

1. An upper bound of electron density when the payload bay faces close to the velocity vector is $10^7/\text{cm}^3$.
2. Density during wake conditions drops to below the instrument sensitivity of $10^4 \text{ e}/\text{cm}^3$.

The SRPA measurements are difficult to interpret since the peak in the second derivative as a function of sweep voltage for the dominant ionospheric O^+ ion is often contaminated by locally produced H_2O^+ and NO^+ . When the O^+ peak is clearly observable, several observations prevail:

1. Densities consistent with ambient ionospheric O^+ are observed for most conditions which shall be referred to as non-wake.
2. > 2 orders of magnitude depletion occurs in the near wake.

ADDITIONAL EVIDENCE FOR LARGE DEPLETION

Additional evidence for a many order of magnitude depletion in the electron density in the near wake is provided by what amounts to a sounder experiment. Recall that the VCAP SRPA is excited with a signal at 8.5 and 10.7 kHz. The PDP contains a 16 channel ($\pm 15\%$ bandwidth) spectrum analyzer capable of detecting electrostatic or electromagnetic waves over a frequency range from 30 Hz to 178 kHz. The instrument has a saturation of approximately 1 V/m electric field amplitude and a usable dynamic range of about 95 dB.

Summary of VCAP Langmuir Probe (dotted line) and SRPA (solid line) results as a function of vehicle attitude.

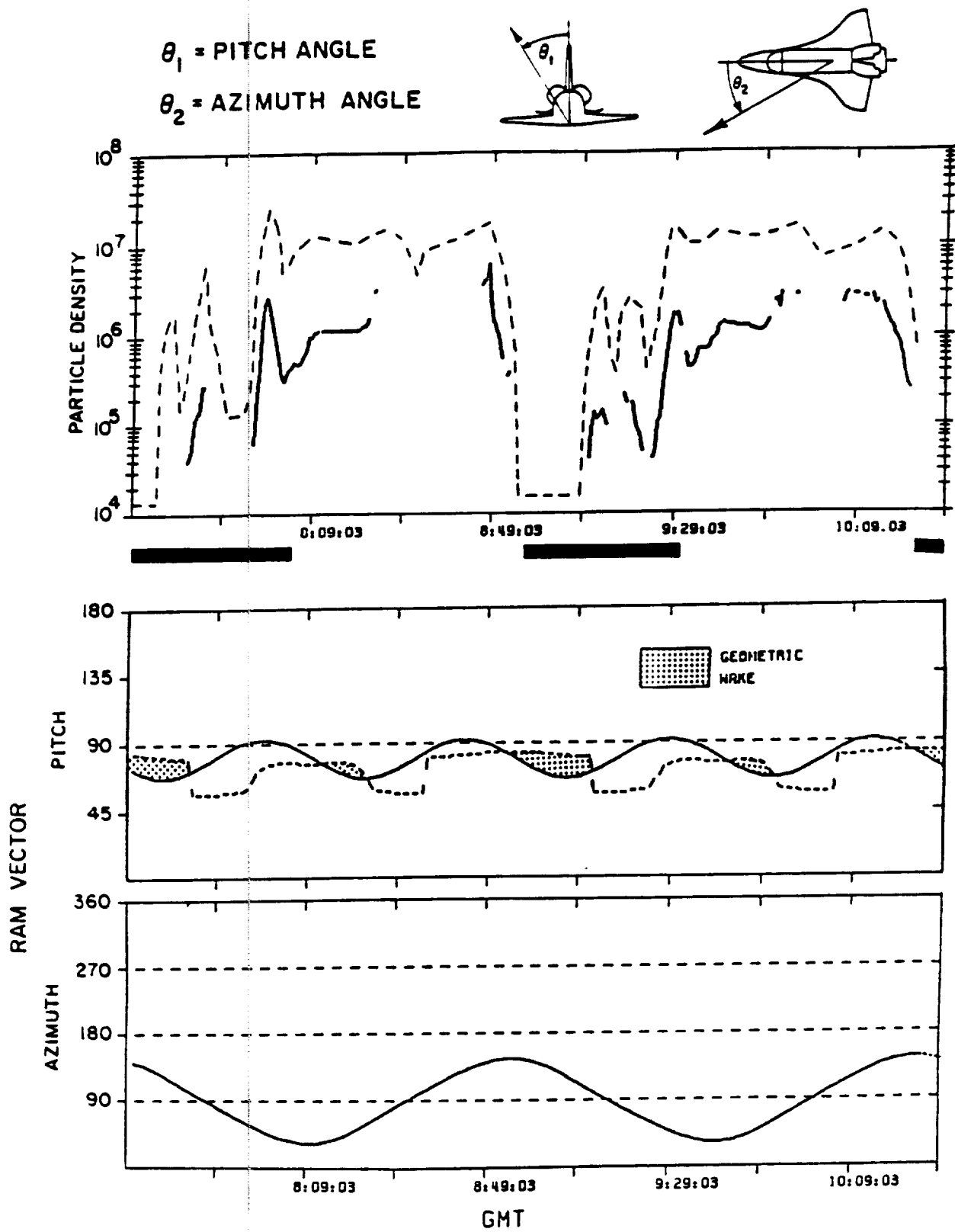


Figure 3

During most of the orbit, the Spectrum Analyzer output is dominated by broad-band orbiter generated electrostatic noise, (ref. 4) thruster firings or other events. Figure 4 illustrates that as the wake boundary is approached, the electrostatic noise disappears in all channels simultaneously and as the payload bay is immersed deeper in the orbiter's wake a signal in the 10 kHz channel grows to a point of dominance in the spectrum. This in fact is the VCAP SRPA signal. As the density drops so that the plasma frequency nears or drops below 10.7 kHz, this signal can propagate to the PDP sensor. Detailed calculations and modeling are being done taking field strengths and sensor separation into account, but preliminary work suggests that although the PDP Langmuir Probe infers densities, $< 50/\text{cm}^3$, the density probably drops at least another order of magnitude to $< 5/\text{cm}^3$. This would be approximately six orders of magnitude of plasma depletion in the near wake from that measured under ram condition.

The VLF electric field spectrum showing the increasing intensity of the received SRPA signal.

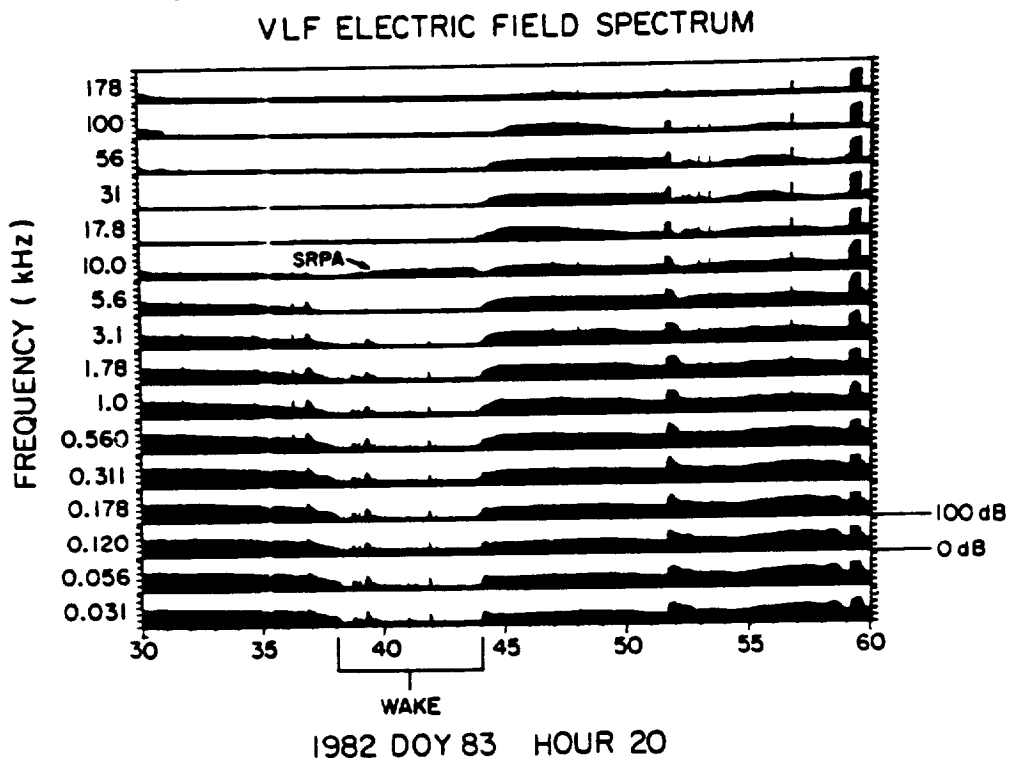


Figure 4

SUMMARY

Although measurements are still in a primitive state, several conclusions can be drawn from the STS-3 PDP and VCAP data.

1. Ram conditions seem to result in a higher than expected electron density.

2. Density depletions of at least 4 orders of magnitude in the wake plasma are observed and there is evidence to suggest this depletion may be as high as six orders of magnitude.
3. Effective temperature measured by the thermal plasma probes indicate an increase in electron temperature in the wake to $> 6000^{\circ}\text{K}$.
4. The thermal ions are excluded rapidly as the orbiter bay rolls into wake and only those locally produced H_2O^+ and NO^+ are measurable.
5. Both LP's and the SRPA indicate a degree of plasma density or velocity turbulence which peaks in the transition region between ram and wake.

Several concerns about these measurements are that: first, the VCAP probes' outputs are often contaminated by the turbulence which causes bias in the data; second, the ability of the PDP LP to measure density and temperature reliably beyond a certain limited range is questionable; and third, whether the sounder experiment setup between the VCAP SRPA and PDP Spectrum Analyzer is "calibratable" is still an open question.

The first concern is being worked and there is confidence that corrections for the turbulence can be computed. Recall that the PDP LP has a $\Delta N/N$ mode which can provide upper bounds on the turbulence within a given frequency band.

The second concern, which applies to a lesser degree to the VCAP LP, is harder to solve. As the density decreases and temperature increases, the size of the probe in relation to a debye length and thermal electron gyroradius changes drastically. This means that approximations used to derive temperature and density are no longer valid and new formulations must be used. A long-term research effort is underway to better understand the behavior of swept probes in these extreme regimes. (See ref. 5 for a description of the probe theory). Meanwhile, effort has been made to include data in this report derived from regimes where approximations hold. Thus, the densities and temperatures are probably good to a factor of two.

It is encouraging to note that when comparisons are made to measurements made by the DE satellite, which flew through the same altitude and latitude regime within the same day, general agreement is found. The DE data show dayside conditions of $N_e = .9 - 1.1 \times 10^6/\text{cm}^3$ and $T_e = 1500^{\circ} - 2000^{\circ}$ while the PDP and VCAP data taken dayside out of wake and also out of maximum ram condition indicate $N_e = 2$ to $10 \times 10^6/\text{cm}^3$ and $T_e = 1000^{\circ} (\pm 30\%)$.

The third concern is currently being worked and if the "sounder" is calibratable, it should provide valuable input for theory.

The fact that elevated temperatures are observed in the near wake of a spacecraft is not without precedence. Samir et al. (ref. 6) found evidence for elevated electron temperatures in the wake of Explorer 31, a much smaller vehicle than the Shuttle Orbiter.

Additional measurements by the PDP and VCAP instruments will be made on Spacelab-2 where detailed experiments have been designed to study the structure of the wake out to approximately one kilometer from the vehicle.

REFERENCES

1. Samir, U.; Wright, K. H., Jr.; and Stone, N. H.: The Expansion of a Plasma into a Vacuum--Basic Phenomena and Processes and Applications to Space Plasma Physics. Submitted to Reviews of Geophysics and Space Physics Space Science Laboratory, MSFC, Preprint #83-102.
2. Paterson, W.; Frank, L. A.; Owens, H.; Pickett, J. S.; Murphy, G. B.; and Shawhan, S. D.: Suprathermal Plasma Observed on the STS-3 Mission by the Plasma Diagnostics Package. Submitted to Proceedings of the Spacecraft Environmental Interactions Conference, October 4-6, 1983.
3. Raitt, W. J.; Dorling, E. B.; Sheather, P. H.; and Blades, J.: Ionospheric Measurements from the ESRO-4 Satellite. Planet Space Sci., 23, 1085-1101, 1975.
4. Shawhan, S. D.; Murphy, G. B.; and Pickett, J. S.: Plasma Diagnostics Package Initial Assessment of the Shuttle Orbiter Plasma Environment. Accepted for publication, December 1983, J. Spacecraft and Rockets.
5. Rubinstein, J. and Laframboise, J. G.: Theory of a Spherical Probe in a Collisionless Magnetoplasma. Phys. Fluids 25 (7), July 1982, 1174-1182.
6. Samir, U. and Wrenn, G. L.: Experimental Evidence of an Electron Temperature Enhancement in the Wake of an Ionospheric Satellite. Planet. Space Sci., 1972, Vol. 20, 889-904.



Effects of Chemical Releases by the STS 3 Orbiter on the Ionosphere

JOLENE S. PICKETT, GERALD B. MURPHY, WILLIAM S. KURTH,
AND CHRISTOPH K. GOERTZ

Department of Physics and Astronomy, University of Iowa, Iowa City

STANLEY D. SHAWHAN

NASA Headquarters, Washington, D. C.

The Plasma Diagnostics Package, which was flown aboard STS 3 as part of the Office of Space Science first shuttle payload (OSS 1), recorded the effects of various chemical releases from the orbiter. Changes in the plasma environment were observed to occur during flash evaporator system releases, water dumps, and maneuvering thruster operations. During flash evaporator operations, broadband orbiter-generated electrostatic noise was enhanced, and plasma density irregularities ($\Delta N/N$) were observed to increase by 3-30 times with a spectrum which rose steeply and peaked below 6 Hz. Ions with energies up to several hundred eV were also observed during one flash evaporator operation. In the case of water dumps, background electrostatic noise was enhanced at frequencies below about 3 kHz and suppressed at frequencies above 3 kHz during the dump, and $\Delta N/N$ was also seen to increase by 5-6 times. Various changes in the plasma environment were effected by primary and vernier thruster operations, including increases in electron density by as much as 3 orders of magnitude, neutral pressure increases to as high as 10^{-4} torr from the nominal 10^{-7} torr, and perturbations in the spacecraft potential by several volts, particularly when measured in relation to the plasma potential in the wake. Thruster activity also stimulated electrostatic noise with a spectrum which peaked at approximately 0.5 kHz. In addition, ions with energies up to 1 keV were seen during some thruster events.

1. INTRODUCTION

Since the first space shuttle launch, in April of 1981, considerable interest has been generated in ionospheric modifications effected by the shuttle, both during launch and during orbital operations. The effects of rocket exhaust on the ionosphere have been studied and recorded in considerable detail since Booker [1961] first reported a local diminution in ionization density forming a hole through the *F* region associated with the firing of Vanguard II in 1959. A review of the findings to date, particularly with regard to large space systems, was given by Rote [1980] and included such environmental effects as plasma depletion, temperature change, and airglow excitation. A brief history of rocket-induced perturbations upon the upper atmosphere was also given by Mendillo [1980]. In addition, he described a method for assessing how the space shuttle's engines would affect the ionosphere in the vicinity of the engine burns. A review of the effects on the ionosphere due to the deliberate release of known quantities of highly reactive chemicals such as H_2O and CO_2 was given by Pongratz [1981]. The environmental impact on the *D* and *E* regions of the ionosphere of chronic discharges of water vapor from large rockets was investigated by Forbes [1980]. While most of the previously mentioned papers deal with large-scale chemical releases, whether planned releases for scientific study or whether released as a result of rocket transit through the ionosphere, shuttle-produced chemical releases, although much smaller by comparison, do perturb the environment near the shuttle. These perturbations tend to be more localized than the large-scale releases; however, they do affect the ambient ionosphere and therefore help us understand the effects of larger releases. On the other hand, it is important to understand the distinction between these two types of releases.

The foregoing discussion of large-scale releases provides the impetus and background for studying the smaller shuttle-produced releases.

The purpose of this paper is to present observational evidence of ionospheric modification by using data taken by the Plasma Diagnostics Package (PDP) [Neupert *et al.*, 1982] during Space Shuttle orbiter chemical releases. The space shuttle is an ideal vehicle for experiments involving ionospheric modification. Not only does it initiate chemical releases, but it also provides the platform from which to monitor the effect of those releases. While not intended to be scientific ventures, the orbiter water dumps, flash evaporator system (FES) releases and thruster operations are, in effect, chemical releases. It is to be understood that the study of these effects is limited to the near vicinity of the orbiter and indeed to the gaseous and plasma envelope of the shuttle itself. However, the measurements of the effects should not be ignored simply because they cannot tell us what the end result of the release will be. The first few seconds of any release are very important in that many of the critical chemical reactions and kinetic effects happen during that time. By being in the bay of the shuttle near the point of release, the first few seconds of these releases can be studied in detail giving us a clue to the early chemistry that takes place in larger releases. An underlying theme of this paper is that orbiter operations produce effects which are measurable by a wide range of instruments. Hence, it is obvious that a potential shuttle experimenter should be aware of the nonambient nature of the ionosphere in close proximity to his or her detectors.

An outline of the paper is as follows: Section 2 contains STS 3 mission and operational considerations, including an overview of orbit and ionospheric characteristics, shuttle operations, and PDP instrumentation. The observations of the effects of flash evaporator system releases, water dumps, and thruster operations are presented in Section 3. Finally, some concluding remarks and possible explanations for the physical processes involved are offered in Section 4.

Copyright 1985 by the American Geophysical Union.

Paper number 4A1380.
0148-0227/85/004A-1380\$05.00

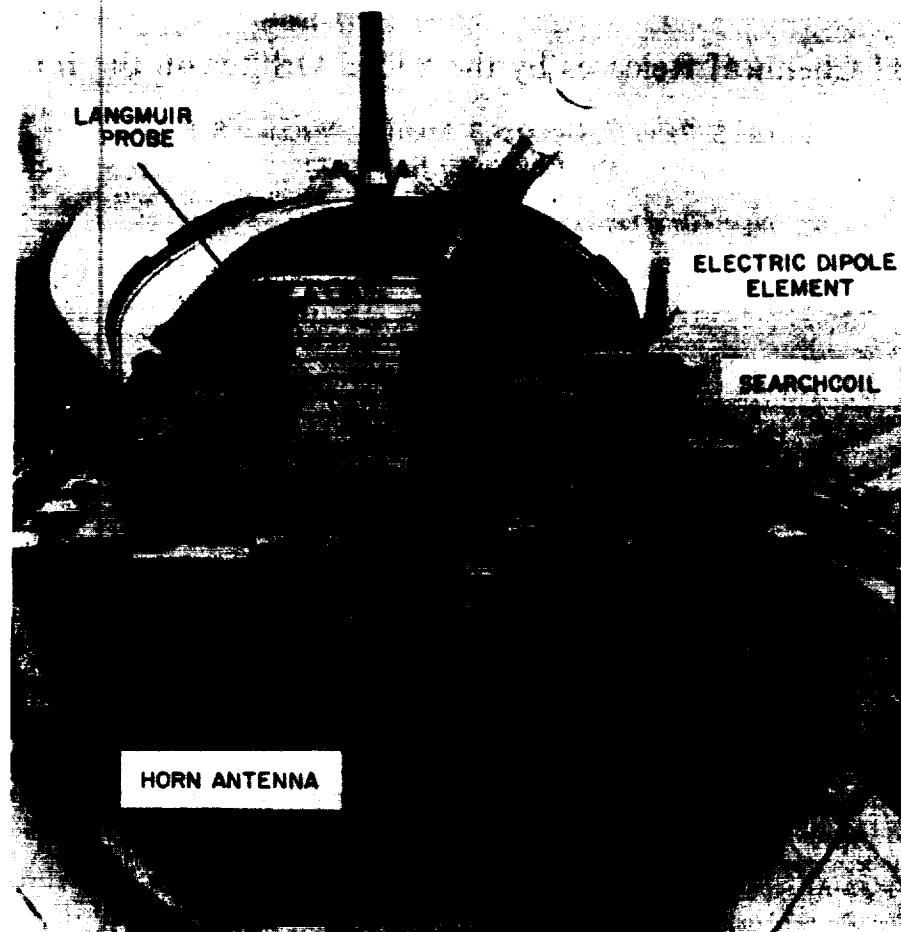


Fig. 1. Plasma Diagnostics Package in pallet location as part of the Office of Space Science first shuttle payload. The various wave sensors are identified on the Plasma Diagnostics Package.

2. MISSION AND OPERATIONAL CONSIDERATIONS

2.1. STS-3 Mission

During March 22–30, 1982, the Plasma Diagnostics Package was flown on the third space shuttle mission (STS 3) as part of the Office of Space Science (OSS 1) first shuttle payload [Neupert *et al.*, 1982]. Figure 1 shows the OSS 1 instruments as they were mounted on the aft pallet and points out the external sensors on the PDP. The orbiter was placed in a circular orbit at an altitude of 241 km and an inclination of 38°, which resulted in an orbit period of approximately 1½ h. The STS 3 mission's primary objective was to analyze the orbiter's operation over a wide range of thermal extremes; thus many different orbiter attitudes were achieved. Eighty hours out of approximately 192 were spent in a nose-to-sun attitude to cause low temperature extremes in the engine compartments, with a roll rate which was twice the orbit rate (see Figure 2); this attitude interval was when most of the PDP data were taken. At the ascending node (equator crossing moving northward), the orbiter attitude was such that atmospheric gases were ramming into the bay. As the orbiter headed toward descending node and night, it completely blocked the flow of gases into the bay, and a wake condition prevailed in and just above the bay.

2.2. Ionospheric Characteristics

Using satellite measurements as well as numerical models, the F2 region of the ionosphere can be characterized as fol-

lows: It extends from approximately 225 to 400 km with a neutral component of $\leq 10^9 \text{ cm}^{-3}$ and an average plasma density of $10^5\text{--}10^6 \text{ cm}^{-3}$. The dominant ion of this region is O^+ , which is created by ionizing UV, and the dominant neutral is O. In addition, N_2 and O_2 are important constituents since they are believed to play an important role in the principal loss process of the O^+ ion [Banks and Kockarts, 1973].

2.3. Shuttle Operations

During orbital operations the flash evaporator may discharge water to supplement heat rejection when the orbiter attitude is thermally unfavorable. A secondary function of the evaporator is to expend excess potable water produced by the fuel cells that has accumulated in the potable water tanks. The vaporized water produced by the FES during these two processes is discharged through two thrust-balancing sonic nozzles, one on each side of the aft fuselage, which are known as topping FES vents (see Figure 3). An FES plume study was conducted in June of 1978 at Johnson Space Center (S. Jacobs, personal communication, 1984). The results of this study were inconclusive owing to some of the equipment malfunctioning and the fact that the tests took place in a large chamber with many exposed cold surfaces. However, these tests did suggest that 100% water vapor (no particulates) was released by the FES during topping releases. In fact, the FES topping system was specifically designed to be 100% efficient at releasing steam. No crews of any shuttle flights to date have reported seeing any particulates released through the FES topping vents

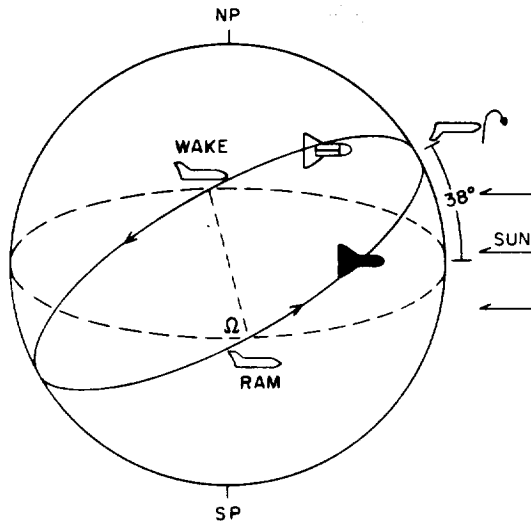


Fig. 2. Sketch of the orbit of the third space shuttle flight during the nose-to-sun attitude with the Orbiter roll at 2 times the orbit rate leading to a ram condition near the ascending node and a wake condition at the descending node.

(S. Jacobs, personal communication, 1984). The water vapor is discharged in pulses with a variable pulse rate and a pulse width equal to 200 ± 30 ms. The maximum pulse rate is 4 Hz at 22.7 kg/h [Hamilton Standard Engineering, 1982]. For example, for an average FES release of 2.3 kg/hr., the pulse rate is 0.4 Hz, which means every $2\frac{1}{2}$ s there is a 0.2-s pulse of water vapor and a 2.3-s gap. It should be noted that a plot of mass flow rate versus pulse rate is not linear since mass flow rate also depends on feedwater pressure. Therefore if the mass flow rate is known, only an estimate of the pulse rate can be obtained. The plume expands along the $\pm Y_0$ axes of the orbiter and in some cases is reflected by the wings [European Space Agency (ESA), 1982]. A high-load FES vent is also pointed out on Figure 3 which was used primarily at the beginning and end of the mission when the payload bay doors were closed. During the STS 3 mission there were 20 FES releases of varying lengths from a minute to more than 2 h. The PDP was turned on during four of these FES releases, all of which

were topping FES releases. Table 1 lists these releases and the location of the PDP.

Water management on the orbiter includes storing, distributing, and disposing of excess water generated by the fuel cells. This excess water is dumped overboard in a nonpropulsive fashion at predetermined times [ESA, 1982]. The water relief vent for water dumps is located on the port side, rearward of the forward bulkhead and about 1.5 m down from the door hinge (see Figure 3). A total of nine water dumps were made during the mission, each of which lasted for approximately 45 min to an hour. The average dump rate was 64 kg/h, with the amount of water being dumped varying from 41 to 93 kg. Most of the water dumps began around sunset and ended shortly after sunrise. The water dumped at night turned to ice upon release. The ice sublimated as the Orbiter passed into sunlight.

The Reaction Control System (RCS) is used on the orbiter to control attitude. The system consists of 38 primary (395 kg) thrusters and 6 vernier (11 kg) thrusters. Figure 3 shows the location of these thrusters from a side view. Both verniers and primaries are located in the front and rear of the orbiter. In this view the circular designation means the thrust is directed sideways, and the oval means the thrust is directed down. The other side of the orbiter has a matching set of these thrusters. In addition, there are a set of primaries which thrust up and forward in the front of the orbiter and a set of primaries which thrust up and back in the rear of the orbiter. Because of the location and direction of thrust of some of the RCS thrusters, a certain number of the thruster plume molecules are reflected off orbiter surfaces [ESA, 1982] as well as returned to payload instruments, resulting in contamination [Ehlers, 1984].

Table 2 shows thruster plume characteristics for both the vernier and primary thrusters, including composition of the exhaust and numbers of ions and neutrals ejected in a typical firing (while maintaining orbit) and in a long firing event (while maneuvering to a new orbit attitude). It should be noted that the stated composition of the exhaust plume, both neutral and ionic, is based on thermodynamic equilibrium calculations since actual measurements are very difficult to make. These predictions are the result of a thermodynamic one-dimensional model program called CONTAM III, which was

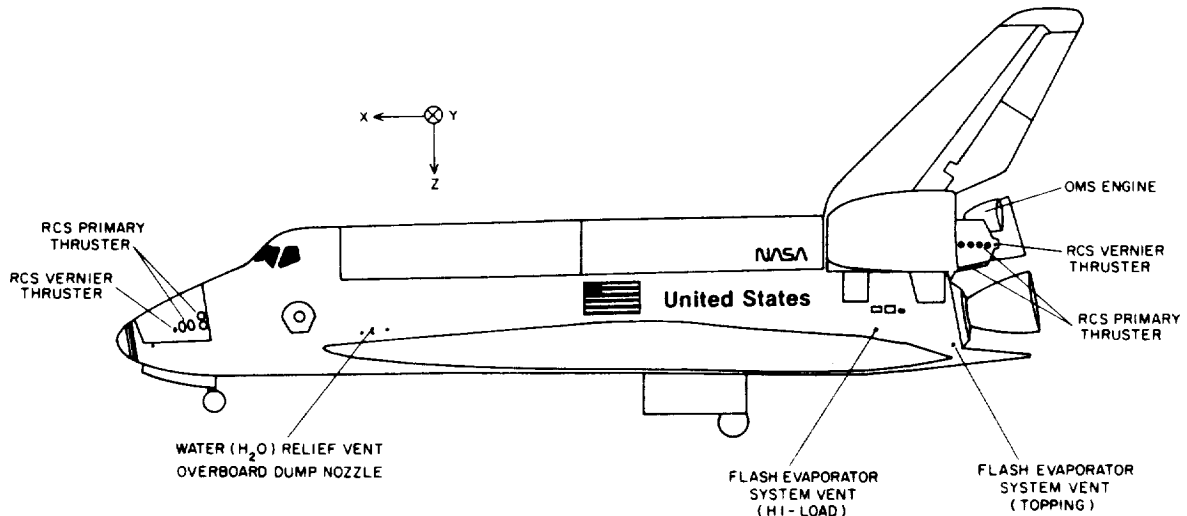


Fig. 3. Identification of the flash evaporator system vents which release water vapor, the water relief vent which releases liquid water, and the maneuvering thrusters (primary and vernier) which release many neutrals and ions as shown in Table 2.

TABLE 1. STS-3 FES Water Usage

Start Time		Duration, h:min	Type	Location of PDP	Usage, kg
Day	UT				
82	0117:58	0:02	Topping	Pallet	<.45
85	1230:00	2:32	Topping	RMS*	26
85	1501:44	1:30	Topping	RMS	15
86	2010:00	0:01	Topping	Pallet	<.45

*Remote Manipulator System Arm

developed for the purpose of predicting plume contamination effects [Hoffman and Hetrick, 1982]. The model does not take into account kinetic effects, chemical reactions, or charge interchanges that may occur immediately after a thruster firing. Thus, although such ions as CO_2^- are unstable and predicted to be a part of the thruster exhaust, these ions most likely undergo immediate chemical reactions with other components of the exhaust or even neutrals and ions present in the ionosphere. We would also like to point out the following regarding Table 2: (1) MMH- NO_3 is only a suspected constituent of the plume and is believed to be a condensable, and (2) Only the most dominant ions (mole fraction $> 10^{-10}$) are listed in the table. The model actually predicts several other ions to be present, such as OH^+ and NO_2^- ; however, the maximum mole fraction of each of these ions is predicted to be $\leq 10^{-10}$, and thus we have not included them in the table. The velocity of the exhaust gases at all points in the plume after all energy has been converted is predicted to be 3.5 km/s based on a given temperature of approximately 3000° K (using the CONTAM III model). During the mission, there were over 40,000 thruster firings of varying lengths from 0.08 s to tens of seconds. When the PDP was turned on and taking data, nearly all of these firings as well as every FES release and water dump were evident in the data through one or more measured parameters.

2.4. PDP Instrumentation

A primary objective of the PDP was to measure aspects of the orbiter's induced environment both in the payload bay at the pallet level and above the bay to a 15-m height through use of the Remote Manipulator System (RMS). The PDP carried a complement of 14 instruments that measured electrostatic and electromagnetic waves, dc magnetic and electric fields, ion composition and flow, ion and electron energy distribution functions, plasma temperature and density, and neutral pressure. Some of the instruments which showed effects during chemical releases are briefly described below. A more detailed description of the instrument complement, the associated receiver systems, and the range of measurements possible can be found in works by Shawhan *et al.* [1984a, b].

A 5-cm-diameter, gold-plated spherical Langmuir Probe measured electron density and temperature and electron density irregularities ($\Delta N/N$) in the frequency range 0–40 Hz. Two spectrum analyzers were used to look at electrostatic and electromagnetic waves and $\Delta N/N$ irregularities in the frequency range 31 Hz to 178 kHz. One of the spectrum analyzers was dedicated to observing the electric component of waves using a double probe with two 20-cm-diameter black spherical sensors separated by 1.6 m. The other analyzer was periodically switched between the electric dipole antenna, the magnetic search coil, and the Langmuir Probe (see Figure 1 for location of these sensors on the PDP). The dc electric fields in the

range ± 4.8 V/m were measured using the electric dipole antenna, and spacecraft potential with range ± 8.2 V was measured by taking the average potential between the two spheres with respect to the PDP ground, which was the same as the orbiter ground. A cold cathode ionization gauge measured ambient pressures from 10^{-7} to 10^{-3} torr. Finally, pitch angle and flux of energetic electrons and ions with energies 2 eV to 36 keV were detected with a low-energy proton and electron differential energy analyzer.

3. OBSERVATIONS

3.1. Flash Evaporator System Releases

Figure 4 provides Langmuir Probe and plasma wave data taken during the 2-min FES release on day 82 (UT) under daytime conditions. The top panel shows that for every 1.6-s sample plotted during the release the Langmuir Probe saw peak to peak voltage outputs which covered the full dynamic range of the instrument. By applying a fast Fourier transform (FFT) algorithm to these data, the $\Delta N/N$ plasma turbulence spectrum shown at the top of Figure 5 was obtained. This spectrum shows that the turbulence was increased by as much as 30 times over background below 10 Hz and increased by approximately 3 times at frequencies 10–40 Hz. The FES release spectrum was seen to rise steeply below 6 Hz and peak at approximately 0.5 Hz, which was, in all probability, the pulse rate of the FES release at this time. The basis for this assumption will be discussed at the end of this subsection.

TABLE 2. Thruster Plume Characteristics

Primary Thruster (PRCS)		Vernier Thruster (VRCS)	
$\dot{m} = 1419.8$ g/s/engine		$\dot{m} = 40.8$ g/s/engine	
Species	Molecular Weight	Mole Fraction	
<i>Composition, Neutrals</i>			
H ₂ O	18	0.328	
N ₂	28	0.306	
CO ₂	44	0.036	
O ₂	32	0.0004	
CO	28	0.134	
H ₂	2	0.17	
H	1	0.015	
MMH-NO ₃	108	0.002	
<i>Composition, Dominant Ions</i>			
NO ⁺	30	1.7×10^{-8}	
CO ₂ ⁺	44	2.7×10^{-10}	
OH ⁺	17	4.3×10^{-10}	
Electrons	—	2.4×10^{-9}	
Total Number of Neutrals and Ions Ejected			
	Number of Neutrals	Number of Ions (Electrons)	
<i>VRCS</i>			
Typical*	1.3×10^{25}	3.1×10^{17}	
Longest†	1.7×10^{26}	3.8×10^{18}	
<i>PRCS</i>			
Typical‡	9.2×10^{24}	2.1×10^{17}	
Longest§	5.5×10^{25}	1.2×10^{18}	

*Based on 2 firings ejecting 163 g over 2 s.

†Based on 14 firings ejecting 2100 g over 30 s.

‡Based on 1 firing ejecting 114 g over 80 ms.

§Based on 5 firings ejecting 682 g over 720 ms.

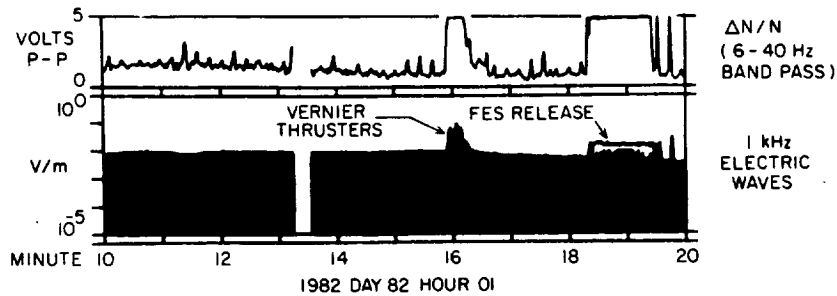


Fig. 4. Effects of a flash evaporator system release at 0118. The top panel shows that the Langmuir Probe registered peak-to-peak voltage outputs covering the full dynamic range of the instrument. The bottom panel shows that the peak intensity of 1-kHz electric waves rose substantially over the background during the release while the average did not. A vernier thruster firing is also pointed out at 0116.

Associated with the $\Delta N/N$ increase was an enhancement in the background orbiter-generated electrostatic noise [Shawhan *et al.*, 1984b], which in panel 2 of Figure 4 was shown to be 10^{-2} V/m at 1 kHz before the release. The average value of the 1-kHz electric field (based on the average seen during each 1.6-s sample) during the release rose only slightly while the peak value (the maximum encountered during each 1.6-s sample) was at least half an order of magnitude greater than before the release. An effect in the electric field during FES releases was seen at all frequencies from 31 Hz to 31 kHz and sometimes as great as 100 kHz, depending on Orbiter attitude and on day/night and ram/wake conditions. The bottom half of Figure 5 shows electric field spectral density for the FES release on day 82. It can be seen here that electric field spectral density was clearly enhanced by as much as 20 dB up to 31 kHz. Other data available show there were no obvious effects on the wave magnetic field, spacecraft potential, dc electric field, or neutral pressure.

The FES release discussed above took place during the nose-to-sun attitude. It is apparent from Figure 1 that the PDP sensors, i.e., Langmuir Probe and electric field sensors, were located well inside the bay and were shielded by other instrument packages from flow in some directions. Since the plume of water vapor expands along the $\pm Y_0$ axes of the orbiter, a more ideal location for the PDP would be on the RMS near the back of the orbiter. Of the two releases that took place while the PDP was on the RMS, essentially the same effects as noted above were seen. In addition, a pulsing effect was seen in the fluxes of low-energy electrons and ions. This was particularly obvious in the ion data when the PDP was on the RMS near the back of the orbiter as seen in Figure 6a. At this time, which was shortly after noon, we saw a pulsing effect in the ion fluxes up to about 1 keV. A line plot of counts versus time for 92.1-eV ions, shown at the bottom of this figure, clearly shows the variation.

A careful analysis of the data, which showed a cycle of about 5/min, the sweep time of the particle detector (1.4 s plus 0.2 s rest), and the pulse rate of the flash evaporator system (which we know to be less than 4 Hz) indicated that the pulsing effect was due to a beat frequency between the sweep of the particle detector and the FES pulse rate. In fact, computer modeling has shown that a FES pulse rate of 1.8 Hz would give a spectrum similar to that shown at the top of Figure 6a. In addition, output amplitude versus time from the Langmuir Probe clearly showed a periodic variation at 1.8 Hz for this release (see Figure 6b), and the $\Delta N/N$ plasma turbulence spectrum peaked between $1\frac{1}{2}$ and 2 Hz. A pulse rate of 1.8 Hz for the FES at this time is consistent with what engi-

neering models from Hamilton Standard predict (A. Decrisantis, personal communication, 1984). The production of hot ions up to 1 keV is not yet fully understood; however, a few remarks concerning a mechanism which could possibly explain this phenomenon are given in Section 4.

3.2. Water Dumps

Figure 7 is a plot which shows Langmuir Probe and plasma wave measurements as a water dumping operation ended. The water dump had begun 35 min prior to the beginning of this plot. The end of the dump was characterized by an abrupt decrease in $\Delta N/N$ turbulence at 1654 UT on day 83. A total of 42 kg of water was dumped at an average dump rate of 65 kg/hr. Panel 1 shows that during the water dump the Langmuir Probe recorded peak to peak voltage outputs which covered the full dynamic range of the instrument. At water shut-off the voltage output dropped to background level almost immediately, which was the case with FES releases. However,

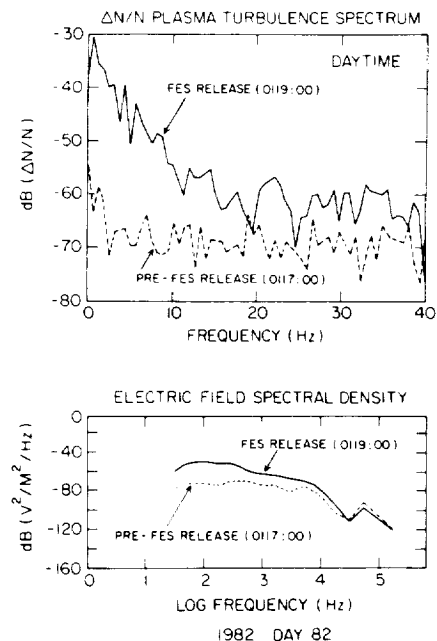


Fig. 5. $\Delta N/N$ plasma turbulence spectrum and electric field spectral density for the flash evaporator system release shown in Figure 4. The $\Delta N/N$ spectrum rose steeply below 6 Hz and peaked at about 0.5 Hz, which was the pulse rate of the flash evaporator at this time. The bottom plot shows that background electrostatic noise was enhanced at all frequencies up to about 31 kHz. Zero dB corresponds to $1 \text{ V}^2/\text{M}^2/\text{Hz}$.

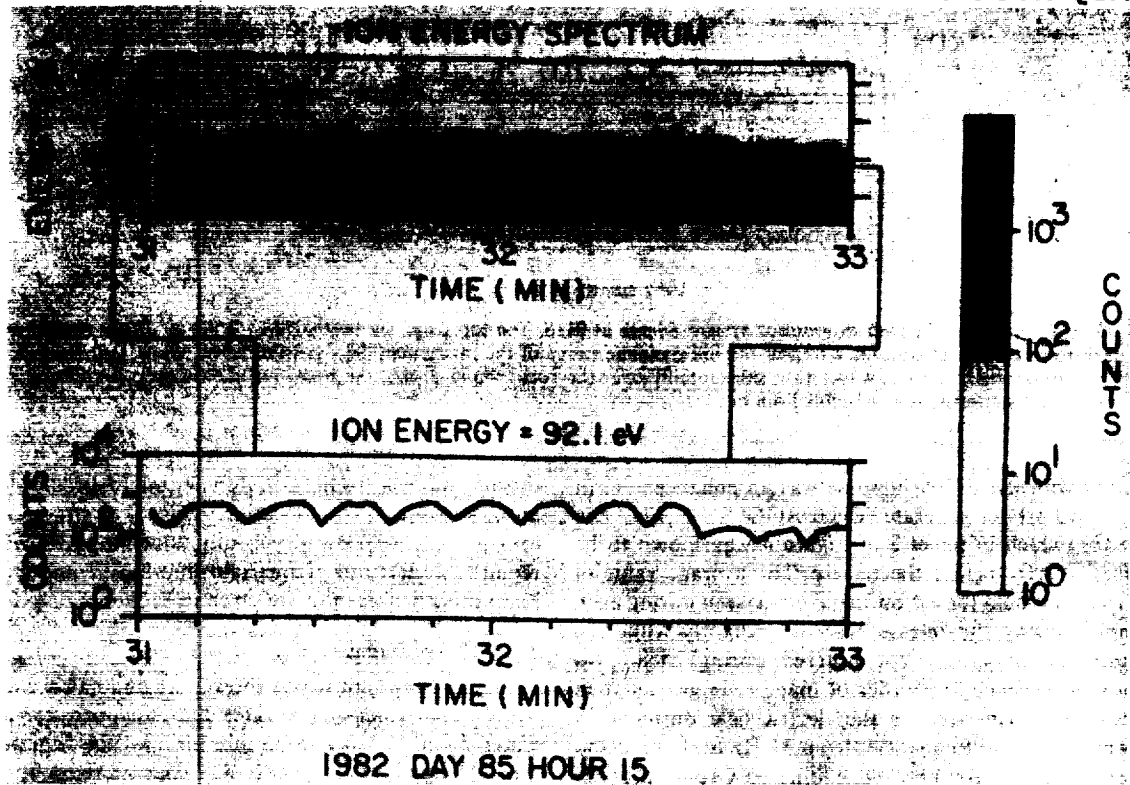


Fig. 6a. Ion energy spectrum during a flash evaporator system release while the Plasma Diagnostics Package was on the Remote Manipulator System. The spectrum shows a beat frequency between the sweep time of the ion detector and the pulse rate of the flash evaporator. Ions with energies up to about 1 keV are seen at this time (see discussion in 4.1). The bottom panel shows the 92.1-eV energy channel plotted to show the flux variation with time.

the turbulence spectrum was much broader and extended to higher frequencies than that observed during FES operations as shown at the top of Figure 8. Plasma turbulence appeared to be increased 5 to 6 times over background at all frequencies 0-40 Hz.

Panel 2 of Figure 7 shows that the background noise at 0.178 kHz had been elevated slightly during the water dump. Figure 8 shows that in fact, amplitudes at all frequencies up to about 3 kHz were elevated during the dump and amplitudes at all frequencies from 3 to 100 kHz were suppressed. However, this spectrum depression was not seen in the FES releases as shown at the bottom of Figure 5. It should be noted that sunrise occurred at approximately 1651 UT on day 83 in Figure 7, which is also a near-ram condition. Even though the water dump had begun during nighttime conditions, peak to peak voltage outputs covering the full dynamic range from the Langmuir Probe were seen during most of the dump. A water dump that occurred on day 84 also showed similar effects. As seen in Figure 9, the beginning of this water dump at 0111 was evident only at the low frequencies, possibly because the bay was in a wake condition at this time and the orbiter-generated noise was almost absent. The near lack of effects seen when the electrostatic noise was absent might imply that the effect of the water dump was not to generate the noise but merely to amplify it if it was already present. Wave magnetic field, spacecraft potential, and dc electric field were not affected by the water dumps, as was the case with FES releases. However, neutral pressure appeared to be affected only during that part of the orbit in which density was lowest, i.e., in wake. During this part of the orbit, neutral pressure readings were slightly greater with water being dumped than without it.

Smiddy *et al.* [1983] reported that on another shuttle mis-

sion during a water dump there was a $\Delta N/N$ increase at frequencies between 30 and 503 Hz, an enhancement of electrostatic noise, a decrease in the spacecraft potential, and an unchanged dc field. With the exception of a decrease in spacecraft potential the results seem to be similar to those of the PDP.

3.3. Thruster Operations

Most of the plasma effects observed by the PDP during thruster firings are shown in Figure 10. This plot covers a 10-min time period during the daytime (sunset occurred at 1540) with the payload bay in a near-wake condition up to 1536 and during which several primary thrusters were fired. The PDP was in the bay at this time, but the effects were similar when the PDP was on the RMS. Note that the PDP provided a resolution of 1.6 s for most of these measurements, which was considerably longer than the typical 80-ms firing of

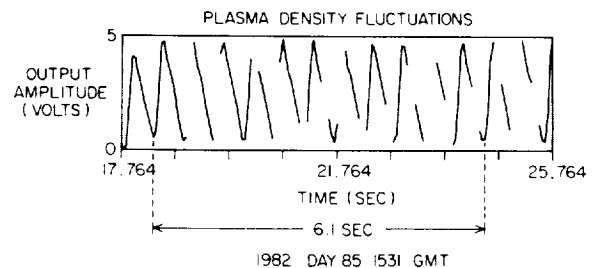


Fig. 6b. Plasma density fluctuations during an FES release while the PDP was on the remote manipulator system (see Figure 6a). The data show 11 cycles in 6.1 s for a periodic variation at 1.8 Hz, which other data and modeling show to be the pulse rate of the flash evaporator at this time.

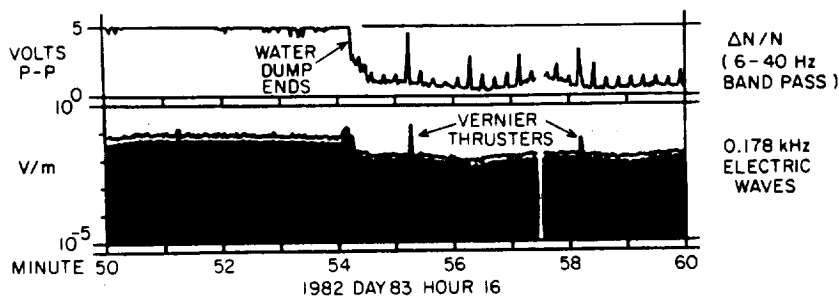


Fig. 7. Effects of a water dump that ended at 1654. The top panel shows that the Langmuir Probe registered peak-to-peak voltage outputs covering the full dynamic range of the instrument during most of the dump. The bottom panel shows that 1-kHz electric waves were elevated over background during the dump. Vernier thruster firings are also pointed out at 1655 and 1658.

a primary thruster. When thrusters fired, the Langmuir Probe, which responded to variations in the electron density near the PDP, typically saw peak to peak voltage outputs which covered the full dynamic range of the instrument with frequency components in the 0- to 40-Hz range (see Panel 1 of Figure 10). In addition, the Langmuir Probe measured electron density. As shown in Panel 2, the density was seen to increase by 2-3 orders of magnitude every time a thruster fired. Please note that the absolute density scale as labeled is still subject to revision at this time. However, the relative change seen in density with every thruster firing will be unchanged should the scale be revised. At the same time the electric field at frequencies from 30 Hz to ≥ 10 kHz was seen to increase by almost 2 orders of magnitude to 0.1 V/m. The 1-kHz channel, which is representative, is shown in Panel 3. In the fourth and fifth panels, low-energy ions (58.9 eV) and electrons (2.56 eV) are displayed which showed increases in flux with nearly every thruster firing up to 1536. Ions with energies up to 1 keV were seen with some thruster firings during the mission. Pressure

spikes (Panel 6) were seen for several firings, with some producing increases up to 2×10^{-6} torr. Pressure spikes up to 10^{-4} torr were observed during certain thruster firings tests [Shawhan et al., 1984b]. The resolution of the pressure gauge is 1.6 s, which explains why many of the thruster firings showed no effect on pressure. In Panel 7 the potential of the PDP spacecraft and orbiter with respect to the plasma (SC POT.) shows a 2-V change with each firing up to 1536. The electric field in the vicinity of the PDP (E_{DIFF}) was occasionally perturbed by as much as a 1 V/m. Finally, Panel 8 shows that only primary thrusters were fired during this 10-min time period. The firing of one thruster is indicated by a half line, with a full line indicating the firing of two or more thrusters at approximately the same time.

As mentioned in the preceding paragraph, electron density was seen to increase by 2-3 orders of magnitude during a thruster firing. This effect was most pronounced, however, when the orbiter was in a wake condition, i.e., low initial density ($< 10^3 \text{ cm}^{-3}$). At higher electron density ($> 10^5 \text{ cm}^{-3}$) and thus at a different attitude a thruster firing tended to reduce the density. In addition, the ion mass spectrometer which was flown on the PDP [Grebowsky et al., 1983] saw order of magnitude enhancements in H_2O^+ and NO^+ during thruster firings. Although NO^+ is a constituent of the exhaust

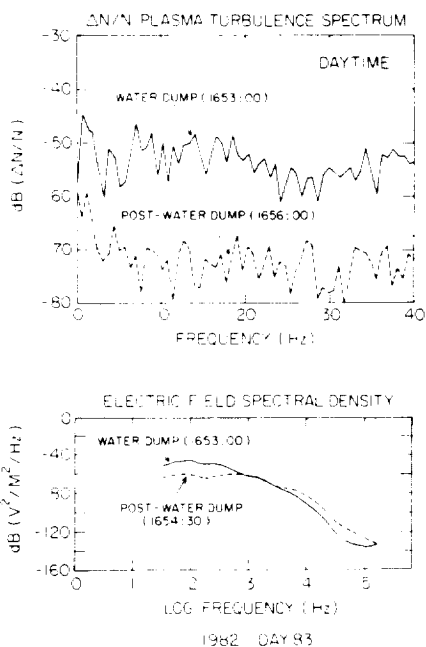


Fig. 8. $\Delta N/N$ plasma turbulence spectrum and electric field spectral density for the water dump shown in Figure 7. The $\Delta N/N$ spectrum was elevated over background at all frequencies from 0 to 40 Hz. The bottom plot shows that background electrostatic noise was enhanced at all frequencies up to about 3 kHz and suppressed at all frequencies above that. Zero dB corresponds to $1 \text{ V}^2/\text{M}^2 \text{ Hz}$.

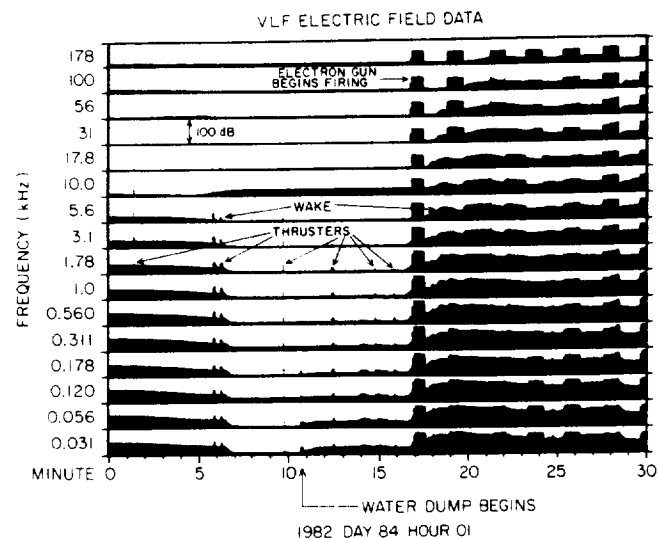


Fig. 9. A 30-min plot of VLF electric field data which shows that a water dump began at about 0111. Effects are noticed only at low frequencies since the bay of the orbiter was in a wake condition. Vernier thruster firings are also pointed out.

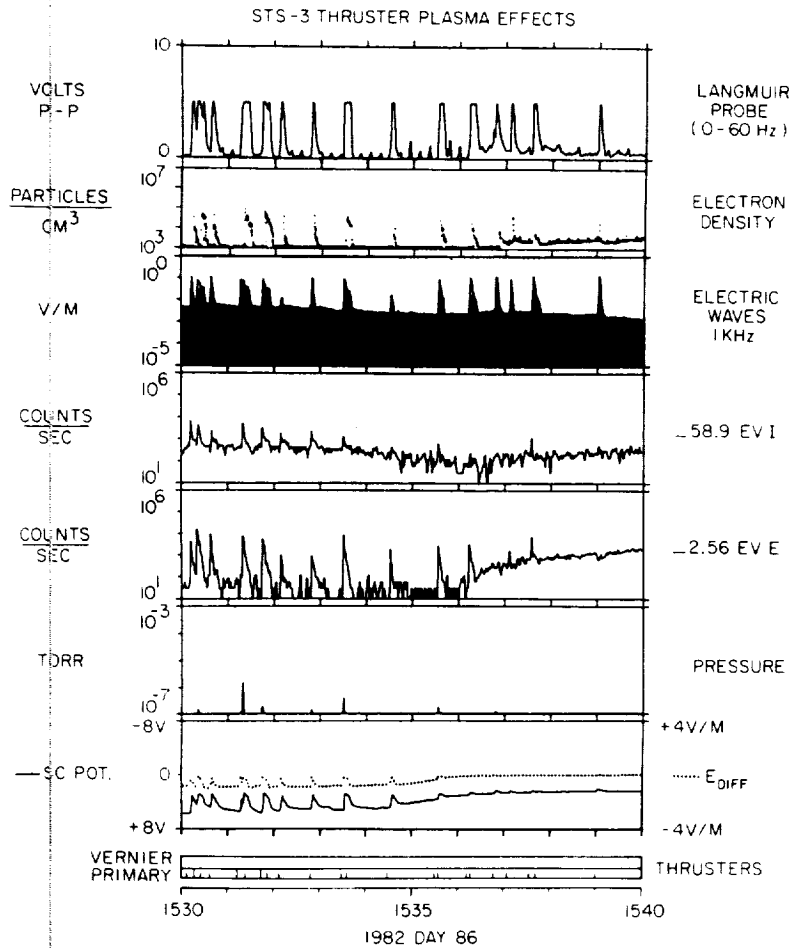


Fig. 10. A 10-min sample plot of measurements made by the PDP indicating the pressure and plasma effects of primary thruster firings. Some of the effects disappeared as the bay came out of a near-wake condition at about 1536.

plume (see Table 2), these momentary enhancements of NO^+ are most likely due to the reaction $\text{O}^+ + \text{N}_2 \rightarrow \text{NO}^+ + \text{N}$, which takes place at the rate of $1.3 \times 10^{-12} \text{ cm}^3/\text{s}$ [Ferguson, 1973]. Thus, it is the dominant neutral N_2 constituent of the plume which reacts with the ambient O^+ to produce the enhanced NO^+ . Likewise, the H_2O^+ must be produced by charge exchange between ambient O^+ and neutral water, which is a dominant constituent of the plume. It should be noted that the lack of effects in the ion and electron data and in the electric field and spacecraft potential after 1536 was certainly a result of the payload bay coming out of wake and/or approaching the day/night terminator.

Vernier thruster firings produced the same effects as noted above, although in many cases the effects were minimized owing to the smaller amount of gas being ejected. Some vernier thruster firings are noted on Figures 4, 7, and 9. The spikes seen in the $\Delta N/N$ data (panel 1) in Figures 4 and 7 and not noted as thruster firings are an instrumental effect and are in no way related to thruster firings. In addition, the turbulence spectrum and electric field spectral density spectrum for a vernier thruster firing are shown in Figure 11. These plots show that $\Delta N/N$ electron density irregularities during thruster firings were increased over background by as much as 10 times at all frequencies 0–40 Hz and background electrostatic noise stimulated by the thruster firing was most intense at frequencies below 10 kHz and peaked around 0.5 kHz. For more details on the effects of thruster firings during STS 3, see Murphy *et al.* [1983]. Similar effects to the ones mentioned

above have been reported on other shuttle flights [Smiddy *et al.*, 1983; McMahon *et al.*, 1983; and Narcisi *et al.*, 1983].

4. DISCUSSION AND CONCLUSIONS

The Space Shuttle perturbs the ambient ionosphere in many ways as it carries out its planned missions. A foreknowledge of these perturbations will aid all researchers who wish to use the shuttle as a platform from which to conduct their experiments, whether they be astronomy-related or physics-related experiments. The results of the PDP on STS 3, as presented in this paper, show clearly the early effects on the ionosphere of shuttle-produced chemical releases. These results are valuable in helping to understand the early effects on the ambient ionosphere of the larger releases from rockets for which measurements close to the release are nearly impossible. A summary of the effects observed by the PDP and possible explanations for them are as follows.

4.1. Flash Evaporator System Releases

The flash evaporator system released vaporized water at a variable pulse rate. During this time the plasma density irregularities ($\Delta N/N$) were increased by 3–30 times. In addition, the fast Fourier transform of the Langmuir Probe data showed a spectrum that rose steeply and peaked below 6 Hz, in agreement with the possible pulse rates, and extended to 40 Hz, which was the limit of the detector. At the same time the plasma wave data (Figure 4) showed an enhancement in the background orbiter-generated electrostatic noise at fre-

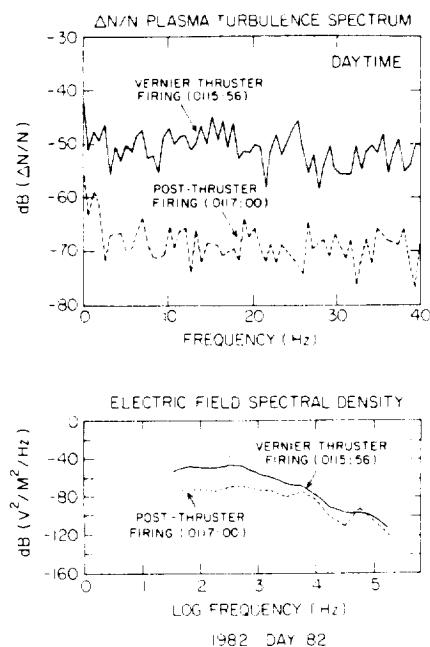


Fig. 11. $\Delta N/N$ plasma turbulence spectrum and electric field spectral density for the vernier thruster firings shown in Figure 4. The $\Delta N/N$ spectrum was elevated over background at frequencies from 0 to 40 Hz. The bottom plot shows that electrostatic noise was stimulated at all frequencies up to about 10 kHz. The spectrum peaked at about 0.5 kHz. Zero dB corresponds to $1 \text{ V}^2/\text{M}^2/\text{Hz}$.

quencies 30 Hz to 31 kHz and as high as 100 kHz depending on the orbit and attitude characteristics. Figure 6a illustrates the periodic variation in energetic ion particle flux which was consistent with an FES pulse rate of 1.8 Hz. The fact that this variation exists is evidence that the time scale of the onset of plasma modification by the water vapor was fast. For releases of only a few grams of water vapor per pulse the plume dispersed rapidly (within a few seconds), which reasonably explains the decay time of any plasma effect. The fast (< 1 s) onset time is consistent with the $\text{O}^+/\text{H}_2\text{O}$ charge exchange reaction which occurs at the kinetic rate ($2.4 \times 10^{-9} \text{ cm}^3/\text{s}$) [Ferguson, 1973]. The fact that this charge exchange reaction occurs 1000 times faster than the dominant F region O^+ loss process [Mendillo et al., 1975] causes it to dominate the local ionospheric chemistry.

Additional evidence of the rapidity of the plasma/ H_2O interaction is provided by the Lagopedo ionospheric depletion experiments conducted in September 1977 [Pongratz et al., 1978; Sjolander and Szuszczewicz, 1979] which involved releasing water vapor into the F region of the ionosphere. These experiments confirmed that charge exchange and dissociative recombination took place shortly after the releases and persisted for nearly a half hour. The hole was nearly isotropic and Gaussian in profile, with a thickness at half depletion of 60 km.

Day versus night effects are summarized by Bernhardt [1976] when he states that water vapor is acceptable as a daytime release from the Shuttle but loses efficiency at creating a hole in the plasma at night owing to its condensation into ice crystals upon release. Zinn and Sutherland [1980] pointed out that such ice crystals have an evaporative lifetime of about 5 min, which is long enough for them to traverse a great distance (kilometers) before they evaporate. This would seem to indicate that the PDP should see little or no change in electron or ion flux during night releases. This prediction

can neither be confirmed nor denied for the case of FES operation since not enough data were taken under appropriate conditions.

During the time the PDP was on the RMS (see Figures 6a and 6b) the flash evaporator was releasing an average of 0.6 g of water vapor each time it pulsed. This means that approximately 4×10^{22} water vapor molecules were being released every second. Because this release is pulsed and occurs in vapor form, the FES should be very efficient at creating a plasma hole at F region altitudes. The PDP data taken during the daytime support this. Section 4.4 further examines the plasma/ H_2O physics, seeking to understand the phenomenon which would take place after the charge exchange reaction occurs.

4.2. Water Dumps

Plasma effects noted during water dumps include increased pressure in the shuttle wake, plasma turbulence increases at all frequencies up to 40 Hz, and enhancement of the background orbiter-generated electrostatic noise at frequencies from 30 Hz to approximately 3 kHz and a suppression at frequencies above 3 kHz. This observation is consistent with a theory proposed by Papadopoulos [1984], which attributes the broadband electrostatic noise and glow phenomena to lower hybrid drift instabilities driven by plasma density gradients. When the bay is in ram and thus the density is very high ($\sim 10^6 \text{ cm}^{-3}$), there appears to be a critical frequency which determines whether the background orbiter-generated electrostatic noise is enhanced or suppressed. PDP data show this critical frequency to be approximately 3–4 kHz, which is near the lower hybrid resonance frequency. Electromagnetic noise was recorded during the large liquid water release at 105 km on the second flight test of the Saturn booster in 1962 [Debus et al., 1964]. Signal strength measurements during that release at frequencies ranging from 10 kHz to 230 MHz indicated that radio frequency waves generated by electrical discharge were associated with the cloud that developed after the release.

It is expected that liquid water would be less efficient at creating a plasma hole in the ionosphere than vaporized water since at release, only a small amount would be vaporized and the remainder would become ice particles, as was the case with the Saturn booster experiment [Debus et al., 1964]. In view of the PDP measurements and the releases which were recorded during STS 3 it is not possible to state whether or not liquid water was less efficient at creating a hole than vaporized water.

4.3. Thruster Operations

Finally, a summary of the effects of thruster firings includes the following: an increase in plasma turbulence over the 0- to 40-Hz spectrum, increases or decreases in electron density which were orbit dependent, enhancement of the background electrostatic noise from 30 Hz to above 10 kHz, neutral pressure spikes up to 10^{-4} torr, perturbations to the spacecraft potential by as much as 2 V and to the dc electric field by as much as 1 V/m primarily under wake conditions, and occasional changes in the low-energy ion and/or electron fluxes. It is likely that the enhancement in electron density during thruster firings, which was seen primarily during the times when the orbiter was in a wake condition, was due to ion scattering into the wake as a result of the high pressure gas cloud which surrounded the shuttle and to other chemical reactions. With regard to the high-energy ions and electrons which were seen during some thruster firings, it is not possible,

with the data available, to absolutely determine whether these ions and electrons were due to neutral or ionic effluents of the thruster exhaust. Most of the other effects noted during thruster firings, including enhancement of the background electrostatic noise and perturbation to the spacecraft potential and dc electric field, could have an explanation rooted in the qualitative description of plasma/H₂O physics contained in the next section.

4.4. Physics in a Cloud of Water

Further examination of the physics which could take place in a cloud of water (from FES releases, water dumps, or thruster operation) released into the ionosphere hints at some possible explanations for the observed phenomena.

Charge exchange between the ambient O⁺ ions moving at 8 km/s relative to the H₂O molecules in a plume produces stationary H₂O⁺ ions (in the reference frame of the plume) and fast O atoms which are rapidly lost from the plume. Since in this moving frame there is a motional electric field ($E = -V \times B \approx 2 \text{ mV/m}$), the newly created ions experience a force $F \propto E + V \times B$. The subsequent motion is cycloidal, thus the guiding centers of the H₂O⁺ ions are displaced in the direction of the electric field. This displacement contributes a current, the so-called pickup current [Goertz, 1980], which will lead to a buildup of charge at the end of the plume. These charges will partially screen the motional electric field from the inside of the magnetic flux tube connected to the plume. The electric field in the plume must then be calculated by balancing the pickup current with field aligned currents carried by Alfvén waves [Goertz, 1980].

It can be shown that if the plume is fairly dense, $N_{\text{H}_2\text{O}} \gtrsim 10^{14} \text{ cm}^{-3}$, (which would occur during the first few tenths of a second after an FES release) the electric field in the plume flux tube (PFT) is significantly reduced.

Ambient ions overtaken by the Alfvén wave will be accelerated perpendicularly to the magnetic field and form a ring distribution in velocity space. In addition, ambient O atoms entering this nearly field-free region are photoionized and also form a ring distribution in velocity space which is unstable to electrostatic waves [Harris, 1959]. It is known that such a ring distribution will quasilinearly diffuse in velocity space with a rapid formation of a high-energy tail [Kulygin et al., 1971].

It needs to be investigated quantitatively what the plasma density and composition is in the PFT and whether the O⁺ ions stay in the plume long enough to be affected by charge exchange with the H₂O molecules. If charge exchange occurs before the O⁺ ions leave the plume along magnetic field lines, the ring distribution may not be strong enough to cause rapid growth of electrostatic waves and heating.

In addition to the foregoing, we would like to point out that it has been suggested that the observed spacecraft potential changes, electrostatic noise, and plasma turbulence during FES releases may be due to nozzle spray electrification (triboelectric effects). While this is an interesting suggestion, its investigation is beyond the scope of this paper. The paper's main purpose is to present observational evidence of effects noted during shuttle-produced chemical releases and to suggest possible explanations for the effects observed. In light of this, a thorough study of all of the suggested explanations contained in this paper needs to be undertaken.

Further measurements by the Plasma Diagnostics Package coordinated with ground-based observations, both of which are investigations of the Spacelab 2 mission scheduled for a July 1985 launch, will provide an opportunity to further study

the plasma/H₂O interactions through orbiter chemical releases. In situ measurements by the PDP will be extended to the regime around the orbiter far beyond the reaches of the RMS (the PDP will be released as a free-flying satellite) and coordinated with simultaneous ground observations to provide much more extensive input to theory. Further, it is hoped that the measurements obtained by the PDP on Spacelab 2 will aid other experimenters who plan to use the space shuttle as an experimental platform.

Acknowledgments. The authors wish to thank the PDP co-investigators, Nicola D'Angelo, Louis A. Frank, and Donald A. Gunnert, for use of their data; Steve Jacobs and Lubert Leger of Johnson Space Center, Paul Campbell of Rockwell International, and Angelo Decrisantis of Hamilton Standard for their assistance in obtaining the necessary Orbiter data and information; and Christine Joyner for her patient typing. Helpful discussions with R. A. Smith are gratefully acknowledged. Credit for the suggestion of triboelectric effects goes to one of the referees. This research was supported by NASA through contract NAS8-32807 with Marshall Space Flight Center and through grant NAG3-449 from Lewis Research Center.

The Editor thanks R. S. Narcisi and J. M. Forbes for their assistance in evaluating this paper.

REFERENCES

- Banks, P. M., and G. Kockarts, *Aeronomy, Part B*, pp. 175-186, Academic, Orlando, Fla., 1973.
- Bernhardt, P. A., The response of the ionosphere to the injection of chemically reactive vapors, *Tech. Rep. 17*, pp. 1-247, Stanford University, Stanford, Calif., 1976.
- Booker, H. G., A local reduction of F region ionization due to missile transit, *J. Geophys. Res.*, **66**, 1073-1079, 1961.
- Debus, K. H., W. G. Johnson, R. V. Hembree, and C. A. Lundquist, A preliminary review of the upper atmosphere observations made during the Saturn high water experiment, in *Proceedings of the XIIIth International Astronautical Congress*, pp. 182-196, Springer-Verlag, New York, 1964.
- Ehlers, H. K. F., An analysis of return flux from the space shuttle orbiter RCS engines, paper presented at the AIAA 22nd Aerospace Sciences Meeting, Am. Inst. of Aeronaut. and Astronautics, Reno, Nev., January 9-12, 1984.
- Eur. Space Agency, Spacelab Payload Accommodation Handbook, *Doc. SLP/2104*, Neuilly, France, 1982.
- Ferguson, E. E., Rate constants of thermal energy binary ion-molecule reactions of aeronomic interest, *At. Data Nucl. Data Tables*, **12**, 159-178, 1973.
- Forbes, J. M., Upper atmosphere modifications due to chronic discharges of water vapor from space launch vehicle exhausts, in *Space Systems and Their Interactions With Earth's Space Environment*, edited by H. B. Garrett and C. P. Pike, pp. 78-98, American Institute of Aeronautics and Astronautics, New York, 1980.
- Goertz, C. K., Io's interaction with the plasma torus, *J. Geophys. Res.*, **85**, 2949-2956, 1980.
- Grebowsky, J. M., M. W. Pharo III, H. A. Taylor, Jr., and I. J. Eberstein, Measured thermal ion environment of STS-3, paper presented at the Shuttle Environment and Operations Meeting, Am. Inst. of Aeronaut. and Astronautics, Washington, D. C., October 31, 1983.
- Hamilton Standard Engineering, Flash evaporator controller operation, *Memo. SEM 62408*, Windsor Locks, Conn., January 25, 1982.
- Harris, E. G., Unstable plasma oscillations in a magnetic field, *Phys. Rev. Lett.*, **2**, 34, 1959.
- Hoffman, R. J., and M. A. Hetrick, Jr., Plume contamination effects prediction: CONTAM III Computer Program, *Tech. Rep. AFRPL TR82-033*, Air Force Rocket Propul. Lab., Edwards AFB, Calif., 1982.
- Kulygin, V. M., A. B. Mikhailovskii, and E. S. Tsapelkin, Quasi-linear relaxation of fast ions moving transverse to a magnetic field, *Plasma Phys.*, **13**, 1111-1116, 1971.
- McMahon, W., R. Salter, R. Hills, and D. Delorey, Measured electron contribution to shuttle plasma environment, paper presented at the Shuttle Environment and Operations Meeting, Am. Inst. of Aeronaut. and Astronautics, Washington, D. C., October 31, 1983.
- Mendillo, M., Modification of the ionosphere by large space vehicles,

- in *Space Systems and Their Interactions With Earth's Space Environment*, edited by H. B. Garrett and C. P. Pike, pp. 99-117, American Institute of Aeronautics and Astronautics, New York, 1980.
- Mendillo, M., G. S. Hawkins, and J. A. Klobuchar, A sudden vanishing of the ionospheric F region due to the launch of Skylab, *J. Geophys. Res.*, **80**, 2217-2228, 1975.
- Murphy, G. B., S. D. Shawhan, and J. S. Pickett, Perturbations to the plasma environment induced by the orbiter's maneuvering thrusters, paper presented at the Shuttle Environment and Operations Meeting, Am. Inst. of Aeronaut. and Astronautics, Washington, D. C., October 31, 1983.
- Narcisi, R., E. Trzcinski, G. Frederico, L. Wlodyka, and D. Delorey, The gaseous and plasma environment around space shuttle, paper presented at the Shuttle Environment and Operations Meeting, Am. Inst. of Aeronaut. and Astronautics, Washington, D. C., November 2, 1983.
- Neupert, W. M., et al., Science on the space shuttle, *Nature*, **296**, 193-197, 1982.
- Papadopoulos, K., On the shuttle glow (The plasma alternative), *Radio Science*, **19**, 571-577, 1984.
- Pongratz, M. B., Large scientific releases, *Adv. Space Res.*, **1**, 253-273, 1981.
- Pongratz, M. B., G. M. Smith, C. D. Sutherland, and J. Zinn, Lagopedo-F-region ionospheric depletion experiments, in *Effect of the Ionosphere on Space and Terrestrial Systems*, edited by J. M. Goodman, pp. 438-441, U.S. Government Printing Office, Washington, D. C., 1978.
- Rote, D. M., Environmental effects of space systems: A review, in *Space Systems and Their Interactions With Earth's Space Environment*, edited by H. B. Garrett and C. P. Pike, pp. 3-53, American Institute of Aeronautics and Astronautics, New York, 1980.
- Shawhan, S. D., G. B. Murphy, and D. L. Fortna, Measurements of electromagnetic interference on OV102 Columbia using the Plasma Diagnostics Package, *J. Spacecraft and Rockets*, **21**, 392-397, 1984a.
- Shawhan, S. D., G. B. Murphy, and J. S. Pickett, Plasma Diagnostics Package initial assessment of the shuttle orbiter plasma environment, *J. Spacecr. Rockets*, **21**, 387-391, 1984b.
- Sjolander, G. W., and E. P. Szuszczewicz, Chemically depleted F₂ ion composition: measurements and theory, *J. Geophys. Res.*, **84**, 4393-4399, 1979.
- Smiddy, M., W. Sullivan, D. Girouad, and P. Anderson, Shuttle electrical environment, paper presented at the Spacecraft Environmental Interactions Technology Conference, U.S. Air Force/Nat. Aeronaut. and Space Admin., Colorado Springs, Colorado, October 4, 1983.
- Zinn, J. and C. D. Sutherland, Effects of rocket exhaust products in the thermosphere and ionosphere, *Space Sol. Power Rev.*, **1**, pp. 109-132, 1980.
-
- C. K. Goertz, W. S. Kurth, G. B. Murphy, and J. S. Pickett, Department of Physics and Astronomy, University of Iowa, Iowa City, IA 52242.
- S. D. Shawhan, Code EE, NASA Headquarters, Washington, D. C., 20546.

(Received February 27, 1984;
revised November 11, 1984;
accepted November 13, 1984.)



MEASUREMENTS OF PLASMA PARAMETERS IN THE VICINITY OF THE SPACE SHUTTLE

G. MURPHY, J. PICKETT, N. D'ANGELO and W. S. KURTH

Department of Physics and Astronomy, The University of Iowa, Iowa City, IA 52242, U.S.A.

(Received 29 April 1986)

Abstract—A Langmuir probe flown as part of the Plasma Diagnostics Package aboard the third space shuttle flight was used to determine electron densities, temperatures and plasma potential in the vicinity of the shuttle orbiter. Measurements taken both in the cargo bay and 10 m above the cargo bay on the Remote Manipulator System arm are consistent with small satellite and laboratory results in that reduced densities and elevated temperatures are observed in the shuttle wake. The primary difference in the shuttle measurements is one of magnitude, i.e. orders of magnitude density decreases and factor of five temperature enhancements.

Analysis of data taken in $\Delta N/N$ mode (used to measure plasma density fluctuations) reveals large plasma fluctuations with a significant spectral component up through the lower-hybrid frequency. The peak amplitude of this $\Delta N/N$ turbulence can be as high as a few percent, and the most intense turbulence seems to occur near regions with a steep gradient in plasma pressure.

1. INTRODUCTION

Measurements of temperature and densities behind a body immersed in a flowing plasma which have thus far been reported in the literature can be divided into three categories: (1) those obtained in the laboratory under controlled conditions, (2) those obtained in the wake of small scientific satellites, and (3) those recently reported from experiments aboard the space shuttle (Raitt *et al.*, 1984; Siskine *et al.*, 1984). This paper will discuss the plasma parameter measurements made by the Plasma Diagnostics Package (PDP) which flew as part of the third shuttle payload.

Subdividing plasma measurements in this way is quite natural, since these categories correspond to an ever-increasing ratio of object size to Debye length. Laboratory measurements have typically achieved scaling in the range of 1–50 λ_D (Stone, 1981). Measurements from small satellites (e.g. Samir and Willmore, 1965) and the *Gemini-Agena* (Troy *et al.*, 1970) rocket experiment have been in a range of up to $\sim 100 \lambda_D$, while the space shuttle has typical dimensions on the order of 1000 λ_D . For the *F*-region in which the orbiter typically flies, densities of 10^6 cm^{-3} and temperatures of 1000 K are common. There are some other variables which complicate the picture and make comparisons between the small satellite and shuttle cases more difficult; namely, the small satellites are typically conducting bodies, whereas the shuttle is primarily an insulator on surfaces exposed to the plasma; also, there is evidence to indicate that the shuttle outgassing products constitute a large portion

of the neutral atmosphere (Shawhan *et al.*, 1984) near the vehicle. This neutral gas may be enough to alter details of the wake structure. Despite these difficulties, measurements by the PDP Langmuir probe indicate an overall consistency with the information provided by data from small satellites and laboratory experiments.

This paper will discuss in detail the methodology of the shuttle observations and then summarize the results within the framework of previous experiments.

2. INSTRUMENTATION

The PDP Langmuir probe is a relatively simple instrument which has two operational modes, the first as an electron density/temperature measurement tool, the second as a diagnostic for $\Delta N/N$ fluctuations in electron density over the frequency range 0.5–40 Hz. The instrument uses a 6 cm diameter gold-plated spherical sensor mounted on a fixed boom approximately 30 cm from the body of the PDP. The location of the probe is illustrated in Fig. 1. The electronics operates in two modes, alternated by a timing signal generated by the PDP spacecraft encoder. The total cycle lasts for approximately 13 s and consists of a 12-s "lock" period where the probe is held at +10 V relative to the PDP chassis, followed by a 1-s 120-sample sweep from +10 to -5 V. Figure 2 illustrates this cycle. During the lock cycle, the probe is in the $\Delta N/N$ mode and the output current fluctuations are sensed by a logarithmic sensor and sampled through

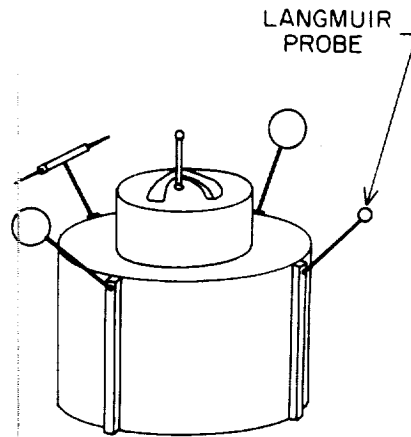


FIG. 1. A SIMPLIFIED DIAGRAM OF THE PDP STRUCTURE SHOWS THE LOCATION OF THE LANGMUIR PROBE ON A BOOM APPROXIMATELY 30 cm IN LENGTH.

three filters: 1 Hz low pass, 1–6 Hz bandpass, and 6–40 Hz bandpass. A fourth filter (30 Hz high pass) routes the output to a wide-band receiver and spectrum analyzer which, when in the Langmuir probe mode (51.2 s out of a total sensor switching cycle of 409.6 s), can look at details of the current fluctuations

up to a frequency of 178 kHz. The sample rates of the filters were adjusted such that the Nyquist criterion was satisfied, that is 5, 20 and 120 Hz, respectively, for the first three filters. The 30 Hz high-pass filter which was sampled by the spectrum analyzer was peak detected and each of the 16 channels sampled once each 1.6 s.

The voltage sweep cycle of the probe had a step size of 0.125 V, which is relatively coarse for a plasma with ambient temperatures of 1000 K and presented some difficulties which will be discussed later. The probe was sampled once each voltage step. Since the probe steps from +10 to –5 V and then jumps back to +10 V, it was not possible to check for possible hysteresis effects on the probe. The output of this mode is a voltage, proportional to log of the current, vs sweep voltage. Unlike the probe described by Raitt *et al.* (1984), no differentiation takes place; the probe, in fact, works much like manually swept probes used in the laboratory giving the I – V (current–voltage) curve directly.

A word is in order about the reference potential for the Langmuir probe. The voltage on the probe is referenced to the PDP chassis. The PDP chassis is grounded to the orbiter both while in the payload bay and on the Remote Manipulator System (RMS) arm.

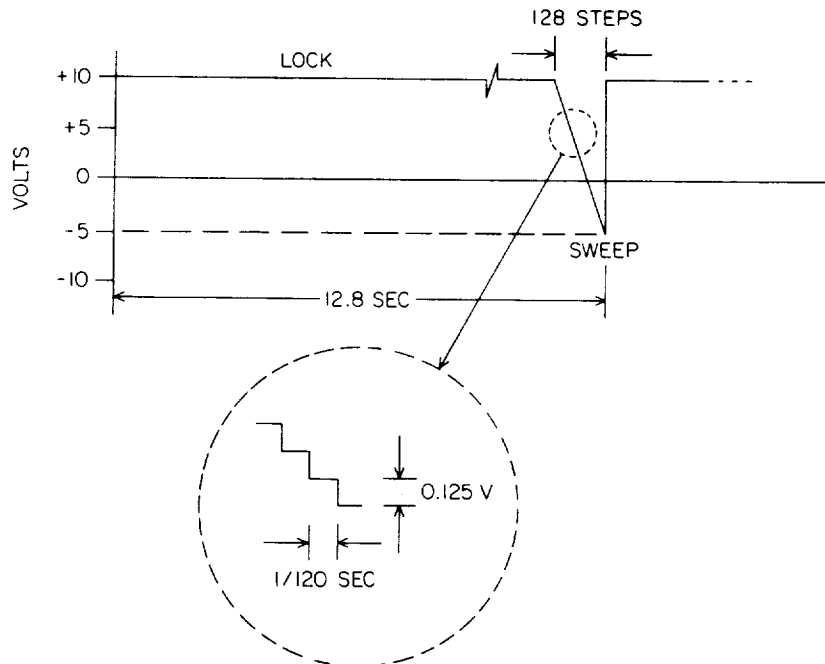


FIG. 2. THE LANGMUIR PROBE INSTRUMENT CYCLE HAD A PERIOD OF 12.8 s (EIGHT MAJOR DATA FRAMES). At the end of the cycle, a sweep consisting of a series of 0.125 V steps is driven by a 120 Hz clock. The wide sweep range accommodates swings in the PDP potential due to charging effects.

TABLE I. LANGMUIR PROBE PERFORMANCE PARAMETERS

Current sensor	0.1 μ A–1 mA
T_e	(800–5000 K)
n_e	(10^3 – 10^7 cm $^{-3}$)
$\Delta N/N$	
< 1 Hz	1.8–460%
1–6 Hz	0.12–30%
6–40 Hz	0.012–3%
> 30 Hz (spectrum analyzer)	–30 to –80 db $\Delta N/N$

Thus the probe is swept with respect to orbiter chassis ground and a measurement of the potential of the vehicle with respect to the plasma is possible. This is relevant considering that the orbiter is primarily an insulating body and its principal conducting surfaces are the engine nozzles at the rear of the vehicle.

The sensitivities and dynamic ranges of the two modes of the Langmuir probe are summarized in Table I. It should be noted that it is difficult to state an absolute temperature measurement range since that range is density dependent. For that reason, the current sensitivity of the log current sensor is given as the primary specification, with temperature and density dynamic ranges in parentheses.

3. DATA ANALYSIS

The process of deriving electron temperature, density and plasma potential from a Langmuir I - V characteristic is straightforward in the ideal case but has several limitations in practice that the reader needs to be aware of in order to fairly judge the results of this research.

As noted previously, the Langmuir probe is stepped from +10 to –5 V in 0.125 V increments with its current sampled at each step. Even though this voltage range extends well below the floating potential, the electronics uses a transistor's base-emitter junction to detect directly the log of the current and therefore cannot measure negative (ion) current. Thus, we see two fundamental limitations in the probe design which were engineering compromises necessary for operation in the uncertain shuttle environment.

The relatively large step size (0.125 V) implies there will not be very many samples of current in the retardation region for typical ionospheric electron temperatures of ~ 0.1 eV. For example, at a density of $\sim 10^6$ cm $^{-3}$, the electron current at plasma potential for our probe would be $I_p \cong 10^{-3}$ A. Considering that the minimum detectable current for the electronics is 10^{-7} A approximately six points would lie on the electron retardation region of the charac-

teristic. Clearly at densities $< 10^3$ cm $^{-3}$ it would not be possible to accurately determine temperatures. The software used to calculate temperature and density thus uses a number of first and second derivative tests to determine if a statistically significant number of points lie beyond the "knee" of the curve and in the retardation region of the characteristic. If statistically good fits are not possible, the analysis of that sweep is halted and the data are written to a "bad record" file where records are examined further by hand. Comparison of machine calculations to those done by hand for a large number of sweeps over the full range of these data were used to refine the "intelligence" of the software to a point where high confidence can be placed in the results.

The second limitation, the fact that the probe does not measure ion current, results in an underestimate of temperature and overestimate of density at high ambient densities. To see why this is so we look at two sample sweeps in detail.

Figure 3 illustrates a log- I vs V curve taken at 21:47:38 U.T. yielding electron "density" of $\sim 1 \times 10^4$ and "temperature" of ~ 2600 K. In this particular case, the dotted lines are fit by the computer routine and the plasma density (proportional to saturation current), temperature and plasma potential determined accordingly. What is the effect of the unmeasured ion current? Once the measured current falls below a certain threshold, the ion current may become a significant portion of it. Since the ion current subtracts from the electron current, the measured current is less than it would be if only electron current were present, thus increasing the slope of the curve and causing the computed temperature to be too low. An upper bound for the ion current can be calculated as $I_i = A \cdot q \cdot n_i \cdot v_s$, where A is the projected area of the probe, n_i the ion density, q the elementary charge and v_s the shuttle velocity through the plasma. For the case in Fig. 3, the ion current would be $3.6 \times 10^{-12} \cdot n_i$ or $\sim 3.6 \times 10^{-8}$ A, a correction which is below the instrument sensitivity. As one can see from Fig. 3, the corrected and uncorrected slopes are indistinguishable.

Since the ion current is variable—it depends on ram-wake conditions, detailed geometry in the payload bay, etc.—it was found that no consistently accurate correction could be calculated and implemented under all conditions. Therefore, the decision was made to let the software fit the data uncorrected for ion current, and determine instead what worst-case effect this has on the calculated "temperature" and "density". In these data, presented in the next section, the reader will find that, under ram conditions, densities are high by about a factor of two

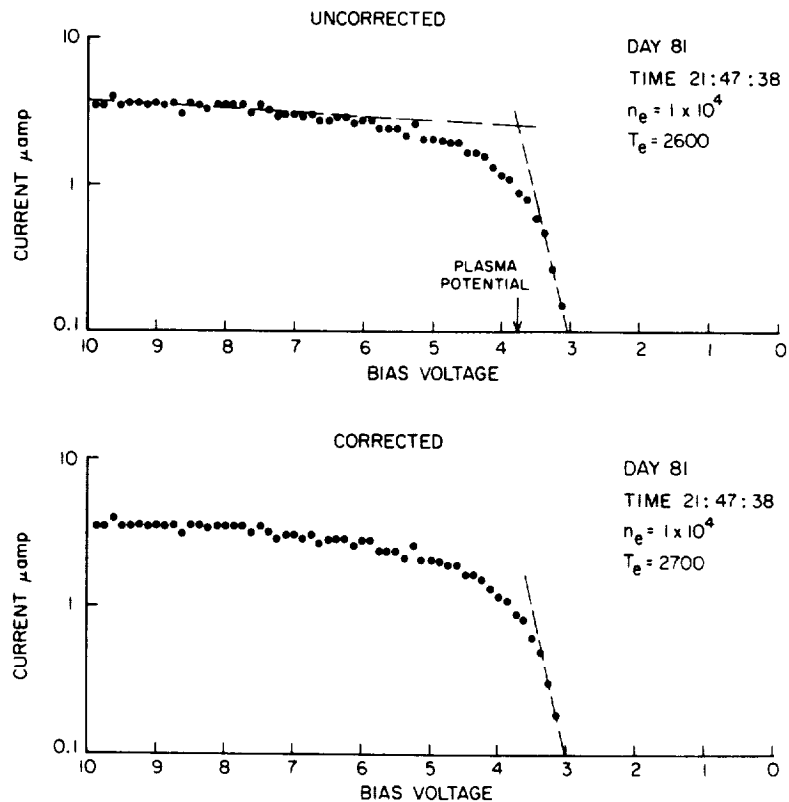


FIG. 3. A TYPICAL LANGMUIR CHARACTERISTIC IS GIVEN FOR A DENSITY OF 1×10^4 . Note how density, temperature and plasma potential are determined by using two straight-line fits. This method slightly overestimates plasma potential but does so fairly consistently by a few KT_{ev} . In this case, the lower curve corrected for ion current is not significantly different from the uncorrected version.

and temperatures correspondingly low by ambient daytime ionosphere standards. It is important to realize that no elaborate physics need be invoked to explain these results; it is simply an ion current effect. The above formula can be used to calculate ion current, but one must keep in mind that due to lower ion densities in wake and semi-wake conditions and the fact that ions impacting the probe under these conditions must have a velocity less than v_s , the calculation gives an upper limit valid only in undisturbed plasma flow regions (ram).

Figure 4 illustrates data taken in these ram conditions and shows the effect of correcting for ion current which is not negligible in this case ($I_i \sim 1.4 \times 10^{-5}$ A). A look at the effect under various conditions gives the following general rule for the underestimate of temperature as a function of actual ambient electron density:

$$10^6 \text{ cm}^{-3} \rightarrow 100\%; \quad 10^5 \text{ cm}^{-3} \rightarrow 50\%; \\ \text{and } 10^4 \text{ cm}^{-3} \rightarrow \text{negligible.}$$

These effects are accounted for in the plots of the next section by the dashed lines which illustrate the best mean solution for density and temperature consistent with the above rule.

Fortunately, although extremely low densities cannot be accurately measured and high densities have ion current corrections, the range for most of the interesting physics of the wake region discussed here remains free of instrumental limitations.

4. OBSERVATIONS

We will first present a summary of a representative sample of our observations and then discuss each in detail. Details of the STS-3 flight, where these measurements were made, can be found in Shawhan *et al.* (1984). The important aspects from the point of view of this paper are that the orbiter flew just below the peak in the *F*-region in a 240 km circular orbit at an inclination of 37° . Measurements presented here

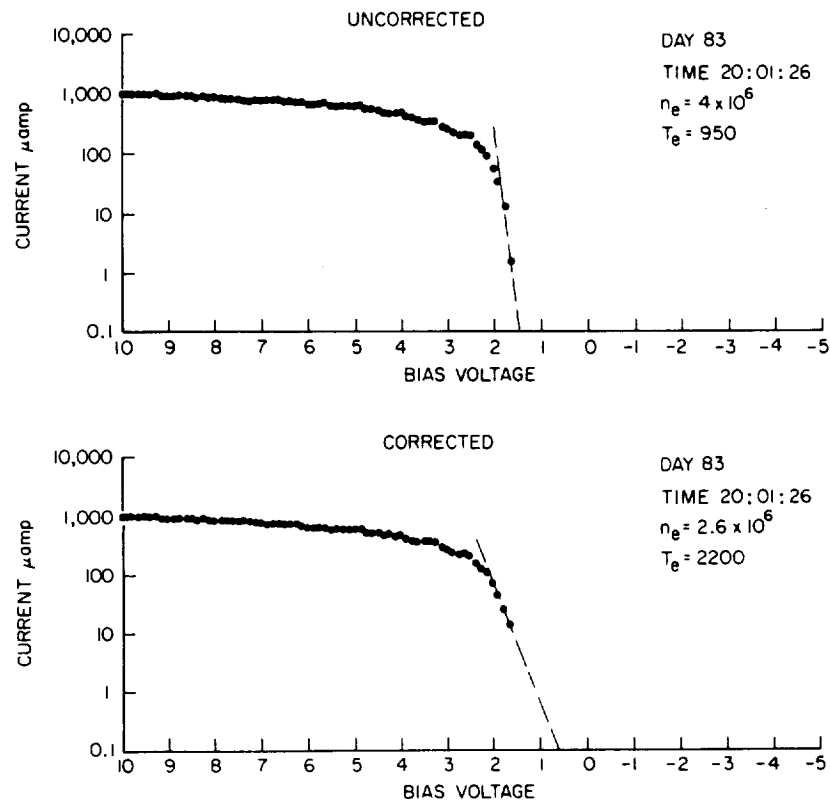


FIG. 4. A LANGMUIR LOG I VS V CURVE AT A DENSITY OF 10^6 NEEDS SIGNIFICANT CORRECTION FOR ION CURRENT.

In this case, the value of ion current is $\sim 1.4 \times 10^{-5}$ A so no data points are available below that value in the corrected curve. The correction of slightly more than a factor of two in temperature implies a corresponding decrease in the estimate of density since $n_e \propto 1/\sqrt{T_e}$.

were taken either while the PDP was stowed in the cargo bay or while it was deployed on the RMS arm 5–10 m above the bay. The location of the PDP in these two cases is illustrated in Figs 5 and 6.

Electron temperature and density are shown as a function of universal time (U.T.) in Fig. 7 for the case of the PDP in the cargo bay. The obvious periodic structure which repeats four times across the plot is due to the "ram-wake cycle" which resulted from a slow orbiter roll about its x -axis (nose-to-tail axis). In order to relate the observed density and temperature variations to the vehicle attitude, we need to set up a coordinate system to describe the direction of plasma flow. This coordinate system is illustrated at the bottom of Fig. 8, which is the attitude plot for the same time period as Fig. 7. The "pitch" angle of plasma flow is θ_1 . When $\theta_1 = 0^\circ$, the plasma flows at the orbiter from its underside; when $\theta_1 = 180^\circ$, the plasma is streaming directly down into the cargo bay. The immediate correlation between plasma density

and θ_1 is evident when comparing Figs 7 and 8. The azimuth angle of the plasma flow is θ_2 and is measured counterclockwise from the nose (as viewed from above the orbiter). Sensitivity to θ_2 is evident only when the angle θ_1 is near 90° . This is primarily due to the vertical stabilizer and other large structures in the cargo bay near the PDP.

The magnitude of the density depletions in Fig. 7, which is greater than three orders of magnitude, is striking. It should be recalled that the computational method used to determine density and temperature is halted when too little of the I - V curve is available for unambiguous interpretation (see Section 3). The probe current is usually at least one order of magnitude above the probe threshold of detectability at this point but continues to fall rapidly until no current is detected at any sweep voltage. Thus, the three orders of magnitude depletion is a conservative estimate of the density change and in reality the $\alpha = N_{\text{wake}}/N_{\text{ambient}}$ probably extends into the 10^{-4} or 10^{-5} range. It should

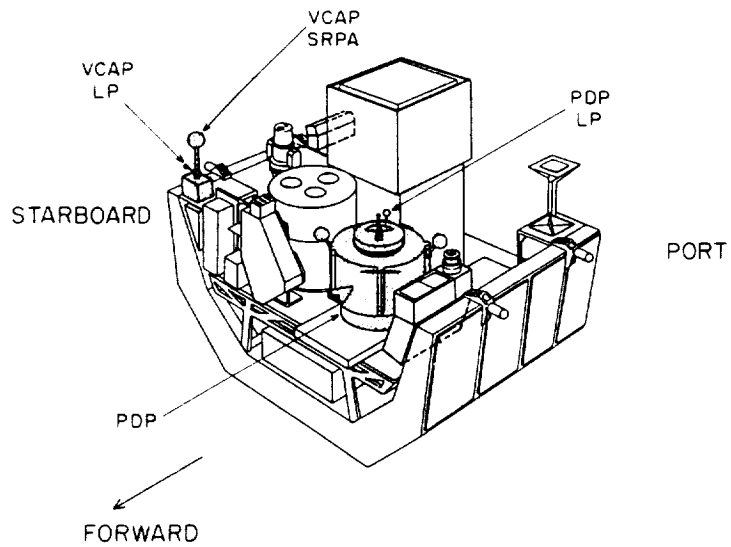


FIG. 5. THE OSS-1 PAYLOAD FOR THE THIRD SHUTTLE FLIGHT HAD THE PDP POSITIONED SUCH THAT THE LANGMUIR PROBE WAS APPROXIMATELY AT STILL LEVEL IN THE CARGO BAY. The VCAP instrumentation is also highlighted. Note that large structures such as the Thermal Cannister Experiment, only inches from the Langmuir probe, complicate geometry in the analysis of plasma flow in the payload bay.

be noted in Fig. 7 that the dotted lines represent a correction for ram ion current to the probe and no real density enhancement or temperature depression in ram is believed to be present, compared to standard ionospheric conditions.

The next and perhaps more interesting result is the remarkable temperature enhancement seen as the probe enters the wake region. The fact that the temperature shows no evidence of "leveling off" at a stable value before calculations are stopped (refer to the gaps in the data at ~ 21:30 and 22:08 U.T.) implies that temperature may rise considerably higher in the

extreme rarefaction region. Since the probe voltage has a step size of 0.125 V, it is inherently less accurate at determining low temperatures in the range of 1000 K (0.1 eV) (see Section 3), but that accuracy improves as the temperature rises and statistical fits to the straight line portion of the $I-V$ curve are very good. In summary, although the absolute accuracy of the probe in measurements of temperature is probably no better than 50%, and the low end temperatures are underestimated, the trend in Fig. 7 is apparent and cannot be attributed to instrumental effects.

To determine the variation of the density depletion in the wake region as a function of distance behind the vehicle, it is useful to compare the above results obtained while the PDP was in the payload bay with those obtained while on the RMS at a distance of 10 m above the payload bay. This is, of course, equivalent to having a probe further behind the obscuring plate in the laboratory experiments or mounting a sensor on the boom of a small satellite.

Figure 9 shows data from one orbit while the PDP is on the RMS arm. Figure 10 is the corresponding orbiter attitude. Note that the density rarefaction from ~17:00 to 17:20 U.T. is not nearly as pronounced as those in Fig. 7 and that the temperature enhancement is also less dramatic. The fine structure in the plot (sharp peaks of a few minutes duration) correlates well with the predicted wake of the PDP

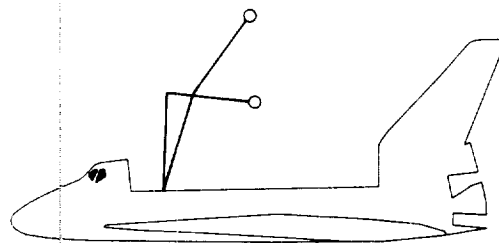


FIG. 6. THE LOCATION OF THE PDP ABOVE THE CARGO BAY FOR THE "RMS" DATA ILLUSTRATED IN THIS PAPER PLACES IT WELL OUT OF THE WAY OF STRUCTURES IN THE BAY ITSELF, MAKING THE ORBITER BODY THE DOMINANT OBJECT IN ALL WAKE ANALYSIS.

(The RMS is 50 ft long when fully extended.)

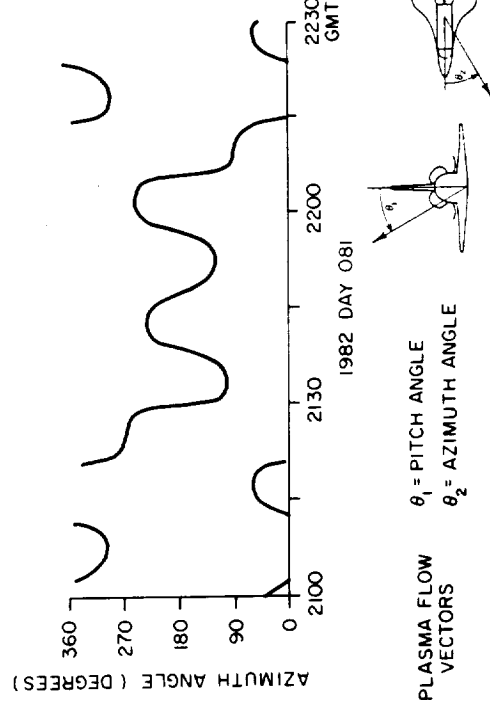
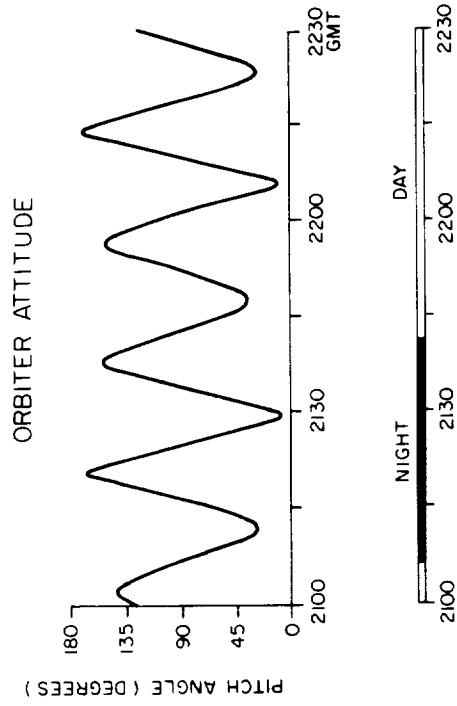


FIG. 8. θ_1 AND θ_2 INDICATE THE PLASMA FLOW VECTORS FOR THE TIME PERIOD ILLUSTRATED IN FIG. 7. The ram-wake effect is dominated by θ_1 , the "pitch" angle or co-elevation of the flow. When θ_1 is less than 90° , the flow is from underneath the orbiter and the PDP is in the plasma wake. θ_2 has little effect except when θ_1 is near 90° .

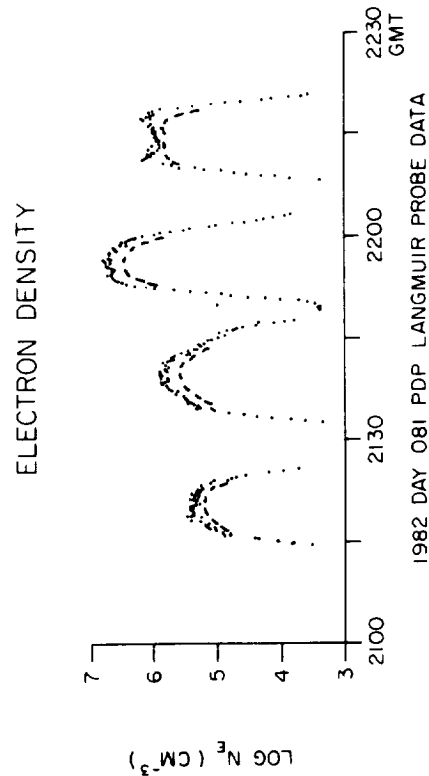
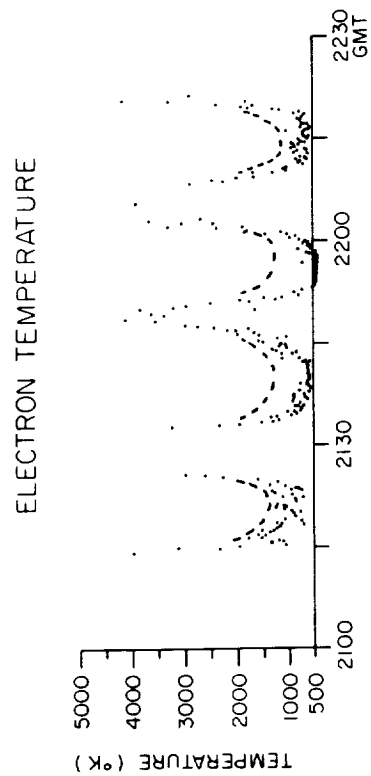


FIG. 7. ELECTRON TEMPERATURE AND DENSITY MEASUREMENTS TAKEN WHILE THE PDP IS IN THE ORBITER BAY ARE DOMINATED BY THE WAKE STRUCTURE RESULTING FROM A PASSIVE THERMAL CONTROL (PTC) ATTITUDE, WHICH ROLLS THE ORBITER ABOUT AN AXIS THROUGH ITS NOSE AT A RATE OF $24^\circ/\text{min}$. The low-end temperatures are underestimated by approximately a factor of two by processing software (see Section 3 for details). Dotted lines represent ion current corrections.

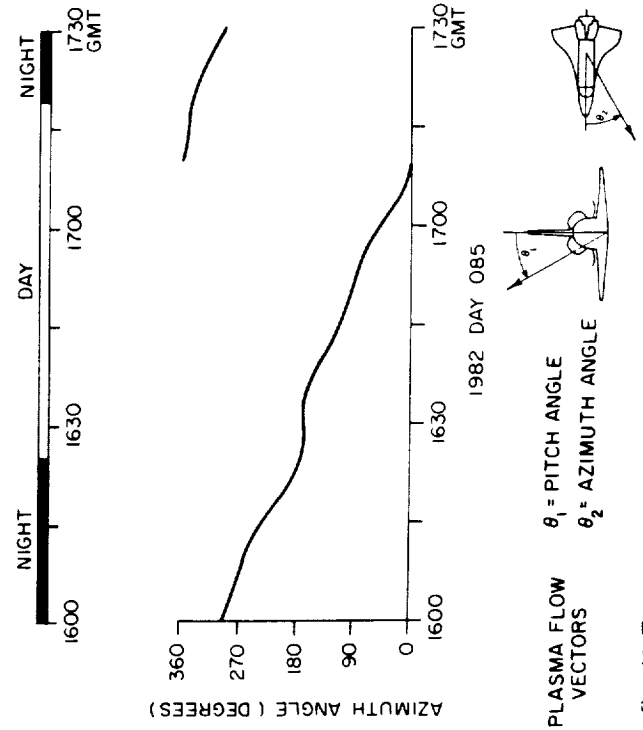
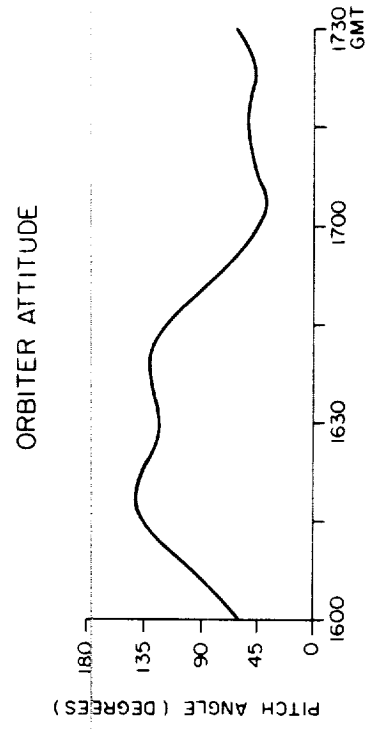


FIG. 10. THE ORBITER ATTITUDE DURING THE TIME INTERVAL FOR DATA SHOWN IN FIG. 9 WAS "NOSE-TO-SUN" WITH AN 8°min^{-1} ROLL. This resulted in a once-per-orbit "ram wake" cycle as illustrated by the θ_1 and θ_2 plasma flow vectors.

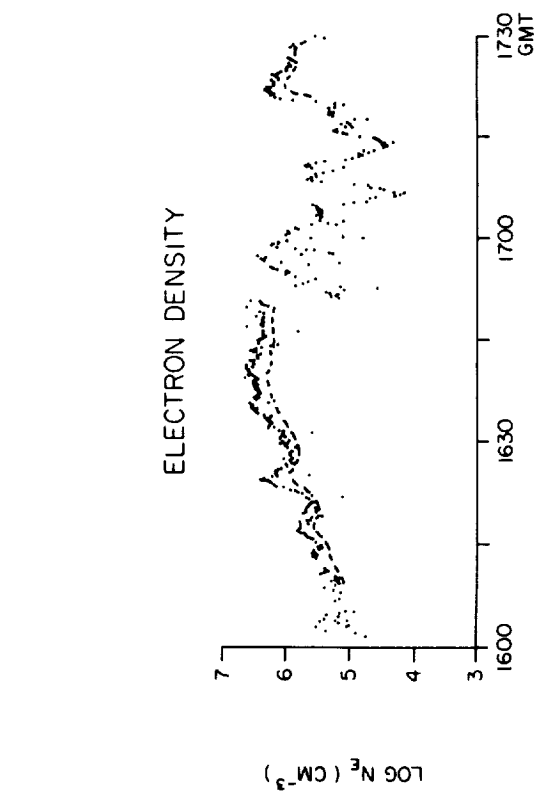
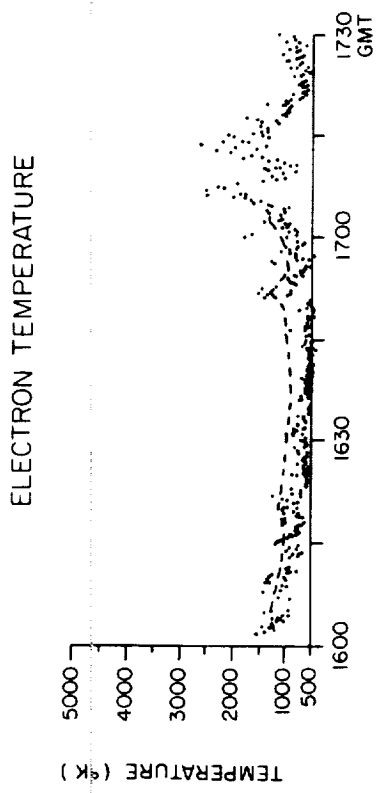


FIG. 9. ELECTRON TEMPERATURE AND DENSITY MEASUREMENTS ON THE RMS DO NOT SHOW THE DEEP WAKE OBSERVED IN THE PAYLOAD BAY, BUT INDICATE THE SUPERPOSITION OF A SHALLOWER ORBITER WAKE COMBINED WITH A WAKE DUE TO THE PDP ITSELF AS IT IS ROTATED ON THE RMS. Note that low end temperatures are underestimated (see Section 3 for details). Dotted lines represent corrections due to ion current.

and RMS. Since the PDP was being rotated while on the RMS, the orientation of the Langmuir probe with respect to plasma flow around the PDP and RMS (angle of attack) varies, producing this fine structure variation. It would be useful to compare these data to those from the small satellite category since the PDP is approximately 1 m in diameter and the RMS is approximately 0.3 m in diameter. Again, as with Fig. 7, the dotted line represents temperature and density measurements corrected for worse-case ion current.

The third set of raw data which this paper will address is the $\Delta N/N$ output. The plasma turbulence (Raitt *et al.*, 1984) present in the vicinity of the shuttle has received some attention, and understanding its nature can give us greater insight into the special problems associated with large vehicles interacting with the ionospheric plasma. Figure 11(a) is a plot of the RMS value (averaged over 1.6 s) of $\Delta N/N$ in the 6–40 Hz region. This plot covers the same time period as Figs 7 and 8 and was taken while the PDP was in the orbiter's payload bay. The turbulence in this

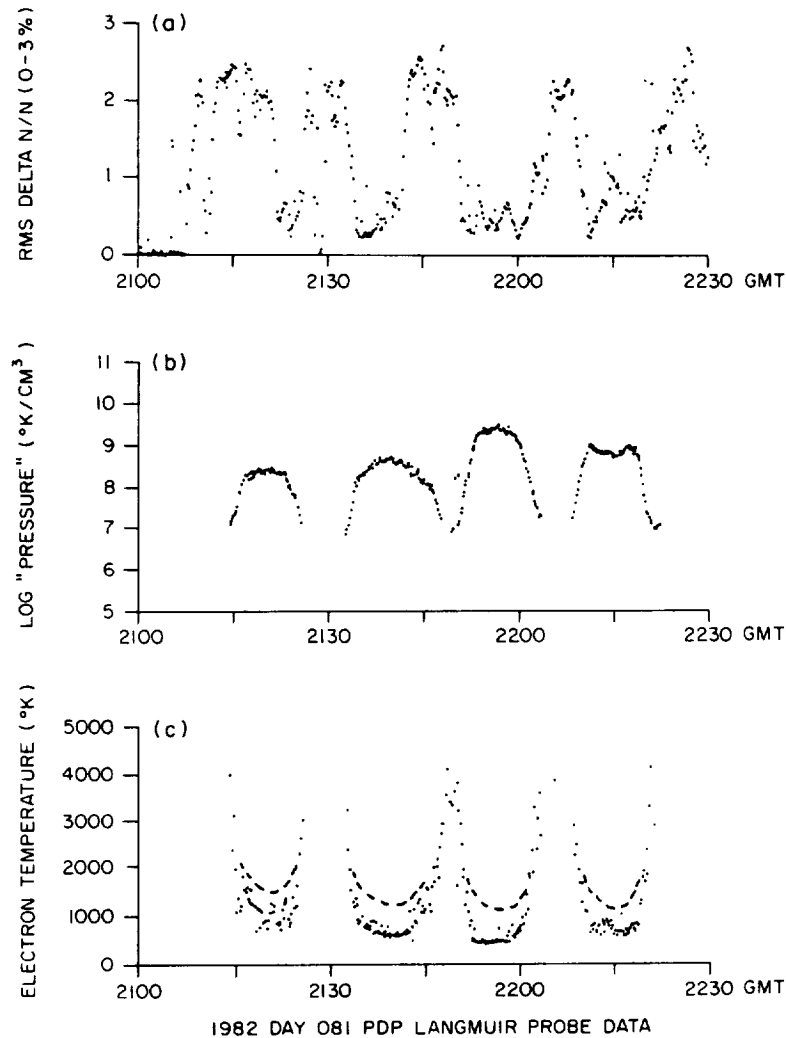


FIG. 11. (a) THE RMS VALUE OF THE PERCENTAGE OF DENSITY FLUCTUATIONS ($\Delta N/N$) IN THE FREQUENCY RANGE 6–40 Hz IS PLOTTED FOR THE SAME TIME PERIOD AS THE FIG. 7 DATA.

Note the peaks have a "double-humped" character with maxima at rising and falling edges of the electron temperature curve.

(b) DENSITY AND TEMPERATURE IN THE PLASMA YIELDS A VALUE PROPORTIONAL TO ELECTRON PRESSURE.

Note that maxima in (a) correlate well with the steepest pressure gradients.

(c) THE TEMPERATURE DATA FROM FIG. 7 HAVE BEEN REPLOTTED FOR EASE OF COMPARISON TO (a).

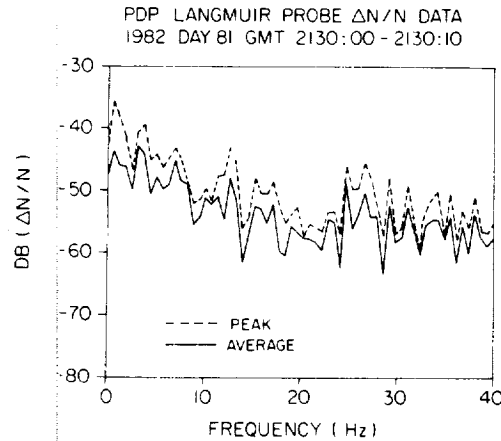


FIG. 12. A FFT OF THE $\Delta N/N$ DATA FOR THE FREQUENCY RANGE 1–40 Hz SHOWS NO PARTICULAR STRUCTURE. This plot is typical of data taken during a time of moderate turbulence.

frequency range is not observed to be highest in ram as reported by Raitt *et al.* (1984) but highest, generally, in a transition zone between ram and wake. For ease of comparison, the temperature and pressure are also shown in Fig. 11, and one can see a "double-humped" character to the noise, the two peaks appearing more or less at the beginning and end of the wake boundary.

In order to understand the nature of this turbulence, its frequency spectrum needs to be examined as well. Figure 12 is a plot of the Fast Fourier Transform (FFT) of the turbulence from 1 to 40 Hz. The spectrum shows little structure and a typical magnitude of $\Delta N/N$ at any given frequency is less than 1%. Extended frequency analysis up to 178 kHz has been done by using the special Langmuir probe mode on the spectrum analyzer. The noise shows a relatively flat spectral response up through the lower hybrid resonance frequency. This extended analysis has been combined with that at low frequency and a typical spectrum shown in Fig. 13.

5. DISCUSSION AND COMPARISON WITH PREVIOUS RESULTS

Since measurements of the wake characteristics of very large objects are quite new, an assessment needs to be made of how these observations stand against the following: (1) instrumental or systematic problems, (2) other measurements, and (3) predictions from theory and the scaling of observations made in a regime where the object is much smaller.

The Langmuir probe instrument itself seems to perform well. The probe is believed to be quite clean due

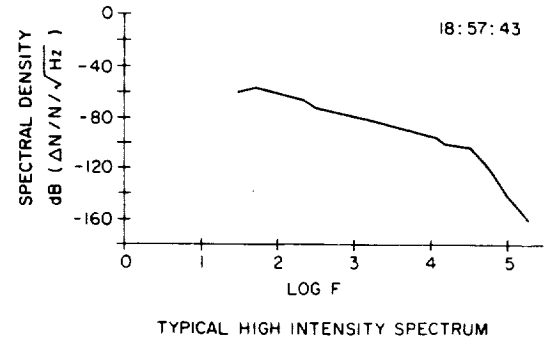
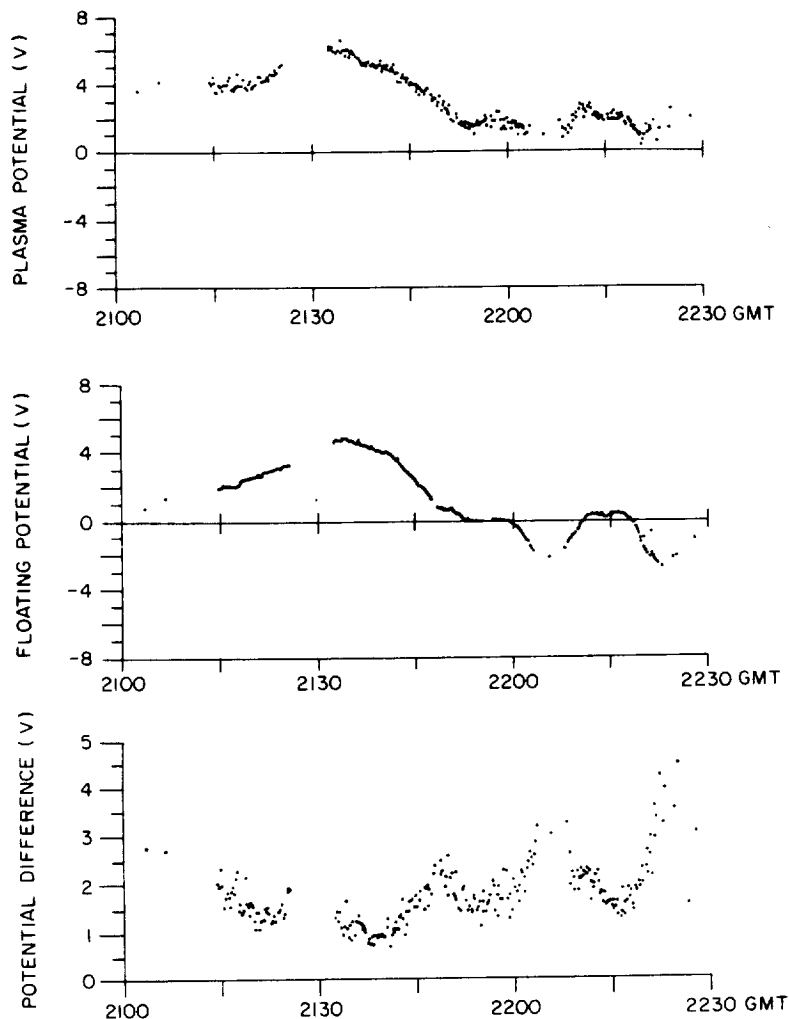


FIG. 13. EXTENDED FREQUENCY ANALYSIS OF THE $\Delta N/N$ SPECTRUM FOR A TYPICAL SAMPLE OF THE NOISE SHOWS A RELATIVELY FLAT SPECTRUM UP TO APPROXIMATELY 30 kHz. This data was taken in the payload bay (D.O.Y. = 083).

to atomic oxygen bombardment. It is also relevant that there seemed to be no significant shift in data over the time frame of the mission, leading one to believe the probe condition is a constant. Although absolute accuracy is difficult to achieve, the probe gives (after correcting for ion current) temperatures and densities within approximately 50% of the expected values at peak *F*-region altitudes and since it is the change in density and temperature which is significant here, the absolute accuracy is not at issue. Further evidence that the probe is measuring plasma characteristics correctly is given in Fig. 14. Here we have plotted the plasma potential as measured by the Langmuir probe, the floating potential as measured by dual-floating probes on the PDP and the difference between plasma and floating potential (ΔV) for the same time interval as the data plotted in Fig. 7. Note that the "cusps" or increases in ΔV correspond to the wake region and are consistent with the increasing plasma temperature observed there. These regions of increasingly negative plasma potential have been observed in the laboratory and are a principal mechanism driving the self-similar ion expansion that has been studied by several investigators (Raychaudhuri *et al.*, 1986). Thus, even without actually measuring the slope of the $\log I$ vs V curve to determine temperature, we can independently verify that temperature must, in fact, be increasing at these times.

Comparison with other measurements must first take place where spacecraft scales are similar. The *Gemini/Agena*, *Explorer 31* and *AE-C* spacecraft (Medved, 1969; Samir and Wrenn, 1972; Samir and Fontheim, 1981) were similar in size to the PDP and sampled regions of similar plasma density at comparable Mach number. The temperature and density data shown in Fig. 9 while the PDP is on the RMS arm show small-scale depletions in density (~50%)



1982 DAY 081 DC AND LANGMUIR PROBE DATA

FIG. 14. THE TOP TWO PANELS ARE A COMPARISON OF THE PLASMA POTENTIAL DATA MEASURED BY THE LANGMUIR PROBE WITH THE FLOATING POTENTIAL MEASURED BY THE SPHERICAL FLOATING PROBES. THE THIRD PANEL IS A PLOT OF PLASMA POTENTIAL MINUS FLOATING POTENTIAL AND SHOULD BE PROPORTIONAL TO THE PLASMA TEMPERATURE. NOTE THE 1-2 V OFFSET IS CONSISTENT WITH THAT EXPECTED IN THIS TEMPERATURE DENSITY REGIME BUT IS PERIODICALLY ENHANCED DURING WAKE ENCOUNTERS.

and increases in temperature (50–100%), which are entirely consistent with the previous results on small spacecraft.

Comparison of our results to those of Siskind *et al.* (1984), which were also made on the *STS-3*, shows both experiments agree on the magnitude of electron density depletions. However, while the PDP Langmuir probe indicates an elevated temperature in wake, Siskind *et al.* (1984) interpret the VCAP Langmuir probe data to indicate an elevated temperature in ram. Although the PDP and VCAP instruments were not always operating simultaneously, data were taken

under similar circumstances and general agreement would be expected. Samir *et al.* (1986) have systematically compared the results of laboratory and small satellite experiments, as well as the predictions of several theories, to the Siskind *et al.* (1984) data. They state that "No electron temperature enhancement, known to the authors, has been found for ram conditions on small satellites. Therefore, we submit that the results of Siskind *et al.* (1984) and Siskind (1983) are in contrast with all earlier results." While the PDP Langmuir probe temperature measurements are contrary to the Siskind *et al.* (1984) measurements.

they do agree with the majority of other experimental results.

It is difficult to scale measurements from bodies of the 50–100 λ_D size range to those of the orbiter, but the enhancement in T_e has been seen to be a function of body size up through the *Gemini-Agena* experiment. Plasma chamber experiments performed by Oran *et al.* (1975), Illiano and Storey (1974) and Stone (1981) all indicate temperature enhancement in the near wake. In particular, Stone (1981) carried the measurements farther downstream and supports the result that the temperature enhancement is a near-wake phenomenon, extending spatially downstream only to about $z = SR_0$, where S = Mach number and R_0 = body size. This is consistent with the comparison made between our pallet and RMS data. At a distance of $\lesssim R_0$ downstream, the density depletion was only two orders of magnitude and the temperature enhancement was only $\sim 100\%$, compared to more than three orders of magnitude density depletions and factors of five temperature enhancement seen in the near wake during pallet measurements. This suggests that a rough scaling law may indeed work for objects the size of the shuttle orbiter, at least for the gross wake structure.

An explanation for the elevated electron temperature observed in the wake of orbiting spacecraft has been addressed by various authors (e.g. Samir and Wrenn, 1972; Troy, 1975; Gurevich *et al.*, 1973). It has been speculated that the hot electrons may result: (1) from a selection effect by the negative potential generally found in the spacecraft wake, or (2) from energization of the electrons by wave-particle interactions in the plasma turbulence present in or near the wake. A third and alternative explanation, which does not involve turbulence, may be along the lines indicated by Fried and Wong (1966) to explain ion cooling when ions from a high potential expand into a low-potential region in a laboratory double-plasma device. In the case of an orbiting spacecraft, electrons reaching the spacecraft within the wake would be nearly adiabatically compressed (and heated) as they enter the low-potential region attached, at the wake, to the spacecraft. Simple estimates indicate that this effect may account for the observed heating.

The final observation to discuss is that of the plasma turbulence. Turbulence similar to that reported herein has been observed in the wake region of other satellites, e.g. *Ariel 1* (Samir and Wilmore, 1965). The PDP Langmuir probe results again seem inconsistent with those of Siskind *et al.* (1984) in that Siskind *et al.* report this turbulence to be greatest in ram, whereas the PDP results show that the turbulence is generally greatest in the transition region between ram and

wake. The key difference in the observations may be due to the spectral content of the noise. Components between 2 and 3 kHz which is the frequency range observed by Siskind *et al.* with the VCAP instrumentation region may show a different ram-wake dependence than those in the 6–40 Hz frequency range plotted in Fig. 12. Since the whole spectrum of turbulence is only available when the 16-channel spectrum analyzer is in Langmuir probe mode (approximately 1 min out of every 8), a study of the spectral dependence vs angle of attack has not been possible.

Acknowledgements—The authors wish to thank Professor D. Gurnett for the use of his potential data and Fahad Jalawi for his hard work in developing a very "smart" code for automation of the Langmuir probe data analysis. Special thanks are extended to Uri Samir for his interest and advice and to Nobie Stone and Ken Wright for helpful discussions in relation to laboratory work. The hard work and special help from the reviewer in calling attention to the ion-current effect has enhanced understanding of the data and added to the strength of the work. This help was greatly appreciated.

This paper was supported by NASA Lewis Research Center Grant NAG3-449. The hardware and flight of the PDP on OSS-1 was supported by MSFC Contract No. NAS8-32807.

REFERENCES

- Fried, B. D. and Wong, A. Y. (1966) *Physics Fluids* **9**, 1084.
 Gurevich, A. V., Pariiskaya, L. V. and Pitaevskii, L. P. (1973) *Sov. Phys. JETP* **36**, 274.
 Illiano, J. M. and Storey, L. R. O. (1974) *Planet. Space Sci.* **22**, 873.
 Medved, D. B. (1969) Rarefied gas dynamics, *Sixth Int. Symp. Proc.* p. 1525.
 Oran, W. A., Samir, U., Stone, N. H. and Fonrhwim, E. G. (1975) *Planet. Space Sci.* **23**, 1081.
 Raitt, W. J., Siskind, D. E., Banks, P. M. and Williamson, P. R. (1984) *Planet. Space Sci.* **32**, 457.
 Raychaudhuri, S., Hill, J., Chang, H. Y., Tsikis, E. K. and Lonngren, K. E. (1986) *Physics Fluids* **29**, 289.
 Samir, U. and Fontheim, E. G. (1981) *Planet. Space Sci.* **29**, 975.
 Samir, U., Stone, N. H. and Wright, K. H., Jr. (1986) *J. geophys. Res.* **91**, 277.
 Samir, U. and Willmore, A. P. (1965) *Planet. Space Sci.* **13**, 285.
 Samir, U. and Wrenn, G. L. (1972) *Planet. Space Sci.* **20**, 899.
 Shawhan, S. D., Murphy, G. B. and Pickett, J. S. (1984) *J. Spacecraft Rockets* **21**, 387.
 Siskind, D. E. (1983) Ph.D. Thesis, Utah State University.
 Siskind, D. E., Raitt, W. J., Banks, P. M. and Williamson, P. R. (1984) *Planet. Space Sci.* **32**, 881.
 Stone, N. H. (1981) The aerodynamics of bodies in a rarefied ionized gas with applications to spacecraft environmental dynamics, NASA Technical Publication 1933.
 Troy, B. E., Jr., Medred, D. B. and Samir, U. (1970) *J. Astronautical Sci.* **18**, 173.
 Troy, B. E., Jr., Maier, E. J. and Samir, U. (1975) *J. geophys. Res.* **80**, 993.

From: Proceedings of the Workshop on Space Technology Plasma Issues in
2001, Jet Propulsion Laboratory, Pasadena, CA, Sept. 24-16, 1986.

**A Review of the Findings of the Plasma Diagnostic Package and Associated
Laboratory Experiments: Implications of Large Body/Plasma
Interactions for Future Space Technology**

Gerald B. Murphy and Karl E. Lonngren

University of Iowa, Iowa City, Iowa 52242

1.0 Introduction

The purpose of this report is to review the discoveries and experiments of the Plasma Diagnostic Package (PDP) on the OSS 1 and Spacelab 2 missions, to compare these results with those of other space and laboratory experiments, and to discuss the implications for the understanding of large body interactions in a LEO plasma environment. The paper is logically divided into three sections. First a brief review of the PDP investigation, its instrumentation and experiments is presented. Next a summary of PDP results along with a comparison of those results with similar space or laboratory experiments is given. Last of all the implications of these results in terms of understanding fundamental physical processes that take place with large bodies in LEO is discussed and experiments to deal with these vital questions are suggested.

2.0 PDP instrumentation and experiments

The PDP is a small cylindrical satellite with a complement of instruments designed to measure plasma density and temperature, give ion composition, temperature and flow direction, provide complete electron and ion distribution functions, and measure electron flux from electron beams. In addition to these comprehensive particle measurements the PDP contains instrumentation to provide a complete set of single axis wave and field measurements. Waves (both electric and magnetic) are measured from approximately 10^1 to 10^5 hz and electric fields are measured both at DC and from 10^1 to 10^7 hz. A complete description of the PDP instrumentation is available in Shawhan 1984c.

The PDP was designed not only as a satellite, but because it was to be flown and deployed from the Orbiter; it was also capable of measuring the plasma environment in and around the orbiter bay by being maneuvered through various positions on the Shuttle Remote Manipulator System (RMS) arm. The initial experiments and measurements made by the PDP on the OSS-1 (STS-3) Mission were all made either in the payload bay on a pallet or within approximately 10 meters of the bay on the RMS. As will be seen in the next section these early shuttle experiments helped provide insight into the shuttle orbiter environment, conducted the first orbiter-based active plasma experiments, and provided some of the first insights in large body interactions at LEO. In addition, the OSS-1 experiments provided the baseline from which many of the future detailed interaction issues could be addressed. Spacelab 2, which repeated (with some modifications) some of the OSS-1 experiments and extended the range of interaction studies to nearly a kilometer from the orbiter, benefited greatly from the earlier OSS-1 experience. The PDP investigation was initiated by Prof. Stanley D. Shawhan (who is now at NASA Headquarters) and is currently under the leadership of Prof. Louis A. Frank at the University of Iowa. Other members of the PDP team

include Donald A. Gurnett and Nicola D'Angelo (U. of Iowa), Nobie H. Stone, David L. Reasoner (NASA/MSFC) and Joseph M. Grebowsky (NASA/GSFC). Numerous other scientists and engineers both at the U. of Iowa and NASA have played a major role in the program since its inception in 1978.

3.0 The early results

Early papers from the OSS-1/PDP program focused on defining the environment of the shuttle orbiter. This environment was a critical question mark in the eyes of many future users of the shuttle particularly in the areas of contamination, plasma, and electromagnetic environment.

3.1 The neutral environment

Early measurements of the neutral pressure environment of the orbiter revealed that the ambient pressure at orbital altitudes was only obtainable in the near wake of the vehicle and then only after a long period of outgassing. Even after seven days in orbit, pressure averaged at least an order of magnitude greater than ambient (Shawhan, 1984c). Not until Spacelab-2 analysis was available would the probable source of such a large vapor cloud be revealed.

More detailed investigation of the source of large pressure enhancements led to the study of thruster operations. It was reported that the thrusters (in particular Primary RCS and to a much less degree Vernier RCS) introduce major changes in plasma density, ion composition, neutral density, electric fields, and electrostatic plasma waves (Shawhan, 1984c; Murphy, 1983; Pickett, 1985). Other investigators have since reported similar results noting neutral density increase of up to $10^{18}/\text{m}^3$ inside the payload bay ($\sim 7 \times 10^{-5}$ Torr) with NO a major component of the enhancement (Wulf, 1986).

3.2 The plasma environment

The plasma density and apparent DC electric field shifts observed near the orbiter are not yet totally understood but may be related to interactions of the neutral constituent of the gas plume with the ambient plasma or to the plasma component per se.

Grebowsky et al. (1983) reported the surprising result that H_2O^+ is a major constituent of the plasma near the orbiter sometimes even dominating the ambient O^+ ionosphere. The source of these water ions is believed to be in charge exchange reactions between the ambient O^+ ions and a cloud of H_2O molecules generated by outgassing around the orbiter. This H_2O cloud may indeed be a major contributor to the enhanced neutral pressure environment.

The plasma environment near the orbiter not only has an altered ion composition but reveals the influence of a large body moving supersonically through its medium. Stone et al. (1986) observe the ions streaming by the orbiter and study in detail the structure of the wake behind the vehicle. They took particular note of multiple "beams" of ions with different apparent source directions and theorize that this is consistent with not only an additional source of ions close to the orbiter but may imply an E-field sheath associated with a boundary between the ion source region and the undisturbed plasma. It could in fact be that this additional source region is consistent

with observations of Grebowsky (1983) on the production of H_2O^+ near the orbiter.

Reasoner et al. (1986) have underscored the problem of making reliable ambient ionospheric density/temperature measurements near the orbiter. Combinations of contaminant ions, plasma turbulence generating heating, and ram/wake effects make it imperative to move well away from the orbiter before relying on an RPA to reliably characterize the ionosphere. This observation is of course consistent with all previously discussed results.

Electron densities and temperatures near the orbiter are reported by Murphy et al. (1986). To first order electron densities are dominated by the ram/wake effects associated with large bodies. The orbiter is not only large compared to the debye length ($10^3-10^4 \lambda_D$) but also large compared to the electron and ion gyroradius. This size results in the investigation of a unique and unexplored region in parameter space and creates perhaps more questions than it answers. Murphy et al. (1986) report density depletions of as much as 5 orders of magnitude in the near wake of the orbiter (within the payload bay) and less dramatic though significant depletions of 1-2 orders of magnitudes at distances reachable by the RMS. Moreover, apparent temperature enhancements of \sim factors of 5 are observed in the wake transition region. This transition region is also characterized by plasma "turbulence" with $\Delta N/N$ values of typically several per cent. Secondary effects controlling the electron density spacial variation involve: 1.) the possible enhancement of electron density in ram (compared to ambient), Shawhan (1984c), Raitt (1984); 2.) the effect of the neutral cloud around the vehicle and the photoionization of that cloud, Pickett (1985); 3.) the role of the magnetic field both in the filling in of the wake and the production of $V \times B$ potentials in the orbiter reference frame.

3.3 Electromagnetic environment

The AC and DC electric and magnetic fields on and near the orbiter are driven by two sources: 1.) orbiter EMI associated with the hardware per se; 2.) fields associated with the interaction between the orbiter and its environment.

The orbiter EMI under JSC's leadership and Rockwell's cooperation proved to be much more benign than the original ICD specifications would indicate. Shawhan (1984b) and Murphy (1984b) reported in detail the measurement of that environment. By using the PDP's sensitive plasma wave receivers and various RMS maneuvering sequences a "map" of orbiter EMI revealed that the environment was dominated not by orbiter generated noise but by plasma interaction noise. This Broadband Orbiter Generated Electrostatic (BOGES) noise (Shawhan, 1984b) seemed to be associated with plasma turbulence around the orbiter and had field strengths as great as .1 v/m with a relatively flat spectrum up to \sim 10 khz. Although the exact mechanism was not understood, Murphy et al. (1984a), suspecting that it was similar to the turbulence observed by the Langmuir probe, indicated that it was noise of relatively short wavelength (\lesssim 1 m). This noise was observed to be enhanced by any sort of gas release (thruster, water dump, etc.) implicating the gas cloud as a production mechanism. Theoretical work by Papadopolous (1984) suggested that the gas

cloud may provide the "fuel" for enhanced plasma densities by the critical ionization velocity phenomenon and may be intimately involved in the production of this BOGES noise.

Thus we see that the understanding and characterization of the orbiter environment requires detailed investigation of the inter-reactions between the orbiter body, its contaminant cloud, and the ionospheric plasma.

For purposes of completeness it should also be emphasized that a large part of both the OSS-1 and Spacelab-2 missions were devoted to detailed study of the behavior and interactions of an electron beam propagating in the ionosphere. These studies were conducted jointly with the Vehicle Charging and Potential (VCAP) experiment (Banks, 1986). The OSS-1 results are reviewed by Banks (1986) and Shawhan (1984a). Since another paper in this proceedings describes the VCAP/PDP results in detail no further discussion will be given here.

4.0 Spacelab 2, laboratory results, and the emerging picture

Many of the results discussed above began to be published after the Spacelab-2 mission which was launched in July 1985 but early results had a significant influence on the science objectives and experiment planning of Spacelab-2. The landmark nature of the plasma experiments of Spacelab-2 will gradually emerge over the next several years and, in particular, the importance of the PDP free-flight activity, described briefly below, in understanding large vehicle interactions, will become quite obvious. This is especially true in light of the hiatus of Spacelab type missions in the coming years.

After performing about 12 hours worth of experiments on the RMS which consisted of wake studies, EMI surveys, and joint experiments with VCAP, the PDP was prepped for release as a sub-satellite of the orbiter. The PDP free-flight scenario consisted of approximately 6 hours of complex maneuvers by the shuttle orbiter which controlled, in a carefully planned sequence, the relative positions of the PDP and orbiter.

First, a release and back-away maneuver moved the PDP down the "throat" of the orbiter wake to a distance of ~ 100 meters. After several station-keeping experiments the orbiter began a "fly-around" of the PDP. Part of the fly-around was executed in plane so the PDP would transit the orbiter wake at distances from 40 to 200 meters. The other part of the fly-around was out of plane moving the orbiter above and behind the PDP and targeting two flux-tube-connections (FTC's) per orbit. These FTC's were planned so that they occurred out of the orbiter's wake with one in the daytime ionosphere and one at night. The FTC's were quite successful in placing the PDP and the orbiter on the same magnetic field line at a relative distance of ~ 200 meters. These FTC's were believed to be accurate to within several meters at best to a little more than 10 meters at worst. After two "fly-arounds" and several wake transits were completed the orbiter approached and captured the PDP along the velocity vector, again allowing the PDP to examine the near wake. Dealing with topics as a continuation and refinement of the OSS-1 results we first discuss the neutral environment.

4.1 Neutral environment and the contaminant gas cloud

Further measurements by the PDP neutral pressure gauge taken during pallet operations verified the high pressure environment due to early on-orbit outgassing. Analysis of vernier thruster operations verified that only the aft down pointing verniers affected pressure in the bay (Pickett, 1986). No further observations of primaries are possible because of an instrument malfunction. A strong point to be made from Pickett's observations are that large instruments which vent gases can also have dramatic effects of the payload bay environment, raising pressure to as high as 10^{-5} Torr. The orbiter's outgassing is now known to have a major effect on the local environment.

The contaminant ion gas cloud observations were extended to $\sim .5$ km from the orbiter. Grebowsky, 1986 observed contaminant H_2O^+ ions in all directions around the orbiter. The presence of contaminant NO and O_2^+ ions was also reported. It is important to note that the dominant ion in the wake of the shuttle appeared to be H_2O^+ instead of ambient O^+ .

If these ions are created by charge exchange with O^+ analysis of their distribution function would indicate a ring in velocity space. Reports by Paterson, 1986 provide evidence that this is indeed the case and an attempt to model the outgassing and chemical reactions associated with it is currently under way. Observations of the Infrared telescope on Spacelab-2 may provide additional data on outgassing rates and the structure of the water cloud which appears to surround the vehicle.

4.2 Further studies of the orbiter wake

Investigation of the structure and dynamics of the orbiter wake both on the RMS and as a free flyer are being continued. More detailed examination of the wake turbulence indicate that the magnetic field orientation may affect the structure of the turbulent zone (Tribble, 1986). Comparisons of the electron density observed in the wake are being made with predictions of the NASA POLAR code (Katz et al., 1984) and early results indicate the code may be quite accurate at predicting at least the first order effects on electron density. The details associated with magnetic field effects, the role of the plasma turbulence and pickup ions, and processes which produce the heated electrons (Murphy, 1986) still must be investigated. Although a detailed review of wake investigations conducted both in the laboratory and in space is presented elsewhere in the proceedings it is relevant to discuss briefly some laboratory results which complement the Spacelab studies.

4.3 Complementary laboratory investigations

In addition to observing the wake region behind large objects as they pass through the near earth plasma, it is found profitable to perform laboratory experiments in order to gain some insight into the plasma-wake environment. Although the parameters may not scale directly to the plasma that has been examined above, such experiments suggest new avenues for the spacelab investigations of the future. Herein, we shall review a few recent experiments performed in laboratory plasma environments whose volume is of the order one cubic meter, possessing plasma numbers of $n_e = n_i = 10^6 - 10^8$ electrons/cm³; $T_e = 1-3$ eV and $T_i < T_e/10$.

Alikhanov et al. (1971) studied the flow into the wake region created by a flowing plasma passing a rectangular plate that was at floating potential. In an extended study, Eiselevich and Fainshtein (1980) noted that the expansion of the plasma from the undisturbed region into the wake could be modeled with a self similar description. This can be understood from the governing fluid equations of continuity

$$v_b \delta n / \delta z + \delta(nv) / \delta x = 0$$

and motion

$$v_b \delta / \delta z + v \delta v / \delta x = -c_s^2 \delta(\ln n) / \delta x$$

where the quasineutral plasma has been assumed to be moving as a beam in the z direction with a velocity of v_b . The ion acoustic velocity is c_s . These equations are identical to the problem of a neutral gas or a quasineutral plasma expanding into a vacuum and solutions in terms of the self similar variable $\zeta = x/(z/v_b)$ can be obtained. The POLAR model discussed previously uses such a quasineutral approximation. Similar results concerning the self similar expansion into the wake region behind a grounded metal plate were reported by Wright et al. (1985). In the very near wake region where quasineutrality would be violated, it was found that the potential would be the important self similar dependent variable by Diebold et al. (1986). In this case, the dependent self similar variable becomes $\zeta = x/(z/v_b)^2$ as shown by Lonngren and Hershkowitz (1979).

As the wake region has a lower density than the ambient flowing plasma, one might conjecture that the electrons due to their higher mobility would rapidly enter the wake, creating an electric field which would accelerate the ions to velocities greater than the ion acoustic velocity. The accelerated ions have been noted in the experiments of Wright et al. (1985), (1986) and Raychaudhuri et al. (1986). The potential well that would result from such a space charge was observed in the orbiter wake by Murphy et al. (1986). That the electrons can speed ahead of the ions was recently detected by Chan et al. (1986). Ions could also enter the wake region by being deflected around the perturbing objects as was recently noted by D'Angelo and Merlino (1986a), (1986b) in an experiment performed in a plasma in a weak magnetic field oriented in the direction of the plasma flow. These experiments show results reminiscent of those by Stone 1986 where streams of converging ions were observed behind the orbiter. Finally, a series of experiments designed to examine the flow of plasma around magnetized objects has been described by Hill et al. (1986). These would be related to the TERRELLA type of experiments except that the present experiments were performed in a very low β plasma environment ($\beta = 10^{-4}$). A general characteristic of the observations in this experiment was that the magnetic object "appeared" to be larger for the electrons than the ions since the electron wake had dimensions that were larger than the ion wake.

Hence, we see that the laboratory experiment provides a controllable environment in which to suggest future paths for space experiments or to explain certain space observations. Future work needs to better define the role of the magnetic field and the charge on the object in question. It should be noted however that it is difficult to simulate in the laboratory conditions similar to the orbiter where the magnetic field can be perpendicular to the flow vector and where gas cloud interactions modify the

observations.

4.4 Electromagnetic environment and active experiments

Further definition of the electromagnetic environment has shown that the BOGES noise extends as far from the orbiter as the PDP observed, and was strongest along field lines connecting to the orbiter and in the turbulent wake zone (Gurnett, 1986a). Gurnett has also verified that the noise is electrostatic in nature and has very short wavelength. Considerable theoretical efforts are currently under way to determine the fundamental process creating such noise.

Of further interest may be a series of joint experiments with VCAP where, during two flux tube connection experiments, dramatic comparisons to the physics of whistler mode radiation in auroral arcs has been discovered (Gurnett, 1986b).

Further active experiments conducted by using the orbiter OMS engines to produce a cloud of water vapor and deplete the ionosphere (Mendillo, 1981; Mendillo et al., 1978) showed significant plasma depletion, as measured in the orbiter payload bay, recovering on the timescale of seconds after engine shutdown (Tribble et al. 1985). Tribble also reported a high level of plasma "turbulence" which lasted tens of seconds indicating the presence of instabilities. This phenomenon may be similar to that observed by RCS ignition and reported by Murphy et al., 1984a, and Shawhan et al., 1984b.

5.0 Summary

It is important, with such a wide range of data, to put together an emerging picture of the Shuttle orbiter interactions and then systematically address the experiments which need to be conducted in order to further the science/technology of large body interactions.

Although laboratory and small satellite observations can shed light on details of wake structures, and the electric fields associated with them, large bodies such as the orbiter pose some unique problems. Is the orbiter a comet? In many respects, there are similarities. It definitely carries its own gas cloud and understanding how large objects such as the orbiter, platforms, or space station interact with the plasma demands on more than a scaling of laboratory experiments.

Part of the interactions around large objects are due to the "scale size" effect while others are distinctly interrelated to outgassed products and the change in the balance of the ambient chemical equilibrium. As described by Grebowsky et al., 1986, the instrumentation required to completely disgrace the ionospheric chemistry and simultaneously determine all key plasma parameters requires careful consideration of the specific problems the spacecraft must study. The PDP is only a first generation experiment with instrumentation that was not optimized for studies such as "comet" problems.

Future experiments must be designed both for space and in complementary laboratory setting which can, if not solve the following problems, at least determine by appropriate empirical means their impact on future technologies. These problems include:

1. What is the effect of gas clouds associated with large objects on their interaction with the neutral atmosphere and plasma?
 - a. How does the cloud affect the wake fill process?
 - b. Is the orbiter cloud large enough to create a pick-up current of such magnitude that it partially screens the motional electric field? (Pickett, et al., 1985; Goertz, 1980; Katz et al., 1984).
 - c. For large objects such as space station, could the energy dissipation associated with such a cloud create significant anomalous drag?
 - d. How does the cloud affect the charge neutralization process and current loops associated with tethers, or particle beams?
 - e. What is the effect of such a cloud on the operation of a plasma contactor?
2. The interactions of large structures with the ionosphere through electromotive forces associated with differential charging, absolute charging, and closed current loops are not well understood.
3. The phenomena of vehicle glow, its relationship with the plasma, the neutral cloud and the interacting surface has given rise to conflicting theories with insufficient data to resolve the issue. (Green, 1985)
4. Understanding of the total picture associated with large body wakes involves more than models of electron and ion density. Wave particle interactions, atmospheric chemistry, vehicle charge, and magnetic fields must be included in the analysis.
5. Joint particle beam experiments such as those between PDP and VCAP have raised many questions about the propagation of beams from structures like the orbiter. This is an immature experiment because until SL-2 no experiments (other than short sounding rocket flights) have provided remote diagnostics on such beams. (See the paper by Banks et al. in this proceedings for more detail.)

6.0 Recommendations

The Challenger accident has dealt a severe setback to the space experiments associated with large body/plasma interactions. It is unfortunate that the space station is set to proceed on course with little opportunity in the next 6 years for detailed study of the technical issues that should be resolved before it proceeds.

Studying such problems requires a commitment by NASA to a program which must involve the development of instrumentation adequate to measure the appropriate parameters, flights of opportunity within the next five to six years for such instruments, support of working groups consisting of experimentalists who may have relevant data from past missions and theorists attempting to model the phenomena and, last of all, well designed and executed laboratory experiments.

Last of all it is of paramount importance that those scientists and engineers evolved with the state of the art of large body interactions, gas cloud dynamics, high voltage effects, etc. have effective knowledge transfer to those individuals and organizations making the design decisions of the future.

Acknowledgements

The authors wish to thank the PDP principal investigator, Professor Louis A. Frank and all co-investigators for their cooperation and input to this manuscript. We also acknowledge the efforts of Henry Garrott, Steve Gabriel and Joan Feynman for the organization of the conference. The PDP program has been supported by NASA/MSFC contract NAS832807 and NASA/Lewis Grant NAG 3-449. Laboratory investigations at the University of Iowa have been supported by NSF Grant # ECS 8519510.

References

- Alikhanov, S. G., V. G. Belen, G. N. Kichigin and P. Z. Chebotaev, Expansion of a Plasma in Vacuum and Flow of Collisionless Plasma Around a Plate, Sov. Phys. JETP, 32, 1061-1063, 1971.
- Banks, P.M., W. J. Raitt, P. R. Williamson, A. B. White and R. I. Bush, Results from the Vehicle Charging and Potential Experiment on STS-3, J. Spacecraft and Rockets, (in press), 1986.
- Chan, C., M. A. Morgan and R. C. Allen, Electron dynamics in the Near Wake of a Conducting Body, IEEE Transactions on Plasma Science, to be published, 1986.
- D'Angelo, N. and R. L. Merlino, The Effect of a Magnetic Field on Wake Potential Structures, IEEE Transactions on Plasma Science, PS-14, 609-610, 1986a.
- Diebold, D. N. Hershkowitz, T. Intrator and A. Bailey, Self-similar Potential in the Near Wake, Physics of Fluids, to be published, 1986.
- Eselevich, V. G. and V. G. Fainshtein, Expansion of Collisionless Plasma in a Vacuum, Sov. Phys. JETP, 52, 441-448, 1980.
- Goertz, C. K., Io's Interaction with the Plasma Torus, J. Geophys. Res., 85, 2949-2956, 1980.
- Grebowsky, J. M., M. W. Pharo III, H. A. Taylor, Jr., and I. J. Eberstein, Measured Thermal Ion Environment of STS-3, AIAA Pub., 83-2597, 1983.
- Grebowsky, J. M., H. A. Taylor, Jr., M. W. Pharo III, and N. Reese, Thermal Ion Perturbations Observed in the Vicinity of the Space Shuttle, submitted to Planetary and Space Science, May, 1986.
- Green, B. D., Review of Vehicle Glow, AIAA reprint #85-6095-CP, 1985.

- Gurnett, D. A., J. T. Steinberg, and W. S. Kurth, Short Wavelength Electrostatic Noise Observed in the Vicinity of the Shuttle During the SL-2 Mission, presented at URSI, Boulder, CO, Jan., 1986.
- Gurnett, D. A., W. S. Kurth, J. T. Steinberg, P. M. Banks, R. I. Bush, and W. J. Raitt, Whistler Mode Radiation from the SL-2 Electron Beam, Geophys. Res. Lett., 13, 225, 1986.
- Green, B. D., 'Review of Vehicle Glow, AIAA reprint #85-6095-CP, 1985.
- Hill, J. L., A. Seyhonzadeh, H. Y. Chang and K. E. Lonngren, Radio Science, to be published, 1986.
- Katz, I., D. E. Parks, D. L. Cooke, J. R. Lilley, Jr., Geophys. Res. Lett., 11, 1115-1116, 1984.
- Katz, I., D. L. Cooke, D. E. Parks, J. J. Mandrell, A. G. Rubin, Three Dimensional Wake Model for Low Earth Orbit, J. of Spacecraft and Rockets, 21, 125, 1984.
- Lonngren, K. E. and N. Hershkowitz, A Note on Plasma Expansion into a Vacuum, IEEE Transactions on Plasma Science, PS-7, 107-108, 1979.
- Mendillo, M., J. Forbes, Artificially Created Holes in the Ionosphere, J. of Geophys. Res., 83, 151, 1978.
- Mendillo, M., The effect of Rocket Launches on the Ionosphere, Advances in Space Research, 1, 275, 1981.
- Merlino, R. L., and N. D'Angelo, The Interaction of a Conducting Object With a Supersonic Plasma Flow: Ion Deflection Near a Negatively Charged Obstacle, J. Plasma Physics, to be published, 1986.
- Murphy, G. B., N. D'Angelo, J. S. Pickett and S. D. Shawhan, Characteristics of Strong Plasma Turbulence Created by the STS Orbiter, presented at URSI, Jan, 1984.
- Murphy, G. B., J. S. Pickett, N. D'Angelo, and W. S. Kurth, Measurements of Plasma Parameters in the Vicinity of the Space Shuttle, Planetary and Space Science, (in press), 1986.
- Murphy, G. B., S. D. Shawhan, Radio Frequency Fields Generated by the S-band Communication Link on OV102, J. of Spacecraft and Rockets, 21, #4, 398, 1984.
- Murphy, G. B., S. D. Shawhan, L. A. Frank, N. D'Angelo, D. A. Gurnett, J. M. Grebowsky, D. L. Reasoner, and N. H. Stone, Interaction of the Space Shuttle Orbiter With the Ionospheric Plasma, Proc. 17th ESLAB Symposium on Spacecraft/Plasma Interactions and Their Influence on Field and Particle Measurements, European Space Agency Publ., ESA SP-178, p. 73, Dec. 1983.
- Papadopolous, K., On the Shuttle Glow - the Plasma Alternative, Radio Sci., 19, 571, 1984.

- Paterson, W. R., L. A. Frank, and P. M. Banks, Charged Particle Distributions Measured in the Vicinity of the Space Shuttle, presented at Fall AGU, San Francisco, CA, 1985.
- Pickett, J. S., G. B. Murphy and W. S. Kurth, The Gaseous Environment of the Space Shuttle Early in the Spacelab-2 Mission, submitted to J. of Spacecraft and Rockets, 1986. (Presented as paper 85-6064-CP at AIAA Conference Shuttle Environment and Operations II, Nov. 1985)
- Pickett, J. S., G. B. Murphy, W. S. Kurth, C. K. Goertz, and S. D. Shawhan, Effects of Chemical Releases by the STS-3 Orbiter on the Ionosphere, J. Geophys. Res., 90, 3487, 1985.
- Raitt, W. J., D. E. Siskind, P. M. Banks, P. R. Williamson, Measurements of the Thermal Plasma Environment of the Space Shuttle, Planet. Space Sci., 32, 457, 1984.
- Raychaudhuri, J. Hill, H. Y. Chang, E. K. Tsikis and K. E. Lonngren, An Experiment on the Plasma Expansion into a Wake, Physics of Fluids, 29, 289-293, 1986.
- Reasoner, D. L., S. D. Shawhan, and G. B. Murphy, Plasma Diagnostics Package Measurements of Ionospheric Ions and Shuttle-Induced Perturbations, J. Geophys. Res., (in press), 1986.
- Shawhan, S. D., G. B. Murphy, P. M. Banks, P. R. Williamson and W. J. Raitt, Wave Emissions from DC and Modulated Electron Beams on STS-3, Radio Sci., 19, 471, 1984.
- Shawhan, S. D., G. B. Murphy, D. L. Fortna, Measurements of Electromagnetic Interference on OV102 Columbia Using the Plasma Diagnostics Package, J. Spacecraft and Rockets, 21, 392, 1984.
- Shawhan, S. D., G. B. Murphy, and J. S. Pickett, Plasma Diagnostics Package Initial Assessment of the Shuttle Orbiter Plasma Environment, J. Spacecraft and Rockets, 21, 387, 1984.
- Stone, N. H. and U. Samir, The Plasma Dynamics of Hypersonic Spacecraft: Applications of Laboratory Simulations and Active In Situ Experiments, this issue.
- Stone, N. H., K. H. Wright, Jr., K. S. Hwang, U. Samir, G. B. Murphy, and S. D. Shawhan, Further Observations of Space Shuttle Plasma - Electrodynamic Effects from OSS-1/STS-3, Geophys. Res. Lett., 13, 217, 1986.
- Tribble, A. C., J. S. Pickett, N. D'Angelo, and G. B. Murphy, Plasma Densities and Temperatures Near the Shuttle Orbiter, presented at Fall AGU, San Francisco, CA, 1985.
- Tribble, A. C., N. D'Angelo, G. B. Murphy, and J. S. Pickett, The Effect of the Earth's Magnetic Field on Plasma Turbulence Near the Shuttle Orbiter, presented at Fall AGU, San Francisco, CA, 1986.

Wulf, E., and U. von Zahn, The Shuttle Environment: Effects of Thrust Firings on Gas Density and Composition in the Payload Bay, J. of Geophys. Res., 19, 3270, 3278, 1986.

Wright, Jr., K. H., D. E. Parks, I. Katz, N. H. Stone and U. Samir, More on the expansion of a collisionless plasma into the wake of a body, J. Plasma Physics, 35, 119-123, 1986.

Wright, Jr., K. H., N. H. Stone and U. Samir, A study of plasma expansion phenomena in laboratory generated plasma wakes: Preliminary Results, J. Plasma Physics, 33, 71-82, 1985.

PLASMA WAVE TURBULENCE AROUND THE SHUTTLE: RESULTS FROM THE SPACELAB-2 FLIGHT

D. A. Gurnett, W. S. Kurth, J. T. Steinberg

Department of Physics and Astronomy, The University of Iowa, Iowa City

S. D. Shawhan

NASA Headquarters, Washington, DC

Abstract. During the Spacelab-2 flight, which occurred from July 29, to August 6, 1985, a spacecraft called the Plasma Diagnostics Package (PDP) was released from the shuttle to explore the plasma environment around the shuttle. The plasma wave instrument on the PDP detected a region of intense broadband turbulence around the shuttle at frequencies extending from a few Hz to about 10 kHz. The noise has broadband intensities ranging from 1 to 5 mV/m and was observed at distances of up to 400 m from the shuttle. The highest intensities occurred in the region downstream of the shuttle and along magnetic field lines passing near the shuttle. The intensities also tended to increase during periods of high thruster activity, which provides strong evidence that the noise is caused by an interaction of the ionosphere with gaseous emissions from the shuttle, similar in many respects to the interaction of a comet with the solar wind. Antenna interference patterns observed in the wideband data show that the wavelength of the turbulence is very short, a few meters or less.

Introduction

In this report we describe plasma wave turbulence observed around the shuttle by a spacecraft called the Plasma Diagnostics Package (PDP) which was released from the shuttle during the Spacelab-2 flight. The PDP was designed and constructed at the University of Iowa and is a reflight of the same spacecraft previously flown on the STS-3 flight (Shawhan et al., 1984a). On STS-3 the PDP was carried on the remote manipulator arm, which restricted the measurements to about 15 meters from the shuttle. The principal new feature of the Spacelab-2 flight is that the PDP was released from the shuttle, thereby providing measurements at much greater distances. During the free-flight phase of the mission, the shuttle was maneuvered to provide two complete fly-arounds of the PDP at radial distances out to about 400 meters. The fly-arounds provided measurements both upstream and downstream of the shuttle, and along the magnetic field line through the shuttle. In addition to the fly-arounds, a series of maneuvers, called wake transits, were performed to survey the wake region directly downstream of the shuttle.

Included among the various experiments on the PDP was a plasma wave receiver designed to measure electric and magnetic disturbances produced by the motion of the shuttle through the ionosphere. The results presented here are mainly from this instrument. For a description of this and other instruments on the PDP, see Shawhan [1982]. The Spacelab-2 mission, which was launched on July 29, 1985, was flown in a nearly circular low-inclination orbit with a nominal altitude of 325 km and an inclination of 49.5°. The PDP was in free flight for a roughly 6-hour period, from 0010 to 0620 UT on August 1, 1985.

Observations

An electric field spectrogram showing the plasma wave intensities during the first of the two fly-arounds is shown in the bottom panel of Figure 1. The shuttle position relative to the PDP is given by the x, y, z coordinates at the bottom of each plot. The +z axis is directed downward toward the center of the Earth, the x axis is in the orbital plane with the positive axis in the direction of motion, and the y axis completes the right-handed coordinate system. The electric field spectral density, $E^2/\Delta f$, is indicated by the color code, with blue being least intense and red being most intense. The white line labeled f_{ce} is the electron cyclotron frequency, which is a basic characteristic frequency of the plasma. The points labeled 1 and 2 at the top of the spectrogram indicate magnetic conjunctions, which are times when the shuttle was maneuvered to intercept a magnetic field line through the PDP.

The spectrogram shows two types of noise. At selected times during the flight an electron gun on the shuttle was used to inject a beam of electrons into the ionosphere for purposes of studying beam-plasma interactions. This beam produced the series of whistler-mode emissions identified as "electron beam emissions" in Figure 1. These emissions have been described in a previous series of papers [Gurnett et al., 1986; Bush et al., 1987; Farrell et al., 1988] and will not be discussed further. In addition to the electron beam emissions, a broad band of noise can be seen at frequencies below about 10^4 Hz. No comparable type of noise is evident in the magnetic field spectrogram. From the known noise level of the magnetic antenna, the ratio of the electric field energy density to the magnetic field energy density is found to be at least 10 to 100, which is much larger than would be expected for any known electromagnetic mode of propagation. Therefore, the noise is electrostatic. The same type of noise was detected on the STS-3 mission [Shawhan et al., 1984b; 1984c], and is usually referred to as "broadband electrostatic noise."

As can be seen, the broadband electrostatic noise consists of many impulsive short-term variations superimposed on a slowly varying, nearly continuous background. Most of the impulsive variations can be associated with thruster firings. For comparison, the rate of gas ejection from the thrusters averaged over one-minute intervals is shown in the top panel of Figure 1. Major trajectory correction maneuvers, which typically involve gas injection rates of 10^2 to 10^3 gm/sec over periods of 30 sec or more, almost always produce an intense burst of broadband noise. Examples of such maneuvers occur near the first magnetic conjunction, at 0157 and 0204 UT. In addition to the trajectory correction maneuvers, an almost continuous level of thruster activity occurs in association with minor attitude corrections. These firings, which have durations of about 80 msec and occur at a rate of several per minute, may be responsible for the nearly continuous low level of noise that is present most of the time.

Comparisons of the electric field spectrograms from the two fly-arounds and the wake transits indicate that the intensity varies systematically with the position of the PDP relative to the shuttle. This dependence is illustrated in Figure 2 which shows the x-z projection of the shuttle trajectory relative to the

Copyright 1988 by the American Geophysical Union.

Paper number 8L6829.
0094-8276/88/008L-6829\$03.00

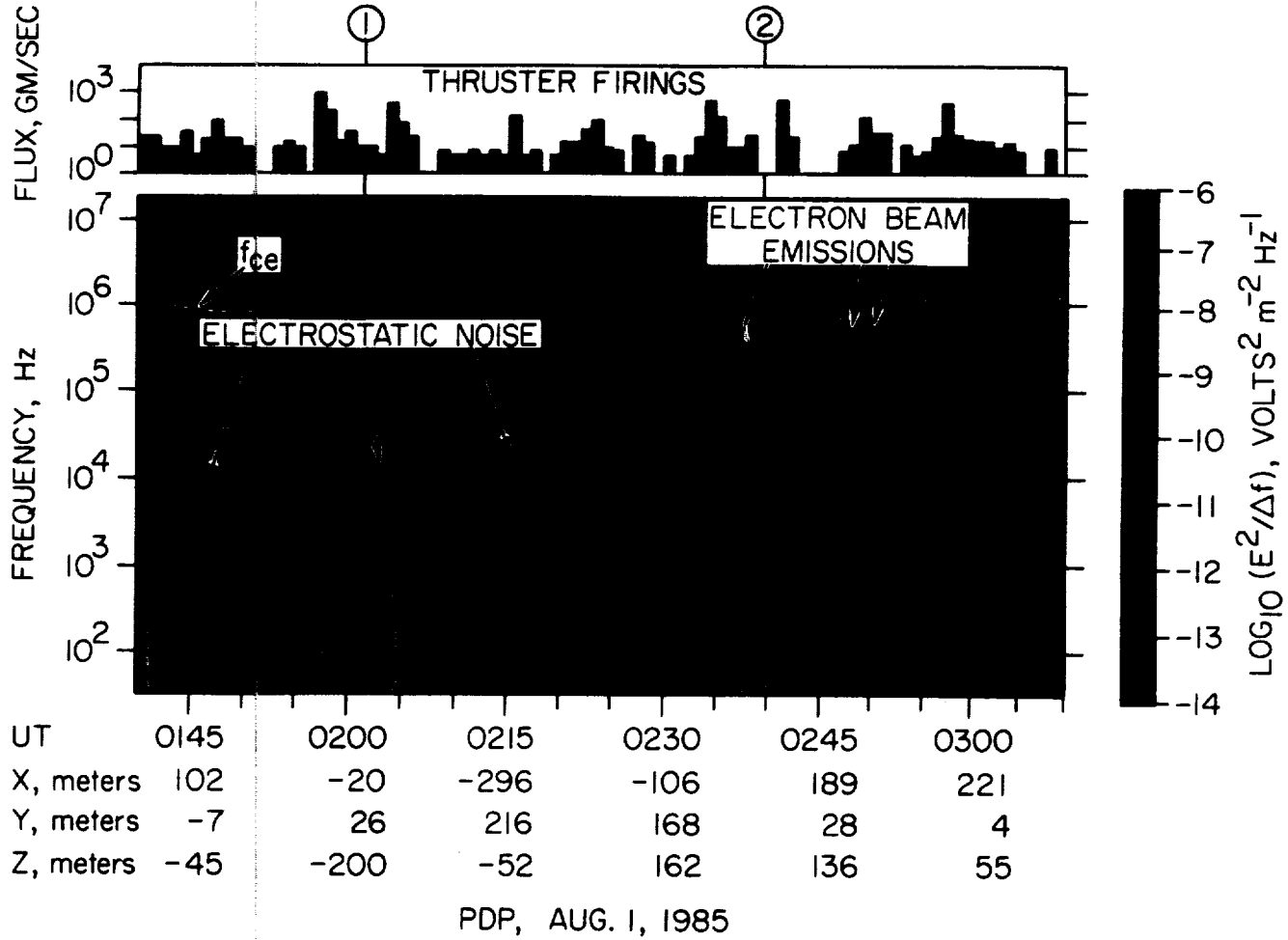


Fig. 1. The bottom panel shows a spectrogram of the electric field intensities observed by the PDP during the first fly-around and the top panel shows the gas flux associated with thruster firings on the shuttle. The broad band of noise below about 10^4 Hz is closely associated with the thruster firings and is believed to be caused by an interaction between a cloud of neutral gas around the shuttle and the ionosphere, which is streaming by at ~ 8 km/sec.

PDP. The solid black dots show the regions where the broadband electric field strength, integrated from 35 Hz to 31 kHz, exceeds 1 mV/m. As can be seen, the electrostatic noise tends to be strongest and most persistent along the +x axis, when the PDP is downstream of the shuttle, and weakest along the -x axis, when the PDP is upstream of the shuttle. The noise is also strong near the four magnetic conjunctions, which are labeled 1 through 4 in Figure 2.

The interpretation of the noise enhancements near the magnetic conjunctions is complicated by the fact that the thruster firing rate tends to be higher in these regions as the shuttle was maneuvered to intercept the magnetic field line through the PDP. Nevertheless, we believe that the intensification in this region is controlled to some degree by the magnetic field geometry. As evidence of this relationship note that thruster firings when the PDP is upstream of the shuttle, for example at 0216 and 0224 UT (see Figure 1), do not have nearly as large an effect as thruster firings near the magnetic conjunction, for example at 0157 and 0204 UT. Also, even when the gas ejection rate is low, for example from 0159 to 0203 UT, the noise level in the magnetic conjunction region is higher than for comparable gas ejection rates when the PDP is upstream of the shuttle.

Representative electric field spectrums of the broadband electrostatic noise are shown in Figure 3. The top panel shows two spectrums selected from near the first and second magnetic

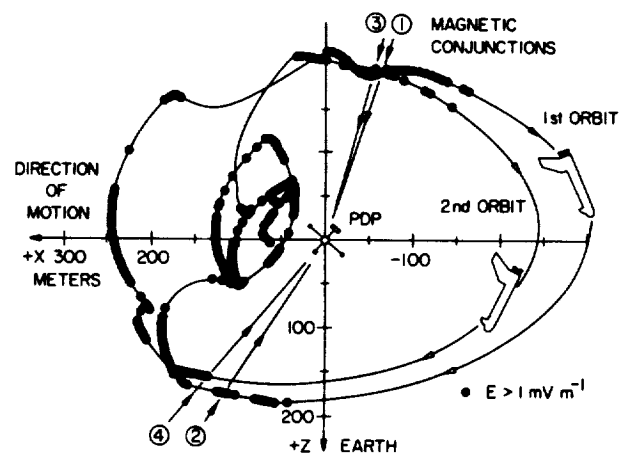


Fig. 2. An orbital plane plot showing the regions (black dots) where the broadband shuttle-induced noise exceeds 1 mV/m. The noise is strongest and most persistent in the region downstream of the shuttle and weakest in the region upstream of the shuttle. Strong enhancements also occur near the magnetic conjunctions.

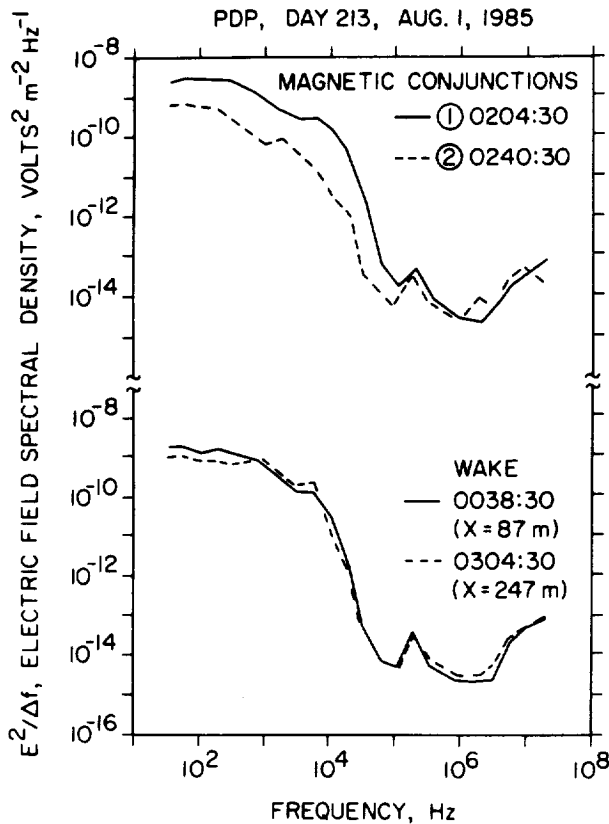


Fig. 3. Selected spectrums of the broadband noise near the first and second magnetic conjunctions, and at two positions in the wake region downstream of the shuttle.

conjunctions, and the bottom panel shows spectrums at two different distances ($x = 247$ m and $x = 87$ m) in the wake region directly downstream ($y = 0$, $z = 0$) of the shuttle. All four spectrums are remarkably similar. Typically, the spectrum is almost flat from 10 Hz to about 10^4 Hz, and then drops below the instrument noise level by 10^6 Hz. Sometimes a peak can be seen at a frequency of a few kHz, which is near the lower hybrid resonance frequency. This peak can be seen at various times in Figure 1, for example at 0150 and 0255 UT. The broadband electric field strength during the most intense thruster-related events ranges from about 2 to 5 mV/m. The nearly continuous background level in the wake region directly downstream of the shuttle is about 1 to 2 mV/m.

High-resolution wideband spectrograms of the electrostatic noise sometimes show a "fingerprint" pattern that repeats with a period of one-half of the spacecraft rotation period. An example of such a pattern is shown in Figure 4. This type of spin modulation pattern is well known in space plasma wave data and is an antenna pattern effect caused by wavelengths short compared to the antenna length [Temerin, 1979; Fuselier and Gurnett, 1984; Gallagher, 1985]. The nulls occur when the antenna separation projected in the direction of propagation is an integral number of wavelengths. Since the antenna length is only 3.9 meters, the existence of these nulls implies that the wavelengths of the electrostatic noise is substantially less than one meter. For such short wavelengths, the frequency spectrum is almost entirely determined by Doppler shifts. From the nulls in the fingerprint pattern, one can in principle determine the wave frequency in the plasma rest frame. Although a more detailed analysis will be necessary to provide an exact mode identification, our preliminary estimates indicate that the wave frequency in the plasma rest frame is quite low, 500 Hz or less. The fingerprint pattern tends to be most pronounced and easily

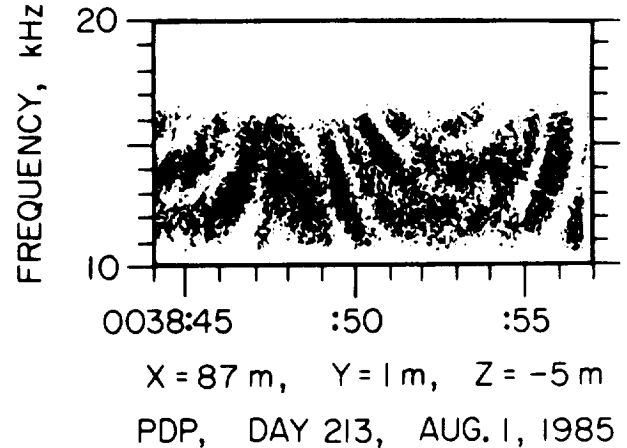


Fig. 4. A high-resolution wideband spectrogram showing "fingerprints" in the broadband noise. This effect is caused by nulls in the antenna pattern as the spacecraft rotates and is indicative of wavelengths shorter than the 3.9 meter length of the electric antenna.

recognized near the upper frequency cutoff (~ 10 to 20 kHz) and in the region directly downstream of the shuttle.

Interpretation

The close correlation between thruster firings and enhancements in the broadband electrostatic noise provides a strong indication that the noise is associated with neutral gas emissions from the shuttle. Previous measurements [Shawhan et al., 1984b; 1984c; Pickett et al., 1985] have shown that the shuttle is surrounded by a neutral gas cloud with pressures as much as 10^2 to 10^3 above ambient. This gas cloud originates from a variety of transient and steady-state sources including thruster firings, water dumps, outgassing of water absorbed in the tiles, and leaks from pressurized compartments on the shuttle. The fact that the electrostatic noise displays both an impulsive component as well as a nearly steady component simply reflects the complex time variability of these various sources.

Since a neutral atom does not interact with an electric field, some mechanism is needed to generate the noise. This mechanism is believed to be charge exchange between the shuttle gas cloud and the surrounding ionosphere. Studies of the plasma distribution around the shuttle by Paterson and Frank [1987] and Frank et al. [1988] show that the shuttle is surrounded by an energized distribution of H_2O^+ ions and other heavy ions. These ions are believed to be produced by charge exchange between the shuttle gas cloud, which is primarily H_2O and ionospheric O^+ ions, which are streaming by at ~ 8 km/s. Once ionized, the newly born H_2O^+ ions are immediately accelerated by the $\vec{v} \times \vec{B}$ electric field and carried downstream, more or less as illustrated in Figure 5.

The pick-up process causes two effects that could possibly account for the intense electrostatic noise observed around the shuttle. First, since the newly born ions are moving with respect to the ionosphere, these ions produce a beam or ring-like velocity distribution that should be highly unstable [Krall and Trivelpiece, 1973; Papadopoulos, 1984]. Second, the pick-up process produces both perpendicular and parallel currents, J_{\perp} and J_{\parallel} , which ultimately must close in the ionosphere via an Alfvén wave, more or less as shown in Figure 5. If the current density exceeds a critical value, then current-driven electrostatic waves could be excited, similar to the processes that are believed to occur in the auroral zone [Kindel and Kennel, 1971]. Just which mechanism provides the free-energy

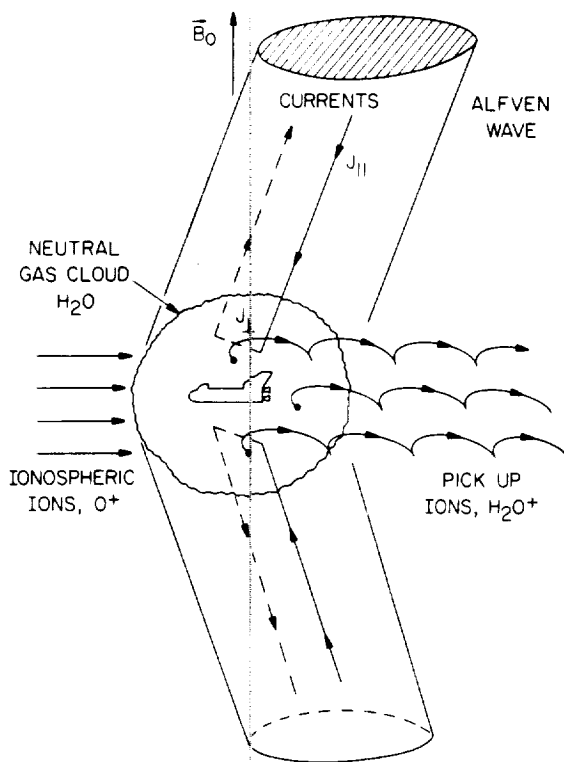


Fig. 5. Charge exchange interactions with ionospheric ions are believed to partially ionize the neutral gas cloud around the shuttle, thereby producing pick-up ions which are accelerated and carried downstream by the convection electric field. The pick-up ions produce a highly unstable ion distribution which is believed to be responsible for the intense electrostatic noise observed downstream of the shuttle.

source for generating the intense electrostatic noise around the shuttle remains to be established. The unstable ion distributions associated with the pick-up ions appears to be the best possibility, since current-driven instabilities usually have a rather high threshold. However, the enhanced noise intensities near the magnetic conjunctions suggest that field-aligned currents may play some role. Although the main energization of the pick-up ions comes from acceleration by the $\vec{V} \times \vec{B}$ electric field, the electrostatic turbulence may play an important role in thermalizing these ion distributions.

In comparing these results with other measurements, it is interesting to note the very close similarity between the noise observed near the shuttle and the electrostatic noise observed near the AMPTE artificial comet [Gurnett et al., 1985; 1986] and the comets Giacobini-Zinner [Scarf et al., 1986], and Halley [Grard, 1986]. Since charge exchange and ion pick-up are believed to be one of the dominant processes in the interaction of a comet with the solar wind, it appears that the interaction of the shuttle with the ionosphere may have a close similarity to the plasma processes occurring near a comet.

Acknowledgements. The research at the University of Iowa was supported by NASA through contract NAS8-32807, and grants NGL 16-001-043 and NAG3-449.

References

Bush, R. I., G. D. Reeves, P. M. Banks, T. Neubert, P. R. Williamson, W. J. Raitt, and D. A. Gurnett, Electromagnetic fields from pulsed electron beam experiments in space: Spacelab-2 results, *Geophys. Res. Lett.*, **14**, 1015-1018, 1987.

- Farrell, W. M., D. A. Gurnett, P. M. Banks, R. I. Bush, and W. J. Raitt, An analysis of whistler mode radiation from the Spacelab 2 electron beam, *J. Geophys. Res.*, **93**, 153-161, 1988.
- Frank, L. A., W. R. Paterson, P. M. Banks, R. I. Bush, and W. J. Raitt, Plasma observations in the vicinity of the shuttle, 1988 National Radio Science Meeting, Boulder, Colorado, Jan. 5-8, 1988.
- Fuselier, S. A., and D. A. Gurnett, Short wavelength ion waves upstream of the earth's bow shock, *J. Geophys. Res.*, **89**, 91-103, 1984.
- Gallagher, D. L., Short-wavelength electrostatic waves in the earth's magnetosheath, *J. Geophys. Res.*, **90**, 1435-1448, 1985.
- Grard, R., A. Pedersen, J.-G. Trotignon, C. Beghin, M. Mogilevsky, Y. Mikhailov, O. Molchanov, and V. F. Formisano, Observations of waves and plasmas in the environment of comet Halley, *Nature*, **321**, 290-291, 1986.
- Gurnett, D. A., R. R. Anderson, B. Häusler, G. Haerendel, O. H. Bauer, R. A. Treumann, H. C. Koons, R. H. Holzworth, and H. Lühr, Plasma waves associated with the AMPTE artificial comet, *Geophys. Res. Lett.*, **12**, 851-854, 1985.
- Gurnett, D. A., W. S. Kurth, J. T. Steinberg, P. M. Banks, R. I. Bush, and W. J. Raitt, Whistler-mode radiation from the Spacelab-2 electron beam, *Geophys. Res. Lett.*, **13**, 225-228, 1986.
- Gurnett, D. A., T. Z. Ma, R. R. Anderson, O. H. Bauer, G. Haerendel, B. Häusler, G. Paschmann, R. A. Treumann, H. C. Koons, R. Holzworth, and H. Lühr, Analysis and interpretation of shock-like electrostatic noise observed during the AMPTE solar wind lithium releases, *J. Geophys. Res.*, **91**, 1301-1310, 1986.
- Kindel, J. M., and C. F. Kennel, Topside current instabilities, *J. Geophys. Res.*, **76**, 3055-3078, 1971.
- Krall, N., and A. W. Trivelpiece, *Principles of Plasma Physics*, McGraw-Hill, N. York, 473, 1973.
- Papadopoulos, K., On the shuttle glow (the plasma alternative), *Radio Science*, **19**, 571-577, 1984.
- Paterson, W. R., and L. A. Frank, Observations and modeling of ion pickup in the vicinity of the orbiter, *EOS*, **68**, 1399, 1987.
- Pickett, J. S., G. B. Murphy, W. S. Kurth, C. K. Goertz, and S. D. Shawhan, Effects of chemical releases by the STS-3 orbiter in the ionosphere, *J. Geophys. Res.*, **90**, 3487-3497, 1985.
- Scarf, F. L., F. V. Coroniti, C. F. Kennel, D. A. Gurnett, W.-H. Ip, and E. J. Smith, Plasma wave observations at comet Giacobini-Zinner, *Science*, **232**, 377-381, 1986.
- Shawhan, S. D., Description of the plasma diagnostics package (PDP) for the OSS-1 shuttle mission and JSC chamber test in conjunction with the fast pulse electron gun (FPEG), *Artificial Particle Beams in Space Plasma Studies*, ed. B. Grandel, Plenum, N. York, 419-430, 1982.
- Shawhan, S. D., G. B. Murphy, P. M. Banks, P. R. Williamson, and W. J. Raitt, Wave emissions from dc and modulated electron beams on STS-3, *Radio Science*, **19**, 471-486, 1984a.
- Shawhan, S. D., G. B. Murphy, and J. S. Pickett, Plasma Diagnostics Package initial assessment of the shuttle orbiter plasma environment, *J. Spacecraft and Rockets*, **21**, 387-391, 1984b.
- Shawhan, S. D., G. B. Murphy, and D. L. Fortna, Measurements of electromagnetic interference on OV102 Columbia using the Plasma Diagnostics Package, *J. Spacecraft and Rockets*, **21**, 392-397, 1984c.
- Temerin, M., Doppler shift effects on double-probe-measured electric field power spectra, *J. Geophys. Res.*, **84**, 5929-5934, 1979.

(Received: April 26, 1988;
accepted May 26, 1988.)

Exposed High-Voltage Source Effect on the Potential of an Ionospheric Satellite

A. C. Tribble, N. D'Angelo, G. B. Murphy,
J. S. Pickett, J. T. Steinberg

Reprinted from



Journal of Spacecraft and Rockets

Volume 25, Number 1, January-February 1988, Pages 64-69

AMERICAN INSTITUTE OF AERONAUTICS AND ASTRONAUTICS, INC.
370 L'ENFANT PROMENADE, SW • WASHINGTON, DC 20024



Exposed High-Voltage Source Effect on the Potential of an Ionospheric Satellite

A. C. Tribble,* N. D'Angelo,† G. B. Murphy,‡ J. S. Pickett,§ and J. T. Steinberg¶
 University of Iowa, Iowa City, Iowa

A pulsed, high-voltage source, which is able to draw a current from the surrounding plasma, is seen to induce large changes in the potential of an ionospheric satellite (the Iowa Plasma Diagnostics Package flown on Space Shuttle flight STS-51F). This, in turn, may affect the operation of other instruments that use the chassis of the satellite as a ground for electrical circuits. The magnitude of the change in satellite potential is dependent upon both the orientation of the high-voltage source, relative to the plasma flow, and the characteristics of the high-voltage source. When the satellite is grounded to the Shuttle Orbiter, this effect is sufficient to change the potential of the Orbiter by a small, but noticeable, amount.

Nomenclature

- A_e = surface area of the PDP that will collect electrons
- A_i = surface area of the PDP that will collect ions
- e = charge of the electron
- h = height of the main body of the PDP
- h' = height of the "top cap" of the PDP
- $I_{e, ins}$ = electron current collected by all of the PDP's instruments
- $I_{e, pr}$ = electron current collected by the Langmuir probe
- $I_{e, LEP}$ = electron current collected by the LEPEDA
- $I_{e, sc}$ = electron current collected by the PDP chassis
- $I_{i, ins}$ = ion current collected by all of the PDP's instruments
- $I_{i, sc}$ = ion current collected by the PDP chassis
- k = Boltzmann's constant
- m_e = mass of the electron
- n_e = electron density
- n_i = ion density
- r = radius of the main body of the PDP
- r' = radius of the "top cap" of the PDP
- T_e = electron temperature
- v_o = orbital velocity of the PDP

Introduction

A SPACECRAFT traveling in the Earth's ionosphere has no external electrical ground available for it to use as a reference for potential measurements. As a consequence, such spacecraft are susceptible to different types of charging phenomena that may alter the potential of the spacecraft chassis.^{1,2} From July 29 to August 6, 1985, a satellite designed and built by the University of Iowa's Department of Physics and Astronomy, the Plasma Diagnostics Package (PDP), was flown as part of the Spacelab 2 payload on Space Shuttle flight STS-51F at an altitude of 325 km. The PDP is a cylindrical spacecraft 106.68 cm (42 in.) in diameter and 66.04 cm (26 in.) in height composed of 14 different instruments designed to study the plasma and electromagnetic environment near the Shuttle Orbiter. A diagram is shown in Fig. 1.

Received March 9, 1987; revision received June 23, 1987. Copyright © American Institute of Aeronautics and Astronautics, Inc., 1987. All rights reserved.

*Graduate Research Assistant, Member AIAA.

†Professor of Physics, Department of Physics and Astronomy.

‡Research Engineer, Department of Physics and Astronomy. Member AIAA.

§Staff Research Assistant, Department of Physics and Astronomy. Member AIAA.

¶Graduate Research Assistant, Department of Physics and Astronomy.

The PDP skins are constructed of aluminum and are covered by multilayered insulation (MLI) blankets followed by an outer dielectric layer of beta cloth (teflon-coated fiberglass) overlaid with a conducting aluminum wire mesh electrically grounded to the chassis of the PDP via bolts and staples through the MLI. The MLI consists of a singly aluminized kapton layer on the outside (aluminum sides facing inward) and 10 layers of doubly aluminized mylar separated by dacron net on the inside with grounding straps used to electrically bond the MLI to the structure.

During the Spacelab 2 mission, the PDP made measurements from the payload bay, from the Remote Manipulator

PDP BOOMS DEPLOYED CONFIGURATION

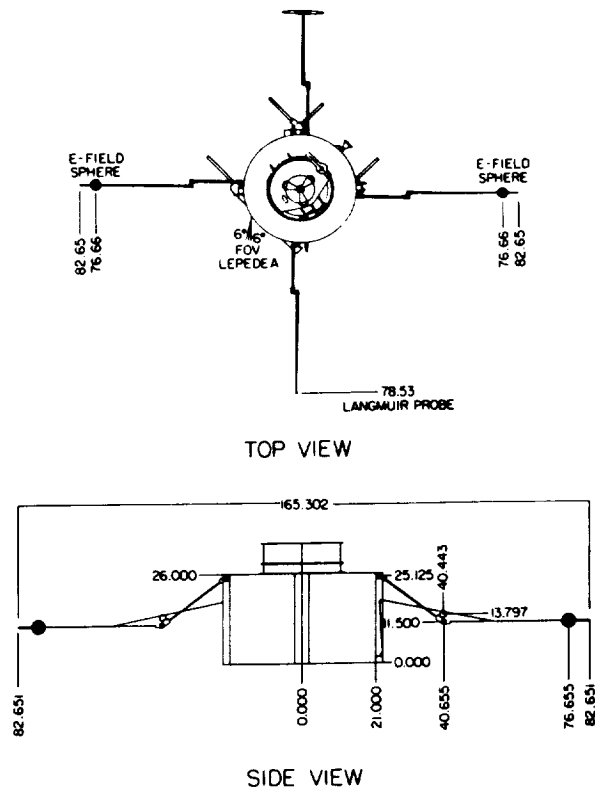


Fig. 1 Diagram of the PDP with booms deployed. Relevant distances are indicated in inches.

System (RMS), and for a period of 6 h as a free-flying subsatellite. This paper will show how some of the measurements made with a Langmuir probe and a dc Electric Fields instrument (utilizing the E-field spheres) on the PDP were affected by a pulsed, high-voltage source (LEPEDEA).

Instrumentation

A Langmuir probe on the PDP was used to make measurements of electron temperature, electron density, fluctuations in the electron density, and plasma potential. The Langmuir probe consisted of a 3-cm-diam spherical, gold-plated sensor and supporting circuitry. This circuitry was designed to alternate between two modes, which we refer to as the sweep mode and the lock mode.

During the sweep mode the bias voltage of the Langmuir probe was swept from 10 to -5 V, relative to the chassis of the PDP, in discrete steps of 0.125 V at a rate of 120 steps/s. A graph of the log of the current collected by the Langmuir probe during this time as a function of the bias voltage is typically referred to as a Langmuir curve. As shown, for example, by Huddleston and Leonard,³ a Langmuir curve allows us to calculate the electron density, electron temperature, and plasma potential. An example of a typical Langmuir curve is shown in Fig. 2a. In Fig. 2a and in all subsequent figures, the times given are in Universal Time (UT).

Following the sweep mode, the bias voltage on the Langmuir probe returned to 10 V where it remained for 11.8 s. During this time, the data collected by the probe, which were again sampled at a rate of 120 steps/s, allow us to measure electron density fluctuations. An example of the lock mode data, sampled through a 6-40-Hz filter, is shown in Fig. 2b. A Langmuir probe similar to the one used on the Spacelab 2 mission is discussed in more detail by Murphy et al.⁴

The dc Electric Fields instrument on the PDP consisted of two spherical unbiased high-impedance probes and associated electronics. The two sensors are visible in Fig. 1 and are labeled E-field spheres. In this paper, we are concerned with only one type of dc measurement that was made. The average of the dc potentials of the two spheres, V_a and V_b , relative to the chassis of the PDP, $(V_a + V_b)/2$, was measured once every 1.6 s. It is important to note that the measurements made by the Langmuir probe and the dc Electric Fields instrument complement each other in that the Langmuir probe was a low-impedance sensor that measured current at a controlled bias level and the dc Electric Fields instrument utilized high-impedance floating probes that measured the potential at near-zero current.

The last instrument that will be discussed in this paper is the Low Energy Proton Electron Differential Energy Analyzer (LEPEDEA). As can be seen in Fig. 1, the LEPEDEA was mounted on the circumference of the PDP. It has two particle collectors open to the ionosphere, one designed to detect electrons and the other, ions. The two openings are separated by a curved plate to which a pulsed high-voltage is applied. The combined cross-sectional area of the openings to the electron and ion detectors is 6.69 cm² (1.04 in.²). The high-voltage plate is 5.26 cm (2.07 in.) wide and extends into the LEPEDEA for a distance of 9.83 cm (3.87 in.). At time $t = 0$, the bias voltage on the LEPEDEA plate switched from 0 to 2.2 kV, relative to the chassis of the PDP, where it remained for 0.2 s. During the following 1.4 s, the bias voltage then decayed exponentially with a $1/e$ time of 0.16 s, the entire cycle requiring 1.6 s. The operation of the LEPEDEA is discussed in more detail by Frank et al.⁵

Anomalous Results

During the 6 h of free flight, an anomaly was detected in both the sweep and lock mode data collected by the Langmuir probe. An example is shown in Fig. 3. Figure 3a indicates that the normal Langmuir curve is interrupted by a "bite out" in the current collection. This bite out always maximizes approximately 0.2 s after the start of the voltage sweep.

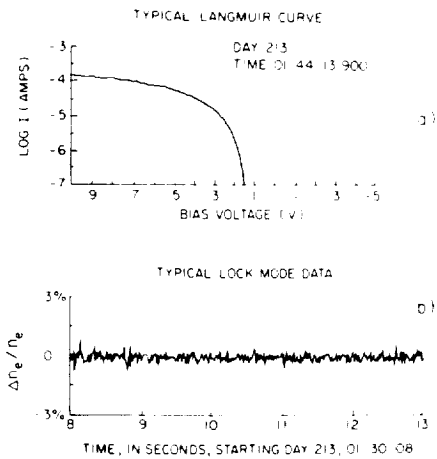


Fig. 2 Examples of: a) a typical Langmuir curve and; b) typical lock mode data.

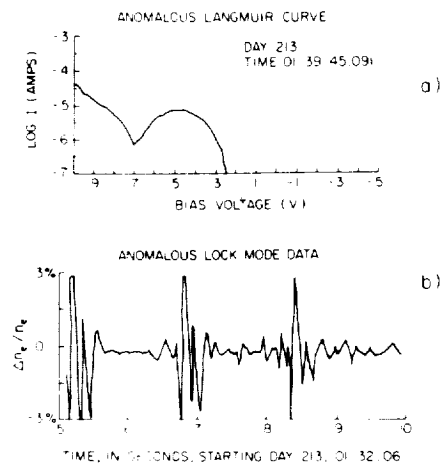


Fig. 3 Examples of: a) an anomalous Langmuir curve and; b) anomalous lock mode data.

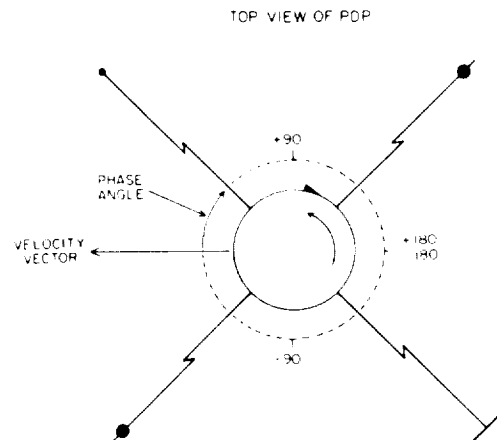


Fig. 4 Definition of the Langmuir probe phase angle. The PDP is rotating counterclockwise in the plane of the paper.

Further examination of a series of Langmuir curves indicates that the magnitude of the anomaly is dependent upon the orientation of the PDP, which was spinning about its cylindrical axis with an inertial period of 13.06 s. This orientation is defined by a phase angle, which is the angle between the velocity vector of the PDP and the vector that points from the center of the PDP to the Langmuir probe.

Fig. 4. In this figure, the PDP is rotating counterclockwise in the plane of the paper. The Langmuir probe entered the sweep mode every 12.8 s. Consequently, if the PDP started a voltage sweep when the phase angle was -180 deg, the next sweep would have begun when the phase angle was -172.9 deg. The difference in phase angles occurs because the PDP rotates through 352.9 deg in 12.80 s. Therefore, even though the PDP is rotating in a counterclockwise direction, a graph of phase angle at the start of a sweep mode vs time would show the Langmuir probe apparently precessing in a clockwise direction. A series of Langmuir curves that shows the dependence of the anomaly on the phase angle is shown in Fig. 5. These data indicate that the anomaly maximized at a phase angle of about -55 deg.

As seen in Fig. 3b, the lock mode data indicate that some type of interference, which we hereafter refer to as noise, was affecting the Langmuir probe once every 1.6 s. The anomaly in the lock mode data was present even during times when the PDP was grounded to the RMS of the Shuttle Orbiter. However, the magnitude of the resulting anomaly was reduced in comparison to that seen during free flight.

Like the Langmuir probe measurements, the dc potential measurements taken during free flight also had an unexpected character. As is shown in Fig. 6, the average potential of the spheres relative to the PDP varied with the spin phase of the spacecraft. In Fig. 6, the potential between the spheres and the PDP varies by about 2.1 V over the spin cycle. At other times during free flight, this variation in potential was as much as 3.0 V, depending on the local plasma conditions. The variation in potential always reached its maximum positive value when the phase angle of the Langmuir probe was about -55 deg.

Source of the Interference

Several reasons led us to believe that the noise detected by the Langmuir probe during PDP free flight was not due to an instrument malfunction. First, at all other times throughout the mission, the probe appeared to function as expected, and no anomaly was detected until data reduction had begun. Second, noise seen by the dc Electric Fields Instrument was coincident in time with the noise seen by the Langmuir probe. Also significant was the fact that the Langmuir probe noise recurred with a period of 1.6 s. This is important in that several instruments on the PDP were designed so that one complete "cycle" would require 1.6 s. As was mentioned previously, the LEPEDA is just such an instrument. The temporal relation between the bias voltage on the LEPEDA and the bias voltage on the Langmuir probe is illustrated in Fig. 7. The "ringing" detected in the lock mode data occurred at precisely the times that the bias voltage on the LEPEDA switched from 0 to 2.2 kV. This, and the fact that, throughout the mission, whenever the LEPEDA was turned off, the anomalies seen by the Langmuir probe and the dc Electric Fields Instrument disappeared, led us to believe that, in some way, the LEPEDA was responsible for the anomalous data.

This suspicion was strengthened by the fact that the phase-angle dependence, Fig. 5, shows strong indications of being a dependence upon the orientation of the LEPEDA. In Fig. 5, we see that the Langmuir curves, which have an anomalous character, occur between a phase angle of about -110 and 30 deg. This corresponds to time when the LEPEDA phase angle was between -53 and 87 deg. Sweeps taken when the Langmuir probe phase angle was -55 deg corresponded to times when the LEPEDA was approximately in ram. Thus, the anomalies were largest when the LEPEDA was in the ram of the plasma flow and smallest when it was in wake. The reason for this dependence will be discussed in the next section.

Discussion

When working with laboratory plasmas, it is possible to use an externally grounded electrode, whose potential will not change, as a reference point for potential measurements.

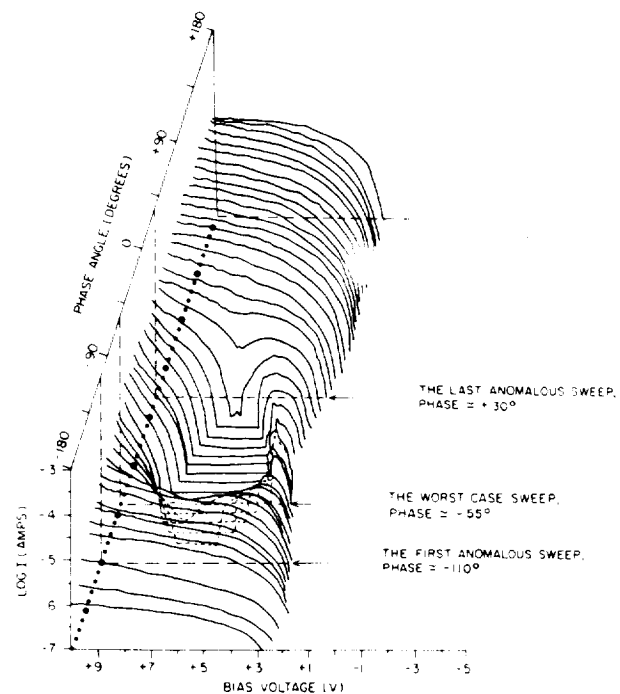


Fig. 5 Series of Langmuir curves taken at various phase angles. Time increases with increasing phase angle.

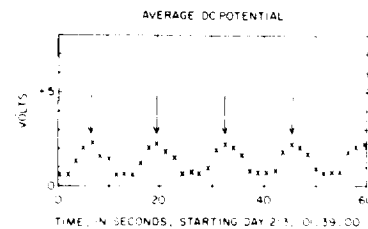


Fig. 6 Average dc potential of the PDP as measured by the dc Electric Fields instrument. The arrows indicate the times when the LEPEDA is approximately in ram.

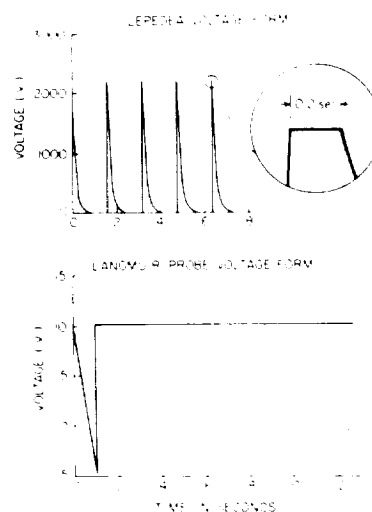


Fig. 7 Temporal relation between the Langmuir probe and the LEPEDA bias voltages.

However, no such electrical ground is available when dealing with a spacecraft in the ionosphere. In such a situation, we must treat the system of the spacecraft and the instruments

mounted on it as a "double probe," following the method originally proposed by Johnson and Malter.⁶ When two probes are biased with respect to one another but insulated from ground, the entire system will "float." An important consequence of this is that the total current collected by the system must be zero. That is, any electron current collected by the system must be balanced by an equal ion current. In our case, the condition that the system be floating is

$$I_{i,sc} + I_{i,ins} - I_{e,sc} - I_{e,ins} = 0 \quad (1)$$

where $I_{i,sc}$, $I_{e,sc}$, $I_{i,ins}$, and $I_{e,ins}$ are defined as the ion and electron currents to the PDP spacecraft structure and the instruments, respectively. We are able to obtain expressions for $I_{i,sc}$ and $I_{e,sc}$ in the following manner.

After release from the Shuttle, the PDP had an orbital velocity of about 7.7 km/s. Analysis of the uncontaminated Langmuir probe data indicated that the electrons had a typical temperature of about 2500 K and a typical density of $1.5 \times 10^5 \text{ cm}^{-3}$, in general agreement with previous measurements. If we assume that the ions and electrons are in thermal equilibrium, we find that the thermal velocity of an electron was about 180 km/s and the thermal velocity of atomic oxygen, the predominant ion in the F2 region, about 1.1 km/s. Since the orbital velocity of the PDP was approximately a factor of 7 greater than the thermal velocity of the ions, most of the ions would have impacted the PDP on the side facing the ram of the plasma flow, the ion current thus consisting of the ions swept out by the front surface of the PDP. The equation describing ion current collection by the spacecraft is

$$I_{i,sc} = A_i e n_i v_o \quad (2)$$

where A_i is the front surface area of the PDP, e the charge of the ion, n_i the ambient ion density (we assume $n_i = n_e$), and v_o the orbital velocity of the PDP. Since the ion current consists of those ions that are rammed out by the motion of the PDP, we will approximate A_i by $(2rh + 2r'h')$, where r , h are the radius and height of the main body of the PDP, and r' , h' are the radius and height of the "top cap," Fig. 1.

The thermal velocity of the electrons is greater than the orbital velocity of the PDP by almost a factor of 25. Consequently, all surfaces of the PDP will collect electron current, not just the ram side. We assume that the electrons had a Maxwellian distribution given by

$$f_e(v) = n_e \left[\frac{m_e}{2\pi k T_e} \right]^{3/2} \exp \left[\frac{-m_e v^2}{2k T_e} \right] \quad (3)$$

The electron current to the PDP at a potential V less than the plasma potential V_p , and measured relative to V_p , consists of those electrons with energies greater than $|eV|$ that strike the PDP, and is given by

$$I_{e,sc} = A_e e n_e \left[\frac{k T_e}{2\pi m_e} \right]^{1/2} \exp \left[\frac{eV}{k T_e} \right] \quad (4)$$

where A_e is the surface area of the PDP that will collect electrons, e the charge on the electron, n_e the electron density, k Boltzmann's constant, T_e the electron temperature, and m_e the electron mass. Since the electrons may strike all surfaces of the PDP, we approximate A_e by $(2\pi r^2 + 2\pi r h + 2\pi r' h')$.

We now need expressions for $I_{i,ins}$ and $I_{e,ins}$. The cross-sectional collecting areas of all of the instruments on the PDP are several orders of magnitude smaller than A_i ; consequently, we should be justified in neglecting $I_{i,ins}$ altogether. The only instruments on the PDP expected to draw significant amounts of electron current from the plasma, due to their positive bias voltages, are the Langmuir probe and the LEPDEA. We can rewrite Eq. (1) as

$$I_{i,sc} - I_{e,sc} - I_{e,pr} - I_{e,LEP} = 0 \quad (5)$$

where the subscripts pr and LEP refer to current collected by the Langmuir probe and LEPDEA, respectively. We can solve the preceding equation to determine the potential of the chassis of the PDP. Since the LEPDEA has a very small collecting area and its bias voltage is large only for about 0.3 s, during most of its 1.6-s operational cycle it should draw negligible current from the ionosphere. Therefore, we will first solve for the floating potential by setting $I_{e,LEP}$ to zero. Substituting Eqs. (2) and (4) into Eq. (5), with $I_{e,LEP}$ set to zero, we find that the "floating potential" of the PDP is given by

$$V = \frac{+k T_e}{e} \ln \left[\frac{A_i e n_i v_o - I_{e,pr}}{A_e e n_e (k T_e / 2\pi m_e)^{1/2}} \right] \quad (6)$$

Using the values for n_e , T_e , and the additional constants given in Table 1, we may determine the nominal floating potential of the PDP once we know $I_{e,pr}$. Analysis of Langmuir curves collected under the plasma conditions listed in Table 1 reveals that the corresponding value of $I_{e,pr}$ is approximately 14 μA , which would give a value of -0.90 V for the floating potential of the PDP. The resulting magnitudes of $I_{e,sc}$ and $I_{i,sc}$ would be about 93 and 107 μA , respectively. (Ignoring the presence of $I_{e,pr}$, i.e., setting $I_{e,pr}$ to zero, would have given a value for V_f of -0.86 V . As we shall see momentarily, a change of 0.04 V is about 2 orders of magnitude smaller than the effect that is responsible for the appearance of the anomalous data. Consequently, we would be justified in ignoring $I_{e,pr}$ altogether.)

We turn next to the intervals when the LEPDEA voltage was large and positive. As was mentioned previously, we believe that the cause of the anomalous data discussed in the preceding sections was somehow related to the operation of the LEPDEA. The most likely explanation for the appearance of the anomalous Langmuir curves is that the bias voltage of the Langmuir probe, relative to the plasma, was changing unexpectedly during the course of a sweep. One other possible explanation, that the conditions in the plasma itself were changing, was not supported by data from other instruments on the PDP. An examination of all anomalous Langmuir curves showed that, by the time the Langmuir probe bias voltage had stepped to 4 V, the cause of the anomaly seemed to have subsided, as the remainder of the anomalous Langmuir curve appeared nominal. Under the assumption that whatever was responsible for the anomaly had completely subsided by the time the probe's bias voltage was 4 V and that the conditions in the plasma remained unchanged during the course of a sweep, we were able to analyze the anomalous sweeps as follows. The Langmuir curve shown in Fig. 8 was taken when the plasma conditions were similar to those given in Table 1. In this figure, when the bias voltage of the Langmuir probe was 9 V, the probe collected about 6 μA of current from the plasma. Under normal conditions we would not collect this current until the bias voltage of the probe was 7.3 V. Therefore, we conclude that, at the time the probe bias voltage was supposed to be 9 V, relative to the original floating potential of the PDP, it was actually 7.3 V. As is shown in Fig. 9, this procedure allowed us to determine the potential of the PDP, relative to the original floating

Table 1 Constants used in the calculation of the floating potential

Geometry of satellite:	
Electron collecting area A_e , m^2	4.395
Ion collecting area A_i , m^2	0.830
Height of main body h , cm (in.)	66.04 (26)
Height of "top cap" h' , cm (in.)	21.97 (8.65)
Radius of main body r , cm (in.)	53.34 (21)
Radius of "top cap" r' , cm (in.)	28.58 (11.25)
Orbital parameters:	
Electron density n_e , $\times 10^5 \text{ cm}^{-3}$	1
Ion density n_i , $\times 10^5 \text{ cm}^{-3}$	1
Electron temperature T_e , K	2500
Orbital velocity of PDP v_o , km/s	7.7

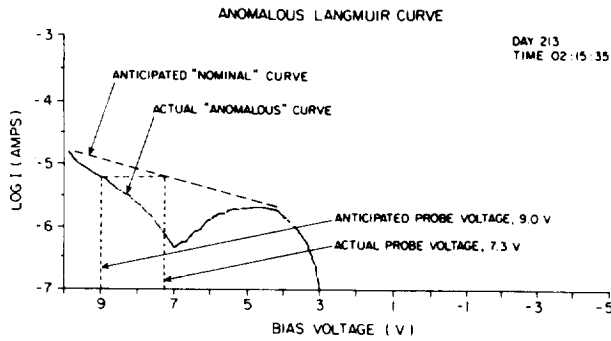


Fig. 8 Illustration of the method used to determine the actual Langmuir probe bias voltage, relative to the original floating potential of the spacecraft.

potential, as a function of time. (This cannot be done with the average dc potential measurements by the E-field spheres, since the dc potential is sampled only once every 1.6 s.) The potential of the PDP dropped for about 0.2 s after the beginning of a sweep and then spent the next 0.2 s recovering to its original value. The implications of this are as follows.

Recall that the current balance equation, Eq. (5), must be satisfied at all times. We have four currents contributing to current balance. $I_{i,sc}$ is a constant, independent of the floating potential of the PDP, $I_{e,sc}$ depends on the floating potential, which we can determine as in Fig. 9, and $I_{e,pr}$ was measured directly. This allows us to solve for our one remaining unknown, $I_{e,LEP}$. A graph of $I_{e,LEP}$ as a function of time, assuming the plasma conditions given in Table 1, is given in Fig. 10. Time $t = 0$ is the time when the bias voltage on the LEPEDA switches from 0 to 2.2 kV. Due to the sampling rate of the Langmuir probe data, 120 Hz, we were unable to determine the form of $I_{e,LEP}$ between 0 and 0.050 s. Consequently, this portion of the graph has been left blank. Also, we were unable to obtain $I_{e,LEP}$ after about 0.4 s, since it was difficult to establish with any accuracy when the predominant source of electron current changed from $I_{e,LEP}$ to $I_{e,sc}$.

In spite of these difficulties, the significance of Fig. 10 is that it shows conclusively that the LEPEDA must be drawing significant amounts of electron current from the ionosphere. At time $t = 0.2$ s, the LEPEDA is drawing about 100 μ A of electron current, compared with 107 μ A for the magnitude of $I_{i,sc}$. Thus, the LEPEDA current is large enough that the potential of the PDP must drop by several volts in order to maintain current balance. In the example presented here, $n_e = 1 \times 10^5 \text{ cm}^{-3}$, $T_e = 2500 \text{ K}$, the potential of the PDP dropped by about 4 V. However, in some cases, when the Langmuir probe phase angle was about -55 deg, the resulting Langmuir curves indicated an even larger drop in spacecraft potential, Fig. 5. Also, by comparing the magnitude of the noise seen in the lock mode data during these worst-case events with the noise seen when the plasma conditions were similar to those in Fig. 8, we believe that, in some cases, the potential of the PDP may have dropped by as much as 10 V.

The previous discussion indicates that it is current collection by the LEPEDA that is responsible for the anomalous data reported by both the Langmuir probe and the dc Electric Fields instrument. We must now show that this can explain the actual appearance of the anomalous data and also the dependence of the anomaly on the phase angle. We begin with a discussion of the Langmuir probe sweep mode data. As was shown in Fig. 7, the bias voltage on the LEPEDA switches from 0 to 2.2 kV at the same time that the Langmuir probe enters the sweep mode. However, as was shown in Fig. 9, the maximum change in spacecraft potential does not occur until 0.2 s after the start of the sweep. This 0.2-s delay occurs because at time $t = 0$ the bias voltage on the LEPEDA switches from 0 to 2.2 kV and remains at this level for 0.2 s. The situation is similar to what happens when one charges/

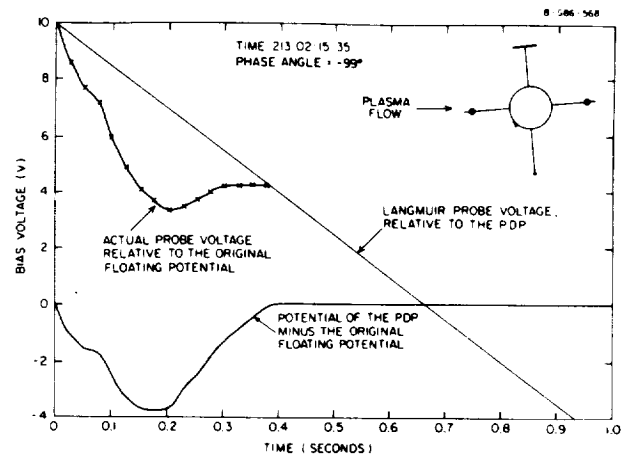


Fig. 9 Potential of the Langmuir probe and the PDP relative to the original floating potential.

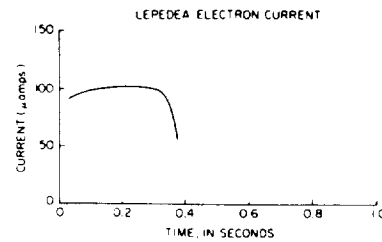


Fig. 10 Predicted value of the LEPEDA electron current, $I_{e,LEP}$, vs time. Time $t = 0$ corresponds to the time when the LEPEDA bias voltage switched from 0 to 2.2 kV.

discharges a capacitor. At $t = 0$, the LEPEDA bias voltage is large and positive, thus the LEPEDA can draw a large electron current from the ionosphere and the PDP begins to charge to a negative potential. At $t = 0.2$ s, the bias voltage on the LEPEDA begins to decrease. Consequently, the electron current collected by the LEPEDA also decreases and the PDP begins to "discharge" to its original potential.

As can be seen in Fig. 9, the PDP potential wave form appears "rounded off" at early times. We have examined the possibility that this rounding could be related to a spacecraft-plasma circuit. Based on an electron density of $1 \times 10^5 \text{ cm}^{-3}$, we calculate a plasma sheath resistance of about 10 k Ω , ignoring magnetic field effects. If the rounding off of the spacecraft potential waveform occurred because the current to the spacecraft could only vary with a time constant given by $\tau = L/R \approx 0.2$ s or $\tau = RC \approx 0.2$ s, for a simple circuit this would require values for the inductance L or the capacitance C , which are unrealistically large. Similarly, an examination of the Langmuir probe circuit gives no indication that any of its components could be responsible for producing the effect either. We have been informed that the LEPEDA voltage form was nominal in the high-voltage range during the time of observation,⁷ consequently, a satisfactory explanation of the PDP potential waveform is lacking.

The appearance of the lock mode (6-40 Hz) data is understood as follows. As was shown in Fig. 9, we were able to deduce the potential of the chassis of the PDP, as a function of time, after the voltage pulse to the LEPEDA. Consequently, we also know that the actual bias voltage of the Langmuir probe would be, relative to the plasma, during the lock mode. This is shown in Fig. 11a, where time $t = 0$ again corresponds to the start of the voltage pulse on the LEPEDA and the plasma conditions are those given in Table 1. Using a nominal Langmuir curve, Fig. 2a, we then determine the current collected by the Langmuir probe during the lock mode by reversing the process illustrated in Fig. 8. The current curve in the lock mode is shown in Fig. 11b for the initial 1.0 s of the 1.6-s cycle of the LEPEDA voltage. By taking the fast

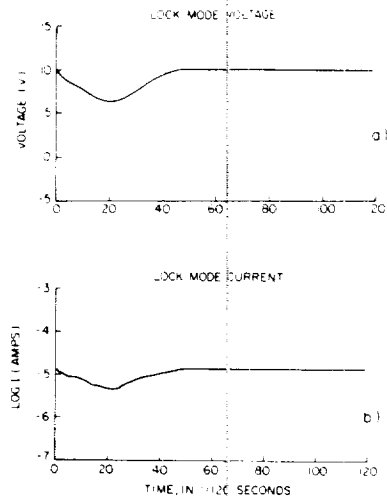


Fig. 11 Actual Langmuir probe bias voltage during the lock mode, relative to the original floating potential (a) and computation of the current collected by the Langmuir probe during lock mode (b). Time $t = 0$ corresponds to the time when the LEPEDA bias voltage switched from 0 to 2.2 kV.

Fourier transform of these data, Fig. 11b, we then isolate the contribution of the 6-40-Hz components, see Fig. 12. In comparing Fig. 12 with Fig. 3b, we notice that the general oscillatory form seen in Fig. 12 is very similar to that seen in the actual data, although the finer details appear somewhat different. We should note that, in an attempt to recreate the ringing seen in Fig. 3b, we have ignored the presence of any rapid density fluctuations, and, thus, cannot expect our prediction, Fig. 12, to agree entirely with the actual data, Fig. 3b.

Next, we need to explain the dependence that the anomaly has on the orientation of the PDP. As was previously mentioned, the magnitude of the anomaly recorded by both the Langmuir probe and the dc Electric Fields instrument maximizes whenever the LEPEDA is in ram. We would expect the LEPEDA to draw less current when the local electron density, i.e., the electron density near its opening, is small, and more current when the local electron density is large. If we ignore $I_{e,pr}$, we may rewrite Eq. (5) as

$$I_{e,LEP} = e n_e^*(\theta) f(V) \\ = en_e(A_1 v_0 - A_e [kT_e / 2\pi m_e]^{1/2} \exp[eV/kT_e]) \quad (7)$$

where $n_e^*(\theta)$ is the local electron density "seen" by the LEPEDA, θ the LEPEDA phase angle, and $f(V)$ some function of its bias voltage. It is well established that the wake of an ionospheric satellite is a region of depleted electron densities. Therefore, when the LEPEDA is facing the wake of the PDP, the local electron density, $n_e^*(\theta)$, will be significantly less than the local electron density seen in ram. Thus, the magnitude of $I_{e,LEP}$ when the LEPEDA is in the wake will be correspondingly reduced and current balance will be achieved with virtually no change in spacecraft potential. Consequently, no anomaly is detected when the LEPEDA is in the wake.

Finally, the measurements of the average potential on the E-field spheres, relative to the chassis of the PDP, can also be easily understood. With the LEPEDA voltage pulsed to 2.2 kV, the potential between the PDP (which becomes more negative) and the spheres (still close to the original floating potential) must increase. We note that this potential measurement was taken once every 1.6 s and always 0.166 s after the LEPEDA voltage pulse. We can compare the potential change measured by the dc Electric Fields instrument with that determined from the Langmuir probe as in Fig. 9. In so doing, we find that the former is generally somewhat smaller

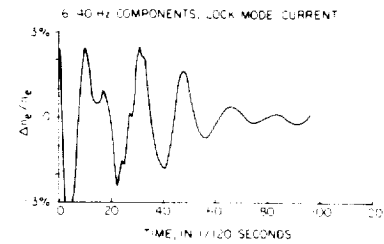


Fig. 12 Computed lock mode output from the 6-40-Hz channel. Time $t = 0$ corresponds to the time when the LEPEDA bias voltage switched from 0 to 2.2 kV.

than the latter, an effect due to low-pass filtering in the dc Electric Fields instrument. The Langmuir probe measurements and the dc potential measurements are, however, in general agreement.

Conclusions

Our experience suggests that an exposed, positive high-voltage source on an ionospheric satellite can act as a source of electron current to the spacecraft chassis. This may, in turn, affect the operation of other instruments that use the chassis of the satellite as an electrical ground by altering the spacecraft potential. This change in spacecraft potential is dependent upon the orientation of the high-voltage source, relative to the plasma flow. It is believed that this problem can be minimized in the future by placing a grounded grid on the opening of the high-voltage source so as to limit the collection of thermal electrons.

The fact that the effect was also detectable in the lock mode data when the PDP was grounded to the Orbiter indicates that the pulse of electron current collected by the LEPEDA was sufficient to change the potential of the Shuttle by a small, but noticeable, amount. Most of the body of the Shuttle is covered with an insulating material. The area of the Shuttle believed to be most responsible for current collection is the main engines. Because the surface area of the main engines is approximately one order of magnitude greater than that of the PDP, the current pulse to the LEPEDA may have shifted the potential of the Orbiter by as much as -1 V when the main engines were in the Orbiter's wake. If the potential of the Orbiter had shifted by more than -1 V the appearance of the Langmuir probe sweep mode data would have been affected. Since this did not occur, -1 V is an upper bound on the change in potential of the Shuttle.

Acknowledgments

This work was supported by Grant NAG3-449 from the NASA Lewis Research Center and Contract NAS8-32807 from the NASA Marshall Space Flight Center. We gratefully acknowledge the assistance of Prof. Donald A. Gurnett for providing the dc Electric Fields data and of the LEPEDA science/engineering team, in particular Bill Paterson, for their help in describing the operation of the LEPEDA.

References

- ¹DeForest, S. E., "Spacecraft Charging at Synchronous Orbit," *Journal of Geophysical Research*, Vol. 77, No. 4, Feb. 1972, p. 651.
- ²Olsen, R. C. and Purvis, C. K., "Observations of Charging Dynamics," *Journal of Geophysical Research*, Vol. 88, No. A7, July 1983, p. 5657.
- ³Huddleston, R. H., and Leonard, S. L., eds., *Plasma Diagnostic Techniques*, Academic Press, New York, 1965.
- ⁴Murphy, G., Pickett, J., D'Angelo, N., and Kurth, W. S., "Measurements of Plasma Parameters in the Vicinity of the Space Shuttle," *Planetary and Space Science*, Vol. 34, Oct. 1986, p. 993.
- ⁵Frank, L. A., Yeager, D. M., Owens, H. D., Ackerson, K. L., and English, M. R., "Quadrifurcated LEPEDAs for ISEE's-1 and -2 Plasma Measurements," *IEEE Transactions on Geoscience Electronics*, Vol. GE-16, July 1978, p. 221.
- ⁶Johnson, E. O. and Malter, L., "A Floating Double Probe Method for Measurements in Gas Discharges," *Physical Review*, Vol. 80, Oct. 1950, p. 58.
- ⁷Cravens, J., private communication, 1987.

The Plasma Wake of the Shuttle Orbiter

G. B. MURPHY,¹ D. L. REASONER,² A. TRIBBLE,³ N. D'ANGELO, J. S. PICKETT, AND W. S. KURTH

Department of Physics and Astronomy, The University of Iowa, Iowa City

One of the objectives of the Plasma Diagnostics Package (PDP) instrumentation on Spacelab 2 was to obtain information about the plasma wake of the shuttle orbiter. We present plasma density and electron temperature data obtained (1) while the PDP was attached to the shuttle remote manipulator system and (2) while the PDP was a free-flying satellite. Wake crossings by the PDP from ~40 m to ~240 m behind the orbiter provide information about the structure of the mid and far wake of the orbiter. As expected, the wake is characterized by density depressions, relative to the ambient ionospheric plasma, and by enhancements of the electron temperature, particularly in the near and mid wake. The observed electron temperature enhancements appear to be in line with previous spacecraft observations.

INTRODUCTION

For many years, wakes of bodies of different sizes and shapes in supersonic plasma flows have been studied both experimentally and theoretically. The experimental work has been performed both in the laboratory [e.g., Stone, 1979, 1981a, b; Bogashchenko et al., 1971; Schmitt, 1973; Merlino and D'Angelo, 1987] and on various ionospheric spacecraft [e.g., Samir and Wrenn, 1972; Stone et al., 1986; Shawhan et al., 1984; Murphy et al., 1986; Raitt et al., 1987; Reasoner et al., 1986]. For a review of the theoretical work (and an extensive bibliography), see, for example, Stone [1979].

Both ionospheric observations and laboratory experiments are generally performed under the conditions $C_s \ll v \ll v_{e,th}$, where C_s is the ion acoustic speed, $v_{e,th}$ is the electron thermal speed, and v is the speed of plasma flow relative to the "body." Thus the plasma flow is supersonic ($M = v/C_s \gg 1$) in relation to the ions but slow in relation to the electron thermal motion.

Other parameters characterizing the plasma flow-body interaction are (1) the ratio L/λ_D between the body transverse dimension L and the Debye length λ_D , and (2) the ratio L/ρ_i , where ρ_i is the ion gyroradius. In laboratory experiments the ratio L/λ_D is $\sim 10^2$ [e.g., Schmitt, 1973; Merlino and D'Angelo, 1987]. This is also true for spacecraft of ~1-m size, interacting with the *F* region ionospheric plasma ($\lambda_D \approx 1$ cm). For the case of the shuttle orbiter, with dimensions transverse to the plasma flow of 10–15 m, the ratio L/λ_D is $\sim 10^3$.

As far as the ratio L/ρ_i is concerned, a direct comparison of conditions prevailing in the laboratory with those realized in spacecraft/plasma interaction may not be entirely meaningful, since in the laboratory experiments performed so far, the plasma flow was always magnetic field aligned, while in the case of a spacecraft in the ionosphere the angle between the Earth's magnetic field and the flow varies over a wide range. However, for orientation purposes, it may still be

useful to compare the L/ρ_i of some laboratory experiments with those of different spacecraft. In the *Q*-machine experiment of Schmitt [1973], $L/\rho_i \geq 1$, while in the argon plasma of Merlino and D'Angelo [1987], $L/\rho_i \approx 0.1$. For a typical *F* region O^+ ion, $\rho_i \approx 5$ m. Thus with a spacecraft of about 1-m size, $L/\rho_i \approx 0.2$. In the case of the shuttle orbiter, on the other hand, since $L \approx 10$ –15 m, we have $L/\rho_i \approx 2$ –3.

This paper is organized as follows: The second section ("experiment") contains a brief description of the relevant experimental conditions during the Spacelab 2 mission. In the third section ("observations") the observations of the shuttle plasma wake are described. Finally, the fourth section ("discussion") presents a discussion of the results.

EXPERIMENT

The Plasma Diagnostics Package (PDP), a small recoverable scientific satellite designed and built at the University of Iowa, was one of 13 experiments aboard Spacelab 2 on Shuttle 51F in July–August 1985. One of its principal objectives was to determine the characteristics of the wake associated with plasma flow past a large-scale structure such as the orbiter. The plasma conditions and some other typical parameters for the Spacelab 2 mission are given in Table 1.

A description of the PDP and its instrumentation can be found in the work of Shawhan et al. [1984]. The present paper will focus on electron density and temperature data collected by the Langmuir probe (LP) instrument similar to the one described by Murphy et al. [1986] and on ion density measurements taken by the retarding potential analyzer (RPA) described by Reasoner et al. [1986]. It will enlarge the database of previous shuttle investigations, such as those of Murphy et al. [1986], Stone et al. [1986], and Raitt et al. [1987].

Two sets of experiments were performed during the mission, which enabled the PDP to investigate the orbiter wake at downstream distances ranging from ~10 m to ~240 m. The first set of observations was designed to study the near wake, while the second was devoted to an investigation of the mid and far wake:

1. For a study of the near wake, the PDP was positioned by the remote manipulator system (RMS) at approximately 10 m directly above the orbiter cargo bay (Figure 1). The orbiter then underwent a slow roll, at the rate of 1 degree per second, so that the PDP would pass alternately from the ram of the plasma flow into the orbiter wake, 9 times during a

¹Now at Jet Propulsion Laboratory, Pasadena, California.

²Also at NASA Marshall Space Flight Center, Huntsville, Alabama.

³Now at Rockwell International, Satellite and Space Electronics Division, Seal Beach, California.

Copyright 1989 by the American Geophysical Union.

Paper number 89JA00149.
0148-0227/89/89JA-00149\$05.00

TABLE 1. Typical Parameters for Spacelab 2

Parameter	Value
Electron density n_0 , cm^{-3}	$1-5 \times 10^5$
Electron T_e (and ion T_i) temperature ($T_e \approx T_i$), °K	2500
Debye length λ_D , cm	1
Ion acoustic speed C_s , km/s	2.3
Electron thermal speed $v_{e,th}$, km/s	200
Orbital velocity v , km/s	7.7
Orbital altitude h , km	320
Electron plasma frequency $f_{p,e}$, MHz	2.8-6.3
Ion plasma frequency $f_{p,i}$, kHz	17-38
Ion gyroradius ρ_i , m	5

1-hour period. This allowed us to explore the near wake of the orbiter by crossing it repeatedly across its narrowest dimension (along the Y axis in Figure 1). The coordinate system shown in Figure 1 is a noninertial frame, moving along with the shuttle in its orbit with, at all times, Y positive downward toward nadir, Z positive in the direction of the orbiter velocity vector (opposite to plasma flow), and the X axis completing the right-handed coordinate system.

2. For a study of the mid and far wake, a second set of experiments was performed during a 6-hour period, during which the PDP was released from the orbiter and operated as a spin-stabilized satellite. For this portion of the flight, the shuttle was rotated to fly "nose up." A coordinate system more appropriate during the PDP free flight is obtained by a -90° rotation about the Z axis shown in Figure 1, i.e., X' positive upward toward zenith, Z' positive in the direction of the orbiter velocity vector, and the Y' axis completing the right-handed coordinate system. Note, however, that in Figure 2 the PDP is at the origin of this coordinate system,

with the shuttle moving in the $X'Z'$ plane. The orbiter performed a series of maneuvers designed to cause the PDP to pass through the orbiter wake at varying distances downstream. All of these wake crossings occurred close (within ~ 10 m) to the shuttle orbital plane (the $X'Z'$ plane), so that the shuttle wake was explored along its widest dimension. At the end of the 6-hour free flight period the orbiter approached the PDP, which was then recaptured by the RMS.

Two portions of the free flight period were studied separately, namely: (1) the orbiter back-away maneuver in which, after releasing the PDP from the RMS, the orbiter separated along the velocity vector, and (2) several PDP transits of the shuttle wake, as the orbiter performed an "elliptical fly-around." These maneuvers are illustrated in Figure 2a, while the wake transits resulting from fly-around are highlighted and numbered in Figure 2b. In Figure 2 the orbital maneuver in the orbital plane is presented in a reference frame which has the PDP at its origin and local horizontal and local vertical axes.

The trajectory reconstruction for Figure 2 was done using a procedure discussed by *Huysman and Pieniasek* [1985] and *Pieniasek* [1985]. The reconstructed trajectory is believed to be accurate to a typical 1-sigma sphere of ~ 10 -m diameter. Reconstruction of the trajectory during back-away out to approximately 40 m was performed by integration of the separation velocity obtained from on-board navigation software.

OBSERVATIONS

We begin this section by showing LP electron density and temperature data obtained during the orbiter roll maneuver, with the PDP on the RMS as shown in Figure 1. Figure 3a shows the density measured by the Langmuir probe as a function of the phase angle Φ defined as the angle between

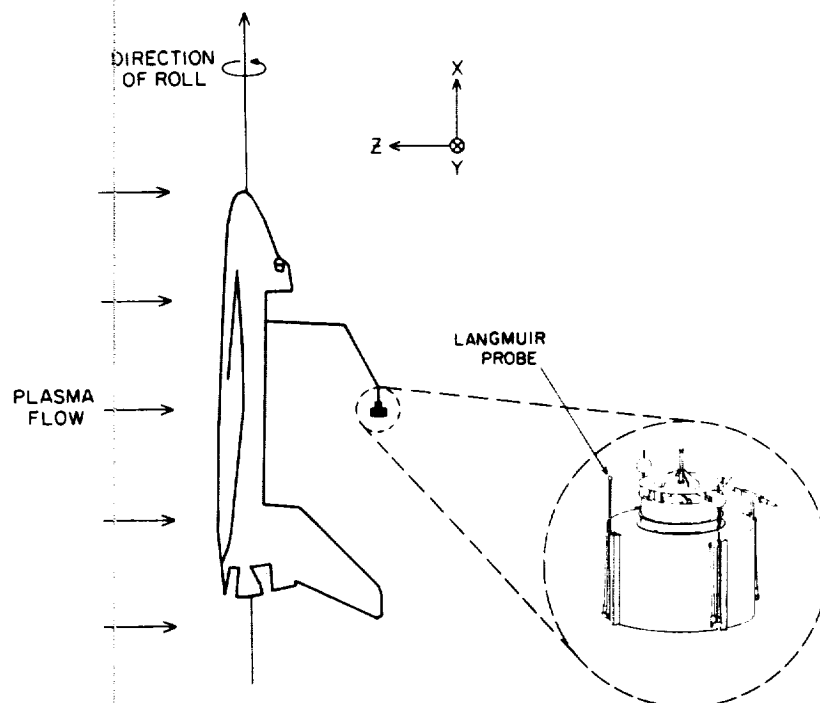


Fig. 1. The orbiter roll maneuver. The position of the PDP with respect to the orbiter is fixed, but the PDP is rotated about an axis parallel to the orbiter's X axis to maintain constant orientation to the velocity vector (except for the first orbiter roll). The orbiter's X axis is perpendicular to the orbit plane.

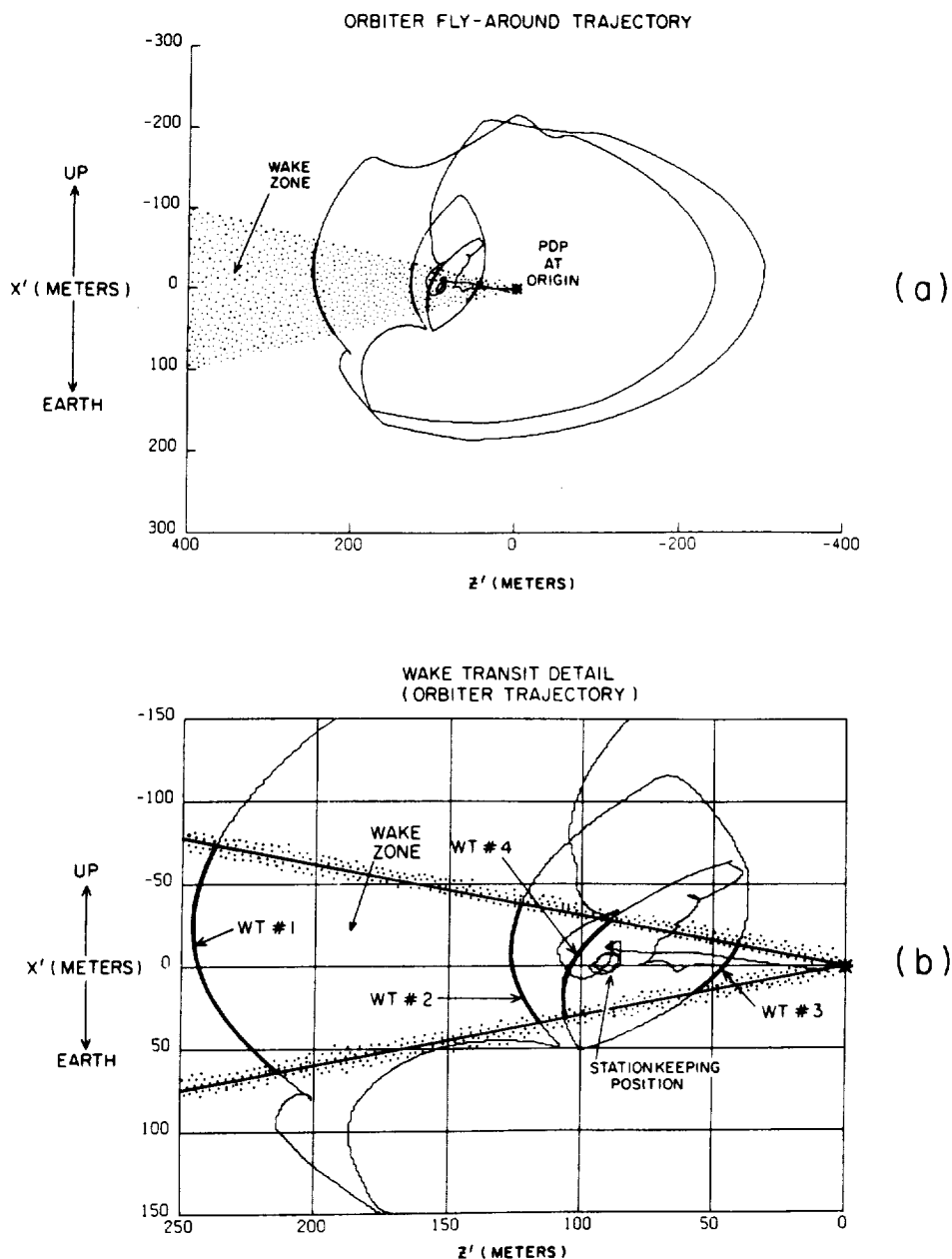


Fig. 2. (a) The entire 6-hour PDP free flight. The orbiter has been rotated (it flies nose up); the X' axis now points toward zenith, and the Z' axis points along the orbiter velocity. Thus the $X'Z'$ plane is the orbital plane. The PDP is at the origin of the coordinate system, and the times of interest for the mid and far wake study occur when the orbiter is within the shaded region. Note that unlike laboratory experiments, the object (orbiter) is moved here around the probe (PDP). (b) The "wake transits" are enlarged and labeled 1 through 4 for future reference. The orbiter-PDP distance varies along Z' from ~ 40 m to ~ 240 m.

the orbiter velocity vector and a line joining the "center" of the orbiter with the center of the PDP. A phase angle equal to zero thus means that the PDP is in ram, while for an angle of 180° the PDP is at the center of the orbiter wake. The density depression associated with the orbiter wake is clearly seen near $\Phi = 180^\circ$, while two less deep depressions are also present at $\Phi \approx 50^\circ$ and $\Phi \approx 320^\circ$. These latter features are associated with two smaller wakes produced by the RMS "wrist" grappled to the top of the PDP. For each of the following 360° orbiter rolls the PDP was continuously rotated by the RMS so as to avoid that the Langmuir Probe be affected by either the wake of the RMS or of the PDP. With this last arrangement, only the orbiter wake was detected. Figure 3b shows the electron temperature, as a

function of phase angle, for the same orbiter roll as Figure 3a. Large temperature enhancements are seen in the orbiter wake, and smaller enhancements in the RMS wakes.

Figure 4 presents measurements of the wake density for another orbiter roll. Here the abscissa is expressed as distance, in meters, from wake center, and the density is expressed in terms of the ram (or ambient) density.

We turn next to measurements performed after the PDP was released from the orbiter and operated as a spin-stabilized satellite (see the second section ("experiment"), point 2). Figure 5a shows the observed electron and ion densities during the back-away maneuver as functions of UT. The dots are the electron density (small periodic depressions are seen for the times the boom-mounted probe

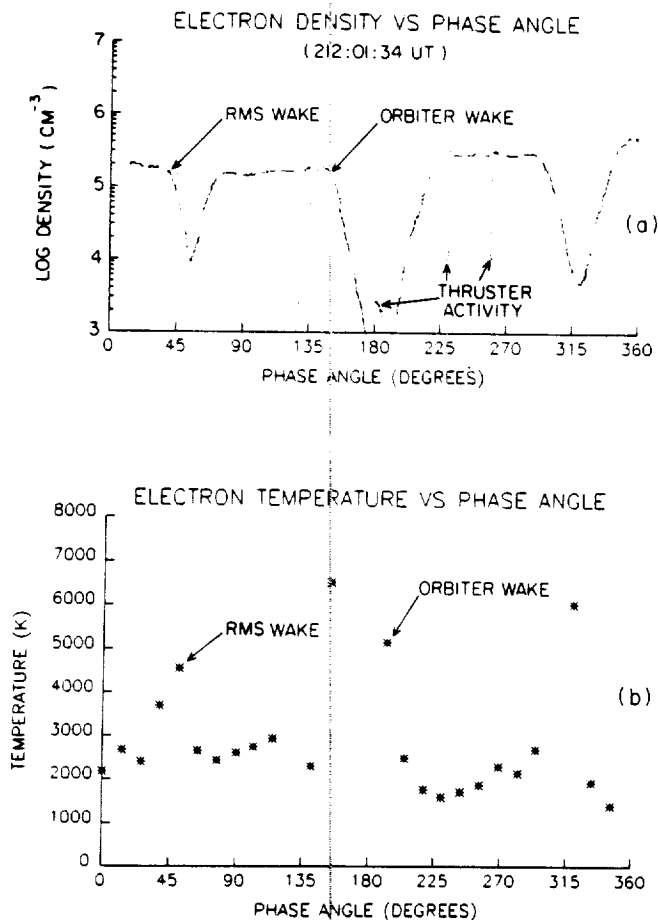


Fig. 3. (a) Electron density roll data showing the orbiter wake, the smaller wakes associated with the RMS, and the effect of thruster operations. (b) The temperature enhancements typical of the wake boundary region are evident.

passes through the wake of the spinning PDP). The ion density is shown only for times during spin-up of the PDP when the ion instrument is pointed in the ram direction ("plus" symbols). Between 0014 and 0020 UT the RPA and LP data agree to $\sim 10\%$. The dot-dash curve in Figure 5a represents the orbiter-PDP distance, in meters, during back-away. For purposes of comparison, Figure 5b shows the electron density as a function of time one orbit later when the PDP was far from the orbiter. The portion of the orbit referred to here extends from $\sim -15^\circ$ to $\sim +40^\circ$ latitude in early afternoon local time. Evidently, some of the density variation seen in Figure 5a must be interpreted as normal variations along the orbit. However, the density depression between 0010 UT and approximately 0020 UT in Figure 5a must be associated with the orbiter near wake.

Finally, Figure 6 shows electron and ion density data in the mid and far wake of the orbiter, obtained during the shuttle "fly-around" maneuver (see the second section, point 2). The wake transits (WT) 3, 4, 2, and 1 are arranged in order of increasing downstream distance between the PDP and the orbiter. The "ambient" density, indicated by the dashed lines, is obtained by simple interpolation from the opposite sides of the wake (WT 1 and 2) or by actually measuring the densities, with the PDP out of the orbiter wake, one orbit later (WT 3) or one orbit earlier (WT 4). Knowledge of the unperturbed "ambient" density allows us to estimate the maximum density depression for each wake

transit. We thus estimate the minimum $N_{\text{wake}}/N_{\text{ambient}}$ to be 0.18 for WT 3, 0.87 for WT 4, 0.61 for WT 2, and 0.8 for WT 1.

DISCUSSION

We have presented electron and ion data obtained by two instruments on The University of Iowa Plasma Diagnostics Package flown on Shuttle 51F in July–August 1985. Two sets of experiments were performed to study (1) the near wake and (2) the mid and far wake of the shuttle orbiter. For the near-wake study the PDP was held by the remote manipulator system at approximately 10 m directly above the cargo bay, while the orbiter rotated around its X axis. This made it possible to cross repeatedly (nine times) the shuttle near wake. For the mid- and far-wake study the PDP was released from the orbiter and operated as a free-flying satellite. The orbiter then performed a series of maneuvers which allowed the PDP to obtain information on the orbiter wake at various distances from the orbiter.

The near-wake observations (Figures 3 and 4) show a deep wake behind the orbiter, with the plasma density dropping, on the axis of the wake, to values more than 3 orders of magnitude below the ram density. The electron temperature is seen to rise in the wake by a factor ≥ 3 relative to the ram temperature of $\sim 2000^\circ\text{K}$. Both results are in line with those reported for a previous shuttle flight by Murphy *et al.* [1986]. On that occasion the PDP was located in the shuttle bay, while the shuttle revolved around its X axis.

Coming next to that portion of the mission in which the PDP operated as a free-flying satellite, we deal separately with the back-away maneuver (see Figure 5 for the density data) and with wake crossings at mid and far distances from the orbiter (see Figure 6).

The data in Figure 5 show good agreement between the electron and the ion density measurements. In the first 10 min or so of the back-away maneuver the density rises by 1–2 orders of magnitude as the PDP leaves the shuttle deep (near) wake. This result is, of course, in agreement with expectations. However, the plasma density measured when the PDP is still at a distance of ~ 10 m from the shuttle is, in this case (see Figure 5a), more than 1 order of magnitude larger than the density measured, on wake axis, with the PDP on the RMS (see Figures 3 and 4). A possible reason for the discrepancy may be a large contaminant ion population

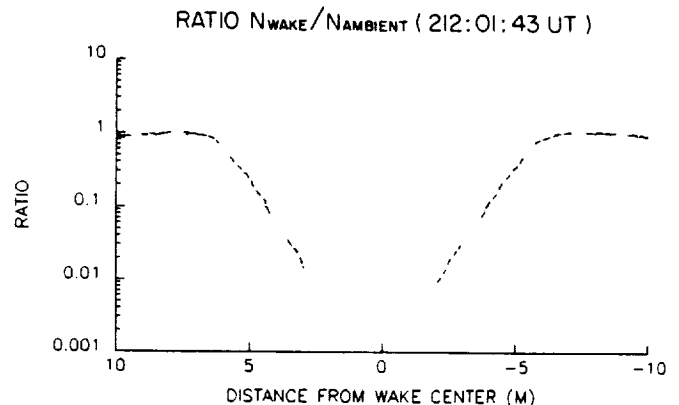


Fig. 4. Electron density for a second orbiter wake encountered during the orbiter roll maneuver, normalized to the ambient (ram) density.

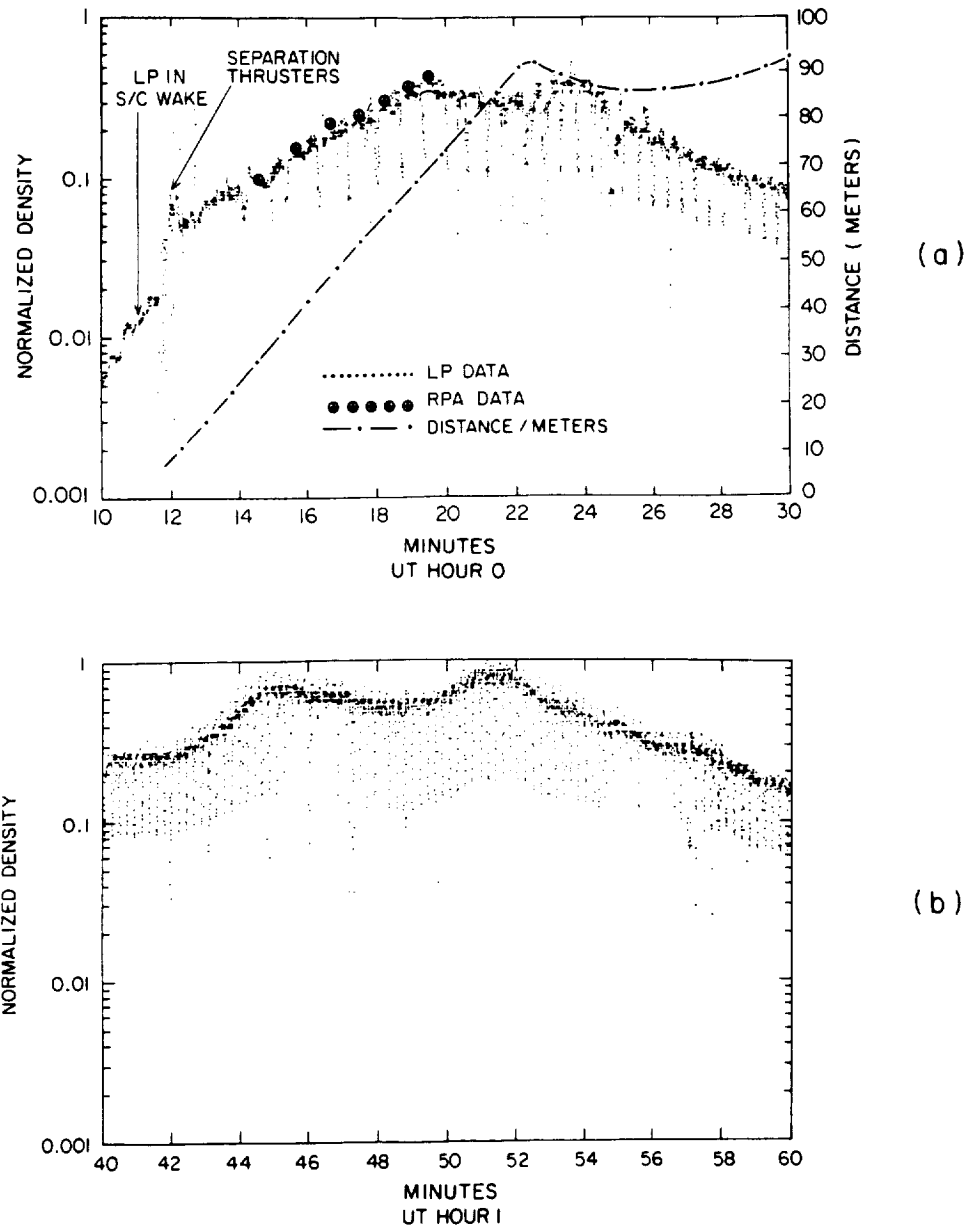


Fig. 5. (a) Ion and electron data during the back-away maneuver. (b) Data obtained one orbit later at approximately the same location.

being present in one case but not (or to a smaller extent) in the other. A number of authors have investigated the contaminant ion population in the vicinity of the orbiter. *Hunton and Calo* [1985] observe that at a particular time early in the STS-4 mission, ion species in the orbiter bay consisted of 36% ambient O^+ , 13% H_2O^+ , and 48% H_3O^+ . *Shawhan et al.* [1984] indicate payload bay pressures in the 10^{-5} torr range near ram, which would be consistent with high outgassing rates. *Pickett et al.* [1985] report on the effects of chemical releases by the orbiter FES, thrusters and outgassing, consistent with a halo of H_2O^+ pickup ions around the orbiter. *Grebowsky et al.* [1987] discuss the ion composition measurements made with a Bennett ion mass spectrometer which was also a part of the PDP instrumentation. In a study of the ion composition they find the first ion peak detected after PDP release (at a distance from the orbiter of ~12–15 m) to be H_2O^+ , not O^+ . In fact, O^+ does not become the dominant ion species until the PDP is at a distance of ≥ 25 m.

We comment, finally, on the data of Figure 6, namely, the wake crossings at distances from the orbiter in the range ~40 m to ~240 m. The most obvious feature of this set of wake crossings is that as distance from the orbiter increases, the density depression on the axis of the wake (relative to the ambient ionospheric density) becomes less and less noticeable, as expected. One exception to this general trend is represented, however, by WT 4 (at ~100 m downstream), where the observed density is larger than at WT 2 (~125 m) and WT 1 (~240 m). It seems unlikely that the density determination in WT 4 is in error to the extent that would be needed to remove the exceptional behavior. Thus one is justified in looking for a physical mechanism that may help in explaining the relatively high density near the center of WT 4.

No ion species data are available to us for WT 4; so contaminant ions may not be totally ruled out. As discussed above, these contaminants are time variable and can repre-

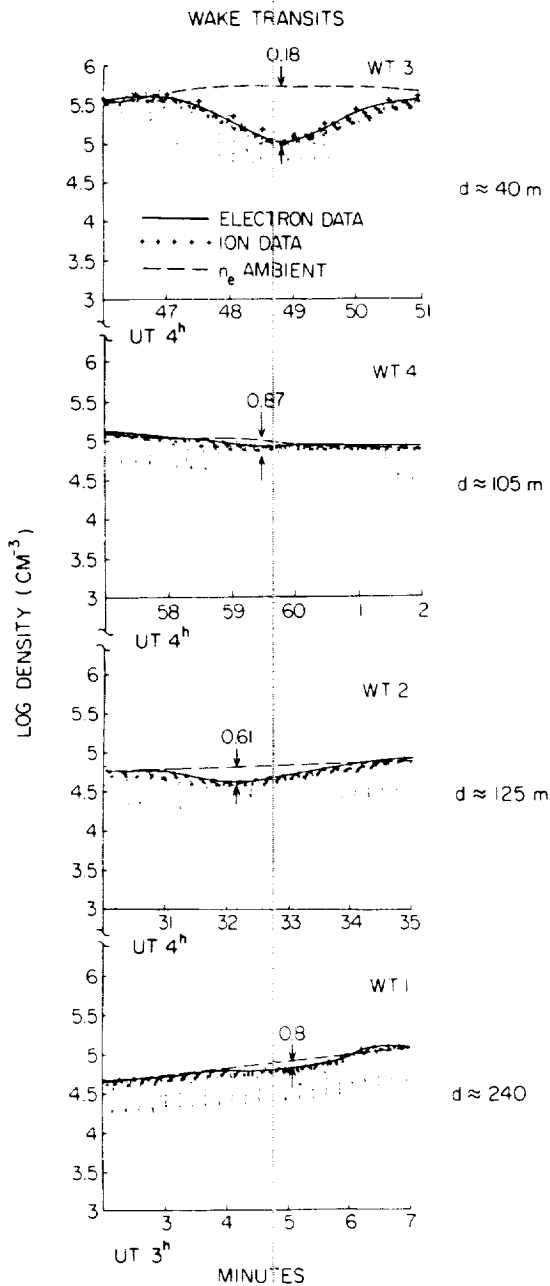


Fig. 6. Electron/ion densities for four wake transits. The number at each wake center indicates $N_{\text{wake}}/N_{\text{ambient}}$. The PDP-orbiter distance d is also shown for each transit.

sent significant contributions to the density. On the other hand, it is difficult to see why contaminant ions should be so significant just at a downstream distance from the orbiter of ~ 100 m.

Turning to possible magnetic field effects, one is reminded of the phenomenon of "ion bunching" observed in the laboratory, for example, by Schmitt [1973]. Schmitt's experiment, however, was conducted in a situation in which the supersonic plasma flow was entirely magnetic field aligned, a situation hardly ever realized in the case of the shuttle observations.

A third possibility, which has some appeal, is suggested, for example, by the laboratory experiments of Merlino and D'Angelo [1987], who observed the deflection of ions in the sheath of a negatively charged body, which is very thin in the direction of the supersonic plasma flow. Ions passing within

a few λ_D of the edge of a thin disk would receive enough transverse momentum for their subsequent trajectories to converge on the axis of the wake, at some distance l downstream, determined by the initial velocity of the ions, the potential of the disk V_b , and its radius R . One finds [Merlino and D'Angelo, 1987] that

$$l \approx R \frac{E_i}{|V_b|}$$

where E_i is the ion beam energy.

In the case of the shuttle the role of the "thin" object interacting with the plasma flow would be played by the radiators at the door edges. If we now take V_b negative, with $|V_b| \sim k T_e \sim 0.2$ eV, $E_i \sim 5$ eV, and $R \sim 5$ m, we obtain $l \sim 125$ m. This is of the order of the distance downstream from the orbiter (WT 4) where the "anomalous" density was observed. We note, in addition, that the ion focusing effect observed by Merlino and D'Angelo [1987], with a body potential of $\sim (-2kT_e/e)$, was a very prominent one (see, for example, their Figure 6). However, the prominence of this effect would be expected to increase with an increase of the parameter λ_D/L between the Debye length and the body transverse dimension, since a larger λ_D means that more ions come close enough to the negatively charged body to be deflected. As was noted in the introduction, $\lambda_D/L \approx 10^{-3}$ for the case of the shuttle, while $\lambda_D/L \approx 10^{-2}$ for the experiment of Merlino and D'Angelo [1987]. The focusing effect should then be less pronounced (although still observable) in the former case. It is also worth keeping in mind that, as was discussed in the introduction, the ratio between the orbiter size and an O^+ gyroradius is $L/\rho_i \sim 2-3$, while the corresponding ratio in the laboratory experiment is only ~ 0.1 . In addition, the plasma flow in the laboratory is magnetic field aligned, while in the shuttle-ionosphere interaction the angle between the shuttle velocity and the Earth's magnetic field varies over a wide range.

Acknowledgments. This work was supported by NASA MSFC contract NAS8-32807, NASA LeRC grant NAG 3-449, and NASA Headquarters grant NGT-50402.

The Editor thanks W. J. Raitt and N. H. Stone for their assistance in evaluating this paper.

REFERENCES

- Bogashchenko, I. A., A. V. Gurevich, R. A. Salimov, and Yu. I. Eidel'man, Flow of rarefied plasma around a body, *Sov. Phys. JETP, Engl. Transl.*, **32**, 841, 1971.
- Grebowsky, J. M., H. A. Taylor, Jr., M. W. Pharo III, and N. Reese, Thermal ion perturbations observed in the vicinity of the space shuttle, *Planet. Space Sci.*, **35**, 501, 1987.
- Hunton, D. E., and J. M. Calo, Low energy ions in the shuttle environment: Evidence for strong ambient-contaminant interactions, *Planet. Space Sci.*, **33**, 945, 1985.
- Huysman, B. P., and L. A. Pieniasek, STS post-flight on-orbit relative trajectory and ancillary data products, *Rep. 85: W482-1-57*, TRW, Houston, Tex., 1985.
- Merlino, R. L., and N. D'Angelo, The interaction of a conducting object with a supersonic plasma flow: Ion deflection near a negatively charged obstacle, *J. Plasma Phys.*, **37**, 185, 1987.
- Murphy, G., J. Pickett, N. D'Angelo, and W. S. Kurth, Measurements of plasma parameters in the vicinity of the space shuttle, *Planet. Space Sci.*, **34**, 993, 1986.
- Pickett, J. S., G. B. Murphy, W. S. Kurth, C. K. Goertz, and S. D. Shawhan, Effects of chemical releases by the STS-3 orbiter on the ionosphere, *J. Geophys. Res.*, **90**, 3487, 1985.
- Pieniasek, L. A., Relbet user's manual V.2 update, *Rep. 85: W482.8-24*, TRW, Houston, Tex., 1985.

- Raitt, W. J., J. V. Eccles, D. C. Thompson, P. M. Banks, P. R. Williamson, and R. I. Bush, Plasma parameters in the near wake of the space shuttle, *Geophys. Res. Lett.*, *14*, 359, 1987.
- Reasoner, D. L., S. D. Shawhan, and G. B. Murphy, Plasma Diagnostics Package measurements of ionospheric ions and shuttle-induced perturbations, *J. Geophys. Res.*, *91*, 13,463, 1986.
- Samir, U., and G. L. Wrenn, Experimental evidence of an electron temperature enhancement in the wake of an ionospheric satellite, *Planet. Space Sci.*, *20*, 899, 1972.
- Schmitt, J. P. M., Wake past an obstacle in a magnetized plasma flow, *Plasma Phys.*, *15*, 677, 1973.
- Shawhan, S. D., G. B. Murphy, and J. S. Pickett, Plasma Diagnostics Package initial assessment of the shuttle orbiter plasma environment, *J. Spacecr. Rockets*, *21*, 387, 1984.
- Stone, N. H., The aerodynamics of bodies in a rarefied ionized gas with applications to spacecraft environmental dynamics, Ph.D. thesis, Univ. of Ala., Huntsville, Ala., 1979.
- Stone, N. H., The plasma wake of mesosonic conducting bodies, Part 1, An experimental parametric study of ion focusing by the plasma sheath, *J. Plasma Phys.*, *25*, 351, 1981a.
- Stone, N. H., The plasma wake of mesosonic conducting bodies, Part 2, An experimental parametric study of the mid-wake ion density peak, *J. Plasma Phys.*, *26*, 385, 1981b.
- Stone, N. H., K. H. Wright, Jr., K. S. Hwang, U. Samir, G. B. Murphy, and S. D. Shawhan, Further observations of space shuttle plasma—Electrodynamic effects from OSS-1/STS-3, *Geophys. Res. Lett.*, *13*, 217, 1986.
- N. D'Angelo, W. S. Kurth, and J. S. Pickett, Department of Physics and Astronomy, The University of Iowa, Iowa City, IA 52242.
- G. B. Murphy, Jet Propulsion Laboratory, Pasadena, CA 91109.
- D. L. Reasoner, Code ES53, NASA Marshall Space Flight Center, Huntsville, AL 35812.
- A. Tribble, Rockwell International, Satellite and Space Electronics Division, Seal Beach, CA 90740.

(Received December 23, 1987;
revised November 14, 1988;
accepted December 15, 1988.)



Gaseous Environment of the Shuttle Early in the Spacelab 2 Mission

Jolene S. Pickett,* Gerald B. Murphy,* and William S. Kurth†
University of Iowa, Iowa City, Iowa

A cold-cathode ionization gage was flown on Space Shuttle flight STS-51F as part of the Spacelab 2 payload. Neutral pressure data that were taken in the payload bay during the first few hours on orbit are presented. These data show that when the payload bay is oriented such that the atmospheric gases are ramming into it, the pressure rises to a peak of 4×10^{-6} Torr. Pressure is also slightly higher during the sunlit portion of each orbit. Outgassing of the payload bay causes the pressure to be elevated to a few times 10^{-6} Torr early in the mission. In addition, several effects on pressure have been identified that are due to chemical releases. Substantial increases (50-150%) are seen during another experiment's gas purge. Orbiter chemical-release effects include: pressure increases of 200% up to 7×10^{-6} Torr due to Orbital Maneuvering System (OMS) burns, minor perturbations in pressure due to vernier thruster firings and little or no increase in pressure due to water dumps. In the case of vernier thruster firings, effects are seen only from down-firing thrusters in the back of the Orbiter, which are probably due to reflection of thruster gases off Orbiter surfaces.

Introduction

THE Plasma Diagnostics Package (PDP) is a cylindrical subsatellite that has flown on two Space Shuttle flights to date. The PDP carried a complement of 14 instruments, including a cold-cathode ionization gage that measured various plasma parameters. Data were taken in the payload bay and on the Remote Manipulator System (RMS) arm on both flights and as a free-flying satellite on its most recent shuttle flight.

The PDP first flew on STS-3 (Space Shuttle Columbia) as part of the Office of Space Science's first payload (OSS-1) from March 22-30, 1982.¹ The pressure gage on that flight obtained approximately 100 h of neutral pressure measurements from two locations: in the payload bay and on the RMS arm up to 15 m (~ 50 ft) from the Orbiter. Neutral pressure results from that flight may be found in Shawhan et al.² and Shawhan and Murphy.³

The PDP's second flight was on STS-51F (Space Shuttle Challenger) as part of the Spacelab 2 (SL-2) payload from July 29-Aug. 6, 1985.⁴ On this flight the pressure gage obtained only 3 h of data on the first day of the mission due to a mechanical failure in the gage electronics box, which occurred 7.5 h after launch. However, these data were obtained during a time in which other instruments were being activated, the payload bay was still outgassing, and two OMS burns occurred. For these reasons, these data are vital in understanding the neutral pressure environment of the Space Shuttle early in a mission.

Instrumentation

The vacuum measurement system on the PDP utilizes a cold-cathode magnetron gage similar in configuration to the Redhead magnetron gage developed in the late 1950's.⁵ The gage aperture contains a baffle to prevent ram effects of neutrals and ions. A 6-in. extension tube is added to the

aperture to allow access to the orbiter payload bay pressure environment outside the PDP skin. The gage works on the principle that a discharge current in a transverse magnetic field is dependent on the pressure of the gas. The gage transforms the vacuum-input signal into a 0-5 V output signal that is proportional to the logarithm of the input pressure. The range of the instrument on SL-2 was 10^{-7} - 10^{-3} Torr of equivalent nitrogen pressure. The sampling frequency of the pressure gage on SL-2 was 20 Hz.

Since all of the data presented here were obtained while the PDP was located in the payload bay, it is important to know the orientation of the pressure gage. Figure 1 shows the PDP in its stowed (i.e., pallet) configuration. As may be seen, the pressure gage tube is located near the bottom of the spacecraft and points in a direction midway between starboard and aft of the Orbiter. The extension tube exits the PDP skin 45 deg to the radial direction. The tube aperture is only 0.5 in. from the PDP skin at its closest point. Figure 2 shows the location of the PDP within the SL-2 payload. It is obvious from this figure that other experiments closely surround the pressure gage. In fact, the pressure gage looks directly at the Infrared Telescope (IRT) instrumentation, which is located only a few inches from the PDP structure. This is in contrast to the pressure gage on OSS-1 that had an open field of view in the middle of the pallet where no other instrument was mounted close to it.

Neutral Pressure Results

Orbit-related Effects

A plot of the 3 h of neutral pressure data obtained by the PDP cold-cathode ionization gage on Spacelab 2 is shown in Fig. 3. This plot shows neutral pressure in Torr (equivalent N_2) vs time. The time of this plot, which begins about 4.5 h after launch, is from 0130 to 0430 Greenwich Mean Time (GMT) on day 211 of 1985. The pressure gage actually received power at the time the spacecraft was powered up at 0039 GMT. However, it did not begin to ionize until 50 min later. The possible reasons for this will be discussed below.

One feature to note in Fig. 3 is the rise in pressure from a low of about 1.5×10^{-6} Torr, which begins shortly before 0300 GMT. At this time the payload bay is rapidly rotating into the ram of the gas flow, reaching maximum ram at 0302 GMT, and then gradually rotating out of it as indicated by the angle of attack in Fig. 3. The angle of attack is defined as the angle between the $-Z$ axis of the orbiter (up from the payload bay) and the velocity vector. Thus, maximum ram is

Presented as Paper 85-6054 at the AIAA Shuttle Environment and Operations II Conference, Houston, TX, Nov. 13-15, 1985; received Feb. 9, 1987; revision received July 2, 1987. Copyright © American Institute of Aeronautics and Astronautics, Inc., 1987. All rights reserved.

*Staff Research Assistant, Department of Physics and Astronomy. Member AIAA.

†Research Scientist, Department of Physics and Astronomy. Member AIAA.

obtained at an angle of attack equal to 0 deg and deep wake at 180 deg. During the ram event centered at 0302 GMT, the pressure is seen to rise rapidly and then gradually decrease to its previous level, indicating a dependence on the direction of gas flow with respect to the payload bay. The rise actually begins to occur during a 1-min interval of lower pressure, which will be explained in the following section. The PDP is in wake at 0203-0206 GMT, but this wake appears to have no significant effect on pressure. The entire payload bay is briefly in a deep-wake condition (i.e., angle of attack equal to 180 deg) around 0250 GMT, but, once again, no significant effect is noted.

It is also evident that there is some outgassing in the payload bay since ambient pressure for an altitude around 300 km would be $\leq 10^{-7}$ Torr, and contributions from ram flow would only increase the pressure to about 1×10^{-6} Torr. Also evident are the brief, random one-order of magnitude increases in pressure to about 2×10^{-5} Torr throughout the plot. These increases are believed to be due to outgassing in the gage itself. This effect was also seen on the OSS-1 flight³ and during thermal-vacuum testing prior to the SL-2 launch.

There is also an indication in Fig. 3 that the neutral pressure in the payload bay is slightly less on the nightside than on the day. For example, the slight rise in pressure (approximately 50%) seen at 0350 GMT is probably attributable to the shuttle entering daylight.

Payload-related Effects

One of the more striking features of the plot shown in Fig. 3 is a periodic variation in pressure that begins at 0216:44 GMT. At this time the pressure is seen to rise, thus beginning a cycle of 20 min at a higher pressure and 1 min at the lower pressure that was being recorded before the cycle began. Subsequent to the flight it was discovered that at about 0216:00 GMT the Cosmic Ray Nuclei Experiment (CRNE) of the Univ. of Chicago, shown in Fig. 2, began a gas purge that consisted of releasing a mixture of 80% N₂ and 20% CO₂ for 20 min, pausing for 1 min, and then releasing the gas for another 20 min, etc. The amount of gas being released was about 500 l/h. Its composition changed from the N₂, CO₂

mixture to a mixture of 15% CH₄, 25% Xe, and 50% He with a time constant of about 1 h.⁶ Before the CRNE release we assume that the gaseous environment of the payload bay is predominantly water, based on measurements taken by an ion mass spectrometer mounted on the PDP on SL-2.⁷ Summers⁸ states that the relative sensitivity of H₂O normalized to N₂ is 0.97 over the pressure range 10^{-7} - 10^{-5} Torr for a cold-cathode ionization gage. Therefore, when the CRNE release (consisting primarily of N₂) begins, we expect to see a maximum increase in pressure of 3% due to the gage's greater sensitivity to N₂ than H₂O. Since the increase (about 150%) is, in fact, quite large, we know that the CRNE release has a marked effect on the payload environment.

If the payload bay environment is not dominated by water as reported in Ref. 7, but instead, consists primarily of atomic oxygen as expected at shuttle altitudes, then a lower limit on the pressure increase due to the CRNE release can be derived. Since the sensitivity of the gage to atomic oxygen is not given in Ref. 8, we can arrive at an approximate value based on the data given by Summers⁸ and the ionization cross sections published in the literature. Redhead et al.⁹ state that provided the ions, which are produced within the gage, are formed with zero kinetic energy, the relative gage sensitivities should be nearly proportional to the magnitude of the ionization cross sections near their maximum (approximately 100 eV electron

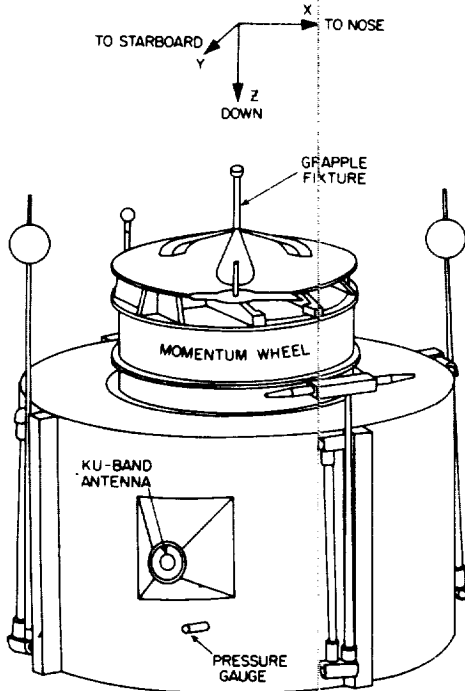


Fig. 1 The Plasma Diagnostics Package subsatellite with neutral pressure gage aperture pointed out.

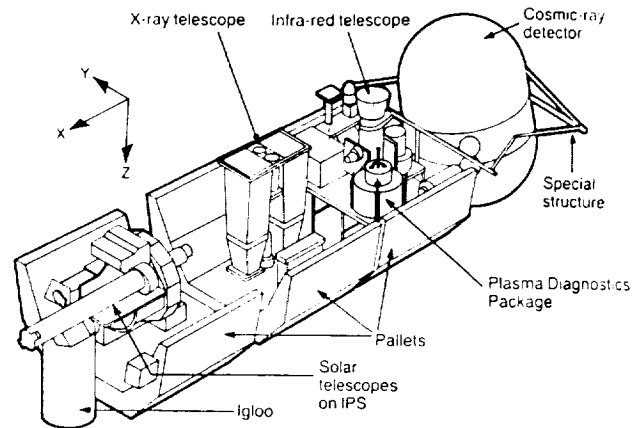


Fig. 2 Layout of the Spacelab 2 pallets showing location of the PDP in relation to the other instruments.

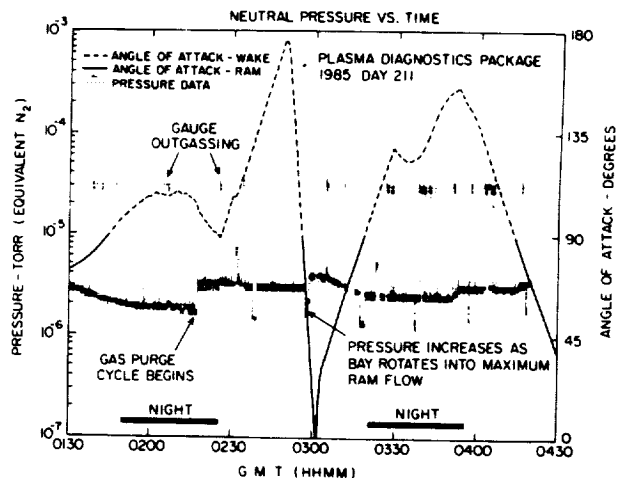


Fig. 3 Three-hour neutral pressure plot from early in the Spacelab 2 mission.

energy). Assuming this to be the case, the sensitivity of the gage to atomic oxygen would be ≥ 0.5 . This implies that the increase in pressure due to the CRNE release is only around 50% rather than 150% for the case of a water-dominated environment.

At least two other experiments on SL-2—the Infrared Telescope (IRT) from the Smithsonian Astrophysical Observatory and Super Fluid Helium Experiment (SFHE) from the Jet Propulsion Laboratory—were steadily venting helium at the sill of the Orbiter payload bay at the rate of 20–30 mg/s (approximately 0.4–0.6 l/h at STP). The relative sensitivity of He normalized to N_2 for this stage is 0.15.⁸ The effects, if any, from helium ventings, cannot be determined.

Another effect on the pressure that we believe may be due to one of the other experiments located in the payload bay is shown in Fig. 4. This plot covers 30 min from 0200–0230 GMT on day 211. At about 0205 GMT we see a square wave pattern in the data with a period of about 3.5 min. At about 0216:00 GMT the square wave begins to look more like a rectified sine wave with a period of about 0.5 min. (Note that the jump at 0216:44 GMT is the result of the CRNE gas purge.) We considered the possibility that the scanning IRT, which is located very close to the pressure sensor, was the cause of this effect; however, available data appear to rule this out. The drop to zero output seen at 0204 GMT is probably an indication of the impending mechanical failure.

Orbiter-related Effects

Figure 5 shows the effects of two types of chemical releases associated with thruster activity on the Orbiter: a continuous firing of two vernier thrusters, which takes place over about 1.1 s, and an Orbital Maneuvering System (OMS) burn. The effect of the OMS-3 burn, which was used on SL-2 to circularize the orbit at approximately 325 km altitude, begins at 0230:27 GMT during daylight, lasts for about 35 s, and is directed antiparallel to the velocity vector. This burn raises the neutral pressure by about a factor of 2 up to 7×10^{-6} Torr. Once the OMS engines are shut off, the pressure returns to its previous level after only 3–4 s. Acceleration data from the SFHE experiment¹⁰ show a sharp drop at 0231:01.0 GMT until about 0231:01.7 GMT and then an exponential decay that approaches zero at about 0231:05 GMT, which is consistent with the pressure data. The reason for the pressure spike (lasting about 0.5 s) at the beginning of the burn is not known. However, the post-mission flightcrew report¹¹ states that exceptional ignition transients were associated with all OMS burns on STS-51F with the exception of the final deorbit burn. The ignition transient was termed a "hard light" by the crew and was manifested by larger than normal acceleration at the beginning of the burn. The report states further that Johnson Space Center has been unable to confirm this effect or show a cause for it. It is possible that the momentary sharp pressure increase to 10^{-5} Torr, seen at the beginning of the OMS-3 burn, is related to the effect reported by the crew.

Another OMS burn that occurs at 0322:17 GMT during nighttime (not shown in Fig. 5) and that is directed antiparallel to the velocity vector over Millstone Hill Observatory in Westford, Massachusetts also raises the pressure by about a factor of 2 over its preburn level. The pressure spike is also present at the beginning of this burn. We are not able to determine the recovery time associated with this burn since there is a data dropout that begins in the middle of the burn and lasts well past engine shutoff. During the two OMS burns just discussed, both OMS engines were fired, each of which has a thrust of 26,688 N (6000 lb) and burn at a rate of about 85.27 N/s (19.17 lb/s) using a propellant of monomethylhydrazine (MMH) as fuel and nitrogen tetroxide (N_2O_4) as an oxidizer.

The Reaction Control System (RCS) thruster firings, pointed out at 0229:38 GMT in Fig. 5, are vernier thrusters, which have a thrust of 111 N (25 lb) and use a propellant of MMH/ N_2O_4 . The effect of this series of continuous firings is

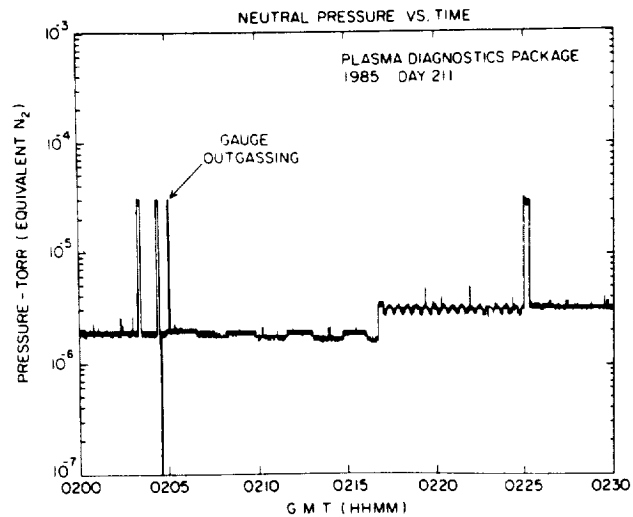


Fig. 4 Neutral pressure changes on a short time scale possibly related to another experiment.

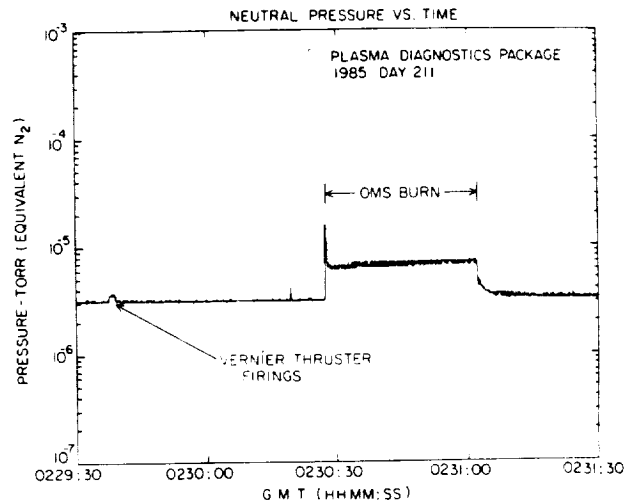


Fig. 5 Effects on neutral pressure of Orbiter gas releases.

to raise the neutral pressure in the vicinity of the payload bay by only a small amount. A more detailed analysis of all thruster firings that occur during the time in which pressure data were taken was done in order to determine whether specific thrusters affect the pressure more than others. The authors ascertained that no primary RCS thrusters, which have a thrust of 3870 N (870 lb), were fired during the 3 h of interest. That leaves only six vernier thrusters. Two of them are located in the nose section of the Orbiter and have thrust vectors that point down and slightly starboard or port (F5R, F5L). The remaining four are in the RCS pods in the tail section of the Orbiter. Two of these four are located on the starboard side and point in the starboard (or + Y) direction (R5R) and down along + Z (R5D). The other two in the tail section are on the port side of the Orbiter and point in the port (or - Y) direction (R5L) and down along + Z (L5D).

Figure 6 is a 2-min plot that shows two sets of vernier thruster firings. Notice that at 0202:22 GMT, the continuous firing of two vernier thrusters in the back of the Orbiter for a period of 2.8 s has a noticeable effect on the pressure, whereas the continuous firing of one forward and one aft vernier for a period of 2.1 s has no effect. Our analysis of all thruster firings from 0130–0430 GMT on day 211 shows that all vernier thruster firings from the back of the Orbiter that involve

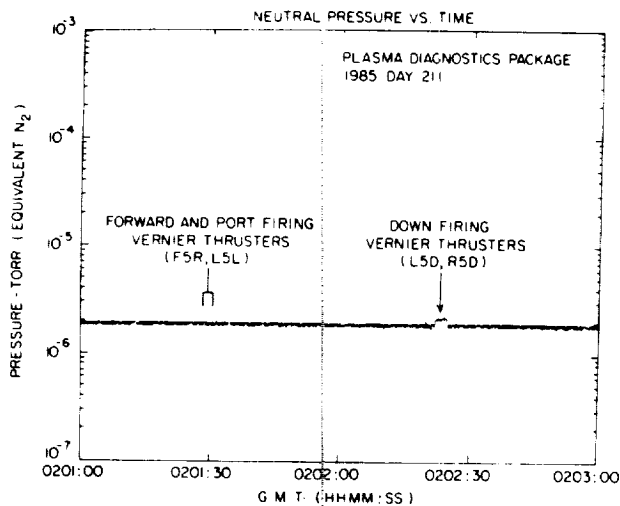


Fig. 6 Comparison of vernier thruster firing effects on neutral pressure.

thrust vectors directed down along the Orbiter + Z axis (R5D, L5D), produce similar effects on neutral pressure as those shown in Fig. 6 at 0202:22 GMT. Vernier thruster firings from the front directed down and slightly out (F5R, F5L) and from the back directed along the +/− Y axes (R5R, L5L) have little or no effect on the neutral pressure as shown in Fig. 6.

Other factors that may be important in the study of thruster-firing effects are discussed in the following section. More details on the thrusters and their effects on the ionosphere during the OSS-1 flight are provided in Refs. 12 and 13.

Finally, an Orbiter water dump that begins at 0414 GMT (see Fig. 3) and continues for about 40 min may be the cause of the slight increase in pressure seen at about that time. However, because the angle of attack has significantly started to decrease and the pressure increase is so slight, no definite conclusions can be drawn.

Discussion and Conclusions

The unusually long time taken for the pressure gage to begin to ionize (about 50 min) may be related to several factors, such as the length of time it was stored at sea level, the temperature at which it is powered up, and the degree to which it has been contaminated during preflight testing. The PDP was at sea level for a considerable length of time due to its integration into the SL-2 payload at Kennedy Space Center over a year prior to launch. The temperature of the deck on which the pressure gage is mounted was about 20° C at the time it was powered up on orbit, and so temperature was probably not a factor. One of the biggest factors could have been that the pressure gage was not cleaned after completion of all preflight testing and prior to launch. Thus, it is possible that contamination may have contributed to the delay in onset of ionization.

Neutral pressure in the payload bay depends to a great extent on the orientation of the gas flow to it and to a lesser extent on the day/night conditions prevailing at the time. SL-2 results show slightly higher pressures during daytime than nighttime, which is in accord with the MSIS-83 atmospheric model,¹⁵ and enhancements in the pressure under ram conditions. The wake conditions encountered produce no significant effects on the pressure probably due to payload bay outgassing. OSS-1 results show a definite modulation in the pressure from ram to wake conditions.^{2,3} This effect has also been reported by Yanagisawa et al.¹⁶ from measurements obtained by a BN-type ionization pressure gage that was part of the SEPAC investigation flown on Spacelab 1.

A relation is given by Hedin et al.¹⁷ for determining ram pressure for a gage consisting of an enclosure within a rocket with a small entrance hole or orifice. Hedin et al.¹⁷ state that if the diameter of the entrance hole is large compared to the length of the hole, but small with respect to the mean free path of the gas, and the gas in the gage comes to thermal equilibrium with the walls of the gage, the result is

$$n_g = n_a \left(\frac{T_a}{T_g} \right)^{1/2} F(S) \quad (1)$$

where

$$\begin{aligned} n_g &= \text{number density of particles in gage} \\ n_a &= \text{ambient particle number density} \\ T_g &= \text{temperature of gage walls} \\ T_a &= \text{ambient temperature} \end{aligned}$$

$$F(S) = \exp(-S^2) + S\pi^{1/2}(1 + \text{erf } S) \quad (2)$$

where

$$\begin{aligned} S &= V/C_{pa} \\ V &= \text{component of rocket velocity normal to gage opening} \\ C_{pa} &= \text{most probable speed of ambient particles} \end{aligned}$$

The significance of Eq. (1) is that the number of particles entering the gage per unit time is equal to those leaving. Substituting gage pressure P_g and ambient pressure P_a for n_g and n_a , respectively, in Eq. (1) we obtain

$$P_g = P_a \left(\frac{T_a}{T_g} \right)^{1/2} F(S) \quad (3)$$

For the one maximum ram condition on SL-2 (0302 GMT), the authors ran the MSIS-83 atmospheric model¹⁵ and found that $P_a = 7.7 \times 10^{-8}$ Torr, $T_a = 894$ K, and $C_{pa} = 1.07$ km/s. At 0302 GMT, $T_g \sim 293$ K and $V =$ orbiter velocity normal to the payload bay = 7.8 km/s. Substituting these values in Eq. (3) gives $P_g = 3.5 \times 10^{-6}$ Torr, which is in good agreement with the SL-2 data. In applying Eq. (3) to the orbiter, it is assumed that the orifice is the payload bay.

The enhancement under ram conditions is most likely primarily related to the fact that under ram conditions there is a great increase in the number of atmospheric molecules in the vicinity of the payload bay, which are reflected from various Orbiter and instrument surfaces at thermal velocities corresponding to temperature of the bay.^{16,18} A much smaller contribution may come from erosion of materials due to atomic oxygen bombardment.

Outgassing in the payload bay and ram flow to the bay as discussed above cause the neutral pressure in the bay to be elevated to a few times 10^{-6} Torr early in the mission. Shawhan et al.² state that it took nearly 24 h for the payload bay to outgas to the ambient level on OSS-1. Koch¹⁴ reports that pressure measurements obtained by an identical pressure gage to the PDP's as a part of the IRT investigation on SL-2 are around an order of magnitude higher than the PDP's. However, the IRT pressure gage, including sensor, were located inside a box that had only a 2-in.-diam opening at the top. Due to the greatly decreased volume of this box compared to the relative openness of the payload bay and the outgassing within the box itself, it is expected that the IRT gage would obtain consistently higher pressure measurements than the PDP gage. Scialdone¹⁹ derived an equation for open-bay pressure as a function of time based on previous measurements from the payload bay. The pressure for open bay is

$$P_s(t) = 1.3 \times 10^{-5} t^{-1} \text{ (Torr)} \quad (4)$$

where t is in hours and greater than 0240 MET (Mission Elapsed Time). The data shown in this paper appear to follow

this relationship until the CRNE gas purge begins. Scialdone¹⁹ states that the outgassing pressure will vary depending on temperatures of outgassing materials, which are related to the angle of the payload bay to the sun and length of time at that angle.

Experiments that release gas in the operation of their instruments can and do affect the neutral pressure environment in the payload bay. These gas releases, together with outgassing of the payload bay and ram flow pressure enhancements early in a shuttle mission, can lead to a substantial increase in the neutral pressure over ambient.

Orbiter OMS burns on SL-2 are shown to increase the neutral pressure in the payload bay by a factor of 2. A review of PDP pressure gage data from OSS-1 shows no increase in pressure during the two OMS burns that occur late in the mission. However, these two burns are performed under ram conditions that produce higher pressures than those shown to be associated with OMS burns. Further, the pressure spikes seen at the beginning of the SL-2 OMS burns are not present at the beginning of the OSS-1 burns. However, the sampling frequency was only 1 Hz on the earlier flight. Thus, if these sharp pressure increases, which last about 0.5 s, are present, they would probably not be evident in the data. Narcisi et al.²⁰ report results similar to those shown in the present paper for OMS burns. Their instrument, a quadrupole mass spectrometer flown on an early shuttle flight, shows the spike at the beginning of the burn, a pressure pulse of about 10^{-6} Torr, and a return to background in 1-2 s.

Although no primary thrusters are fired during the time of interest on SL-2, it is important to mention them since they can affect neutral pressure more than an OMS burn. The L2U primary thruster firing sequence that occurs during the OSS-1 flight raises the pressure to 3×10^{-4} Torr.^{2,3,12} This sequence consists of the pulsed firing of two primary thrusters in the back and the continuous firing of one in the front, all of which have thrust vectors that point up (parallel to the Orbiter - Z axis).

Even though the emission rate for the OMS firing is twice as great as for the combination of the three up-firing primary thrusters, the OMS burn on SL-2 causes pressure in the payload bay to rise to a value that is at least 1.5 orders of magnitude less than that for the L2U primary thruster sequence test. There are several factors that probably contribute to this. The L2U sequence takes place when the payload bay is in the wake of the orbiter. There is probably some reflection of the thruster plumes of the two primaries in the back off of the vertical stabilizer. Further, the PDP is closer to the primary thruster plumes than to the OMS plumes, thus being in a better position to see any backscatter from the plumes and their interactions with each other. Finally, the PDP is in a more open environment during the L2U event on OSS-1.

A summary of the questions that must be given consideration in order to adequately analyze the effects from any thruster firings are the following:

1) Is the payload bay in wake or ram? If in wake, any measurements made during thruster firings will probably show a much greater pressure increase in a relative sense than at nonwake times due to the lower background pressure in the wake. If in ram, effects may not be seen at all if ram pressure is extremely high.

2) What is the location of the pressure gage with respect to each thruster? The closer the gage is to the thruster and its exhaust plumes, the greater the possibility of recording an effect due to backscatter from the plume. This means that the emission pattern of the plume is also important. For instance, the exhaust plume of the primary thrusters is much broader than that of the verniers. Coupled with this is that certain thruster plumes are reflected into the payload bay by various Orbiter surfaces, such as the wings, elevons, and vertical stabilizer. Another important consideration is the presence of barriers and obstructions between the pressure gage and the

thruster, which may tend to hinder the gage's ability to detect an effect.

3) What is the direction of the velocity vector with respect to the thrust vector? Although no one has yet done a thorough study of this, the possibility exists that a thruster fired upstream of the Orbiter may have a different effect than one fired downstream. If such an effect was detected for a thruster fired upstream, it would most likely be a second-order effect. Although the velocity of the Orbiter is much greater than the thruster exhaust, the thruster plume interacts with the environment on a much faster time scale.

4) How many thrusters are firing simultaneously? In the case of vernier thrusters, generally, two or three will fire simultaneously throughout a given period of time. It is, therefore, very difficult to determine the effects due to any one thruster. Thus, it is often necessary to study the effects of groups of thrusters, such as the down-pointing ones. In this connection it has been reported by Wulf and von Zahn²¹ that there is some evidence that the simultaneous firing of several vernier thrusters produces higher signals than would be calculated for the sum of the individual contributions. Primary thrusters are more likely to be fired one at a time; however, they are not used as extensively on orbit as verniers and so the study of their effects may be limited.

In the authors' analysis of vernier thruster firing effects on neutral pressure, the following conclusions are drawn based on the above:

1) In general, vernier thruster firings are only minor perturbations to the pressure. Although the authors have no examples of firings while the payload bay is in wake, the ones made while in ram show a very small enhancement in pressure.

2) Effects observed from downward-pointing verniers (along + Z) in the back are probably due to the thruster plume impinging on Orbiter surfaces, such as the body flap, elevons, main engines, etc., and thus being reflected into the payload bay. The two forward-mounted vernier thrusters have a relatively unobstructed path in the primary direction of the expanding thruster plume compared to the aft verniers, which could partially explain why little or no effect is seen on neutral pressure during those firings. In addition, the location of the pressure gage on SL-2, well down in the center of the payload bay near other structures, may have been another factor, particularly for the aft, sideways-pointing verniers whose plumes can be reflected off the wings. It is not possible to do a thruster direction dependence analysis on the OSS-1 data set since the sampling frequency was only 1 Hz. However, the SL-2 thruster direction dependence results with regard to forward and aft downward-firing verniers are certainly borne out by Wulf and von Zahn,²¹ from neutral mass spectrometer results from the SPAS-01 subsatellite on the STS-41B flight, and by Narcisi et al.²⁰ on an early shuttle flight. Their results for these thrusters differ from the SL-2 results only in that the effects they see are substantially greater. In addition, they see effects from port- and starboard-firing verniers that may be due, in part, to their instruments being located in a more advantageous position with respect to these thrusters than the SL-2 pressure gage.

3) No conclusions can be drawn with regard to the relationship of the velocity vector to the direction of thrust since the data set is limited.

4) No conclusions can be drawn with regard to the effects of one thruster firing vs several firing simultaneously since single-firing events were not available.

A definitive conclusion as to whether Orbiter water dumps affect the neutral pressure in the payload bay cannot be made since enough cases under varying conditions have not been tested. The data seem to indicate, however, that the effect, if any, is minimal. As reported by Pickett et al.,¹³ neutral pressure readings on OSS-1 are slightly greater with water being dumped than without when the payload bay is in wake. Narcisi et al.²⁰ report that there is no increase in neutral pressure during a water dump.

Finally, a comment is in order with regard to the magnitude of effects seen by the SL-2 pressure gage vs those seen by other pressure monitors on this and other shuttle flights. Effects of thruster firings seen by the PDP pressure gage are less in magnitude than those seen on previous shuttle flights. This could be related to a number of things such as location of the sensor in relation to other instruments, Orbiter altitude and attitude, and degree of outgassing in the payload bay. In fact, had the PDP pressure gage on SL-2 been able to obtain measurements later in the flight when outgassing in the payload bay had decreased significantly, the relative effects of thruster firings, OMS burns, and payload bay into ram may have been much greater, although the absolute magnitude may have remained about the same due to the gage's location in the bay. Further measurements on future Space Shuttle flights need to be made in order to adequately quantify the various effects on neutral pressure seen as a result of Orbiter and payload operations.

Acknowledgments

This research was supported by NASA through Grant NAG3-449 from NASA Lewis Research Center and through Contract NAS8-32807 with Marshall Space Flight Center. The authors wish to thank Dr. S. Swordy of the University of Chicago, Dr. D. Koch of the Smithsonian Astrophysical Observatory, and Dr. P. Mason and Dr. D. Petrac of the Jet Propulsion Laboratory for supplying them with the times of their experiments' gas releases and results from their experiments. Thanks are also due to Mr. P. Simeth of Sentran Company for providing useful information about the pressure gage and Dr. L. Leger of the Johnson Space Center and Col. G. Fullerton of Dryden Flight Center for helpful comments on thruster firing and OMS engine effects. The authors gratefully acknowledge the permission granted by Cambridge University Press to use and modify Fig. 2 of this paper, which originally appeared on p. 158 of *Spacelab Research in Earth Orbit* by David Shapland and Michael R. Rycroft, published in 1984.

References

- ¹Neupert, W. M., "OSS-1: A Pathfinder Mission for Space Science on the Space Shuttle," *Journal of Spacecraft and Rockets*, Vol. 21, July-Aug. 1984, pp. 382-386.
- ²Shawhan, S. D., Murphy, G. B., and Pickett, J. S., "Plasma Diagnostics Package Initial Assessment of the Shuttle Orbiter Plasma Environment," *Journal of Spacecraft and Rockets*, Vol. 21, July-Aug. 1984, pp. 387-391.
- ³Shawhan, S. D. and Murphy, G. B., "Plasma Diagnostics Package Assessment of the STS-3 Orbiter Environment and Systems for Science," AIAA Paper 83-0253, Jan. 1983.
- ⁴"Spacelab 2 90 Day Post-Mission Science Report," Marshall Space Flight Center, AL, edited by E. W. Urban, Nov. 1985.
- ⁵Redhead, P. A., "The Magnetron Gauge: A Cold-Cathode Vacuum Gage," *Canadian Journal of Physics*, Vol. 37, Nov. 1959, pp. 1260-1271.
- ⁶Swordy, S., Private communication, Univ. of Chicago, Chicago, IL, April 1986.
- ⁷Grebowsky, J. M., Taylor, H. A. Jr., Pharo, M. W. III, and Reese, N., "Thermal Ion Perturbations Observed in the Vicinity of the Space Shuttle," *Planetary and Space Science*, Vol. 35, April 1987, pp. 501-513.
- ⁸Summers, R. L., "Gas Sensitivity Tables," NASA TN D-5285, June 1969.
- ⁹Redhead, P. A., Hobson, J. P., Kornelsen, E. V., "The Physical Basis of Ultrahigh Vacuum," Chapman and Hall Ltd., London, 1968.
- ¹⁰Mason, P., private communication, Jet Propulsion Laboratory, Pasadena, CA, Dec. 1986.
- ¹¹"S1-F Flightcrew Report," Johnson Space Center, Houston, TX, 1985.
- ¹²Murphy, G. B., Shawhan, S. D., and Pickett, J. S., "Perturbations to the Plasma Environment Induced by the Orbiter's Maneuvering Thrusters," AIAA Paper 83-2599, Oct. 1983.
- ¹³Pickett, J. S., Murphy, G. B., Kurth, W. S., Goertz, C. K., and Shawhan, S. D., "Effects of Chemical Releases by the STS 3 Orbiter on the Ionosphere," *Journal of Geophysical Research*, Vol. 90, April 1985, pp. 3487-3497.
- ¹⁴Koch, D., private communication, Smithsonian Astrophysical Observatory, Cambridge, MA, Oct. 1986.
- ¹⁵Hedin, A. E., "A Revised Thermospheric Model Based on Mass Spectrometer and Incoherent Scatter Data: MSIS-83," *Journal of Geophysical Research*, Vol. 88, Dec. 1983, pp. 10, 170-10, 188.
- ¹⁶Yanagisawa, M., Kawashima, N., Sasaki, J., and Obayashi, T., "Vacuum-Environment around Spacelab-1," *The Institute of Space and Astronautical Science, Tokyo, Japan, ISAS Rept. No. 617*, Aug. 1985.
- ¹⁷Hedin, A. E., Avery, C. P., and Tschetter, C. D., "An Analysis of Spin Modulation Effects on Data Obtained with a Rocket-Borne Mass Spectrometer," *Journal of Geophysical Research*, Vol. 69, Nov. 1964, pp. 4637-4648.
- ¹⁸Scialdone, J. J., "Self-Contamination and Environment of an Orbiting Satellite," NASA TM TN-D-6645, May 1972.
- ¹⁹Scialdone, J. J., "Shuttle Measured Contaminant Environment and Modeling for Payloads—Preliminary Assessment of the Space Telescope Environment in the Shuttle Bay," NASA TM-8511, Dec. 1983.
- ²⁰Narcisi, R., Tazcinski, E., Federico, G., Weodyka, L., and Delorey, D., "The Gaseous and Plasma Environment around Space Shuttle," AIAA Paper 83-2659, Oct. 1983.
- ²¹Wulf, E. and von Zahn, U., "The Shuttle Environment: Effects of Thruster Firings on Gas Density and Composition in the Payload Bay," *Journal of Geophysical Research*, Vol. 91, No. A3, March 1986, pp. 3270-3278.

Hot Ion Plasmas From the Cloud of Neutral Gases Surrounding the Space Shuttle

W. R. PATERSON AND L. A. FRANK

Department of Physics and Astronomy, University of Iowa, Iowa City

Large intensities of hot positive ions are observed out to distances of several hundred meters from the space shuttle *Challenger* (Spacelab 2) with a plasma analyzer on board a small free-flying satellite, the Plasma Diagnostics Package. This ion plasma is inferred to be generated by the charge exchange of ionospheric O^+ ions with a large cloud of water molecules from the space shuttle. The measured ion density ranges from ~ 30 to 10^4 H_2O^+ ions cm^{-3} . The hot ion plasma forms an ion trail in the wake of the space shuttle. A model for the water vapor cloud provides the basis for density estimates as high as 10^9 H_2O molecules cm^{-3} at a distance of 50 m from the space shuttle. Thus the space shuttle possesses a substantial coorbiting atmosphere.

1. INTRODUCTION

We report on a series of measurements of hot ion plasmas in the vicinity of the space shuttle *Challenger* on August 1, 1985. These observations are made with a plasma instrument capable of determining the energy spectra of electrons and positive ions, separately and simultaneously, in the range of energy-per-unit charge extending from 2 V to 36 kV. This plasma analyzer is included with other fields and plasma instrumentation in the free-flying, recoverable small satellite PDP, i.e., the Plasma Diagnostic Package.

The PDP spacecraft was one of the components of the Spacelab 2 mission flown on the space shuttle *Challenger*, referred to herein as the orbiter. Spacelab 2 was carried into orbit on July 29, 1985, and was landed on August 6, 1985. The orbital altitude and inclination were ~ 320 km and 49.5° , respectively. Instrumentation for the PDP includes the plasma analyzer, a Langmuir probe, an ion mass spectrometer, a retarding potential analyzer, a differential ion flux probe, a plasma wave receiver and electric field detector, an electrometer, a neutral pressure gauge, and radio receivers [Shawhan, 1982]. The plasma analyzer is also known in the literature as a Lepedea (low energy proton and electron differential energy analyzer) [Frank *et al.*, 1978]. The diameter (without booms) and height of the PDP are 1.1 and 1.3 m, respectively, and the total mass is 285 kg.

Prior to the Spacelab 2 flight the PDP was flown as part of the OSS 1 payload aboard the space shuttle *Columbia* [Shawhan *et al.*, 1984]. During that flight the PDP was operated, while berthed in the payload bay and in the immediate vicinity of the shuttle, by means of the remote manipulator system (RMS). During the Spacelab 2 mission the PDP also made measurements from within the bay and while attached to the RMS. In addition, the PDP was released from the orbiter and flown as an independent satellite. Release of the PDP occurred at 0010 UT on August 1, and retrieval was successfully accomplished at 0620 UT on the same day. Our present interest lies in the plasma observations during free flight of the PDP at distances ranging to ~ 400 m from the orbiter. Remarkably intense, hot ion plasmas are found in the vicinity of the orbiter. We interpret these plasmas in terms of a dense cloud of neutral gases from and coorbiting with the orbiter.

Copyright 1989 by the American Geophysical Union.

Paper number 88JA04201.
0148-0227/89/88JA-04201\$05.00

2. OBSERVATIONS OF PICKUP IONS

The electrostatic analyzers are constructed of concentric, spherical-segment plates, across which a known, variable potential is supplied in order to separate ions and electrons according to their energy-per-unit charge. Because it is necessary to measure the charged particle intensities with respect to both the directions of the local magnetic field \mathbf{B} and of the instantaneous orbital velocity \mathbf{V} of the orbiter and PDP, and because these directions vary as the spacecraft orbit Earth, the electrostatic analyzer is configured to utilize the rotation of the PDP spacecraft to measure the particle intensities from almost all directions. One analyzer each for positive ions and electrons employs seven detectors and one entrance aperture for measurements in seven directions in a wide, fan-shaped field of view. The plane of this field of view is aligned parallel to the spin axis of the PDP, such that, with the spin motion of this satellite, most of the 4π sr solid angle for particle velocity vectors is observed with the plasma analyzer. Such surveys of the entire angular distributions of hot electron and ion plasmas are acquired once each spin period of the PDP spacecraft, 13.1 s.

After the release of the PDP from the RMS, the orbiter's primary and vernier thrusters were fired to increase the distance between the two spacecraft to 90 m. This separation was maintained until 0120 UT. At that time the crew began maneuvering the orbiter around the PDP. The orbiter was flown around the PDP twice, with each circuit taking place during one 90-min orbit of Earth. The trajectory of the orbiter relative to the PDP between 0130 and 0430 UT is depicted in Figure 1. This motion is shown projected into the orbital plane. The relative out-of-plane separation during this time was as large as 340 m and the total distance between the spacecraft ranged from 100 to 420 m. After these orbits the orbiter was flown several times across the path of the PDP, so that the PDP passed directly through the orbiter's wake. At 0527 UT, spin-down of the PDP was begun, and the PDP was subsequently captured with the RMS.

An example of the hot ion spectra observed in the vicinity of the orbiter is shown in Figure 2. The position of the free-flying PDP is at a distance of 280 m from the orbiter. The differential, directional intensities of positive ions as a function of energy-per-unit charge are shown in Figure 2. These measurements are taken in the direction parallel to the velocity vector of the spacecraft, i.e., as seen looking into the ram

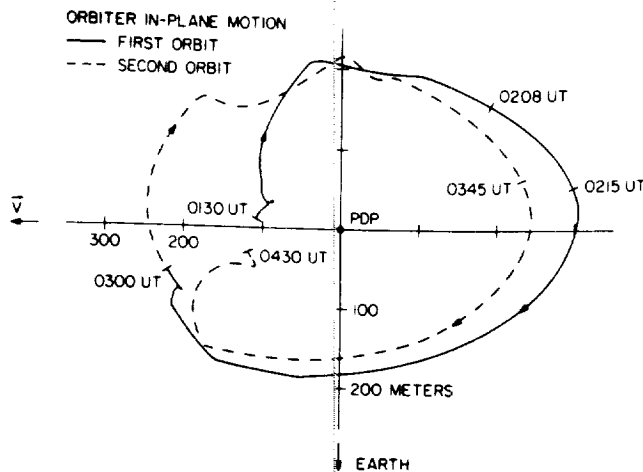


Fig. 1. Orbiter trajectory during the free flight. The orbiter motion relative to the Plasma Diagnostics Package (PDP) is shown projected into the orbital plane. The out-of-plane separation ranged from 0 to 340 m. Maximum out-of-plane excursions occurred near 0215 and 0350 UT.

direction due to the spacecraft orbital motion. At these altitudes of ~ 320 km above Earth's surface, the primary ionospheric ion is O^+ [Banks and Kockarts, 1973]. Because the orbital velocity of the spacecraft is 7.8 km s^{-1} , the ram energy-per-unit charge of the ambient O^+ ions is about 5 V. The large intensities of these O^+ ions can be seen in Figure 2. The characteristic thermal energies of the ambient ionospheric O^+ ions are ~ 0.1 eV, an energy less than that of the energy resolution of the hot plasma analyzer. Thus the presence of the ambient O^+ ions in the ionosphere is detected, but their temperatures and densities are not determined.

Large intensities of positive ions are detected at energies significantly greater than those expected for ambient ions. These hot ions are seen at energies-per-unit charge ≥ 10 V in Figure 2. Of particular interest is the maximum of the intensities at ~ 18 V and the significant intensities of hot ion plasmas extending to ~ 60 V. We show here that these ion velocity distributions are consistent with ion production by charge exchange in a large cloud of neutral gases that are outflowing from and corbiting with the orbiter.

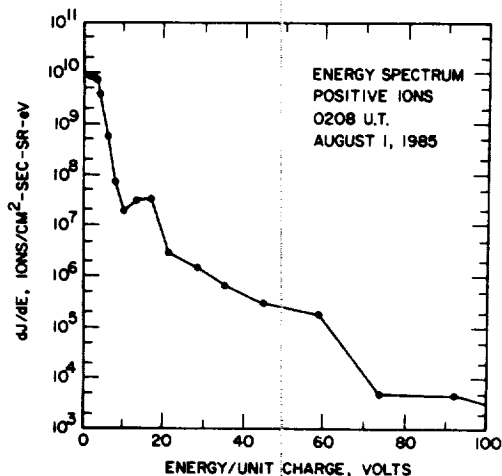


Fig. 2. Energy spectrum of positive ions, as observed in the orbital ram direction with an electrostatic analyzer on the free-flying spacecraft PDP.

Consider the neutral gas cloud of the orbiter. There are a variety of sources of neutral gases from the orbiter, including waste water, water as a by-product of power generation by fuel cells, combustion from the orbiter thrusters for attitude control, and He from the cooling of the infrared telescope. The thrusters utilize the reaction between monomethyl hydrazine and N_2O_4 , and several of the combustion products are H_2O , N_2 , CO_2 , and CO [Pickett et al., 1985].

Outgassing of volatiles, in particular H_2O , is expected from the surfaces of the orbiter. These neutral gases should radially outflow from the orbiter at thermal speeds, around hundreds of meters per second. This cloud of neutral gases is moving with a bulk velocity of 7.8 km s^{-1} , i.e., the orbiter orbital velocity, through the plasmas of Earth's ionosphere. The densities of the ambient ionospheric ions are $\sim 10^4$ – 10^6 cm^{-3} at these altitudes and are sufficiently large to ionize a measurable fraction of the neutral molecules in the cloud by charge exchange, i.e., $O^+ + H_2O \rightarrow O + H_2O^+$. Momentum transfer is negligible. These positive ions produced by charge exchange are observed with our plasma instrument. After charge exchange the H_2O^+ ions do not corbit with the orbiter gas cloud but are trapped in the terrestrial magnetic field by the Lorentz force, i.e., these ions form an ion trail in the wake of the orbiter. The motion of these so-called "pickup" ions in the reference frame of the orbiter and PDP are of interest for our present analysis. In this reference frame these ions appear to be executing cycloidal motion, with an average drift speed due to an electric field $E = -V \times B$. In other words, if the orbiter velocity V is directed perpendicular to the local magnetic field B , then the apparent motion of the pickup ions is such that during one period of circular motion of the ion in the plane perpendicular to B , the ion speed increases to a maximum of twice V and then decreases to values nearly zero. The average drift velocity of the ion with respect to the orbiter is $-V$ in the direction of the wake. As the angle α between V and B decreases or increases from 90° , the maximum ion energy decreases in proportion to $\sin^2 \alpha$. At angles near 0° and 180° , the energies of the pickup ions are sufficiently low that the pickup ions cannot be distinguished from ionospheric ions with the plasma analyzer. The phenomenon of pickup ions in magnetized plasmas moving with respect to neutral gases is of general interest to space plasma physics, e.g., the production of He^+ in the solar wind by infalling interstellar gas [Möbius et al., 1985], the formation of a plasma torus from volcanic gases of the Jovian satellite Io [Goertz, 1980], and the interaction of cometary comae with the solar wind [Ip and Axford, 1986; Ipavich et al., 1986; Mukai et al., 1986].

Two features of the distributions of pickup ions are noted here in the case of the orbiter, which is in motion nearly perpendicular to the magnetic field. First, because the maximum ion speed is twice the orbiter and PDP orbital speeds, the maximum energy of the ion is equal to 4 times that of an ambient ionospheric ion of the same mass as seen at the PDP. Second, in a coordinate system referenced to the velocity components of the observed ions in the rest frame of the orbiter, the distributions are pancake-shaped in a plane perpendicular to B and are offset from the origin by the spacecraft velocity vector. For example, these ion velocity distributions are shown in Figure 3 as taken at 0208 UT on August 1, 1985. The distribution function for ion densities, i.e., ions per unit volume $\Delta x \Delta y \Delta z$, and per unit volume of velocity space $\Delta v_x \Delta v_y \Delta v_z$, is given for a plane perpendicular to the local magnetic field. The direction of the orbiter motion is approxi-

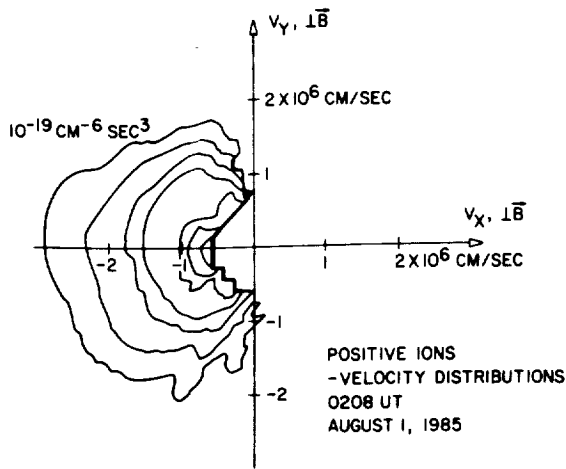


Fig. 3. The velocity distribution for hot ions in the vicinity of the orbiter. The velocity vector for the orbiter orbital motion is approximately along the $+V_x$ axis. The geomagnetic field vector is directed perpendicular to the plane of the figure. The density value for the outer contour is shown. Each successive inner contour corresponds to a factor of 10 increase in densities.

mately $+V_x$. Thus the ambient ionospheric plasma is in bulk motion with respect to the orbiter and is expected to appear as a compact series of circles at $V_x \approx -0.8 \times 10^6 \text{ cm s}^{-1}$. Evidence for this ambient ion plasma can be seen in Figure 3, although, as mentioned earlier, this plasma is too cool to fully resolve with the instrument. The pancake distribution of pickup ions with higher energies is the dominant feature to be seen in Figure 3. For Figure 3 and Figure 4 the ion mass-per-unit charge is assumed to be 16 amu (O^+). The results are changed little for masses nearly equal to this value, e.g., H_2O^+ , but they must be recomputed if the ion is CO^+ or CO_2^+ . In order to demonstrate that the ion velocity distribution is pancake-shaped, i.e., that the motions of the ions are mainly directed perpendicular to the magnetic field B , it is necessary to exhibit these ion distribution functions in a plane parallel to B . These ion distributions are shown in Figure 4, with the V_z axis taken parallel to B ; V_x is perpendicular to B and almost along the direction of the orbiter orbital motion. It is seen that the component of ion motion, V_z along B , is smaller relative to that perpendicular to B , V_x . Thus the observed ions are found to be in motion primarily in a direction

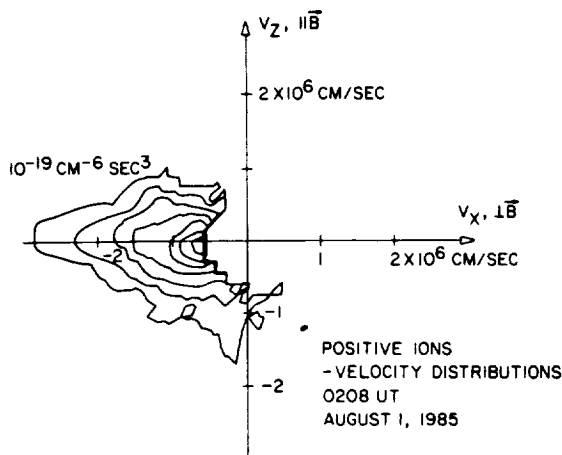


Fig. 4. Continuation of Figure 3, but for a plane rotated by 90° to include the direction of the geomagnetic field vector ($+V_z$).

perpendicular to the magnetic field (the pancake distribution) with an offset from the coordinate origin (the average drift speed of the ions with respect to the orbiter and PDP). These are the expected signatures of pickup ions from the interaction of the ionosphere with the neutral gas cloud of the orbiter.

The species of the pickup ions are not directly determined with the plasma instrumentation but may be inferred from energy spectra, such as that shown in Figure 2. The energy-per-unit charge for the secondary peak is $\sim 18 \text{ V}$. The most likely ion with this energy at twice the orbiter speed is H_2O^+ . At higher energies, $\geq 20 \text{ V}$, the ions are heavier, CO^+ , CO_2^+ , and others from the thrusters. The identification of H_2O^+ as the dominant pickup ion in the lower mass range is in agreement with independent ion mass analyses at lower energies [Grebowsky et al., 1987]. This identification is also consistent with observations of neutral water [Carignan and Miller, 1983; Narcisi et al., 1983; Wulf and Von Zahn, 1986] and water ions [Grebowsky et al., 1983; Narcisi et al., 1983; Hunton and Calo, 1985] in the near vicinity of the orbiter during other shuttle flights.

3. MODEL OF THE WATER CLOUD

We can use the observations of the densities of pickup H_2O^+ ions to develop a model of the water vapor cloud that coorbits with the orbiter. We assume that the radial velocity of the water molecules from the orbiter is similar to that for thermal velocities corresponding to a temperature $\sim 300 \text{ K}$, or $V_t \approx 5 \times 10^4 \text{ cm s}^{-1}$. This velocity is much less than the spacecraft orbital velocity of $V \approx 8 \times 10^5 \text{ cm s}^{-1}$. The water vapor expands radially outwards from the orbiter until the molecules collide with those of the ambient neutral atmosphere, primarily atomic oxygen, O I. The densities of O I, [O I], are in the range of $\sim 1-3 \times 10^8 \text{ cm}^{-3}$. The MSIS 83 model [Hedin, 1983] for the neutral ambient atmosphere is used for our calculations. To estimate the cross section for collisions of H_2O with O I, we assume hard-sphere collisions and diameters of $4.6 \times 10^{-8} \text{ cm}$ for H_2O and $2.6 \times 10^{-8} \text{ cm}$ for O I [McDaniel, 1964], where the diameter for Ne is used for O I. The cross section estimated in this way is $4 \times 10^{-15} \text{ cm}^2$, and the mean free paths Λ are about 10 km. Thus relative to the orbiter, a water molecule moves an average distance $d \approx (V_t/V)\Lambda$, or $\sim 700 \text{ m}$, before its first collision with an atmospheric oxygen atom. From the continuity equation the number density of water molecules, $[H_2O]$, then varies with radial distance R from the orbiter as

$$[H_2O] = C(R_0/R)^2 \exp[-(R - R_0)/d] \quad (1)$$

where R_0 is taken as 10 m, or the approximate linear dimension of the orbiter.

The relationship between the densities of pickup H_2O^+ ions and of the neutral water molecules must be found in order to determine the constant C in (1). The primary source of the H_2O^+ ions is charge exchange of H_2O with the ambient ionospheric O^+ . Photoionization by solar ultraviolet radiation and impact ionization by atmospheric photoelectrons proceed at much slower rates. Because O^+ is the dominant ionospheric ion at the orbiter altitudes, the O^+ densities, $[O^+]$, are taken to be equal to the electron densities that are simultaneously measured by the Langmuir probe on the PDP spacecraft (data courtesy of N. D'Angelo). The cross section for the charge exchange $H_2O + O^+ \rightarrow H_2O^+ + O$ appears uncertain. For the 5-eV energy of O^+ relative to the water cloud, values of $2.6 \times 10^{-15} \text{ cm}^2$ [Turner and Rutherford, 1968] and 0.6

$\times 10^{-15} \text{ cm}^2$ [Murad and Lai, 1986] have been reported. We adopt the cross section reported by Turner and Rutherford [1968], $2.6 \times 10^{-15} \text{ cm}^2$. The relationship between the water molecule densities, $[\text{H}_2\text{O}]$, and the ion densities, $[\text{H}_2\text{O}^+]$ and $[\text{H}_3\text{O}^+]$, is given by the following equations:

$$\frac{\partial}{\partial t} [\text{H}_2\text{O}^+] = \gamma_1 [\text{H}_2\text{O}][\text{O}^+] - \gamma_2 [\text{H}_2\text{O}^+][\text{H}_2\text{O}] - \alpha_1 [\text{H}_2\text{O}^+][e^-] \quad (2)$$

$$\frac{\partial}{\partial t} [\text{H}_3\text{O}^+] = \gamma_2 [\text{H}_2\text{O}^+][\text{H}_2\text{O}] - \alpha_2 [\text{H}_3\text{O}^+][e^-] \quad (3)$$

where the rate coefficients are given in Table 1. To calculate the rate coefficient γ_1 for charge exchange between H_2O and O^+ , we multiply the cross section for this reaction with the relative speed of the reactants, $7.8 \times 10^5 \text{ cm s}^{-1}$. The rate constant γ_2 is for the reaction $\text{H}_2\text{O}^+ + \text{H}_2\text{O} \rightarrow \text{H}_3\text{O}^+ + \text{OH}$. The kinetic energy of the H_2O^+ ions relative to the water cloud ranges from approximately 0 to 23 eV because of the gyratory motion of the H_2O^+ ions. For γ_2 we have used the rate at 300 K [Albritton, 1978]. The coefficients α_1 and α_2 for the dissociative recombination of H_2O^+ and H_3O^+ with electrons are estimates by Sjolander and Szuszczewicz [1979]. Equations (2) and (3) are expected to be applicable for ions and neutral atoms within distances up to $\sim 10 \text{ km}$ from the orbiter. Also, the densities of ionospheric O^+ ions are found to be sufficiently unperturbed that they may be taken as a constant as the water cloud moves through the ionosphere for distances $\geq 20 \text{ m}$ from the orbiter. Equation (1) for the radial dependence of water molecule densities and (2) and (3) for the relationship of the neutral water molecule and water ion densities are solved numerically with a fifth-order Runge-Kutta algorithm, in a reference frame at rest with respect to the instantaneous position of the center of curvature for pickup ion motion, i.e., the guiding center. The constant C in (1) is then found by determining the H_2O^+ density, $[\text{H}_2\text{O}^+]$, by numerical integration of ion velocity distributions, such as that shown in Figures 3 and 4. The specific time for determination of $[\text{H}_2\text{O}^+]$, and then C , is 0350 UT on August 1. If $[\text{H}_2\text{O}]$ is in units of molecules cm^{-3} , then $C = 4 \times 10^{10}$. The corresponding ionospheric density, as measured with the Langmuir probe, is $2 \times 10^5 \text{ electrons cm}^{-3}$ (N. D'Angelo, private communication, 1986). For our following analyses we assume that the water release rate from the orbiter is constant. No major waste water releases occur during the PDP free-flight.

Figure 5 gives an example of the results from the model calculations for the water vapor cloud surrounding the orbiter and for the ion densities in its wake. The abscissa is taken parallel to the orbiter motion but is offset in such a manner that this coordinate axis lies at a distance of 50 m from the orbiter at closest approach (at 0 km on abscissa scale). For this example the orbiter velocity \mathbf{V} is perpendicular to the geomagnetic field \mathbf{B} . The water vapor densities at 50 m from

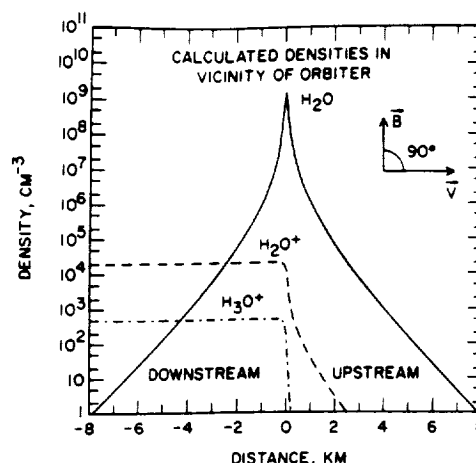


Fig. 5. Densities of H_2O , H_2O^+ , and H_3O^+ , as computed from a model based upon observations of pickup ion densities. The abscissa is taken along a line parallel to the velocity vector of the orbiter, but displaced by 50 m, i.e., 0 km corresponds to a distance of 50 m from the orbiter. The ambient densities of O I and O^+ are $2.3 \times 10^8 \text{ cm}^{-3}$ and $4 \times 10^5 \text{ cm}^{-3}$, respectively. For this calculation the direction of orbital motion relative to the magnetic field is taken to be at an angle of 90° .

the orbiter are large, $\sim 10^9 \text{ H}_2\text{O molecules cm}^{-3}$, and greater than that of the ambient atmosphere. These densities decrease to $\sim 1 \text{ cm}^{-3}$ at a distance of 8 km from the orbiter. The column density as seen from the orbiter is also large, $4 \times 10^{13} \text{ H}_2\text{O molecules cm}^{-2}$. This column density exceeds that corresponding to the threshold of the infrared telescope (IRT) in the bay of the orbiter by about an order of magnitude [Fazio, 1982]. Column densities as observed with this helium-cooled IRT during the SL 2 mission ranged from 10^{13} to $10^{14} \text{ H}_2\text{O molecules cm}^{-2}$ [Koch et al., 1987]. The rate of water release from the orbiter that is necessary to sustain the water cloud is $\sim 2.5 \times 10^{22} \text{ molecules s}^{-1}$. This rate implies a total water loss from the orbiter of 500 kg, if the rate is constant during the 8-day mission. If the space shuttle surface area is coarsely approximated by a sphere of 15-m radius, then this water loss is $\sim 18 \text{ mg cm}^{-2}$. During the 8-day mission, a coarse estimate of the water loss by engine and thruster burns, flash evaporator, and water dumps is $\sim 3000 \text{ kg}$. Although there are inaccuracies inherent in our simple model, such as those due to atmospheric ram effects in the immediate vicinity of the orbiter, this assessment of the properties of the neutral water cloud is probably accurate to within factors of about 3.

4. THE WATER ION TRAIL

The computed water ion densities in the wake of the orbiter are also shown in Figure 5. The maximum H_2O^+ densities are in the range of 5% of the ionospheric O^+ densities. This ion trail is long, $\geq 10 \text{ km}$, and is expected to be dissipated primarily by recombination with electrons and the impact of the hot water ions with the ambient oxygen atoms. This latter loss term is not included in (2), which is used for the water ion and molecule densities at closer distances to the orbiter. The pickup ion velocity distributions are in substantial nonequilibrium with those of the ionospheric ions, a situation likely to drive plasma instabilities responsible for the generation of the observed broadband electrostatic noise in the wake [cf. Gurnett et al., 1986, 1988; Scarf et al., 1986]. In order to obtain measurements of the unperturbed ionospheric plasmas, it is

TABLE 1. Reactions and Reaction Rates

Reaction	Rate, $\text{cm}^3 \text{ s}^{-1}$
$\text{H}_2\text{O} + \text{O}^+ \rightarrow \text{H}_2\text{O}^+ + \text{O}$	$\gamma_1 = 2 \times 10^{-9}$
$\text{H}_2\text{O}^+ + \text{H}_2\text{O} \rightarrow \text{H}_3\text{O}^+ + \text{OH}$	$\gamma_2 = 1.7 \times 10^{-9}$
$\text{H}_2\text{O}^+ + e^- \rightarrow \text{OH} + \text{H}$	$\alpha_1 = 1.7 \times 10^{-7}$
$\text{H}_3\text{O}^+ + e^- \rightarrow \text{products}$	$\alpha_2 = 1.9 \times 10^{-7}$

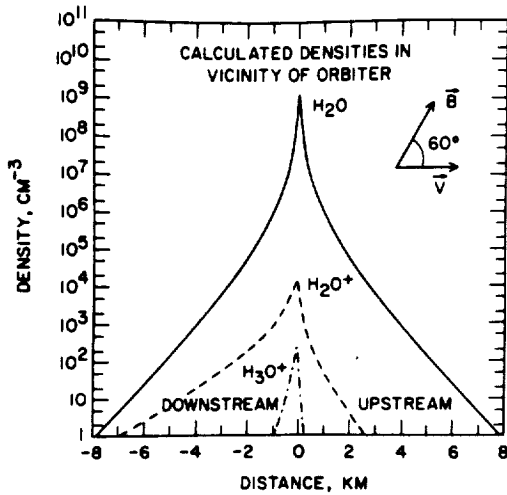


Fig. 6. Densities of H_2O , H_2O^+ , and H_3O^+ computed from the model. The ambient densities of $O I$ and O^+ are the same as for Figure 5. The direction of orbital motion relative to the magnetic field for this case is at an angle of 60° .

evident from Figure 5 that these observations must be made at distances beyond 1–2 km upstream from the orbiter.

In the rest frame of the ionosphere the pickup ions move along the magnetic field with a component of velocity equal to $V \cdot B/B$. The results of calculations with B and V at an angle of 60° are shown in Figures 6 and 7. Figure 6 is similar to Figure 5 in that the abscissa is parallel to the direction of motion of the spacecraft and passes within 50 m of the center of the water cloud. Ahead of the orbiter the ion densities are nearly equal to the densities calculated for B and V at an angle of 90° (Figure 5). Behind the orbiter, however, the ion densities decrease along this axis as a result of the ion motion along the magnetic field. Figure 7 displays contours of constant $[H_2O^+]$ in the coordinate plane parallel to B and V . It is clear from this figure that the trail of ions behind the orbiter does not extend directly opposite V , but points in a direction that is perpendicular to B . The ion trail extends directly behind the orbiter only when B and V are at an angle of 90° .

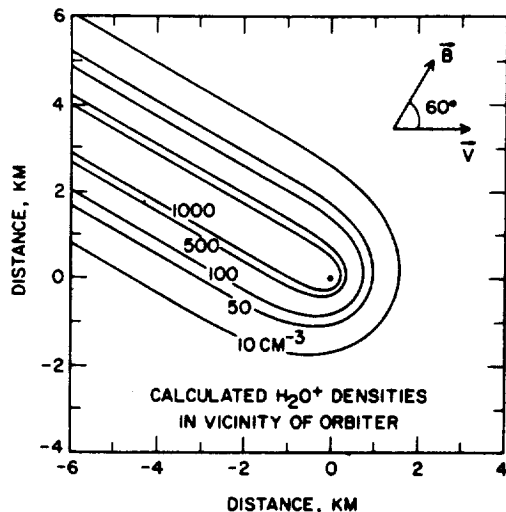


Fig. 7. Contours of constant water ion densities calculated from the model for the case where B and V are at an angle of 60° . The coordinate origin is at the center of the water cloud (the orbiter).

5. OBSERVED WATER ION DENSITIES

Observations of the densities of pickup H_2O^+ ions during approximately two Earth orbits of the PDP while this spacecraft is in free flight are shown in Figure 8. Also shown in Figure 8 are the calculated pickup ion densities as expected from the model of the water vapor cloud that surrounds the orbiter, as presented in our previous discussion. The water vapor cloud is assumed to be time-independent for this period. The position angle θ is the angle between the velocity vector V of the spacecraft orbital motion and the direction from the orbiter to the PDP. The distance between the PDP and the orbiter is given as R in Figure 8. In order to compute the pickup ion densities from the model of the water vapor cloud, the ambient O^+ density is assumed to be equal to the ionospheric electron densities, as measured with the Langmuir probe on the PDP. Reliable measurements of these electron densities are not available during the two periods of ~ 0230 – 0250 UT and ~ 0405 – 0420 UT. The densities are assumed to be 10^4 cm^{-3} for these two periods. Inspection of Figure 8 shows that there is general qualitative agreement between the observed and computed H_2O^+ densities and, for a substantial fraction of this series of observations, quantitative agreement as well. However, for certain time periods, e.g., 0310 – 0330 UT and 0445 – 0500 UT, discrepancies between observed and computed densities are evident. Such disparity may arise from a temporal fluctuation of the water vapor cloud of the orbiter or from our inability to accurately separate the pickup ion densities from those of the ambient ionosphere. The diurnal variations of pickup ion densities as seen in Figure 8 are primarily due to a similar variation of the ionospheric O^+ densities that charge exchange with the neutral water molecules along the path of the orbiter. No hot ion densities that greatly exceed those due to charge exchange are

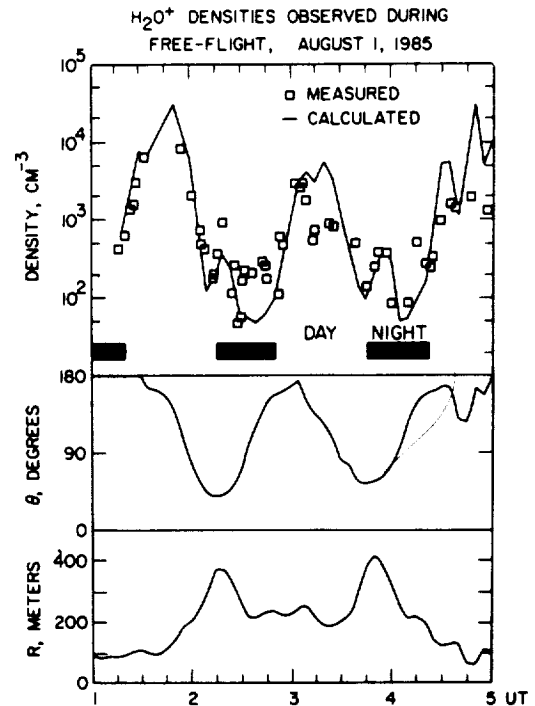


Fig. 8. Comparison of the observed densities of pickup water ions with computed values from the model of the water vapor cloud that coorbits with the orbiter. Observations are shown for most of the free-flight period of the PDP. Orbiter thruster firings do not occur during the periods selected for determining the water ion densities.

found with our observations. The somewhat higher densities relative to those from the model during the period 0230–0250 UT do not exceed the observational uncertainties.

6. DISCUSSION

The velocity distributions of hot, positive ions observed during the PDP free flight are characteristic of ions picked up from a cloud of neutral gases coorbiting with the orbiter. Because the cloud moves with orbiter speed V through the ionosphere the ions form flat velocity distributions in the plane perpendicular to Earth's magnetic field. Distributions of this type were observed throughout the free flight with densities ranging from ~ 30 to 10^4 ions cm^{-3} . In the reference frame of the spacecraft, these ions are expected to have a maximum energy 4 times greater than the energy of ionospheric ions of similar mass. The observed energy spectra indicate that the dominant ion species is most likely H_2O^+ , although more massive species appear to be present as well. This identification is consistent with measurements from the Ion Mass Spectrometer, which is also on board the PDP [Grebowsky *et al.*, 1987]. From these observations we conclude that the orbiter is surrounded by a substantial cloud of neutral gases and that water is a major constituent of this cloud. We infer that the observed ions are produced primarily by reactions of gases within the cloud with ambient ionospheric ions, the dominant reaction being charge exchange between O^+ and H_2O .

In contrast to the shell-like velocity distributions of pickup ions observed at comet Halley [Mukai *et al.*, 1986; Wilken *et al.*, 1987] and in the solar wind [Möbius *et al.*, 1985], the pickup ions observed during the PDP free flight are seen to have retained their initial pancake-shaped distributions. These ions are swept from the neutral cloud by the terrestrial magnetic field. Because the time constant of recombination of H_2O^+ with electrons is approximately 10 s, an ion tail with a length of ≥ 10 km is expected to extend behind the orbiter. The Lorentz force on the ions acts transverse to the direction of the magnetic field, and the ion motion along the field is unaffected. In this way the ion tail can be driven either downward into the atmosphere or upward away from the atmosphere, depending on the relative orientation of \mathbf{B} and \mathbf{V} .

Our simple model of the water cloud and the ion chemistry within that cloud accounts for much of the variation observed for the pickup densities. We find that our assumption of radial flow at a constant rate is adequate in providing qualitative agreement between measured and calculated H_2O^+ densities. In particular, no increase in flow seems to occur at sunrise when orbiter surfaces are suddenly exposed to sunlight. Instead, the observed increase in H_2O^+ density at sunrise appears to be due to the coincident increase in the density of ionospheric O^+ . Higher ion densities could also be the signature of another heating mechanism for ions in the water cloud of the orbiter. Enhanced ionization in the neutral water vapor cloud is not expected from the critical ionization velocity effect proposed by Alfvén [1954] for gases in bulk motion with respect to a plasma and with bulk speeds exceeding that corresponding to the ionization potential of the neutral molecules. The ionization potential for H_2O is 12.6 eV, and the kinetic energy of the H_2O molecules with respect to the ionospheric plasmas is only 5.7 eV.

Acknowledgments. We express our appreciation to N. D'Angelo for kindly allowing us the use of the electron density measurements from the Langmuir probe. Our gratitude is also conveyed to the flight

crew C. G. Fullerton, R. D. Bridges, Jr., and S. Musgrave, the mission specialists A. England and K. Henize, and the payload specialists L. Acton and J.-D. Bartoe, whose skills and efforts made our measurements possible. Similar acknowledgments are given to the alternate payload specialists D. Prinz and G. Simon, to the mission scientist E. W. Urban and his assistant K. S. Clifton, and to the mission manager R. C. Lester. At the University of Iowa the efforts of the project manager for the PDP spacecraft, R. F. Randall, and his engineering staff were essential to the successful implementation of our scientific investigation. This research was supported in part by the National Aeronautics and Space Administration under contract NAS8-32807 and grant NGL-16-001-002.

The Editor thanks K. Wilhelm and another referee for their assistance in evaluating this paper.

REFERENCES

- Albritton, D. L., Ion-neutral reaction-rate constants measured in flow reactors through 1977, *At. Data Nucl. Tables*, 22, 1–101, 1978.
- Alfvén, H., *On the Origin of the Solar System*, 194 pp., Clarendon, Oxford, 1954.
- Banks, P. M., and G. Kockarts, *Aeronomy, Part B*, 355 pp., Academic, San Diego, Calif., 1973.
- Carignan, G. R., and E. R. Miller, Mass spectrometer, STS-2, -3, -4, Induced Environment Contamination Monitor (IECM) Summary Report, edited by E. R. Miller, *NASA Tech. Memo., NASA TM-82524*, 87–101, 1983.
- Fazio, G. G., A small helium-cooled infrared telescope, Spacelab Mission 2 Experiment Descriptions, edited by K. S. Clifton, *NASA Tech. Memo., NASA TM-82477*, pp. 13–16, Marshall Space Flight Center, Ala., 1982.
- Frank, L. A., D. M. Yeager, H. D. Owens, K. L. Ackerson, and M. R. English, Quadrilateral LEPEDEAS for ISEE's-1 and -2 plasma measurements, *IEEE Trans. Geosci. Electron.*, 16, 221–225, 1978.
- Goertz, C. K., Io 's interaction with the plasma torus, *J. Geophys. Res.*, 85, 2949–2956, 1980.
- Grebowsky, J. M., M. W. Pharo III, H. A. Taylor, Jr., and I. J. Eberstein, Measured thermal ion environment of STS-3, *AIAA Pap.*, 83-2597, 1983.
- Grebowsky, J. M., H. A. Taylor, Jr., M. W. Pharo III, and N. Reese, Thermal ion perturbations observed in the vicinity of the space shuttle, *Planet. Space Sci.*, 35, 501–513, 1987.
- Gurnett, D. A., et al., Analysis and interpretation of the shocklike electrostatic noise observed during the AMPTE solar wind lithium releases, *J. Geophys. Res.*, 91, 1301–1310, 1986.
- Gurnett, D. A., W. S. Kurth, J. T. Steinberg, and S. D. Shawhan, Plasma wave turbulence around the shuttle: Results from the Spacelab 2 flight, *Geophys. Res. Lett.*, 15, 760–763, 1988.
- Hedin, A. E., A revised thermospheric model based on mass spectrometer and incoherent scatter data: MSIS 83, *J. Geophys. Res.*, 88, 10,170–10,188, 1983.
- Hunton, D. E., and J. M. Calo, Low energy ions in the shuttle environment: Evidence for strong ambient-contaminant interactions, *Planet. Space Sci.*, 33, 945–951, 1985.
- Ip, W.-H., and W. I. Axford, The acceleration of particles in the vicinity of comets, *Planet. Space Sci.*, 34, 1061–1065, 1986.
- Ipavich, F. M., A. B. Galvin, G. Gloeckler, D. Hovestadt, B. Klecker, and M. Scholer, Comet Giacobini-Zinner: In situ observations of energetic heavy ions, *Science*, 232, 366–369, 1986.
- Koch, D. G., G. G. Fazio, W. Hoffmann, G. Melnick, G. Rieke, J. Simpson, F. Witteborn, and E. Young, Infrared observations of contaminants from Shuttle Flight 51-F, *Adv. Space Res.*, 7(5), 211–221, 1987.
- McDaniel, E. W., *Collision Phenomena in Ionized Gases*, 775 pp., John Wiley, New York, 1964.
- Möbius, E., D. Hovestadt, B. Klecker, M. Scholer, G. Gloeckler, and F. M. Ipavich, Direct observations of He^+ pick-up ions of interstellar origin in the solar wind, *Nature*, 318, 426–429, 1985.
- Mukai, T., W. Miyake, T. Terasawa, M. Kitayama, and K. Hirao, Plasma observations by Susei of solar-wind interaction with comet Halley, *Nature*, 321, 299–303, 1986.
- Murad, E., and S. T. F. Lai, Some charge exchange reactions involving H_2O , *Chem. Phys. Lett.*, 126, 427–429, 1986.
- Narcisi, R., E. Trzcinski, G. Federico, L. Wlodyka, and D. Delorey, The gaseous and plasma environment around space shuttle, *AIAA Pap.*, 83-2659, 1983.
- Pickett, J. S., G. B. Murphy, W. S. Kurth, C. K. Goertz, and S. D.

- Shawhan, Effects of chemical releases by the STS 3 orbiter on the ionosphere. *J. Geophys. Res.*, *90*, 3487-3497, 1985.
- Scarf, F. L., F. V. Coroniti, C. F. Kennel, D. A. Gurnett, W.-H. Ip, and E. J. Smith, Plasma wave observations at comet Giacobini-Zinner. *Science*, *232*, 377-381, 1986.
- Shawhan, S. D., Description of the Plasma Diagnostics Package (PDP) for the OSS-1 shuttle mission and JSC chamber test in conjunction with the fast pulse electron gun (FPEG), *Artificial Particle Beams in Space Plasma Studies*, edited by B. Grandel, pp. 419-430, Plenum, New York, 1982.
- Shawhan, S. D., G. B. Murphy, and J. S. Pickett, Plasma Diagnostics Package initial assessment of the shuttle orbiter plasma environment, *J. Spacecraft*, *21*, 387-391, 1984.
- Sjolander, G. W., and E. P. Szuszczewicz, Chemically depleted F_2 ion composition: Measurements and theory, *J. Geophys. Res.*, *84*, 4393-4399, 1979.
- Turner, B. R., and J. A. Rutherford, Charge transfer and ion-atom interchange reactions of water vapor ions, *J. Geophys. Res.*, *73*, 6751-6758, 1968.
- Wilken, B., A. Johnstone, A. Coates, H. Borg, E. Amata, V. Formisano, K. Jockers, H. Rosenbauer, W. Stüdemann, M. F. Thomson, and J. D. Winningham, Pick-up ions at comet P. Halley's bow shock: Observations with the IIS spectrometer on Giotto, *Astron. Astrophys.*, *187*, 153-159, 1987.
- Wulf, E., and U. von Zahn, The shuttle environment: Effects of thruster firings on gas density and composition in the payload bay, *J. Geophys. Res.*, *91*, 3270-3278, 1986.

L. A. Frank and W. R. Paterson, Department of Physics and Astronomy, University of Iowa, Iowa City, IA 52242.

(Received August 4, 1988;
revised November 30, 1988;
accepted November 30, 1988.)



Double-Probe Potential Measurements Near the Spacelab 2 Electron Beam

J. T. STEINBERG¹ AND D. A. GURNETT

Department of Physics and Astronomy, University of Iowa, Iowa City

P. M. BANKS

STAR Laboratory, Stanford University, Stanford, California

W. J. RAITT

Center for Atmospheric and Space Sciences, Utah State University, Logan

As part of the Spacelab 2 mission the plasma diagnostics package (PDP) was released from the shuttle as a free-flying satellite. The PDP carried a quasi-static electric field instrument which made differential voltage measurements between two floating probes. At various times during the free flight, an electron beam was ejected from the shuttle. Large differential voltages between the double probes were recorded in association with the electron beam. However, analysis indicates that these large signals are probably not caused by ambient electric fields. Instead, they can be explained by considering three effects: shadowing of the probes from streaming electrons by the PDP chassis, crossing of the PDP wake by the probes, and spatial gradients in the fluxes of energetic electrons reaching the probes. Plasma measurements on the PDP show that energetic electrons exist in a region 20 m wide and up to at least 170 m downstream from the electron beam. At 80 or more meters downstream from the beam, the double probe measurements show that the energetic electron flux is opposite to the injection direction, as would be expected for a secondary returning electron beam produced by scattering of the primary electron beam.

1. INTRODUCTION

As part of the Spacelab 2 mission, a spacecraft called the plasma diagnostics package (PDP) was released from the shuttle to survey the plasma environment around the orbiter. At various times, an electron beam was ejected from the shuttle so that the effects produced in the plasma might be studied. In this paper we report on efforts to measure the quasi-static electric fields in the plasma with the PDP, focusing on those times when the electron beam generator was operating. The PDP, a scientific instrument package containing 14 instruments, was designed and constructed at the University of Iowa, and is described by *Shawhan* [1982]. The electron beam generator, flown as part of the vehicle charging and potential (VCAP) experiment provided by Stanford University and Utah State University, is described by *Banks et al.* [1987]. The PDP and the electron beam generator were previously flown on the STS-3 flight [*Shawhan et al.*, 1984].

Prior to the shuttle flights, a number of electron beam experiments were performed in plasma chambers and from rockets. Using the same PDP and the same electron beam generator later flown onboard Spacelab 2, quasi-static electric fields of the order of a few volts per meter were measured within a few meters of the beam in a large plasma chamber at Johnson Space Flight Center [*Shawhan*, 1982]. *Denig* [1982] questioned the reliability of these measurements because of the possibility of differential charging on the measuring probes, and because the fields seemed too large to be sustained in the

given apparatus. *Kellogg et al.* [1982] also reported measuring fields of a few volts/m in a similar chamber test. Measurements of the quasi-static electric fields have also been reported in association with electron beams emitted from rockets in the ionosphere. In the Polar 5 experiment, fields of the order of 0.1 V/m were detected over 100 m away from the beam source [*Jacobsen and Maynard*, 1978]. During the Echo 6 experiment, *Winckler and Erickson* [1986] measured fields of the order of 0.2 V/m at a distance of 40 m from the flux tube on which the beam was expected to be centered. All the measurements mentioned here involved differential voltage measurements on floating probes. Considering the chamber and rocket experiments, we expected on the Spacelab 2 mission to detect fields on the order of 1 V/m associated with the electron beam.

The Spacelab 2 mission was launched into a nearly circular orbit, of inclination 49.5°, at a nominal altitude of 325 km. The PDP was in free flight roughly 6 hours, during which the shuttle performed two complete fly-arounds of the PDP. During the fly-around the shuttle was maneuvered to regions upstream and downstream of the PDP. The fly-around included four magnetic conjunctions during which the shuttle was targeted to pass through the magnetic field line passing through the PDP. The electron beam generator was operated at various times throughout the free flight, both in a steady (dc) mode, and in a pulsed mode. During several of these times large signals were detected by the quasi-static electric field instrument. The purpose of this paper is to describe the large signals associated with the electron beam firings and to determine the origin of these signals.

¹Now at Center for Space Research, Massachusetts Institute of Technology, Cambridge.

Copyright 1988 by the American Geophysical Union.

Paper number 7A9230.
0148-0227/88/007A-9230\$05.00

2. INSTRUMENTATION

The PDP quasi-static electric field instrument made potential measurements on two floating probes. These floating probes consisted of conducting spheres mounted on insulated

PDP CONFIGURATION

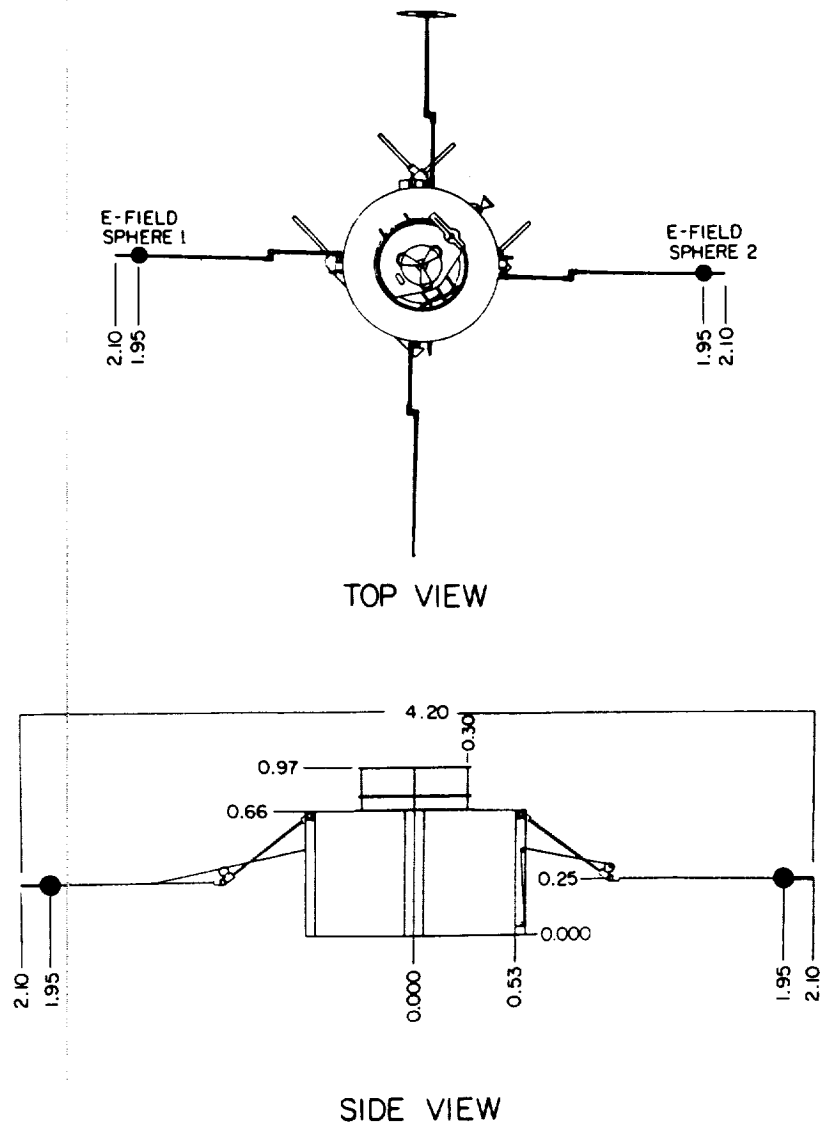


Fig. 1. The plasma diagnostics package. Dimensions are given in meters.

booms on opposite sides of the spacecraft. The sphere-to-sphere separation was 3.89 m, and the diameter of the spheres was 10.2 cm. A diagram of the PDP, showing the dimensions of the main chassis and the locations of spherical probes 1 and 2, is presented in Figure 1. Two types of measurements were made: the differential voltage, V_{diff} , between the two probes was measured at both a high gain and a low gain, and the average potential, V_{ave} , of the two probes relative to the PDP chassis was measured. The following relations describe the two measurements:

$$V_{diff} = V_2 - V_1$$

$$V_{ave} = (V_2 + V_1)/2$$

where V_1 and V_2 are respectively the potentials of sphere 1 and sphere 2 relative to the PDP chassis. Typically, the differential

voltage divided by the antenna length is interpreted as a measurement of the electric field. The basic instrument parameters and dynamic ranges are given in Table 1. Since the floating potential of an object in a plasma is dependent on the

TABLE 1. Instrument Parameters and Dynamic Ranges

	Value
Electric field high gain range	± 0.064 V/m
Electric field high gain precision	± 0.51 mV/m
Electric field low gain range	± 2.0 V/m
Electric field low gain precision	± 0.017 V/m
Electric field sample rate	20.0 samples/s
Average potential range	± 8.0 V
Average potential sample interval	1.6 s/sample
Spherical probe separation	3.89 m
Spherical probe diameter	10.2 cm

surface materials, it is also important to describe the surface properties of the spacecraft and spheres. The PDP chassis was covered with a teflon-coated fiberglass cloth which in turn was covered with an aluminum mesh to provide a uniform conducting surface. Potential measurements were referenced to the aluminum mesh. The spherical antenna probes were coated with a conducting graphite-epoxy paint.

After release from the shuttle, the PDP was made to spin by the action of an inertia wheel within the PDP. When spinning at its maximum rate, the spacecraft had a spin period of 13.1 s. The spin axis was oriented approximately perpendicular to the orbital plane. Thus the spacecraft velocity vector lay approximately in the PDP spin plane.

The electron beam generator was mounted in the shuttle payload bay. A beam was produced as electrons emitted from a heated tungsten wire filament were accelerated through a 1-kV potential. The generator operated at beam currents of either 50 mA or 100 mA, producing either a steady or a pulsed beam. The beam was pulsed at frequencies up to 800 kHz.

3. OBSERVATIONS

During most of the free flight, the V_{diff} signals were of the order of the induced potential due to the orbital motion of the spacecraft, $|(V \times B) \cdot L|$, where V is the spacecraft velocity and L is a vector pointing from sphere 2 to sphere 1. These signals were typically 0.4 and 0.8 V. The V_{ave} signal was usually between zero and a few volts positive. That is, the PDP normally floated at a slightly lower potential than the antenna probes. The V_{ave} signal also showed a periodic variation synchronous with the spacecraft spin period. The periodic variation was found to be related to the operation of the PDP low energy proton and electron differential energy analyzer (LEPEDEA) [Tribble et al., 1988]. The LEPEDEA utilized a current collecting plate whose voltage jumped to +2 kilovolts every 1.6 s. The plate collected a large thermal electron current, and the PDP potential decreased by several volts, recovering to its initial value within 1.0 s. The V_{ave} signal was spin modulated because the degree of charging of the spacecraft was less when the LEPEDEA aperture faced the spacecraft wake, than when the aperture faced the ram direction. For the V_{diff} measurement, a large negative potential on the PDP was equivalent to a large positive common mode signal on the probes. Because of limitations in the common mode rejection, the V_{diff} signal was disturbed whenever the PDP potential exceeded several volts negative. The magnitude of the instrument output due to the common mode signal was generally much less than $|(V \times B) \cdot L|$. Thus the common mode signal was large enough to make the interpretation of the measurements difficult when the difference between the V_{diff} and $|(V \times B) \cdot L|$ was small. However, for V_{diff} signals larger than $|(V \times B) \cdot L|$, the common mode rejection problem was not important.

At five times during the free flight when the electron beam generator was operating, V_{diff} signals were recorded that were significantly larger than $|(V \times B) \cdot L|$. The signals for these events are shown in Figure 2, and the events are numbered 1-5. At no other times during the PDP free flight were signals this large recorded. Of these five events, the beam was operated in a steady mode for three events, and in a pulsed mode for two events. The beam injection pitch angle varied widely among the events. Table 2 lists the beam operation mode, injection pitch angle, beam current, and several other important parameters regarding these five events.

The basic periodicity of the V_{diff} signals in Figure 2 is due to

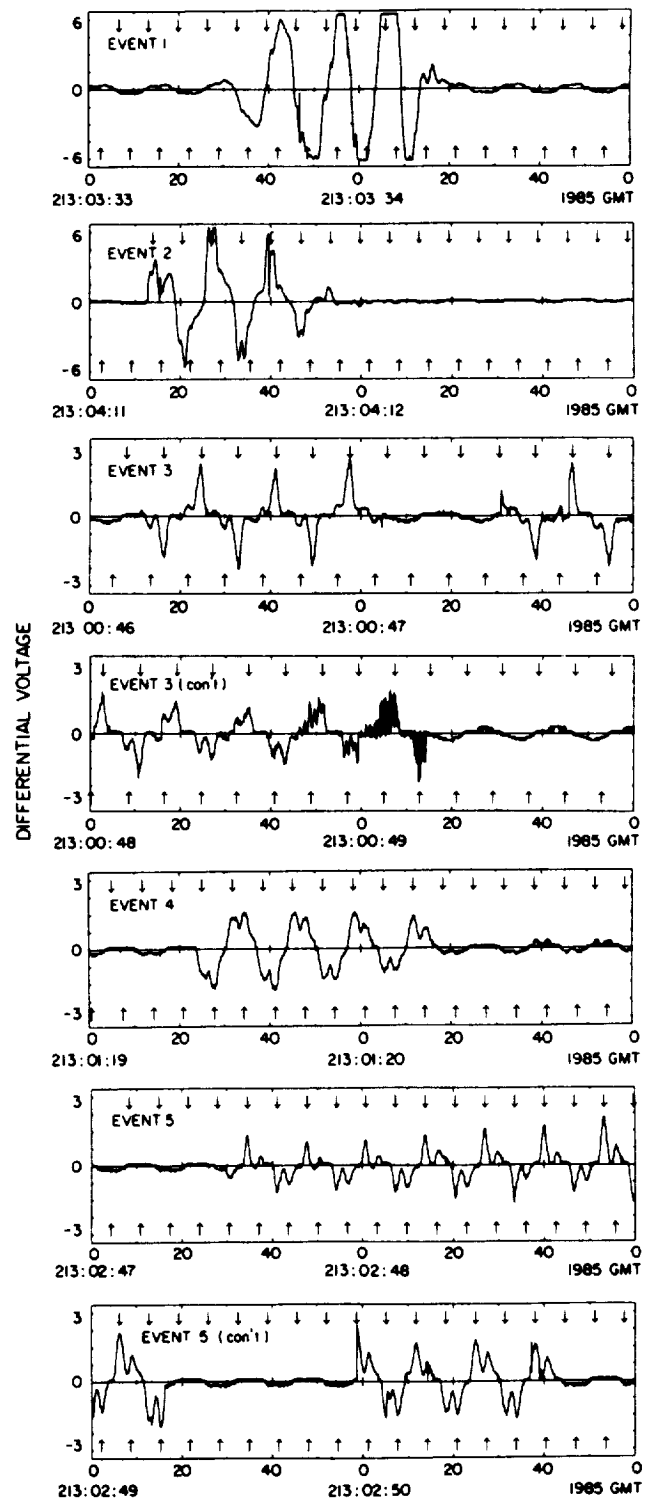


Fig. 2. Large differential voltage signals associated with times of the electron beam generator operation. Arrows at the top indicate times the antenna was aligned with the spacecraft velocity vector. Arrows at the bottom indicate times the antenna was aligned with the magnetic field.

the spinning of the spacecraft. In addition to the overall variation at the spin period, the signals have a number of unusual features. During event 1 the instrument saturates. Thus, the difference voltage on the probes is greater than 8 V, which corresponds to an inferred electric field strength in the spin

TABLE 2. Beam Parameters, Sunlight Conditions, PDP Orientation

Event	1	2	3	4	5
Distance from PDP to shuttle	206 m	218 m	93 m	90 m	235 m
Distance from PDP to flux tube of beam	26-3 m	9-40 m	87 m	84 m	143 m
Θ , Angle of B to spin plane	22.9°-23.6°	15.4°-15.7°	15.1°-19.4°	10.8°-12.1°	15.4°-16.6°
Day/night	day	night	night	night-sunrise	night-sunrise
Beam current	50 mA	100 mA	100 mA	100 mA	100 mA
Beam injection direction	down	up	down	up	up
Beam injection pitch angle	<7.5°	2.4°-10°	54°-70°	68°-69°	38°-45°
Beam mode	dc	1.2 kHz	54 s dc 115 s pulsed 600 Hz stepped down to 10 Hz	dc	dc

plane greater than 2 V/m. Event 2 has a "spiky" character, and events 3, 4, and 5 all show a "double peak" character. At the end of event 3 (around 0049), there is an apparent higher frequency structure to the signal. This structure is associated with the pulsing of the electron beam. Note that as long as the beam pulse frequency is much greater than the V_{diff} sample rate, then no effect of the pulsing should be apparent in the V_{diff} signal. Such is the case for event 2, where the beam was pulsed at 1.2 kHz. However, during event 3 the beam pulse frequency was lower in steps from 600 Hz down to frequencies near the V_{diff} sample frequency of 20 Hz. The apparent higher frequency structure is the result of a beating effect that occurs between the beam pulse rate and the V_{diff} sample rate.

In order to understand the origin of the large signals, the phase angle of the spinning PDP was investigated. Arrows are plotted in Figure 2 at the top of the graph to indicate the times when the electric antenna was aligned with the spacecraft velocity vector. Recall that the velocity vector lay approximately in the PDP spin plane. Arrows are plotted in Figure 2 at the bottom of the graph to indicate times when the antenna was aligned with the magnetic field projected onto the spin plane. In general, the magnetic field vector did not lie exactly in the spin plane, but made an angle of between 10° and 24° with the spin plane. The angle for each event is given in Table 2. Inspection of Figure 2 reveals that for cases 2, 3, 4, and 5 a voltage peak occurs when the antenna is aligned with the spacecraft velocity vector, and for cases 3, 4, and 5 a second peak occurs when the antenna is aligned parallel to the magnetic field projected onto the spin plane.

Figure 3 shows the trajectory of the PDP in a plane perpendicular to the magnetic field during all times that the electron beam generator was operating. The direction V_1 indicated in the figure is along the component of the velocity perpendicular to B . The origin represents the position of the magnetic field line on which the electron beam should be centered. The beam is assumed to lie on a magnetic field line which intersects the electron beam generator, and the field is determined from a multipole model of the Earth's magnetic field. Although shown in Figure 3 only as a point, the beam will have a cyclotron motion about the magnetic field. The injection pitch angles are listed in Table 2. The pitch angles vary over a large range, but are relatively small (less than 10°) for events 1 and 2, and large (greater than 30°) for events 3, 4, and 5. The beam also has some spreading due to beam divergence, space charge repulsion of the beam electrons, and beam instability. The actual width of the beam is unknown; however, previous beam experiments indicate that the cyclotron radius of a beam electron with pitch angle 90° is a reasonable approximation

for the beam radius. For a 1-keV electron in a magnetic field of 0.25-0.5 G, the cyclotron radius is approximately 2-4 m.

The trajectories during the five large events are shown in Figure 3 as solid segments, and the trajectories during times when the beam generator was operating but the measured differential voltage was small (i.e., less than $(V \times B)$), are shown by the dashed lines. During events 1 and 2, the length of time the electron beam generator was turned on was longer than the length of time large signals were recorded, indicating that the spatial region over which large signals occur is limited. For each of events 3, 4, and 5, large signals were recorded for the entire period the beam generator was on. Note that events 1-5 occur at times when the PDP was in a region downstream of the flux tube carrying the electron beam. Except briefly during event 1, the perpendicular distance from the PDP to the flux tube of the electron beam was much greater than the 2 to 4 m predicted beam radius, so that the PDP was well outside of the region of the primary beam. Events 1 and 2 occur when the PDP was closest to the flux tube of the electron beam, and are the largest in magnitude.

The average potential measurements for events 1-5 are

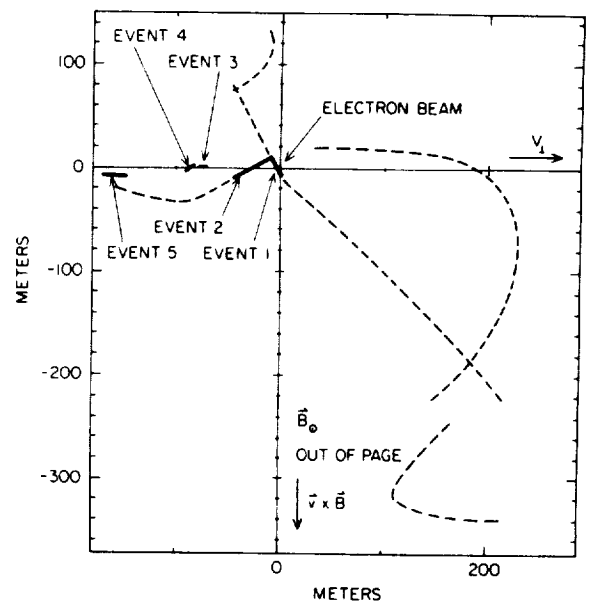


Fig. 3. Dashed lines indicate the trajectory of PDP in the plane perpendicular to B during times of electron beam generator operation. The trajectories for events 1-5 are shown as solid segments. The origin represents the position of the magnetic field line on which the beam lies. V_1 is the component of velocity perpendicular to B .

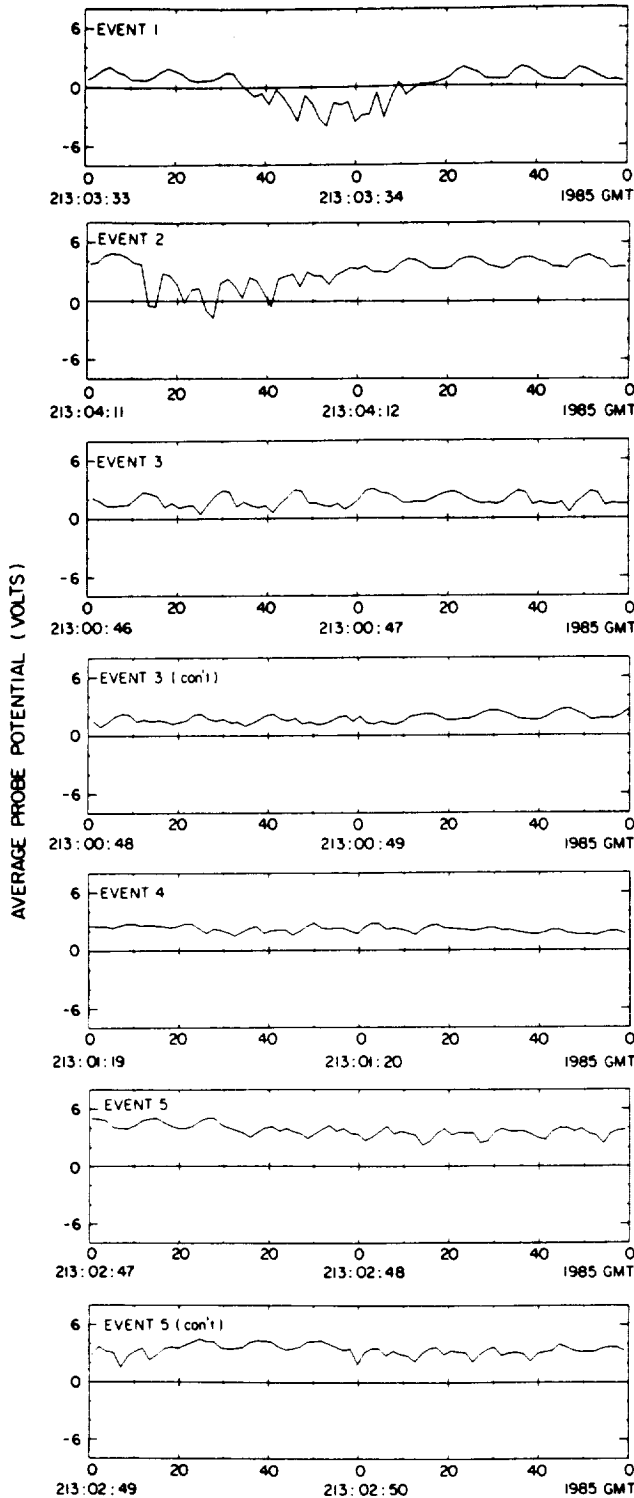


Fig. 4. Average potential measurements during times when large differential voltage signals were detected.

shown in Figure 4. The largest changes in the average potential measurements associated with the electron beam are seen during events 1 and 2, where the average potential of the probes goes from positive values of +2 to +4 V to negative values of -2 to -4 V. The spin period variation of the signal discussed above can be seen in the graphs for events 1 and 2 during the times before and after the large negative excursions of the signal. During events 3, 4, and 5, the average potential

does not change by a large amount, but the smooth spin period variation of the signal is disrupted.

4. INTERPRETATION

Because the determination of the quasi-static electric field with the PDP is based on measurements of the differential voltage between two floating probes, the results can be affected by energetic beam electrons striking the probes. It is easily shown that a small flux of energetic electrons may alter the floating potential of the probes by a large amount [Fahleson, 1967]. Arnoldy and Winckler [1981] reported a population of energetic electrons in the region around an electron beam, causing the floating potential of the Echo 3 rocket to become several volts negative. A similar observation was made on Echo 6 [Winckler *et al.* 1984]. Thus we might expect to find that the PDP potential is affected by energetic electrons around the beam. In fact, during each of events 1-5 discussed here, the LEPDEA on the PDP detected energetic electrons at energies nearly up to the beam energy (W. R. Paterson, personal communication, 1987). Further, data from the PDP Langmuir probe seems to indicate that the PDP charged to at least -4.3 V during event 2, and to at least -7.6 V during event 1 (A. C. Tribble, personal communication, 1987). Therefore there is reason to suspect that the probes also charged. If the charging is different for the two probes, then V_{diff}/L cannot be safely interpreted as a good measure of the electric field.

To determine the possible effect of energetic electrons on our measurements, we perform a simple calculation of the floating potential. This is done by considering the balance of currents to the object of concern (see, for example, Kasha [1969]). The possible current sources are (1) thermal (background) electrons, (2) thermal (background) ions swept up by the motion of the spacecraft, (3) energetic electrons (energies $\gg kT_e$), (4) energetic ions (energies $\gg 5.0$ eV, the ramming energy), (5) secondary electron emission, and (6) photoelectron emission. Measurements made with the LEPDEA indicate that the current from energetic ions is much less than that from the ramming ions (W. R. Paterson, personal communication, 1987), so this current can be neglected. The maximum secondary electron yields for aluminum (PDP surface material) and graphite (probe surface material), are 1.0 secondaries/primary for 300-eV primaries [Whetten, 1985]. Thus secondary production would reduce the negative charging effect of the energetic electrons by some fraction. Photoemission would also reduce the negative charging. But since we wish to obtain a worst case estimate of the spacecraft potential, we neglect both secondary production and photoemission. We consider then the following current balance equation for an object at potential $V < 0$:

$$A_x n_e u_{sc} (1 - eV/E_e) - A_s n_e (kT_e/2\pi m_e)^{1/2} \exp(eV/kT_e) - A_s J_b = 0 \quad (1)$$

The first term in the above equation includes the ion current due to the sweeping up of the ionospheric ions by the spacecraft motion plus some effect of the attraction of ions to the negatively charged object. The second term is the electron current from the thermal electrons. The third term is the current to the object due to energetic electrons. The variables in (1) are identified in Table 3.

Using the representative parameters given in Table 3, equation (1) was solved numerically for various values of J_b and n_e . The floating potential was determined from (1) for both the

TABLE 3. Parameters Used in Evaluation of Equation (1)

	Value
U_{sc} spacecraft velocity	7.8×10^3 m/s
A_x cross-sectional area for ion collection:	
PDP	0.869 m ²
probe	8.11×10^{-3} m ²
A_s total surface area: PDP	4.52 m ²
probe	3.24×10^{-2} m ²
E_i ion energy in spacecraft reference frame	5.08 eV
T_e electron temperature	0.2 eV
n_e plasma density	5.0×10^{11} m ⁻³
J_b current density of energetic electrons	$0-5.5 \times 10^{-4}$ amp/m ²

spherical probes and for the PDP chassis. The current collecting area of the PDP was taken to be its surface area. Unfortunately, the current collecting properties of the spacecraft body are complicated, and this estimate is to be taken only as a rough approximation. The solution for the floating potential as a function of the energetic electron current density is plotted in Figure 5. Measurements from the LEPDEA during beam event 1 indicate that J_b was as high as 4×10^{-4} amp/m² (W. R. Paterson, personal communication, 1987). The Langmuir probe measurements indicate that during event 1, n_e was of the order of 1×10^{11} m⁻³ (A. C. Tribble, personal communication, 1987). From Figure 5 one can see that under the conditions of event 1 the PDP floating potential could easily be lower than -10 V. This is consistent with the Langmuir probe observation mentioned previously that the PDP charged to at least -7.6 V during event 1. More importantly for the V_{diff} measurements, under the conditions of event 1 differences in J_b on the order of 10^{-5} amp/m² lead to floating potential differences on the probes of several volts. During events 2, 3, 4, and 5 the Langmuir probe measurements indicate that n_e was of the order of 1×10^{10} m⁻³ (A. C. Tribble, personal communication, 1987). For this lower ambient density, Figure 5 shows that differences in J_b of the order of 10^{-6}

amp/m² lead to floating potential differences on the probes of several volts. Figure 5 also shows that for a fixed value of J_b , small differences in the ambient plasma density lead to floating potential differences of several volts.

Using the differential voltage between the probes to infer electric field values can produce erroneous results if the two antenna probes receive different amounts of current from any of the various current sources. Current differences can occur if one of the probes is shielded by the PDP chassis from a current source, or if the plasma environment is nonuniform over the length of the antenna. During events 2, 3, 4, and 5 the peaks in V_{diff} are associated with specific orientations of the antenna with respect to the velocity and the magnetic field, and therefore can be primarily attributed to shadowing effects. Shadowing effects of this type were observed by Winckler *et al.* [1984] during the Echo 6 experiment. In that experiment, large signals at the payload spin frequency were attributed to shadowing of one probe from a magnetic field aligned plasma flow. At the time, the electric probes were stowed in the payload body. During events 3, 4, and 5 the "double peak" character of the signals indicates that two different shadowing effects are occurring. These two effects are discussed separately below.

For events 3, 4, and 5 one finds a voltage peak, and therefore a probable shadowing of one probe, when the antenna is aligned with the magnetic field projected onto the spin plane. Because the local ion larmor radius is much larger than the PDP, a shadowing along field lines suggests a shadowing of electrons. We explain the signal peak in the following manner. For events 3, 4, and 5 the beam was injected in the direction of **B**. At the time when the antenna was aligned with **B** in the spin plane, the probe on the boom pointing in the direction of **B** was at a lower potential than the probe on the boom pointing in the direction of $-\mathbf{B}$. Thus we conclude that some energetic electrons are moving in the direction of $-\mathbf{B}$, and one probe is shielded from them. So, for the three events when the PDP is 80 or more meters from the beam, the energetic elec-

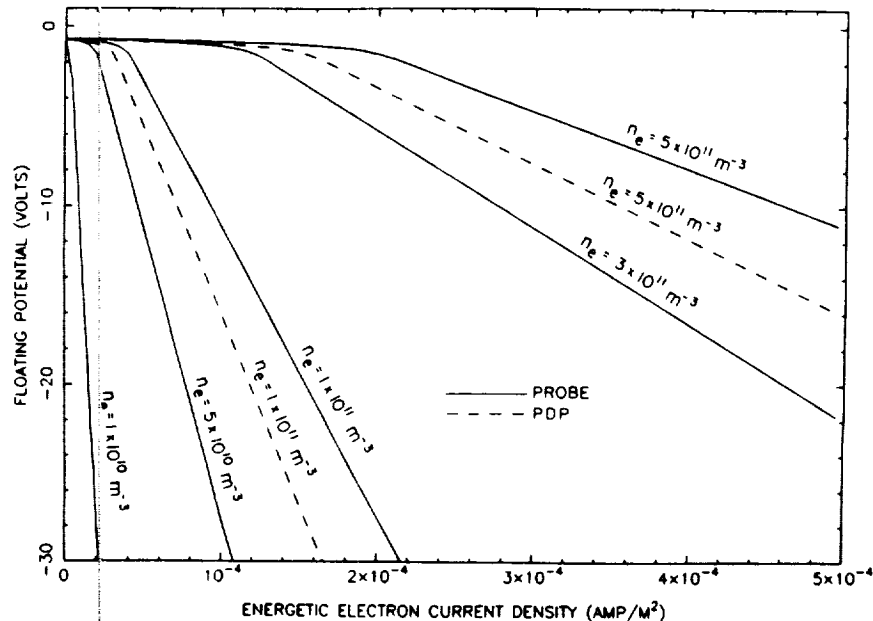


Fig. 5. Solution of equation (1) using values from Table 3. Model of floating potential as a function of energetic electron current. Antenna probe and PDP chassis have different floating potentials because of their different current collecting surface areas.

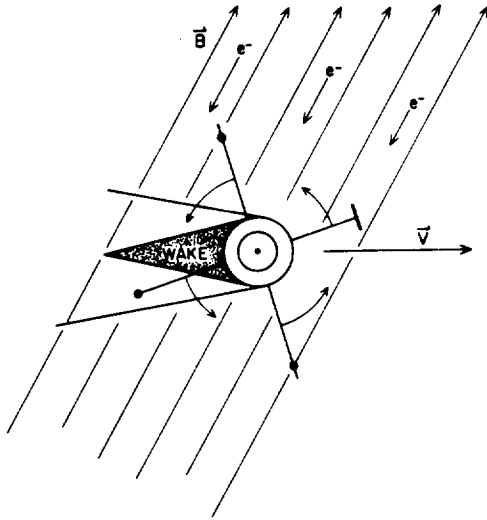


Fig. 6a. The PDP with the spin plane corresponding to the plane of the page. Energetic electrons move along the field lines. As the PDP spins, the antenna periodically becomes aligned with the magnetic field, and one probe is shielded from the electron flux. The probe also passes through the PDP wake.

trons have a preferred direction, which is opposite to the injection direction. This explanation is consistent with the report by the LEPEDA group of a secondary electron beam in the shuttle wake [Frank *et al.*, 1987]. The shadowing of one probe from electrons moving down the field lines is pictured in Figure 6a. Consideration of Figure 6b shows that if the angle θ of the magnetic field to the spacecraft spin plane is too large, then shadowing along the field lines will not occur. The range of angles where shadowing is possible is $\theta < 20.4^\circ$. Referring to the values of θ listed in Table 2, one finds that shadowing along field lines is possible for events 2, 3, 4, and 5.

The energetic electrons moving down the field lines and charging the probes in events 3, 4, and 5, may be attributed to reflection of beam electrons by collisions with atmospheric neutrals, or to a beam plasma interaction. First, consider reflection of electrons by collisions. Given the distance of the PDP downstream from the beam for these events, and the spacecraft velocity, one can determine the time of flight for the energetic electrons to be around 10 to 20 ms. For 1-keV electrons, the corresponding total distance traveled is about 200 to 400 km. For comparison, the mean free path of electrons for collisions with oxygen atoms can be roughly estimated by $\lambda = 1/(n_n \sigma)$, where n_n is the atomic oxygen density and σ is the collision cross section. We use a value for σ of $7 \times 10^{-16} \text{ cm}^2$, the total scattering cross section for 100 eV electrons measured by Sunshine *et al.* [1967]. At an altitude of 300 km, n_n is approximately 10^8 cm^{-3} [Johnson, 1965], which yields a mean free path $\lambda \approx 140 \text{ km}$. Because the atomic oxygen density is larger at lower altitudes, λ will become shorter at lower altitudes. Thus for events 1 and 3 where the beam was injected downward, it is quite reasonable that electrons reflected by collisions with neutrals could reach the PDP. Since the atomic oxygen density is smaller at higher altitudes, λ becomes longer at higher altitudes. At an altitude of 400 km, n_n is approximately 10^7 cm^{-3} , which yields $\lambda \approx 1400 \text{ km}$. So for electrons injected upward, the effective mean free path will be $\gg 1400 \text{ km}$. For events 2, 4, and 5 where the beam was injected upward, it may seem unlikely that the PDP could be affected by reflected electrons. However, it is not necessary that most

of the beam particles be reflected. The solution of (1) showed that the measured signals are explained by differential energetic electron currents of the order of 10^{-6} amp/m^2 , and this current can result from only a small percentage of beam particles being reflected. An alternative explanation for the presence of energetic electrons is considered by Wilhelm *et al.* [1985]. In the SCEX experiment, Wilhelm *et al.* measured energetic electrons in the region downstream of an electron beam. They discuss the possibility that the energetic electrons are the product of a beam plasma interaction. Both explanations are possible, and without a further more detailed analysis we cannot say which is correct.

A different shadowing effect occurs for events 2, 3, 4, and 5 when the antenna is aligned with the velocity vector. Because the local ion thermal speed is less than the spacecraft velocity, ions are swept up by the spacecraft motion. The electron thermal velocity is much greater than spacecraft velocity, so the electrons are not swept up. However, because quasi-neutrality must be maintained, both the ion and the electron densities are reduced behind the spacecraft, forming a plasma wake. The sweeping of the antenna through the wake as the PDP spins is indicated in Figure 6a. Because the velocity vector lies in the PDP spin plane as shown, the antenna always passes through the wake region. In order to estimate the plasma density in the wake at the location of the antenna probe, we use the self-similar solution for the expansion of a plasma into a vacuum as shown by Samir *et al.* [1983] and Singh and Schunk [1982]. In the standard treatment one assumes initially a plasma of density N_0 for the region $x < 0$, and a vacuum for the region $x > 0$. At time $t = 0$ the plasma is allowed to expand into the vacuum region. The solution for the density at later times is given by

$$N = N_0 \exp \left[\left(\frac{x}{S_0 t} + 1 \right) \right] \quad (2)$$

where S_0 is the ion sound speed. To obtain an estimate of the density at the probe when the probe is in the wake, we use (2) and take for x the radius of the PDP, $x = 0.53 \text{ m}$, and for t the time for the ionospheric plasma to flow a distance of half of the antenna length relative to the PDP, $t = 2.5 \times 10^{-4} \text{ s}$. Assuming an electron temperature of 0.2 eV, and assuming ions are atomic oxygen, the ion sound speed is estimated to be

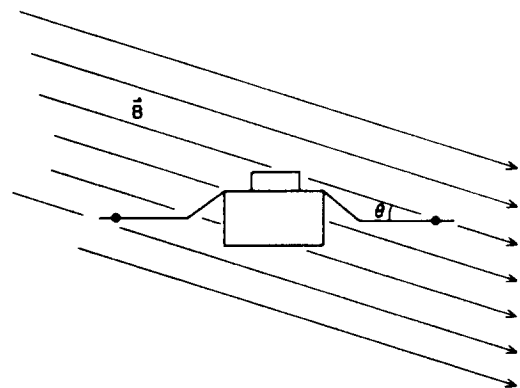


Fig. 6b. The PDP viewed with the spin axis in the plane of the page. The angle θ of the magnetic field to the spin plane is shown. If θ is small, then particles moving along field lines can be shadowed from one probe.

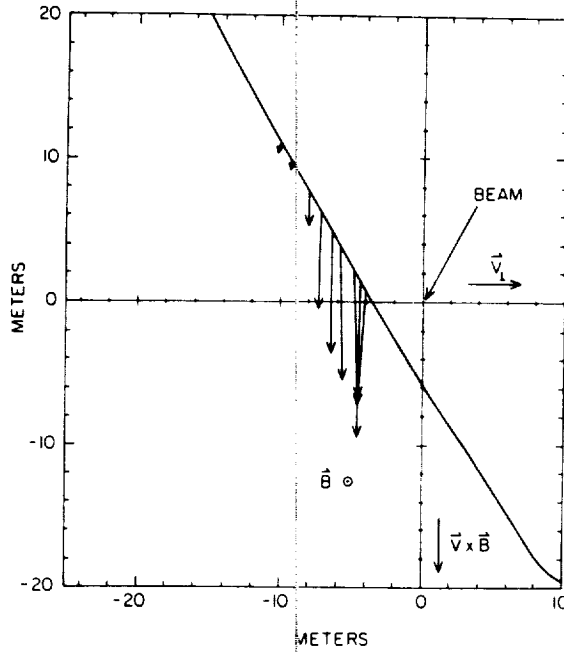


Fig. 7. Vectors showing the gradient in energetic electron flux along the trajectory of the PDP during event 1. Note that the beam will have a finite width, and the location of the beam center shown is accurate only to within a few meters.

about 1.4×10^3 m/s, yielding a wake density

$$N = 0.08N_0 \quad (3)$$

This solution corresponds to the expansion of the plasma in one direction only. The wake fills in from all directions, so we expect the density in the wake at the location of the antenna probe to be greater than $0.08 N_0$, but still significantly less than N_0 . Examination of Figure 5 shows that if both probes receive the same amount of energetic electron current, but one probe is in the wake where the density is lower, then the probe in the wake will be several volts lower in potential than the probe upstream. This explanation is consistent with the observed signals.

Event 1 does not lend itself to explanation in terms of probe shadowing, as the other events do. The angle θ between the magnetic field and the spin plane (see Table 2) is greater than 20.4° , so that probes are not shadowed along field lines. Figure 2 shows that the peaks in voltage are not consistently centered about the times the antenna is aligned with the velocity vector or the magnetic field. The peaks are also broader than expected if due only to a shielding effect. Thus the signal is due either to a gradient in the fluxes of energetic electrons reaching the probes, or both a gradient in fluxes of energetic electrons and an electric field. We cannot rule out the possibility that we have measured the electric field. However, because the entire region where the large electric field signals and the energetic electrons are observed is only 20 meters wide (refer to Figure 3), gradients over the antenna length are expected. As will be discussed below, we consider it likely that the large V_{diff} signal in event 1 is caused mainly by a gradient in energetic electron fluxes.

In order to investigate the possible interpretation of the large signals associated with event 1, the V_{diff} signals were analyzed as follows. Due to the spacecraft rotation, the V_{diff} signal varies sinusoidally with the PDP spin period of 13.1 s, and we assume that V_{diff} attains peak value when the antenna

is aligned with the direction of strongest gradient in the energetic electrons. The direction and relative magnitude of the gradient is then obtained by using a least squares method to fit a 13.1-s segment of the V_{diff} signal to the function

$$F(t) = F_1 + F_2 \cos(2\pi t/T - \Phi) \quad (4)$$

where $T = 13.1$ s, and F_1 , F_2 , and Φ are parameters determined by the fit procedure. If the signal is interpreted as a measure of the gradient of the energetic electron flux, then the constant F_2 gives the magnitude of the gradient and Φ gives the direction of the gradient in the spin plane. We do not expect the energetic electron flux to vary much along the direction of \mathbf{B} , so we assume that the gradient lies in the plane perpendicular to \mathbf{B} and that we have measured the component of the gradient projected onto the PDP spin plane. Using this assumption, the magnitude of the gradient vector in the plane perpendicular to \mathbf{B} was determined. In order to establish a "goodness of fit" of the curve fit performed for each measurement, the following test variable was calculated:

$$X = [\sum (F(t_i) - x_i)^2 / (N - 3)]^{1/2} / F_2 \quad (5)$$

where x_i is the V_{diff} signal at time t_i , and N is the number of sample points used in one curve fit. Measurements were retained if $X < 0.25$, corresponding roughly to 25% error.

The vectors obtained by the above analysis are shown in Figure 7. The vectors are plotted along the trajectory of the PDP relative to the electron beam where the coordinate directions are the same as in Figure 3. The V_{diff} signals first become larger than $|(\mathbf{V} \times \mathbf{B}) \cdot \mathbf{L}|$, and the gradient in the energetic electron flux first becomes significant, when the PDP is about 10 m away from a line extending directly downstream from the center of the beam. The V_{diff} signal, and thus the gradient in the electron flux, become larger as the PDP gets closer to this line. The gradient vectors tend to point toward the line. The indicated picture is that of a region of energetic electrons downstream from the primary electron beam. The region is not homogeneous but rather the electron flux is peaked along the line extending directly downstream from the primary beam.

The presence of a gradient in energetic electron flux can account for the large magnitude (larger than 8 V) of the V_{diff} signals during event 1. If the magnitude of the gradient in J_b is estimated from the LEPEDA measurements, then the V_{diff} signal that would result from such a gradient can be estimated. As stated previously, the LEPEDA measured a peak value of J_b of about 4×10^{-4} amp/m². We assume that the flux of energetic electrons is peaked on a line extending directly downstream from the center of the beam, and is symmetric about that line. Since the region where large signals are detected is about 20 m wide, the spatial gradient $\Delta J_b / \Delta x$ is approximately $(4 \times 10^{-4} \text{ amp/m}^2) / (10 \text{ m}) = 4 \times 10^{-5}$ amp/m. The resulting V_{diff} can be estimated by

$$V_{diff} = (\Delta J_b / \Delta x) (\Delta V / \Delta J_b) (L \sin \theta) \quad (6)$$

where the quantity $\Delta V / \Delta J_b$ must be determined from Figure 5, L is the antenna length, and θ is the angle of \mathbf{B} to the spin plane. For $n_e = 1 \times 10^{11}$ m⁻³ and $J_b > 4 \times 10^{-5}$ amp/m², $\Delta V / \Delta J_b$ is -1.6×10^5 V/amp/m². The antenna length is 3.89 m (see Table 1) and θ is about 23° (see Table 2). Using equation (4) with the given values, we obtain $V_{diff} \approx 9.7$ V. Thus a gradient in the energetic electron flux of the magnitude indicated by the LEPEDA measurements could easily produce the V_{diff} signals recorded during event 1.

Analysis of all five events suggests that energetic electrons are found in a region about 20 m wide extending up to 170 m downstream from the injected electron beam. Consideration of event 1 indicates that very close to the beam, there is a large spatial gradient in the energetic electron flux: the flux increases as one approaches the line extending directly downstream from the center of the beam. We expect that the energetic electron flux is symmetric about this line. For events 3, 4, and 5, in which the PDP was 80 or more meters away from the beam, the signals are explained by the presence of energetic electrons having a preferential direction of motion along the magnetic field line, but in a direction opposite to the beam injection.

Although the main features of the V_{diff} signals during events 1-5 are understood in terms of the discussion given above, some features remain unexplained. For example, the voltage peaks during event 4 are bumps on a signal that is otherwise sinusoidal. The peaks in event 4 are explained by alignment of the antenna with the magnetic field or with the velocity vector in the presence of energetic electrons. However, the V_{diff} signal for event 4 shown in Figure 2 would also provide a reasonably good fit to the function in (4). Yet, since the shadowing effects are apparent in the measurements, a fit of the signal to (4) would be difficult to interpret. It is not clear why event 4 has a more sinusoidal character than events 3 or 5. Similarly, the large peaks in the signal during event 2 can be attributed to alignment of the antenna with the velocity vector in the presence of energetic electrons, but the signal remains $> |(\mathbf{V} \times \mathbf{B}) \cdot \mathbf{L}|$ when the probes are not in the spacecraft wake.

Finally, we consider the average potential measurements. The measurements show that during periods of no beam operation, the average probe floating potential was several volts higher than the PDP chassis floating potential. The solution of (1) (see Figure 5) indicates that the probes should float to a potential which is much less than a volt higher than the PDP potential. During events 1 and 2 the average probe floating potential became lower than the PDP potential. The solution of (1) indicates that the average probe floating potential should always be higher than the PDP chassis potential. The reasons for these discrepancies are not clear. However, we speculate that explanation involves the properties of the PDP surface materials. In solving (1) for the PDP potential, we assumed the PDP to have a uniformly conducting surface. However the potential of the aluminum mesh on the PDP surface may be influenced by the fiberglass cloth which underlies it. The fiberglass cloth may be charging to a different potential than the aluminum mesh. Katz and Davis [1987] analyze some of the effects of the fiberglass cloth-aluminum mesh arrangement for the situation of the PDP attached to the shuttle. The ultimate effect on the mesh potential for the PDP in free flight is uncertain.

5. CONCLUSIONS

Our conclusion from this analysis is that the large signals measured by the PDP quasi-static electric field instrument during electron beam operation can primarily be attributed to three causes. First, at times when the electric antenna is aligned with the projection of the magnetic field into the spin plane, the spacecraft body shields one probe from energetic electrons moving along the magnetic field lines. The two probes receive different amounts of electron current, thereby causing large signals. Second, at times when energetic electrons are reaching both probes, but one probe is in the PDP

wake, the wake produces asymmetries in the plasma density at the two probes, thereby causing large signals. Finally, spatial gradients in the energetic electron fluxes between the two antenna probes produce differences in the energetic electron current to the two probes, thereby causing large signals. When the electron beam generator is operating, energetic electrons are found in a region about 20 m wide and up to 170 m downstream from the injected electron beam. Because the region is so narrow, the spatial gradients are significant even over the length of the PDP antenna. For events 80 or more meters away from the beam, the electric field results are explained by the presence of energetic electrons having a preferential motion back down the magnetic field line on which the beam was injected.

On the Spacelab 2 mission, it was demonstrated that with the shuttle it is possible to carry out detailed studies of electron beam effects under carefully controlled conditions. Thus, it should be possible to obtain a good map of the electric field near an electron beam. However, our experience indicates that double probe floating potential measurements are not reliable in the region near the beam. The floating potential of an object in a region with substantial fluxes of energetic electrons can be many times kT_e/e more negative than the plasma potential. A small difference in energetic electron current collected by each probe of a double probe system can then lead to differential voltages much higher than those due to any electric field in the plasma. Reliable potential measurements probably will require biased probes, such as described by Fahleson [1967], or emissive probes such as described by Bettinger [1965]. These active potential measurements are not as sensitive to energetic electrons. An example of a biased probe system is found on the ISEE-1 spacecraft [Mozer et al., 1978]. In general, though, active potential measurements have not been widely used because of the appealing simplicity of floating potential measurements. However, for future spacecraft electron beam experiments, active instead of passive potential measurements will probably have to be considered.

Acknowledgments. The authors thank Louis A. Frank and William R. Paterson for the use of the LEPEDEA measurements, and for their help. We thank Nicola D'Angelo for use of the Langmuir probe measurements. We also acknowledge the useful discussions with Rock Bush, William M. Farrell, Karl Lonngren, Gerald B. Murphy, Jolene S. Pickett and Alan C. Tribble. This research was supported by NASA through contract NAS8-32807 with Marshall Space Flight Center, contract NAG3-449 with the Lewis Research Center, and grant NGL 16-001-043 with NASA Headquarters.

The Editor thanks B. A. Whalen and J. R. Winckler for their assistance in evaluating this paper.

REFERENCES

- Arnoldy, R. L., and J. R. Winckler, The hot plasma environment and floating potentials of an electron beam-emitting rocket in the ionosphere, *J. Geophys. Res.*, **86**, 575-584, 1981.
- Banks, P. M., W. J. Raitt, A. B. White, R. I. Bush, and P. R. Williams, Results from the Vehicle Charging and Potential Experiment on STS-3, *J. Spacecr. Rockets*, **28**, 138-149, 1987.
- Bettinger, R. T., An in situ probe system for measurement of ionospheric parameters, in *Interactions of Space Vehicles With an Ionized Atmosphere*, edited by S. F. Singer, pp. 163-270, Pergamon, New York, 1965.
- Denig, W. F., Wave and particle observations associated with the beam plasma discharge in a space simulation chamber, Ph.D. thesis, Utah State Univ., Logan, 1982.
- Fahleson, U., Theory of electric field measurements conducted in the magnetosphere with electric probes, *Space Sci. Rev.*, **7**, 238-262, 1967.
- Frank, L. A., D. A. Gurnett, M. Ashour-Abdalla, W. R. Paterson,

- W. S. Kurth, N. Omidi, P. M. Banks, and W. J. Raitt, The secondary electron beams and plasma waves associated with electron beam injection in space (abstract), *Bull. Am. Phys. Soc.*, **32**, 1823, 1987.
- Jacobsen, T. A., and N. C. Maynard, Polar 5—An electron acceleration experiment within an aurora, 3, Evidence for significant spacecraft charging by an electron accelerator at ionospheric altitude, *Planet. Space Sci.*, **28**, 291–307, 1978.
- Johnson, F. S., Structure of the upper atmosphere, in *Satellite Environment Handbook*, edited by F. S. Johnson, pp. 3–20, Stanford University Press, Stanford, Calif., 1965.
- Kasha, M. A., *The Ionosphere and Its Interaction With Satellites*, Gordon and Breach, New York, 1969.
- Katz, I., and V. A. Davis, Ram ion scattering caused by space shuttle $V \times B$ induced differential charging, *J. Geophys. Res.*, **92**, 8787–8791, 1987.
- Kellogg, P. J., H. R. Anderson, W. Bernstein, T. J. Hallinan, R. H. Holzworth, R. J. Jost, H. Leinbach, and E. P. Szuszczewicz, Laboratory simulation of injection particle beams in the ionosphere, in *Artificial Particle Beams in Space Plasma Studies*, edited by B. Grandel, p. 289, Plenum, New York, 1982.
- Mozer, F. S., R. B. Torbert, U. V. Fahlson, C. G. Falthammer, A. Gonfalone, and A. Pedersen, Measurements of quasi-static and low-frequency electric fields with spherical double probes on the ISEE-1 spacecraft, *IEEE Trans. Geosci. Electron.*, *GE-16*, 258–261, 1978.
- Samir, U., K. H. Wright, Jr., and N. H. Stone, The expansion of a plasma into a vacuum: Basic phenomena and processes and applications to space plasma physics, *Rev. Geophys.*, **21**, 1631, 1983.
- Shawhan, S. D., Description of the plasma diagnostics package (PDP) for the OSS-1 shuttle mission and JSC chamber test in conjunction with the fast pulse electron gun (FPEG), in *Artificial Particle Beams in Space Studies*, edited by B. Grandel, pp. 419–430, Plenum, New York, 1982.
- Shawhan, S. D., G. B. Murphy, P. M. Banks, P. R. Williamson, and W. J. Raitt, Wave emissions from dc and modulated electron beams on STS-3, *Radio Sci.*, **19**, 471–486, 1984.
- Singh, N., and R. W. Schunk, Numerical calculations relevant to the initial expansion of the polar wind, *J. Geophys. Res.*, **87**, 9154, 1982.
- Sunshine, G., B. B. Aubrey, and B. Bederson, Absolute measurements of total cross sections for the scattering of low-energy electrons by atomic and molecular oxygen, *Phys. Rev.*, **154**, 1–8, 1967.
- Tribble, A. C., N. D'Angelo, G. Murphy, J. Pickett, and J. T. Steinberg, Exposed high-voltage source effect on the potential of an ionospheric satellite, *J. Spacecr. Rockets*, **25**, 64–69, 1988.
- Whetten, N. R., Secondary electron emission, in *CRC Handbook of Chemistry and Physics*, 65th ed., CRC Press, Boca Raton, Fla., 1985.
- Wilhelm, K., W. Bernstein, P. J. Kellogg, and B. A. Whalen, Fast magnetospheric echoes of energetic electron beams, *J. Geophys. Res.*, **90**, 491–504, 1985.
- Winckler, J. R., and K. N. Erickson, Plasma heating, plasma flow and wave production around an electron beam injected into the ionosphere, JPL Symposium on Space Technology Plasma Issues in 2001, edited by H. Garrett, J. Feynman, and S. Gabriel, *JPL Publ.*, **86-49**, 295–306, Oct. 1, 1986.
- Winckler, J. R., J. E. Steffen, P. R. Malcolm, K. N. Erickson, Y. Abe, and R. L. Swanson, Ion resonances and ELF wave production by an electron beam injected into the ionosphere: Echo 6, *J. Geophys. Res.*, **89**, 7565–7571, 1984.

P. M. Banks, STAR Laboratory, Stanford University, Stanford, CA 94305.

D. A. Gurnett, Department of Physics and Astronomy, University of Iowa, Iowa City, IA 52242.

J. T. Steinberg, Center for Space Research, Massachusetts Institute of Technology, Cambridge, MA 02139.

(Received July 28, 1987;
revised April 22, 1988;
accepted May 26, 1988.)

The POLAR Code Wake Model: Comparison With in Situ Observations

G. MURPHY

Jet Propulsion Laboratory, Pasadena, California

I. KATZ

S-Cubed, La Jolla, California

Measurements of the ion and electron densities associated with the wake of the shuttle orbiter were made by the Plasma Diagnostics Package (PDP) during the 1985 Spacelab 2 mission. Cross sections of the wake at distances of 50–250 m downstream and measurements along the wake axis from 5 to 100 m were obtained. The POLAR wake model, developed for The Air Force Geophysics Laboratory to study charging of spacecraft in low-altitude high-inclination orbits, was used to perform a three-dimensional simulation of the plasma wake evaluated at points along relative trajectory of the PDP. The POLAR code uses several simplifying assumptions to predict wake densities. These include neglecting the magnetic field and assuming that the plasma is quasi-neutral. The code models plasma density ahead of the expansion front, using a neutral approximation, and models the plasma density behind the expansion front by using the self-similar solution of the expansion of a plasma into a vacuum. For cases where $T_i \approx T_e$, the front is not sharp and thermal motion can account for most of the expansion. This approach is computationally very efficient. The results presented here are the first known comparison between such a model and actual in situ data obtained for objects of scale size $\approx 10^4 \lambda_D$. Excellent qualitative and quantitative agreement are found at distances greater than ≈ 30 m, indicating that at least to first order, the model's approximations are justified. An intriguing disparity between the model and data suggests that the orbiter's near wake may be filled predominantly by a pick-up ion population created from neutral contaminants and that these would have to be included if accurate wake models of large gas-emitting objects are required.

INTRODUCTION

In this paper we discuss measurements made by the Plasma Diagnostics Package (PDP) during Spacelab 2, which are presented by *Murphy et al.* [1989], and compare those results with predictions from the Air Force Geophysics Laboratory (AFGL) POLAR wake code, which uses a complex geometric model of the orbiter and the self-similar solution of the expansion of a plasma into a vacuum as its model basis. Previous reports [*Katz et al.*, 1985] have compared the predictions of POLAR to observations of $T_i \approx T_e$ plasmas in the laboratory.

Caution should be exercised in extending conclusions about the accuracy of the POLAR model to conclusions regarding verification of the underlying physical processes it contains. Several other investigations have studied the applicability of the self-similar mathematics [*Samir et al.*, 1983; *Raychaudhuri et al.*, 1986; *Gurevich et al.*, 1969; *Diebold et al.*, 1987; *Kozima et al.*, 1988] to wakes. It is our purpose only to determine if POLAR provides a reasonable model for the wakes of "large" objects in the ionosphere, as it has for $T_i \approx T_e$ plasmas in the laboratory.

We describe briefly the POLAR model and review the physics it contains, compare the data with the model, and then discuss the range of validity of the code.

THE POLAR CODE

To develop a code that can adequately describe the plasma wake behind a large object, particularly one of complex geom-

etry, careful consideration of assumptions and approximations are required, as are simplifications allowing for computational efficiency. The POLAR code has evolved with such considerations in mind. A detailed description of the POLAR wake model is given by *Katz et al.* [1985], and it is the purpose here only to review the basic physics and processes in POLAR so the reader may have some insight into the validity of the code.

The model of the wake structure used by POLAR depends on the position relative to the so-called ion front. This ion front marks the boundary where electron density begins to change on a scale commensurate with the Debye length and the ion density takes a sudden and dramatic drop. Several authors have discussed the relationship between the wake fill process and the theoretical problem of the expansion of a plasma into a vacuum. In particular, problems applicable to ionospheric conditions have been treated by *Gurevich et al.* [1966], *Gurevich and Pitaevskii* [1975], and *Singh and Schunk* [1982], to name a few.

The solution to the Vlasov-Poisson equation system is in general quite difficult to obtain, but for the expansion of a plasma into the void it can be solved explicitly [*Gurevich et al.*, 1969]. Ahead of the ion front the plasma is treated as rarefied; its motion is controlled by the thermal spread in ion velocities. Behind the front the motion is controlled by the electron temperature and ion mass. Figure 1 illustrates these regimes and defines the coordinate system used.

The governing equations in the region behind the front, considering that electrons are more mobile than ions and that they maintain equilibrium with a local potential, are

The Boltzman relation

$$n_e = n_0 \exp(e\phi/kT_e) \quad (1)$$

Copyright 1989 by the American Geophysical Union.

Paper number 89JA00582.
0148-0227/89/89JA-00582\$05.00

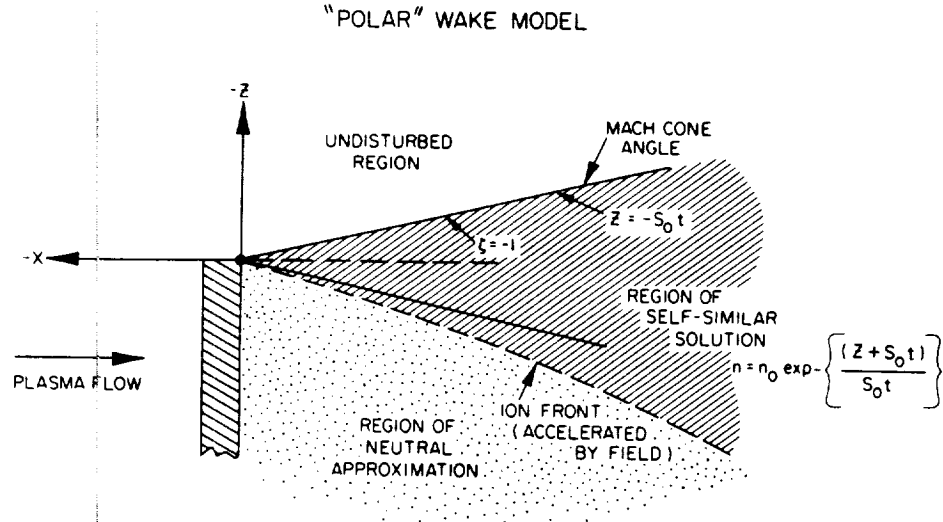


Fig. 1. The POLAR wake code distinguishes three regions of interest. The ambient plasma, the region of self-similar model, and the neutral approximation spaces are bounded by the Mach cone $Z = -S_0 t$ and ion front, respectively. The coordinate system used is consistent with equations (1) through (10).

Continuity

$$\frac{\partial n_i}{\partial t} + \frac{\partial(n_i v)}{\partial z} = 0 \tag{2}$$

Equation of motion

$$\frac{\partial v}{\partial t} + v \frac{\partial v}{\partial z} = \frac{-e \partial \phi}{M \partial z} \tag{3}$$

Poissons equation

$$\frac{\partial^2 \phi}{\partial z^2} = 4 \pi e (n_e - n_i) \tag{4}$$

where

- n_0 ambient density;
- n_i ion density;
- n_e electron density;
- T_e electron temperature;
- e electron charge;
- ϕ local potential;
- k Boltzman's constant.

and where z is a variable representing distance parallel to the front velocity or, in this case, perpendicular to the orbital velocity.

Crow *et al.* [1975] have numerically solved (1) through (4) to predict the position of the ion front. Katz *et al.* [1985] developed an analytical fit to the Crow results:

$$Z_F(t) = 2 \lambda_d \left\{ \left(\omega t + \frac{1}{\alpha} \right) \ln (1 + \alpha \omega t) - \omega t - \left(1 - \frac{0.429}{\alpha} \right) \left(\omega t - \frac{1}{\alpha} \ln (1 + \alpha \omega t) \right) \right\} \tag{5}$$

where

$$\omega = \frac{(4 \pi n_0 e^2)^{1/2}}{M} \quad \lambda_d = \frac{(k T_e)^{1/2}}{4 \pi n_0 e^2}$$

are the ion plasma frequency and Debye length, respectively, and α is a free parameter determined to be ≈ 1.6 .

Katz *et al.* [1985] showed that this formula agrees well with laboratory data from Wright *et al.* [1985] and incorporated it in POLAR. Ahead of this front Z_F , the plasma is assumed to expand owing to thermal motion, the so-called "neutral approximation." Behind Z_F the plasma evolves into a state which is self-similar [Chan *et al.*, 1984]. The self-similar solution of (1)–(4) for $z > -S_0 t$ is

$$n = n_0 \exp \left[- \frac{(z + S_0 t)}{S_0 t} \right] \tag{6}$$

where $S_0 = (k T_e / M)^{1/2}$ is the ion acoustic speed.

The time variable is defined as

$$t = \frac{x}{V_0} \tag{7}$$

where x is the distance behind the object (perpendicular to z) and V_0 is the orbital velocity. We define the self-similar variable ζ as

$$\zeta = \frac{z}{S_0 t} \tag{8}$$

Thus the self-similar solution essentially states that between the region bounded in positive z by the front Z_F and in negative z by the line $z = -S_0 t$, the density rises exponentially to be equal to the ambient value along $z = -S_0 t$. This is an intuitively reasonable result.

In summary, the wake routines in POLAR employ two limiting cases. (1) Ahead of the ion front the electric field is negligible and the motion of ions is identical to neutrals. (2) Behind the ion front, whose position is determined by (5), the quasi-neutral self-similar solution of (6) is implemented.

POLAR has routines which model accurately the geometry of the object, and the "neutral ion" trajectories are calculated from

$$f_i(\mathbf{x}, v) = g(\mathbf{x}, \Omega) f_{i0}(v) \tag{9}$$

where $f_{i0}(v)$ is the unperturbed distribution function for a drifting Maxwellian, and $g(\mathbf{x}, \Omega)$ has value "0" if a ray starting from \mathbf{x} and going in the direction Ω would strike the vehicle and "1" if it would not.

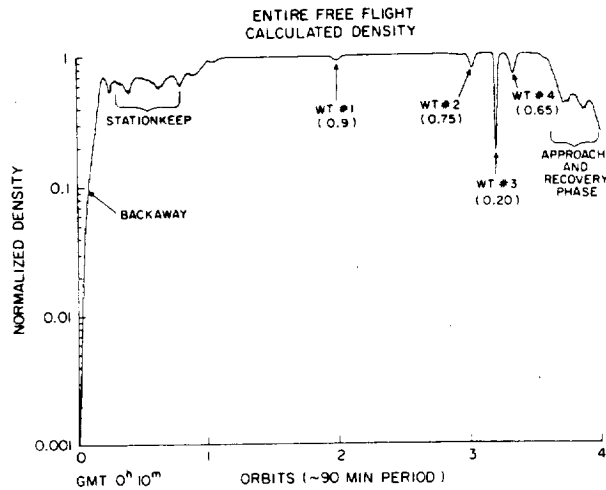


Fig. 2. Using the relative trajectory of the PDP and orbiter, POLAR calculates the density as a function of time for the entire free-flight time period. Areas of interest are labeled in the figure. The assumed normalization values for the plasma are $n_e = 1 \times 10^5 \text{ cm}^{-3}$ and $T_e = 2500^\circ\text{K}$.

The local density is given by

$$n_i(\mathbf{x}) = \int f_i(\mathbf{x}, \mathbf{v}) = \int g(\mathbf{x}, \Omega) \left\{ \int f_{i0}(\mathbf{v}, \Omega) v^2 dv \right\} d\Omega \quad (10)$$

This initial density calculated in three dimensions for neutral particles is compared with density calculated assuming the complex geometric object is replaced by a flat plate at a position where the dominant source appears at the object edge. This ratio provides a "geometric correction factor," which is applied to the quasi-neutral one-dimensional solution discussed earlier for positions behind Z_F . In this way, POLAR can calculate quite rapidly an approximate value for the ion and electron densities in the wakes of complex objects.

Note that the assumptions behind the front are (1) that the electron temperature and ion mass govern the equation of motion, (2) that the plasma is quasi-neutral, (3) that the magnetic field does not affect the ion or electron motion, (4) that equation (5) serves as a good approximation for determining the boundary of the ion front, and (5) that the geometric correction factor calculated in detail with the three-dimensional neutral model can be approximately applied to correct the plasma densities as well. Therefore the algorithm can address complex geometries but takes advantage of the smooth wake structure characteristic of ionospheric plasmas where $T_i/T_e \approx 1$. Additionally, the model ignores fields existing in a sheath near the body surface, which should not be of concern in our case where the orbiter is near plasma potential. This implies that ion acceleration calculated by POLAR is dominated by electric fields due to space charge separation in the wake.

COMPARISON OF RESULTS

Figure 2 is a plot of the normalized density as a function of time predicted by POLAR for the PDP/orbiter relative trajectory. The density ratio $N_{\text{wake}}/N_{\text{ambient}}$ varies from approximately 0.9 for wake transit (WT) 1, which is at a distance of 245 m, to 0.2 for the closest, WT 3, at 45 m.

One must be careful when comparing the model to the data, since the model assumes a fixed background density of

10^5 cm^{-3} , whereas the actual ionospheric density can and does vary considerably. The background density chosen for the model is typical of that observed in the dayside ionosphere. The assumed model temperature is also a constant 2500°K . The observed temperature varies plus or minus $\approx 25\%$ from this assumed value during times of interest. The wake transits were all planned to occur in the relatively stable dayside ionosphere, and over the time span of a given wake transit the background density is believed to be stable to $\pm 10\%$ [Murphy *et al.*, 1989]. In the following discussion we will always compare the observed density ratio during a wake transit to the percentage change predicted by the model.

Figure 3a plots the observed electron and ion density depression during the back-away maneuver, with a constant 10^6 cm^{-3} as the reference density [Murphy *et al.*, 1989]. The density chosen for normalization is arbitrary and does not affect the shape of the profile as long as it is constant. It is the shape and relative depth of the profile we wish to compare with POLAR. The dots in Figure 3a are the electron density (small periodic depressions result when the boom-mounted probe passes through the wake of the spinning PDP). The plus symbols are the ion density obtained once per spin cycle. During the back-away, the PDP and orbiter pass from a latitude of approximately -20° to $+30^\circ$ in early afternoon, local time. Figure 3a also shows the predicted normalized density calculated by the POLAR model described earlier. As can be seen, good agreement exists at distances from ≈ 30 to ≈ 75 m. It should also be noted that over the range of the data shown, the RPA and LP data agree on density within $\approx 30\%$.

As discussed by Murphy *et al.* [1989], we cannot easily normalize to either the previous or following orbit, so we use a constant value of 10^6 cm^{-3} for N_{ambient} . This value appears to be the peak density observed after the PDP has left the wake approximately 1 hour and 40 min later. Over the relatively long period of this maneuver, the ionosphere has surely changed by more than 10%, and this may explain the disparity after $t \approx 20$ min, since the PDP to orbiter distance is changing relatively little. Figure 3b is a plot of the predicted density calculated by the IRI ionosphere model and the measured density one orbit later (same local time and latitude). Note that the gradual variations observed owing to changing local time and latitude are consistent with the general trend predicted by the IRI model.

Let us turn now to the wake transit observations. Table 1 lists the wake transits and compares the predicted and observed depletions as well as conditions at the time of the center of the wake. Note that in this entire range of ≈ 50 –250 m, the calculations and observations agree to within $< 30\%$.

Since the orbiter has a complex geometry, the details of the wake structure at a distance of 45 m (WT 3) downstream may be affected. Figure 4 plots a detail of that wake transit and the POLAR model as a function of time. The data are normalized to a constant value, since it is clear some variation in background density occurs but it is not clear exactly what that variation is. To normalize to any unknown value other than a constant would introduce artificial variation and skew the results. Murphy *et al.* [1989] discuss this issue in detail and in that case, WT 3 is normalized by the data from the prior orbit. However, Murphy *et al.* [1989] are attempting no comparison to a model. During this wake transit the background is believed to vary by as much as 10%

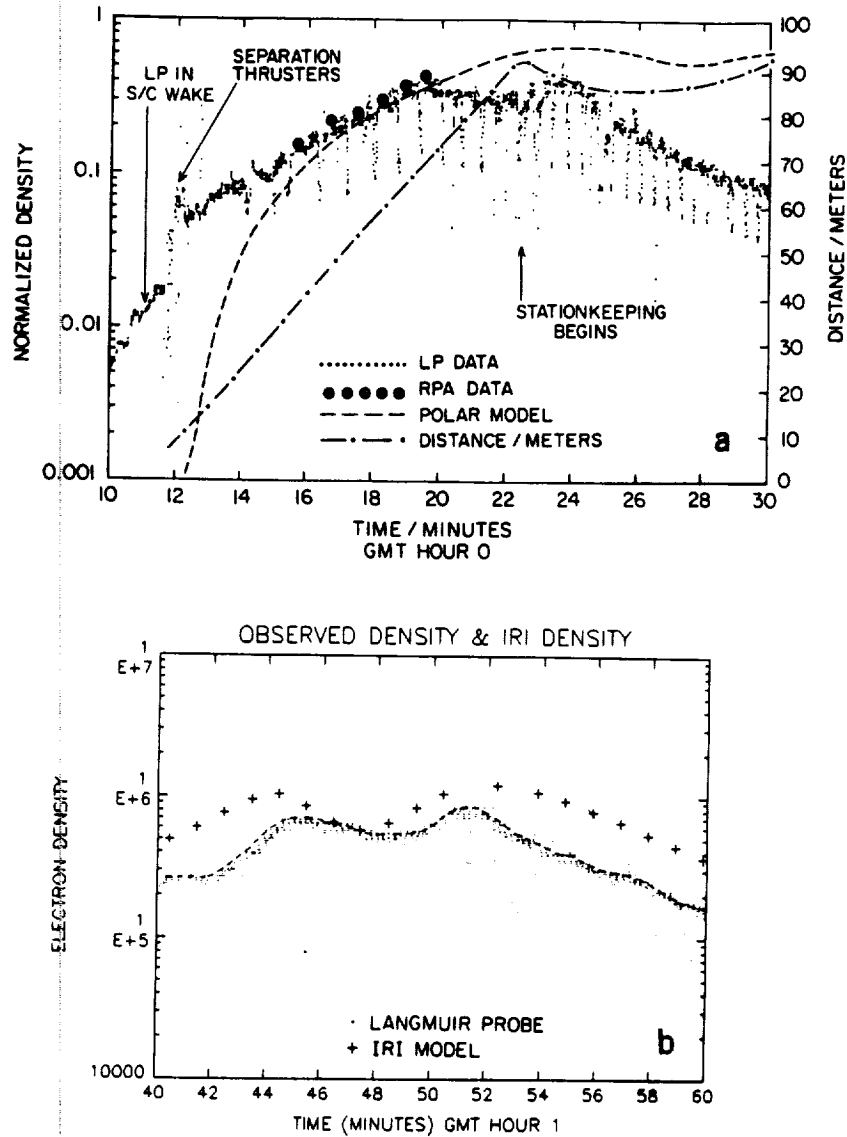


Fig. 3. Ion and electron data during the back-away are plotted in Figure 3a, normalized to $n_e = 1 \times 10^6 \text{ cm}^{-3}$. Note the relatively good agreement between model and data between 30 and 75 m. Beyond $t = 20 \text{ min}$ (75 m), background density varies considerably, as is illustrated in Figure 3b, which includes data for one orbit later than Figure 3a, at approximately the same station-keeping position, superimposed on a predicted density for this orbit from the IRI ionosphere model.

[Murphy *et al.*, 1989] so the model cannot be tested to an accuracy greater than that.

DISCUSSION

In examining the back-away density profile, we find three relevant observations from Figure 3.

1. Close to the orbiter (<30 m) the model underestimates the observed density by 1 to 2 orders of magnitude.
2. In the range 30–75 m the model predicts quite accurately the gradual increase in density until the time $t = 20 \text{ min}$. (Figure 3). After $t = 20 \text{ min}$ the observed density seems to have a variation, which is not believed to be wake-related. These density changes result from ionospheric variability as the spacecraft approaches the dawn-dusk meridian plane and are predicted by empirical models such as IRI.

Considering the first observation, recall that the assumptions incorporated within the POLAR wake model require a quasi-neutral plasma, assume a self-similar solution, and

neglect magnetic fields. Since the electron and ion densities observed even at the beginning of the release and back-away period agree within 10%, it would seem that quasi-neutrality would be valid. It has been shown by Chan *et al.* [1984] that after a few ion plasma periods ($\approx 0.1 \text{ ms}$ in this case) the plasma expansion becomes self-similar. For the case of the shuttle orbiter, this takes place within the first $\approx 1 \text{ m}$ of the wake. The magnetic field, if it is to be considered for this

TABLE 1. Comparison of Observations From Murphy *et al.* [1989] With POLAR Predictions

Wake	Latitude, deg	T_e , K	Distance, m	POLAR Normalized Density	Observed Normalized Density
1	-35	2500	242	0.9	0.80
2	-45	3000	125	0.75	0.61
3	+10	1500	45	0.20	0.18
4	+35	2000	105	0.65	0.90

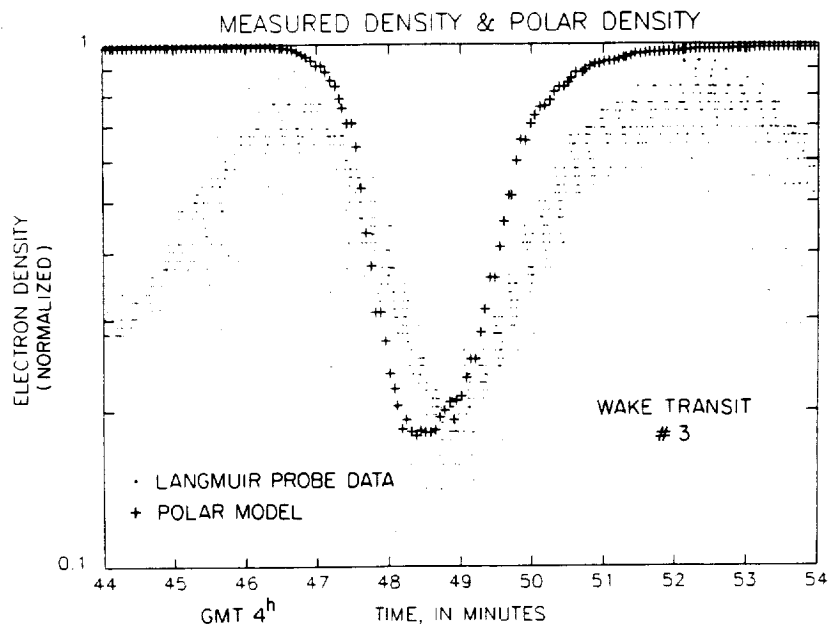


Fig. 4. Detail of data from WT 3 is compared to POLAR predictions. Data are normalized to a constant. Since there may be variation in background of $>10\%$, differences of that order between data and model are not significant.

case, would always act to limit plasma flow, rather than enhance it. Therefore it too can be eliminated from serving as an explanation for the poor fit at less than 30 m.

The answer to the disparity between model and observation would seem to lie in the role played by contaminant ions. *Murphy et al.* [1989] discuss these ions and offers their presence as an explanation for the disparity between these data and that taken at similar distances while on the remote manipulator system (RMS).

Let us turn now to the 30- to 75-m distance region. The most dominant characteristic of both the data and model is the relatively smooth increase in density as the PDP moves axially along the orbiter wake.

This midwake region has been studied extensively in the laboratory and the wake-fill process depends strongly on the body size, body potential, and ratio of ambient ion to electron temperature. *Stone* [1981], *Fournier and Pigache* [1975], *Hester and Sonin* [1970], and many others have performed laboratory experiments and observed fine structure in wakes, including ion density peaks along the wake axis and wavelike condensation disturbances. It is important, however, to note that for the case of large bodies in low earth orbit (LEO) (1) the body potential is not too different from the plasma potential (a few kT_e at most, since the body surface is an insulator and does not expose $v \times B$ potential to the plasma); (2) the plasma is a cold Maxwellian (lev) and collisionless; and (3) the ambient ion and electron temperatures are close to being equal.

An excellent review of laboratory work before 1975 is given by *Fournier and Pigache* [1975]. Another excellent review of the subject of expansion of plasma into the wake is given by *Samir et al.* [1983]. In these cases the authors agree with the basic finding of *Gurevich and Pitaevskii* [1969] that the fine structure and ion peaks observed in certain laboratory investigations vanish as T_i approaches T_e . We see in this case that in spite of (or perhaps because of) the effect of contaminant ions, we have a large-scale wake which is basically devoid of any fine structure, at least in the sense of total electron or ion density. It should be emphatically

noted, however, that this does not imply knowing all there is to know about the wake structure. The overall plasma density is only the zeroth order parameter. Ion and electron composition [*Grebowsky et al.*, 1987]; vector measurements of ion velocities [*Stone et al.*, 1983, 1988]; electron temperature [*Murphy et al.*, 1986; *Raitt et al.*, 1984]; plasma turbulence [*Raitt et al.*, 1984] all play roles in understanding the total physics of the wake structure for such a complex, gas-emitting, large object.

As discussed earlier, the structural differences between predictions and observations after $t \approx 20$ min in Figure 3a are attributed to natural ionospheric variation (not modeled by POLAR). Figure 3b illustrates the density profile one orbit after the back-away maneuver and shows this similar structure.

Let us compare the model predictions to observations for WT 1 through WT 4. The agreement is quite remarkable and affirms that the "well-behaved" wake structures associated with $T_i/T_e \approx 1$ plasmas can be adequately modeled by the physics contained in the POLAR model. There is only one significant difference between model and data. WT 2, which occurs at ≈ 125 m, seems to be considerably deeper than WT 4, which occurs at a little more than 100 m. *Murphy et al.* [1989] discuss this extensively, and we do not believe that, considering approximations made by the model and errors made in normalization, we could expect any better agreement. If the magnetic field, contaminant ions, and orbiter sheath do play some role, it is clear from both the model and the data that it must be a secondary one.

Studying the detail of WT 3 observations and POLAR's predicted profile, we also find good agreement. This is significant because at 45 m downstream the details of the orbiter geometry and its effect on the wake can not yet be "washed out" (the long dimension of the orbiter is ≈ 36 m). The agreement between model and data seems to imply that the geometric assumptions are valid and that it is permissible to use the geometric correction factor calculated from the neutral flow model, at least to first order.

Note that the center of the predicted wake seems to be

offset slightly from that observed and that the predicted density gradient seems slightly greater than observed. Murphy *et al.* [1989] discuss the accuracy with which the trajectory reconstruction takes place. This offset error is consistent with that level of precision. It is also possible that errors in normalization (constant background assumed) could produce this effect.

The difference in density gradients may be due to a slightly different plasma temperature than that modeled or may be consistent with the role played by contaminant ions in the neutralization of the space charge electric field.

Electric field data is difficult to discern from the PDP measurements because of interference from another instrument, but J. Steinberg (private communication, March 1988) has examined data from the time period of WT 3 and finds an electric field which changes sign at the wake center. This field is within a factor of 2 of that expected from a self-similar expansion. No attempt has been made to compare the predicted field computed by POLAR to the actual data, since error bars on the data are rather large. The authors may examine this as well as the RMS data [Tribble *et al.*, 1989] in more detail in a future paper. The RMS roll data may be more useful for comparison, since those data are taken at <10 m downstream, where the density depletion and electric fields are greater.

CONCLUSIONS

The sampling of PDP ion and electron densities verify that for ionospheric plasma conditions ($T_i \approx T_e$), the orbiter wake is relatively smooth in its structure from ≈ 30 m to distances of ≈ 250 m downstream. POLAR predicts this smooth wake structure and agrees with the observations to an accuracy of <30% (Table 1). For large and complex systems such as the orbiter, outgassed products may play a significant role in the structure of its wake at distances less than the characteristic body dimension. Adequate modeling in this regime requires input that details the outgassed species and rates, chemistry describing their interaction with the ionosphere, and inclusion of magnetic field to account for the pick-up ion population in the wake.

At midwake distances the magnetic field effects, if any, would appear to be secondary to the dominant role of the electric field and thermal motion already modeled by POLAR in the wake-fill process. However, for slightly larger objects or high-inclination orbits the magnetic field may have to be considered if accurate results are required. In addition, the fundamental scientific questions associated with large-body wakes will eventually require its inclusion.

For comparisons between in situ observations and models such as POLAR to be meaningful at levels better than a few tens of percent, more than simple axial or planar profiles of density are needed. Future experiments will also require good background measurements and inclusion of vector ion velocity, electric field, and particle distribution functions.

Acknowledgments. The authors wish to express their thanks to the reviewers for their constructive comments and suggestions. This work was supported by NASA MSFC contract NAS8-32807, NASA LeRC grant NAG 3-449, and by the Air Force Geophysics lab under contract F19628-86-C-0056.

The Editor thanks W. J. Raitt and two other referees for their assistance in evaluating this paper.

REFERENCES

- Chan, C., N. Hershkowitz, A. Ferreira, T. Intrator, B. Nelson, and K. Lonngren, Experimental observations at self-similar plasma expansion, *Phys. Fluids*, **27**, 266, 1984.
- Crow, J. E., P. J. Aver, and J. E. Allen, The expansion of a plasma into a vacuum, *J. Plasma Phys.*, **14**, 65, 1975.
- Diebold, D., N. Hershkowitz, T. Intrator, and A. Bailey, Self-similar potential in the near wake, *Phys. Fluids*, **30**, 579, 1987.
- Fournier, G., and D. Pigache, Wakes in collisionless plasma, *Phys. Fluids*, **18**, 1443, 1975.
- Grebowsky, J. M., H. A. Taylor, Jr., M. W. Pharo III, and N. Reese, Thermal ion perturbations observed in the vicinity of the space shuttle, *Planet. Space Sci.*, **35**, 501, 1987.
- Gurevich, A. V., and L. P. Pitaevskii, Non-Linear Dynamics of a Rarefied Ionized Gas, *Prog. Aerospace Sci.*, **16**, 227, 1975.
- Gurevich, A. V., L. V. Pariiskaya, and L. P. Pitaevskii, Self-similar motion of a rarefied plasma, *Sov. Phys. JETP (Engl. Transl.)*, **22**, 449, 1966.
- Gurevich, A. V., L. P. Pitaevskii, and V. V. Smirnova, Ionospheric aerodynamics, *Space Sci. Rev.*, **9**, 805, 1969.
- Hester, S. D., and A. A. Sonin, A laboratory study of wakes of ionospheric satellites, *AIAA J.*, **8**, 1090, 1970.
- Katz, I., D. E. Parks, and K. H. Wright, Jr., A model of the plasma wake generated by a large object, *IEEE Trans. Nucl. Sci.*, **NS-32(6)**, 4092, 1985.
- Kozima, H., H. Shimizu, K. Yamada, T. Mieno, K. Yamagiwa, Self-similar flow and related phenomena of plasma around obstacles, *J. Phys. Soc. Jpn.*, **57**, 1136, 1988.
- Murphy, G. B., J. Pickett, N. D'Angelo, and W. S. Kurth, Measurement of plasma parameters in the vicinity of the space shuttle, *Planet. Space Sci.*, **34**, 993, 1986.
- Murphy, G. B., D. L. Reasoner, A. Tribble, N. D'Angelo, J. S. Pickett, and W. S. Kurth, The plasma wake of the shuttle orbiter, *J. Geophys. Res.*, in press, 1989.
- Raitt, W. J., D. E. Siskind, P. M. Banks, and P. R. Williamson, Measurements of the thermal plasma environment of the space shuttle, *Planet. Space Sci.*, **32**, 357, 1984.
- Raychauduri, S., J. Hill, H. Chang, E. Tsikis, and K. Lonngren, An experiment on the plasma expansion into a wake, *Phys. Fluids*, **29**, 289, 1986.
- Samir, U., K. H. Wright, Jr., and N. H. Stone, The expansion of a plasma into a vacuum-based phenomena and processes and application to space plasma physics, *Rev. Geophys.*, **21**, 1631, 1983.
- Shawhan, S. D., G. B. Murphy, and J. S. Pickett, Plasma Diagnostics Package initial assessment of the shuttle orbiter plasma environment, *J. Spacecraft Rockets*, **21(4)**, 387, 1984.
- Singh, N., and R. W. Schunk, Numerical calculations relevant to the initial expansion of the polar wind, *J. Geophys. Res.*, **87**, 9154, 1982.
- Stone, N. H., The aerodynamics of bodies in a rarefied, ionized gas with applications to spacecraft environmental dynamics, NASA Tech. Pap. 1933, 1981.
- Stone, N. H., U. Samir, K. H. Wright, Jr., D. L. Reasoner, and S. D. Shawhan, Multiple ion streams in the near vicinity of the space shuttle, *Geophys. Res. Lett.*, **10**, 1215, 1983.
- Stone, N. H., K. H. Wright, Jr., U. Samir, and K. S. Hwang, On the expansion of ionospheric plasma into the near wake of the shuttle orbiter, *Geophys. Res. Lett.*, **15**, 1169, 1988.
- Tribble, H. C., J. S. Pickett, N. D'Angelo, and G. B. Murphy, Plasma density, temperature and turbulence in the wake of the shuttle Orbiter, *Planet. Space Sci.*, in press, 1989.
- Wright, K. H., Jr., N. H. Stone, and U. Samir, A study of plasma expansion phenomena in laboratory-generated plasma wakes: Preliminary results, *J. Plasma Phys.*, **33**, 71, 1985.
- I. Katz, S-Cubed, P.O. Box 1620, La Jolla, CA 92038.
G. Murphy, Jet Propulsion Laboratory, MS 301-460, 4800 Oak Grove Drive, Pasadena, CA 91109.

(Received December 23, 1987;
revised March 20, 1989;
accepted March 22, 1989.)

Coherent Cerenkov Radiation From the Spacelab 2 Electron Beam

W. M. FARRELL, D. A. GURNETT, AND C. K. GOERTZ

Department of Physics and Astronomy, University of Iowa, Iowa City

During the Spacelab 2 mission, a spacecraft called the Plasma Diagnostics Package (PDP) was released from the space shuttle to investigate the surrounding plasma environment. During an interval when the shuttle and PDP were magnetically connected, a continuous 1-keV/50-mA electron beam was ejected along a field line from an electron generator on board the shuttle. As the PDP flew by the beam, the PDP plasma wave instrument detected intense whistler mode radiation originating from the beam. It is believed that coherent Cerenkov radiation from bunches of beam electrons is responsible for the whistler mode radiation, where an electrostatic beam-plasma instability forms the coherently radiating bunches. In this paper a detailed model of the coherent Cerenkov emission process is presented. A one-dimensional computer simulation of the beam is used to model the expected phase space structure of the electrons, and power emitted from Cerenkov radiation is computed using an analytical expression. The calculated power from the modeled 200-m beam segment is $\sim 5 \times 10^{-8}$ W/Hz, which can easily account for the measured whistler mode wave power. The inclusion of coherent effects in the beam increases the wave powers by nearly 90 dB above incoherent power levels. These calculations demonstrate that a spontaneous emission process, alone, can account for the observed whistler mode wave powers.

1. INTRODUCTION

During the Spacelab 2 (SL 2) mission, intense whistler mode radiation from an electron beam ejected from the space shuttle was detected by radio receivers on board the Plasma Diagnostics Package (PDP) which was in free flight around the shuttle [Gurnett *et al.*, 1986]. Simple calculations have indicated that coherent Cerenkov radiation emitted by bunches of beam electrons may produce such whistler mode signals [Bell, 1968; Farrell *et al.*, 1988], with the bunches being formed by a beam-plasma instability. This paper presents a detailed model of this wave generation process, including a determination of the expected radiated power.

In July of 1985, the space shuttle carried the SL 2 payload into the upper ionosphere. One of the experiments on board was the University of Iowa's Plasma Diagnostics Package, which contained 10 experiments designed to study the plasma environment around the shuttle orbiter. Another experiment, the Vehicle Charging and Potential Experiment (VCAP), also flew on the mission to study the charging and potential of the shuttle. Part of this package included a fast pulsed electron generator (FPEG) designed to eject a 1-keV/50-mA electron beam.

The PDP was released from the shuttle for a 6-hour period on August 1, 1985, to investigate the plasma environment in an extended region around the shuttle. At specific times the PDP intersected geomagnetic field lines that connected to the shuttle orbiter. These times are known as magnetic conjunction. During one magnetic conjunction event, the FPEG, located in the shuttle cargo bay, continuously ejected a 1-keV/50-mA electron beam with a pitch angle that varied from 0° to 20°. The PDP, located 200 m from the shuttle, passed within 6 m of the magnetic flux tube containing the beam. During this magnetic conjunction, the PDP plasma wave instrument detected intense whistler mode radiation. Figure 1 displays a frequency-versus-time spectrogram from the PDP plasma wave instrument during the 1-keV/50-mA beam ejection

(0330-0337 UT). The whistler mode emission is the funnel-shaped structure extending in frequency from about 30 kHz to about 1 MHz.

Whistler mode signals like those detected during the SL 2 beam ejection are commonly detected from both artificially and naturally created electron beams in the Earth's ionosphere. In particular, rocket-launched electron beam experiments performed in the 1970s clearly showed the occurrence of whistler mode radiation in association with injected electron beams (Cartwright and Kellogg [1974], Monson *et al.* [1976], and Dechambre *et al.* [1980], just to name a few). With the advent of the shuttle program, these experiments were continued at a new level of sophistication which was due, in part, to the diagnostics packages, such as the PDP, that could be placed in favorable positions relative to the ejected electron beams. During beam ejections from the shuttle, many strong LF and VLF emissions were detected [Shawhan *et al.*, 1984; Beghin *et al.*, 1984; Neubert *et al.*, 1986], including intense whistler mode radiation [Gurnett *et al.*, 1986; Farrell *et al.*, 1988]. For a comprehensive review of the many wave modes excited by artificially generated electron beams, see Grandel [1982]. Besides artificial beams, whistler mode radiation called auroral hiss is also emitted from field-aligned electron beams that occur naturally in the auroral regions [Gurnett, 1966; Lin *et al.*, 1984]. Like the whistler mode radiation detected from the SL 2 electron beam, these emissions appear funnel shaped on a radio spectrogram. It has been demonstrated that this shape results from a propagation effect of whistler mode waves with normal angles near the resonance cone [see Gurnett, 1983]. Based on the striking similarities between auroral hiss and the whistler mode radiation from the SL 2 electron beam, further investigation of the latter was performed.

In particular, the whistler mode emission from the 1-keV/50-mA SL 2 electron beam has been the subject of two studies [Gurnett *et al.*, 1986; Farrell *et al.*, 1988]. Evidence presented in both indicates that the emission is quasi-electrostatic and is propagating with wave normals near the resonance cone. The emission is also believed to be generated by a Landau resonance interaction, since its index of refrac-

Copyright 1989 by the American Geophysical Union.

Paper number 88JA03335.
0148-0227/89/88JA-03335\$05.00

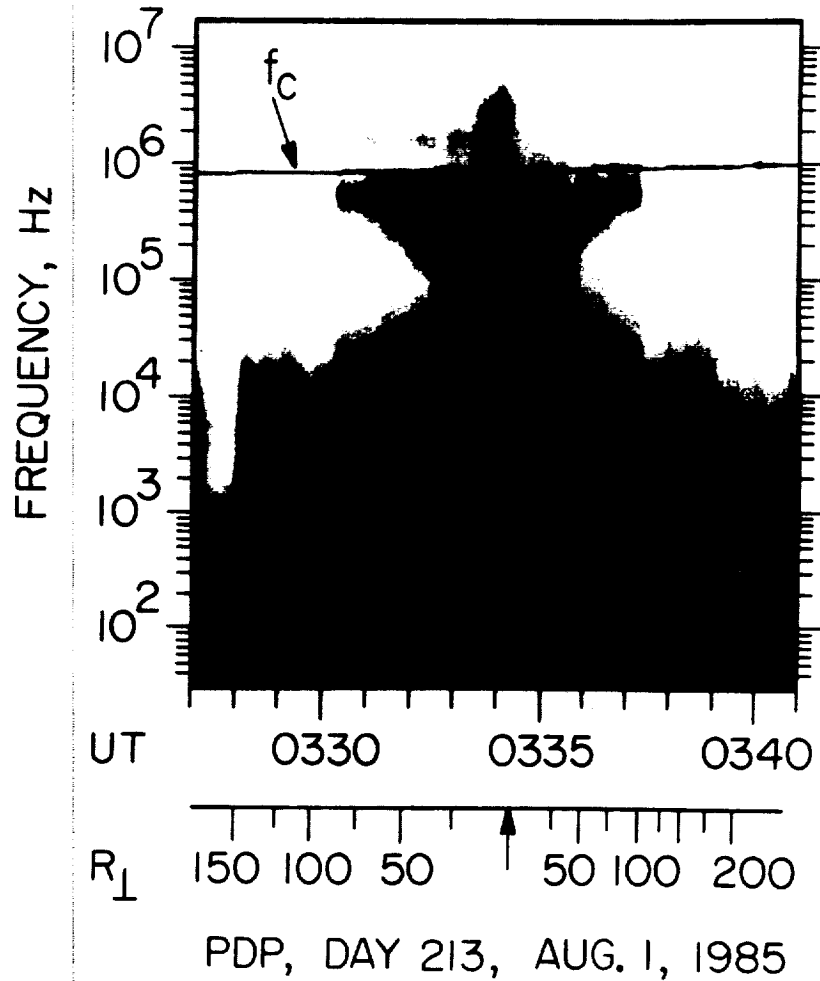


Fig. 1. Frequency versus time spectrogram from the PDP plasma wave instrument showing intense emissions during a continuous electron beam event (0330-0337 UT). The funnel-shaped structure that extends from the electron cyclotron frequency f_c to about 30 kHz is whistler mode radiation from the beam.

tion values are near those expected for such an interaction [Farrell *et al.*, 1988] and $k \cdot v_b > 0$ [Gurnett *et al.*, 1986]. The radiated whistler mode power from the first 200 m of the beam was calculated by integrating the Poynting flux through a surface that contained the PDP trajectory [Farrell *et al.*, 1988]. The resulting power spectrum is displayed in Figure 2. Note that the power spectral density, dP/df , is $\sim 10^{-9}$ W/Hz. The total power radiated in the whistler mode from the 200-m beam segment has been estimated to be 1.6 mW, which corresponds to a linear emissivity of about 8×10^{-6} W/m. Since the total power in the beam is 50 W, the beam converted only 3.2×10^{-5} of its power to whistler mode radiation in the first 200 m of its trajectory.

Owing to the low efficiency of converting beam power to wave power, incoherent Cerenkov radiation from the beam electrons was initially considered as the source of the emission. However, the estimated power from this radiation process is 10^7 times smaller than that detected [Farrell *et al.*, 1988]. In reality, the beam cannot be considered an incoherent radiator since a beam-plasma instability is operating in the beam forming quasi-periodically spaced density perturbations or "bunches" which can radiate coherently. Therefore an emission process involving coherent Cerenkov radiation from these bunches was considered [Farrell *et al.*, 1988]. Strong

instability-related electrostatic turbulence near the local plasma frequency, f_{pe} , was detected in the beam by the PDP plasma wave instrument. These waves interact with the beam and form the "bunches" which can spontaneously emit powerful Cerenkov radiation due to the increased coherence of the beam electrons. The Cerenkov radiation emitted from these coherent structures is then detected by the PDP plasma wave receiver as the whistler mode radiation. As demonstrated previously [Farrell *et al.*, 1988], the frequency range of the emitted Cerenkov radiation closely corresponds to that of the detected whistler mode radiation, and the bunching may create enough coherence among the beam electrons to yield the measured wave powers.

In this paper we will present a model of the coherent Cerenkov radiation from a bunched electron beam like that on the SL 2 experiment. We note that there are other possible mechanisms for generating the whistler mode radiation, such as a whistler mode instability in the beam [Lin and Wong, 1988] or some nonlinear mode conversion process. However, we will only consider the coherent Cerenkov radiation model and attempt to demonstrate that this process alone can account for the measured wave powers. In section 2 an expression is derived that describes the coherent Cerenkov radiated power from a field-aligned electron beam. This expression

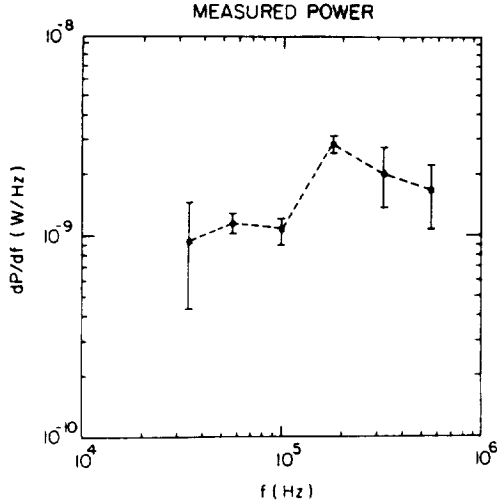


Fig. 2. Calculated power spectral density from the first 200 m of the beam in the whistler mode as a function of frequency.

will be applied to a model of the SL 2 electron beam obtained from a one-dimensional particle simulation, the results of which are outlined in section 3. In section 4, the power from the modeled beam is calculated and compared with the measured power in the whistler mode from the actual SL 2 electron beam.

2. EXPRESSION FOR THE RADIATED POWER

In this section an expression is derived for the power emitted from an electron beam by a coherent Cerenkov radiation process. The derivation presented here is similar to that of Mansfield [1967], who calculated the radiated power from a single test particle in a plasma medium using the Fourier transforms of the source current and radiated electric field. Using a similar analytical technique, Harker and Banks [1983] derived an expression for the power radiated from a pulsed electron beam in a plasma medium which included coherent effects between the radiating electrons in the pulses. In their derivation it was assumed that all beam electrons traveled with the same velocity \bar{v} in pulses of length l with a distance d separating each pulse and that the pulsing is imposed by the generator that produces the beam. Compared with the incoherently radiated power from a beam, the inclusion of coherent effects between radiating beam electrons in a pulse leads to much higher powers. The calculations performed in our analysis are similar to theirs, except that we are now considering the radiation from an initially continuous beam that becomes modulated or "bunched" owing to the beam-plasma instability.

In the derivation of the radiated power presented here, it is assumed that the beam is a line source radiator of electromagnetic radiation. This assumption is valid since the whistler mode wavelength λ_{cm} is of the order of 20 m and is several times greater than the beam diameter d , which is at most 2 cyclotron radii or about 6 m [Farrell et al., 1988]. As will soon be demonstrated, this assumption will allow the current from the field-aligned SL 2 electron beam to be adequately represented by a delta function.

We also assume that the beam electrons only act as test particles which do not significantly alter the ambient plasma medium. Consequently, the medium is represented by a homo-

geneous, cold, collisionless plasma in a static magnetic field, and the terms in the dielectric tensor \bar{K} describing the beam are not included. Very near the electron generator this assumption is probably not valid, since the SL 2 electron beam is overdense ($n_b > n_a$), and thus the beam-related terms in \bar{K} cannot be ignored. However, as pictures of shuttle-launched beams indicate [Banks and Raitt, 1988], the beams tend to expand and become tenuous as they propagate from their source. Gendrin [1974] has demonstrated that this expansion will cause an initially overdense beam to become underdense within a few meters from the point of injection, and it is in the underdense region where the test particle assumption is considered valid. From Banks and Raitt the expansion of a 1-keV/100-mA electron beam with an initial density of $n_b \cong 100n_a$ is about 13° . At this expansion rate the average beam density can become less than that of the ambients with the first meter (or $100\lambda_D$) of the injection point. Note that the beam expands from the generator opening of a couple centimeters to at most 1–2 cyclotron radii [Gendrin, 1974; Banks and Raitt, 1988] and is never larger than the whistler mode wavelength. Consequently, the assumption of a line source radiator still applies even though the beam diameter is increasing.

We write the equation for a wave in a cold plasma including the external current source, $J_q(\bar{k}, \omega)$, as

$$\mathbf{T} \cdot \bar{E}(\bar{k}, \omega) = \frac{iJ_q(\bar{k}, \omega)}{\omega\epsilon_0} \quad (1)$$

where $\mathbf{T} \cdot \bar{E}(\bar{k}, \omega) = \bar{n} \times \bar{n} \times \bar{E}(\bar{k}, \omega) + \mathbf{K} \cdot \bar{E}(\bar{k}, \omega)$ and \mathbf{K} is the cold plasma dielectric tensor. The form of the dielectric tensor used here can be found in the work of Mansfield [1967]. The electric field, $\bar{E}(\bar{r}, t)$, is obtained by taking the inverse Fourier transform of $\bar{E}(\bar{k}, \omega)$,

$$\bar{E}(\bar{r}, t) = \frac{1}{\epsilon_0} \iint \mathbf{T}^{-1} \cdot J_q(\bar{k}, \omega) e^{i(\omega t - \bar{k} \cdot \bar{r})} d\bar{k} \frac{d\omega}{\omega} \quad (2)$$

The current density can be expressed in a generalized form for a line source as

$$\bar{J}_q(\bar{r}, t) = [\hat{x}J_x(x, t) + \hat{y}J_y(y, t) + \hat{z}J_z(z, t)] \cdot \delta(x - R_c \cos \omega_c t) \delta(y - R_c \sin \omega_c t) \quad (3)$$

where the beam displacement is

$$\mathbf{r} = \hat{x}R_c \cos \omega_c t + \hat{y}R_c \sin \omega_c t + \hat{z}z \quad (4)$$

and R_c and ω_c are the cyclotron radius and frequency, respectively. The Fourier transform of this current is

$$\begin{aligned} \bar{J}_q(\bar{k}, \omega) &= \frac{1}{(2\pi)^4} \int J_q(\bar{r}, t) e^{i(\bar{k} \cdot \bar{r} - \omega t)} d\bar{r} dt \\ &= \frac{1}{(2\pi)^4} \int [\hat{x}J_x(x, t) + \hat{y}J_y(y, t) + \hat{z}J_z(z, t)] \\ &\quad \cdot e^{i(k_x z - \omega t)} (e^{ik_x R_c \cos \omega_c t} + e^{ik_y R_c \sin \omega_c t}) dz dt \end{aligned} \quad (5)$$

The exponential factors in the parentheses can be reexpressed as

$$e^{ik_x R_c \cos \omega_c t} = \sum_{s=-\infty}^{\infty} J_s(k_x R_c) e^{-is\omega_c t}$$

and

$$e^{ik_y R_c \sin \omega_c t} = \sum_{s'=-\infty}^{\infty} J_{s'}(k_y R_c) e^{is'\omega_c t} \quad (6)$$

where J_s is the s order Bessel function. Inserting these into (5) yields the following expression for the transformed current:

$$\bar{J}_q(\vec{k}, \omega) = \frac{1}{(2\pi)^4} \int (\hat{x}J_x(x, t) + \hat{y}J_y(y, t) + \hat{z}J_z(z, t))e^{i(\vec{k}\cdot\vec{z} - \omega t)} \cdot \left[\sum_{x=-x}^x J_s(k_x R_c) e^{-is\omega_c t} \right] \left[\sum_{y=-y}^y J_s(k_y R_c) e^{is'\omega_c t} \right] dz dt \quad (7)$$

During the SL 2 beam firing, the beam pitch angle was at most 20° , and for a 3-min period, from 0332:30 to 0335:30 UT, it was less than 10° . As a consequence, $V_{||} \gg V_{\perp}$, which implies that $J_z(z, t) \gg J_x(x, t)$ and $J_y(y, t)$. Also, $R_c = V_{||}/\omega_c \ll \lambda_{em}$ and, therefore, the factors in the brackets in (7) are near unity. Equation (7) then becomes

$$\bar{J}_q(\vec{k}, \omega) = \frac{\hat{z}}{(2\pi)^4} \iint J_z(z, t) e^{i(\vec{k}\cdot\vec{z} - \omega t)} dz dt \quad (8)$$

Consider a group of particles ejected from a particle generator. Ideally, if all the particles are moving at the same velocity, V_s , a simple transformation can be made to a frame moving with the particles, $z' = z - V_s t$. In this frame the current density does not depend explicitly on time,

$$J_z(z, t) = J_z(z') \quad (9)$$

and consequently, the beam particles appear stationary. In order to solve the time integral in (8), a transformation to z' is made where the current density is considered time independent. In reality, it is not expected that all particles have identical velocities (i.e., they may have a spread ΔV about V_s), and the validity of the power expression derived assuming (9) must be established for the particular case in question.

Assuming that a transformation can be made to a frame where (9) is valid, expression (8) becomes

$$\bar{J}_q(\vec{k}, \omega) = \frac{\hat{z}}{(2\pi)^4} \int_{-x}^x J_z(z') e^{ik_z z'} dz' \int_{-\infty}^{\infty} e^{i(k_z V_s - \omega)t} dt \quad (10)$$

The quantity $\int_{-x}^x J_z(z') e^{ik_z z'} dz' = (2\pi)^{1/2} J_z(k_z)$, where $J_z(k_z)$ is the Fourier transform of $J_z(z')$. Using the definition of the delta function, $\int_{-\infty}^{\infty} e^{i(k_z V_s - \omega)t} dt = 2\pi \delta(k_z V_s - \omega)$, and the fact that $k_z = n\omega \cos \theta/c$, (10) reduces to

$$\bar{J}_q(\vec{k}, \omega) = \frac{\hat{z}}{(2\pi)^3} [(2\pi)^{1/2} J_z(k_z)] \delta(n\omega \cos \theta\beta - \omega) \quad (11)$$

where $\beta = V_s/c$.

In order to determine the radiated electric field, (11) is substituted into (2) to obtain

$$\vec{E}(\vec{r}, t) = \frac{1}{(2\pi)^3 \epsilon_0} \iint (T^{-1} \cdot \hat{z}) [(2\pi)^{1/2} J_z(k_z)] \cdot \delta(n\omega \cos \theta\beta - \omega) e^{i(\omega t - \vec{k} \cdot \vec{r})} d\vec{k} \frac{d\omega}{\omega} \quad (12)$$

Knowing the electric field and source current, an expression for the radiated power can now be found:

$$P(t) = \int \vec{E}(\vec{r}) \cdot \vec{J}(r) dr = \frac{1}{(2\pi)^2 \epsilon_0} \iint (\hat{z} \cdot T^{-1} \cdot \hat{z}) \{ (2\pi) J_z[k_z(n, \theta)] J_z^*[k_z(n, \theta)] \} \cdot \delta(n\omega \cos \theta\beta - \omega) e^{i(\omega t - n\omega \cos \theta\beta r)} n^2 \omega^2 dn \sin \theta d\theta d\omega \quad (13)$$

where $n^2(\omega^3/c^3) dn \sin \theta d\theta d\phi$ has been substituted for the

element $d\vec{k}$ and the trivial integration over ϕ has been performed. Integrating over θ , an integral of the form

$$I = \int f(x) \delta(Ax - B) dx = \frac{f(x_0)}{A}$$

must be solved, where $A = |n\omega\beta|$, $B = \omega$, and $x_0 = \cos \theta_0 = 1/n\beta$. It should be noted that to obtain a nonzero solution to the integral, the condition $\cos \theta_0 = 1/n\beta$ must be satisfied, which is the Landau resonance condition. Upon evaluating the integral, the radiated power becomes

$$P(t) = \frac{-i}{(2\pi)^2 \epsilon_0 c^3 \beta} \iint (\hat{z} \cdot T^{-1} \cdot \hat{z}) \{ (2\pi) J_z[k_z(n, \theta_0)] \cdot J_z^*[k_z(n, \theta_0)] \} |n| |\omega| dn d\omega \quad (14)$$

From Mansfield, the quantity $(\hat{z} \cdot T^{-1} \cdot \hat{z})$ is

$$(\hat{z} \cdot T^{-1} \cdot \hat{z}) = \frac{T_{33}(n)}{\epsilon_1(n^2 - n_2^2)(n_2 - n_1^2)} \quad (15)$$

where

$$T_{33} = \epsilon_1^2 - \epsilon_2^2 - \epsilon_1 n^2 + (n^4 - \epsilon_1 n^2) \cos^2 \theta_0 \quad (16)$$

$$n_{1,2}^2 = [-B \pm (B^2 - 4C\epsilon_1)^{1/2}] / 2\epsilon_1 \quad (17)$$

$$B = \left(\frac{c}{V_s}\right)^2 (\epsilon_3 - \epsilon_1) + \epsilon_2^2 - \epsilon_1^2 - \epsilon_1 \epsilon_3 \quad (18)$$

and

$$C = \left(\frac{c}{V_s}\right)^2 (\epsilon_1^2 - \epsilon_2^2 - \epsilon_1 \epsilon_3) + \epsilon_3(\epsilon_1^2 - \epsilon_2^2) \quad (19)$$

Using the Plemelj formula, the complex integration over dn is performed to yield the final expression for the radiated power:

$$P(t) = \bar{P} = \int_{-\infty}^{\infty} \left(\frac{\omega d\omega}{8\pi\epsilon_0 \epsilon_1 c^2 V_s} \right) \frac{1}{(n_2^2 - n_1^2)} \sum_{k=1}^2 T_{33}(n_k) \cdot \{ 2\pi J_z[k_z(n_k, \theta_0)] J_z^*[k_z(n_k, \theta_0)] \} \quad (20)$$

Note that the radiated power is proportional to the square of the Fourier transform of the current density. This result is similar to that obtained by *Harker and Banks* [1983], who found that the radiated power varies as the square of the transform of the current pulses. Once the current density and its transform are known, it can be used in (20) to easily calculate the radiated power. We will use a modeled beam to obtain the beam current, $J_z(z, t)$, since the available plasma instruments flown on the PDP cannot directly measure the electron bunching which occurs on time scales of $1/\omega_{pe} \sim 10^{-7}$ s. The results of the beam simulation are presented in the next section.

3. A ONE-DIMENSIONAL ELECTROSTATIC SIMULATION OF THE SL 2 ELECTRON BEAM

To obtain the required beam current, a one-dimensional electrostatic model of an electron beam propagating through an ambient plasma is simulated on a computer. A one-dimensional beam model was chosen, since the length scales being considered are very long, about 200 m (many thousand Debye lengths), and cannot be reasonably modeled using a two- or three-dimensional system owing to the practical limits on computer CPU time. In the one-dimensional model it is assumed that the velocity of the particles is directed along a

static magnetic field line, which allows the particle trajectories to be unaffected by this field. Since the SL 2 electron beam was nearly field aligned during injection, this assumption is acceptable. In this analysis we also assume that the magnitude of the electric field of the generated Cerenkov radiation is much smaller than that of the electrostatic wave generated within the beam, $E_{ES} \gg E_{RAD}$. This assumption implies that the radiated electric field did not significantly alter the SL 2 beam electron trajectories and is consistent with the modeling of the beam where radiation field effects are neglected. This assumption is also consistent with observations made during the SL 2 experiment, where $E_{ES} \geq 0.3$ V/m in the beam while $E_{RAD} \sim 10^{-3}$ V/m for the whistler mode waves.

The simulation is designed so that initially the system is charge neutral. The particles representing the ambient electrons can move freely; however, they are confined to the system by reinjection boundaries. Ambient electrons leaving the system at these boundaries are reinjected with a Gaussian-weighted velocity between zero and the electron thermal speed. The electron beam is represented by particles of negative charge that are injected into the system at the $z = 0$ boundary with velocities greater than the ambient electron thermal speed. In order to keep the net charge in the system equal to zero, a positive charge equal in magnitude to the amount of negative beam charge in the system is placed at the $z = 0$ boundary. This boundary charge draws a return flow of ambient electrons which, for low beam flux ($n_b V_b A < n_a V_A A$), is sufficient to keep the boundary almost completely neutralized.

In a one-dimensional simulation the particles are charged sheets of infinite extent in the transverse direction and of finite thickness ($\sim \lambda_D$) along the direction being modeled. Consequently, the modeled beam has an infinite cross section. This infinite cross-section model, however, is contrary to the true SL 2 electron beam, which had a cross-sectional radius of no more than 6 m [Farrell et al., 1988]. Assuming such a model ignores finite radius electrostatic effects associated with the SL 2 electron beam and is only justified if the wavelength of the longitudinal electrostatic mode, λ_{ES} , is less than the SL 2 electron beam diameter d , which is not the case. Therefore we must demonstrate that the electrostatic nature of a finite radius beam, like the SL 2 electron beam, is similar to that of an infinite radius beam. To show this, a comparison will be made between our one-dimensional beam model and a two-dimensional radially finite beam model [Winglee and Pritchett, 1988] to verify such similarities.

Figure 3 displays a beam phase space configuration from Winglee and Pritchett's [1988] two-dimensional simulation of a radially finite beam. In their simulation an initially overdense beam is injected into a model ionosphere, with the ratio of the beam density to ambient density, n_b/n_a , equal to 4 and beam velocity to ambient thermal velocity, V_b/V_{TH} , equal to 20. Both ratios used in the simulation are representative of the conditions during SL 2 electron beam injections. From this figure we see that the beam can freely propagate from the injection boundary (located at $x/\Delta = 125$). In this case, the spacecraft charging potential at the injection boundary is much less than the initial beam energy, $\phi < \frac{1}{2} m_e V_b^2$, and will allow the beam to escape from the near-injection region. This low spacecraft potential is consistent with potential measurements made during the SL 2 mission where the shuttle obtained only a 40-V potential during ejections of a 1-keV electron beam [Williamson et al., 1985; Hawkins et al., 1987]. As

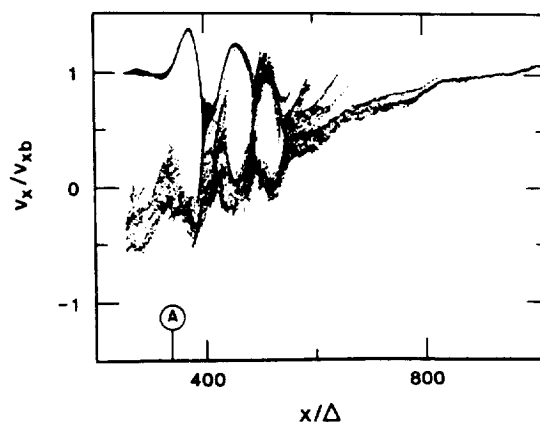


Fig. 3. Phase space configuration of beam electrons from Winglee and Pritchett's [1988] two-dimensional simulation. In this model the beam is initially injected overdense ($n_b/n_a = 4$). The ratio $V_b/V_A = 20$ and the figure displays the beam phase space after about $38\omega_{pe}^{-1}$. Note that the wave-trapping structures created in the beam are very similar to those typically created in one-dimensional simulations of underdense beams.

can be seen in the figure, the classic trapping structures created in this beam are very similar to those obtained in one-dimensional simulations [Okuda et al., 1987; Okuda and Kan, 1987; Winglee et al., 1987], thereby verifying that similar electrical forces are occurring in the two beams.

Owing to the limitations of a one-dimensional simulation, we will not self-consistently model the overdense region of the beam very near the electron generator as was done by Winglee and Pritchett, but instead, we will model the beam after it has propagated $\sim 100\lambda_D$. In this region and beyond, the average beam density is considered less than that of the ambients. In a qualitative sense we can consider the modeling of the beam to start at point A labeled in Figure 3, where the average beam density is reduced and the beam temperature is still relatively cold.

Figures 4a, 4b, and 4c display the beam phase space config-

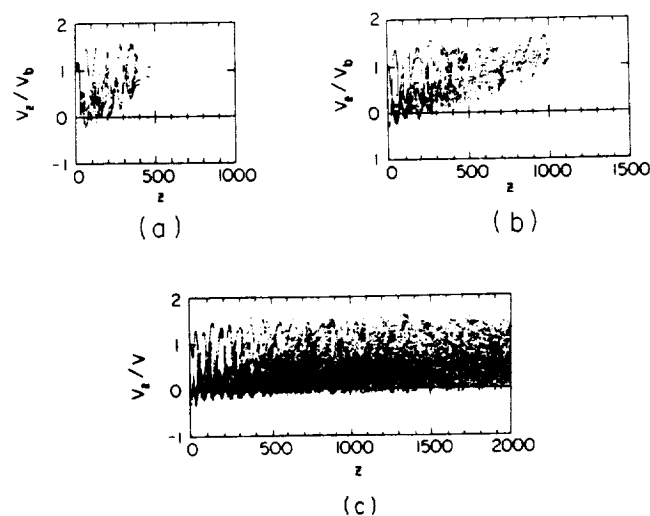


Fig. 4. Beam phase space configuration from our one-dimensional simulation after (a) $50\omega_{pe}^{-1}$, (b) $100\omega_{pe}^{-1}$ and (c) $840\omega_{pe}^{-1}$. In this simulation the beam model represents the underdense part of the beam displayed in Figure 3 starting from point A. The simulation was run with $n_b/n_a = 1/16$ and $V_b/V_A = 20$.

uration from our one-dimensional simulation after 50, 100, and $840\omega_{pe}^{-1}$, respectively. In this model, $n_b/n_A = 1/16$, $V_b/V_{TH} = 20$, and the beam is initially cold at $z = 0$. Each unit of distance represents $2\lambda_D$, or about 10 cm; thus Figure 4c displays the beam phase space configuration for a 200-m beam segment. The simulation was run for $840\omega_{pe}^{-1}$ to allow the transient front edge of the beam to leave the system. Consequently, the model displayed in Figure 4c represents the steady state beam. Note from the figures that the wave-particle trapping structures are similar to those of the two-dimensional beam displayed in Figure 3, implying that both are undergoing similar electrostatic interactions. Also note that the beam phase space configuration appears very similar to those modeled by Okuda *et al.* [1987], who performed a one-dimensional simulation similar to the one presented here. Figures 5a, 5b, and 5c display the number of beam particles as a function of z at times corresponding to those in Figure 4. Note from both Figures 4 and 5 that the beam is undergoing strong interactions with the background ionospheric medium. In the first 100 m ($z = 0$ to 1000), the beam-plasma instability is creating the classic trapping structures associated with such instabilities, which gives rise to significant perturbations in the density. Beyond 100 m ($z > 1000$), the beam is strongly thermalized, with the beam particles becoming randomized in phase space owing to the wave-particle interactions. Such randomization of the particles signifies the transfer of free energy from the beam to the electrostatic turbulence. Even though the beam becomes randomized, some significant density fluctuations are still present out past 100 m ($z > 1000$), as is indicated in Figure 5c.

According to expression (20) the current density of the beam is needed to obtain the radiated power. Figure 6a displays the beam current density, $J_z(z, t = 840\omega_{pe}^{-1})$, in the 200-m beam segment. Note from the figure that current density perturbations are clearly evident in the beam. It is the radiative coherence within and between these perturbations that yield significant wave powers, since the randomized background beam component only contributes to the incoherent power level. Figure 6b displays the Fourier transform of the current, $J_z(k_z)$, as a function of k_z . The resulting transform appears as a white noise type k spectra for $k_z > 20$; however, for $k_z < 20$, $J_z(k_z)$ appears to increase as k_z decreases. The white noise type k spectra found in $k_z > 20$ results from the randomized component of the electrons in the computer model. Although not feasible, if electrons with real mass and charge had been modeled, this noise would be significantly reduced. The average noise level was obtained by calculating the arithmetic average of the $J_z(k_z)$ values between 23.6 and 31.4. This level is represented by the line in Figure 6b. The increase in $J_z(k_z)$ found at $k_z < 20$ results from wave-particle interactions within the beam that create current density perturbations or "bunches." If bunching had not occurred, the simulated beam electrons would be completely randomized in phase space, and the resulting values of $J_z(k_z)$ would appear as white noise at all k_z values.

4. RADIATED POWER FROM A MODEL OF THE SL 2 ELECTRON BEAM

Equation (20) will now be applied to the simulated SL 2 electron beam discussed in the last section. In applying this expression to waves propagating in the SL 2 electron beam environment, some further approximations can be made. Specifically, in the frequency range of consideration, $n_1 \gg n_2$,

$n_1 \approx n$, where n is the whistler mode index of refraction obtained from cold plasma theory, and $T_{33}(n_1) \approx 10^3 T_{33}(n_2)$. Also, based on arguments of the typical density structure size in the beam, $J_z[k_z(n_2, \theta_0)] > J_z[k_z(n_1, \theta_0)]$. Consequently, the $k = 2$ term in the summation of (20) is very small and can be neglected. The radiated power can then be expressed as

$$P(t) = \bar{P} \approx \int_{-\infty}^{\infty} \left[\frac{-|\omega| d\omega}{8\pi\epsilon_0\epsilon_1 c^2 V_s (n_2^2 - n_1^2)} \right] \cdot 2\pi J_z(k_z') J_z^*(k_z') T_{33}(n_1) \quad (21)$$

where $k_z' = n \cos \theta_0 \omega/c$. Note that $n_1 > n_2$, which makes the term in brackets positive for the frequency range considered. To derive (21), it was assumed that a frame of reference exists where the current density is time independent, and thus all current density perturbations propagate at the same speed, V_s . In this case, the transform of the current density is properly represented by (11), where the delta function specifies the propagation speed V_s of the perturbations. In reality, however, all the perturbations may not be propagating at the same speed, and the validity of using (21) to estimate the coherent radiated power must be established. Consider a more realistic case where the density perturbations propagate with a speed $V \pm \Delta V$, where ΔV represents a velocity spread of the perturbations. In this case, the delta function in (11) should be replaced by a function that approximates this spread in velocity, such as a Gaussian function. As is demonstrated in the appendix, as long as this spread is not too great, the values of the radiated power are not significantly different from those obtained from perturbations all moving at identical velocities.

The velocity of the perturbations, V_s , must be determined in order to obtain a solution to (21). This velocity can be found by examining the spatial and temporal evolution of the current density perturbations in the simulation. By plotting the current density values above the average, $J_z(z, t) > 0.05$ A, as a function of z and t , the evolution of the individual perturbations can be followed. Such a plot is displayed in Figure 7. From this figure we see that the current density perturbations drift from the injection point at nearly the initial beam speed of 1.89×10^7 m/s. However, not all the perturbations move at the same identical speed, since at certain times, merging of a number of perturbations occurs. Examples of such current density enhancements are at $x = 100$ m, $t = 2.1 \times 10^{-5}$ s and at $x = 85$ m, $t = 3 \times 10^{-5}$ s and are circled in the figure. It is the creation of these structures coupled with the perturbations near the injection boundary that yield the large values of $J_z(k_z)$ at small wave numbers ($k_z < 0.2$) shown in Figure 6b. The Fourier transform of the current density, $J_z(k_z, \omega)$, is displayed in Figure 8. Note from this figure that the most intense values of the current corresponding to the perturbations lie near $V_s = 1.89 \times 10^7$ m/s, which is represented by the solid line in the figure. We also see that there is a spread in these values about V_s , but this spread is not very large and (21) can be readily applied. It is interesting to note that even though the beam itself develops a significant velocity spread, as indicated in Figure 4, the perturbations which generate significant radiation continue to propagate at the injection speed with little spread.

Recently, Omura and Matsumoto [1988] suggested that the bunches in their two-dimensional periodic beam simulation quickly reached a "quasi-linear phase" where they became "smoothed out," and thus significant radiation from these bunches could not occur. In the simulation presented here, we

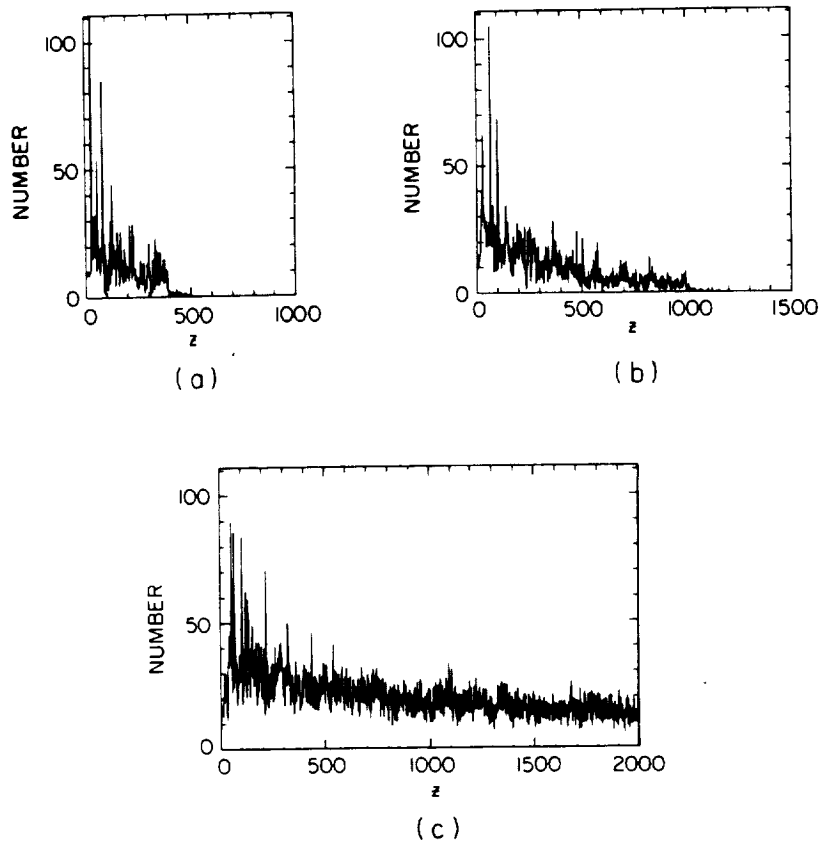


Fig. 5. Number of beam electrons as a function of z at times corresponding to those of Figure 4. Note from all three figures that significant density perturbations are created in the beam.

also see the bunches in the beam quickly reach this quasi-linear phase between 50 and 100 m from the injection point (see Figure 4). However, as is indicated in Figure 7, significant current density enhancements still exist out as far as 200 m,

and these fluctuations affect the Cerenkov radiation. In particular, they couple to the strong perturbations found in the first 50 m, increasing the values of $J_z(k_z)$ in the whistler mode wave number regime (see Figure 6). This coupling effect is best mod-

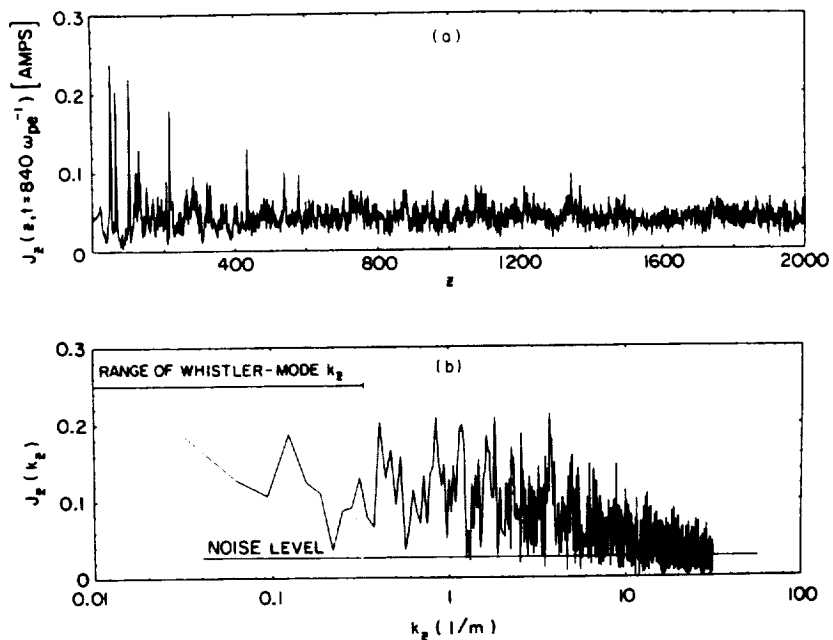


Fig. 6. Beam current density as a function of z at $840\omega_{pe}^{-1}$; (b) corresponding transform of this current. Note from Figure 6a that significant perturbations in the current density are present in the beam, which increases the values of $J_z(k_z)$ displayed in Figure 6b at wave numbers of less than 20.

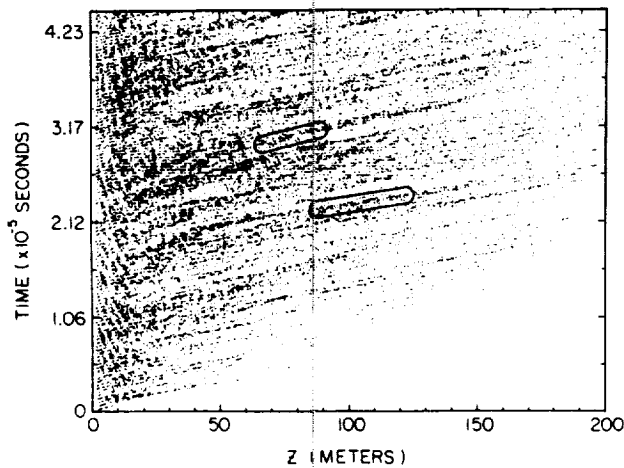


Fig. 7. Current density values, $J_z(z, t)$, above the average of 0.05 A as a function of z and t . The evolution of the current density perturbations is clearly displayed. Note that these perturbations drift at $V \sim 1.89 \times 10^7$ m/s, which is the beam injection speed. Also, note that merging of the current density perturbations occurs in the beam, as indicated by the circled structures.

eled using an injection simulation, which may possibly explain the different conclusions reached by *Omura and Matsumoto* [1988].

To obtain the radiated power from (21), $J_z(k_z)$ evaluated at $k_z(\omega) = n \cos \theta_0 \omega/c$ is required, where the wave number $k_z(\omega)$ represents those of the whistler mode that satisfy the Landau resonance condition. This wave number varies from 0.01 at 31.1 kHz to 0.332 at 1 MHz. The current density values that correspond to these wave numbers are indicated in Figure 6b. Using (21) and the calculated values of $J_z(k_z)$ with the noise level subtracted, the radiated power spectral density, dP/df , from the modeled 200-m beam segment is evaluated. These power spectral density values are plotted as a function of wave frequency in Figure 9 (represented by crosses), along with the log average of these values (represented by the straight line). The calculated incoherent Cerenkov power spectra (represented by open circles) and measured whistler mode power spectra (represented by dots) from the 200-m SL 2 electron beam segment is also displayed in the figure. Note from the figure that the inclusion of coherent effects among the beam electrons increases the wave powers by nearly a factor of 10^9 (90 decibels) above incoherent power levels and yields values that are relatively close to the measured whistler mode powers. It is clear from the figure that coherent Cerenkov radiation from the beam can indeed account for the measured whistler mode wave power.

It can also be seen from Figure 9 that the calculated power from the modeled beam actually overestimates the measured power by a factor of 40. This overestimate may result from the fact that the SL 2 electron beam is not an ideal line source radiator as assumed in our analysis, and a more accurate estimate of the power may be obtained by including the beam's radial dimension. The overestimate of the power may also be due to the assumption that the beam electrons are completely field aligned. Even if the electron generator is perfectly aligned with the geomagnetic field, electrical and fluid edge effects between the beam and the generator orifice may impart enough perpendicular momentum to the beam electrons to reduce the size of the density perturbations as we have modeled them. Consequently, the radiated power will be

reduced. Interactions between the beam electrons and neutrals may also impart significant perpendicular momentum to the beam electrons, which will again reduce the size of the density perturbations and the radiated power. It might be expected that Landau damping of the Cerenkov radiation as it propagates in the ionospheric plasma will also reduce wave powers; but it is suspected that this effect is not significant, since the Cerenkov wave phase speed from the current density perturbations is still well above the thermal velocity of the ionosphere. On the basis of the limiting assumptions used in our model, the calculated power should be considered as an upper limit of the possible whistler mode wave power. The effects mentioned above should all tend to reduce the beam's radiative coherence as compared to our one-dimensional model and, consequently, lower the radiated powers. Therefore it is not surprising that the powers obtained via the one-dimensional analysis are higher than those measured.

5. CONCLUSION

Previously, the measured power of the whistler mode waves emitted by a continuous electron beam ejected from the shuttle was found to be almost 10^7 greater than the expected power from an incoherent Cerenkov radiation process. Owing to this discrepancy, it was suggested that these waves might result from coherent Cerenkov radiation effects in a beam naturally modulated by a beam-plasma instability. In this case, the enhanced radiated power would result from the coherence between electrons in the instability-related density perturbations or "bunches."

In order to verify that this process is indeed viable, a one-dimensional electrostatic simulation of the beam was performed that verified the existence of the bunches. The coherent Cerenkov-radiated power from the modeled beam was then calculated using an analytical expression similar to that pre-

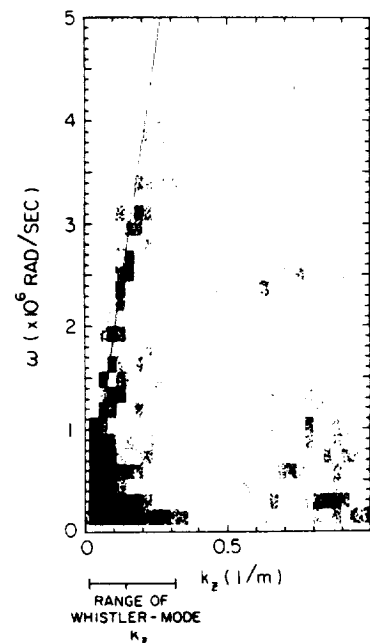


Fig. 8. To determine the velocity of the perturbations, the Fourier transform of the current density in time and space, $J_z(k_z, \omega)$, was calculated and plotted as a function of k_z and ω . Note that the values lie near $\omega/k_z = 1.89 \times 10^7$ m/s.

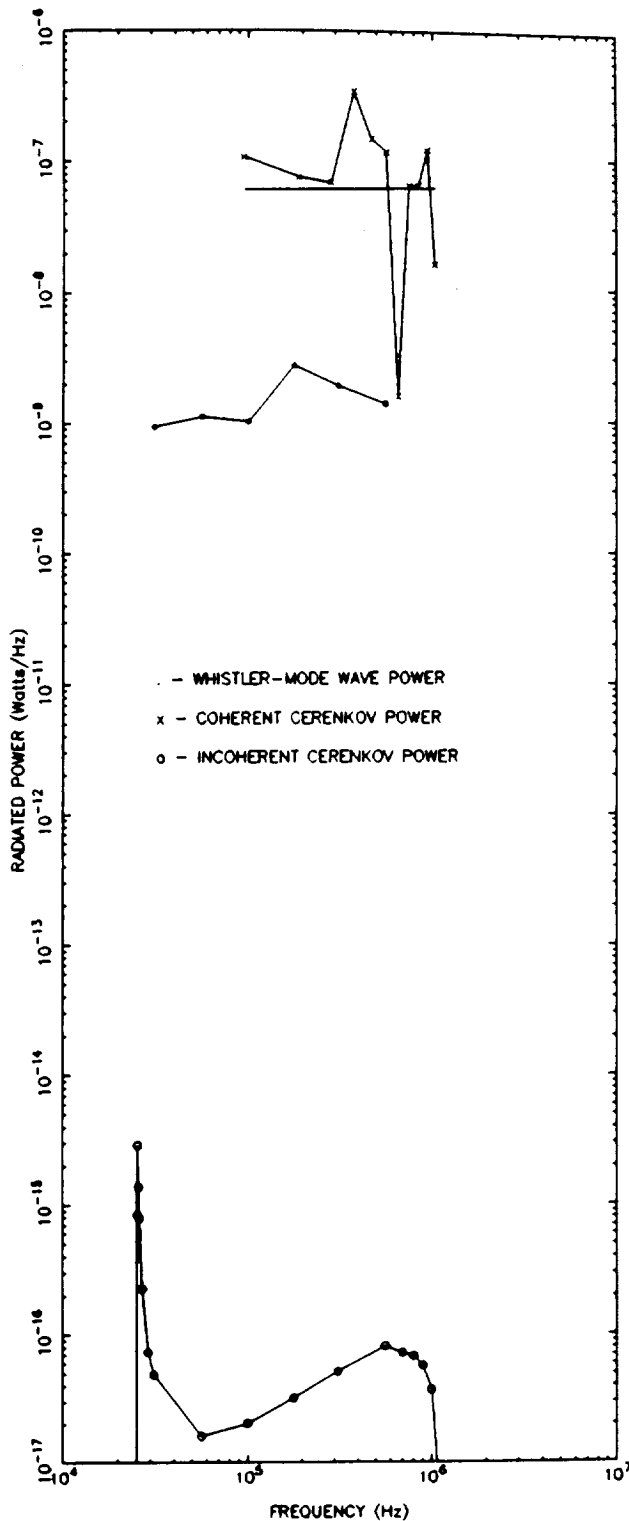


Fig. 9. Power spectra of the measured whistler mode radiation from the first 200 m of the SL 2 electron beam along with the calculated power spectra of the incoherent and coherent Cerenkov radiation from a 200-m beam segment. Note that the inclusion of coherent radiation effects increases the calculated powers near to those measured from the SL 2 electron beam. On the basis of these results, it is concluded that coherent Cerenkov radiation from a bunched electron beam can generate the detected whistler mode radiation.

sented by *Harker and Banks* [1983] and was found to be within a factor of 40 of the measured wave power.

It should be noted that two very critical assumptions were made to simplify the above analysis. The first assumption was that the beam could be treated as a line source radiator of the whistler mode waves and was invoked to obtain a manageable expression for the radiated power. Although the beam was not an ideal line source, the electromagnetic wavelengths were still significantly greater than the beam diameter, making the assumption valid. The second assumption is that similar electrostatic effects occur in beams of finite and infinite radius, which allowed us to model the beam using only a one-dimensional simulation. As was mentioned previously, a one-dimensional simulation was advantageous, since a long beam length was required. We demonstrated, via simulation, that the phase space structure of a two-dimensional, radially finite beam was indeed comparable to that of a one-dimensional beam. Without these two simplifying assumptions, the expression for the radiated power and the modeled beam could not have been used in the analysis.

Since we have demonstrated that a spontaneous emission process alone can account for the whistler mode wave powers, other more sophisticated emission processes operating in the beam, such as a whistler mode instability, are not required. Both a Cerenkov radiation process and a whistler mode instability could be present in the beam, but in this case, the powers from the Cerenkov process are at least comparable to those from the instability. Consequently, effects from spontaneous Cerenkov radiation processes cannot be ignored in the generation of the whistler mode waves from the SL 2 electron beam.

APPENDIX

As was mentioned in the text, all the current density perturbations or bunches in the modeled SL 2 electron beam are not propagating at exactly V_s but, instead, propagate in a range of velocities, $V_s \pm \Delta V$, where ΔV is the typical velocity spread. Consequently, in the frame moving with these bunches, they are not all stationary, as was assumed in the derivation of (21), but have second-order temporal variations that can alter the radiative coherence of the beam. The effect of these temporal variations on the radiated power can be accounted for by changing the delta function in (11) to a Gaussian function that represents the spread in bunch velocity. The corresponding transform of the current density in space and time is then written as

$$\bar{J}_q(\vec{k}, \omega) = \frac{\hat{z}}{(2\pi)^3} (2\pi)^{1/2} J_z(k_z) \left[\frac{t_0}{2(\pi)^{1/2}} e^{-a^2 t_0^2 / 4} \right] \quad (\text{A1})$$

where $J_z(k_z)$ is the spatial transform of the current density, $a = k_z V_s - \omega$, and t_0 is the typical coherence time scale of the temporal variations in the current density. If the transform of the current density is peaked at $\omega/k_z = V_s$ with little or no spread in ω or k_z , then the current density is properly represented by (11). However, as Figure 8 indicates, the transform of the current density, $J_z(k_z, \omega)$, has some spread about $V_s = \omega/k_z = 1.89 \times 10^7$ m/s. Consequently, this transform is best represented by (A1), where the Gaussian function is used to represent the spread in ω - k_z space. Note as $t_0 \rightarrow \infty$, (A1) and (11) become identical.

Following a similar analysis as was done previously, the power spectral density from a current density, $J_z(k_z, \omega)$, with a

spread is found to be

$$\left. \frac{dP}{d\omega} \right|_{\omega=\omega_0} = \int F(k_z, \omega_0) \frac{t_0}{2(\pi)^{1/2}} e^{-a^2 t_0^2 / 4} dk_z \quad (\text{A2})$$

where

$$F(k_z, \omega_0) = \frac{1}{(2\pi)^2 \epsilon_0 c^2} \int (\hat{z} \cdot \mathbf{T}^{-1} \cdot \hat{z}) [2\pi J_z(k_z) J_z^*(k_z)] n \omega_0 dn \quad (\text{A3})$$

Thus to obtain the power spectra density, a Gaussian-weighted integration of $F(k_z, \omega_0)$ over dk_z must be performed. Using (13), a similar expression can be written when $J_z(k_z, \omega)$ has no spread about $\omega/k_{\parallel} \approx V_s$:

$$\begin{aligned} \left. \frac{dP}{d\omega} \right|_{\omega=\omega_0} &= \int F(k_z, \omega_0) \delta(k_z V_s - \omega_0) e^{i(k_z V_s - \omega_0)t} dk_z \\ &= \left. \frac{F(k_{z0}, \omega_0)}{V_s} \right|_{k_{z0}=\omega_0/V_s} \end{aligned} \quad (\text{A4})$$

Expressions (A2) and (A4) should yield similar results as long as $F(k_z, \omega_0)$ approximates $F(k_{z0}, \omega_0)$ in dk_z . A numerical integration of (A2) was performed, and this result was indeed found to be true. The radiated power varied by only about 10% when considering a spread in $J_z(k_z, \omega)$ equal to k_{z0} . From these results it is evident that the radiated power does not vary significantly when considering a spread in $J_z(k_z, \omega)$ about $\omega/k_z = V_s$. Consequently, the radiated power calculated using the much simpler expression (21) should be a sufficiently accurate estimate of the radiated power from the modeled beam.

Acknowledgments. We would like to thank Terry Whelan and Shinobu Machida for their timely ideas concerning the simulation and radiated power calculations, John Steinberg for his useful discussions, Terry Averkamp for his valuable input on PDP data analysis, and John Birkbeck for a fine drafting job. Part of this research was funded by NASA graduate student researchers training grant NGT-50034. The research at the University of Iowa was also supported by NASA through contract 32807 and grants NAG3-449, NSG-7632, NGL 16-001-002, and NGL 16-001-043. The research at Stanford University was supported by NASA through grant NAGW-235.

The Editor thanks three referees for their assistance in evaluating this paper.

REFERENCES

- Banks, P. M., and W. J. Raitt, Observations of electron beam structure in space experiments, *J. Geophys. Res.*, **93**, 5811, 1988.
- Beghin, C., J. P. Lebreton, B. N. Maehlum, J. Troim, P. Ingsoy, and J. L. Michau, Phenomena induced by charged particle beams, *Science*, **225**, 188, 1984.
- Bell, T. F., Artificial production of VLF hiss, *J. Geophys. Res.*, **73**, 4409, 1968.
- Cartwright, D. G., and P. J. Kellogg, Observations of radiation from an electron beam artificially injected into the ionosphere, *J. Geophys. Res.*, **79**, 1439, 1974.
- Dechambre, M., Yu. V. Kushnerevsky, J. Lavergnat, R. Pellot, S. A. Pulinets, and V. V. Seleger, Waves observed by the ARAKS experiment: The whistler mode, *Ann. Geophys.*, **36**, 351, 1980.
- Farrell, W. M., D. A. Gurnett, P. M. Banks, R. I. Bush, and W. J. Raitt, An analysis of whistler mode radiation from the Spacelab 2 electron beam, *J. Geophys. Res.*, **93**, 153, 1988.
- Gendrin, R., Initial expansion phase of an artificially injected electron beam, *Planet. Space Sci.*, **22**, 633, 1974.
- Grandel, B. (Ed.), *Artificial Particle Beams in Space Plasma Studies*, Plenum, New York, 1982.
- Gurnett, D. A., A satellite study of VLF hiss, *J. Geophys. Res.*, **71**, 5599, 1966.
- Gurnett, D. A., High latitude electromagnetic plasma wave emissions, in *High Latitude Space Physics*, edited by B. Hultqvist and T. Hagfors, Plenum, New York, 1983.
- Gurnett, D. A., W. S. Kurth, J. T. Steinberg, P. M. Banks, R. I. Bush, and W. J. Raitt, Whistler-mode radiation from the Spacelab-2 electron beam, *Geophys. Res. Lett.*, **13**, 225, 1986.
- Harker, K. J., and P. M. Banks, Radiation from pulsed electron beams in space plasmas, *Radio Sci.*, **19**, 454, 1983.
- Hawkins, J. G., P. M. Banks, P. R. Williamson, R. I. Bush, and W. J. Raitt, Rise times in the vehicle charging and return current measurements during electron beam emission experiments from the shuttle orbiter (abstract), *Eos Trans. AGU*, **68**, 1400, 1987.
- Lin, C. S., and H. K. Wong, Plasma instabilities of a finite size electron beam-plasma system, paper presented at 1988 URSI Meeting, Union Radio Scientifique Internationale, Boulder, Colo., 1988.
- Lin, C. S., J. L. Burch, S. D. Shawhan, and D. A. Gurnett, Correlation of auroral hiss and upward electron beams near the polar cusp, *J. Geophys. Res.*, **89**, 925, 1984.
- Mansfield, V. N., Radiation from a charged particle spiraling in a cold magnetoplasma, *Astrophys. J.*, **147**, 672, 1967.
- Monson, S. J., P. J. Kellogg, and D. G. Cartwright, Whistler mode plasma waves observed on Electron Echo 2, *J. Geophys. Res.*, **81**, 2193, 1976.
- Neubert, T., W. W. L. Taylor, L. R. O. Storey, N. Kawashima, W. T. Roberts, D. L. Reasoner, P. M. Banks, D. A. Gurnett, R. L. Williams, and J. L. Burch, Waves generated during electron beam emissions from the space shuttle, *J. Geophys. Res.*, **91**, 11,321, 1986.
- Okuda, H., and J. D. Kan, Injection of an electron beam into a plasma and spacecraft charging, *Phys. Fluids*, **30**, 209, 1987.
- Okuda, H., R. Horton, M. Ono, and M. Ashour-Abdalla, Propagation of a nonrelativistic electron beam in a plasma in a magnetic field, *Phys. Fluids*, **30**, 200, 1987.
- Omura, Y., and H. Matsumoto, Computer experiments on whistler and plasma wave emissions for Spacelab-2 electron beam, *Geophys. Res. Lett.*, **15**, 319, 1988.
- Shawhan, S. D., G. B. Murphy, P. M. Banks, P. R. Williamson, and W. J. Raitt, Wave emissions from dc and modulated electron beams on STS 3, *Radio Sci.*, **19**, 471, 1984.
- Williamson, P. R., J. G. Hawkins, R. I. Bush, P. M. Banks, and W. J. Raitt, Vehicle charging measured during electron beam emission on Spacelab-2 (abstract), *Eos Trans. AGU*, **66**, 1051, 1985.
- Winglee, R. M., and P. L. Pritchett, Comparative study of cross-field and field-aligned electron beams in active experiments, *J. Geophys. Res.*, **93**, 5823, 1988.
- Winglee, R. M., P. L. Pritchett, and G. A. Dulk, Energy transport by energetic electrons released during solar flares. 1. Thermal versus nonthermal processes, *Astrophys. J.*, in press, 1987.

W. M. Farrell, C. K. Goertz, and D. A. Gurnett, Department of Physics and Astronomy, G375, University of Iowa, Iowa City, IA 52242.

(Received October 27, 1987;
revised July 22, 1988;
accepted July 26, 1988.)

CONTAMINANT IONS AND WAVES IN THE SPACE STATION ENVIRONMENT

G. B. Murphy

Department of Physics and Astronomy
The University of Iowa
Iowa City, IA 52242

Introduction

It is a difficult task to estimate, with any degree of certainty, the probable environment of any large space structure or system given that the system has not been firmly defined. This environment is a product of the natural environment and its interactions with that structure and system. We shall distinguish between the so-called induced environment, the molecular, particulate, photon and wave environment which results from the disturbing effects of a large object flying at orbital speeds through the ionosphere, and the contaminant environment which is produced when solids, liquids or gases are released from the system and interact with the induced environment in an array of chemical and physical processes. Our task is made particularly difficult by two important unknowns: a firm definition of the system and its contaminants; incomplete knowledge of the chemical and physical processes which can take place. In this paper we will address the probable plasma environment of Space Station. That is, we will discuss the particles (ions and electrons) and waves which will likely exist in the vicinity of the Space Station and how these may affect the operation of proposed experiments. Differences between quiescent operational periods (as defined by JSC 30426) and non-operational periods as well as probable effects from Shuttle operations will also be discussed. Areas which need further work are identified and a course of action suggested.

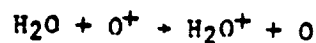
Background

Much of our knowledge about the interactions between large bodies and the ionospheric plasma had, until the time before Shuttle flights, been obtained from observations aboard small scientific satellites and various scaled laboratory investigations. The recent era of Spacelab-type payloads aboard the Shuttle orbiter has provided a wealth of heretofore unobtainable information. The Shuttle is not only the largest body flown to date but, as was discovered over a period of time, carries with it a large gas cloud. The discovery of "Shuttle glow" (Banks et al., 1983), broadband electrostatic noise (Shawhan et al., 1984a), heated electron populations (McMahan et al., 1983), a modified ion environment (Hunton and Carlo, 1985), and contaminant ions in the wake (Grebowsky et al., 1987) have begun to fill in pieces in what appears to be a complex puzzle associated with the large body induced environment and contaminant interactions. Recent studies of the neutral and ion population during thruster operations (Wulf and Von Zahn, 1986; Narcisi et al., 1983; Shawhan et al., 1984b), modification of the plasma during FES

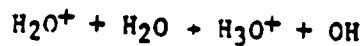
operations and H₂O dumps (Pickett et al., 1985), the discovery of pick-up ions consistent with chemistry of the H₂O, O⁺ interaction (Paterson, 1987), as well as observations by neutral mass spectrometers (Wulf and Von Zahn, 1986; Miller, 1983), have helped to sort out the differences between interactions which are of the induced variety and those which result from release of contaminants by the orbiter. Observations by IR, optical, and UV instruments on board the orbiter (Torr, 1983; Torr and Torr, 1985; Koch et al., 1987), and by IR on the ground (Witteborn et al., 1987) have provided insight into the effects of both absorption and emission by this contaminant population. It is now clear as a result of these pathfinder experiments that in order to conduct experiments in plasma physics, provide long-term monitoring and a data base for the ionosphere, observe astronomical targets over a broad range of wavelengths, and provide sensitive remote sensing capability, the Space Station environment must be cleaner than that of the orbiter in many respects. Much work has already been done in assessing just how clean that environment must be in order to meet the minimum science requirements (Space Station Payload Contamination Compatibility Workshop, 1987). It will be the purpose of this paper to assess what the particle and wave environment might be and whether the current specifications are adequate in this regard. This assessment will be based on current contamination control requirements, knowledge of proposed space station configuration, and our best guess about the scaling laws for certain plasma interactions.

Particle Environment

A number of investigators have studied the composition of the Shuttle ion environment and compared it to that which was expected of the natural environment at the orbiter altitude (Grebowsky et al., 1987; Siskind et al., 1984; Reasoner et al., 1986). The studies observe large amounts of H₂O⁺ which results from the rapid charge exchange reaction



as well as smaller amounts of H₃O⁺.



The amount of H₂O⁺ (and H₃O⁺) observed appears to be directly proportional to the surface temperature leading to the conclusion that most of this observed water is offgassed from Shuttle tiles or other porous surfaces (Narcisi et al., 1983). The amount of water can be estimated by neutral mass spectrometers but caution must be taken since frequently these instruments can only observe molecules which are scattered back toward the orbiter either by collisions with ambient molecules or the cloud itself. Several attempts have been made to estimate water density or by observing the ion population and then doing a kinetic analysis. This has been done with observations obtained within the orbiter bay (Narcisi, 1983) and with data which were obtained during the PDP free-flight on Spacelab 2 (Paterson, 1987). Other estimates have been obtained by observing the infrared signature and then estimating column densities (Koch et al., 1987). The remarkable thing about all of these methods is that although they have shown some decay in the amount of water during the lifetime of the mission and variation among missions, the neutral

observations, ion observations, and IR observations give a consistent picture which can be modeled within the accuracy of the known cross sections for the charge exchange reaction. The significance of this is that if we know one of the above parameters accurately, e.g., column density from IR observations, we can predict another, e.g., contaminant ion population, through a modeling of the chemistry and kinetics of the gas cloud. Several authors have developed models of this "gas-cloud" interaction; notably Patterson (1987) has modeled a steady state cloud and shown the production of H_2O^+ to scale with background O^+ density and Hastings et al. (1987a) have developed time-dependent models of clouds which would be associated with a brief gas release, such as the opening of a gas relief valve or a thruster operation.

This contaminant ion population can be a source of several problems.

(1) These ions create an additional wake which trails the object in a sense which is perpendicular to the magnetic field line instead of parallel to the velocity vector.

(2) Depending on the nature of the ions they may result in a deposition problem on some surfaces facing the ram direction.

(3) Depending on the excitation state of the ions, they may add to the IR, optical or UV spectrum which is sensed by a particular instrument.

(4) The current created by these pick-up ions is believed to be responsible for plasma instabilities which enhance the background wave environment.

(5) Molecules which have low ionization potential may be susceptible to the critical ionization velocity (CIV) process causing enhanced plasma density, production of wave turbulence, and possible photon emission.

Let us look at the above possibilities in light of Space Station operations. Although much of our shuttle experience has been gained by observing the H_2O/O^+ interaction, any process such as charge exchange, photoionization, ionization by CIV, etc., will produce the pick-up ion cloud and present a similar set of problems to experiments or the Space Station.

Figure 1 presents a cartoon of the composite nature of the Shuttle environment to illustrate the first point above. Superimposed on the induced environment (i.e., the neutral and plasma wake) is the wake produced by the pick-up ions. Generated in the orbiter rest frame they will appear to move past the vehicle perpendicular to field lines. Any experiment expecting to be in the neutral or plasma wake may in fact be in a location dominated by these contaminant ions. As mentioned in point 2, it is clear that these ions could interact with or stick to surfaces when they were presumed to be part of a freely expanding cloud. Possible surface degradation could result from the fact that they can strike the ram surfaces with near orbital velocity (their energy is dependent on the reaction that creates them as well as their mass). This implies chemistry which takes place in front of ram surfaces (e.g., glow) and that which takes place on surfaces must take these ions into account.

Regarding point 3, since these ions form an asymmetric distribution about the vehicle and since their column density is greatest in the wake direction, it is important to evaluate not only the atomic physics associated with the neutral molecule but its ionized and possibly excited state as well. If the

ionized species has a particular emission line which is undesirable optically, this may be particularly noticeable in the wake direction.

We will discuss in more detail the effects described by points 4 and 5 in the next section. Let us first, however, summarize the primary contributors to the ion environment.

Molecular contaminants resulting from outgassed or vented products can interact with the ambient population through several processes creating an ionized cloud which will trail behind the Space Station much like the tail of a comet. If the ionizable contaminants are held to levels well below that of the Shuttle (how much below will be discussed in the next section), the ion environment during operational periods should be acceptable to most experimenters. However, a very important gap exists in our knowledge. A study of the OSSA Space Station waste inventory (Bosley et al., 1986) reveals a large number of possible waste gas and liquid products. Although interactions of simple molecules like H_2O , N_2 , and CO_2 with the O^+ plasma are reasonably well understood, the chemistry of this large possible "soup" of waste products involves many unknowns. It would seem prudent to assess the possible interaction of some of these waste gases by realistic laboratory experiments before deciding that they are allowable vent gases.

Wave Environment

It will be difficult to assess whether the wave environment described in JSC 30420 and JSC 30237 can be met in its entirety. Analysis of the wave environment aboard the orbiter based on PDP data from OSS 1 and Spacelab 2 have led to the emerging picture, again depicted by the cartoon of Figure 1, that the broadband noise environment may be dominated not by the induced environment associated with the large body interaction as was originally believed, but by production of waves by the gas cloud itself. If this is the case it may be possible to correlate the general level of this background noise to the density of the water cloud. In Figure 2, we present data that have been compiled from the published literature (Pickett et al., 1985). The level of noise at 1 kHz (chosen as typical of the broadband noise spectra for these data) is plotted for three different cases of "small" gas cloud releases. The level of uncertainty in the measurement of H_2O density is represented by the vertical error bars. The three cases chosen represent almost 3 orders of magnitude in gas quantity. In all cases the dominant gas is H_2O . The first is the H_2O vapor cloud associated with the orbiter outgassing per se, the second an operation of the Flash Evaporator System (FES), and the third a typical operation of a VRCS thruster. In all cases the releases were on the dayside and in an ambient density of O^+ plasma of $\sim 10^5 \text{ cm}^{-3}$. Note that the data indicate that the noise is linearly proportional to the density of gas released. The best fit to the data is that the intensity (at 1 kHz) of electrostatic noise is proportional to the product of H_2O and O^+ density. The constant of proportionality is such that at a 1 g s^{-1} release rate the measured electric field anywhere within the general interaction region will be $\sim 1 \text{ mV m}^{-1}$ in a 150 Hz bandwidth. (150 Hz is the approximate bandwidth at which these measurements were made.) This law is certainly not absolute but leads the author to believe that most of the observed noise can be tied to this contaminant release. Further examination of turbulence measured by the Langmuir probe and electrostatic waves observed near the orbiter wake by the PDP on Spacelab 2 leads one to speculate that the wake

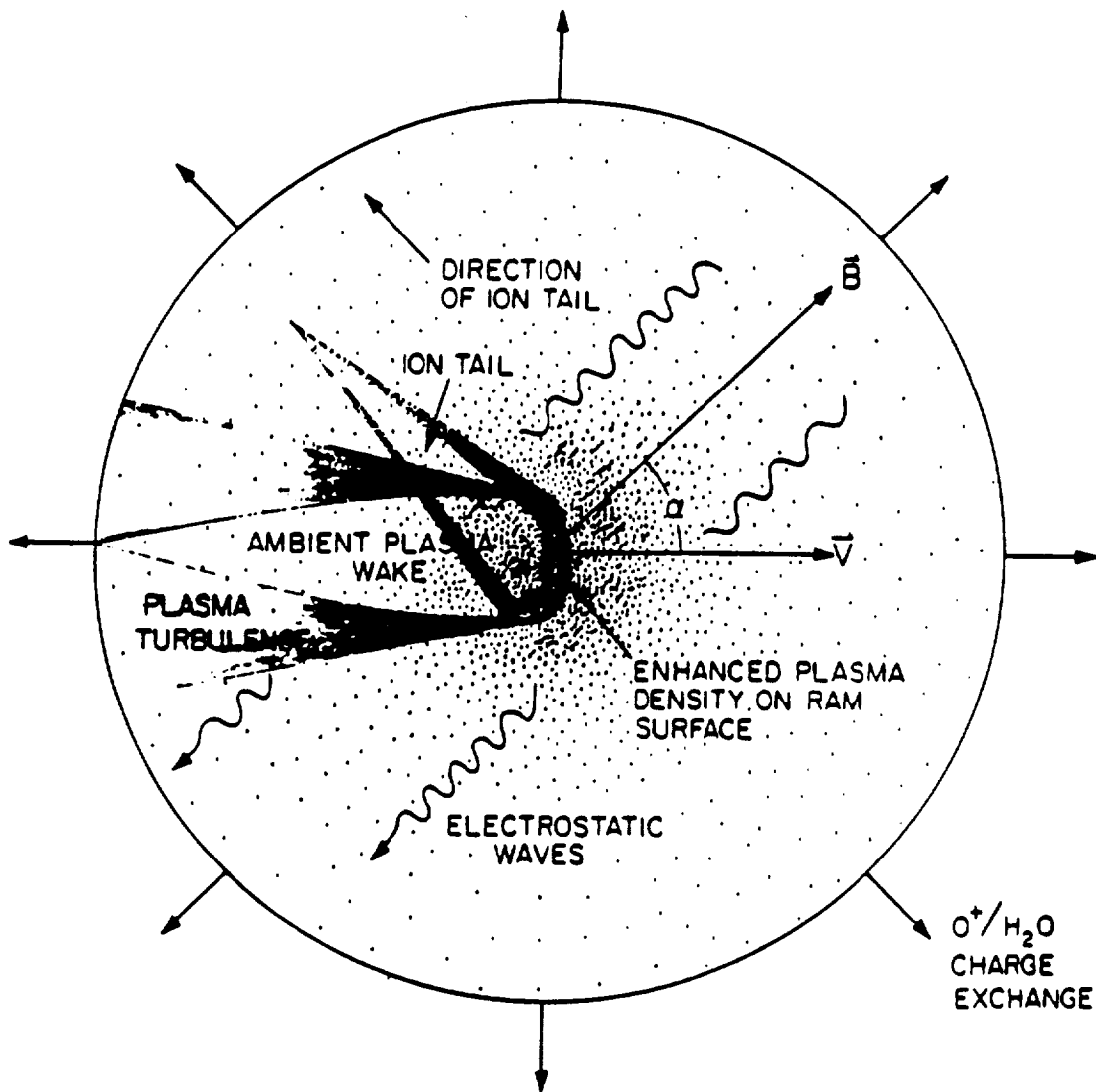


Fig. 1. The neutral cloud of gas which expands from the orbiter undergoes chemical interactions such as charge exchange which results in an ion tail and creates plasma waves presumed to be driven by the ion currents.

noise is dominant only in a region confined to the wake and wake boundaries and most wake noise observed elsewhere is dominated by the production of noise associated with instabilities resulting from ion pick-up current generated by the contaminant water cloud.

In order to properly scale this phenomena we must establish more firmly the instability that causes the wave growth and the process that saturates the

ELECTROSTATIC NOISE

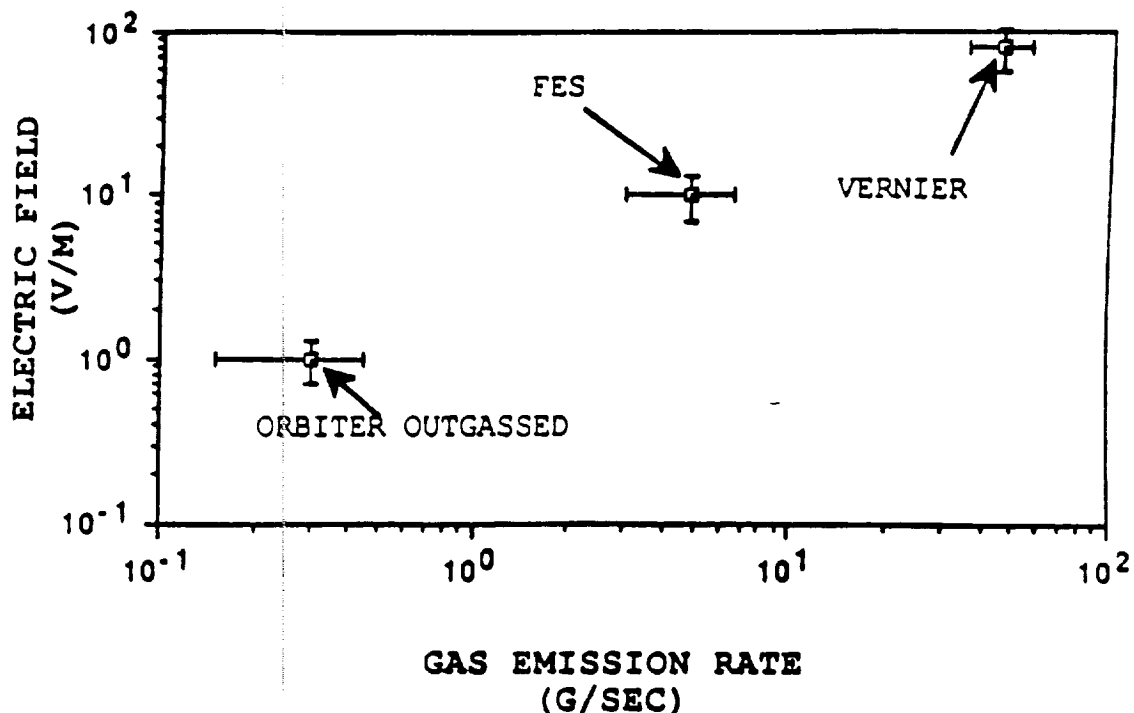


Fig. 2. Gas releases of three different magnitudes and the measured electrostatic noise show roughly a linear correlation. Estimates of outgassing rates for the first data point are a consensus of observations of inferred column density from IR and measurements of both ion and neutral densities. Emission rates of FES and VRCS are well defined.

instability. CIV may play a role in this process (Papadopoulos, 1984) but will again be very dependent on the gas composition. More experiments are required before we can definitely say that the above scaling law applies to molecules other than water, since the importance of a particular instability or CIV varies with molecular species.

Extrapolating this insight into the Space Station environment we are again led to conclude that the plasma environment will be acceptable and the JSC requirements met only during periods where ionizing components of the contaminant gases are minimized. Although the large modules and solar arrays may be a source of plasma noise generated by turbulence in their wake, at points midway along the transverse boom or on the upper or lower keel, this noise may be at an acceptable level at least for some geometric configurations of the velocity vector and magnetic field. Other sources of noise, currents carried by the structure to complete the $\vec{V} \times \vec{B}$ current loop (Hastings and Wang, 1987), radiation of noise by the cable trays or solar arrays or currents

(Hastings et al., 1987b), conduction of noise by sheath waves, etc. must be solved by appropriate design and are not within the scope of this discussion.

What numerical limits must be placed on the ionizing contaminants in order to meet the JSC 30237 specification and provide an environment free of this source of noise? Examining JSC 30237 for the spec on broadband emission for systems at standard locations, we find that at 1 kHz we must be less than $103 \text{ dB } \mu\text{V m}^{-1} \text{ MHz}^{-1}$. Scaling to the 150 Hz bandwidth of the measurements taken in compiling Figure 2, we find that these emissions must be less than $\sim 0.02 \text{ mV m}^{-1}$ which, using the linear scaling law of Figure 2, implies an emission rate of water of $< 20 \text{ mg s}^{-1}$. This should be manageable for a structure like the Space Station which will not be covered with a material that continually outgasses water. The mass release rate of other ionizable molecules could be scaled appropriately depending on their cross section for ionization. The sum total of all of these easily ionizable molecules would then have to be such that their emissions are below JSC 30237 specifications. This compares favorably with recommendations from the Space Station Payload Contamination Compatibility Workshop which recommended lower column densities of most species.

In January 1987 the OSSA contamination compatibility workshop recommended several changes in JSC 30426, which included lowering total acceptable column densities of O_2 , N_2 , and H_2 , as well as noble gases and other UV and non-IR active molecules. A further specification should be included which defines ionizable gases and the acceptable release rates for them. Furthermore, it is very important that we gain a detailed understanding of the chemistry and physics of reactions which occur between the ambient environment and the large shopping list of molecules which may be released during the non-operational periods to insure that experiments and the Space Station hardware are not subjected to effects described earlier.

Non-Quiescent Environment

JSC 30426 states that the Space Station be capable of supporting quiescent operation periods of up to 14 days. This period of minimum perturbation is essential for many science investigations and any disturbances during this period, however minor, must be noted. It is not clear that the requirement to record such disturbances is fully satisfied. Section 5.0 simply states that "...monitoring of the environment to a limited extent will be required." Since the IOC phase Space Station will not be gravity gradient stable, some fine tuning of attitude will be required. Whether it is accomplished with jets only or some combination of jets and gyros is unclear. It is clear, however, that during the long "quiescent" periods there will undoubtedly be some disturbances whether they be occasional jet firings, experiment vents, purges, or relief valve operations, EVA crew activity, etc. A clear requirement to monitor specific critical aspects of the environment must be in place. Space Station elements must have a way of "notifying the system" of an impending disturbance. Some monitoring can and should be real time and some may only be required after the fact. Whether PIMS or some other monitoring package is responsible is yet to be determined but the requirement must be a system responsibility with data accessible to all.

Non-quiescent periods, such as Shuttle docking, will provide significant disturbances. It is the consensus of a number of independent observations that the Shuttle orbiter carries with it a large amount of contaminant material, particularly water. Column densities near the orbiter of 10^{12} to

10^{13} should be expected. There is some disagreement over the decay time of the associated cloud. IECM observations (STS-2, STS-3, STS-4) indicated an initial decay time of ~10 hours. However, Narcisi et al. (1983) has observed wide variations in the water density cloud with some overall decrease in H_2O density with time, but a much stronger correlation between density and surface temperature. Raitt (private communication, 1987) reports that an ion signature, characteristic of H_2O^+ in his retarding potential analyzer, practically disappeared by the end of mission 51P. (51P spent a lot of time in a hot attitude due to a several day long solar observation cycle.)

The conclusion that may be reached from all of this is that the amount of contamination that will be carried into the space station environment by the orbiter may be reduced by simply waiting some minimum period of time (224 hours) in a relatively hot attitude behind the station, then going to a cool attitude for several hours before beginning the approach and docking. Clearly it will not be possible to operate some experiments while the orbiter is in rendezvous phase, both because of the outgassed cloud and thruster plume impingement. Docking procedures which minimize plume impingement and thruster activity will be preferred. Operation of experiments while the orbiter is present may be possible and is dependent on the type of experiment.

Other disturbances to the environment, such as EVA activity, should be scheduled as much as is practical for the non-quiet periods since gaseous products associated with the EVA suit can provide significant disturbances.

Summary

The developing requirements for Space Station must be responsive to the needs of the user and in line with the reality of Space Station logistics. They must also be internally consistent, be carried out to as full an extent as possible, and be "living documents" which can incorporate new knowledge as it becomes available. The PWWG (Particle and Waves Working Group) has been responsive to the user's needs in writing requirements and assuring that the proper tools are in place to implement them. The definition and control of the particle, plasma, and wave environment has incorporated specific needs from a wide range of potential users. The Contamination Working Group has likewise been responsive and JSC 30426 reflects the panel's concern for the cleanliness of the Space Station environment for the user, the Station safety and longevity, and for the preservation of the delicate natural chemical balance of the ionosphere. It is not clear whether some oversight group such as the CWG will be responsible for continual evaluation and enforcement of the requirements. Some mechanism will be required to do this.

Only minor modifications to the documents may be required, but the importance of these modifications cannot be over emphasized. Let us first deal with recommendations to changes in JSC 30426:

(1) Incorporate specific requirements relating to easily ionizable molecules which contribute to the plasma environment. This should be stated in $g\ s^{-1}$ emission instead of column density; e.g. total water emission should be less than $\sim 1\ mg\ s^{-1}$ for adequate margin. Other common gases which contribute to this environment are N_2 , CO_2 , and H_2 , e.g.:



(2) Analysis of proposed vented products during non-operational periods must be performed to determine if the proposed contaminants are acceptable.

(3) More specific requirements for monitoring the environment should be in place. These should include real time or "warn" flags for certain releases which must be accounted for in data analysis or known about ahead of time.

JSC 30252, the Plasma Effects Control Process Requirements Document, must be consistent with the expected contamination levels and reflect the difference between operational and non-operational periods. Further recommendations in regards to operational considerations are the following:

(1) The orbiter should be allowed to outgas for ≥ 24 hours before docking with the Station (the orbiter should be behind the Station).

(2) Procedures minimizing thruster activity and plume impingement should be implemented for docking activity.

(3) Any plan which includes continuous thrusting for reboost should be eliminated for environmental considerations.

(4) Brief gaseous releases, either by Station hardware or other equipment, must be minimized, documented, and made available in a common data base.

(5) EVA activity should be confined to non-quiet periods whenever possible.

(6) It may be appropriate to include a section on operational guidelines in the JSC 30426 document.

Last of all, several recommendations regarding uncertainties about the physical processes involved are appropriate:

(1) The cross sections for charge exchange reactions of a broad range of molecules are not well known for O^+ at 5 eV.

(2) The susceptibility of certain molecules to CIV at Space Station altitudes is unknown. Laboratory and Shuttle experiments are appropriate.

(3) The precise cause of "Shuttle glow" must be determined.

(4) Models which predict line-of-sight emissions and absorption must take into account possible ionized species that are present. In order to do this, accurate models of cross sections for reactions are required.

(5) The mechanism for production of broadband instabilities must be better understood so scaling laws can be used with more assurance.

All of the above physical considerations may also be applied to co-orbiting platforms. The environmental constraints may be similar or tighter depending on experiment complements.

References

- Banks, P. M., P. R. Williamson, and W. J. Raitt, Space Shuttle glow observations, Geophys. Res. Lett., 10, 118, 1983.
- Bosley, J. and G. Curran, OSSA Space Station Waste Inventory, NASA/Ames Research Center, SS Projects Office, November 1986.
- Grebowsky, J. M., H. A. Taylor, Jr., M. U. Pharo, III, and N. Reese, Thermal ion perturbations observed in the vicinity of the Space Shuttle, Planet. Space Sci., in press, 1987.
- Hastings, D. E. and J. Wang, Induced emission of radiation from a large Space Station-like structure in the ionosphere, J. Spacecraft & Roc, submitted, 1987.
- Hastings, D. E., N. A. Gatsonis, and T. Mogstad, A simple model for the initial phase of a water plasma cloud about a large structure in space, J. Geophys. Res., in press, 1987a.
- Hastings, D. E., A. Barnett, and S. Olbert, Radiation from large space structures in low earth orbit with induced AC currents, J. Spacecraft & Roc, submitted, 1987b.
- Hunton, D. E. and J. M. Calo, Low energy ions in the Shuttle environment: Evidence for strong ambient-contaminant interactions, Planet. Space Sci., 33, 8, 1985.
- Koch, D. G., et al., Infrared observation of contamination from Shuttle flight 51F, Adv. Space Res., in press, 1987.
- McMahan, W., R. Salter, R. Hills, and D. Delorey, Measured electron contribution to Shuttle plasma environment, AIAA-83-2598, AIAA Shuttle Environment and Operations Meeting, October 31-November 3, 1983.
- Miller, E. R. (ed.), STS-2, -3, -4 Induced Environment Contamination Monitor (IECM) Summary Report, NASA TM-82524, 1983.
- Narcisi, R. S., R. E. Trzcinski, G. Federico, L. Wlodyka, and D. Delorey, The gaseous and plasma environment around the Space Shuttle, paper #83-2659 AIAA Conference on Shuttle Environment and Operations, Washington, D.C., 1983.
- Narcisi, R. S., Quantitative determination of the outgassing water vapor concentrations surrounding space vehicles from ion mass spectrometer measurements, Adv. Space Res., 2, 10, 1983.
- Papadopoulos, K., On the Shuttle glow (the plasma alternative), Radio Science, 19, 2, 1984.
- Paterson, W. R., Ion plasmas in the vicinity of the Orbiter: Observations and modeling, M.S. Thesis, University of Iowa, July 1987.
- Pickett, J. S., G. B. Murphy, W. S. Kurth, and C. K. Goertz, Effects of chemical releases by the STS-3 orbiter on the ionosphere, J. Geophys. Res., 90, 3487-3497, 1985.
- Reasoner, D. L., S. D. Shawhan, and G. B. Murphy, Plasma Diagnostics Package measurements of ionospheric ions and Shuttle-induced perturbations, J. Geophys. Res., 91, 13463-13471 1986.
- Shawhan, S. D., G. B. Murphy, and D. L. Fortna, Measurements of electromagnetic interference on OV102 Columbia using the Plasma Diagnostic Package, J. Spacecraft & Roc, 21, 4, 1984a.

- Shawhan, S. D., G. B. Murphy, and J. S. Pickett, Plasma Diagnostics Package initial assessment of the Shuttle orbiter plasma environment, J. Spacecraft & Roc, 21, 387, 1984b.
- Siskind, D. E., W. J. Raitt, P. M. Banks, and P. R. Williamson, Interactions between the orbiting Space Shuttle and the ionosphere, Planet. Space Sci., 32, 7, 1984.
- Space Station Payload Contamination Compatibility Workshop: Final Report, NASA, OSSA Washington, D.C., June 1987.
- Torr, M. R., Optical emissions induced by spacecraft-atmosphere interactions, Geophys. Res. Lett., 10, 114, 1983.
- Torr, M. R. and D. G. Torr, A preliminary spectroscopic assessment of the Spacelab 1/Shuttle optical environment, J. Geophys. Res., 90, 1683, 1985.
- Witteborn, F., L. J. Caroff, D. M. Rank, and G. Ashley, Nighttime spectroscopic and photometric observations of Spacelab-2 and other satellites, Geophys. Res. Lett., submitted, 1987.
- Wulf, E. and U. Von Zahn, The Shuttle Environment: Effects of thruster firings on gas density and composition in the payload bay, J. Geophys. Res., 91, 3270-3278, 1986.



Spacelab 2 Plasma Diagnostics Package

W. S. Kurth* and L. A. Frank†
University of Iowa, Iowa City, Iowa

The Plasma Diagnostics Package is a small, deployable satellite designed to study the interaction of the Space Shuttle Orbiter with the ionospheric environment as well as to be used in joint experiments with the plasma depletion and the vehicle charging and potential investigations during the Spacelab 2 mission. This paper provides a brief description of the small spacecraft, its instrumentation and operation, and the scientific objectives of the investigations. A brief summary of the scientific results obtained thus far is also presented.

Introduction

THE Plasma Diagnostics Package (PDP) was one of 13 investigations that were a part of the Spacelab 2 mission that occurred during July 29–August 6, 1985. As its name implies, the PDP is equipped with a coordinated set of sensors and instruments designed to measure a wide range of parameters characterizing the ionospheric environment surrounding the Orbiter. The objectives of the investigation are to study the interaction of the Orbiter with the ionosphere, the interaction of an electron beam with the ionospheric plasma, and various naturally occurring ionospheric phenomena.

During the Spacelab 2 mission, the PDP was operated in its launch configuration in the payload bay, at various vantage points around the Orbiter while being maneuvered by the Remote Manipulator System (RMS), and at distances of up to about 400 m from the Orbiter while operating as a free-flying subsatellite of the Orbiter. In each of these operational configurations the PDP obtained measurements supporting the various scientific objectives. During much of the mission, the PDP was operated jointly with the plasma depletion and the vehicle charging and potential (VCAP) experiments for correlative studies.

The PDP had been flown previously on STS-3 as part of the first Office of Space Science (OSS-1) payload in March 1982.¹ The instrument complement was similar to the Spacelab 2 PDP, although not identical, and observations were obtained only from the payload bay and the RMS. There was no provision for the PDP to operate as a free flyer on STS-3.

Some of the primary conclusions obtained during the Spacelab 2 PDP flight are as follows:

- 1) The influence of the Shuttle Orbiter on the ionosphere extends beyond the 0.4-km region sampled by the PDP.
- 2) The Orbiter is surrounded by a water cloud that extends to distances as great as 8 km.
- 3) Ions formed by the "pickup" of contaminant water molecules are likely to be the source of intense, broadband electrostatic waves observed in the vicinity of the Shuttle Orbiter.
- 4) The Orbiter forms a well-developed wake in the ionosphere with a length of at least 250 m.
- 5) The injection of a 1-keV electron beam produces whistler mode waves analogous to very low frequency (VLF) hiss found naturally in conjunction with auroral electron beams.
- 6) The injection of the electron beam forms a narrow sheet of energetic electrons in the wake of the Orbiter that is accompanied by broadband electrostatic waves.

In this paper, we outline the general scientific objectives of the PDP for the Spacelab 2 mission, describe the PDP and its complement of instruments, provide an overview of the operations of the PDP during the mission, and summarize the results gained to date from the PDP.

Scientific Objectives

One of the major scientific objectives of the PDP investigation on Spacelab 2 was to characterize and understand the interaction of the Orbiter with the ionospheric environment through which it flies. The Orbiter is a large object; in fact, it is large with respect to virtually all of the important plasma scale lengths at its approximately 325-km altitude orbit, including the thermal ion gyroradius. Furthermore, the Orbiter moves with great speed through the ionospheric plasma, typically about 8 km/s. This situation provides the opportunity to study the formation of wakes and turbulence generated by a large body moving through the plasma. All previous satellite measurements were of much smaller bodies and often in plasma regimes with much larger scale sizes.^{2,3}

On Spacelab 2, the PDP carries out a coordinated set of wake observations at distances ranging from very close (i.e., a few meters) to nearly 400 m. In addition, the Orbiter provides its own set of active experiment opportunities in the form of chemical contamination experiments. The most obvious examples of these are the joint experiments with the Spacelab 2 plasma depletion experiment for which the PDP provides supporting in situ data for the ground-based observation of the effects of firing the Orbital Maneuvering System (OMS) engines in the plasma.^{4,5} The Orbiter, however, is almost continuously depositing large quantities of contaminants into the ionosphere through outgassing leaks from pressurized vessels, the operation of the Reaction Control System (RCS) jets required to jet and maintain various attitudes, and the deliberate discharging of both liquid and gaseous water as normal maintenance operations.^{6,7}

Another primary objective of the PDP on Spacelab 2 was to operate jointly with the Fast Pulse Electron Generator portion of the VCAP experiment provided by Stanford University and Utah State University.⁸ The primary purpose of VCAP was to investigate the interaction of an energetic (1 keV) beam of electrons with the ionospheric environment. This experiment has importance for the study of naturally occurring auroral phenomena observed elsewhere in the ionosphere but takes advantage of the active control of the electron beam to isolate various aspects of the beam-plasma interaction. The electron beam studies were also undertaken during STS-3, but Spacelab 2 offered experiments that benefited from the STS-3 RMS experience and the important opportunity to observe at distances a factor of 10 or more larger in the free-flight configuration.

Finally, it was planned to investigate naturally occurring ionospheric phenomena with the PDP while in free flight, but

Received Dec. 19, 1988; revision received April 17, 1989. Copyright © 1989 American Institute of Aeronautics and Astronautics, Inc. All rights reserved.

*Research Scientist, Department of Physics and Astronomy.

†Professor of Physics, Department of Physics and Astronomy.

one of the most important discoveries of the Spacelab 2 PDP is that one must move much further away from the Orbiter than the 400-m distances achieved during Spacelab 2 to fully escape the influence of the Orbiter.^{6,7,9} Hence, the ambient ionospheric studies have been overshadowed by the Orbiter and electron beam interaction studies. It should be noted that some natural phenomena were observed, such as VLF whistlers, therefore, some such studies are still possible.

Instrumentation

Spacecraft Description

The PDP was designed and fabricated by the University of Iowa and is a unique Spacelab experiment in that it is designed to make observations while 1) attached to the Spacelab pallet in the payload bay, 2) being maneuvered about the Orbiter by the RMS, and 3) operating as an independent satellite in orbit near the Orbiter. To accomplish the third goal, the PDP had to be designed primarily as a free-flying satellite, but with provisions to be carried aloft within the payload bay and to be grappled and articulated by the RMS. Modifications late in the development of the PDP further allowed its recapture, preserving the possibility of reusing all or part of the spacecraft in future programs.

The PDP, shown in free flight during the Spacelab 2 mission in Fig. 1 and in schematic form in Fig. 2, is cylindrically shaped with a diameter of about 42 in. (1.07 m) and a weight of about 625 lb (284 kg). Various sensors are mounted on the four deployable booms, and numerous instruments have apertures through the spacecraft skin. The appendage at the top of the spacecraft is an electrical grapple fixture that allows the PDP to be manipulated by the RMS as well as operated electrically through cables in the RMS that are connected to a special switch panel on the aft flight deck of the Orbiter.

The small cylinder just below the grapple fixture contains a momentum wheel loaned by the Smithsonian Institution from the ATS-G satellite. The wheel is used to store angular momentum in the PDP prior to release for free flight. The stored angular momentum was subsequently used to spin the PDP up to about 4.6 rpm during the free-flight phase by allowing the momentum wheel to spin down with respect to the PDP structure. Prior to recovery, the wheel was spun up again to transfer the angular momentum back out of the structure, thereby despinning the spacecraft to allow recapture by the RMS.

Instrument Summary

The PDP contains an integrated set of instruments to provide a broad range of measurements of plasmas, dc and oscillatory electric and magnetic fields, and neutral pressure. Because of funding limitations, many of the scientific instruments are flight spare units from such projects as IMP, Helios, and ISEE. Table 1 provides an overview of the various scientific instruments flown on the Spacelab 2 PDP, the investigators providing the instrumentation, and a brief summary of the measured parameters. The sensor locations are shown in Fig. 2.

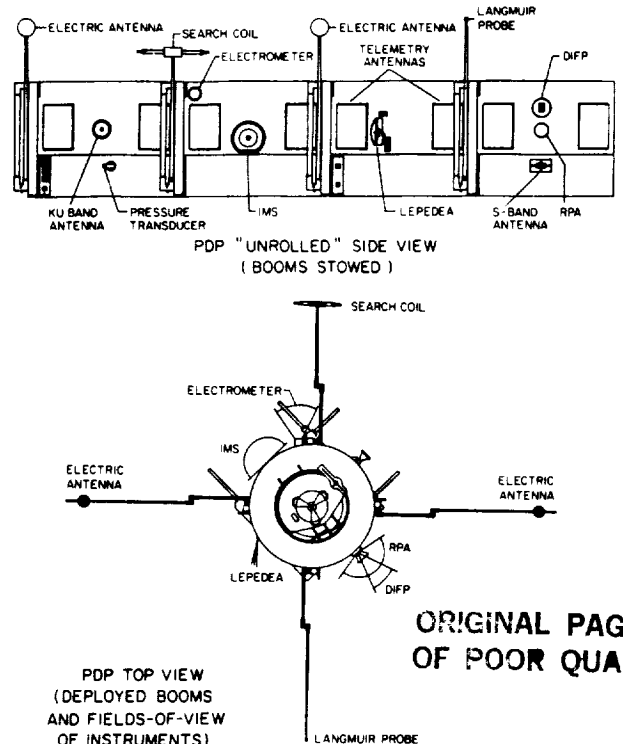
PDP Operations

The PDP operations performed during the Spacelab 2 mission can be organized best by separating them into operations performed while 1) on the Spacelab pallet, 2) being manipulated by the RMS, and 3) functioning as a free-flying satellite in orbit with the Orbiter. In the following subsections, we will describe briefly the operations in each of these phases. Table 2 summarizes the major PDP in-flight operations.



Fig. 1 Photograph of the PDP deployed in its free-flight configuration during the Spacelab 2 mission.

PDP SENSOR LOCATIONS



ORIGINAL PAGE IS OF POOR QUALITY

Fig. 2 Top panel shows locations of the various instrument viewports and sensors (see Table 1) in a schematic of the PDP shown with the sidewall of the spacecraft "unrolled." The bottom panel is a view of the PDP from the top showing the locations of the booms and the boom-mounted sensors in the fully extended configuration. The fields of view of the plasma analyzers are also indicated.

Table 1 Spacelab 2 PDP scientific instruments

Instrument	Provider	Measurement
Ion mass spectrometer (IMS)	J. M. Grebowsky Goddard Space Flight Center	Thermal ions; 1-64 amu; $20-2 \times 10^6$ cm ⁻³
Retarding potential analyzer (RPA)	D. L. Reasoner Marshall Space Flight Center	Ions; 0-15 eV; $20-10^7$ cm ⁻³
Differential ion flux probe (DIFP)	N. H. Stone Marshall Space Flight Center	Ions; 0-15 eV; $6 \times 10^{-2}-3 \times 10^5$ cm ⁻³ ; 3-deg angular resolution in range of ± 45 deg from PDP equator
Lepedea	L. A. Frank Univ. of Iowa	Ions and electrons; three-dimensional velocity distributions; 2 eV-36 keV; plus electrometer with range 10^9-10^{14} electrons/cm ⁻² s ⁻¹
Langmuir probe	N. D'Angelo Univ. of Iowa	Thermal electrons; 10^3-10^7 cm ⁻³ ; $500 < T_e < 4000$ K; $\Delta N/N$ spectrum up to 178 kHz
Neutral pressure gage	J. S. Pickett Univ. of Iowa	$10^{-7} < P < 10^{-3}$ Torr
Triaxial fluxgate magnetometer	S. D. Shawhan NASA Headquarters	± 1.5 G with 0.012 G resolution; 3 axes; 10-Hz sample rate per axis
dc electric field detector	D. A. Gurnett Univ. of Iowa	± 2 -V/m single axis; 0.5-mV/m resolution (booms extended); 20-Hz rate; plasma potential ± 8 V; 20-mV resolution
Plasma wave receivers	D. A. Gurnett Univ. of Iowa	Electric: 30 Hz-17.8 MHz in 24 channels; magnetic: 35 Hz-~10 kHz in 11 channels; wideband analog: 5 Hz-30 kHz electric and magnetic
S- and K _u -band monitors	G. B. Murphy Jet Propulsion Lab.	S-band: 1.4-3.0 GHz; K _u -band: 13.5-14.5 GHz

Table 2 Spacelab 2 PDP significant events timeline

Event	Date 1985	GMT
Launch	7/29	2100
PDP activation in bay	7/30	0039
PDP grappled by RMS	7/30	2326
RMS-mounted observations begin	7/30	2338
PDP parked over port wing	7/31	0835
RMS-mounted observations resume	7/31	1840
PDP parked over port wing	7/31	1928
RMS-mounted observations resume	7/31	2023
PDP parked over port wing	7/31	2114
PDP released for free-flight	8/1	0010
PDP captured, end of free flight	8/1	0620
PDP parked over port wing	8/1	0644
Additional RMS-mounted observations ^a	8/2	1824
PDP latched in bay ^b	8/2	2241
PDP deactivation	8/6	0528
Landing	8/6	2000

^aPDP was used as a target for infrared glow observations.

^bPower to the PDP was occasionally cycled off for thermal considerations.

Pallet Operations

The PDP was carried into orbit while latched onto the Spacelab pallet and was returned to Earth in the same configuration. The initial activation and checkout were performed just a few hours after launch as soon as the payload bay doors were opened and the Spacelab support systems were activated. During the on-pallet operations early in the mission, the PDP was able to monitor the activation of other instruments from an electromagnetic interference point of view as well as observe the initial outgassing of the Orbiter and its payload.¹⁰ All PDP instruments were activated soon after the PDP was covered up with the exception of the Lepedea, which uses a

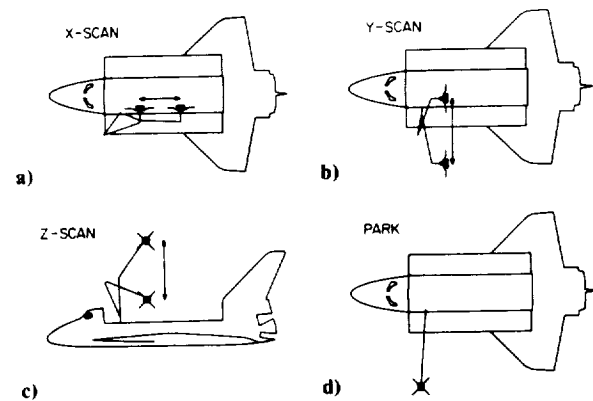


Fig. 3 Most of the RMS manipulations of the PDP during Spacelab 2 were the series of motions parallel to the principal axes of the Orbiter shown here. A few other special sequences were also used that are not shown here.

high-voltage power supply and is susceptible to coronal discharge prior to complete outgassing.

The PDP also spent the final four days of the mission positioned on the pallet while intensive solar and dark sky observations were being performed by other Spacelab investigations. During this time, the PDP passively monitored the payload bay environment and supported the VCAP electron beam experiments. The solar observations required a bay-toward-sun attitude for many orbits in succession, which led to overheating of a few of the PDP subsystems. In response to the overheating, the PDP was deactivated occasionally to allow tem-

peratures to return to acceptable values. No thermal damage was experienced despite the elevated temperatures.

RMS Operations

The PDP was grappled by the RMS at 1 day, 2 h, and 26 min into the mission (or mission elapsed time), corresponding to 2326 Greenwich Mean Time (GMT) on July 30, 1985. During the next 3 days, the PDP was manipulated actively by the RMS in studies of the Orbiter-ionosphere interaction and electron beam interactions, for a total data-gathering period of about 11 h. During the remaining portion of those 3 days, the PDP was either stowed in a noninterfering position over the port wing at a park point (Fig. 3d) or was in free flight.

During the active portion of the RMS operations, the PDP was moved about the Orbiter in a number of preprogrammed maneuvers in support of the various scientific objectives. Several of these maneuvers are depicted in Figs. 3a-c. The primary maneuvers moved the PDP longitudinally parallel to the roll axis of the Orbiter (*X* scans), or parallel to the pitch axis of the Orbiter (*Y* scans), or vertically up and down over a fixed location in the bay (*Z* scans). The maximum extension of the RMS is about 15 m. However, the PDP was never more than about 13 m from the Orbiter while attached to the RMS. At various times during the scans, the PDP could be rotated about its spin axis by the wrist actuator of the RMS so that instruments with directed fields of view could be swept through different look angles or pointed in various special directions, such as the velocity vector of the Orbiter.

The RMS programs were specialized to the PDP scientific objectives. For example, the *X* and *Y* scans were used to execute beam searches, i.e., to move the PDP through the electron beam to sample the region of direct beam-plasma interaction as well as the surrounding environment. One particularly useful maneuver coupled the rotation of the PDP about the

RMS wrist axis in one direction with the roll of the Orbiter in the opposite direction at identical rates such that the PDP was swept alternately through ram and wake orientations while holding a specific instrument's look direction parallel to the velocity vector of the Orbiter. This particular maneuver was designed to allow detailed studies of the near wake of the Orbiter.

Free Flight

The free-flight portion of the PDP operations was the most innovative part of the Spacelab 2 PDP investigation. This activity was not undertaken during the previous STS-3 mission, and we believe that the PDP free-flight experiments were the first of their type in space plasma physics. Several rocket experiments have included detached payloads for the diagnosis of beam interactions, but none have included both the active control of relative position and attitude for the purposes of studying vehicle-plasma interactions as well as the beam-plasma interactions, especially in conjunction with a large body such as the Orbiter.

The constraints on the free-flight activities were severe, especially from the point of view of time allotted against the requirements of other Spacelab 2 investigations and RCS propellant usage. The latter constraint was much more severe than planned due to the loss of about 2000 kg of OMS propellant during the abort-to-orbit procedure executed as a result of the premature shutdown of the center main engine on ascent.

The free-flight phase of the mission can be broken down into deployment and back-away, fly-around "ellipses," wake transits, and approach and recovery. The total time for the free flight was about 6 h. Figure 4 shows the relative trajectory of the Orbiter with respect to the PDP. The first panel shows the back-away and first fly-around ellipse. The second panel shows the second fly-around ellipse, wake transits, and approach. Three hours were utilized during the two orbits of fly-arounds depicted in Fig. 4. During the fly-around ellipses, the Orbiter was flown out of the orbit plane and to positions along the magnetic field line threading the PDP to look for Alfvén waves generated by the Orbiter and to do electron beam experiments. During the portion of the orbit when the Orbiter preceded the PDP in flight, the Orbiter was brought back into the PDP orbit plane to study the Orbiter's wake at distances between 50 and 250 m. When the Orbiter was in the cone on the left side of the panels in Fig. 4, it was in the plane of orbit of the PDP so that the Orbiter's wake would pass over the PDP at varying distances. In the remainder of the ellipses, the Orbiter was flown out of the PDP's orbit plane to intercept the magnetic field line threading the PDP.

The back-away and approach maneuvers were completed with the Orbiter upstream from the PDP, i.e., with the PDP in or near the wake of the Orbiter. This configuration allowed additional observations of the Orbiter's wake to be made at distances intermediate to those achieved while on the RMS and in the free-flight fly-around maneuvers. It was anticipated that, during the intervals when the PDP preceded the Orbiter at distances of over 300 m, the PDP might be able to sample the unperturbed ionospheric medium. However, the PDP was never far enough upstream to avoid the neutral gas cloud and its associated effects so that a truly ambient ionospheric observation could be made.

Summary of Results

Studies of the Shuttle Environment

Perhaps the most profound discovery of the PDP flight aboard Spacelab 2 is that the Orbiter is accompanied in the ionosphere by an extensive gas cloud of contaminants consisting primarily of water.^{6,7,10,11} This conclusion is consistent with observations made by the ion mass spectrometer,^{6,11} pressure gage,¹⁰ and Lepedea⁷ on the PDP. The Orbiter releases contaminants through the operation of the RCS thrusters, normal operation of the Orbiter fuel cells and cooling systems, leakage from pressurized vessels, and outgassing.

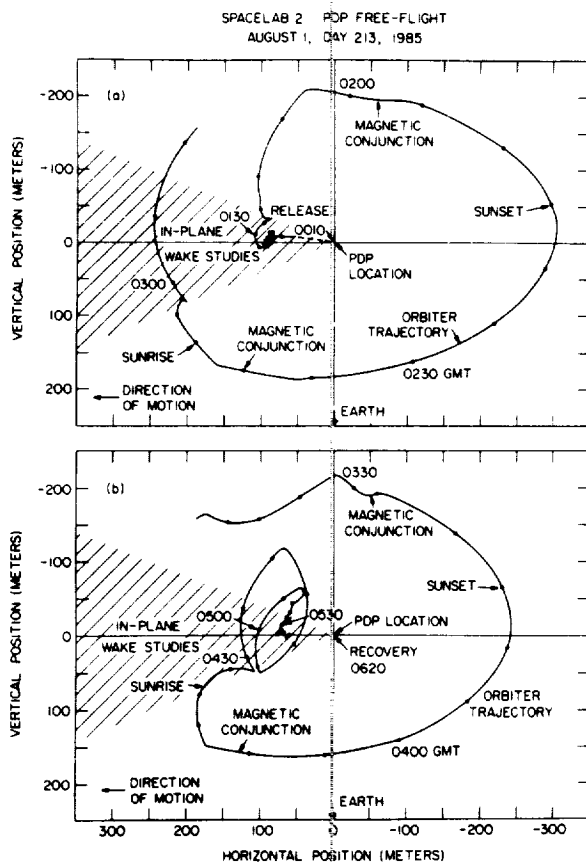


Fig. 4 Trajectory of the Orbiter with respect to the PDP during the free-flight portion of the Spacelab 2 mission. Top panel summarizes the release of the PDP through the completion of the first fly-around ellipse. Lower panel shows the second ellipse, final wake transits, and the approach for recovery.

The neutral water is subject to ionization by a number of processes in low Earth orbit with charge exchange with the ambient O^+ ions being the primary reaction. As ions are created, they are "picked up" immediately by the magnetic field sweeping through the cloud at the orbital velocity of the Orbiter, about 8 km/s, and, hence, form a highly anisotropic distribution of ions known as a "ring distribution." The Lepedea has measured these ring distributions from free-flight vantage points at several locations around the Orbiter.⁷ The measurements indicate a neutral water production rate of about $2.5 \times 10^{22} \text{ s}^{-1}$ from the Orbiter.⁷ The pickup ions form a long ion trail behind the Orbiter. At certain times, the contaminant water ions can actually be the dominant species in the region within a few meters of the Orbiter.⁶ A model of the neutral water cloud suggests that it has a density of 6×10^9 molecules cm^{-3} at 50 m from the Orbiter and extends to ~ 8 km with densities of $\geq 1 \text{ cm}^{-3}$.⁷

Since ring distributions are typically unstable to the generation of plasma waves, it is possible that these distributions are responsible for the broadband electrostatic waves observed in the vicinity of the Orbiter by the plasma wave receiver.^{9,12} This noise typically has a broad spectrum from a few hertz to 20–30 kHz. The broadband electric field strength of the turbulence is about 1–5 mV/m. The waves are generally most intense in the region downstream of the Orbiter, although high intensities are also observed near magnetic conjunctions. The wave intensity is correlated with RCS thruster activity, although some noise is still present when no thrusters are being fired.

The S- and K_u -band receivers were used to survey the electric fields associated with the operation of the Orbiter communication links at various locations around the payload bay.¹³ For those systems that avoid the main beam of the radar, the maximum field strength is less than 2 V/m. For those payload elements subjected to the main beam, a design guideline of 300 V/m provides an adequate safety margin at K_u band. The S-band fields measured were several decibels below the worst-case predictions. An instrument in the payload bay can expect to be subjected to S-band fields of magnitude < 2 V/m.

Wake Studies

The motion of the Orbiter through the ionosphere leads to the formation of a well-developed wake in the downstream region.^{14,15} The PDP was operated both on the RMS and in a free-flight path specifically designed to provide information on the characteristics of the wake both in the near vicinity of the Orbiter (within a body radius of the obstacle of about 10 m) and in the distant wake, out to about 250 m. From RMS and back-away observations, the density in the near wake can be two or more orders of magnitude less than the ambient density, whereas the electron temperature on the boundary of the wake region can be observed to increase by more than a factor of 2. At greater distances, the magnitude of the density depletion is less, sometimes only about 10%. One striking result, however, is that even at distances of 250 m, the wake is still well defined and of simple structure. There is no evidence of large-scale turbulence in the distant wake. It should be mentioned, however, that small-scale wavelike turbulence often characterizes the boundary of the wake region¹⁵; it is possible that this turbulence is similar in character to the broadband electrostatic noise discussed earlier.

Some work on comparisons of the Spacelab 2 PDP wake observations with wake models has been completed.¹⁶ The model used in these comparisons is the Polar code,¹⁷ which neglects the magnetic field and uses a self-similar solution to the expansion of a plasma into a vacuum as its foundation. The observed electron and ion densities measured by the PDP during passages through the Orbiter's wake at distances out to a few hundred meters are compared with predictions of the model. In the distance range less than 30 m, the model underestimates the density by as much as an order of magnitude; the presumption is that outgassing from the Orbiter can be a substantial contributor to the wake density within a few body

scale sizes. Beyond 30 m, the agreement is very good (within about 10%) between the model and observations, provided one allows for variations in the ambient density with position as predicted by the International Reference Ionosphere model.¹⁸ The observations show a lack of fine structure in the density of the wake and are, therefore, consistent with the behavior of wakes in regimes where the ion and electron temperatures are similar. Comparisons of the wake observations and the collisionless plasma expansion model¹⁹ suggest that the plasma wake of the Orbiter closes much faster than predicted by simple thermal expansion, implying that the ions filling the wake have been accelerated. Furthermore, some minor inconsistencies in the depth of the wake as a function of distance from the Orbiter observed by the PDP are evidence for crossing ion streams¹⁵ such as those observed in laboratory plasmas.²⁰

Beam-Plasma Interactions

The PDP and VCAP jointly designed numerous experiments for the Spacelab 2 mission for the purpose of understanding various aspects of the interaction of an energetic (1 keV) electron beam with the ionospheric plasma. One of the primary characteristics of the interaction is the generation of waves. Early studies have concentrated on whistler mode waves, called "VLF hiss"²¹ which are thought to be generated via a coherent Cerenkov process associated with bunching of electrons in the continuously firing beam.^{22,23} The VLF hiss was detected easily because of a funnel-shaped frequency-time signature observed in the plasma wave data set. The funnel-shaped spectrum is a result of well-understood propagation characteristics of the whistler mode waves and leads to an understanding of the beam emissivity as a function of distance along the beam. Further studies^{8,24,25} involve wave generation by a pulsed beam, where the pulsing frequency of the beam is in the VLF range. The resultant waves are found at harmonics of the pulsing frequency.

Other studies concerning the interaction of the electron beam with the ionosphere include the dc electric fields set up in the vicinity of the beam in response to the current systems driven by the beam.²⁶ Analysis of the PDP Lepedea measurements of electrons associated with the beam-plasma interaction demonstrates that there is a narrow sheet of energetic electrons in the wake of the Orbiter.²⁷ This sheet of electrons is threaded by magnetic field lines from the upstream injection of the primary electron beam. Numerical simulations of the beam-plasma interaction show the generation of low-frequency, broadband electrostatic waves similar to those observed by the plasma wave receiver.

Conclusions

The Plasma Diagnostics Package investigation on the Spacelab 2 mission was extremely successful. Virtually 95% of the objectives of the investigation were achieved, and the results referred to in the previous section attest to the scope of the science results obtained during the flight. Those 5% of the objectives that were not met owing to the shortage of Reaction Control System (RCS) propellant were primarily experiments that involved the firing of RCS thrusters in a predetermined way to measure their effects and those experiments that were to have been performed during a planned, third orbit of fly-around. The thruster-associated objectives were partially achieved via coincidental firings of RCS thrusters during the execution of various maneuvers. The loss of the third orbit of fly-arounds resulted primarily in the loss of repetitions of experiments achieved during the first two orbits.

Acknowledgments

The research at the University of Iowa was supported by NASA through Contract NAS8-32807 with the Marshall Space Flight Center (MSFC) and Grant NAG3-449 from Lewis Research Center.

The Plasma Diagnostics Package (PDP) project would not have been possible without the support of a large number of people at the University of Iowa and within NASA. Unfortunately, we cannot mention all of those persons here. However, we do wish to commend the flight crew—C. G. Fullerton, R. D. Bridges Jr., A. England, S. Musgrave, K. G. Henize, J. -D. Bartoe, and L. W. Action—and the alternate payload specialists—G. Simon and D. Prinz—for their excellent job of carrying out the mission. We would also like to acknowledge the MSFC mission management team under R. C. Lester, the planning and operations teams under S. Perrine and A. Roth, and the data management team under M. Rives. B. Gwynes, D. Talley, R. Adams, W. Claunch, and B. Soutullo all served the PDP project as our MSFC liaison and assured the success of the project. We thank E. Urban for his role as mission scientist. We are indebted to the mission planning and operations team at the Johnson Space Center, including K. Cannon, A. Austin, and M. Veres, as well as the payload integration team at the Kennedy Space Center, especially E. Lunceford. At the University of Iowa, we express our appreciation for the professional job performed by the spacecraft engineering team under the direction of R. F. Randall, the operations team led by G. B. Murphy, and the data analysis team headed by R. L. Brechwald and J. S. Pickett. Finally, we would like to take this opportunity to recognize S. D. Shawhan as the individual responsible for conceiving the PDP and its implementation through its first flight on STS-3 and through a substantial portion of its refurbishment for Spacelab 2.

References

- ¹Shawhan, S. D., Murphy, G. B., and Pickett, J. S., "Plasma Diagnostics Package Initial Assessment of the Shuttle Orbiter Plasma Environment," *Journal of Spacecraft and Rockets*, Vol. 21, July-Aug. 1984, pp. 387-391.
- ²Samir, U. and Wrenn, G. L., "Experimental Evidence of an Electron Temperature Enhancement in the Wake of an Ionospheric Satellite," *Planetary and Space Science*, Vol. 20, No. 6, 1972, pp. 899-904.
- ³Samir, U. and Fontheim, E. G., "Comparison of Theory and 'In Situ' Observations for Electron and Ion Distributions in the Near Wake of the Explorer 31 and AE-C Satellites," *Planetary and Space Science*, Vol. 29, No. 9, 1981, pp. 975-987.
- ⁴Mendillo, M., Baumgardner, J., Allen, D. P., Foster, J., Holt, J., Ellis, G. R. A., Klekocivk, A., and Reber, G., "Spacelab 2 Plasma Depletion Experiments for Ionospheric and Radio Astronomical Studies," *Science*, Vol. 238, 1987, pp. 1260-1264.
- ⁵Bernhardt, P. A., Swartz, W. E., Kelley, M. C., Tepley, C. A., and Sulzer, M. P., "Radar and Optical Observations During the Spacelab 2 Plasma Depletion Experiment over Arecibo," Symposium on Active Experiments, Communications on Space Research, Toulouse, France, June 1986.
- ⁶Grebowsky, J. M., Taylor, H. A., Jr., Pharo, M. W. III, and Reese, N., "Thermal Ion Perturbations Observed in the Vicinity of the Space Shuttle," *Planetary and Space Science*, Vol. 35, No. 4, April 1987, pp. 501-513.
- ⁷Paterson, W. R. and Frank, L. A., "Hot Ion Plasmas from the Cloud of Neutral Gases Surrounding the Space Shuttle," *Journal of Geophysical Research*, Vol. 94, No. A4, 1989, pp. 3721-3727.
- ⁸Bush, R. I., Reeves, G. D., Banks, P. M., Neubert, T., Williamson, P. R., Raitt, W. J., and Gurnett, D. A., "Electromagnetic Fields from Pulsed Electron Beam Experiments in Space: Spacelab 2 Results," *Geophysical Research Letters*, Vol. 14, No. 10, 1987, pp. 1015-1018.
- ⁹Gurnett, D. A., Kurth, W. S., Steinberg, J. T., and Shawhan, S. D., "Plasma Wave Turbulence Around the Shuttle: Results from the Spacelab-2 Flight," *Geophysical Research Letters*, Vol. 15, No. 8, 1988, pp. 760-763.
- ¹⁰Pickett, J. S., Murphy, G. B., and Kurth, W. S., "Gaseous Environment of the Shuttle Early in the Spacelab 2 Mission," *Journal of Spacecraft and Rockets*, Vol. 25, March-April 1988, pp. 169-174.
- ¹¹Grebowsky, J. M., Taylor, H. A., Jr., Pharo, M. W. III, and Reese, N., "Thermal Ion Complexities Observed Within the Spacelab 2 Bay," *Planetary and Space Science*, Vol. 35, No. 11, 1987, pp. 1463-1469.
- ¹²Hwang, K. S., Stone, N. H., Wright, K. H., Jr., and Samir, U., "The Emissions of Broadband Electrostatic Noise in the Near Vicinity of the Shuttle Orbiter," *Planetary and Space Science*, Vol. 35, No. 11, 1987, pp. 1373-1379.
- ¹³Murphy, G. B. and Cutler, W. D., "Orbiter Environment at S- and K_u-Band Frequencies," *Journal of Spacecraft and Rockets*, Vol. 25, Jan.-Feb. 1988, pp. 81-87.
- ¹⁴Murphy, G. B., Reasoner, D. L., Tribble, A., D'Angelo, N., Pickett, J. S., and Kurth, W. S., "The Plasma Wake of the Shuttle Orbiter," *Journal of Geophysical Research* Vol. 94, No. A6, 1989, pp. 6866-6872.
- ¹⁵Tribble, A. C., Pickett, J. S., D'Angelo, N., and Murphy, G. B., "Plasma Density, Temperature, and Turbulence in the Wake of the Shuttle Orbiter," *Planetary and Space Science* (to be published), 1989.
- ¹⁶Murphy, G. and Katz, I., "The Polar Code Wake Model: Comparison with In-Situ Observations," *Journal of Geophysical Research*, Vol. 94, No. A7, 1989, pp. 9065-9070.
- ¹⁷Katz, I., Parks, D. E., and Wright, K. H. Jr., "A Model of the Plasma Wake Generated by a Large Object," *IEEE Transactions on Nuclear Science*, Vol. NS-32, No. 6, 1985, pp. 4092-4096.
- ¹⁸Lincoln, J. V. and Conkright, R. O., "International Reference Ionosphere—IRI 79," Rept. UAG-82, World Data Center A for Solar-Terrestrial Physics, Boulder, CO, 1981.
- ¹⁹Stone, N. H., Wright, K. H., Samir, U., and Hwang, K. S., "On the Expansion of Ionospheric Plasma into the Near-Wake of the Space Shuttle Orbiter," *Geophysical Research Letters*, Vol. 15, No. 10, 1988, pp. 1169-1172.
- ²⁰Merlino, R. L. and D'Angelo, N., "The Interaction of a Conducting Object with a Supersonic Plasma Flow: Ion Deflection Near a Negatively Charged Obstacle," *Journal of Plasma Physics*, Vol. 37, Pt. 2, 1987, pp. 185-198.
- ²¹Gurnett, D. A., Kurth, W. S., Steinberg, J. T., Banks, P. M., Bush, R. I., and Raitt, W. J., "Whistler-Mode Radiation from the Spacelab 2 Electron Beam," *Geophysical Research Letters*, Vol. 13, No. 3, 1986, pp. 225-228.
- ²²Farrell, W. M., Gurnett, D. A., Banks, P. M., Bush, R. I., and Raitt, W. J., "An Analysis of Whistler Mode Radiation from the Spacelab 2 Electron Beam" *Journal of Geophysical Research*, Vol. 93, No. A1, 1988, pp. 153-161.
- ²³Farrell, W. M., Gurnett, D. A., and Goertz, C. K., "Coherent Cerenkov Radiation from the Spacelab 2 Electron Beam," *Journal of Geophysical Research*, Vol. 94, No. A1, 1989, pp. 443-452.
- ²⁴Reeves, G. D., Banks, P. M., Fraser-Smith, A. C., Neubert, T., Bush, R. I., Gurnett, D. A., and Raitt, W. J., "VLF Wave Stimulation by Pulsed Electron Beams Injected from the Space Shuttle," *Journal of Geophysical Research*, Vol. 93, No. A1, 1988, pp. 162-174.
- ²⁵Neubert, T., Hawkins, J. G., Reeves, G. D., Banks, P. M., Bush, R. I., Williamson, P. R., Gurnett, D. A., and Raitt, W. J., "Pulsed Electron Beam Emission in Space," *Journal of Geomagnetism and Geoelectricity*, Vol. 40, No. 10, 1988, pp. 1221-1233.
- ²⁶Steinberg, J. T., Gurnett, D. A., Banks, P. M., and Raitt, W. J., "Double-Probe Potential Measurements Near the Spacelab 2 Electron Beam," *Journal of Geophysical Research*, Vol. 93, No. A9, 1988, pp. 10,001-10,010.
- ²⁷Frank, L. A., Paterson, W. R., Ashour-Abdalla, M., Schriver, D., Kurth, W. S., Gurnett, D. A., Omid, N., Banks, P. M., Bush, R. I., and Raitt, W. J., "Electron Velocity Distributions and Plasma Waves Associated with the Injection of an Electron Beam into the Ionosphere," *Journal of Geophysical Research*, Vol. 94, No. A6, 1989, pp. 6995-7001.

PLASMA DENSITY, TEMPERATURE AND TURBULENCE IN THE WAKE OF THE *SHUTTLE ORBITER*

A. C. TRIBBLE,* J. S. PICKETT, N. D'ANGELO and G. B. MURPHY†

Department of Physics and Astronomy, The University of Iowa, Iowa City, IA 52242, U.S.A.

(Received in final form 21 February 1989)

Abstract—Plasma density, temperature, and turbulence in the near, mid, and far wake of the *Shuttle orbiter* are examined on the basis of *in situ* observations by The University of Iowa *Plasma Diagnostics Package (PDP)*. These observations, the only such measurements in the mid and far wake of the *orbiter*, indicate that plasma disturbances produced by the passage of the *orbiter* extend downstream for a distance of several hundred meters behind the *orbiter*. The electron density profile is found to exhibit nonmonotonic behavior. Most of the 6–40 Hz turbulence in the wake is confined to a region ≈ 20 m downstream of the *orbiter*. $\Delta N_e/N_e$ spectra show a rapid decline in the 10^3 – 10^5 Hz decade, both in the ambient ionosphere and in the wake.

INTRODUCTION

The interaction of a large object with a flowing plasma is an important topic of study in the field of space physics. A satellite in the Earth's ionosphere is a practical example of such a situation and a number of studies have been conducted regarding the interaction of small satellites with the ionosphere (Martin, 1974; Samir and Wrenn, 1969, 1972; Illiano and Storey, 1974; Troy *et al.*, 1975; Samir and Willmore, 1965; Henderson and Samir, 1967; Samir, 1981; Stone and Samir, 1981). However, it is only very recently that measurements of plasma parameters in the vicinity of the *Shuttle orbiter* have allowed researchers to study the interaction of a large body with the ionospheric plasma (Murphy *et al.*, 1986; Raitt *et al.*, 1984). Unfortunately, these large body observations have been restricted to measurements of the electron density and temperature in the near wake of the object. An examination of conditions in the far wake of a large orbiting satellite, such as the *Shuttle orbiter*, is needed to help determine the spatial extent of the wake. At the same time, an examination of the density fluctuations in the wake is warranted since density fluctuations often affect the behavior of the plasma phenomena (Kadomtsev, 1965). In this paper we shall present measurements of the plasma turbulence in the near, mid, and far wake of the *orbiter* and relate these to the spatial density and temperature gradients.

* Presently at: Rockwell International, Satellite and Space Electronics Division, Seal Beach, CA 90740, U.S.A.

† Presently at: Jet Propulsion Laboratory, Pasadena, CA 91109, U.S.A.

THE INSTRUMENT

From 29 July to 6 August 1985 a University of Iowa satellite, the *Plasma Diagnostics Package (PDP)* (Fig. 1) was flown as part of the payload on *Space Shuttle* flight STS-51F, the *Spacelab 2* mission. A Langmuir probe on the *PDP* was used to make measurements of the electron density, the electron temperature, and the fluctuations in electron density. The Langmuir probe experiment consisted of a 3 cm diameter, gold-plated sphere, which was mounted on one of the *PDP*'s extendable booms, and supporting electronics.

The electronics that controls the probe alternates between two different modes, one complete cycle requiring 12.8 s. The first part of the cycle is an 11.8 s "lock" mode. During this time the Langmuir probe is biased at +10 V, relative to the *PDP* chassis. The current that is collected by the probe is passed through three filters, 1 Hz low-pass, 1–6 Hz band-pass, and 6–40 Hz band-pass, with sampling rates of 5, 20, and 120 Hz, respectively. These three channels give density fluctuation data in their respective frequency ranges. The 1 Hz low-pass filter also provides a continuous density monitoring. Following the lock mode is a 1.0 s "sweep" mode where the bias voltage on the probe is swept from +10 to –5 V in discrete steps of 0.125 V, and then returned to +10 V. The sweep mode data are used to determine the electron density and temperature in the usual manner. In addition, once every 6.83 min, for a period of 51.2 s the output from the Langmuir probe is routed through a 30 Hz high-pass filter to a wideband receiver and spectrum analyzer which can look at details of the current fluctuations up to a frequency of 178 kHz.

PDP BOOMS DEPLOYED CONFIGURATION

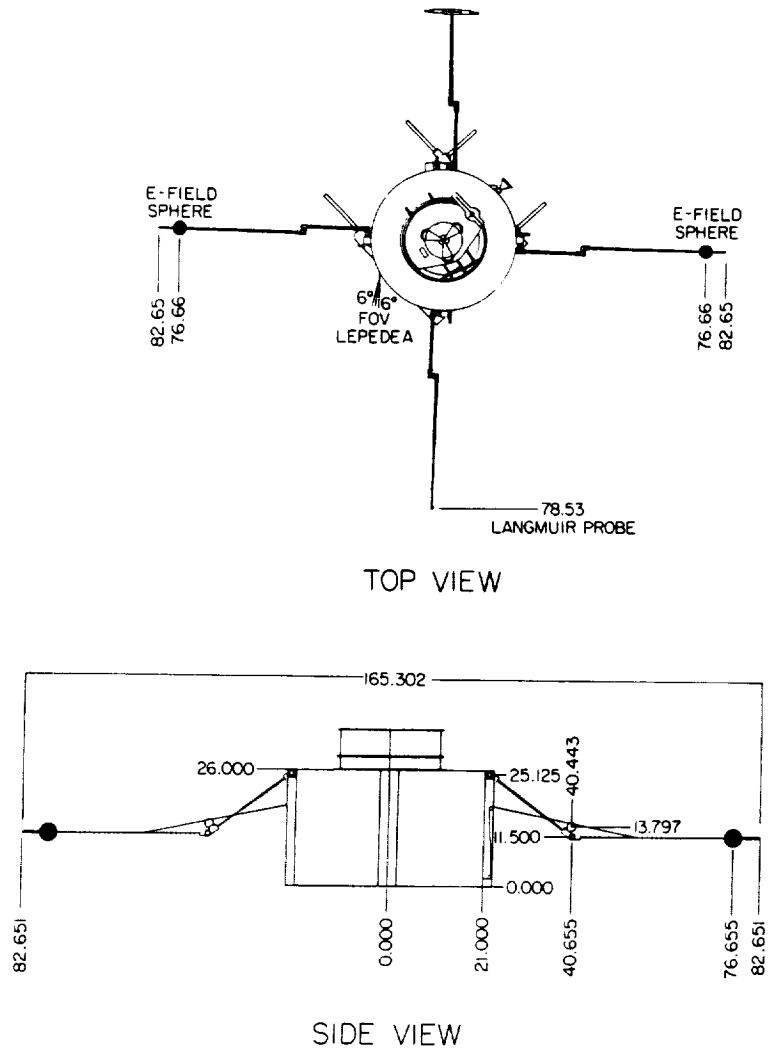


FIG. 1. THE *Plasma Diagnostics Package*.
Relevant distances are indicated in inches from the center of the *PDP*.

The spectrum analyzer consists of 16 channels. Their outputs provide an amplitude spectrum of the turbulence. Table 1 shows channel numbers, center frequencies, saturation $\Delta N_e/N_{cs}$ and bandwidths. Subsequent to the mission, four of the channels (3, 5, 7, 9) were found to behave unsatisfactorily and have, thus, been excluded from the analysis.

For a more complete discussion of the operation of the Langmuir probe, including a discussion of the errors associated with the measurement of the plasma parameters in question, see Murphy *et al.* (1986). A list of some of the ionospheric plasma characteristics

associated with the *Spacelab 2* mission is presented in Table 2.

THE EXPERIMENT

The data that we will present were obtained during two separate maneuvers designed to allow the *PDP* to study both the near and far wake of the *orbiter*. The maneuver designed for near wake studies involved placing the *PDP* on the Remote Manipulator System (RMS) a distance of 10.5 m above the center of the payload bay with the *PDP*'s booms partially

TABLE 1. SPECTRUM ANALYZER CHARACTERISTICS

Channel	Center frequency (kHz)	Saturation $\Delta N_e/N_e$	Bandwidth (Hz)
0	0.0355	0.113	16
1	0.0633	0.057	22
2	0.120	0.090	35
3	0.200	—	—
4	0.311	0.226	89
5	0.562	—	—
6	1.00	0.226	353
7	1.78	—	—
8	3.11	0.113	910
9	5.62	—	—
10	10.0	0.113	2,000
11	16.5	0.226	2,780
12	31.1	0.226	3,550
13	56.2	0.226	7,110
14	100	0.226	11,300
15	178	0.180	12,200

TABLE 2. TYPICAL PARAMETERS FOR Spacelab 2

Electron density	$n_0 \approx 1-5 \times 10^5 \text{ cm}^{-3}$
Electron (and ion) temperature	$T_e \approx T_i \approx 2500 \text{ K}$
Debye length	$\lambda_D \approx 1 \text{ cm}$
Ion acoustic speed	$C_s \approx 2.3 \text{ km s}^{-1}$
Electron thermal speed	$v_{e,th} \approx 200 \text{ km s}^{-1}$
Orbital velocity	$v_0 \approx 7.7 \text{ km s}^{-1}$
Orbital altitude	$h \approx 320 \text{ km}$
Electron plasma frequency	$f_{p,e} \approx 2.8-6.3 \text{ MHz}$
Ion plasma frequency	$f_{p,i} \approx 17-38 \text{ kHz}$
Ion gyroradius	$\rho_i \approx 5 \text{ m}$

extended. By keeping the *X*-axis of the orbiter perpendicular to the orbital plane and rolling the orbiter at a rate of 1° s^{-1} , the *PDP* was moved into and out of the orbiter's wake (Fig. 2). This maneuver is referred to as XPOP roll. At the same time, the RMS was rotated at the same rate as the orbiter roll so that the orientation of the *PDP*, relative to the plasma flow,

remained unchanged. In the plane of rotation the biggest obstacles to plasma flow were the orbiter's payload bay doors, which are $\approx 10.6 \text{ m}$ wide. If we define *W* to be the width of our obstacle, 10.6 m , and *R* the downstream distance of the Langmuir probe, 10.5 m , the relevant *W/R* during the XPOP roll was ≈ 1 .

Later in the mission, for a period of 6 h, the *PDP* was released as a free-flying satellite in order to allow the *PDP* to study the mid and far wake of the orbiter. During this time the booms seen in Fig. 1 were extended to their full length. After release from the orbiter the *PDP* was spin stabilized with an inertial spin period of 13.06 s. The plane of *PDP* rotation was

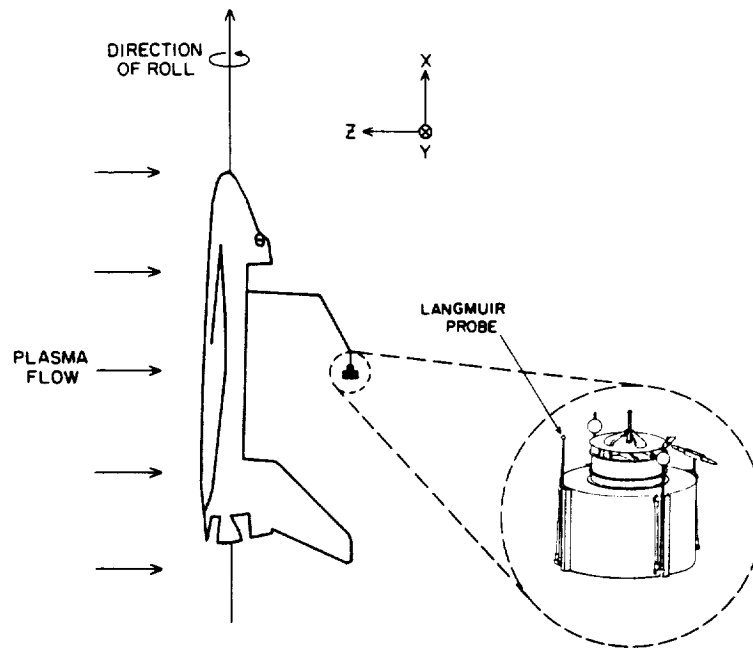


FIG. 2. XPOP ROLL. This maneuver was used to study the near wake of the Shuttle orbiter.

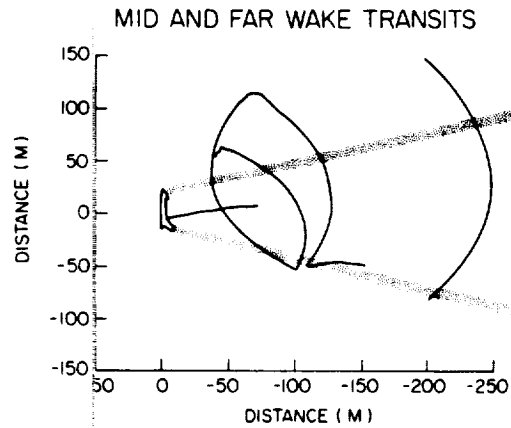


FIG. 3. THE TRAJECTORY OF THE PDP, RELATIVE TO THE Shuttle orbiter, DURING TRANSITS OF THE orbiter'S MID AND FAR WAKE.

coincident with the orbital plane. During this period of 6 h the orbiter executed a series of maneuvers around the PDP designed to allow the PDP to study the wake of the orbiter. The trajectory of the PDP, in a non-inertial coordinate system which uses the orbiter as its origin, during the time that the PDP was in the orbiter's wake is shown in Fig. 3. Table 3 gives times and geographical coordinates of wake transits. The data obtained during the "wake transits" seen in Fig. 3 represent the only *in situ* observations of the mid and far wake of the Shuttle orbiter.

ELECTRON DENSITIES AND TEMPERATURES

Electron density and temperature data obtained while the PDP was on the RMS were presented by Murphy *et al.* (1986) for the OSS-1 mission. Some near wake density profiles for the Spacelab 2 mission are given in the next section for purposes of comparison with the 6-40 Hz turbulence. In this section we concentrate on density and temperature measurements obtained during the PDP free flight.

TABLE 3. UNIVERSAL TIME AND GEOGRAPHICAL COORDINATES FOR WAKE TRANSITS OF FIG. 3

Wake transit downstream distance (m)	U.T.		
	Day 213, 1985 (h:min)	Latitude (degrees)	Longitude (degrees)
45	04:49	+5	125 E
100	04:59	+34	153 E
120	04:32	-41	77 E
240	03:04	-35	111 E

Due to the spin of the PDP some measurements in the wake of the orbiter were unusable because the Langmuir probe periodically passed through the wake of the PDP itself. That is, some measurements were affected by the electron density depletions and temperature enhancements associated with the PDP wake. These are illustrated, for times when the PDP was not in the wake of the orbiter, in Fig. 4. Fortunately, knowing the orientation of the PDP allows us to restrict our attention to data taken when the Langmuir probe was not in the PDP wake. Similarly, problems that arose due to spacecraft charging, Tribble *et al.* (1988), further limited the amount of available data. However, a sufficient amount of "unaffected" data remained to allow for an extensive analysis of the orbiter wake conditions.

For brevity the data obtained during each wake transit (Fig. 3) will not be presented here. However, by combining the data obtained during each of the individual wake transits, we were able to obtain one large scale picture of the conditions in the orbiter's wake. Knowledge of the electron density depletions,

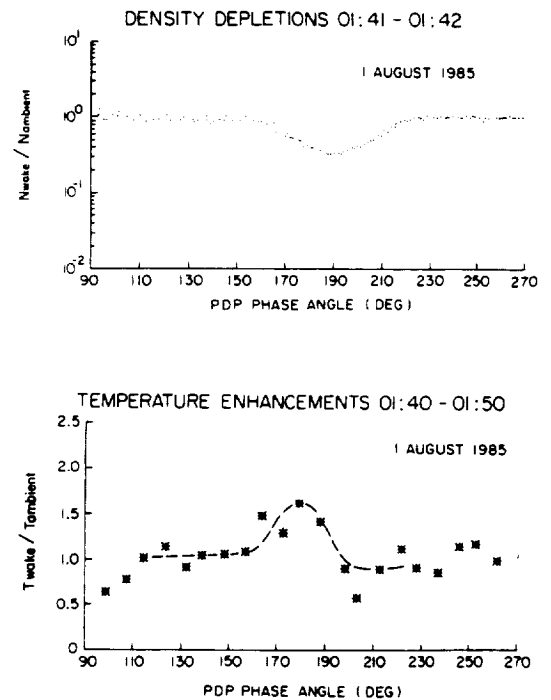


FIG. 4. THE ELECTRON DENSITY DEPLETIONS AND TEMPERATURE ENHANCEMENTS ASSOCIATED WITH THE WAKE OF THE PDP. The PDP phase angle is defined as the angle between the PDP velocity vector and the vector that points from the center of the PDP to the Langmuir probe, when viewed from the top of the PDP.

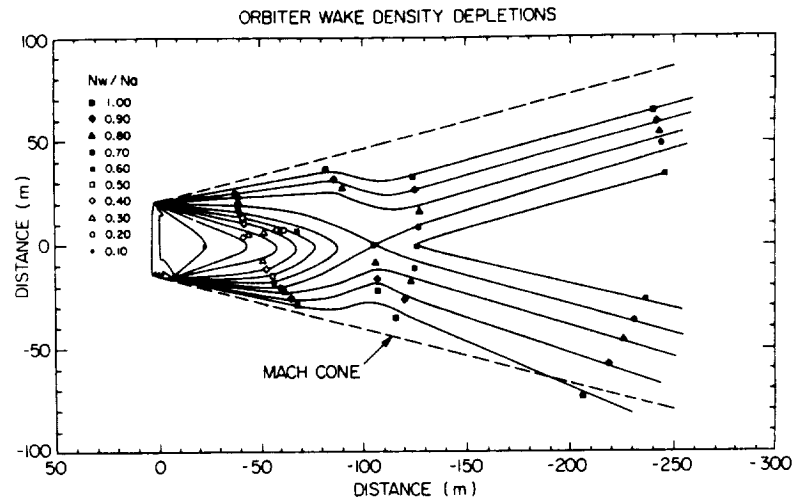


FIG. 5. ELECTRON DENSITY DEPLETIONS IN THE WAKE OF THE Shuttle orbiter. The contours represent constant values of N_w/N_a . The Mach cone was calculated assuming an electron/ion temperature of 2500 K.

N_w/N_a , for each transit (N_w being the electron density measured in the wake and N_a the ambient density) can be used to define the contours of constant density in the wake of the orbiter (Fig. 5). In Fig. 5 plasma flow is from left to right and the orbiter's Mach cone is indicated by the dashed lines. Again, this figure is particularly significant in that it represents the only *in situ* observations of the mid and far wake of a large object in low Earth orbit. In Fig. 5 we calculated N_a by interpolating the ambient density from one side of the wake to the other during the course of each wake transit. The wake transit 240 m downstream of the orbiter had a slight inclination with respect to the orbital plane of Fig. 3. Some of these data points were taken when the PDP was as much as 15 m out of the orbital plane. The largest obstacles to plasma flow perpendicular to the orbital plane are the orbiter's payload bay doors. Since the orbiter's bay doors are only ≈ 10.6 m wide when fully opened, the density depletions downstream of the orbiter in the orbital plane at the distance of the farthest wake transit may be somewhat greater than those measured by the PDP.

Attempts to obtain contours for the electron temperature enhancements measured in the orbiter's wake were not as successful. Since measurements of T_e are obtained only during the sweep mode, once every 12.8 s, many of the temperature data points in the wake of the orbiter happened to be taken when the Langmuir probe was in the wake of the PDP as well. Those points cannot be used to obtain a good estimate of

the temperature enhancement that is associated with the wake of the orbiter since they will, at least in part, be affected by the temperature enhancement that is associated with the wake of the PDP itself. However, the data taken when the Langmuir probe was not in the wake of the PDP indicate a definite temperature enhancement in the wake of the orbiter, all the way to $Z \approx -240$ m (Fig. 6).

NEAR WAKE TURBULENCE

Turning to the turbulence data, we begin by presenting the XPOP roll data in terms of an orbiter phase angle, which we define as the angle, in the orbiter's YZ-plane, between the orbiter velocity vector and the vector that points from the center of mass of the orbiter to the PDP. A phase angle of 180° indicates that the center of the PDP is directly in the orbiter wake. We will restrict our attention initially to the 6–40 Hz plasma turbulence data, typical examples of which are given in Fig. 7. In Figs 7a–c the top panels present the percentage density fluctuations, $\Delta N_e/N_e$, in the 6–40 Hz channel, while the bottom panels provide the corresponding density profiles. For the ionospheric conditions similar to those encountered for Fig. 7 we calculate that the Langmuir probe would cross the orbiter's Mach cone at phase angles of $\approx 140^\circ$ and $\approx 230^\circ$. The turbulence apparently decreases to below ambient levels when the probe is directly on axis. There is also some tendency for the turbulence

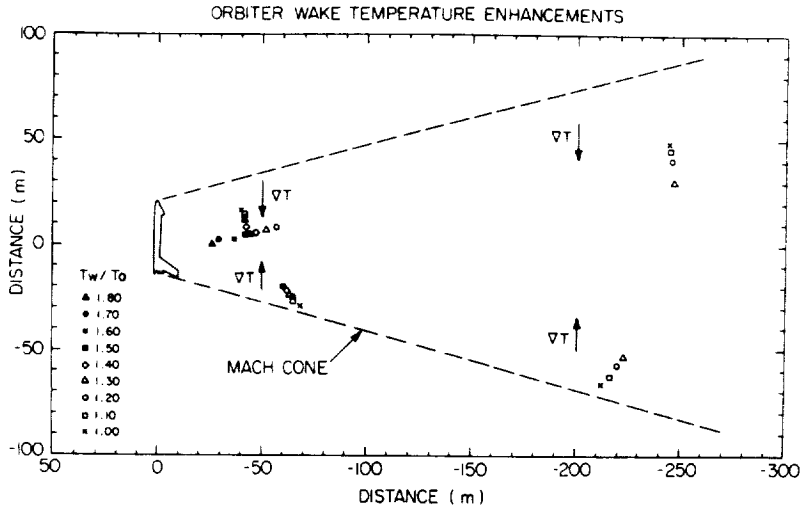


FIG. 6. ELECTRON TEMPERATURE ENHANCEMENTS IN THE WAKE OF THE Shuttle orbiter.

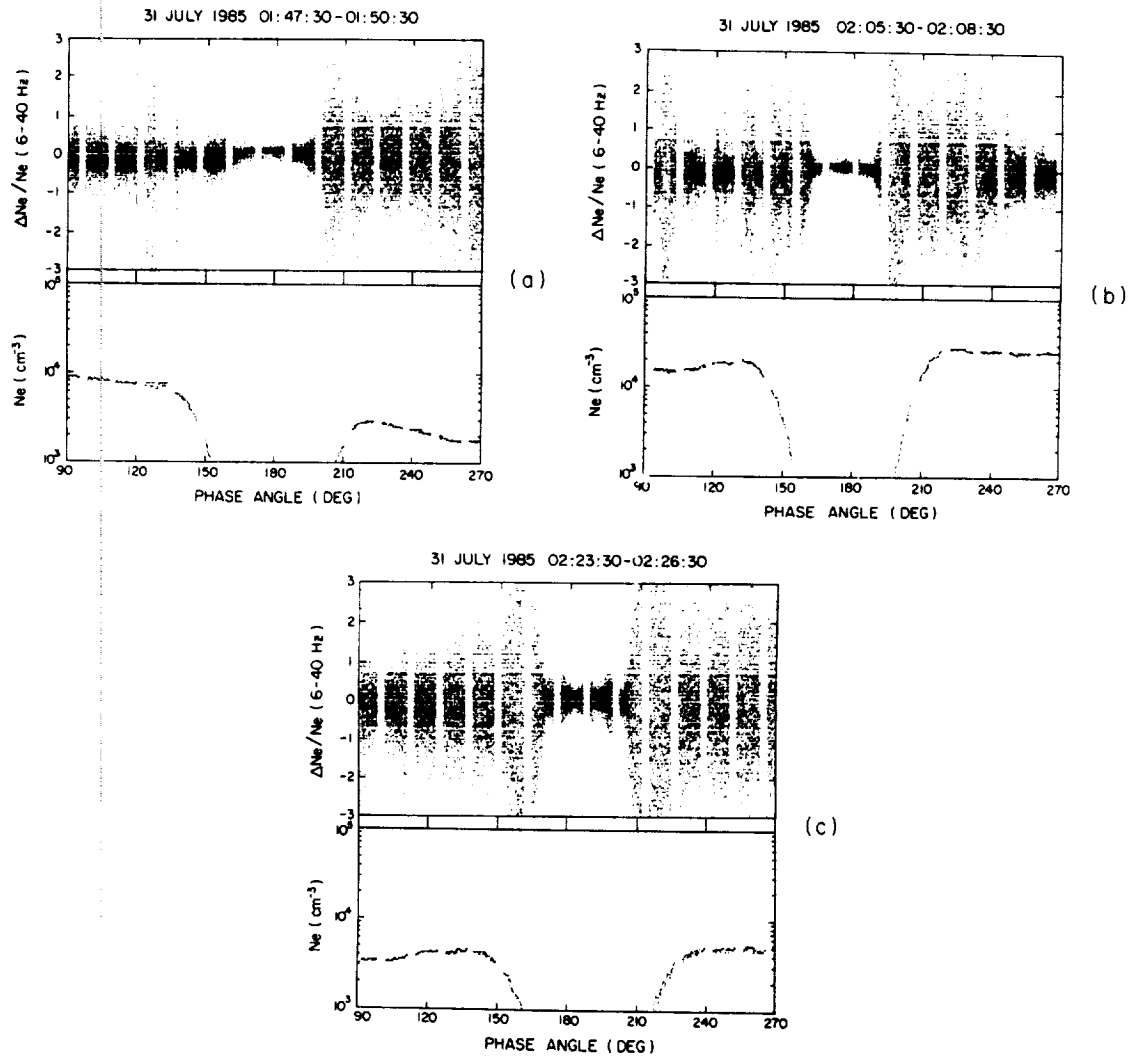


FIG. 7. EXAMPLES OF 6-40 Hz TURBULENCE IN THE NEAR WAKE OF THE Shuttle orbiter (TOP PANELS); CORRESPONDING DENSITY PROFILES (BOTTOM PANELS).

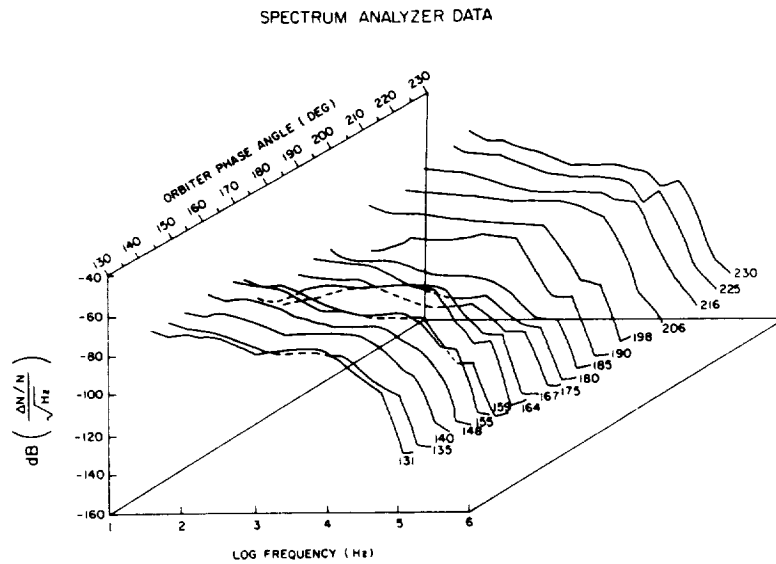


FIG. 8. THE SPECTRAL DENSITY OF $\Delta N_e/N_e$ DURING A TRANSIT OF THE NEAR WAKE OF THE orbiter.

to be stronger near wake edges. The reduction of the turbulence on wake axis may be a result of there being so little plasma that the sensor is operating near the limit of (or outside) its dynamic range. On the other hand, the decrease of $\Delta N_e/N_e$ seen near the wake edges as one moves inward toward the axis, is believed to be a real effect. Further confidence in the reality of turbulence reduction on the axis is gained by comparing the turbulence features of, for example, Fig. 7a with those of Fig. 7b and/or Fig. 7c.

The spectrum analyzer data allow us to look at higher frequency turbulence in the near wake of the orbiter as well (Fig. 8). This figure is composed of data from three separate 51.2 s measuring periods. The data presented in Fig. 8 that correspond to phase angles less than 154° were taken 6.83 min earlier than those corresponding to phase angles between 159° and 204° . Similarly, the data corresponding to phase angles between 159° and 204° were taken 6.83 min earlier than those corresponding to phase angles greater than 209° . Changing ionospheric conditions during these time periods may have an effect on the shape of the signatures seen in Fig. 8, but we do not believe these changes to be significant in comparison with wake effects.

Notice first that in all cases there seems to be an appreciable drop in the spectral density of $\Delta N_e/N_e$ for frequencies higher than $f_{p,i}$, which we calculate to be ≈ 17 kHz assuming an O^+ ion density of $1 \times 10^5 \text{ cm}^{-3}$. Also, there do not appear to be any appreciable changes in the signature of the spectrum analyzer data

until we are well within the Mach cone. When we cross the Mach cone at 142° we must proceed to a phase angle of 155° before we notice a significant difference, an enhancement of about 5 dB in the spectral density in the 31.1 kHz channel. Similarly, this enhancement disappears once we have passed a phase angle of 198° , well before exiting the Mach cone at 228° . It is also worth noting the spectral density signature at phase angles of about 165° . Here the spectral density seen by the lower frequency channels is depressed by about 10 dB while the spectral density of the middle channels seems unaffected. This situation is reversed in the vicinity of 180° where the lower frequency spectral density increases to almost ambient levels and the middle frequency spectral density decreases by about 5 dB. The decrease in the spectral density of the lower frequency channels is repeated, to a lesser degree, at a phase angle of 190° .

MID AND FAR WAKE TURBULENCE

As might be expected, the turbulence measured in the mid and far wake of the PDP was not as intense as the turbulence seen in the near wake. This is especially evident in the 6–40 Hz channel data. An examination of all of the 6–40 Hz data taken when the PDP was in the wake of the orbiter indicated that the only appreciable enhancements occurred very near the orbiter. Figure 9 shows data collected by the PDP immediately after it was released from the orbiter along the trajectory found in Fig. 3 that connects to

6-40 Hz DATA 00:11 - 00:20

1 AUGUST 1985

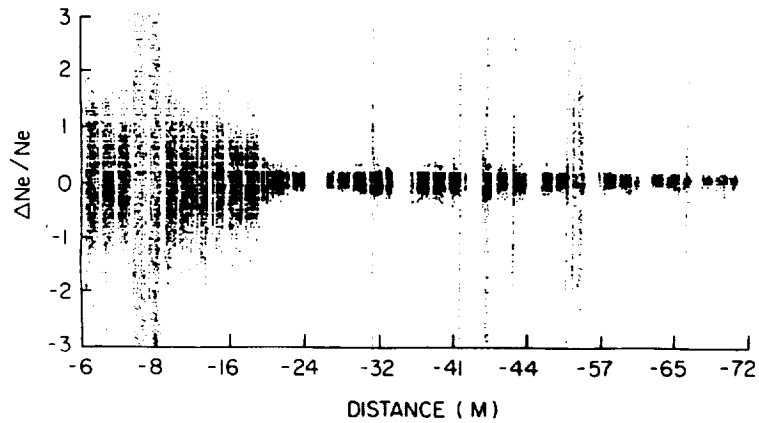


FIG. 9. 6-40 Hz TURBULENCE IMMEDIATELY DOWNSTREAM OF THE *Shuttle orbiter*. The distance scale is not linear due to variations in the velocity with which the orbiter and the PDP separated.

the *orbiter* and extends downstream for a distance of ≈ 75 m. The distance scale in Fig. 9 indicates the downstream distance from the *orbiter* to the PDP. This scale is slightly nonlinear because the velocity of the *orbiter*, relative to the PDP, during the backaway maneuver was not constant. Large "enhancements" associated with the firing of the *orbiter* thrusters are seen at several times during this period. The remaining data indicate that the low frequency turbulence associated with the wake of the *orbiter* is mainly confined to a region within ≈ 20 m of the *orbiter* itself.

Figure 10 indicates locations within or near the

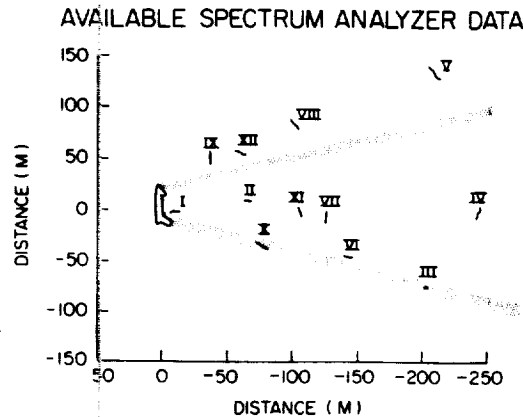


FIG. 10. LOCATIONS IN THE *orbiter*'S MID AND FAR WAKE WHERE THE SPECTRUM ANALYZER DATA ARE AVAILABLE.

orbiter's wake where spectrum analyzer data are available. Examples of the data taken in these 12 locations are given in Fig. 11, the location being indicated by the roman numeral in the lower left-hand corner of each individual graph. The data obtained at location I, the near wake, indicate a higher spectral density at lower frequencies than those obtained at location II, further downstream from the *orbiter*. This is in general agreement with the results from the 6-40 Hz data.

Data collected outside of the *orbiter*'s Mach cone, locations V, VIII, IX, and XII, are all similar in appearance and may be more indicative of conditions in the ambient ionosphere. Data taken along the *orbiter*'s Mach cone, locations III, VI, and X, indicate an enhancement in the spectral density at frequencies between 10 and 17 kHz. Data taken on the wake axis, locations II, IV, VII, and XI, are similar to those obtained outside the Mach cone.

Again, as for the near wake turbulence, the most obvious feature in the $\Delta N_e/N_e$ spectra is the rapid decline, with increasing frequency, in the 10^4 - 10^5 Hz decade. An additional feature (see e.g., panels III and VI) seems to be an enhancement of the turbulence, at wake edges, near $f_{p,i}$ the ion plasma frequency. Whether the "ambient" results are really features of the undisturbed ionosphere or whether disturbance effects are still seen outside the Mach cone, is difficult to say. It is quite conceivable, for instance, that plasma effects could occur well outside the Mach cone from interaction of the ionospheric plasma with the neutral

SPECTRUM ANALYZER DATA

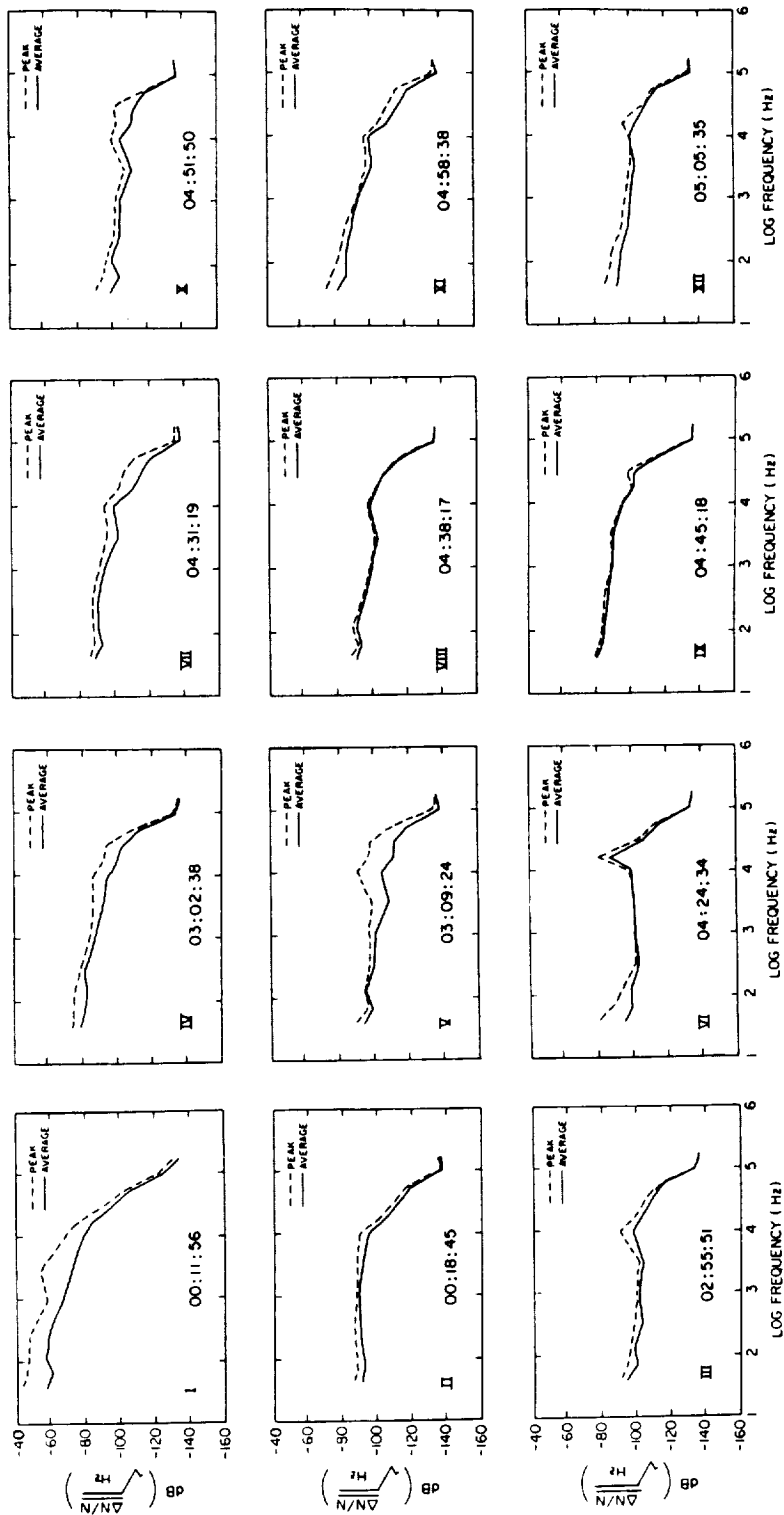


FIG. 11. THE SPECTRAL DENSITY OF $\Delta N_e/N_e$ IN THE MID AND FAR WAKE OF THE Shuttle orbiter.

gas cloud which accompanies the *Shuttle orbiter* along its orbit (e.g. Paterson, 1987).

SUMMARY AND CONCLUSIONS

The electron density depletions and temperature enhancements associated with the wake of the *Shuttle orbiter* extend several hundred meters behind the *orbiter* itself. Figure 5 indicates that the density depletions in the wake of the *orbiter* are bounded by the *orbiter's* Mach cone. Also of significance is the fact that there is a slight density enhancement 100 m downstream of the *orbiter* directly on the wake axis, the horizontal line defined in Fig. 5 by a vertical distance of zero. At this location the value we measure for N_w/N_a is 0.7, whereas 20 m upstream or downstream of this point the value for N_w/N_a is 0.6. This nonmonotonic behavior may be indicative of crossing streams of ions as reported by Merlino and D'Angelo (1987). As seen in Fig. 6, the temperature data taken 240 m downstream from the *orbiter* indicate a general T_e enhancement at this distance on the order of 30%–50%.

We find that most of the plasma turbulence in the wake of the *Shuttle orbiter* is confined to a region ≈ 20 m downstream of the *orbiter* itself. However, there are measurable disturbances along the *orbiter's* Mach cone at downstream distances of at least 200 m.

In the *orbiter's* YZ-plane, the near wake turbulence, at distances of ≈ 10 m downstream, in the 6–40 Hz range exhibits a change from a fraction of a per cent to about 3% near the *orbiter's* Mach cone. This turbulence decreases to a level below that associated with the ambient ionosphere when the PDP is within a few degrees of the *orbiter's* wake center. There a decrease in the spectral density at the lower frequencies is accompanied by a slight increase for frequencies between 200 Hz and 10 kHz.

In the far wake of the *orbiter*, the 6–40 Hz data show a level of turbulence well below that observed within ≈ 20 m from the *orbiter* itself and not very different from that recorded in the ambient ionosphere. A similar behavior is seen in the spectral density data.

Acknowledgements—This work was supported by grant NAG3-449 from the NASA Lewis Research Center, contract NAS8-32807 from the NASA Marshall Space Flight Center, and grant NGT-50402 from NASA Headquarters. We also gratefully acknowledge the assistance of Dr D. Gurnett and Dr J. Steinberg for their contributions with regard to obtaining and calibrating the spectrum analyzer data.

REFERENCES

- Henderson, C. L. and Samir, U. (1967) Observations of the disturbed region around an ionospheric spacecraft. *Planet. Space Sci.* **15**, 1499.
- Illiano, J. M. and Storey, L. R. O. (1974) Apparent enhancement of electron temperature in the wake of a spherical probe in a flowing plasma. *Planet. Space Sci.* **22**, 873.
- Kadomtsev, B. B. (1965) *Plasma Turbulence*. Academic Press, New York.
- Martin, A. R. (1974) Numerical solutions to the problem of charged particle flow around an ionospheric spacecraft. *Planet. Space Sci.* **22**, 121.
- Merlino, R. L. and D'Angelo, N. (1987) The interaction of a conducting object with a supersonic plasma flow: ion deflection near a negatively charged obstacle. *J. Plasma Phys.* **37**, 185.
- Murphy, G., Pickett, J., D'Angelo, N. and Kurth, W. S. (1986) Measurements of plasma parameters in the vicinity of the *Space Shuttle*. *Planet. Space Sci.* **34**, 993.
- Paterson, W. R. (1987) Ion plasmas in the vicinity of the *orbiter*: observations and modeling. Master's Thesis, The University of Iowa, Iowa City, Iowa.
- Raitt, W. J., Siskind, D. E., Banks, P. M. and Williamson, P. R. (1984) Measurements of the thermal plasma environment of the *Space Shuttle*. *Planet. Space Sci.* **32**, 457.
- Samir, U. (1981) Bodies in flowing plasmas: spacecraft measurements. *Adv. Space Res.* **1**, 373.
- Samir, U. and Willmore, A. P. (1965) The distribution of charged particles near a moving spacecraft. *Planet. Space Sci.* **13**, 285.
- Samir, U. and Wrenn, G. L. (1969) The dependence of charge and potential distribution around a spacecraft on ionic composition. *Planet. Space Sci.* **17**, 693.
- Samir, U. and Wrenn, G. L. (1972) Experimental evidence of an electron temperature enhancement in the wake of an ionospheric satellite. *Planet. Space Sci.* **20**, 899.
- Stone, N. H. and Samir, U. (1981) Bodies in flowing plasmas: laboratory studies. *Adv. Space Res.* **1**, 361.
- Tribble, A. C., D'Angelo, N., Murphy, G. B., Pickett, J. S. and Steinberg, J. T. (1988) Exposed high-voltage source effect on the potential of an ionospheric satellite. *J. Spacecraft Rockets* **25**, 64.
- Troy, B. E., Jr., Maier, E. J. and Samir, U. (1975) Electron temperatures in the wake of an ionospheric satellite. *J. Geophys. Res.* **80**, 993.

THE COHERENT CERENKOV RADIATED POWER FROM A GROUP OF FIELD-ALIGNED TEST PARTICLES IN A MAGNETOPLASMA

W. M. FARRELL* and C. K. GOERTZ

Department of Physics and Astronomy, The University of Iowa, Iowa City, IA 52242, U.S.A.

(Received in final form 25 August 1989)

Abstract—In this paper, an expression is derived that describes the coherent Cerenkov radiated power from a group of test particles in a plasma medium moving parallel to a magnetic field. In this analysis, each particle has an arbitrary position and velocity along a field line and, as a consequence, both the spatial and temporal coherence of the radiation are considered. As an example, we demonstrate that a monoenergetic electron beam consisting of small pulses can generate wave powers well above incoherent levels if the pulse spacing is comparable to an integer number of emission wavelengths. It is also shown that if the beam particles have a velocity spread, ΔV , the wave powers will decrease in time due to the reduced temporal coherence of the particle radiators, where this coherence scales as $1/\Delta V$. This latter effect applies to any charged particle beam propagating in a magnetoplasma, because even an initially monoenergetic beam becomes thermalized by electrostatic wave-particle interactions reducing the radiated power.

INTRODUCTION

The association of whistler-mode radiation with electron beams is a well-known phenomenon. In the Earth's auroral regions, such radiation called auroral hiss is commonly detected from naturally-occurring auroral electron beams by radio receivers onboard satellites (Gurnett, 1966; Jorgensen, 1968; Barrington *et al.*, 1971; Laaspere *et al.*, 1971; Gurnett *et al.*, 1983; Lin *et al.*, 1984). A characteristic of the emission is that it usually appears "saucer"- or "funnel"-shaped on a frequency vs time spectrogram, which is a result of the emission propagating with wave normals near the resonance cone (for a review of this process, see Gurnett, 1983). Similar funnel-shaped whistler-mode emissions have now been detected at Jupiter, near to the Io plasma torus, where strong electron beaming is again suspected (Gurnett *et al.*, 1979). Whistler-mode emissions are also detected from artificial electron beams ejected from rockets and the space shuttle (Cartwright and Kellogg, 1974; Monson *et al.*, 1976; Dechambre *et al.*, 1980; Shawhan *et al.*, 1984; Beghin *et al.*, 1984) and, in particular, during the shuttle's *Spacelab-2* mission, a funnel-shaped whistler-mode signal was detected that appeared almost identical to those observed from natural auroral electron beams (Gurnett *et al.*, 1986; Farrell *et al.*, 1988). Based on over 20 years of observations, it is now clearly evident that whistler-mode emissions are closely related to electron beams.

There are two well-known theories that attempt to

explain the generation of the whistler-mode emissions from electron beams. In the first theory, the electrons in the beam are considered incoherent spontaneous radiators of Cerenkov radiation. This mechanism has been tested for whistler-mode emissions from both natural (Taylor and Shawhan, 1974) and artificial (Farrell *et al.*, 1988) electron beams. In many cases the estimated powers from this process are too low to account for the measured wave powers, indicating that some coherent mechanism must be involved in wave generation. Such a coherent mechanism is the whistler-mode instability, whereby the waves gain energy directly via the unstable beam distribution. It is strongly suspected that this stimulated emission process generates auroral hiss emissions (Maggs, 1976; James, 1976; Maggs and Lotko, 1981; Lin *et al.*, 1984).

Recently, a third wave generation theory has been introduced involving coherent Cerenkov radiation from beam electrons (Harker and Banks, 1983). This mechanism is particularly relevant for artificial electron beams, since the two mechanisms discussed above may not readily apply. In particular, incoherent Cerenkov radiation from beam electrons yields power values too low to account for those measured (Farrell *et al.*, 1988) and the amplification path length for the whistler-mode instability in an artificial beam may be too small for significant wave growth (Jones and Kellogg, 1973). Harker and Banks derived an expression for the Cerenkov-radiated power from a pulsed monoenergetic electron beam in a plasma medium which included the spatial coherence between the pulses. In their derivation, it was assumed that all beam electrons travelled at the same velocity, v , in

* Present address: Laboratory of Extraterrestrial Physics, NASA/Goddard Space Flight Center, Greenbelt, MD 20771, U.S.A.

pulses of length, l , with a distance, d , separating each pulse and that the pulsing is imposed by the generator that produces the beam. A monoenergetic continuous beam ($d \rightarrow 0$) would have no spatial coherence and consequently only emit incoherent Cerenkov radiation. However, it is an observational fact that even a continuous beam emits whistler-mode radiation at powers well above the estimated incoherent Cerenkov radiation level (Farrell *et al.*, 1988). It has been demonstrated that continuous beams in magnetoplasmas naturally break up into pulses or "bunches" due to a beam-plasma instability, and it is this "bunched" beam that radiates wave powers above incoherent levels (Farrell *et al.*, 1988, 1989).

In this paper, a derivation is presented for the coherent Cerenkov radiated power from a group of field-aligned test particles that includes not only spatial, but also temporal coherence effects. The approach taken is very similar to that used by Mansfield (1967), who derived the radiated power for a single test particle in a magnetoplasma. The steps include calculating the total current by summing up the contribution from each of the N test particles, and then using the Fourier transform of this quantity to determine the radiated electric field and power. The formalism will then be applied to a field-aligned beam of particles of generalized velocity and position, $f(v)$ and $g(z)$, respectively. Unlike Harker and Banks, the motion of the beam particles is only considered in one dimension, along the magnetic field. However, by assuming arbitrary field-aligned velocities for the particles, the effects of a beam's thermal spread can now be included in the calculation.

THE POWER RADIATED FROM FIELD-ALIGNED TEST PARTICLES

In the derivation of the radiated power, some assumptions are usually made that will now be discussed. First, it is assumed that the particles do not significantly alter the ambient plasma medium. Hence, the particles are considered "test" particles in the surrounding magnetoplasma. Second, it is assumed that the ambient plasma is cold, homogeneous, collisionless, contains a static magnetic field, and thus can be described by the cold plasma dielectric tensor defined by equation (1-20) in Stix (1962). Third, it is assumed that the particles have zero pitch angle. This choice makes the integrals in the derivation easily solvable. This condition differs from that used in Harker and Banks (1983), who derived the radiated power assuming gyrotropic beam particle trajectories and identical particle velocities. Our approach concentrates on the effects associated with the beam's

temporal coherence which have not been considered previously. Therefore, for simplicity, we use particles with zero pitch angle. Fourth, it is assumed that the Cerenkov radiation, itself, does not significantly alter the surrounding ambient plasma and has a magnetic field strength much weaker than the static magnetic field.

The inhomogeneous wave equation including a current source $J_q(\vec{k}, \omega)$ can be written as:

$$\vec{n} \times \vec{n} \times \vec{E}(\vec{k}, \omega) + \vec{k} \cdot \vec{E}(\vec{k}, \omega) = \vec{T} \cdot \vec{E}(\vec{k}, \omega) = \frac{i J_q(\vec{k}, \omega)}{\omega \epsilon_0} \quad (1)$$

The static magnetic field, \vec{B}_0 , in the plasma medium points along the \hat{z} -axis. Radiation from a field-aligned test particle will be azimuthally symmetric. Hence, $k_\phi = 0$ while k_ρ and k_z have finite, real values. For simplicity, it is assumed that \vec{k} is entirely in the $y-z$ plane at an angle θ relative to the \hat{z} -axis. This coordinate system can be rotated to analyze radiation from any specific azimuth angle, hence this assumption can be made without any loss of generality. The tensor \vec{T} can be expressed as:

$$\vec{T} = \begin{bmatrix} \epsilon_1 - n^2 & i \epsilon_2 & 0 \\ -i \epsilon_2 & \epsilon_1 - n^2 \cos^2 \theta & n^2 \sin \theta \cos \theta \\ 0 & n^2 \sin \theta \cos \theta & \epsilon_3 - n^2 \sin^2 \theta \end{bmatrix} \quad (2)$$

where

$$\begin{aligned} \epsilon_1 &= 1 + \frac{f_{pe}^2}{f_{ce}^2 - f^2} + \frac{f_{pi}^2}{f_{ci}^2 - f^2}, \\ \epsilon_2 &= \frac{f_{pe}^2 f_{ce}}{f(f^2 - f_{ce}^2)} + \frac{f_{pi}^2 f_{ci}}{f(f_{ci}^2 - f^2)}, \\ \epsilon_3 &= 1 - \frac{f_{pe}^2}{f^2} - \frac{f_{pi}^2}{f^2}. \end{aligned}$$

f is the wave frequency, f_{ce} and f_{pe} are the electron cyclotron and plasma frequencies, respectively, and f_{ci} and f_{pi} are the ion cyclotron and plasma frequencies, respectively.

The electric field, $\vec{E}(\vec{r}, t)$, is obtained by taking the inverse Fourier transform of $\vec{E}(\vec{k}, \omega)$:

$$\vec{E}(\vec{r}, t) = \frac{i}{\epsilon_0} \iiint \vec{T} \cdot J_q(\vec{k}, \omega) \exp[i(\omega t - \vec{k} \cdot \vec{r})] d\vec{k} \frac{d\omega}{\omega} \quad (3)$$

For N test particles in the medium, the source current is expressed as:

J_q
where $\vec{V}_i(t)$ at
 $\vec{V}_i(t) = V_i \hat{z}$, a

for field-align
particle's initi
that \vec{k} equals
the delta func

the Fourier tr
expressed as:

$$J_q(\vec{k}, \omega) =$$

Substituting (f
field in the pla

$$\vec{E}(\vec{r}, t) =$$

Expressing $d\vec{k}$
using the fact
loss and hence
can be written

$$P(t) = q \sum_{i=1}^N \vec{E}$$

$$\times \frac{q^2 i V_i V_j}{(2\pi)^3 \epsilon_0 c}$$

$$\times \exp \left[\frac{i n \omega}{c} \right]$$

$$\times \delta(n \omega \cos$$

where the tri

$$J_q(\vec{r}, t) = \sum_{i=1}^N q \vec{V}_i(t) \delta(\vec{r} - \vec{r}_i(t)) \quad (4)$$

where $\vec{V}_i(t)$ and $\vec{r}_i(t)$ are

$$\vec{V}_i(t) = V_i \hat{z}, \text{ a constant in time,} \\ \text{and } \vec{r}_i(t) = (z_{i0} + V_i t) \hat{z} \quad (5)$$

for field-aligned trajectories. The variable z_{i0} is the particle's initial position along the field line. Given that \vec{k} equals $\vec{n}\omega/c$, that β_i is defined as V_i/c , and that the delta function, $\delta(x - x_0)$, is defined as

$$\int \exp [i(x - x_0)t] \frac{dt}{2\pi},$$

the Fourier transform of the source current can be expressed as:

$$J_q(\vec{k}, \omega) = \frac{1}{(2\pi)^4} \iint J_q(\vec{r}, t) \exp [i(\vec{k} \cdot \vec{r} - \omega t)] d\vec{r} dt \\ = \sum_{i=1}^N \frac{\hat{z} q V_i}{(2\pi)^4} \int \exp [i(\vec{k} \cdot \vec{r}_i - \omega t)] dt \\ = \sum_{i=1}^N \frac{\hat{z} q V_i}{(2\pi)^3} \exp \left[\frac{i n \omega}{c} \cos \theta z_{i0} \right] \\ \times \delta(n \omega \cos \theta \beta_i - \omega). \quad (6)$$

Substituting (6) into equation (3) yields the electric field in the plasma

$$\vec{E}(\vec{r}, t) = \sum_{i=1}^N \frac{q_i V_i}{(2\pi)^3 \epsilon_0} \iint (\vec{T}^{-1} \cdot \hat{z}) \\ \times \exp \left[\frac{i n \omega}{c} \cos \theta z_{i0} \right] \delta(n \omega \cos \theta \beta_i - \omega) \\ \times \exp [i(\omega t - \vec{k} \cdot \vec{r})] d\vec{k} \frac{d\omega}{\omega}. \quad (7)$$

Expressing $d\vec{k}$ as $n^2 \omega^2 dn \sin \theta d\theta d\phi/c^3$ and, again, using the fact that $\vec{k} = \vec{n}\omega/c$, the instantaneous energy loss and hence the radiated power from the N particles can be written as

$$P(t) = q \sum_{i=1}^N \vec{E}(\vec{r}_i, t) \cdot \vec{V}_i(t) = \sum_{i=1}^N \sum_{j=1}^N \\ \times \frac{q^2 i V_i V_j}{(2\pi)^2 \epsilon_0 c^3} \iint (\hat{z} \cdot \vec{T}^{-1} \cdot \hat{z}) \\ \times \exp \left[\frac{i n \omega}{c} \cos \theta (z_{i0} - z_{j0}) \right] \exp [i(\omega - n \omega \cos \theta \beta_j) t] \\ \times \delta(n \omega \cos \theta \beta_i - \omega) n^2 \omega^2 dn \sin \theta d\theta d\omega, \quad (8)$$

where the trivial integration over ϕ has been per-

formed. Integrating equation (8) over θ yields:

$$P(t) = \sum_{i=1}^N \sum_{j=1}^N \frac{q^2 i V_i V_j}{(2\pi)^2 \epsilon_0 c^3 \beta_i} \iint (\hat{z} \cdot \vec{T}^{-1} \cdot \hat{z}) \\ \times \exp \left[\frac{i n \omega}{c} \cos \theta_{i0} (z_{i0} - z_{j0}) \right] \\ \times \exp \left[i \omega \left(1 - \frac{\beta_j}{\beta_i} \right) t \right] |n| |\omega| dn d\omega, \quad (9)$$

where $\cos \theta_{i0} = (1/n) \beta_i$, the Cerenkov condition. The quantity $(\hat{z} \cdot \vec{T}^{-1} \cdot \hat{z})$ was calculated by Mansfield (1967) as

$$(\hat{z} \cdot \vec{T}^{-1} \cdot \hat{z}) = \frac{T_{33}(n)}{\epsilon_1 (n_1^2 - n^2)(n_2^2 - n^2)}, \quad (10)$$

where $T_{33}(n) = \epsilon_1^2 - \epsilon_2^2 - \epsilon_1 n^2 + (n^4 - \epsilon_1 n^2) \cos^2 \theta_{i0}$. The quantities n_1^2 and n_2^2 are

$$n_{1,2}^2 = [-B \pm (B^2 - 4C\epsilon_1)^{1/2}] / 2\epsilon_1, \quad (11)$$

where

$$B = \left(\frac{c}{V_i} \right)^2 (\epsilon_3 - \epsilon_1) + \epsilon_2^2 - \epsilon_1^2 - \epsilon_1 \epsilon_3 \quad (12)$$

and

$$C = \left(\frac{c}{V_i} \right)^2 (\epsilon_1^2 - \epsilon_2^2 - \epsilon_1 \epsilon_3) + \epsilon_3 (\epsilon_1^2 - \epsilon_2^2). \quad (13)$$

After performing the complex integration over n via the residue theorem, we find that the radiated power is:

$$P(t) = \int_{-\infty}^{\infty} \sum_{i=1}^N \sum_{j=1}^N \frac{q^2 |\omega| d\omega}{8\pi \epsilon_0 \epsilon_1} \frac{1}{(n_1^2(\beta_i) - n_1^2(\beta_j))} \\ \times \left(\frac{V_j}{c^2} \right) \left\{ \exp \left[i \omega \left(1 - \frac{\beta_j}{\beta_i} \right) t \right] \right\} \sum_{k=1}^2 (-1)^k T_{33}(n_k(\beta_i)) \\ \times \left\{ \exp \left[i \frac{n_k(\beta_i) \omega}{c} \cos \theta_{i0} (z_{i0} - z_{j0}) \right] \right\}, \quad (14)$$

where $n_{1,2}$ are functions of β_i . The two factors in brackets represent the temporal and spatial coherence, respectively, between particle i and j .

Equation (14) can be generalized to describe the radiated power from particles with field-aligned velocity distribution $f(v)$ and spatial configuration $g(z)$ defined by:

$$N = \int_{-\infty}^{\infty} f(v) dv \int_0^z g(z) dz. \quad (15)$$

In this case, the power is expressed as:

$$P(t) = \iiint d\omega \left(\frac{q^2 |\omega|}{8\pi\epsilon_0\epsilon_1} \right) \int \frac{f(v)}{n_z^2(v) - n_1^2(v)} \Phi(v) \times \sum_{k=1}^2 (-1)^k T_{33}(n_k(v)) \times \exp \left[i \frac{n_k(v)\omega}{c} \cos \theta_0(z-z') \right] dv g(z) dz g(z') dz', \tag{16}$$

where

$$\Phi(v) = \int f(v') \frac{v'}{c} \exp [i\omega(t - v'/v)t] dv'$$

It should be recognized that expression (16) represents the solution to the initial value problem. Given the particle's velocity and position at $t = 0$, the instantaneous radiated power at later times is determined. Both Mansfield (1967) and Harker and Banks (1983) also determined the instantaneous power, but then averaged this quantity over a complete gyroperiod. Since monoenergetic particles were assumed, their time-averaged power also represented the solution to the boundary value problem. A similar time-averaging of (16) would not necessarily yield such a solution since we have assumed arbitrary particle energies. As we shall demonstrate in the next section, if monoenergetic particle distributions are used, we obtain a time-independent solution which will also apply to the boundary value problem. However, if the distribution has a thermal spread, the radiated power will remain explicitly dependent on time, solving the initial value problem but making applications to the boundary value problem difficult.

A measurable quantity is the angular distribution of radiated power, $dP/d\Omega$, where $d\Omega$ represents the infinitesimal solid angle. The integrand of (16) is

$$\frac{dP}{d\omega} = \iiint \left(\frac{q^2 |\omega|}{8\pi\epsilon_0\epsilon_1} \right) \int \frac{f(v)}{n_z^2(v) - n_1^2(v)} \Phi(v) \times \sum_{k=1}^2 (-1)^k T_{33}(n_k(v)) \times \exp \left[i \frac{n_k(v)\omega}{c} \cos \theta_0(z-z') \right] dv g(z) dz g(z') dz', \tag{17}$$

and relates to $dP/d\Omega$ by

$$\frac{dP}{d\Omega} = \frac{1}{2\pi \sin \theta} \frac{d\omega}{d\theta} \frac{dP}{d\omega} \tag{18}$$

The quantity $d\omega/d\theta$ is $\omega_{ce} C_N/C_D$ where C_N and C_D are defined by equations (88) and (97)-(101) of Harker and Banks (1983).

APPLICATIONS

We shall now apply equation (16) to a number of simplified examples that will demonstrate the variation of the radiated power with the $f(v)$ and $g(z)$ chosen. First, consider a single ($N = 1$) field-aligned test particle of velocity, V_0 , located at the origin, $z = 0$. In this case, $f(v) = \delta(v - V_0)$, and $g(z) = \delta(z)$. The radiated power can be easily calculated for this particle by substituting the velocity and spatial distribution into (16), which yields:

$$P_1 = \int_{-\infty}^{\infty} d\omega \left(\frac{q^2 |\omega|}{8\pi\epsilon_0\epsilon_1} \right) \frac{V_0}{c^2} \left(\frac{1}{n_z^2(V_0) - n_1^2(V_0)} \right) \times \sum_{k=1}^2 (-1)^k T_{33}(n_k(V_0)), \tag{19}$$

where P_1 designates the spontaneous Cerenkov power from a single particle. An identical expression is obtained using equation (32) of Mansfield (1967) for field-aligned particle trajectories.

Now consider the radiation from a series of p particles each of charge, Nq , and velocity, V_0 . This example may represent a pulsed beam with the length of each pulse much less than the parallel wavelength of the emitted wave, $l \ll \lambda_{\parallel}$. This condition allows the N particles within each pulse to radiate in complete coherence. However, spatial coherent effects between the pulses alters the radiated power. Since all particles have the same speed, temporal coherent effects are not important. The particle distributions can be written as

$$f(v) = Nq\delta(v - V_0) \quad \text{and} \quad g(z) = \sum_{i=1}^p \delta(z - z_i),$$

where z_i is the initial position of the i -th point source, respectively. Figure 1 displays the phase space configuration of such a system. Inserting $f(v)$ and $g(z)$ into (16) yields the following expression for the radiated power:

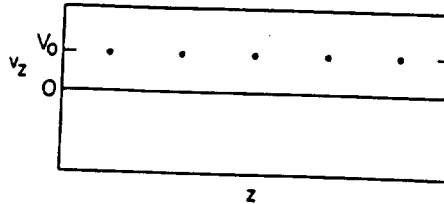


FIG. 1. DISPLAYED IS THE PHASE-SPACE CONFIGURATION FOR p POINT CHARGES ALL HAVING IDENTICAL VELOCITIES. If the spacing between the charges is equal and comparable to the Cerenkov-radiated parallel wavelength, then increased wave powers will result.

$$P(t) = \int \sum_{i=1}^p \times \left(\frac{1}{n_z^2(v)} \right)$$

This result c
Expression (dependent o
the spatial c
 p pulses are
an integer 1
 $|z_i - z_j| = m\lambda_{\parallel}$
integer), then
unity and the
is well above
The spatial co
each propagat
sidered in gre
and thus othe
pursued any f

We will now
ence on a gro
effect, a veloci
required, such
 V_0 , defined by
of particles in
spread. We as
distributed ovr
density of the
integrations in
nitestimally s
 $g(z) = \delta(z)$. T
of electrons in
we are consid
that describes
 $\exp [im\omega \cos$
only tempora

FIG. 2. DISPLAYED DISTRIBUTION OF

$$P(t) = \int \sum_{j=1}^p \sum_{k=1}^p d\omega \left(\frac{N^2 q^2 |\omega|}{8\pi\epsilon_0\epsilon_1} \right) \frac{V_0}{c^2} \times \left(\frac{1}{n_2^2(V_0) - n_1^2(V_0)} \right) \sum_{k=1}^2 (-1)^k T_{33}(n_k(V_0)) \times \exp \left[i \frac{n_k(V_0)\omega}{c} \cos \theta_0 (z_i - z_j) \right]. \quad (20)$$

This result can also be directly obtained using (14). Expression (20) indicates that the power is highly dependent on the exponential term that describes the spatial coherence of the point particles. If the p pulses are equally spaced, with $|z_i - z_j|$ equal to an integer number of parallel wavelengths (i.e. $|z_i - z_j| = m\lambda_1 = 2\pi mc/n\omega \cos \theta$ with m being an integer), then the exponential term in (20) is close to unity and the power is $p^2 \times (Nq)^2 \times P_1$. Such a value is well above the incoherent level at $p \times (Nq)^2 \times P_1$. The spatial coherence of a pulsed beam of particles each propagating at identical velocities has been considered in great detail in Harker and Banks (1983), and thus other than this demonstration, will not be pursued any further here.

We will now discuss the effects of temporal coherence on a group of particles. In order to quantify this effect, a velocity distribution with a thermal spread is required, such as a plateau distribution centered about V_0 , defined by $f(v) = N/\Delta V$, where N is the number of particles in the group and ΔV is the particle velocity spread. We assume that the N particles are uniformly distributed over ΔV . Figure 2 displays the phase space density of the particles in this case. To simplify the integrations in (16), we will only examine an infinitesimally small slice in phase space, so that $g(z) = \delta(z)$. This distribution may represent a pulse of electrons in a plasma with thermal spread ΔV . Since we are considering a small pulse, the exponential term that describes the spatial coherence of the particles, $\exp [in_k\omega \cos \theta_0(z - z')/c]$, goes to unity, and now only temporal coherent effects will be important.

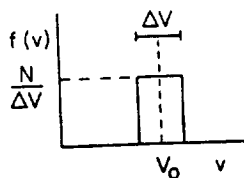


FIG. 2. DISPLAYED IS THE PHASE-SPACE DENSITY FOR A PLATEAU DISTRIBUTION OF AVERAGE VELOCITY, V_0 AND VELOCITY SPREAD, ΔV .

Inserting $f(v')$ into $\Phi(v)$ defined in (16) and keeping the real terms yields:

$$\Phi(v) = \frac{V_0}{c^2} N \exp [i\omega(1 - V_0/v)t] \frac{\sin x}{x}, \quad (21)$$

where

$$x = \frac{\Delta V \omega t}{v} \frac{x}{2}.$$

The radiated power is then given by:

$$P(t) = \int d\omega \left(\frac{q^2 |\omega|}{8\pi\epsilon_0\epsilon_1} \right) \frac{V_0}{c^2} \frac{N^2}{\Delta V} \times \int dv \frac{1}{n_2^2(v) - n_1^2(v)} \left(\sum_{k=1}^2 (-1)^k T_{33}(n_k(v)) \right) \times \exp [i\omega(1 - V_0/v)t] \frac{\sin x}{x}. \quad (22)$$

To perform the integration over v , we will assume that $\Delta V < V_0$, so that in (22), we can approximate dv by ΔV , v by V_0 , and $\sin x/x$ by $1 + x^2/3$ with $x = \Delta V \omega t / 2V_0$. The radiated power from this slice then becomes

$$P(t) = \int d\omega \left(\frac{N^2 q^2 |\omega|}{8\pi\epsilon_0\epsilon_1} \right) \frac{V_0}{c^2} \frac{1}{n_2^2(V_0) - n_1^2(V_0)} \times \left(\sum_{k=1}^2 (-1)^k T_{33}(n_k(V_0)) \right) \left[1 - \left(\frac{\Delta V}{V_0} \right)^2 \frac{\omega^2 t^2}{12} \right] = N^2 P_1 \left[1 - \left(\frac{\Delta V}{V_0} \right)^2 \frac{\omega^2 t^2}{12} \right] \quad (23)$$

which holds for $x < 1$ or $t < \sqrt{12} V_0 / \Delta V \omega$. If ΔV is zero, the power goes as $N^2 \times P_1$, and radiation is in complete coherence. However, with a velocity spread, the particle radiators become separated in space for $t > 0$, hence decreasing the coherence of the particles. This coherence can be quantified by defining a coherence time, $T = \pi V_0 / \Delta V \omega$, when the power from the particles is reduced by about a factor of five due to temporal coherence effects.

To better understand expression (23), we can substitute in the Cerenkov condition, $\omega = k_1 V_0$, and the particle's spatial dispersion, $\Delta z = \Delta V t$, with the result that

$$P \cong N^2 P_1 \left(1 - \left(\frac{\Delta z}{\lambda_1/2} \right)^2 \right). \quad (24)$$

Initially, all the particles are located at the same spatial location, and the group acts as a coherent radiation source (i.e. $\Delta z = 0$). However, since particles are moving at different speeds the group will spatially disperse

as it propagates which tends to reduce the radiated power. When $\Delta z \approx \lambda_1/2$, the phase of the particles relative to the wave will vary by nearly 180° from the front to the back of the pulse. For a nearly uniform distribution, this will yield a small value of power. Consequently, we can interpret the coherence time, T , as the time required for the group of particles to disperse to half the emission's parallel wavelength, and thus radiate effectively out of phase.

The temporal coherence of an electron beam is particularly important to consider since it has been demonstrated that such beams undergo strong thermalization from wave/particle interactions right after injection (Winglee and Pritchett, 1988; Farrell *et al.*, 1989). In particular, an electrostatic beam-plasma instability tends to diffuse a large fraction of the beam particles in phase space, which reduces their coherence time, T , and radiated power.

As an example, we can consider the case of an initially monoenergetic electron pulse propagating in a plasma medium with an initial length, l , much less than the parallel Cerenkov-radiated wavelength, λ_1 . The interaction of this pulse with the ambient plasma causes a thermal spread in velocity (and hence a spread in space) with a resulting loss of coherence. In this case, equation (23) derived above may be applied. To quantify the effects of thermalization, a simulation of such a pulse has been performed using the one-dimensional electrostatic particle code described in Farrell *et al.* (1989). In the model, an initially cold beam pulse of density $1/8$ that of the ambient plasma and length $130 \lambda_D$ was injected into the system at the $z = 0$ boundary with a speed ten times the ambient thermal speed. The resulting phase space configuration for the electrons is displayed in Figs 3a, b, and c after 40, 80, and $120 \omega_{pe}^{-1}$, respectively. The phase space structures that develop appear very similar to those modeled by Okuda *et al.* (1987). As indicated in Fig. 3, the electrostatic wave/particle interactions within the beam are strong, and cause the initially cold pulse to diffuse in phase space. Consequently, a significantly thermal spread develops among the beam particles. In applying (23) to the simulated pulse, some of the assumptions used to derive the expression have to be relaxed. In particular, the electrons in the pulse do not act as true test particles, since they appear to slightly alter the ambient plasma medium as they propagate. However, this effect is limited only to the region where the beam is located, and not outside. Also, the average current carried by the ambient plasma is much less than that of the beam and thus will not contribute significantly to the generation of Cerenkov radiation. Another limitation is that the pulse electron distribution is not

a truly uniform plateau distribution, like that shown in Fig. 2, since the density fluctuations in phase space occur. However, since $\lambda_1 > l$, the modulation of electron density within the pulse does not significantly affect the radiated power in this particular case. We can now estimate the radiative coherence time, T , of the pulse. As calculated from the simulation, the average value of ΔV is $0.76 \bar{V}$, where \bar{V} is the average beam velocity. Using the value of $\Delta V/\bar{V} = 0.76$ and assuming that Cerenkov radiation is emitted from the pulse with frequency $\omega = 0.1 \omega_{pe}$, the coherence time of the pulse, T , is estimated to be about $42 \omega_{pe}^{-1}$. Whistler-mode waves, possibly originating by Cerenkov processes, are detected at $\omega = 0.1 \omega_{pe}$ during *Spacelab-2* beam ejections (Gurnett *et al.*, 1986; Farrell *et al.*, 1988). For typical ionospheric densities, ω_{pe} is about $7 \times 10^6 \text{ rad s}^{-1}$ and thus the N particles remain in relative coherence for only about $6 \mu\text{s}$ in such regions. In contrast, had no wave/particle interactions occurred (i.e. no velocity spread), the pulse would remain almost completely coherent for all times, since $\Delta V = 0$ and $l \ll \lambda_1$, and the power would remain proportional to N^2 . Clearly, from this simple example, we see that wave/particle interactions and beam thermal effects are very important to consider when determining the radiated power from a particle beam.

As a final example, we shall consider the radiated power from a series of p small electron pulses, each like the one shown in Fig. 3. Again, the initial length of each pulse, l , is assumed to be much less than the parallel Cerenkov-radiated wavelength, λ_1 , so the spatial distribution can be approximated by

$$g(z) = \sum_{i=1}^p \delta(z - z_i).$$

Representing the velocity distribution by $f(v) = N/\Delta V$, the power [from equation (16)] can be expressed as:

$$P(t) \approx \sum_{i=1}^p \sum_{j=1}^p \left[\frac{N^2 q^2 |c\omega|}{8\pi\epsilon_0 \epsilon_1} \right] \times \frac{V_0}{c^2} \frac{1}{n_1^2(V_0) - n_1^2(V_0)} \left[1 - \left[\frac{\Delta V}{V_0} \right]^2 \frac{\omega^2 t^2}{12} \right] \times \sum_{k=1}^2 (-1)^k T_{33}(n_k(V_0)) \times \exp \left[\frac{in_k(V_0)\omega}{c} \cos \theta_0 (z_i - z_j) \right] \quad (25)$$

for times $t < T = \sqrt{12} V_0 / \Delta V \omega$. As indicated in (25), for early times ($t \ll T$), the spatial coherence deter-

FIG.
Show
120 c
instal

mines the ra
sitation bei
pression (20)
broaden in s
reduces their
sider small
spaced at mu
wavelength.
calculate the
radiated pow
would be the
formalism (1
spread, ΔV ,
interactions,
 $P(t) = p^2 \times ($
which holds
decreases as t
wave/particle
phase-space a
ence, and are i
the Cerenkov-
beam.

We have de
Cerenkov-radi

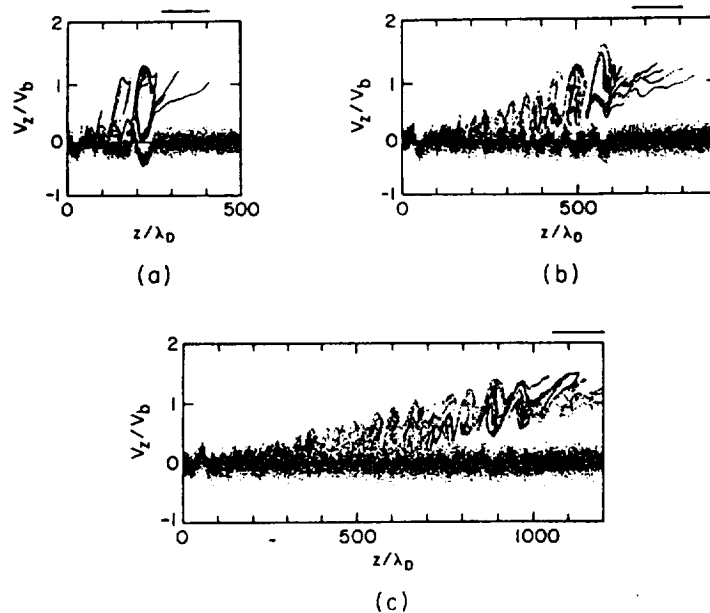


FIG. 3. THE RESULTS OF A ONE-DIMENSIONAL, ELECTROSTATIC PARTICLE SIMULATION OF A SMALL ELECTRON PULSE IN A PLASMA ARE DISPLAYED. Shown are the phase-space configurations of the pulse and ambient electrons after (a) 40, (b) 90, and (c) 120 ω_{pe}^{-1} . We can see that the initially cold pulse becomes thermalized via the electrostatic beam/plasma instability as it propagates in the medium. The line in each panel represents the position of the unaltered beam, initially injected at $V_z/V_b = 1$.

mines the radiated power from the pulses with the situation being similar to that associated with expression (20). However, as time increases, the pulses broaden in space due to their thermal spread, which reduces their radiative coherence. As an example, consider small pulses with $\Delta V/\bar{V} = 0.76$, all initially spaced at multiples of the parallel Cerenkov-emitted wavelength. Like the previous example, we wish to calculate the power at $\omega = 0.1 \omega_{pe}$. Initially, the radiated power is $P(t=0) \approx p^2 \times (Nq)^2 \times P_1$, which would be the power for all times in Harker and Banks' formalism (1983). However, by including a thermal spread, ΔV , created by electrostatic wave/particle interactions, the power at later times becomes $P(t) = p^2 \times (Nq)^2 \times P_1 \times [1 - A^2 t^2]$ where $A = \omega_{pe}/46$, which holds for $t < 1/A$. Notice that the power decreases as time increases. As in the previous case, wave/particle interactions that diffuse the beam in phase-space act to reduce the beam's radiative coherence, and are important to consider when determining the Cerenkov-radiated power from a pulsed electron beam.

CONCLUSION

We have derived an expression that describes the Cerenkov-radiated power from a group of field-

aligned test particles in a plasma medium that includes both spatial and temporal coherent effects. This expression was then applied to some simplified cases. For example, it was demonstrated that the expression for the radiated power from a single point charge using (16) is identical to that obtained from Mansfield (1967) for field-aligned trajectories. Also, the radiated power from a group of equally-spaced point sources all moving at identical velocities can be increased well above incoherent levels if the source spacing is comparable to the emission parallel wavelength, $|z_i - z_j| \sim \lambda_i$. These results are similar to those found in Harker and Banks (1983). The temporal coherence of a single electron pulse with a thermal spread was also calculated using the results of a particle simulation. It was demonstrated that such a pulse undergoes strong wave/particle interactions which tend to reduce the radiative coherence time and emitted Cerenkov power. In particular, for a small pulse with $\Delta V/\bar{V} \sim 0.75$ emitting in the MF range, the radiative coherence time, T , was calculated to be on the order of about 10 μs . After this time, the different parts of the broadened pulse are radiating out of phase, significantly reducing the power level.

This result has dramatic implications on the use of a pulsed electron beam as a radio wave antenna.

ORIGINAL PAGE IS OF POOR QUALITY

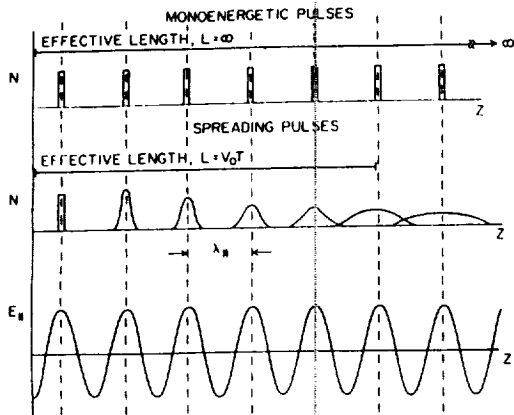


FIG. 4. A SCHEMATIC REPRESENTATION OF A MONOENERGETIC AND SPREADING PULSED ELECTRON BEAM.

Note that the effective radiation length for a spreading beam is shortened due to a reduction in the pulse's temporal coherence. For small pulses located where E_1 is a maximum, the radiation is emitted in phase. The ideal case is depicted in the top panel, where the pulses remain coherent for all times, giving an effective radiation length of the pulsed beam, L , at infinity. However, if the pulses have a thermal spread, then the coherence of an individual pulse changes as it propagates downstream. The case of a spreading pulsed beam is pictorially represented in the second panel. When the electrons in a pulse spread to $\lambda_1/2$, their relative phasing varies by nearly 180° , making the pulse an incoherent radiator. Hence, the effective radiation length of the pulsed beam, L , is now $V_0 T$.

Specifically, without including a thermal spread, the pulses in a beam would remain coherent for all times. Hence, for spacing at integer multiples of λ_1 , the radiated power would vary as p^2 where p is the total number of emitted pulses. This result is similar to our second example in the application section and to that presented in Harker and Banks (1983). In contrast, if we include a thermal spread resulting from wave/particle interactions, then pulses with lifetimes greater than T would not contribute to the radiation process since they no longer radiated coherently. Thus, only those pulses lying from the point of injection out to about $L = V_0 T$ would contribute to the emitted power. Figure 4 illustrates this point by displaying a schematic representation of two pulsed beams, one being monoenergetic and the other having a thermal spread. As indicated in the figure, when the thermalized pulses extend to about $\lambda_1/2$, they can no longer be considered coherent radiators. Hence, beyond $z = L$, the radiated power is small, where L corresponds to the effective radiation length. The quantity L is similar to $1/B$ in Harker and Banks (1985), who incorporated a phenomenological parameter to describe the beam coherence length. The total energy

loss of the beam can be expressed as $P_{\text{EFF}} \times T$, where P_{EFF} is the power from the coherent pulses. This energy loss changes from an infinite, unrealistic value for a monoenergetic beam to a finite, realistic value for a beam with a velocity spread.

Acknowledgements—The authors wish to thank Donald A. Gurnett for his valuable input throughout all aspects of this research, and Terry Whalen and Shinobu Machida for their timely advice on particle simulations. We also thank Joyce Chrisinger for a fine drafting job, and Kathy Kurth and Tami Thompson for typing the manuscript. Part of this research was funded by NASA Graduate Student Researchers Training Grant NGT-50034. The research at the University of Iowa was also supported by NASA through contract 32807, and grants NAG3-449, NSG-7632, and NAGW-1488.

REFERENCES

- Barrington, R. E., Hartz, T. R. and Harvey, R. W. (1971) Diurnal distribution of ELF, VLF, and LF noise at high latitudes as observed by *Alouette 2*. *J. geophys. Res.* **76**, 5278.
- Beghin, C., Lebreton, J. P., Maehlum, B. N., Troim, J., Ingsy, P. and Michau, J. L. (1984) Phenomena induced by charged particle beams. *Science* **225**, 188.
- Cartwright, D. G. and Kellogg, P. J. (1974) Observations of radiation from an electron beam artificially injected into the ionosphere. *J. geophys. Res.* **79**, 1439.
- Dechambre, M., Kushnerevsky, Yu. V., Lavergnat, J., Pellar, R., Pulnits, S. A. and Seleger, V. V. (1980) Waves observed by the ARAKS experiment: the whistler mode. *Ann. Geophys.* **36**, 351.
- Farrell, W. M., Gurnett, D. A., Banks, P. M., Bush, R. I. and Raitt, W. J. (1988) Analysis of the whistler-mode radiation from the *Spacelab-2* electron beam. *J. geophys. Res.* **95**, 153.
- Farrell, W. M., Gurnett, D. A. and Goertz, C. K. (1989) Coherent Cerenkov radiation from the *Spacelab-2* electron beam. *J. geophys. Res.* **94**, 443.
- Gurnett, D. A. (1966) A satellite study of VLF hiss. *J. geophys. Res.* **71**, 5599.
- Gurnett, D. A. (1983) High latitude electromagnetic plasma wave emissions, in *High Latitude Space Physics* (Edited by Hultqvist, B. and Hagfors, T.). Plenum Press, New York.
- Gurnett, D. A., Kurth, W. S. and Scarf, F. L. (1979) Auroral hiss observed near the Io plasma torus. *Nature* **280**, 767.
- Gurnett, D. A., Kurth, W. S., Steinberg, J. T., Banks, P. M., Bush, R. I. and Raitt, W. J. (1986) Whistler-mode radiation from the *Spacelab-2* electron beam. *Geophys. Res. Lett.* **13**, 225.
- Gurnett, D. A., Shawhan, S. D. and Shaw, R. R. (1983) Auroral hiss, Z-mode radiation, and auroral kilometric radiation in the polar magnetosphere: DE-1 observations. *J. geophys. Res.* **88**, 329.
- Harker, K. J. and Banks, P. M. (1983) Radiation from pulsed electron beams in space plasmas. *Radio Sci.* **19**, 454.
- Harker, K. J. and Banks, P. M. (1985) Radiation from long pulse train electron beams in space plasmas. *Planet. Space Sci.* **33**, 953.
- James, H. G. (1976) VLF saucers. *J. geophys. Res.* **81**, 501.
- Jones, T. W. and Kellogg, P. J. (1973) Plasma waves arti-

cially induced
2166.
Jorgensen, T.
sured in OC
Cerenkov r
Laaspere, T.
Observatio
phenomen
OGO-6. J.
Kin, C. S., B
(1984) Cor
beams near
Maggs, J. E.
geophys. R
Maggs, J. E.
model of t
trostatic no
spiraling in

ORIGINAL PAGE IS
OF POOR QUALITY

- officially induced in the ionosphere. *J. geophys. Res.* **75**, 2166.
- Jorgensen, T. S. (1968) Interpretation of auroral hiss measured in OGO-2 and at Byrd Station in terms of incoherent Cerenkov radiation. *J. geophys. Res.* **73**, 1055.
- Laaspere, T., Johnson, W. C. and Semperebon, L. G. (1971) Observations of auroral hiss, LHR noise, and other phenomena in the frequency range 20 Hz to 540 kHz on OGO-6. *J. geophys. Res.* **76**, 4477.
- Kin, C. S., Burch, J. L., Shawhan, S. D. and Gurnett, D. A. (1984) Correlation of auroral hiss and upward electron beams near the polar cusp. *J. geophys. Res.* **89**, 925.
- Maggs, J. E. (1976) Coherent generation of VLF hiss. *J. geophys. Res.* **81**, 1707.
- Maggs, J. E. and Lotko, W. (1981). Altitude dependent model of the auroral beam and beam-generated electrostatic noise. *J. geophys. Res.* **86**, 3439.
- Mansfield, V. N. (1967) Radiation from a charged particle spiraling in a cold magnetoplasma. *Astrophys. J.* **147**, 672.
- Monson, S. J., Kellog, P. J. and Cartwright, D. G. (1976) Whistler-mode plasma waves observed on Electron Echo II. *J. geophys. Res.* **81**, 2193.
- Okuda, H., Horton, R., Ono, M. and Ashour-Abdalla, M. (1987) Propagation of a nonrelativistic electron beam in a plasma in a magnetic field. *Phys. Fluids* **30**, 200.
- Shawhan, S. D., Murphy, G. B., Banks, P. M., Williamson, P. R. and Raitt, W. J. (1984) Wave emissions from D. C. and modulated electron beams on STS-3. *Radio Sci.* **19**, No. 2, 471-486.
- Stix, T. H. (1962) *The Theory of Plasma Waves*. McGraw-Hill, New York.
- Taylor, W. W. L. and Shawhan, S. D. (1974) A test of incoherent Cerenkov radiation for VLF hiss and other magnetospheric emissions. *J. geophys. Res.* **79**, 105.
- Winglee, R. M. and Prichett, P. L. (1988) Comparative study of cross-field and field-aligned electron beams in active experiments. *J. geophys. Res.* **93**, 5823.



Electron Velocity Distributions and Plasma Waves Associated With the Injection of an Electron Beam Into the Ionosphere

L. A. FRANK,¹ W. R. PATERSON,¹ M. ASHOUR-ABDALLA,^{2,3} D. SCHRIVER,^{3,4}
W. S. KURTH,¹ D. A. GURNETT,¹ N. OMIDI,³ P. M. BANKS,⁵
R. I. BUSH,⁵ AND W. J. RAITT⁶

An electron beam was injected into Earth's ionosphere on August 1, 1985, during the flight of the space shuttle *Challenger* as part of the objectives of the Spacelab 2 mission. In the wake of the space shuttle a magnetically aligned sheet of electrons returning from the direction of propagation of the beam was detected with the free-flying Plasma Diagnostics Package. The thickness of this sheet of returning electrons was about 20 m. Large intensifications of broadband electrostatic noise were also observed within this sheet of electrons. A numerical simulation of the interaction of the electron beam with the ambient ionospheric plasmas is employed to show that the electron beam excites electron plasma oscillations and that it is possible for the ion acoustic instability to provide a returning flux of hot electrons by means of quasi-linear diffusion.

INTRODUCTION

Spacelab 2 was carried into an orbit with altitude ~ 320 km and inclination 49.5° on the space shuttle *Challenger* on July 29, 1985. During August 1 the Plasma Diagnostics Package (PDP) was put into free flight around *Challenger* in order to measure phenomena associated with the passage of a large vehicle through the ionosphere, the injection of electron beams, the release of volatiles, and the ambient ionosphere. The PDP provided observations out to a distance of ~ 400 m from the space shuttle before it was retrieved on the same day. A Langmuir probe, an ion mass spectrometer, a hot plasma analyzer, a differential ion flux probe, and a plasma wave receiver were among the instruments on board the PDP. For a description of this instrumentation the reader is referred to *Shawhan* [1982]. Of relevance to the present investigation are the measurements of the three-dimensional velocity distributions of electrons in the energy range 2 eV to 36 keV with the hot plasma analyzer, the LEPEDDA, and of the spectral energy density of the electric fields of plasma waves in the frequency range from 31 Hz to 17.8 MHz. These two instruments were used to observe the electrons and plasma waves produced by the 1-keV electron beam injected into the ionosphere with the fast pulse electron generator (FPEG) that was located in the bay of the shuttle. The implementation of the FPEG was the joint responsibility of Stanford University and Utah State University [see *Raitt et al.*, 1982], and the PDP was designed and constructed at The University of Iowa. We present initial observations of hot electrons and plasma waves that are produced by the electron beam. The effects are confined to a narrow, mag-

netically aligned sheet in the wake of the shuttle. The results of a numerical simulation are used in order to interpret the large intensities of hot electrons that return from the direction of beam injection and the presence of intense broadband electrostatic noise.

The first artificial injection of an electron beam into the ionosphere was reported by *Hess et al.* [1971]. Even for this early experiment it was noted that the ambient electron plasmas were heated by the electron beam. The early rocket-borne experiments were primarily focused on exciting artificial auroras and providing a means for investigating the motion of electrons between their geomagnetic mirror points. More recently, the scientific thrust has been directed toward understanding the heating of electron plasmas and the generation of plasma waves by the electron beam because of the relevance of these phenomena to mechanisms for the interaction of the naturally occurring auroral electron beams with the ionosphere. The artificial electron beams offer a unique opportunity to determine the beam-plasma interactions that can heat ionospheric electron plasmas greatly in excess of that expected from direct Coulomb interactions [cf. *Maehlum et al.*, 1980, and references therein]. An extensive review of early experiments with artificial electron beams is given by *Winckler* [1980].

Previous injections of an artificial electron beam from the space shuttle were accomplished during the STS 3 and Spacelab 1 missions. During the Spacelab 1 mission a large flux of returning hot electrons was observed [*Wilhelm et al.*, 1984], and whistler mode, narrow-band emissions near $3f_c$ and $4f_c$ (f_c , electron cyclotron frequency) and broadband electrostatic noise were clearly present [*Beghin et al.*, 1984]. These plasma and plasma wave measurements were obtained in the bay of the space shuttle. The instrumentation used for the STS 3 mission was similar to that for the Spacelab 2 mission, except that the PDP was not released into free flight from the space shuttle. Observations of electromagnetic radiation during the electron beam firings of the STS 3 mission are reported by *Reeves et al.* [1988a]. *Winglee and Pritchett* [1988] give the results of a numerical simulation model to account for the complex behavior of the electron beam in the immediate vicinity of the electron gun nozzle when the beam electrons are expected to execute a coherent helical motion about the local magnetic field. The

¹Department of Physics and Astronomy, University of Iowa, Iowa City.

²Department of Physics, University of California, Los Angeles.

³Institute of Geophysics and Planetary Physics, University of California, Los Angeles.

⁴Now at Max-Planck Institute for Extraterrestrial Physics, Garching, Federal Republic of Germany.

⁵STAR Laboratory, Stanford University, Stanford, California.

⁶Center for Atmospheric and Space Sciences, Utah State University, Logan.

Copyright 1989 by the American Geophysical Union.

Paper number 89JA00507.
0148-0227/89/89JA-00507\$02.00

VIEWING GEOMETRY FOR RETURN ELECTRON FLUX
FROM ELECTRON BEAM (0411 UT, 1 AUGUST 1985)

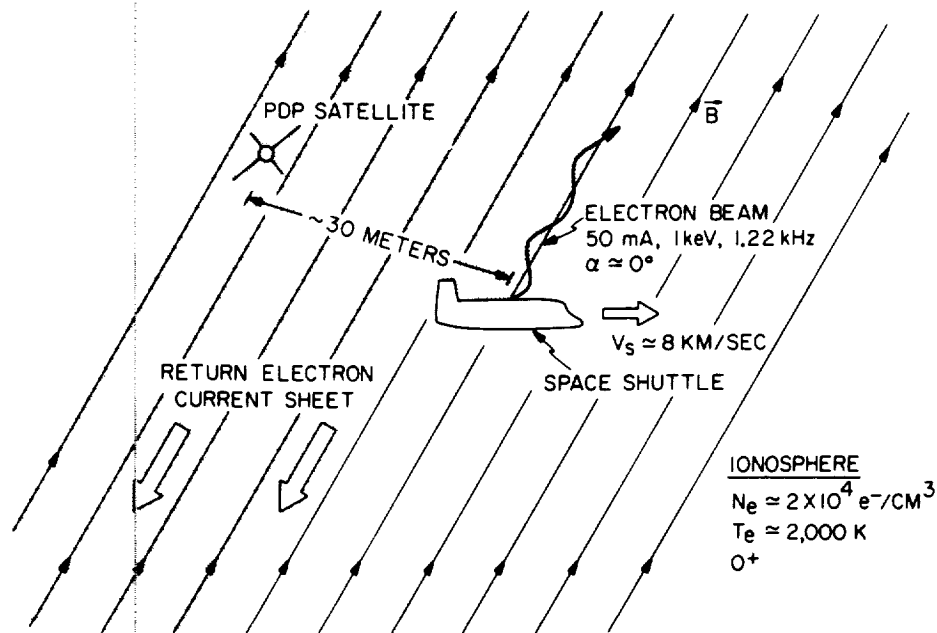


Fig. 1. Viewing geometry for observing the electron velocity distributions and plasma waves produced by the launching of an electron beam from the bay of the space shuttle *Challenger*.

beam density is large in relation to the ambient ionospheric density, and the beam is expected to lose its coherency, i.e., its collimated spiral motion along the ambient magnetic field, within scale lengths of meters from the injection point. This simulation was not carried forward in time sufficiently long to identify the presence of low-frequency ion waves. Our present study uses observations of the effects of the beam electrons at much larger distances from the space shuttle during the Spacelab 2 mission, i.e., the escaping electrons, and a numerical simulation that reveals the probable generation of ion acoustic waves. Our presently reported observations were taken with instruments on board the PDP during its several-hour free flight around the space shuttle and hence are relatively uncompromised by shuttle-associated effects. These unique observations of electron plasmas and plasma waves provide the basis for a significant extension of knowledge of electron beam-plasma interactions.

OBSERVATIONS

The PDP encountered the sheet of returning electrons during eight FPEG beam launching sequences. Our presentation concentrates on the sequence that occurred for 430 s beginning at 0411:13 UT. The situation is depicted in Figure 1. The 1-keV electron beam was modulated at a 1.22-kHz frequency with a 50% duty cycle. The current was 50 mA. Inspection of observations when the beam was unmodulated shows that the modulation of the current has no apparent effect on the phenomena reported here. During the period 0411:13–0412:02 UT a large flux of hot electrons was encountered. The velocity distribution function is anisotropic with measurable densities at all pitch angles and with maximum densities corresponding to fluxes returning to the ionosphere. The injected electron beam was propagating away

from the ionosphere. The thickness of this field-aligned current sheet was about 20 m as measured for several crossings during operation of the FPEG. For comparison the gyroradius of a 1-keV electron moving perpendicular to the local magnetic field vector is 4.9 m. For the measurements of electrons presented here, the electron beam is injected nearly parallel to the magnetic field. During the above time period the PDP moved from a position ~ 15 m downstream from field lines intersecting the shuttle to ~ 45 m as it crossed out of the current sheet. During another electron beam injection this electron sheet was seen to extend at least to 170 m behind the shuttle. Such field-aligned electron distributions were not observed when the PDP was positioned outside the expected location of the sheet when the electron gun was activated. The velocity distribution of hot electrons returning along the magnetic field ($\alpha \approx 165^\circ$) at 0411:26 UT is shown in Figure 2. The anisotropy is large. For electrons with pitch angle $\alpha \approx 15^\circ$, $f \approx 10^{-28}$ s³/cm⁶ at $v = 6 \times 10^8$ cm/s, i.e., a factor of ~ 100 less than that of the returning electron flux at $\alpha \approx 165^\circ$. The phase space density increases with decreasing electron speed, and the electron number density integrated over all pitch angles is ~ 100 el/cm³ for $E \geq 2$ eV. The energy spectrum and angular distributions are qualitatively similar to those observed previously during beam injections into the ionosphere from rockets [Winckler *et al.*, 1975; Duprat *et al.*, 1983; Wilhelm *et al.*, 1985]. The upper limit for the electron velocity distribution at similar pitch angles but just outside the sheet while the FPEG was still activated at 0412:19 UT is also shown in Figure 2.

The possibility that the returning electrons are due to backscattering from the ambient neutral atmosphere must be evaluated in order to identify the current sheet as a signature of a beam-plasma interaction. We have numerically esti-

mated the contribution from atmospheric scattering using the relationship

$$\frac{d^2 j_s}{dE d\Omega} = j\rho \frac{d^2 \sigma}{dE d\Omega} \frac{Vt \sin \alpha}{(V \cos \alpha / V_b - 1)^2} \quad (1)$$

where j_s is the secondary flux, V is the speed of these electrons, α is their pitch angle, V_b is the speed of the beam electrons, j is the beam directional flux, and ρ is the atmospheric number density. The mass spectrometer incoherent scatter 1983 (MSIS-83) model [Hedin, 1983] is used for atmospheric densities. The differential cross section $d^2 \sigma / dE d\Omega$ is approximated using the laboratory measurements reported by Opal et al. [1971] for several gases, but not atomic oxygen. The total scattering cross section for O I was taken to be one-half that given for O₂. It should be noted by the reader that the electron gun is moving with respect to the ambient atmospheric molecules and that numerical integration of equation (1) must include the condition of appropriate combinations of V , α , and t in order that the secondary electron from a given distance from the shuttle reaches the PDP at energy E . Then the time t is the elapsed time since the injection of the beam electron. The electron beam is injected at an altitude of ~ 320 km and in the direction away from the atmosphere. Further scattering of the secondary electrons before arrival at the PDP is neglected in these calculations. For the purpose of this estimate the primary electron beam is assumed to be monoenergetic, 1 keV, with no significant energy and pitch angle diffusion due to beam-plasma interactions. The computed field-aligned intensities of electrons from atmospheric scattering are shown in Figure 2. Open circles indicate the energies at which equation (1)

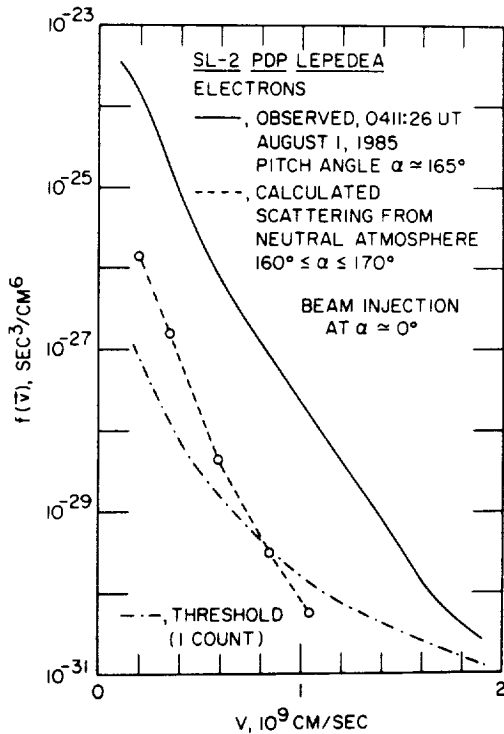


Fig. 2. Electron velocity distribution observed at pitch angle $\alpha = 165^\circ$ in the sheet of returning electrons in the wake of the space shuttle. The velocity distribution expected for secondary electrons from the neutral atmosphere is also shown. The observed upper limit for the velocity distribution just outside the electron sheet is given for comparison.

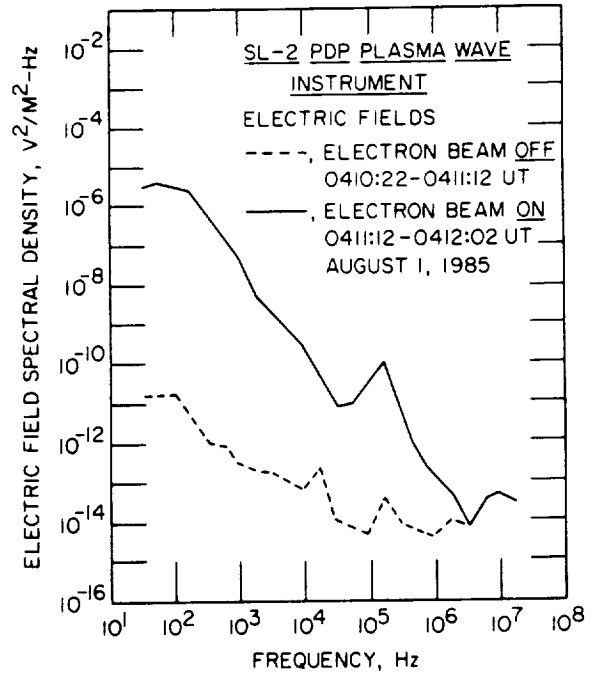


Fig. 3. Electric field spectral densities in the current sheet of returning electrons. Spectral densities for the immediately preceding period when the electron beam is not present are shown for comparison.

was evaluated. At low energies these intensities are lower than the observed intensities by factors of ~ 100 . Confidence in the calculated scattered intensities is supported by reasonable agreement of these intensities with those observed further downstream in the electron sheet where the electron intensities may be expected to be due mainly to atmospheric scattering. No evidence was found in the LEPEDEA ion measurements for significant increases of thermal or suprathermal ion densities that are expected to occur from ionization of the ambient neutral atmosphere by a beam-plasma discharge (see Grandal [1982] for discussions of this phenomenon). Thus the field-aligned intensities reported here are likely to be due to a beam-plasma interaction.

The spectral densities of the electric fields increased dramatically in the sheet of returning electrons relative to the densities observed prior to injection of the electron beam. These spectral densities are shown in Figure 3. At 100 Hz the increase is by a factor of $\sim 10^5$ during operation of the electron gun. The local electron plasma frequency, f_{pe} , is ~ 1.3 MHz as determined from measurements of ionospheric densities with a Langmuir probe (courtesy of N. D'Angelo, 1988). Thus the increases of broadband electrostatic noise as shown in Figure 3 occur at frequencies $\leq f_{pe}$. Because the electron gyrofrequency f_c is ~ 0.6 MHz and no well-defined feature of the spectral densities is present at frequencies $\sim 1-2$ MHz, the upper frequency cutoff for the broadband electrostatic noise cannot be firmly identified as f_{pe} or the upper hybrid resonance frequency $f_{UHR} = (f_{pe}^2 + f_c^2)^{1/2}$. Simultaneous measurements of the magnetic field spectral densities for the range ~ 30 Hz to 200 kHz are not available for this crossing of the electron sheet because of the cyclic sampling mode for the search coil which shares the data channel with the electric antenna and Langmuir probe. No increases in magnetic field spectral densities at low frequencies were observed during another, more distant sheet

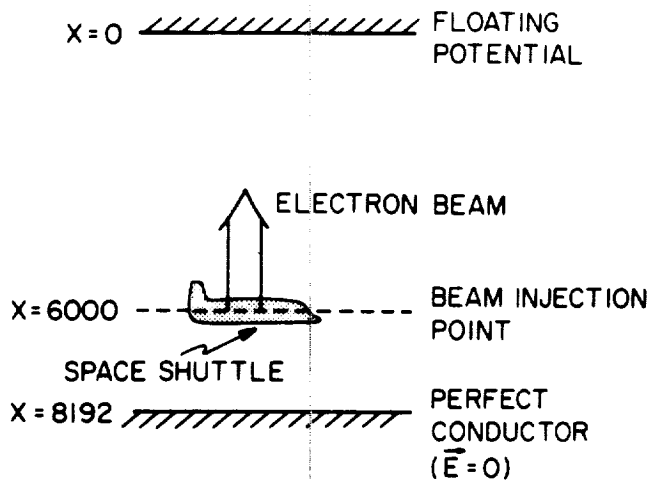


Fig. 4. Geometry assumed for the computer simulation of the injection of the electron beam into the ionosphere with a nonperiodic, one-dimensional electrostatic code.

crossing at 0248 UT. The increases of broadband electrostatic noise were similar to those shown in Figure 3. Gurnett *et al.* [1986] have reported observations of whistler mode radiation from the electron beam during the Spacelab 2 mission as the PDP approached within ~ 10 m of the magnetic field lines of the electron beam. At these small distances the low-frequency broadband noise is observed in electric and magnetic components, and the relative contributions from electromagnetic and electrostatic modes to the electric field spectral densities cannot be resolved. Bush *et al.* [1987] and Reeves *et al.* [1988b] also present observations of the electromagnetic radiation associated with the electron beam during the Spacelab 2 mission. The presence of this whistler mode radiation during the presently discussed observations is identified by the spectral peak at ~ 200 kHz in Figure 3. This conclusion is based upon the funnel-shaped frequency-time spectrum that is evident in the electric field spectrograms (not shown here).

INTERPRETATION AND DISCUSSION

In order to model electron beam injection into an ambient plasma from the space shuttle for a comparison with observations, a nonperiodic one-dimensional electrostatic particle code is used [Okuda *et al.*, 1987]. The reader is referred to Birdsall and Langdon [1985] for a discussion of basic algorithms used in these simulations. As illustrated in Figure 4, the top boundary at $X = 0$ is free whereby plasma crossing the boundary to $X < 0$ is lost from the system and the electric potential can float to any value according to the charge density. The bottom boundary at $X = L = 8192\Delta$ (where Δ is the grid size, set equal to the electron Debye length λ_e) is modeled as a perfect conductor with the electric field at $X = L$ set equal to zero, and the plasma particles are reflected with $v \rightarrow -v$ when they reach the bottom boundary. The beam is injected at $X = 6000\Delta$ into a charge neutral background plasma and moves toward $X = 0$ (which is in the negative x direction in simulation coordinates) with a drift speed $V_d = -20v_{te}$. It is assumed that the shuttle injects the beam from a position $X = 6000\Delta$. Thus the boundary at $X = L$ represents the conducting ionosphere, and the PDP which measures the plasma diagnostics (and lags behind the shuttle) would arrive at some position $0 < X < 6000\Delta$ after beam

injection, according to the observational geometry of Figure 1.

Because low-frequency ion waves and ion time scales are of interest here, the full dynamics of both ions and electrons must be followed, and a reduced mass ratio $m_i/m_e = 100$ is used. The density of ambient plasma particles n_0 is initially 40 per grid space, and the beam density is $n_b = n_0/8$. The ion and electron temperatures are initially equal ($T_e = T_i$). The electron beam temperature $T_b = T_e$. When the beam electrons (injected at $X = 6000\Delta$ with $V_d = -20v_{te}$) reach the top boundary at $X = 0$, the simulation run is stopped.

At $t = 0$, only a charge neutral ambient plasma is present in the system, and for $t > 0$ the introduction of the beam electrons at $X = 6000\Delta$ creates a net negative charge in that region. This charge imbalance creates an electric field in front of the beam, from $X = 0$ to $X = 6000\Delta$, while behind the beam ($6000\Delta < X < L$) the electric field is zero because of the conducting ionosphere at $X = L$. The electric field in front of the beam accelerates the ambient electrons to the top so that, in effect, the injected beam pushes the electrons ahead such that charge neutrality can be maintained in the plasma. The ambient electrons pushed ahead of the beam are lost from the system at $X = 0$, and a rough balance is achieved such that the number of new electrons introduced by beam injection is about equal to the number of ambient electrons that exit the system at the top under the influence of the induced electric field.

The drift of the ambient electrons caused by the induced electric field is not a return current like that found in the beam injection simulations of Ashour-Abdalla and Okuda [1986] and Okuda and Ashour-Abdalla [1988], because the drifting electrons move away from the spacecraft (and injected beam) rather than back toward it. However, there are

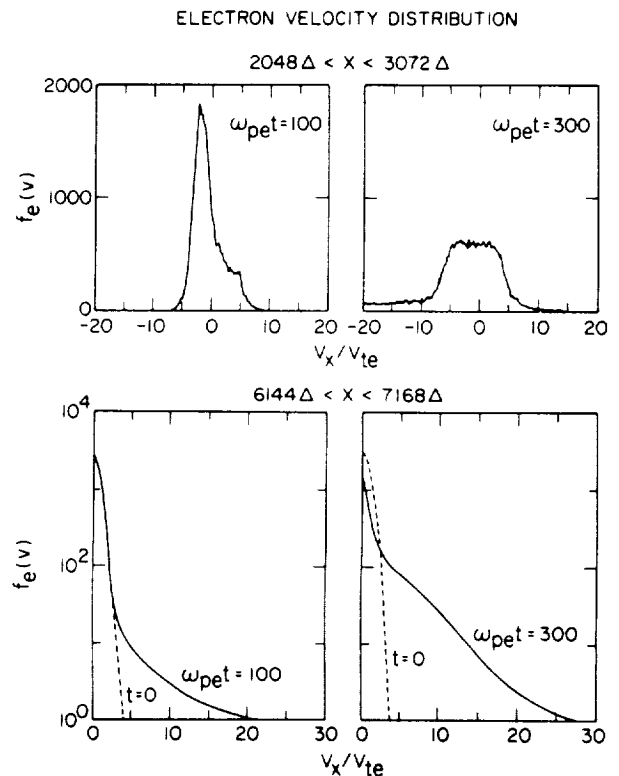


Fig. 5. Temporal evolution of the electron velocity distribution for two different locations in the simulation model shown in Figure 4.

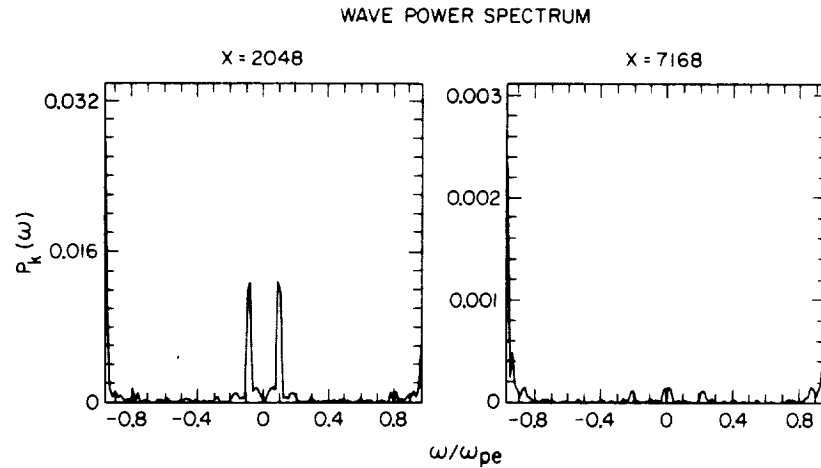


Fig. 6. Computed wave power spectral densities at two locations in the simulation model for $\omega_{pe}t = 300$.

electrons that can be accelerated in the direction opposite to the beam velocity and can be detected by the PDP. This occurs as a result of wave-particle interactions due to plasma instabilities excited by the drifting ambient electrons. The induced electric field caused by the injection of the electron beam at $X = 6000\Delta$ accelerates the ambient electrons at $X < 6000\Delta$ to the top, and the net drift between the ambient ions and drifting ambient electrons can then drive the ion acoustic instability. This process is similar to that described by *Okuda and Ashour-Abdalla* [1988], for which an ion acoustic instability was excited not by the injected beam but by the return current.

The ion acoustic instability is excited by an electron-ion drift [*Fried and Gould*, 1961; *Hasegawa*, 1975] where in the ion rest frame, the ion acoustic phase velocity will occur on the negative slope of the electron velocity distribution function and the instability results from inverse electron Landau damping. The ion acoustic mode propagates parallel to the ambient magnetic field, and for short wavelengths ($k\lambda_e > 1$) the frequency approaches the ion plasma frequency. The velocity threshold at which the instability is excited decreases as T_e/T_i increases greater than 1, but for $T_e = T_i$, the instability can still be unstable for high enough drift velocity [*Gary and Omid*, 1987]. This critical drift velocity is reached by the ambient electrons in the simulation run, and the ion acoustic instability is excited.

To illustrate how the instability is excited in the simulation run, the electron velocity distribution is shown in Figure 5. The top two panels show the ambient electron velocity distribution at $2048\Delta < X < 3072\Delta$, which is in front of the beam. The top left panel is for $\omega_{pe}t = 100$, and the distribution is seen to be shifted to a negative drift velocity by the induced electric field. The negative slope is unstable to the ion acoustic instability, and the slope already shows plateauing due to quasi-linear diffusion which accelerates the electrons to $v > 0$ and forms a positive velocity high-energy tail. The top right panel shows that at the end of the simulation, when $\omega_{pe}t = 300$, the unstable slope is completely eliminated by diffusion due to the ion acoustic instability and the high-energy tail for $v > 0$ is much more pronounced than at earlier times. These high-energy electrons, accelerated by the wave-particle interactions, flow to the bottom and can penetrate the region behind the beam at $X > 6000\Delta$. This is seen in the bottom two panels of Figure 5, which show (on a

semilog plot) the electron velocity distribution at $6144\Delta < X < 7168\Delta$, which is behind the injection of the beam. At $\omega_{pe}t = 100$, shown in the bottom left panel, there is no net drift velocity evident in the velocity distribution, as is expected because the electric field is zero in the region behind the beam. However, a few of the high-energy particles with $v > 0$ created at $X < 6000\Delta$ have already reached this spatial region, and a slight high-energy tail is present. By the end of the simulation, as shown in the bottom right panel, a number of the high-energy electrons have reached $X > 6144\Delta$, and a considerable high-energy tail is formed, similar to that observed with the PDP. Note that the PDP is not located in a position such that the electron plasma oscillations in the beam can be observed, but is positioned behind the electron beam as it propagates along the magnetic field.

An examination of the wave spectrum from the simulation run confirms that ion acoustic waves are excited. Figure 6 shows the wave power spectrum at two different locations along the simulation box. The left panel is taken for $X = 2048\Delta$, which is in front of the beam injection, and two types of waves are excited. At high frequencies near ω_{pe} , plasma oscillations are excited by the injected beam. This excitation is expected because the primary beam is unstable to a Buneman type two-stream instability excited by the relative drift between the injected beam and the ambient plasma background. Lower-frequency waves are also present at just less than ω_{pi} . These ion acoustic waves are excited by the background electron drift as already described. (Note that because of the reduced mass ratio, $\omega_{pi}/\omega_{pe} = (m_e/m_i)^{1/2} = 0.1$.) The observed broadband electrostatic noise spectrum extends to frequencies above ω_{pi} and could be explained in terms of Doppler shifting of the waves. The right panel shows the power spectrum for $X = 7168\Delta$, which is behind the beam, and it is clear that no ion acoustic waves are excited because there is no drift of the ambient plasma in this region. The ordinate scale is a factor of ~ 0.1 less than that of the left panel. A weak plasma oscillation is present, but the wave power is nearly an order of magnitude less than that shown in the left panel.

For numerical simulation that is intended to account for observed plasma phenomena it is useful to compare the parameters. The beam density n_b used in the numerical simulation is $n_0/8$, where n_0 is the ambient thermal density. The actual electron beam was injected nearly parallel to the

magnetic field. If the range of pitch angles for beam injection is $\alpha = 0^\circ\text{--}10^\circ$, then the beam density for a homogeneous electron distribution over these pitch angles is about $n_0/2.9$, where $n_0 = 2 \times 10^4$ el/cm³. For the simulation the drift speed V_d for the beam electrons is assumed to be $20v_{te}$, where v_{te} is the characteristic thermal speed of the ambient electrons. A reduced mass ratio m_i/m_e is used. For the injection of the electron beam from the space shuttle, $V_d = 75v_{te}$. The simulation was performed over times extending to about $\omega_{pe}t = 300$. Observations of the electron plasmas and plasma waves with the PDP as reported here occurred at a distance of ~ 30 m from the space shuttle, or $\omega_{pe}t = 3 \times 10^4$. The PDP is not simultaneously located on the magnetic field line when the electron beam is injected (see Figure 1). For a given field line and pitch angles for electron injection of $0^\circ \leq \alpha \leq 10^\circ$, the length of the electron column along the field line is ~ 4 km, i.e., the propagation distance of a 1-keV electron as the shuttle moves a distance across the magnetic field of twice the gyroradius for $\alpha = 10^\circ$. The numerical simulation follows the beam propagation ~ 0.7 km along the field line. By the time that the field line is intercepted by the PDP the beam electrons have propagated ~ 70 km from this spacecraft. As shown in Figure 1, the PDP intercepts plasmas along the field line that the beam has previously traversed. The simulation model appears to demonstrate that it is the electron beam and not the return flux of electrons that excites the broadband electrostatic noise. Thus the observed waves may represent only the decaying waves that were previously excited directly in the electron beam. Further numerical simulations, together with observations at various distances in the sheet of returning electrons, are required to resolve this issue. The parameters chosen for the present numerical model are sufficiently similar to the observed plasma parameters that a possible mechanism for beam interaction with the ambient ionosphere can be initially identified and pursued in later studies.

The simulation results can be summarized as follows: (1) the injected electron beam excites plasma oscillations due to the relative beam-background drift and also creates a charge imbalance in the plasma which induces an electric field in front of the beam, (2) the induced electric field forces the background electrons to drift in relation to the background ions, exciting the ion acoustic instability, and (3) the ion acoustic instability, through quasi-linear diffusion, creates an electron high-energy tail in the direction opposite of the injected beam, and these hot electrons are observed by the PDP.

Acknowledgments. The authors are grateful to N. D'Angelo for the use of thermal electron plasma measurements from the Langmuir probe. This research was supported in part at The University of Iowa by NASA under contract NAS8-32807 and grants NAG3-449 and NGL-16-001-002, at the University of California, Los Angeles, by the Air Force under contracts F19628-88-K-0011 and F19628-88-K-0022, and at Stanford University and Utah State University by NASA under contract NAS8-36011 and grant NAGW-235. Part of the computing was performed at the San Diego Supercomputer Center supported by the National Science Foundation.

The Editor thanks W. Bernstein and another referee for their assistance in evaluating this paper.

REFERENCES

Ashour-Abdalla, M., and H. Okuda, Electron acoustic instabilities in the geomagnetic tail, *Geophys. Res. Lett.*, **13**, 366, 1986.

- Beghin, C., J. P. Lebreton, B. N. Maehlum, J. Troim, P. Ingsoy, and J. L. Michau, Phenomena induced by charged particle beams, *Science*, **225**, 188, 1984.
- Birdsall, C. K., and A. B. Langdon, *Plasma Physics via Computer Simulation*, McGraw-Hill, New York, 1985.
- Bush, R. I., G. D. Reeves, P. M. Banks, T. Neubert, P. R. Williamson, W. J. Raitt, and D. A. Gurnett, Electromagnetic fields from pulsed electron beam experiments in space: Spacelab-2 results, *Geophys. Res. Lett.*, **14**, 1015, 1987.
- Duprat, G. R. J., B. A. Whalen, and A. G. McNamara, Measurements of the stability of energetic electron beams in the ionosphere, *J. Geophys. Res.*, **88**, 3095, 1983.
- Fried, B. D., and R. W. Gould, Longitudinal ion oscillations in a hot plasma, *Phys. Fluids*, **4**, 139, 1961.
- Gary, S. P., and N. Omid, The ion-ion acoustic instability, *J. Plasma Phys.*, **37**, 45, 1987.
- Grandal, B. (Ed.), *Artificial Particle Beams in Space Plasma Studies*, Plenum, New York, 1982.
- Gurnett, D. A., W. S. Kurth, J. T. Steinberg, P. M. Banks, R. I. Bush, and W. J. Raitt, Whistler-mode radiation from the Spacelab 2 electron beam, *Geophys. Res. Lett.*, **13**, 225, 1986.
- Hasegawa, A., Plasma instabilities and nonlinear effects, in *Physics and Chemistry in Space*, vol. 8, edited by J. Roederer and J. T. Wasson, p. 17, Springer-Verlag, New York, 1975.
- Hedin, A. E., A revised thermospheric model based on mass spectrometer and incoherent scatter data: MSIS-83, *J. Geophys. Res.*, **88**, 10,170, 1983.
- Hess, W. N., M. C. Trichel, T. N. Davis, W. C. Beggs, G. E. Kraft, E. Stassinopoulos, and E. J. R. Maier, Artificial auroral experiment: Experiment and principal results, *J. Geophys. Res.*, **76**, 6067, 1971.
- Maehlum, B. N., B. Grandal, T. A. Jacobsen, and J. Troim, Polar 5—An electron accelerator experiment within an aurora, 2. Scattering of an artificially produced electron beam in the atmosphere, *Planet. Space Sci.*, **28**, 279, 1980.
- Okuda, H., and M. Ashour-Abdalla, Ion acoustic instabilities excited by injection of an electron beam in space, *J. Geophys. Res.*, **93**, 2011, 1988.
- Okuda, H., R. Horton, M. Ono, and M. Ashour-Abdalla, Propagation of a nonrelativistic electron beam in a plasma in a magnetic field, *Phys. Fluids*, **30**, 200, 1987.
- Opal, C. B., W. K. Peterson, and E. C. Beatty, Measurements of secondary-electron spectra produced by electron impact ionization of a number of simple gases, *J. Chem. Phys.*, **55**, 4100, 1971.
- Raitt, W. J., P. M. Banks, W. F. Denig, and H. R. Anderson, Transient effects in beam-plasma interactions in a space simulation chamber stimulated by a fast pulse electron gun, in *Artificial Particle Beams in Space Plasma Studies*, edited by B. Grandal, p. 405, Plenum, New York, 1982.
- Reeves, G. D., P. M. Banks, A. C. Fraser-Smith, T. Neubert, R. I. Bush, D. A. Gurnett, and W. J. Raitt, VLF wave stimulation by pulsed electron beams injected from the space shuttle, *J. Geophys. Res.*, **93**, 162, 1988a.
- Reeves, G. D., P. M. Banks, T. Neubert, R. I. Bush, P. R. Williamson, A. C. Fraser-Smith, D. A. Gurnett, and W. J. Raitt, VLF wave emissions by pulsed and DC electron beams in space, 1, Spacelab 2 observations, *J. Geophys. Res.*, **93**, 14,699, 1988b.
- Shawhan, S. D., Description of the plasma diagnostics package (PDP) for the OSS-1 shuttle mission and JSC plasma chamber test in conjunction with the fast pulse electron gun (FPEG), in *Artificial Particle Beams in Space Plasma Studies*, edited by B. Grandal, p. 419, Plenum, New York, 1982.
- Wilhelm, K., W. Stüdemann, and W. Riedler, Electron flux intensity distributions observed in response to particle beam emissions, *Science*, **225**, 186, 1984.
- Wilhelm, K., W. Bernstein, P. J. Kellogg, and B. A. Whalen, Fast magnetospheric echoes of energetic electron beams, *J. Geophys. Res.*, **90**, 491, 1985.
- Winckler, J. R., The application of artificial electron beams to magnetospheric research, *Rev. Geophys.*, **18**, 659, 1980.
- Winckler, J. R., R. L. Arnoldy, and R. A. Hendrickson, Echo 2: A study of electron beams injected into the high-latitude ionosphere from a large sounding rocket, *J. Geophys. Res.*, **80**, 2083, 1975.
- Winglee, R. M., and P. L. Pritchett, Comparative study of cross-field and field-aligned electron beams in active experiments, *J. Geophys. Res.*, **93**, 5823, 1988.

M. Ashour-Abdalla and N. Omid, Institute of Geophysics and Planetary Physics, University of California, Los Angeles, CA 90024.
P. M. Banks and R. I. Bush, STAR Laboratory, Stanford University, Stanford, CA 94305.

L. A. Frank, D. A. Gurnett, W. S. Kurth, and W. R. Paterson, Department of Physics and Astronomy, University of Iowa, Iowa City, IA 52242.

W. J. Raitt, CASS, Utah State University, Logan, UT 84322.
D. Schriver, Max-Planck-Institut für Extraterrestrische Physik, 8046 Garching, Federal Republic of Germany.

(Received January 3, 1989;
revised February 16, 1989;
accepted March 8, 1989.)



Plasma Density Fluctuations Observed During Space Shuttle Orbiter Water Releases

J. S. PICKETT, N. D'ANGELO, AND W. S. KURTH

Department of Physics and Astronomy, University of Iowa, Iowa City

Observations by the Langmuir probe on the Plasma Diagnostics Package flown as part of the Spacelab 2 mission in the summer of 1985 show a strong increase in the level of turbulence near the shuttle orbiter during operations in which liquid water is released. The spectrum of the plasma density fluctuations peaks at the lowest frequencies measured (a few hertz) and extends up to a few kilohertz, near the lower hybrid frequency. We suggest two potential mechanisms for generating the plasma turbulence which are both based on the production of water ions as a result of charge exchange with the ambient oxygen ions in the ionosphere. The first mechanism proposed is the ion-plasma instability which arises from the drift of the contaminant ions with respect to the ambient oxygen ions. The other mechanism proposed is the Ott-Farley instability which is a result of the ring distribution formed by the "pick-up" water ions.

1. INTRODUCTION

One of the objectives of flying the Plasma Diagnostics Package on the Spacelab 2 mission was to study the interaction of the shuttle orbiter with the ionospheric environment [Kurth and Frank, 1989]. In particular, Pickett *et al.* [1985] have shown that there are numerous observable effects associated with the introduction of contaminants into the orbiter environment through such normal operations as thruster firings, water dumps, and flash evaporator operations. These effects include increases in neutral density, increases or decreases in plasma density, variations in the plasma potential, and increases in turbulence in the vicinity of the shuttle orbiter.

In this paper we focus on the plasma turbulence associated with the release of liquid water by the shuttle orbiter. Such releases are required to get rid of the excess water produced by the fuel cells or of other wastewater produced within the orbiter. This is a normal operation for the shuttle orbiter, and similar water dumps might be required by the space station; an understanding of the effects on the environment is important for some experiments being performed on either of these platforms. In addition, the shuttle orbiter mimics some of the characteristics of comets by being a copious source of contaminant ions and, hence, provides a convenient laboratory from which to study some of the cometlike interactions with an impinging plasma. As with both comets Giacobini-Zinner and Halley, ion "pick-up" is a particularly important process in the vicinity of the shuttle orbiter. An advantage provided by the orbiter is that some of the sources of contaminants can be turned on and off, thus affording a measure of control in experiments designed to study the effects.

In section 2 of this paper we describe the essential features of the Plasma Diagnostics Package and the Langmuir probe with which the observations were made, as well as some of the details of the water dump operations. In section 3 we present the observations of plasma density fluctuations associated with typical water dumps. In section 4 we offer two possible mechanisms for producing the observed turbu-

lence, the ion-plasma instability and the Ott-Farley instability.

2. THE EXPERIMENT

The Plasma Diagnostics Package (PDP) is one of 13 experiments which was flown as part of the Spacelab 2 (SL 2) payload on space shuttle flight 51-F from July 29 to August 6, 1985. A description of the PDP, its instrumentation, its operation, and the scientific objectives of the investigation are given by Kurth and Frank [1989]. One of the PDP instruments, a Langmuir probe, was used to obtain measurements of electron density (10^3 - 10^7 cm⁻³), temperature (800°-5000°K), and density fluctuations (1 Hz to 178 kHz). The PDP Langmuir probe that was flown on SL 2 is described in detail by Tribble *et al.* [1989]. A similar instrument was flown as part of the PDP experiment on the third space shuttle flight [Murphy *et al.*, 1986].

One of the scientific objectives of the PDP experiment on SL 2 was to investigate the effects of shuttle orbiter water dumps on the orbiter environment. Two kinds of water dumps took place during the SL 2 flight: namely, supply and waste (H. Rotter, personal communication, 1989). The supply water dump is used to dispose of excess water produced by the fuel cells. A typical operation consists of releasing approximately 45 kg of liquid water in a nonpropulsive fashion along the -Y axis of the orbiter (see Figure 1) at a rate of about 55 kg/h. The waste water dump is used to dispose of a mixture which consists of ~50% humidity condensate water and 50% urine by dumping it overboard (also along the -Y axis). The quantity of wastewater released and the rate at which it is released are comparable to the supply water dump. The two differ, however, not only in their individual liquid components, but also in the amount of dissolved gases they contain. The wastewater contains ~20% dissolved gases by volume, whereas the supply water contains only ~2%.

In order to more effectively carry out the scientific objective of studying effects of water releases, certain times and PDP locations were set aside for this purpose. During times when the SL 2 solar experiments were scheduled for prime viewing, the PDP was positioned on the remote manipulator system (RMS) at a designated location called "point solar,"

Copyright 1989 by the American Geophysical Union.

Paper number 89JA01203.
0148-0227/89/89JA-01203\$02.00

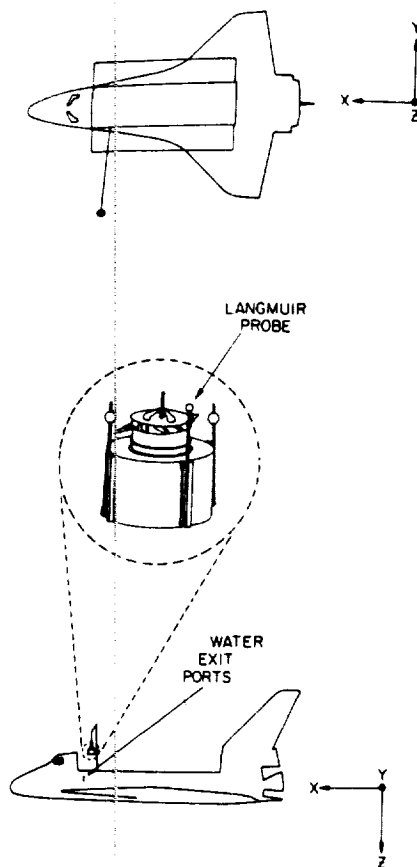


Fig. 1. Schematic of the shuttle orbiter in the XY and XZ planes (in an orbiter-based coordinate system), showing the location and orientation of the PDP and Langmuir probe on the RMS. This configuration was used during many of the orbiter water dumps.

as shown in Figure 1. The term "point solar" refers to the stationary position of the PDP on the RMS with the PDP upright ~ 12 m from the port side of the orbiter. Point solar is an ideal position from which to obtain measurements during water dumps because the water exit ports are located on the port side of the orbiter just below the forward payload bay door and only ~ 12 m from the PDP (see Figure 1).

Figure 1 provides an accurate perspective of the position of the PDP, at point solar, with respect to the orbiter. The enlarged view of the PDP shows the location of the Langmuir probe instrument's 3-cm-diameter, gold-plated sphere mounted on one of the four extendable booms. The PDP was occasionally rotated by 180° so that certain instruments could point in different directions and thermal control could be maintained.

There were a total of 16 supply and three wastewater dumps performed on SL 2, many of which took place during times when the PDP was positioned at point solar. Their effects on the orbiter environment, as determined by analysis of Langmuir probe data, are described in the next section.

3. OBSERVATIONS

The effects of a supply water dump, which occurred on day 212 from 1531 to 1642 UT, are evident in Figure 2. Plotted in this figure are measurements of electron density fluctuations as a function of time in two frequency ranges.

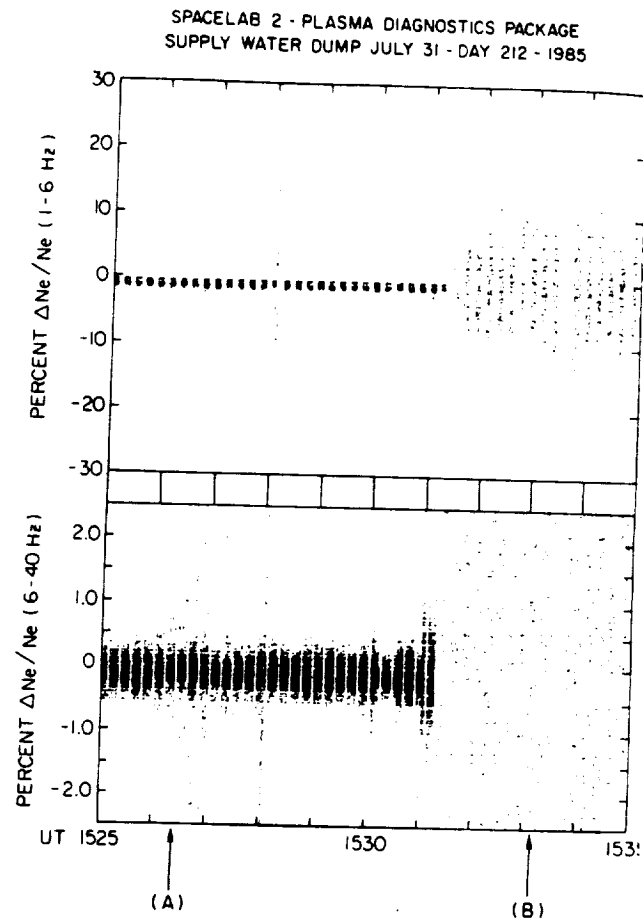


Fig. 2. $\Delta N_e/N_e$ data in the 1- to 6-Hz range (top panel) and 6- to 40-Hz range (lower panel) before and during an orbiter supply water dump. Turbulence is significantly increased in both frequency ranges when the outlet water valve is opened at ~ 1531 UT. The A and B pointers refer to times for which spectral density plots are provided in Figure 3.

The fluctuations are normalized to the density and expressed as percentages. During this time the PDP is positioned on the RMS at point solar as shown in Figure 1. Turbulence associated with the start of the water dump at approximately 1531 UT is seen in Figure 2. At that time, $\Delta N_e/N_e$ is seen to increase by about a factor of 25 in the 1- to 6-Hz channel (upper panel). A substantial increase is also seen in the 6- to 40-Hz channel data (lower panel), although the magnitude of the increase cannot be determined since that channel becomes saturated. The scale that is shown on the ordinate of each panel in Figure 2 represents the full dynamic range of each respective channel. The effects of a thruster firing are noted at 1528 UT.

Spectra of the higher frequency (35 Hz to 178 kHz) $\Delta N_e/N_e$ data are shown in Figure 3. Typical peak and average spectra are plotted both before and during the water dump. (The times of these "before" and "during" spectra are pointed out as A and B, respectively, at the bottom of Figure 2.) There appears to be a significant enhancement over ambient (up to 40 dB at $f \sim 100$ Hz) at all frequencies below about the lower hybrid frequency (f_{LH}) while water is being released from the orbiter into the environment.

During the time period encompassed by Figure 2 the orbiter is in sunlight, and the angle between the velocity

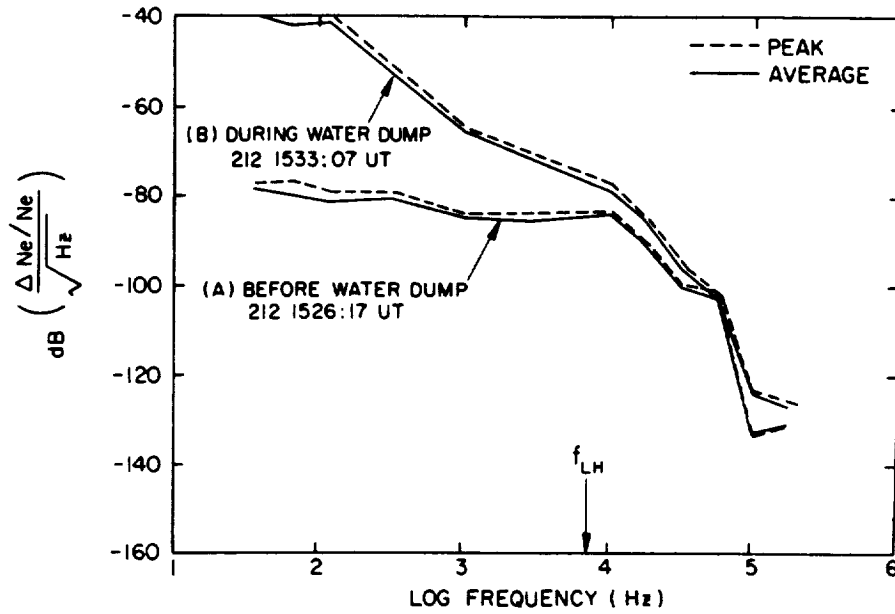


Fig. 3. Density fluctuation spectra (35 Hz to 178 kHz) before (A) and during (B) the water dump of Figure 2. During the time water is being released, spectral density is increased over ambient at all frequencies below about the lower hybrid frequency.

vector and the magnetic field increases from 73° to 91°, with 90° occurring at about 1534:30 UT. The measured electron density is $\sim 10^4 \text{ cm}^{-3}$ with a slight increase occurring at the time the water dump begins.

Figure 4 shows the effects of a wastewater dump which occurred on day 214 at 0042–0052 UT. This wastewater dump is shorter because it is only one segment (~ 10 min) of a three-segment dump (total time ~ 30 min). Once again, the PDP is stationed on the RMS at point solar, but it is rotated 180° from the orientation shown in Figure 1. The results for this water dump are similar to those for the case in Figures 2 and 3. During the release of water the turbulence is increased by a factor of 20–25 in the 1- to 6-Hz channel (upper panel of Figure 4) and by an indeterminable, but substantial, amount in the 6- to 40-Hz channel (lower panel). A high level of turbulence is seen to continue throughout the entire water dump. After the water valve is closed at about 0052 UT, the turbulence decreases to a pre-water dump level after approximately 2.5 min (see, for example, lower panel of Figure 4).

Typical higher-frequency spectra for times before, during, and after the day 214 water dump are presented in Figure 5 (noted as C, D, and E, respectively, on Figure 4). The characteristic increase over ambient (up to 50 dB at $f \sim 100$ Hz) at all frequencies below $\sim f_{LH}$ is seen during the time water is being released. The “after” spectrum was taken before the environment had fully recovered after the water valve was closed. As expected, this spectrum still shows an increase over ambient at frequencies below f_{LH} .

This wastewater dump occurs while the orbiter is in the sunlight, and the angle between the velocity vector and the magnetic field increases from 64° to 103°, with 90° occurring at about 0050 UT. The measured electron density decreases from about 10^4 cm^{-3} at 0040 UT to $\leq 10^3 \text{ cm}^{-3}$ at 0055 UT.

Figures 2 through 5 provide typical examples from SL 2 of the effects of dumping water into the orbiter environment. The turbulence is almost always increased over ambient during

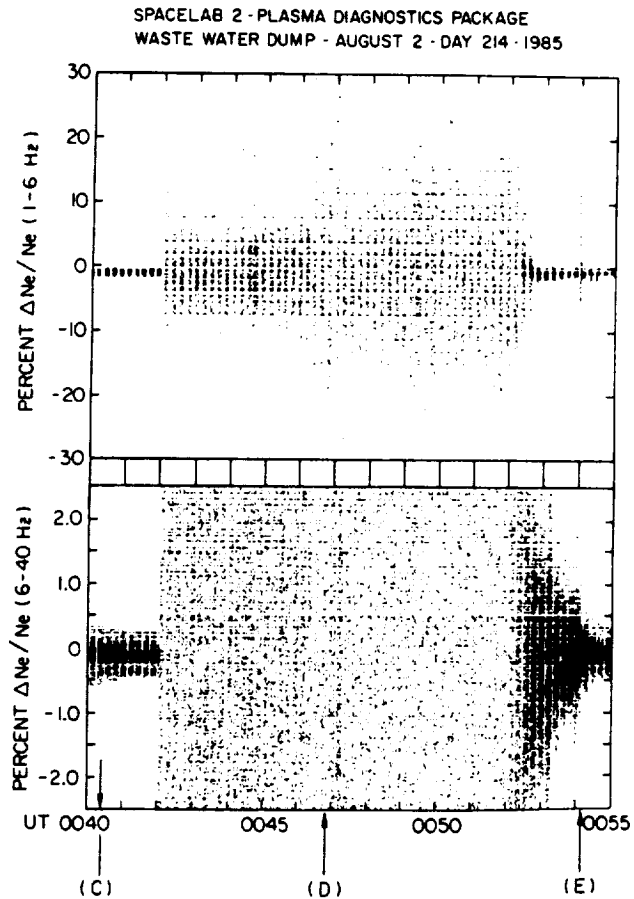


Fig. 4. $\Delta N_e/N_e$ data in the 1- to 6-Hz range (top panel) and 6- to 40-Hz range (lower panel) before, during, and after an orbiter wastewater dump. The level of turbulence is greatly increased during the water dump and decreases to ambient over a time period of about 2.5 min once the water valve is closed at ~ 0052 UT. The C, D, and E pointers refer to times for which spectral density plots are available in Figure 5.

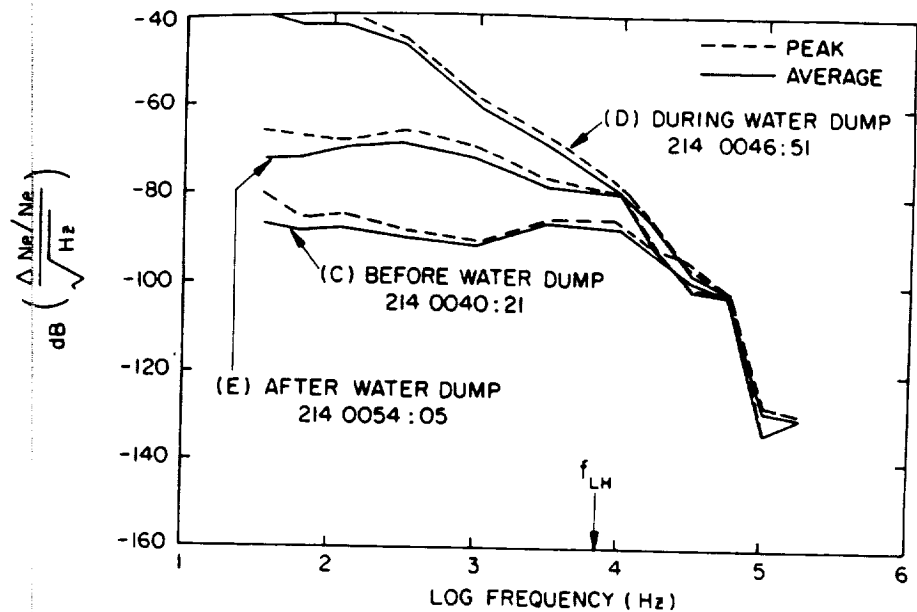


Fig. 5. Density fluctuation spectra (35 Hz to 178 kHz) before (C), during (D), and after (E) the water dump of Figure 4. Enhancement over ambient occurs only at frequencies below about the lower hybrid frequency. The "after" spectrum was taken before the environment had fully recovered and thus still shows enhancements over ambient (up to ~ 20 dB at $f \sim 100$ Hz).

the time the water is being released. Electron density is seen to increase, decrease, or remain the same depending on, for example, whether the Langmuir probe is in ram or wake. This is in line with the results reported by Pickett *et al.* [1985] for thruster firings, which released about 30% water by mole fraction.

Effects of water releases which took place while the PDP was located in the payload bay of the orbiter were similar, in most cases, to those for times when the PDP was on the RMS. However, the level of turbulence was often less. This could be due, in part, to the Langmuir probe being in the wakes of the various orbiter structures and other instruments.

4. DISCUSSION

In attempting to understand the generation of the plasma turbulence during water dumps, we have considered two different processes, both related to the production of H_2O^+ ions by charge exchange of the shuttle cloud water molecules with ionospheric O^+ ions. The first mechanism relies on the fact that, in general, the total ion (O^+ and H_2O^+) population, viewed as a function of the velocity, v_{\parallel} , parallel to the Earth's magnetic field, \mathbf{B} , is double-peaked and may be unstable to an ion-plasma instability [i.e., Fried and Wong, 1966]. The second mechanism is the instability discussed by Ott and Farley [1975] for the lower F region, which requires a "toroidal" ion velocity distribution perpendicular to \mathbf{B} , of the type reported recently by Paterson [1987] and Paterson and Frank [1989] and analyzed by St.-Maurice and Schunk [1974]. For both mechanisms a non-Maxwellian character of the ion velocity distribution is required; in the parallel velocity component for the first and in the perpendicular component for the second.

4.1. The Ion-Plasma Instability

Viewed in a frame of reference fixed to Earth, the ion velocity distribution along \mathbf{B} consists of stationary ionospheric O^+ ions and of a group of H_2O^+ ions drifting with velocity $v_{\parallel} = v_{\text{shuttle}} \cos(\beta)$, where β is the angle between the Earth's magnetic field and the shuttle velocity. Up to tens of meters from the shuttle the density of the H_2O^+ ions may be as large as (or even larger than) the density of O^+ [Grebowsky *et al.*, 1987]. The thermal spread of the O^+ ions corresponds to a temperature of the order of $T_i \sim 1000^\circ\text{K}$ whereas the "beam," or H_2O^+ , ions should be much cooler. In the first place, water exits the shuttle at a temperature $\leq 300^\circ\text{K}$. Furthermore, as the water cloud around the shuttle expands, it cools by a very large factor [e.g., Bernhardt, 1982], before it has any chance of being partially reheated by collisions with the ambient atomic oxygen. We may estimate a ratio, α , between the O^+ thermal speed and the H_2O^+ thermal speed, as large as ~ 4 (or more). The ratio $T = \bar{T}_i/\bar{T}_e$ between the O^+ temperature and the electron temperature is, probably, of the order of 0.3–0.5. With these values of α and T , and a ratio $n \approx 1$, between the H_2O^+ density and the O^+ density, we may use, for example, Figure 3 or Figure 4 of Fried and Wong [1966], to estimate a range for the angle β within which the instability should occur. A (very approximate) range $40^\circ \leq \beta \leq 85^\circ$ is obtained from this procedure. In addition, from Fried and Wong [1966, Figure 5], who show the phase velocity of the unstable waves versus the "beam" velocity, we estimate that frequencies as low as ~ 1 Hz may be seen by an observer on the shuttle, if wavelengths comparable with the "size" of the H_2O^+ cloud of ~ 500 m [Paterson, 1987; Paterson and Frank, 1989] are allowed.

It appears to us that the ion-plasma instability described by Fried and Wong [1966] has many of the features required

to account for our noise observations during water releases from the shuttle. It must be pointed out, however, that one aspect of the observations appears to be at odds with this interpretation. We observe that the noise persists, during water releases, throughout a range of β which includes $\beta = 90^\circ$. When the shuttle velocity is at right angles to the Earth's magnetic field, the instability would not be expected to occur. As seen, for example, in the lower panel of Figure 4, the 6- to 40-Hz turbulence decreases to a pre-water dump level after approximately 2.5 min. The time required for the shuttle orbiter to transit the range of β for which the instability is not expected ($85^\circ \leq \beta \leq 95^\circ$) is approximately 5 min. Thus it does not seem likely that the turbulence observed near $\beta = 90^\circ$ could be attributed to previously created turbulence that had not yet dissipated and, somehow, been carried along with the orbiter. On the other hand, with ions produced at ~ 7.8 km/s, their gyroradius is large enough compared to that of the electrons that a modified two-stream (MTS) instability is possible. The MTS peak at essentially 90° and may explain the observations for $\beta \approx 90^\circ$.

4.2. The Ott-Farley Instability

This instability may occur when a plasma $\mathbf{E} \times \mathbf{B}$ drifts through a neutral gas background and new ions are continuously produced by charge exchange between the ions in the drifting plasma and the background neutrals. *St.-Maurice and Schunk* [1974] have analyzed the ion velocity distributions that are produced by the combined effects of the $\mathbf{E} \times \mathbf{B}$ drift and of the charge exchanges, for several values of the drift velocity and of the ratio, v_{in}/ω_{ci} , between the ion-neutral collision frequency and the ion gyrofrequency. The distributions are of the "ring" or "toroidal" type, with peak at $v_{\perp} > 0$, v_{\perp} being the ion velocity component perpendicular to the magnetic field. In fact, such ring distributions have been measured by *Paterson* [1987] and *Paterson and Frank* [1989] within the water cloud that surrounds the shuttle orbiter.

Ott and Farley [1975], on the basis of earlier work by *Post and Rosenbluth* [1966], have argued that these ion distributions should be unstable if the following conditions are satisfied: (1) The dominant collisions between ions and neutrals are charge exchange collisions, with $v_{in}/\omega_{ci} \ll 1$. (2) The ion-ion collisions can be neglected compared to ion-neutral collisions ($\nu_{ii} < \nu_{in}$). (3) The $\mathbf{E} \times \mathbf{B}/B^2$ drift velocity of the plasma through the neutral background is larger than $\sim 1.8v_n$, where v_n is the thermal speed of the neutral particles. In the case of the *F* region of the ionosphere, this last condition is equivalent to having an electric field larger than ~ 50 mV/m.

The instability has frequency and maximum growth rate of the order of the lower hybrid frequency, $\omega \sim \gamma \sim (\omega_{ci}\omega_{ce})^{1/2}$. Also, an estimate of nonlinear limits suggests that the relative wave amplitude, $\Delta N_e/N_e$, should be at least several percent and, probably, more.

In the case of interest to us here, the \mathbf{E} field seen by an observer on the shuttle orbiter can be as large as ~ 350 mV/m (the shuttle speed is ~ 7.8 km/s), well above the ~ 50 mV/m threshold. Also, for a water cloud with partial water pressure $\sim 10^{-6}$ torr, the ratio v_{in}/ω_{ci} is estimated to be $\approx 10^{-2}$. The condition $\nu_{ii} < \nu_{in}$ is also seen to be satisfied. Thus the flow of ionospheric plasma through the water cloud produced around the shuttle orbiter by water releases should be

conductive to the Ott-Farley instability. This would account for the very pronounced increase in turbulence observed at frequencies of the order ~ 1 kHz to ~ 10 kHz. However, a problem remains for the noise observed at frequencies well below 1 kHz. If the Ott-Farley instability is the primary agent responsible for the observed noise, it would appear that an inverse cascading of the wave energy, from small wavelengths to large wavelengths, takes place in the nonlinear regime, so that most of the noise energy is finally concentrated at the largest wavelength allowed by the system, i.e., by the "size" of the H_2O^+ cloud. Small-scale "whirls" would continuously coalesce into large-scale whirls, all the way to the size of the cloud. A similar argument for two-dimensional magnetohydrodynamic turbulence is given, for example, by *Knorr* [1974] and was invoked by *Kustom et al.* [1985] in an attempt at understanding similarly puzzling features of observations of the so-called "high-frequency" Farley-Buneman instability. A possible way out of the inverse cascade to large wavelengths may be suggested by the analysis of barium cloud striations by *Simons et al.* [1980]. A weak density gradient would couple the Ott-Farley instability to a drift mode which is unstable all the way from the ion cyclotron frequency, f_{ci} , up to the lower hybrid frequency. On the other hand, since $f_{ci} \approx 40$ Hz, the observations of turbulence in the 1- to 6-Hz band would remain unexplained by this process.

In conclusion, fluctuations in the electron density are consistently observed in the vicinity of the shuttle orbiter during water dump operations. The fluctuations can be as large as tens of percent at the lowest frequencies (below 6 Hz) and substantially above ambient level up to about the lower hybrid frequency. The Langmuir probe signatures are quite similar for waste and supply water dumps and also for different PDP orientations. Two mechanisms are suggested for producing the turbulence. The ion-plasma instability appears to be a likely candidate because of the relative drift along \mathbf{B} of H_2O^+ ions with respect to the ambient O^+ ions. However, it seems unable to explain the observations when $\beta \approx 90^\circ$. A second possibility is the Ott-Farley instability produced by a ring distribution of contaminant ions. In the latter case an inverse cascade in wavelength may be required to account for the broad spectrum of turbulence extending down from the lower hybrid frequency to the lowest frequency measured (a few hertz).

Acknowledgments. We thank L. A. Frank and W. R. Paterson for useful discussions. This work was supported by grant NAG3-449 from the NASA Lewis Research Center.

The Editor thanks J. G. Hawkins and D. J. Simons for their assistance in evaluating this paper.

REFERENCES

- Bernhardt, P. A., Environmental effects of plasma depletion experiments, *Adv. Space Res.*, 2, 129, 1982.
- Fried, B. D., and A. Y. Wong, Stability limits for longitudinal waves in ion beam-plasma interaction, *Phys. Fluids*, 9, 1084, 1966.
- Grebowsky, J. M., H. A. Taylor, Jr., M. W. Pharo III, and N. Reese, Thermal ion perturbations observed in the vicinity of the space shuttle, *Planet. Space Sci.*, 35, 501, 1987.
- Knorr, G., Stationary and quasistationary solutions of a guiding-center plasma, *Plasma Phys.*, 16, 423, 1974.
- Kurth, W. S., and L. A. Frank, The Spacelab 2 plasma diagnostics package, *J. Spacecr. Rockets*, in press, 1989.
- Kustom, B., N. D'Angelo, and R. L. Merlino, A laboratory inves-

- tigation of the high-frequency Farley-Buneman instability, *J Geophys. Res.*, **90**, 1698, 1985.
- Murphy, G., J. Pickett, N. D'Angelo, and W. S. Kurth, Measurements of plasma parameters in the vicinity of the space shuttle, *Planet. Space Sci.*, **34**, 993, 1986.
- Ott, E., and D. T. Farley, Microinstabilities and the production of short-wavelength irregularities in the auroral F region, *J. Geophys. Res.*, **80**, 4599, 1975.
- Paterson, W. R., Ion plasmas in the vicinity of the orbiter: Observations and modeling, master's thesis. University of Iowa, Iowa City, 1987.
- Paterson, W. R., and L. A. Frank, Hot ion plasmas from the cloud of neutral gases surrounding the space shuttle, *J. Geophys. Res.*, **94**, 3721, 1989.
- Pickett, J. S., G. B. Murphy, W. S. Kurth, C. K. Goertz, and S. D. Shawhan, Effects of chemical releases by the STS 3 orbiter on the ionosphere, *J. Geophys. Res.*, **90**, 3487, 1985.
- Post, R. F., and M. N. Rosenbluth, Electrostatic instabilities in finite mirror confined plasmas, *Phys. Fluids*, **9**, 730, 1966.
- Simons, D. J., M. B. Pongratz, and S. P. Gary, Prompt striations in ionospheric barium clouds due to a velocity space instability, *J. Geophys. Res.*, **85**, 671, 1980.
- St.-Maurice, J.-P., and R. W. Schunk, Behavior of ion velocity distributions for a simple collision model, *Planet. Space Sci.*, **22**, 1, 1974.
- Tribble, A. C., J. S. Pickett, N. D'Angelo, and G. B. Murphy, Plasma density, temperature, and turbulence in the wake of the shuttle orbiter, *Planet. Space Sci.*, in press, 1989.
- N. D'Angelo, W. S. Kurth, and J. S. Pickett, Department of Physics and Astronomy, University of Iowa, Iowa City, IA 52242.

(Received April 11, 1989;
revised June 2, 1989;
accepted June 8, 1989.)

Spacelab 2 Electron Beam Wave Stimulation: Studies of Important Parameters

G. D. REEVES¹, P. M. BANKS, T. NEUBERT, AND K. J. HARKER

Space Telecommunications and Radioscience Laboratory, Stanford University, Stanford, California

D. A. GURNETT

Department of Physics and Astronomy, University of Iowa, Iowa City

W. J. RAITT

Center for Atmospheric and Space Science, Utah State University, Logan

The Spacelab 2 space shuttle mission included experiments on the production of waves in the ionospheric plasma by the injection of pulsed electron beams. The Spacelab 2 mission took place during July and August of 1985 and provided an extensive data set which continues to yield new results. The experimental results reported here were obtained with the combined use of the University of Iowa plasma diagnostics package (PDP) and the Stanford/Utah State vehicle charging and potential experiment (VCAP). To date most of the analysis has focused on the sequences performed during the release of the PDP as a free-flying satellite. However, over 300 beam sequences were conducted with the PDP mounted in the orbiter's payload bay. The results of these experiments provide important new information which helps answer some of the outstanding questions which remain. The wave environments which exist in the orbiter payload bay and at several hundred meters away are compared both during ambient conditions and during electron beam injections. The dependence of beam-generated wave characteristics on the duty cycle and the frequency of the pulsed beam are investigated. The duty cycle of the beam is found to be one of the most important parameters affecting the amplitude and the harmonic structure of the waves. Maximum amplitudes are produced by 50% duty cycles and amplitudes are proportional to instantaneous, rather than average, beam current. Harmonic structure also provides insight into the spatial integrity of the propagating beam. The dependence on pulsing frequency is found to show good agreement with theory for whistler mode waves produced through the Cherenkov resonance confirming previous results. Theoretical predictions for the dependence of wave amplitudes on parameters which could not be experimentally investigated are also provided. The results of both the experimental and theoretical studies have important practical consequences for experiments attempting to produce and detect propagating radiation using artificial electron beams.

1. INTRODUCTION

The Spacelab 2 electron beam experiments were part of a long and on-going series of active experiments using electron beams as probes of plasma processes in the ionosphere. Reviews can be found in *Winckler et al.* [1980] and *Reeves* [1989]. Spacelab 2 carried the Stanford/Utah State vehicle charging and potential (VCAP) instruments and the University of Iowa plasma diagnostics package (PDP) as well as a variety of instruments relating to other investigations. The VCAP instruments were designed primarily for the investigation of vehicle charging and return current neutralization

processes and descriptions of the instruments and results can be found in *Banks et al.* [1987] and *Hawkins* [1988]. The PDP contained an extensive array of instruments used to study the ambient plasma environment and the modification of that environment caused by the orbiter, its motion through the plasma, its attendant effluents, and the modifications produced by the injection of the electron beam. The PDP instruments are described by *Shawhan et al.* [1984].

The main VCAP instrument of interest in the wave stimulation experiments is the fast pulse electron generator (FPEG). The FPEG produced a 1 keV beam of electrons with a current of 100 mA. It was mounted in a fixed orientation out of the orbiter payload bay, perpendicular to the plane of the wings. The wave receivers are part of the PDP. A single axis electric dipole antenna and a single axis magnetic search coil antenna were connected to a wideband wave receiver. The wideband wave receiver provides wave data with high time and frequency resolution. It simultaneously recorded signals in two frequency ranges. The ELF channel monitored the frequency range 0-1 kHz and the VLF channel monitored the frequency range 0-30 kHz. While the ELF channel recorded 0-1 kHz continuously, the VLF

¹Now at Earth and Space Science Division, Los Alamos National Laboratory, Los Alamos, New Mexico.

channel incorporated a frequency switching pattern. The wideband receiver did not record electric and magnetic signals simultaneously. Both included an antenna switching pattern which alternated between the electric and the magnetic antennas every 52 s. As a final point, the ELF and VLF channels each used automatic gain control (AGC) circuits to keep the total output signal strength within strict limits. Each has its own independent AGC.

The PDP and the VCAP instruments were first used together on the space shuttle flight STS 3 in 1982. The FPEG and the PDP instruments were essentially identical to the instruments which were flown on the later Spacelab 2 mission but the PDP was at all times mounted in the payload bay. The wave stimulation experiment results from the STS 3 mission have been presented by *Reeves et al.* [1988a]. That investigation established the primary wave responses to the injection of a low power pulsed electron beam. The primary results included (1) pulsed electron beam operation produces both broadband and narrow-band waves, (2) both electric and magnetic wave response is observed, (3) narrow-band waves are produced at harmonics of the pulsing frequency, (4) the harmonic structure varies from one pulsing sequence to another, and (5) narrow-band beam-generated waves are also produced at non-harmonic frequencies and these included "satellite lines" and "subharmonics."

The Spacelab 2 experiments used enhanced experimental and analytic techniques to continue this investigation. Over 300 separate electron beam experiments were performed. Two of the most important were the so-called "Pulsed" and "DC" flux tube connection sequences which provided information on the wave response at distances from the beam of ≈ 5 –250 m during a six hour free flight of the PDP. Observations of wave fields produced by electron beam operations during the free flight of the PDP using the wideband receiver have been reported by *Bush et al.* [1987], *Reeves et al.* [1988b], and *Neubert et al.* [1988, 1990].

Analysis of the wideband wave receiver data after the mission was aided by the development of an algorithm to extract absolute wave amplitudes from the wideband receiver data using information on the gain applied to the signals by the AGC. (See *Reeves* [1989] or *Reeves et al.* [1990].) This capability allowed more quantitative analysis of the data from Spacelab 2 than was possible for STS 3. The primary results from the investigations during the free flight of the PDP were (1) the amplitudes of the beam-generated ac fields were determined, (2) an electromagnetic component of both the broadband and the narrow-band radiation was observed, (3) this component was determined to be whistler mode radiation produced through the Cherenkov resonance. *Gurnett et al.* [1986] and *Farrell et al.* [1988] used filter bank data to identify a funnel-shaped emission between the lower hybrid frequency (ω_{LHR}) and the electron cyclotron frequency (ω_{ce}) as quasi-electrostatic whistler mode waves with wave normal angles near the resonance cone. *Reeves et al.* [1990] used wideband receiver data to show that broadband and narrow-band waves observed below ≈ 30 kHz were whistler mode waves with wave normal angles in the central hump of the index of refraction surface (e.g., the wave normal angle is less than the Gendrin angle [$\theta < \theta_G$]).

2. PAYLOAD BAY SEQUENCES

Investigations of wave generation during the free flight of the PDP yielded important information about electron

beam wave generation. The experiments were carefully coordinated and provided unique data on the wave environment at a variety of locations with respect to the orbiter and the beam for several different FPEG operations. However, the free flight was not the only period which produced interesting data. Literally hundreds of separate FPEG modulation sequences were conducted while the PDP was mounted in the orbiter's payload bay. The results of these investigations are the subject of this paper.

The FPEG was command controlled and could be operated in either preprogrammed modes or through up-linked commands. Operation in preprogrammed modes was the most common and typically several modes were programmed back-to-back in what are referred to as "beam sequences." An interval of FPEG operation at a particular frequency and duty cycle is referred to as a "pulsing period" (which should not be confused with the period of the square-wave modulation). A pulsing period could have a duration of microseconds to minutes but was typically several seconds long. Frequencies were typically several tens of hertz to several tens of kilo-hertz. The FPEG was square-wave modulated and the ratio of the on time of a single pulse to the period between pulses is defined as the duty cycle and could range from nearly 0% to 100%. A beam sequence could consist of one or several pulsing periods. For sequences comprised of several pulsing periods the frequency and duty cycle were varied from one pulsing period to the next in order to investigate specific phenomena.

Figures 1–5 show the beam sequences which are most important to this investigation. The upper plot in each figure shows the frequency of each pulsing period. The lower plot shows the duty cycle for each pulsing period. Duty cycle is plotted relative to 50% (which represents equal beam-on and beam-off times) for reasons which will become apparent. Although, on these plots, each pulsing period is shown with a gap between it and the next this is just for visual clarity. In fact, each pulsing period occurred immediately after its predecessor with no FPEG-off interval between them.

Figure 1 shows one such sequence; the Duty 41 sequence. In this sequence there are 10 pulsing periods. During the first two periods the FPEG is pulsed at 3.9 kHz and the FPEG is operated in pairs of pulsing periods with successively descending frequencies — 3.9 kHz, 976 Hz, 244 Hz, 122 Hz, and 31 Hz (Figure 1a). The first period in each pair has a duty cycle of 4/5 or 80% and the second has a duty cycle of 1/5 or 20% (Figure 1b). Each period has a duration of 10 s. The Duty 21 sequences were similar to the Duty 41 sequences but the frequencies were 3.25 kHz, 814 Hz, 203 Hz, 102 Hz, and 25 Hz and the duty cycles were 2/3 (67%) and 1/3 (33%) (Figure 2). The Duty 41 and Duty 21 sequences were designed to investigate the dependence of the wave characteristics on the duty cycle of the beam pulses to determine if the length of beam on-time affected the characteristics of the waves.

The Beam Energy sequences are depicted in Figure 3. In these sequences the pulsing frequency was held roughly constant (between ≈ 500 –600 Hz) for each of the 19 pulsing periods while the duty cycle was varied from 0.2% to 99.8%. The beam energy sequences investigated the dependence on the total average current injected by the beam. Note that the twelfth pulsing period in the sequence does not follow the steady progression of duty cycles. Rather, it repeats pulsing period 8 in order to check that there is no systematic change

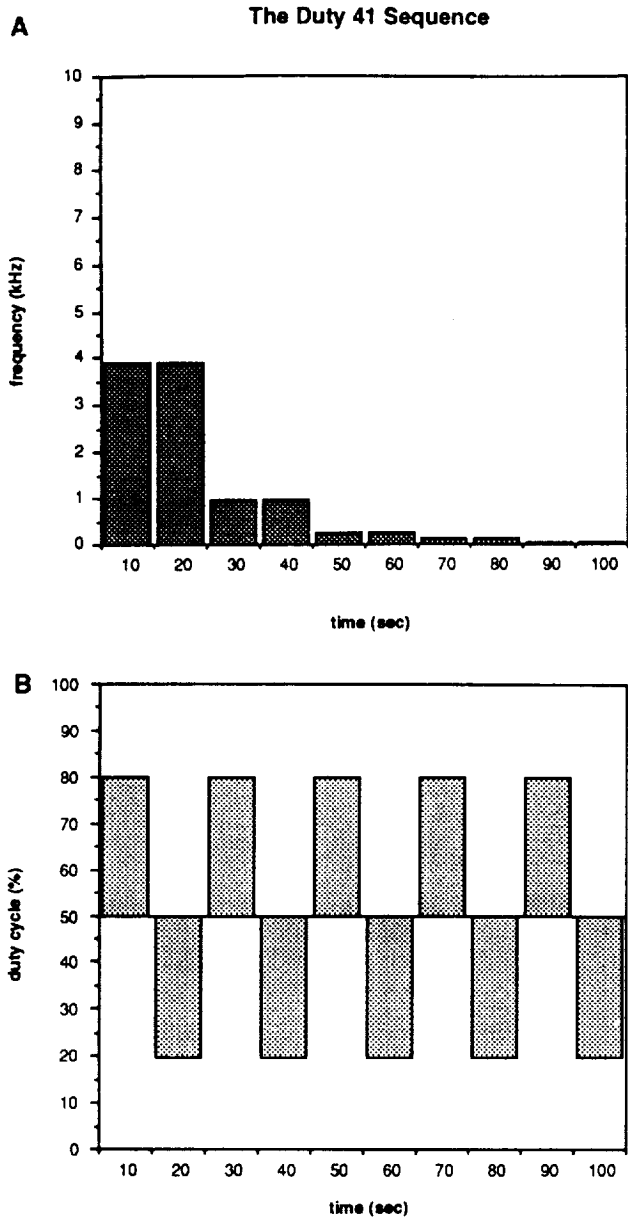


Fig. 1. A schematic representation of the Duty 41 beam sequence. (a) The frequency of the various pulsing periods. (b) The duty cycle of the various pulsing periods. The duty cycles are plotted relative to 50% because the wave response is symmetric about this value (see text). Although they are drawn with a gap between them the actual pulsing periods in a beam sequence took place back-to-back with no FPEG off time between them.

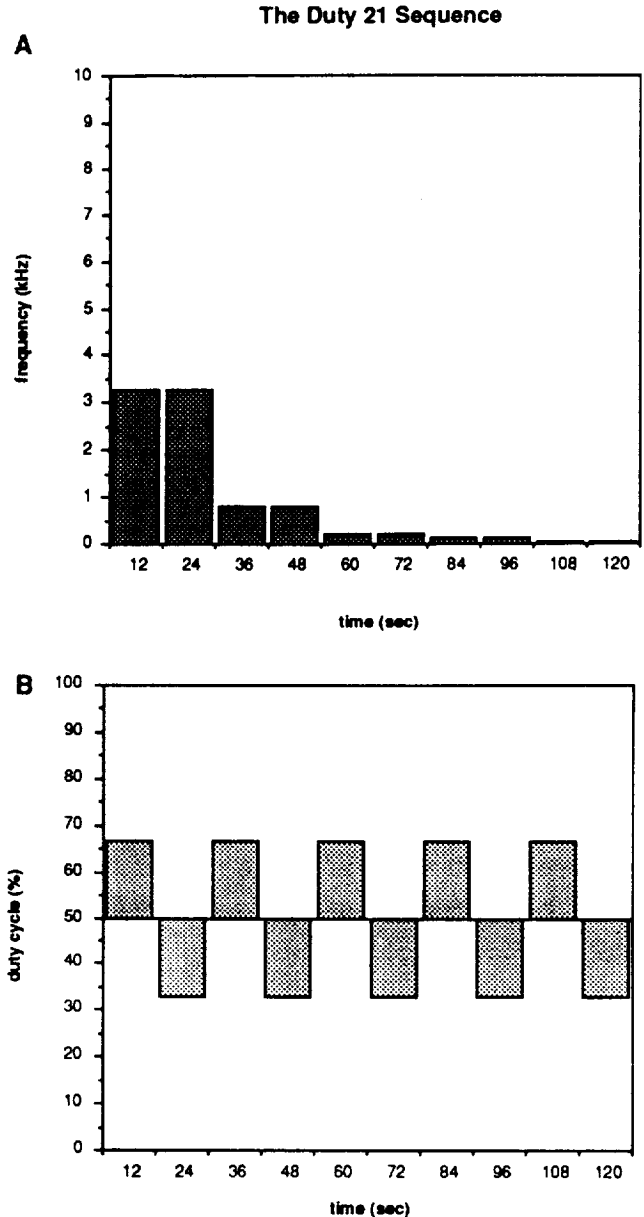


Fig. 2. Similar to Figure 1, this figure shows the pulsing periods for the Duty 21 sequence.

in wave amplitudes due to effects other than changing duty cycle.

The ELF Sweep sequence is shown in Figure 4. The frequency is increased from 51 Hz to 976 Hz in nine steps. At each step the pulsing frequency is increased by approximately a factor of two. The duty cycles of 20%, 33%, or 50% were chosen to be as constant as possible while obtaining the desired frequencies. After nine steps the pattern is repeated twice for a total of 18 pulsing periods. The VLF Sweep sequence (Figure 5) was similar to the ELF Sweep sequence but was designed to span the 0-10 kHz range. The primary purpose of these sequences was to investigate the dependence of wave emissions on beam pulsing frequency

and in particular to look for cut-offs or resonances in the wave mode at characteristic wave frequencies.

The Duty 41 and Duty 21 sequences were conducted 17 and 15 times respectively. There were 17 Beam Energy sequences, 10 ELF Sweep sequences, and 28 VLF Sweep sequences. This study concentrates on the results of these five types of beam sequences. In addition there were 13 other types of FPEG sequences whose purposes included study of spacecraft charging and operations attempting to propagate radiation to remote receivers on the ground and on the DE satellite.

3. COMPARISON OF FREE FLIGHT AND PAYLOAD CONDITIONS

During the payload bay wave generation sequences (referred to here as simply "payload bay sequences") the PDP

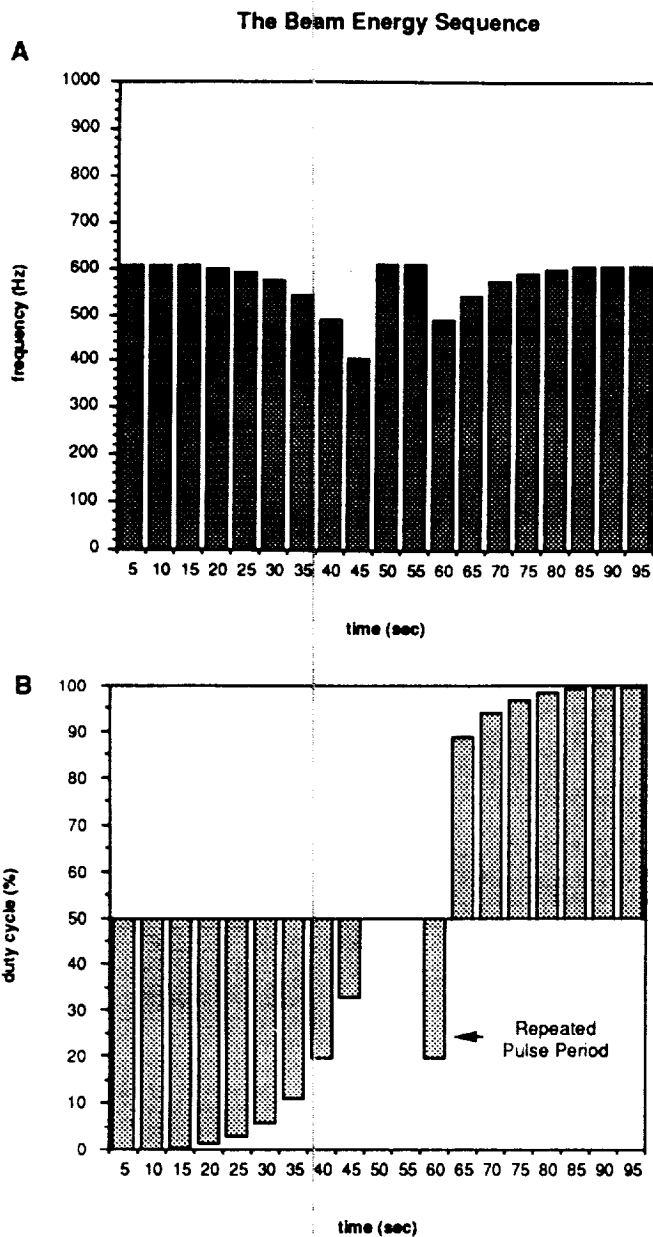


Fig. 3. Similar to Figure 1, this figure shows the pulsing periods for the Beam Energy sequence.

was located 6.62 m from the FPEG in the orbiter payload bay. Figure 6 shows the relative locations of the FPEG, the PDP, and several other instruments in the Spacelab 2 payload bay. Both the plasma and the ambient wave environments can be quite different in the payload bay than they are at some distance from the orbiter. (See for example *Raitt et al.* [1987], *Shawhan et al.* [1984], and *Hastings et al.* [1988].) Therefore data taken with the PDP in the payload bay are somewhat different than data acquired during the free flight. Most noticeable is the level of background electromagnetic interference (EMI). The interaction of the orbiter moving at ≈ 7.7 m/s through the plasma and the presence of on-board electrical systems create both broadband and narrow-band EMI. Vehicle outgassing, thruster operation, and waste releases can introduce new ion species into the environment, vehicle charging can introduce poten-

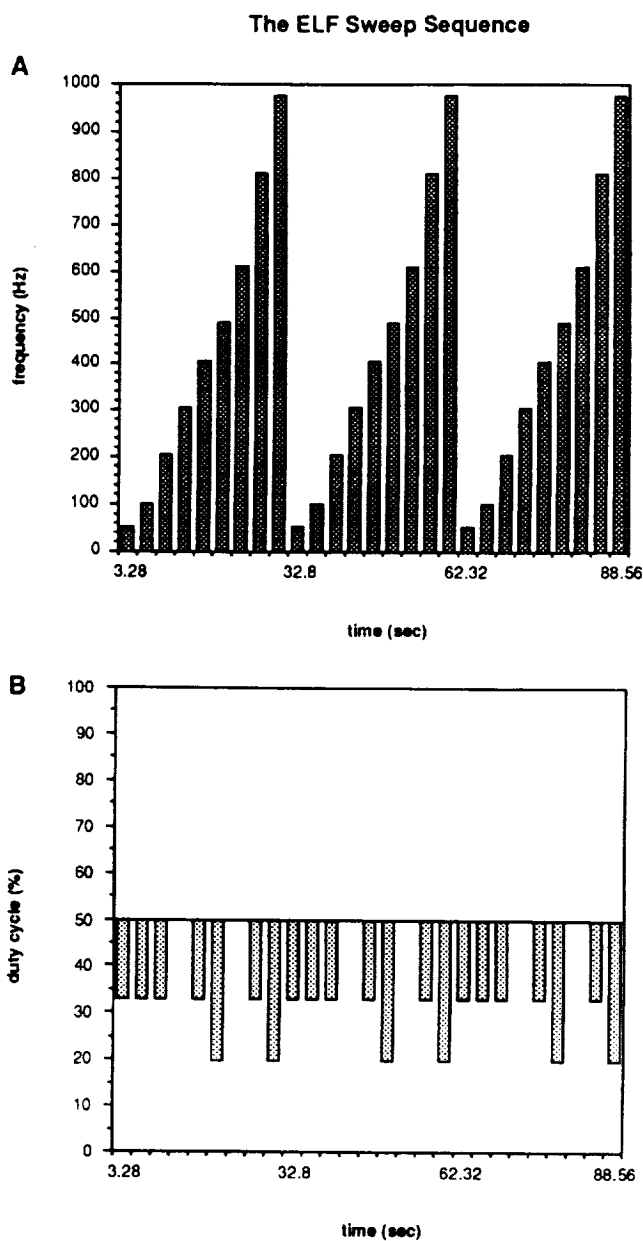


Fig. 4. Similar to Figure 1, this figure shows the pulsing periods for the ELF Sweep sequence.

tial structures around the orbiter, and ram/wake conditions can provide dramatically different plasma densities than in the surrounding medium. Although these phenomena are generally assumed to have an effect on the production of waves by electron beams, the magnitude of those effects is not completely understood. It will be seen below that these effects do not substantially alter the basic characteristics of the electron beam-generated waves. Therefore, for the purposes of this investigation, the payload bay can be thought of as similar to, but more noisy than, the undisturbed, ambient plasma environment.

Figures 7-10 show spectrograms produced from the magnetic wideband receiver data. They illustrate both the similarities and the differences between the waves observed during the free flight and during payload operations. All four spectrograms show data in the range 0-30 kHz. The first

The VLF Sweep Sequence

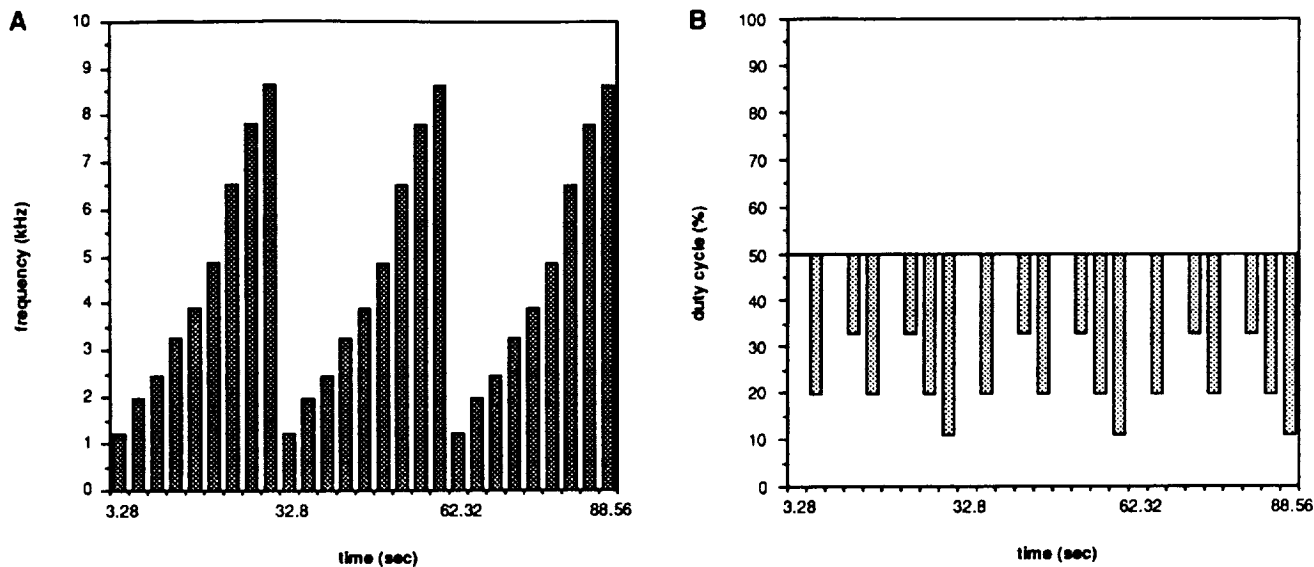


Fig. 5. Similar to Figure 1, this figure shows the pulsing periods for the VLF Sweep sequence.

SPACELAB-2 PAYLOAD LAYOUT

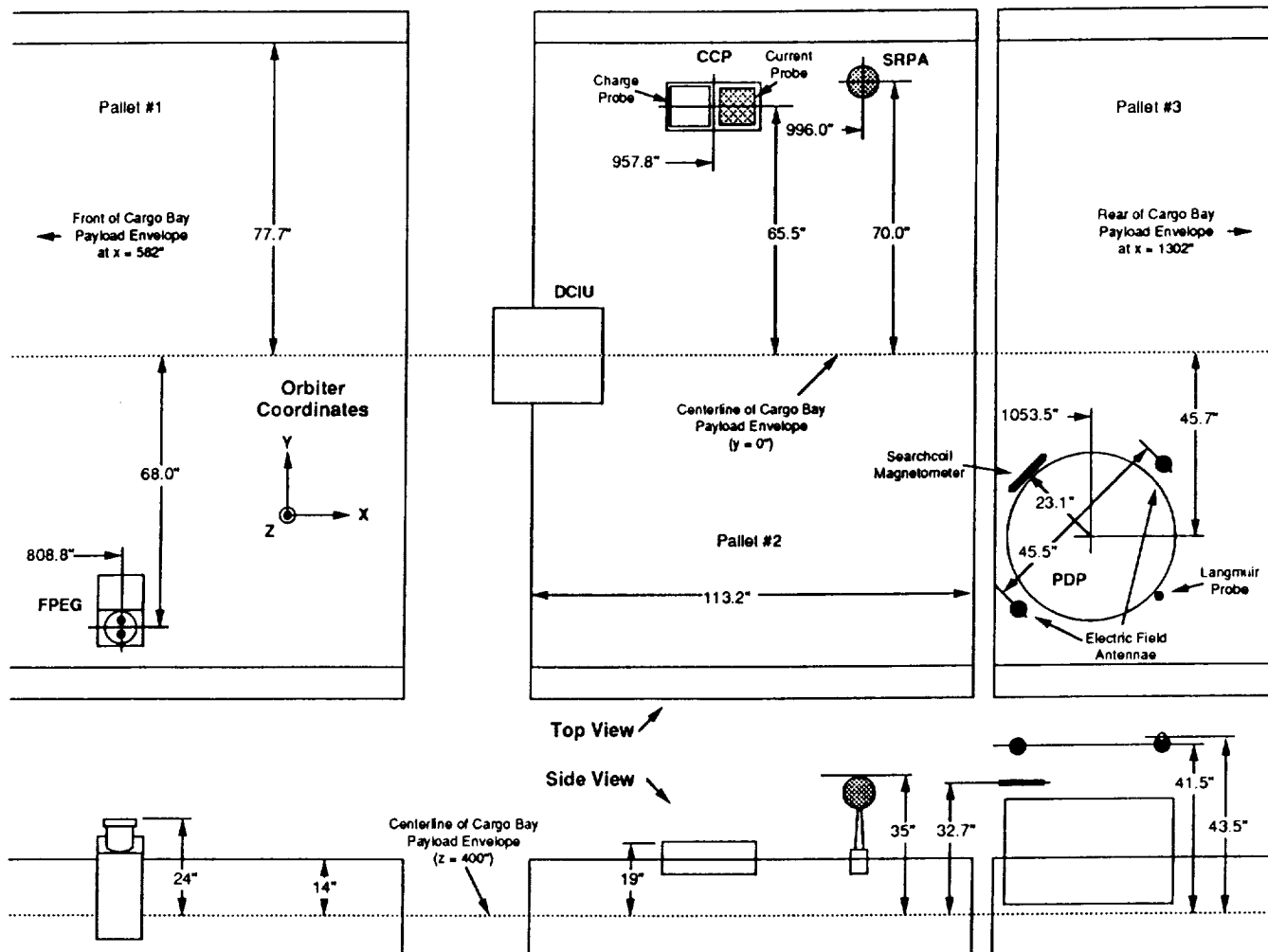


Fig. 6. The location of various VCAP and PDP instruments in the Spacelab 2 payload bay.

≈ 26 s of each shows the 0–10 kHz range. The next ≈ 13 s shows the 10–20 kHz range which was heterodyned down into the 0–10 kHz band. The frequency is also inverted in this range so 10 kHz is at the top of the scale and 20 kHz is at the bottom. In the final ≈ 13 s the 20–30 kHz range is shown with 20 kHz at the bottom of the scale and 30 kHz at the top. The spectrograms shown here are uncalibrated data. The dynamic effects of the gain applied by the AGC have not been removed and therefore amplitudes are relative. (Reeves *et al.* [1988a, 1988b] show other spectrograms from the Spacelab 2 mission and describe the format in more detail.)

Figure 7 shows the ambient wave environment during the free flight of the PDP. The FPEG is not operating at this time and the PDP is ≈ 200 m from the orbiter. Highly time varying emissions are observed in the 0–10 kHz range. Most are natural atmospheric whistlers but some are effects of orbiter thruster operations which were frequent during the free flight. In the 10–20 kHz and 20–30 kHz ranges strong interference lines dominate. The line at ≈ 11.4 kHz is most likely a source on the PDP because its amplitude is always on the order of 10^{-6} nT. The line at ≈ 24 kHz is mostly likely a source on the orbiter. It shows modulation at the spin period of the PDP (≈ 6.5 s for a half rotation) and varies in amplitude with the location of the PDP with respect to the orbiter.

The latter half of the spectrogram in Figure 8 can be compared with Figure 7. During the first ≈ 28 s the FPEG is operated in a VLF Sweep sequence. During the remainder of

the interval shown the FPEG is off and background fields as measured in the payload bay are shown. It is apparent that in the payload the level of EMI is significantly higher than it is at several hundred meters from the orbiter. The interference lines at ≈ 11.4 kHz and ≈ 24 kHz are still present and have the comparable amplitudes as were observed near the beam during the free flight. In addition a multitude of other interference lines are also observed with comparable amplitudes. Some of the sources can be identified. For example, harmonics of 60 Hz and 400 Hz (the orbiter power converter frequency) are common.

Figure 8 also shows the response to FPEG operations as measured from the payload bay. Pulsing periods during a VLF Sweep sequence with frequencies 1.95 kHz to 8.65 kHz are seen in the 0–10 kHz range. The final pulsing period at 1.22 kHz starts in the 0–10 kHz range and continues as the antenna switches to the 10–20 kHz range. The sequence is prematurely terminated after this pulsing period. It is seen that the narrow-band magnetic wave fields produced by the beam are significantly stronger than the background EMI. The gain applied by the AGC at this time is such that essentially only beam-generated waves are measured.

Figures 9 and 10 show the wave response to a pulsing sequence which was conducted both during the free flight (Figure 9) and with the PDP in the payload bay (Figure 10). The FPEG is pulsed at 1.22 kHz with a duty cycle of 50% and a current of 100 mA. This sequence, known as the Proximate Operations sequence is referred to as the "Pulsed flux tube connection" sequence during the free flight and

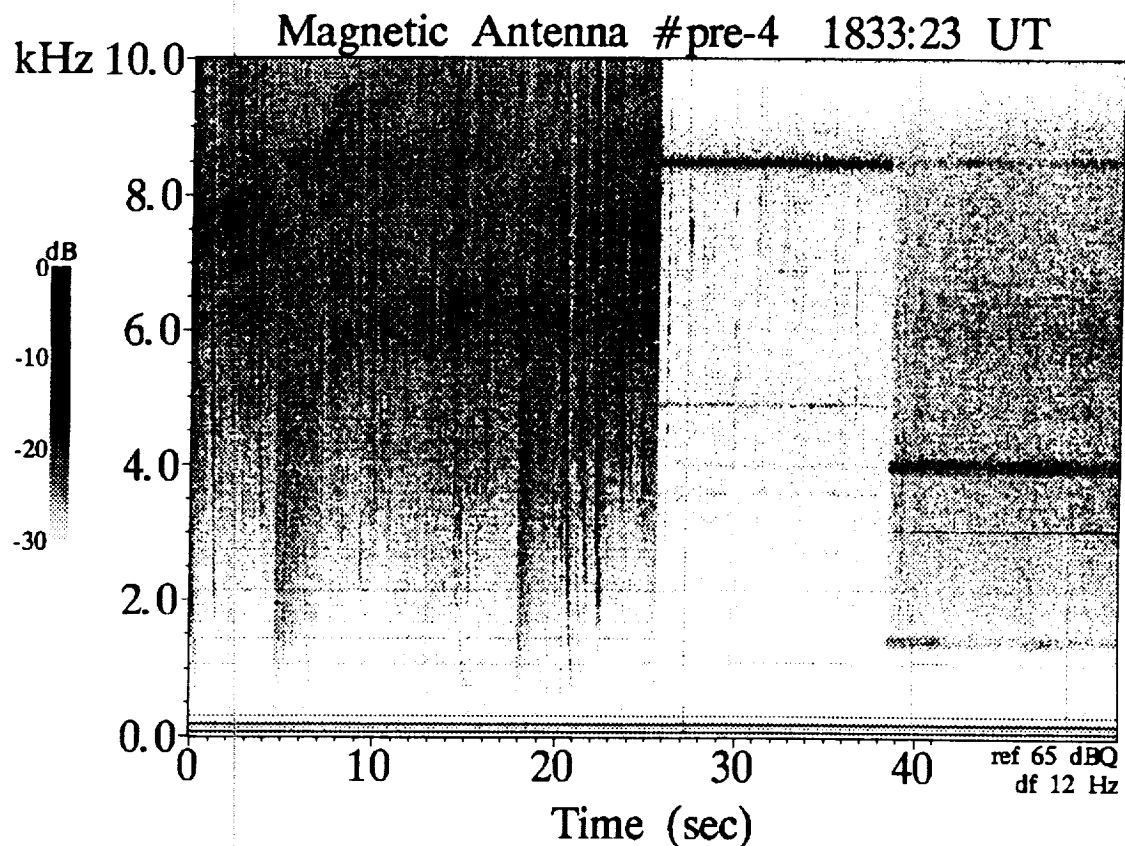


Fig. 7. A spectrogram showing the wave response measured by the PDP magnetic search coil during the free-flight of the PDP. The FPEG is off during this period and ambient fields are measured. The antenna switching pattern and the gain applied by the AGC are both super-imposed on the data.

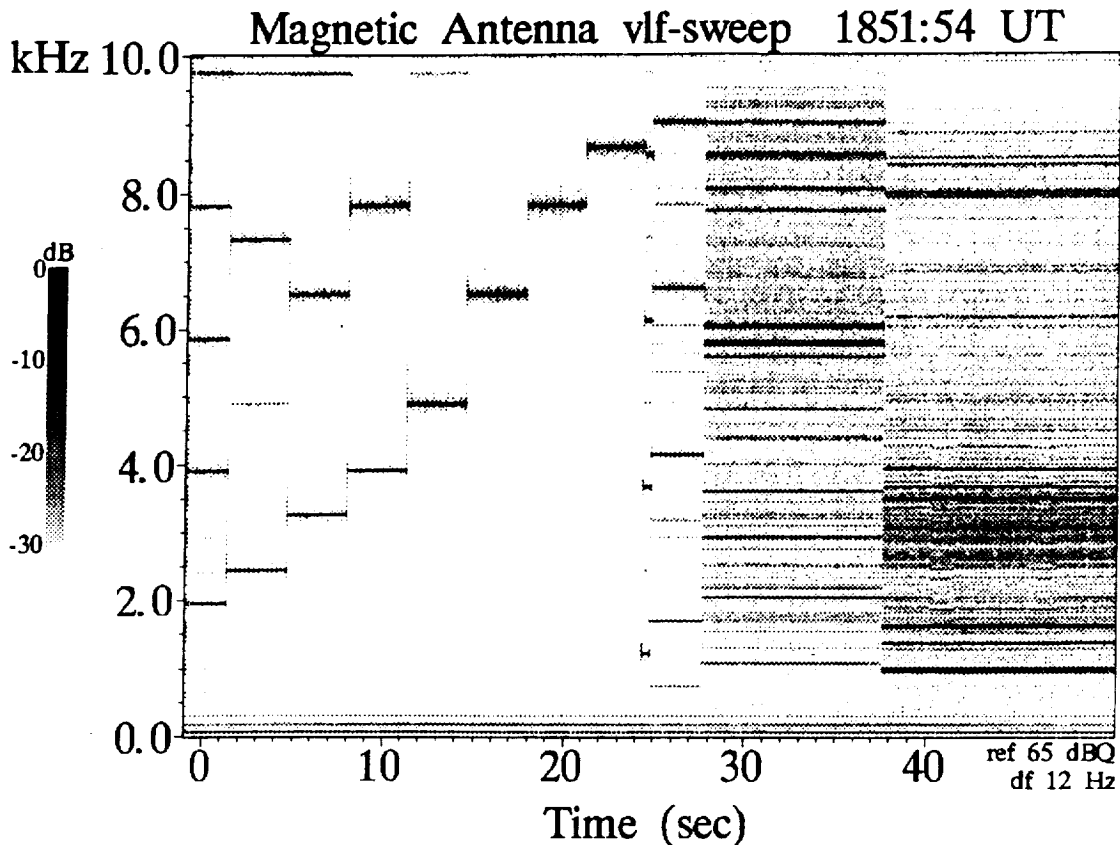


Fig. 8. A spectrogram showing the wave response measured by the PDP magnetic search coil when the PDP is in the payload bay. From ≈ 0 –28 s in the figure the FPEG is operated in a VLF Sweep sequence. In the remainder of the figure background EMI is measured.

the “Prox Ops” sequence in the payload bay [Reeves *et al.*, 1988b, 1990]. The wave response is seen to be nearly identical. Harmonics of the pulsing frequency are observed up to the limit of the receiver. Broadband waves are also generated in both cases but are approximately one to two orders of magnitude lower in amplitude than the narrow-band emissions. In Figure 10 the amplitude of the fundamental is $\approx 5 \times 10^{-3}$ nT and is fairly constant over time. In Figure 9 the amplitude of the fundamental is an order of magnitude lower due to the separation between the PDP and the beam (≈ 70 m). Ambient wave fields are more comparable in amplitude to the beam-generated waves during the free flight even though they are lower in absolute amplitude than the EMI in the payload bay. The other major difference between the two spectrograms is that the free flight signals are modulated by the spin of the PDP while in the payload the PDP is in fixed orientation.

4. THEORY OF NARROW-BAND WAVE PRODUCTION

There are several advantages to a pulsed mode of electron beam operation. As seen, pulsed electron beams produce narrow-band emissions at discrete, predictable frequencies. These waves can be readily distinguished from background emissions. In addition pulsing the electron beam produces a current source which can radiate coherently and can therefore produce more intense radiation than an in-

coherent source [Bell, 1968]. As a result there has been considerable effort to develop a theoretical model for wave production by pulsed electron beams.

Harker and Banks [1983] considered the radiation from a finite train of pulses injected into a magnetized plasma. For simplicity, each pulse was assumed to traverse an unbounded path length ($-\infty$ to $+\infty$). Radiation was considered in the frequency range from the lower hybrid frequency to the ion cyclotron frequency. Harker and Banks [1985] extended that theory to cover the frequency range below the lower hybrid frequency. They also assumed an infinite train of pulses which were injected into a half space (0 to $+\infty$) which is more appropriate to experiments. A later paper, Harker and Banks [1987] considered the near-field radiation from such an electron beam. Neubert and Harker [1988] extended this work to include expressions for magnetic field amplitudes. We will review the theory of near-field radiation from a semi-infinite pulsed electron beam propagating in a magnetized plasma in this section. The results of Harker and Banks [1987] and Neubert and Harker [1988] will be used extensively in this paper. They will often be referred to, collectively, as “HBN.”

Other treatments of radiation from electron beams in space plasmas have been presented by Lavergnat and Lehner [1984] and Ohnuki and Adachi [1984] who consider radiation from pulsed electron beams for the special case of zero pitch angle. Lavergnat *et al.* [1984] have presented results for a sinusoidally modulated beam with arbitrary pitch angle.

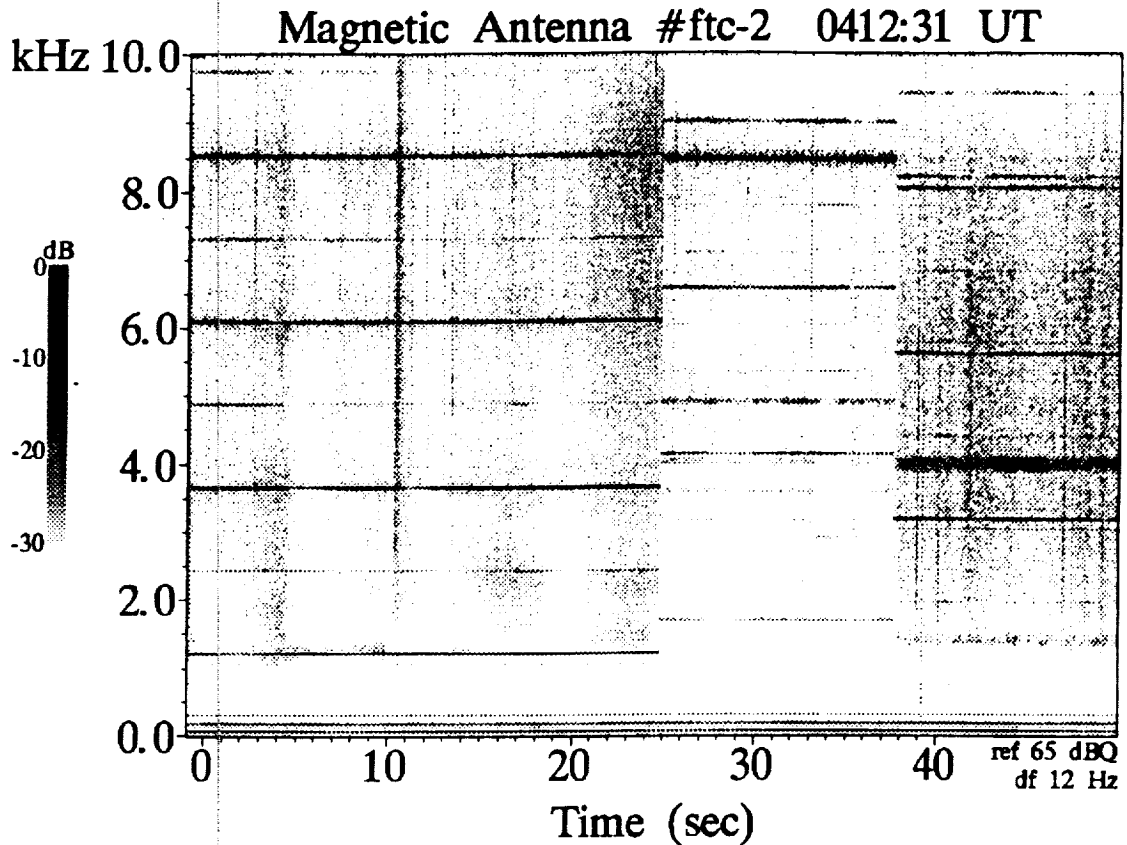


Fig. 9. A spectrogram showing the wave response measured by the PDP magnetic search coil during the free-flight of the PDP. The FPEG is pulsed at 1.22 kHz with a 50% duty cycle. Throughout this interval.

The Theory of HBN

HBN apply a treatment which is based upon the works of McKenzie [1967], Liemohn [1965], and Harker and Banks [1983, and 1985]. They assume an infinitely thin electron beam spiraling around the geomagnetic field (B_0) under the influence of the Lorentz force. The beam is square-wave modulated, (pulsed), and extends into an infinite half space. Within each pulse the electrons are assumed to be evenly distributed and have no motion other than the helical motion of the beam as a whole. Thus such effects as Coulomb spreading of the beam along the magnetic field or across it, are not considered. B_0 is taken to define the z axis of a coordinate system and the electron source is located at $(a, 0, 0)$ which defines the x axis. (Here, $a = v_{\perp}/\omega_{ce}$ is the Larmor radius). An exponential attenuation factor, which assumes that the ability of the beam to radiate decays exponentially as $e^{-\beta z}$ over an arbitrary length, $1/\beta$, may also be applied. The factor β could not be estimated for the Spacelab 2 experiments. Therefore we assume here that the coherence length is long and therefore that $\beta \approx 0$.

The electric field and the current density are expressed in a rotating cylindrical coordinate system, Fourier transformed into frequency-wave number space, and the dispersion equation is applied. The fields are then transformed back into coordinate space but are left as functions of frequency. The integrals which must be done are over the components of the wave number vector (k_{\parallel} , ϕ , and k_{\perp}). The

integral over k_{\parallel} has simple poles at $n^2 = n_a$, $n^2 = n_b$, and $n^2 = n_c$ where n_a and n_b are functions of the cold plasma dielectric tensor and the perpendicular index of refraction (μ_{\perp}) and $n_c = (k_{\parallel} c)/\omega$, where $k_{\parallel} = (\omega - s\omega_{ce})/v_{\parallel}$. In addition it has been determined that there is a branch cut whose contribution to the integrals was neglected. The possible effects of this omission will be discussed below.

The reader will recognize the expression for k_{\parallel} as the familiar resonance condition which picks out the Cherenkov ($s = 0$), cyclotron ($s = 1$), and anomalous cyclotron ($s = -1$) resonances. The cylindrical shape of the beam trajectory naturally leads to the use of Bessel functions (J) and Hankel functions (H). After transforming the fields back from rotating to polar coordinates the final expressions for the electric field components are obtained and are given in Harker and Banks [1987]. Magnetic field components are obtained through the relation $\nabla \times \mathbf{E} = -\partial \mathbf{B}/\partial t$. They are given in Neubert and Harker [1988]. The reader is referred to those papers for the exact expressions.

Each component of the magnetic fields can be written as

$$B_i = C \sum_{\eta=-\infty}^{\infty} \sum_s \sum_{\nu} \sum_q D F G$$

The electric field components have similar form. The subscript i is over the polar coordinates (ρ, ψ, z). C is a constant which includes the factor $\omega_m I_B v_{\perp}/v_{\parallel}$ where ω_m is the beam modulation frequency, I_B is the instantaneous beam

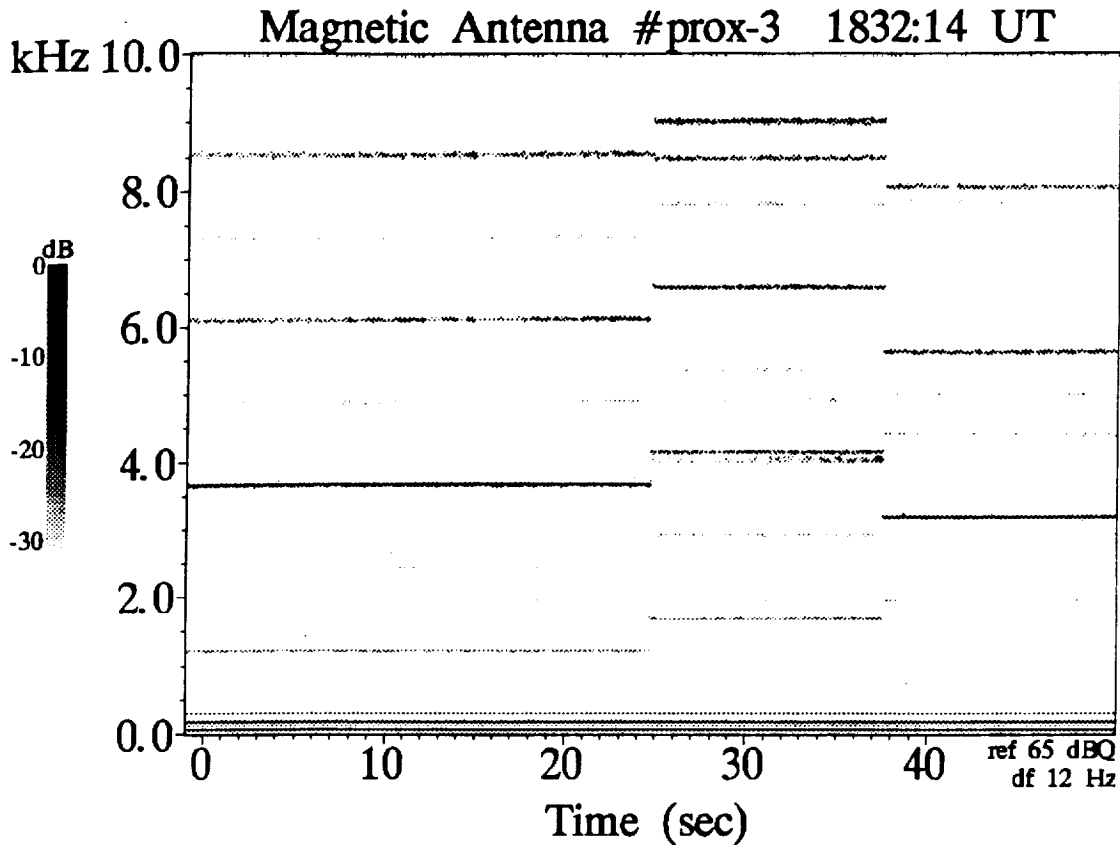


Fig. 10. A spectrogram showing the wave response measured by the PDP magnetic search coil with the PDP in the payload bay. The FPEG is pulsed at 1.22 kHz with a 50% duty cycle. Throughout this interval.

current, and v_{\perp} and v_{\parallel} are components of the beam velocity. The summations are over the harmonic number η , the resonance condition s , a spatial coordinate index ν , and an index q which is used to insure that waves are outgoing. The function \mathcal{G} contains factors which depend on the index of refraction and the dielectric tensor elements and also contains the Hankel functions $H_j^{(2)}(\mu_{\perp} k_0 \rho)$ where $j = s, s + 1$, or $s - 1$. The function \mathcal{F} includes the Bessel function $J_{s-\nu}(\mu_{\perp} k_0 a)$. The function \mathcal{D} is what we will call the duty cycle factor, $\mathcal{D} = 1/\eta \sin(\eta\pi b/d)$. Here b/d is the duty cycle where b is the on-time for a pulse and d is the period of the square wave modulation. (We note that equation 36 of *Harker and Banks* [1987] and equation 5 of *Neubert and Harker* [1988] are missing the term $1/\eta$.) The dependences described here will be important when we consider the predictions of this theory.

Applications of the Theory

The expressions for the electric or magnetic field components given by HBN can be evaluated numerically for the specific conditions which existed during the Spacelab 2 experiments. The conditions include frequency, duty cycle, beam current, beam energy, the geomagnetic field vector, the plasma density, and the distance of observation. Given those values, an electric or magnetic field vector can be calculated for each of the resonance conditions and for each of the two complex perpendicular indices of refraction (μ_{\perp}).

This has been done for the Pulsed flux tube connection during the free flight of the PDP [*Reeves et al.*, 1988b and 1990]. The results showed the best agreement between predictions and observations for the $s = 0$ root 2 solutions. The Cherenkov resonance is given by $s = 0$. Root 1 solutions are waves with wavenormal angles near the resonance cone ($\theta \approx \theta_{res}$). They are evanescent below the lower hybrid frequency (f_{LHR}). The root 2 solutions are continuous across f_{LHR} and for $f > f_{LHR}$. Above f_{LHR} they are waves with wavenormal angles in the central hump of the index of refraction surface ($\theta < \theta_G$). For the $s = 0$ root 2 solutions the agreement between predictions and observations was better than a factor of 30 for all harmonics at all distances at which waves were measured. Within the context of this type of experiment this agreement is considered quite good. The predictions for the other resonance conditions disagreed with observations by many orders of magnitude.

Broadband waves generated through the Cherenkov resonance were also observed during the free flight. Root 1 (resonance cone) waves were observed to produce a funnel-shaped feature between the lower hybrid and the electron cyclotron frequencies [*Gurnett et al.*, 1986]. Root 2 (central hump) waves contributed to broadband emissions observed below ≈ 30 kHz [*Reeves et al.*, 1990]. No wave fields were observed which suggested measurable contributions from the cyclotron or anomalous cyclotron resonances ($s = \pm 1$). For the narrow-band emissions there appeared to be no measured contribution from the root 1 solutions.

In applying the predictions of HBN to payload bay beam operations we again find no evidence for contributions from the cyclotron or anomalous cyclotron resonances and no predictions are presented here for those solutions. For the Cherenkov resonances we cannot exclude the possibility of both the root 1 and root 2 solutions because of the proximity of the beam and the PDP.

The ≈ 7 m separation between the beam and the PDP raises another issue. The wavelength of whistler mode waves generated through the Cherenkov resonance can range from meters to several kilometers. The theory of HBN is fully valid in the near-field of the waves provided the point of observation is outside the beam itself.

Two problems exist when applying the theory of HBN to the results from the payload bay beam operations. The first is that the electron density could not be measured accurately when the PDP was in the payload bay [Raitt et al., 1987]. This is a result of the turbulent conditions produced in the payload bay by the motion of the orbiter through the plasma. Thus an approximate value must be used. The second problem is that the theory of HBN, as it stands, is not complete. As noted above, the contributions to the integrals from the simple poles are included but a contribution from a branch cut was neglected. We have evaluated the contributions from the branch cut in the asymptotic far-field limit. The relative contribution of the branch cut will be greater at larger distances from the beam but its effect at the short distances at which the Spacelab 2 experiments were conducted is not known. Nevertheless the theory of HBN in its present form proved quite useful in the interpretation of the free flight wave stimulation results and lacking a complete theory it will again be used here. We will see that it again shows good general agreement and provides an important framework for the interpretation of the experimental results.

5. THE BEAM DUTY CYCLE

The duty cycle of the beam is defined as the ratio of the beam on-time to the period of the beam modulation. It is one of the most easily controlled of the beam parameters and turns out to be one of the most important. The duty cycle controls the spatial structure of the beam. This, in turn, controls the amplitude and the spectral characteristics of the waves generated by the beam.

The duty cycle enters into the equations of HBN through the Fourier integral over the spatial structure of the beam. This implies that the dependence of the amplitude on the duty cycle is relatively insensitive to the details of the theory. In HBN the dependence on the duty cycle is very simple. It appears only in the duty cycle factor, $\mathcal{D} = 1/\eta \sin(\eta\pi b/d)$. The factor \mathcal{D} is the same in the equations for each component of the electric and magnetic field vectors and is independent of the mode of the radiation or the resonance condition.

Variation at the Pulsing Frequency

The duty cycle factor is dependent on both the duty cycle and the harmonic number. We begin by considering the dependence of the amplitude of the fundamental ($\eta = 1$) on the duty cycle. The Beam Energy sequence is particularly well suited to this investigation. The Beam Energy sequence consists of 19 pulsing periods (Figure 3). During the sequence the duty cycle for each pulsing period was in-

creased from 0.2% to 99.8%. The frequency for each pulsing period was kept as constant as possible and ranged between 488–608 Hz. The entire sequence lasted 95 s and the local plasma conditions can be considered constant over this interval. With all other variables held constant the dependence of the amplitude of the fundamental on the duty cycle is simply $\sin(\pi b/d)$.

Figure 11 shows that the measured dependence agrees very well with predictions. The function $\sin(\pi b/d)$ is plotted with a solid curve. The amplitude is normalized to an arbitrary value of 0.1 and plotted on a logarithmic scale. The amplitude of narrow-band waves at the pulsing frequency are taken from the magnetic antenna data during two Beam Energy sequences. Each sequence spans an electric and a magnetic antenna period so the full range of duty cycles cannot be compared in a single sequence. Some care was taken to find two sequences which took place under similar conditions. The sequence labeled "bmn" took place at 1900 UT on day 215 and the sequence labeled "bvd" took place at 1738 UT on the same day. During both sequences the payload bay was in light wake conditions with an ambient magnetic field strength of $B_0 \approx 0.45$ G on the Earth's day-side. The most likely cause of the difference in amplitudes at $b/d = 20\%$ and 50% is a difference in plasma density. The IRI predicted densities [Bilitza, 1986] for the two sequences were 3.5×10^5 and $2.6 \times 10^5 \text{ cm}^{-3}$ respectively. The higher amplitude waves are observed for the higher density estimate.

The variation with the duty cycle of the beam can be understood in terms of a physically simple model. For a duty cycle of $b/d = 0\%$ there is no emitted current and no radiation is expected. For a duty cycle of 100% the beam is on continuously (the dc case) and only broadband waves are emitted. The amplitude of narrow-band radiation is again expected to vanish. The presence of narrow-band radiation depends on periodically changing current densities.

One unanswered question from previous investigations was which portion of the beam pulse was responsible for producing the narrow-band radiation. One might expect radiation from, say, only the leading and trailing edges of each beam pulse in which case the wave amplitude should be independent of the duty cycle. The theory of Harker and Banks

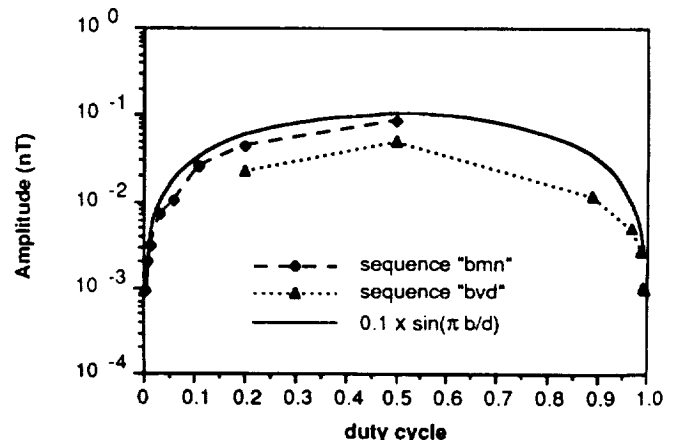


Fig. 11. The variation of the amplitude at the fundamental frequency with duty cycles between 0% and 100%. The solid line is $\sin(\pi b/d)$ arbitrarily normalized to 0.1. Data for two Beam Energy sequences show good agreement with the predicted behavior.

predicts amplitudes based on coherent radiation from the entire length of the pulse. The amplitudes from the Beam Energy sequences indicate that, in fact, the entire pulse radiates. This conclusion is important for understanding the production of narrow-band radiation from pulsed electron beams.

An equally important conclusion is that the amplitude of narrow-band radiation is not dependent on the average current injected by the beam. The beam current which appears in the expressions of HBN is $I_B = -Nev$. N is the density per unit length in a beam pulse and v is the velocity of the beam electrons. Therefore I_B is the instantaneous current when the beam is on (100 mA). The average current is $I_B \times b/d$. The results from the Beam Energy sequence experiments show that a duty cycle of 50% produces the maximum amplitudes even though duty cycles greater than 50% inject larger average currents. These results are expected to be independent of the value of the instantaneous current.

Harmonic Structure and the Duty Cycle Factor

Since the duty cycle factor, $1/\eta \sin(\eta\pi b/d)$, contains the harmonic number, η , the harmonic structure of the observed wave fields is also expected to depend on the duty cycle of the beam. Two major effects are predicted. The first is a decrease in wave amplitude with harmonic number due to the factor $1/\eta$. The second is the exclusion of harmonics for which $\eta b/d$ is an integer. Those harmonics are known as "forbidden harmonics."

Two sequences designed to investigate the variation with duty cycle are Duty 41 and Duty 21 sequences (Figures 1 and 2). Figure 12a shows the harmonic structure for two pulsing periods during a Duty 21 sequence. The pulsing frequency for both periods is 814 Hz. For the Duty 21 sequences the duty cycles were 2/3 and 1/3 or $\approx 33\%$ and 67% and for each, every third harmonic is forbidden. Figure 12b shows the predicted variation in amplitude with harmonic number.

Several features are apparent. We note that the tendency is for higher harmonics to appear with lower amplitudes, as expected. The amplitudes of the forbidden harmonics tends to be lower than the harmonics which give nonintegral $\eta b/d$ but are not zero. For both the 33% and the 67% duty cycles, forbidden harmonics are observed with amplitudes up to an order of magnitude above the background noise levels of $\approx 1-5 \times 10^{-4}$ nT. These results are consistent with the observations from STS 3 and the Spacelab 2 free flight experiments.

The presence of measurable narrow-band waves at the forbidden frequencies is likely to be the result of loss or partial loss of the spatial coherence of the beam pulses. Figure 13 shows how sensitive the amplitude is to the duty cycle. The predicted amplitude of the second harmonic is plotted for duty cycles in the vicinity of 50%. It is seen that even a 1% change in the actual duty cycle of the beam pulses can result in a substantial and measurable wave amplitude for a forbidden frequency.

An interesting point is that the duty cycle factor is a spatial parameter rather than a temporal one. This is seen in the theory from the fact that the integral which produces the duty cycle factor is over the coordinate space. Evidence of this subtle distinction is also found in the data from the Prox Ops sequence. As mentioned above, the Prox Ops sequence

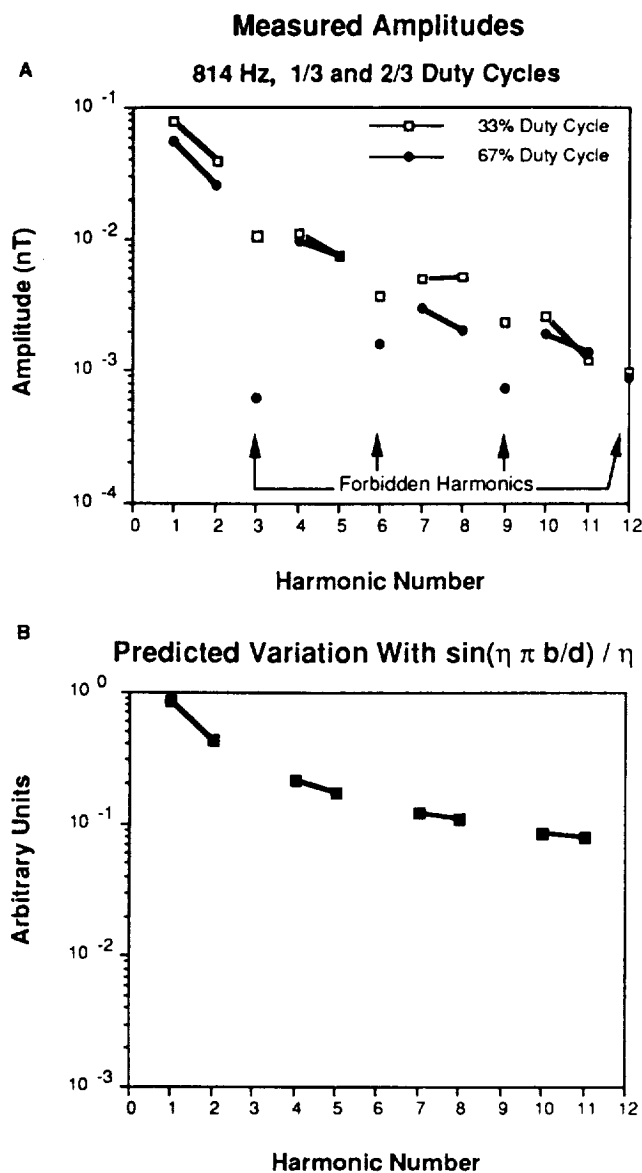


Fig. 12. (a) The amplitude of the harmonics of two pulsing periods during a Duty 21 sequence. The pulsing frequency for both is 814 Hz and the duty cycles are 1/3 and 2/3. (b) The predicted harmonic structure for both pulsing periods ($\sin(\eta\pi b/d)/\eta$).

used a 1.22 kHz pulsing frequency and a 50% duty cycle. It lasted for ≈ 10 min. Over this interval the pulsing mode was kept constant but the orientation of the orbiter with respect to the geomagnetic field changed. In the early part of the sequence the beam trajectory was such that it could exit the payload bay freely. Computer simulations have shown that in the later part of the sequence the pitch angle of the beam changed from 120° to 114° from the orbiter z axis and that the electron beam trajectory intersected the orbiter's starboard payload bay door approximately 4 m from the FPEG aperture.

Figure 14 shows the change in harmonic structure. The amplitude of the harmonics of the 1.22 kHz pulsing is shown for two different times. The dark bars show the amplitude when the beam is escaping from the payload bay. The even harmonics are the forbidden harmonics for this sequence and

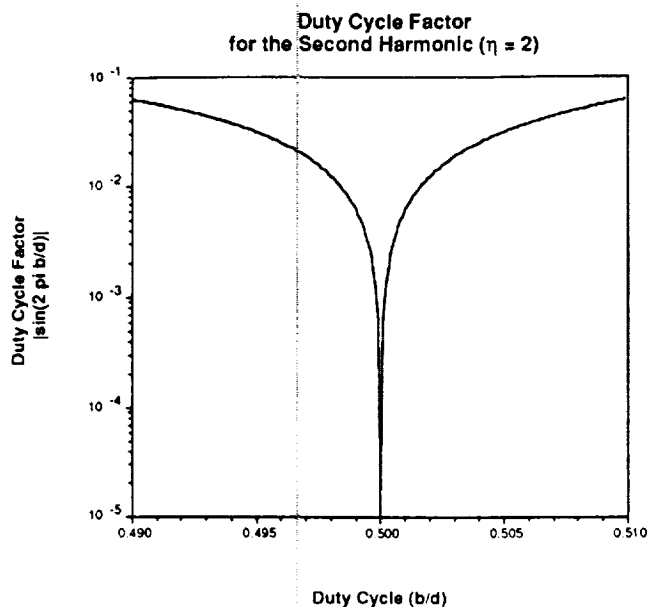


Fig. 13. The duty cycle factor $|\sin(\eta\pi b/d)|$ for the second harmonic ($\eta = 2$) versus the duty cycle b/d . Very sensitive dependence on the duty cycle is expected. Note the relative values of this factor for duty cycles of 50% and 50.5%.

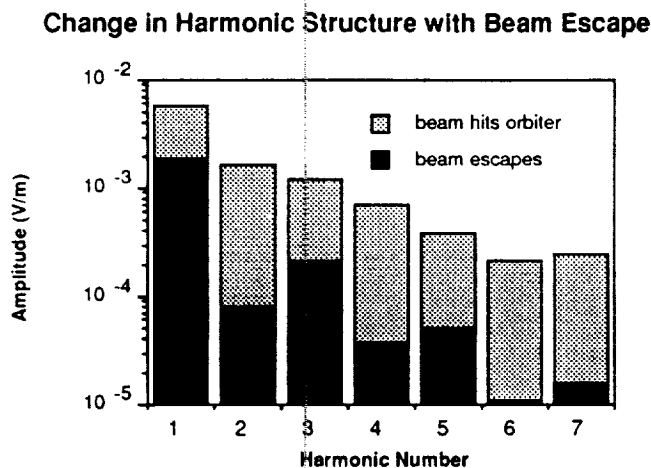


Fig. 14. The harmonics of a 1.22 kHz pulsing with a 50% duty cycle. Dark bars show harmonics with the beam freely escaping the orbiter. Even (forbidden) harmonics have lower amplitudes than odd harmonics. Light bars show harmonics when the beam trajectory hits the orbiter payload bay door. A $1/\eta$ harmonic structure is observed and even harmonics have comparable amplitude to odd harmonics.

they are observed with reduced amplitude compared to the odd harmonics. The light bars show the amplitude when the beam hits the orbiter. The beam is still on for 50% of the time but the length of the beam is essentially restricted to a few meters. In this situation the harmonic structure is roughly $1/\eta$ and the even, forbidden harmonics are of comparable amplitude to the odd harmonics.

There are many factors which could produce a change in the spatial coherence of the beam pulses. As well as the con-

ditions of beam escape, vehicle charging, beam plasma interactions, interactions with return currents, and the Coulomb repulsion of electrons within the beam can produce changes in the effective length of the radiating current source. Any propagation effect which spreads the beam pulses along the magnetic field or retards the leading electrons in a pulse can alter the spatial structure of the current source and hence the physical duty cycle of the beam. Two constraints on any process which can be proposed are (1) that the beam current structure is not drastically different from a square-wave and (2) that the effect on each pulse in the beam is approximately the same since the harmonic structure remains constant over times which are long compared to the duration of a pulse.

6. VARIATION WITH THE BEAM PULSING FREQUENCY

The other FPEG pulsing parameter which was actively controlled is the pulsing frequency of the beam. The pulsing frequency can be varied over the full 0–30 kHz range of the receiver. The narrow-band structure of the wave response to pulsed electron beams allows specific frequencies to be singled out for investigation. Study of the wave response at the fundamental eliminates the dependence on the harmonic structure of the wave response but does not eliminate the dependence on the duty cycle.

When one considers the plots of predicted amplitude versus frequency presented in *Harker and Banks* [1987] two main characteristics are apparent. (1) The amplitude of the different wave modes ($s = 0, 1, -1$) have very different behavior with varying frequency. (2) Within each wave mode there may be a complex dependence of the wave amplitude on frequency. That dependence includes cut-offs and resonances at characteristic frequencies of the plasma and nulls which are a result of destructive interference in the wave fields. Unlike the dependence of wave amplitude on the duty cycle the dependence on frequency cannot be isolated as a simple factor. Therefore, to examine the dependence of wave amplitude on frequency it is necessary to determine the wave mode and compare observations with the full numerical predictions of HBN.

Figure 15 shows the measured and the predicted variation with the frequency of the pulsed beam. The measured data is taken from an ELF Sweep and a VLF Sweep sequence and is plotted with dots connected by a bold line. The numeric predictions using the theory of HBN are plotted with solid lines. For the predictions a set of "typical" values of various parameters were used. The values for those parameters is given in Table 1 with the exception that both the root 1 (resonance cone) and root 2 (central hump) modes are plotted.

The measurements show the best agreement with the root 2 solutions. The root 1 solutions are predicted to have higher amplitudes than are measured at these distances but do not show the right frequency dependence. These results are the same as the results from the free flight [Reeves et al., 1988b and 1990]. The measured values deviate from the predicted amplitudes for the Cherenkov root 2 solutions in two ways. Firstly the behavior of the measured amplitudes at frequencies between 1 kHz and 10 kHz shows two systematic decreases which are not predicted. This is a result of the influence of the duty cycle factor. The predictions are made for a duty cycle of 50%. In the VLF Sweep sequence

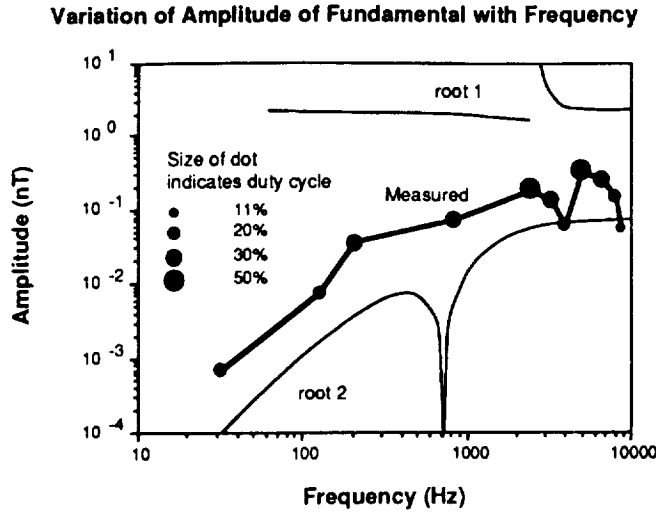


Fig. 15. The variation of the amplitude of the fundamental with the frequency of the pulsing. Predicted curves are shown for the Cherenkov root 1 and root 2 modes (light lines). Measured values are shown for an ELF Sweep and a VLF Sweep sequence (dots connected by bold line). The size of the dot represents the duty cycle for that pulsing period.

the duty cycle ranged from 11% to 50%. The duty cycle for each frequency is represented on the plot by the size of the dot. Frequencies with duty cycles which are less than 50% appear with systematically lower amplitudes. Secondly, the amplitude of the measured amplitudes is consistently higher than predicted. This is most likely due to an inappropriate estimate of the electron density which could not be accurately measured.

7. PREDICTED VARIATIONS WITH IMPORTANT PARAMETERS

The duty cycle and the frequency of a particular pulsing period were actively controlled during the Spacelab 2 mission. These two parameters are particularly important in the study of wave generation by electron beam injection. In this section we consider the dependence of wave amplitude on parameters which could not be controlled. Again we use the predictions of HBN. The parameters we will consider are the beam current (I_B), the beam energy (E_B), the geomagnetic field strength (B_0), the pitch angle (ϕ), the ambient

Table 1. Default Parameters for Predicted Amplitudes

Parameter	Description
resonance condition mode	Cherenkov ($s=0$) root 2 (central hump)
beam current I_B	100 mA
beam energy E_B	1 keV
harmonic number η	1
duty cycle b/d	50%
ambient electron density n_e	10^5 cm^{-3}
distance to beam r_{\perp}	5 m
geomagnetic field strength B_0	0.2 G
beam pitch angle ϕ	45°

electron density (n_e), and the distance from the receiver to the beam (r_{\perp}).

For each calculation a set of default parameters were used (Table 1). Based on the comparison of measured and predicted waves, both during the PDP free flight and with the PDP in the payload bay, we identify the Cherenkov, root 2 (central hump) mode as the most important for these experiments. The beam current and beam energy are the values used for the experiments. For all studies the fundamental frequency ($\eta = 1$) and a duty cycle of 50% are used. The ambient electron density and the geomagnetic field strength are typical values for the experimental conditions. The distance to the beam is defined as the perpendicular distance from the center of the PDP to the center of the beam helix which was typically ≈ 5 m for the payload bay sequences. The pitch angle is chosen arbitrarily to be 45° . In each study all the parameters were kept fixed except the parameter being studied. In Figures 16-20 the default value is shown on the axis in bold type. Numerical calculations are presented for pulsing frequencies of 100 Hz, 1 kHz, and 10 kHz.

Beam Current

The dependence of the wave amplitude on the average beam current has already been considered in our discussion of the duty cycle. For the Spacelab 2 and STS 3 missions the instantaneous beam current, I_B was set at 100 mA for all the pulsed beam operations. Figure 16 shows the predicted dependence of wave amplitude on the instantaneous beam current. In the theory of HBN, I_B appears as a constant in the expressions for each of the wave field components. Figure 16 shows the expected linear variation with beam current at all three frequencies (log scale).

Beam Energy

The beam acceleration voltage was 1 keV for all Spacelab 2 FPEG operations. Figure 17 shows the variation in amplitude for beam energies in the range 0-2 keV. The dependence of the expressions for wave amplitude on E_B is primarily a function of the velocity of the electrons. That

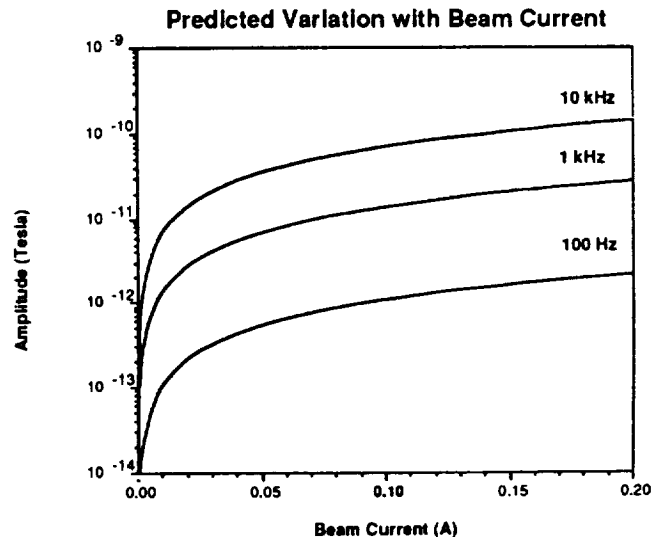


Fig. 16. The predicted variation of amplitude with the beam current, I_B , at frequencies 100 Hz, 1 kHz, and 10 kHz. The default value of 0.1 A is shown in bold type.

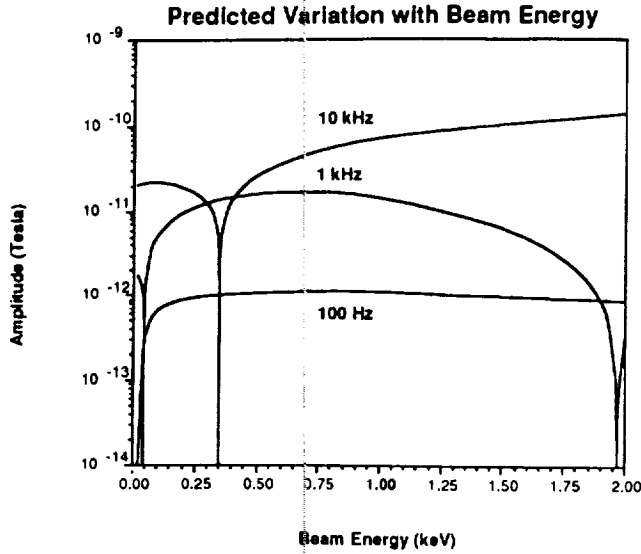


Fig. 17. The predicted variation of amplitude with the beam energy, E_B , at frequencies 100 Hz, 1 kHz, and 10 kHz.

velocity, however, determines the gyroradius (which appears in the Bessel functions) and the resonance condition which picks out the values of the parallel index of refraction. Although the dependence of the final expressions on E_B is not simple, the wave amplitudes are predicted to vary little over this range of beam energies.

Although the nominal beam energy for the Spacelab 2 mission was 1 keV it is anticipated that the actual energy of the electrons in the beam could be significantly different. The dynamics of beam escape and the thermalization and Coulomb repulsion of beam electrons are anticipated to change the energy of a substantial population of beam electrons. Figure 17 indicates that changes of energy up to a factor of 2 will not significantly effect the wave amplitudes provided the beam energy alone is changed. Another interesting prediction is that the wave amplitude may actually decrease for higher beam energies at some frequencies.

Geomagnetic Field

The variation with the geomagnetic field strength is shown in Figure 18. The magnetic field strength determines the characteristic frequencies in the plasma including the electron cyclotron, the ion cyclotron, and the lower hybrid frequencies which in turn appear in the elements of the permittivity tensor and the dispersion relation. B_0 also determines the gyroradius and hence appears in the Bessel functions. Again, in spite of the complex dependence of the field expressions on B_0 , the variation over the range $B_0 = 0.1-0.5$ G is fairly smooth and gradual.

The pitch angle (Figure 19) varies significantly in the experiments and can take values in the full range of $0-90^\circ$. The pitch angle influences the gyroradius along with B_0 and E_B . It is the dependence of the argument of the Bessel function ($k_\perp m V_\perp / e B_0$) which causes the nulls in the amplitude seen in the figure. Physically these nulls are caused by destructive interference of waves generated in different parts of the beam. The dependence of the wave amplitude is also seen to be quite different for different frequencies reflecting the

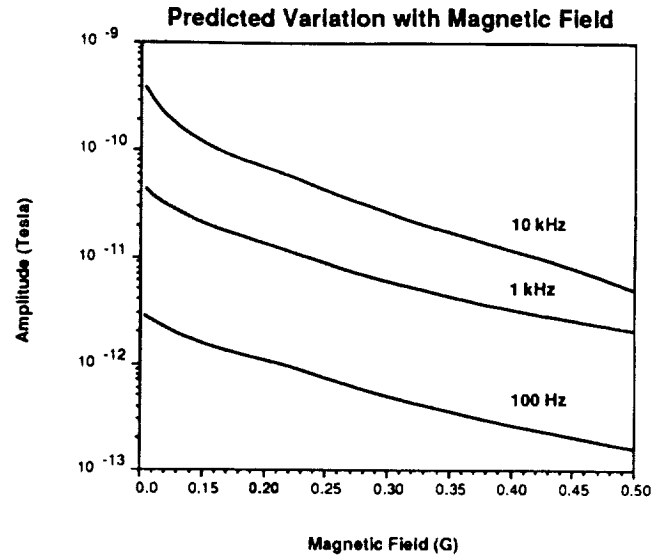


Fig. 18. The predicted variation of amplitude with the geomagnetic field strength, B_0 , at frequencies 100 Hz, 1 kHz, and 10 kHz.

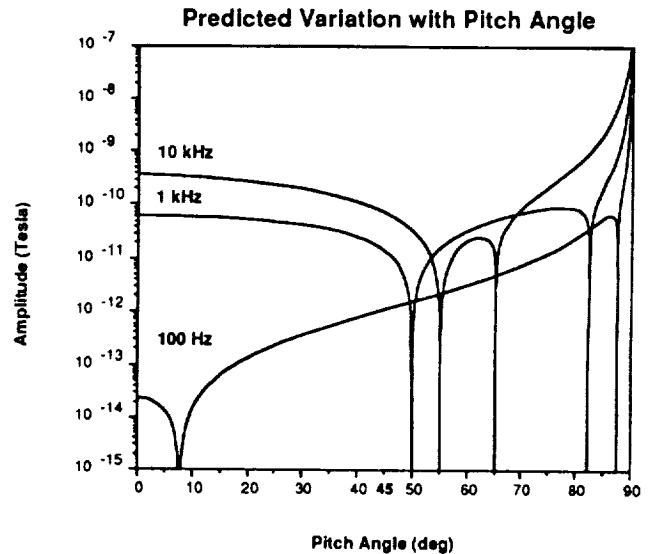


Fig. 19. The predicted variation of amplitude with the pitch angle, ϕ , at frequencies 100 Hz, 1 kHz, and 10 kHz.

dependence of the resonance condition on V_{\parallel} and hence on ϕ .

We note that the variation of amplitude with pitch angle could provide a very sensitive test of the theory of HBN. The orientation of the FPEG was fixed and therefore on Spacelab 2 the pitch angle was determined by the orbiter orientation with respect to the geomagnetic field. For this reason the Spacelab 2 data set is not adequate for a study of pitch angle variations. Such an investigation may be more easily conducted on a rocket flight.

Electron Density

The local electron density is one of the hardest parameters to determine for sequences in the payload bay because

of the strong and variable effects of ram/wake conditions which may change the plasma density in the payload bay by several orders of magnitude from the ambient levels. The electron density also affects many of the terms in the expressions for the wave amplitudes. It determines the plasma frequencies and the lower hybrid frequency. Therefore it affects the permittivity tensor elements, the index of refraction, and all the terms which depend on them. Those terms include the Bessel function which is again responsible for the nulls in the wave fields plotted in Figure 20. The abrupt drop in wave amplitudes for the 10 kHz predictions at $\log(n_e) \approx 5.75 \text{ cm}^{-3}$ is due to the fact that the Cherenkov root 2 resonance condition cannot be satisfied above a critical frequency. This effect was discussed in *Reeves et al.* [1990] in relation to the cut-off in broadband waves during the DC flux tube connection.

Distance

In contrast to the parameters considered above, the dependence on the distance to the electron beam is rather straight forward. In the treatment with no loss of coherence along the path of the beam the distance which is relevant is the perpendicular distance to the center of the beam, r_{\perp} . The perpendicular distance contributes only through the Hankel functions $H_s^{(2)}(\mu_{\perp} k_0 r_{\perp})$ and $H_{s+1}^{(2)}(\mu_{\perp} k_0 r_{\perp})$ and therefore show a smooth decrease with increasing distance.

Although the effect of varying parameters have been considered here individually, under real conditions they are generally observed to vary simultaneously. In addition, the effects of changing a particular parameter may be different at different frequencies. For example, during the free flight of the PDP, as the orbiter moved through space the electron density and the magnetic field strength both vary and as the orbiter maneuvered for the flux tube connections the distance to the receiver and the pitch angle of the beam were altered.

8. CONCLUSIONS

Electron beam pulsing sequences conducted with the PDP in the Spacelab 2 payload bay confirm and extend the re-

sults of the free flight investigations. The duration of the free flight was 6 hours. Therefore considerably more time was available for experiments when the PDP was in the payload bay. Several distinct beam modulation sequences were designed to investigate the wave response to series of pulsing periods with different frequencies and duty cycles. These sequences include the Duty 41, Duty 21, Beam Energy, ELF Sweep, and VLF Sweep sequences.

The wave environment in the payload bay was compared to that measured during the PDP free flight. The ambient wave fields are found to be quite different. Ambient fields measured several hundred meters from the orbiter consist primarily of natural atmospheric. In the payload bay orbiter-associated EMI dominates the measured fields. In contrast, the beam generated wave response is found to be similar. The most significant differences can be attributed to differences in the position and motion of the PDP relative to the electron beam.

In this analysis the theory of *Harker and Banks* [1987] on wave production by pulsed electron beams is used extensively. Although the theory is not complete it is valid in the near field of the waves and has proven useful for the analysis of free flight and payload bay experiments. Experimental results have shown good agreement with both the qualitative and quantitative predictions of the theory.

The dependence of the narrow-band wave amplitudes on the duty cycle of the beam has been the subject of extensive investigation. The predicted dependence occurs only in the duty cycle factor $D = (1/\eta)\sin(\eta\pi b/d)$. The results from the Beam Energy sequences show the predicted variation at the fundamental frequency. They establish that the wave amplitude depends upon the instantaneous beam current rather than the average beam current and that maximum wave amplitudes are produced by 50% duty cycles.

The duty cycle is also found to control the harmonic structure of the narrow-band waves. Good agreement with the predicted dependence is observed for all frequencies except at forbidden harmonics. Measured amplitudes at forbidden harmonics are generally lower in amplitude but are not zero. The presence of narrow-band emissions at the forbidden harmonics is attributed to the sensitive dependence of the wave amplitude on the actual spatial extent of the beam pulses.

Investigation of the wave amplitude as a function of beam pulsing frequency also shows good agreement with theory. The dependence on frequency is predicted to be different for the different wave modes. The best agreement is found for the Cherenkov, root 2 solutions in the whistler mode. This is the same conclusion as for the results of the free flight wave experiments.

The beam duty cycle and frequency were actively controlled. Numerical calculations of the expected variation of the wave amplitude with other parameters were also performed. The amplitude of the narrow-band waves are not expected to show strong dependence on the beam current, the beam energy, or the geomagnetic field strength for values of these parameters near the Spacelab 2 conditions. The dependence of the wave amplitude on the beam pitch angle and the ambient electron density is expected to be more complex. In the Spacelab 2 experiments, in general, several parameters varied simultaneously and controlled investigations of a single parameter were not possible. It would be possible in future experiments to actively control the pitch angle and thus keep an important variable fixed or to vary

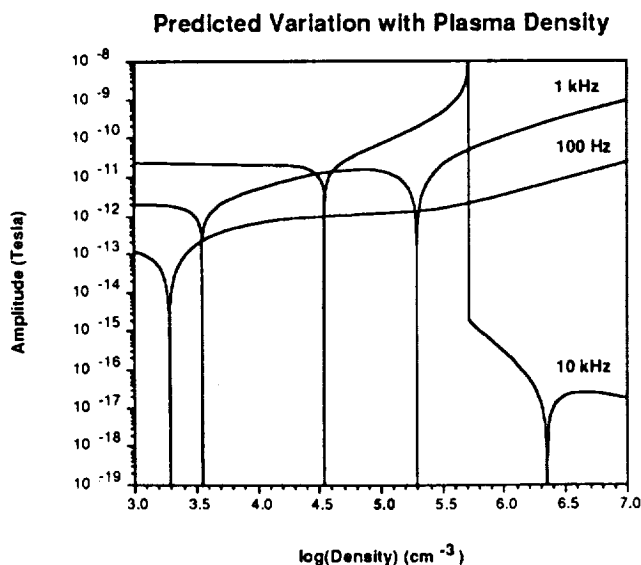


Fig. 20. The predicted variation of amplitude with the ambient electron density, n_e , at frequencies 100 Hz, 1 kHz, and 10 kHz.

it in a controlled manner and thus provide a sensitive test of the theory.

Acknowledgments. This work was conducted at Stanford University under NASA grant NAGW-225.

The Editor thanks B. A. Whalen and another referee for their assistance in evaluating this paper.

REFERENCES

- Banks, P. M., W. J. Raitt, A. B. White, R. I. Bush, and P. R. Williamson, Results from the vehicle charging and potential experiment on STS-3, *J. Spacecr. Rockets*, **24**, 138-149, 1987.
- Bell, T. F., Artificial production of VLF hiss, *J. Geophys. Res.*, **73**, 13, 1968.
- Bilitza, D., International reference ionosphere: Recent developments., *Radio Sci.*, **21**, 343, 1986.
- Bush, R. I., G. D. Reeves, P. M. Banks, T. Neubert, P. R. Williamson, W. J. Raitt, and D. A. Gurnett, Electromagnetic fields from pulsed electron beam experiments in space: Spacelab 2 results, *Geophys. Res. Lett.*, **14**, 1015-1018, 1987.
- Farrell, W. M., D. A. Gurnett, P. M. Banks, R. I. Bush, and W. J. Raitt, An analysis of whistler-mode radiation from the Spacelab 2 electron beam, *J. Geophys. Res.*, **93**, 153-161, 1988.
- Gurnett, D. A., W. S. Kurth, J. T. Steinberg, P. M. Banks, R. I. Bush, and W. J. Raitt, Whistler-mode radiation from the Spacelab 2 electron beam, *Geophys. Res. Lett.*, **13**, 225, 1986.
- Gurnett, D. A., W. S. Kurth, J. T. Steinberg, and S. D. Shawhan, Plasma wave turbulence around the shuttle: Results from the Spacelab 2 flight, *Geophys. Res. Lett.*, **15**, 760-763, 1988.
- Harker, K. J., and P. M. Banks, Radiation from pulsed electron beams in space plasmas, *Planet. Space Sci.*, **19**, 454-470, 1983.
- Harker, K. J., and P. M. Banks, Radiation from long pulse train electron beams in space plasmas, *Planet. Space Sci.*, **33**, 953-963, 1985.
- Harker, K. J., and P. M. Banks, Near fields in the vicinity of pulsed electron beams in space, *Planet. Space Sci.*, **35**, 11-19, 1987.
- Hastings, D. E., N. A. Gatsonis, and T. Mogstad, A simple model for the self-consistent water plasma cloud about an outgassing structure in the ionosphere, *J. Geophys. Res.*, **93**, 1961, 1988.
- Hawkins, J. G., Vehicle charging and return current measurements during electron beam emission experiments from the shuttle orbiter, Ph.D. Dissertation, Stanford Univ., Stanford, Calif., 1988.
- Lavergnat, J., and T. Lehner, Low frequency radiation characteristics of a modulated electron beam immersed in a magnetized plasma, *IEEE Trans.*, **AP-32**, 177, 1984.
- Lavergnat, J., T. Lehner, and G. Matthieussent, Coherent spontaneous emission from a modulated beam injected in a magnetized plasma, *Phys. Fluids*, **27**, 1632, 1984.
- Liemohn, H. B., Radiation from electrons in a magnetoplasma, *J. Res. Natl. Bur. Stand., Sect. D* **69**, 741, 1965.
- McKenzie, J. F., Radiation losses from a test particle in a plasma, *Phys. Fluids*, **10**, 12, 1967.
- Neubert, T., J. G. Hawkins, G. D. Reeves, P. M. Banks, R. I. Bush, P. R. Williamson, D. A. Gurnett, and W. J. Raitt, Pulsed electron beam emission in space, *J. Geomagn. Geoelectr.*, **40**, 1221-1233, 1988.
- Neubert, T., and K. J. Harker, Magnetic fields in the vicinity of pulsed electron beams in space, *Planet. Space Sci.*, **36**, 469, 1988.
- Neubert, T., K. J. Harker, P. M. Banks, G. D. Reeves, and D. A. Gurnett, Waves generated by pulsed electron beams., *Adv. Space Sci.*, **10**, 137, 1990.
- Ohnuki, S., and S. Adachi, Radiation of electromagnetic waves from and electron beam antenna in an ionosphere, *Radio Sci.*, **19**, 925, 1984.
- Raitt, W. J., J. V. Eccles, D. C. Thompson, P. M. Banks, P. R. Williamson, and R. I. Bush, Plasma parameters in the near wake of the Space Shuttle, *Geophys. Res. Lett.*, **14**, 359-362, 1987.
- Reeves, G. D., P. M. Banks, A. C. Fraser-Smith, T. Neubert, R. I. Bush, D. A. Gurnett, and W. J. Raitt, VLF Wave stimulation by pulsed electron beams injected from the space shuttle, *J. Geophys. Res.*, **93**, 162, 1988a.
- Reeves, G. D., P. M. Banks, T. Neubert, R. I. Bush, P. R. Williamson, A. C. Fraser-Smith, D. A. Gurnett, and W. J. Raitt, VLF Wave emissions by pulsed and DC electron beams in space 1: Spacelab 2 observations, *J. Geophys. Res.*, **93**, 14699-14718, 1988b.
- Reeves, G. D., Very low frequency radio waves produced by electron beam injection in space plasmas, Ph. D. dissertation, Stanford Univ., Stanford, Calif., 1989.
- Reeves, G. D., P. M. Banks, T. Neubert, K. J. Harker, and D. A. Gurnett, VLF wave emissions by pulsed and DC electron beams in space, 2, Analysis of Spacelab 2 results, *J. Geophys. Res.*, **95**, 6505, 1990.
- Shawhan, S. D., G. B. Murphy, J. S. Pickett, Plasma diagnostics package initial assessment of the shuttle orbiter plasma environment, *J. Spacecr. Rockets*, **21**, 387, 1984.
- Winckler, J. R., The application of artificial electron beams to magnetospheric research, *Rev. Geophys.*, **18**, 659-682, 1980.

P. M. Banks, K. J. Harker, T. Neubert, and G. D. Reeves, Space Telecommunications and Radioscience Laboratory, Durand 202, Stanford University, Stanford CA 94305.

D. A. Gurnett, Department of Physics and Astronomy, University of Iowa, Iowa City, IA 52242.

W. J. Raitt, Center for Atmospheric and Space Science, Utah State University, Logan, UT 84322

(Received August 22, 1989;
revised January 17, 1990;
accepted February 9, 1990.)

Comments on "Pulsed Electron Beam Emission in Space"
by Neubert *et al.* (1988)

W. M. FARRELL

Laboratory of Extraterrestrial Physics, NASA/Goddard Spaceflight Center,
Greenbelt, MD 20771, U.S.A.

(Received May 15, 1989; Revised September 25, 1989)

Recently, NEUBERT *et al.* (1988) described the potential and return currents at the space shuttle during ejection of 1 keV, 50-150 mA DC and pulsed electron beams. Their measurements were taken during the shuttle's Spacelab-2 (SL-2) mission. One of the author's main objectives was to determine the ability of the electron beams to escape the near vicinity of the spacecraft. They show that potential and wave measurements during some beam injections are consistent with beams that are freely-propagating into the ambient plasma. The issue of beam escape has become an important one, particularly since recent theoretical particle simulations that study the injection process predict that overdense beams ($n_b \gg n_a$) such as those from the shuttle should be strongly disrupted and reflected backwards due to the development of a large spacecraft potential (OKUDA and KAN, 1987; WINGLEE and PRITCHETT, 1987, 1988; PRITCHETT and WINGLEE, 1987). Experimental measurements from the SL-2 mission obtained during some overdense ejections seem to contradict these theories. Hence, the purpose of this comment is to supplement Neubert *et al.*'s findings by presenting more evidence for the escape of overdense electron beams from the shuttle.

Neubert *et al.* presented a set of potential measurements obtained by the Charge and Current Probe (CCP) during beam ejections. They showed that when the ambient electron density was greater than about $1.5 \times 10^5 \text{ cm}^{-3}$, the measured potentials remained small, less than about 5 V. However, below this ambient density level, the measured potentials could become quite large, approaching nearly 60 V. In this case, the true vehicle potentials may have possessed even larger values, since the plasma sheath surrounding the shuttle now extended beyond the characteristic measuring length of the CCP. The threshold densities of $1.5 \times 10^5 \text{ cm}^{-3}$ corresponded to the densities at which the thermal electron current from the ionosphere balanced the emitted beam flux for a 50 mA current. The importance of this observation is that above the threshold ambient electron density, the potentials were relatively small and should have allowed for the escape of overdense electron beams. Further evidence of escape was presented by the authors using the waves generated during pulsed electron beam ejections. For an ideal square wave pulse, amplitude increases at the odd harmonics of the pulsing frequency should be observed. This wave signature was seen during ejections, indicating that the electron pulses escaped with minimal distortion.

To illustrate the point further, the SL-2 electron beam ejection occurring on

DOY 213 of 1985 from 03:30 to 03:37 UT will now be examined. During this period, a continuous 1 keV-50 mA electron beam was ejected from the shuttle bay along a magnetic field line with a varying pitch angle of $<20^\circ$. The beam density at injection, n_b , was estimated to be $1.6 \times 10^7 \text{ cm}^{-3}$ (or half the density of the 100 mA electron beam described in BANKS and RAITT (1988)), while the ambient electron density, n_a , was determined to be $1.3 \times 10^5 \text{ cm}^{-3}$ (based on the electron plasma frequency value given in GURNETT *et al.* (1986)). Hence, n_b/n_a is about 100 and the beam is considered extremely overdense. According to one-dimensional simulations, n_b must be less than n_a for a beam to escape (OKUDA and KAN, 1987; WINGLEE and PRITCHETT, 1987), while the two-dimensional BIG code requires the ratio of the plasma response time to beam stagnation time to be less than 0.4, $t_{rp}/t_s < 0.4$ (WINGLEE and PRITCHETT, 1988). Since $n_b \sim 100n_a$ and $t_{rp}/t_s = 2$ to 6 (NEUBERT *et al.*, 1988) during injection, neither theoretically-derived condition for beam escape was met; thus one might expect the development of a large spacecraft potential and the reflection of the beam very near the generator. However, the free-flying Plasma Diagnostics Package (PDP) made a close encounter to the connecting magnetic flux tube at a distance of 200 meters from the shuttle. At this time, the PDP detected strong wave turbulence near the plasma frequency and in the whistler-mode (GURNETT *et al.*, 1986; FARRELL *et al.*, 1988), along with a relatively intense backscattered beam electron component (FRANK *et al.*, 1989). Back at the shuttle, the Vehicle Charging and Potential (VCAP) Experiment measured potentials of only 3 V during the 1-keV beam ejections (NEUBERT *et al.*, 1988). This potential is not large enough to significantly alter the beam's propagation. Hence, the experimental results seem to contrast the simulation's predictions.

The whistler-mode waves emitted by this beam can be used as a diagnostic tool to estimate the beam's extension from the shuttle. As demonstrated in GURNETT *et al.* (1986) and FARRELL *et al.* (1988), these waves were emitted with their normal angles very near the resonance cone angle. Hence, for the waves at a given frequency, their ray path orientation with respect to the magnetic field is specified by equation (1) of GURNETT *et al.* (1986). Given this wave geometry, consider a beam reflected (or stopped) very near the shuttle (ideally, to form a point source) and a spacecraft flying past the active field line, such as the PDP during the SL-2 mission. Figure 1(a) schematically represents this situation. For a point source radiating at frequency f_2 , there will be two points where the spacecraft will intercept the whistler-mode rays, at A and A'. At a lower frequency, f_1 , again two points will be intercepted, but at locations B and B', which are located closer to the active field line. Hence, on a radio spectrogram, the emission pattern appears as a hollow or partially-filled funnel. As the radiation source (i.e., the beam) becomes more extended along the field line, the funnel-shaped emission pattern becomes more complete, as indicated in (b). Whistler-mode emissions detected as incomplete funnel-shaped patterns are found in nature, and are called VLF saucers (SMITH, 1969). If the source extends completely to the spacecraft, the funnel-shaped pattern is completely filled in, as shown in (c). During the SL-2 beam ejection described above, the wave receiver on the PDP detected a complete, intense whistler-mode funnel (see Fig. 2 of GURNETT *et al.*, 1986; or Fig. 1 of FARRELL *et al.*, 1988) verifying the propagation of the beam out to at least 200 meters from its point of injection. Also, near the active flux tube, very strong electrostatic turbulence near f_{pe}

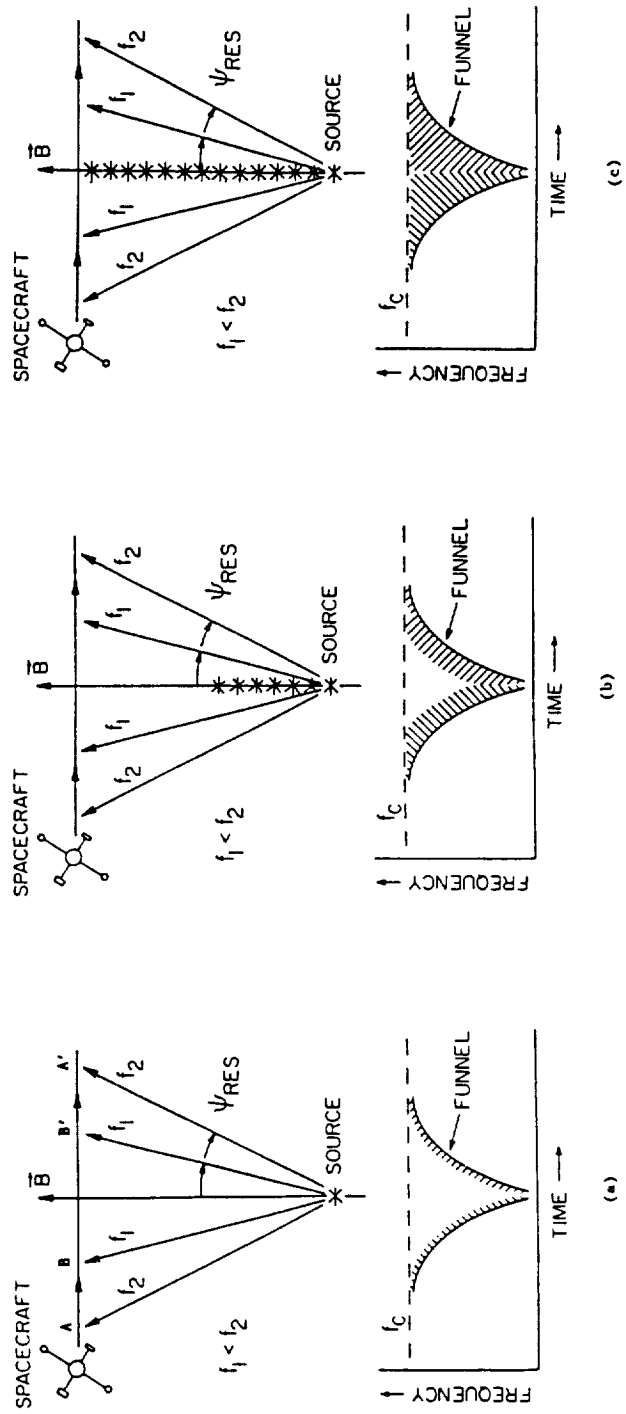


Fig. 1. The whistler-mode emission pattern for different beam configurations.

was detected, further implying the presence of the beam distant from its injection point.

The whistler-mode wave power was also determined for this particular event by calculating the Poynting flux through a surface containing the PDP trajectory (FARRELL *et al.*, 1988). The only assumption involved in calculating this quantity was that the emissions were generated by a Landau resonance process, as suggested by GURNETT *et al.* (1986) and verified by FARRELL *et al.* (1988). The measured power was found to be about 10^{-9} W/Hz, which is a value almost 10^7 times greater than the expected incoherent Cerenkov radiation level from the fully-escaping beam. A number of coherent radiation processes have been suggested to account for this power difference (FARRELL *et al.*, 1988, 1989; LIN and WONG, 1988; OMURA and MATSUMOTO, 1988; PRITCHETT *et al.*, 1988; NISHIKAWA *et al.*, 1989). These high power levels suggest that a significant fraction of beam electrons get away from the near-shuttle region, although the exact number escaping is difficult to determine. This number depends upon knowing the exact coherent process operating in the beam, which is still the subject of some debate, as mentioned in NEUBERT *et al.* (1988).

The inconsistency between experimental and simulated beam ejections might possibly lie in the return current collecting areas, A_{sc} , of the two systems. On the shuttle, this area is at least 30 m^2 (NEUBERT *et al.*, 1988), which is more than 10^4 times larger than the cross-sectional area of the beam at injection, A_b . This large collecting area can allow for ample return flux to the shuttle even during highly overdense ejections. In contrast, one-dimensional simulations have A_{sc} equal to A_b (both of infinite size), making the condition for beam escape ($n_b/n_a < 1$) independent of area (OKUDA and KAN, 1987; PRITCHETT and WINGLEE, 1987). Such a condition is unrealistic for the modeling of shuttle ejections. Like the one-dimensional case, the condition for escape derived from the BIG code ($t_{rp}/t_s < 0.4$) has a very strong dependency on beam and ambient electron density, and only a mild dependency on areas (WINGLEE and PRITCHETT, 1988). Hence, it too may be inadequate for shuttle applications involving large return current areas. The fact that it predicts beam disruption and large spacecraft potentials when the opposite is sometimes observed indicates that some inadequacy exists. Despite the inadequacies, some two-dimensional simulations do show the proper trend of improved beam escape with increasing spacecraft area (PRITCHETT and WINGLEE, 1987; OKUDA and BERCHEM, 1988). In the future, it may be possible to replicate shuttle injections using advanced three-dimensional models (like OKUDA and ASHOUR-ABDALLA, 1989) run with realistic shuttle-like parameters.

A final point considering overdense beam escape can be made using the published results from the Echo-7 rocket experiment. During this flight, a mother payload ejected a powerful electron beam (38 keV-180 mA) and various diagnostics packages recorded its optical, radio, and return current signatures. A picture published in Aviation Week and Space Technology (HUGHES, 1988) indicates that the beam not only escaped the near vicinity of the rocket, but remained coherent for at least eight gyrations about the magnetic field line. Also, this beam escape occurred at the very low altitude of 99 km, where the ambient electron density was significantly reduced in comparison to the SL-2 values. Hence, here is another example of an overdense beam escaping its source.

To conclude, Neubert *et al.* have presented evidence that overdense electron beams can escape the near vicinity of the shuttle using the potentials measured from the CCP and the signature of the harmonic emissions generated by pulsed electron beams. To supplement their results, further indication of beam escape and propagation out to at least 200 meters was presented in this comment, using the whistler-mode wave signature obtained during a continuous beam ejection. Combined, these results lend strong support to the thesis that overdense electron beams can and will escape from the space shuttle (and other spacecraft, such as Echo-7), despite the predictions based upon idealized simulations of the injection process which show otherwise.

I would like to thank Jolene Pickett and Bill Paterson for reviewing and discussing this comment. Part of this research was funded by a NASA graduate student researchers training grant NGT-50034.

REFERENCES

- BANKS, P. M. and W. J. RAITT, Observations of electron beam structure in space experiments, *J. Geophys. Res.*, **93**, 5811-5822, 1988.
- FARRELL, W. M., D. A. GURNETT, P. M. BANKS, R. I. BUSH, and W. J. RAITT, An analysis of the whistler-mode radiation from the Spacelab-2 electron beam, *J. Geophys. Res.*, **93**, 153-161, 1988.
- FARRELL, W. M., D. A. GURNETT, and C. K. GOERTZ, Coherent Cerenkov radiation from the Spacelab-2 electron beam, *J. Geophys. Res.*, **94**, 443-452, 1989.
- FRANK, L. A., W. R. PATERSON, M. ASHOUR-ABDALLA, D. SCHRIEVER, W. S. KURTH, D. A. GURNETT, N. OMIDI, P. M. BANKS, R. I. BUSH, and W. J. RAITT, Electron velocity distributions and plasma waves associated with the injection of an electron beam into the ionosphere, *J. Geophys. Res.*, **94**, 6995-7002, 1989.
- GURNETT, D. A., W. S. KURTH, J. T. STEINBERG, P. M. BANKS, R. I. BUSH, and W. J. RAITT, Whistler-mode radiation from the Spacelab-2 electron beam, *Geophys. Res. Lett.*, **13**, 225-228, 1986.
- HUGHES, D., Echo-7 photographs electron spiraling around earth's magnetic field lines. *Aviation Week and Sp. Tech.*, 115-118, September, 12, 1988.
- LIN, C. S. and H. K. WONG, Plasma instabilities of a finite-sized electron beam-plasma system, paper presented at 1988 URSI meeting, Union Radio Scientifique Internationale, Boulder, Colo., 1988.
- NEUBERT, T., J. G. HAWKINS, G. D. REEVES, P. M. BANKS, R. I. BUSH, P. R. WILLIAMSON, D. A. GURNETT, and W. J. RAITT, Pulsed electron beam emission in space, *J. Geomag. Geoelectr.*, **40**, 1221-1233, 1988.
- NISHIKAWA, K.-I., L. A. FRANK, and C. Y. HUANG, Three-dimensional simulation of whistler mode excited by the Spacelab 2 electron beam, *J. Geophys. Res.*, **94**, 6855-6865, 1989.
- OKUDA, H. and M. ASHOUR-ABDALLA, Propagation of a nonrelativistic electron beam in three dimensions, *J. Geophys. Res.*, submitted, 1989.
- OKUDA, H. and J. BERCHEM, Injection and propagation of a nonrelativistic electron beam and spacecraft charging, *J. Geophys. Res.*, **93**, 175-195, 1988.
- OKUDA, H. and J. D. KAN, Injection of an electron beam into a plasma and spacecraft charging, *Phys. Fluids*, **30**, 209-220, 1987.
- OMURA, Y. and H. MATSUMOTO, Computer experiments on whistler and plasma wave emissions for Spacelab-2 electron beam, *Geophys. Res. Lett.*, **15**, 319-322, 1988.
- PRITCHETT, P. L. and R. M. WINGLEE, The plasma environment during particle beam injection into space plasmas, I, Electron beams, *J. Geophys. Res.*, **92**, 7637-7688, 1987.
- PRITCHETT, P. L., H. KARIMABADI, and N. OMIDI, Electromagnetic waves generated during electron beam experiments in space (abstract), *Eos Trans. AGU*, **69**, 1372, 1988.
- SMITH, R. L., VLF observations of auroral beams as sources of a class of emissions, *Nature*, **224**, 351-352, 1969.

- WINGLEE, R. M. and P. L. PRITCHETT, Space charge effects during the injection of dense electron beams into space plasmas, *J. Geophys. Res.*, **6**, 6114-6126, 1987.
- WINGLEE, R. M. and P. L. PRITCHETT, Comparative study of cross-field and field-aligned electron beams in active experiments, *J. Geophys. Res.*, **93**, 5823-5844, 1988.

Transition From Ring to Beam Arc Distributions of Water Ions Near the Space Shuttle Orbiter

IVER H. CAIRNS

Department of Physics and Astronomy, University of Iowa, Iowa City

The distribution function of water ions produced near the space shuttle by charge exchange between ionospheric oxygen ions and outgassed water molecules is investigated using solutions of Liouville's equation with a source term modeling the charge exchange process. A transition from ring distributions to beamlike distributions termed "beam arc" distributions is found with decreasing distance upstream from the orbiter. This beam arc distribution corresponds to a finite section of a ring distribution and not to a conventional beam distribution. The ratio of water ion number density to oxygen ion number density is calculated; typical values within 50 m of the shuttle are in excess of 2% with a maximum value of the order of 20% for nominal parameters, suggesting that these ions must be considered when interpreting particle data from near the space shuttle. An argument for a plasma density enhancement of the order of 10% very close to the shuttle, due to kinematic effects (corresponding to pileup of plasma) and not to plasma creation, is also presented. This kinematic density enhancement is insufficient, by an order of magnitude, to explain the plasma density enhancements inferred from Spacelab 2 data.

1. INTRODUCTION

One major aim of the OSS 1 and Spacelab 2 missions was to investigate the interaction of the shuttle's atmosphere with the ionospheric plasma, and so the gaseous and plasma environment of the space shuttle. These and other missions found the shuttle environment to be surprisingly active [Shawhan *et al.*, 1984] with high levels of several types of plasma waves [Gurnett *et al.*, 1988], energetic particles [Paterson and Frank, 1989], multiple ion streams [Stone *et al.*, 1983], and many ionic species [Narcisi *et al.*, 1983; Hunton and Calo, 1985; Grebowsky *et al.*, 1987]. Measurements of these phenomena were performed with instruments mounted on a pallet within the orbiter's payload bay and exposed to space, and on a small independent spacecraft, the Plasma Diagnostics Package or PDP [Shawhan, 1982; Kurth and Frank, 1990]. This PDP spacecraft probed the shuttle's environment both while attached to the shuttle and while flying free of the shuttle (the so-called "free-flight" mission) to distances of the order of 400 m.

The general scenario envisaged [e.g., Shawhan *et al.*, 1984; Gurnett *et al.*, 1988; Paterson and Frank, 1989; Eccles *et al.*, 1989] for the shuttle's interaction with the ionospheric plasma involves the outgassing of water vapor from the shuttle orbiter, the subsequent collisional charge exchange of these water molecules with ionospheric oxygen ions (O^+) to form water ions, the generation of plasma waves by these water ions, and subsequent plasma heating. Evidence exists for a cloud of neutral water surrounding the shuttle [Carignan and Miller, 1983; Narcisi *et al.*, 1983], and water ions have indeed been observed, both by the shuttle's payload instruments [Narcisi *et al.*, 1983; Hunton and Calo, 1985] and by the PDP instruments [Grebowsky *et al.*, 1987; Paterson and Frank, 1989]. During the PDP's free-flight portion of the Spacelab 2 mission, Paterson and Frank [1989] observed "ringlike" distributions of ions with the basic characteristics expected of water ions produced by the charge exchange

process. They also found that the observed number densities of the ringlike distributions were qualitatively and often quantitatively consistent with those predicted by a theoretical model for production of water ions by charge exchange from a water cloud surrounding the shuttle orbiter out to distances of at least 400 m. This theoretical analysis ignored the particle distribution function in favor of a fluid description and did not consider the effects of the large water ion gyroradius (~ 40 m). Eccles *et al.* [1989] have also assumed a (magnetized) fluid description for the plasma species in their simulations of water ion production and plasma electrodynamics in the vicinity of the shuttle; their supposition, that ion-molecule collisions might randomize the water ions sufficiently rapidly to justify a fluid description, is not addressed here.

In this paper we discuss the spatial variation in the expected distribution function of water ions produced by the charge exchange process with position relative to the space shuttle: in particular, we show that a gradual transition from a ring distribution to a beamlike distribution should occur between about 30 and 100 m upstream from the shuttle. Magnetization effects are included in the model. We show that the water ion distribution, although beamlike in a gyrospeed-gyrophase phase space, covers a significant region of velocity space corresponding to a finite section of a ring and is most correctly described as a "beam arc" distribution (i.e., a finite section of a ring distribution). We describe the spatial variation in the number density and shape of the water ion distribution function and compare these variations with those for a fluid description. This leads to comments on the observed enhancements in plasma density in the vicinity of the shuttle [Siskind *et al.*, 1984; Eccles *et al.*, 1989]. We also discuss the PDP spacecraft's orbit around the shuttle, concluding that the absence of anisotropies in gyrophase (i.e., beam arc distributions) in Paterson and Frank's [1989] observations in the upstream region are not inconsistent with the theory presented here. In addition to presenting these immediate results, our paper has two more general motivations. First, knowledge of the distribution functions and sources of free energy is a prereq-

Copyright 1990 by the American Geophysical Union.

Paper number 90JA00887.
0148-0227/90/90JA-00887\$05.00

uisite for constructing theories for the active and complex wave environment associated with the space shuttle [Hwang *et al.*, 1987; Gurnett *et al.*, 1988]. The technique described here is capable of obtaining this information, and the results presented herein are of direct relevance to the shuttle-associated waves. Second, the calculated distribution functions and relative number densities (likely to be in excess of 1% of the O^+ number density) of water ions presented here emphasize Paterson and Frank's [1989] finding that water ions produced by charge exchange should be present in detectable amounts throughout the shuttle missions. This suggests that the possible presence of ring or beam arc distributions of water ions should be strongly considered in interpreting and modeling the data from the OSS 1, Spacelab 2, and other shuttle missions.

The distribution function of water ions, the focus of this paper, is calculated by solving Liouville's equation with a source term describing the charge exchange process. The plasma model and method of solution for the distribution function are given in the next section. The transition from a ring to a beam arc distribution function is shown in section 3. Section 4 contains a discussion of the ring-to-beam arc transition of the water ion distribution function, the relative number density of water ions in the plasma, and evidence of a small plasma density enhancement. The conclusions of the paper are given in section 5.

2. MODEL FOR THE CHARGE EXCHANGE PROCESS IN THE ORBITER'S WATER CLOUD

We consider a reference frame (X_p, Y_p, Z_p) moving with the space shuttle in which the ionospheric magnetic field B_0 is along the Z_p axis. The origin of this reference frame is taken to coincide with the center of mass of the shuttle orbiter. Without loss of generality we assume the velocity of the background plasma in this reference frame is of the form $(-V_\perp, 0, -V_\parallel)$; positive values of X_p then correspond to the region upstream of the shuttle. The motion of the background plasma across the magnetic field then implies the presence of a self-consistent electric field $E = (0, -V_\perp B_0, 0)$ in this reference frame. Velocity is conserved during the charge exchange process. Now, however, the newly born water ion must respond to the crossed electric and magnetic fields, resulting in a cycloidal motion in the X_p - Y_p plane. The equations of motion for the particle motion may be solved for the position and velocity of the particle as a function of time given the position and velocity at some reference time. This motion may be summarized as follows: first, any particle speed along the magnetic field (the Z_p axis) remains constant; second, ignoring thermal motions for the moment, a newly born water ion starts out at zero velocity and is accelerated by the crossed electric and magnetic fields into motion with a gyrospeed V_\perp centered on a velocity $(-V_\perp, 0, 0)$, and a gyroradius $V_\perp / (2\pi f_{gw})$ where f_{gw} is the water ion gyrofrequency. This gyromotion maps out a ring in the V_{X_p} - V_{Y_p} plane in velocity phase space. A "ring" distribution results if water ions are found at all gyrophases in this V_{X_p} - V_{Y_p} plane, while a "beam" distribution results if the water ions are found in a well-defined range of gyrophases. Thermal motions produce a spread in gyrospeed and velocity along the magnetic field. Figure 1 is a schematic illustration of a partial ring distribution, which will be called a beam arc distribution below. Beam arc distributions of water ions are

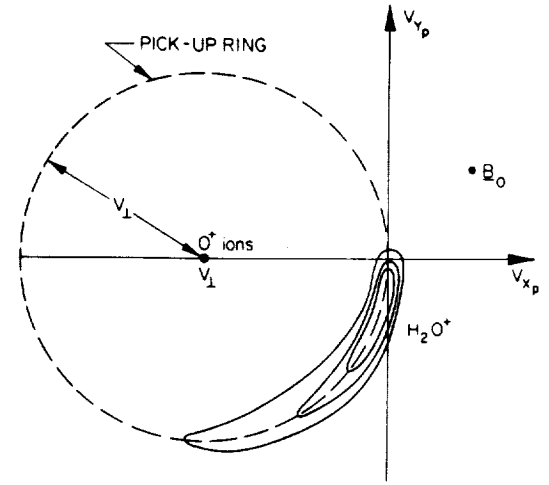


Fig. 1. A beam arc distribution displayed in V_{X_p} - V_{Y_p} space. Water ions are created near zero velocity and follow their gyromotion clockwise around the dashed ring with gyrospeed V_\perp centered on the oxygen flow speed $-V_\perp$. Zero gyrophase corresponds to zero velocity.

predicted in this paper to occur near to and upstream from the space shuttle. The (X_p, Y_p, Z_p) reference frame is the natural one for studies of water ion pickup around the shuttle.

Liouville's equation for the distribution function of charge-exchanged water ions, $f_w(\mathbf{r}, \mathbf{p}, t)$, is

$$\frac{d}{dt} f_w(\mathbf{r}, \mathbf{p}, t) = F_w(\mathbf{r}, \mathbf{p}, t) \quad (1)$$

where $F_w(\mathbf{r}, \mathbf{p}, t)$ is the source term. A formal solution exists [White *et al.*, 1983; Cairns, 1987]:

$$f_w(\mathbf{r}, \mathbf{p}, t) = \int_{-t}^0 d\tau F_w(\mathbf{r}'(\mathbf{r}, \mathbf{p}, t; \tau), \mathbf{p}'(\mathbf{r}, \mathbf{p}, t; \tau), t + \tau) \quad (2)$$

where

$$\mathbf{r}'(\mathbf{r}, \mathbf{p}, t; 0) = \mathbf{r} \quad (3)$$

$$\mathbf{p}'(\mathbf{r}, \mathbf{p}, t; 0) = \mathbf{p} \quad (4)$$

and $-\tau$ is the travel time from $(\mathbf{r}', \mathbf{p}')$ to (\mathbf{r}, \mathbf{p}) along the particle path. The effects of wave-particle scattering on the particle distribution function are ignored in this treatment.

An expression for the source term $F_w(\mathbf{r}, \mathbf{p}, t + \tau)$ for the collisional charge exchange follows from the binary nature of the collision and conservation of velocity for the particles:

$$F_w(\mathbf{r}, \mathbf{p}, t + \tau) = \gamma n_{O^+}(\mathbf{r}, t + \tau) f_m(\mathbf{r}, \mathbf{p}, t + \tau) \quad (5)$$

where n_{O^+} is the number density of oxygen ions. This equation is consistent with the usual charge exchange equation involving number densities, allowing identification of the reaction rate γ as $2 \times 10^{-9} \text{ cm}^3 \text{ s}^{-1}$ [Paterson and Frank, 1989]. The remaining quantity f_m is the distribution function of the water gas molecules, which for time-steady outflow with thermal speed V_m from the shuttle may be written

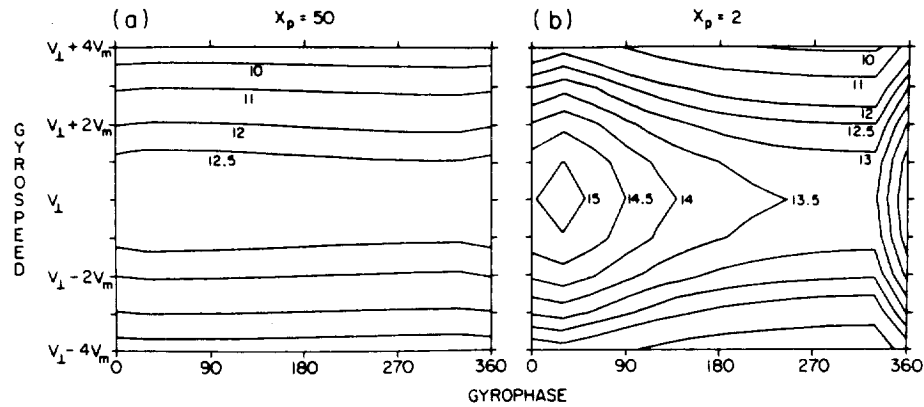


Fig. 2. Contour plots of the water ion distribution functions at two positions along the X_p axis in a gyrospeed-gyrophase phase space formed by unwrapping the ring feature in Figure 1. (a) At $X_p = 50$ the logarithmically spaced contours do not vary significantly with gyrophase, corresponding to a ring distribution. (b) At $X_p = 2$ the contours close at small gyrophase, implying a beamlike feature. Recognition of the large extent in V_{X_p} and V_{Y_p} leads to the term beam arc for the distribution function.

$$f_m(\mathbf{r}, \mathbf{p}, t + \tau) = \frac{n_0(r_0)r_0^2}{r^2} \frac{1}{(2\pi)^{3/2}V_m^3} e^{-v^2/2V_m^2} \quad (6)$$

Here $n_0(r_0)$ is the number density of water molecules at a radial distance r_0 from the shuttle; note that n_0 obeys an inverse square law in time-steady outflow. The symbol v denotes the speed corresponding to momentum \mathbf{p} . For convenience we now assume that the velocity and density of the background plasma, the magnetic field strength, and water \mathbf{g} as thermal speed are constant over the time scales of interest. Normalizing all speeds by the water thermal speed $V_m (= (kT_m/M_m)^{1/2})$ and distances by the characteristic distance V_m/f_{gw} , these assumptions and equations (5) and (6) allow (2) to be rewritten as the product of constants times a "probability" integral for the charge exchange:

$$f_w(\mathbf{r}, \mathbf{p}, t) = \frac{\gamma n_0 \cdot n_0 r_0^2}{(2\pi)^{3/2}} \int_{-t}^0 d\tau \frac{\exp[-v'^2(\mathbf{r}, \mathbf{v}, t + \tau)/2]}{r'^2(\mathbf{r}, \mathbf{p}, t + \tau)} \quad (7)$$

with r' and v' implied by (3) and (4) and the equations of motion for the water ions. The "probability" integral, essentially an integral over travel time $-\tau$ of the probability of ions producing charge exchange at earlier times $t + \tau$ with eventual momentum \mathbf{p} at the observation time t and position \mathbf{r} may be performed numerically using standard techniques. The shape of the distribution function is specified by the probability integral alone.

Before proceeding we specify the parameters used in the calculations below. Assuming a constant water gas temperature of 300 K, the normalized range of V_{\perp} for the PDP free-flight mission is from about 7 to 21 clustered primarily near 20, and we choose the value 20. During this time the shuttle's orbital speed V remained nearly constant with $V \sim 21$; smaller values of V_{\perp} therefore correspond to times when the orbiter's velocity is more nearly parallel to the ionospheric magnetic field. Smaller values of V_{\perp} tend first to increase the probability integral and so the total water ion number density for a given position and second to decrease the contrast in the distribution function over gyrophase for a given gyrospeed (i.e., decrease the parameter R defined below), making the distribution function more ringlike. The distance scale V_m/f_{gw} similarly varies from about 8 to 21 m,

with a characteristic value of the order of 15 m, which is used hereinafter. In contrast, the water ions have gyroradii $V_{\perp}/(2\pi f_{gw}) \sim 40$ m.

3. PICKUP DISTRIBUTION FUNCTIONS DIRECTLY UPSTREAM FROM THE SHUTTLE

Figure 2 shows the water ion distribution functions resulting from charge exchange at two distances directly upstream from the shuttle ($Y_p = Z_p = 0$) and demonstrates the transition from a ring distribution to a beamlike distribution with decreasing distance from the shuttle. These distributions are displayed as contour plots in a gyrospeed-gyrophase phase space formed by unfolding the ring feature in X_p - Y_p velocity space (e.g., Figure 1) centered on the velocity $(-V_{\perp}, 0, 0)$ for particles with zero speed along the magnetic field. For reference an ion formed by pickup of a water molecule with zero initial velocity in the shuttle frame has gyrospeed V_{\perp} and has a gyrophase which is initially zero but which increases with time as the ion follows its gyromotion. A ring distribution then has contours which do not vary greatly with gyrophase, as is the case at the position $X_p = 50$, far upstream from the shuttle orbiter, shown in Figure 2a. A beam distribution has contours which delineate a limited range of gyrophases; Figure 2b shows that the distribution at $X_p = 2$ (close to the shuttle) has some beamlike characteristics at small gyrophases. In these figures the contours are logarithmically spaced (to base 10) in arbitrary units.

This transition from ring to beamlike distributions is investigated further in Figure 3 using cuts from Figure 2 (and analogues) along the line of constant gyrospeed $V_g = V_{\perp}$ normalized to the maximum value of the distribution function along the cut. For instance, the curves $X_p = 50$ and 2 in Figure 3 are the cuts from Figures 2a and 2b, respectively. (Calculating the distribution function with smaller steps in gyrophase smooths the sharp turnover in the cuts near a gyrophase of 10° .) The range of gyrophases $\Delta\phi$ in which the distribution function has over one half of its maximum value decreases significantly as X_p decreases, and the ratio of this range in gyrophase to the total available (360°) also decreases significantly. It is important to note, however, that even at

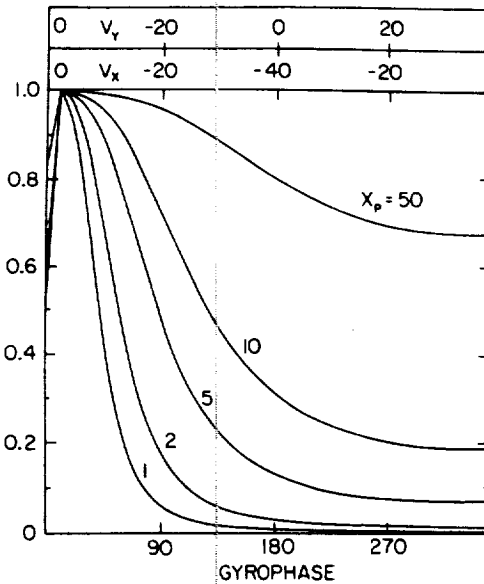


Fig. 3. Normalized cuts of distribution functions along lines of constant gyrospeed V_{\perp} and zero parallel velocity for positions along the positive X_p axis. Note the narrowing range of gyrophases and increasing contrast in the distribution functions with decreasing distance from the shuttle. The V_{X_p} and V_{Y_p} scales indicate the great extent in velocity space covered by the distribution even at $X_p = 1$.

$X_p \sim 1$, corresponding to the approximate outer surface of the shuttle and so an inner limit for the theory's applicability, this width $\Delta\phi$ is of the order of 40° while for $X_p = 5$, $\Delta\phi \sim 90^\circ$. The speeds in the X_p and Y_p directions are shown at the top of Figure 3 above the gyrophase axis and show that even at $X_p = 1$ the range of velocities in the $V_{X_p}-V_{Y_p}$ plane for which the distribution function is significant is large, as shown schematically in Figure 1. A conventional beam distribution is expected to be restricted to a narrow range of velocities centered on some velocity. It is therefore not appropriate to term these water ion distributions "beam" distributions in an absolute sense. Rather, we suggest the term "beam arc" distributions, corresponding to a finite segment of a ring, to describe these distributions found close to the shuttle. We note, however, that these beam arc distributions do have some beamlike characteristics so that instability calculations assuming conventional beams may provide a reasonable first description of an instability.

Figure 4 further describes this transition from ring to beam arc distribution functions and the continuously increasing water ion number density. The plotted parameters are R (dotted line), the ratio of the maximum to minimum of the distribution function for gyrospeed V_{\perp} and zero speed along the magnetic field, and the quantity N (solid line), proportional to the water ion number density, calculated by integrating the probability integral in (7) over velocity space. For a ring distribution, $R \sim 1$, as found at large values of X_p , while a beam arc distribution has a large value of R as found close to the shuttle. For definiteness we define the distribution function to be a beam arc if $R > 50$, corresponding to positions $X_p < 2$.

The spatial variation in N may be compared with the predictions of an (unmagnetized) fluid representation of the water ion distribution, shown by the dashed line in the figure, and found to be in good agreement at large $X_p > 10$.

These fluid model predictions are calculated by analytically integrating analogues of (1) and (5) for the water ion number density along a particle path in the X_p-Y_p plane with mean speed equal to V_{\perp} and zero gyroradius for the above gas cloud model; note that the oxygen ions move with this velocity in this plane (ignoring their minor gyromotion with a thermal gyroradius of the order of 3 m). The fluid prediction is for a water ion number density which varies inversely with distance X_p and convection speed V_{\perp} (for $Y_p = Z_p = 0$). The differences at small X_p may be ascribed to magnetization and pickup motion effects not included in the fluid model. These differences are further discussed in terms of enhanced plasma densities in the near vicinity of the shuttle in the next section.

This transition from ring to beam arc distribution function with position upstream from the shuttle may be understood in terms of the spatial gradient in water molecule number density and the characteristics of the charge exchange process. Figure 5 illustrates the development of beam arc and ring distributions at $X_p = 1$ and $X_p = 15$, respectively, in the X_p-Y_p plane for $V_{\perp} = 20$. The solid lines are contours of constant inverse distance squared $1/R_p^2$, and so constant charge exchange rate, spaced in powers of 10. The characteristics of the water ion distribution function at $X_p = 1$ and $X_p = 15$ follow on considering the primary source of particles with zero velocity (stars) and velocity $(-2V_{\perp}, 0, 0)$ (squares) at the observation points. Ignoring thermal motions (i.e., $V_m \ll V_{\perp}$), all picked-up water ions initially have zero velocity. Particles observed at zero velocity are therefore primarily produced (at the star symbols) very close to the observation point. Particles observed at velocity $(-2V_{\perp}, 0, 0)$ have, however, followed their gyromotion along the dashed lines from their primary production points (squares) where they had zero velocity. At $X_p = 1$, therefore, the production rate of water ions observed at velocity $(-2V_{\perp}, 0,$

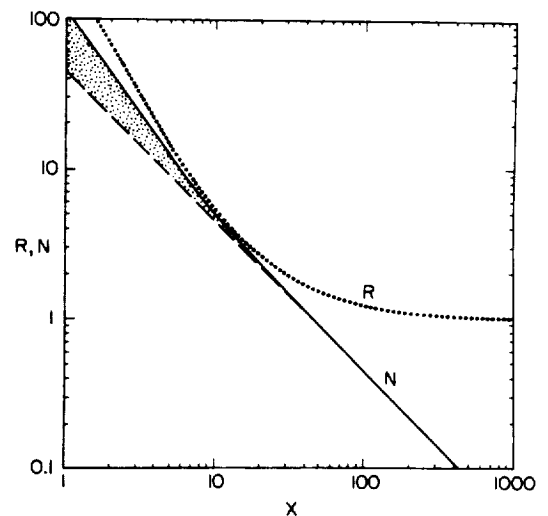


Fig. 4. Plots of the quantities N (solid line) and R (dotted line) versus position along the X_p axis. These quantities are defined in the text. The speckled area is bounded by the exact curve for N and the fluid model prediction of N given by the dashed line and is evidence of a plasma density enhancement. For parameters typical of the Spacelab missions a value $N = 10$ corresponds to a relative water to oxygen ion number density of 1.6%. The transition to a beam arc distribution from a ring distribution is implied by the monotonic increase in R as X_p decreases.

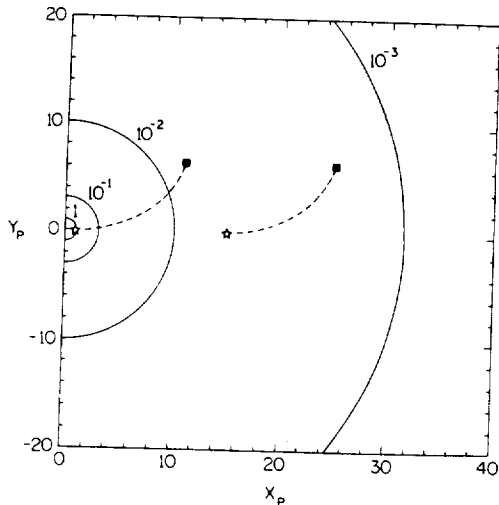


Fig. 5. Explanation of the formation of beam arc and ring distributions of water ions close to and far from the space shuttle, respectively. Solid lines show contours of constant charge exchange rate, spaced by factors of 10. The stars and squares show the positions (and so rates of charge exchange) at which ions observed near zero velocity and velocity $(-2V_{\perp}, 0, 0)$, respectively, at the observation positions are produced. Greatly differing rates of charge exchange imply a beam arc distribution at $X_p = 1$, while similar rates imply a ring distribution at $X_p = 15$.

0) is less than one-hundredth that for ions observed near zero velocity, implying that the distribution function is a well-defined beam arc with $R \sim 100$. In contrast, at $X_p = 15$ the production rates for ions with near-zero velocity and velocity $(-2V_{\perp}, 0, 0)$ differ by only a factor $(15/25)^2 \sim 0.4$, implying a ring distribution function with small $R < 10$. Further from the shuttle the ratio R continues to decrease toward 1, and the ring distributions become more uniform. The beam arc's formation near zero gyrophase follows from the charge exchange process always loading the water ions near zero gyrophase (since $V_m \ll V_{\perp}$) and the monotonically increasing rate of pickup as one approaches the shuttle along the X_p axis from upstream. The beam arc does not form exactly at zero gyrophase due to the thermal spread of the water molecules; this and the position of beam arc features when downstream of the shuttle will be discussed in detail in another publication. Notice that the value of the distribution function at a particular velocity monotonically increases as the observing point is moved closer to the shuttle along the X_p axis.

Beam arc water distributions are also formed away from the X_p axis in the upstream region in regions where the charge exchange rate is large; this implies that the condition $X_p < 2$ may be generalized to radial distances $R_p < 2$ with $X_p > 0$. The contrast in the distribution functions, i.e., the parameter R , does decrease with distance from the X_p axis, as does the probability integral and so the number density of water ions. We reiterate here that results directly analogous to those in Figures 2-5 follow for all values of V_{\perp} ; quantitatively, smaller values of V_{\perp} than 20, as appropriate for the Spacelab 2 mission, correspond to higher water ion number densities and more ringlike distributions at the same position compared with the results for $V_{\perp} = 20$. In summary, the water ions should have a beam arc distribution function when upstream and within a radial distance of the order of 20-40 m ($R_p < 2$) and have a ringlike distribution function

when more than about 100 m ($R_p > 10$) from the shuttle in the upstream hemisphere.

4. DISCUSSION

The above results clearly show that beam arc distributions of water ions, with considerable gyrophase anisotropies, should exist at positions close to and upstream from the space shuttle. In contrast, *Paterson and Frank* [1989] do not report observations of gyrophase anisotropies for the pickup ions observed during the PDP's free-flight mission. This is not inconsistent with the work described in this paper. There are two reasons for this. First, the PDP spacecraft's orbit around the space shuttle did not pass through the required upstream region (i.e., $X_p < 5$ with $Y_p, Z_p < 5$), thereby precluding direct testing of the theoretical results presented above. The beam arc distributions produced in the upstream region do, of course, move into the downstream region due to the effects of the crossed convection electric field and ionospheric magnetic field. This downstream region was extensively investigated by the PDP spacecraft. However, we shall show elsewhere that even in the downstream region the PDP's orbit was such as to limit the theoretically predicted contrast parameter R defined above to be less than 15 with a typical value of the order of 2. Second, in the upstream region close to the shuttle ($R_p < 5$, say) the dominant gyrophase anisotropy (and most of the ion number density) occurs in the range of gyrophases 0° - 90° with corresponding kinetic energies 0-5 eV. Particles with these energies are subject to confusion with the observed ambient oxygen plasma (ram energy of the order of 5 eV) due to the effects of the typically negative spacecraft potential (which moves the oxygen peak to a lower energy) and saturation of the ion detector by the oxygen plasma, as shown for example in Figure 2 of *Paterson and Frank's* paper. *Paterson and Frank*, quite properly, therefore removed these particles from their calculations of the water ion number density, thereby potentially underestimating the water ion number density. This effect is likely to be less important in the downstream region due to the ion gyromotion moving the beam arc into ranges of gyrophase, and thus of measured particle energy, not obscured by the ambient oxygen plasma for much of the PDP orbit. In summary, *Paterson and Frank's* observations are not inconsistent with the theoretical work presented in this paper. We note the present absence of published ion distribution functions measured while the PDP spacecraft was on the remote manipulator system arm, within 10 m of the orbiter, during the OSS 1 and Spacelab 2 missions. These data should permit further testing of the theory in this paper.

We now turn to the number density of pickup ions. The relative number density of water ions to ambient oxygen ions, or the number density of water ions, may be estimated using equation (7) and Figure 4. *Paterson and Frank* [1989] found their observations to be consistent with a water gas number density of approximately $4 \times 10^{10} \text{ cm}^{-3}$ at a radial distance of 10 m. With the rate constant γ and distance scale of 15 m given in section 2, a value $N = 10$ corresponds to a relative water ion to oxygen number density of 1.6%. At $X_p = 1$ the model therefore predicts that the water ion number density is approximately 20% of the (far) upstream oxygen number density for these parameters. This estimate is an upper limit for these assumed parameters due to the

decrease in oxygen ion number density not being included in (7). However, larger relative water ion number densities are predicted when the shuttle is moving more nearly parallel to the ionospheric magnetic field (V_{\perp} smaller than 20); note that the fluid water ion number density is inversely proportional to V_{\perp} . These estimates suggest that non-Maxwellian distributions of water ions with densities at least a few percent of the ambient oxygen ion number density should be prevalent in the near vicinity of, and the region downstream from, the space shuttle and should be strongly considered when interpreting data from the OSS 1 and Spacelab 2, and perhaps other, shuttle missions.

Siskind et al. [1984] have interpreted ion data from the vehicle charging and potential (VCAP) instrument on the OSS 1 flight in terms of plasma density enhancements by a factor of 10 over the ambient number density close to the space shuttle; this factor assumes the particles to have Maxwellian distribution functions. *Eccles et al.* [1989] have suggested that the plasma density enhancement is by a factor of 2–3 instead, with non-Maxwellian particle distributions being important. We show now that our Figure 4 suggests plasma density enhancements in the near vicinity of the shuttle of the order of 10% due simply to the motions of newly picked-up water ions, or equivalently to plasma "pileup." The argument proceeds as follows. First, oxygen ions move with speed V_{\perp} in the $-X_p$ direction in the X_p - Y_p plane exactly as assumed in the fluid model for the number density of charge-exchanged water ions described briefly in the last section. The assumed constancy of the oxygen ion number density for the Liouville calculation, and the small oxygen gyroradius $R_g \sim 0.2$, allow neglect of the oxygen ion gyromotion. The gyromotion of newly created water ions is also not included in the fluid model but will be vital to the argument here. Second, since charge exchange between the oxygen ions and water molecules leads to no change in the total number of charged ions in the plasma, the fluid model (the dashed line in Figure 4) gives the number density of water ions corresponding to no change in total ion number and to this assumed ion motion (for $V_{\parallel} \sim 0$). The significant excess in predicted water ion number density (solid line in Figure 4) at small values of $X_p < 10$, a factor of 2 at $X_p = 1$, then corresponds to an enhancement in plasma density close to the shuttle orbiter. This enhancement is due to the creation of the water ions near zero velocity in the X_p - Y_p - Z_p frame and not at the oxygen ion velocity $-V_{\perp}$ in the X_p - Y_p plane and the substantial time required (of the order of a gyroperiod with great corresponding motion downstream) for a water ion to attain the oxygen ion velocity on average; that is, this plasma enhancement is due purely to the different motions of the newly ionized water ions and the ambient oxygen ions, and not to creation of new plasma, and so may be understood in terms of pileup of plasma. Using the estimates above for the relative numbers of water ions and oxygen ions at $X_p = 1$ (and Figure 4) one estimates a plasma enhancement of the order of 10%. We note that these estimates are upper limits (for $V_{\perp} = 20$) due to neglect of the spatial gradient in oxygen ion number density resulting from the charge exchange. Further calculations with smaller values of the convection speed V_{\perp} show that the water ion number density approaches the result predicted by the fluid model, so that the relative enhancement in plasma density due to kinematic effects decreases. Accordingly, this purely kinematic mechanism cannot explain the magnitudes of the

plasma enhancements near the shuttle orbiter inferred by *Siskind et al.* [1984] and *Eccles et al.* [1989]. This is consistent with the findings of *Eccles et al.* [1989], who found that the effects of collisions and charge exchange are required to explain plasma enhancements by factors of the order of 2–3 in the vicinity of the space shuttle.

The results of this paper indicate that the distribution function of water ions found at small distances upstream from the shuttle is best described as a beam arc rather than a conventional beam due to the extended region of velocity space in which water ions are found. This is due to the relatively small ratios V_{\perp}/V_m of 6–20 appropriate to the shuttle-ionosphere interaction; calculations indicate that ratios $V_{\perp}/V_m > 100$ are required for the distribution function at $X_p \sim 2$ to be properly described as a conventional beam. Elastic and charge exchange collisions between the water ions and water gas molecules offer another means of establishing more beamlike water ion distribution functions: the beam arc distributions occur due to the water ions following their gyromotion; disruption of the regular ion gyromotion by collisions with low-velocity water neutrals might then limit the water ions to a more limited range of gyrophases and so to a more beamlike distribution function. Further work is required to see whether such collisions are important in determining the water ion distribution function close to the shuttle, as assumed by *Eccles et al.* [1989] in partial justification of a fluid description for the plasma in their simulations.

5. CONCLUSIONS

We have studied the distribution function of water ions produced near the space shuttle by charge exchange between ionospheric oxygen ions and water molecules outgassed from the shuttle using Liouville's equation with a source term representing the charge exchange process. Our analysis here is restricted to the region upstream from the shuttle; the downstream region, containing the shuttle's wake, will be considered elsewhere. We note that this analysis could be adapted to apply to ionization of heavy ions near comets. We find that the water ions have ring distribution functions far upstream (i.e., more than about 100 m) from the shuttle but that a transition from ring distributions to beamlike distributions termed beam arc distributions occurs with decreasing distance upstream from the shuttle. These beam arc distributions correspond to a finite section of a ring distribution (near zero velocity in the shuttle frame), with a gyrophase width in excess of 40° and a corresponding significant extent in velocity space, and do not correspond well in the shuttle case to conventional beam distributions. Well-defined beam arc distributions (with ratios $R > 50$ in the distribution function at the central gyrospeed V_{\perp} and zero parallel velocity) correspond to positions less than about 20–30 m upstream from the shuttle. We find that the PDP observations of *Paterson and Frank* [1989], which do not show significant gyrophase anisotropies, are not inconsistent with the theory reported here, due to the PDP spacecraft's orbit around the shuttle not sampling the required region where such anisotropies are significant, and due to the beam arc distributions being near zero velocity in the upstream region and so being removed from *Paterson and Frank's* analysis due to possible confusion with the ambient oxygen plasma.

The number density of water ions is found to increase monotonically with decreasing distance from the shuttle, as expected. Once within 100 m (upstream) of the shuttle the relative number density of water ions to ionospheric oxygen ions is at least of the order of 1%, with an expected value of the order of 20% near the shuttle's surface for the nominal plasma parameters assumed here. The value of the orbiter's speed perpendicular to the magnetic field chosen in the paper, $V_{\perp} = 20$ near the upper range of expected values, is expected to correspond to the most strongly peaked distributions and smallest water ion number densities relevant to the Spacelab 2 mission. This strongly suggests that the presence of these water ions should be fully considered when interpreting data from the OSS 1, Spacelab 2, and other shuttle orbiter missions. We also find that the increase in water ion number density close to the shuttle is faster than that predicted by a fluid model with no creation of new plasma. This excess in plasma density near the shuttle, by a maximum amount of the order of 10% for Spacelab 2 parameters, is due solely to kinematic effects corresponding to plasma pileup; namely, the creation of the water ions near zero velocity and not at the oxygen (or fluid) velocity, and the time and convection distance required for the water ions to attain the oxygen velocity on average in their gyromotion. This plasma enhancement is an order of magnitude less than those discussed by Siskind *et al.* [1984] and Eccles *et al.* [1989]. Eccles *et al.* [1989] find that plasma density enhancements by a factor of 3 can be explained when the effects of collisions are included in their simulations.

Further work is required to correlate the observed plasma waves with their position in the water ion pickup frame X_p - Y_p - Z_p and the characteristics of the local particle distributions. Qualitative models for the instabilities generating the waves, including the particle distribution functions, will then be constructed and tested using linear instability theory and simulations. At the present time we briefly note that ring distributions of water ions appear strangely ineffective in producing observable waves upstream from the shuttle orbiter, while beam arc distributions of water ions appear important in generating some of the broadband electrostatic waves [Hwang *et al.*, 1987; Gurnett *et al.*, 1988] observed near the space shuttle by the PDP spacecraft.

Acknowledgments. The author thanks D. A. Gurnett, J. S. Pickett, C. K. Goertz, W. R. Paterson, and L. A. Frank for helpful discussions and comments on this paper, and acknowledges financial support from NASA grant NAGW-1488.

The Editor thanks Associate Editor R. J. Walker for handling the

review process on this paper and P. L. Pritchett and N. H. Stone for their assistance in evaluating this paper.

REFERENCES

- Cairns, I. H., The electron distribution function upstream from the Earth's bow shock, *J. Geophys. Res.*, **92**, 2315, 1987.
- Carignan, G. R., and E. R. Miller, Mass spectrometer, STS-2, -3, -4 induced environment contamination monitor (IECM) summary report, *NASA Tech. Memo.*, TM-82524, 87-101, 1983.
- Eccles, J. V., W. J. Raitt, and P. M. Banks, A numerical model of the electrodynamics of plasma within the contaminant gas cloud of the space shuttle orbiter at low Earth orbit, *J. Geophys. Res.*, **94**, 9049, 1989.
- Grebowsky, J. M., H. A. Taylor, Jr., M. W. Pharro III, and N. Reese, Thermal ion perturbations observed in the vicinity of the space shuttle, *Planet. Space Sci.*, **35**, 501, 1987.
- Gurnett, D. A., W. S. Kurth, J. T. Steinberg, and S. D. Shawhan, Plasma wave turbulence around the shuttle: Results from the Spacelab-2 flight, *Geophys. Res. Lett.*, **15**, 760, 1988.
- Hunton, D. E., and J. M. Calo, Low energy ions in the shuttle environment: Evidence for strong ambient-contaminant interactions, *Planet. Space Sci.*, **33**, 945, 1985.
- Hwang, K. S., N. H. Stone, K. H. Wright, Jr., and U. Samir, The emissions of broadband electrostatic noise in the near vicinity of the shuttle orbiter, *Planet. Space Sci.*, **35**, 1373, 1987.
- Kurth, W. S., and L. A. Frank, The Spacelab-2 Plasma Diagnostics Package, *J. Spacecr. Rockets*, **27**, 70, 1990.
- Narcisi, R., E. Trzcinski, G. Federico, L. Wlodyka, and D. Delorey, The gaseous and plasma environment around space shuttle, *AIAA Pap.*, 83-2659, 1983.
- Paterson, W. R., and L. A. Frank, Hot ion plasmas from the cloud of neutral gases surrounding the space shuttle, *J. Geophys. Res.*, **94**, 3721, 1989.
- Shawhan, S. D., Description of the Plasma Diagnostics Package (PDP) for the OSS-1 shuttle mission and JSC chamber test in conjunction with the fast pulse electron gun (FPEG), in *Artificial Particle Beams in Space Plasma Studies*, edited by B. Grandel, p. 419, Plenum, New York, 1982.
- Shawhan, S. D., G. B. Murphy, and J. S. Pickett, Plasma Diagnostics Package initial assessment of the shuttle orbiter plasma environment, *J. Spacecr. Rockets*, **21**, 387, 1984.
- Siskind, D. E., W. J. Raitt, P. M. Banks, and P. R. Williamson, Interactions between the orbiting space shuttle and the ionosphere, *Planet. Space Sci.*, **32**, 881, 1984.
- Stone, N. H., U. Samir, K. H. Wright, Jr., D. L. Reasoner, and S. D. Shawhan, Multiple ion streams in the near vicinity of the space shuttle, *Geophys. Res. Lett.*, **10**, 1215, 1983.
- White, S. M., D. B. Melrose, and G. A. Dulk, Electron cyclotron masers following a solar flare, *Proc. Astron. Soc. Aust.*, **5**, 188, 1983.

I. H. Cairns, Department of Physics and Astronomy, Van Allen Hall, University of Iowa, Iowa City, IA 52242.

(Received November 16, 1989;
revised March 20, 1990;
accepted April 2, 1990.)



Control of Plasma Waves Associated With the Space Shuttle by the Angle Between the Orbiter's Velocity Vector and the Magnetic Field

IVER H. CAIRNS AND DONALD A. GURNETT

Department of Physics and Astronomy, University of Iowa, Iowa City

The interaction between water outgassed from the space shuttle and the ionospheric plasma leads to production of water ions by charge exchange and an active and complex plasma wave environment for the space shuttle. We show that the amplitude and spectral character of some of these waves are controlled by the angle between the magnetic field and the shuttle's velocity vector V_T relative to the ionospheric plasma. When the flow is approximately perpendicular to the magnetic field ($V_{\parallel}/V_T \sim 0$), large wave amplitudes and characteristic "mushroom" wave structures are observed, whereas more nearly parallel flows $|V_{\parallel}| \sim V_{\perp}$ are characterized by low wave levels. We show that linear instability theory predicts the growth of Doppler-shifted lower hybrid waves in the observed frequency range when driven by the ring and/or beam distributions of water ions produced by charge exchange in the vicinity of the space shuttle. Two mutually compatible interpretations for the V_{\parallel}/V_T effect exist. The first interpretation involves the path lengths available for growth of waves driven by pickup ions varying with the quantity V_{\parallel}/V_T and being limited by spatial variations in the water ion distribution. The second interpretation follows directly from the linear theory: decreasing the ring/beam speed V_{\perp} of the pickup ions driving the waves (increasing V_{\parallel}/V_T) results in smaller growth rates, with zero growth rate below some threshold value of V_{\perp} . The linear theory shows that decreased growth lengths or growth rates should naturally produce the observed amplitude and bandwidth changes constituting the V_{\parallel}/V_T effect. These results have immediate implications for future shuttle missions and orbiting platforms subject to outgassing of water. If these facilities are used for ionospheric plasma studies or active experiments involving plasma waves, the plasma wave background due to pickup ions associated with the orbiter should be minimized. This requires orbits with large $|V_{\parallel}| \geq V_{\perp}$; that is, orbital velocities within about 45° of the magnetic field over as much of the orbit as possible. These constraints favor more nearly polar orbits and argue strongly against equatorial orbits. Alternatively, free-flying spacecraft situated upstream from the orbiter's water cloud should be used.

1. INTRODUCTION

Plasma measurements on the OSS 1, Spacelab 2, and other space shuttle missions have found the shuttle environment to be surprisingly active with high levels of several types of plasma waves [Shawhan *et al.*, 1984; Murphy *et al.*, 1983; Hwang *et al.*, 1987; Gurnett *et al.*, 1988], energetic particles [Paterson and Frank, 1989], multiple ion streams [Stone *et al.*, 1983], and many ionic and neutral species [Narcisi *et al.*, 1983; Hunton and Calo, 1985; Grebowsky *et al.*, 1987]. Kurth and Frank [1990] provide a recent review of the shuttle's plasma environment. The qualitative picture envisaged for the shuttle's interaction with the ionospheric plasma involves the steady outgassing of water vapor from the orbiter, the subsequent collisional charge exchange of these water molecules with ionospheric oxygen ions to form water ions, and the generation of plasma waves by "pickup" instabilities resulting from the different motions of the water ions and ambient plasma. Evidence exists for a cloud of neutral water surrounding the shuttle [Carignan and Miller, 1983; Narcisi *et al.*, 1983]. Water ions have been observed in the vicinity of the orbiter with the expected characteristics of the charge exchange process [Paterson and Frank, 1989]. The number densities of the water ions are qualitatively and often quantitatively consistent with theoretical models for the charge exchange process [Paterson and Frank, 1989; Cairns, 1990]. These number densities are substantial: $n_{H_2O^+}/n_{O^+} \geq 10\%$ within 10 m of the shuttle and $n_{H_2O^+}/n_{O^+} \sim 1\%$ within 100 m of the shuttle.

Copyright 1991 by the American Geophysical Union.

Paper number 90JA02564.
0148-0227/91/90JA-02564\$05.00

This paper focuses on the observation and interpretation of plasma waves during the Spacelab 2 mission. The Spacelab 2 mission was launched on July 29, 1985, into a nearly circular, low-inclination orbit with an altitude of about 320 km and an inclination of 49.5° . One major objective of the mission was to investigate the shuttle-ionospheric plasma interaction at distances up to about 400 m from the orbiter. This study involved a small independent spacecraft, the Plasma Diagnostics Package or PDP spacecraft [Shawhan, 1982; Kurth and Frank, 1990], flying free of the shuttle during the so-called "free-flight" mission. The PDP spacecraft carried a full complement of particle and field instruments including a plasma wave receiver. This free-flight mission included two complete fly-arounds of the shuttle orbiter, as well as multiple traversals of the orbiter's plasma wake.

Previous work on the plasma waves associated with the space shuttle during the free-flight mission has been primarily directed toward explaining emissions generated by the FPEG experiment (fast pulse electron gun) [Gurnett *et al.*, 1986; Bush *et al.*, 1987; Farrell *et al.*, 1988; Neubert *et al.*, 1988; Reeves *et al.*, 1988] and describing the effects of thruster firings and magnetic conjunctions [Gurnett *et al.*, 1988]. Langmuir probe data have also been used to investigate low-frequency waves (below about 40 Hz) associated with water dumps and the shuttle's orbital maneuvering system and plasma wake [Murphy *et al.*, 1989; Pickett *et al.*, 1989; Tribble *et al.*, 1989, and references therein]. In this paper we will show that many of the variations in amplitude and spectral properties of the plasma waves from 31 Hz to 31 kHz observed well away from the shuttle during the free-flight mission, the so-called "mushroom" spectral features

to be discussed below, can be understood in terms of the variation of the angle between the orbiter's velocity vector relative to the plasma and the magnetic field vector, the so-called V_{\parallel}/V_T effect. A linear theory is developed in which the waves are Doppler-shifted lower hybrid waves driven by pickup instabilities involving ring or beamlike distributions of water ions. Similar situations arise at comets [e.g., Coroniti *et al.*, 1986, and references therein] and with chemical release experiments [e.g., Hudson and Roth, 1988, and references therein]. The observed V_{\parallel}/V_T effect is interpreted in terms of variations in both the path length available for wave growth and the growth rate of the pickup instability in response to orbital variations in V_{\parallel}/V_T . These results constitute a significant advance in the understanding of the plasma waves associated with the space shuttle. They also provide a criterion for design of future space shuttle missions, and the planned space station, in which minimizing the orbiter-associated plasma wave (and ion) background is important for passive and/or active space plasma investigations. To present these new results, this paper is organized as follows: the motions of charge-exchanged water ions and the background plasma particles are discussed in section 2, and the observational data are presented in section 3. Section 4 contains both an interpretation and a discussion of the observational results. A linear theory for generation of the plasma waves is developed in section 5. The implications of these works for design of future shuttle missions and the space station are discussed in section 6. The conclusions of the paper are given in section 7.

2. A REVIEW OF THE PICKUP PROCESS

The coordinate system used in this paper, the so-called "pickup" system [Cairns, 1990] developed for studies of charge-exchanged water ions in the vicinity of the shuttle, moves with the space shuttle and is centered on the orbiter's center of mass. This reference frame (X_P, Y_P, Z_P) has the ionospheric magnetic field \mathbf{B} along the Z_P axis. Without loss of generality the velocity of the background plasma may be written in the form $(-V_{\perp}, 0, -V_{\parallel})$. Positive values of X_P then correspond to the region upstream from the shuttle. Motion of the background plasma across the magnetic field implies the existence of a self-consistent convection electric field $\mathbf{E} = V_{\perp} \mathbf{B}$ along the Y_P axis. A water ion born at zero velocity (the shuttle velocity) then moves in a cycloidal orbit in the X_P - Y_P plane with gyrospeed V_{\perp} and gyrocenter velocity $(-V_{\perp}, 0, 0)$. Thermal motions lead to a distribution of gyrospeeds and gyrophases about this convection drift velocity $(-V_{\perp}, 0, 0)$ perpendicular to the magnetic field, as well as to a thermal distribution of gyrocenter drifts along the magnetic field (with zero average drift). In contrast, the ionospheric plasma particles have the same gyrocenter speed V_{\perp} as the water ions in the X_P - Y_P plane, but have a gyrocenter drift speed V_{\parallel} along the magnetic field. Plasma waves in regions where the water ions do not dominate the plasma convect with the ionospheric plasma. During the shuttle's orbital motion around the Earth, the angle between the velocity vector (relative to the ionospheric plasma) and the magnetic field varies from about 30° to 150° , where 90° corresponds to a velocity vector perpendicular to the magnetic field. Corotation of the ionospheric plasma is included when calculating the velocity of the ionospheric plasma relative to the shuttle orbiter; the plasma's corotation speed

is of order 0.5 km s^{-1} , small compared to the orbital speed of order 7.8 km s^{-1} .

The space shuttle acts as an obstacle to the ionospheric plasma flow, resulting in the formation of a plasma wake behind the shuttle [Murphy *et al.*, 1989; Tribble *et al.*, 1989]. Since the wave data presented in this paper are primarily from the region downstream of the shuttle, we need to carefully consider the possibility that the observed plasma waves are associated with the wake rather than with pickup ions. The wake is expected to be centered directly behind the shuttle along the line of the shuttle's velocity vector (with respect to the ionospheric plasma). In the pickup coordinate system defined above, the expected center of the wake is at $Y_P = 0$ and $Z_P = X_P V_{\parallel}/V_{\perp}$. Positions relative to the expected wake center, and times of wake transits, can therefore be calculated and used to investigate the characteristics of any purely wake-associated plasma waves. For convenience here two new coordinates X' and Z' are defined by rotating the X_P - Z_P axes so that the X' axis is parallel to the plasma flow velocity and aligned along the center of the wake. That is, the expected center of the wake has coordinates $Z' = Y_P = 0$. Negative values of X' imply that the PDP spacecraft is a distance $|X'|$ downstream from the orbiter along the wake direction. Noting that the electron thermal speed ($\sim 200 \text{ km s}^{-1}$) greatly exceeds the shuttle's orbital speed ($\sim 8 \text{ km s}^{-1}$) and the ion thermal speed ($\sim 1 \text{ km s}^{-1}$), one expects that the magnetic field will influence the structure of the wake and make the Z' coordinate of the PDP a more sensitive indicator of position relative to wake structures than the Y_P coordinate. Wake transits are therefore defined below as transits $Z' = 0$ at small $Y_P \leq 10 \text{ m}$. Plasma waves associated with the orbiter's plasma wake will be discussed elsewhere.

3. OBSERVATIONAL RESULTS

The data presented here are from the Helios subsystem of the plasma wave instrument on the PDP spacecraft [Shawhan, 1982; Gurnett *et al.*, 1988] and were obtained during the free-flight portion of the Spacelab 2 mission. The Helios instrument provides electric field measurements from 31.1 Hz to 178 kHz using 16 logarithmically spaced channels, four per frequency decade. A double-sphere antenna with a sphere separation of 3.89 m is used for detecting the electric fields during free flight. Each channel provides a data point every 1.6 s; only the peak signal during each measurement interval is used.

Plate 1 shows Helios data in a spectrogram format with wave amplitude color coded. The white curve at about 8 kHz shows the lower hybrid frequency computed using the square root of the electron to oxygen ion mass ratio times the electron gyrofrequency. There are three effects which complicate the interpretation of the data. First is the modulation at the spacecraft spin period of 13.6 s, most visible as a periodic blue spike in the spectrogram near 20 kHz, at all frequencies up to about 20 kHz. This modulation corresponds not to natural waves (the modulation period would be half the spacecraft spin period in this case), but to some presently unidentified source of spacecraft-associated interference. This effect leads to spurious signals during times of relatively low wave levels. The second interference effect is the impulsive production of intense waves by the orbiter's thrusters. These thruster signals are the yellow (typically)

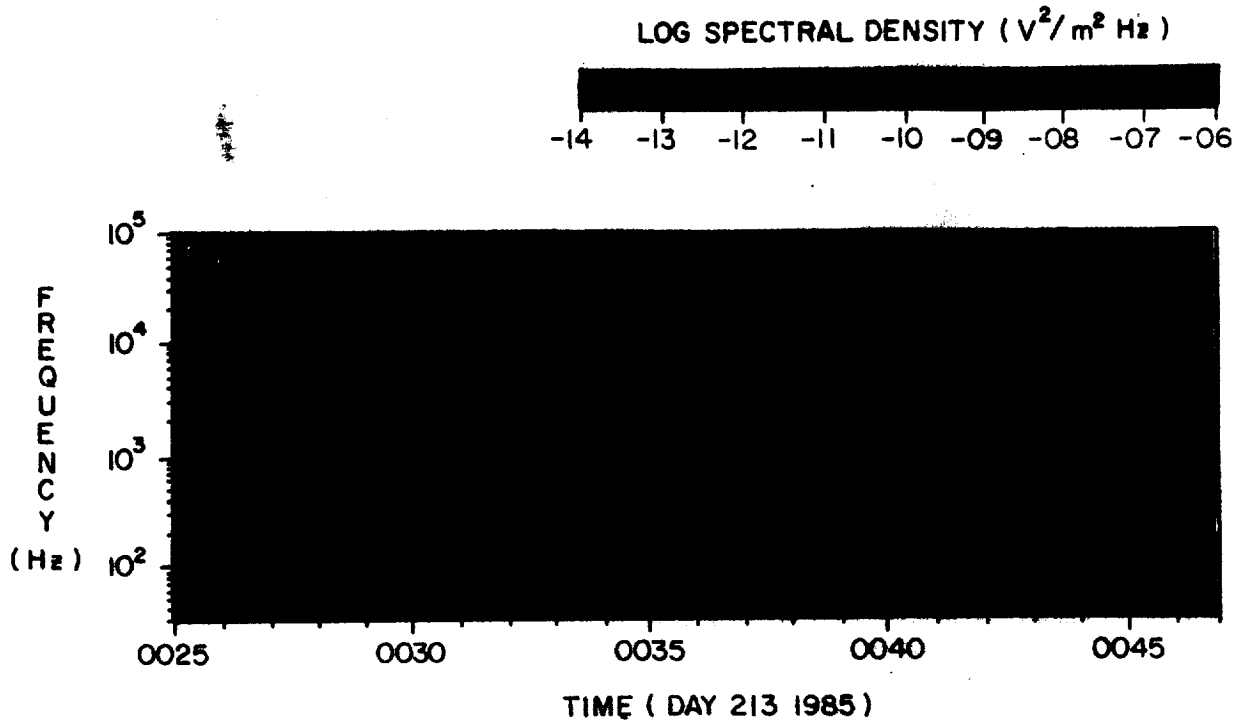


Plate 1. A frequency-time spectrogram with color-coded amplitude for the period 0025-0047 UT, day 213, 1985, during the PDP's free-flight mission. The white curve shows the lower hybrid frequency. A "mushroom" spectral feature is seen between about 0031 and 0042. Wake transits occur near 0028, 0032, and 0041 with no accompanying changes in the wave spectrum.

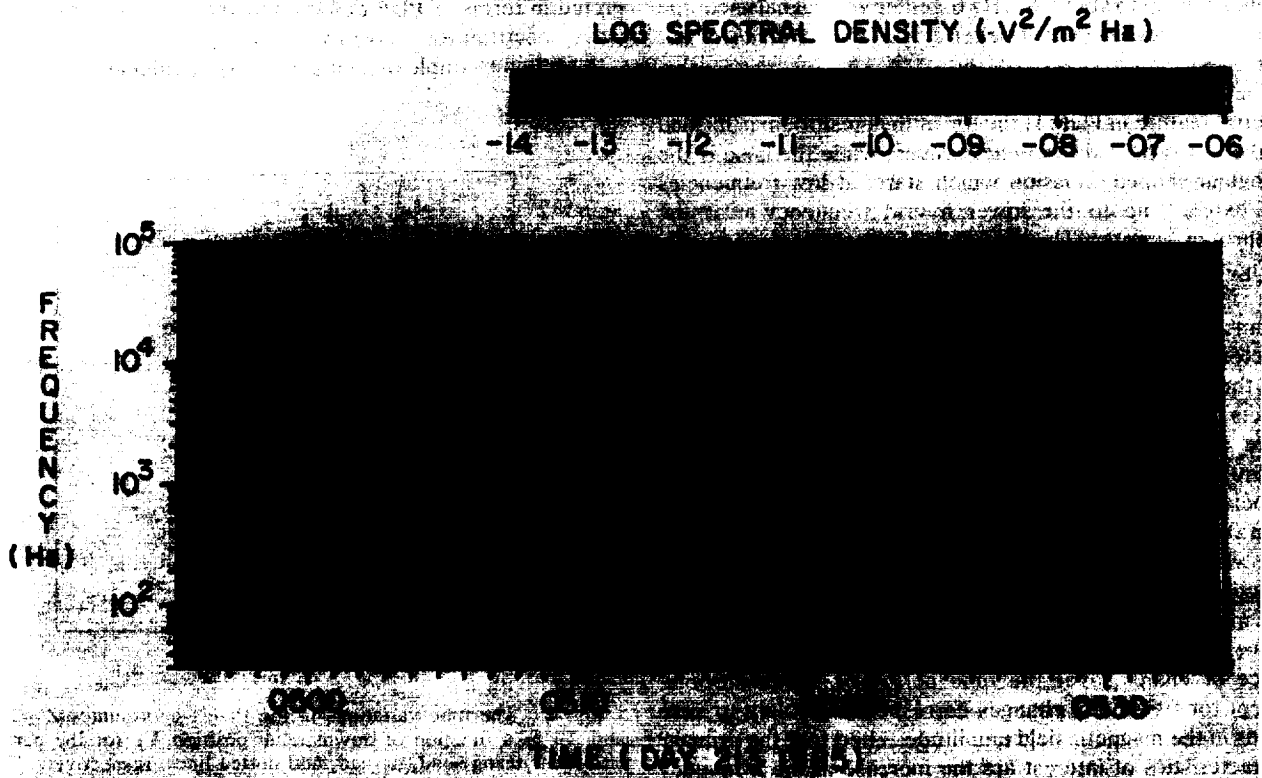


Plate 2. Another example of a "mushroom" spectral feature (in Plate 1's format) consistent with control of the waves by the parameter $|V_{\perp}/V_{\parallel}|$. Differences between this figure and Plate 1 indicate that position is not unimportant in determining the wave amplitude and detailed characteristics of the mushroom feature.

ORIGINAL PAGE IS
OF POOR QUALITY

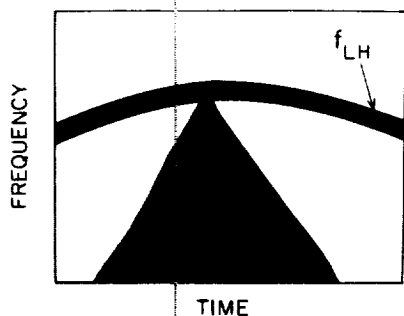


Fig. 1. An idealized "mushroom" spectral feature.

spikes which are most intense at low frequencies but extend up to about the lower hybrid frequency. Illustrative examples of these thruster signals, visible throughout this time period, occur at 0025:42, 0026:28, and 0037:40 (time format hour-minute:second; all times are universal time). Not all thruster firings result in intense, impulsive signals: the diffuse, relatively weak, broadband (up to f_{LH}) enhancement shown in Plate 1 from 0025:00 to about 0025:30 (but which starts at 0024:48) does correspond in time with almost continuous thruster firings from 0024:48 to 0025:05 and is almost certainly a thruster signal. Some thruster firings also produce no observable wave signals at the PDP spacecraft. All wave signals were therefore carefully checked against the record of thruster firings to eliminate thruster-associated waves from further consideration. No water dumps [e.g., Pickett *et al.*, 1989] occurred during the PDP free-flight mission. The third interference effect is that of the FPEG experiment, visible as the intense red signals from about 0046:10 to 0047:00 in Plate 1, with intense signals at all frequencies up to about 20 kHz together with signals near the electron gyrofrequency [Gurnett *et al.*, 1986; Farrell *et al.*, 1988].

The feature of interest in this paper is the "mushroom" spectral feature in Plate 1: the top of the mushroom is formed by the lower hybrid frequency waves, while the base is the triangular-shaped emission which starts at low frequencies and extends up to the lower hybrid frequency near the mushroom's center. This feature is illustrated schematically in Figure 1. This mushroom-shaped feature also corresponds to a significant and smooth (punctuated by thruster firings) enhancement in the intensity of the low-frequency waves by a factor of order 10. The time record of thruster firings shows that the smoothly varying mushroom feature is not due to the effects of thruster firings. For instance, the smooth enhanced wave levels (light yellow color) for the period 0038:00–0039:07 near the center of the mushroom feature are not associated with thruster firings: no thruster firings occurred from 0037:58 until 0039:07. Correspondingly, all the impulsive yellow and red signals in the data either correspond directly to the times of thruster firings or are associated with the modulated spacecraft interference pattern discussed above. The lower hybrid frequency waves show little evidence of change over the time period of the mushroom, except for frequency changes corresponding solely to variations in the magnetic field amplitude. Therefore the primary characteristics of interest are the increase in the frequency bandwidth of the triangular-shaped features (up to the lower hybrid frequency) and the smooth increase in amplitude of the low-frequency waves near the mushroom's apex. During

the time period of Plate 1, the first "station-keeping" period, the PDP spacecraft is located in the wake region downstream from the shuttle and remains almost stationary relative to the shuttle's plasma wake (coordinates X' , Y_p , and Z'), as shown in Figure 2. Wake transits occur near 0028:40, 0031:45, and 0041:15 with no accompanying changes in the plasma waves. This time period does, however, coincide with a transition from positive to negative values for $V_{||}$. The quantity $V_{||}/V_T$ passes through zero near 0037:00, coinciding with the maximum intensities of the low-frequency waves and the apex of the mushroom spectral feature. This feature in the plasma waves therefore apparently corresponds to variations in the quantity $V_{||}/V_T$ and not to plasma waves associated purely with the orbiter's plasma wake.

Figure 3 shows the variation in the quantity $V_{||}/V_T$ during the free-flight mission, giving the times of further predicted mushroom spectral features, the PDP's position relative to the orbiter at these times, and times of wake transits. Stylized mushroom features on the figure indicate where mushroom spectral features were indeed observed. In each case when the PDP was in the downstream region, mushroom spectral features were indeed observed to be centered near times when $V_{||}/V_T = 0$, although the event near 0128 is somewhat problematical. While many of these mushroom features occur within a few minutes of transits of the center of the orbiter's wake, the events near 0037 and 0515 and the many wake transits not accompanied by mushroom features show that mushroom features are not associated with the orbiter's plasma wake. These mushroom spectral features are usually not as well defined as in the station-keeping period of Plate 1; most mushroom features occur while the PDP is moving significantly relative to the orbiter. Below, deviations from the idealized mushroom shape are interpreted in terms of PDP motion and spatial variations of the wave spectrum for a given value of $V_{||}/V_T$.

A second example of a mushroom spectral feature is given

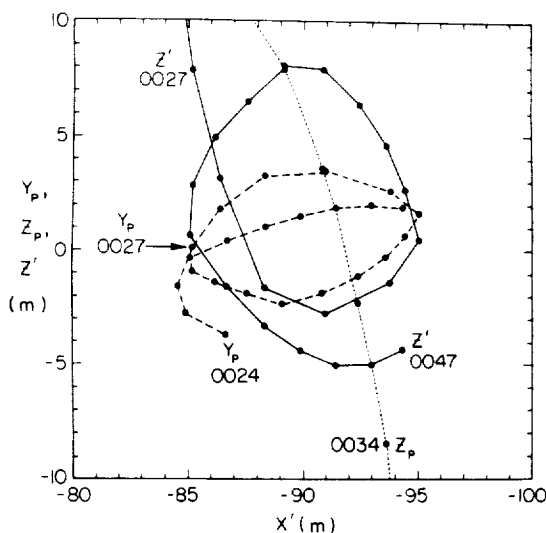


Fig. 2. The time variations in the PDP's coordinates Z' , Y_p , and Z_p as a function of downstream position X_p for the period 0025–0047 using solid, dashed, and dotted lines, respectively. The solid circles are separated in time by 1 min. Noting the PDP's antenna length is approximately 4m, the PDP remains almost stationary relative to the orbiter's plasma wake (coordinates X' , Y_p , and Z'). Wake transits occur near 0028, 0032, and 0041.

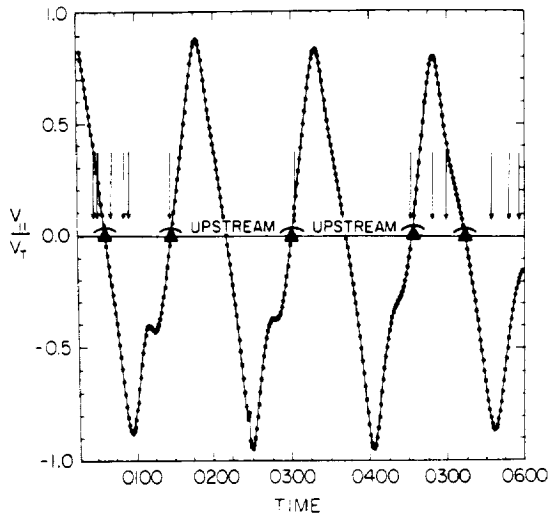


Fig. 3. The variation of V_{\parallel}/V_T during the PDP's free-flight mission. Stylized mushrooms indicate where "mushroom" spectral features are observed, and arrows indicate transits of the center of the orbiter's wake. Times when $V_{\parallel}/V_T = 0$ and the PDP is not downstream from the orbiter are specified. Mushroom features are observed whenever $V_{\parallel}/V_T = 0$ and the PDP is downstream from the shuttle.

in Plate 2. The time scale extends from 0448 to 0536, with a mushroom spectral feature visible from about 0456 to 0530. Figure 4 shows the motion of the PDP spacecraft relative to the orbiter's plasma wake and the orbiter itself during this period. The PDP moves distances of order 50 m in all four coordinates shown, thereby implying significant motions relative to both the plasma wake and the orbiter during this time period. Wake transits take place at 0459 and 0534. These transits have no effects on the mushroom spectral feature. The quantity V_{\parallel}/V_T passes through zero near 0514 and has a value greater than 0.5 from 0508 to 0520. These data are consistent with a mushroom spectral feature (1) occurring in conjunction with the variations in V_{\parallel}/V_T and (2)

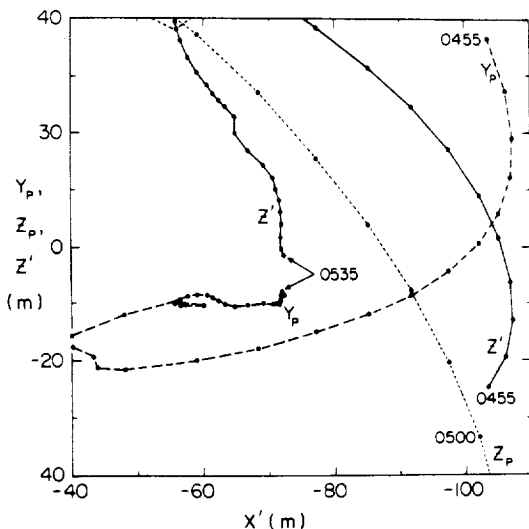


Fig. 4. The PDP's position relative to the orbiter for the period 0455–0535 in Figure 2's format. The PDP moves significantly relative to the orbiter's plasma wake. Wake transits occur near 0459 and 0534.

not being associated with specific structures in the orbiter's plasma wake. The differences between the events in Plate 1 and Plate 2 are interpreted in terms of the PDP's motion and of spatial variations in the wave characteristics in the orbiter's downstream region at constant V_{\parallel}/V_T .

4. INTERPRETATION AND DISCUSSION OF THE OBSERVATIONS

We have shown that the so-called "mushroom" spectral features of plasma waves found downstream of the space shuttle orbiter during the Spacelab 2 mission are strongly correlated with the parameter V_{\parallel}/V_T : in particular the maximum amplitude, frequency bandwidth, and apex of a mushroom occur near where V_{\parallel} goes through zero and the orbiter's velocity vector is perpendicular to the ionospheric magnetic field. We now argue that this correlation between mushroom spectral features and V_{\parallel}/V_T has a natural interpretation in terms of the optimum conditions for wave growth driven by pickup water ions and the time available for evolution of the wave spectrum. Consider the growth of localized wave packets with sizes small compared with the water cloud (and water ion trail) and group velocities that lie in the X_p - Y_p plane and are small compared with the plasma flow velocity. (The argument below indicates that group velocities significantly out of the X_p - Y_p plane are inconsistent with the occurrence of the mushroom apexes near $V_{\parallel} = 0$.) These wave packets then move essentially with the background plasma through the water ion trail. When the orbiter moves perpendicular to the magnetic field, water ions produced by charge exchange of outgassed water molecules move in the same plane (the X_p - Y_p plane) and have the same gyrocenter velocity as the ionospheric plasma and the convected wave packets of plasma waves. Maximum path lengths for the growing waves, the maximum time for evolution of the wave spectrum, and a symmetry axis for the mushroom feature at $V_{\parallel} = 0$ can be envisaged in this case. In contrast, when the orbiter velocity has a significant component along the magnetic field, the pickup ions and the ionospheric plasma (and wave packets) move in different planes with significantly different gyrocenter velocities. The finite sizes of the orbiter's water cloud and water ion trail then imply a significant limitation of the growth length available for the waves. For instance, in a time equal to one ion cyclotron period a convected wave packet and a pickup water ion suffer a separation of order $250 \sin \alpha$ meters along the magnetic field, where α is the angle between the magnetic field and the plasma flow velocity, and a periodic separation of order $40 \sin \alpha$ meters in the X_p - Y_p plane due to the water ion gyromotion. In contrast, the characteristic scale of the water molecule cloud is of order 10–100 m in the high-density region of the cloud which might be expected to be the source region for the water ions driving the waves (i.e., pickup ion number densities in excess of 1%) [Paterson and Frank, 1989; Cairns, 1990], and the linear theory developed below predicts wavelengths of order 1–2 m. These strong spatial inhomogeneities in the water ion distribution function and number density imply considerable spatial variations in the dispersion relations of locally generated waves (as found, but not shown here, for the linear theory developed below) and so sensitivity to the effects of convection. There is therefore considerable scope for limitation of wave growth due to the different motions of the background plasma, plasma waves, and pickup ions. Here our intent is only to show the

plausibility of this mechanism for the observed V_{\parallel}/V_T effect under a wide variety of unrestrictive conditions. Indeed, only slight modifications are necessary before this mechanism fits into the framework of the linear theory developed for the waves in the next section. In addition the linear theory for the waves also implies a separate, but compatible, mechanism for the V_{\parallel}/V_T effect due to the nature of the pickup instability itself. We emphasize that the existence of the observed V_{\parallel}/V_T effect is strong evidence that the waves are driven by water pickup ions.

Recent work on the plasma waves observed within 10 m of the space shuttle (called "near zone" waves here) during the XPOP roll (I. H. Cairns and D. A. Gurnett, Plasma waves in the near vicinity of the space shuttle, submitted to *Journal of Geophysical Research*, 1990; hereinafter Cairns and Gurnett, submitted manuscript, 1990; see also Tribble *et al.* [1989]) shows that the amplitude and spectral characteristics of the near zone plasma waves vary significantly with orbital variations in V_{\parallel}/V_T . Again, times with large $|V_{\parallel}/V_T| \geq 0.5$ show very low wave amplitudes. This provides further support for the observational results reported here.

The source region of the plasma waves forming the mushroom spectral features may be addressed as follows. In the first of two simple models the waves are generated throughout the region containing water ions produced from the orbiter's water cloud (this region might be referred to as the shuttle's water ion trail). In the second model the waves are generated within the near zone region of the orbiter and convected downstream. These models are not mutually incompatible, and both are plausibly consistent with the observed V_{\parallel}/V_T effect. The first model permits the possibility that waves similar to the mushroom features might be observable when $|V_{\parallel}/V_T|$ is large during the PDP's two upstream excursions. Unfortunately, the PDP's path was not propitious for testing this possibility: both such time periods with $|V_{\parallel}/V_T| \geq 0.2$, 0206-0214 and 0338-0347, occurred at large Y_P or Z_P where small water ion number densities (and wave growth rates) are expected. (The absence of upstream waves during these times is not inconsistent with the linear theory developed in the next section.) The second model predicts that the waves should be observed only when downstream from or in the near vicinity of the space shuttle. Observational data [Gurnett *et al.*, 1988; Tribble *et al.*, 1989; Cairns and Gurnett, submitted manuscript, 1990] show that the intense near zone waves are strongly localized to the near vicinity of the space shuttle and are not convected downstream in recognizable form. Furthermore, the observed mushroom features show no well-defined variation in amplitude with downstream distance. These arguments suggest that the first source model for the waves is more consistent with the available data. However, further analysis of these wave data, as well as theoretical work on the models, is necessary before drawing firm conclusions on the source of the observed mushroom features. We note, moreover, that both models imply the possibility of significant spatial variations in the characteristics of both locally generated and convected waves, as appears necessary to understand the characteristics of the observed waves.

5. LINEAR INSTABILITY THEORY RELEVANT TO THE ORBITER-ASSOCIATED WAVES

Theoretical calculations of the water ion distribution function in the vicinity of the space shuttle [Cairns, 1990] argue

that the water ions have a ring distribution far from the orbiter, as observed by Paterson and Frank [1989]. However, with decreasing distance to the shuttle the water ion distribution function becomes increasingly well represented as a beam near zero velocity (superposed onto a ring with much lower number density). Both source models for the generation of the waves given in the last paragraph may therefore be discussed in terms of linear instabilities involving ring or beam distributions of water ions. In particular, the source model with wave growth throughout the water ion trail involves wave generation by primarily ringlike distributions of water ions [Cairns, 1990], while the second source model involves wave generation by primarily beamlike distributions of water ions. We now show that linear instability theory predicts that both ring and beam distributions of water ions should drive Doppler-shifted lower hybrid waves in the observed range of frequencies. A detailed development of the linear theory will be performed elsewhere; here we restrict our discussion to waves with wave vectors exactly perpendicular to the magnetic field, but note that calculations for wave vectors with components parallel to the field give similar results.

The electrostatic dispersion equation for plasma waves propagating exactly perpendicular to the magnetic field and observed in the shuttle frame may be written

$$1 - \frac{\omega_{pe}^2}{k_{\perp}^2 V_e^2} e^{-r_e^2} \sum_{m=-\infty}^{m=\infty} \frac{m\Omega_e}{\omega - k_x V_{\perp} - m\Omega_e} I_m(r_e^2) - \frac{\omega_{pO}^2}{k_{\perp}^2 V_O^2} e^{-r_O^2} \sum_{m=-\infty}^{m=\infty} \frac{m\Omega_O}{\omega - k_x V_{\perp} - m\Omega_O} I_m(r_O^2) - \frac{\omega_{pw}^2}{k_{\perp}^2 V_w} \sum_{m=-\infty}^{m=\infty} \frac{2mJ_m(R_w)J'_m(R_w)}{(\omega - k_x V_{\perp} - m\Omega_w)} = 0 \quad (1)$$

In this equation the ionospheric electrons and oxygen ions are represented by magnetized Maxwellian distributions drifting with velocity $(-V_{\perp}, 0, 0)$ and have the standard forms for their contributions to the dispersion equation, while the water ions produced by charge exchange are represented by a magnetized delta function ring in perpendicular velocity (the functional form over parallel velocity is unimportant) [Tataronis and Crawford, 1970; Hudson and Roth, 1988, and references therein]. We restrict our attention to the case when the shuttle moves exactly perpendicular to the magnetic field. The functions J_m and I_m are the m th-order Bessel functions of the first and second kind, respectively. The arguments are $r_{\alpha} = k_{\perp} V_{\alpha}/\Omega_{\alpha}$ for the electrons and water ions, and $R_w = k_{\perp} V_{\perp}/\Omega_w$ for the water ions. Subscripts e , O , and w refer to the electrons, oxygen ions, and water ions, respectively. Standard definitions apply to the angular plasma frequencies $\omega_{p\alpha}$, gyrofrequencies Ω_{α} , and thermal speeds V_{α} for species α . Below, the water ions are also represented by an unmagnetized Maxwellian beam at zero velocity; in this case the sum over Bessel functions is replaced by the standard form involving the Fried-Conte function $Z(z_w)$ with $z_w = \omega/(2^{1/2}kV_w)$ and $k = k_{\perp}$ (by assumption). The dispersion equation is then

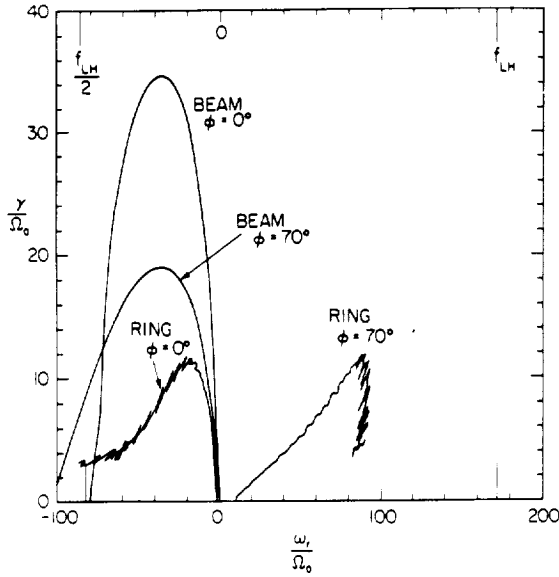


Fig. 5. Growth rates versus wave frequency for numerical solutions of equation (1) for both ring and beam distributions of water ions as marked. Curves are shown for two wave vector directions $\phi = 0^\circ$ and $\phi = 70^\circ$. Negative real frequencies result from Doppler-shifting, but only the magnitude of the wave frequency is directly observable. The plasma parameters are given in the text. The linear theory clearly predicts growth over the frequency bandwidth of the low-frequency component of the mushroom features.

$$\begin{aligned}
 1 - \frac{\omega_{pe}^2}{k_\perp^2 V_e^2} e^{-r_e^2} \sum_{m=-\infty}^{\infty} \frac{m\Omega_e}{\omega - k_x V_\perp - m\Omega_e} I_m(r_e^2) \\
 - \frac{\omega_{pO}^2}{k_\perp^2 V_O^2} e^{-r_O^2} \sum_{m=-\infty}^{\infty} \frac{m\Omega_O}{\omega - k_x V_\perp - m\Omega_O} I_m(r_O^2) \\
 + \frac{\omega_{pw}^2}{k_\perp^2 V_w^2} [1 + z_w Z(z_w)] = 0 \quad (2)
 \end{aligned}$$

All quantities are defined in the "pickup" coordinate system described in section 2; in particular, the magnetic field defines the Z_P axis, and the X_P axis points upstream from the shuttle. Most important, however, is that the angular frequency ω is the frequency observable in the shuttle (or PDP) frame of reference. The quantity $\omega - k_x V_\perp$ is the Doppler-shifted wave frequency seen by the ionospheric electrons and water ions. A wave vector with a positive component k_x is directed upstream along the X_P axis. When solving this equation we normalize all quantities relative to those for the oxygen ions. Nominal ratios for the Spacelab 2 mission are $T_e/T_O = 2$, $T_w/T_O = 0.3$ (typically $T_O \sim 1000$ K), $V_\perp/V_O = 11$, and $\omega_{pO}/\Omega_O \sim 1000$ with an oxygen gyrofrequency of order 30 Hz. All frequencies calculated below are given in units of the oxygen gyrofrequency. In these units the nominal lower hybrid frequency f_{LH} , given by the square root of the electron to oxygen mass ratio times the electron gyrofrequency, is 172 units.

Figure 5 shows numerical solutions of the dispersion equation (1) for the growth rate as a function of the wave frequency ω , for ring distributions of water ions, together with the analogous solutions when the water ions are repre-

sented as a beam centered at zero velocity. The relative water to electron number density is fixed at 5%. Curves are shown for two wave vectors in the X_P - Y_P plane: the $\phi = 0^\circ$ curve corresponds to a wave vector directed upstream along the X_P axis. Linear theory clearly predicts that these particle distributions should drive waves from zero frequency to about the lower hybrid frequency with sizable growth rates. For all these solutions the waves with the maximum growth rates have positive frequencies near the lower hybrid frequency in the ionospheric plasma frame. The waves are therefore interpretable as Doppler-shifted lower hybrid-like waves. Strictly speaking, as described below, these waves do not lie on the lower hybrid mode; nevertheless, we follow standard practice [i.e., Papadopoulos, 1984] and refer to the waves as Doppler-shifted lower hybrid waves in the remainder of the paper. Negative values of ω_r in the shuttle frame result from Doppler-shifting of waves with frequency $\omega_{rest} \leq kV_\perp$ in the ionospheric plasma's rest frame. Note that only the absolute value of the wave frequency is observable.

More detailed comments on the waves driven by the ring distribution are as follows. In the ionospheric plasma frame the growing plasma waves form a series of flute modes with $\omega_{rest} \sim kV_\perp$ and maximum growth rates for wave frequencies near the lower hybrid frequency. These waves are similar to those of Lee and Birdsall [1979] in their "intermediate" and "strong ring" regimes. Only the dominant member of this series of modes is shown in Figure 5, i.e., mode "a" in Lee and Birdsall's Figure 5; this mode has the largest growth rate for a given wave frequency in the shuttle frame. For smaller ring densities this dominant mode breaks up into a forest of flute modes unstable over a limited range of wave frequencies, as hinted at by the series of jagged lines making up the ring-driven curves in Figure 5. Since the particle distribution functions are symmetric about zero velocity in the ionospheric plasma frame (corresponding to velocity $(-V_\perp, 0, 0)$ in the shuttle frame), the growth rates and frequencies of these flute modes in the ionospheric plasma frame do not depend on the angle ϕ ; however, the Doppler shift, and so the wave frequency observed in the shuttle frame, does depend on ϕ . This Doppler shift moves the frequency of the maximum growth rate mode from near zero frequency for $\phi = 0^\circ$ to near twice the lower hybrid frequency for $\phi = 180^\circ$. Accordingly, linear theory implies that waves in the frequency range from zero frequency to several times the lower hybrid frequency could be generated by a ring distribution of water ions. The wavelengths of the growing modes should be of order 1-2 m, compared with the antenna length of 3.98 m.

A detailed discussion of the expected frequency spectrum of the waves requires careful consideration of both the angular dependence of the Doppler shift and the convective growth rate of the waves. In particular, even for a spectrum of waves with identical electric fields and wave numbers distributed uniformly over propagation angle ϕ , the cosine dependence of the Doppler shift on the angle ϕ concentrates the observed wave energy at $\phi = 0^\circ$ and 180° [e.g., Boardson et al., 1990]. This effect would then lead to enhanced wave levels near zero frequency (i.e., $\phi \sim 0^\circ$) and twice the lower hybrid frequency ($\phi \sim 180^\circ$). The convective growth rates of these two peaks in the Doppler-shifted wave spectrum are quite different: in the shuttle frame the propagation speed (corresponding to the vector sum of the plasma convection velocity and the group velocity) of the upshifted plasma

waves near $2f_{\text{LH}}$ is $\sim 2V_{\perp} \sim 16 \text{ km s}^{-1}$ in the downstream direction, greatly exceeding that for the downshifted waves ($\sim 0.1V_{\perp} \sim 800 \text{ m s}^{-1}$). Therefore, since the convective growth rate in the shuttle frame is given approximately by the temporal growth rate divided by the wave propagation speed, it is clear that the downshifted waves will grow much more effectively than the upshifted waves (a factor of 16 in convective growth rate). For the plasma described in Figure 5, the propagation/convection distance required for the waves to reach saturation (10 e -folding distances) is 4 m in the plasma frame, corresponding to 40 m in the shuttle frame. Detailed discussions of the distances available for effective wave growth must await development of a spatially inhomogeneous wave theory and comparison with theories for spatial variations in the water ion distribution function [cf. Cairns, 1990]. Qualitatively, however, the water ion distribution function is expected to show substantial spatial variations on the scale of the water ion gyroradius $V_{\perp}/\Omega_w \sim 40 \text{ m}$ (for $V_{\perp} \gg V_{\parallel}$) in the shuttle frame. Distances of order 10–40 m (in the shuttle frame) are then sufficient for the above theory to predict the generation of significant levels, but not necessarily the saturation levels, of the downshifted waves. In this connection we note that the low-frequency waves in the mushroom features shown in Plates 1 and 2 have maximum energy densities of approximately $1\text{--}10 \times 10^{-18} \text{ J m}^{-3}$. The ratios of wave energy density to water ion energy density and thermal plasma energy density are then approximately 10^{-9} and 3×10^{-10} (for $n_e = 10^{11} \text{ m}^{-3}$), respectively. These wave levels are therefore qualitatively consistent with the pickup instability not proceeding to saturation. In summary, the linear theory predicts that observable levels of the downshifted waves should grow at low frequencies in the shuttle frame, exactly as observed. At this stage, no interpretation of the lower hybrid frequency waves comprising the tops of the mushroom spectral features is apparent in terms of this theory.

A water ion beam centered at zero velocity, modeling the highly peaked beam arc distributions expected in the very near vicinity of the space shuttle [Cairns, 1990], may also drive rapidly growing waves at frequencies below the lower hybrid frequency as shown in Figure 5 (also Cairns and Gurnett, submitted manuscript, 1990). In fact, the ion beam produces larger growth rates (by a factor of order 3) than the ring distribution for the same number density of water ions. However, a ring distribution produces waves peaked at significantly lower frequencies, in better agreement with the observed waves. In the plasma rest frame the beam-driven waves have dispersion relations $\omega_{\text{rest}} \sim kV_{\perp}$ with maximum growth rates for wave frequencies near the lower hybrid frequency. The distribution of wave vectors is, however, different: waves driven by the ion beam are restricted to wave vectors with $\phi \leq 75^\circ$, and also to negative real frequencies. The two curves show an extension to more negative frequencies with increasing angle ϕ , thereby potentially permitting an explanation involving linear theory for the increased frequency range of the observed low-frequency component of the "mushroom" spectral features. Again, no interpretation for the lower hybrid frequency waves in the mushroom features is apparent.

Two interpretations for the observed V_{\parallel}/V_T effect are consistent with this linear theory. First, as suggested in section 4, coupling the different motions of pickup ions and convected wave packets with spatial inhomogeneity should

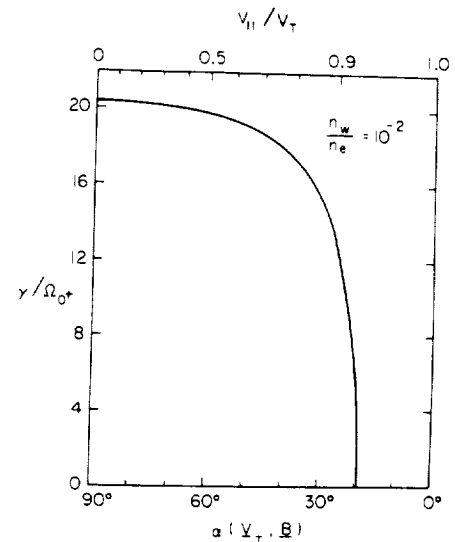


Fig. 6. Variation in the maximum growth rate for the beam-driven waves with the angle α (between V_T and B) and the quantity V_{\parallel}/V_T . Significant growth requires $\alpha \geq 30^\circ$ for a relative water ion beam density of 1%.

lead to growth lengths for the waves which vary with V_{\parallel}/V_T . Figure 5 then shows that increasing the growth length for the waves (decreasing V_{\parallel}/V_T) should lead naturally to enhancements in the wave levels, an increased range of wave vectors, and a greater frequency bandwidth for the observable waves. This is consistent with the observed amplitude-bandwidth correlation for the "low-frequency" component of the mushroom spectral features. The linear theory predicts that the observed waves should consist of wave packets elongated along the magnetic field that are convected downstream (in the shuttle frame), but with group speeds of order $0.9V_{\perp}$ antiparallel to the plasma flow velocity. The V_{\parallel}/V_T argument in section 4 may be repeated without substantive changes with these specifications for the wave packets. Now, however, spatial variations in the water ion distributions and the characteristics of the locally growing waves are vital in limiting both the spatial extent of the wave packets along the magnetic field and the growth lengths of the waves: note, in particular, that separations along the magnetic field would have no effects on the growth length of ideal flute modes in an infinite homogeneous plasma (since the wave fronts are aligned along the magnetic field). Further discussion of this mechanism must await development of analytic theories or simulations that fully include spatially inhomogeneous wave growth and convection in a shuttle environment with more realistic water ion distributions [cf. Cairns, 1990]. Second, the ring speed V_{\perp} driving the unstable waves decreases as the quantity V_{\parallel}/V_T increases, thereby leading to a decrease in the amount of free energy available for wave growth and to decreases in the growth rate and frequency bandwidth of the waves. Similar effects are well known for ion acoustic instabilities [e.g., Gary and Omidi, 1987] and electron beam instabilities. Application of this idea to the shuttle environment is complicated by both the expected variation in the pickup ion number density with variations in V_{\parallel}/V_T [Cairns, 1990] and the idealized (delta function) ring feature in the linear theory. Using a beam representation for the water ion distribution, Figure 6 shows

that the linear growth rate varies markedly with the quantity V_{\parallel}/V_T and the angle α between the plasma velocity V_T and the magnetic field. In particular, when $\alpha \leq 30^\circ$, very low path-integrated wave levels are expected. Calculations for ring distributions show similar results; however, due to the idealized delta function ring features used in this paper, significant growth occurs until $\alpha \leq 20^\circ$. A realistic, thermally broadened ring is expected to have significantly lower growth rates than the delta function ring feature, implying that significant growth will only be possible for values of V_{\parallel}/V_T smaller than or comparable to those for the beam.

The water ions produced near the space shuttle are expected [Cairns, 1990] to have characteristics intermediate to those of the pure ring and pure beam distributions described above. The linear theory discussed here predicts that both ring and beam distributions of water ions may drive Doppler-shifted lower hybrid waves in the range of observed frequencies (and observable wave numbers) for the low-frequency component of mushroom spectral features. Plausible means for producing the mushroom features (i.e., the V_{\parallel}/V_T effect) are also apparent. At this stage, ring distributions appear to be more likely sources for the observed mushroom waves than beam distributions, based on (1) the ring instability producing waves at significantly lower frequencies than the beam instability, (2) the observed spatial localization and different characteristics of the near zone waves [Tribble *et al.*, 1989; Cairns and Gurnett, submitted manuscript, 1990], and (3) the natural interpretation of the near zone waves in terms of Doppler-shifted lower hybrid waves driven by beamlike distributions of water ions (Cairns and Gurnett, submitted manuscript, 1990). We note, however, that the effects of spatial inhomogeneity appear to be a vital ingredient for a complete theory for the waves and that nonlinear processes are often important, even dominant, in determining the evolution of the amplitude and frequency spectrum of plasma waves. Therefore further work on linear instability theory and computer simulations that address in detail the effects of spatial inhomogeneity are required to construct a detailed quantitative theory for the mushroom spectral features.

6. IMPLICATIONS FOR FUTURE SPACE MISSIONS IN LOW EARTH ORBIT

The role of the quantity V_{\parallel}/V_T in controlling the amplitude and spectral characteristics of waves associated with the space shuttle may have important implications for the design of future missions involving orbital platforms subject to outgassing, such as the space shuttle or the proposed space station, which have a requirement that the background of plasma waves driven by outgassed pickup ions be minimized. This requirement for minimal levels of platform-associated plasma waves is a natural one for missions focused on either natural ionospheric plasma waves or active space plasma experiments involving plasma waves as either a diagnostic tool or the focus of the research. We note that both the plasma waves observed in the space shuttle's outgas cloud during the PDP free-flight mission (this paper) and the intense near zone plasma waves observed in the near vicinity of the space shuttle (Cairns and Gurnett, submitted manuscript, 1990; see also Murphy *et al.* [1983] and Shawhan *et al.* [1984]) show evidence of the V_{\parallel}/V_T effect. Our comments therefore apply to both platform-based (i.e.,

the shuttle's payload bay) and free-flying experiments. Aside from the obvious comment that outgassing of potential pickup ions should be minimized, the primary implication of our observational research is that the platform's orbit should be designed so that $|V_{\parallel}| \geq V_{\perp}$. Both our theoretical interpretations imply that large values of $|V_{\parallel}/V_T|$ should be pursued. This means that polar orbits are strongly favored, whereas equatorial orbits are contraindicated.

We note, however, that a maximum value of $|V_{\parallel}/V_T|$ may exist: for $V_{\perp} = 0$ there is no convection electric field, and the pickup ions and background plasma once again move in the same plane, thereby again permitting more efficient wave growth. The pickup instability described in the last section has zero growth rate in this case; however, more familiar ion acoustic-type instabilities [e.g., Gary and Omidi, 1987] may grow in this case provided the temperature ratios T_e/T_o and T_o/T_w are sufficiently high. Therefore, in the absence of observational data with larger values of $|V_{\parallel}/V_T|$ than 0.95 during this shuttle mission, our primary recommendation is for future missions with a requirement for low levels of plasma waves associated with the orbiting platform to have orbits with $0.7 \leq |V_{\parallel}/V_T| \leq 0.95$. These orbits are highly inclined with respect to Earth's equatorial plane.

Our secondary recommendation, which must be qualitative due to the limited data set from the PDP free-flight mission, is that orbiter-based experiments involving plasma waves should be performed outside and upstream from the orbiter's water cloud and water ion trail so as to avoid confusion with the wide variety, large spectral width, and significant levels of orbiter-associated plasma waves. A similar recommendation follows for other orbiting platforms, such as the proposed space station, which are inhabited or suffer significant outgassing. The PDP free-flight data and theoretical extent of the shuttle orbiter's water cloud [Patterson and Frank, 1989] indicate that upstream distances of at least 400 m should be chosen, thereby arguing strongly for such research to be performed using independent, free-flying spacecraft.

7. CONCLUSIONS

The plasma wave receiver on the PDP spacecraft observed "mushroom" spectral features with accompanying amplitude enhancements during the free-flight portion of the Spacelab 2 mission. The top of a mushroom feature is formed by a band of lower hybrid frequency waves, while the base of the mushroom is formed by low-frequency waves whose frequency bandwidth increases to meet the lower hybrid frequency band at the apex of the mushroom. The lower hybrid band shows little change during the mushroom feature. Our interest here is primarily in the significant intensity (by a factor of order 10) and bandwidth variations (by a factor of order 10 again) of the low-frequency waves. These mushroom spectral features are centered near times when the shuttle orbiter's velocity (relative to the ionospheric plasma) is perpendicular to the ionospheric magnetic field, i.e., V_{\parallel}/V_T is small, and when the PDP is downstream from the orbiter. These features are not associated with the orbiter's plasma wake or with the effects of thruster firings or water dumps. The near zone plasma waves observed in the near vicinity of the orbiter also show major changes in amplitude and spectral characteristics with V_{\parallel}/V_T (Cairns and Gurnett, submitted manuscript, 1990); times of low wave amplitude have $|V_{\parallel}/V_T| \geq 0.5$.

The existence of a V_{\parallel}/V_T effect for the waves is strong evidence that the waves are driven by water pickup ions associated with the shuttle orbiter. Two mutually compatible interpretations exist, one in terms of the optimum conditions for wave growth driven by pickup ions, and one in terms of the pickup instability driving the waves. In the first interpretation, maximum growth lengths for the waves are envisaged when the orbiter moves perpendicular to the magnetic field since water ions produced by charge exchange of outgassed water molecules move in the same plane and have the same gyrocenter velocity as the ionospheric plasma and the convected (and growing) plasma waves. In contrast, when the orbiter velocity has a significant component along the magnetic field, the pickup ions and ionospheric plasma (and the plasma waves) move in different planes with significantly different gyrocenter velocities; spatial inhomogeneities in the properties of the water ion distributions driving the waves and the finite size of the orbiter's water cloud then imply a significant limitation of the growth length available for the waves. The second interpretation follows from the mechanism of the pickup instability driving the waves: the instability is driven by the ring speed or beam speed V_{\perp} of the pickup ions; decreasing the speed V_{\perp} causes a decrease in the growth rate of the waves with no growth possible below some threshold value of V_{\perp} .

A linear instability theory has been constructed for growth of waves driven by the ring and beam distributions of water ions expected near the space shuttle due to charge exchange. This theory predicts the generation of Doppler-shifted lower hybrid waves in the frequency band of the low-frequency component of the mushroom features. These waves have large growth rates and have wavelengths capable of being detected by the PDP antenna. The theory suggests that variations in the distances available for growth and/or variations in the ring/beam speed V_{\perp} should permit waves to grow to larger amplitudes over a larger range of wave vectors and so naturally (due to the varying Doppler shift) produce a broader frequency spectrum of waves, thereby explaining the observed V_{\parallel}/V_T effect. The available observational data appear to favor ring distributions as the source of instability for the observed waves. The waves are then predicted to be generated throughout the region populated with water ions produced in the orbiter's water cloud (the so-called water ion trail). At this stage the waves observed near the lower hybrid frequency appear to have no interpretation in terms of the linear theory developed in this paper. Further work on the linear theory and simulations are required before the theory suggested here may be regarded as an adequate explanation for the plasma waves comprising the mushroom spectral features (or other orbiter-associated waves). In particular, inhomogeneity effects must be considered in detail due to their essential role in the theory, and nonlinear effects may have some influences on the observed spectrum of waves. Nevertheless, the homogeneous linear theory developed here provides considerable support for the interpretation of the mushroom spectral features advanced, and so for the resulting implications for further research on plasma waves in the vicinity of orbiting platforms.

This work has significant implications for the orbits of future shuttle missions and space platforms subject to outgassing that are intended for ionospheric research or active space experiments involving plasma waves: to avoid confusion with the orbiter-associated waves discussed in this

paper, (1) the orbit should have $0.7 \leq |V_{\parallel}/V_T| \leq 0.95$, thereby favoring more nearly polar orbits and arguing strongly against equatorial orbits, and/or (2) the research should be performed using free-flying spacecraft situated well upstream of the orbiter- or platform-associated water ion trail and associated plasma waves.

Acknowledgments. We acknowledge the financial support of NASA grant NAGW-1488 from NASA Headquarters and NASA grant NAG 3-449 with NASA/Lewis Research Center. Helpful discussions with J. S. Pickett concerning the PDP's free-flight mission are also gratefully acknowledged.

The Editor thanks Associate Editor J. U. Kozyra for handling the review process on this paper and M. K. Hudson and T. Neubert for their assistance in evaluating this paper.

REFERENCES

- Boardsen, S. A., D. A. Gurnett, and W. K. Peterson, Double-peaked electrostatic ion cyclotron harmonic waves, *J. Geophys. Res.*, **95**, 10,591, 1990.
- Bush, R. I., G. D. Reeves, P. M. Banks, T. Neubert, P. R. Williamson, W. J. Raitt, and D. A. Gurnett, Electromagnetic fields from pulsed electron beam experiments in space: Spacelab-2 results, *Geophys. Res. Lett.*, **14**, 1015, 1987.
- Cairns, I. H., Transition from ring to beam arc distribution functions of water ions with distance upstream from the space shuttle orbiter, *J. Geophys. Res.*, **95**, 15,167, 1990.
- Carignan, G. R., and E. R. Miller, Mass spectrometer STS-2, -3, -4 induced environment contamination monitor (IECM) summary report, edited by E. R. Miller, *NASA Tech. Memo.*, NASA TM-82524, 87, 1983.
- Coroniti, F. V., C. F. Kennel, F. L. Scarf, E. J. Smith, B. T. Tsurutani, S. J. Bame, M. F. Thomsen, R. Hynds, and K. P. Wenzel, Plasma wave turbulence in the strong coupling region at comet Giacobini-Zinner, *Geophys. Res. Lett.*, **13**, 869, 1986.
- Farrell, W. M., D. A. Gurnett, P. M. Banks, R. I. Bush, and W. J. Raitt, An analysis of whistler mode radiation from the Spacelab 2 electron beam, *J. Geophys. Res.*, **93**, 153, 1988.
- Gary, S. P., and N. Omidi, The ion-ion acoustic instability, *J. Plasma Phys.*, **37**, 45, 1987.
- Grebowsky, J. M., H. A. Taylor, Jr., M. W. Pharro III, and N. Reese, Thermal ion perturbations observed in the vicinity of the space shuttle, *Planet. Space Sci.*, **35**, 501, 1987.
- Gurnett, D. A., W. S. Kurth, J. T. Steinberg, P. M. Banks, R. I. Bush, and W. J. Raitt, Whistler-mode radiation from the Spacelab-2 electron beam, *Geophys. Res. Lett.*, **13**, 225, 1986.
- Gurnett, D. A., W. S. Kurth, J. T. Steinberg, and S. D. Shawhan, Plasma wave turbulence around the shuttle: Results from the Spacelab-2 flight, *Geophys. Res. Lett.*, **15**, 760, 1988.
- Hudson, M. K., and I. Roth, Simulations of active ion injection experiments on ARCS 3, *J. Geophys. Res.*, **93**, 8768, 1988.
- Hunton, D. E., and J. M. Calo, Low energy ions in the shuttle environment: Evidence for strong ambient-contaminant interactions, *Planet. Space Sci.*, **33**, 945, 1985.
- Hwang, K. S., N. H. Stone, K. H. Wright, Jr., and U. Samir, The emissions of broadband electrostatic noise in the near vicinity of the shuttle orbiter, *Planet. Space Sci.*, **35**, 1373, 1987.
- Kurth, W. S., and L. A. Frank, The Spacelab-2 Plasma Diagnostics Package, *J. Spacecr. Rockets*, **27**, 70, 1990.
- Lee, J. K., and C. K. Birdsall, Velocity space ring-plasma instability, magnetized, I, Theory, *Phys. Fluids*, **22**, 1306, 1979.
- Murphy, G. B., S. D. Shawhan, L. A. Frank, N. D'Angelo, D. A. Gurnett, J. M. Grebowsky, D. L. Reasoner, and N. Stone, Interaction of the space shuttle orbiter with the ionospheric plasma, *Spacecraft/Plasma Interactions and Their Influence on Field and Particle Measurements*, *Eur. Space Agency Spec. Publ.*, ESA SP-198, 73, 1983.
- Murphy, G. B., D. L. Reasoner, A. Tribble, N. D'Angelo, J. S. Pickett, and W. S. Kurth, The plasma wake of the shuttle orbiter, *J. Geophys. Res.*, **94**, 6866, 1989.
- Narcisi, R., E. Trzcinski, G. Federico, L. Wlodyka, and D. Deloey, The gaseous and plasma environment around space shuttle, *AIAA Pap.*, 83-2659, 1983.

- Neubert, T., G. D. Reeves, J. G. Hawkins, P. M. Banks, R. I. Bush, P. R. Williamson, W. J. Raitt, and D. A. Gurnett, Pulsed electron beam emissions in space, *J. Geomagn. Geoelectr.*, **40**, 1221, 1988.
- Papadopoulos, K. D., On the shuttle glow (the plasma alternative), *Radio Sci.*, **19**, 571, 1984.
- Paterson, W. R., and L. A. Frank, Hot ion plasmas from the cloud of neutral gases surrounding the space shuttle, *J. Geophys. Res.*, **94**, 3721, 1989.
- Pickett, J. S., N. D'Angelo, and W. S. Kurth, Plasma density fluctuations observed during space shuttle orbiter water releases, *J. Geophys. Res.*, **94**, 12,081, 1989.
- Reeves, G. D., P. M. Banks, T. Neubert, R. I. Bush, P. R. Williamson, A. C. Fraser-Smith, D. A. Gurnett, and W. J. Raitt, VLF wave emissions by pulsed and DC electron beams in space, 1, Spacelab 2 observations, *J. Geophys. Res.*, **93**, 14,699, 1988.
- Shawhan, S. D., Description of the Plasma Diagnostics Package (PDP) for the OSS-1 shuttle mission and JSC chamber test in conjunction with the fast pulse electron gun (FPEG), in *Artificial Particle Beams in Space Plasma Studies*, edited by B. Grandel, p. 419, Plenum, New York, 1982.
- Shawhan, S. D., G. B. Murphy, and J. S. Pickett, Plasma Diagnostics Package initial assessment of the shuttle orbiter plasma environment, *J. Spacecr. Rockets*, **21**, 387, 1984.
- Stone, N. H., U. Samir, K. H. Wright, Jr., D. L. Reasoner, and S. D. Shawhan, Multiple ion streams in the near vicinity of the space shuttle, *Geophys. Res. Lett.*, **10**, 1215, 1983.
- Tataronis, J. A., and F. W. Crawford, Cyclotron harmonic wave propagation and instabilities, I, Perpendicular propagation, *J. Plasma Phys.*, **4**, 231, 1970.
- Tribble, A. C., J. S. Pickett, N. D'Angelo, and G. B. Murphy, Plasma density, temperature, and turbulence in the wake of the shuttle orbiter, *Planet. Space Sci.*, **37**, 1001, 1989.
-
- I. H. Cairns and D. A. Gurnett, Department of Physics and Astronomy, University of Iowa, Iowa City, IA 52242.

(Received April 6, 1990;
revised October 29, 1990;
accepted November 13, 1990.)



Plasma Waves Observed in the Near Vicinity of the Space Shuttle

Iver H. Cairns and Donald A. Gurnett

University of Iowa, Iowa City, IA 52242, USA

Abstract

The OSS-1 and Spacelab-2 missions found intense broadband waves in the near vicinity of the space shuttle. This paper contains a detailed observational characterization of the plasma waves observed within about 10 meters of the space shuttle during the XPOP roll period of the Spacelab-2 mission. High wave levels are found from 30 Hz to 10 KHz (near the lower hybrid frequency). Above 10 KHz the wave levels decrease with frequency, reaching the background level near 56 KHz. The frequency distribution of wave electric fields is best interpreted in terms of three components below about 10 KHz and a high frequency tail. The first, and primary, component is a fairly uniform, high level of waves covering the frequency range from 31 Hz to 10 KHz. The two superposed components in this frequency range have electric fields of order twice the uniform level. The second component corresponds to a low frequency peak in the range 100-178 Hz. The third component is found near the lower hybrid frequency. The spectral density and electric field amplitude of this component follow both the magnitude and the trend of the theoretical lower hybrid frequency. No evidence is found for a high frequency component localized above about 10 KHz due to the smooth fall-off in the spectral density and integrated electric field profiles seen at these frequencies. The waves show a pronounced amplitude and frequency variation with the quantity V_{\parallel}/V_T which measures the angle between the ionospheric

magnetic field and the shuttle's velocity vector. Very low wave levels and small frequency extents are observed when V_{\parallel}/V_T is near its maximum value, i.e., the shuttle is moving as close to parallel to the magnetic field as possible. This implies that the waves are probably driven by water pick-up ions. Observations of the waves below about 20 KHz during the free-flight mission imply that the near zone waves have wavevectors oriented perpendicular to the magnetic field. The observed nulls in the wave data as the PDP spacecraft moves through the orbiter's wake imply that the higher frequency waves have higher wavenumbers (shorter wavelengths) than the lower frequency waves.

Detailed theoretical work on the near zone waves is also performed in the paper. Hwang et al. 's theory for the near zone waves is shown to be inconsistent with the frequency distribution and wavevector orientations of the observed waves. A new theory involving doppler-shifted lower hybrid waves driven by beam-like distributions of water ions near the space shuttle is developed using linear theory. This linear theory can explain generation of waves with (1) frequencies ranging from near zero frequency to the lower hybrid frequency, (2) wavevectors essentially perpendicular to the magnetic field, (3) wavenumbers increasing with wave frequency, (4) wavelengths observable by the PDP antenna, and (5) natural explanations for the V_{\parallel}/V_T effect. These properties are all consistent with the properties of the observed near zone waves and provide strong support for this theory. However, the linear theory cannot explain the details of the observed frequency spectrum of the waves. Explanations for the differences between the linear theory and the observed wave spectrum are discussed in terms of refining the linear theory, the effects of the strongly spatially inhomogeneous near zone environment and nonlinear effects. The ratio of electric field energy to thermal plasma energy for the observed waves is of order 10^{-5} , sufficient for nonlinear and strong turbulence effects to be potentially important.

Lastly, the observed V_{\parallel}/V_T effect implies optimum conditions for use of the space shuttle as a base for observing plasma waves generated by active experiments or natural ionospheric waves. Ideally, the shuttle's orbit should be designed so that V_{\parallel}/V_T exceeds about 0.7, thereby favoring polar orbits and arguing against equatorial orbits.

1 Introduction

One of the unexpected results from the OSS-1 mission was the observation of high levels of broadband electrostatic waves in the very near vicinity of the space shuttle [Murphy et al., 1983; Shawhan et al., 1984]. These waves were observed using the plasma wave receiver on the PDP spacecraft. During this mission the PDP remained in the orbiter's payload bay or on the RMS arm (within about 10 meters from the orbiter). The waves had their greatest spectral densities between 31 Hz (the lowest frequency measured) and about 31 KHz, with a peak between 100 Hz and 300 Hz, but extended in frequency above 100 KHz. In comparison, during this mission, the ion gyrofrequency was of order 50 Hz, the lower hybrid frequency was of order 5 KHz, and the oxygen ion plasma frequency was of order 15 - 55 KHz. Hwang et al. [1987] suggested that these broadband electrostatic waves are driven by the secondary ion streams observed [Stone et al., 1983, 1986] in the near vicinity of the orbiter. The relevant instabilities are the ion acoustic and ion-ion acoustic instabilities [e.g., Omidi and Gary, 1987]. Hwang et al. claimed that these theoretical ideas predicted waves with frequencies in good agreement with the observational data of Murphy et al. [1983] and Shawhan et al. [1984].

The PDP spacecraft performed further investigations into the shuttle's interaction with the ionosphere during the Spacelab-2 mission. This mission, launched on 29 July 1985, had a nearly circular, low inclination orbit with a typical altitude of 320 Km and an inclination of 49.5 degrees. In preparation for the Spacelab-2 mission, steps were taken to reduce the noise level of the plasma wave receivers on the PDP spacecraft. The PDP probed the shuttle's environment both while attached to the spacecraft on the RMS arm (distances less than about 10 meters) and while flying free of the shuttle (the so-called "free-flight" mission) out to distances of order

400 meters. While the PDP was on the RMS arm the shuttle performed a roll manoeuvre (the XPOP roll) designed to allow investigation of the broadband near zone waves as a function of phase relative to the orbiter's velocity vector. The free-flight mission included two complete fly-arounds of the shuttle orbiter, including two pairs of transitions from the region downstream of the shuttle (defined by the orbiter's velocity relative to the ionospheric plasma) to the upstream region. Previous papers discussing plasma wave data from the Spacelab-2 mission include those of Gurnett et al. [1988], Tribble et al. [1989], and Cairns and Gurnett [1990].

This paper focuses on the observation and theory of plasma waves in the very near vicinity (within 10 meters) of the space shuttle during the Spacelab-2 mission. The observational data presented are from the XPOP roll period and from one upstream-downstream transition during the free-flight period. These data allow demonstration of the control of the amplitude and spectral characteristics of the near zone waves by the angle between the orbiter's velocity vector and the magnetic field direction (Section 2), the so-called V_{\parallel}/V_T effect, analogous to the results of Cairns and Gurnett [1990] for some waves during the free-flight mission. Detailed investigations into the spectral characteristics of the near zone waves are undertaken. These investigations reveal that the wave spectrum is most plausibly composed of three components: a uniform component covering the frequency range from 30 Hz to about 10 KHz, together with superposed components near about 100 Hz and near the lower hybrid frequency ($\sim 5 - 10$ KHz). Comparisons are made with the results of Murphy et al. [1984] and Shawhan et al. [1984]. Variations in the wave characteristics with roll phase are briefly discussed in Section 3. Section 4 contains data from a period in which the PDP moves from upstream to downstream of the shuttle while magnetically connected. These data suggest that the near zone waves have wavevectors approximately perpendicular to the magnetic field. Theoretical discussions of the near zone waves are

presented in Sections 5 and 6. Hwang et al.'s [1987] theory is discussed in Section 5. Arguments are presented that the frequency spectrum of the observed waves is not even qualitatively consistent with this theory. The inferred wavevector orientation and the existence of the effect involving the angle between the orbiter's velocity vector and the magnetic field provide further arguments against Hwang et al.'s model. A new theory involving doppler-shifted lower hybrid waves driven by pick-up water ions via the modified-two-stream instability [Krall and Liewer, 1971; Papadopoulos, 1984] is suggested for the general characteristics of the broadband near zone waves. These pick-up water ions are produced by charge-exchange interactions between ionospheric oxygen ions and water molecules outgassed from the space shuttle [Paterson and Frank, 1989; Cairns, 1990]. A linear theory is developed that is capable of explaining growth of waves with many of the observed characteristics, in particular the 'uniform' broadband component of the waves. The theory is consistent with the inferred wavevector directions and the V_{\parallel}/V_T effect. However, the theory cannot presently explain the low frequency and lower hybrid frequency components of the wave spectrum. Suggestions are made and discussed that nonlinear effects and the effects of spatial inhomogeneity produce the detailed frequency structure of the observed waves. Further discussion of the paper, in particular the implications of the V_{\parallel}/V_T effect described in Section 2 for design of future shuttle missions, is given in Section 6, followed by the conclusions of the paper in Section 7.

2 Observations of the Near Zone waves during the XPOP roll

The results presented in this paper are from the Helios and MFR (Medium Frequency Receiver) subsystems of the plasma wave receiver on the PDP spacecraft [Shawhan, 1982; Gurnett et

al., 1988]. The Helios instrument measures narrowband electrostatic signals from 31.1 Hz to 178 KHz using 16 logarithmically spaced channels, four per frequency decade. The frequency bandwidths are nominally $\pm 15\%$ below 1 KHz and $\pm 7.5\%$ above 1 KHz. Eight additional higher frequency channels from 311 KHz to 17.8 MHz constitute the MFR subsystem. A double sphere antenna is used with these instruments. The sphere separation (and effective antenna length) is 1.15 meters while on the RMS arm (e.g., during the XPOP roll) and 3.89 meters during the free-flight mission. Each channel provides a data point each 1.6 seconds; both peak and average signals during each measurement interval are recorded. Only the average values are presented here.

The geometry of the XPOP roll is described in Figure 1. The PDP spacecraft is attached to the RMS arm, and remains in the same position (but in various orientations) relative to the orbiter during the XPOP roll. At about 01:34 thruster firings induce the orbiter to roll around the X_{OBAS} axis, corresponding to the nose-tail axis of the orbiter, with the orbiter oriented so that the X_{OBAS} axis is essentially perpendicular to the shuttle's orbital motion around the Earth. Accordingly, the orbiter rotates about an axis perpendicular to the ram velocity direction. This rotation is designed to move the PDP into the orbiter's wake region and upstream region at a constant distance and position relative to the orbiter. The rotation rate is 0.933 degrees per second, corresponding to one wake transit about every six minutes.

The upper panel in Figure 2 shows a spectrogram formed from Helios and MFR data with spectral density (in $V^2m^{-2}Hz^{-1}$) color-coded for the time period of the XPOP roll during the Spacelab-2 mission: 01:34 - 02:40, Day 212, 1985. The white curve is the lower hybrid frequency computed as the product of the square root of the electron to (oxygen) ion mass ratio times the electron gyrofrequency. The data invariably show the highest spectral densities at low frequencies

below 1 KHz, and the lowest spectral densities at high frequencies of order 100 KHz and above. The data show many depletion features, for example near 01:40::00 and the periodic events marked with arrows at 01:48::40, 01:54::40 etc. These 6 minute period events are associated with the PDP's motion through the orbiter's plasma wake and the arrows mark the times when the PDP is in the center of the orbiter's wake. The features at 01:34 and 01:40 occur while the PDP is directly upstream (in the ram direction) from the orbiter. Correlations between the wave characteristics and the PDP's phase (or position) relative to the velocity vector are discussed briefly in the next section. The present section is devoted to discussion of more general characteristics of the waves.

The bottom panel in Figure 2 shows the variation in the quantity V_{\parallel}/V_T for this time period. We define the quantities V_{\parallel} , V_{\perp} and V_T as the components of the orbiter's velocity vector (relative to the ionospheric plasma) parallel and perpendicular to the magnetic field and the orbiter's speed, respectively. Co-rotation of the ionospheric plasma is assumed: the plasma's co-rotation speed is of order 0.5 Kms^{-1} , compared to the shuttle's orbital speed of order 7.8 Kms^{-1} . A strong correlation is visible in Figure 2 between the spectral density of the waves at any frequency below about 10 KHz and the ratio V_{\parallel}/V_T . When the quantity V_{\parallel}/V_T is near its maximum around 01:35 and 02:15, in other words when the shuttle's velocity vector is most nearly parallel to the magnetic field, dramatically lower wave amplitudes are observed and the waves have much smaller extents in frequency. On the other hand, when V_{\parallel}/V_T is small and the shuttle moves almost perpendicular to the magnetic field, the wave amplitudes are always larger than those for large V_{\parallel}/V_T and the waves extend to much higher frequencies. Note that two distinct periods of very low wave levels, separated by one half the shuttle's orbital period, occur near the peaks in V_{\parallel}/V_T . This fact argues against a peculiar region of ionospheric

plasma being responsible for this phenomenon. Density data from the PDP's Langmuir Probe [J.S. Pickett, private communications, 1990] show, however, that the electron density decreases below measurable levels between 02:14 and 02:21, indicating entry into an unusually low density region of the ionosphere at this time. Nevertheless, the absence of a similar density depletion for the first plasma wave null (01:32 - 01:41) and timing differences between the second wave null (02:11 - 02:17) and the observed density depletion show that the wave nulls cannot be explained in terms of unusual ionospheric density depletions.

Careful comparisons show that the centers of the wave nulls do not coincide with the peaks in $V_{||}/V_T$. In particular, the centers of the null periods both occur between the two peaks in $V_{||}/V_T$ and less than one half orbital period apart. Potentially, this observation might cast doubt on the simple correlation drawn above between the wave nulls and large values of $V_{||}/V_T$. However, the ionospheric density depletion overlapping the period of the second wave null may have associated plasma waves. Interpreting the waves observed between 02:17 and 02:19 as being associated with the ionospheric density feature would explain the difference in length (2 minutes) of the two wave nulls and the failure of the second wave null to include the peak in $V_{||}/V_T$ (in contrast to the first null period). Some support for this interpretation comes from observations of plasma waves associated with a similar ionospheric density depletion during the free-flight mission. This suggestion therefore significantly strengthens the correlation drawn above between wave nulls and large values of $|V_{||}/V_T|$. Furthermore, we note that some relatively strong, transient wave features occur during the first wave null which are not directly associated with thruster firings. Thruster firing occur at 01:34::1,2,3,44,45, 01:36::7,15,16,59, 01:37::0-4,48-50, 01:38::17-18, 01:40::42-45 and 01:44:34 (format hour:minute::second). Accordingly, the waves preceding the 01:36 firings and the waves during minute 01:39 are not directly thruster-associated. These

waves do not appear to be part of the usual orbiter-associated spectrum and may be associated with particular roll phases of the orbiter and the attitude of the PDP spacecraft itself. Thus, these phase complications between the wave nulls and the peaks in V_{\parallel}/V_T may also be due to waves that are usually weaker than the usual correlated wave spectrum becoming observable when $|V_{\parallel}/V_T|$ is large.

This V_{\parallel}/V_T effect for the near zone shuttle waves is strongly analogous to the V_{\parallel}/V_T effect reported by Cairns and Gurnett [1990] for some plasma waves (called mushroom spectral features) downstream from the orbiter during the free-flight mission. In particular, these mushroom features showed their largest amplitudes and spectral bandwidths (from zero frequency to the lower hybrid frequency) near where $V_{\parallel}/V_T = 0$ and showed small amplitudes and small frequency bandwidths (restricted to low frequencies) when V_{\parallel}/V_T was large. Cairns and Gurnett pointed out that this effect has a natural interpretation in terms of the optimum conditions for wave growth driven by pick-up ions. In particular, when $V_{\parallel} = 0$ the pick-up ions and ionospheric plasma (convecting the plasma waves) move in the same plane, thereby permitting longer path lengths for wave growth. Cairns and Gurnett also developed a linear theory capable of explaining waves in the observed frequency range and broadening of the wave spectrum with increased growth lengths for the waves. This theory involves doppler-shifted lower hybrid waves driven by ring distributions of pick-up water ions. One might infer, then, that the strong V_{\parallel}/V_T effect reported here is evidence for pick-up ions being involved with the generation of the orbiter's near zone waves.

Figure 3 shows another spectrogram for the XPOP roll; in this case the color coding represents the average squared electric field in the frequency bandwidth of the channel at frequency f . It can be seen that each channel up to a frequency of 56 KHz has an rms electric field at least of

order 0.1 mV/m. The maximum electric field in a channel is of order 3 mV/m. Two distinct peaks in the electric field are visible: one centered at about 178 Hz and one near the lower hybrid frequency $\sim 5.6 - 10$ KHz. The low frequency peak is clearly not in the lowest frequency channel (center frequency 31 Hz), although fields of order 1 mV/m sometimes extend down to the lowest observed frequencies. Strong levels of waves are observed between the two peaks. The high frequency peak follows the time variations and magnitude of the theoretical lower hybrid frequency determined by changes in the local ionospheric magnetic field. This behaviour is strong evidence that the high frequency peak is associated with lower hybrid waves. Except for the sudden extensions of the high frequency waves to 178 KHz discussed briefly in the next section, e.g. at 01:41::40, 01:47::00, and 01:58::30, the high frequency waves only have significant spectral densities up to about 56 KHz.

Murphy et al. [1984] and Shawhan et al. [1984] have previously recognised the existence of the low frequency peak. However, the peak near the lower hybrid frequency has not been recognised before in the near zone data. The presence of strong low frequency waves and a high frequency peak near the lower hybrid frequency is strongly reminiscent of the plasma waves observed during the free-flight mission [Gurnett et al., 1988; Cairns and Gurnett, 1990]. In particular, Figure 2 of Cairns and Gurnett's paper shows the presence of strong waves at low frequencies together with a high frequency band near the lower hybrid frequency. This strong similarity provides a further hint that these Near Zone waves are driven by pick-up ion instabilities, as is presently believed for the aforementioned waves observed during the free-flight mission.

The presence of two peaks in the wave spectrum is also visible in spectral density plots for the waves. Figures 4a and b show spectral density plots for the typical period 01:56 - 01:58 and the period 01:45 - 02:10, respectively. Both clearly show the fall-off at low frequencies, the presence

of a low frequency peak near 178 Hz, a region with spectral densities decreasing approximately inversely with frequency between the low frequency peak and the lower hybrid frequency, a bulge around the lower hybrid frequency marking the second component, and a rapid fall-off at higher frequencies. Channels above 178 KHz (in the MFR receiver) show essentially background levels. The rapid fall-off at high frequencies is believed to be real: the whistler mode emissions seen during some FPEG events on the free-flight missions [Gurnett et al., 1986; Farrell et al., 1989] show no evidence for a significant difference in sensitivity between the 100 and 178 KHz Helios channels and the 311 KHz and higher channels of the MFR receiver. In addition, ignoring the usual spike in the 178 KHz channel at low signal levels (e.g., the constant light blue band at 178 KHz in Figure 2), the decreasing trend in the 10 - 100 KHz Helios channels plausibly connects to the very low levels seen in the MFR channels. We note that this fall-off might also be partially associated with the wavelengths of the high frequency portion of a wave spectrum becoming very short relative to the antenna length, and so becoming undetectable.

Figure 5 shows the relative contribution of the electric fields centered on the n 'th channel to the total average broadband, frequency-integrated electric field E_T plotted versus the frequency of the n 'th channel. The detailed definition of this quantity is $R(f_i) = E_i / \sum_i E_i$ with $E_i^2 = \int_{\sqrt{f_i f_{i-1}}}^{\sqrt{f_{i+1} f_i}} S(f) df$ where $S(f)$ is the spectral density in units of $V^2 m^{-2} Hz^{-1}$. The frequency intervals chosen for the integration correspond to equally-spaced intervals in logarithmic frequency. The data plotted are for the period 0145-0210 shown also in Figure 4b. The total average broadband electric field E_T was 51.1 mV/m. Two peaks are visible. The first is at low frequencies centered on 178 Hz, with a broad shoulder at significant amplitudes to the second peak which is situated between 5.6 KHz and 10 KHz. As described above, the lower hybrid frequency varies between 5 and 10 KHz during this time period, providing an excellent identifi-

cation for the higher frequency peak. Above 56 KHz the measured electric fields are essentially negligible. We note now that the linear theory in Section 6 predicts maximum wave growth at wavelengths of order 0.8 meters, commensurable with the antenna length (1.15 meters) for these observations. It is therefore likely that the broadband wave electric field estimated above (51 mV/m) is smaller than the field present in the plasma.

The interpretation of these data in Figures 2-5 in terms of components in the wave spectrum is not unique. However, the peaks in Figure 5 are only a factor of 2 greater than the level between the peaks and at lower frequencies than the first peak. It therefore seems most appropriate to interpret the wave spectrum in terms of a fairly constant high level of waves (electric fields of order 2.5 mV/m per frequency interval) from 31 Hz to 10 KHz with two superposed peaks, one around 178 Hz and one near the lower hybrid frequency. These superposed peaks have electric fields a factor of two higher than the constant level of waves between 30 Hz and 10 KHz. These data require any high frequency waves above about 20 KHz to smoothly merge with the lower hybrid frequency waves; no evidence is found for any sharply peaked wave components in the frequency range of 10 to 40 KHz. These identifications are referred to below as the 'uniform' component, the low frequency component and the lower hybrid component. We will show below (Section 6) that a simple linear theory can explain growth of waves over a broad frequency bandwidth between zero frequency and the lower hybrid frequency, thereby providing an explanation for the uniform component. It is suggested below that the effects of nonlinearities and spatial inhomogeneities lead to the developments of the low frequency and lower hybrid frequency enhancements. Despite the above interpretation adopted in this paper we recognize that an interpretation in terms of only two wave components with broad extents in frequency, one centered at 178 Hz and one at the lower hybrid frequency, is not precluded by the available

observational data. No theoretical interpretation is presently available for this two-component interpretation.

3 Variations of the Near Zone waves with roll phase

The periodic patterns at the XPOP roll period in Figures 2 and 3 indicate that the plasma waves associated with the space shuttle show significant and often reproducible variations with position relative to the ram direction. Figure 6 shows the time variation of the phase angle ϕ between the ram direction and the PDP's position vector relative to the orbiter. Times when the PDP is directly in the orbiter's wake region ($\phi = 0^\circ$) are denoted by white arrows in Figure 2. It is clear that the high frequency null features occur when the PDP is in the orbiter's wake region [Murphy et al., 1983; Gurnett et al., 1990, in preparation]. Tribble et al. [1989] find that the low frequency waves in the range 6 – 40 Hz also show a null region when the PDP is in the orbiter's wake. Gurnett et al. [1990] provide a detailed discussion of these null features. In particular, they note that the higher frequency waves always decrease in amplitude before the lower frequency waves when approaching the center of the shuttle's plasma wake, with the increases in amplitude while leaving the wake center in a symmetrical fashion. They suggest that this behaviour is consistent with the higher frequency waves having shorter wavelengths, thereby having greater difficulty propagating into the deep null observed in the plasma density [Murphy et al., 1983; Tribble et al., 1989] in the orbiter's wake. We will show that a theoretical model for the plasma waves at frequencies below the lower hybrid frequency developed in Section 6 below is consistent with this interpretation. Further discussion of these wake features is presented in Gurnett et al.'s [1990] paper.

In distinction to the usual plasma wave null when the PDP is in the orbiter's plasma wake, it is usual for the wave intensities to be largest when the PDP is located directly upstream from the orbiter ($\phi = -180^\circ$ or 180°). However, during the times of maximum V_{\parallel}/V_T , nulls in the plasma waves are seen when the PDP is in the ram direction (near 01:34, 01:40, and 02:16) or in the wake. Low level waves are observed at other roll angles during these periods.

Two further aspects of the Near Zone plasma waves are deferred to the paper by Gurnett et al. [1990] and future work. The first concerns the existence and characteristics of the low frequency 6 - 40 Hz wave enhancements suggested by Tribble et al. [1989] to occur near where the PDP enters the shuttle's Mach cone. Consideration of Figures 1 and 2 provides little support for this suggestion; however, the survey slides for the PDP instruments clearly show Langmuir probe data supporting this notion for several wake transits. At present, no consistent trend in the data is apparent. Further work is warranted on this matter. The second topic deferred to further work involves the sudden extensions of the high frequency waves to near 178 KHz visible, for example, near 01:41:30 and 01:58:30. At the present time we have no viable explanations for these events.

4 Observations of the Near Zone waves during the free-flight mission

Figure 7 shows wave data from 02:30 to 02:47 Day 213, 1985, during the PDP spacecraft's free-flight mission. The motion of the PDP spacecraft in $X_P - Y_P - Z_P$ coordinates is described in Figure 8. The "pick-up" coordinate system $X_P - Y_P - Z_P$ is defined by Cairns [1990]. The origin is situated at the orbiter's center of mass and moves with the space shuttle. The ionospheric

magnetic field is directed along the Z_P axis, and the ionospheric plasma is constrained to move in the $X_P - Z_P$ plane with velocity $(-V_{\perp}, 0, -V_{\parallel})$. In contrast the water pick-up ions move in a cycloidal path in the $X_P - Y_P$ plane with convection velocity $(-V_{\perp}, 0, 0)$ and gyrospeed of order V_{\perp} , together with thermal motions along the magnetic field. A summary of the PDP's motion is as follows. The PDP spacecraft is initially moving downstream from the upstream region with small Y_P at a large and approximately constant distance along the magnetic field (Z_P coordinate) of order 215 m. The PDP has position $X_P = 0$ near 02:39::15 (i.e., the PDP is magnetically connected to the orbiter's center of mass), and $Y_P = 0$ near 02:41::10 when downstream from the shuttle (i.e., probing the center of the wake).

FPEG interference is visible in Figure 7 as spikes extending from low frequencies to the electron gyrofrequency from about 02:30 to 02:38. Thruster firings occur frequently from 02:25 to 02:38, and thereafter at 02:38::54, 02:39::22,57, 02:42::2-6,10,13,14,16,18,19,23,27,30-31 and 02:43::12,16 and 57. However, plasma waves are observed in association with the upstream-downstream transition $X_P = 0$. A strong broadband burst of waves extending up to the lower hybrid frequency is observed as the PDP becomes magnetically connected to the space shuttle (i.e., $X_P = 0$). The maximum frequency of these broadband waves abruptly decreases from near the lower hybrid frequency to about 500 Hz at about 02:41::00, and then tends to about 300 Hz with increasing distance downstream. At 02:41::10 the PDP is magnetically connected to the center of the wake with $X_P \sim -50$ m, $Y_P \sim 0$ and $Z_P \sim 220$ m. Note the relative lack of waves between the lower hybrid frequency and 1 KHz from 02:41::00 to 02:41::30. Waves near the lower hybrid frequency start near 02:41::30, leading into the mushroom spectral feature centered near 03:02 discussed briefly by Cairns and Gurnett [1990]. Notice also the band of waves between 10 and 20 KHz from about 02:43 to 02:47. This band is not discussed further in this paper; we note

that these waves have frequencies near the oxygen plasma frequency implied by the Langmuir probe data (of order 14 - 9 KHz at the above times, respectively) and frequencies of order three times the lower hybrid frequency.

The important observation here is the onset of strong waves at frequencies up to and above the lower hybrid frequency when the PDP spacecraft becomes magnetically connected to the space shuttle. Inspection of the PDP survey slides indicate no obvious increases in electron or ion fluxes measures by the LEPDEEA, RPA, IMS or other particle instruments or changes in the DC electric field instrument. It does not appear correct, therefore, to interpret the observed plasma wave event in terms of waves generated locally (to the PDP spacecraft) due to particles originating at the space shuttle. Electrostatic waves with wavevectors perpendicular to the magnetic field have wavefronts aligned along the magnetic field. That is, the electric field of the wave does not vary along the magnetic field in an infinite inhomogeneous plasma. We therefore interpret the burst of waves observed between 02:39::30 and 02:41::00 in terms of the intense waves generated in the near vicinity of the space shuttle being observed along the magnetic field from the shuttle. This implies that the near zone waves, at least at frequencies below a few times the lower hybrid frequency, have wavevectors oriented perpendicular to the magnetic field. This interpretation places significant restrictions on theories attempting to explain the near zone waves. The evident decrease in amplitude for the free-flight waves compared with the near zone waves, and the restriction in the frequency spectrum of the waves, may be qualitatively explained in terms of the inhomogeneous plasma environment of the shuttle and the smaller wavelengths for the higher frequency waves inferred from the high frequency nulls in the orbiter's wake (see last section and Gurnett et al. [1990]). We now proceed to gather additional supporting evidence for our interpretation of the wavevectors of the near zone waves.

Figure 9 compares the spectral density of the burst of waves for the time period 02:39:40-50 with the average spectral density of the near zone waves shown in Figure 4b (time period 01:45 - 02:10 Day 212). These spectral density profiles are surprisingly similar. The free-flight data shows two low frequency peaks, one near 178 Hz and one near the lower hybrid frequency of about 3 KHz, which compare well with the XPOP roll observations. Note that the lower hybrid frequency during this period of near zone data was above about 5 KHz, consistent with the frequency of the second peak. The high frequency fall-off above the lower hybrid frequency shows similar forms in both the free-flight and near zone data. These spectral density profiles coincide well if one multiplies the free-flight curve by a factor of 10, corresponding to electric fields a factor of 3 stronger. These spectral density profiles are therefore consistent with the interpretation of the free-flight data in terms of observing flute mode (i.e., wavevectors perpendicular to the magnetic field) plasma waves from the Near Zone region around the shuttle. In addition, in Section 6 we show that the linear theory predicts maximum growth at wavelengths of order 1 meter: the longer antenna length during free-flight (3.89 meters) compared with the XPOP roll (1.15 meters) then implies less efficient measurement of the wave electric fields. An additional point of interest involves the extension of the wave spectrum to 20 KHz in the free-flight data when the lower hybrid frequency is of order 3 KHz. During the free-flight mission it is unusual to observe waves above about two times the lower hybrid frequency (except for thruster- and FPEG-associated waves and the interference spikes) except perhaps when well downstream in the wake region. Thus, the observation of waves above about 10 KHz during this connection event provides some weak additional support for the interpretation in terms of the broadband near zone waves advanced above. Evidence for spin modulation of the waves was sought to provide further support for the wavevector directions inferred above. However, except

for a spacecraft-associated signal with one maximum-null pair per spacecraft rotation, the data showed no evidence of consistent spin modulation.

Another event similar to the 02:39 upstream-downstream transition occurred near 02:03. This event is a transition from downstream to upstream, but which suffers from confusion with thruster firings, with similar characteristics to the 02:39 event discussed above. In this case the lower hybrid frequency is of order 8 KHz and the wave spectrum is observed to continue up to about 56 KHz, well above the interference spikes at this time. This provides further support that the PDP is observing the the broadband near zone waves during this event, and thereby that the near zone waves have wavevectors oriented essentially perpendicular to the magnetic field up to frequencies at least four times the lower hybrid frequency.

5 Previous theories for the near zone waves

5.1 Discussion of Hwang et al.'s theory

Hwang et al. [1987] suggest a linear theory for these electrostatic, broadband Near Zone waves on the basis of the observations of Murphy et al. [1983] and Shawhan et al. [1985]. This theory involves ion acoustic and ion-ion acoustic instabilities [e.g., Gary and Omidi, 1987] driven by the secondary ion streams observed by Stone et al. [1983, 1986] in the near vicinity of the space shuttle. Hwang et al. solve the electrostatic dispersion equation with Maxwellian distributions of magnetized ionospheric electrons, unmagnetized ionospheric oxygen ions and an unmagnetized species of ions which drift relative to the ionospheric plasma particles and to the space shuttle. This last species represents the secondary ion stream. At the present time the origin and detailed characteristics of these secondary ion streams are not known [see, however, Stone et al., 1983,

1986]. Published plasma characteristics for the ion streams are few. Hwang et al. state that these streams have temperatures of several hundred degrees Kelvin (similar to the expected temperature $\sim 300\text{K}$ of water molecules outgassed from the shuttle) and have current densities of order 30 – 70% of the ionospheric ram current. These current densities imply that the ion streams have number densities of order 30 – 70% of the observed ionospheric plasma flow's number density.

Hwang et al. [1987] claim that their linear theory gives results which are consistent with the wave observations of Murphy et al. [1983] and Shawhan et al. [1984]. Below we show that Hwang et al.'s theory is not consistent with the detailed properties of the broadband waves identified in this paper. In brief, Hwang et al.'s paper implies the following characteristics for the unstable waves and their corresponding instabilities: (1) the instabilities are the ion acoustic and ion-ion acoustic instabilities [e.g., Gary and Omidi, 1987], (2) the instabilities are essentially unmagnetized (no mention is made of the angle between the magnetic field and the wavevector being important), (3) the important variable determining the angular characteristics of the unstable waves is $\theta_D = \cos^{-1}(\underline{k} \cdot \underline{V}_D)$, where V_D is the drift velocity of the secondary ion stream relative to the ionospheric plasma, (4) the unstable waves have wavevectors concentrated near $\theta_D = 0^\circ$ or 77° depending on the ion stream density and temperature, (5) the growth rate of the waves as a function of wave frequency shows a single well-defined maximum at frequencies of order 10 KHz and essentially negligible wave growth below 1 KHz, (6) decreasing the relative ion stream number density from its maximum value (100%) moves the peak in the growth rate from a wave frequency of 10 KHz to higher wave frequencies of order 40 KHz (50%) and above. Lastly, (7) ion streams with relative number density less than about 10% do not show effective growth.

Detailed comments on the disagreement between the characteristics of the observed waves (see previous three sections) and Hwang et al.'s theory are as follows. Firstly, and most importantly, almost all the observed wave energy is concentrated at frequencies well below those predicted by the theory ($\sim 10 - 40$ KHz). Therefore no explanation exists in the theory for the low frequency component and strong wave levels below 1 KHz in the observed wave spectrum. Secondly, the theory cannot explain the second primary component (near the lower hybrid frequency) in the observed waves since the theory predicts essentially unmagnetized waves with no dependence or importance for the lower hybrid frequency. Thirdly, the wavevectors inferred from the available wave data are essentially perpendicular to the magnetic field, thereby contradicting the theoretical predictions.

Additional problems for Hwang et al.'s theory include the absence of a direct interpretation for the V_{\parallel}/V_T effect described in Section 2 and the temperature ratios chosen for the instability analysis. Ion acoustic and ion-ion acoustic instabilities are strongly dependent on the electron-to-ion and ion-beam temperature ratios T_e/T_i and T_i/T_b being sufficiently large [e.g., Gary and Omidi, 1987] for growth to overcome damping. A beam temperature of 200 – 300K [e.g. Hwang et al., 1987] implies oxygen ion temperatures $T_i \sim 1500 - 2250$ K and electron temperatures $T_e \sim 3000 - 4500$ K for Hwang et al.'s assumed temperature ratios. In contrast, nominal ionospheric temperatures are $T_e/T_i \sim 2$ with $T_i \sim 1000$ K. During the PDP free-flight mission the oxygen ion temperature inferred from the RPA instrument's data [Reasoner et al., 1988] is of order 1100 K whenever confidence may be attached to the fitting routine [Reasoner, personal communication, 1989]. Reducing the ion-beam temperature ratio to more plausible values will reduce the wave growth rates and range of growing modes, if not lead to elimination of the instability for shuttle parameters.

In summary, Hwang et al.'s theory is unable to account for the broadband near zone waves at frequencies below several times the lower hybrid frequency. A possibility remains that Hwang et al.'s theory may still apply to the broadband waves above about 20 KHz or to the high frequency extension events near 01:41::30 and 01:58::30 for example. This first possibility is discussed at the end of the next section.

5.2 Discussion of Papadopoulos' [1984] theory

Papadopoulos [1984] suggested that the waves observed by Murphy et al. [1983] and Shawhan et al. [1984] evolve from a linear spectrum of lower hybrid waves driven by a beam of oxygen ions reflected from the space shuttle. The relevant instability is the modified-two-stream instability [Krall and Liewer, 1971]. No role is played in the theory by water 'pick-up' ions and the nature of the required reflection process for the oxygen ions is not specified. Severe theoretical problems exist for efficient reflection of low energy ions (ram energy of order 5 eV) off metallic or ceramic surfaces [e.g., Hagstrum, 1961; Meyer et al., 1985; J.E. Borovsky, private communication, 1989]. The majority of such ions are reflected as neutrals and typically the ion reflection yield is much less than 1%. In contrast, the theory suggested in this paper involves doppler-shifted lower hybrid waves driven by beam distributions of water 'pick-up' ions via the modified-two-stream instability. These water ions naturally have much greater relative number densities ($\geq 20\%$) in the near vicinity of the shuttle, as observed [Grebowsky et al., 1987] and predicted theoretically [Cairns, 1990]. These greater water ion beam densities imply much higher growth rates for the waves than for the reflection theory. This water ion theory is therefore greatly more favored over Papadopoulos' theory. Further problems for Papadopoulos' theory include the absence (not shown here) of an asymmetry predicted in the ion beam density and wave growth due to

magnetization of the reflected ion beams, similar to the observed asymmetry in Titan's wake [Ma and Gurnett, 1987], and the kinematic requirement that the reflected ions should be constrained to be at most one gyroradius ($\sim 4\text{m}$) upstream from the space shuttle. Observations of the near zone waves at least ten meters upstream from the shuttle during the XPOP roll are inconsistent with these predictions for Papadopoulos' theory. In addition, no simple explanation for the observed V_{\parallel}/V_T effect is apparent in terms of this theory. We conclude that Papadopoulos' [1984] is inconsistent with the available wave data.

6 A new theory for the Near Zone Waves

In this section we develop a linear theory capable of explaining generation of waves with the general characteristics of the near zone waves. This theory involves the generation of doppler-shifted lower hybrid waves driven by beam-like distributions of water ions [Cairns, 1990] via the modified-two-stream instability [Krall and Liewer, 1971; Papadopoulos, 1984] in the near vicinity of the space shuttle. These water ions are produced by charge-exchange between ionospheric oxygen ions and water molecules outgassed from the space shuttle. Use of water 'pick-up' ions as the source of instability is the principal difference between our theory and that of Papadopoulos [1984]; as argued in the last section, Papadopoulos' theory is not consistent with the observable wave data. A linear theory for the characteristics of the waves is then developed and discussed. This new theory is shown to explain the characteristics of the observed waves except for the detailed frequency structure of the observed wave spectrum. The roles of spatial inhomogeneity and nonlinear effects in producing the observed wave spectrum are then discussed. Preliminary simulation results providing some support for inhomogeneity and nonlinear effects being impor-

tant are summarized. The section ends with comments on the generation of waves at frequencies above several times the lower hybrid frequency.

6.1 Linear theory: doppler-shifted lower hybrid waves

Water ions are produced in the vicinity of the space shuttle by charge-exchange between ionospheric oxygen ions and water molecules outgassed from the space shuttle [Paterson and Frank, 1989; Cairns, 1990]. Cairns [1990] has considered the distribution function of the pick-up water ions and shown that a transition between a ring-like distribution and a beam-like distribution function occurs with decreasing distance upstream from the space shuttle. In addition the water ions increase monotonically in number density with decreasing distance upstream from the shuttle [Cairns, 1990]: within 10 meters of the shuttle the water ions are observed [Grebowsky et al., 1987] and expected theoretically to comprise in excess of 10% of the plasma ions. Within about 30 meters from the shuttle (but not in the wake region) the water ion distributions are best described as “beam arc” distributions, corresponding to the water ions being found primarily in a finite section near zero velocity (relative to the shuttle) of a ring. Figure 10 shows these distribution functions in the $X_p - Y_p - Z_p$ “pick-up” coordinate system. Reviews of the pick-up ion motions are given in the papers by Paterson and Frank [1989], Cairns [1990] and Cairns and Gurnett [1990]. Briefly, however, the water ions are born in a thermal distribution centered at zero velocity relative to the shuttle but experience a convection electric field due to the ionospheric plasma’s motion across the magnetic field. The water ions then move with cycloidal orbits in the $X_P - Y_P$ plane comprised of a gyrocenter drift $(-V_{\perp}, 0, 0)$ and gyro speed of order V_{\perp} (modified by the initial thermal velocity of the ion) and thermal motions along the magnetic field. In contrast, the ionospheric plasma moves with velocity $(-V_{\perp}, 0, -V_{\parallel})$ in this

frame.

Within 30 meters from the shuttle it appears appropriate to initially model the pick-up water ions in terms of a Maxwellian beam distribution centered at zero velocity while the ionospheric plasma drifts relatively (the influence of the ring component is discussed briefly below). We work in the “pick-up” coordinate system, in which case the calculated wave frequencies are directly comparable with the observed wave frequencies. For now we restrict our attention to the case in which the orbiter moves exactly perpendicular to the magnetic field and $V_{\parallel} = 0$. The electrostatic dispersion equation is then

$$1 + \frac{\omega_{pe}^2}{k^2 V_e^2} \left(1 + \frac{\omega - k_x V_{\perp}}{\sqrt{2} k_{\parallel} V_e} e^{-r_e^2} \sum_{m=-\infty}^{m=\infty} Z(y_{em}) I_m(r_e^2)\right) + \frac{\omega_{pO}^2}{k^2 V_O^2} \left(1 + \frac{\omega - k_x V_{\perp}}{\sqrt{2} k_{\parallel} V_O} e^{-r_O^2} \sum_{m=-\infty}^{m=\infty} Z(y_{Om}) I_m(r_O^2)\right) + \frac{\omega_{pw}^2}{k^2 V_w^2} \left(1 + \frac{\omega}{\sqrt{2} k V_w} Z(y_w)\right) = 0 \quad (1)$$

In this equation the ionospheric electrons and oxygen ions are represented by magnetized Maxwellian distributions drifting with velocity $(-V_{\perp}, 0, 0)$ and have the standard forms for their contributions to the dispersion equation. The water ions are represented by an unmagnetized Maxwellian beam at zero velocity. Subscripts e , O , and w refer to the electrons, oxygen ions and water ions, respectively. The functions J_m and I_m are Bessel functions of order m of the first and second kind, respectively. The arguments of these functions and the Friede-Conte function Z_y are $r_{\alpha} = k_{\perp} V_{\alpha} / \Omega_{\alpha}$ and $y_{\alpha m} = (\omega - k_x V_{\perp} - m \Omega_{\alpha}) / \sqrt{2} k_{\parallel} V_{\alpha}$ for the electrons and oxygen ions, and $R_w = k_{\perp} V_{\perp} / \Omega_w$ and $y_w = \omega / \sqrt{2} k_{\parallel} V_w$ for the water ions. Standard definitions apply to the angular plasma frequencies $\omega_{p\alpha}$, gyrofrequencies Ω_{α} , number densities n_{α} , and thermal speeds V_{α} for species α .

The quantity $\omega - k_x V_{\perp}$ is the doppler-shifted wave frequency seen by the ionospheric electrons

and water ions. A positive component k_x for a wavevector implies the wavevector is directed upstream along the X_p axis. When solving this equation we normalize all quantities relative to those for the oxygen ions. Nominal ratios for the Spacelab-2 mission are $T_e/T_O = 2$, $T_w/T_O = 0.3$ (typically $T_O \sim 1000\text{K}$), $V_\perp/V_O = 11$, and $\omega_{pO}/\Omega_O \sim 1000$ with an oxygen gyrofrequency $\Omega_O/2\pi$ of order 30 Hz. All frequencies and growth rates calculated below are given in units of the oxygen gyrofrequency. In these units the nominal lower hybrid frequency f_{LH} , given by the square root of the electron to oxygen mass ratio times the electron gyrofrequency is 172 units.

Analytically one expects this situation to give rise to doppler-shifted lower hybrid waves via the so-called “modified two stream” instability [e.g., Krall and Liewer, 1971; Papadopoulos, 1984]. This may be seen as follows. The electron terms are treated by retaining only the $m = 0, \pm 1$ terms in the electron magnetization, expanding the modified Bessel functions in the limit $r_e^2 \ll 1$, retaining only first order terms and assuming that $k_\parallel \ll k_\perp$. The oxygen ions are treated by assuming that $\gamma \gg 1$ (in units of the oxygen gyrofrequency), so that the oxygen ions are effectively unmagnetized, and expanding the Friede-Conte function using the high phase speed expansion ($\omega/\sqrt{2}kV_O \gg 1$). Finally after expanding the water ion contribution using the high phase speed approximation, one finds an equation of the form

$$1 - \frac{\omega_{pe}^2}{(\omega - k_x V_\perp)^2 - \Omega_e^2} - \frac{\omega_{pO}^2}{(\omega - k_x V_\perp)^2} - \frac{\omega_{pw}^2}{\omega^2} = 0. \quad (2)$$

Rearranging this equation with the definition of the lower hybrid frequency above and the assumptions (1) $\omega_{pO}^2/\Omega_O^2 \gg 1$, (2) $(\omega - k_x V_\perp)^2 \ll \Omega_e^2$, and (3) $n_e = n_O + n_w$, gives the dispersion equation

$$1 - \frac{n_O}{n_e} \frac{\Omega_{LH}^2}{(\omega - k_x V_\perp)^2} - \frac{n_w}{n_e} \frac{\Omega_{LH}^2}{\omega^2} = 0. \quad (3)$$

This equation is directly analogous to the dispersion equation for the usual two stream instability

in which Langmuir waves are generated by an electron beam and viewed in the reference frame of the beam [e.g, Cairns, 1989]. Accordingly [Cairns, 1989], for beams which satisfy the condition $n_w/n_e > 2.5(V_w/V_\perp)^3$ ($\sim 10^{-3}$ here), this equation predicts generation of strongly growing waves with dispersion relation $\omega_{rest} \sim k_x V_\perp$, frequencies near the lower hybrid frequency in the ionospheric plasma rest frame, and relatively small wave frequencies in the shuttle's rest frame.

Figure 11 shows the wave dispersion relation and growth rate in the ionospheric plasma frame for waves propagating along the X_P direction with an angle $\theta = 89.9^\circ$ between the wavevector and the magnetic field direction (the Z_P axis). The relative water ion number density $n_w/n_e = 0.05$. The dashed line shows the dispersion relation $\omega_{rest} = k_x V_\perp$ for comparison. A strong resemblance to the ordinary beam instability for "Langmuir" waves is apparent [e.g., Figure 1 of Cairns, 1989]. Four important results may be inferred from this figure: (1) These waves are essentially beam driven waves with $\omega_{rest} \sim k_x V_\perp$. (2) The waves have strong growth rates. (3) Noting that $\omega_r < k_x V_\perp$ for all wavenumbers k_x , these waves will be doppler-shifted to low and negative frequencies (only the magnitude of the frequency is directly observable, however). (4) The higher wavenumber waves will be doppler-shifted to larger observable wave frequencies than the smaller wavenumber waves.

Figures 12a and b present the dispersion relations and growth rate curves, respectively, for the waves in the PDP (or shuttle) frame for propagation at various polar angles θ between the magnetic field and the wavevector (and fixed propagation angle $\phi = 0^\circ$ in the $X_P - Y_P$ plane. The angle ϕ is defined by $k_x = k_\perp \cos\phi$. Figure 12a explicitly shows results (3) and (4) above; note that the fastest growing waves always occur on portions of the dispersion curve where the higher wavenumber waves have higher frequencies. This is consistent with Gurnett et al.' [1990] interpretation (see Section 3 too) of the null patterns in the orbiter's plasma wake. The growing

waves are clearly confined to angles $\theta > 88.8^\circ$, with maximum growth occurring near $\theta \sim 89.6^\circ$. Thus the waves are flute modes (with wavevectors almost perpendicular to the magnetic field), as expected for lower hybrid-like waves. The waves are unstable over a range of wavenumbers from 0 - $70 \Omega_O/V_O$. In comparison, a wavenumber of $30\Omega_O/V_O$ corresponds to a wavelength of 0.8 m for the nominal ionospheric parameters defined above.

Figure 13 compares the growth rate versus frequency plots of the waves for wavevectors directed at various angles θ and a fixed angle $\phi = 0^\circ$. The frequency range over which growth occurs shows little variation with angle θ . Maximum growth is centered on a frequency of order $0.25f_{LH}$; growth should occur over the frequency range from zero frequency to about $0.5f_{LH}$. Variations in the angle ϕ for fixed θ show more effects. Figure 14 shows curves relating the wave frequency and growth rate for wavevectors directed at various angles ϕ and fixed $\theta = 89.5^\circ$. ($k_x = k_\perp \cos\phi$) for the situation in Figures 11 and 12. The fastest growing waves remain concentrated near a frequency of order $0.25f_{LH}$ while the bandwidth of growing waves decreases with increasing ϕ . However, the growth rates for the waves decrease rapidly with ϕ once $\phi > 50^\circ$ and the waves are damped for $\phi > 66^\circ$. As ϕ increases from zero the wavenumbers k_\perp of the fastest growing waves increase, so as to permit the resonance condition $\omega_{rest} \sim \Omega_{LH} \sim k_\perp \cos(\phi)V_\perp$ to be satisfied.

Lastly, we show in Figure 15 the effect of increasing the relative water ion number density n_w/n_e on the wave frequency at which the growth rate is maximum. Increasing the water ion number density increases both the center frequency and bandwidth of the growing waves. Accordingly, linear theory predicts that the spatial gradient in water ion number density near the shuttle [Cairns, 1990] (when not in the wake region) implies an increase in the center frequency, bandwidth and growth rate of the unstable waves with decreasing distance from the shuttle.

The linear theory can therefore explain wave growth from near zero frequency up to a frequency of order f_{LH} .

6.2 Discussion of the linear theory: a role for inhomogeneity and nonlinear effects.

The linear theory described above is capable of explaining the generation of waves (1) with large growth rates in the observed frequency range and range of observable wavenumbers, (2) with wavevectors essentially perpendicular to the magnetic field, as required by the free-flight observations, and (3) with wavenumber increasing with frequency, as required by Gurnett et al.'s [1990] explanation of the high frequency wave nulls during wake transits. Unusual species temperatures, densities, or preheating of the electrons are not required. Indeed higher electron temperatures should tend to damp the waves and reduce their angular range. The linear theory permits two natural explanations for the $V_{||}/V_T$ effect described in Section 2. Firstly, as argued by Cairns and Gurnett [1990], the different motions of the pick-up ions driving the waves and the ionospheric plasma convecting the waves imply that the waves will have minimum (maximum) growth lengths when $|V_{||}/V_T|$ is large (small), thereby explaining the differences in amplitude. Secondly, by analogy with the ordinary two stream instability [e.g., Gary, 1985], large values of $|V_{||}/V_T|$ imply small effective beam speeds driving the waves, and eventually zero growth rates once below some threshold speed. This latter idea will be checked in future work.

The above points show that the linear theory predicts waves in very good agreement with the observed characteristics of the intense near zone waves in the frequency range $0 - f_{LH}$. However, the linear theory is not capable of explaining the details of the frequency spectrum for the intense near zone waves or the generation of the weak near zone waves above f_{LH} . In particular, the

linear theory predicts growth between zero frequency and about the lower hybrid frequency with a peak (corresponding to the maximum growth rate) in the range $0.25 - 0.75 f_{LH}$ depending on the relative number density of water ions (Figure 15). During the XPOP roll this frequency range for the peak growth rate corresponds to a range from 1.5 – 7.5KHz, well above the observed low frequency peak at about 178 Hz and well below the observed peak near the lower hybrid frequency. This difficulty in explaining the details of the observed frequency spectrum should be expected for at least three reasons. Firstly, the preliminary nature of this linear theory, secondly the neglect of inhomogeneous effects in the strongly inhomogeneous shuttle environment, and thirdly the neglect of nonlinear effects which are often vital in determining the wave spectrum.

Improvements to the linear theory can be expected in a number of ways. A more exact representation of a beam arc distribution might involve superposing a beam distribution onto a lower level ring distribution and considering both components in the linear theory. Cairns and Gurnett [1990] have considered generation of doppler-shifted lower hybrid waves by a ring distribution. They find that growth is likely to be most effective near zero frequency, although wave growth up to frequencies of order $2f_{LH}$ is possible. Thus, considering the contribution of the ring component to the water ion distribution function might lead to a second peak in the growth rate at low frequencies, thereby leading to an explanation for the observed peak near 178 Hz for the near zone waves. In addition, waves driven by ring distributions well away from the immediate vicinity of the shuttle [Cairns and Gurnett, 1990] and convecting into the near zone region might explain some of the low frequency near zone waves. However, the free-flight data generally show low wave levels when upstream from the shuttle. Further improvements to the linear theory could be made by including the effects of charge-exchange and neutral-ion collisions to the linear dispersion equation. However, test solutions including these effects

show little change from the corresponding solutions of equation (1). Therefore, in this paper, although we recognize that potential exists for modifying the linear theory to better explain the observational data, we defer further examination of the linear theory to future work on the grounds that inhomogeneity effects and nonlinear effects are greatly more favored means to produce the details of the observed wave spectrum.

Inhomogeneity effects may be expected to limit effective linear growth of the waves (i.e., the wavevector for a wave with frequency ω must change with position for linear theory to predict further growth) and cause evolution of the wave spectrum away from the predictions of linear theory. Figure 15 above demonstrates the significant changes in wave frequency and growth rate that should accompany the increasing water ion number density expected near to the space shuttle [Cairns, 1990]. The arguments of Cairns and Gurnett [1990] indicate that the existence of the V_{\parallel}/V_T effect described in Section 2 is consistent with spatial inhomogeneity limiting growth of the waves. Spatial inhomogeneity can also couple drift modes to sources of free energy [e.g., Simon et al., 1980; Pickett et al., 1989]. Thus, as suggested by Pickett et al. [1988] in another, related context, a drift mode instability coupling to the source of free energy in the water ion beam near to the shuttle may provide an explanation for the low frequency peak near 178 Hz in the near zone waves. This suggestion will be pursued elsewhere.

Nonlinear processes involving lower hybrid waves, such as scattering off thermal ions, decay processes involving ion acoustic waves, modulational instabilities and strong turbulence processes, have been discussed in the literature [e.g., Musher et al., 1986]. Detailed discussions of these possibilities are not appropriate here. However, we note that the ratio of wave electric field energy to thermal plasma energy is of order 10^{-5} (for $n_e = 10^{11} m^{-3}$) while the ratio of the total water ion kinetic energy to the thermal plasma energy is of order 5 for $n_w/n_e = 0.1$.

Moreover, we point out that the linear theory predicts growth at wavelengths similar in magnitude, but usually smaller for the higher frequency waves, to the effective antenna length during the XPOP roll (1.15 meters) and free-flight mission (3.89 meters). It is therefore probable that the high wave levels seen (total average broadband field of order 50 mV/m) are smaller than the actual wave levels in the plasma. These wave levels are considerable and imply that nonlinear processes, including strong turbulence processes, warrant considerable attention. Further support for consideration of nonlinear effects comes on comparing the timescales for growth and convection of the waves. For waves with a linear growth rate of $50\Omega_O$ typical in Figure 15, 10 e-folding periods corresponds to a time of 10^{-3} seconds. During this time period a wave packet would be convected a maximum distance of 8 meters (given the shuttle's orbital speed of 7.8 Kms^{-1}) while a wave electric field would increase by a factor of 2×10^4 . This distance is small compared with the expected extent of the region near the shuttle with beam distributions of water ions ($\sim 30m$ [Cairns, 1990]) and comparable in size with the expected scale length of the gradient in the neutral water number density within 10 meters of the space shuttle.

Nonlinear processes appear to be occurring in simulations relevant to the shuttle problem which we have performed in collaboration with G. Lu and C.K. Goertz. The 2-D electrostatic code used, the code PANIC [Machida and Goertz, 1988], incorporates a time- and spatially-varying rate of charge-exchange, consistent with collisional charge-exchange between ionospheric oxygen and a spherical water gas cloud whose number density varies inversely with radial distance squared. This code is therefore suitable for studying the long timescale behaviour of waves near the shuttle. Preliminary simulation runs show an initial growth phase of low frequency waves (relative to the lower hybrid frequency), followed by a later phase in which the wave spectrum splits into two components, one near zero frequency and one near the lower hybrid frequency.

These simulations therefore appear to produce a two peaked frequency spectrum similar to the observed wave spectrum. Further work is required to see whether this agreement is fortuitous and to investigate the physics of these processes.

6.3 Waves observed above several times the lower hybrid frequency

The wave data indicate that the broadband near zone waves extend up to frequencies of order 50 KHz, corresponding to 5 - 10 times the lower hybrid frequency. The wave spectrum above the lower hybrid frequency shows only a smooth decrease without apparent structure. Linear theory for doppler-shifted lower hybrid waves driven by a ring distribution of water ions [Cairns and Gurnett, 1990] can explain wave frequencies up to about two times the lower hybrid frequency. Similarly the beam-driven doppler-shifted lower hybrid waves considered in this paper are restricted (by the linear theory) to frequencies below the lower hybrid frequency. Therefore, linear theories involving ring or beam distributions of water ions appear incapable of explaining the weak observed waves above about $2f_{LH}$. We note that Hwang et al.'s [1987] theory predicts growth above the lower hybrid frequency. However, Hwang et al.'s waves do not have wavevectors perpendicular to the magnetic field as implied by the free-flight data in Section 4 even for wave frequencies well above $2f_{LH}$. Combining this point with the absence of a localized peak in the observed wave spectrum above f_{LH} at frequencies similar to those in Hwang et al.'s theory (10 - 40 KHz) implies that Hwang et al.'s theory is not a viable explanation for the observed waves above a few times the lower hybrid frequency. Investigations into nonlinear effects and mechanisms involving spatial inhomogeneity appear promising directions for further research into the origin of these high frequency waves.

7 Implications of the V_{\parallel}/V_T effect for shuttle missions

Detailed observations of plasma waves constitute an important diagnostic for active space experiments and investigations into the natural ionosphere. The data presented in this paper show that the intense broadband waves in the immediate vicinity of the space shuttle have total average electric fields of order 50 mV/m in the frequency range from 30 Hz to 10 KHz (the lower hybrid frequency). Removing this high, and probably dominating, background of waves should therefore be an important consideration in designing shuttle missions and orbiting facilities, such as the proposed space station, intended as bases for research involving plasma waves. The dramatic V_{\parallel}/V_T effect observed for the near zone waves (Figure 2) offers a means to minimize the levels of orbiter-associated waves, as pointed out previously by Cairns and Gurnett [1990] for waves observed during the free-flight portion of the Spacelab-2 mission. In particular, the orbit of the platform should be designed so that $|V_{\parallel}/V_T|$ is close to 1 for as much of the orbit as possible. Figure 2b indicates that a minimum value $|V_{\parallel}/V_T| = 0.7$ should be chosen at this orbital height. These orbits are highly inclined with respect to Earth's equatorial plane. However, due to orbital constraints, present-day launching sites and political realities, another approach is likely to be more attainable [e.g., Cairns and Gurnett, 1990]: the observing instruments and experiment package should be placed at a sufficient distance upstream from the shuttle or other outgassing facility to be outside the water/outgas cloud. Data from the PDP free-flight mission suggest that distances of order 1 Km are appropriate [Paterson and Frank, 1989].

Nevertheless, further research into the origin and usefulness of the observed V_{\parallel}/V_T effect is advisable. Explanations for the offsets between the centers of the wave nulls and the peaks in V_{\parallel}/V_T should be pursued. Furthermore, as pointed out by Cairns and Gurnett [1990], an

upper limit on $|V_{\parallel}/V_T|$ may exist due to driving of ion acoustic-like wave instabilities by the parallel drift between the water pick-up ions and the ionospheric plasma. These instabilities are expected to be strongly temperature-dependent, implying possible variations with height and time of day in the ionosphere. Further work is required to investigate this possibility.

8 Conclusions

This paper contains a detailed observational characterization of the plasma waves observed within about 10 meters of the space shuttle during the XPOP roll period of the Spacelab-2 mission. The frequency distribution of wave electric fields is best interpreted in terms of three components. The first, and primary, component is a uniform high level of waves covering the frequency range from 31 Hz to 10 KHz with only minor variations in amplitude with frequency. Two superposed peaks in this frequency range mark the two other components, and the wave levels decrease rapidly with increasing frequency above 10 KHz. The two superposed components have electric fields of order twice the steady level. The second component is defined by the low frequency peak in the range 100-178 Hz. This low frequency component merges smoothly back into the steady level of waves. The third component is found near the lower hybrid frequency. The spectral density and electric field amplitude of this component follow both the magnitude and the trend of the theoretical lower hybrid frequency. Wave power is observed consistently out to frequencies of order 56 KHz. No evidence is found for a high frequency component localized above about 10 KHz due to the smooth fall-off in the spectral density and integrated electric field profiles seen at these frequencies. The waves show a pronounced amplitude and frequency variation with the quantity V_{\parallel}/V_T which measures the angle between the ionospheric magnetic

field and the shuttle's velocity vector. Very low wave levels and small frequency extents are observed when V_{\parallel}/V_T is near its maximum value, i.e., the shuttle is moving as close to parallel to the magnetic field as possible, and the highest wave levels and extents in frequency are observed when V_{\parallel}/V_T is near zero. This implies that the waves are plausibly driven by water pick-up ions [e.g., Cairns and Gurnett, 1990]. Strong analogies with the spectral characteristics (two peaks, one at the lower hybrid frequency and one near zero frequency) and the V_{\parallel}/V_T effect observed during the free-flight portion of the Spacelab-2 provide further hints that the near zone waves are driven by pick-up water ions. Observations of the waves below about 20 KHz during the free-flight mission imply that the near zone waves have wavevectors oriented perpendicular to the magnetic field. The observation of nulls in the wave data which occur first at higher frequencies as the PDP spacecraft enters the density hole in the orbiter's wake imply that the higher frequency waves have higher wavenumbers (shorter wavelengths) than the lower frequency waves [Gurnett et al., 1990]. Lastly, the observed near zone waves have a total measured average broadband (frequency-integrated) electric field of order 50 mV/m. This field strength implies a ratio of electric field energy density to thermal plasma energy density of order 10^{-5} . Together with the prediction from linear theory that waves should grow with linear wavelengths smaller than the antenna length, so that the true field strength in the plasma is underestimated, this wave level implies that nonlinear effects may be important in understanding the evolution of the waves.

Detailed theoretical work on the near zone waves is also performed in the paper. Recently, Hwang et al. [1987] developed a theory for the near zone waves involving ion acoustic and ion-ion acoustic instabilities driven by the secondary ion streams observed in the near vicinity of the shuttle [Stone et al., 1983; 1986]. Here, we showed that this theory is inconsistent

with the frequency distribution and wavevector orientations of the observed waves. A new theory involving doppler-shifted lower hybrid waves driven by beam-like distributions of water ions [Cairns, 1990] in the near vicinity of the space shuttle is proposed and developed using linear theory. The relevant instability is the modified-two-stream instability. This linear theory can explain generation of waves with (1) frequencies ranging from near zero frequency to the lower hybrid frequency, (2) wavevectors essentially perpendicular to the magnetic field, (3) wavenumbers increasing with wave frequency, (4) wavelengths observable by the PDP antenna, and (5) natural explanations for the V_{\parallel}/V_T effect. These properties are all consistent with the properties of the observed near zone waves and provide strong support for this theory. However, the linear theory cannot explain the details of the observed frequency spectrum of the waves. In particular, the theory predicts growth over the frequency range of the primary, uniform component of the waves, but with a peak growth rate in the range $0.25 - 0.75 f_{LH}$ and no peaks at the frequencies of the two observed peaks (or components) in the wave spectrum at low frequencies 100 - 178 Hz and the lower hybrid frequency itself. The linear (beam) theory cannot explain the observed low level waves above the lower hybrid frequency. Explanations for the differences between the linear theory and the observed wave spectrum are discussed in terms of refining the linear theory, the effects of the strongly spatially inhomogeneous near zone environment and nonlinear effects. Including the effect of the ring component to the beam-arc distributions of water ions in the near vicinity of the space shuttle [Cairns, 1990] should lead primarily to increased growth at low frequencies, as well as less favoured growth up to frequencies near $2f_{LH}$ [Cairns and Gurnett, 1990]. Convection of the growing waves through the spatially inhomogeneous shuttle environment, and so the varying wavenumbers required for a wave of a given frequency to be linearly unstable, is expected to modify the frequency spectrum of growing

waves. Furthermore, coupling of a drift mode associated with the density gradients to the free-energy source in the water ions might lead to an instability at low frequencies [e.g., Simon et al., 1980; Pickett et al., 1989] thereby perhaps explaining the component near 100 - 178 Hz. The high wave levels imply that nonlinear effects, such as decay processes involving ion acoustic waves, modulational instabilities and strong turbulence processes [e.g., Musher et al., 1986], may be very important in determining the frequency spectrum of the waves. Preliminary simulations of the shuttle environment run in collaboration with G. Lu and C.K. Goertz also indicate that nonlinear processes are important. In summary, while the linear theory developed here successfully explains many of the characteristics of the near zone waves, further theoretical work involving the effects of wave nonlinearities and spatial inhomogeneity is required to explain the details of the observed wave frequency spectrum. Finally, we note that the V_{\parallel}/V_T effect observed for the near zone waves has similar implications for design of future shuttle missions to those described by Cairns and Gurnett [1990]: orbits for shuttle missions requiring minimal plasma wave backgrounds should be highly inclined to Earth's equatorial plane with $|V_{\parallel}/V_T| > 0.7$ over as much of the orbit as possible. Otherwise, these missions should be performed using free-flying spacecraft located at least 1 Km upstream of any outgassing facility.

Acknowledgements

We acknowledge financial support from NASA Grant NAGW-1488 from NASA Headquarters and NASA Grant NAG3-449 from NASA/Lewis Research Center. Helpful discussions with J.S. Pickett and W.S. Kurth concerning the Spacelab-2 mission are also gratefully acknowledged.

References.

- Cairns, I.H., Electrostatic wave generation above and below the plasma frequency by electron beams, Phys. Fluids B, 1, 204, 1989.
- Cairns, I.H., Transition from ring to beam arc distribution functions of water ions with distance upstream from the space shuttle orbiter, J. Geophys. Res., in press, 1990.
- Cairns, I.H., and D.A. Gurnett, Control of plasma waves associated with the space shuttle by the angle between the orbiter's velocity vector and the magnetic field, submitted, J. Geophys. Res., 1990.
- Gary, S.P., and N. Omidi, The ion-ion acoustic instability, J. Plasma Physics, 37, 45, 1987.
- Grebowsky, J.M., H.A. Taylor, Jr., M.W. Pharro III, and N. Reese, Thermal ion perturbations observed in the vicinity of the space shuttle, Planet. Space Sci., 35, 501, 1987.
- Gurnett, D.A., W.S. Kurth, J.T. Steinberg, and S.D. Shawhan, Plasma wave turbulence around the shuttle: Results from the Spacelab-2 flight, Geophys. Res. Lett., 15, 760, 1988.
- H.D. Hagstrum, Reflection of noble gas ions at solid surfaces, Phys. Rev., 123, 758, 1961.
- Hwang, K.S., N.H. Stone, K.H. Wright, Jr., and U. Samir, The emissions of broadband electrostatic noise in the near vicinity of the shuttle orbiter, Planet. Space Sci., 35, 1373, 1987.
- Krall, N.A., and P.C. Liewer, Low-frequency instabilities in magnetic pulses, Phys. Rev. A, 4, 2094, 1971.

- Ma, T.-Z., and D.A. Gurnett, Interpretation of electrostatic noise observed by Voyager 1 in Titan's wake, J. Geophys. Res., 92, 8595, 1987.
- Machida, S, and C.K. Goertz, The electromagnetic effect on the critical ionization velocity process, J. Geophys. Res., 93, 11495, 1988.
- Meyer, O., G. Linker, and F. Kappeler, Ed.s, Ion Beam Surface Layer Analysis, Plenum, New York, 1985.
- Murphy, G.B., S.D. Shawhan, L.A. Frank, N. D'Angelo, D.A. Gurnett, J.M. Grebowsky, D.L. Reasoner and N. Stone, Interaction of the space shuttle orbiter with the ionospheric plasma, Spacecraft/Plasma Interactions and their Influence on Field and Particle Measurements, ESA SP-198, 73, 1983.
- Musher, S.L., A.M. Rubenchik, and I.Ya. Shapiro, Nonlinear effects in the propagation of an ion beam across a magnetic field, Sov. Phys. JETP, 63, 519, 1986.
- Papadopoulos, K.D., On the shuttle glow (the plasma alternative), Radio Science, 19, 571, 1984.
- Paterson, W.R., and L.A. Frank, Hot ion plasmas from the cloud of neutral gases surrounding the space shuttle, J. Geophys. Res., 94, 3721, 1989.
- Pickett, J.S., N. D'Angelo, and W.S. Kurth, Plasma density fluctuations observed during space shuttle orbiter water releases, J. Geophys. Res., 94, 12081, 1989.
- Shawhan, S.D., Description of the Plasma Diagnostics Package (PDP) for the OSS-1 shuttle mission and JSC chamber test in conjunction with the fast pulse electron gun (FPEG), Artificial particle Beams in Space Plasma Studies, ed. B. Grandel, Plenum, New York, 419, 1982.

- Shawhan, S.D., G.B. Murphy, and J.S. Pickett, Plasma Diagnostics Package initial assessment of the shuttle orbiter plasma environment, J. Spacecraft Rockets, 21, 387, 1984.
- Simons, D.J., M.B. Pongratz, and S.P. Gary, Prompt striations in ionospheric barium clouds due to a velocity space instability, J. Geophys. Res., 85, 671, 1980.
- Stone, N.H., U. Samir, K.H. Wright, Jr., D.L. Reasoner, and S.D. Shawhan, Multiple ion streams in the near vicinity of the space shuttle, J. Geophys. Res., 10, 1215, 1983.
- Stone, N.H., K.H. Wright, Jr., K.S. Hwang, U. Samir, G.B. Murphy, and S.D. Shawhan, Further observations of space shuttle plasma-electrodynamic effects from OSS-1/STS-3, Geophys. Res. Lett., 13, 217, 1986.
- Tribble, A.C., J.S. Pickett, N. D'Angelo, and G.B. Murphy, Plasma density, temperature, and turbulence in the wake of the shuttle orbiter, Planet. Space Sci., 37, 1001, 1989.

Figure Captions

Figure 1. The geometry of the XPOP roll during the Spacelab-2 mission. The shuttle rolls about the nose-tail or \underline{X}_{OBAS} axis while its orbital velocity is perpendicular to the \underline{X}_{OBAS} axis. The 'pick-up' coordinate system $X_p - Y_p - Z_p$ is also defined.

Figure 2. (a) A Helios-MFR color spectrogram for the period of the XPOP roll. Spectral density is color-coded. Black lines show the variation in the electron gyrofrequency f_g and the lower hybrid frequency f_{LH} . (b) The variation in the quantity $V_{||}/V_T$, measuring the ratio of the shuttle's orbital velocity parallel to the magnetic field and the orbital speed, during the XPOP roll. The nulls in the wave data are correlated with large values of $V_{||}/V_T$.

Figure 3. Spectrogram of Helios-MFR data showing the color-coded squared electric field measured in each channel bandwidth. Two peaks are evident, one near 100 Hz and one at the lower hybrid frequency.

Figure 4 (a) Spectral density as a function of channel frequency for the period 01:56 to 01:58 during the XPOP roll. The solid curve shows the average spectral density, while the long and short dashed curves show the maximum and minimum observed spectral densities, respectively, during this period. The dotted line shows the calibrated receiver noise level (before launch). (b) Similar to (a), but for the period 01:45 - 02:10.

Figure 5. Ratio $R(f)$ of the average electric field in a frequency bandwidth divided by the total average broadband field as a function of frequency (see text for a detailed definition). The wave fields are essentially constant from 30 Hz to 10 KHz and sharply lower at higher frequencies, reaching the background level by 100 KHz. Two peaks, by a factor of 2, are

seen in the average wave fields: one at low frequencies near 178 Hz, and one at the lower hybrid frequency.

Figure 6. Roll angle versus time for the period 01:30 to 02:30 during the XPOP roll. A phase angle of 0° corresponds to the PDP being in the center of the shuttle's wake.

Figure 7. A Helios-MFR spectrogram for the period 02:30 - 02:47, Day 213, during the free-flight mission. Spectral density is color-coded. White lines show the electron gyrofrequency and lower hybrid frequency. Signals associated with spacecraft interference, the FPEG experiment and thruster firings are indicated in the figure and text. The signals marked 'connection event' occur while the PDP is magnetically connected to the space shuttle. These data are interpreted in terms of observations of the shuttle's near zone waves, implying that these waves are flute modes with wavevectors approximately perpendicular to the magnetic field.

Figure 8. Variations in the coordinates X_p , Y_p and Z_p of the PDP relative to the space shuttle as a function of time for the data shown in Figure 7.

Figure 9. Comparisons of the spectral density profiles of the waves observed during the free-flight connection event (02:39:40 - 50, day 213) and during the XPOP roll (01:45 - 02:10, day 212). These curves are qualitatively similar with magnitudes differing by a factor of order 30 (the antenna lengths differ by a factor of order 3). These data support the interpretation that the connection event corresponds to observation of the near zone waves at a 200 meter distance along the magnetic field, implying that the near zone waves are flute modes.

Figure 10. Illustration of a ‘beam arc’ distribution function of water ions in the $V_{X_p} - V_{Y_p}$ phase space. Water ions have a gyrocenter drift $(-V_{\perp}, 0, 0)$ and gyrospeed of order V_{\perp} . Particle gyromotion corresponds to movement along the ‘pick-up’ ring in the clockwise direction.

Figure 11. Dispersion diagram for a water ion beam with $n_w/n_e = 0.05$, $V_{\parallel} = 0$, other plasma parameters as given in the text and waves with wavevectors defined by $\theta = 89.9^\circ$ and $\phi = 0^\circ$. The damped lower hybrid mode and growing beam mode waves are shown. This figure is strongly reminiscent of the ordinary beam instability for growth of Langmuir waves.

Figure 12. (a) Observable wave frequencies (magnitudes) as a function of wavenumber for various angles θ (but $\phi = 0^\circ$) and the plasma parameters of Figure 11. (b) Growth rates as a function of wavenumber for various angles θ . The waves are flute mode waves tightly restricted to perpendicular propagation and the (observable) wave frequency increases with wavenumber.

Figure 13. Growth rates versus (observable) wave frequencies as a function of angle θ (with $\phi = 0^\circ$). Maximum growth rates occur near $0.25 f_{LH}$.

Figure 14. Growth rates versus (observable) wave frequency as a function of angle ϕ and fixed angle $\theta = 89.5^\circ$. Growth is restricted to angles $\phi < 66^\circ$.

Figure 15. Growth rates versus (observable) wave frequency as a function of beam density n_w/n_e for angle $\phi = 0^\circ$ and angles θ with the maximum growth rate. Increasing the beam density increases the maximum growth rate, the frequency at which maximum growth occurs, and the extent of the growing waves in frequency, wavenumber and wavevector directions.

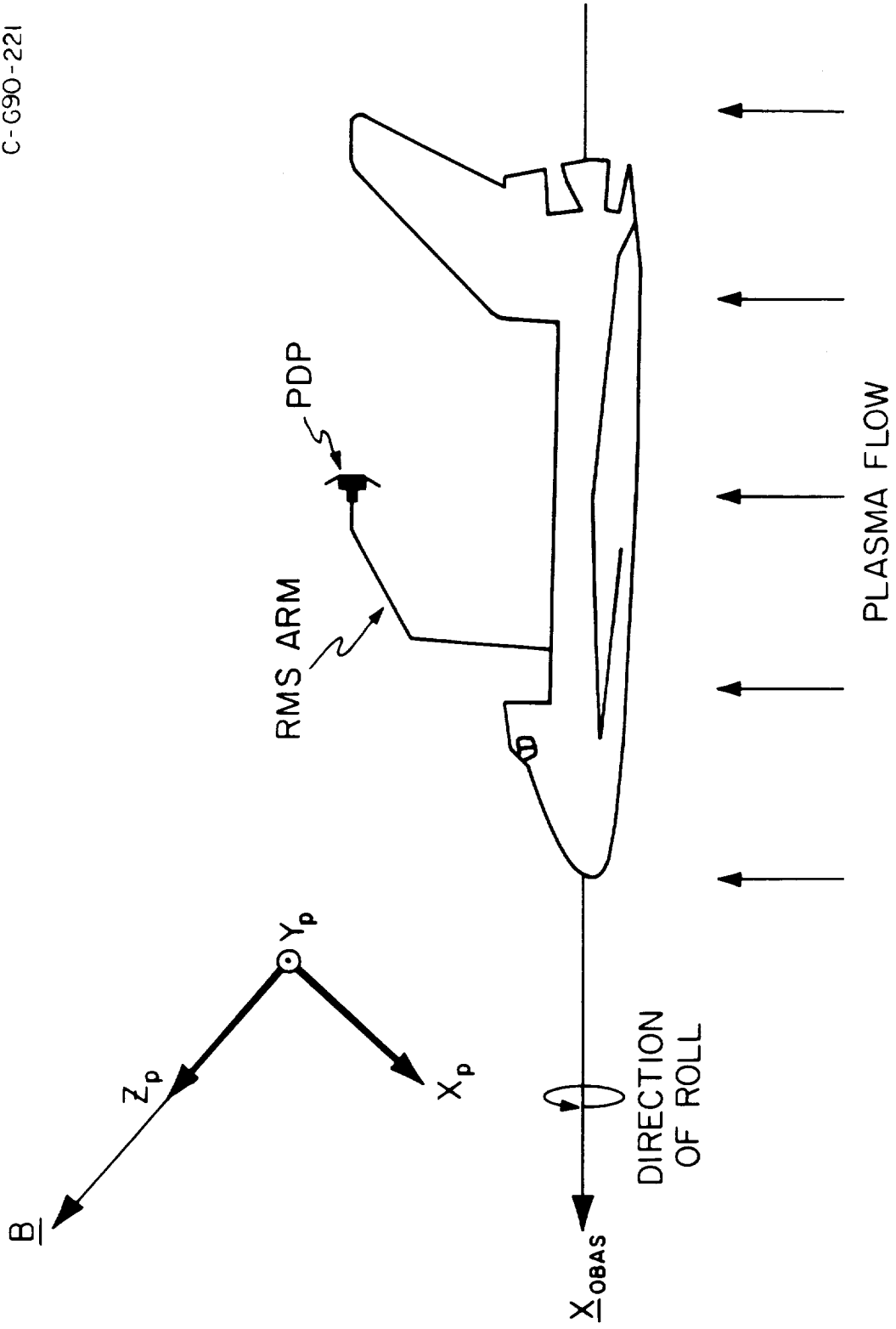
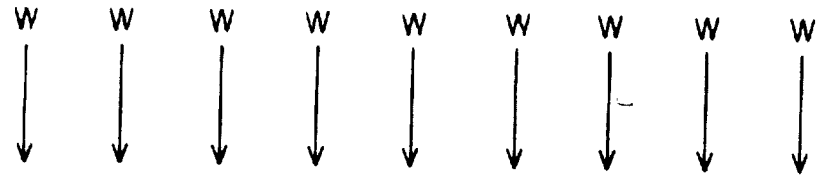
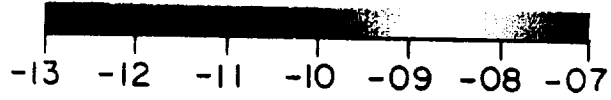


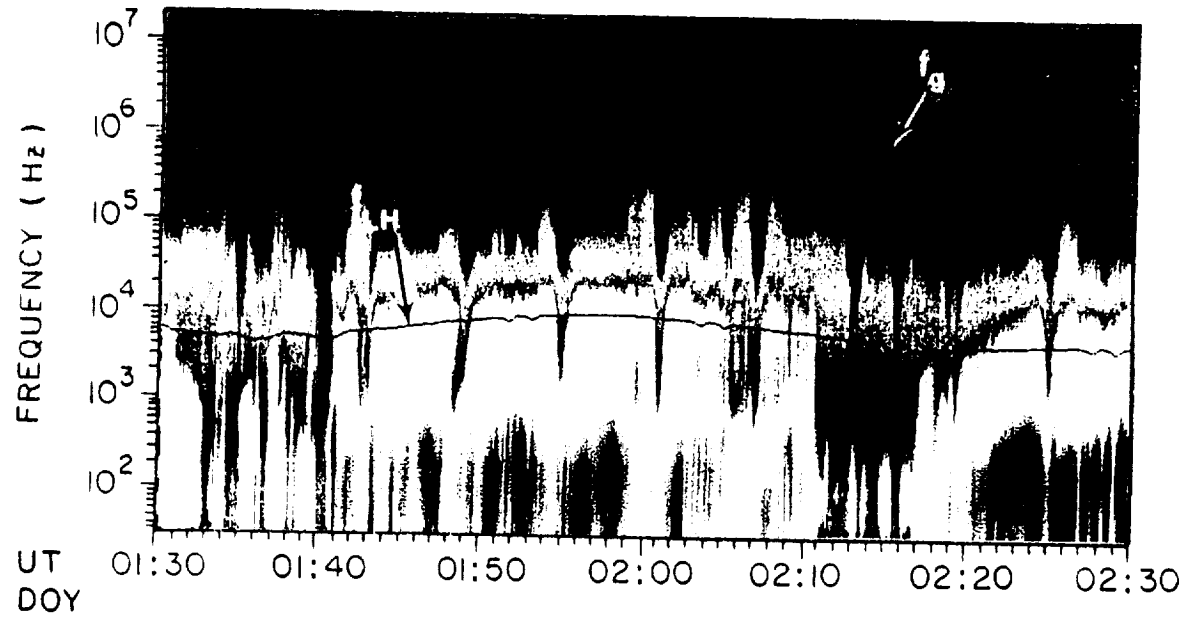
Figure 1



LOG SPECTRAL DENSITY ($V^{**2}/M^{**2}/Hz$)



(a)



(b)

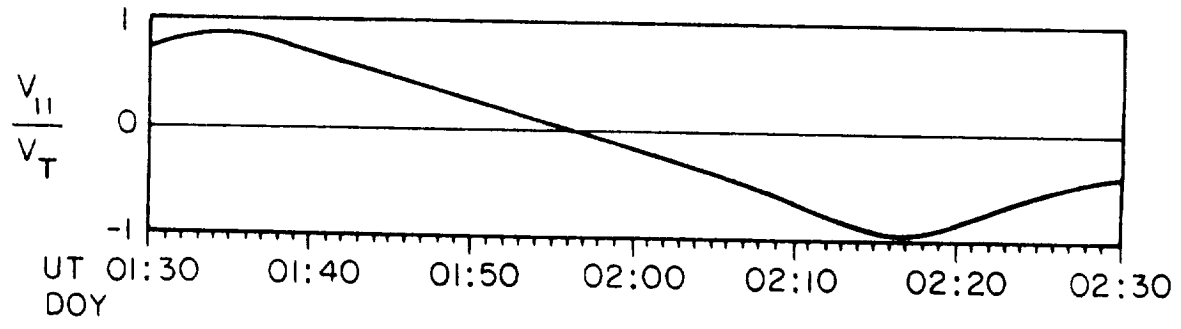


Figure 2

A-690-183

LOG ELECTRIC FIELD SQUARED (V**2/M**2)

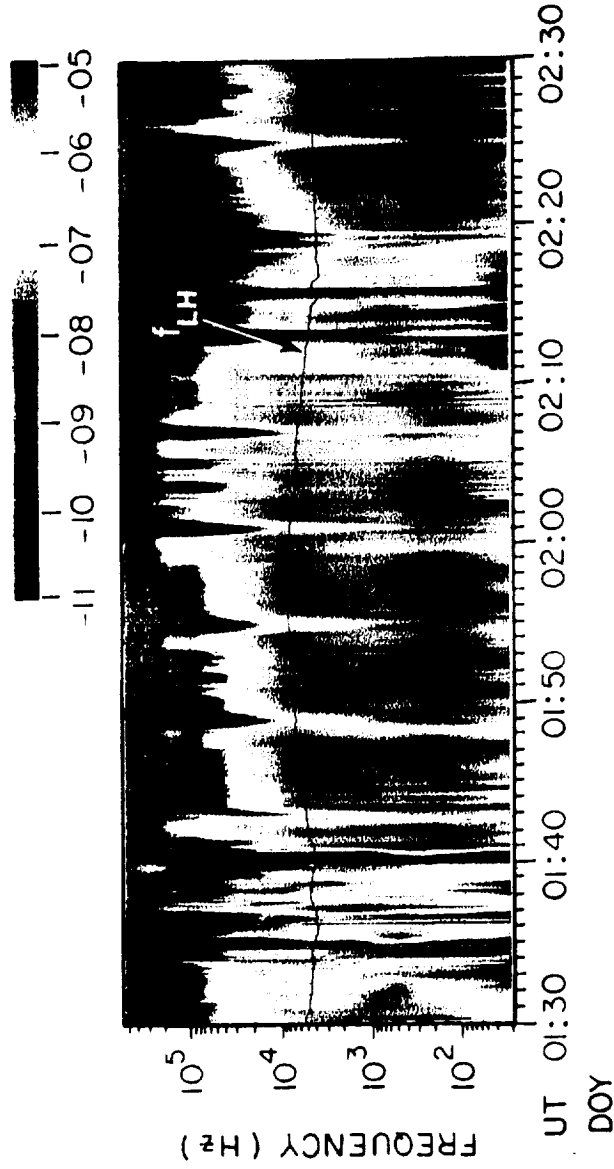


Figure 3

PDP PWS
85/212/01:56:00.000
85/212/01:58:00.000

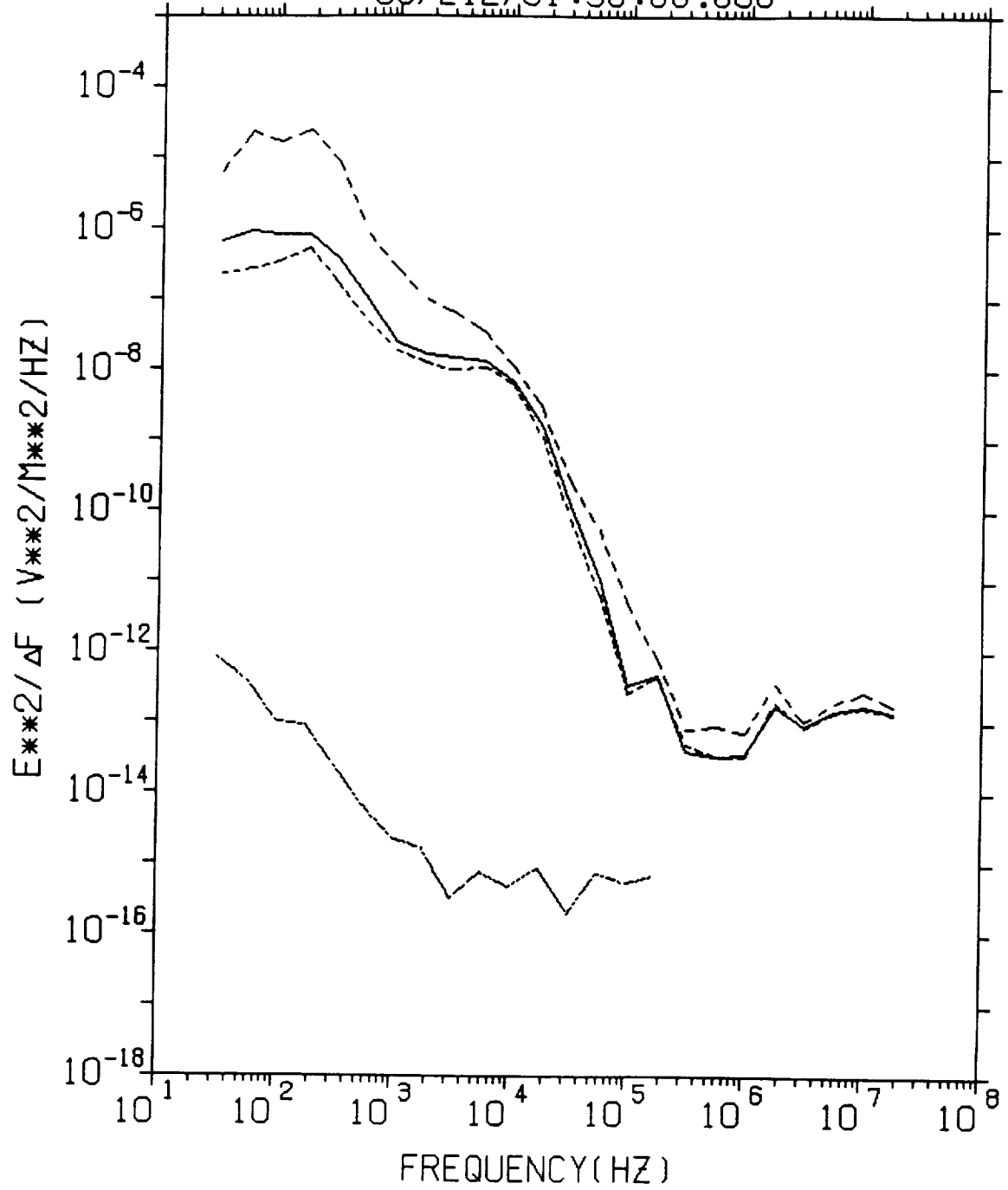


Figure 4a

PDP PWS
85/212/01:45:00.000
85/212/02:10:00.000

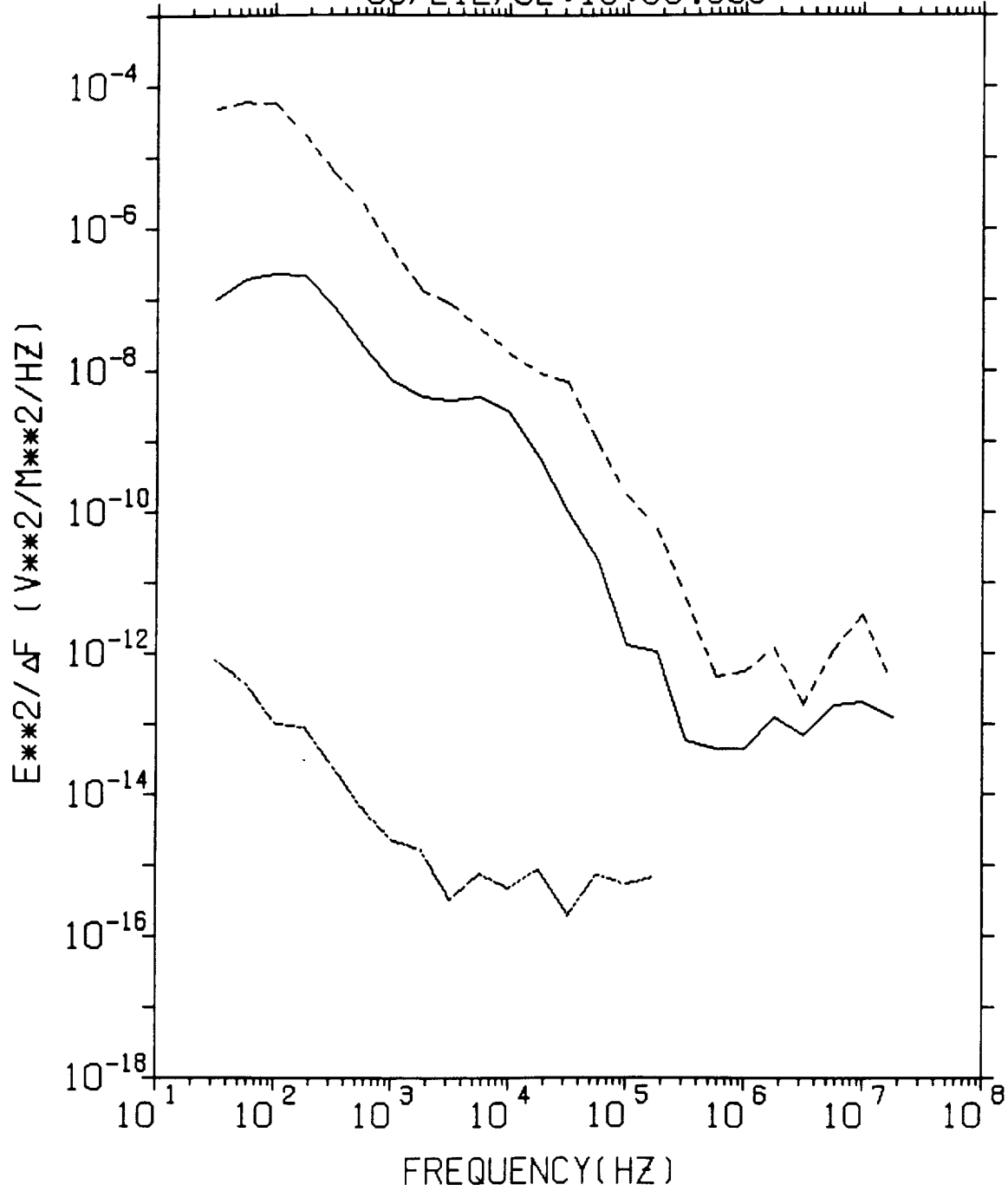


Figure 4b

POP ROLL RELATIVE ELECTRIC FIELDS

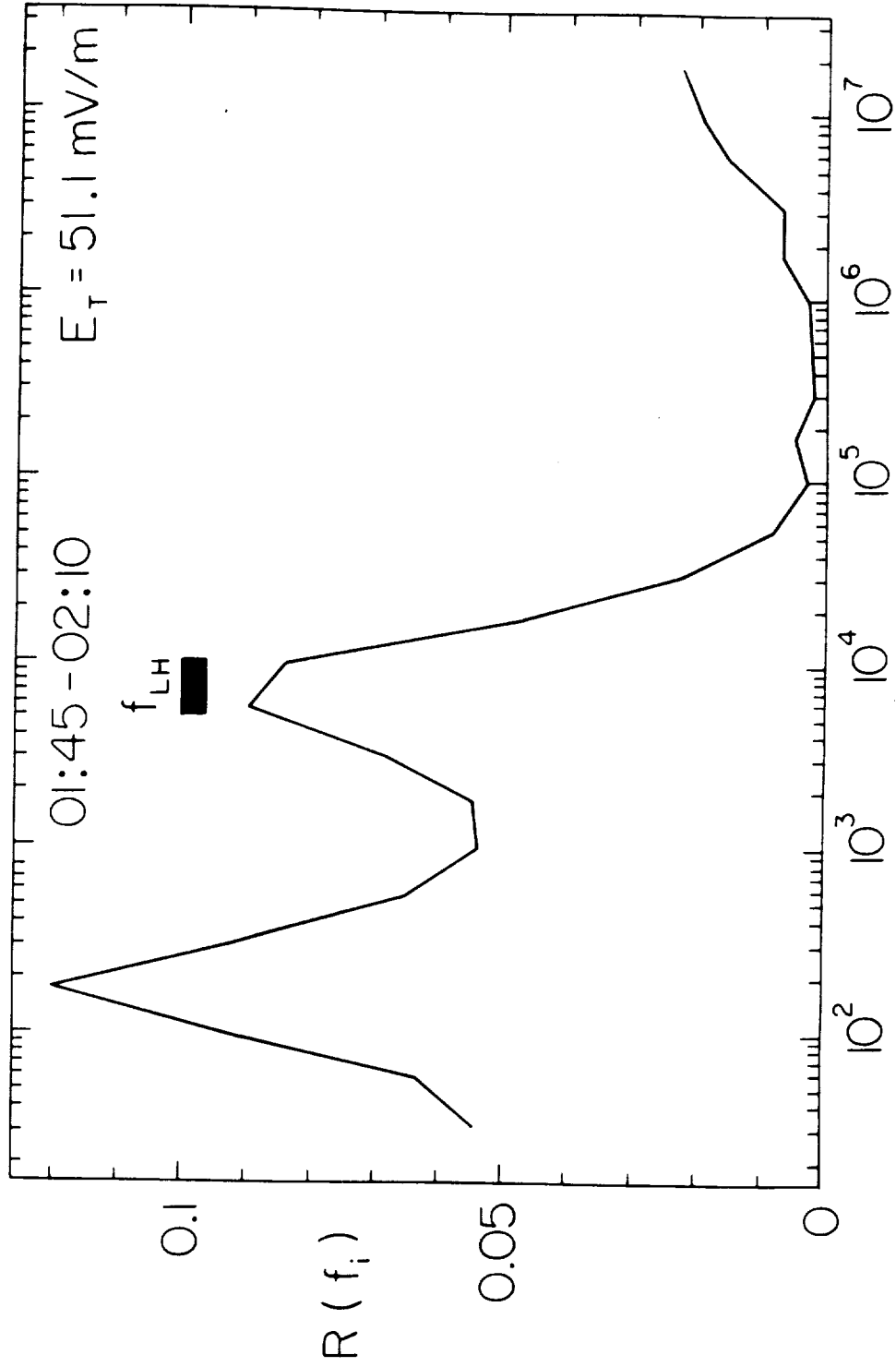


Figure 5

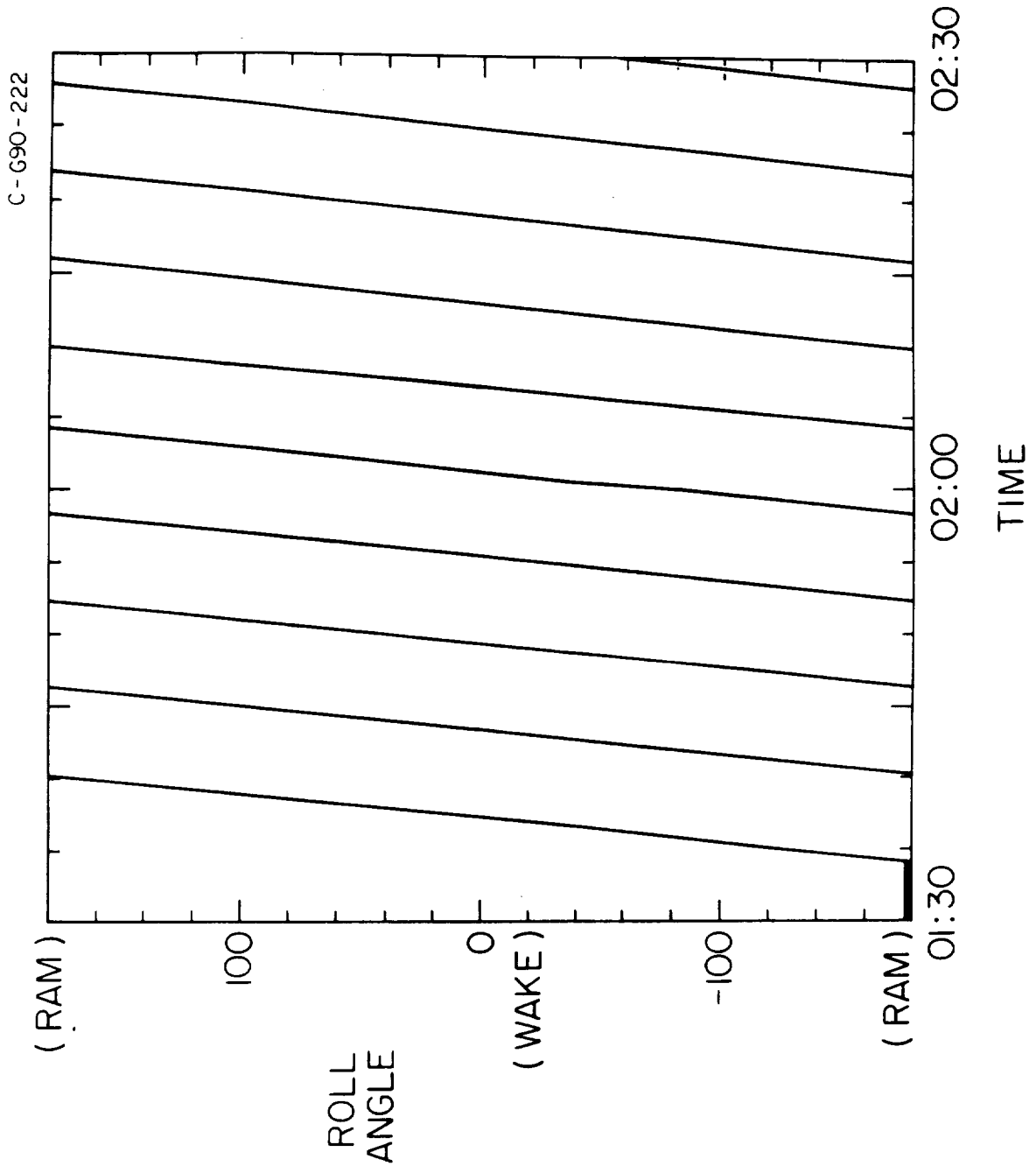


Figure 6

B. G90 174

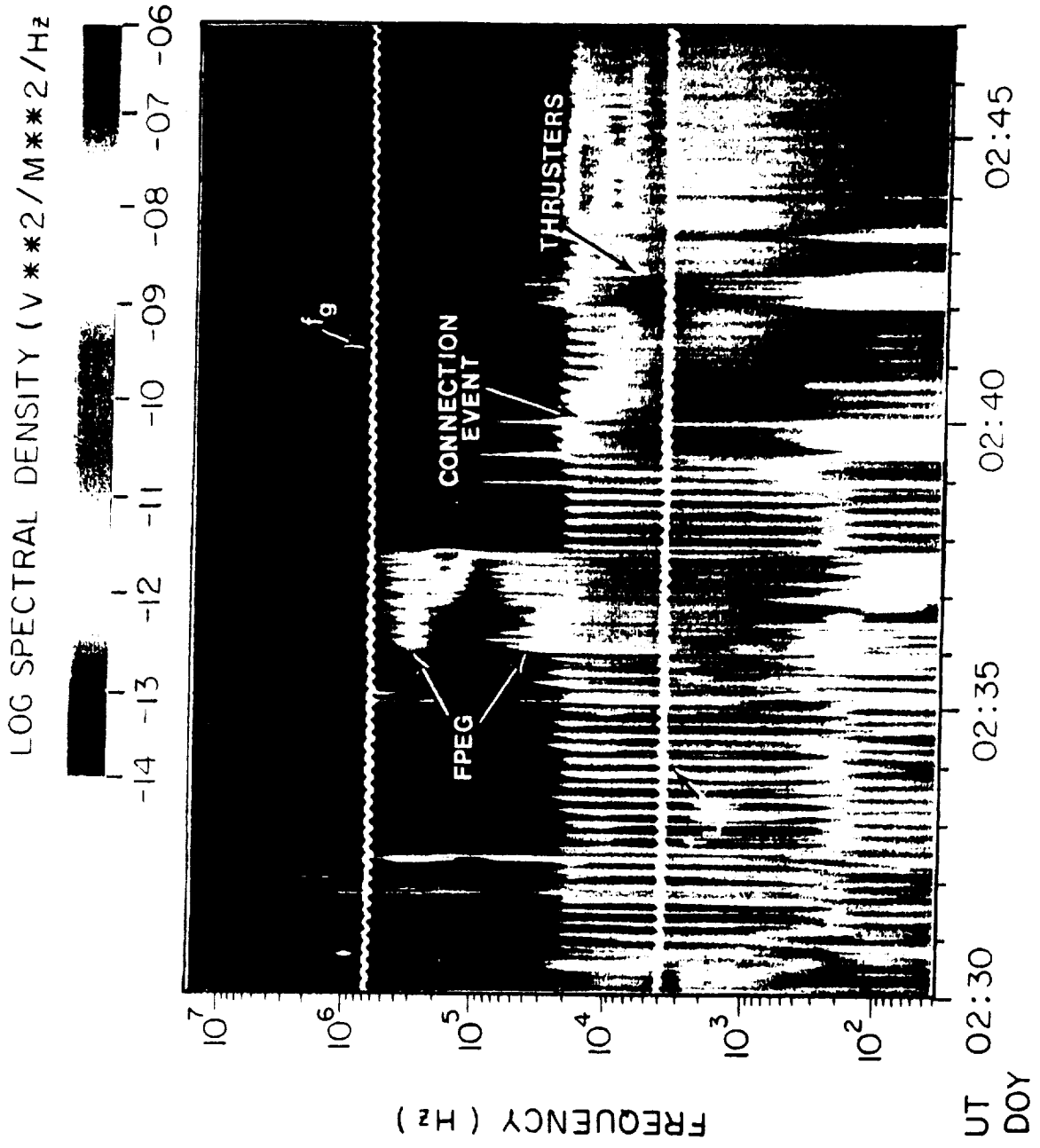


Figure 7

FREE-FIGHT CONNECTION EVENT

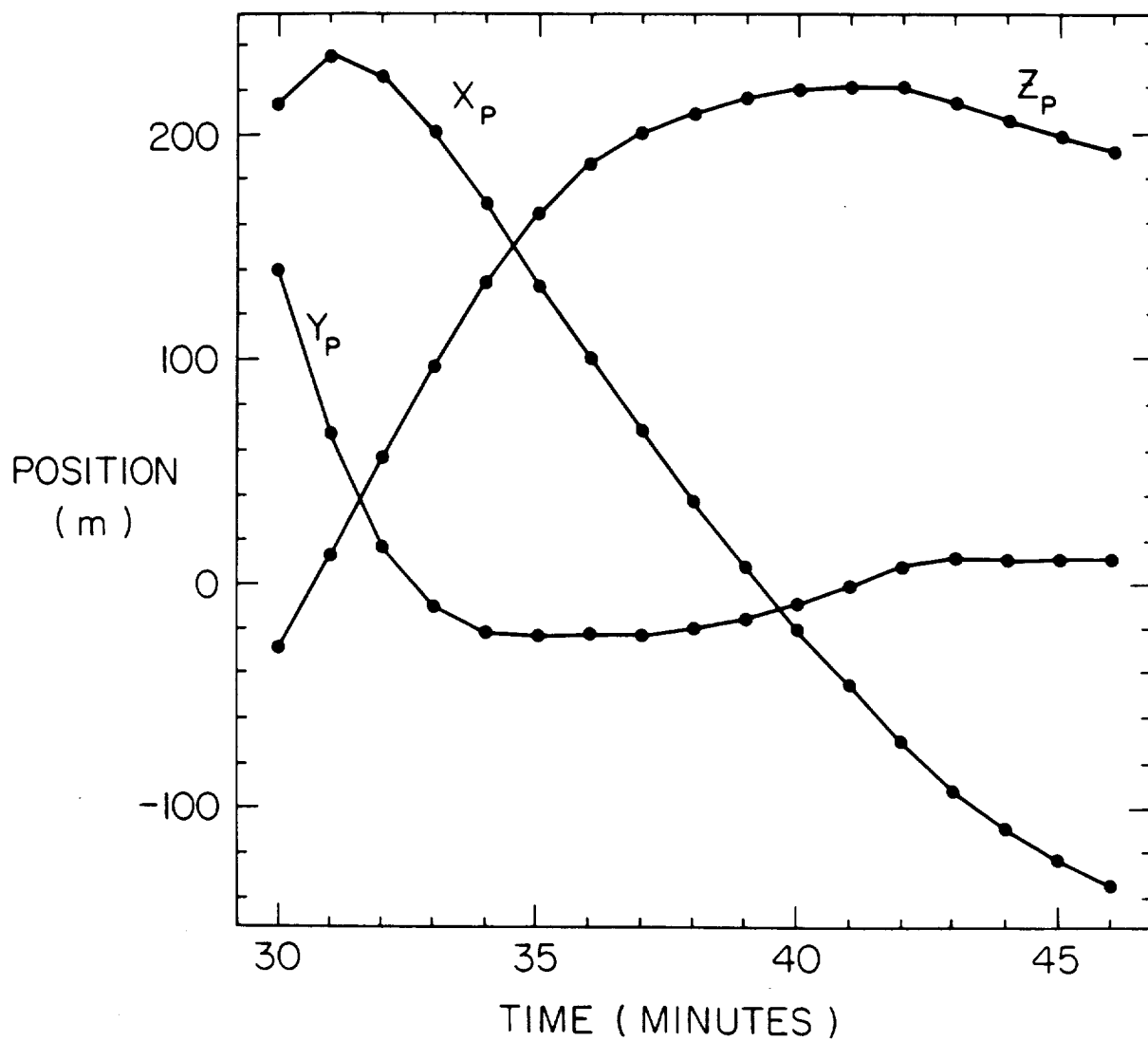


Figure 8

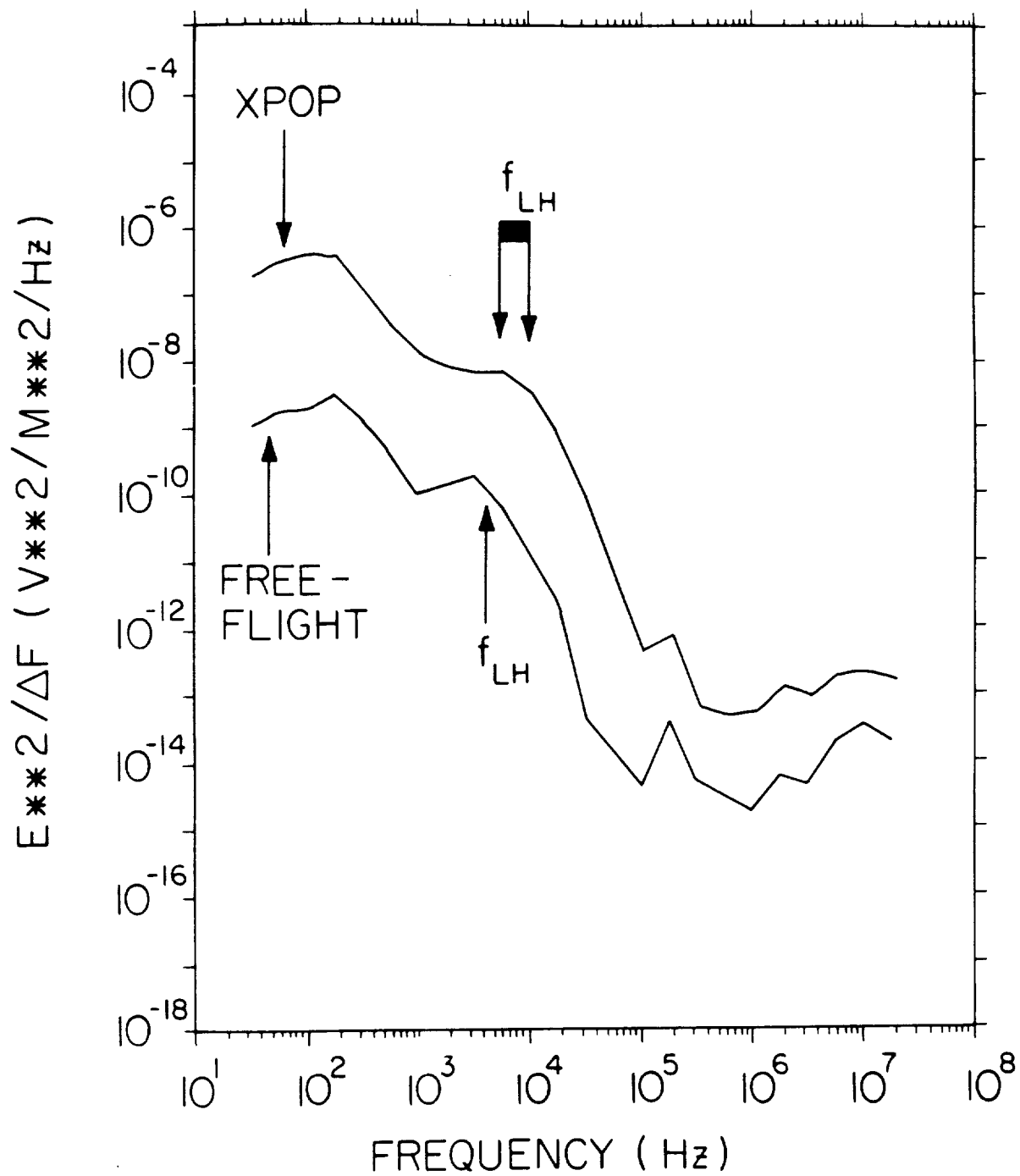


Figure 9

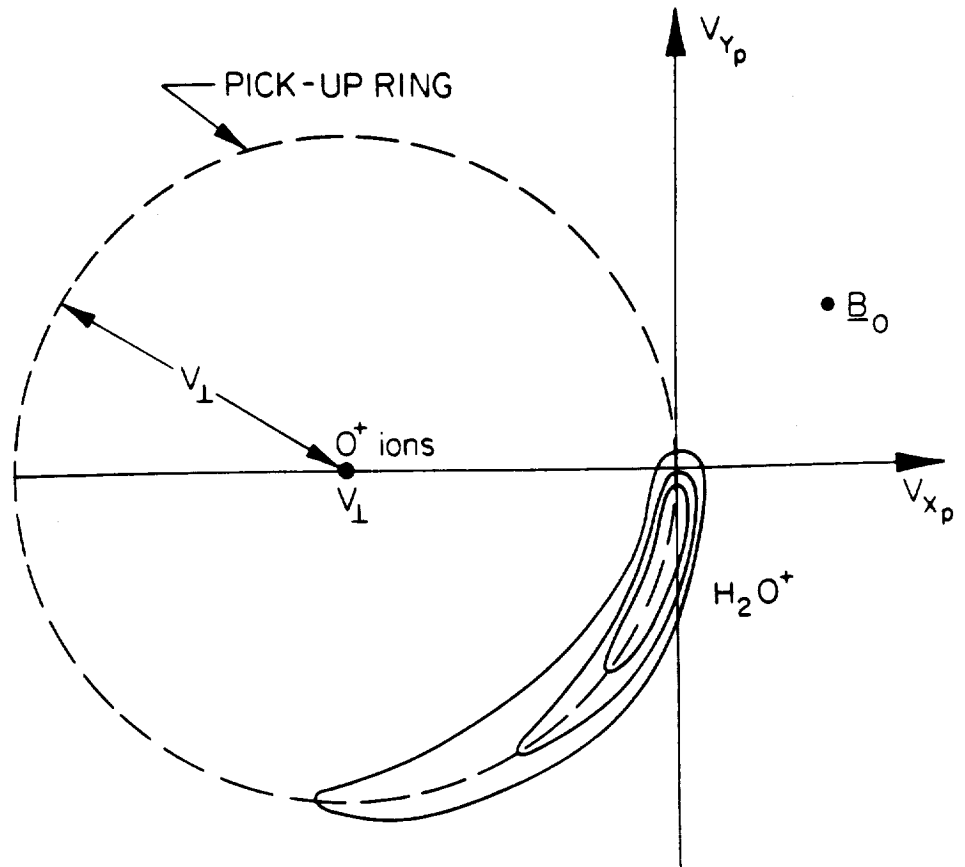


Figure 10

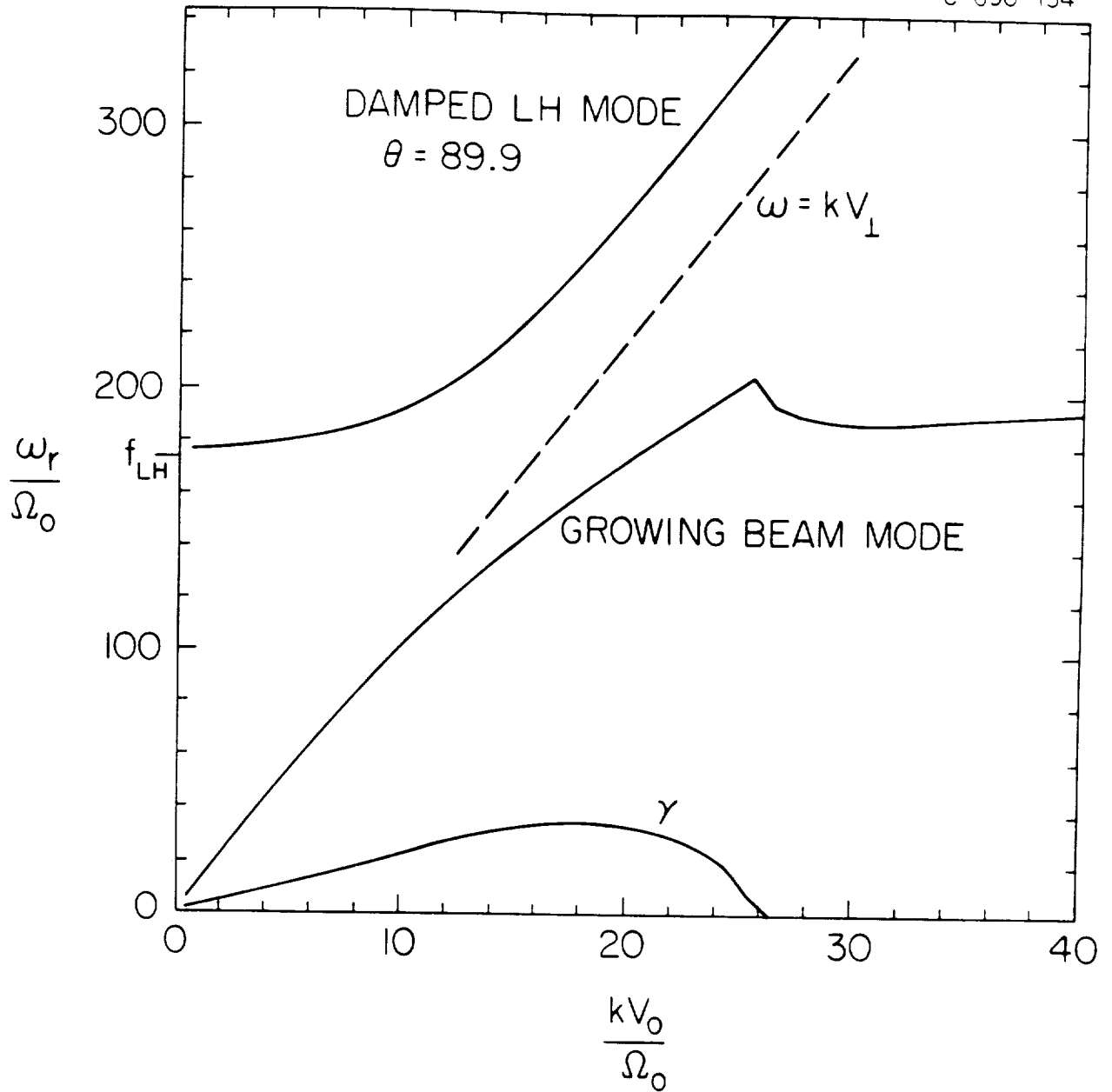


Figure 11

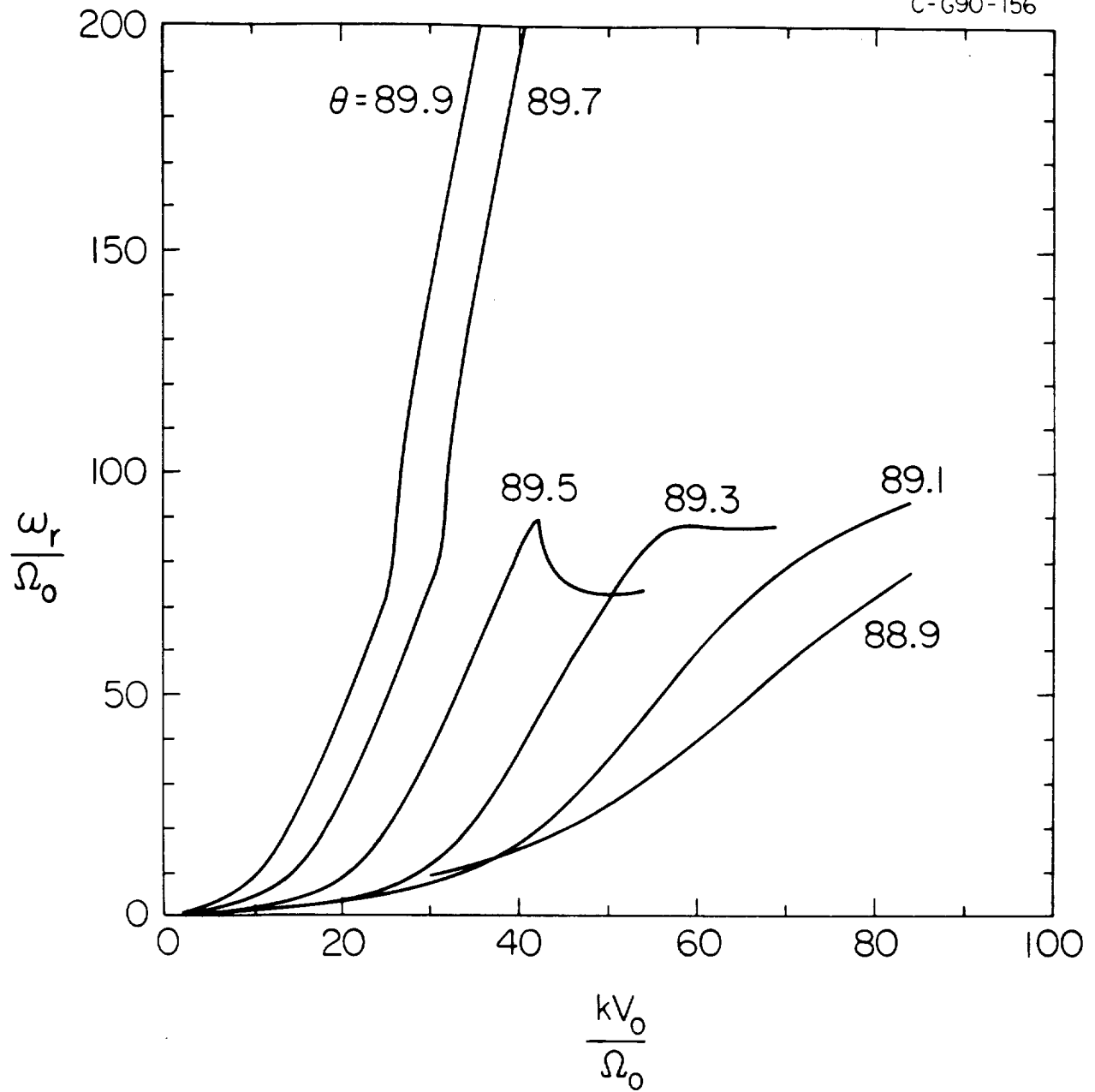


Figure 12a

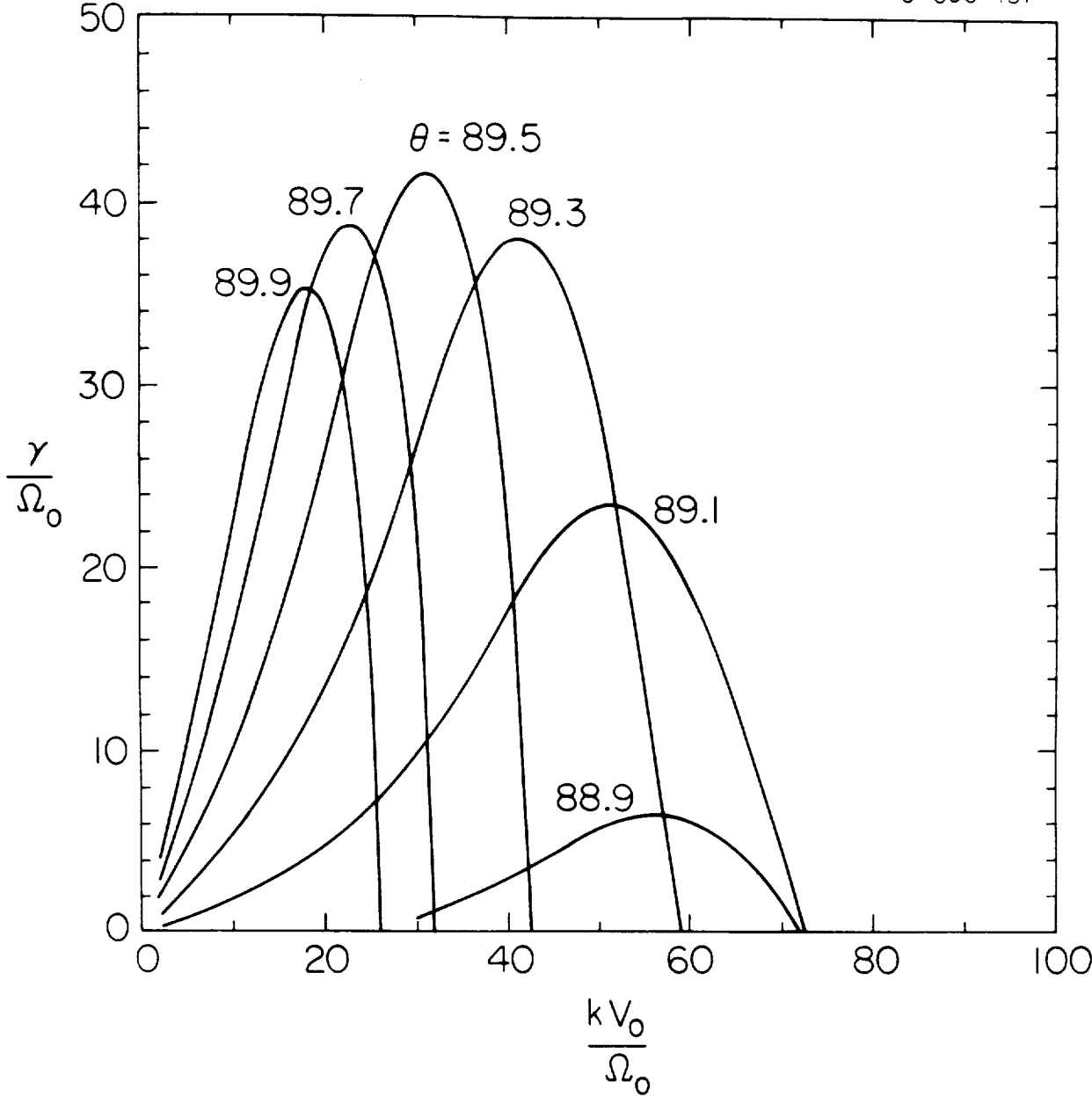


Figure 12b

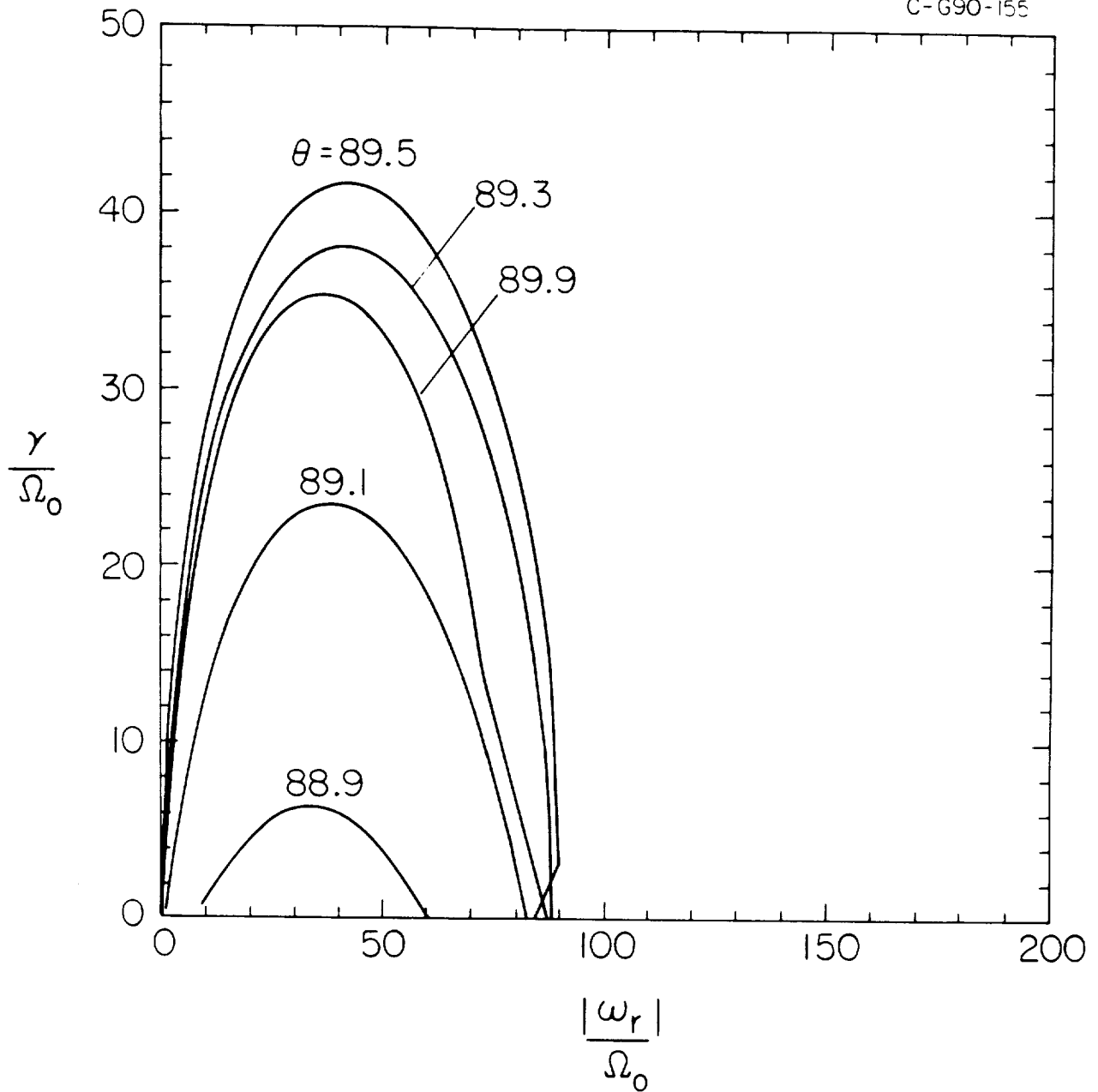


Figure 13

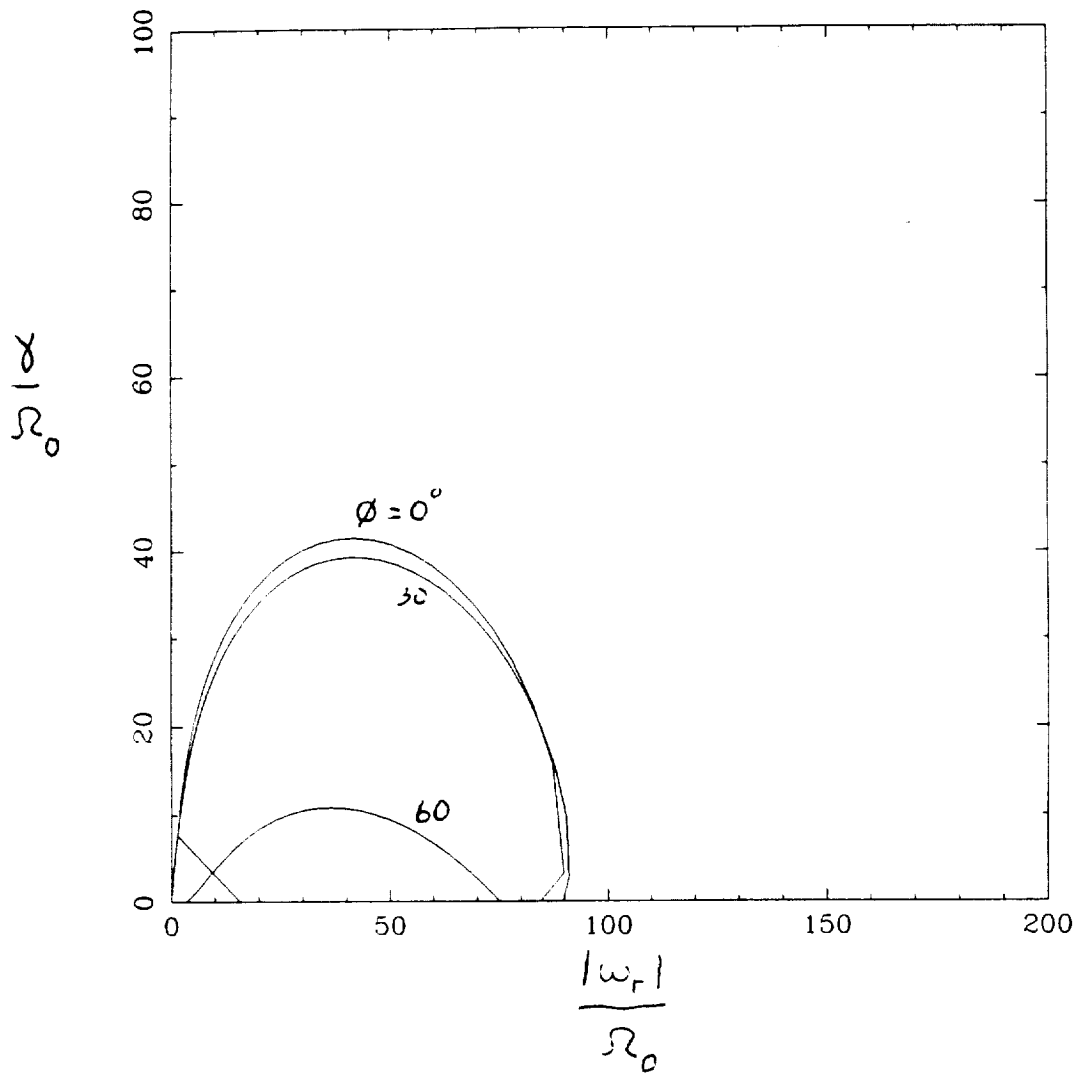


Figure 14

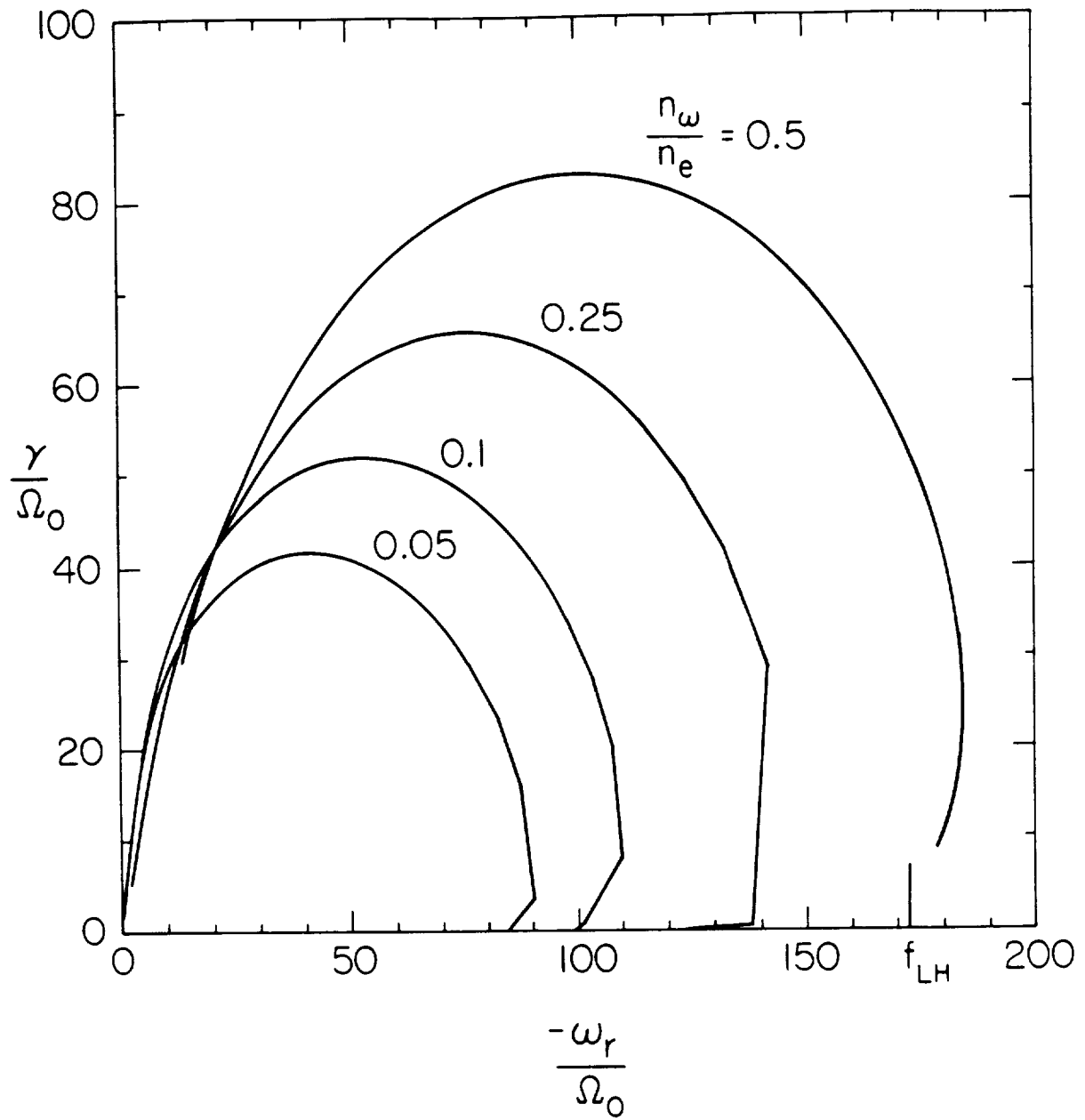


Figure 15

PLASMA WAVES ASSOCIATED WITH THE SPACE SHUTTLE

I.H. Cairns & D.A. Gurnett

Department of Physics & Astronomy, University of Iowa, Iowa City, USA

ABSTRACT

Water molecules outgassed from the US/NASA space shuttle suffer collisional charge-exchange with ionospheric oxygen ions, thereby forming unstable distributions of pick-up water ions and leading to high levels of plasma waves near the shuttle. Liouville's equation with a charge-exchange source term is solved for the water ion distribution function as a function of position relative to the shuttle. The observational characteristics of the near zone shuttle waves are summarized. A linear theory in which beam-like distributions of water ions drive Doppler-shifted lower hybrid waves via the modified-two-stream instability is developed. This theory explains many characteristics of the near zone waves. However, further work on the effects of wave nonlinearities and spatial inhomogeneity is required to explain the detailed frequency spectrum of the waves. The observed wave levels apparently satisfy the threshold condition for modulational instability of lower hybrid waves.

Key words: Waves; Instabilities; Pick-up ions; Lower hybrid; Space shuttle.

1. INTRODUCTION

This paper discusses the water ions and high levels of plasma waves found in the immediate vicinity of the USA/NASA space shuttle. At first sight then, the presentation of this paper at a conference on Plasma Astrophysics might appear rather unusual. Three justifications for including this paper are: (1) Water ion pick-up phenomena strongly influence the plasma and wave environment of the shuttle, very similar to the case of comets in our solar system (e.g., Ref. 1 and references therein). (2) The paper addresses issues in basic plasma physics and space plasma physics such as the modified-two-stream instability and possible strong turbulence collapse of lower hybrid waves (e.g., Ref. 2 and references therein). (3) The increasing importance of space-based instruments in astrophysics requires that any perturbations to the local plasma caused by the orbiting platform be understood. More complete descriptions of the work presented here will be available shortly (Refs. 3-5).

The gaseous and plasma environment of the space shuttle and the interaction of the shuttle's atmosphere with the ionospheric plasma has been investigated by the OSS-1 and Spacelab-2 shuttle missions. These and other missions found the shuttle environment to be surprisingly active, as reviewed by Shawhan et al. (Ref. 6) and Kurth and Frank (Ref. 7), with high levels of several types of plasma waves (Refs. 4, 5, 8, 9), energetic pick-up ions and other particles (Ref. 10), multiple ion streams (Ref. 11), and many ionic species such as H_2O^+ and H_3O^+ (references in Ref. 10). Measurements of these phenomena were performed with instruments mounted on a pallet within the shuttle's pay-

load bay and exposed to space, and on a small independent spacecraft, the Plasma Diagnostics Package or PDP (Refs. 12 and 7). This PDP spacecraft probed the shuttle's environment both while attached to the shuttle and while flying free of the shuttle (the so-called "free-flight" mission) to distances of order 400 m.

The general scenario envisaged (e.g., Refs. 6,9,10) for the shuttle's interaction with the ionospheric plasma involves the outgassing of water vapour from the shuttle orbiter, the subsequent collisional charge-exchange of these water molecules with ionospheric oxygen ions (O^+) to form water ions, the generation of plasma waves by these water ions, and subsequent plasma heating and the production of energetic particles. Evidence exists for a cloud of neutral water vapour surrounding the shuttle (Refs. 13-15), and water ions have indeed been observed, both by the shuttle's payload instruments (Refs. 14,15) and by the PDP instruments (Ref. 10). During the PDP's free-flight around the space shuttle (Spacelab-2), Paterson and Frank (Ref. 10) observed "ring-like" distributions of ions with the basic characteristics expected of water ions produced by the charge-exchange process. They also found that the observed number densities of the ring-like distributions were qualitatively and often quantitatively consistent with those predicted by a theoretical model for production of water ions by charge-exchange from a water cloud surrounding the space shuttle out to distances of at least 400 m.

This paper presents an overview of progress on 3 problems corresponding to plasma waves associated with the space shuttle. In Section 2 we construct a theory for the water ion distribution function close to the space shuttle using solutions to Liouville's equation with a charge-exchange source term; in particular we show that the distribution function smoothly varies from a ring-like distribution to a beam-like distribution with distance from the space shuttle. The spatial variation in the number density of water ions is also addressed. In Section 3 we present observational data on the characteristics of the near zone (within 10 m) shuttle waves and summarize data presented in Ref. 5. In Section 4 we present a linear theory for the observed waves in terms of Doppler-shifted lower hybrid waves driven by beam-like water ions via the modified-two-stream instability. This linear theory predicts wave characteristics consistent with the characteristics of the observed waves except for the detailed form of the frequency spectrum. The effects of spatial inhomogeneity and nonlinearities due to the high wave levels present are appealed to as the cause of the observed wave frequency spectrum. Brief conclusions to the paper are provided in Section 5.

2. THE DISTRIBUTION FUNCTION OF WATER IONS

Knowledge of the particle distribution functions and sources of free energy is a prerequisite for constructing

theories for the active and complex wave environment in the near vicinity of the space shuttle. However, at the present time published observational data on the distribution functions of the pick-up water ions within 50 m of the shuttle do not exist. Accordingly, the problems of the water ion distribution function and the source of free energy driving the observed waves in the very near vicinity of the space shuttle must be attacked theoretically. We note that Paterson and Frank's (Ref. 10) previous theoretical analysis ignored the particle distribution function in favour of a fluid description and did not consider the effects of the large water ion gyroradius (~ 40 m).

2.1 Physical Model

We consider a reference frame (X_p, Y_p, Z_p) moving with and centered on the space shuttle in which the ionospheric magnetic field \mathbf{B}_0 is along the Z_p axis. The velocity of the background plasma in this reference frame is generally of the form $(-V_L, 0, -V_p)$; positive values of X_p then correspond to the region upstream of the shuttle. The motion of the background plasma across the magnetic field implies the presence of a self-consistent electric field $\mathbf{E}=(0, -V_L B_0, 0)$ in this reference frame. Velocity is conserved during the charge-exchange process. Now, however, the newly-born water ion must respond to the crossed electric and magnetic fields, resulting in a cycloidal motion in the X_p - Y_p plane. The equations of motion for the particle motion may be solved for the position and velocity of the particle as a function of time given the position and velocity at some reference time. This motion may be summarized as follows: firstly, any particle speed along the magnetic field (the Z_p axis) remains constant; secondly, ignoring thermal motions for the moment, a newly-born water ion starts out at zero velocity and is accelerated by the crossed electric and magnetic fields into motions with a gyro-speed V_L centered on a velocity $(-V_L, 0, 0)$. This gyromotion maps out a ring in the X_p - Y_p plane. A "ring" distribution results if water ions are found at all gyrophases in this X_p - Y_p plane, while a "beam" distribution results if the water ions are found in a well-defined range of gyrophases. Thermal motions produce a spread in gyrospeed and velocity along the magnetic field. Fig. 1 illustrates a partial ring distribution, which will be called a beam arc distribution below.

Liouville's equation for the distribution function of charge-exchanged water ions, $f_w(\mathbf{r}, \mathbf{p}, t)$, is

$$\frac{d}{dt} f_w(\mathbf{r}, \mathbf{p}, t) = F_w(\mathbf{r}, \mathbf{p}, t) \quad (1)$$

where $F_w(\mathbf{r}, \mathbf{p}, t)$ is the source term. A formal solution exists:

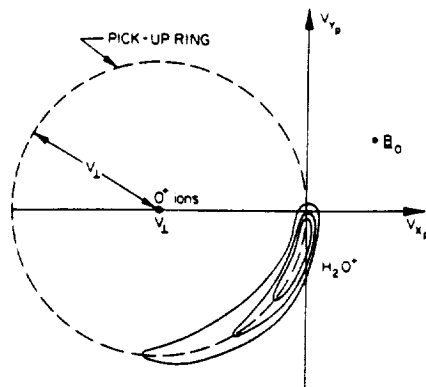


Fig. 1. Beam arc distribution displayed in V_{X_p} - V_{Y_p} space. Water ions are created near zero velocity and follow their gyromotion clockwise around the dashed 'pick-up' ring.

$$f_w(\mathbf{r}, \mathbf{p}, t) = \int_{-t}^0 d\tau F_w(\mathbf{r}'(\mathbf{r}, \mathbf{p}, t; \tau), \mathbf{p}'(\mathbf{r}, \mathbf{p}, t; \tau), t + \tau) \quad (2)$$

where $\mathbf{r}'(\mathbf{r}, \mathbf{p}, t; 0) = \mathbf{r}$, $\mathbf{p}'(\mathbf{r}, \mathbf{p}, t; 0) = \mathbf{p}$, and τ is the travel time from $(\mathbf{r}', \mathbf{p}')$ to (\mathbf{r}, \mathbf{p}) along the particle path. The effects of wave-particle scattering on the particle distribution function are ignored in this treatment.

An expression for the source term $F_w(\mathbf{r}, \mathbf{p}, t + \tau)$ for the collisional charge-exchange follows from the binary nature of the collision and conservation of velocity for the particles:

$$F_w(\mathbf{r}, \mathbf{p}, t + \tau) = \gamma n_{O^+}(\mathbf{r}, t + \tau) f_m(\mathbf{r}, \mathbf{p}, t + \tau) \quad (3)$$

where n_{O^+} is the number density of oxygen ions. This equation is consistent with the usual charge-exchange equation involving number densities, allowing identification of the reaction rate γ as $2 \times 10^{10} \text{ cm}^3 \text{ s}^{-1}$ (Ref. 10). The remaining quantity f_m is the distribution function of the water gas molecules, which for time-steady outflow with thermal speed V_m from the shuttle may be written as the product of the oxygen ion number density, which varies inversely with radial distance squared, and a Maxwellian velocity distribution with isotropic thermal speed V_m . For convenience we now assume that the velocity and density of the background plasma, the magnetic field strength, and water gas thermal speed are constant over the timescales of interest. Normalizing all speeds by the water thermal speed V_m and distances by the characteristic distance V_m / f_{gw} (f_{gw} is the gyrofrequency of a water ion) these assumptions and Eq. 3 allow Eq. 2 to be rewritten as the product of constants times a "probability" integral for the charge-exchange:

$$f_w(\mathbf{r}, \mathbf{p}, t) = \frac{\gamma n_{O^+} n_0 r_0^2}{(2\pi)^{3/2}} \int_{-t}^0 d\tau \frac{e^{-v'^2(\mathbf{r}, \mathbf{p}, t + \tau)/2}}{r'^2(\mathbf{r}, \mathbf{p}, t + \tau)} \quad (4)$$

with r' and v' implied by Eqs. 3 and 4 and the equations of motion for the water ions. Here $n_0(r_0)$ is the number density of water molecules at a radial distance r_0 from the shuttle and the symbol v denotes the speed corresponding to momentum \mathbf{p} . The "probability" integral, essentially an integral over travel time $|\tau|$ of the probability of charge-exchange producing ions at earlier times $t + \tau$ with eventual momentum \mathbf{p} at the observation time t and position \mathbf{r} , may be performed numerically using standard techniques. The shape of the distribution function is specified by the probability integral alone. Before proceeding we specify the nominal parameters used in the calculations below. Assuming a constant water gas temperature of 300K, a typical (normalized) value of V_L is 20 and the distance scale V_m / f_{gw} is 15 m.

2.2 Distribution Functions Directly Upstream from the Shuttle

Fig. 2 shows the water ion distribution functions resulting from charge-exchange at two distances directly upstream from the shuttle ($Y_p = Z_p = 0$) and demonstrates the transition from a ring distribution to a beam-like distribution with decreasing distance from the shuttle. These distributions are displayed as contour plots in a gyrospeed-gyrophase phase space formed by unfolding the ring feature in X_p - Y_p velocity space (e.g., Fig. 1) centered on the velocity $(-V_L, 0, 0)$ for particles with zero speed along the magnetic field. For reference, an ion formed by pick-up of a water molecule with zero initial velocity in the shuttle frame has gyrospeed V_L , initially has zero gyrophase, and has a gyrophase which increases with time as the ion follows its gyromotion. A ring distribution then has contours which do not vary greatly with gyrophase, as is the case at the position $X_p = 50$, far upstream from the shuttle orbiter, shown in Fig. 2(a). A beam distribution has contours which delineate a limited range of gyrophases; Fig. 2(b) shows that the distribution at $X_p = 2$ (close to the shuttle) has some beam-

like characteristics at small gyrophases. In these figures the contours are logarithmically spaced (to the base 10) in arbitrary units. We note that the significant velocity spread of the distribution even at $X_p=1$ implies that it is therefore not appropriate to term these water ion distributions "beam" distributions in an absolute sense. Rather, we suggest the term "beam arc" distributions, corresponding to a finite segment of a ring, to describe these ion distributions found close to the shuttle. We note, however, that these beam arc distributions do have some beam-like characteristics so that instability calculations assuming conventional beams may provide a reasonable first description of an instability.

This transition from ring to beam arc distribution function with position upstream from the shuttle may be understood in terms of the spatial gradient in water molecule number density and the characteristics of the charge-exchange process. Fig. 3 illustrates the development of beam arc and ring distributions at $X_p=1$ and $X_p=15$, respectively, in the X_p - Y_p plane for $V_1=20$. The solid lines are contours of constant inverse distance squared $1/R_p^2$, and so constant charge-exchange rate, spaced in powers of 10. The characteristics of the water ion distribution function at $X_p=1$ and $X_p=15$ follow on considering the primary sources of particles with zero velocity (stars) and velocity $(-2V_1, 0, 0)$ (boxes) at the observation points. Ignoring thermal motions (i.e., $V_m \ll V_1$), all pick-up water ions initially have zero velocity. Particles observed at zero velocity are therefore primarily produced (at the star symbols) very close to the observation point. Particles observed at velocity $(-2V_1, 0, 0)$ have, however, followed their gyromotion along the dashed lines from their primary production points (boxes) where they had zero velocity. At $X_p=1$, therefore, the production rate of water ions observed at velocity $(-2V_1, 0, 0)$ is less than one hundredth that for ions observed near zero velocity, implying that the distribution function is a well-defined beam arc. In contrast, at $X_p=15$ the production rates for ions with near-zero velocity and velocity $(-2V_1, 0, 0)$ differ by only a factor $(15/25)^2 \sim 0.4$, implying a ring distribution function with small contrast as in Fig. 2a. Farther from the shuttle the ring distributions become more uniform. Beam arcs do not form exactly at zero gyrophase due to the thermal spread of the water molecules.

Beam arc water distributions are also formed away from the X_p axis in the upstream region in regions where the charge-exchange rate is large. A general condition for formation of a beam arc distribution is that $R_p < 2$ with $X_p > 0$. In summary, the water ions should have a beam arc distribution function when upstream and within a radial distance of order 20-40 m ($R_p < 2$) from the shuttle in the upstream hemisphere.

2.3 Discussion

The above results show that beam arc distributions of water ions, with considerable gyrophase anisotropies, should exist at positions close to and upstream from the space shuttle. In contrast, Paterson and Frank [1989], and

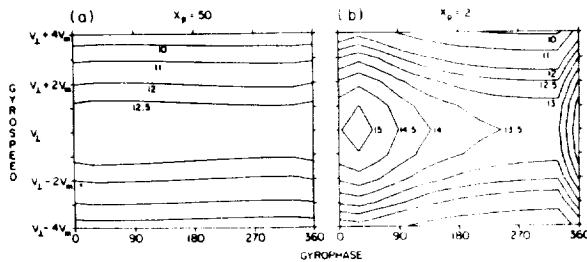


Fig. 2. Contour plots of the water ion distribution function in a gyrospeed-gyrophase phase space at two positions along the X_p axis. Contours are logarithmic to the base 10. (a) A ring distribution at $X_p=50$. (b) A beam arc distribution of $X_p=2$.

Paterson [1987], do not report observations of gyrophase anisotropies for their pick-up ions. This is not inconsistent with the work described in this paper due to (1) the PDP spacecraft's orbit around the shuttle not sampling the required region where such anisotropies are significant, and (2) the beam arc distributions being near zero velocity in the upstream region and so being removed from Paterson and Frank's analysis due to potential confusion with ambient oxygen plasma. Furthermore, elsewhere we will show that the water ion distribution functions predicted by our Liouville calculation are primarily ring-like (with no well-defined beam arcs) for the entire duration of the PDP's free-flight motion around the space shuttle during the Spacelab-2 mission.

The water ion distribution functions derived using the Liouville code may be integrated numerically to give the water ion number density as a function of position relative to the space shuttle (Ref. 3). This work may be summarized as follows: (1) Relative water ion (to plasma) densities should exceed 1% within approximately 150 m of the shuttle. (2) Within 10 m of the shuttle water ions should comprise at least 20% of the plasma density. (3) Pile-up of water ions due to kinematic effects leads to an increase in plasma density close to the shuttle. This pile-up is not included in fluid predictions for the water ion number density. We note that water ions and other pick-up ions sometimes comprise at least 50% of the plasma density in the near vicinity of the space shuttle (e.g., Ref. 7). Accordingly, non-Maxwellian distributions of water ions with significant densities should be strongly considered when interpreting the data from the OSS-1 and Spacelab-2, and perhaps other, shuttle missions.

Lastly, elastic and charge-exchange collisions between the water ions and water gas molecules offer another means of establishing more beam-like water ion distribution functions: the beam arc distributions occur due to the water ions following their gyromotion; disruption of the regular ion gyromotion by collisions with low velocity water neutrals might then limit the water ions to a more limited range of gyrophases and so to a more beam-like distribution function. Further work is required to see whether such collisions are important in determining the water ion distribution function close to the shuttle.

3. CHARACTERISTICS OF THE NEAR ZONE SHUTTLE WAVES

One of the unexpected results from the OSS-1 mission was the observation of high levels of broadband electrostatic

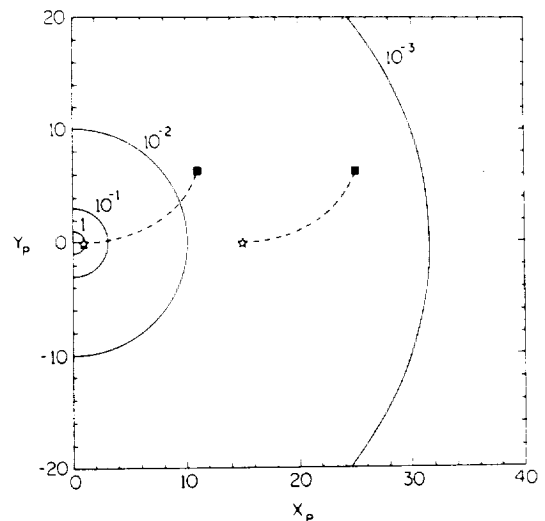


Fig. 3. Formation of beam arc and ring distributions close to and far from the space shuttle, respectively. See text for explanation.

waves in the very near vicinity (within 10 meters) of the space shuttle (Refs. 6,8). The waves had their greatest spectral densities between 31 Hz (the lowest frequency measured) and about 31 KHz, with a peak between 100 Hz and 300 Hz, but extended in frequency above 100 KHz. In comparison, during this mission, the ion gyrofrequency was of order 50 Hz, the lower hybrid frequency was of order 5 KHz, and the oxygen ion plasma frequency was of order 15-55 KHz. Here we summarize observational data from the XPOP roll during the Spacelab-2 mission, presented in detail in Ref. 5, which characterize the waves in sufficient detail for theoretical progress to be made.

Fig. 4 shows the time-averaged spectral density of the near zone waves as a function of frequency. This figure clearly shows a fall-off at low frequencies, the presence of a low frequency peak near 178 kHz, a region with spectral densities decreasing approximately inversely with frequency between the low frequency peak and the lower hybrid frequency, a bulge around the lower hybrid frequency, and a rapid fall-off at higher frequencies. One implication of these data is that the electric field in the waves should be approximately constant between 100 Hz and the lower hybrid frequency, and essentially negligible at higher frequencies.

Fig. 5 shows the relative contribution of the electric fields centered on the *i*'th channel to the total average broadband, frequency-integrated electric field E_T plotted versus the frequency of the *i*'th channel. The detailed definition of this quantity is $R(f_i) = E_i / \sum E_i$ with $E_i^2 = \int S(f) df$ with upper and lower limits of integration $f_U = \sqrt{f_i f_{i+1}}$ and $f_L = \sqrt{f_i f_{i-1}}$, respectively. Here $S(f)$ is the spectral density, and the frequency intervals for integration are equally spaced in logarithmic frequency. The data plotted are for the period 0145-0210 shown in Fig. 4. The total average broadband electric field E_T was 51.1 mV/m. As anticipated above, the electric field is essentially constant between 100 Hz and the lower hybrid frequency, and essentially negligible at higher frequencies. Two peaks, a factor of order 2 above the uniform level, are visible. The first is at low frequencies centered on 178 Hz, with a broad shoulder at significant amplitudes to the second peak which is situated between 5.6 KHz and 10 KHz. As described above, the lower hybrid frequency varies between 5 and 10 KHz during this time period, providing an excellent identification for the higher frequency peak. Above 56 KHz the measured electric fields are essentially negligible. Murphy

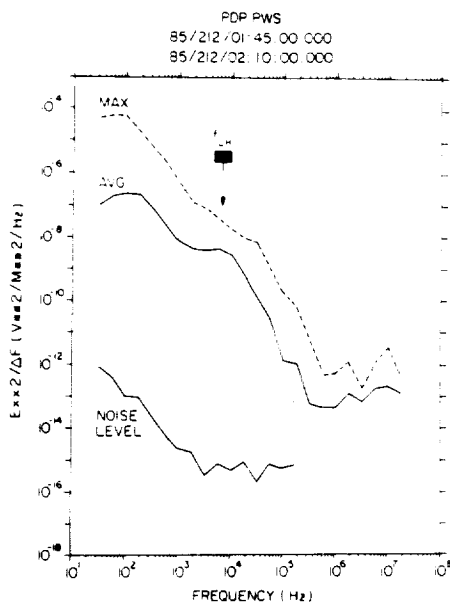


Fig. 4. Spectral density as a function of frequency for the period 01:45-2:10, day 212, 1985, during the XPOP roll.

et al. (Ref. 8) and Shawhan et al. (Ref. 6) have previously recognized the existence of the low frequency peak. However, neither the essentially constant level of waves between the 100 Hz and the lower hybrid frequency, nor the peak near the lower hybrid frequency have been recognized before.

The interpretation of these data in terms of components in the wave spectrum is not unique. However, it seems most appropriate to interpret the wave spectrum in terms of a fairly constant high level of waves (electric fields of order 2.5 mV/m per frequency interval) from 31 Hz to 10 KHz with two superposed peaks, one around 178 Hz and one near the lower hybrid frequency. These superposed peaks have electric fields a factor of two higher than the constant level of waves between 30 Hz and 10 KHz. These data require any high frequency waves above about 20 KHz to smoothly merge with the lower hybrid frequency waves; no evidence is found for any sharply peaked wave components in the frequency range of 10 to 40 KHz. These identifications are referred to below as the 'uniform' component, the low frequency component and the lower hybrid component. A theoretical interpretation for the uniform component is developed in the next section, while suggestions for the two peak components are given in Ref. 5.

The other results reported in Ref. 5 are as follows.

- Null features in the wave data as the PDP spacecraft moves through the shuttle's plasma wake imply that the higher frequency near zone waves have smaller wavelengths (higher wavenumbers).
- Observations of the near zone waves while the PDP was magnetically connected to the space shuttle at a distance of order 200 m imply that the near zone waves have wavevectors perpendicular to the magnetic field.
- The near zone waves show a pronounced decrease in amplitude and spectral extent when the shuttle is moving most nearly parallel to the magnetic field. This so-called V_p/V_T effect implies that the near zone waves are driven by water pick-up ions.

4. A NEW THEORY FOR THE NEAR ZONE WAVES: DOPPLER-SHIFTED LOWER HYBRID WAVES

Two previous theories for the near zone shuttle waves are discussed in detail in Ref. 5. Hwang et al. (Ref. 16) proposed that the waves result from ion acoustic or ion-ion acoustic instabilities driven by the secondary ion streams observed (Ref. 11) in the near vicinity of the space shuttle. This theory is inconsistent with the frequency spectrum and wavevector directions of the near zone waves reported in Ref. 5. Papadopoulos (Ref. 17) proposed that the waves are Doppler-shifted lower hybrid waves driven via the modified-two-stream instability by ionospheric oxygen ions reflected from the shuttle. This theory fails on two grounds. Firstly, severe theoretical problems exist for

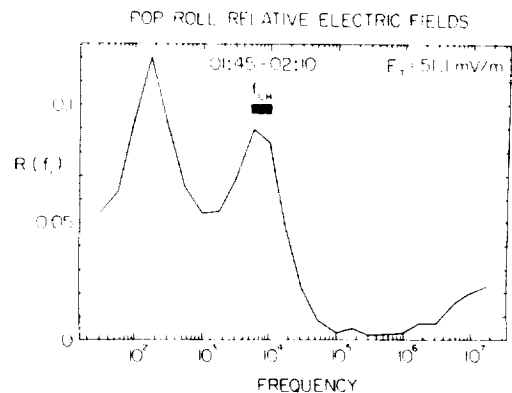


Fig. 5. Radio $R(f)$ of the average electric field in a frequency bandwidth divided by the total average broadband field as a function of frequency (see text for a detailed definition).

reflections of charged oxygen ions at significant yields (>1%) at these low collision energies (5 eV). Secondly, correcting a minor error in Papadopoulos' calculation of the observed wave frequencies leads to the prediction that the waves should have frequencies in the range from 0.5-1.4 f_{LH} , thereby not explaining the large wave levels below 1 KHz. In addition, no simple explanation of the observed V_p/V_T effect is apparent for these theories.

Here we propose a new theory: the waves are Doppler-shifted lower hybrid waves driven via the modified-two-stream instability by beam arc distributions of water ions in the near vicinity of the space shuttle. These water ions naturally comprise at least 20% of the plasma densities, thereby greatly favouring this theory over Papadopoulos' theory. In addition, a natural explanation for the V_p/V_T effect is available. In this first development of the theory we represent the water ions as a Maxwellian beam distribution centered at zero velocity while the ionospheric electrons and oxygen ions have Maxwellian distributions drifting relative to the water ions. We restrict ourselves to the case in which the shuttle moves exactly perpendicular to the magnetic field ($V_T=0$). Making the standard approximations (e.g., Ref. 17) we can reduce the exact electrostatic dispersion equation ($\beta < 10^{-5}$) to the standard form for the modified-two-stream instability:

$$1 - \frac{n_O}{n_e} \frac{\Omega_{LH}^2}{(\omega - k_x V_L)^2} - \frac{n_w}{n_e} \frac{\Omega_{LH}^2}{\omega^2} = 0. \quad (5)$$

Here, the quantity $\omega - k_x V_L$ is the Doppler-shifted wave frequency seen by the ionospheric electrons and oxygen ions. Subscripts e, O, and w refer to the electrons, oxygen ions and water ions, respectively. A positive component k_x for a wavevector implies the wavevector is directed upstream along the X_p axis. This equation is directly analogous to the dispersion equation for the usual two-stream instability in which Langmuir waves are generated by an electron beam and viewed in the reference frame of the beam (Ref. 18). Accordingly, for water ion beams which satisfy the condition $n_w/n_e > 2.5(V_w/V_L)^3$ ($\sim 10^3$ here), this equation predicts generation of strongly growing waves with dispersion relation $\omega_{rest} \sim k_x V_L$, wavevectors approximately perpendicular to the magnetic field, frequencies near the lower hybrid frequency in the ionospheric plasma rest frame, and relatively small wave frequencies in the shuttle's rest frame.

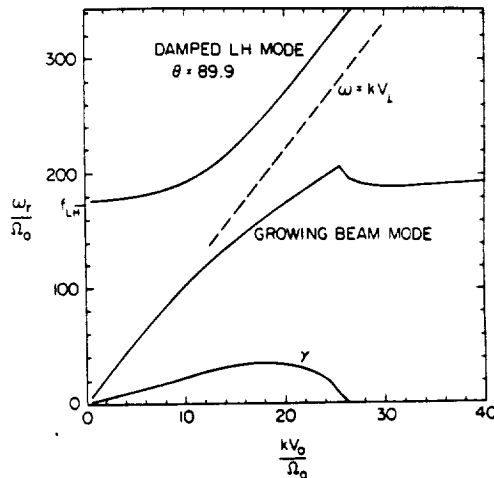


Fig. 6. Dispersion diagram (in the ionospheric plasma frame) for waves driven by a water ion beam with $n_w/n_e = 0.05$ and wavevectors defined by $\theta = 89.9^\circ$. The damped lower hybrid mode and growing beam mode waves are shown. Subtraction of kV_L gives the wave frequency in the observing frame.

Fig. 6 shows the wave dispersion relation and growth rate in the ionospheric plasma frame obtained by solving the full electrostatic dispersion equation numerically (including electron and oxygen ion magnetization) for waves propagating along the X_p direction with an angle $\theta = 89.9^\circ$ between the wavevector and the magnetic field direction (the Z_p axis). The dashed line shows the dispersion relation $\omega_{rest} = k_x V_L$ for comparison. A strong resemblance to the ordinary beam instability for "Langmuir" waves is apparent (e.g., Fig. 1 of Ref. 18). Four important results may be inferred from this figure: (1) These waves are essentially beam driven waves with $\omega_{rest} \sim k_x V_L$. (2) The waves have strong growth rates. (3) Noting that $\omega_r < k_x V_L$ for all wavenumbers k_x , these waves will be Doppler-shifted to low and negative frequencies (only the magnitude of the frequency is directly observable, however). (4) The higher wavenumber waves will be Doppler-shifted to larger observable wave frequencies than the smaller wavenumber waves.

Further calculations show that the growing waves are severely restricted in angle θ , as expected for lower hybrid waves. Fig. 7 shows plots of observable wave frequency versus growth rate for various ratios of water ion to electron number density at the angles θ of maximum growth rate. The theory predicts waves in the observed frequency range. Increasing the water ion number density increases both the center frequency and bandwidth of the growing waves. Accordingly, linear theory predicts that the spatial gradient in water ion number density near the shuttle (Ref. 3), when not in the wake region, implies an increase in the center frequency, bandwidth and growth rate of the unstable waves with decreasing distance from the shuttle. The linear theory can therefore explain wave growth from near zero frequency up to a frequency of order f_{LH} as required.

In summary, this linear theory is capable of explaining the generation of waves (1) with large growth rates in the observed frequency range and range of observable wavenumbers, (2) with wavevectors essentially perpendicular to the magnetic field, (3) with wavenumber increasing with frequency. The theory also admits natural explanations for the observed V_p/V_T effect. Unusual species temperatures, densities, or preheating of the electrons are not required. However, the linear theory is not capable of explaining the details of the frequency spectrum for the intense near zone waves. In particular the linear theory predicts peak growth in the range 0.25-0.75 f_{LH} (depending on the relative number density of water ions as in Fig. 7), well above the

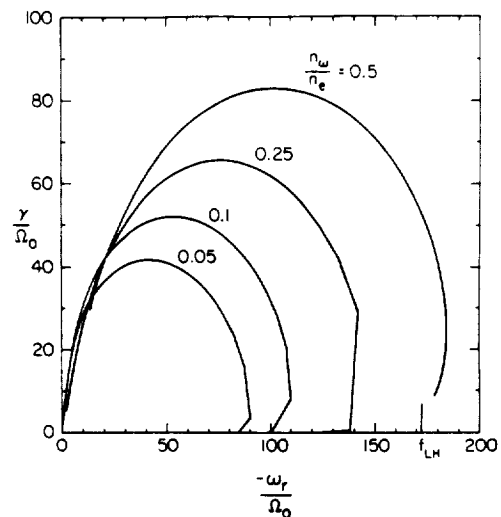


Fig. 7. Growth rates versus (observable) wave frequency as a function of beam density n_w/n_e for angles θ with the maximum growth rate and wavevectors in the X_p-Z_p plane.

observed low frequency peak at about 178 Hz and well below the observed peak near the lower hybrid frequency. This difficulty in explaining the details of the observed frequency spectrum should be expected for at least three reasons. Firstly, the preliminary nature of this linear theory, secondly the neglect of inhomogeneity effects in the strongly inhomogeneous shuttle environment, and thirdly the neglect of nonlinear effects which are often vital in determining the wave spectrum. Further discussion of improvements to the linear theory and the role of inhomogeneity effects is given in Ref. 5. Only nonlinear effects are briefly and qualitatively discussed here.

Nonlinear processes involving lower hybrid waves, such as scattering off thermal ions, decay processes involving ion acoustic waves, modulational instabilities and strong turbulence processes, have been discussed in the literature (e.g., Ref. 2, 19). Detailed discussions of these possibilities are not appropriate here. Here we note that the ratio of wave electric field energy to thermal plasma energy is of order 10^{-5} (for $n_e = 10^{11} \text{ m}^{-3}$) while the ratio of the total water ion kinetic energy to the thermal plasma energy is of order 5 for $n_w/n_e = 0.1$. Moreover, the wavelengths predicted by the linear theory are smaller than (but comparable to) the PDP's effective antenna length during the XPOP roll (1.15 m), indicating that the wave levels in the plasma may be underestimated. These wave levels are considerable and imply that nonlinear processes, including strong turbulence processes, warrant considerable attention. In particular, the equations in Ref. 2 suggest that the threshold for the modulational instability is at least marginally satisfied for these waves. Further support for consideration of nonlinear effects comes on comparing the timescales for growth and convection of the waves. For waves with a linear growth rate of $50\Omega_0$ typical in Fig. 15, 10 e-folding periods corresponds to a time of 10^{-3} seconds. During this time period a wave packet would be convected a maximum distance of 8 m (given the shuttle's orbital speed of 7.8 Kms $^{-1}$) while a wave's electric field would increase by a factor of 2×10^4 . This distance is small compared with the expected extent of the region near the shuttle with beam distributions of water ions (~ 30 m).

5. CONCLUSIONS

This paper shows that ion pick-up phenomena control the plasma wave environment of the USA/NASA space shuttle, similar to the situation at comets. We have developed a theory for the water ion distribution function resulting from charge-exchange of outgassed water molecules. This theory, involving the solution of Liouville's equation with a charge-exchange source term, predicts a transition from ring-like distributions to beam arc distributions with decreasing distance upstream from the shuttle. The characteristics of the observed near zone (within 10 m of the shuttle) waves are summarized. A linear theory involving Doppler-shifted lower hybrid waves driven by beam arc distributions of water ions via the modified-two-stream instability is developed. This theory can explain most characteristics of the observed waves. However, appeals to the effects of wave nonlinearities and spatial inhomogeneity are required to explain the details of the observed frequency spectrum. Further work on these matters is required. The high wave levels present apparently exceed the threshold condition for modulational instability of lower hybrid waves, thereby providing some support for nonlinear effects being important.

6. ACKNOWLEDGEMENTS

The authors thank J.S. Pickett, W.S. Kurth, C.K. Goertz, W.R. Paterson, N. D'Angelo, and L.A. Frank for helpful discussions concerning the PDP data and the shuttle's plasma environment. Financial support from NASA Grants NAGW-1488 and NAG3-449 from NASA Headquarters and NASA/Lewis Research Center, respectfully, is gratefully acknowledged.

7. REFERENCES

1. Johnstone AD et al. 1990, Observations in the bow shock of comet Halley, this issue.
2. Kalinin VP et al. 1990, Lower hybrid collapse dynamics in the space plasma, this issue.
3. Cairns IH 1990, Transition from ring to beam arc distributions of water ions near the space shuttle orbiter, *J. Geophys. Res.*, in press.
4. Cairns IH and Gurnett DA 1990, Control of plasma waves associated with the space shuttle by the angle between the orbiter's velocity vector and the magnetic field, *J. Geophys. Res.*, submitted.
5. Cairns IH and Gurnett DA 1990, Plasma waves observed in the near vicinity of the space shuttle, *J. Geophys. Res.*, submitted.
6. Shawhan SD et al. 1984, Plasma Diagnostics Package initial assessment of the shuttle orbiter plasma environment, *J. Spacecraft Rockets*, **21**, 387-391.
7. Kurth WS and Frank LA 1990, The Spacelab-2 Plasma Diagnostics Package, *J. Spacecraft Rockets*, **27**, 70-75.
8. Murphy GB et al. 1983, Interaction of the space shuttle orbiter with the ionospheric plasma, *Spacecraft/Plasma Interactions and Their Influence on Field and Particle Measurement*, ESA SP-198, 73.
9. Gurnett DA et al. 1988, Plasma wave turbulence around the shuttle: Results from the Spacelab-2 flight, *Geophys. Res. Lett.*, **15**, 760-763.
10. Paterson, WR and Frank LA 1989, Hot ion plasmas from the cloud of neutral gases surrounding the space shuttle, *J. Geophys. Res.*, **94**, 3721-3727.
11. Stone NH et al. 1983, Multiple ion streams in the near vicinity of the space shuttle, *J. Geophys. Res.*, **10**, 1215-1218.
12. Shawhan SD 1982, Description of the Plasma Diagnostics Package (PDP) for the OSS-1 shuttle mission and JSC chamber test in conjunction with the fast pulse electron gun (FPEG), *Artificial Particle Beams in Space Plasma Studies*, ed. B. Grandel, Plenum, New York, 419-430.
13. Carignan GR and Miller ER 1983, Mass spectrometer STS-2, -3, -4 induced environment contamination monitor (IECM) summary report, ed. ER Miller, *NASA Tech. Memo.*, NASA TM-82524, 87-101.
14. Narcisi R et al. 1983, The gaseous and plasma environment around space shuttle, *AIAA Pap.*, 83-2659.
15. Koch DG et al. 1987, Infrared observations of contaminants from shuttle flight 51-F, *Adv. Space Res.*, **7**, 211-221.
16. Hwang KS et al. 1987, The emissions of broadband electrostatic noise in the near vicinity of the shuttle orbiter, *Planet. Space Sci.*, **35**, 1373.
17. Papadopoulos KD 1984, On the shuttle glow (the plasma alternative), *Radio Science*, **19**, 571.
18. Cairns IH 1989, Electrostatic wave generation above and below the plasma frequency by electron beams, *Phys. Fluids B*, **1**, 204.
19. Musher SL et al. 1986, Nonlinear effects in the propagation of an ion beam across a magnetic field, *Sov. Phys. JETP*, **63**, 519.

**INTERFERENCE PATTERNS IN WIDEBAND SPECTRA IN THE SPACELAB-2 PLASMA
WAVE DATA: ION ACOUSTIC WAVES GENERATED BY THE ELECTRON BEAM**

W. Feng, D. A. Gurnett and I. H. Cairns

Department of Physics and Astronomy

The University of Iowa

Iowa City, IA 52242

Journal of Geophysical Research

(In Preparation)

July 1991

SPACELAB 2 POTENTIAL MEASUREMENTS AROUND THE SHUTTLE ORBITER

J. S. Pickett and W. S. Kurth

Department of Physics and Astronomy

The University of Iowa

Iowa City, IA 52242

Planetary and Space Science

(In Preparation)

July 1991

ELECTROSTATIC WAVES ASSOCIATED WITH THE SPACELAB 2 ELECTRON BEAM

W. S. Kurth¹, D. A. Gurnett¹, L. A. Frank¹, W. R. Paterson¹, M. Ashour-Abdalla², D. Schriver², P. M. Banks³, R. I. Bush⁴, and W. J. Raitt⁵

Geophysical Research Letters

(In Preparation)

July 1991

¹ Department of Physics and Astronomy, The University of Iowa, Iowa City, IA 52242

² Institute of Geophysics and Planetary Physics, UCLA, Los Angeles, CA 90024

³ Space Physics Research Lab., University of Michigan, Ann Arbor, MI 48109

⁴ Department of Electrical Engineering, Stanford University, Stanford, CA 94305

⁵ Center for Atmospheric and Space Sciences, Utah State University, Logan, UT 84322

PLASMA PARAMETERS IN THE VICINITY OF
THE SHUTTLE ORBITER

by

Alan C. Tribble

A thesis submitted in partial fulfillment
of the requirements for the Master
of Science degree in Physics
in the Graduate College of
The University of Iowa

May 1986

Thesis supervisor: Professor Nicola D'Angelo

Graduate College
The University of Iowa
Iowa City, Iowa

CERTIFICATE OF APPROVAL

MASTER'S THESIS

This is to certify that the Master's thesis of

Alan C. Tribble

has been approved by the Examining Committee
for the thesis requirement for the Master of
Science degree in Physics at the May 1986
graduation.

Thesis committee: W. D. Angelo
Thesis supervisor

Robert H. Merline
Member

Christopher K. Gail
Member

ACKNOWLEDGMENTS

I wish to thank my advisor Professor Nicola D'Angelo, for his numerous helpful comments concerning the preparation of this manuscript. His suggestions regarding the presentation of the data often aided me in gaining a better understanding of the physics involved. The other members of my committee, Professors Goertz and Merlino, also deserve special mention. In addition, I appreciate the time spent by Gerald Murphy and Jolene Pickett helping to familiarize me with the data reduction process. Thanks are also due Alice Shank for typing this thesis.

ABSTRACT

Plasma parameters in the vicinity of the Space Shuttle are studied using a Langmuir probe on the University of Iowa's Plasma Diagnostics Package. First, we examine electron density, temperature, and plasma potential as well as their dependence on the attitude of the orbiter. We then examine density fluctuations in the ambient ionosphere, in the wake of the orbiter, and during an OMS burn.

TABLE OF CONTENTS

	Page
LIST OF TABLES	v
LIST OF FIGURES	vi
I. INTRODUCTION	1
The Plasma Diagnostics Package	1
Operation of the Langmuir Probe	3
II. TYPICAL DENSITIES AND TEMPERATURES	11
In the Ambient Ionosphere	11
Near the Orbiter's Cargo Bay	12
III. DENSITY FLUCTUATIONS	17
In the Ambient Ionosphere	17
During XPOP Roll	18
After an OMS Burn	20
IV. SUMMARY	22
APPENDIX A. ELECTROSTATIC NOISE	50
APPENDIX B. ERROR ANALYSIS	66
REFERENCES	73

LIST OF TABLES

Table		Page
1.	Performance Characteristics of the Langmuir Probe	24
2.	Free-Flight Sequence of Events	25
B-1.	The Magnitude of the Ion Current	70
B-2.	The Effect of Ion Current on Electron Temperature	71

LIST OF FIGURES

Figure	Page
1. The PDP for the OSS-1 mission	26
2. The PDP for the Spacelab-2 mission	27
3. A typical Langmuir probe sweep	28
4. The rotation of the PDP during free flight	29
5. Position of the Shuttle, relative to the PDP	30
6. Free-flight densities and temperatures	31
7. Free-flight densities and temperatures	32
8. The pallet for the OSS-1 mission	33
9. The pallet for the Spacelab-2 mission	34
10. Shuttle attitudes	35
11. "Nose-to-Sun" data, PDP in cargo bay	36
12. "Nose-to-Sun" data, attitude timeline, PDP in cargo bay .	37
13. "PTC" data, PDP in cargo bay	38
14. "PTC" attitude timeline, PDP in cargo bay	39
15. "Nose-to-Sun" data, PDP on RMS	40
16. "Nose-to-Sun" attitude timeline, PDP on RMS	41
17. XPOP Roll	42
18. The location of the PDP during XPOP Roll	43
19. The Orbiter Body Axis System (OBAS)	44
20. Electron density vs roll angle	45

Figure	Page
21. Free-flight density fluctuations	46
22. The wake of the orbiter	47
23. $\vec{v} \times \vec{B}$	48
24. Density fluctuations during an OMS burn	49
A-1. The phase angle	57
A-2. The density depletion regions	58
A-3. Density depletions as a function of phase angle	59
A-4. An anomaly in the Langmuir probe sweep	60
A-5. An anomaly in the lock mode data	61
A-6. "Cleaned up" lock mode data	62
A-7. Lock mode data during density depletion	63
A-8. LEPEDA firing sequence	64
A-9. Location of LEPEDA at the start of the density depletions	65
B-1. Corrected and uncorrected Langmuir probe sweeps	72

I. INTRODUCTION

The Plasma Diagnostics Package

The region of the Earth's atmosphere higher than 60 km above the surface is chiefly composed of negatively charged electrons and positively charged ions commonly called a plasma. A spacecraft moving through this region of the atmosphere, traditionally referred to as the ionosphere, disturbs the plasma in much the same way water is disturbed by a boat sailing on its surface. Spacecraft have been flying through this region of the Earth's atmosphere for over 25 years, but there have been few opportunities to study the wake generated in the plasma. Many scientific and engineering investigations are underway which will use the Space Shuttle as a platform for experiments in the Earth's ionosphere. Therefore, it is essential that we understand the environment near the orbiter since the orbiter's wake or any electromagnetic emissions from the orbiter may have an effect on in situ observations.

For this reason the Plasma Diagnostics Package (PDP) was built by the University of Iowa Department of Physics and Astronomy under the direction of Professor Stanley D. Shawhan. The PDP contains fourteen instruments which can make measurements of magnetic and electric fields, particle distributions, radio waves, as well as plasma

composition, density, and temperature. In addition to making measurements of the ambient medium, the PDP can be teamed with other experiments to perform "active" experiments. For example, the PDP can be used to measure changes deliberately provoked by the operation of the Fast-Pulse Electron Gun, which is part of the Vehicle Charging and Potential experiment (VCAP).

The PDP has flown on two shuttle missions. First, in March of 1982 the PDP took part in the third shuttle flight as one of the experiments on the Office of Space Science payload, the OSS-1 mission. After returning to Earth, the PDP was modified and took part in the Spacelab-2 flight in July of 1985. For the remainder of this thesis note that all data taken during March, i.e., on day 083, 084, etc., is from the OSS-1 mission. All data taken during July or August, i.e., on day 211, 212, etc., is from the Spacelab-2 mission. The altitude for the OSS-1 mission averaged 240 km while the altitude for the Spacelab-2 mission averaged 380 km. The angle of inclination for the OSS-1 mission was 38° , for the Spacelab-2 mission the angle was 49.5° .

During landing and re-entry the PDP is stowed on a pallet in the orbiter's cargo bay. Over the course of each mission, several hours of data were obtained from this location which yielded a good deal of information about conditions in the bay. In addition, on both missions the crew maneuvered the Remote Manipulation System (RMS), the arm of the shuttle, to grapple the PDP, unlatch it, and moved it

around in predetermined sweeps to map the orbiter's environment near the cargo bay and out to 15 m distance. On Spacelab-2 the PDP was released as a spin-stabilized sub-satellite while the orbiter executed a complex series of maneuvers around it at distances up to 200 m. As the two slowly separated, the PDP was able to make more distant measurements of the orbiter's fields.

At this time plans are currently underway to construct the Recoverable Plasma Diagnostics Package (RPDP). The RPDP will be designed to be released from the orbiter for days at a time so that a great deal of in situ observations can be made of the ambient ionosphere. The RPDP is expected to make its first flight sometime around 1990.

Operation of the Langmuir Probe

The Langmuir probe on the PDP is a relatively simple instrument which has two operational modes. In the first mode the probe can determine the electron density, temperature, and plasma potential. In the second mode the probe can observe density fluctuations over a wide frequency range. The probe that was part of the OSS-1 mission was a 6 cm diameter gold-plated spherical sensor mounted on a fixed boom approximately 30 cm from the body of the PDP (see Figure 1). The probe on the Spacelab-2 mission was a 3 cm diameter gold-plated sphere mounted on a moveable boom. When deployed the probe is 78.53 in from the center of the PDP, this is shown in Figure 2. The probe can measure density fluctuations in the frequency range 0 to 178 kHz,

plasma densities from 10^3 to 10^7 electrons/cm³, and plasma temperatures from about 1000 K to 5000 K.

The electronics that control the probe's operation alternate between two different modes, one complete cycle requires 12.8 seconds. The first is an 11.8 second lock mode. During this time the Langmuir probe is biased at +10 volts relative to the PDP chassis. The lock mode is followed by a 1 second sweep mode where the voltage is swept from +10 volts to -5 volts in increments of 0.125 volts. The performance characteristics of the probe are listed in Table 1.

During the lock mode the probe measures density fluctuations in the following manner. The probe is sampled 120 times a second to see how much charge has accumulated. In this way we are able to obtain the charge collected as a discrete function of time. By taking the Fast Fourier Transform (FFT) of these data, we obtain current fluctuations as a function of frequency. The output is then sampled through three filters: 1 Hz low pass; 1 - 6 Hz bandpass; and 6 - 40 Hz bandpass. The sample rates of the filters are 5 Hz, 20 Hz, and 120 Hz, respectively. A fourth filter (30 Hz high pass) routes the output to a wideband receiver and spectrum analyzer which can look at details of the current fluctuations up to a frequency of 178 kHz. However, data from the fourth filter will not be presented here.

During the sweep mode the data collected by the probe is sent through a 0 - 50 Hz bandpass filter and can be used to determine the electron density, temperature, and the plasma potential. From

elementary plasma physics we know the effect of introducing a potential, such as a point charge or a probe, into a plasma. If we make the assumption that the mobility of the ions can be neglected in comparison to the mobility of the electrons, then, as done by Nicholson [1983], the potential around a test charge q is given by

$$V(r) = \frac{q}{r} \exp\left(\frac{-r}{\lambda_e}\right) ,$$

where

$$\lambda_e = \left(\frac{T_e}{4\pi n_0 e^2}\right) .$$

T_e is the electron temperature and λ_e is the Debye length for electrons. Because the potential falls off so rapidly as r increases, electrons or ions further than one Debye length away from the probe will be virtually unaffected by the probe's presence. If we apply a large positive bias to the probe, we can expect to attract all of the electrons and repel all of the ions within one Debye length of the probe. We can compute the current collected by the probe in the following manner.

If the radius of the probe is much larger than the Debye length, we may assume that all of the particles passing within one Debye length of the probe, through thermal motions, for example, will

hit the probe. If the probe is perfectly absorbing, then the current collected by the probe will be

$$I = J_r A_s \quad .$$

J_r is the random current flux and A_s is the surface area of the sheath one Debye length away from the probe. Since the radius of the probe is much larger than the Debye length, we can approximate the area of the sheath by the surface area of the probe. We now have

$$A_s = 4\pi r^2 \quad .$$

By definition,

$$J_r = Q_s \times (\text{number of particles hitting probe each second}) \quad .$$

Q_s refers to the charge of each species present in the plasma, a sum over each species in the plasma is implied. To determine the quantity in parenthesis, we can look at a differential volume element located at the edge of the sheath farthest from the probe. The particles here are far enough away from the probe that we only need consider their thermal motions. Therefore, half of the particles in this volume element would be entering the Debye sheath, half would be leaving it. We conclude that the number of particles entering the sheath each

second, i.e., the number that will eventually impact the probe, is $(N_S/2)A_S v_S$. N_S is the density of each species in the plasma and v_S is their velocity. This tells us that

$$J_r = Q_S \frac{N_S}{2} A_S v_S \quad .$$

If we assume a Maxwellian distribution, then

$$P(v) = 4 \left(\frac{M_S}{2\pi kT_S} \right)^{3/2} v^2 \exp\left(-\frac{M_S v^2}{2kT_S}\right)$$

is the probability that a given particle will have its velocity between v and $v + dv$. The average velocity is given by

$$\langle v_S \rangle = \int_{-\infty}^{+\infty} v_S P(v_S) dv_S = 2 \left(\frac{2kT_S}{\pi M_S} \right)^{1/2} \quad .$$

The direction of the velocity vector, for the particles entering the sheath, will be randomly distributed over 180° . Therefore, we can define the vector so that the component of velocity directed at the probe is given by $v_S \cos \theta$. When we integrate over the factor $\cos \theta$ to find the average component of velocity in the direction of the probe, we pick up a factor of $1/2$ which cancels a factor of 2 in the previous expression for v_S . Therefore, when we combine this

definition of v_s with the definition of J_r , we find that the current collected by the probe is

$$I = Q_s (4\pi r^2) \frac{N_s}{2} \left(\frac{2kT_s}{\pi M_s} \right)^{1/2} .$$

Again there is an implied sum over all the species present in the plasma.

If we apply a large positive bias voltage to the probe, we may assume that only electrons will contribute to the current collected, since the number of ions impacting the probe will be negligible. Therefore, the value of the electron current, before the probe saturates, is

$$I = -e(4\pi r^2) \frac{N_e}{2} \left(\frac{2kT_e}{\pi M_e} \right)^{1/2} .$$

This equation is dependent on both density and temperature. However, we can make use of the Boltzmann relation from statistical mechanics. In the presence of a potential, in this case the probe, the density is given by

$$N_e = N_0 \exp\left(\frac{-eV}{kT_e}\right) .$$

Plugging this into the previous equation gives

$$I = -e(4\pi r^2) \frac{N_0}{2} \left(\frac{2kT_e}{\pi M_e}\right)^{1/2} \exp\left(\frac{-eV}{kT_e}\right) .$$

Now we have an equation involving the electron temperature and the probe bias voltage V . Taking the natural log of both sides of the equation gives

$$\ln I = \text{constant} + (\text{constant} \ln T_e) + \left(\frac{-e}{kT_e}\right)V .$$

The \ln of T_e will vary much slower than T_e itself, therefore, we may approximate $\ln T_e$ as a constant. The equation becomes

$$\ln I = \text{constant} + \left(\frac{-e}{kT_e}\right)V .$$

If we graph $\ln I$ vs V , before the probe saturates, the slope will be given by $(-e/kT_e)$. Using this we have an expression for T_e ,

$$T_e = \frac{-e}{k \text{ slope}} .$$

Once we have T_e we can plug this into the expression for I and deduce an expression for N_0 , which is

$$N_0 = \text{constant } I T_e^{1/2} .$$

The constant is determined if we know the radius of the probe, the mass of the electron, Boltzmann's constant, etc.

In this manner the Langmuir probe can give us the electron density and temperature. If we define the plasma potential as the bias voltage at which the probe saturates, a graph of $\ln I$ vs V will also give us the plasma potential. A typical sweep is shown in Figure 3. Note that the value of I that we use in the determination of N_0 is chosen so that V is as positive as possible without saturating the probe. For a further discussion of the theory behind Langmuir probes see, for example, Huddlestone and Leonard [1965].

II. TYPICAL DENSITIES AND TEMPERATURES

In the Ambient Ionosphere

On day 213, 1985 the PDP was released from the orbiter as a free-flying sub-satellite for about 6 hours. During this time the Langmuir probe took measurements of the plasma parameters as the orbiter backed away from the PDP and executed a series of maneuvers around it. The booms were deployed throughout free flight so that the Langmuir probe, VLF spheres, and search coil would be further from the body of the PDP. In addition to this, the PDP used a momentum wheel to cause it to spin with a period of 13.06 seconds. As is shown in Figure 4, the PDP was spinning counterclockwise if viewed from the top. The spin plane, i.e., the plane of the paper in Figure 4, was the plane in which the orbiter executed the majority of its maneuvers after releasing the PDP. The predicted position of the shuttle, relative to the PDP, is shown in Figure 5 for the time that it took the orbiter to execute one complete fly-around. The chronological sequence of events is given in Table 2.

The data taken during this first fly-around are shown in Figures 6-7. (We should first point out that the apparent "density depletion regions" that occur approximately every 9 1/2 minutes are attributed to instrumental effects and are not rapid fluctuations in

the ionospheric electron density. This effect is discussed in Appendix A.) The data reveal the daily fluctuations in electron density and temperature that we could expect to see from the orbiter. Two points are worth noting. First, the plasma potential shows little variation during the day but appears to increase after sunset. Second, the electron density appears lowest at sunrise and sunset but also appears to increase after sunset. One possible explanation for this is that the altitude at which the Spacelab-2 mission took place, 380 km, is in the F region of the Earth's ionosphere. The peak in electron density in the F region usually occurs between 250 - 300 km during the day, and about 50 km higher at night. Therefore, what we may be seeing after sunset is the peak in the electron density shifting to a higher altitude. However, while radar observations confirm that the peak of the electron density shifts to a higher altitude at night, they also show that in most cases the value of the peak density is less at night than it was during the day. Consequently, there may be other factors contributing to the increase in the electron density.

The ambient ionosphere has been studied for many years and a great deal of data has accumulated. For comparison see, for example, Hess and Mead [1968] or Kasha [1969].

Near the Orbiter's Cargo Bay

During most of the OSS-1 and Spacelab-2 missions the PDP was kept on a pallet in the orbiter's cargo bay. The location for the

OSS-1 mission is shown in Figure 8, and the location for the Spacelab-2 mission is shown in Figure 9. During the OSS-1 mission the crew of the orbiter placed the shuttle in several different attitudes designed to subject the orbiter to the most extreme temperature differences that could be expected on later flights. The four attitudes used are shown in Figure 10 and are referred to as "nose to sun," "tail to sun," "bay to sun," and "passive thermal control" or PTC. During the "nose-to-sun" and "tail-to-sun" attitudes, the bay is in the shade and is bitterly cold. The "bay-to-sun" attitude places the pallet in direct sunlight which causes the temperature to soar. PTC, also known as the barbecue mode, is designed to equalize temperatures on all surfaces.

Data obtained during the "nose-to-sun" attitude is shown in Figures 11-12. Note that in Figures 12, 14, 16 the pitch and azimuth angles are measured with respect to the plasma flow vector and not the velocity vector of the shuttle. As we can see from Figure 11 when the bay is in the ram of the plasma flow, electron densities are typically $10^6/\text{cm}^3$ and the corresponding electron temperature is less than 1000 K. However, as is discussed in Appendix B, we suspect that we are underestimating the electron temperature when the probe is in ram. Consequently, the corresponding drop in electron density by three orders of magnitude when the bay is facing the wake may be overestimated. Data obtained during PTC is shown in Figures 13-14. Here we see more vividly the effects of rolling the orbiter. Note that the

electron temperature increases in the wake of the shuttle. Similar results have been reported by Oran et al. [1975] and Samir and Wrenn [1972].

For completeness Figures 15-16 show a segment of data obtained during the "nose-to-sun" attitude when the PDP was on the RMS about 7 m above the cargo bay. Even in this position the PDP notices a decrease in the electron density as the orbiter turns so that the PDP is in the wake of the shuttle.

During the Spacelab-2 mission the orbiter executed a series of maneuvers designed to yield information about the extent of the orbiter's near wake. This series of maneuvers is referred to as XPOP (X-axis Perpendicular to Orbital Plane) roll and is described in Figure 17. The location of the PDP during this time is shown in Figure 18. During XPOP roll the orbiter rolls at a rate of $1^\circ/\text{second}$. Consequently, one complete roll requires 6 minutes. At the same time that the orbiter is rolling, the RMS can be unwound at the same rate so that the orientation of the PDP, relative to the plasma flow, remains unchanged.

Unfortunately, the software that computes the electron density and temperature was unable to make use of most of the raw data collected during XPOP roll. However, we are able to use the second point of the Langmuir probe sweep as an approximation to density. By second point of the sweep, we mean the current collected when the probe is biased at +9.875 volts. Past experience has shown that the value of

the second point of the sweep is proportional to the value of the density. Using the Orbiter Body Axis System (OBAS), a noninertial coordinate system that moves with the orbiter, we can compute the roll angle of the orbiter. The OBAS coordinate system is defined in Figure 19 and the roll angle is defined as the angle between the orbiter's velocity vector and the z-axis of the orbiter. Figure 20 shows the relationship between the interpolated electron density and the roll angle.

These data clearly indicate the presence of a density depletion region in the wake of the shuttle. The velocity of the shuttle is approximately 8 km/s. If we make the assumptions that $n_i = n_e = 10^6 \text{ cm}^{-3}$ and $T_i = T_e = 2500 \text{ K}$ then the thermal velocity of atomic oxygen is 1.1 km/s and the thermal velocity of an electron is 180 km/s. Because the electrons are moving much faster than the shuttle, they will be able to move into the region directly in the wake of the orbiter whereas the majority of the ions will be unable to do so. As a result the majority of the particles in the wake of the orbiter will be mostly electrons and this will be a region of negative potential. This negative potential will prevent other electrons from reaching the wake, consequently, the electron density in the near wake of the shuttle will be lower than the electron density in ram. The density depletion region is also associated with enhanced electron temperatures. As postulated by Samir and Wrenn [1972], this temperature enhancement may be due to wave-particle interactions that apply

an energy-filtering mechanism to the electrons that enter the region. One other possible explanation would be heating through adiabatic compression.

We have now given an overview of the characteristic plasma parameters that the Langmuir probe can measure in the vicinity of the shuttle. The next chapter will deal with an examination of how rapidly these parameters fluctuate.

III. DENSITY FLUCTUATIONS

In the Ambient Ionosphere

As was mentioned in Chapter I, when the Langmuir probe is in the lock mode, we are able to use it to determine the current collected by the probe as a function of frequency. Data obtained during the first 15 minutes of free flight, which occurred during the Spacelab-2 mission, is shown in Figure 21. As shown in Table 2, the PDP was released from the orbiter at 0010 on day 213. The 0 - 1 Hz channel remains relatively constant at about 1 volt until this time. After release the voltage rises rapidly for about 10 minutes before finally leveling off at about 0020. This indicates that there is an increase in the DC current collected by the probe as the shuttle backs away from it. This is to be expected because when the PDP was attached to the RMS, it was directly in the wake of the orbiter. However, as the orbiter moves away the density of the plasma near the PDP increases slightly. The voltage from the 1 - 6 Hz filter remains constant after the release of the PDP. However, there is a marked increase in the turbulence in this channel when the PDP is no longer grounded to the orbiter. After its release the PDP used a momentum transfer wheel to spin up so that it would rotate with a period of 13.06 seconds. The turbulence in the 1 - 6 Hz channel exhibits a

periodicity that leads us to suspect that it is related to the spin of the PDP. That is, the turbulence is either a maximum or minimum depending on the orientation of the PDP relative to the plasma flow. The 6 - 40 Hz channel was not shown because it shows similar turbulence during this time. It is believed that this turbulence is actually interference from another instrument on the PDP. This is the same interference alluded to in Chapter II, and an explanation for it is offered in Appendix A. We believe that we can attribute most if not all of the turbulence in the 1 - 6 Hz and 6 - 40 Hz channels to this interference. Therefore, we conclude that the PDP sees very little turbulence in the ambient ionosphere during free flight. The most notable difference is an increase in the DC current collected by the probe. This is due to the fact that the PDP is no longer in the electron density depletion region found in the orbiter's wake.

We should note that Rubin and Besse [1986] have reported that a free-flying satellite, such as the PDP, could charge to a potential of -1400 volts in the wake of the orbiter. If this potential were distributed nonuniformly over the surface of the PDP, it could produce a surface discharge. However, this does not appear to have caused any problems during free flight.

During XPOP Roll

In Chapter II we explained the attitude known as XPOP roll. A set of data for ten wake crossings was obtained on day 212 when the orbiter was in this attitude and shows us the turbulence associated

with the wake of the orbiter. The raw data are shown for two wake crossings in Figure 22. In both cases we see that there is very little turbulence when the PDP is exactly in the wake of the shuttle. However, we see a good deal more turbulence when the PDP passes from the wake of the orbiter into the ram of the plasma flow and vice versa. This may be due to the presence of the negative potential well in the wake of the shuttle. When the probe is exactly in the wake of the the orbiter, at 180° , there will be very few ions present to affect current collection by the probe. However, as we pass into the ram of the plasma flow, the probe will be bombarded by the ions that are flowing past the bay doors on the shuttle. The presence of this ion-density gradient on either side of the geometrical wake of the shuttle is responsible for turbulence which causes the data to look noisier.

We can also point out that the data for both of the wake crossings look noisier when the probe moves from the wake of the orbiter to the ram of the plasma flow than the other way around. This may be due to the $\vec{v} \times \vec{B}$ force on the ions. Using the OBAS coordinate system, we can compute the magnitude of $\vec{v} \times \vec{B}$ as shown in Figure 23. Note that the charge on the ions/electrons has not been included nor has the factor $1/c$. In this figure \vec{v} was taken to be the velocity of the shuttle. However, if we want the force on the ions, we can make use of the fact that the velocity of the ions is comparable to the velocity of the shuttle. Therefore, the majority of the ions

contributing to the turbulence near the wake of the shuttle will be ions moving with their velocity vectors antiparallel to the velocity of the shuttle. Therefore, the $\vec{v} \times \vec{B}$ force on these ions will be in the direction of the positive y-axis during the time that the Langmuir probe is in the wake of the shuttle. Consequently, the turbulence in the negative y-direction has been minimized because the force on the ions that pass the shuttle on this side elongates the ion-density gradient. That is, the force due to $\vec{v} \times \vec{B}$ is in the same direction as the force due to the negative potential well. The turbulence in the positive y-direction is magnified because the $\vec{v} \times \vec{B}$ force opposes the force due to the negative potential well and effectively compresses the density gradient. Other factors, such as the $\vec{E} \times \vec{B}$ drift, will also affect the shape of the orbiter's wake.

After an OMS Burn

During the Spacelab-2 mission a ground-based experiment was conducted to investigate the effects of an OMS (Orbiter Maneuvering System) burn on the plasma cloud surrounding the orbiter. On day 216, 1985 the orbiter conducted a 6 second OMS burn over the radar observatory at Millstone Hill, Massachusetts, starting at 19:14:44. The PDP was located in the bay of the shuttle during this time and made in situ observations of the effects of the burn. The raw data are shown in Figure 24. The data from the 0 - 1 Hz filter shows us that there was a rapid drop in the voltage sent to this filter as the burn started. However, the burn significantly affects this channel only

for about 15 seconds, although there appears to be residual effects which last up to 90 seconds after completion of the burn. The 1 - 6 Hz filter shows an increase in turbulence during and immediately after the burn, although the majority of the turbulence subsides after about 15 seconds here as well. The 6 - 40 Hz filter is essentially saturated during the first 15 seconds after the burn, and it takes another 90 seconds after the burn has stopped for the turbulence to return to the level that it was at before the burn. Therefore, it seems reasonable to conclude that the turbulence associated with an OMS burn affects all three channels for at least 90 seconds after the OMS engines were shut off. The 6 - 40 Hz channel suggests that the decay in the turbulence is roughly exponential. If so, the time required for turbulence to decrease by a factor of $1/e$ is approximately 30 seconds. It is quite possible that the wideband data, which shows us oscillations up to a frequency of 178 kHz, would indicate that the OMS burn induces most of its turbulence at even higher frequencies. However, the wideband data have yet to be examined.

IV. SUMMARY

In conclusion, we have seen that the Langmuir probe on the PDP has made in situ observations of the ambient ionosphere. These observations are in general agreement with previous studies. However, the electron density enhancement that is seen immediately after sunset still lacks a complete explanation. Data taken from the bay of the shuttle indicate a density depletion region in the wake of the shuttle. This density depletion region forms because the electrons are able to "fill in" the near wake of the shuttle more rapidly than the ions. This produced a region of negative potential and, consequently, a region of electron density depletion and enhanced electron temperatures. Explanations for the elevated electron temperatures have been offered by several authors and three realistic possibilities are:

- (i) Hot electrons result from a selection effect by the negative potential found in the wake.
- (ii) Electrons may be energized by wave-particle interactions in the turbulent region.
- (iii) Adiabatic compression of electrons as they enter the region of negative potential results in thermal excitation.

The density fluctuation data reveal that the orbiter's wake is not totally symmetric. Several factors may contribute to this, for example, $\vec{v} \times \vec{B}$ forces and $\vec{E} \times \vec{B}$ drifts. These data also indicate that there is a great deal of turbulence in the bay of the shuttle following an OMS burn. This turbulence is greatest in the 6 - 40 Hz channel and appears to decay exponentially.

Table 1
Performance Characteristics of the Langmuir Probe

Current Sensor	0.1 μ a - 1 ma
T_e	(800 - 5000) $^{\circ}$ K
n_e	(10^3 - 10^7) cm^{-3}
$\Delta N/N$	
< 1 Hz	1.8% - 460%
1 - 6 Hz	0.12% - 30%
6 - 40 Hz	0.012% - 3%
> 30 Hz (spectrum analyzer)	-30 dB $\Delta N/N$ to -80 dB $\Delta N/N$

Table 2
Free-Flight Sequence of Events

Point	GMT	Event Description
1	213/00:10	Deploy and Separation
2	213/00:34	Establish Stationkeeping at 300 feet
3	213/00:52	Begin Electromagnetic Interference Tests
4	213/01:37	Burn to out-of-plane point 1
5	213/01:47	Out-of-plane point 1 midcourse burn
6	213/01:57	Burn to Flux Tube connection
7	213/02:02	Flux Tube connection
8	213/02:04	Burn to Phantom point 1
9	213/02:16	Burn to Flux Tube connection
10	213/02:35	Midcourse burn, lower Flux Tube 1
11	213/02:40	Flux Tube connection
12	213/02:42	Burn to wake transit 1
13	213/02:49	Midcourse burn, wake transit 1
14	213/02:58	Begin wake transit 1
15	213/03:04	Midpoint of wake transit 1

A - G85 - 598

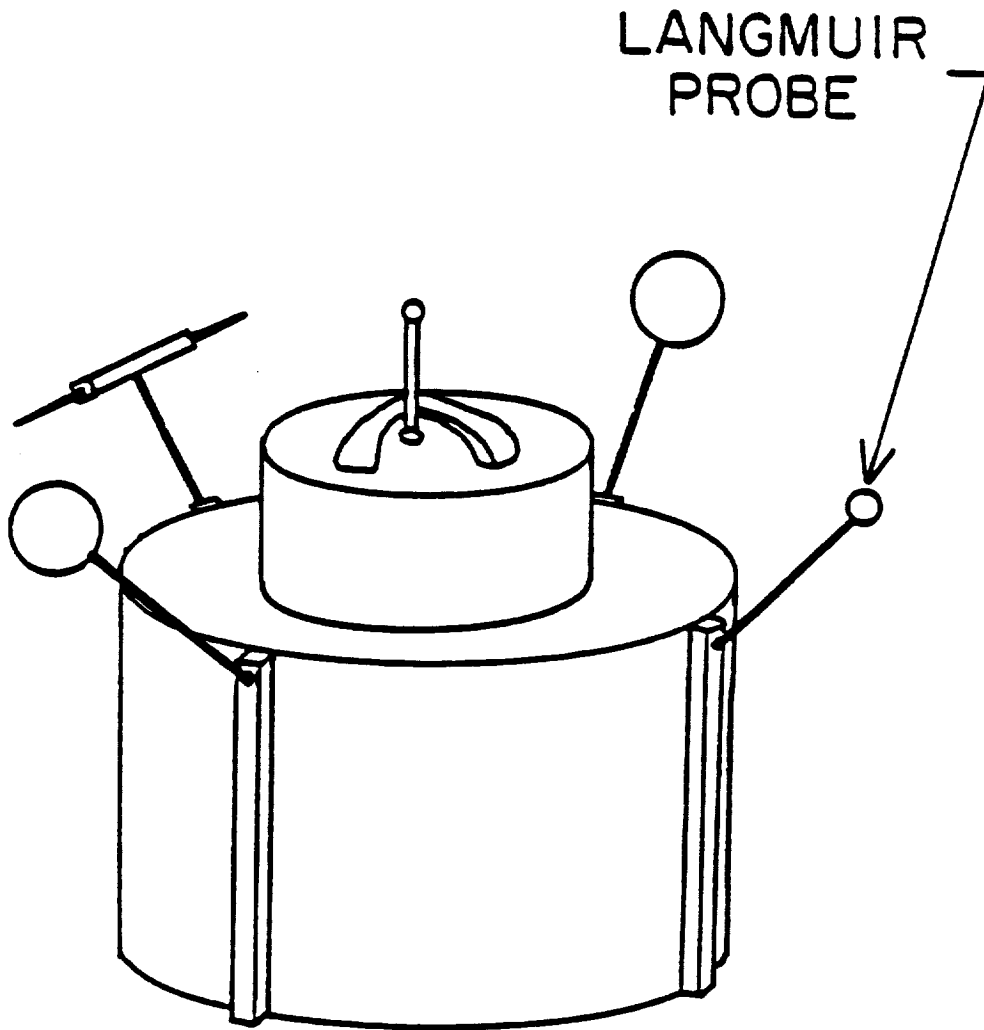
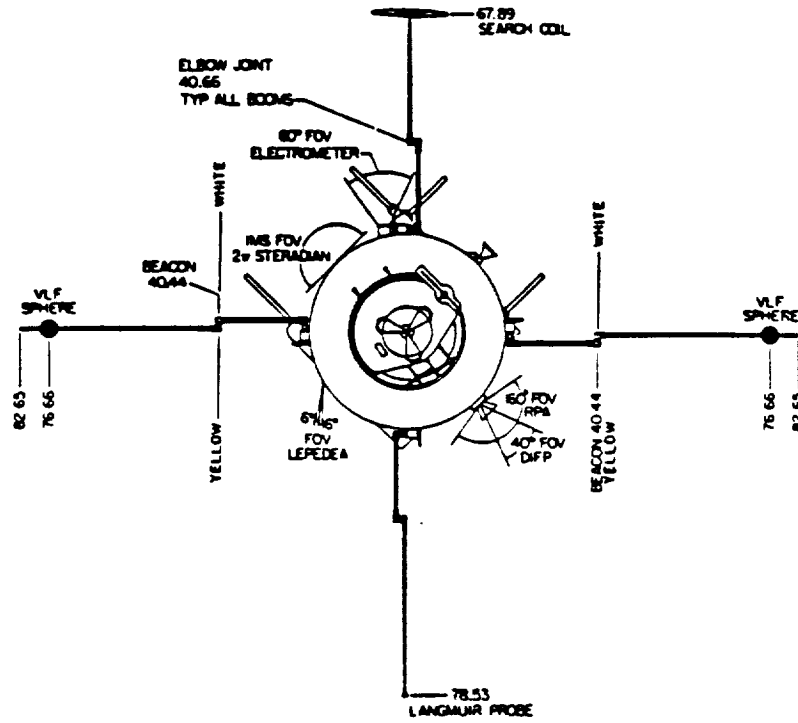
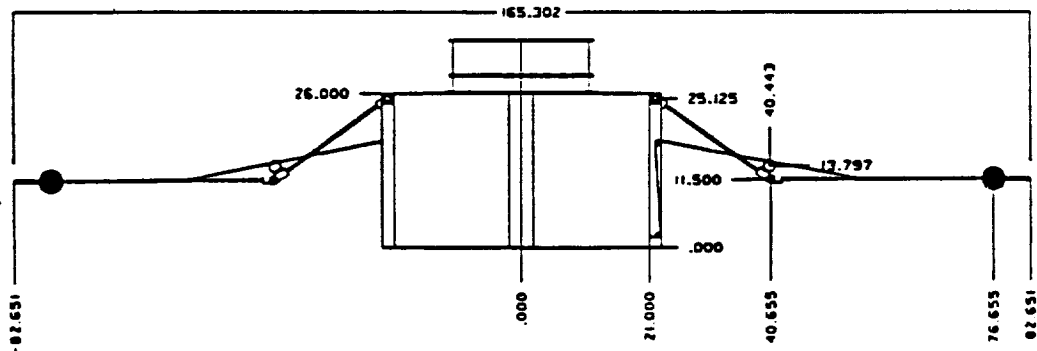


Figure 1. The PDP for the OSS-1 mission.

PDP BOOMS DEPLOYED CONFIGURATION



TOP VIEW



SIDE VIEW

Figure 2. The PDP for the Spacelab-2 mission. The scale is marked in inches.

OSS-1 DATA

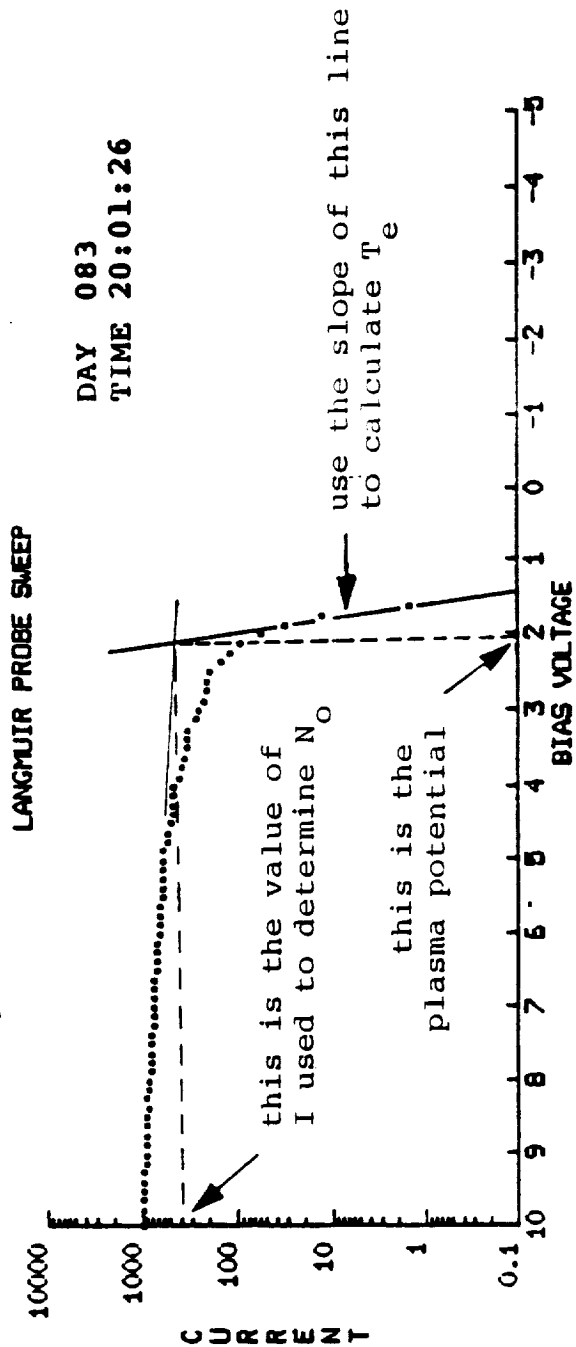
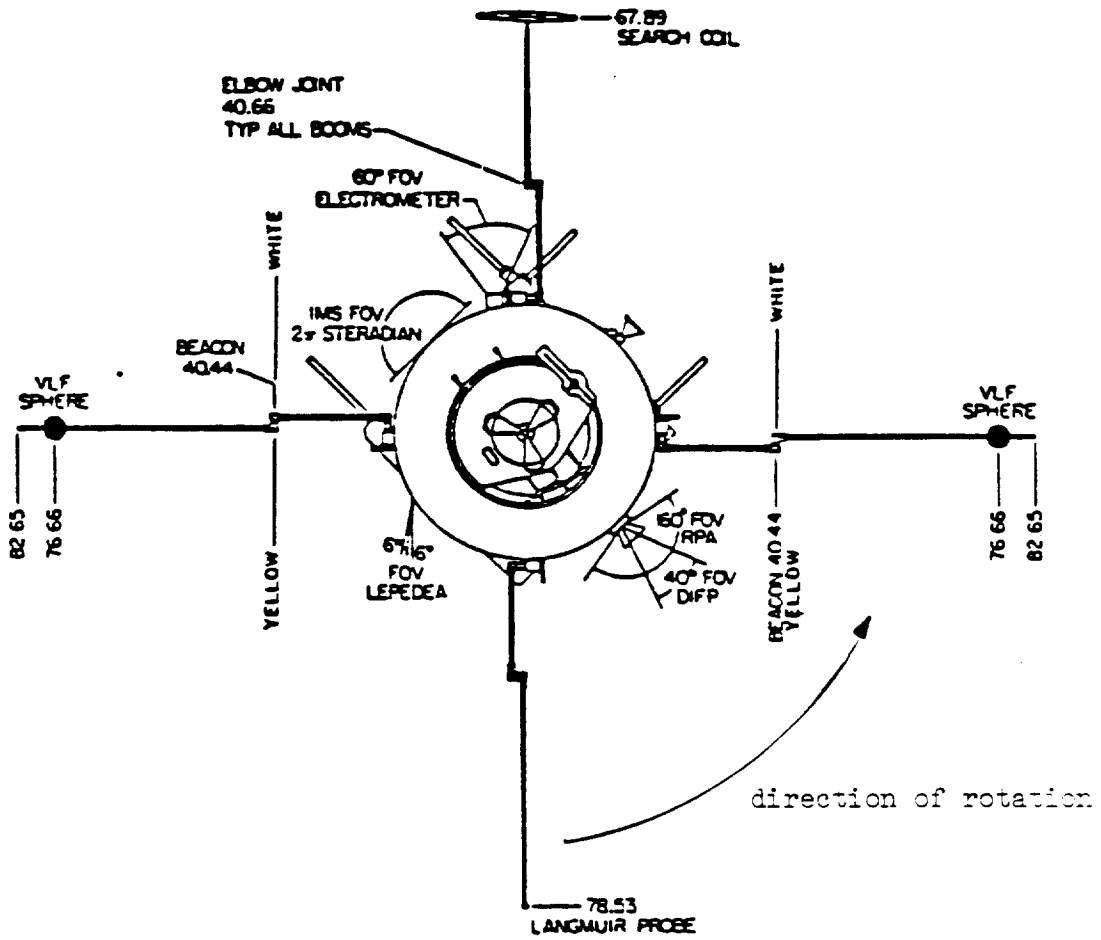


Figure 3. A typical Langmuir probe sweep. The current is in microamperes.



TOP VIEW

Figure 4. The rotation of the PDP during free flight.

**SEPARATION, ROLL MANEUVERS,
& ORBIT 1 IN-PLANE
RELATIVE MOTION SUMMARY
(PDP-CENTERED LVLH RELATIVE MOTION)**

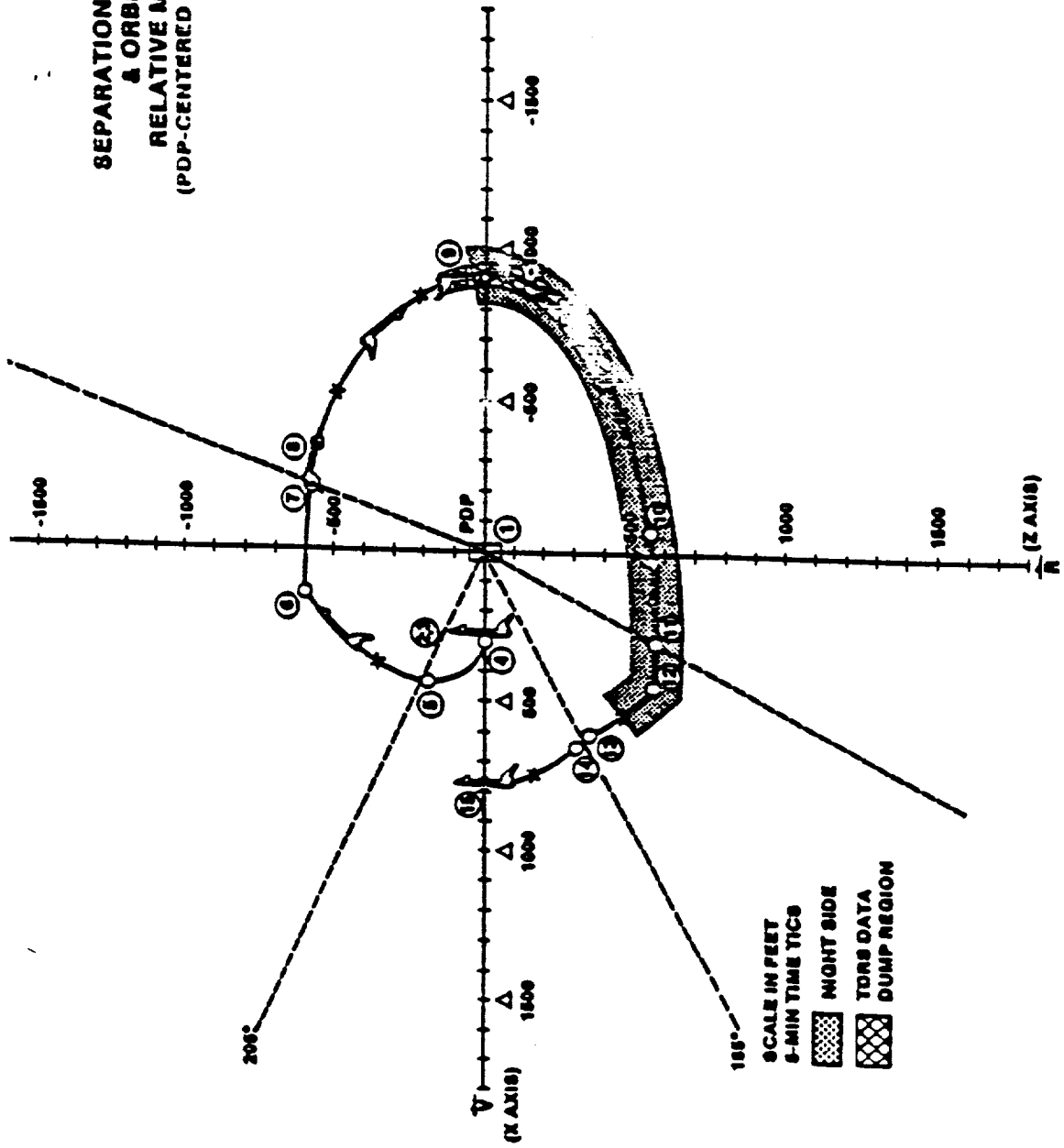


Figure 5. Position of the Shuttle, relative to the PDP.

SPACELAB-2 DATA

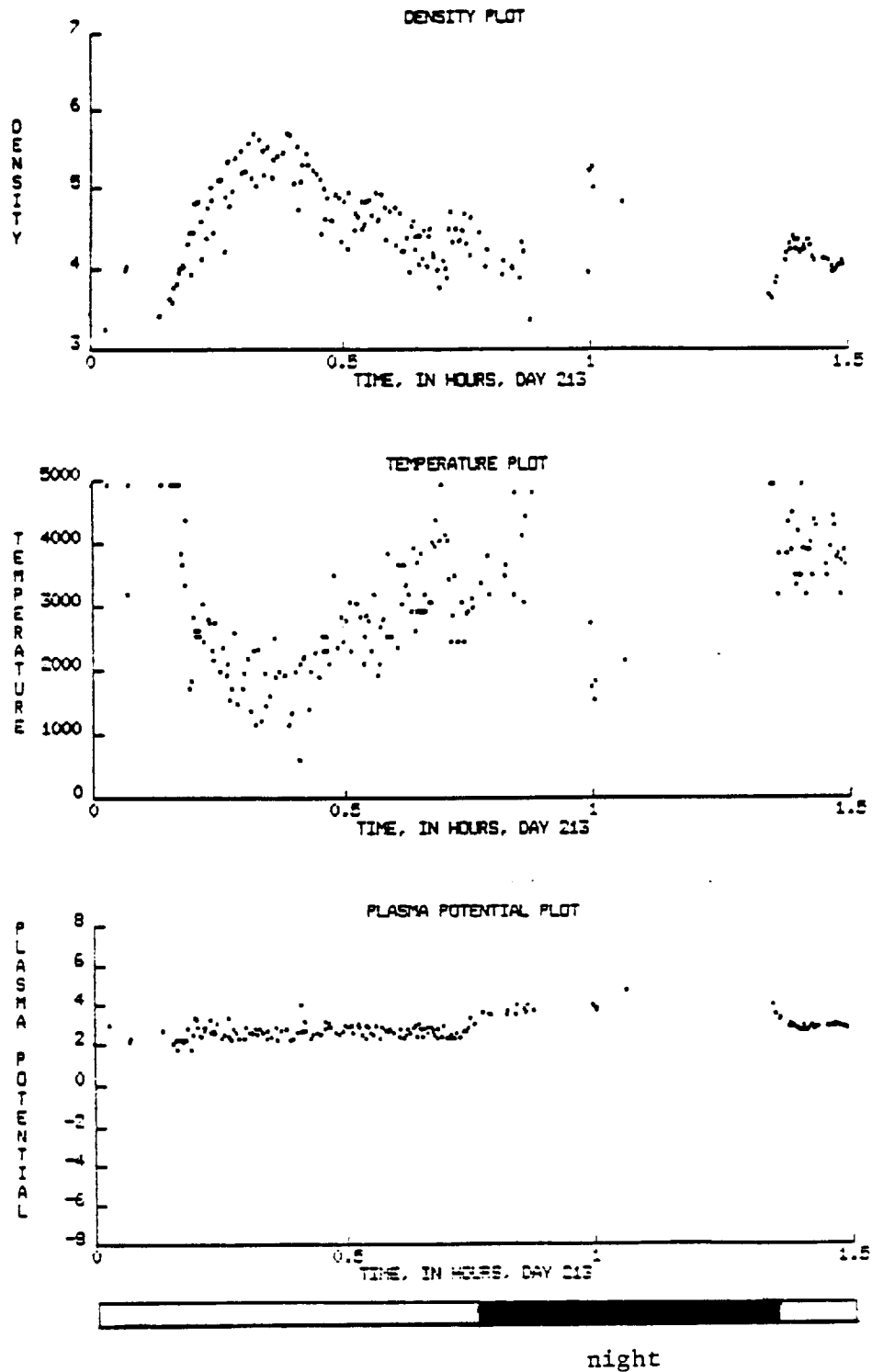


Figure 6. Free-flight densities and temperatures.

SPACELAB-2 DATA

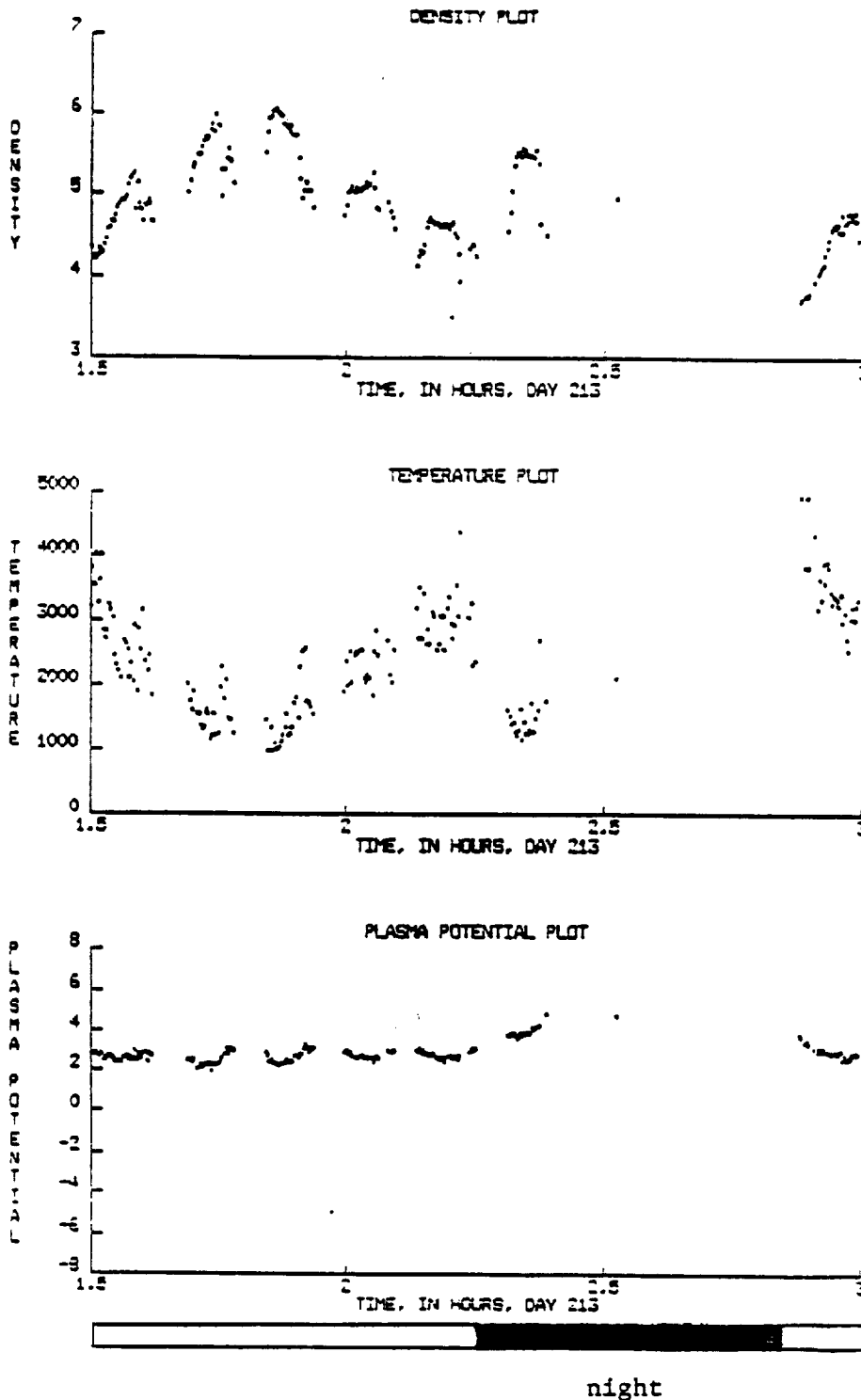


Figure 7. Free-flight densities and temperatures.

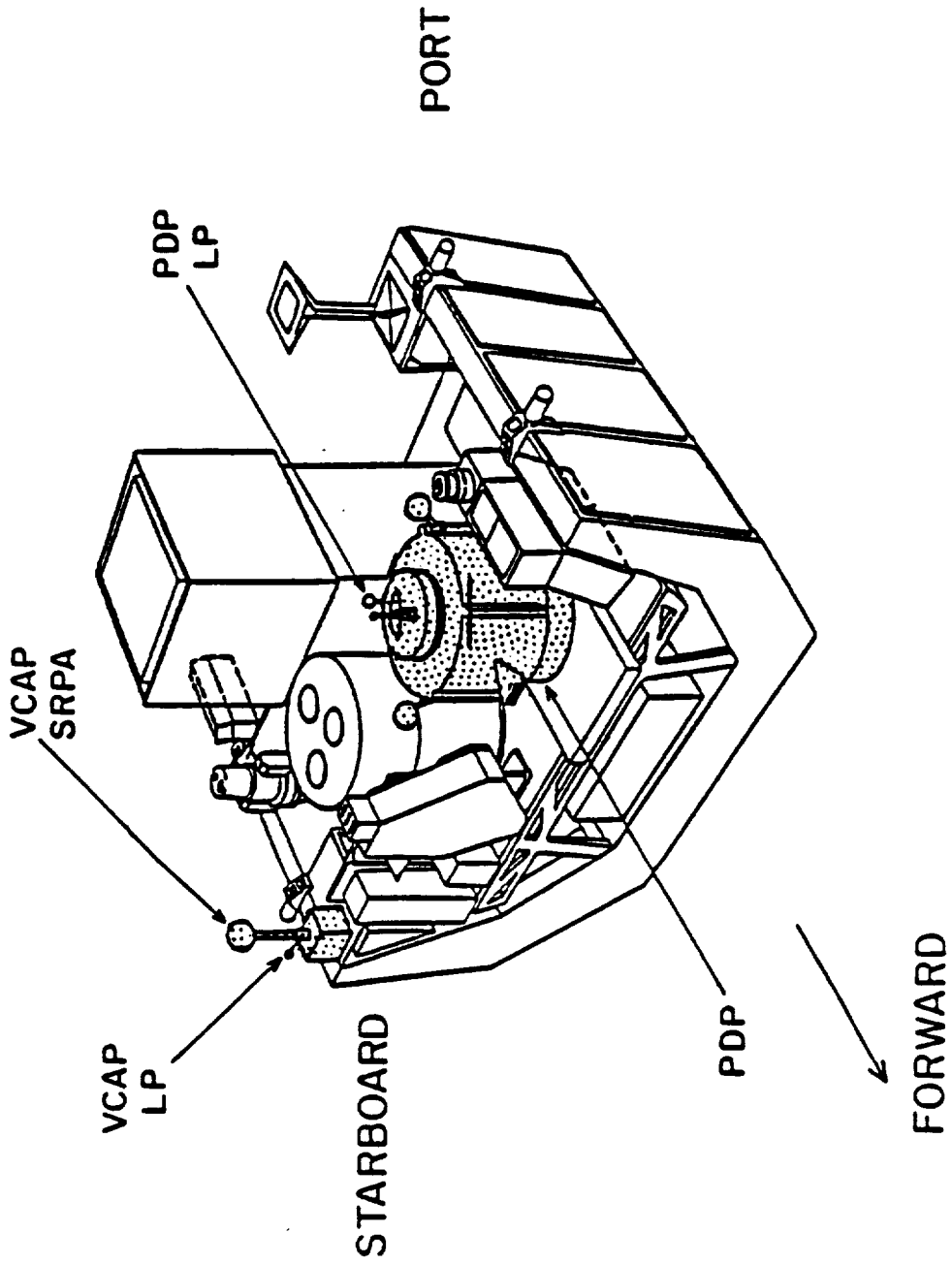


Figure 8. The pallet for the OSS-1 mission.

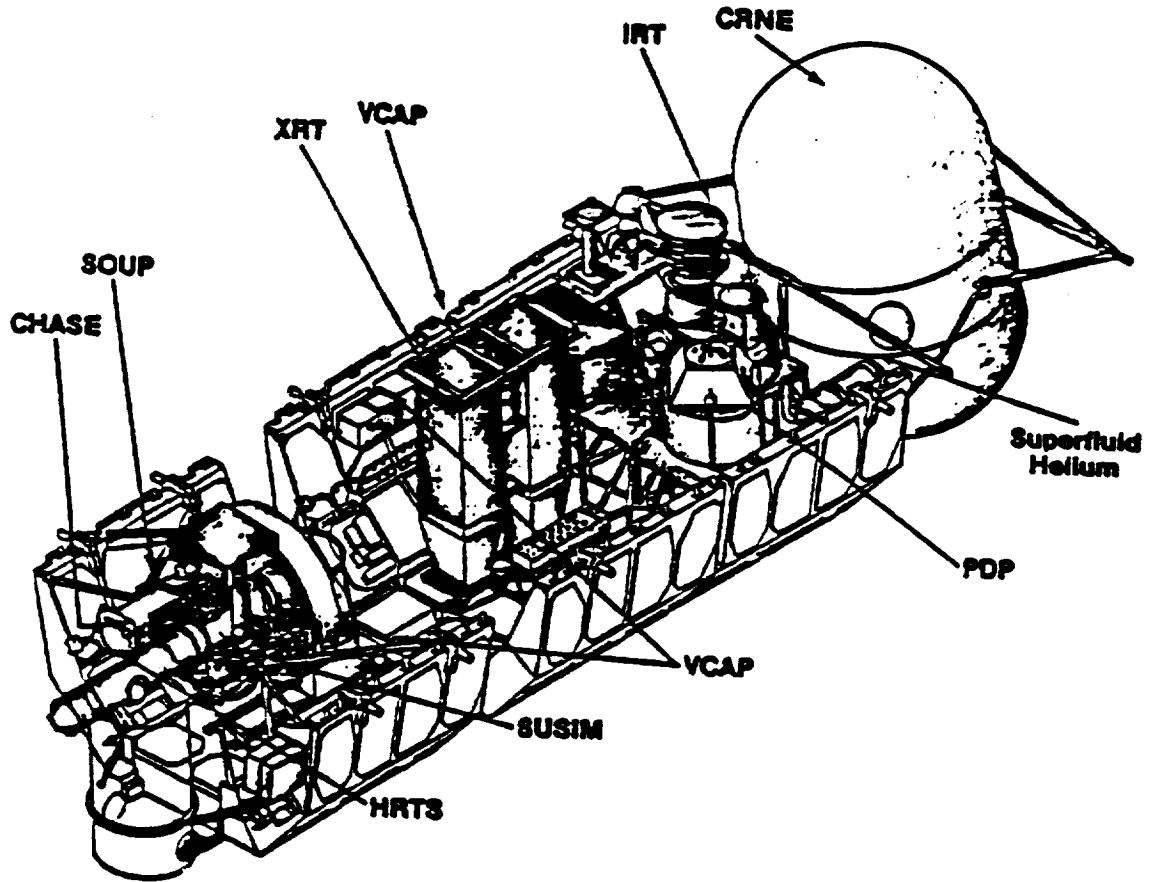


Figure 9. The pallet for the Spacelab-2 mission.

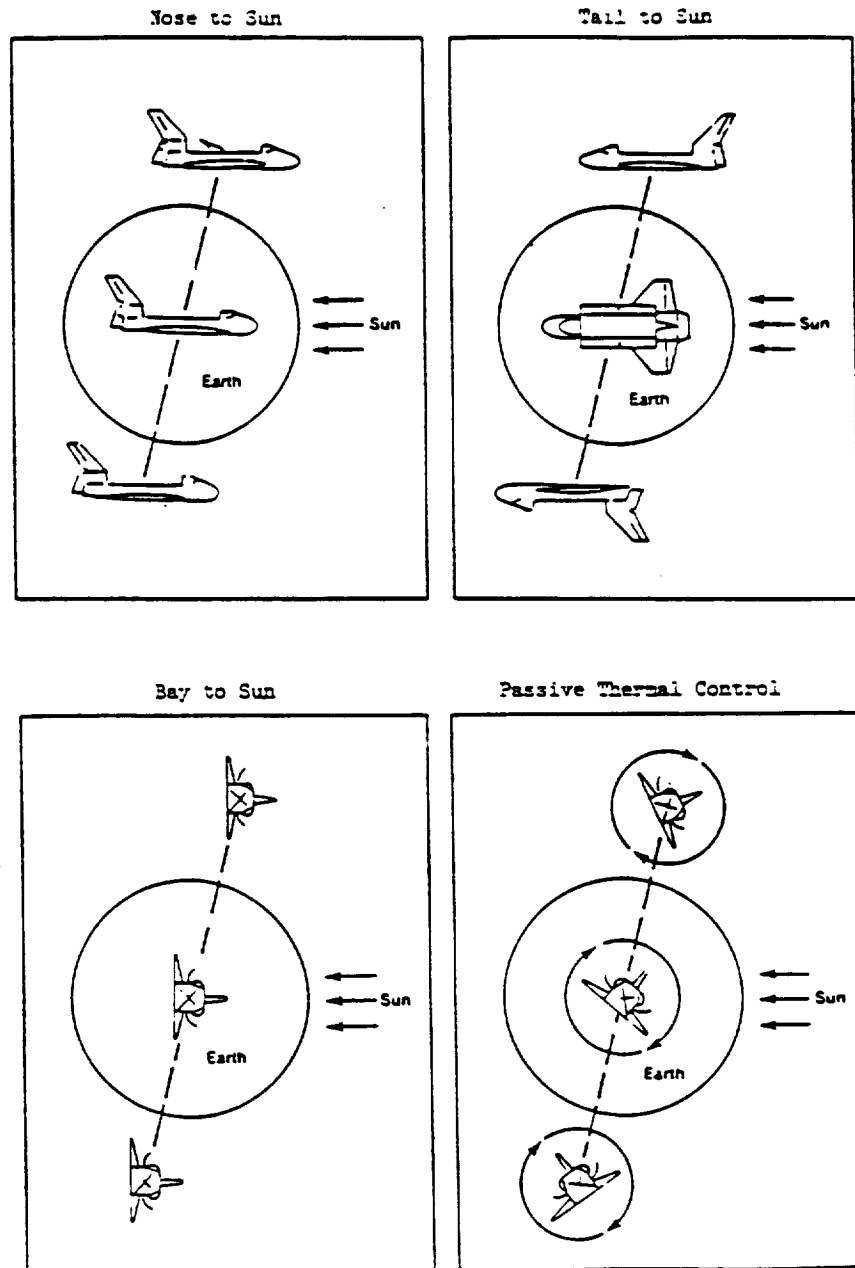
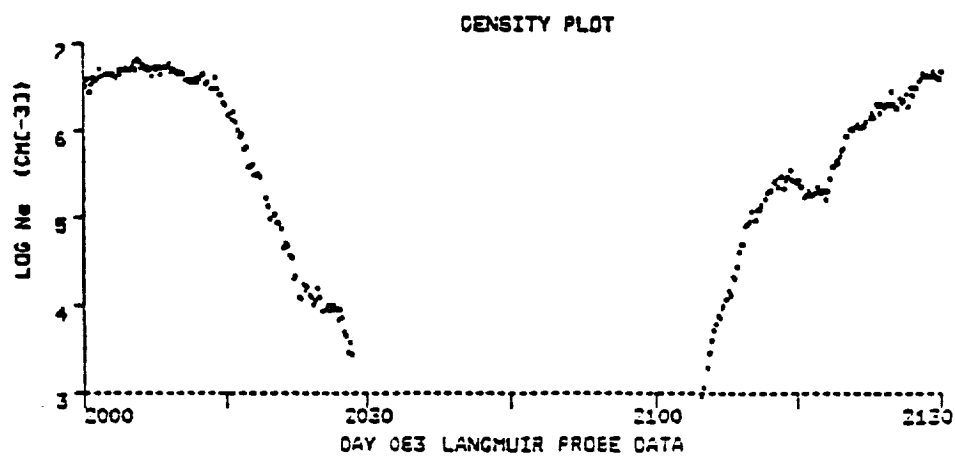
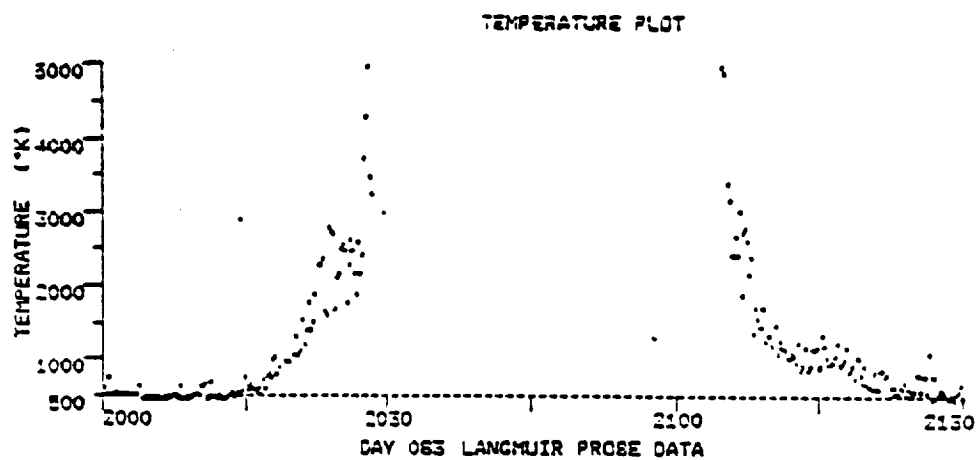


Figure 10. Shuttle attitudes.

OSS-1 DATA

PDP LOCATION: ORBITER BAY



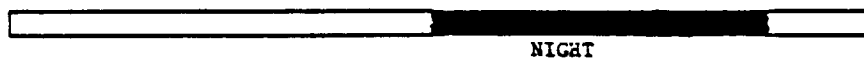
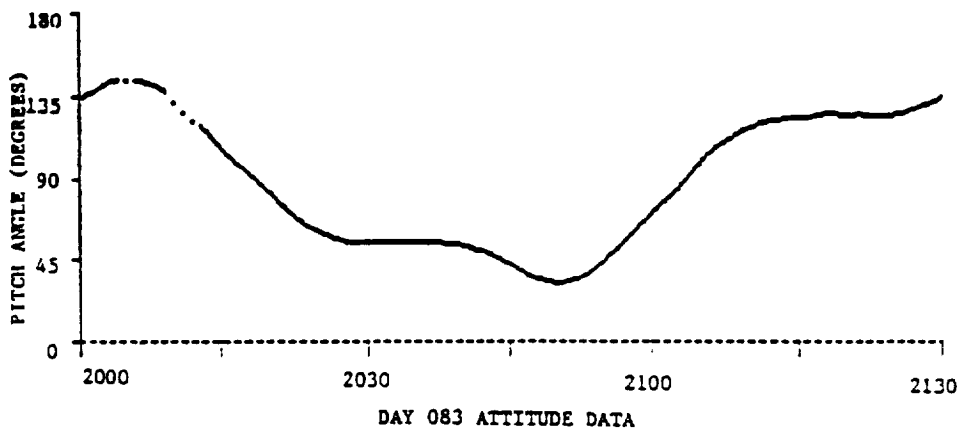
OTHER EVENTS OF INTEREST: Electron Gun Firings, 2013-2029
 2059-2101
 2116-2128

Figure 11. "Nose-to-Sun" data, PDP in cargo bay.

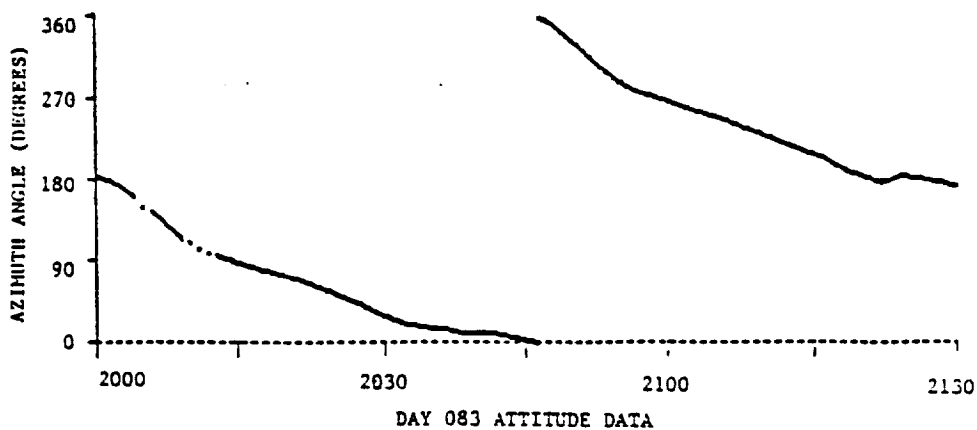
OSS-1 DATA

SHUTTLE ATTITUDE: NOSE-TO-SUN

PITCH ANGLE



AZIMUTH ANGLE



θ_1 = PITCH ANGLE

θ_2 = AZIMUTH ANGLE



Figure 12. "Nose-to-Sun" data, attitude timeline, PDP in cargo bay.

OSS-1 DATA

PDP LOCATION: ORBITER BAY

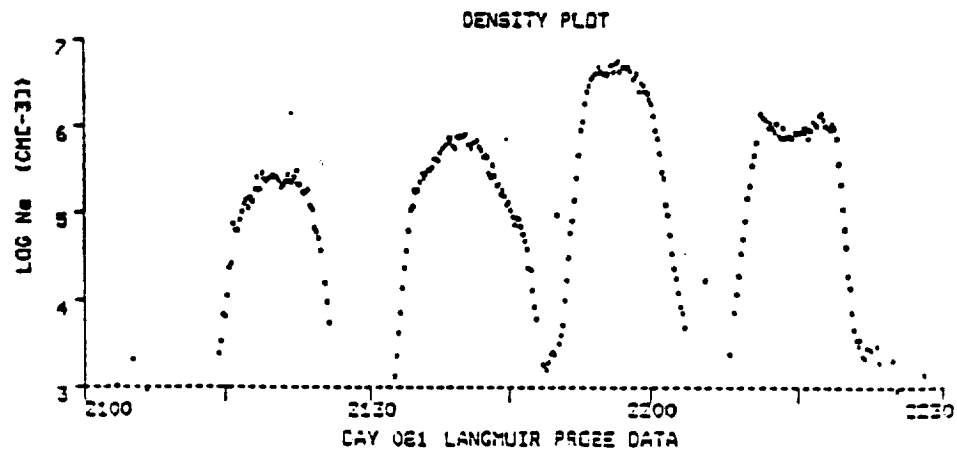
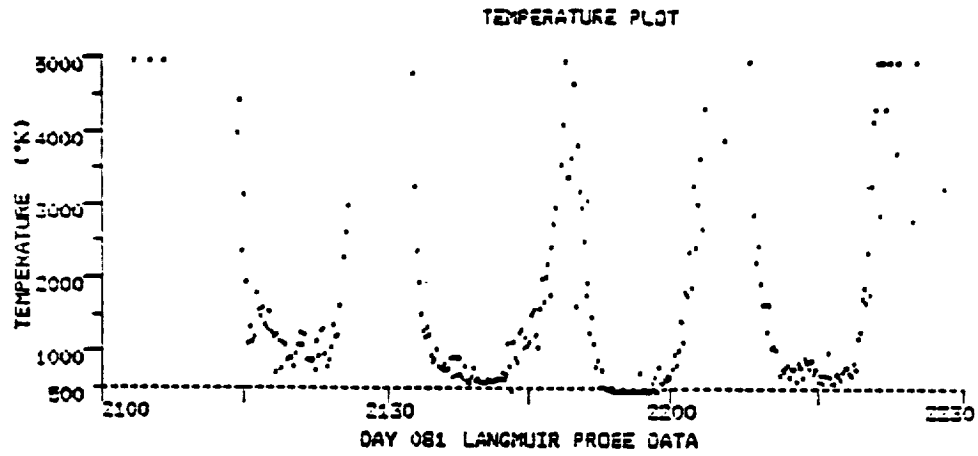
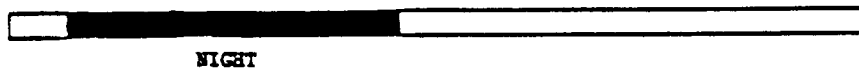
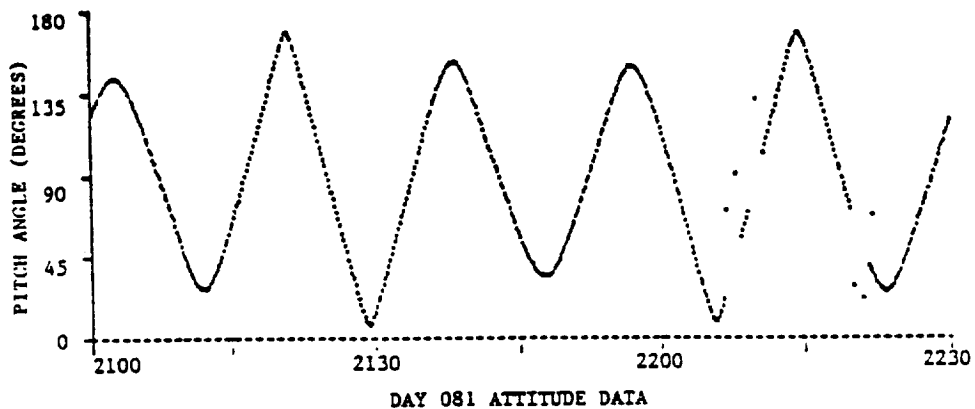


Figure 13. "PTC" data, PDP in cargo bay.

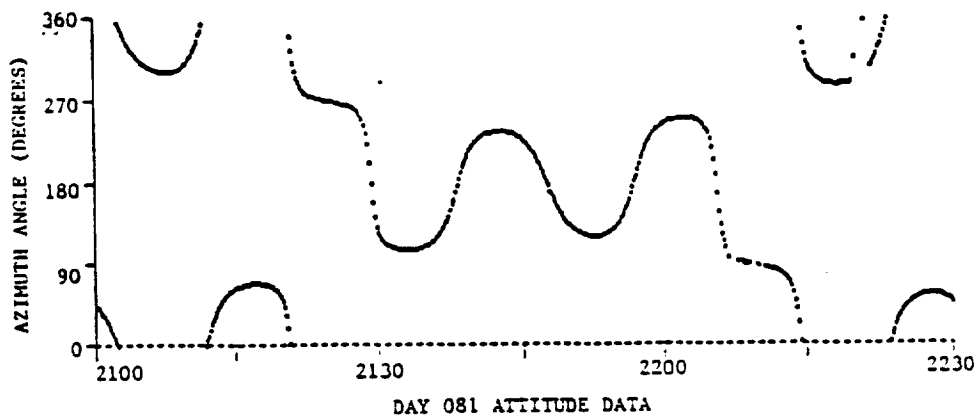
OSS-1 DATA

SHUTTLE ATTITUDE: PTC (BARBECUE MODE)

PITCH ANGLE



AZIMUTH ANGLE



θ_1 = PITCH ANGLE
 θ_2 = AZIMUTH ANGLE

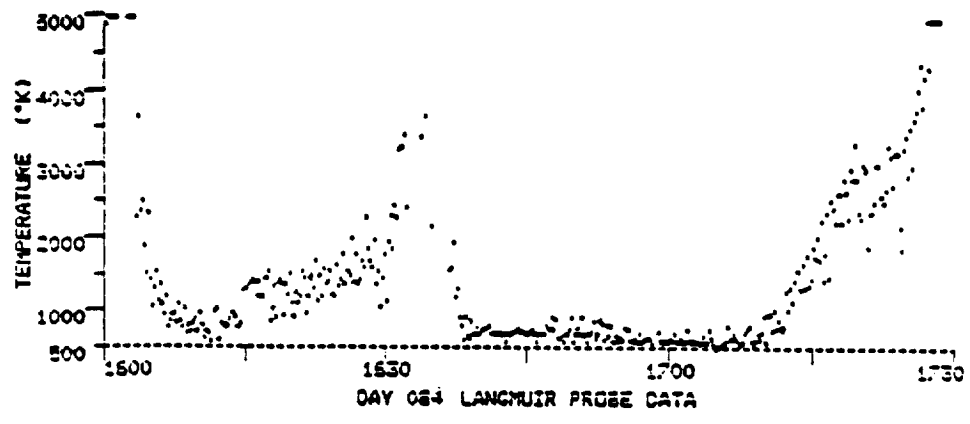


Figure 14. "PTC" attitude timeline, PDP in cargo bay.

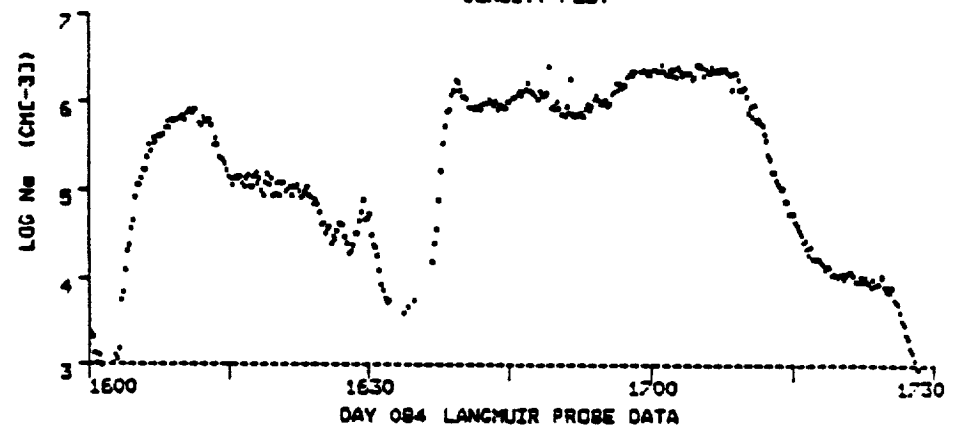
OSS-1 DATA

PDP LOCATION: REMOTE MANIPULATOR SYSTEM ARM

TEMPERATURE PLOT



DENSITY PLOT

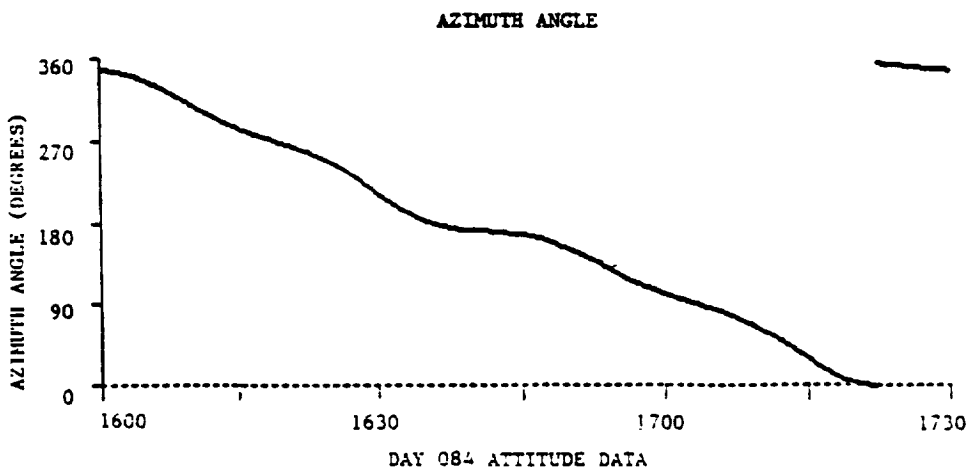
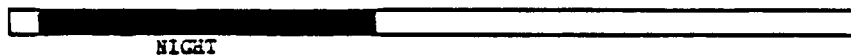
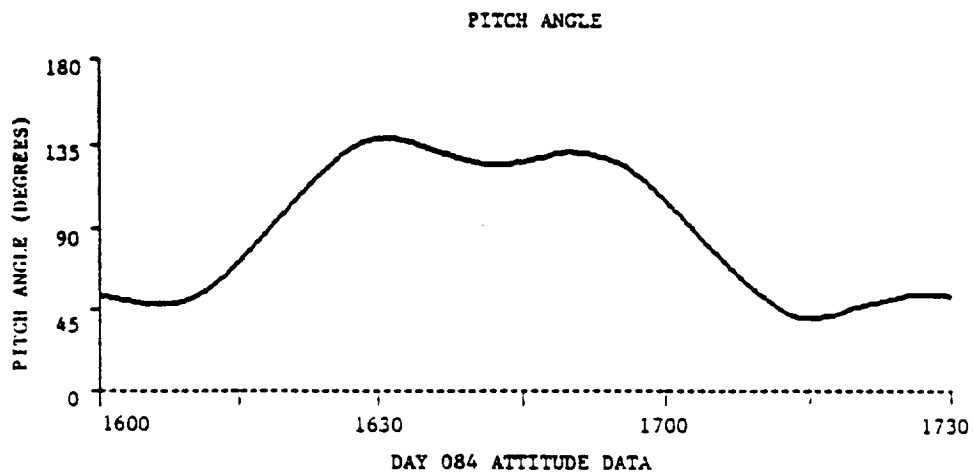


OTHER EVENTS OF INTEREST: Electron Gun Firings, 1653-1710

Figure 15. "Nose-to-Sun" data, PDP on RMS.

OSS-1 DATA

SHUTTLE ATTITUDE: NOSE-TO-SUN



θ_1 = PITCH ANGLE
 θ_2 = AZIMUTH ANGLE



Figure 16. "Nose-to-Sun" attitude timeline, PDP on RMS.

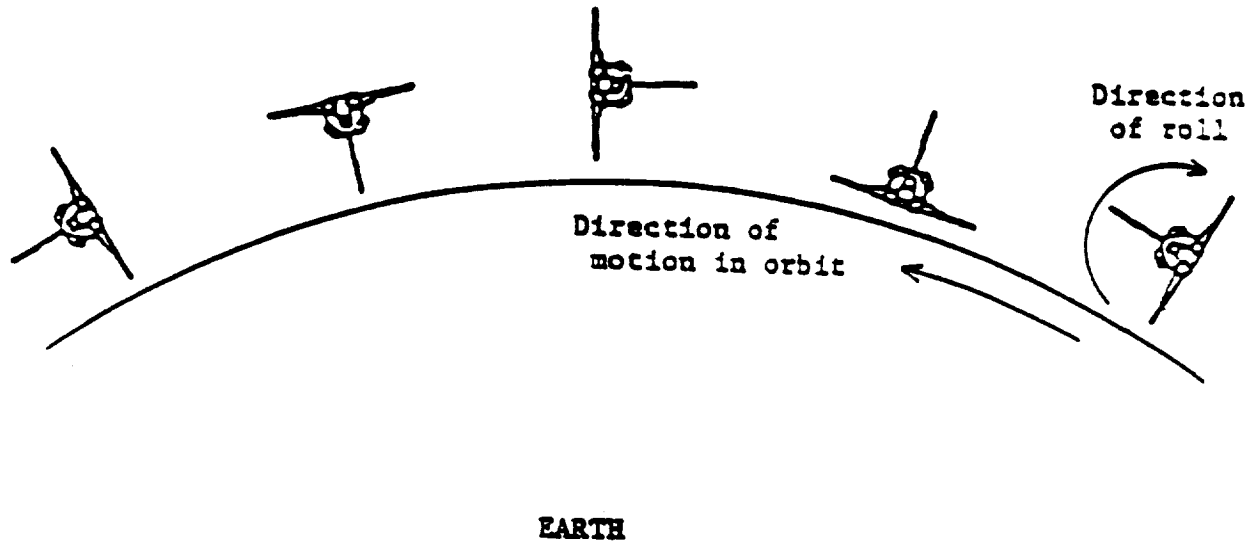


Figure 17. XPOP Roll. Attitude: XPOP Roll (note: tail out of page). Specifics: $0.933^\circ/\text{second}$ retrograde roll around x-axis. x-axis remains perpendicular to the orbit plane. It takes 6 minutes to complete one roll. A total of 10 rolls is made over 1 hour of time. Characteristics: Used to study azimuthal dependence of wake structure.

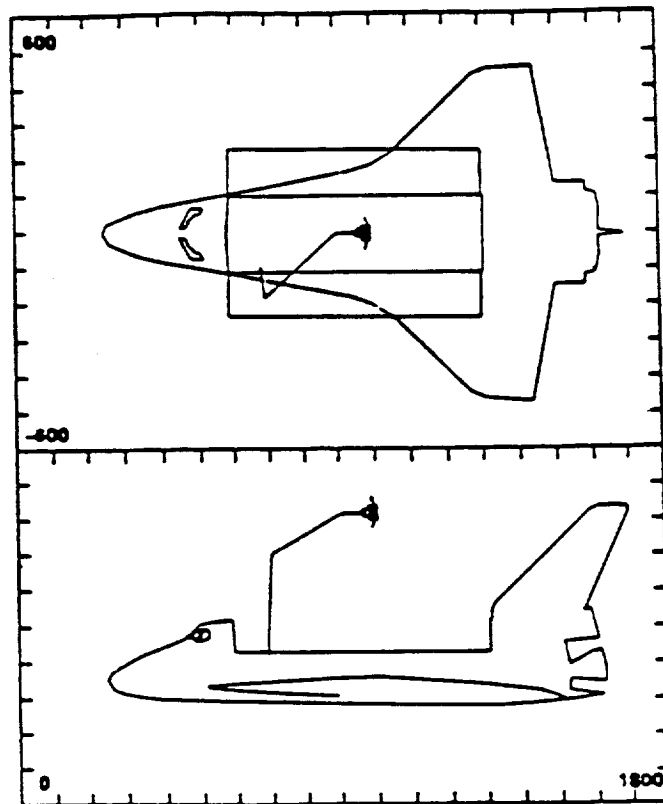


Figure 18. The location of the PDP during XPOP Roll. The scale is marked in inches.

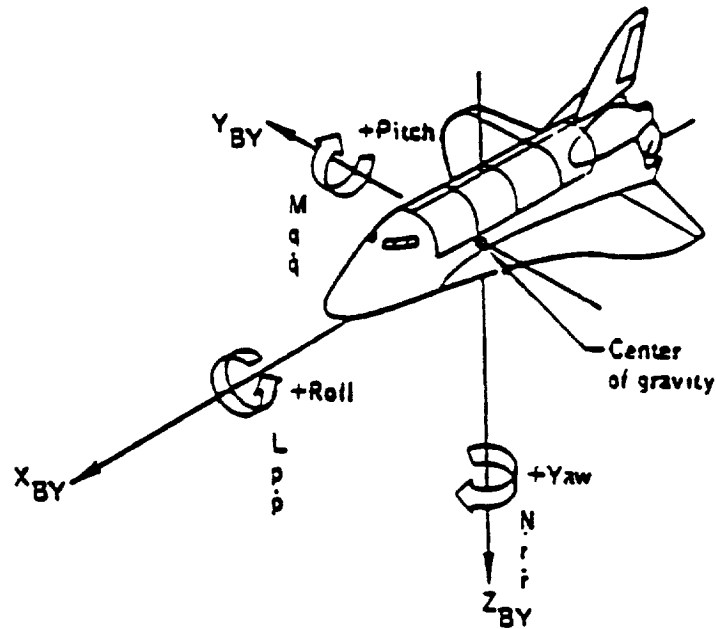


Figure 19. The Orbiter Body Axis System (OBAS). Origin: Center of mass ($X = -1100"$, $Y = 0"$, $Z = -370"$). Orientation: X_{BY} axis is parallel to the orbiter structural body X_0 axis; positive toward the nose. Z_{BY} axis is parallel to the orbiter plane of symmetry and is perpendicular to X_{BY} , positive down with respect to the orbiter fuselage. Y_{BY} axis completes the right-handed orthogonal system. Characteristics: Rotating, right-handed, Cartesian system. L, M, N : Moments about $X_{BY}, Y_{BY},$ and Z_{BY} axes, respectively. p, q, r : Body rates about $X_{BY}, Y_{BY},$ and Z_{BY} axes, respectively. $\dot{p}, \dot{q}, \dot{r}$: Angular body acceleration about $X_{BY}, Y_{BY},$ and Z_{BY} axes, respectively. The Euler sequence that is commonly associated with this system is a yaw, pitch, roll sequence, where $\psi =$ yaw, $\theta =$ pitch, and $\phi =$ roll or bank. This attitude sequence is yaw, pitch, and roll around the $Z_{BY}, Y_{BY},$ and X_{BY} axes, respectively.

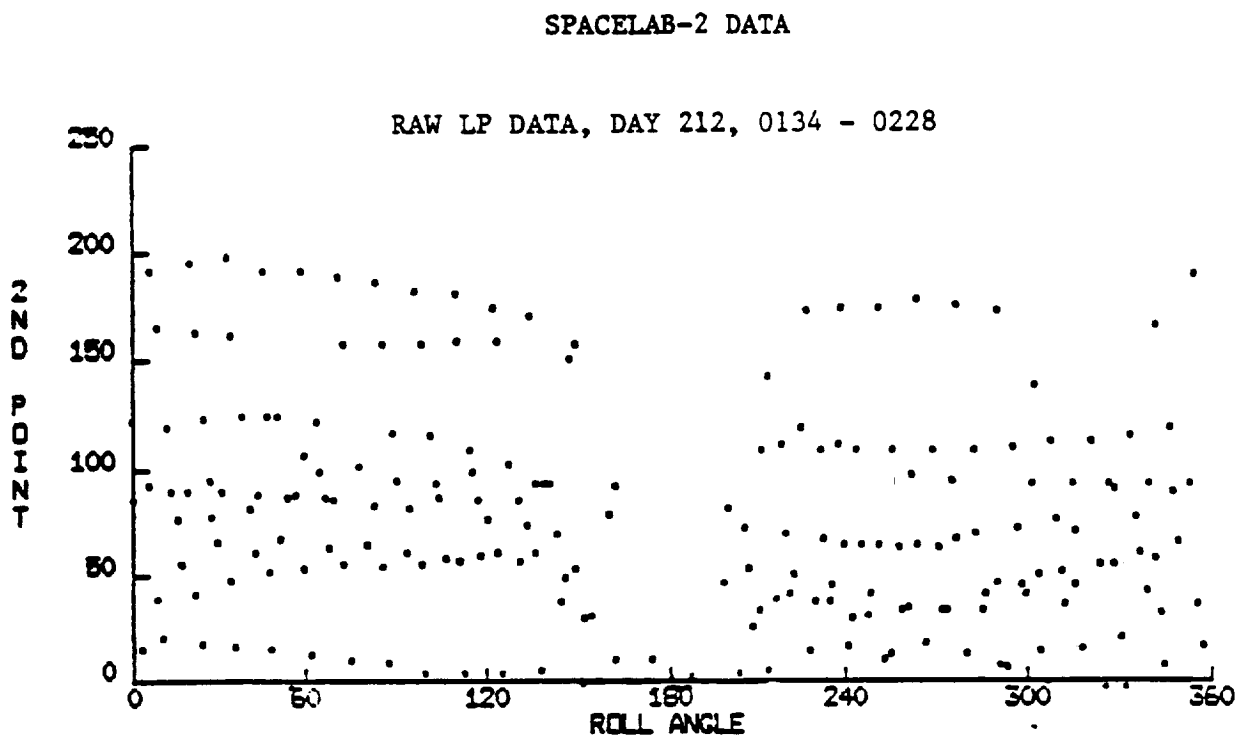


Figure 20. Electron density vs roll angle.

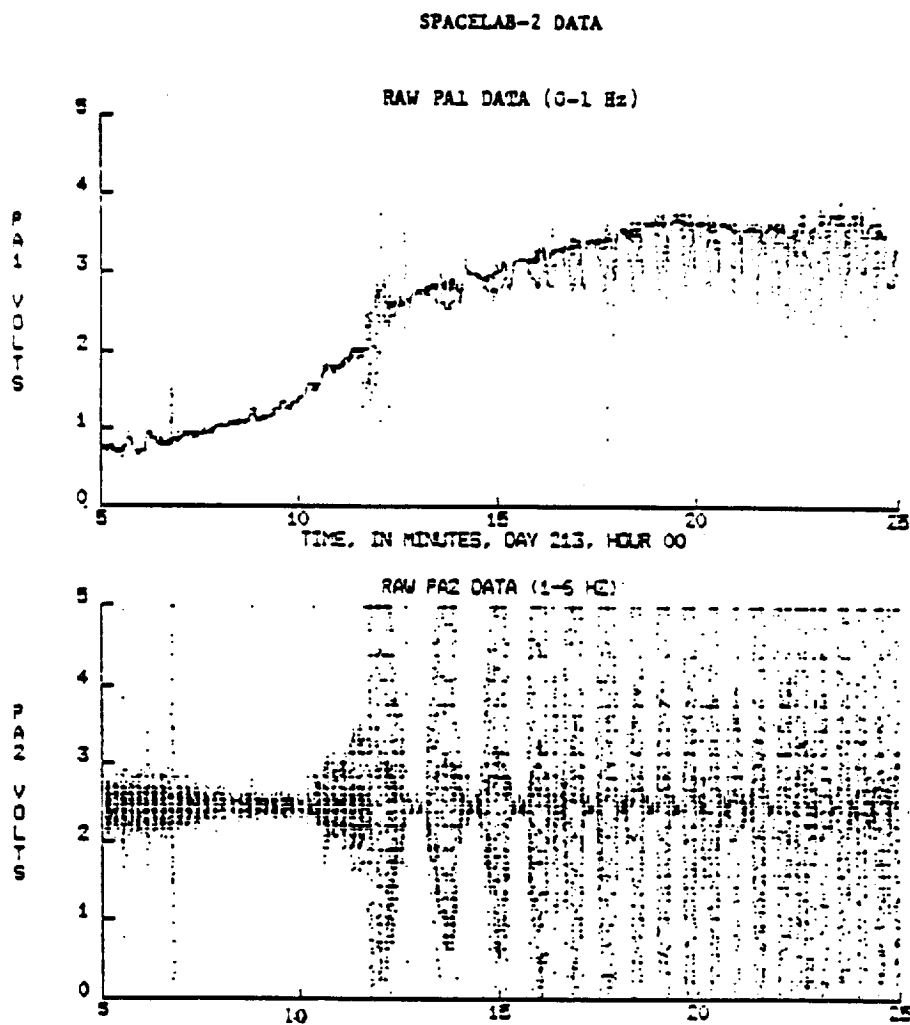
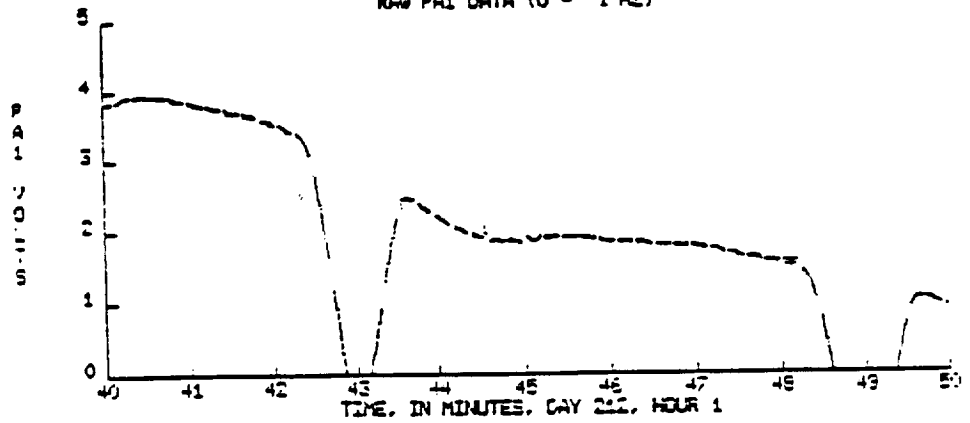


Figure 21. Free-flight density fluctuations.

SPACELAB-2 DATA

RAW PAS DATA (0 - 1 MC)



The PDP is in the wake of the orbiter at 43 and 49 minutes.

RAW PAS DATA (6-40 MC)

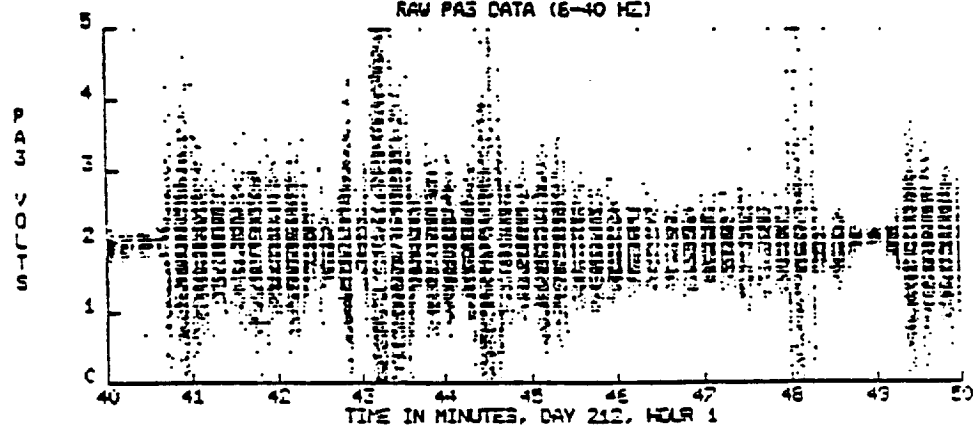
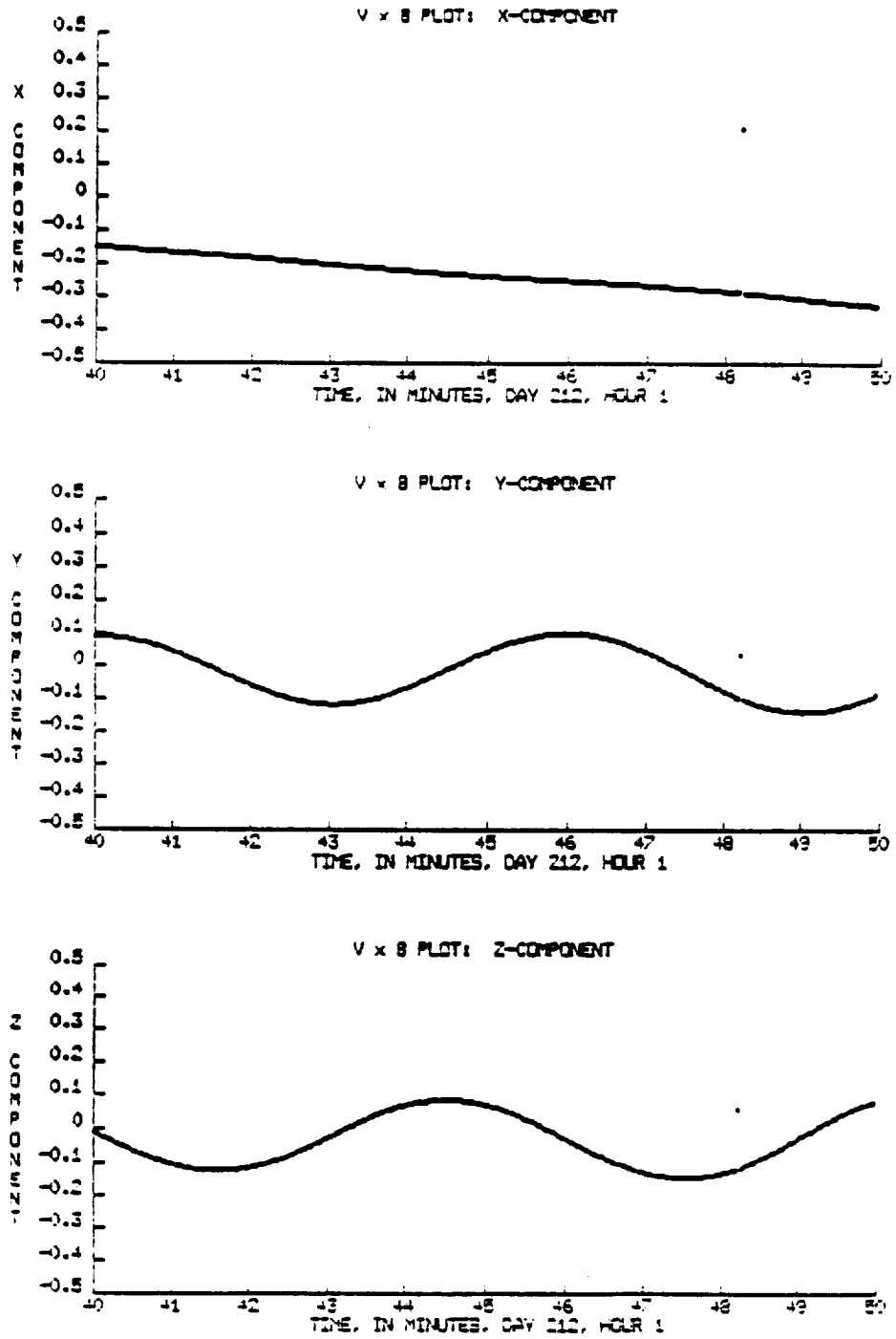


Figure 22. The wake of the orbiter.

SPACELAB-2 DATA

Figure 23. $\vec{v} \times \vec{B}$.

SPACELAB-2 DATA

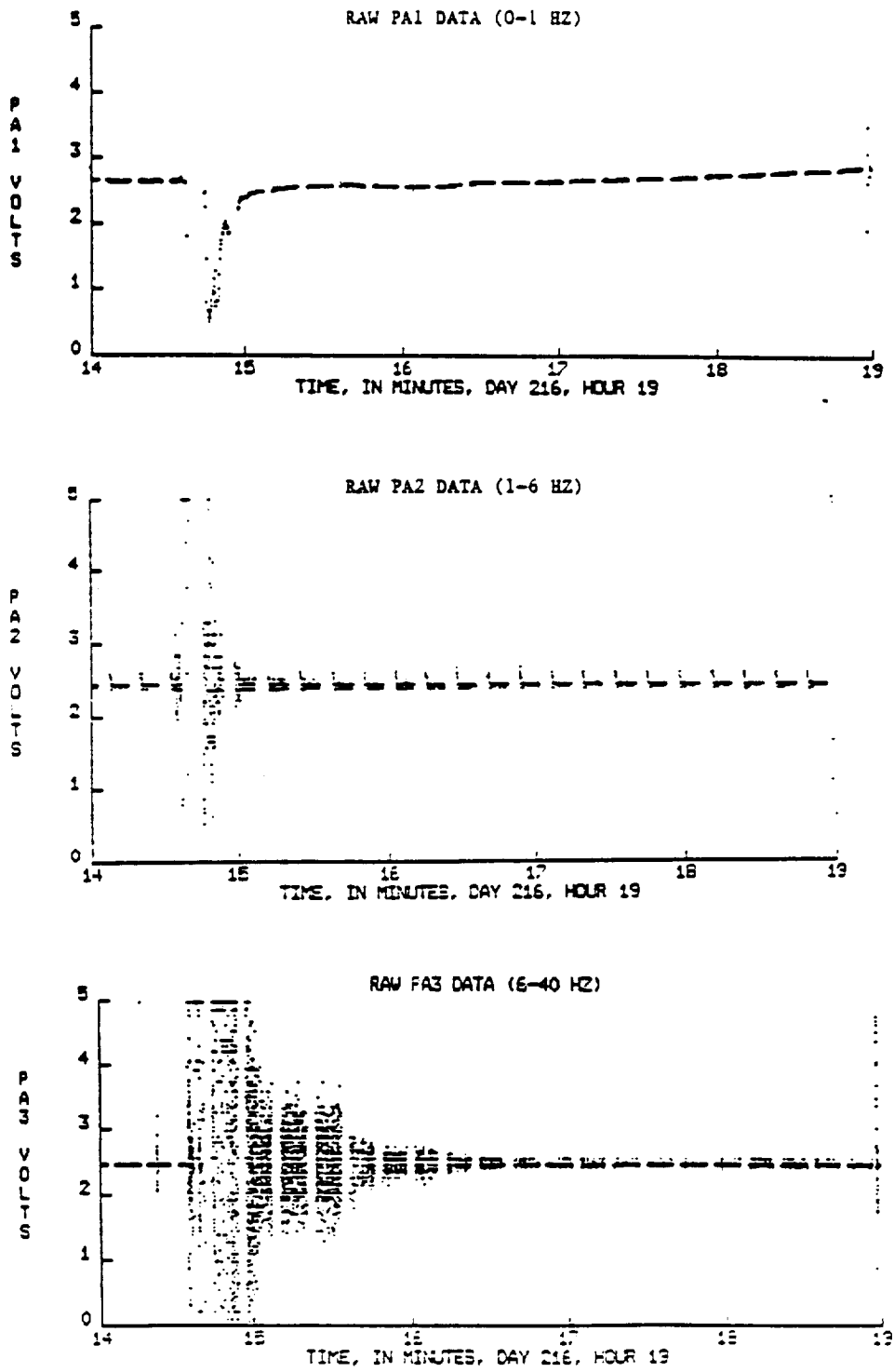


Figure 24. Density fluctuations during an OMS burn.

ORIGINAL PAGE IS
OF POOR QUALITY

APPENDIX A

ELECTROSTATIC NOISE

After the completion of the Spacelab-2 mission, we realized that data reduction for the free-flight times would be complicated because the sweep period of the Langmuir probe was approximately equal to the rotation period of the PDP. The probe has a sweep period of 12.80 seconds. That is, every 12.80 seconds the probe starts a new sweep. During free flight the PDP is rotating with a period of 13.06 seconds. To help visualize some of the consequences of this problem, we define the phase angle as shown in Figure A-1. The phase angle is the angle between the velocity vector of the PDP and the vector that points from the center of the PDP to the Langmuir probe. Thus, if the probe starts a sweep when the phase angle is -180° , the next sweep will begin when the phase angle is approximately -172.9° . The difference in phase angles occurs because the PDP will rotate through 352.9° in 12.80 seconds. Consequently, even though the PDP is rotating in a counterclockwise direction, the probe appears to precess in the clockwise direction.

If the probe travels 7.1° in 12.80 seconds, it will take 10 minutes 42 seconds before the probe will start a new sweep at a

phase angle of -180° . Therefore, the apparent precession period of the probe is just 10 minutes 42 seconds. The velocity vector of the PDP precesses with a period of 90 minutes because this is the time it takes to complete one orbit. Consequently, the probe will start a new sweep in the same position, relative to the velocity vector, after a time T defined by

$$\frac{1}{T} = \frac{1}{10m\ 42s} + \frac{1}{90m} \quad .$$

Solving this gives $T = 9$ minutes 45 seconds.

This is the time between the recurrences of the so-called "density depletion" regions seen during free flight. Part of the data are shown in Figure A-2. Originally, it was thought that these regions were actually times when the probe was in the wake of the PDP. If this was the case then a graph of phase angle vs time would show the phase angle to be approximately 180° during the times associated with the density depletions. However, as we see in Figure A-3, the phase angle is centered at about -60° not 180° . Therefore, the wake of the PDP is not the explanation for the density depletions.

The computer program that calculates densities and temperatures from a given sweep is sometimes unable to do this if the sweep is too noisy. When we examine the sweeps taken during the "density depletions" region, we notice an anomaly in these sweeps. Figure A-4 shows

an example of a Langmuir probe sweep taken during the middle of the first "density depletion" region, which starts at 1 hour 36 minutes on day 213. As we can see from this sweep, there appears to be something affecting the probe's ability to collect current whenever the probe is biased at approximately +7 volts relative to the PDP chassis. However, this problem only manifests itself when the phase angle is between $+30^\circ$ and -150° .

When we look at the data obtained when the PDP is in the lock mode, we notice some anomaly as well. As shown in Figure A-5, the instrument appears to detect some type of noise every 1.6 seconds. Note that in this figure the individual data points have been connected by lines. In order to understand why this is significant, we must first explain how the data are taken from the PDP.

All of the instruments on the PDP have their output formatted so that one complete sampling, what is referred to as one major frame of data, takes 1.6 seconds. Some instruments are sampled every major frame, others may only be sampled periodically. For example, the sweep mode of the Langmuir probe is sampled every eighth major frame. We conclude that the Langmuir probe sees some type of noise at the beginning of every major frame. For this reason we start to suspect that the source of this noise is either the probe itself, or another instrument on the PDP.

When the probe is in the lock mode, it collects 192 data points every major frame. If we look only at the last 100 points, as shown

in Figure A-6, the data clean up immensely, but we are still able to see the effects of this noise. Figure A-7 is a sample of the data obtained during the "density depletion" region starting at 1 hour 36 minutes on day 213. Note that the first 92 points of every major frame have been removed so that we may see the time evolution of the noise more clearly. This is the source of the small gaps in the data. The large gaps in the data are the time intervals when the probe was in the sweep mode. These data are also not plotted. As shown in this figure, we see that there is a shape to the "noise" which we see at the beginning of every major frame. If we follow the maximum of this noise in time, we notice that in some cases the maximum falls in the middle of the lock mode and in some cases the maximum is not present because it falls in the middle of a sweep. The times this noise falls during a sweep mode are also the times that the probe is unable to calculate densities and temperatures. Therefore, we can conclude that the problem we occasionally see during the sweep mode is always present. However, we only notice it during the sweep mode if the noise maximizes there.

As previously mentioned, the fact that we see this "noise" at the beginning of every major frame makes us suspect that there is either a problem with the probe itself or another instrument on the PDP. We are hesitant to place the blame with the probe itself because the instrument appears to have performed as expected at all other times during the Spacelab-2 mission. Also, other instruments on the

PDP record a similar effect. This leads us to believe that the probe is actually measuring some type of physical disturbance, rather than malfunctioning. Most instruments on the PDP, such as the Retarding Potential Analyzer, the Ion Mass Spectrometer, etc., operate at low voltages which would make them unlikely candidates as a source for this disturbance. The most likely source of this noise is the Low Energy Proton Electron Differential Energy Analyzer (LEPEDEA). At the beginning of every major frame LEPEDEA jumps to +2.2 kilovolts, relative to the chassis of the PDP, then decays exponentially, with a time constant of 4 msec, before the start of the next major frame. This is shown in Figure A-8. Also, as shown in Figure A-9, if we examine the orientation of LEPEDEA relative to the velocity vector, we seem to have a plausible explanation for the strange dependence on phase angle that the noise seems to have. The noise begins when the phase angle is +30°, at this point LEPEDEA is just beginning to look into the ram of the plasma flow. The noise ends when the phase angle is -150°, the point at which LEPEDEA looks into the wake. On the basis of this circumstantial evidence, we seem to have good reason for labeling LEPEDEA as the source of the noise.

The velocity of the shuttle is comparable to the thermal velocity of the ions. Therefore, ions will be colliding with the PDP in great numbers only on the side of the PDP facing the ram of the plasma flow. The thermal velocity of the electrons is much greater than the velocity of the shuttle, and they can be expected to impact

the PDP in equal numbers on all surfaces. When LEPEDA jumps to +2.2 kilovolts, this creates a large positive potential hill near its opening. Because the ions are also positively charged, they will be deflected by this well as they approach the LEPEDA. This will cause a number of them to alter their course so that they do not strike the PDP. When LEPEDA is facing the wake, only those ions whose thermal velocities are greater than that of the PDP will be affected. However, when LEPEDA is facing the ram, a substantially greater number of ions will be affected because this is the side of the PDP where most of the collisions with ions take place. As a result when LEPEDA is in ram, there will be less positive current flow to the body of the PDP. This makes the potential of the chassis more negative. Consequently, whenever LEPEDA is in ram the current-collecting ability of the probe is affected because its reference potential changes momentarily as LEPEDA fires.

If the LEPEDA is responsible for changing the reference potential of the PDP, we would expect to see the effect of this within a few milliseconds after LEPEDA fires. However, as was previously mentioned, the anomaly appears to "maximize" whenever the bias voltage is +7 volts. This is 0.2 seconds after the LEPEDA has fired. We believe that this delay is caused by the electronics that controls the operation of the Langmuir probe. Recall that when in the sweep mode the output is sent through a 0 - 50 Hz bandpass filter. Whenever an electrical pulse is sent through such a filter, there will be a delay

between the time that the pulse arrives at the filter and the time that the low-frequency components of the pulse are seen as output. It is believed that this delay could be as long as 0.2 seconds. However, this has yet to be experimentally verified.

At this point we begin to wonder why we did not see this effect at other times during either the Spacelab-2 mission or the OSS-1 mission. However, with the exception of the 6 hours of free-flight data, the remainder of the time we were always grounded to the orbiter. Its larger surface area essentially cancelled the effects of the potential well. Also, LEPEDEA has never before been flown in a region where the ion density is this high. Therefore, we had no reason to expect to see this phenomenon before the free-flight data were collected. As it turns out, when we go back and look at the data for other times, we are able to see the effects of this potential difference. However, the magnitude of the effect appears to have been greatly minimized when the PDP is grounded to the orbiter.

In conclusion, we believe that the regions of "density depletion" are actually regions where LEPEDEA has changed the reference potential of the PDP. This potential difference affects the current-gathering ability of the probe and produces sweeps that we are unable to use when we calculate densities and temperatures.

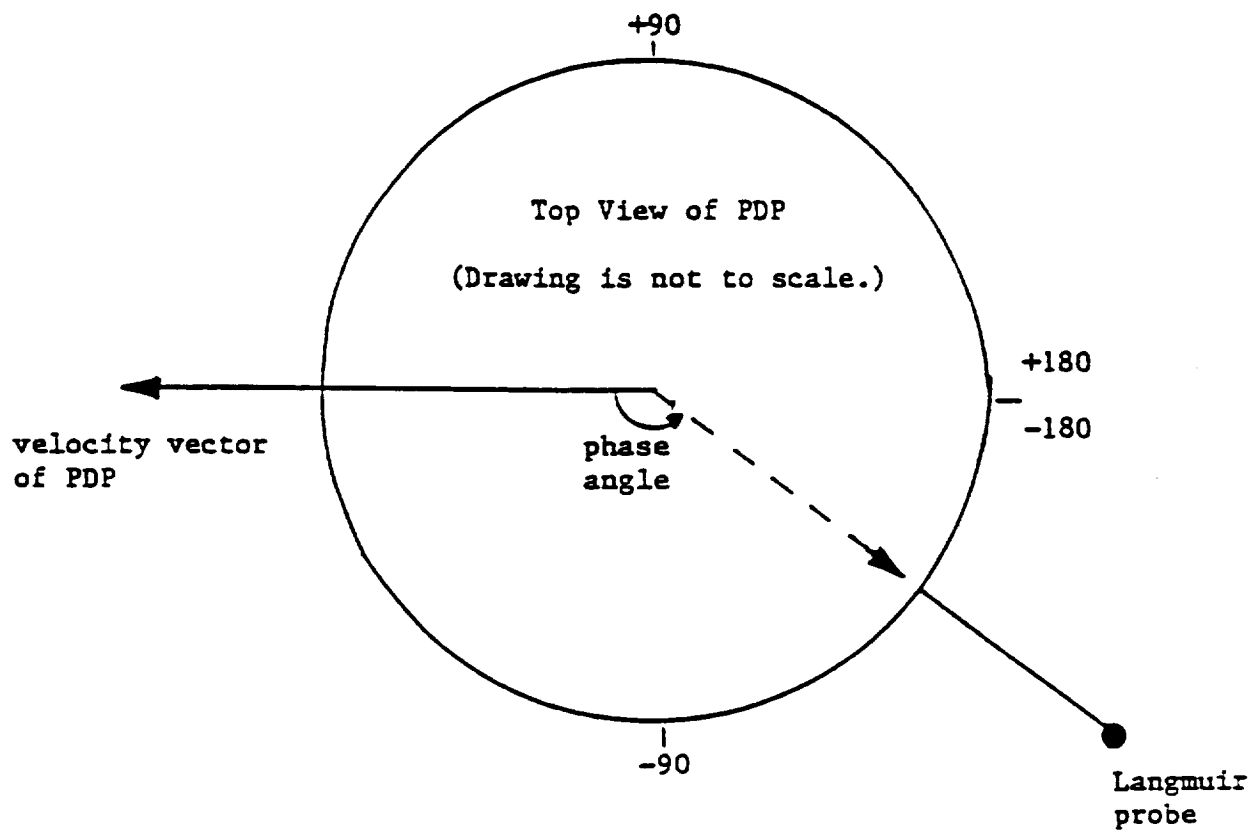


Figure A-1. The phase angle. A phase angle of -90 indicates that the Langmuir probe vector points toward the Earth.

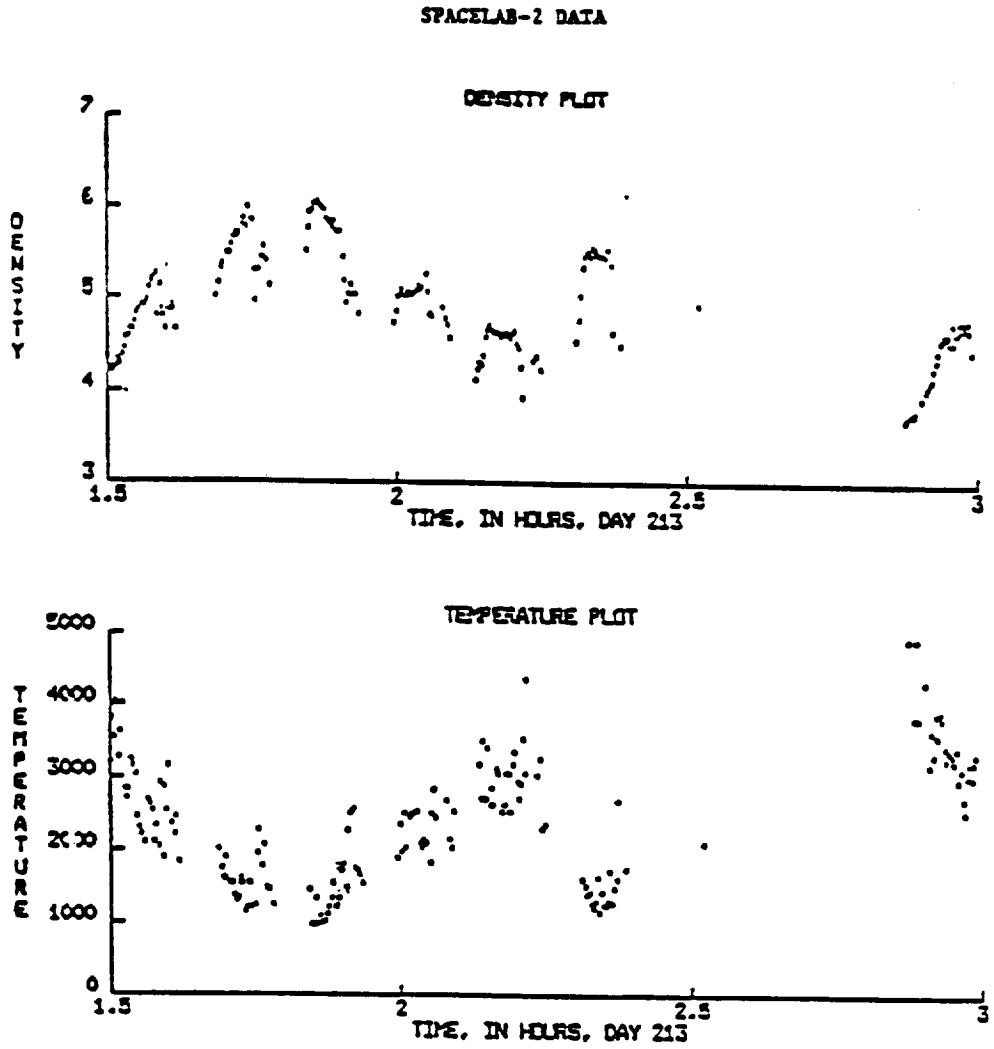


Figure A-2. The density depletion regions.

SPACELAB-2 DATA

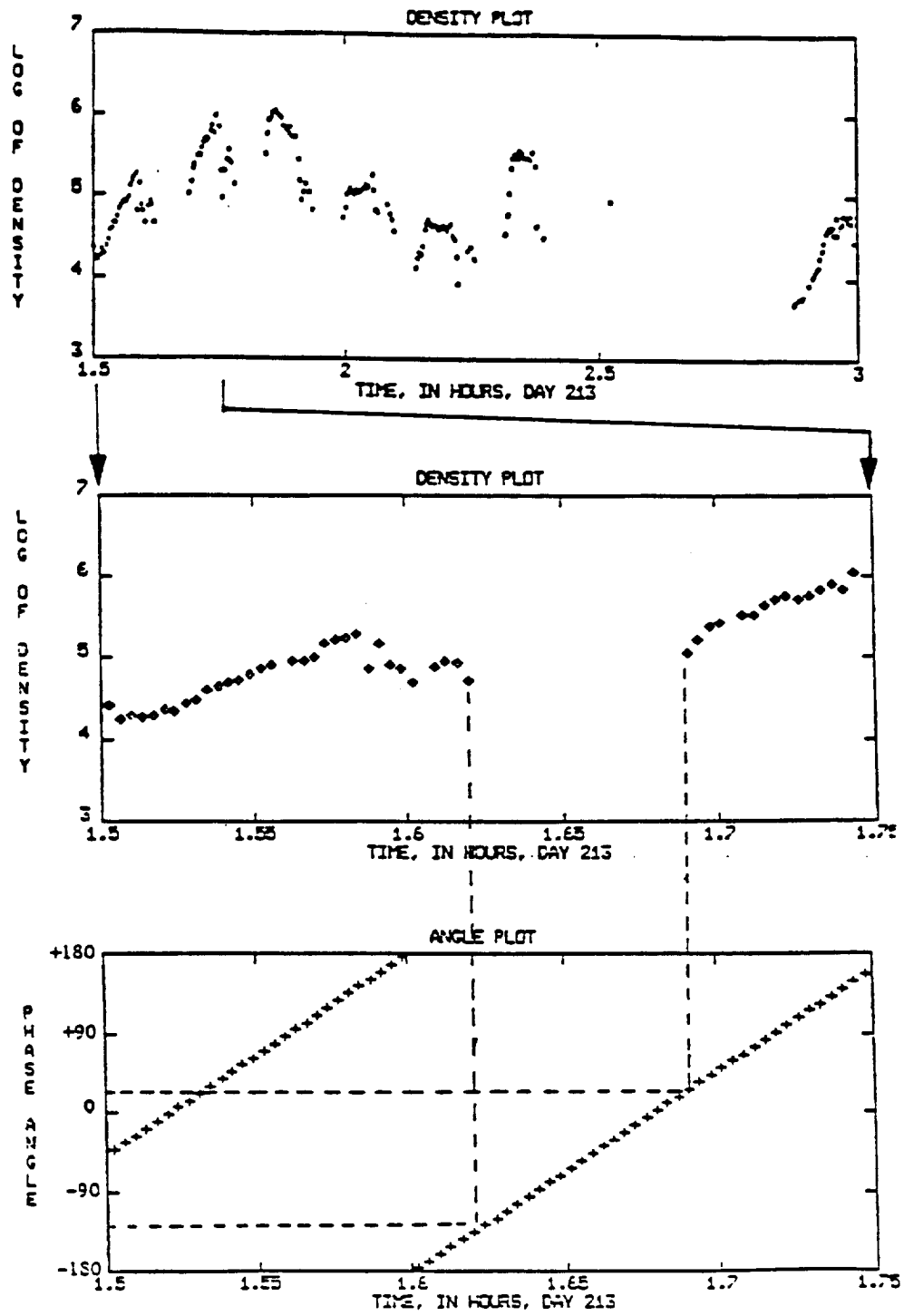


Figure A-3. Density depletions as a function of phase angle.

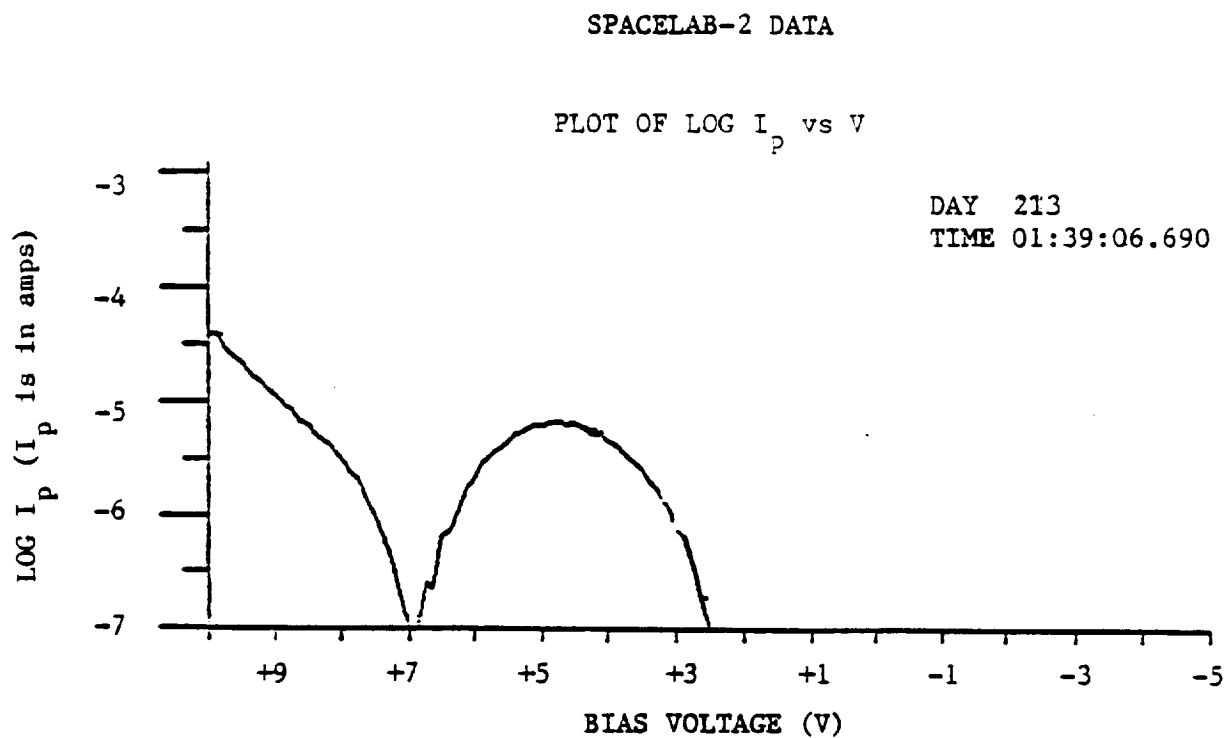


Figure A-4. An anomaly in the Langmuir probe sweep.

SPACELAB-2 DATA

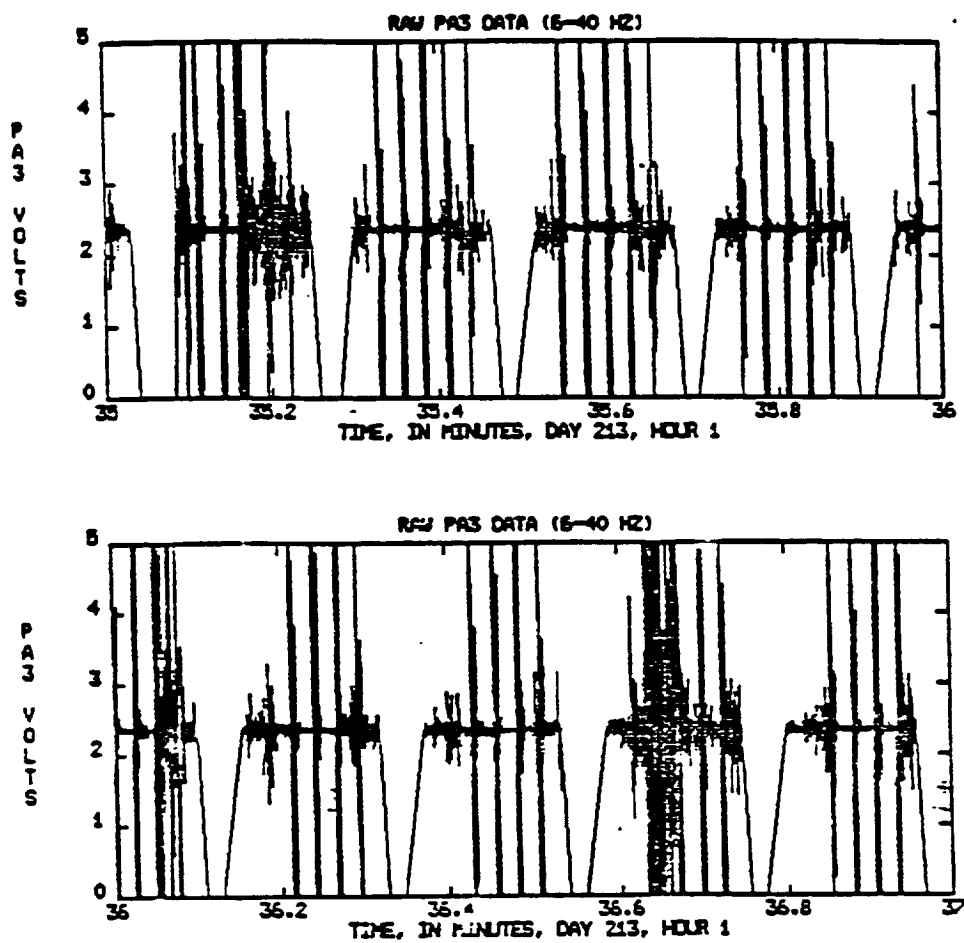


Figure A-5. An anomaly in the lock mode data.

SPACELAB-2 DATA

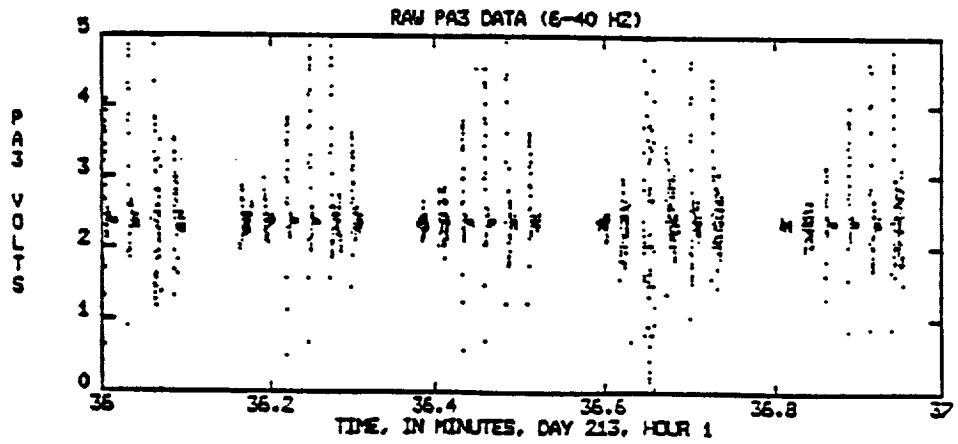
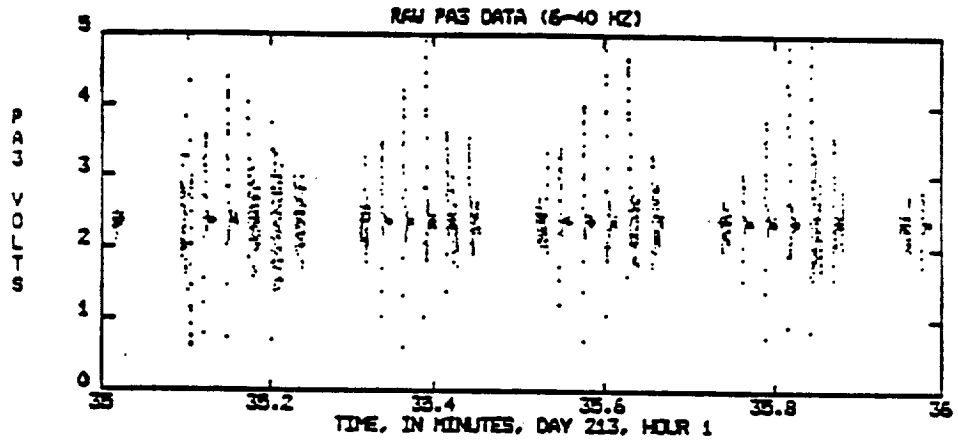
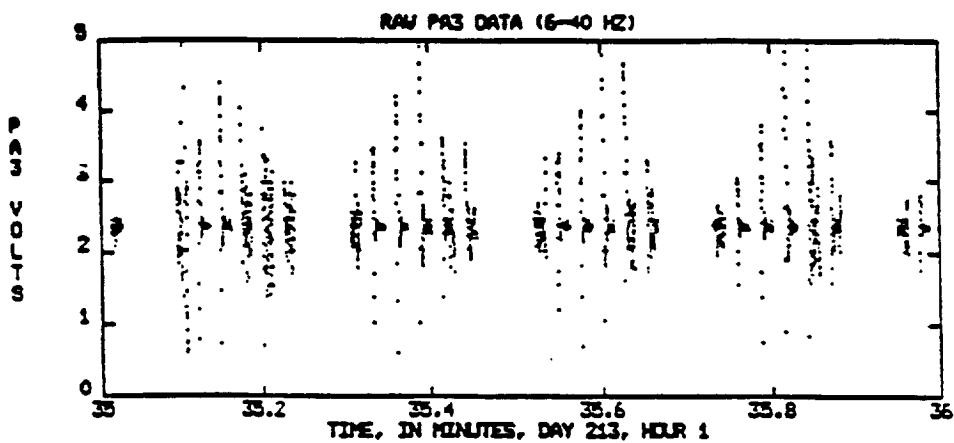


Figure A-6. "Cleaned up" lock mode data.

SPACELAB-2 DATA



A maximum in the middle of a lock mode at 39.4 hours.

A maximum in the middle of a sweep mode at 39.75 hours.

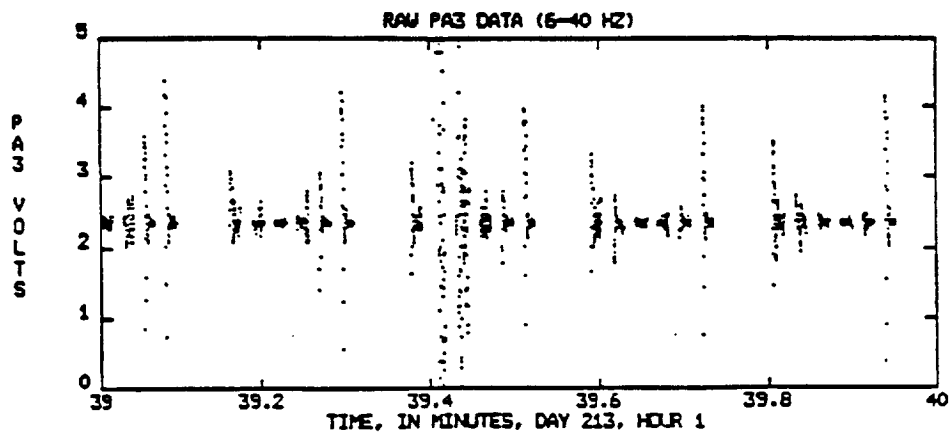


Figure A-7. Lock mode data during density depletion.

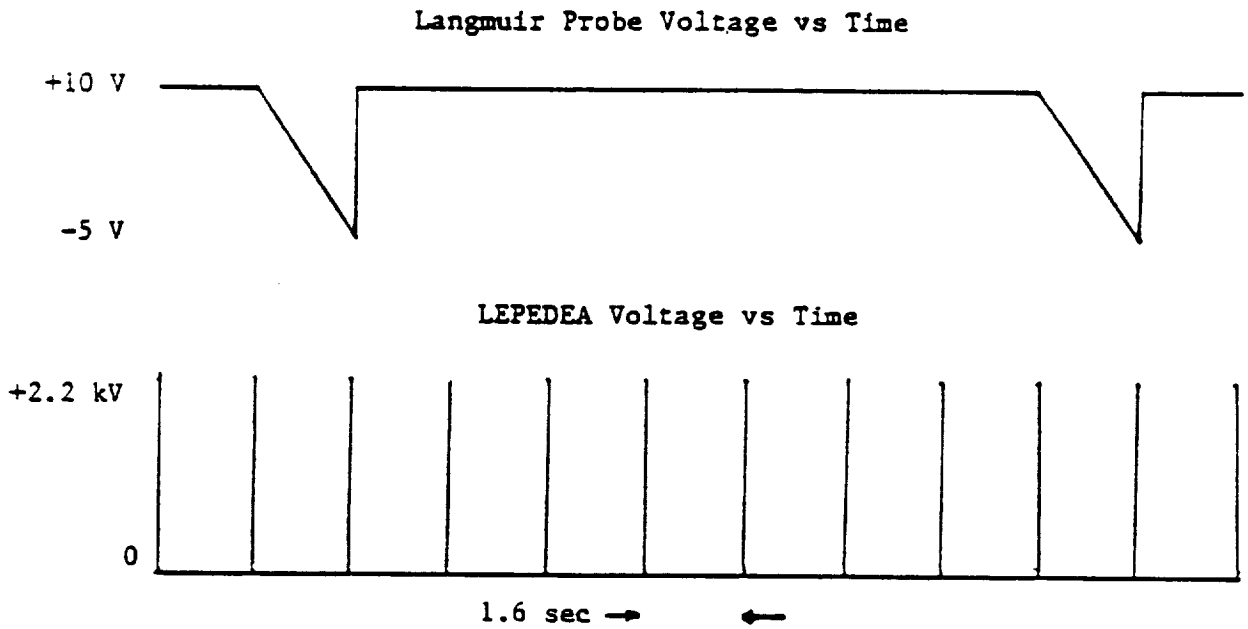


Figure A-8. LEPEDEA firing sequence. LEPEDEA fires at the beginning of the major frame, every 1.6 seconds.

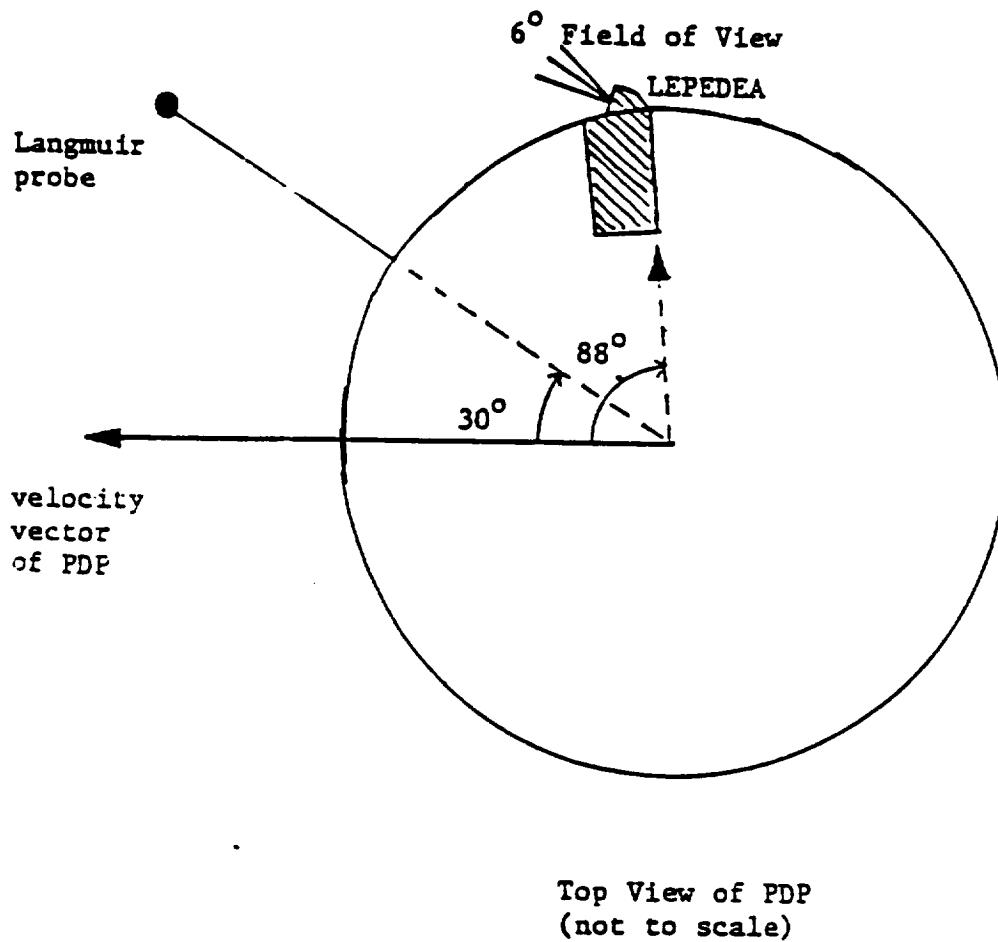


Figure A-9. Location of LEPEDA at the start of the density depletions.

APPENDIX B

ERROR ANALYSIS

Whenever the Langmuir probe is in the sweep mode, there will be some point in the sweep when the bias voltage of the probe is approximately equal to the plasma potential. Whenever this is the case, the current collected by the probe will be independent of the bias voltage and will depend only on the velocity of the particles in the plasma, relative to the PDP. We can give separate expressions for the magnitude of the current due to the electrons and the current due to the ions. That is,

$$I_{i,e} = q_{i,e} A v_{i,e} n \quad ,$$

where $q_{i,e}$ = charge on the ions/electrons, A = area of probe, $v_{i,e}$ = velocity at which the ions/electrons impact the probe, n = density of the plasma. The current collected by the probe is the sum of both the electron and ion currents. However, when we use the Langmuir probe sweeps to calculate electron density and temperature, we are only interested in the electron current which is given by

$$I_e = I_{total} - I_i \quad .$$

Originally it was thought that the ion current, I_i , would be so small that it could be neglected. However, this is not always the case. The ions are moving with a velocity that is comparable to the speed of the shuttle. Therefore, assuming $v_i = 8$ km/s, we find that for the OSS-1 mission, when the probe is in ram, the ion current is given by

$$I_i = 3.6 \times 10^{-12} n(\text{cm}^{-3}) \text{ amperes} \quad .$$

For the Spacelab-2 mission, which used a smaller probe, the value is

$$I_i = 0.9 \times 10^{-12} n(\text{cm}^{-3}) \text{ amperes} \quad .$$

When the probe is in the wake, I_i is small enough to be neglected.

In Figure 3 we showed a typical Langmuir probe sweep taken during the OSS-1 mission. When taking the slope of the line as shown, we ignored the presence of the ion current, assuming it would be small enough to neglect. However, this particular sweep yielded an electron density of $3.9 \times 10^6 \text{ cm}^{-3}$. Using this as the value for n , we find that the magnitude of the ion current is 14 microamps. Adding 14 microamps to the value of each of the points taken when the bias voltage is approximately equal to the plasma potential, we obtain a corrected Langmuir probe sweep. Table B-1 shows the value of the ion

current for three typical density values. By comparing the two sweeps shown in Figure B-1, we immediately see that the slope of the "corrected" line is different from that of the "uncorrected" line. As a result we find that the uncorrected slope provides an electron temperature of 950 K, whereas the corrected slope provides an electron temperature of 2190 K. The difference that the ion current makes in calculating the electron temperature is shown in Table B-2.

As shown in Table B-2 for OSS-1, when $n = 10^6 \text{ cm}^{-3}$ we underestimate the magnitude of the electron temperature by about 100%. When $n = 10^5 \text{ cm}^{-3}$, we underestimate the temperature by about 50%, and when $n = 10^4 \text{ cm}^{-3}$ the value of the ion current is so small we do not notice a difference in temperatures.

Because we have failed to take into account the presence of the ion current, we conclude that electron temperatures less than 500 K are not accurate. Data reduction for OSS-1 had been completed and was well underway for the Spacelab-2 mission before this problem was noticed. However, most of the data analysis was concerned with noting differences in the plasma parameters depending on the attitude of the shuttle, orientation of the PDP, etc., and not with determining the exact value of these parameters. Consequently, the values of the electron temperature shown in this thesis have not been changed to reflect the presence of the ion current even though this causes us to underestimate the electron temperature at high densities.

Another problem encountered during data reduction is due to the large step size used by the probe during the sweep mode, 0.125 volts. As is shown in Figure B-1, in some cases this allows us only 3-4 points to use when we take the slope of the line in the log I vs V graph. This limits the accuracy of the probe by introducing an uncertainty in the value of the slope used to calculate the electron temperature and density.

Table B-1
The Magnitude of the Ion Current

n (cm^{-3})	OSS-1 I_i (amps)	Spacelab-2 I_i (amps)
3.9×10^6	14.04×10^{-6}	3.51×10^{-6}
1.5×10^5	0.54×10^{-6}	0.14×10^{-6}
9.8×10^3	0.03×10^{-6}	0.01×10^{-6}

Table B-2

The Effect of Ion Current on Electron Temperature

$n_e(\text{cm}^{-3})$	Uncorrected $T_e(\text{K})$	Corrected $T_e(\text{K})$
3.9×10^6	950	2190
1.5×10^5	1084	1680
9.8×10^3	2221	2221

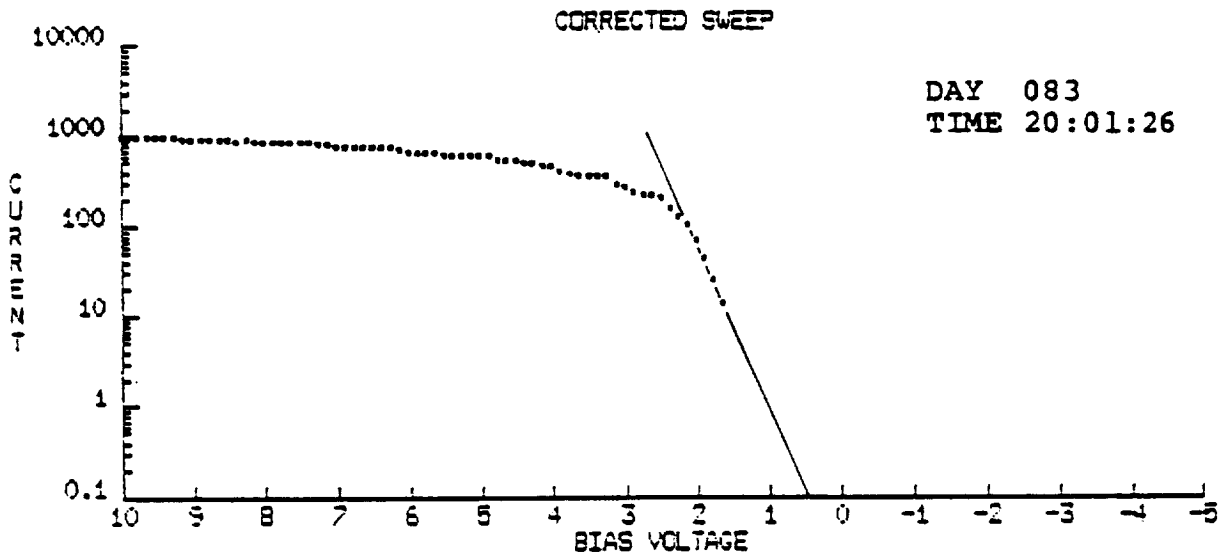
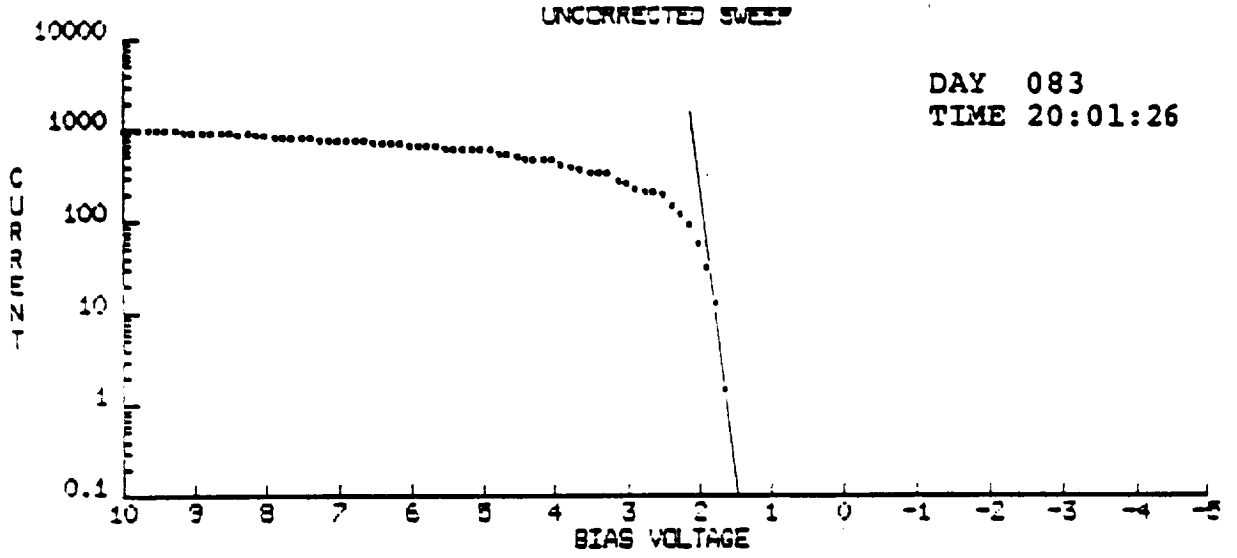


Figure B-1. Corrected and uncorrected Langmuir probe sweeps. The current is in microamperes.

REFERENCES

- Hess, W. N., and G. D. Mead (Eds.), Introduction to Space Science, 2d ed., Gordon and Breach, Science Publishers, New York, 1968.
- Huddlestone, R. H., and S. L. Leonard (Eds.), Plasma Diagnostic Techniques, Academic Press, New York, 1965.
- Kasha, M. A., The Ionosphere and Its Interaction with Satellites, Gordon and Breach, Science Publishers, New York, 1969.
- Murphy, G., J. Pickett, N. D'Angelo, and W. S. Kurth, Measurements of plasma parameters in the vicinity of the Space Shuttle, Planet. Space Sci., submitted, 1985.
- NASA, Spacelab 2, U.S. Government Printing Office, Washington, DC, n.d.
- Nicholson, D. R., Introduction to Plasma Theory, John Wiley & Sons, New York, 1983.
- Office of Space Science and Applications, First Goddard Space Flight Center Payload Developed for Flight on Space Shuttle, NASA, Washington, DC, n.d.
- Oran, W. A., U. Samir, N. H. Stone, and E. G. Fontheim, Laboratory observations of electron temperature in the wake of a sphere in a streaming plasma, Planet. Space Sci., 23, 1081-1083, 1975.
- Rubin, A. G., and A. Besse, Charging of a manned maneuvering unit in the shuttle wake, J. Spacecr. Rockets, 23, No. 1, 1986.
- Samir, U., and Wrenn, G. L., Experimental evidence of an electron temperature enhancement in the wake of an ionospheric satellite, Planet. Space Sci., 20, 899-904, 1972.
- Solar-Terrestrial Science in Earthspace: A Strategy for Shuttle-Spacelab Missions, H-81-05, Essex Corporation, n.d.

AN ANALYSIS OF WHISTLER-MODE RADIATION
FROM THE SPACELAB-2 ELECTRON BEAM
by
William Michael Farrell

An Abstract

Of a thesis submitted in partial fulfillment
of the requirements for the Doctor of
Philosophy degree in Physics
in the Graduate College of
The University of Iowa

July 1987

Thesis supervisor: Professor Donald A. Gurnett

AN ANALYSIS OF WHISTLER-MODE RADIATION
FROM THE SPACELAB-2 ELECTRON BEAM

by

William Michael Farrell

A thesis submitted in partial fulfillment
of the requirements for the Doctor of
Philosophy degree in Physics
in the Graduate College of
The University of Iowa

July 1987

Thesis supervisor: Professor Donald A. Gurnett

ABSTRACT

During the Spacelab-2 mission, the University of Iowa's Plasma Diagnostics Package (PDP) was released from the space shuttle to investigate plasma effects in the near-shuttle environment. At times during this freeflight when the PDP was magnetically connected to the shuttle, an electron gun in the shuttle cargo bay ejected a nearly field-aligned 1 keV - 50 mA electron beam. During these beam ejections, the plasma wave instrument onboard the Plasma Diagnostics Package detected intense whistler-mode radiation from the beam. This thesis presents a detailed study of a whistler mode emission detected during one period when the beam was ejected continuously for about 7 minutes. The electric field polarization of the detected whistler mode signal is consistent with propagation near the resonance cone. Calculations indicate that the beam radiated approximately 1.6 mW in the whistler mode as the beam traversed the 200 meters from the shuttle to the PDP. The emissivity also decreased by about a factor of 10 over this same distance. The measured wave powers are 10^7 greater than wave powers expected from incoherent Cerenkov radiation, verifying that the radiation is generated by a coherent process.

One coherent wave generation mechanisms considered in this study is the whistler-mode instability in the beam; however, it has been concluded that this instability cannot sufficiently amplify the

radiation to the measured power levels since the path length for wave growth in the beam is much smaller than the estimated whistler-mode wavelength.

Another wave generation process considered is coherent Cerenkov radiation from electron bunches formed in the beam by an electrostatic beam-plasma instability. A one-dimensional simulation of the SL-2 electron beam verifies the existence of these electron bunches, and the calculated coherent power radiated from this modeled beam is near the power levels measured from the SL-2 electron beam in the whistler mode. Including coherent Cerenkov radiation effects in the calculation of the power increases their values by nearly 90 dB's above incoherent power levels. Consequently, this mechanism can account for the whistler-mode radiation detected by the PDP during its encounter with the 1 keV - 50 mA electron beam.

TABLE OF CONTENTS

	Page
LIST OF TABLES	vii
LIST OF FIGURES	viii
CHAPTER	
I. GENERAL INTRODUCTION	1
II. POLARIZATION AND POWER MEASUREMENTS OF THE WHISTLER-MODE RADIATION FROM THE SL-2 ELECTRON BEAM . . .	8
A. Electric Field Polarization	8
B. Emitted Power	10
III. POSSIBLE WHISTLER-MODE WAVE GENERATION MECHANISMS	18
A. Incoherent Generation Mechanisms	18
B. Coherent Generation Mechanisms	20
IV. EMITTED POWER VIA CERENKOV RADIATION PROCESSES	26
A. Derivations	28
1. Radiated Power From a Single Test Charge in a Plasma Medium	29
2. Radiated Power From N Particles in a Plasma Medium	36
B. Practical Applications	45
V. A ONE-DIMENSIONAL ELECTROSTATIC SIMULATION OF THE SL-2 ELECTRON BEAM	48
A. Results of the Simulation of the SL-2 Electron Beam	55
B. The Radiated Power From a Model of the SL-2 Electron Beam	62

VI. THE ELECTRON BEAM AS AN EFFICIENT ANTENNA	77
VII. CONCLUSIONS	80
APPENDIX	144
REFERENCES	153

LIST OF TABLES

Table		Page
1.	Simulation Parameters	56
2.	Values of $J_z(k_z)$	69
3.	The Change in Radiated Power From Considering a Current Density With a Spread, Δk	76

LIST OF FIGURES

Figure		Page
1	A frequency vs. time spectrogram from the PDP plasma wave instrument showing intense emissions during a D.C. electron gun firing. The funnel-shaped structure that extends from the electron cyclotron frequency, f_c , to about 30 kHz is whistler-mode radiation from the beam.	82
2	This diagram shows the index of refraction surface for the whistler mode and the associated \bar{E} , \bar{k} , and \bar{v}_g vectors for propagation near the resonance cone ($\theta \approx \theta_{Res}$). For propagation near the resonance cone, \bar{k} and \bar{E} are parallel and nearly perpendicular to \bar{v}_g . In this limit \bar{E} is linearly polarized and quasi-electrostatic.	84
3	This diagram shows the ray path and \bar{E} , \bar{k} , and \bar{v}_g vectors used to confirm the electric field polarization. The assumed electric field is projected into the PDP spin plane and the angle relative to the projection of the sun vector is calculated. The projected electric field direction can then be compared to the measured directions calculated from spin modulation maximums in the electric field intensity (see Figure 4).	86
4(a), (b), (c), and (d)	These plots show the relative directions of the computed and measured electric-field vectors in the PDP spin plane for the 562 kHz, 311 kHz, 178 kHz, and 100 kHz frequency channels. The dots represent the computed electric field directions assuming that the wave vector is near the resonance cone with $\bar{k} \cdot \bar{v}_b > 0$, and the x's represent measured electric-field directions. The close agreement between the measured and modeled directions indicates that the whistler-mode radiation is propagating near the resonance cone in the same direction as the beam.	88

5	This diagram shows the integration surface used to calculate the power emitted from the beam in the whistler mode. At closest approach, the PDP passed within 3 meters of the beam at a distance of about 200 meters from the shuttle.	90
6	The calculated power spectral density from the beam in the whistler mode is shown as a function of frequency.	92
7(a) and (b)	The linear emissivity, $dP/dfdl$, is shown as a function of the distance, L , along the beam for the 562 kHz and 311 kHz frequency channels. Note that the emissivity starts to decrease rapidly beyond about 100 meters.	94
8	The power spectra from a single electron radiating via the Cerenkov processes is shown in a plasma environment similar to that surrounding the SL-2 beam. These calculations assume the wave/beam interaction is by a Landau resonance process and that the particle pitch angle is 10° . This power calculation is based on formulas derived by Mansfield [1967].	96
9	This figure displays the radial expansion of a field-aligned electron beam after it is initially ejected from a gun of radius r_0 . As the beam propagates, the radius expands according to $r = r_0 + \frac{V_{\perp \text{exp}}}{V_b} z$	98
10	This figure is a V_z versus z phase-space configuration of electrons from a beam of density $n_b = 1/16 n_A$ and $V_b = 10 V_{th}$ after (a) $32 \omega_{pe}^{-1}$ and (b) $64 \omega_{pe}^{-1}$. This configuration is obtained from Pritchett and Winglee's two-dimensional simulation [1986]. The beam is injected from a spacecraft located at $z = 125$	100
11	This figure is a V_z versus z phase-space configuration of an electron beam with similar density and velocity as that of Figure 10 taken from the one-dimensional simulation developed in this study. Note that $L = 100$	102

12	Again, a beam phase-space configuration is shown from the one-dimensional simulation developed in this study run with similar parameter as those of Figures 10 and 11, only now $L = \infty$ (no radial beam expansion).	104
13	This V_z versus z beam phase-space configuration is from the one-dimensional simulation run with $n_b = 8 n_A$, $V_b = 15 V_{TH}$ and $L = 10$ for two different times: (a) $20 \omega_{pe}^{-1}$ and (b) $30 \omega_{pe}^{-1}$	106
14	This figure is a beam phase-space configuration taken from Winglee and Pritchett [1986] for an overdense beam ($n_b/n_A = 2$). Note that the beam structure looks similar to that of Figure 13.	108
15	This figure is a beam phase-space configuration taken from Pritchett and Winglee [1986] for an overdense beam ($n_b = 8 n_A$) at two different times: (a) $16 \omega_{pb}^{-1}$ and (b) $32 \omega_{pb}^{-1}$	110
16	This figure is a V_z versus z phase-space configuration of the modeled SL-2 electron beam obtained from the one-dimensional simulation run with the parameters shown in Table 1, with $L = 10$	112
17	This figure displays E_z versus z from the one-dimensional simulation run with $L = 10$. Note that a strong electric field is located near $z = 0$	114
18	This figure displays the number of electrons, N , versus z from the modeled beam run with $L = 10$	116
19	This figure is a V_z versus z phase-space configuration of the modeled SL-2 electron beam obtained from the one-dimensional simulation run with the parameters shown in Table 1, with $L = 5$	118
20	This figure displays E_z versus z from the one-dimensional simulation run with $L = 5$. Note that a strong electric field is located near $z = 0$	120

21	This figure displays the number of electrons, N , versus z from the modeled beam run with $L = 5$	122
22	This figure is a V_z versus z phase-space configuration of the modeled SL-2 electron beam obtained from the one-dimensional simulation run with the parameters shown in Table 1, with $L = 3$	124
23	This figure displays E_z versus z from the one-dimensional simulation run with $L = 3$. Note that wave activity is present in the beam.	126
24	This figure displays the number of electrons, N , versus z from the modeled beam run with $L = 3$	128
25	This figure is a V_z versus z phase-space configuration of the modeled SL-2 electron beam obtained from the one-dimensional simulation run with the parameters shown in Table 1, with $L = 2$	130
26	This figure displays E_z versus z from the one-dimensional simulation run with $L = 2$. Note that wave activity is present in the beam.	132
27	This figure displays the number of electrons, N , versus z from the modeled beam run with $L = 2$	134
28	This figure is a V_z versus z phase-space configuration of the modeled SL-2 electron beam obtained from the one-dimensional simulation run with $L = 3$ and a length of 3600 grids corresponding to 180 meters. Note that the beam phase-space configuration is similar to that shown in Figure 22 for a 60-meter beam segment.	136
29	This diagram is a plot of $J_z(k_z, \omega)$ as a function of ω and k_z for the 175-meter beam segment. The largest values of $J_z(k_z, \omega)$ are completely dark, while o's and .'s represent continually lower intensities. Note that the values of $J_z(k_z, \omega)$ peaks at about $\omega/k_z = 2.8 \times 10^7$ m/s.	138
30	This figure shows the variation of $J_z(k_z)$ for the 175 meter beam segment as a function of k_z . Note for $k_z < 22$ that $J_z(k_z)$ increases as k_z decreases. This variation in $J_z(k_z)$ results from the density perturbations in the beam created by a beam-plasma instability. Also shown in the figure is the simulation noise level. This noise is obtained since simulation electrons many times the mass and charge of real	

electrons were used in the computer model. The range of k_z' of the whistler-mode waves is also shown in the figure. 140

31 This figure shows the power spectra of the measured whistler-mode radiation from the first 200 meters of the SL-2 electron beam along with the calculated power spectra of the incoherent and coherent Cerenkov radiation from a 200-meter beam segment. Note that the inclusion of coherent radiation effects increases the calculated powers to those measured from the SL-2 electron beam. Based on these results, it is concluded that coherent Cerenkov radiation from a bunched electron beam generates the detected whistler-mode radiation. 142

CHAPTER I
GENERAL INTRODUCTION

The results of a study of a whistler-mode emission detected from an artificial electron beam during the space shuttle's Spacelab-2 (SL-2) mission are presented in this thesis. The study includes a measurement of the total radiated power from the beam in the whistler-mode and a comparison of this power to the power predicted by various whistler-mode radiation mechanisms.

The Spacelab-2 flight, which was launched on July 29, 1985, included an electron gun called the Fast Pulsed Electron Generator (FPEG) from Stanford University, and a spacecraft called the Plasma Diagnostics Package (PDP) from the University of Iowa. During a 6-hour period on August 1, 1985, the PDP was released from the shuttle to investigate plasma effects in the vicinity of the shuttle. During the PDP free flight, the shuttle was maneuvered so that the PDP passed near magnetic field lines connected to the shuttle. Four such magnetic conjunctions were achieved. During one of these magnetic conjunctions a 1 keV - 50 mA electron beam was continuously ejected from the shuttle so that radiation effects could be monitored as the PDP passed near the magnetic field line carrying the beam. Figure 1 shows a frequency vs. time spectrogram from the PDP plasma wave instrument during this electron beam event. The funnel-shaped signal extending from the electron cyclotron frequency, f_c , down to approximately 30

kHz is whistler-mode radiation from the electron beam. This whistler-mode radiation was first described by Gurnett et al. [1986] and is the subject of this thesis.

The observation of this beam-generated whistler-mode signal is not unusual; in fact, whistler-mode radiation is frequently detected from both artificial and natural electron beams in the ionosphere. The following briefly describes some of these electron beams and the corresponding radiation detected.

The first artificial electron beam experiment was performed in the ionosphere in 1969. An electron accelerator was flown on an Aerobee 350 rocket and injected a 9.5 keV/490 mA pulsed electron beam into the ionospheric medium [Hess et al., 1971]. Although ground-based radio receivers did not detect any beam-generating emissions, the beam did propagate ~ 200 km into the lower ionosphere where it was observed optically. This experiment demonstrated that artificial electron beams could propagate great distances without being destroyed by beam-generated instabilities.

During the seventies and eighties, an investigative group at the University of Minnesota performed a number of electron beam experiments in the ionosphere with two stated purposes: first, to study the electron beam, including its emitted radiation and its effect on the beam-ejecting spacecraft; and second, to use the beam as a diagnostic tool to further understand processes occurring in the magnetosphere and ionosphere [Winckler, 1980]. Specifically, their electron Echo experiments were designed to inject an electron beam on closed field lines

into the conjugate hemisphere and analyze the returning electrons (electron "echoes") to identify any physical processes involved. To study the plasma and radio waves emitted from these beams, a radio receiver, typically located in the rocket nose cone, was separated from the main payload. During beam injections these receivers detected waves in the whistler mode, at the upper hybrid/plasma frequencies and at electron cyclotron harmonics (ECH) [Cartwright and Kellogg, 1974; Kellogg et al., 1976; Monson et al., 1976; Winckler, 1980]. Recently, the scientific objectives of the latest Echo experiment, Echo 7, were presented and again include an extensive electron beam investigation [Winckler et al., 1986].

Observations of beam-generated emissions were also made during the joint Franco-Soviet Artificial Radiation and Aurora between Kerguelen and the Soviet Union (ARAKS) experiments in 1975 (Lavergnat et al., 1980). Like the Echo experiments, a diagnostics package was carried in the nose cone of the rocket and separated from the main payload. During electron beam injections, radio receivers flown on this package detected waves in the whistler mode, near the local plasma frequency, and near the fourth harmonic of the electron cyclotron frequency (an ECH emission) [Lavergnat et al., 1980; Dechambre et al., 1980a, Dechambre et al., 1980b].

Electron beams have also been used to probe structures occurring in the auroral region. Such an example is the "E#B" experiment that was launched into an auroral arc. During the flight, an electron beam was injected along geomagnetic field lines to locate the regions of

parallel electric field that generated the arc. It was believed that part of the injected electron beam would reflect from these regions; however, few reliable signatures of the returning electrons were detected during the experiment [Wilhelm et al., 1980]. A second flight under the same investigation, the NVB-06 flight, was launched in December of 1979. During pulsed electron beam injections, Kellogg et al. [1986] again reported observing waves in the whistler mode, at the upper hybrid frequency, and at the fundamental and first harmonic of the electron cyclotron frequency. The relative intensity and frequency spectra of the waves were also observed to vary with the beam energy and current, and may have been associated with beam plasma discharge (BPD) effects (see Bernstein et al. [1979]).

A unique facility used for beam-plasma research is the Johnson Space Center (JSC) plasma chamber. This cylindrical chamber has a height of 27.4 m and a diameter of 16.8 m, and is large enough to allow space-like experiments to be performed in a laboratory environment. Such experiments performed on injected electron beams include measurements of the emitted radiation and a study of BPD effects [Shawhan, 1982]. For a review of the results from these experiments, see Grandel [1982].

Electron beam injection experiments in the ionosphere have also been performed on the space shuttle. Since the electron beams and corresponding diagnostics packages (particularly the PDP) could be maneuvered into favorable positions, wave and particle measurements unobtainable from rocket experiments were made in and around the beam

environment. The first electron beam experiment performed on the shuttle was in March of 1982 as part of the STS-3 mission. On this flight, the PDP was maneuvered using the shuttle's Remote Manipulator Arm (RMS) while the FPEG, located in the shuttle cargo bay, produced an electron beam. During beam injections, strong emissions near the local plasma frequency and possibly in the whistler mode were detected by the PDP radio receivers [Shawhan et al., 1984]. In December of 1983, the shuttle carried the PICPAB (Phenomenon Induced by Charged Particle Beams) and SEPAC (Space Experiments with Particle Accelerators) investigations into the ionosphere as part of the Spacelab-1 mission. During electron beam injections, the PICPAB radio receivers detected emissions in the whistler mode, at the plasma frequency and at the fourth harmonic of the cyclotron frequency [Beghin et al., 1984] while the SEPAC radio receivers detected an intense VLF signal between 0.7 and 10 kHz that varied in intensity depending on the beam pitch angle [Neubert et al., 1986]. As mentioned previously, in July/August of 1985, the shuttle again carried the PDP and FPEG into the ionosphere as part of the Spacelab-2 mission. The PDP was released to fly around the shuttle and during magnetic conjunction with the shuttle the FPEG was fired. Besides detecting the whistler-mode radiation, emissions near the local plasma frequency and intense electrostatic emissions below 30 kHz were detected by the PDP during beam injections [Gurnett et al., 1986]. During pulsed electron beam events electromagnetic waves at the fundamental and harmonics of the pulsing frequency were also observed [Reeves et al., 1986; Bush et al., 1986].

From the discussion above, it seems evident that whistler-mode radiation is commonly detected from artificial electron beams. This radiation is also produced naturally in the auroral zone in association with the field-aligned electron beams that are responsible for the aurora [Gurnett, 1966] and is usually called auroral hiss. Both upward and downward propagating auroral hiss has been observed [Mosier and Gurnett, 1969]. The downward propagating auroral hiss is associated with downward moving electron beams with characteristic energies of a few hundred eV [Gurnett, 1966; Hartz, 1969; Gurnett and Frank, 1972; Laaspere and Hoffman, 1976]. The upward propagating auroral hiss often has a V-shaped spectrum called a "saucer" [Smith, 1969; Mosier and Gurnett, 1969; James, 1976] or a "funnel" [Gurnett et al., 1983]. Upward propagating auroral hiss has been observed in association with upward moving field-aligned electron beams [Lin et al., 1984]. The characteristic frequency-time shape of the "saucer" or "funnel" is a propagation effect that occurs for whistler-mode waves propagating near the resonance cone.

Although whistler-mode waves and electron beams are closely related, the exact wave-particle interaction generating the waves is unknown. It is hoped that the study of the whistler-mode radiation from the SL-2 electron beam will aid in the understanding of the processes that create these other artificial and natural beam-generated whistler-mode emissions.

The specific outline of this thesis is as follows. In Chapter II measurements of the polarization and power of the whistler-mode

radiation from the SL-2 electron beam are presented. In Chapter III, the measured power is compared and contrasted to the calculated power predicted from possible incoherent and coherent wave generation mechanisms. By the end of Chapter III, it will be evident that coherent Cerenkov radiation from electron bunches in the beam is the only mechanism able to account for the measured power in the whistler mode. Chapters IV and V involve the detailed modeling of the electron bunches responsible for the coherent Cerenkov radiation. Specifically, an expression for the radiated power from an electron beam is derived in Chapter IV and the Appendix. In Chapter V, the results of a computer simulation of the SL-2 electron beam are presented, which includes the modeling of the electron beam distribution. Electron bunches in the simulated beam resulting from a beam-plasma instability are clearly evident. The radiated power from this simulated beam will then be calculated using the derived power expressions and will be compared to the measured power from the SL-2 electron beam in the whistler-mode.

CHAPTER II
POLARIZATION AND POWER OF THE WHISTLER-MODE
RADIATION FROM THE SL-2 ELECTRON BEAM

In this section, measurements of the electric field polarization and radiated power of the whistler-mode emission from the 1 keV - 50 mA SL-2 electron beam are presented. As will be shown, both measured quantities are important in determining the wave generation mechanism of the whistler-mode emission.

A. Electric Field Polarization

The whistler mode has a polarization that depends on the wave frequency, f , the wave normal angle, θ , the cyclotron frequency, f_c , and the plasma frequency, f_p . Using cold plasma theory [Stix, 1962], the electric-field and index of refraction vectors can be calculated as a function of these parameters. The variation of the index of refraction as a function of θ is often presented as an index of refraction surface $\bar{n}(\theta)$, which defines the locus of points the index of refraction vectors make as a function of the wave normal angle for constant f , f_p and f_c . Figure 2 shows a typical index of refraction surface for the whistler mode. At a limiting wave normal angle, known as the resonance cone angle, θ_{Res} , the index of refraction goes to infinity. This angle is defined by $\tan^2 \theta_{Res} = -P/S$, where $P = 1 - f_p^2/f^2$ and $S = 1 - f_p^2/(f^2 - f_c^2)$. As the wave normal approaches the resonance cone,

the electric field \vec{E} becomes linearly polarized with \vec{E} parallel to \vec{n} . In this limit the electric field is quasi-electrostatic and the group velocity, \vec{v}_g , is perpendicular to \vec{E} and \vec{n} (see Figure 2).

In a previous paper [Gurnett et al., 1986], the funnel-shaped frequency versus time pattern of the radiation from the SL-2 electron beam was explained as a frequency dependent propagation effect for whistler-mode emissions propagating near the resonance cone. As the wave frequency increases, the resonance cone angle, θ_{Res} , decreases and the ray path direction, \vec{v}_g , becomes increasingly oblique to the magnetic field, approaching 90° as the frequency approaches the electron cyclotron frequency. As the PDP approaches the beam, emissions near the gyrofrequency are detected first, since their ray paths are almost perpendicular to the beam. Lower and lower frequencies are then detected as the distance between the PDP and beam decreases. This frequency dependent wave propagation effect causes the funnel-shaped emission pattern observed in Figure 1 and provides strong evidence that the radiation is propagating near the resonance cone.

In order to provide further confirmation that the radiation from the SL-2 electron beam is propagating near the resonance cone, an additional test was performed. This test compares model electric-field directions in the PDP spin plane to their actual directions as measured by the PDP plasma wave instrument. To perform this test a computer program was developed that calculates the angle, ϕ , between the projection of a model electric field onto the spin plane and a fixed reference direction. The fixed reference direction selected was

the spin plane projection of the spacecraft-sun vector. To compute ϕ , the group velocity was assumed to be directed from a point on the beam toward the PDP with the electric field vector, \bar{E} , at an angle θ_{Res} relative to the beam. This field geometry is the expected configuration for an upward propagating whistler-mode wave near the resonance cone. Figure 3 shows the corresponding geometry of \bar{E} , \bar{v}_g and \bar{k} .

The electric-field directions in the spin plane calculated using the model described above are compared to the measured electric-field directions found from spin modulation maximums in the receiver data. The spin modulation maximums occur when the PDP electric antennas are aligned with the measured electric field in the spin plane, thus allowing a direct determination of this measured electric field direction. Figure 4 shows the results of this comparison at four frequencies: 562, 311, 178, and 100 kHz. This figure shows the phase angle, ϕ , between the projected electric field and the sun vector as a function of time. The dots represent the modeled electric-field directions computed assuming a resonance cone propagation scheme while the X's represent the measured electric-field directions. The close agreement between the computed and measured electric field directions provides strong confirmation that the waves are propagating near the resonance cone and in the beam direction (i.e., $\bar{k} \cdot \bar{v}_b > 0$), as indicated in Figure 3.

B. Emitted Power

In this section the total power radiated from the beam in the whistler mode is estimated. By comparing the radiated power to the

total power in the beam, the efficiency of the wave-beam interaction can be determined and compared with various generation mechanisms.

The power emitted from the beam in the whistler mode is obtained by integrating the Poynting flux over a surface surrounding the beam. An inherent difficulty with this calculation is the determination of the phase and magnitude of the electric and magnetic fields in the Poynting flux expression, $\bar{S} = \bar{E} \times \bar{H}$. Since three axis measurements are not available and since phase measurements were not made, the Poynting vector cannot be determined directly. The situation is further complicated by the fact that the emission is propagating near the resonance cone and is quasi-electrostatic. Consequently, the ratio of the electromagnetic to electrostatic components of the wave electric field is a sensitive function of the wave normal angle. Therefore, to compute the wave normal angle it is assumed that the radiation is produced by the Landau resonance, i.e., $\frac{\omega}{k_{\parallel}} = \frac{c}{n_{\parallel}} = v_b$. Since the beam velocity is known, this assumption gives a well-defined value for the wave normal direction. The fact that the radiation is propagating in the same direction as the beam ($\bar{k} \cdot \bar{v}_b > 0$) provides a strong indication that the Landau resonance is involved. For example, the $s = -1$ cyclotron resonance produces radiation propagating in the opposite direction of the beam and is therefore completely ruled out, since the radiation is observed to be propagating in the direction of the beam. Also, as will be discussed later, the Landau resonance gives the best agreement with the measured electric to magnetic field ratios.

To compute the Poynting vector, \bar{S} , the electrostatic and electromagnetic component of the whistler-mode electric field must be determined. Since the PDP did not measure the relative phase between \bar{E} and \bar{H} , these important components of \bar{E} cannot be directly calculated. However, by using the assumption that the waves are generated via a Landau resonance, \bar{n} and \bar{E} can be calculated exactly using cold plasma theory. Consider, first, the whistler-mode wave electric field. Since the emission is propagating near the resonance cone, \bar{E} lies almost entirely in the plane defined by \bar{n} and the geomagnetic field (see Figure 3). The electrostatic and electromagnetic components of \bar{E} are then given by $E_0 \cos \Delta\theta$ and $E_0 \sin \Delta\theta$, respectively, where $\Delta\theta$ is the angle between \bar{E} and \bar{n} , and E_0 is amplitude of the total electric field. The angle $\Delta\theta$ is determined by the Landau resonance condition and cold plasma theory. The Landau resonance condition specifies the component of n parallel to the geomagnetic field, i.e.,

$$n_{\parallel} = n \cos \theta = c/v_b \quad . \quad (2-1)$$

where c is the speed of light. For a 1 keV electron beam moving parallel to the magnetic field n_{\parallel} is approximately 15.9. A program was written that solves Equation (1-20) of Stix [1962] for the magnitude and directions of \bar{n} and \bar{E} . Using this program, \bar{n} and $\Delta\theta$ at a particular wave frequency can be calculated by constraining values of $\bar{n}(\theta)$ using (2-1). Since $\Delta\theta$ is now determined, the electrostatic and electromagnetic components of \bar{E} can be calculated. The calculated $\Delta\theta$ values are very small, typically ranging from $.06^\circ$ to 1.1° from 31.1

kHz to 562 kHz, indicating that the wave is nearly electrostatic. It is easy to show that the magnitude of the Poynting vector is given by

$$|\bar{S}| = \frac{n E_0^2}{2} \left(\frac{\epsilon_0}{\mu_0} \right)^{1/2} (A^2 + B^2)^{1/2} \quad , \quad (2-2)$$

where $A = 1 - \cos^2 \Delta\theta$ and $B = \sin \Delta\theta \cos \Delta\theta$. In the derivation of Equation 2 Faraday's Law was used to eliminate the magnetic field in the $\bar{E} \times \bar{H}$ term. Note, also, that as θ approaches the resonance cone angle, \bar{n} and \bar{E} become parallel and $|\bar{S}|$ goes to zero. This behavior near θ_{Res} is similar to an expression derived by Mosier and Gurnett [1971] in their paper addressing Poynting flux measurements of VLF hiss emissions.

Figure 5 shows, pictorially, the PDP trajectory during the 1 keV - 50 mA electron beam event. As can be seen, near the magnetic conjunction, the PDP trajectory was nearly perpendicular to the beam, and, at closest approach, passed within about 3 meters of the beam at a distance of about 200 meters along the field line from the shuttle. To compute the total radiated power, the Poynting flux is integrated over an imaginary surface perpendicular to the beam that includes the PDP trajectory. Assuming that the sampled intensities along this trajectory are constant around an annular ring of the area, $dA = 2\pi R dR$, centered on the beam, the radiated power from the beam segment can be obtained by evaluating the integral $P = \int S_{\parallel} 2\pi R dR$, where S_{\parallel} is the field-aligned component of the Poynting vector and R is the

perpendicular distance from the beam to the PDP. Note that the evaluation of this integral will yield two values for the radiated power: one value from the inbound pass where the limits of integration extend from $R = \infty$ to $R \cong 0$ and one value from the outbound pass where the limits of integration now extend from $R \cong 0$ to $R = -\infty$. Figure 6 shows the average power spectral density from these two passes as a function of wave frequency. The error bars in the figure represent the standard deviations of the power values. Note that the power spectral density, dP/df , is on the order of 10^{-9} W/Hz in the frequency range extending from 30 kHz to 1 MHz. Adding $\frac{dP}{df}$ over the 30 kHz to 1 MHz frequency range, the total emitted power in the 200-meter beam segment from the shuttle to the PDP is found to be $P = 1.6$ mW. If the power were emitted uniformly along the beam, the radiated power per unit length, dP/dl , would be approximately $1.6 \text{ mW}/200 \text{ m} = 8 \times 10^{-6}$ W/m. Since the total power of the beam was 50 W, the beam converted approximately $1.6 \text{ mW}/50 \text{ W} = 3.2 \times 10^{-5}$ of its power to whistler-mode radiation in the first 200 meters. As a rough indication of the radiation efficiency, if the beam continued to radiate at this level and this radiation was the only beam energy dissipation mechanism, the beam would only propagate about 6000 km before converting all of the beam energy to radiation.

The linear emissivity of the whistler-mode radiation, $dP/dfd\ell$, from different locations along the beam can also be calculated. To calculate the linear emissivity, a knowledge of a signal's exact source location from the beam is required; however, by using the ray

path, the source of the signal at a particular point along the PDP trajectory can be located. The power radiated from an infinitesimal beam radiation source, $d\ell$, is $P = \int S_{\perp} 2\pi R d\ell$, where S_{\perp} is the perpendicular component of the Poynting vector measured at the perpendicular distance R from the beam and corresponds to the Poynting flux emitted from a cylinder of radius, R , and length, $d\ell$, surrounding the beam. The linear emissivity from this source, $dP/dfd\ell$, is then obtained by using the differential form of the power integral. The calculated linear emissivity of the whistler-mode waves is shown in Figure 7. Note that the emissivity drops by a factor of ten from 100 to 200 meters along the beam. This decrease in emissivity indicates that the efficiency of whistler-mode generation decreases with increasing distance along the beam and that the generation mechanism is capable of dynamic changes in tens of meters. If the emissivity continues to drop at the rate observed between 100 to 200 meters, the radiation would be undetectable by the PDP at source distances more than about 1 km from the shuttle. This result may explain why DE-1, which was magnetically connected to the shuttle during a gun firing on the STS-3 mission, did not see beam-generated whistler-mode radiation in the vicinity of the streaming electrons [Inan et al., 1984]. From the SL-2 measurements, it appears that strong whistler-mode emissions are probably generated only in close proximity to the source of the beam.

As mentioned earlier, the electric and magnetic field measurements also provide direct evidence that the whistler-mode waves were generated via a Landau resonance process. This evidence comes from a

comparison of computed and measured cB/E ratios. Assuming a specific resonance condition and using the solution of Equation (1-20) of Stix [1962], a unique value for \bar{n} and $\Delta\theta$ can be computed. Faraday's law can then be used to obtain the relationship

$$\bar{n} \times \bar{E} = c\bar{B} \quad (2-3)$$

where \bar{E} is the electric component and \bar{B} is the magnetic component of the whistler-mode waves. For the assumed field geometry, Equation 3 can be rewritten as

$$n E_0 \sin \Delta\theta = cB_0 \quad ,$$

or

$$\frac{cB_0}{E_0} = n \sin \Delta\theta \quad . \quad (2-4)$$

Using Equation (2-4), $n \sin \Delta\theta$ is computed for various resonance conditions and compared with the measured cB/E ratio. The spectrum analyzer used with the PDP search coil can only provide measurements up to 178 kHz; therefore, the magnetic to electric field ratio can only be obtained in the 56 kHz, 100 kHz, and 178 kHz frequency channels. Also, the measured values of B at high frequencies using the search coil are highly uncertain, due to inaccuracies in the calibration of the instrument. The preflight calibration was performed by placing a calibration

coil in the search coil and surrounding the system in a μ -metal can. A problem arises at high frequencies (>10 kHz), where frequency dependent capacitances and inductances affect the current and the expected value of \bar{B} from the calibration coils. Unfortunately, post-flight calibrations under more ideal condition (specifically, without the μ -metal can) have failed to reproduce the preflight calibrations. This suggests that the high frequency gain of the search coil may have shifted during the flight. Our current best estimates are that B (and cB/E) are accurate only to within a factor of 2 - 4 at high frequencies. The range of measured cB/E values lies between 1.3 and 15.3. Assuming a Landau resonance, $n \sin \Delta\theta$ is computed to be .54, .52, and .54 for 56 kHz, 100 kHz, and 178 kHz, respectively. Note that these values lie just outside the range of measured cB/E values, and fall in the range when considering the factor of 2 - 4 uncertainty in the calibrations. For an $s = +1$ cyclotron resonance, however, $n \sin \Delta\theta$ is computed to be between .05 to .08 for 56 kHz, 100 kHz, and 178 kHz. These values are about a factor of 20 smaller than the lowest measured cB/E value. Similar computed values are obtained for the $s = -1$ cyclotron resonance. These comparisons show that the measured cB/E ratio is closest to those expected for a Landau resonance.

CHAPTER III

POSSIBLE WHISTLER-MODE WAVE GENERATION MECHANISMS

From the power measurements alone it is not clear whether the beam-generated whistler-mode radiation detected by the PDP during the SL-2 mission results from a coherent or incoherent generation process. A coherent mechanism involves large numbers of particles acting together to generate the emitted waves. The total power from a coherent source goes as N^2 , where N is the number of particles in coherence. Common coherent sources are plasma instabilities, lasers and radio antennas. Incoherent mechanisms involve particles that are radiating independently. The power from the individual radiators must be added to get the total power emitted; thus the total power is proportional to N , the number of radiators. A common incoherent source is an incandescent light bulb. In this chapter possible incoherent and coherent mechanisms for generating whistler-mode radiation are described.

A. Incoherent Generation Mechanisms

One possible incoherent mechanism involves incoherent Cerenkov radiation from beam electrons. Cerenkov radiation is generated by charged particles moving with speeds greater than the phase speed of the wave in the medium. The whistler-mode waves from the SL-2 electron beam are propagating near the resonance cone with large indices of refraction, typically $n \sim 30$ to 500. The phase speed of the wave is therefore much

less than the speed of a 1 keV electron. Since the beam electrons are moving faster than the phase speed of the whistler mode, Cerenkov radiation should be produced.

The measured whistler-mode power from the beam is next compared to the calculated power from Cerenkov radiation, assuming that the beam electrons are incoherent radiators. This calculation is similar to those performed by Jorgenson [1968] and Taylor and Shawhan [1973], who both calculated the power from this process and compared it to the radiated powers from VLF hiss. Mansfield [1967] derived an equation that gives the power spectral density radiated from a single electron moving through an ambient ionized gas with a speed greater than the wave phase speed. For an incoherent mechanism, the total power radiated from the beam is the power radiated from each electron $(\frac{dP}{df})_e$, added up over all the electrons in a given beam volume, N_v :

$(\frac{dP}{df})_{total} = N_v(\frac{dP}{df})_e$. Using Mansfield's formula, the radiated power from each beam electron can be calculated and is shown in Figure 8.

In obtaining this result, it is assumed that the radiation is produced via a Landau resonance. It is also assumed, for this calculation, that the pitch angle of the electrons is 10° . The actual pitch angles varied from 0° to 20° ; however, the results are relatively insensitive to pitch angles in this range. From Figure 8 it can be seen that the most intense radiation occurs between the electron cyclotron frequency and the lower hybrid frequency, f_{LHR} . Outside this range the power drops by a factor of 10^4 . Note that this frequency range corresponds rather well to the frequency range of the radiation observed by the

PDP. Multiplying the power from each electron by the number of electrons in the first 200 meter segment of the beam (3×10^{12} particles) yields $(\frac{dP}{df})_{\text{total}} \sim 10^{-16}$ W/Hz in the frequency range from f_c to f_{LHR} . These power spectral densities are much lower than the measured power spectral densities, by about a factor of 10^7 (compare with Figure 6, where $dP/df \sim 10^{-9}$ W/Hz). Therefore, an incoherent process cannot account for the measured wave powers. Some coherent wave process must be involved. In Taylor and Shawhan's [1973] analyses of the generation of VLF hiss emissions by auroral electron beams, the calculated powers for the incoherent Cerenkov process were found to be a factor of $10^2 - 10^3$ lower than those measured, again indicating a coherent process.

B. Coherent Generation Mechanisms

As concluded in the previous section, some coherent process must be involved in the whistler-mode wave generation from the SL-2 electron beam. Coherent processes can be divided into two classes: direct and indirect. Direct mechanisms involve the direct conversion of energy from an unstable particle distribution to electromagnetic radiation; whereas indirect mechanisms involve the intermediate generation of one or more electrostatic modes which are coupled to the escaping electromagnetic radiation. This section will discuss possible direct and indirect mechanisms that may explain the whistler-mode radiation.

Since an unstable electron distribution is present in the beam the escaping electromagnetic radiation may result from direct conversion of the beam energy to electromagnetic radiation. Such a mechanism

has been proposed by Maggs [1976] for the generation of auroral hiss. In his model, incoherent Cerenkov radiation produced by an auroral electron beam is directly amplified via a whistler-mode plasma instability within the beam. It seems reasonable that this wave generation mechanism could be applied to the whistler-mode waves emitted from the SL-2 electron beam; however, a problem arises in doing so. Unlike auroral beams, the path length for wave growth in the SL-2 beam is very short, only two to three electron cyclotron radii (6 to 9 meters). Using the Landau resonance condition and the fact that the emission is propagating near the resonance cone, the wavelength of the whistler-mode radiation is given by

$$\lambda \cong \frac{v_b}{f} \cos \theta_{\text{Res}} \quad , \quad (3-1)$$

which, for the nominal parameters has a value of about 20 meters. This wavelength is greater than the path length, which completely invalidates any mechanism involving exponential growth. Even if that were not the case, for typical whistler-mode group velocities of 10^7 m/sec, the amount of time the wave spends in the beam is so short, only about 10^{-6} sec, that unreasonably high growth rates ($\gamma > \omega_c \cong 10^6$ sec^{-1}) would be required to generate the radiation. No whistler-mode instability is known that can produce such large growth rates from realistic electron distribution functions. These same conclusions were also reached by Jones and Kellogg [1973] in their paper

addressing the growth rates of whistler-mode radiation from artificially-created electron beams.

Mechanisms involving the intermediate generation of electrostatic waves in the beam are now considered. Any density perturbation or bunch created by an electrostatic wave in the beam is capable of emitting coherent Cerenkov radiation. The radiated power from a bunch will have a frequency spectrum similar to that of a single radiating electron; however, the wave power will be much greater since the emitted power goes as N^2 , where N is the number of electrons in a bunch. Coherent Cerenkov radiation from a bunched beam has been considered previously by Bell [1968].

Beam-plasma instabilities are known to be capable of creating intense electrostatic waves and density perturbations in the beam. An estimate of the number of coherently bunched electrons required to account for the observed whistler-mode radiation is presented. A first-order expression for the total power emitted from the electron bunches in the beam is $\left(\frac{dP}{df}\right)_{TOT} = \left(\frac{dP}{df}\right)_e (\Delta N)^2 \alpha$, where $\left(\frac{dP}{df}\right)_e$ is the power radiated by each electron, ΔN is the typical number of electrons in a bunch, and α is the number of bunches in the 200-meter segment of the beam. Consequently,

$$\Delta N = \left(\frac{\left(\frac{dP}{df}\right)_{TOT}}{\left(\frac{dP}{df}\right)_e \alpha} \right)^{1/2} \quad . \quad (3-2)$$

Beam-plasma instabilities are known to create an electrostatic wave near the local electron plasma frequency (3 MHz). Such an emission is, in fact, observed near 3 MHz [see Gurnett et al., 1986]. The corresponding wavelength of this emission is $V_b/f_p \approx 7$ meters, which is assumed to be the approximate length of each bunch. This wavelength can then be used to calculate α , the number of bunches in the first 200 meters of the beam. This number is $\alpha \approx 29$. The radiated power from the 200-meter beam segment, $(\frac{dP}{df})_{\text{total}}$, is about 10^{-9} W/Hz. From Mansfield, $(\frac{dP}{df})_e$ is about 10^{-29} W/Hz. Using (3-2), it is calculated that each bunch must contain about $\Delta N = 2 \times 10^9$ electrons in order to account for the observed radiated power.

An estimate can now be made of the required electric field strength of the electrostatic wave in the beam that forms the bunches. Assuming that the beam diameter is about 2 cyclotron radii, the electron number density in the bunch can be estimated using the formula:

$$\Delta n = \frac{\Delta N}{\pi r_c^2 \Delta L} \quad (3-3)$$

where ΔL is the bunch length and r_c is the cyclotron radius (2 to 3 meters). The required number density is found to be about $\Delta n = 1 \times 10^7$ electrons/m³. Again assuming a beam diameter of $2 r_c$, the average beam density is $n_0 = 1 \times 10^9$ electron/m³. Note that the fractional density perturbation in the beam $\Delta n/n_0$ is only about 0.01. Consequently, a relatively small density perturbation can account for the

measured whistler-mode power. Poisson's equation can be used to determine the magnitude of the self-consistent electric field needed to generate this density perturbation

$$\frac{\Delta E}{\Delta L} = \frac{e\Delta n}{\epsilon_0} \quad . \quad (3-4)$$

From Equation (3-4), an electric field on the order of 1-2 V/m is needed to create the required coherence in the beam electrons.

Although the PDP did not fly directly through the beam during free flight, when the PDP was on the Remote Manipulator Arm, it did provide electric field measurements in the beam. During these times, an intense field-aligned electric-field signal near f_{pe} was measured with amplitudes greater than 0.3 V/m, sufficiently large to saturate the receiver. This value is within a factor of 10 of the required amplitudes needed for radiative coherence of the beam electrons. The good agreement between the calculated and measured electrostatic field strengths strongly suggests that electron bunches generated by a beam-plasma instability can account for the observed whistler-mode power.

In the analysis above, it is assumed that the electron beam has fully expanded to a diameter of $2 r_c$ after being injected. This assumption, however, may not actually be valid near the generator since the beam is still expanding after being ejected from the small generator orifice. As will be shown in Chapter V, this expansion can effect beam structure and should be considered in a detailed power calculation.

In the rest of this thesis, a detailed model of the coherent Cerenkov radiation mechanism described above is presented. A computer simulation of the beam is performed, and the radiated power from this beam is calculated and compared to the measured power from the SL-2 beam in the whistler mode.

CHAPTER IV
EMITTED POWER VIA CERENKOV RADIATION PROCESSES

In this chapter an expression will be derived for the power emitted from an electron beam in a plasma by the Cerenkov radiation process. This expression can be used with known electron beam distributions to compute the radiated power from a beam, and can be applied to the SL-2 electron beam to determine its radiated power.

The derivation is similar to that of Mansfield's [1967], who derived an expression for the radiated power from a single test particle in a plasma medium. His approach was to use the Fourier transforms of the source current and electric field to obtain the radiated power; a method that differed from Liemohn [1965], who derived a similar power expression using the solution of the Hamiltonian of the test particle's radiation field. Mansfield [1967] claimed that there was 'excellent quantitative and qualitative agreement' between his expression and Liemohn's.

Either of these expressions for single particle radiation can be used to calculate the incoherently-radiated power from an electron beam. In performing this calculation it is assumed that each electron in the beam radiates independently from all others. The radiated power from each individual electron in a given volume of the beam is then added to obtain the total radiated power.

In the previous section, a calculation of the incoherently-radiated power from the SL-2 electron beam was performed. It was found that this radiation mechanism could not account for the measured whistler-mode wave power, and concluded that coherent effects among the beam electrons must be included in the calculation.

Harker and Banks [1983] derived an expression for the power radiated from a pulsed electron beam in a plasma which included the coherent effects between the radiating electrons in the beam. They, like Mansfield, used the Fourier transforms of the pulsed current source and electric field to obtain the radiated power. In their derivation, it was assumed that all beam electrons travelled with the same velocity, \bar{v} , in pulses of length, l , with a distance, d , separating each pulse. Compared to the incoherently-radiated power from a beam, the inclusion of coherent effects between radiating beam-electrons in a pulse leads to much higher radiated powers; however, the derived expression for radiated power did not include effects from bunches that occur due to instabilities in the beam.

In this section, a general expression will be derived for the radiated power from an electron beam that includes the coherent radiation from particle bunches. The derived expression allows one to calculate the radiated power from N field-aligned particles with arbitrary velocity and position. If a distribution of beam particles is known, the velocity and position of these particles can be used to compute the radiated power.

A. Derivations

There will be two expressions derived in this section: first, the power radiated from a single test particle in a plasma medium will be obtained. Except for a simplification, this derivation will follow the identical steps as Mansfield [1967]. Second, this derivation will be generalized to include the radiated power from N particles of arbitrary velocity and position.

In deriving these expressions, it is assumed that all particles are moving parallel to a static magnetic field in a plasma. This choice of particle trajectory will simplify the integrations involved in the derivations. It will be shown that these field-aligned particle trajectories only allow the $s = 0$ Landau resonance interaction between beam particles and waves. This is not a problem, however, since it is believed that the detected whistler-mode signal from the SL-2 electron beam was generated by the Landau interaction. It should be noted that the SL-2 electron beam was not actually field aligned, but varied in pitch angle from 0° to 20° ; however, this variation causes only a 6% change in the beam electron's parallel velocity and, as mentioned previously, is not enough variation to significantly alter the radiated power from a 1 keV beam electron. Cyclotron motion of the electrons can, however, alter the radiative coherence of the beam. As will be shown, coherent effects between beam electrons is a function of their relative position. If a beam has a relatively large pitch angle, the beam electrons will deviate from their field-aligned trajectories which alter their relative position and

coherence; however, the SL-2 beam had, at most, a pitch angle of 20° and during most of the encounter was nearly field aligned. Consequently, the calculated power assuming a field-aligned beam trajectory should not be significantly different from that of the real SL-2 beam with small variations in pitch angle.

Some further assumptions will be made in deriving the two power expressions in this section. These assumptions are identical to those made by Mansfield [1967] and they are:

- (1) That the plasma medium is represented by a homogeneous, cold, collisionless plasma in a static magnetic field, \bar{B}_0 .
- (2) That the presence of the test particle(s) may be neglected in the description of the medium.
- (3) That the radiated waves from the test particle(s) do not significantly alter the medium and have magnetic fields much weaker than \bar{B}_0 .
- (4) That the magnetic permeability is equal to the free space value.

1. Radiated Power From a Single Test Charge In A Plasma Medium

An expression is now be derived for the radiated power from a single test charge in a plasma medium. The steps taken in this derivation are identical to Mansfield's [1967], except for the simplification of making the particle trajectories field aligned.

The first step is to write Ampere's and Faraday's Laws for the Fourier transforms of $\bar{E}(\bar{r}, t)$ and $\bar{H}(\bar{r}, t)$:

$$\bar{\mathbf{k}} \times \bar{\mathbf{H}}(\bar{\mathbf{k}}, \omega) = -\omega \epsilon_0 \bar{\mathbf{K}} \cdot \bar{\mathbf{E}}(\bar{\mathbf{k}}, \omega) + i \bar{\mathbf{J}}_q(\bar{\mathbf{k}}, \omega) \quad (4-1)$$

$$\bar{\mathbf{k}} \times \bar{\mathbf{E}}(\bar{\mathbf{k}}, \omega) = \omega \mu \bar{\mathbf{H}}(\bar{\mathbf{k}}, \omega) \quad (4-2)$$

where $\bar{\mathbf{J}}_q(\bar{\mathbf{k}}, \omega)$ is the Fourier transform of the external source current and $\bar{\mathbf{K}}$ is the dielectric tensor for the plasma medium. Substituting $\bar{\mathbf{H}}(\bar{\mathbf{k}}, \omega)$ from (4-2) into (4-1) yields the homogeneous equation:

$$\bar{\mathbf{n}} \times \bar{\mathbf{n}} \times \bar{\mathbf{E}}(\bar{\mathbf{k}}, \omega) + \bar{\mathbf{K}} \cdot \bar{\mathbf{E}}(\bar{\mathbf{k}}, \omega) = \frac{i \bar{\mathbf{J}}_q(\bar{\mathbf{k}}, \omega)}{\omega \epsilon_0} \quad (4-3)$$

where $\bar{\mathbf{n}} = \frac{\bar{\mathbf{k}}c}{\omega}$ is the index of refraction. This equation can be reexpressed as

$$\bar{\mathbf{T}} \cdot \bar{\mathbf{E}}(\bar{\mathbf{k}}, \omega) = \frac{i \bar{\mathbf{J}}_q(\bar{\mathbf{k}}, \omega)}{\omega \epsilon_0} \quad (4-4)$$

A static magnetic field, $\bar{\mathbf{B}}_0$, is present in the plasma medium and is assumed to lie along the $\hat{\mathbf{z}}$ -axis. Radiation from a field-aligned test particle will be azimuthally symmetric; however, for simplicity, it is assumed that $\hat{\mathbf{k}}$ is entirely in the y-z plane at an angle θ relative to the $\hat{\mathbf{z}}$ -axis. This coordinate system can be rotated to analyze radiation from any specific azimuth angle, thus these assumptions can be made without any loss of generality. With these assumptions, $\bar{\mathbf{T}}$ can be expressed as:

$$\bar{T} = \begin{bmatrix} \bar{\epsilon}_1 - n^2 & i \epsilon_2 & 0 \\ -i \epsilon_2 & \epsilon_1 - n^2 \cos^2 \theta & n^2 \sin \theta \cos \theta \\ 0 & n^2 \sin \theta \cos \theta & \epsilon_3 - n^2 \sin^2 \theta \end{bmatrix} \quad (4-5)$$

where

$$\epsilon_1 = 1 + \frac{f_{pe}^2}{f_{ce}^2 - f^2} + \frac{.1836 f_{pe}^2}{f_{ce}^2 - (1836f)^2},$$

$$\epsilon_2 = \frac{f_{pe}^2 f_{ce}}{f(f^2 - f_{ce}^2)} + \frac{f_{pe}^2 f_{ce}}{f[f_{ce}^2 - (1836f)^2]},$$

$$\epsilon_3 = 1 - \frac{f_{pe}^2}{f^2} - \frac{f_{pe}^2}{1836f^2};$$

and f , f_{ce} and f_{pe} are the wave frequency, local cyclotron frequency and local plasma frequency, respectively.

The electric field, $\bar{E}(\bar{r}, t)$, is obtained by taking the inverse Fourier transform of $\bar{E}(\bar{k}, \omega)$:

$$\bar{E}(\bar{r}, t) = \frac{1}{\epsilon_0} \iint \bar{T}^{-1} \cdot \bar{J}_q(\bar{k}, \omega) e^{i(\omega t - \bar{k} \cdot \bar{r})} d\bar{k} \frac{d\omega}{\omega} \quad (4-6)$$

For a single test particle in the medium, the source current is expressed as:

$$\bar{J}_q(\bar{r}, t) = q \bar{V}_q \delta(\bar{r} - \bar{r}_q(t)) \quad (4-7)$$

where for field-aligned trajectories, \bar{V}_q is

$$\bar{V}_q = v_o \hat{z} \quad (4-8)$$

and

$$\bar{r}_q = (r_o + v_o t) \hat{z} \quad (4-9)$$

The variable r_o is defined as the particle's initial position. The Fourier transform of the source current is:

$$\bar{J}_q(\bar{k}, \omega) = \frac{1}{(2\pi)^4} \iint \bar{J}_q(\bar{r}, t) e^{i(\bar{k} \cdot \bar{r} - \omega t)} d\bar{r} dt = \frac{\hat{z} q v_o}{(2\pi)^4} \int e^{i(\bar{k} \cdot \bar{r}_q - \omega t)} dt \quad (4-10)$$

As mentioned previously, \hat{k} is assumed to lie in the y-z plane, at an angle θ relative to the \hat{z} -axis, which allows \bar{k} to be expressed as:

$$\bar{k} = \hat{y} k \sin \theta + \hat{z} k \cos \theta \quad (4-11)$$

and

$$\bar{k} \cdot \bar{r}_q = \frac{n\omega \cos \theta_o}{c} r_o + n\omega \cos \theta \beta t \quad (4-12)$$

where $\beta = \frac{V_0}{c}$ and $\frac{n\omega}{c}$ has been substituted for k . The transform of the source current is then:

$$\begin{aligned} \bar{J}_q(\bar{k}, \omega) &= \frac{\hat{z} q V_0}{(2\pi)^4} e^{\frac{i n \omega}{c}} \cos \theta r_0 \int_{-\infty}^{\infty} e^{i(n\omega \cos \theta \beta - \omega)t} dt \\ &= \frac{\hat{z} q V_0}{(2\pi)^3} e^{\frac{i n \omega}{c}} \cos \theta r_0 \delta(n\omega \cos \theta \beta - \omega) \end{aligned} \quad (4-13)$$

where $\int_{-\infty}^{\infty} e^{i(n\omega \cos \theta \beta - \omega)t} dt = 2\pi \delta(n\omega \cos \theta \beta - \omega)$ is used to obtain (4-13). Substituting (4-13) into Equation (4-6) yields:

$$\begin{aligned} \bar{E}(\bar{r}, t) &= \frac{q i V_0}{(2\pi)^3 \epsilon_0} \iiint (\bar{T}^{-1} \cdot \hat{z}) e^{\frac{i n \omega \cos \theta}{c} r_0} \delta(n\omega \cos \theta \beta - \omega) \\ &e^{i(\omega t - \bar{k} \cdot \bar{r})} d\bar{k} \frac{d\omega}{\omega} \end{aligned} \quad (4-14)$$

for the electric field.

The radiated power from this test particle is

$$\begin{aligned} P(t) &= q \bar{E}(\bar{r}_q, t) \cdot \bar{V}_q(t) \\ &= \frac{q^2 i V_0^2}{(2\pi)^3 \epsilon_0} \iiint (\hat{z} \cdot \bar{T}^{-1} \cdot \hat{z}) e^{\frac{i n \omega}{c} \cos \theta r_0} e^{i(\omega t - \bar{k} \cdot \bar{r}_q)} \delta(n\omega \cos \theta \beta - \omega) \partial \bar{k} \frac{d\omega}{\omega} \end{aligned} \quad (4-15)$$

Substituting (4-12) for $\bar{\mathbf{k}} \cdot \bar{\mathbf{r}}_q$ in the exponential term of (4-15) yields:

$$P(t) = \frac{q^2 v_0^2}{(2\pi)^3 \epsilon_0} \iint (\hat{\mathbf{z}} \cdot \bar{\mathbf{T}}^{-1} \cdot \hat{\mathbf{z}}) \delta(n\omega \cos \theta - \omega) e^{i(\omega - n\omega \cos \theta) t} d\bar{\mathbf{k}} \frac{d\omega}{\omega} . \quad (4-16)$$

Note that the dependence of the power on r_0 , the initial position of the particle, cancels out of the expression. The element $d\bar{\mathbf{k}}$ can be reexpressed as

$$d\bar{\mathbf{k}} = n^2 \frac{\omega^3}{c^3} dn \sin \theta d\theta d\phi .$$

Since there is no ϕ dependence in (4-16), the integration over ϕ yields a 2π . The integration over θ is more complicated since $\cos \theta$ is in both the delta function and exponential. An integral of the form

$$I = \int f(x) \delta(Ax+B) dx = \frac{f(x_0)}{|A|}$$

now has to be evaluated. For (4-16), $A = |n\omega\beta|$, $B = \omega$, and $x_0 = \frac{1}{n\beta}$. Note, in the integration, that a nonzero value is obtained only if

$$\cos \theta_0 = \frac{1}{n\beta} \quad (4-17)$$

is satisfied. This is the Landau resonance condition. The expression for radiated power now becomes:

$$P(t) = \frac{-q^2 i V_0^2}{(2\pi)^2 \epsilon_0 c^3 \beta} \iint (\hat{z} \cdot \vec{T}^{-1} \cdot \hat{z}) |n| |\omega| dn d\omega \quad . \quad (4-18)$$

From Mansfield [1967], it is found that

$$(\hat{z} \cdot \vec{T}^{-1} \cdot \hat{z}) = \frac{\epsilon_1^2 - \epsilon_2^2 - \epsilon_1 n^2 + (n^4 - \epsilon_1 n^2) \cos^2 \theta_0}{\epsilon_1 (n^2 - n_1^2) (n^2 - n_2^2)} \quad (4-19)$$

where θ_0 is the angle that satisfies the Landau resonance condition and $n_{1,2}^2 = [-B \pm (B^2 - 4C\epsilon_1)^{1/2}] / 2\epsilon_1$. The quantity $B = (\frac{c}{V_0})^2 (\epsilon_3 - \epsilon_1) + \epsilon_2^2 - \epsilon_1^2 - \epsilon_1 \epsilon_3$ and $C = (\frac{c}{V_0})^2 (\epsilon_1^2 - \epsilon_2^2 - \epsilon_1 \epsilon_3) + \epsilon_3 (\epsilon_1^2 - \epsilon_2^2)$ where ϵ_1 , ϵ_2 and ϵ_3 are those previously defined. If the numerator of (4-19) is defined as $T_{33}(n)$, the power expression can now be written as:

$$P(t) = \frac{-q^2 i V_0^2}{(2\pi)^2 \beta \epsilon_0 c^3 \epsilon_1} \int \left[\int_0^\infty \frac{T_{33}(n) |n| dn}{(n^2 - n_1^2) (n^2 - n_2^2)} \right] |\omega| d\omega \quad . \quad (4-20)$$

Since the real part of the power is needed, the imaginary part of the quantity in brackets in (4-20) has to be calculated. To obtain this imaginary part, the Plemelj formula was used with the result that

$$\begin{aligned}
\int_0^{\infty} \frac{T_{33}(n) |n| dn}{(n^2 - n_1^2)(n^2 - n_2^2)} &= \frac{\pi i}{2(n_2^2 - n_1^2)} [T_{33}(n_2) - T_{33}(n_1)] \\
&= \frac{\pi i}{2(n_2^2 - n_1^2)} \sum_{k=1}^2 (-1)^k T_{33}(n_k)
\end{aligned} \tag{4-21}$$

Equation (4-20) now becomes

$$P(t) = \int_{-\infty}^{\infty} \frac{q^2 |\omega| d\omega}{8\pi\epsilon_0 \epsilon_1 (n_2^2 - n_1^2)} \left(\frac{v_0}{c^2}\right) \sum_{k=1}^2 (-1)^k T_{33}(n_k) \quad . \tag{4-22}$$

This expression for the radiated power can be compared to Equation 32 of Mansfield [1967]. Assuming that the particle's perpendicular velocity is zero and that wave generation is via the $s = 0$ Landau resonance, then out of the six terms in brackets in Mansfield's Equation 32, only one remains. In the limit that the particle's perpendicular velocity goes to zero, the Bessel function, $J_0(L)$, in Mansfield's Equation 32 goes to one. Consequently, Equation (4-22) is identical to Mansfield's Equation 32 when considering the radiated power from a field-aligned test particle.

2. Radiated Power From N Particles in a Plasma Medium

An expression for the radiated power from N field-aligned test particles is now derived. This derivation is similar to the single particle case derived previously; however, coherence effects between these N radiators will be included.

The source current for the N test particles can be written as:

$$\bar{J}_q(\bar{r}, t) = \sum_{i=1}^N q \bar{V}_i(t) \delta(\bar{r} - \bar{r}_i(t)) \quad (4-23)$$

with

$$\bar{V}_i(t) = v_{i0} \hat{z} \quad (4-24)$$

and

$$\bar{r}_i(t) = (r_{i0} + v_{i0} t) \hat{z} \quad (4-25)$$

being the velocity and position of the ith particle. Like the single particle case, each of the N particles are field-aligned and are initially located at point r_{i0} along the \hat{z} -axis. Using (4-12), $\bar{k} \cdot \bar{r}_i$ can be expressed as

$$\bar{k} \cdot \bar{r}_i = \frac{n\omega}{c} \cos \theta r_{i0} + n\omega \cos \theta \beta_i t \quad (4-26)$$

where $\frac{n\omega}{c}$ has been substituted for k and $\beta_i = \frac{v_{i0}}{c}$. The Fourier transform of the source current is

$$\begin{aligned}\bar{J}_q(\bar{k}, \omega) &= \frac{1}{(2\pi)^4} \iiint \bar{J}_q(\bar{r}, t) e^{i(\bar{k} \cdot \bar{r} - \omega t)} d\bar{r} dt \\ &= \sum_{i=1}^N \frac{q_i V_{i0} \hat{z}}{(2\pi)^4} \int e^{i(\bar{k} \cdot \bar{r}_i - \omega t)} dt\end{aligned}\quad (4-27)$$

Substituting (4-26) into (4-27) and using the identity

$$\int_{-\infty}^{\infty} e^{i(n\omega \cos \theta \beta_i - \omega)t} dt = 2\pi \delta(n\omega \cos \theta \beta_i - \omega)$$
 yields:

$$\bar{J}_q(\bar{k}, \omega) = \sum_{i=1}^N \frac{q_i V_{i0} \hat{z}}{(2\pi)^3} e^{\frac{i n \omega}{c} \cos \theta r_{i0}} \delta(n\omega \cos \theta \beta_i - \omega)\quad (4-28)$$

The electric field can now be solved by substituting (4-28) into

(4-6):

$$\bar{E}(\bar{r}, t) = \sum_{i=1}^N \frac{q_i V_{i0}}{(2\pi)^3 \epsilon_0} \iiint (\bar{T}^{-1} \cdot \hat{z}) e^{\frac{i n \omega}{c} \cos \theta r_{i0}} \delta(n\omega \cos \theta \beta_i - \omega)$$

$$e^{i(\omega t - \bar{k} \cdot \bar{r})} d\bar{k} \frac{d\omega}{\omega}$$

The radiated power from these particles is

$$\begin{aligned}
P(t) &= q \sum_{j=1}^N \overline{\mathbf{E}(\overline{\mathbf{r}}_j, t)} \cdot \overline{\mathbf{V}}_j(t) \\
&= \sum_{j=1}^N \sum_{i=1}^N \frac{q^2 i V_{i0} V_{j0}}{(2\pi)^3 \epsilon_0} \iint (\hat{\mathbf{z}} \cdot \overline{\overline{\mathbf{T}}}^{-1} \cdot \hat{\mathbf{z}}) e^{\frac{i n \omega}{c} \cos \theta r_{i0}} \delta(n \omega \cos \theta \beta_i - \omega) \\
&\hspace{20em} (4-30)
\end{aligned}$$

$$e^{i(\omega t - \overline{\mathbf{k}} \cdot \overline{\mathbf{r}}_j)} d\overline{\mathbf{k}} \frac{d\omega}{\omega} .$$

The element $d\overline{\mathbf{k}}$ can be written as:

$$d\overline{\mathbf{k}} = n^2 \frac{\omega^3}{c^3} dn \sin \theta d\theta d\phi$$

and

$$\overline{\mathbf{k}} \cdot \overline{\mathbf{r}}_j = \frac{n\omega}{c} \cos \theta r_{j0} + n\omega \cos \theta \beta_j t$$

where $\beta_j = \frac{V_{j0}}{c}$. The radiated power, after performing the integration over ϕ , then becomes:

$$\begin{aligned}
P(t) &= \sum_{j=1}^N \sum_{i=1}^N \frac{q^2 i V_{i0} V_{j0}}{(2\pi)^2 \epsilon_0 c^3} \iint (\hat{\mathbf{z}} \cdot \overline{\overline{\mathbf{T}}}^{-1} \cdot \hat{\mathbf{z}}) e^{\frac{i n \omega}{c} \cos \theta (r_{i0} - r_{j0})} \\
&\hspace{20em} (4-31) \\
&e^{i(\omega - n\omega \cos \theta \beta_j)t} \delta(n\omega \cos \theta \beta_i - \omega) n^2 \omega^2 dn \sin \theta d\theta d\omega .
\end{aligned}$$

Like the single particle case, the evaluation of the integral

$$I = \int f(x) \delta(Ax+B) = \frac{f(x_0)}{|A|}$$

is needed to complete the integration over θ . For (4-31), $A = |n\omega \beta_i|$, $B = \omega$ and $x_0 = \frac{1}{n \beta_i}$. This integration is nonzero only for

$$\cos \theta_{oi} = \frac{1}{n \beta_i} \quad (4-32)$$

which is the Landau resonance condition for the i th particle. Equation (4-31) can now be expressed as:

$$P(t) = - \sum_{j=1}^N \sum_{i=1}^N \frac{q^2 i V_{i0} V_{j0}}{(2\pi)^2 \epsilon_0 c^3 \beta_i} \iint (\hat{z} \cdot \vec{T}^{-1} \cdot \hat{z}) e^{\frac{in\omega}{c} \cos \theta_{i0} (r_{i0} - r_{j0})} e^{i\omega(1 - \frac{\beta_j}{\beta_i})t} |n| |\omega| dn d\omega \quad (4-33)$$

The quantity $(\hat{z} \cdot \vec{T}^{-1} \cdot \hat{z})$ is, again,

$$(\hat{z} \cdot \vec{T}^{-1} \cdot \hat{z}) = \frac{T_{33}(n)}{\epsilon_1 (n_1^2 - n^2)(n_2^2 - n^2)} \quad (4-34)$$

where $T_{33}(n)$ is the numerator of (4-19) and $n_{1,2} = n_{1,2}(\beta_i)$. Equation (4-33) is reexpressed as

$$P(t) = - \sum_{j=1}^N \sum_{i=1}^N \frac{q^2 v_{i0} v_{j0}}{(2\pi)^2 \epsilon_0 c^3 \beta_i \epsilon_1} \int \left[\int_0^\infty \frac{T_{33}(n) |n| e^{inA} dn}{(n^2 - n_1^2)(n^2 - n_2^2)} \right] e^{i\omega(1 - \frac{\beta_j}{\beta_i})t} |\omega| d\omega \quad (4-35)$$

where $A = \frac{\omega}{c} \cos \theta_{i0} (r_{i0} - r_{j0})$. Since the real part of the power is desired, the imaginary part of the quantity in brackets must be calculated. In this evaluation, only the real part of the exponential, e^{inA} , is considered since only the relative phase of the electron radiators is needed. Using the Plemelj formula, the imaginary part of the integral is

$$\int_0^\infty \frac{T_{33}(n) |n| e^{inA} dn}{(n^2 - n_1^2)(n^2 - n_2^2)} = \frac{\pi i}{2(n_2^2 - n_1^2)} \sum_{k=1}^2 (-1)^k T_{33}(n_k) e^{in_k A} \quad (4-36)$$

Substituting (4-36) for the bracketed expression in (4-35) yields the expression for the radiated power from N particles:

$$P(t) = - \int_{-\infty}^{\infty} \sum_{j=1}^N \sum_{i=1}^N \frac{q^2 |\omega| d\omega}{8\pi \epsilon_0 \epsilon_1} \frac{1}{(n_2^2(\beta_i) - n_1^2(\beta_i))} \left(\frac{v_{j0}}{c^2}\right) e^{i\omega(1 - \frac{\beta_j}{\beta_i})t} \times \sum_{k=1}^2 (-1)^k T_{33}(n_k(\beta_i)) e^{i \frac{n_k(\beta_i) \omega}{c} \cos \theta_{i0} (r_{i0} - r_{j0})} \quad (4-37)$$

The radiated power is reexpressed as

$$\begin{aligned}
P(t) = & \int_{-\infty}^{\infty} \sum_{i=1}^N \frac{q^2 |\omega| d\omega}{8\pi \epsilon_0 \epsilon_1} \left(\frac{1}{n_2^2(\beta_i) - n_1^2(\beta_i)} \right) \left(\frac{v_{i0}}{c^2} \right) \sum_{k=1}^2 (-1)^k T_{33}(n_k(\beta_i)) \\
& + \int_{-\infty}^{\infty} \sum_{i=1}^N \sum_{j \neq i}^N \frac{q^2 |\omega| d\omega}{8\pi \epsilon_0 \epsilon_1} \left(\frac{1}{n_2^2(\beta_i) - n_1^2(\beta_i)} \right) \left(\frac{v_{j0}}{c^2} \right) \\
& \cdot e^{i\omega(1 - \frac{\beta_j}{\beta_i})t} \sum_{k=1}^2 (-1)^k T_{33}(n_k(\beta_i)) \\
& \cdot e^{i \frac{n_k(\beta_i)}{c} \omega \cos \theta_{i0} (r_{i0} - r_{j0})}
\end{aligned} \tag{4-38}$$

In this expression, the first-term represents the incoherently radiated power from the N test particles while the second-term represents the additional power from coherent effects between the N particles. Note these coherent effects depend on a particle's velocity and position relative to all other particles.

The time-averaged power is defined as

$$\bar{P} = \frac{1}{2T} \int_{-T}^T P(t) dt$$

Averaging (4-37) over time yields the expression:

$$\begin{aligned}
\bar{P} = & \int_{-\infty}^{\infty} \sum_{j=1}^N \sum_{i=1}^N \frac{q^2 |\omega| d\omega}{8\pi \epsilon_0 \epsilon_1} \frac{1}{n_2^2(\beta_i) - n_1^2(\beta_i)} \left(\frac{v_{j0}}{c^2} \right) \\
& \frac{\sin x}{x} \sum_{k=1}^2 (-1)^k T_{33}(n_k(\beta_i)) e^{i \frac{n_k(\beta_i)}{c} \omega \cos \theta_{i0} (r_{i0} - r_{j0})}
\end{aligned} \tag{4-39}$$

where $x = \omega T (1 - \beta_j/\beta_i)$. Note that if $\beta_i = \beta_j$ ($V_{i0} = V_{j0}$), then $\sin x/x \rightarrow 1$ and the radiation coming from particles i and j can be coherent, depending only on the particle's relative position. If a distribution of particles exist with $\beta_i \neq \beta_j$ then the power averaged over very long periods will be nearly equal to the incoherently radiated power from the particles. This result is obtained because $\lim_{T \rightarrow \infty} \frac{\sin x}{x} = 0$ for $\beta_i \neq \beta_j$, allowing only the terms that describe the incoherently radiated power to remain in (4-39). Note, from (4-39), that if all particles were moving at the same velocity and each had the same initial position, the exponential terms would be unity and the radiated power would be $P = N^2 P_1$, where P_1 is the radiated power from a single test charge.

As an example, the radiated power from two test particles will be written from (4-39):

$$\begin{aligned} \overline{dP} = & \frac{q^2 |\omega| d\omega}{8\pi\epsilon_0 \epsilon_1} \left[\frac{1}{(n_2^2(\beta_1) - n_1^2(\beta_1))} \frac{V_{10}}{c^2} \sum_{k=1}^2 (-1)^k T_{33}(n_k(\beta_1)) \right. \\ & + \frac{1}{(n_2^2(\beta_2) - n_1^2(\beta_2))} \frac{V_{20}}{c} \sum_{k=1}^2 (-1)^k T_{33}(n_k(\beta_2)) \\ & \left. + \frac{1}{(n_2^2(\beta_2) - n_1^2(\beta_2))} \frac{V_{10}}{c} \frac{\sin x_1}{x_1} \sum_{k=1}^2 (-1)^k T_{33}(n_k(\beta_2)) \right] \end{aligned}$$

$$\begin{aligned}
& \times e^{\frac{in_k(\beta_2)\omega}{c} \cos \theta_{20}(r_{20}-r_{10})} \\
& + \frac{1}{(n_2^2(\beta_1) - n_1^2(\beta_1))} \frac{v_{20}}{c^2} \frac{\sin x_2}{x_2} \sum_{k=1}^2 (-1)^k T_{33}(n_k(\beta_1)) \\
& \times e^{\frac{in_k(\beta_2)\omega}{c} \cos \theta_{10}(r_{10} - r_{20})} \Bigg]
\end{aligned} \tag{4-40}$$

where $x_1 = \omega T (1 - \beta_1/\beta_2)$ and $x_2 = \omega T (1 - \beta_2/\beta_1)$. The first two terms in the brackets represent the radiated power from single test charge #1 and single test charge #2. These two terms, together, represent the incoherent radiation from the two particles. The last two terms in the brackets represent the effects of coherence on the radiated power from these two test particles. Again, if the particles are moving at the same velocity and have the same initial position, the radiated power is

$$P = 4P_1$$

where P_1 is the radiated power from a single test particle.

Although it is not completely obvious in the analysis, expression (4-37) does indeed describe a Cerenkov radiation process. This fact is easily demonstrated using the Cerenkov (Landau) resonance condition:

$$n_{\parallel} = n \cos \theta = \frac{c}{v_b} \quad . \quad (4-41)$$

Recall that if this condition is not met, the radiated power from the beam is zero (see Equation 4-32). Since the phase velocity of the emitted radiation is $v_{PH} = c/n$, the expression

$$v_b = \frac{v_{PH}}{\cos \theta} > v_{PH} \quad (4-42)$$

can be written using (4-41). Consequently, a necessary condition to obtain radiation from the beam is that $v_b > v_{PH}$, which describes a Cerenkov process.

B. Practical Applications

Expressions (4-37) and (4-39) calculates the radiated power by determining the coherence effect amongst the individual beam electron radiators. This calculation represents a microscopic approach to determining the radiated power. A general macroscopic approach has also been derived and is presented in the Appendix. In this approach, the radiated power from a beam with current density $J_z(z,t)$ is calculated. The macroscopic approach has a distinct advantage over the microscopic approach since any real calculation of the radiated power can be computed easier when considering the macroscopic variable $J_z(z,t)$. Using the microscopic approach, the position and velocity of all N particles as a function of time must be considered. Keeping track of all these

variables on a computer requires large amounts of CPU time. Using the macroscopic approach, however, only requires a calculation of the macroscopic variable $J_z(z,t)$, which on a computer is far easier to calculate. Consequently, for any practical power calculation, Equation (A-10) will be used.

The microscopic approach derived in this section is still an important original work since it is the theoretical basis on which the macroscopic approach is derived. This approach also considers explicitly the concept of radiative coherence between the beam particles; a concept that is only implicitly dealt with in the macroscopic approach.

Calculating the radiated power using either approach requires a knowledge of the beam phase-space configuration. Considering the SL-2 electron beam, the phase-space configuration must be modeled from a particle simulation, since beam particle distributions were not obtained experimentally. There are two reasons for not measuring these distributions directly: first, when the PDP was in free flight, it did not fly through the beam [W. R. Paterson, personal communication, 1986]. When it was on the RMS, it was maneuvered into the beam; however, the instrument that obtains these distributions, the Low Energy Proton Electron Differential Energy Analyzer (Lepedea) instrument, was turned off, since it was feared that a direct hit of the beam on the instrument would alter its sensitivity [W. R. Paterson, personal communication, 1986]. In either case, direct measurements of the electron beam distributions were not obtainable. Second, even if the Lepedea instrument had been turned on and in a favorable position to

measure the beam distribution, the instrument's temporal resolution (1.6 seconds) is not fine enough to directly measure instability-related electron bunching which occurs on the order of $1/\omega_{pe} \sim 10^{-7}$ seconds.

In the next section, the results of a one-dimensional electrostatic particle simulation of the SL-2 electron beam will be reviewed. The velocities and positions of the beam electrons obtained from modeled phase-space distributions will be used to calculate $J_z(z,t)$, and, using (A-10), the Cerenkov radiated power from the beam will be calculated. This calculated power will then be compared to the measured whistler-mode power obtained during the PDP/beam encounter.

CHAPTER V
A ONE-DIMENSIONAL ELECTROSTATIC SIMULATION
OF THE SL-2 ELECTRON BEAM

In order to complete a calculation of the radiated power from the SL-2 electron beam, a knowledge of the electron beam phase-space distribution is required. As mentioned in the previous section, no direct measurement of these distributions were made by the Lepedea instrument on the PDP; thus, the distributions must be modeled. In this section, the results of a particle simulation of the SL-2 electron beam is presented that includes modeled phase-space configurations of the beam that can be used to calculate the radiated power.

To obtain the required beam distribution, a one-dimensional electrostatic model of an electron beam propagating through an ambient plasma is simulated on a computer. Generally, these models use simulation particles that are many times the mass and charge of an electron, and modeling the plasma using these particles is valid only when many of these particles are contained in a Debye cube (Debye length for a one-dimensional system). In this simulation, the ambient plasma consists of electrons represented by simulation particles of negative charge and immobile ions represented by a net positive background charge. The simulation is designed so that initially there is no net charge in the system. The simulation particles representing the

ambient electrons can move freely in this one-dimensional system; however, they are confined to the system by re-injection boundaries. Ambient electrons leaving the system at these boundaries are re-injected with a Gaussian-weighted velocity between zero and the electron thermal speed. The electron beam is represented by simulation particles of negative charge that are injected into the system at the $z = 0$ boundary with velocities greater than the ambient electron thermal speed. In this one-dimensional simulation, a cold electron beam is always injected into the system. In order to keep the net charge in the system equal to zero, a positive charge equal in magnitude to the amount of negative beam charge in the system is placed at the $z = 0$ boundary. This boundary charge imitates the spacecraft charging effect observed on the beam-ejecting shuttle [Williamson et al., 1985].

In a one-dimensional simulation, only a particle's velocity and position in one dimension is considered. The total length of the simulation system is divided up into "grids" of a Debye length, λ_D , in size. The charge density in each grid, ρ_n , is calculated and the numerical solution to Poisson's equation, $E_{n+1} = E_n + 1/2(\rho_{n+1} + \rho_n)$, is used to calculate the electric field in the $n+1$ grid. The simulation particles are then allowed to move in the system under the influence of this electric field for a period of time $\Delta t \leq \lambda_D/V_B$, where V_B is the simulation beam speed. If $\Delta t > \lambda_D/V_B$, the simulated beam particles are moving more than one grid in Δt and will skip grids. Since the ambient particles in the skipped grids will not interact with the beam particle, the modeled system no longer represents reality.

After the simulation particles have evolved, a new charge density and electric field is calculated for each grid and the particles are again allowed to move under the influence of the new electric field. This iterative process continues until the beam-plasma interactions reach a steady-state where then the simulation is terminated.

It is assumed that the particle's position and velocity in the one-dimensional simulated electron beam and plasma is along a static magnetic field line. This alignment allows the simulated particle trajectories to be unaffected by this field. Since the SL-2 electron beam was nearly field aligned during injection, this modeling of the electron beam should yield particle distributions that, for the most part, represent the true physical situation.

Generally, near field-aligned electron beams in test chambers and on shuttle flights tend to expand from twice the radius of the electron generator opening to about two electron cyclotron radii in the radial direction, if the generator opening is less than a gyroradius. This radial or perpendicular expansion decreases the density of the beam as it propagates away from its source. Figure 9 shows pictorially this expansion of the beam. Initially, the beam leaves the electron generator ($z=0$) with a radius r_0 and a density n_0 . However, an effect is present that causes the beam to expand perpendicular to the magnetic field with a perpendicular expansion speed of $V_{\perp \text{exp}}$. This expansion may be related to edge effects of the generator opening or to Coulomb repulsion of beam electrons. As the beam propagates along the \hat{z} -axis at a speed of V_B , the beam radius is expanding according to

the first-order expression $r = r_0 + \frac{v_{\perp \text{exp}}}{v_B} z$ with the local density of the beam, $n(z)$, changing proportionally. The beam expansion continues until $r \cong r_c$, where r_c is the cyclotron radius. By equating the current at the generator to that at other points along z ($J_0 A_0 = J(z) A(z)$), a first-order expression for $n(z)$ is obtained:

$$n(z) = \frac{n_0 r_0^2}{\left(r_0 + \frac{v_{\perp \text{exp}}}{v_B} z\right)^2} = \frac{n_0}{\left(1 + \frac{z}{L}\right)^2} \quad (5-1)$$

where

$$L = \left(\frac{v_B}{v_{\perp \text{exp}}}\right) r_0 \quad (5-2)$$

The scale length, L , represents the beam length where the beam density decreases to $n_0/4$, and is expressed in units of gun radii.

This perpendicular expansion is modeled in the simulation of the SL-2 electron beam. To include this effect, the density of the beam electrons in the simulation are weighted by the factor $\frac{1}{(1+z/L)^2}$, where L is treated as a free parameter. Consequently, the simulation is able to model the density decreases associated with beam expansion which affect the modeled electric fields and beam distributions.

The parameter, L , also indirectly affects the amount of positive charge at the $z=0$ boundary during simulated beam injections. As

mentioned previously, the amount of positive charge at the $z=0$ boundary is equal to the amount of negative beam charge in the system. This charge is placed there in order to conserve the total charge in the system, and effectively simulates spacecraft charging known to occur on beam-ejecting spacecraft. As L decreases, the beam density and total beam charge in the system decreases which also causes the amount of positive charge placed at the $z=0$ boundary to decrease. Consequently, by varying L , both the modeled beam expansion and boundary charging are altered.

Including these effects in the modeling of the SL-2 electron beam makes this one-dimensional simulation rather unique. Usually, to observe the beam character under varying beam expansion and boundary charge, a two-dimensional or three-dimensional simulation is needed; however, by weighting the beam particles properly, this simple one-dimensional simulation copies processes occurring in these more advanced simulations. As an example, results from a two-dimensional simulation performed by Pritchett and Winglee [1986] are compared to the results from this one-dimensional simulation under similar simulated plasma conditions. Pritchett and Winglee's simulation is very advanced. In their two-dimensional simulation system, a simulated spacecraft immersed in a simulated plasma is able to eject a simulated electron beam. Diagnostic software is included that analyzes the electric fields and return currents that develop around the beam and spacecraft. Unlike the one-dimensional simulation, both electron and ion motion parallel and perpendicular to the static magnetic field are

modeled. Electric fields and currents are also allowed to develop both inside and outside the region where the beam propagates. It would seem that such an advanced simulation would have very different results for the electron beam distributions as compared to this study's one-dimensional simulation; however, this is not the case. Figure 10(a) and (b) shows the V_z versus z phase-space configuration of the beam electrons from Pritchett and Winglee's two-dimensional simulation. For this particular simulation, the ratio of the beam to ambient electron densities, n_b/n_A , is 1/16 and the ratio of the beam to ambient thermal velocities, V_b/V_{TE} , is 10. These figures show the phase-space distribution of the beam after the simulation has run for 32 and 64 plasma periods. Note, in both cases, that particle trapping is evident by the looping structures in phase space. In Figure 10(b), particle heating is occurring between $0-.5 V_b$ and the front edge of the beam has a filament structure associated with it. Figure 11(a,b) shows the V_z versus z phase-space configuration of the beam electrons from this study's one-dimensional simulation run with similar beam-plasma parameters as Pritchett and Winglee's. For this run, the expansion scale length parameter, L , is 100. Note that the phase-space configuration of the beam has trapping, heating and filament structures very similar to those of Pritchett and Winglee's, and indicates that similar physical processes are being modeled in both simulations.

The beam phase-space configurations from the one-dimensional simulation are dependent on the expansion scale length parameter, L .

Figure 12(a) and (b) show the beam phase-space configuration from the one-dimensional simulation run with similar beam-plasma parameters as Figures 10 and 11, only now $L = \infty$ (no expansion). The phase-space configurations shown in this figure appear noticeably different, particularly at the leading edge of the beam, compared to those shown in Figures 10 and 11 and indicates that particle trapping dominates at this leading edge. Consequently, beam expansion alters the beam phase-space distributions by reducing wave trapping effects.

The modeling of an electron beam using the one-dimensional code works equally well when simulating an overdense beam ($n_b > n_A$) in an ambient plasma. Figure 13 shows a V_z versus z phase-space configuration from the one-dimensional simulation for an overdense beam with $n_b/n_A = 8$, $V_b/V_{TH} = 15$ and $L = 10$. This configuration can be compared with those obtained by Winglee and Pritchett [1986], who also performed a one-dimensional simulation of an overdense beam ($n_b/n_A = 2$). The beam phase-space distribution obtained from their simulation is shown in Figure 14. Note, in both cases, that a large charge build up of the beam particles is present at the injection boundary, with electron bunches forming near the boundary.

The results of these one-dimensional simulations can be compared to the results obtained from Pritchett and Winglee's two-dimensional simulation of an overdense beam. The V_z versus z beam phase-space configuration from their simulation with $n_b/n_A = 8$ and $V_b/V_{TH} \sim 15$ is shown in Figure 15. Note that a charge build up near the injection boundary is again present, along with bunches of slow moving electrons.

For the modeling of both the underdense and overdense beam injections, this study's one-dimensional simulation is capable of replicating the results obtained from the one-dimensional and two-dimensional simulations performed by Pritchett and Winglee. There is one distinct advantage to the one-dimensional simulation and that is, unlike Pritchett and Winglee's two-dimensional simulation, it can run for very long times; thus, allowing the study of the steady-state nature of the beam. Pritchett and Winglee's simulation has to be terminated as soon as about 1% of the beam particles leave the system in order to maintain charge neutrality based on the simulation boundary conditions; and this usually occurs after 60-100 plasma periods when the beam and plasma are still in a transient state. To determine the steady-state beam character, the simulation should be run for longer times.

A. Results of the Simulation of the SL-2 Electron Beam

The one-dimensional electron beam simulation was performed under similar conditions that prevailed during the SL-2 1 keV-50 mA electron beam injection. The simulated plasma parameters during these runs are displayed in Table 1. The 1 keV-50 mA electron beam was initially injected with a density much greater than the ambient electron density. In order to model this overdense beam in the simulation, an electron beam consisting of simulated electron particles was injected into the simulated plasma with a density five times greater than the ambient electron density. This beam was injected with a velocity $V_B > V_{th}$, where V_{th} is the ambient electron thermal velocity. In the

region of the ionosphere where the SL-2 electron beam experiment was performed, $V_b \approx 100 V_{th}$. Simulations were performed with this

Table 1. Simulation Parameters

n_b/n_A at $z = 0$	5
V_b/V_{th}	20
z	1200 λ_D (~ 60 meters)
L	2, 3, 5, 10 Gun Radii
t	270 ω_{pe}^{-1} ($\sim 1.3 \times 10^{-5}$ sec)
Total number of ambient particles	24000

velocity ratio; however, it was found that V_b/V_{th} could be as low as 20 without significantly altering the beam velocity distributions. Lowering this ratio, however, allows the beam-plasma interactions to occur over shorter length scales, which increases the effective length of the simulation system. Consequently, the simulations were run with $V_b/V_{th} = 20$, which then increased the effective beam length being simulated by a factor of five without altering the interactions being modeled.

The length of the simulation system was selected to be 1200 simulation units long, which corresponds to a length of approximately 60 meters. This length was selected since it is much larger than the size of the expected beam density perturbations, and allows the simulation to be run in a couple CPU hours.

The results of four simulations run with different L values (2, 3, 5, 10) will be presented. Based on practical arguments of beam expansion, spacecraft charging and wave activity, the model that is most consistent with the SL-2 electron beam will be selected.

A simulation was performed with the plasma parameters shown in Table 1, with L , the beam expansion parameter, equal to 10. Figure 16 shows the V_z versus z phase-space distribution for the first 60 meters (1200 simulation units) of the beam at $t = 270 \omega_p^{-1}$. Note that the beam is strongly decelerated near the $z=0$ boundary. Figure 17 shows the electric field versus z for this time. The electric field is measured in dimensionless simulation units, where one of these units corresponds approximately to 6 V/m. Note that a very large positive field is present near the $z=0$ boundary. This electric field is similar to those obtained by Pritchett and Winglee for an overdense beam and results from the strong charging at the boundary. Figure 18 shows the total number of electrons in the beam versus z , and indicates that randomly-spaced density fluctuations are present in the beam; however, as Figure 16 indicates, their velocities are significantly smaller than the initially injected 1 keV-beam velocity. Note from Figure 16 that there is an accumulation of electrons almost lying directly on the $z=0$ boundary. Many of these electrons have significant negative velocities ($V \sim -V_b/2$). This return electron current has been described in great detail by Katz et al. [1986] and is a result of the large potential that develops near $z=0$ due to charging.

Beam expansion is increased and spacecraft charging is decreased for the simulation run with $L = 5$. Figure 19 shows the V_z versus z phase-space distribution of the injected beam for the first 60 meters at $t = 270 \omega_p^{-1}$. The distribution does not appear significantly different from that obtained from the run with $L = 10$ (Figure 16); however, more electrons are able to escape the region near the charged boundary. Figure 20 shows the electric field versus z at $t = 270 \omega_{pe}^{-1}$. Note that a strong electric field is again generated near the $z=0$ boundary; a result from charging effects at the boundary. Figure 21 shows the total electron number versus z , again indicating that randomly-spaced density perturbations are escaping from the region near the charged boundary.

Note for both the $L = 5$ and 10 simulation runs that after $270 \omega_{pe}^{-1}$, the bulk of the beam electrons have not propagated 30 meters past the injection boundary. In contrast, if the beam had propagated unperturbed, it would have extended out to 135 meters; thus, spacecraft charging is drastically altering the character of the beam in these runs. In reality, it may be that large return currents are flowing back to the shuttle along paths unrelated to the beam; such as along magnetic field lines connected to a conducting surface on the shuttle. Such currents may neutralize the spacecraft charge substantially. If this charge is significantly reduced, the beam phase-space distribution will appear as that shown in Figure 22. This result was obtained from a simulation run with $L = 3$. Note that the beam can propagate freely from the injection boundary. The initially

cold beam becomes thermalized and bunches of electrons propagate from the $z=0$ boundary. Note that the beam has a significant number of particles with speeds greater than the initial beam velocity. This is an effect of particle acceleration from an electrostatic wave in the beam. This wave is clearly evident in Figure 23, which displays the electric field versus z . Also note from this figure that the strong charging-related electric field near the $z=0$ boundary is reduced. Figure 24 shows the total number of beam electrons versus z , and indicates that nearly periodic, highly-localized bunches of electrons are present and, from Figure 22, it is concluded that the collective bunch velocity is near or above the initial beam velocity.

Figure 25 shows the V_z versus z beam phase-space distribution from the simulation run with $L = 2$ at $t = 270 \omega_p^{-1}$. Note that the beam can again propagate freely from the $z=0$ boundary. Also, note from this figure, that electron bunches are clearly evident at the top of the elongated looping phase-space structures. Figure 26 displays the electric field versus z at this time. Note that strong electrostatic wave turbulence is present in the beam; however, the relative amplitude of this wave decreases as a function of z . This wave amplitude decrease is an effect of the extreme width-wise beam expansion being simulated. This expansion causes the beam density to strongly decrease as a function of $1/z^2$, which strongly decreases the turbulent electric field according to Poisson's equation. The magnitude of the wave then decreases as the density of the perturbing electrons

decreases. Figure 27 shows the total number of beam electrons versus z . Note that highly localized bunches are evident in the beam.

In Chapter III, calculations were made assuming the bunches had a length, ΔL , of about 7 meters. This bunch length is clearly quite different from those obtained from the simulation. For the runs at $L = 2$ and 3, the bunches are highly localized ($\Delta L \sim .1-.5$ m), nearly periodic, fast-moving groups of charges, while for $L = 5$ and 10, only small randomly-spaced density fluctuations exist in the beam. The density character of the beam in both cases differ from that described in Chapter III, since the simulation is modeling nonlinear wave and spacecraft charging effects occurring in the beam. These effects can drastically alter the beam character and were not included in the simple calculations performed in Chapter III.

As mentioned previously, a choice between the four different beam models must be made to determine which correctly models the SL-2 electron beam. The models presented can be classified according to spacecraft charging's influence on beam propagation. For the runs with $L = 5$ and 10, spacecraft charging is able to drastically alter the injected beam, while for runs with $L = 2$ and 3, the beam is only slightly influenced by charging effects. In reality, the importance of charging depends on the ability of the shuttle to effectively conduct return currents that neutralize the positive charge created during electron beam ejections.

Williamson et al. [1985] have shown that during SL-2 electron beam injections, the shuttle only charged up to between 0 and 40

volts. Consequently, enough return current was drawn from the ionospheric plasma to sufficiently neutralize the positive spacecraft charge, and this charge neutralization allowed the beam to propagate freely from the shuttle [Banks et al., 1985]. A beam freely escaping the near-shuttle region is consistent with the simulations run with $L = 2$ and 3, and rules out the $L = 5$ and 10 simulation runs as possible models of the SL-2 beam.

Figure 26 displays E_z versus z for the simulation run with $L = 2$. As mentioned previously, a self-consistent electrostatic wave is present in the beam with an amplitude that decreases with increasing z , and has a frequency near ω_{pe} . From the figure it appears that the wave has an amplitude barely above simulation noise level in regions of the beam where $z > 7$ meters (150 simulation units). This modeled wave activity is inconsistent with observations made by the PDP on the RMS, where strong electrostatic wave turbulence near ω_{pe} was detected by the PDP radio receivers in regions of the beam where $z > 7$ meters. This model of the beam is then ruled out as a realistic model of the SL-2 electron beam.

From the above arguments, it seems that the simulation run with $L = 3$ is the best model of the SL-2 electron beam. There are two more points to support this conclusion. The first point involves the energy spectrum of the backscattered beam electrons detected near magnetic conjunction by the Lepedea instrument. Apparently, these electrons were not monoenergetic, but were observed at all energies from 2 eV, the lowest Lepedea channel, to about 1 keV [W. R. Paterson,

personal communication]. If nearly-elastic collisional processes dominated the backscattering, the beam distribution would also have a similar energy spectra, which is consistent with the $L = 3$ simulation run (see Figure 22). Also, from Figure 23, strong wave activity is present in the beam for this run. These waves have a frequency near ω_{pe} and are similar to those observed by the PDP in the beam. Consequently, the beam model with $L = 3$ is consistent with the observed beam spectra, wave activity, and spacecraft charging during the 1 keV -50 mA electron beam injection, and is clearly the best beam model.

B. The Radiated Power From a Model of the SL-2 Electron Beam

The radiated power from the modeled SL-2 electron beam will now be calculated. This power will be compared to the measured whistler-mode power to determine if coherent Cerenkov radiation from a bunched beam is a viable wave generation mechanism.

It has been assumed throughout this analysis, that the magnitude of the electric field of the generated Cerenkov radiation is much smaller than that of the electrostatic wave generated within the beam, $E_{ES} \gg E_{RAD}$. This assumption implies that the radiation electric field did not significantly alter the SL-2 beam electron trajectories, and is consistent with the modeling of the beam where radiation field effects are neglected. This assumption is also consistent with observations made during the SL-2 experiment, where $E_{ES} > .3$ V/m in the beam while $E_{RAD} \sim 10^{-3}$ V/m for the whistler-mode waves.

The radiated power from N particles in a specific length segment of the beam can be calculated using equations (4-37) and (4-39). To

actually compute the power using these expressions, however, requires large amounts of costly computer time. An easier way to calculate the power is to use the expression (A-10):

$$P(t) = \bar{P} = \int_{-\infty}^{\infty} \left(\frac{|\omega| d\omega}{8\pi \epsilon_0 \epsilon_1 c^2 V_s} \right) \frac{1}{(n_2^2 - n_1^2)} \sum_{k=1}^2 (-1)^k T_{33}(n_k) \quad (A-10)$$

$$\times [2\pi J_z(k_z(n_k, \theta_0)) J_z^*(k_z(n_k, \theta_0))] \quad .$$

In this expression, V_s is the velocity of the frame moving with the beam such that the current density, $J_z(z, t)$, is considered time independent. In deriving (A-10), a transformation to this frame was made in order to calculate the radiated power from a specific beam segment. Consequently, $J_z(z, t)$ becomes $J_z(z')$ in this new frame, where $z' = z - V_s t$. In (A-10), $J_z(k_z)$ represents the spatial Fourier transform of $J_z(z')$. Once $J_z(k_z)$ of a specific beam segment is known, the power radiated from that segment is easily calculated. As mentioned in Chapter IV, calculating the power using macroscopic variable $J_z(z, t)$ requires less computer time than calculating the radiated power from each particle. In deriving expression (A-10), it has been assumed that a frame of reference exists where the current density is completely independent of time. In this frame, all beam density perturbations have to propagate at identically the same speed, V_s . The transform of the current density is then properly expressed as (A-4), with the delta function specifying the speed of the density

perturbations. This subtle condition placed on the propagation speed of the perturbations reduces the generality of equation (A-10) compared to equation (4-37) which expressed the radiated power from N electrons with arbitrary speeds. Despite this reduction in generality, it will be shown that (A-10) is quite capable of yielding a reasonable estimate of the radiated power from the modeled SL-2 electron beam with bunches moving at or near V_s . It should be noted that in the frequency range of consideration, $n_1 \gg n_2$, $n_1 \approx n$ where n is the whistler-mode index of refraction obtained from cold plasma theory and $T_{33}(n_1) \approx 10^3 T_{33}(n_2)$. Also, based on arguments of the typical density structure size in the beam, $J_z(k_z(n_1, \theta_0)) > J_z(k_z(n_2, \theta_0))$. Consequently, the $k=2$ term in the summation of Equation (A-10) is very small and can be neglected. The radiated power can then be expressed as

$$P(t) = \bar{P} \approx \int_{-\infty}^{\infty} \left[\frac{-|\omega| d\omega}{8\pi \epsilon_0 \epsilon_1 c^2 V_s} \frac{1}{(n_2^2 - n_1^2)} \right] [2\pi J_z(k'_z) J_z^*(k'_z)] T_{33}(n_1) \quad (5-3)$$

where $k'_z = \frac{n \cos \theta_0 \omega}{c}$. Note that $n_1 > n_2$ which makes the term in brackets positive in the frequency range considered.

A simulation of the SL-2 electron beam was run with a simulation length three times longer than those run previously. This simulation length now extends 3600 grid lengths and represents a model of the first 180 meters of the SL-2 electron beam. This increased length was

added to improve the resolution of $J_z(k_z)$ in the whistler-mode range of k_z' . The V_z versus z phase-space configuration for this modeled beam at $t = 840 \omega_{pe}^{-1}$ is displayed in Figure 28. Note that this phase-space configuration is very similar to the phase-space configuration of the 60-meter beam segment displayed in Figure 22. Both configurations have two electron components: a strongly heated component found in phase-space regions where $V < V_b$ and electron bunches found in phase-space regions where $V > V_b$. These bunches are particularly pronounced in the first 75 meters of the beam (from $z = 0$ to 1500). Using Equation (5-3), the radiated power will be calculated from a beam-segment extending 175 meters in length from $z = 100$ to 3500. The first five meters of the beam is not included in the calculation since the beam phase-space configuration near the generator ($z = 0$ boundary) is atypical of the rest of the beam. The power radiated from this 175-meter segment is equal to the Poynting flux through a cylindrical surface of radius R and length $L = 175$ meters surrounding the beam:

$$P_{175m} = S_{\perp} 2\pi R L (175m) \quad . \quad (5-4)$$

Since the radiated power varies directly with L , the power from a 200-meter beam segment can be approximated by

$$P_{200m} = (200/175) P_{175m} \quad . \quad (5-5)$$

A quantity that has to be determined in (A-10) is V_s , the velocity where the current density, $J_z(z,t)$, is considered independent of time. This current density consists of two parts, $J_z(z,t) = J_0(z,t) + J_1(z,t)$. The quantity $J_0(z,t)$ represents the current density from the randomized electrons found in regions of phase space where $V_z < V_b$. The current from these electrons is flowing continuously at a nearly constant value thus $J_0(z,t) = J_0(z)$. The quantity $J_1(z,t)$ represents the current density from the density perturbations or bunches in the beam found in regions of phase space where $V_z > V_b$. The current from these perturbations is time dependent, with bunches passing a point $z = z_0$ at a periodicity of approximately $1/\omega_{pe}$. Consequently, the current density can be rewritten as $J_z(z,t) = J_0(z) + J_1(z,t)$. The frame of reference where $J_z(z,t)$ appears stationary is then a frame that is moving with the bunches since $J_1(z,t)$ is the only time-dependent term in the current density. From Figure 28 it is evident that the bunches are propagating at $V \cong 1.5 V_b = 2.8 \times 10^7$ m/s; thus, $V_s = 2.8 \times 10^7$ m/s.

Bunches created by an electrostatic wave in the beam propagate near the phase speed of the wave, $V_{ph} = \omega/k_z$. The frame where $J_z(z,t)$ is considered time independent is then a frame moving with this wave, $V_s = V_{ph}$. To determine the wave phase speed, the Fourier transform of $J_z(z,t)$, in both time and space for the 175-meter beam segment is calculated and plotted as a function of ω and k_z . This plot is displayed in Figure 29. If the perturbations in current density result from beam interaction with an electrostatic wave, then J_z

(k_z, ω) will be most intense near V_{ph} . Note from the figure that $J_z(k_z, \omega)$ does indeed peak near $\omega/k = V_{ph} = 2.8 \times 10^7$ m/sec, which is represented by the solid line in the figure. Consequently, if a transformation is made to a frame moving at $V_s = V_{ph} = 2.8 \times 10^7$ ms/s, the current density appears nearly stationary. Note also from the figure that all the bunches are not moving exactly at V_{ph} , but have a spread in velocity in a range $\pm \Delta V$ about V_{ph} . Consequently, in the moving frame, some second-order temporal perturbations in the current density will be present and must be considered in the calculation of the radiated power. As will be shown later, these second-order perturbations will not significantly alter the calculation of the radiated power.

The current density calculated from the 175-meter segment is considered the density in the frame moving at V_s , $J_z(z')$, where $z' = z - V_s t$; and the Fourier transform of this current density, $J_z(k_z)$, will be used in (5-3) to determine the radiated power from this segment. The transform of a 175-meter beam segment will yield discrete values of $J_z(k_z)$ at each $k_z = 2\pi m/175$ meters where m is an integer from 0 to 1750. A plot of $J_z(k_z)$ versus k_z is displayed in Figure 30. The resulting transform appears as a white-noise type k -spectra for $k_z > 22$; however, for $k_z < 22$, $J_z(k_z)$ appears to increase as k_z decreases. The white-noise type k -spectra found in $k_z > 22$ results from the randomized position and velocity of the simulation electrons used in the computer model. This noise is inherent in the modeled system since simulation electrons many times the mass and charge of real electrons

were used in the model. Although not feasible, if real electrons had been modeled, this noise would be reduced to nearly zero. The average noise level was calculated by summing the $J_z(k_z)$ values between $k_z = 28.7$ and 62.8 and dividing by the number summed. This level is represented by the dotted line in the figure. The increase in $J_z(k_z)$ found in $k_z < 22$ results from wave-particle interactions within the beam that create localized charged regions or bunches. If bunching had not occurred, the simulated beam electrons would be randomly spaced in both velocity and position and the resulting $J_z(k_z)$ would appear as a white noise type k-spectra at all k_z values.

To solve (5-3), $J_z(k_z)$ evaluated at $k_z' = n \cos \theta_0 \omega/c$ is required. This $k_z'(\omega)$ represents the wave numbers that satisfy the Landau resonance condition and varies from .01 at 31.1 kHz to .25 at 1 MHz. The $J_z(k_z)$ values that correspond to k_z' are presented, graphically, in Figure 30. Note from this figure that six values of $J_z(k_z)$ fall in the range of k_z' for the whistler-mode. Table 2 lists these $J_z(k_z)$ values with the simulation noise level subtracted at their corresponding k_z' and $f(= V_S k_z'/2\pi)$. Using Equation (5-3) and (5-5), the radiated power spectral density, dP/df , from a 200-meter beam segment is evaluated at each of the six frequencies. These values are plotted as a function of wave frequency in Figure 31 (represented by x's) along with the calculated incoherent Cerenkov power spectra (represented by o's) and measured whistler-mode power spectra (represented by .'s) from the 200-meter SL-2 electron beam segment.

Table 2. Values of $J_z(k_z)$

k_z (1/m)	f (kHz)	$J_z(k_z)$ (Noise Level Subtracted)
.0395	176	.092
.0790	352	.035
.1185	529	.192
.1580	705	.067
.1975	881	.123
.2370	1057	.112

Note that the inclusion of coherent effects amongst the beam electrons increases the wave powers by almost 10^9 (90 dB's) above incoherent power levels. Also note that the coherent power level is near the measured whistler-mode powers. It is clear from the figure that coherent Cerenkov radiation from the beam can indeed account for the measured whistler-mode wave power. In fact, the calculated power from the modeled beam overestimates the measured power by about a factor of 10. This disagreement may result from the fact that both the computer simulation of the beam and the power calculations were performed in only one dimension. In this case, motion of the beam electrons perpendicular to the static magnetic field have been neglected. Such motion, as the electron's gyromotion, can change the radiative coherence of the beam electrons by giving them a significant displacement perpendicular to the geomagnetic field. Also, the one-dimensional

simulation of the beam has completely neglected any finite radius effects that occurred in the SL-2 electron beam. These effects can reduce the amplitude of the electrostatic wave in the beam, which correspondingly reduces Δn , the beam density perturbations. The radiated power from the SL-2 electron beam with its finite radius should then be less than the predicted radiated power from the model. Landau damping of the whistler-mode waves in the SL-2 electron beam may also reduce wave powers. This damping occurs because the Cerenkov radiation emitted by the bunches with a phase speed, $V_{ph} < V_s$, is able to interact with the heated component of the beam. This damping is not considered significant, however, since the path length for damping (as well as wave growth) in the SL-2 electron beam is very short. Consequently, the radiation will not interact with the thermalized beam component long enough to be altered significantly.

Note in Figure 31 that the frequency range of the modeled coherently radiated power does not extend below 176 kHz. This low frequency limit results from the discreteness of the $J_z(k_z)$ values used in the calculations. For a 175-meter beam segment, values of $J_z(k_z)$ can only be obtained at specific k_z and f values; namely, at $k_z = 2\pi m/175$ meters and $f = mV_s/175$ meters, where m is an integer extending from 0 to 1750. Consequently, the first nonzero frequency where a $J_z(k_z)$ value exists and the power can be determined is at 176 kHz. Values of power spectral density cannot be obtained below this frequency for a beam of this length. Increasing the beam length will allow the radiated power to be determined at lower frequencies;

however, the computer run time will also be increased, possibly beyond practical considerations. As an example, a calculation of the radiated power at 50 kHz would require nine times the CPU time currently used (from 24 to 216 VAX CPU hours) and a similar calculation at 31 kHz would require a twenty-five times increase in CPU time (from 24 to 600 VAX CPU hours). Clearly, power calculations at these lower frequencies are not feasible.

Based on the results of the simulation, the measured whistler-mode powers calculated in Chapter II and displayed in Figures 6 and 31 should be corrected to account for the radiation emitted by bunch electrons moving at speeds 1.5 times greater than the initial injection speed. The original calculation of this power assumed that all the beam electrons were moving at their initial injection velocity of 1.89×10^7 m/sec which, from the Landau resonance condition, corresponds to a value of $n_{\parallel} = 15.9$. This value of n_{\parallel} was used to constrain the values of $\bar{n}(\theta)$ obtained from cold plasma theory and specified the values of n and $\Delta\theta$ used in the magnitude of the Poynting vector, expression (2-2). From the simulation, however, it is evident that the radiation is emitted from electron bunches moving at $V_s = 2.8 \times 10^7$ m/sec, which corresponds to a value of $n_{\parallel} = 10.7$. As a consequence, the measured power is about 50% greater when considering radiation from the faster moving bunches. Although this increase is insignificant compared to the factor of 10 difference between measured and coherent Cerenkov power values, it still should be mentioned. Recall that the Landau resonance had to be incorporated into the

measured power calculations since complete information on \bar{E} and \bar{B} of the measured whistler-mode waves was unavailable. The measured power is then considered a model dependent quantity based on values of n_{\parallel} .

As mentioned previously, all the bunches in the beam are not propagating at exactly V_s , but instead propagate in a range of velocities, $V_s \pm \Delta V$, where ΔV is the typical velocity spread. Consequently, in the moving frame, the current density is not completely independently of time as assumed in the derivation of (5-3), but has second-order temporal variations that can alter the radiative coherence of the beam. The effect of these temporal variations on the radiated power will now be considered.

Consider a current density that varies as $J_z(z') e^{-t^2/t_0^2}$, where t_0 represents the typical time of the temporal variations in the current density. The corresponding transform of this current density in space and time is written as

$$\bar{J}_q(\bar{k}, \omega) = \frac{\hat{z}}{(2\pi)^3} \sqrt{2\pi} J_z(k_z) \left[\frac{t_0}{2\sqrt{\pi}} e^{-a^2 t_0^2/4} \right] \quad (5-6)$$

where $J_z(k_z)$ is the spatial transform of the current density and $a = k_z V_s - \omega$.

If the electrostatic wave in the beam is monochromatic, the corresponding density perturbations propagate at the phase speed of

this wave. The transform of the current density is then peaked at ω/k_z values where $\omega/k_z = V_{ph} = V_s$, with no spread in ω or k_z . In this case, the current density is properly represented by (A-4). However, as Figure 29 indicates, the transform of the current density has a significant spread about $\omega/k_z = V_{ph} = V_s$. Consequently, this transform is best represented by (5-6), where the delta function in (A-4) is replaced by Gaussian function centered at $\omega/k_z = V_s$. Note as $t_0 \rightarrow \infty$, the two expressions become identical.

Following a similar analysis as that of the Appendix, the radiated power is found to be

$$P(t) = \frac{i}{(2\pi)^3 \epsilon_0} \iint (\hat{z} \cdot \vec{T}^{-1} \cdot \hat{z}) [2\pi J_z(k_z) J_z(k_z)^*] \frac{t_0}{2\sqrt{\pi}} e^{-\frac{a^2 t_0^2}{4}} e^{-\left(\frac{t^2}{t_0^2} + iat\right)} dk \frac{d\omega}{\omega} \quad (5-7)$$

The time-averaged radiated power is now calculated. This power is defined to be

$$\bar{P} = \frac{1}{2T} \int_{-T}^T P(t) dt \quad (5-8)$$

where T is the time interval over which the power is averaged. An integral of the form

$$I = \frac{1}{2T} \int_{-T}^T e^{-\left(\frac{t^2}{t_0^2} + iat\right)} dt \quad (5-9)$$

must now be solved. Expression (5-9) can be reexpressed as

$$I = \frac{e^{-a^2 t_0^2}}{2T} \int_{-T}^T e^{-\left(\frac{t}{t_0} + \frac{iat_0}{2}\right)^2} dt \quad (5-10)$$

The whistler-mode radiation detected by the PDP radio receivers at any instant in time is generated from a beam length segment, l . The typical time an electron spends in l is $\epsilon = l/V_b$. Consequently, (5-10) can be rewritten as

$$I = \frac{e^{-a^2 t_0^2}}{\epsilon} \int_0^\epsilon e^{-\left(\frac{t}{t_0} + \frac{iat_0}{2}\right)^2} dt \quad (5-11)$$

Since l is small, $\epsilon \ll t_0$ and (5-11) is near unity.

The average radiated power is then

$$\bar{P} = \frac{1}{(2\pi)^2 \epsilon_0 c^2} \int (\hat{z} \cdot \vec{T}^{-1} \cdot \hat{z}) [2\pi J_z(k_z) J_z^*(k_z)] \frac{t_0}{2\sqrt{\pi}} e^{-\frac{a^2 t_0^2}{4}} n \omega \, dn \, d\omega \, dk_z \quad (5-12)$$

where $d\bar{k} = \frac{n^2 \omega^3}{c^3} \, dn \, \sin \theta \, d\theta \, d\phi = \frac{n \omega^2}{c^2} \, dn \, dk_z \, d\phi$. Equation (5-12) can be expressed as

$$\left. \frac{d\bar{P}}{d\omega} \right|_{\omega=\omega_0} = \int F(k_z, \omega_0) \frac{t_0}{2\sqrt{\pi}} e^{-\frac{a^2 t_0^2}{4}} dk_z \quad (5-13)$$

Thus, to obtain the radiated power, a Gaussian weighted integration of $F(k_z, \omega_0)$ over dk_z must be performed. Using (A-10), a similar expression can be written when $J_z(k_z, \omega)$ has no spread about $\omega/k_{\parallel} = V_s$:

$$\begin{aligned} \left. \frac{dP}{d\omega} \right|_{\omega=\omega_0} &= \int F(k_z, \omega_0) \delta(k_z V_s - \omega_0) e^{i(k_z V_s - \omega_0)t} dk_z \\ &= \left. \frac{F(k_{z0}, \omega_0)}{V_s} \right|_{k_{z0} = \frac{\omega_0}{V_s}} \end{aligned} \quad (5-14)$$

Expression (5-13) and (5-14) should yield similar results as long as $F(k_z, \omega_0)$ approximates $F(k_{z0}, \omega_0)$ in dk_z . A numerical integration of (5-13) was performed and this result was indeed found to be true. The radiated power varied only slightly when considering a spread in $J_z(k_z, \omega)$ equal to k_{z0} . The deviations of the radiated power due to such a spread are shown in Table 3. In this table, the power from a Gaussian-like $J_z(k_z, \omega)$ distribution with a spread, Δk_z , equal to k_{z0} is calculated using (5-13) and compared to the power expected using (5-14). From these results it is evident that the radiated power does not vary significantly when considering a spread in $J_z(k_z, \omega)$ about $\omega/k_z = V_s$. Consequently, the radiated power calculated using (5-3) is an accurate representation of the radiated power from the modeled beam.

Table 3. The Change in Radiated Power From Considering a Current Density With a Spread, Δk .

Frequency	$\frac{dP}{d\omega}(\Delta k_z = k_{z0}) / \frac{dP}{d\omega}(\Delta k_z \rightarrow 0)$
562 kHz	.930
311 kHz	.887
178 kHz	.924
100 kHz	.942
56.7 kHz	.979
31.1 kHz	1.031

CHAPTER VI
THE ELECTRON BEAM AS AN EFFICIENT ANTENNA

In this study, it has been concluded that the whistler-mode emission detection from the SL-2 electron beam is created by coherent Cerenkov radiation from electron bunches in the beam. Consequently, the electron beam is considered an antenna radiating the whistler-mode radiation. As will be shown, by positioning the radiating bunches properly in the beam, the radiation efficiency of this "antenna" can be improved. Consider, first, the bunches formed in the continuous SL-2 electron beam. From Figure 22 it is evident that these bunches have a length, $l = .1-.5$ meters and have a spacing, $d \cong 6$ meters, apart from each other. This bunching of the modeled beam is clearly evident in Figure 30 which displays $J_z(k_z)$ versus k_z . In this figure the maximum $J_z(k_z)$ value is near $k_z \cong 2\pi/d \cong 1$ corresponding to the typical bunch spacing. Note that this maximum value lies outside the range of k_z' of the whistler-mode radiation. More power in the whistler-mode would have been obtained from the beam if this maximum $J_z(k_z)$ value had been in the k_z' range. In this case, the spacing between the bunches would then be equal to the parallel component of a whistler-mode wavelength, $d = \lambda_{\parallel}$; and the coherent radiation from the bunches in the beam at $f = v_s/\lambda_{\parallel}$ would constructively interfere. This

process would significantly increase the wave powers above those measured from the SL-2 electron beam to near 10^{-6} W/Hz at $f = V_b/\lambda_{\parallel}$.

This effect can be artificially induced by pulsing the electron beam near the whistler-mode range of frequencies. Unlike the continuous beam, a beam-plasma instability is now undesirable, since it tends to destroy the highly coherent pulses ejected from the gun. Consequently, to reduce the effects of the instability, the length of the pulses, ℓ , should be $\ell \ll V_b/f_{pe}$, where V_b/f_{pe} represents the characteristic length over which the instability acts and is the wavelength of the instability-related electrostatic wave. Also, the spacing between the pulses, d , should be equal to a parallel component a whistler-mode wavelength, λ_{\parallel} . If these two conditions are met, the radiated power at $f = V_b/d$ will be quite intense. As an example, consider a 1 keV - 50 mA electron beam in the same plasma environment as the continuous SL-2 electron beam, however, pulsed such that

$$J_z(z) = \sum_{n=0}^p NqV \delta(n \text{ 31.4 meters})$$

where p is the number of pulses in a 200-meter segment (equal to 6). In this idealized example, the individual pulses have an infinitesimally small length, ℓ , and are spaced 31.4 meters apart from each other. For a 1 keV -50 mA electron beam, $V = 1.89 \times 10^7$ m/sec and $N = 4.9 \times 10^{11}$ electrons. The value of k_z corresponding to the pulse spacing, d , is $k_z = .2$. The Fourier transform of $J_z(z)$ is

$$J_z(k_z) = \sum_{n=0}^p \frac{NqV}{\sqrt{2\pi}} \int_{-\infty}^{\infty} \delta(n - 31.4) e^{ik_z z} dz = \sum_{n=0}^p \frac{NqV}{\sqrt{2\pi}} e^{in 31.4 k_z} .$$

Note that at $k_z = .2$, $J_z(k_z)$ is a maximum since the exponential term, representing the relative phase difference between the pulses, goes to unity. Consequently,

$$J_z(k_z = .2) = \frac{6NqV}{\sqrt{2\pi}} = 3.56 .$$

From the Landau resonance condition, this value of k_z corresponds to a frequency of 600 kHz. The radiated power is then a maximum at this frequency and is calculated to be $\sim 3 \times 10^{-4}$ W/Hz from a 200-meter pulsed beam segment. Note that this power is over 10^5 greater than those measured by the PDP. Consequently, the constructive interference amongst the pulses increases the radiated powers drastically.

CHAPTER VII

CONCLUSIONS

The whistler-mode radiation detected by the PDP during its flyby of a 1 keV - 50 mA electron beam has these characteristics:

A) The radiation is propagating near the resonance as determined by the electric field polarization.

B) About 1.6 mW of the radiation is emitted from the first 200 meters of the beam, corresponding to about 8×10^{-6} W/m of emitted radiation from the beam.

C) The calculated wave powers from the beam are well above those expected from incoherent Cerenkov radiation processes in the beam.

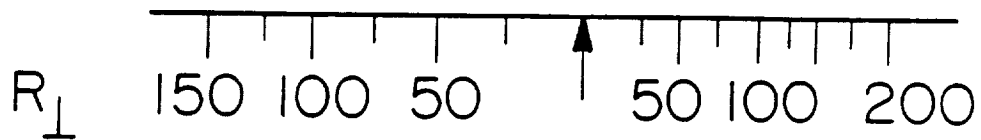
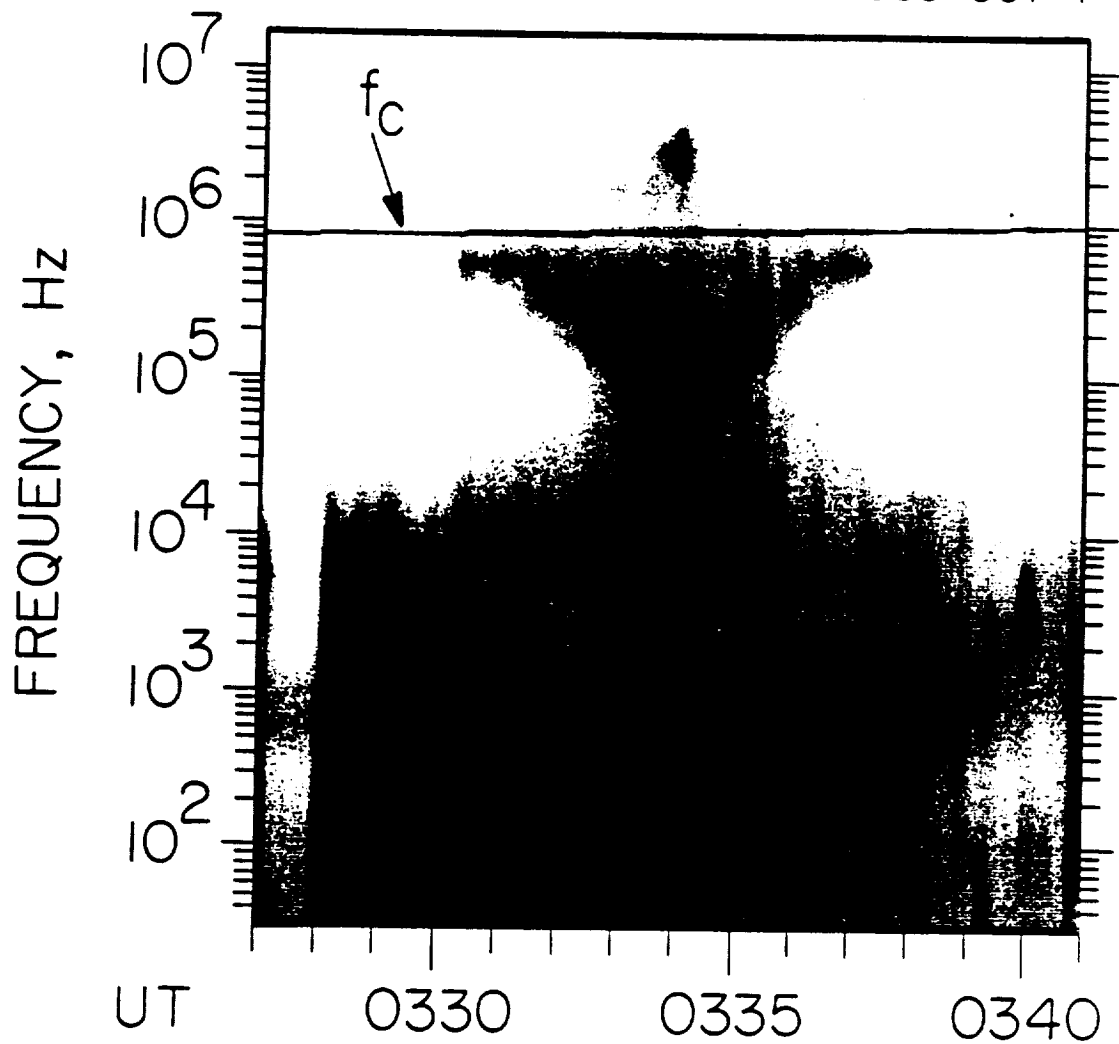
Many mechanisms have been discussed to account for the detected signal; however, the best mechanism is coherent Cerenkov radiation from density perturbations or bunches in the beam. These bunches are created by an electrostatic beam-plasma instability occurring within the beam.

The existence of these bunches is verified in two ways: first, when the PDP was in the beam, radio receivers detected very intense waves near ω_{pe} . These waves are believed to be associated with the instability creating the bunches. Second, a one-dimensional computer simulation of the beam clearly shows the presence of electron bunches in the beam.

The calculated power from the simulated beam indicates that the radiation from electrons in bunches is coherent enough to account for the measured whistler-mode power. Consequently, from this study it is concluded that the whistler-mode radiation from the SL-2 electron beam is generated by coherent Cerenkov radiation from a bunched electron beam.

Figure 1 A frequency vs. time spectrogram from the PDP plasma wave instrument showing intense emissions during a D.C. electron gun firing. The funnel-shaped structure that extends from the electron cyclotron frequency, f_c , to about 30 kHz is whistler-mode radiation from the beam.

A-G85-807-1



PDP, DAY 213, AUG. 1, 1985

Figure 2 This diagram shows the index of refraction surface for the whistler mode and the associated \bar{E} , \bar{k} , and \bar{v}_g vectors for propagation near the resonance cone ($\theta \approx \theta_{Res}$). For propagation near the resonance cone, \bar{k} and \bar{E} are parallel and nearly perpendicular to \bar{v}_g . In this limit \bar{E} is linearly polarized and quasi-electrostatic.

B - 686 - 581 - 1

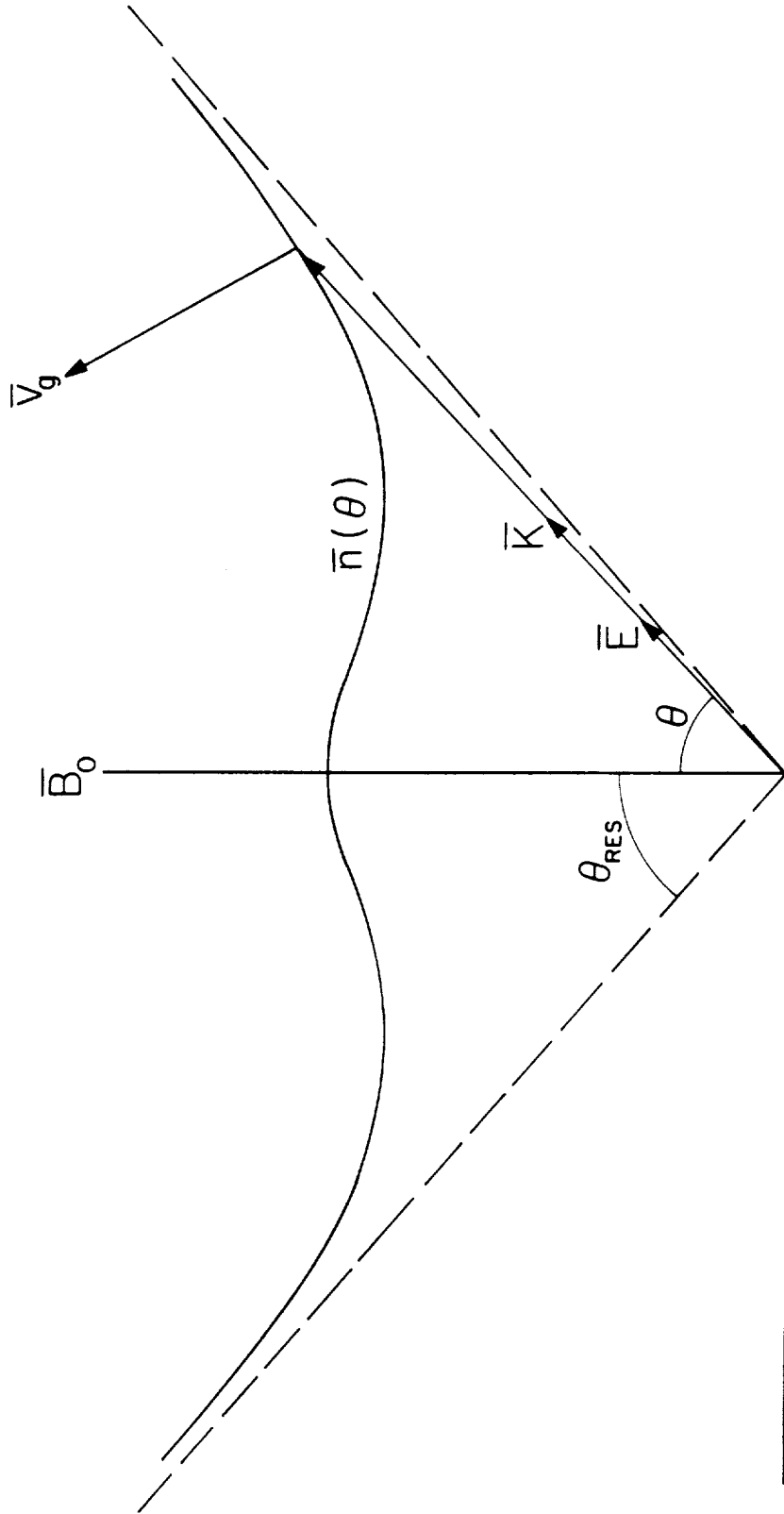


Figure 3 This diagram shows the ray path and \bar{E} , \bar{k} , and \bar{v}_g vectors used to confirm the electric field polarization. The assumed electric field is projected into the PDP spin plane and the angle relative to the projection of the sun vector is calculated. The projected electric field direction can then be compared to the measured directions calculated from spin modulation maximums in the electric field intensity (see Figure 4).

B-G86-582-1

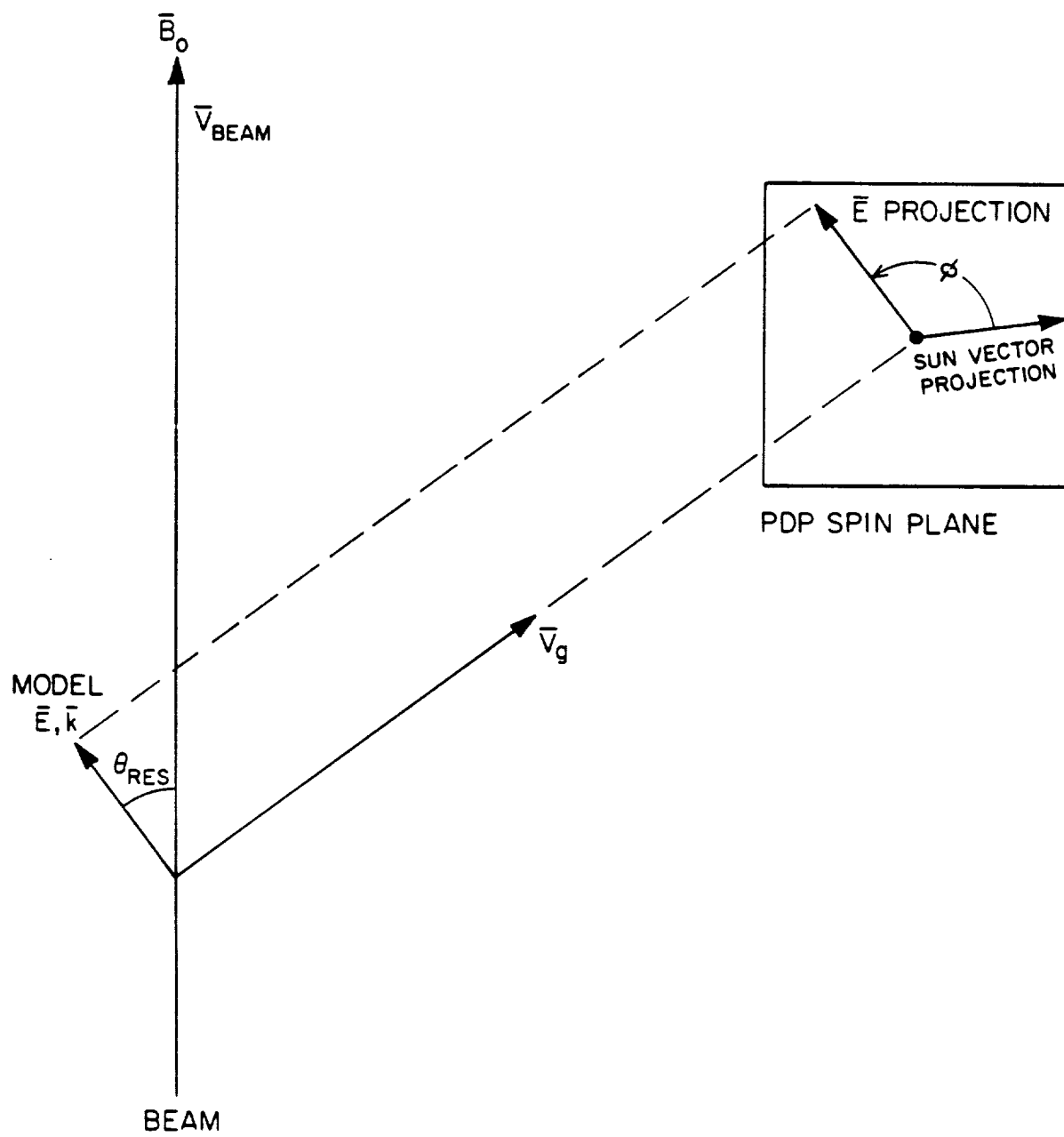


Figure 4(a), (b), (c), and (d) These plots show the relative directions of the computed and measured electric-field vectors in the PDP spin plane for the 562 kHz, 311 kHz, 178 kHz, and 100 kHz frequency channels. The dots represent the computed electric field directions assuming that the wave vector is near the resonance cone with $\bar{k} \cdot \bar{v}_b > 0$, and the x's represent measured electric-field directions. The close agreement between the measured and modeled directions indicates that the whistler-mode radiation is propagating near the resonance cone in the same direction as the beam.

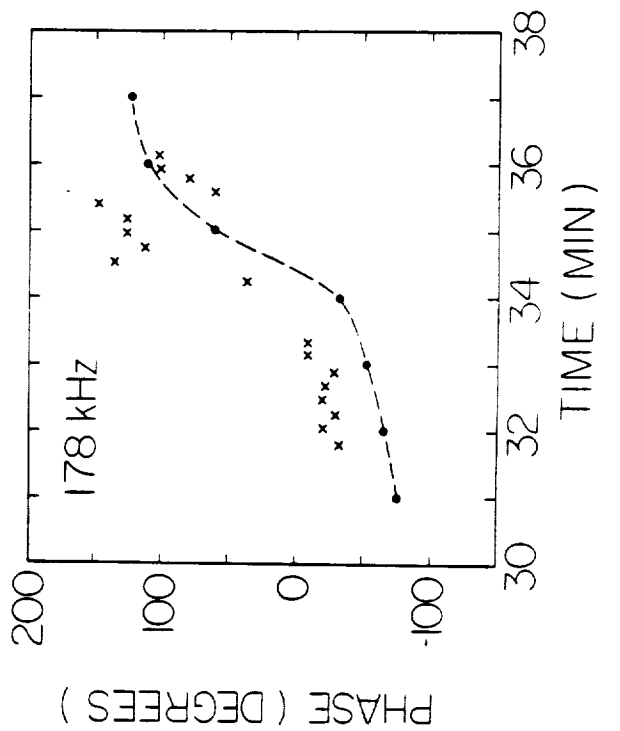
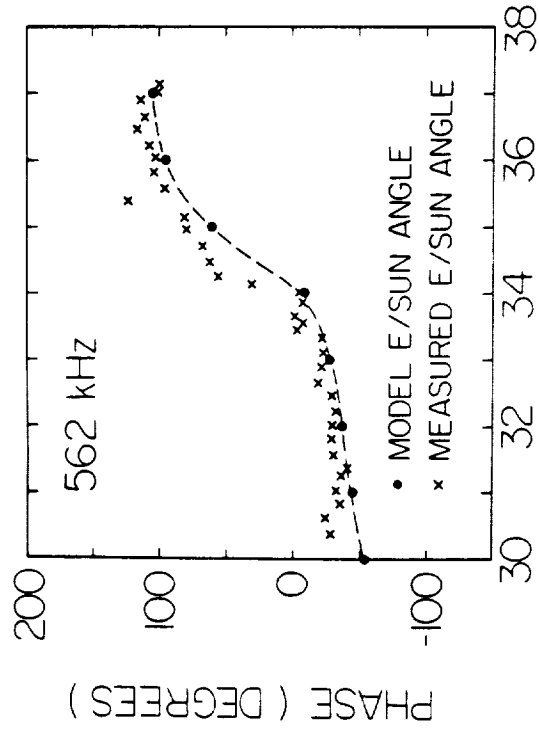
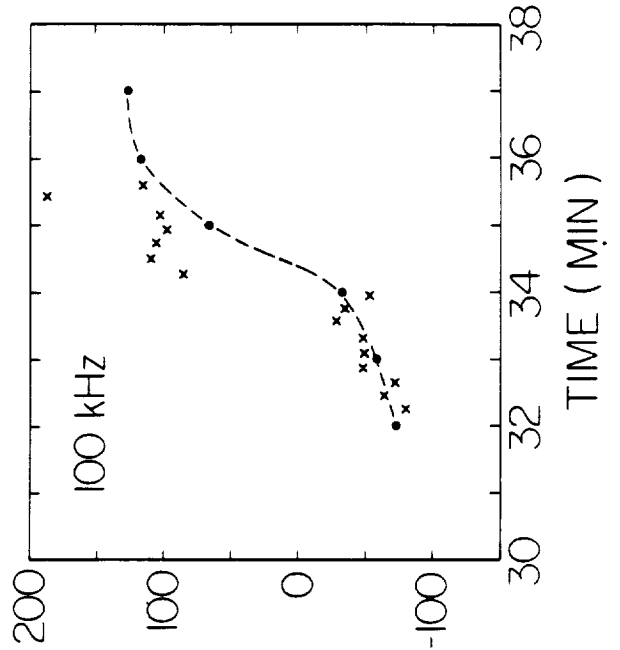
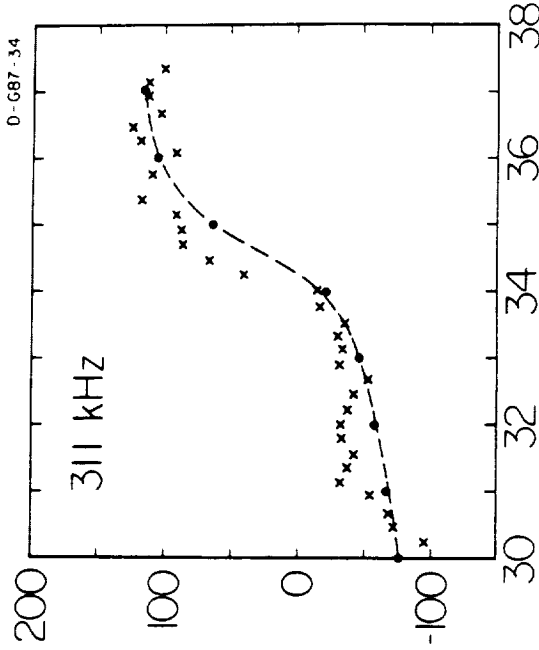


Figure 5 This diagram shows the integration surface used to calculate the power emitted from the beam in the whistler mode. At closest approach, the PDP passed within 3 meters of the beam at a distance of about 200 meters from the shuttle.

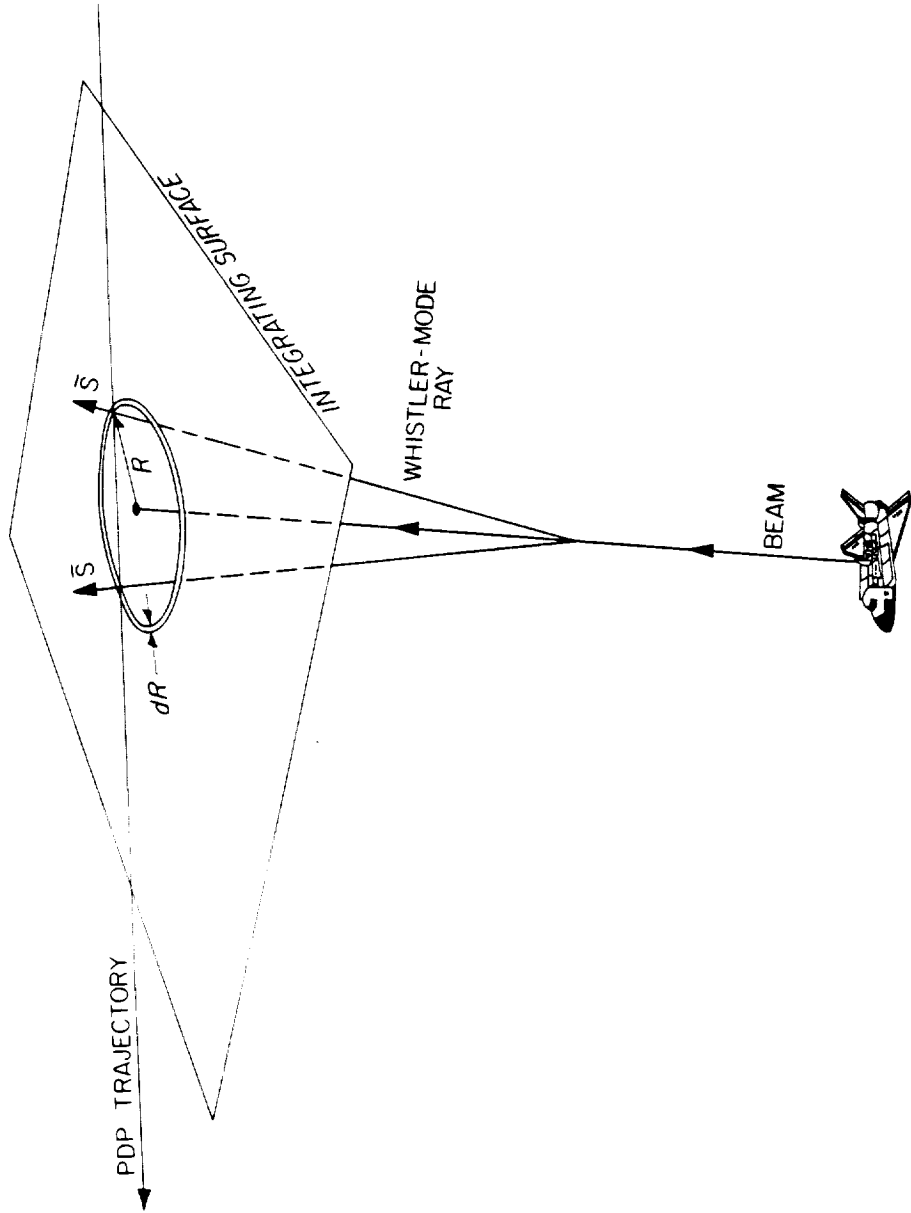


Figure 6 The calculated power spectral density from the beam in the whistler mode is shown as a function of frequency.

A-G86-219

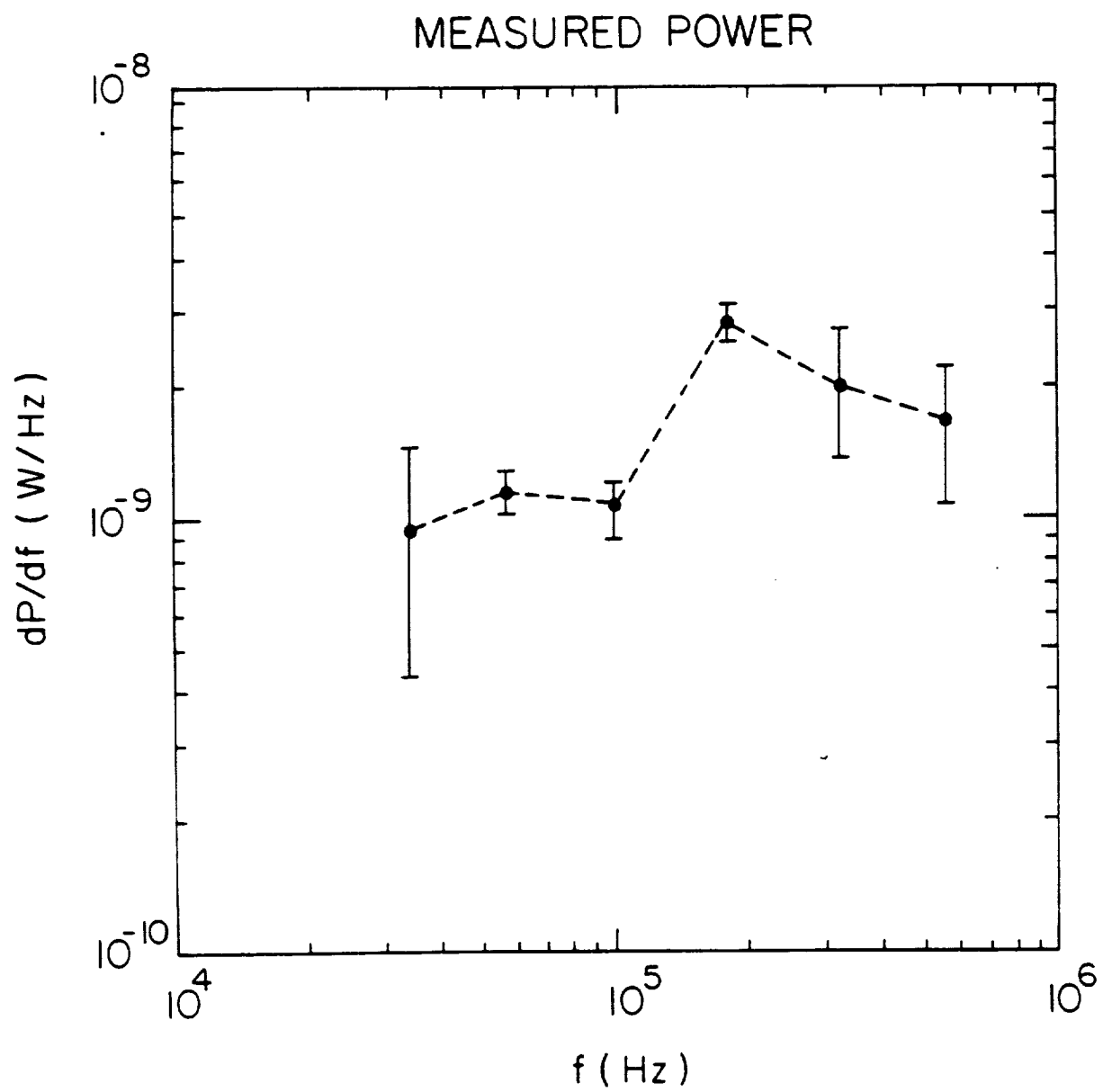


Figure 7(a) and (b) The linear emissivity, $dP/dfdl$, is shown as a function of the distance, L , along the beam for the 562 kHz and 311 kHz frequency channels. Note that the emissivity starts to decrease rapidly beyond about 100 meters.

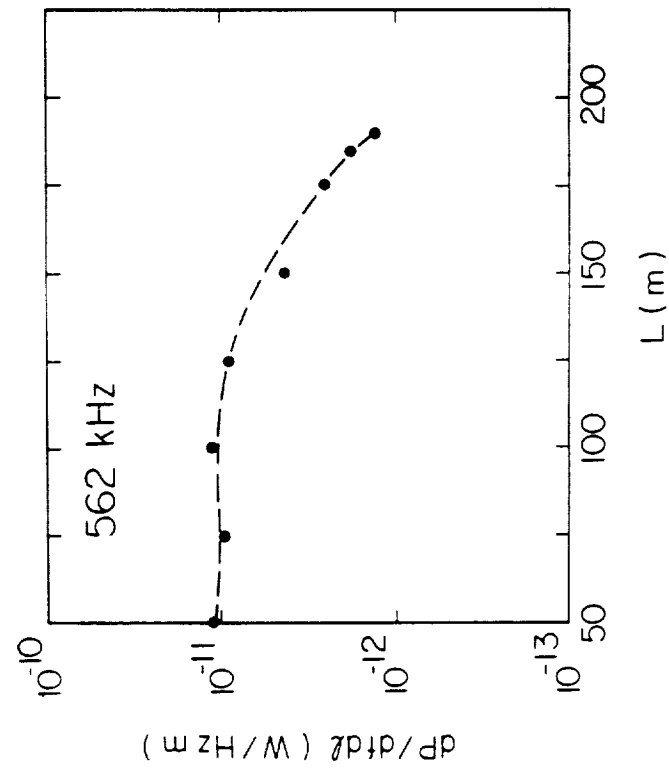
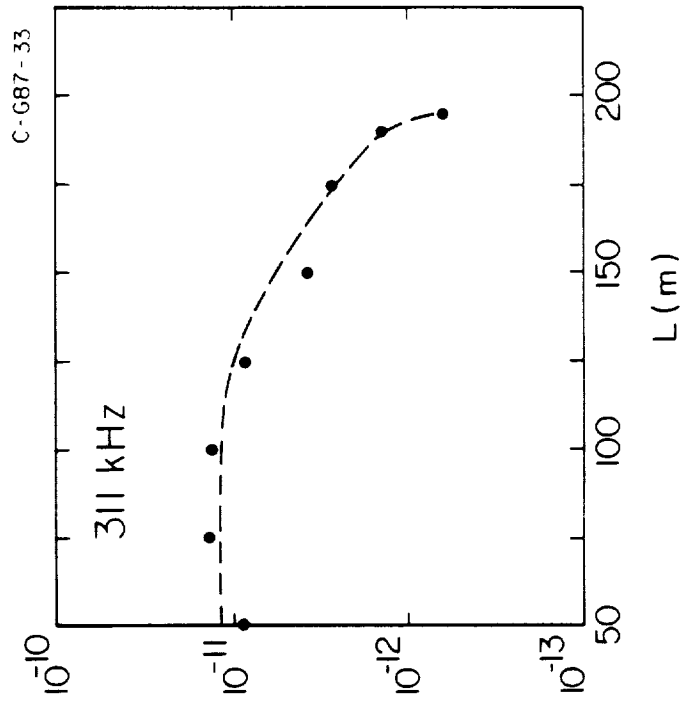


Figure 8 The power spectra from a single electron radiating via the Cerenkov processes is shown in a plasma environment similar to that surrounding the SL-2 beam. These calculations assume the wave/beam interaction is by a Landau resonance process and that the particle pitch angle is 10° . This power calculation is based on formulas derived by Mansfield [1967].

C-G86-450-1

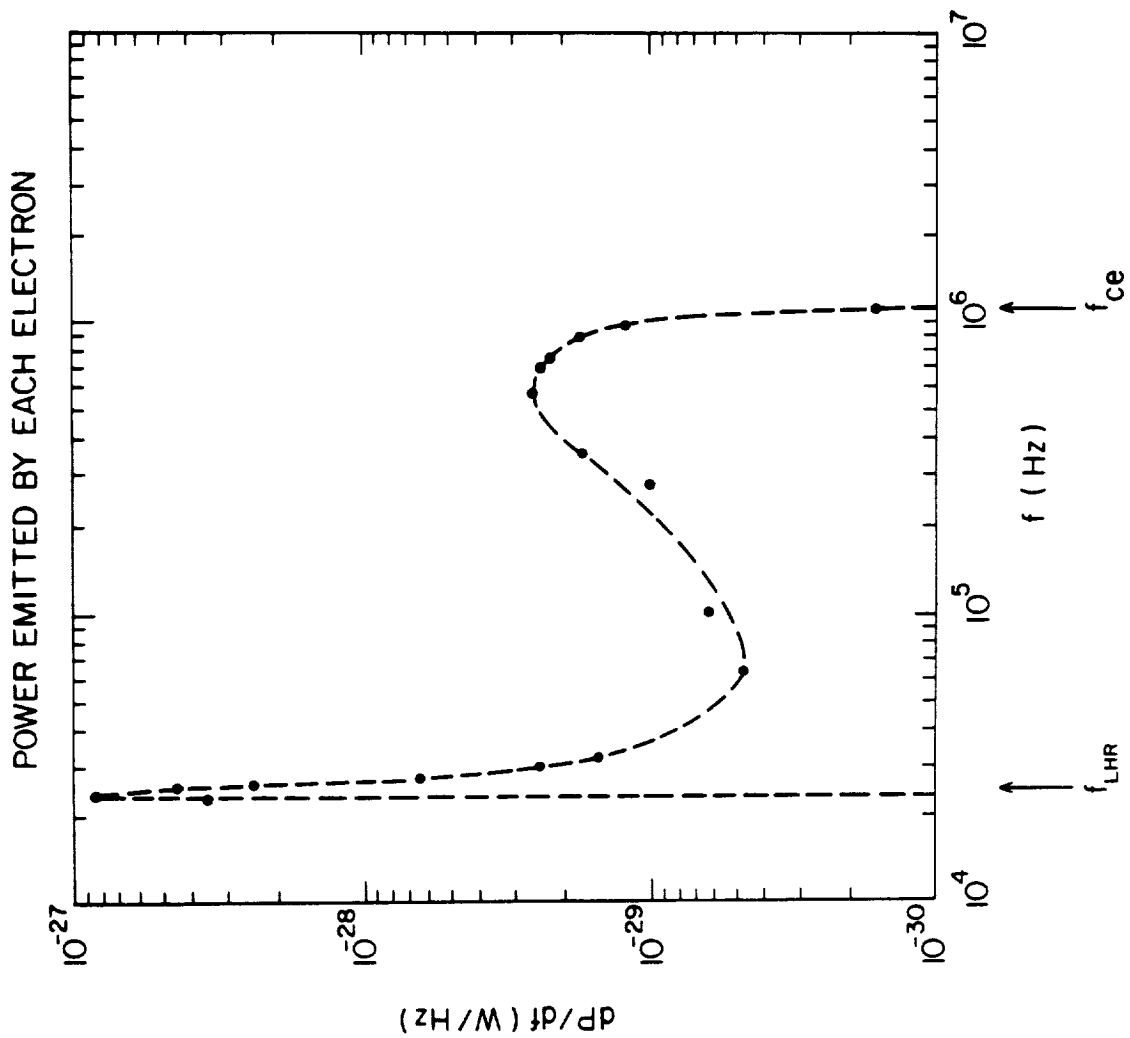


Figure 9 This figure displays the radial expansion of a field-aligned electron beam after it is initially ejected from a gun of radius r_0 . As the beam propagates, the radius expands according to

$$r = r_0 + \frac{v_{\perp \text{exp}}}{v_b} z.$$

B-G87-143

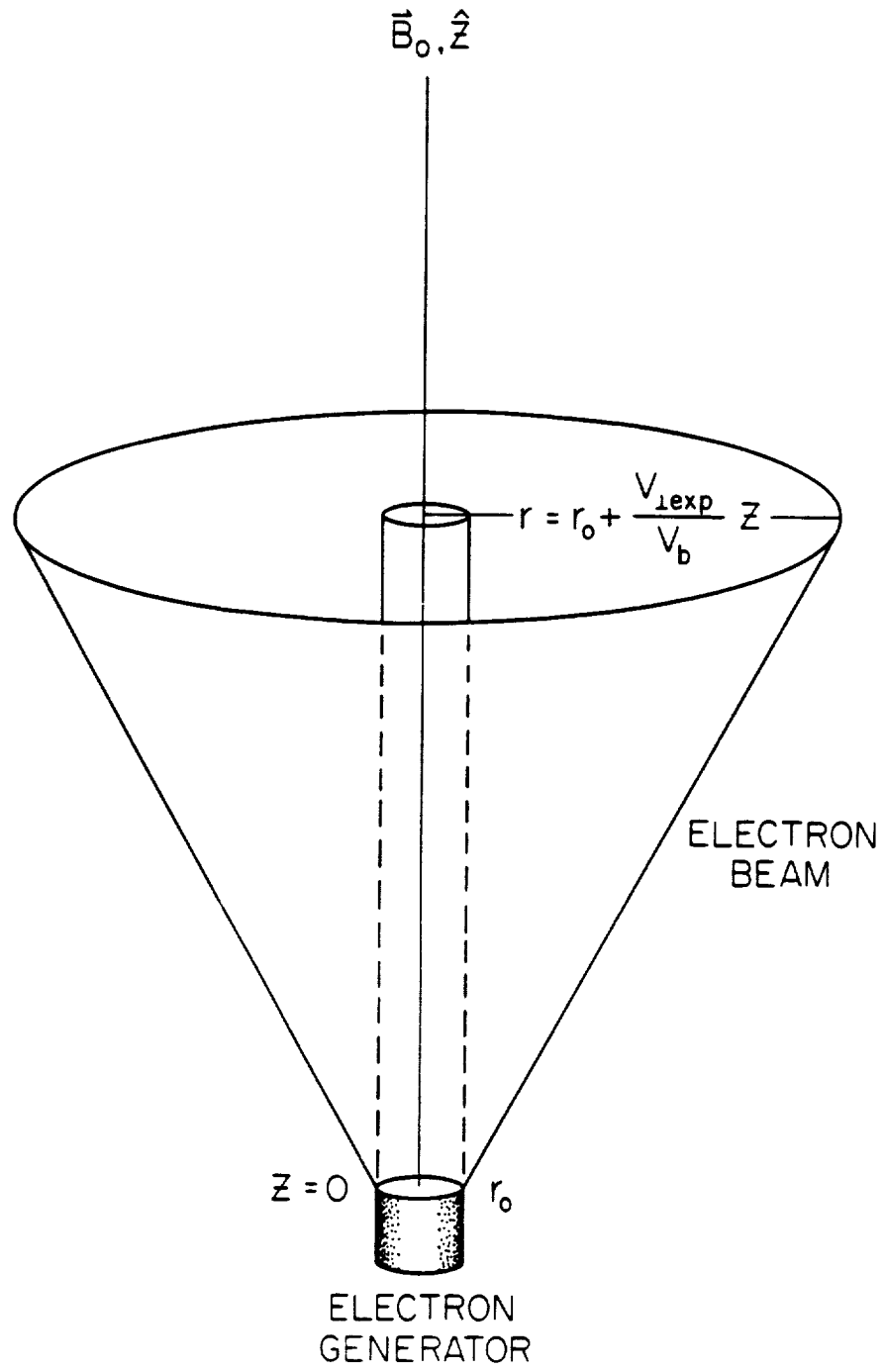


Figure 10 This figure is a V_z versus z phase-space configuration of electrons from a beam of density $n_b = 1/16 n_A$ and $V_b = 10 V_{th}$ after (a) $32 \omega_{pe}^{-1}$ and (b) $64 \omega_{pe}^{-1}$. This configuration is obtained from Pritchett and Winglee's two-dimensional simulation [1986]. The beam is injected from a spacecraft located at $z = 125$.

A - 687 - 149 - 1

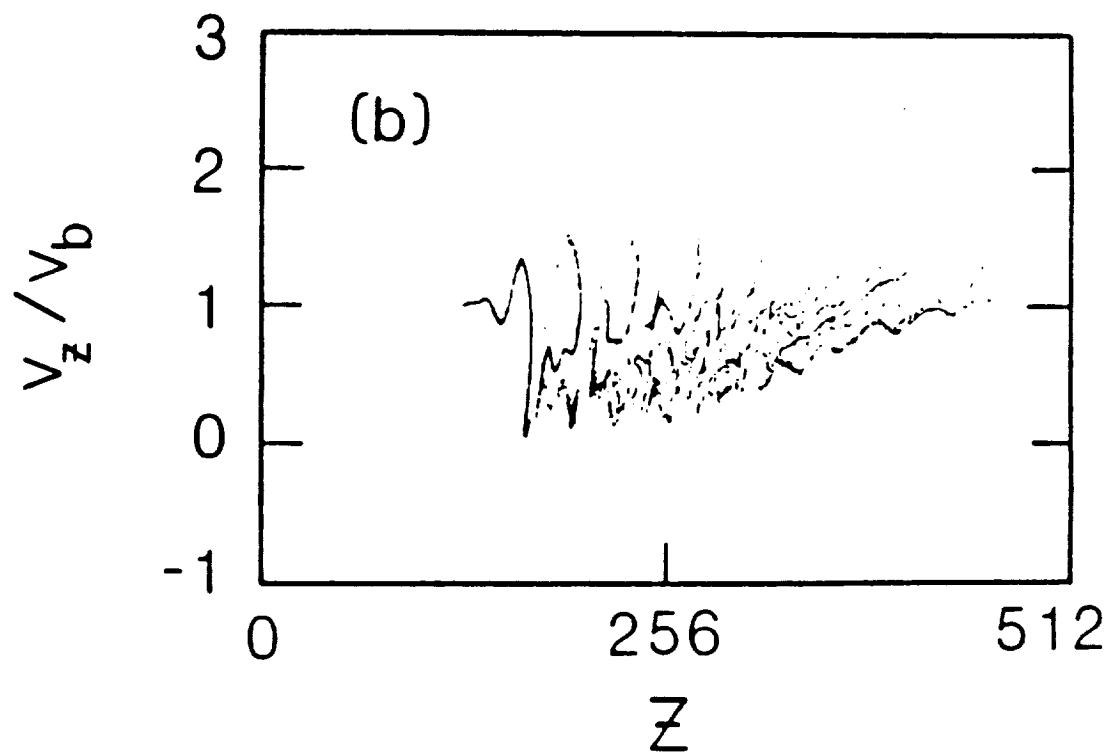
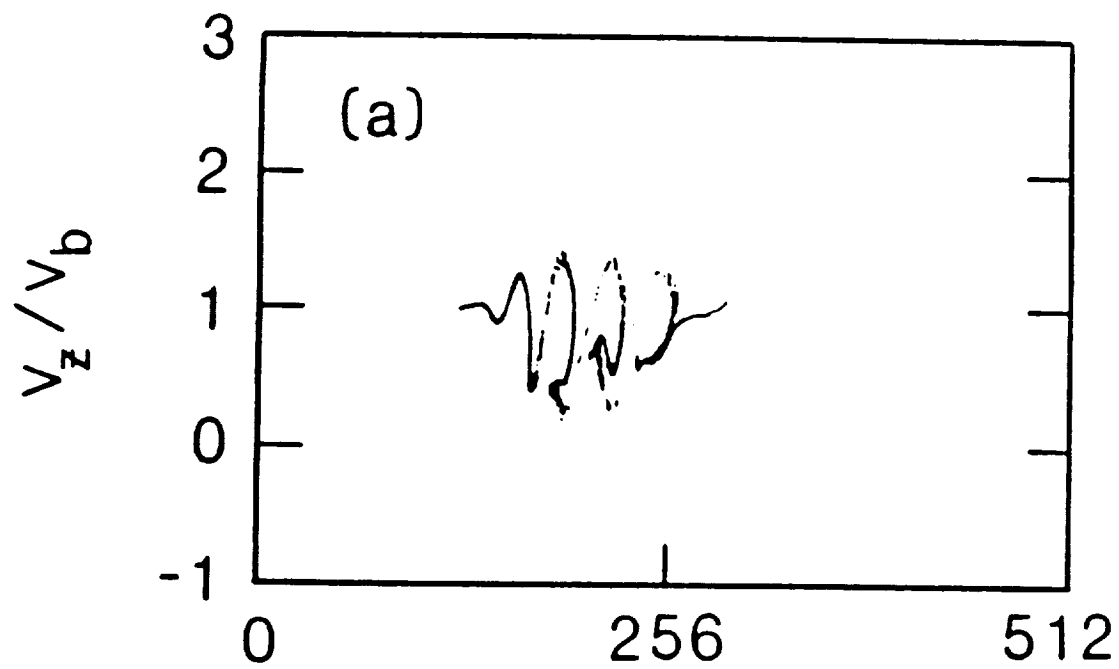


Figure 11 This figure is a V_z versus z phase-space configuration of an electron beam with similar density and velocity as that of Figure 10 taken from the one-dimensional simulation developed in this study. Note that $L = 100$.

A-G87-124

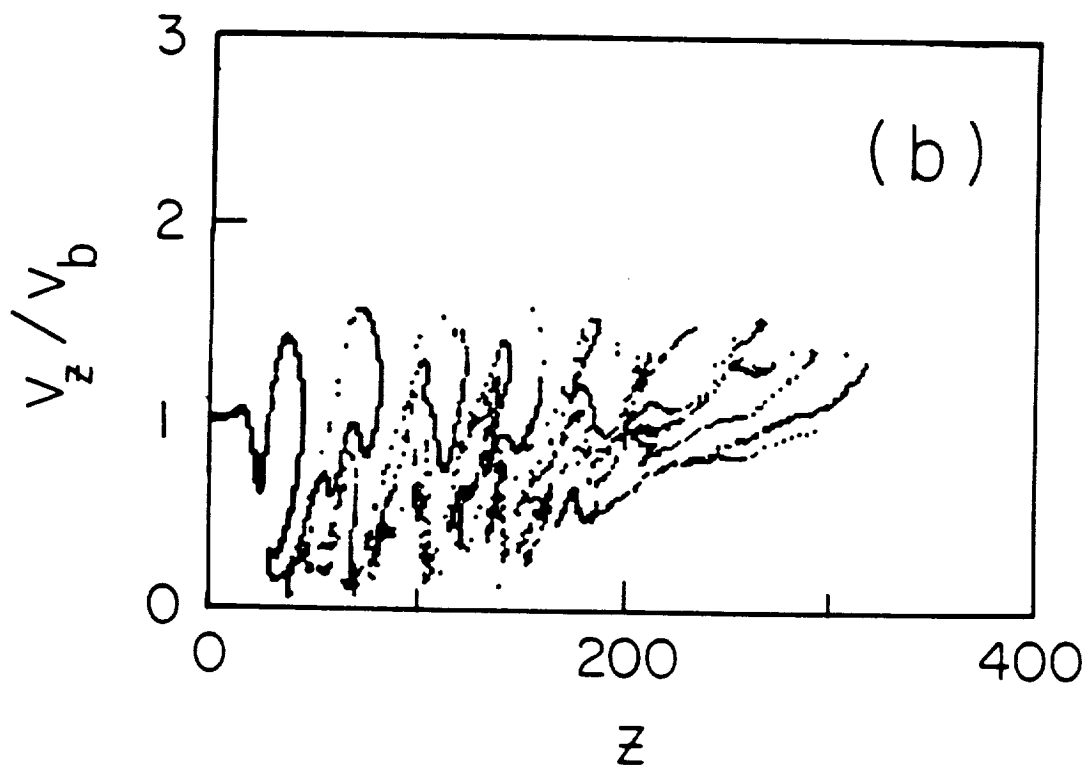
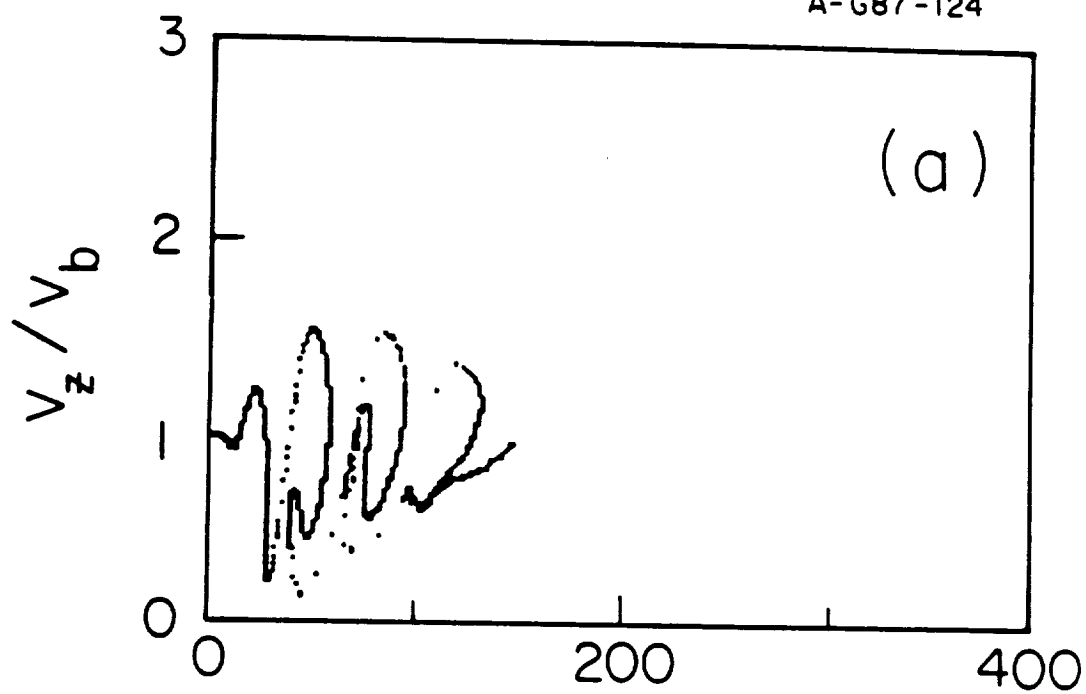


Figure 12 Again, a beam phase-space configuration is shown from the one-dimensional simulation developed in this study run with similar parameter as those of Figures 10 and 11, only now $L = \infty$ (no radial beam expansion).

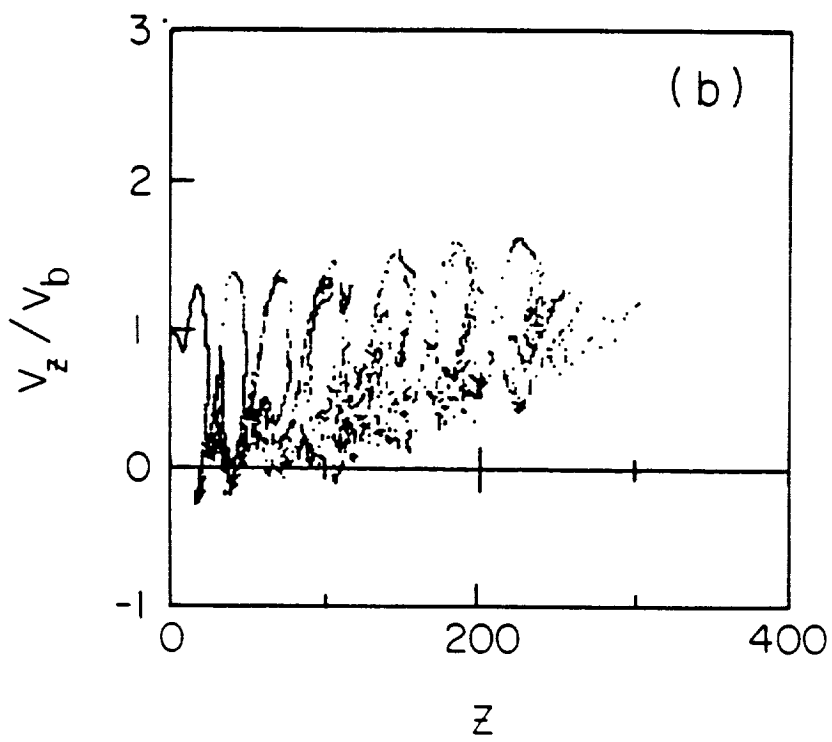
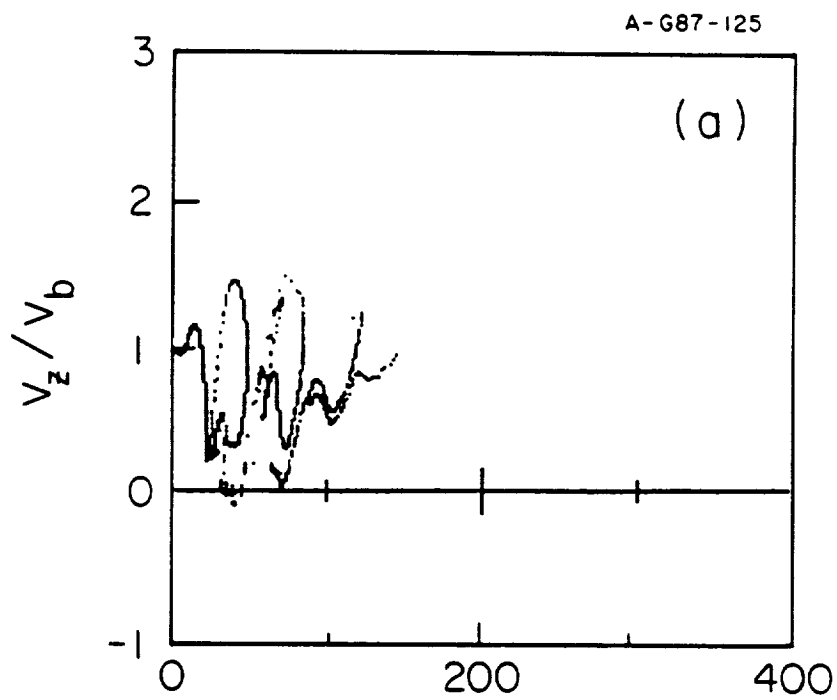


Figure 13 This V_z versus z beam phase-space configuration is from the one-dimensional simulation run with $n_b = 8 n_A$, $V_b = 15 V_{TH}$ and $L = 10$ for two different times: (a) $20 \omega_{pe}^{-1}$ and (b) $30 \omega_{pe}^{-1}$.

A-G87-121

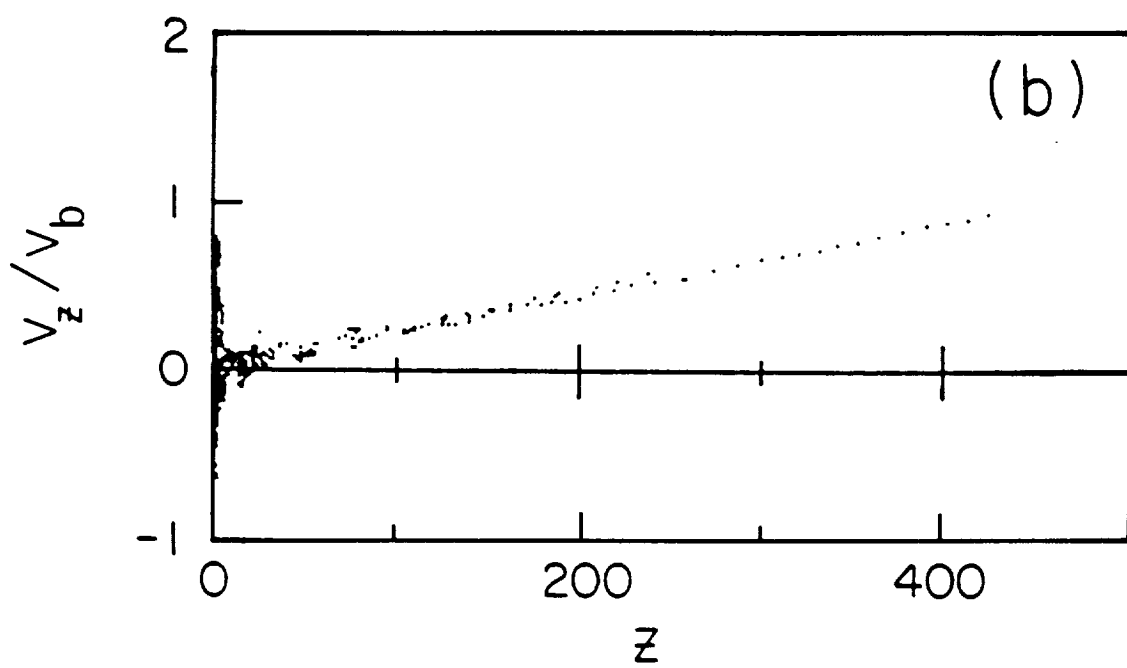
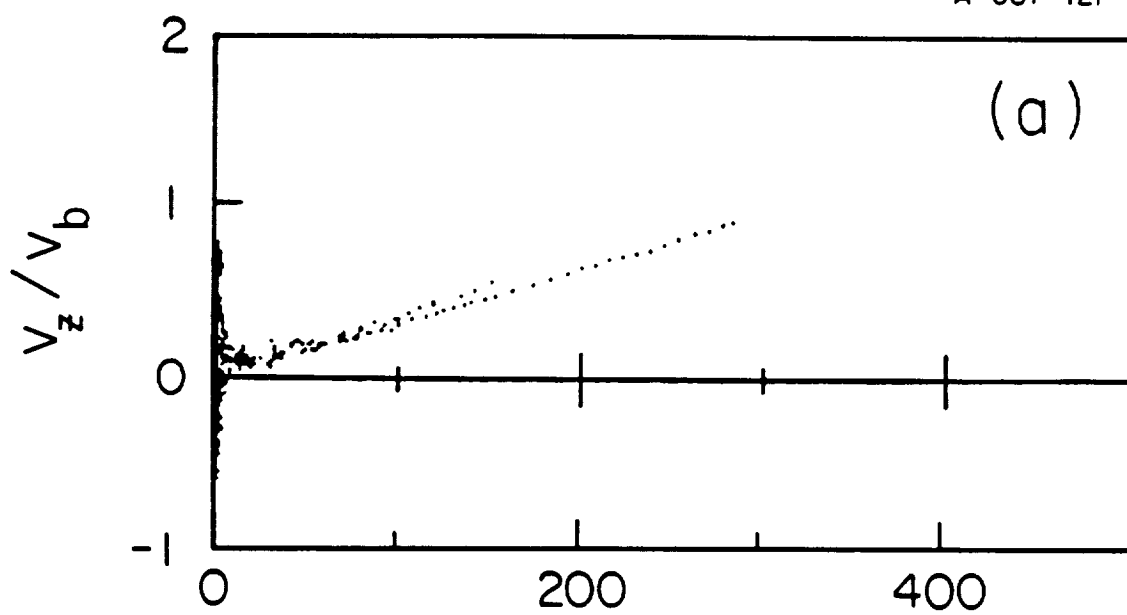


Figure 14 This figure is a beam phase-space configuration taken from Winglee and Pritchett [1986] for an overdense beam ($n_D/n_A = 2$). Note that the beam structure looks similar to that of Figure 13.

A-G87-150

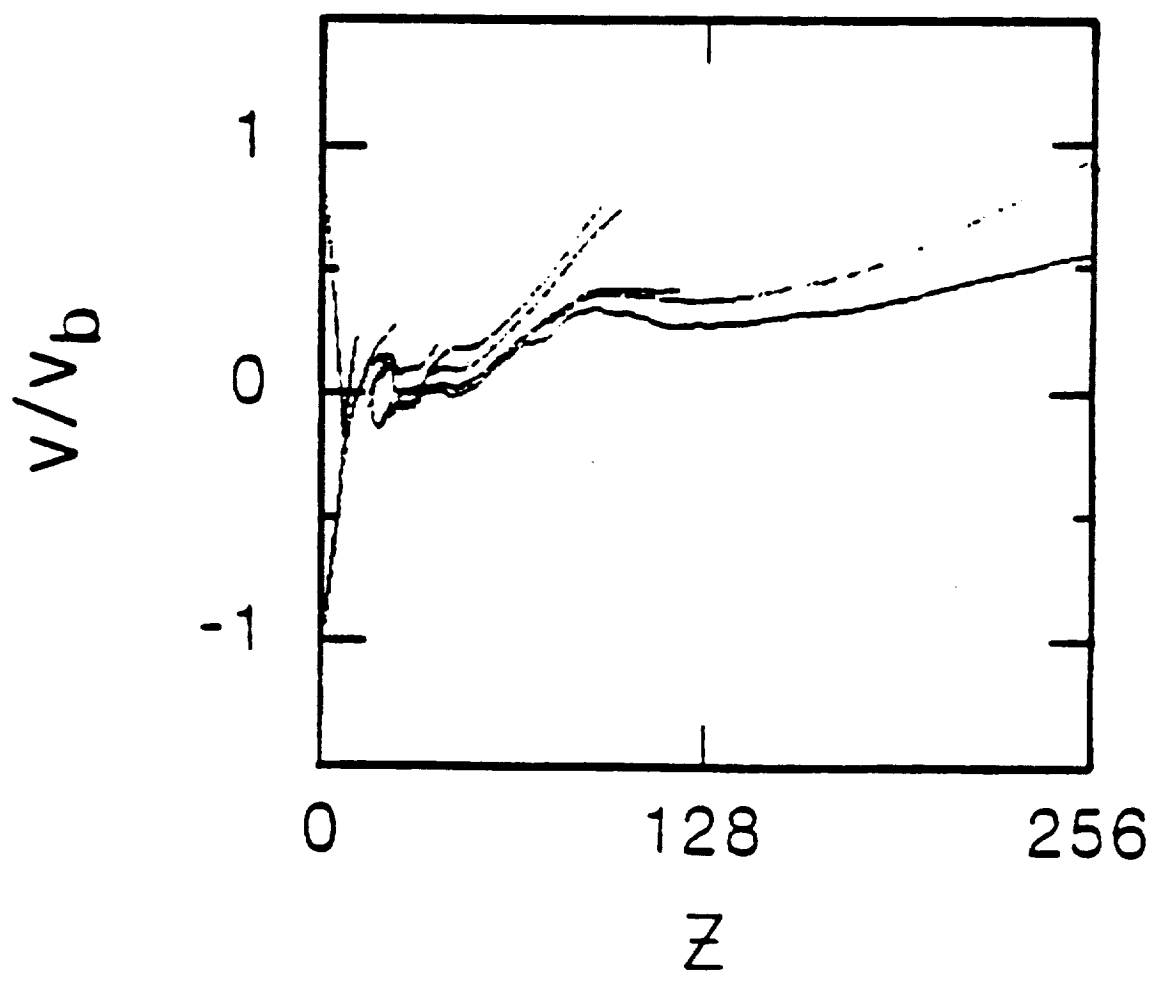


Figure 15 This figure is a beam phase-space configuration taken from Pritchett and Winglee [1986] for an overdense beam ($n_b = 8 n_A$) at two different times: (a) $16 \omega_{pb}^{-1}$ and (b) $32 \omega_{pb}^{-1}$.

A-G87-151-1

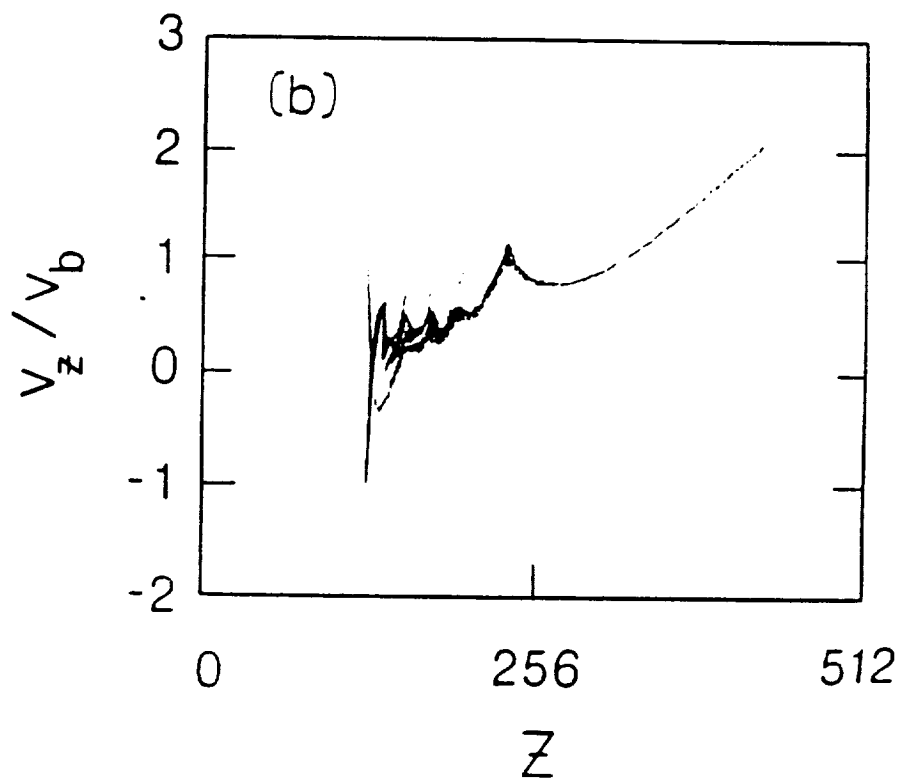
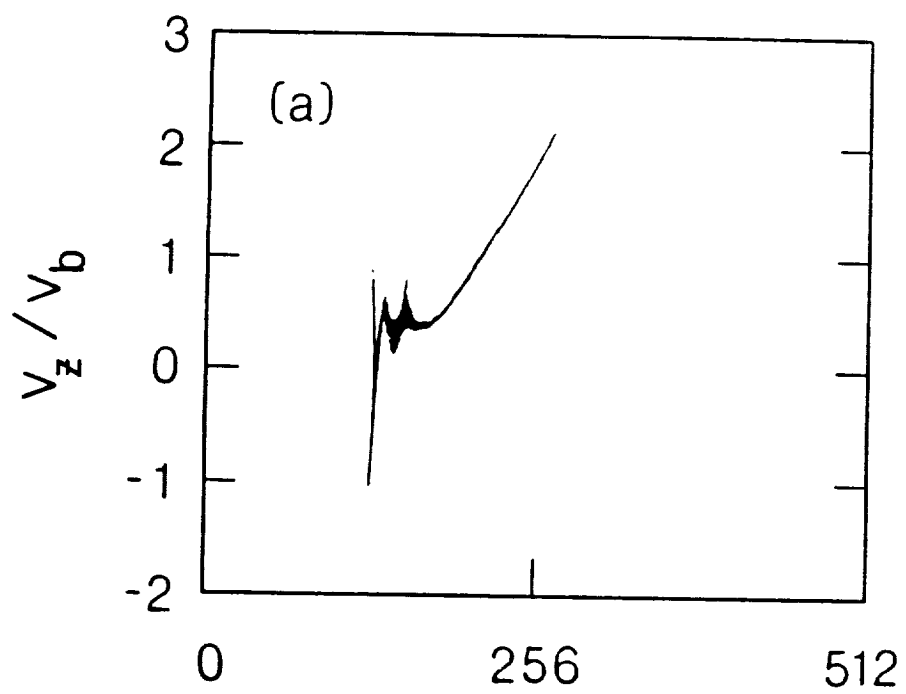


Figure 16 This figure is a V_z versus z phase-space configuration of the modeled SL-2 electron beam obtained from the one-dimensional simulation run with the parameters shown in Table 1, with $L = 10$.

BEAM PARTICLES AT $t = 270 \omega_{pe}^{-1}$

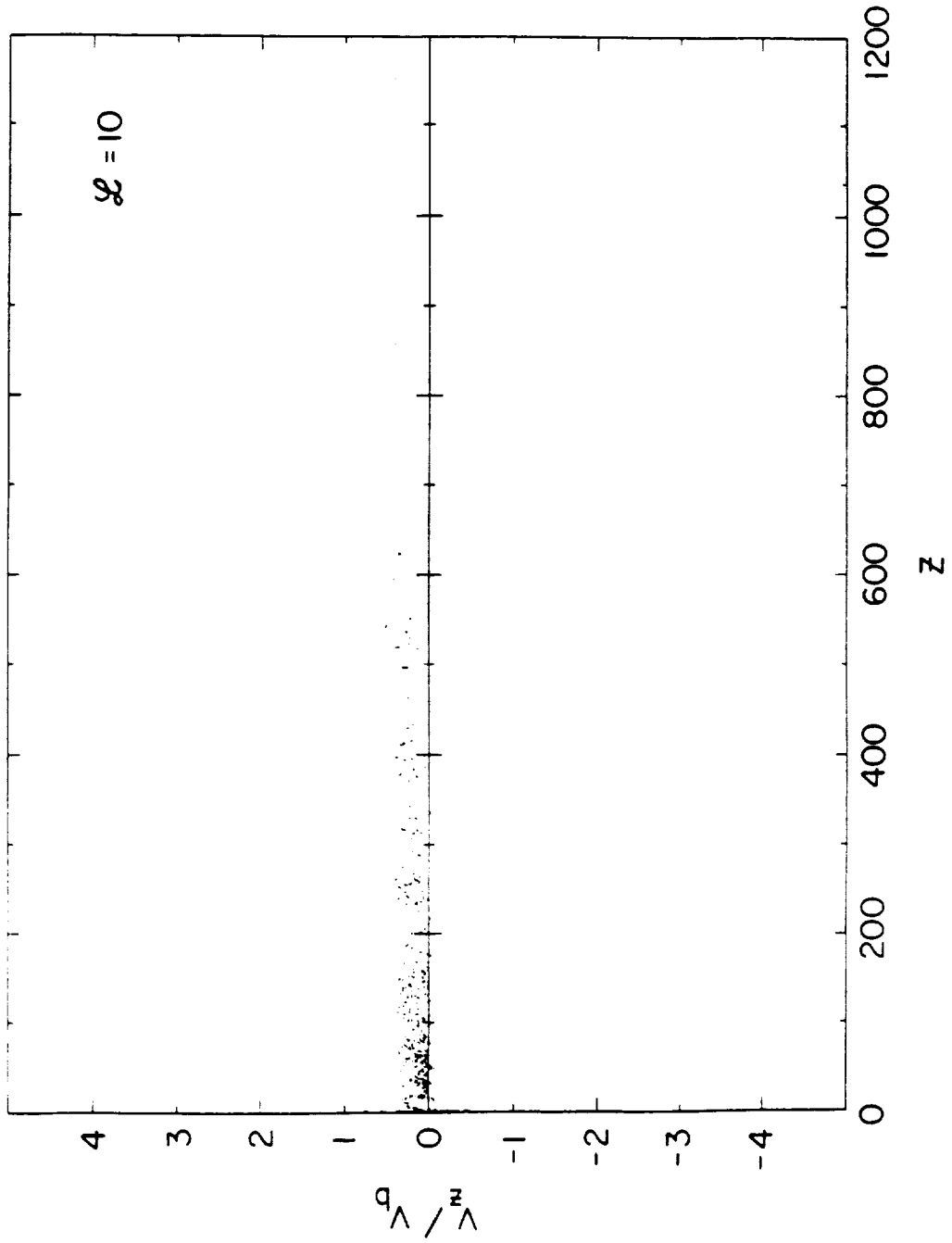


Figure 17 This figure displays E_z versus z from the one-dimensional simulation run with $L = 10$. Note that a strong electric field is located near $z = 0$.

A-687-137

E - FIELD MAGNITUDE AT $t = 270 \omega_{pe}^{-1}$

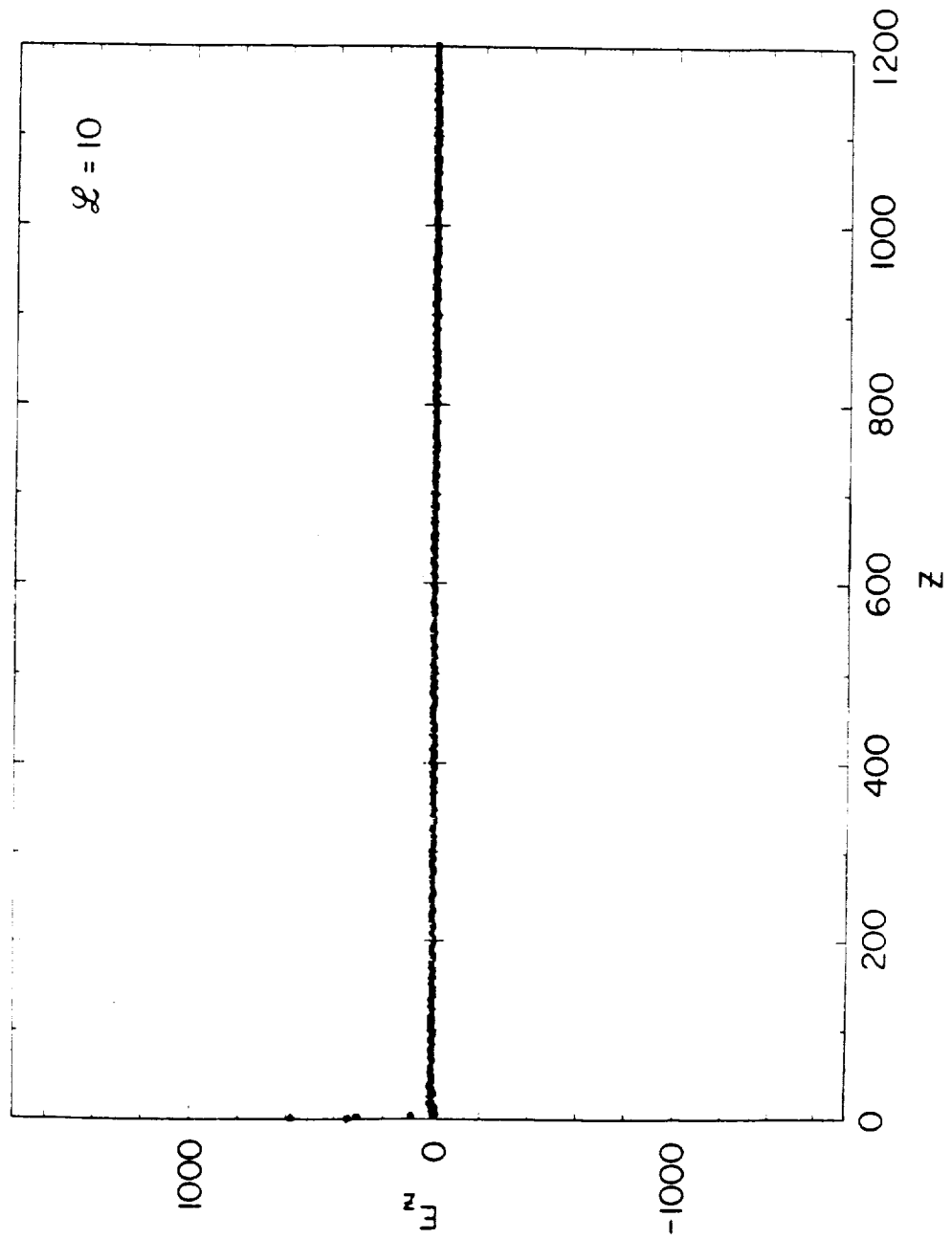


Figure 18 This figure displays the number of electrons, N , versus z from the modeled beam run with $L = 10$.

A - G87 - 138

BEAM ELECTRONS AT $t = 270 \omega_{pe}^{-1}$

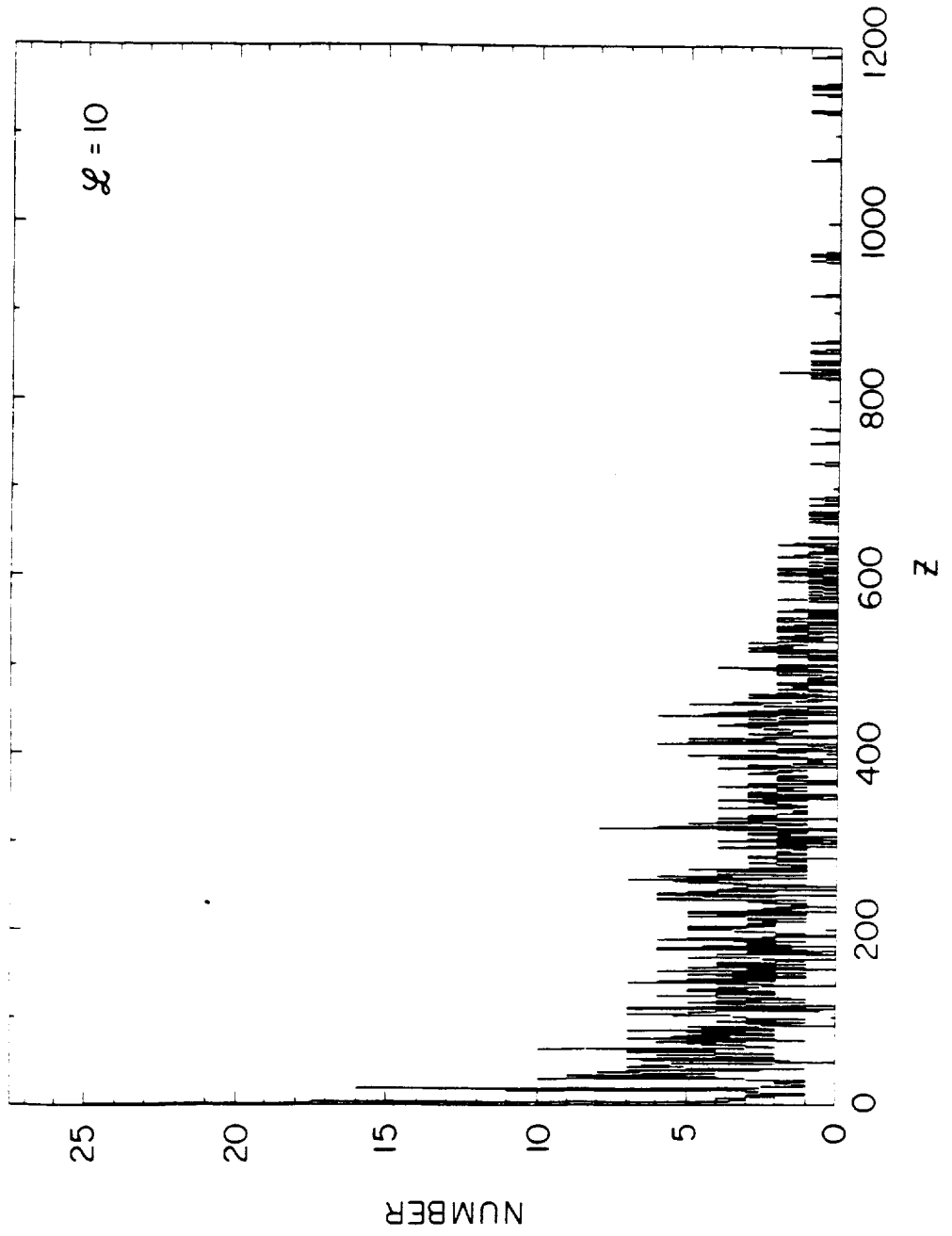


Figure 19 This figure is a V_z versus z phase-space configuration of the modeled SL-2 electron beam obtained from the one-dimensional simulation run with the parameters shown in Table 1, with $L = 5$.

A-G87-133-3

BEAM PARTICLES AT $t = 270 \omega_{pe}^{-1}$

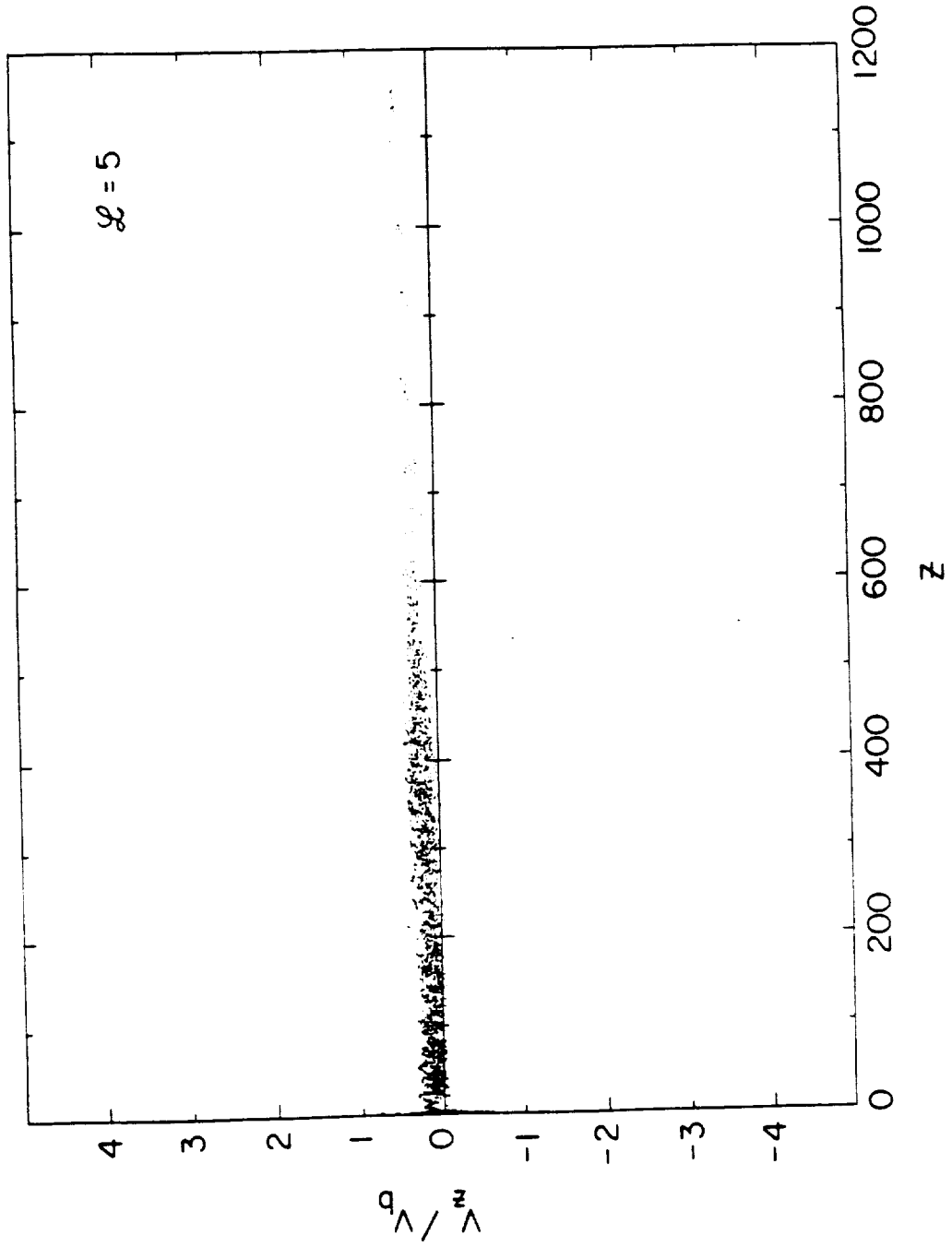


Figure 20 This figure displays E_z versus z from the one-dimensional simulation run with $L = 5$. Note that a strong electric field is located near $z = 0$.

E - FIELD MAGNITUDE AT $t = 270 \omega_{pe}^{-1}$

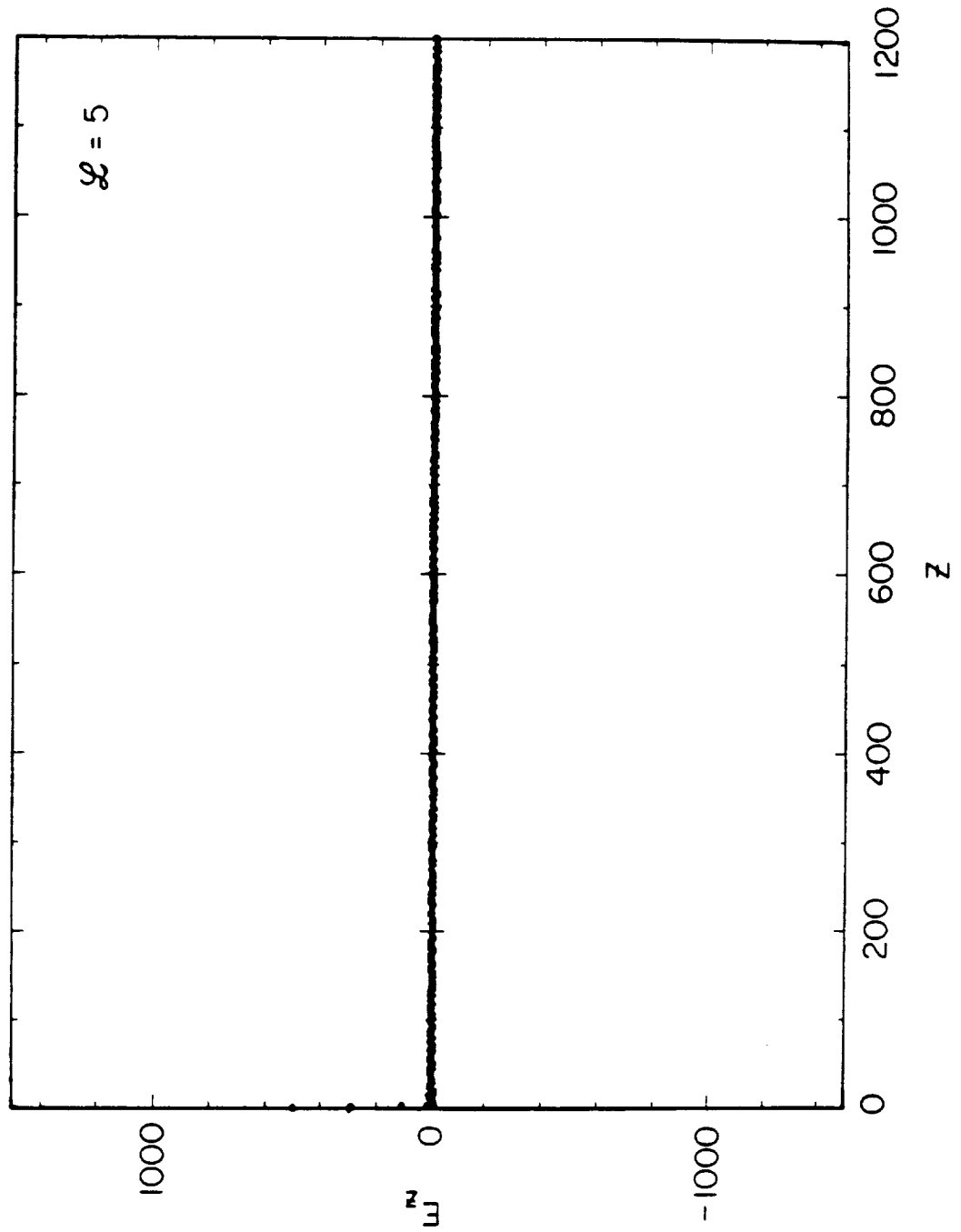


Figure 21 This figure displays the number of electrons, N , versus z from the modeled beam run with $L = 5$.

A-687-135

BEAM ELECTRONS AT $t = 270 \omega_{pe}^{-1}$

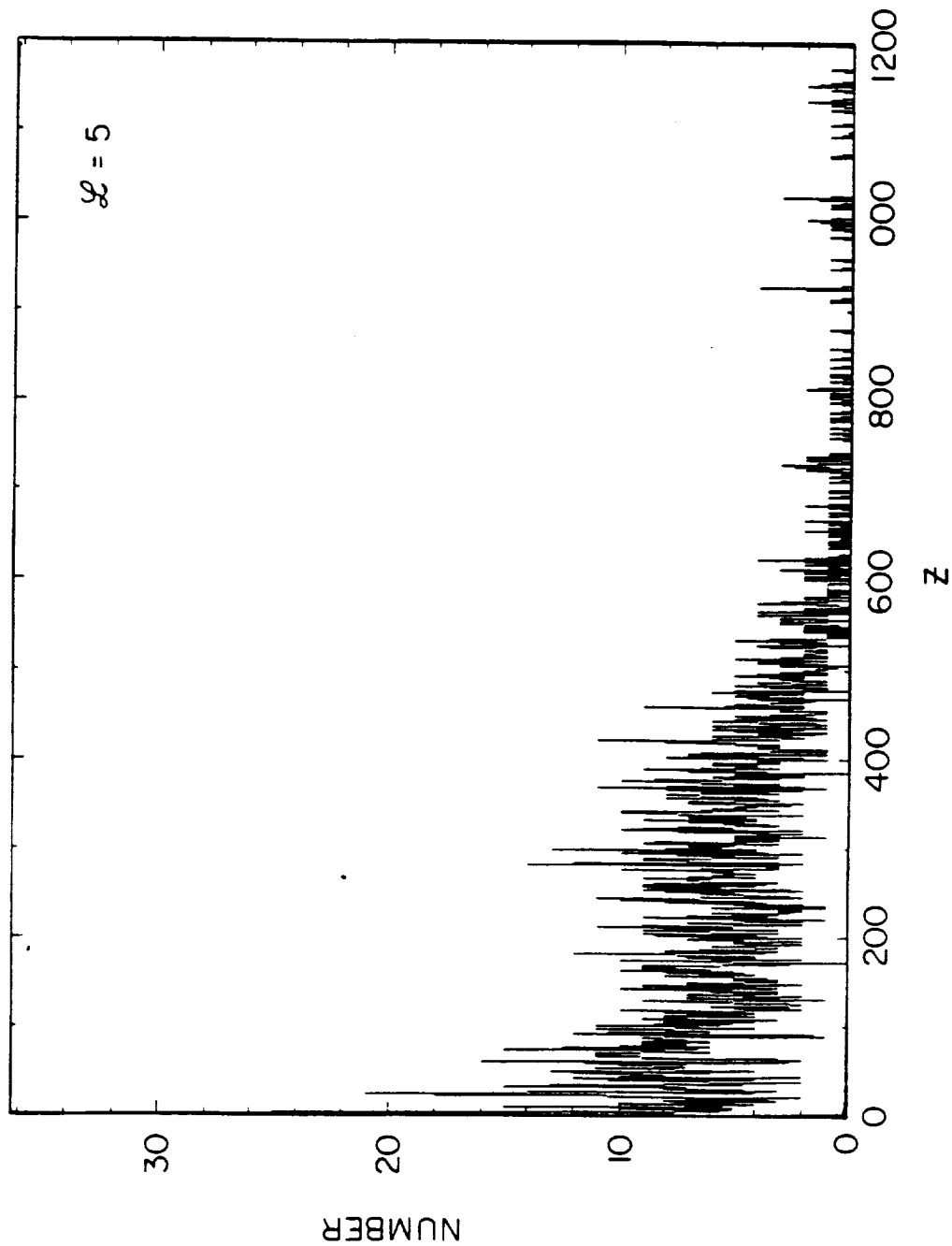


Figure 22 This figure is a V_z versus z phase-space configuration of the modeled SL-2 electron beam obtained from the one-dimensional simulation run with the parameters shown in Table 1, with $L = 3$.

A-G87-130

BEAM PARTICLES AT $t = 270 \omega_{pe}^{-1}$

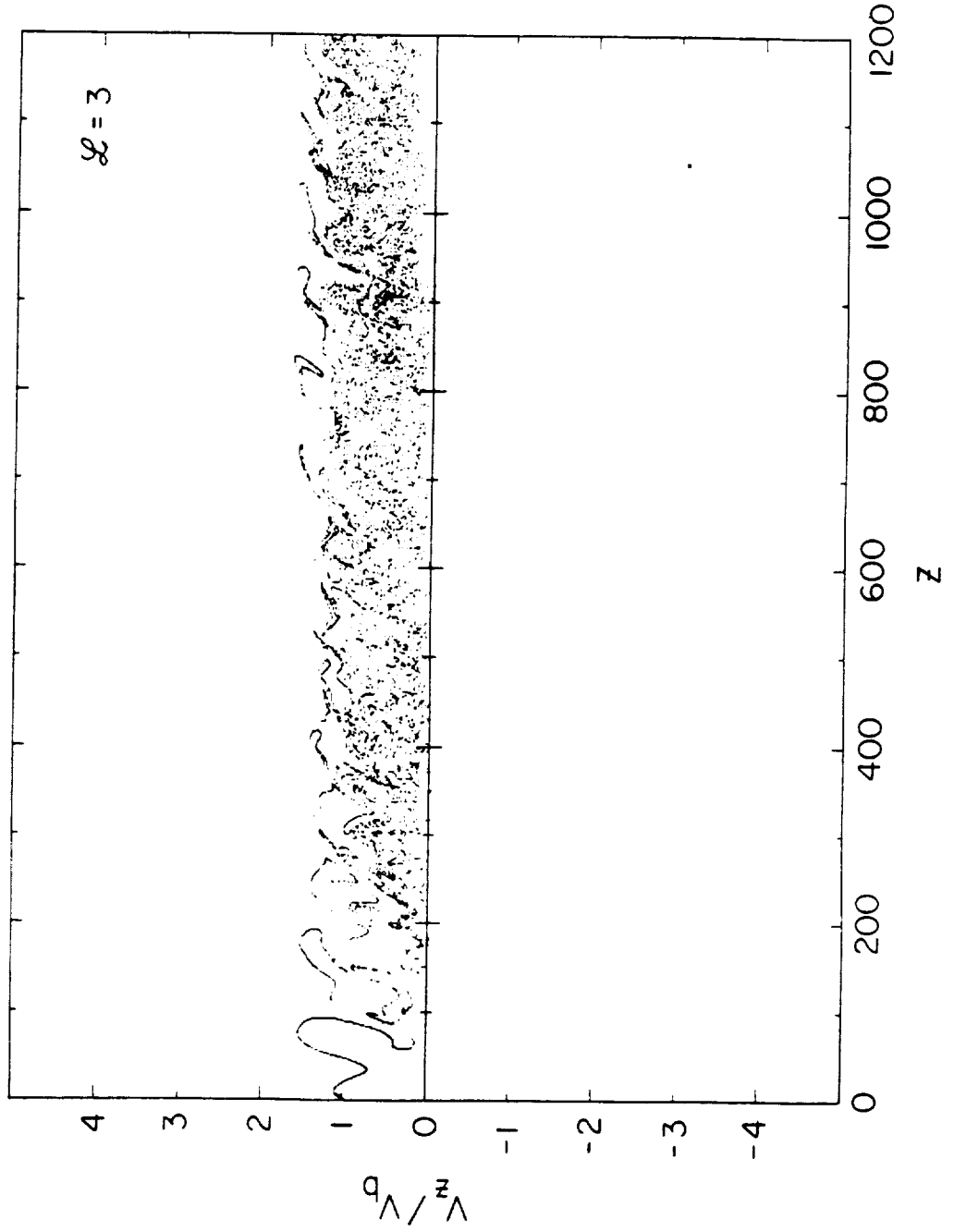


Figure 23 This figure displays E_z versus z from the one-dimensional simulation run with $L = 3$. Note that wave activity is present in the beam.

A-687-131

E - FIELD MAGNITUDE AT $t = 270 \omega_{pe}^{-1}$

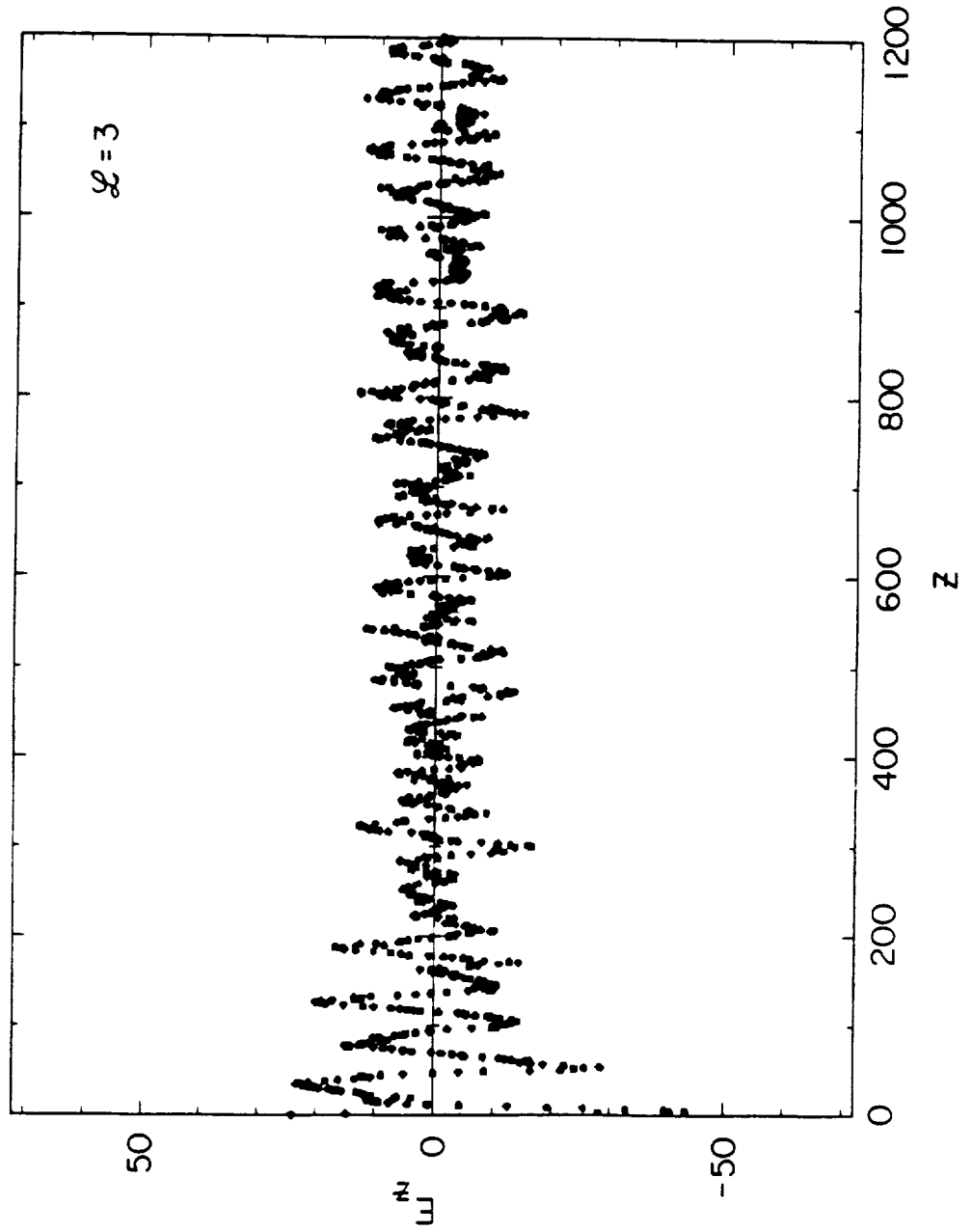


Figure 24 This figure displays the number of electrons, N , versus z from the modeled beam run with $L = 3$.

A - G87 - 132

BEAM ELECTRONS AT $t = 270 \omega_{pe}^{-1}$

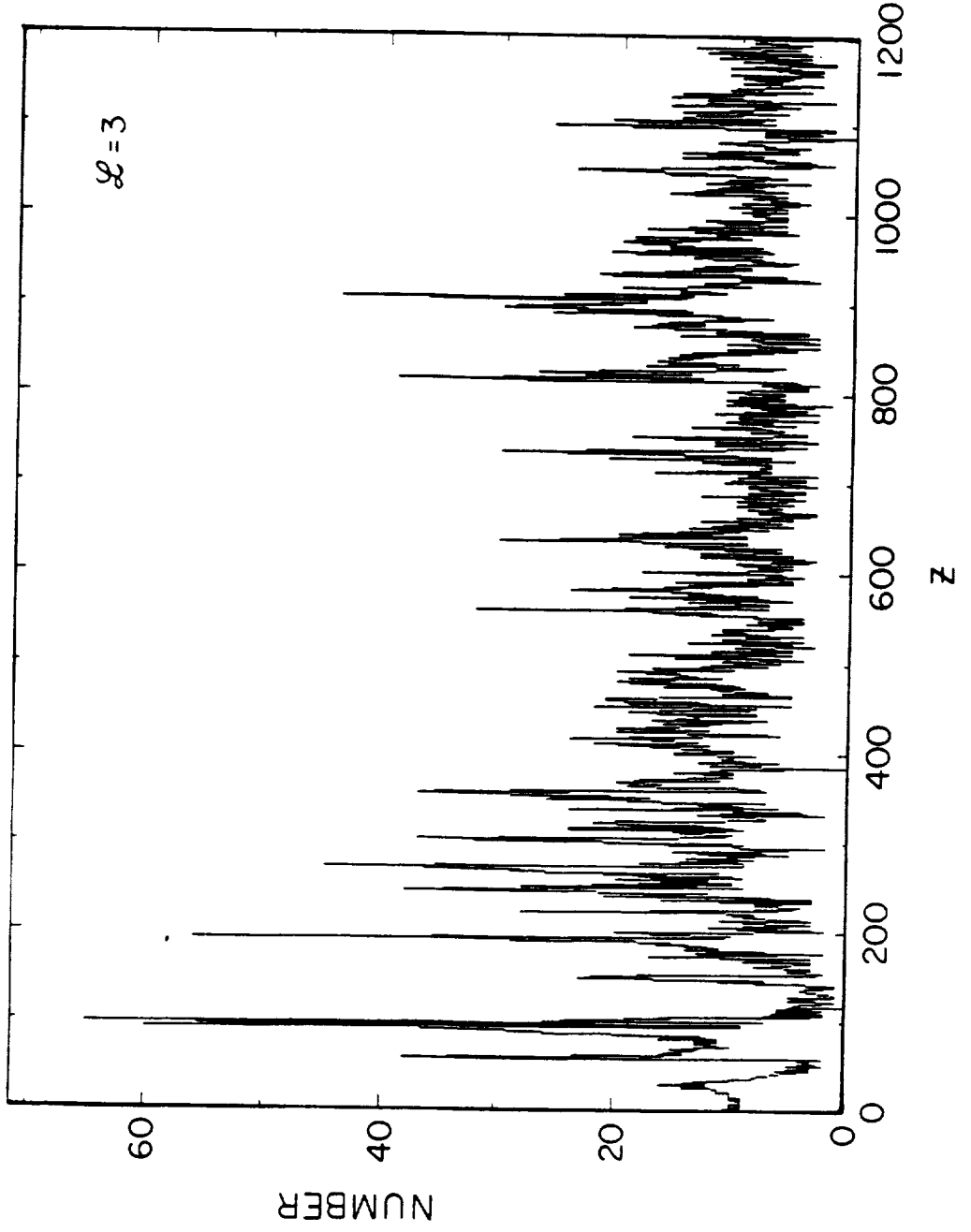


Figure 25 This figure is a V_z versus z phase-space configuration of the modeled SL-2 electron beam obtained from the one-dimensional simulation run with the parameters shown in Table 1, with $L = 2$.

A-687-127

BEAM PARTICLES AT $t = 270 \omega_{pe}^{-1}$

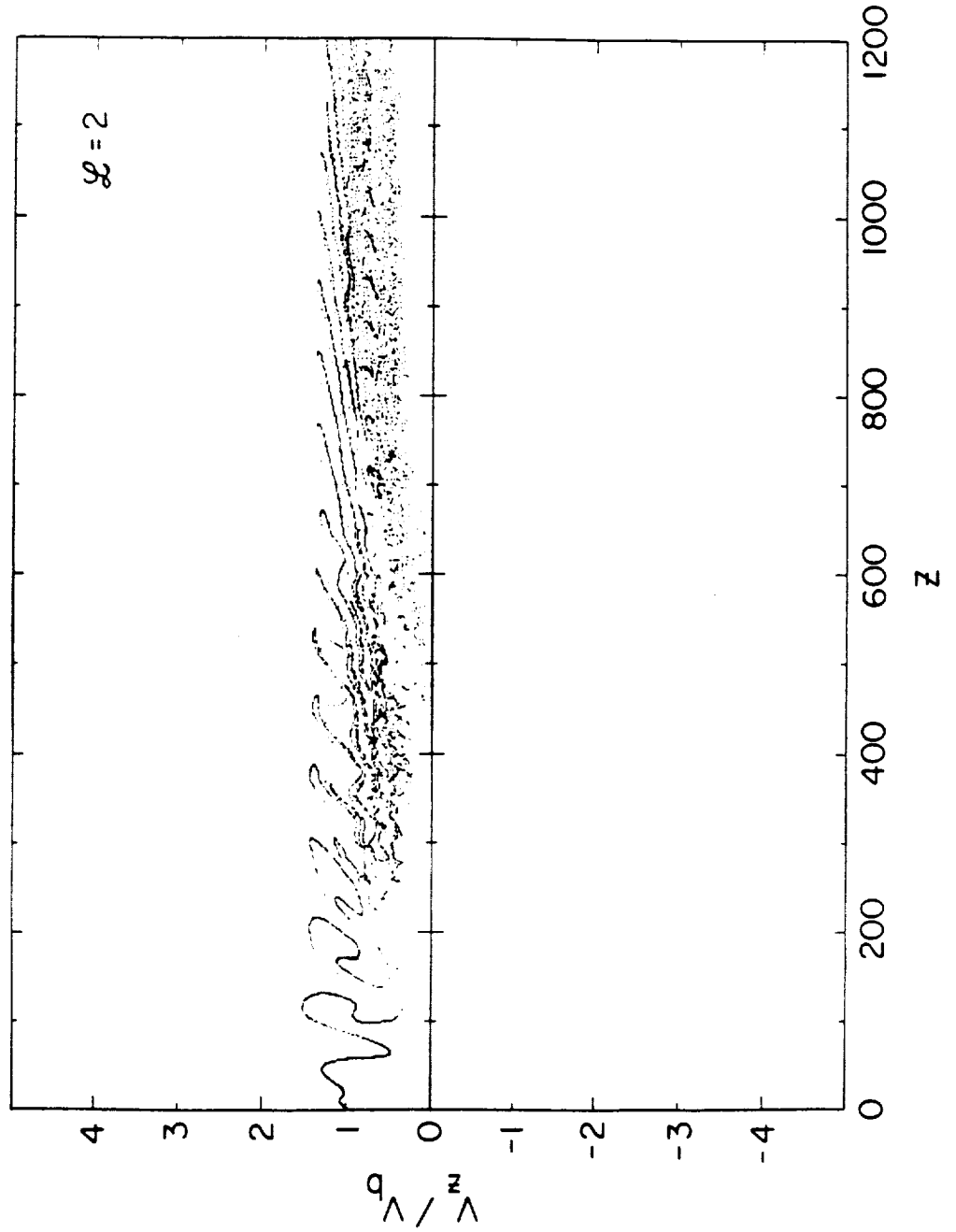


Figure 26 This figure displays E_z versus z from the one-dimensional simulation run with $L = 2$. Note that wave activity is present in the beam.

A-G87-128

E - FIELD MAGNITUDE AT $t = 270 \omega_{pe}^{-1}$

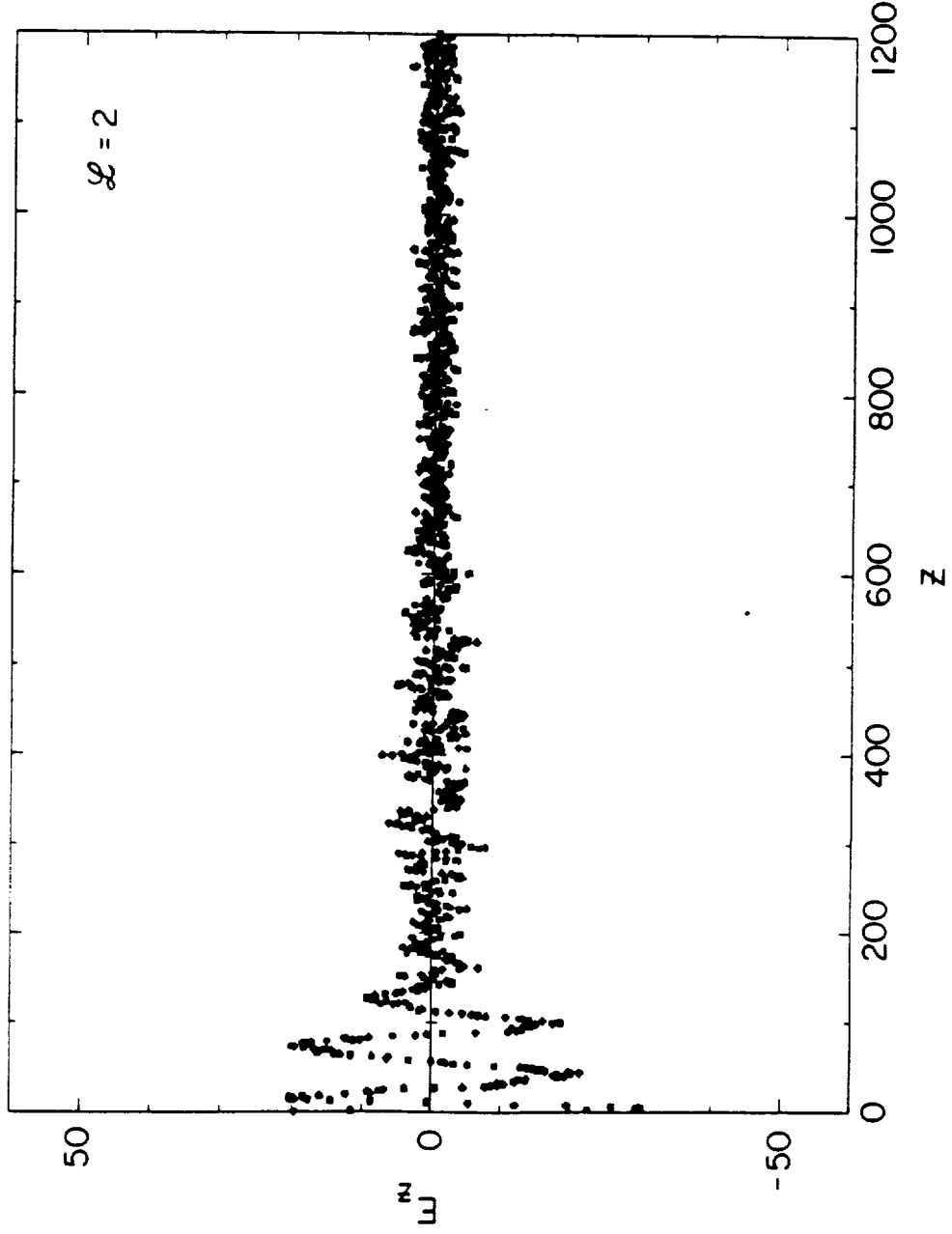


Figure 27 This figure displays the number of electrons, N , versus z from the modeled beam run with $L = 2$.

A-687-129

BEAM ELECTRONS AT $t = 270 \omega_{pe}^{-1}$

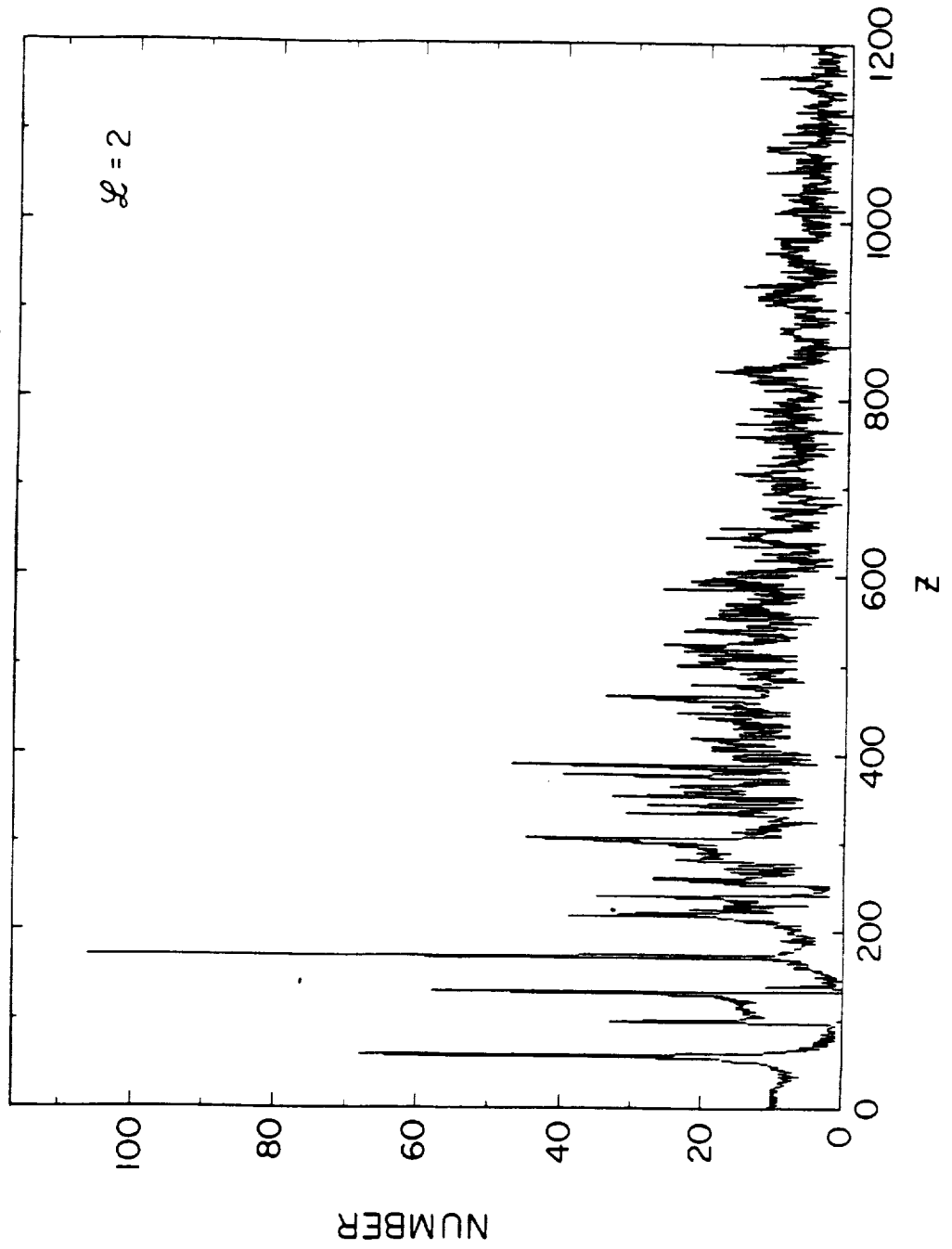


Figure 28 This figure is a V_z versus z phase-space configuration of the modeled SL-2 electron beam obtained from the one-dimensional simulation run with $L = 3$ and a length of 3600 grids corresponding to 180 meters. Note that the beam phase-space configuration is similar to that shown in Figure 22 for a 60-meter beam segment.

BEAM PARTICLES AT $t = 840 \omega_{pe}^{-1}$

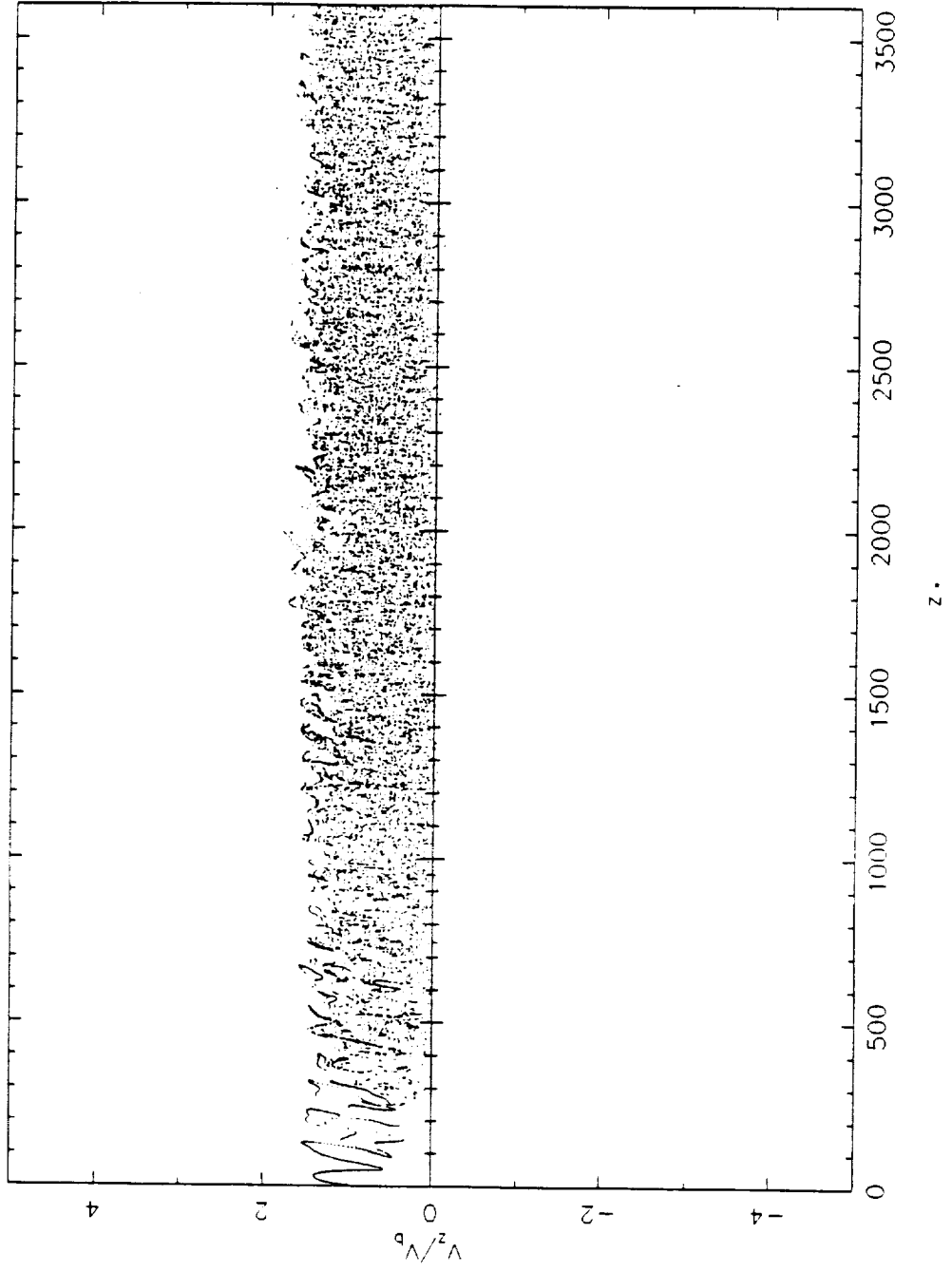


Figure 29 This diagram is a plot of $J_z(k_z, \omega)$ as a function of ω and k_z for the 175-meter beam segment. The largest values of $J_z(k_z, \omega)$ are completely dark, while o's and .'s represent continually lower intensities. Note that the values of $J_z(k_z, \omega)$ peaks at about $\omega/k_z = 2.8 \times 10^7$ m/s.

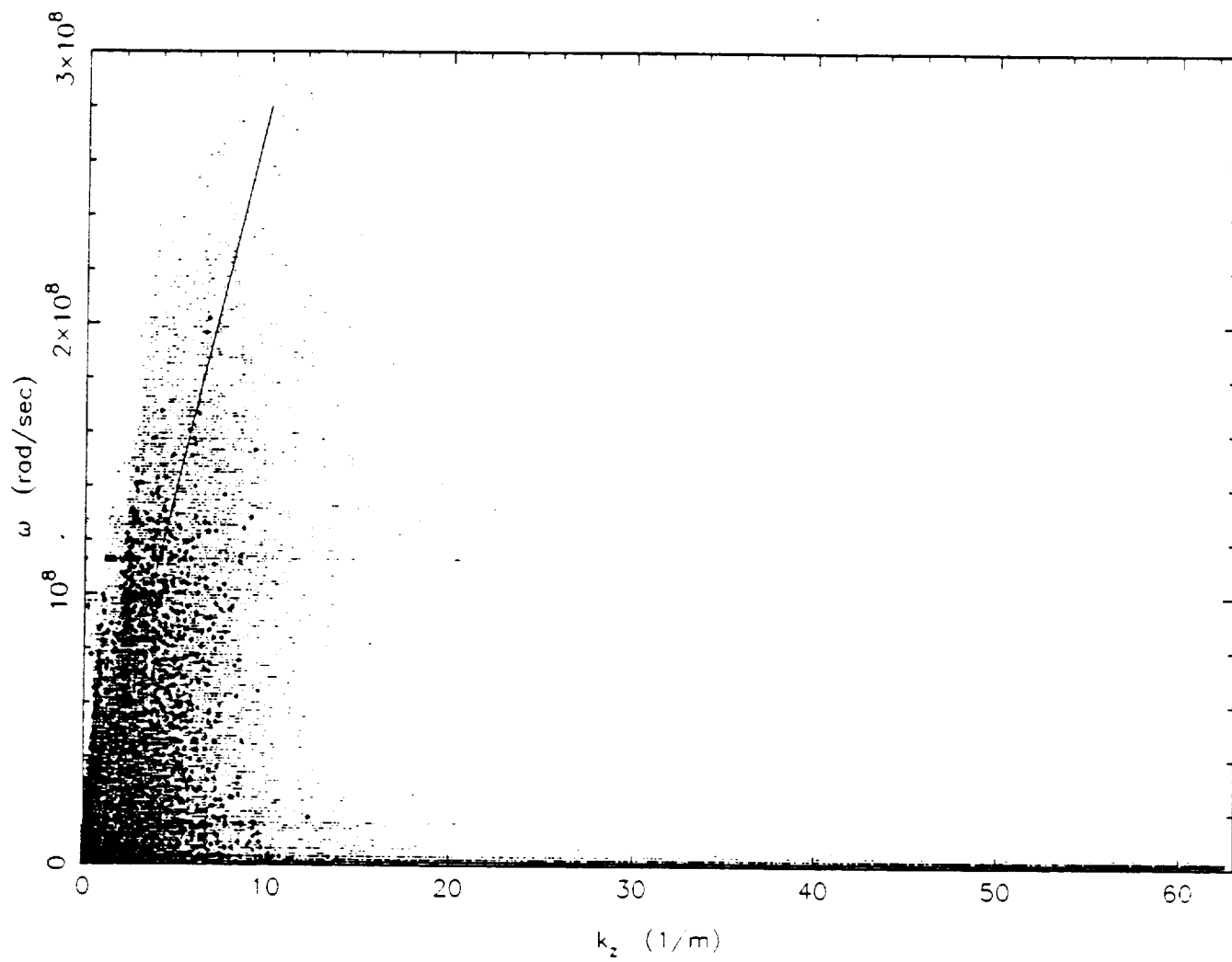


Figure 30 This figure shows the variation of $J_z(k_z)$ for the 175 meter beam segment as a function of k_z . Note for $k_z < 22$ that $J_z(k_z)$ increases as k_z decreases. This variation in $J_z(k_z)$ results from the density perturbations in the beam created by a beam-plasma instability. Also shown in the figure is the simulation noise level. This noise is obtained since simulation electrons many times the mass and charge of real electrons were used in the computer model. The range of k_z' of the whistler-mode waves is also shown in the figure.

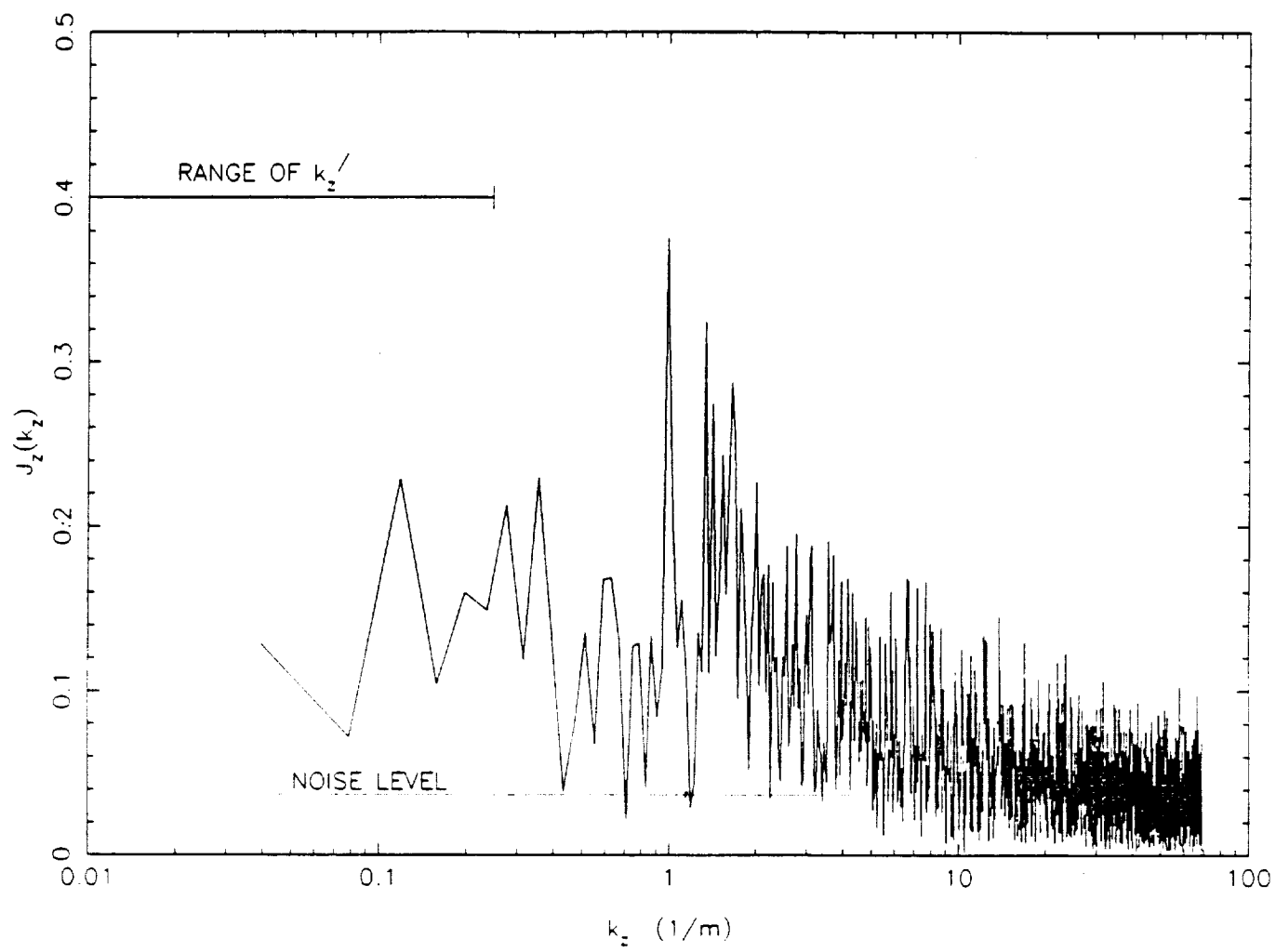
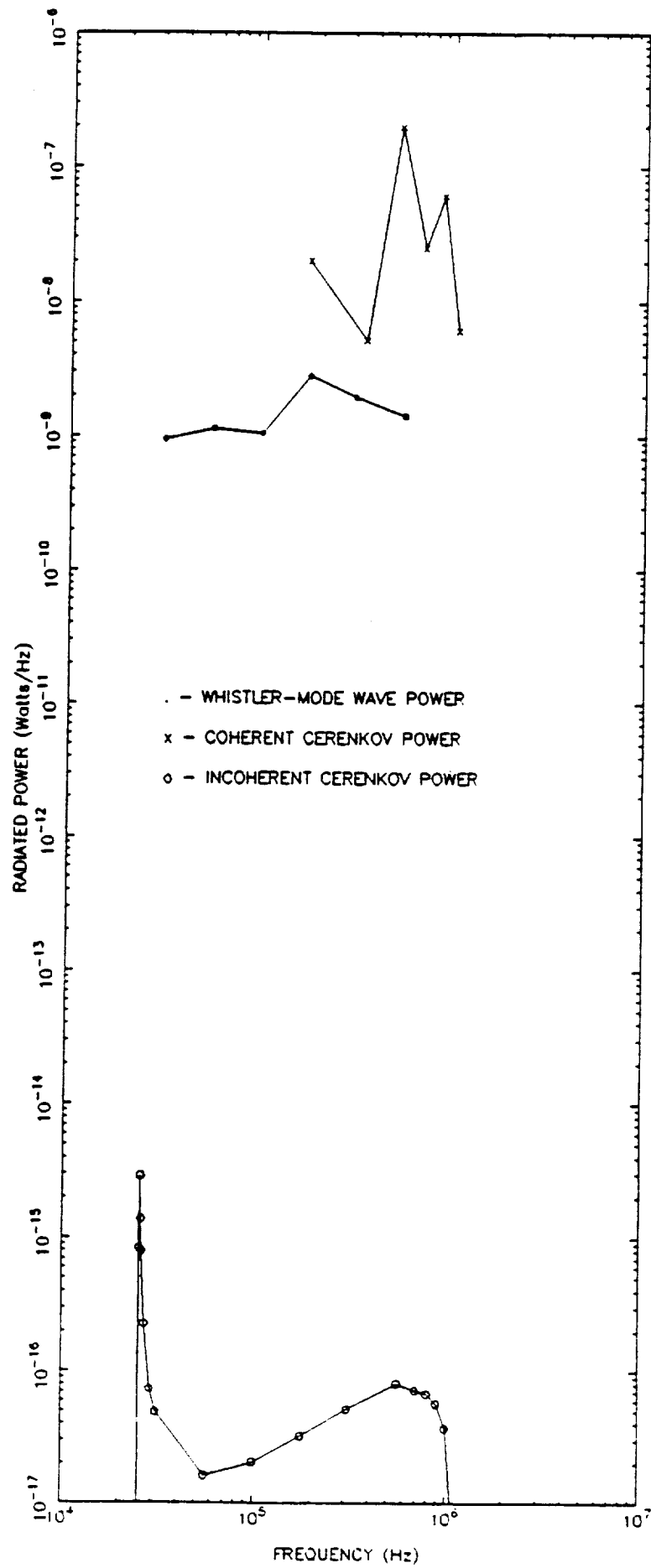


Figure 31 This figure shows the power spectra of the measured whistler-mode radiation from the first 200 meters of the SL-2 electron beam along with the calculated power spectra of the incoherent and coherent Cerenkov radiation from a 200-meter beam segment. Note that the inclusion of coherent radiation effects increases the calculated powers to those measured from the SL-2 electron beam. Based on these results, it is concluded that coherent Cerenkov radiation from a bunched electron beam generates the detected whistler-mode radiation.



APPENDIX

A general formula for the radiated power from a field-aligned beam of current density $J_z(z)$ has been derived by C. K. Goertz. From this very general formalism, the radiated power from a single particle, N particles and a pulsed beam can be easily obtained.

First, the current density is written as

$$\bar{J}_q(\bar{r}, t) = \hat{z} \langle nev \rangle_z \delta(x) \delta(y) = \hat{z} J_z(z, t) \delta(x) \delta(y) \quad (\text{A-1})$$

where $J_z(z)$ is the field-aligned component of the current density.

The Fourier transform of the current can be written as

$$\bar{J}_q(\bar{k}, \omega) = \frac{\hat{z}}{(2\pi)^4} \iint J_z(z, t) e^{i(k_z z - \omega t)} dz dt \quad . \quad (\text{A-2})$$

In order to calculate the radiated power from a group of charges, a transformation must be made to a frame of reference moving with the charges. In this frame, the current density becomes independent of time:

$$J_z(z, t) = J_z(z') \quad .$$

And, consequently, the current density appears stationary. The new coordinate z' is defined as $z' = z - V_S t$, where V_S represents the velocity of this moving frame. Expression (A-2) is then

$$\bar{J}_q(\bar{k}, \omega) = \frac{\hat{z}}{(2\pi)^4} \int_{-\infty}^{\infty} J_z(z') e^{ik_z z'} dz' \int_{-\infty}^{\infty} e^{i(k_z V_S - \omega)t} dt. \quad (A-3)$$

The quantity $\int_{-\infty}^{\infty} J_z(z') e^{ik_z z'} dz' = \sqrt{2\pi} J_z(k_z)$ where $J_z(k_z)$ is the Fourier transform of $J(z')$. Using the definition of the delta function, $\int_{-\infty}^{\infty} e^{i(k_z V_S - \omega)t} dt = 2\pi \delta(k_z V_S - \omega)$, and using the fact that $k_z = \frac{n\omega}{c} \cos \theta$, (A-3) now becomes

$$\bar{J}_q(\bar{k}, \omega) = \frac{\hat{z}}{(2\pi)^3} (\sqrt{2\pi} J_z(k_z)) \delta(n\omega \cos \theta - \omega) \quad (A-4)$$

where $\beta = V_S/c$.

Using Equation (4-6), the electric field is written as

$$\begin{aligned} \bar{E}(\bar{r}, t) = & \frac{i}{(2\pi)^3 \epsilon_0} \iint (\bar{T}^{-1} \cdot \hat{z}) (\sqrt{2\pi} J_z(k_z)) \\ & \delta(n\omega \cos \theta - \omega) e^{i(\omega t - \bar{k} \cdot \bar{r})} d\bar{k} \frac{d\omega}{\omega} \end{aligned} \quad (A-5)$$

Knowing the electric field and source current, an expression for the radiated power can be obtained:

$$\begin{aligned}
 P(t) &= \int \mathbf{E}(\mathbf{r}, t) \cdot \mathbf{J}(\mathbf{r}, t) d\mathbf{r} \\
 &= \frac{1}{(2\pi)^3 \epsilon_0} \iiint (\hat{\mathbf{z}} \cdot \hat{\mathbf{T}}^{-1} \cdot \hat{\mathbf{z}}) (\sqrt{2\pi} J_z(k_z)) \quad (A-6)
 \end{aligned}$$

$$\delta(n\omega \cos \theta \beta - \omega) e^{i(\omega t - k_z z)} J_z(z, t) dz d\bar{k} \frac{d\omega}{\omega}$$

where the current is again described by (A-1). Moving to the frame $z'' = z - V_s t$, (A-6) can be rewritten as

$$\begin{aligned}
 P(t) &= \frac{1}{(2\pi)^3 \epsilon_0} \iiint (\hat{\mathbf{z}} \cdot \hat{\mathbf{T}}^{-1} \cdot \hat{\mathbf{z}}) (\sqrt{2\pi} J_z(k_z)) \\
 &\quad \delta(n\omega \cos \theta \beta - \omega) e^{i(\omega - n\omega \cos \theta \beta)t} \quad (A-7) \\
 &\quad [J_z(z'') e^{-ik_z z''} dz''] d\bar{k} \frac{d\omega}{\omega} .
 \end{aligned}$$

The quantity in brackets is equal to $\sqrt{2\pi} J_z^*(k_z)$ where $J_z^*(k_z)$ is the conjugate Fourier transform of $J(z'')$. The element $d\bar{k}$ is

$$d\bar{k} = n^2 \frac{\omega^3}{c^3} dn \sin \theta d\theta d\phi \quad \text{and}$$

$$k_z = \frac{n \cos \theta \omega}{c} = k_z(n, \theta) .$$

Substituting these into (A-7) and integrating over ϕ yields:

$$P(t) = \frac{i}{(2\pi)^2 \epsilon_0} \iint (\hat{z} \cdot \vec{T}^{-1} \cdot \hat{z}) (2\pi) J_z(k_z(n, \theta))$$

$$J_z^*(k_z(n, \theta)) \delta(n\omega \cos \theta \beta - \omega) \quad (A-8)$$

$$e^{i(\omega - n\omega \cos \theta \beta)t} n^2 \omega^2 dn \sin \theta d\theta d\omega \quad .$$

Integrating over θ , an integral of the form

$$I = \int f(x) \delta(Ax - B) dx = \frac{f(x_0)}{A}$$

must be solved where $A = |n \omega \beta|$, $B = \omega$ and $x_0 = \cos \theta_0 = \frac{1}{n\beta}$.

The radiated power then becomes

$$P(t) = \frac{-i}{(2\pi)^2 \epsilon_0 c^3 \beta} \iint (\hat{z} \cdot \vec{T}^{-1} \cdot \hat{z}) (2\pi) J_z(k_z(n, \theta_0))$$

$$J_z^*(k_z(n, \theta_0)) |n| |\omega| dn d\omega \quad . \quad (A-9)$$

An explicit form for $(\hat{z} \cdot \vec{T}^{-1} \cdot \hat{z})$ is obtained using Equation (4-34), and upon obtaining the imaginary part to the integral

$$\int_0^\infty \frac{T_{33}(n) |n| f(n) dn}{(n^2 - n_1^2)(n^2 - n_2^2)} = \frac{\pi i}{2(n_2^2 - n_1^2)} \sum_{k=1}^2 (-1)^k T_{33}(n_k) f(n_k)$$

where $f(n)$ is an arbitrary even with no singularities, the radiated power becomes

$$P(t) = \bar{P} = \int_{-\infty}^{\infty} \left(\frac{\omega d\omega}{8\pi \epsilon_0 \epsilon_1 c^2 V_s} \right) \frac{1}{(n_2^2 - n_1^2)} \sum_{k=1}^2 T_{33}(n_k) \quad (A-10)$$

$$\times [2\pi J_z(k_z(n_k, \theta_0)) J_z^*(k_z(n_k, \theta_0))] .$$

Note that the radiated power is proportional to the square of the Fourier transform of the current density. Once the current density and its transform are known, it can be used in Equation (A-10) to easily calculate the radiated power.

As an example, the radiated power from a single field-aligned point charge moving at velocity, V_0 , can be calculated. Moving to a frame where the particle is considered stationary, $V_s = V_0$, the current density becomes

$$J_z(z) = q V_0 \delta(z - z_0),$$

where z_0 represents the position of the particle relative to the center of coordinates for the frame moving at V_s . The current density transform becomes

$$J_z(k_z) = \frac{q V_0}{\sqrt{2\pi}} \int_{-\infty}^{\infty} \delta(z - z_0) e^{ik_z z} dz = q V_0 \frac{e^{i \frac{n\omega}{c} \cos \theta z_0}}{\sqrt{2\pi}}$$

where $k_z = \frac{n\omega}{c} \cos \theta$. Using Equation (A-4), $J_q(\underline{k}, \omega)$ is

$$\bar{J}_q(\underline{k}, \omega) = \hat{z} \frac{q V_0}{(2\pi)^3} e^{i \frac{n\omega}{c} \cos \theta z_0} \delta(n\omega \cos \theta \beta - \omega)$$

and is identical to (4-13). Since $J_z(k_z) J_z^*(k_z) = 1/2\pi$, the radiated power is

$$P = \int_{-\infty}^{\infty} \left(\frac{q^2 \omega d\omega}{8\pi \epsilon_0 \epsilon_1} \right) \left(\frac{V_0}{c^2} \right) \frac{1}{(n_2^2 - n_1^2)} \sum_{k=1}^2 T_{33}(n_k)$$

which is identical to (4-22).

The power radiated from N point charges all moving at velocity V_0 , but located at arbitrary positions along a field line can also be calculated. Again, $V_s = V_0$, however, the current density is now

$$J_z(z) = q V_0 \sum_{i=1}^N \delta(z - z_i) \quad ,$$

where z_i is the particle position relative to the center of coordinates of the frame moving with V_s . The transform becomes

$$J_z(k_z) = \sum_{i=1}^N \frac{q V_0}{\sqrt{2\pi}} \int_{-\infty}^{\infty} \delta(z - z_i) e^{ik_z z} dz$$

$$= \frac{q V_0}{\sqrt{2\pi}} \sum_{i=1}^N e^{ik_z z_i} = \frac{q V_0}{\sqrt{2\pi}} \sum_{i=1}^N e^{i \frac{n \omega}{c} \cos \theta z_i}$$

and

$$J_z^*(k_z) = \frac{q V_0}{\sqrt{2\pi}} \sum_{j=1}^N \frac{e^{-i \frac{n \omega}{c} \cos \theta z_j}}{\sqrt{2\pi}} .$$

The quantity

$$J_z(k_z) J_z^*(k_z) = \frac{q V_0}{2\pi} \sum_{i=1}^N \sum_{j=1}^N e^{i \frac{n \omega}{c} \cos \theta (z_i - z_j)} .$$

Inserting this into Equation (A-10) yields a result identical to that of (4-37) for $\beta_i = \beta_j$ ($V_{i0} = V_{j0}$).

A surprising result is obtained for the radiated power if the beam density is completely uniform. In this case, the particles are moving at velocity, V_0 ; thus, $V_s = V_0$. The current density is

$$J_z(z) = q V_0 \frac{N}{L} = q V_0 \lambda_0 .$$

The transform is then

$$J_z(k_z) = q V_0 \lambda_0 \int_{-\infty}^{\infty} e^{ik_z z} dz = q V_0 \lambda_0 \delta(k_z) = q V_0 \lambda_0 \delta\left(\frac{n \omega}{c} \cos \theta\right)$$

and $J_z^*(k_z) = q V_0 \lambda_0 \delta(\frac{n \omega}{c} \cos \theta)$. After substituting these into (A-10), it is found that radiation only at $\omega = 0$ is possible and consequently the radiated power is zero. Therefore, an unperturbed, uniform beam moving at velocity V_0 along a magnetic field will not radiate.

Finally, the power from a pulsed electron beam is considered. Using Equations (74), (76), (77) and (78) from Harker and Banks [1983], the Fourier transform of the field-aligned current is

$$\bar{J}(\bar{k}, \omega) = \frac{q V_0 \hat{z}}{(2\pi)^3} \delta(k_z V_0 - \omega) N \ell \operatorname{sinc}\left(\frac{k_z \ell}{2\pi}\right) \sum_{m=-\infty}^{\infty} e^{imk_z d}$$

where ℓ is the pulse length and d is the distance between pulses. Comparing this with Equation (A-4), $J_z(k_z)$ is obtained:

$$J_z(k_z) = q V_0 \frac{N \ell}{\sqrt{2\pi}} \operatorname{sinc}\left(\frac{k_z \ell}{2\pi}\right) \sum_{m=-\infty}^{\infty} e^{-imk_z d}$$

and $J_z^*(k_z)$ is

$$J_z^*(k_z) = q V_0 \frac{N \ell}{\sqrt{2\pi}} \operatorname{sinc}\left(\frac{k_z \ell}{2\pi}\right) \sum_{m=-\infty}^{\infty} e^{imk_z d} .$$

The quantity

$$J_z(k_z) J_z^*(k_z) = q^2 v_o^2 \frac{N^2 \ell^2}{2\pi} \operatorname{sinc}^2\left(\frac{k\ell}{2\pi}\right) \left| \sum_{m=1}^p e^{-imk_z d} \right|^2$$

where p is the number of pulses. Since

$$\left| \sum_{m=1}^p e^{-imk_z d} \right|^2 = \frac{\sin^2(pdk_z/2)}{\sin^2(dk_z/2)},$$

$J_z(k_z) J_z^*(k_z)$ is

$$J_z(k_z) J_z^*(k_z) = \left[q v_o \frac{N \ell}{\sqrt{2\pi}} \operatorname{sinc}\left(\frac{k_z \ell}{2\pi}\right) \frac{\sin(pdk_z/2)}{\sin(dk_z/2)} \right]^2.$$

Inserting this into (A-10) yields an expression for the radiated power similar to Equation (91) of Harker and Banks.

REFERENCES

- Banks, P. M., R. I. Bush, W. J. Raitt, Observations of electron beam structure on STS-3 and Spacelab 2 (abstract), EOS Trans. AGU, 66, 1053, 1985.
- Beghin, C., J. P. Lebreton, B. N. Maehlum, J. Troim, P. Ingsoy, J. L. Michau, Phenomena induced by charged particle beams, Science, 225, 188-191, 1984.
- Bell, T. F., Artificial production of VLF hiss, J. Geophys. Res., 73, 4409-4415, 1968.
- Bernstein, W., H. Leinbach, P. J. Kellogg, S. J. Monson, and T. Hallinan, Further laboratory measurements of the beam plasma discharge, J. Geophys. Res., 84, 7271-7277, 1979.
- Bush, R. I., T. Neubert, P. M. Banks, W. J. Raitt, D. A. Gurnett, Observations of enhanced plasma wave production during pulsed beam emissions (abstract), EOS Trans. AGU, 67, 1176, 1986.
- Cartwright, D. G., and P. J. Kellogg, Observations of radiation from an electron beam artificially injected into the ionosphere, J. Geophys. Res., 79, 1439, 1974.
- Dechambre, M., G. A. Gusev, Yu. V. Kushnerevsky, J. Lavergnat, R. Pellat, S. A. Pulinets, V. V. Selegei, I. A. Zhulin, High-frequency waves during the ARAKS experiments, Ann. Geophys., 36, 333-340, 1980a.
- Dechambre, M., Yu. V. Kushnerevsky, J. Lavergnat, R. Pellat, S. A. Pulinets, and V. V. Seleger, Waves observed by the ARAKS experiment: The whistler mode, Ann. Geophys., 36, 351-359, 1980b.
- Grandal, B. (ed.) Artificial Particle Beams in Space Plasma Studies, Plenum, New York, 1982.
- Gurnett, D. A., A satellite study of VLF hiss, J. Geophys. Res., 71, 5599, 1966.
- Gurnett, D. A., Electromagnetic plasma wave emissions from the auroral field lines, J. Geomag. Geoelectr., 30, 257-272, 1978.

- Gurnett, D. A., and L. A. Frank, VLF hiss and related plasma observations in the polar Magnetosphere, J. Geophys. Res., 77, 172, 1972.
- Gurnett, D. A., W. S. Kurth, J. T. Steinberg, P. M. Banks, R. I. Bush, and W. J. Raitt, Whistler-mode radiation from the Spacelab-2 electron beam, Geophys. Res. Lett., 13, 225-228, 1986.
- Gurnett, D. A., S. D. Shawhan, and R. R. Shaw, Auroral hiss, Z-mode radiation, and auroral kilometric radiation in the polar magnetosphere: DE-1 observations, J. Geophys. Res., 88, 329-340, 1983.
- Harker, K. J. and P. M. Banks, Radiation from pulsed electron beams in space plasmas, Radio Sci., 19, 454-470, 1983.
- Hartz, T. R., Radio Noise Levels Within and Above the Ionosphere, Proc. ISEE, 57, 1042, 1969.
- Hess, W. N., M. G. Trichel, T. N. Davis, W. C. Beggs, G. E. Kraft, E. Stassinopoulos, and E. J. R. Maier, Artificial auroral experiment: Experiment and principal results, J. Geophys. Res., 76, 6067, 1971.
- Inan, U. S., M. Pon, P. M. Banks, P. R. Williamson, W. J. Raitt, and S. D. Shawhan, Modulated beam injection from the space shuttle during magnetic conjunction of STS-3 with the DE-1 satellite, Radio Science, 19, 487, 1984.
- James, H. G., VLF observations of auroral beams as sources of a class of emissions, Nature, 224, 351, 1969.
- Jones, T. W., and P. J. Kellogg, Plasma waves artificially induced in the ionosphere, J. Geophys. Res., 75, 2166, 1973.
- Jorgensen, T. S., Interpretation of auroral hiss measured on OGO-2 and at Byrd Station in terms of incoherent Cerenkov radiation, J. Geophys. Res., 73, 1055, 1968.
- Katz, I., G. A. Jongeward, D. E. Parks, D. L. Reasoner, and C. K. Purvis, Energy broadening due to space-charge oscillations in high current electron beams, Geophys. Res. Lett., 13, 64-67, 1986.
- Kellogg, P. J., D. G. Cartwright, R. A. Hendrickson, S. J. Monson, and J. R. Winckler, The University of Minnesota electron Echo experiment, Space Res., XVI, 589-599, 1976.
- Kellogg, P. J., S. J. Monson, W. Bernstein, and B. A. Whalen, Observations of waves generated by electron beams in the ionosphere, J. Geophys. Res., 91, 12065-12078, 1986.

- Lääspere, T., and R. A. Hoffman, New results on the correlation between low-energy electrons and auroral hiss, J. Geophys. Res., 81, 524, 1976.
- Lavergnat, J., M. Dechambre, R. Pellat, Yu. V. Kushnerevsky, S. A. Pulinets, Waves observed by the ARAKS experiments: Generalities, Ann. Geophys., 36, 323-332, 1980.
- Liemohn, H. B., Radiation from electrons in a magnetoplasma, Radio Sci., 690, 741, 1965.
- Lin, C. S., J. L. Burch, S. D. Shawhan, and D. A. Gurnett, Correlation of auroral hiss and upward electron beams near the polar cusp, J. Geophys. Res., 89, 925, 1984.
- Maggs, J. E., Coherent generation of VLF hiss, J. Geophys. Res., 81, 1707-1724, 1976.
- Mansfield, V. N., Radiation from a charged particle spiraling in a cold magnetoplasma, Astrophys. J., 147, 672, 1967.
- Monson, S. J., P. J. Kellogg, and D. G. Cartwright, Whistler-mode plasma waves observed on electron Echo II, J. Geophys. Res., 81, 2193, 1987.
- Mosier, S. R., and D. A. Gurnett, VLF measurements of the Poynting flux along the geomagnetic field with Injun 5 satellite, J. Geophys. Res., 74, 5675-5687, 1969.
- Mosier, S. R., and D. A. Gurnett, Theory of the Injun 5 very-low-frequency Poynting flux measurements, J. Geophys. Res., 76, 972-977, 1971.
- Neubert, T., W. W. L. Taylor, L. R. O. Storey, N. Kawashima, W. T. Roberts, D. L. Reasoner, P. M. Banks, D. A. Gurnett, R. L. Williams, and J. L. Burch, Waves generated during electron beam emissions from the space shuttle, J. Geophys. Res., 91, 11321-11330, 1986.
- Pritchett, P. L., and R. M. Winglee, The plasma environment during particle beam injection into space plasmas, 1. Electron Beams, J. Geophys. Res., submitted.
- Reeves, G. D., P. M. Banks, R. I. Bush, K. J. Harker, An analysis of the harmonic structure of VLF radiation generated by a square wave modulated electron beam in space (abstract), EOS Trans. AGU, 67, 1176, 1986.

- Shawhan, S. D., Description of the Plasma Diagnostics Package (PDP) for the OSS-1 shuttle mission and JSC chamber test in conjunction with the Fast Pulsed Electron Gun (FPEG), Artificial Particle Beams in Space Plasma Studies, ed. by B. Grandel, Plenum, NY, pp. 419-430, 1982.
- Shawhan, S. D., G. B. Murphy, P. M. Banks, P. R. Williamson, and W. J. Raitt, Wave emissions from D. C. and modulated electron beams on STS-3, Radio Science, 19, No. 2, 471-486, 1984.
- Smith, R. L., VLF observations of auroral beams as sources of a class of emissions, Nature, 224, 351, 1969.
- Stix, T. H., The Theory of Plasma Waves, McGraw-Hill, New York, 1962.
- Taylor, W. W. L., and S. D. Shawhan, A test of incoherent Cerenkov radiation for VLF hiss and other magnetospheric emissions, J. Geophys. Res., 79, 105-117, 1974.
- Wilhelm, K., W. Bernstein, B. A. Whalen, Study of electric fields parallel to magnetic lines of force using artificially injected energetic electrons, Geophys. Res. Lett., 7, 117, 1980.
- Williamson, P. R., J. G. Hawkins, R. L. Bush, P. M. Banks, W. J. Raitt, Vehicle charging measured during electron beam emission on Spacelab-2 (abstract), EOS Trans. AGU, 66, 1051, 1985.
- Winglee, R. M., and P. L. Pritchett, Space-charge effects during the injection of dense electron beams into space plasmas, J. Geophys. Res., submitted.
- Winkler, J. R., The application of artificial electron beams to magnetospheric research, Rev. Geophys. Res. and Space Phys., 18, No. 3, 659-682, 1980.
- Winkler, J. R., K. N. Erickson, P. R. Malcolm, A new experiment to investigate the conjugate echoes and plasma physics phenomena produced by an electron beam injected in the ionosphere--Echo 7 (abstract), EOS Trans. AGU, 67, 1180, 1986.

ION PLASMAS IN THE VICINITY OF THE ORBITER:
OBSERVATIONS AND MODELING

by

William R. Paterson

A thesis submitted in partial fulfillment
of the requirements for the Master
of Science degree in Physics
in the Graduate College of
The University of Iowa

July 1987

Thesis supervisor: Professor Louis A. Frank

Graduate College
The University of Iowa
Iowa City, Iowa

CERTIFICATE OF APPROVAL

MASTER'S THESIS

This is to certify that the Master's thesis of

William R. Paterson

has been approved by the Examining Committee
for the thesis requirement for the Master of
Science degree in Physics at the July 1987
graduation.

Thesis committee:

L.A. Frank

Thesis supervisor

David A. Smith

Member

John Dore

Member

ACKNOWLEDGMENTS

I would like to thank Dr. N. D'Angelo for the use of electron density measurements made by the Langmuir probe. Thanks are also due to Dr. L. A. Frank for his advice and support.

ABSTRACT

During the Spacelab-2 mission ions produced from a cloud of neutral gases surrounding the Shuttle-Orbiter were observed by an electrostatic analyzer aboard the PDP spacecraft. These ions, identified primarily as H_2O^+ , are distinguishable from ionospheric ions because they form a velocity-space distribution that has the shape of a ring. Distributions of this type were observed at distances up to 400 m from the Orbiter with densities ranging from $100/\text{cm}^3$ to $10^4/\text{cm}^3$. The production and transport of these ions are modeled in an attempt to reproduce the observed H_2O^+ densities. The water cloud is modeled as radial flow from a spherically symmetric source. Water molecules are removed from the cloud by collisions with atmospheric gases and H_2O^+ ions are produced by charge exchange between neutral H_2O and ionospheric O^+ . Once the H_2O^+ ions are produced they are picked up by Earth's magnetic field and removed from the cloud. The density of neutral water is a free parameter in the model which is determined by comparing the modeled H_2O^+ density to the measured ion density. For the Spacelab-2 mission the water density is inferred in this way to be as high as $10^9/\text{cm}^3$ at a distance of 50 m from the Orbiter, as much as ten times higher than the density of ambient atmospheric gases.

TABLE OF CONTENTS

	Page
LIST OF TABLES	v
LIST OF FIGURES	vi
 CHAPTER	
I. INTRODUCTION	1
Spacelab 2	1
The PDP	1
PDP Free Flight	2
The Lepedea	3
Data Analysis	5
II. IONOSPHERIC IONS AND ION PICK-UP	8
Atmospheric Gases and Ionospheric Ions	8
Orbiter Gas Cloud and Ion Pick-up	13
III. OBSERVATIONS	18
IV. MODELING	26
The Orbiter's Gas Cloud	26
Ionization and Losses	30
V. MODEL RESULTS	35
REFERENCES	66

LIST OF TABLES

Table		Page
1.	Ionospheric Reactions	40
2.	Model Reactions	41

LIST OF FIGURES

Figure	Page
1. Top and side views of the PDP with the booms deployed as in free flight. Distances are in inches	42
2. Orbital-plane motion of the Orbiter relative to the PDP between 0137 and 0304 UT	43
3. Orbital-plane motion of the Orbiter relative to the PDP between 0304 and 0434 UT	44
4. Relative orientations of \vec{R}_e , \vec{V}_{SC} , the PDP spin axis, and the fields-of-view of the Lepedea (adapted from Frank [2])	45
5. Polar plot showing the azimuth angles of samples from the Lepedea during eight consecutive energy sweeps for a spin period of 13.1 sec. Radial distance is proportional to the logarithm of the energy of the sample	46
6. Same as Figure 5 except that 41 consecutive energy sweeps are shown	47
7. Atmospheric temperature and densities at the position of the spacecraft during the free flight. Calculated from the MSIS-83 atmospheric model (Hedin [4])	48
8. The energy spectrum of photoelectrons observed at 0208 UT	49
9. Calculated ion distributions in a reference frame moving with velocity $V = 7.8 \times 10^3$ m/sec with respect to the rest frame of the ions	50
10. Energy spectrum calculated for the distributions of Figure 9	51
11. Motion of a particle in a magnetic field before and after ionization. The particle is ionized at point A. (a) Trajectory of the particle in the X, Z plane before ionization. (b) Trajectory of the particle in the X, Y plane before ionization. (c) Trajectory of the particle in the X, Z plane after ionization. (d) Trajectory of the particle in the X, Y plane after ionization	52

Figure	Page
12. Coordinates used to describe pick-up of ions from a cloud of gases co-orbiting with the Orbiter	53
13. The velocity-space trajectory of a single pick-up ion. The magnetic field is out of the plane of the figure. The ion speed ranges from zero to $2 V_{\perp}$	54
14. The energy spectrum of positive ions observed by the Lepedea at 0208 UT in the direction of orbital motion . .	55
15. Contours of constant $f(\vec{V})$ at 0208 UT in the V_x, V_y plane. Both V_x and V_y are perpendicular to \vec{B} . The projection of \vec{V}_{sc} into the plane is along V_x . At this time, \vec{V}_{sc} and \vec{B} are at an angle of 86° . The outermost contour is for $f = 10^{-19} \text{ sec}^3/\text{cm}^6$. Contours interior to this increase by factors of ten	56
16. Contours of constant $f(\vec{V})$ at 0208 UT in a plane perpendicular to the plane of Figure 15. The magnetic field is parallel to the V_z axis	57
17. Energy spectrum of positive ions at 0237 UT in the direction of V_x	58
18. Contours of constant $f(\vec{V})$ in the V_x, V_y plane at 0237 UT .	59
19. Contours of constant $f(\vec{V})$ in the V_x, V_z plane at 0237 UT. The direction of orbital motion is indicated by the dashed line and the arrow marked \vec{V}_{sc}	60
20. The coordinate system used to integrate equations (22) and (23). The integration is performed at the point P on the field line \vec{B} . The point P moves along \vec{B} with a velocity equal to V_{\perp} . Magnetic field lines sweep past the Orbiter with velocity $-\vec{V}_{sc}$. The PDP lies in the U, V plane at a distance R from the Orbiter	61
21. Comparison of observed and calculated pick-up ion densities during the free flight. The lower panels show the angle θ between \vec{R} and \vec{V}_{sc} , and the distance R between the PDP and the Orbiter	62
22. Calculated H_2O , H_2O^+ , and H_3O^+ densities along a line which is parallel to the V axis of Figure 20 and which passes within 50 m of the center of the water cloud. Parameters used in the calculation are discussed in the text. The angle between \vec{B} and \vec{V}_{sc} is 90°	63

Figure		Page
23.	Same as Figure 22 but calculated for an atmospheric density five times higher than the density of Figure 22	64
24.	Same as Figure 22 but for an angle between \vec{B} and \vec{V}_{sc} of 60°	65

CHAPTER I
INTRODUCTION

Spacelab 2

The Spacelab-2 payload was launched July 29 of 1985 aboard the Shuttle-Orbiter Challenger and landed August 6. This flight was a multidisciplinary science mission which included experiments in physics, astronomy, and biology. Most of the experiments were mounted on a pallet within the Orbiter's payload bay and exposed to space during a major fraction of the eight-day mission. Included among these experiments was the Plasma Diagnostics Package (PDP) designed and built at the University of Iowa. A major role of the PDP during the Spacelab-2 mission was to make measurements of plasmas, plasma waves, and electromagnetic radiation in the vicinity of the Orbiter with the goal of identifying and quantifying the Orbiter environment and the interaction of the Orbiter with the ionosphere.

The PDP

The PDP, shown in Figure 1, is a cylindrical body 1.1 m in height by 1.3 m in diameter with a total mass of 285 kg. Inside are instruments designed to detect and analyze electrically charged particles, electric and magnetic fields, waves, and the neutral gas pressure. Four retractable booms mounted on the PDP allow for the

extension of two electric field probes, a magnetic field probe and a Langmuir probe. The outside of the PDP is covered with a thermal insulation blanket affixed to which is a wire screen so that the surface acts as a conductor. Openings in both the blanket and the screen are provided for instrument apertures.

The PDP is designed so that it can be operated from the pallet within the Orbiter's bay, while attached to the Orbiter's Remote Manipulator System (RMS), or as a free-flying spin-stabilized spacecraft. In March of 1982 the PDP was also flown as part of the STS-3 mission aboard the Orbiter Columbia. During that flight, measurements were made from within the Orbiter's bay and at distances of approximately 15 m from the bay while the PDP was attached to the RMS [1]. During the Spacelab-2 mission measurements were again made from within the bay and from the RMS. In addition, the PDP was operated as a free flyer, and measurements were obtained at distances up to 400 m from the Orbiter. In this thesis these latter free-flight measurements are discussed.

PDP Free Flight

The free flight began on August 1 at 0010 UT, 51 hours into the mission. At this time the PDP was released from the RMS with its spin axis perpendicular to \vec{R}_e , the vector pointing from the spacecraft towards the earth, and to \vec{V}_{sc} , the velocity vector of the spacecraft, i.e., perpendicular to the orbital plane (see Figure 4). The rotation of the PDP was accomplished by means of a mechanical momentum wheel

inside the spacecraft. This wheel was spun-up prior to release while the PDP was attached to the RMS. After release, angular momentum was transferred from the wheel to the rest of the spacecraft causing the spacecraft to rotate. A constant period of rotation equal to 13.1 sec was maintained throughout most of the free flight. During this time, the Orbiter was maneuvered around the PDP. Two circuits of the PDP were completed, essentially one per orbit. The projection of the Orbiter's trajectory into the orbital plane of the PDP during this time is shown in Figures 2 and 3 in a coordinate system centered on the PDP. The distance of the Orbiter out of the orbital plane during the free flight was as much as 300 m. The PDP was recovered by maneuvering the Orbiter to within approximately 15 m of the satellite and grappling it with the RMS. The recovery was successfully completed at 0620 UT.

The Lepedea

During the free flight, the differential directional intensities of charged particles with energy-per-charge in the range of 2 V to 36 kV were observed with an electrostatic analyzer aboard the PDP. This instrument, known as the Low Energy Proton and Electron Differential Energy Analyzer (Lepedea) is of a type described in detail by Frank et al. [2]. The Lepedea simultaneously measures the fluxes of electrons and positively charged ions in seven separate fields-of-view. Each field-of-view includes one detector for electrons and one detector for ions so that there are fourteen separate detectors in

all. Particles of different mass are not distinguished. The fields-of-view of the Lepedea and their orientations with respect to the PDP spin axis are shown in Figure 4. As can be seen in the figure, these fields-of-view form a fan which rotates with the spacecraft, thus providing excellent sampling of the possible particle trajectories.

A single instrument cycle for the Lepedea is 1.6 sec in duration and includes 0.2 sec of dead-time followed by a 1.4 sec energy sweep. Each sweep consists of forty-two 33-msec samples at a sequence of energies-per-charge which approximate a decreasing exponential. Because of the rotation of the PDP the fan of the Lepedea sweeps through 360 degrees in azimuth once every 13.1 sec. During each 1.6 sec instrument cycle the detectors sweep through 44 degrees of azimuth so that approximately 8 energy sweeps occur during each rotation. Figure 5 is a polar plot showing the azimuth angles of samples during a single spacecraft rotation. Radial distance in this plot is proportional to the logarithm of the center energy of the samples. Azimuthal resolution is improved by collecting data for more than one rotation. The samples are then sorted according to azimuth. In Figure 6 the azimuth angles of samples collected during 41 energy sweeps are shown, corresponding to .5 spacecraft rotations or a time period of 65.6 sec. For this situation, samples at a given center energy are separated by approximately 8 degrees in azimuth. Sampling of polar angles is fixed by the geometry of the detectors as shown in Figure 4.

Data Analysis

A useful quantity in the analysis of plasmas is the density of particles per unit volume, $\Delta x \Delta y \Delta z$, and per unit volume of velocity space, $\Delta v_x \Delta v_y \Delta v_z$. This density is known as the particle velocity distribution and is denoted functionally as $f(\vec{x}, \vec{v}, t)$. While the velocity distribution is, in general, a function of position, \vec{x} , and time, t , as well as velocity, \vec{v} , it is often written as simply $f(\vec{v})$.

When the velocity distribution of a group of particles is known, certain bulk properties of the particles can be determined such as the density per unit volume,

$$n = \int f(\vec{v}) dv_x dv_y dv_z \quad ,$$

the mean velocity,

$$\langle \vec{v} \rangle = \frac{1}{n} \int \vec{v} f(\vec{v}) dv_x dv_y dv_z \quad ,$$

or the mean kinetic energy,

$$\langle E \rangle = \frac{1}{n} \int \frac{1}{2} m v^2 f(\vec{v}) dv_x dv_y dv_z \quad ,$$

where the integrals are over all possible values of v_x , v_y , and v_z , and m is the mass of a single particle. The functional form of the velocity distribution is also important for the analysis of plasma

instabilities and waves [3]. In particular, multiply peaked distributions can drive plasma waves which in turn alter the particle velocity distributions.

The velocity distribution, $f(\vec{v})$, is related to the differential particle intensity or differential flux denoted by $j'(E)$. Consider the flux through a surface of unit area of particles with speeds within dv of v and coming from within the differential solid angle $d\Omega$ which is centered about the vector \vec{v} . This flux is given by

$$dj = vf(\vec{v})v^2dv d\Omega \quad .$$

Since $E = 1/2 mv^2$, we may also write

$$\begin{aligned} \frac{d^2j}{dEd\Omega} &= \frac{2}{m^2} Ef(\vec{v}) \quad , \quad \text{or} \\ j'(E) &= \frac{2}{m^2} Ef(\vec{v}) \quad , \end{aligned} \quad (1)$$

where $j'(E) = d^2j/dEd\Omega$.

If an ion plasma consists of more than one species of particle, as is generally the case, then there exist separate velocity distributions, $f_k(\vec{v}_k)$, for each species in the plasma, where the subscript k denotes the particle species. In this case,

$$j'(E) = \sum_k j'_k(E) \quad ,$$

where the summation includes a term for each species, and $E = \frac{1}{2} m_k v_k^2$.

Count rates observed by the Lepedea are proportional to the differential flux into the detectors. In the case of electrons, where only a single species is observed, the conversion to $f(\vec{v})$ is straightforward. In the case of positive ions, however, several species may be observed simultaneously. Because the Lepedea does not distinguish between ions of different mass, it is not possible to unambiguously deconvolve the f_k 's from the total flux $j'(E)$.

At times during the mission the ion flux into the Lepedea was of sufficient intensity to saturate the ion detectors. For these times it is not possible to determine the ion fluxes directly from the ion count rates. Ions impacting surfaces within the instrument, however, give rise to a flux of secondary electrons, and some of these electrons are observed by the electron detectors. Since the flux of secondaries is proportional to the ion flux, the observed electron count rate due to these electrons is proportional to the ion count rate. The constant of proportionality relating the rates is found by comparing the electron rates to the ion rates at times when the ion detectors are not saturated. The flux of secondary electrons is much less than the ion flux, so that when the ion detectors are saturated, the true ion rate can be deduced from the electrons. This analysis assumes that the electron counting rate remains proportional to the ion flux even when the ion detectors are saturated.

CHAPTER II

IONOSPHERIC IONS AND ION PICK-UP

During the PDP free flight, two different kinds of ion distributions are observed by the Lepedea. One of these distributions is due to ambient ionospheric ions which flow past the spacecraft with a velocity equal to $-\vec{v}_{sc}$. The other distribution is interpreted as ions created by the ionization of contaminant gases which co-orbit with the Orbiter. Before presenting these observations it is useful to discuss some of the processes which maintain the ionosphere. The goal of this discussion is to develop an understanding of the kinds of ion distributions which are to be expected at the 320 km altitude of the Orbiter.

Atmospheric Gases and Ionospheric Ions

Ionospheric ions are produced by the ionization of neutral atmospheric gases. At the altitude of the Orbiter the atmosphere is composed primarily of atomic oxygen, OI, molecular nitrogen, N₂, and molecular oxygen, O₂. The density of neutral gases in the ionosphere depends on the atmospheric temperature. Since the upper atmosphere is heated primarily by solar radiation, the temperature depends in turn upon the solar flux incident at Earth. The Spacelab-2 mission was accomplished during conditions approaching solar minimum when the

solar flux and hence the atmospheric temperature and densities were relatively low. Figure 7 shows the atmospheric temperature and the neutral-gas concentrations at the position of the spacecraft during the free flight, as predicted by the MSIS-83 atmospheric model [4]. Variations in temperature and density at the 90-minute period of the orbit are evident, due primarily to diurnal variations in the atmosphere. The dominant species is clearly OI, with a density ranging from 1×10^8 to $3 \times 10^8/\text{cm}^3$. The concentrations of N_2 and O_2 are lower than those for OI, but the amplitude of the diurnal variations is greater. The densities for these molecules range from 4×10^6 to $4 \times 10^7/\text{cm}^3$ for N_2 and from 2×10^5 to $2 \times 10^6/\text{cm}^3$ for O_2 .

Ion production and losses at 320 km are dominated by the reactions



where $h\nu$ and e^- denote photons and electrons respectively,





Reactions (2) through (7) and their associated rates are discussed in detail in reference [5] and are summarized in Table 1. The primary source of ions is photoionization of OI as described by reaction (2). The photoionization rate, I_{ν} , depends upon the flux of solar ultraviolet radiation. For solar-minimum conditions $I_{\nu} = 1.7 \times 10^{-7}/\text{sec}$ [5]. Reaction (3) refers to ionization of OI by energetic photoelectrons created in reaction (2). A sample photoelectron spectrum observed with the Lepedea during the free flight at 0208 UT is shown in Figure 8. The rate, I_e , for reaction (3) is determined by the cross section for electron impact ionization of OI [6] and by the spectrum of the photoelectrons. For the free flight this rate is calculated to be $I_e < 2 \times 10^{-8}/\text{sec}$, approximately 10 percent of the rate for photoionization. The neutral molecules N_2 and O_2 are also subject to photoionization and ionization by electron impact. These molecules, however, form ions more rapidly through reactions (4) and (5). These reactions are also the dominant mechanisms for removal of O^+ since direct recombination of O^+ with electrons is a slow process with a rate $\approx 10^{-12} \text{ cm}^3/\text{sec}$ [7]. The molecular ions NO^+ , and O_2^+ , on the other hand, recombine rapidly via the dissociative recombination processes (6), and (7) with the result that their net concentrations remain low compared to the concentration of O^+ .

The velocity distributions of ionospheric ions are Maxwellian with temperatures approximately equal to the temperature of the

neutral gas, i.e., $T_i = 1000$ °K. The thermal speeds of these ions are given by $C_i = [2kT_i/m_i]^{1/2}$, where m_i is the mass of the ions and k is Boltzmann's constant. This results in speeds of 1000 m/sec for O^+ ions and 700 m/sec for NO^+ and O_2^+ . The Orbiter and the PDP fly through the ionosphere with a speed approximately equal to V_{sc} , where V_{sc} is the orbital speed of these spacecraft, equal to 7800 m/sec. Because V_{sc} is much greater than C_i , in the reference frame of the spacecraft the ions form a narrow beam centered at a velocity equal to $-\vec{v}_{sc}$. The kinetic energies of these ions in the rest frame of the PDP are given approximately by $E = 1/2 m_i v_{sc}^2$, which predicts energies of 5 eV for O^+ ions and 10 eV for NO^+ and O_2^+ .

Reactions (2) through (7) lead to a set of first-order differential equations for the ion concentrations. Denoting the density of species X by $[X]$, these equations are written,

$$\frac{\partial}{\partial t} [O^+] = I[O] - \gamma_1[O^+][N_2] - \gamma_2[O^+][O_2] \quad (8)$$

$$\frac{\partial}{\partial t} [NO^+] = \gamma_1[O^+][N_2] - \alpha_1[NO^+][e^-] \quad (9)$$

$$\frac{\partial}{\partial t} [O_2^+] = \gamma_2[O^+] - \alpha_2[O_2^+][e^-] \quad (10)$$

$$[e^-] = [O^+] + [NO^+] + [O_2^+] \quad (11)$$

where the coefficient, I , in equation (8) is the combined rate for ionization of OI by solar radiation and energetic electrons. Equations (8) through (11) describe the major features of the ionospheric chemistry of interest for the present problem. By assuming steady-state conditions, these equations can be solved to give an estimate of the ambient ion densities to be expected at the 320 km altitude of the Orbiter.

If we assume a combined ionization rate $I = 1.9 \times 10^{-7}/\text{sec}$, and typical daytime atmospheric densities predicted by the MSIS-83 model of $[O] = 2.3 \times 10^8/\text{cm}^3$, $[N_2] = 2.1 \times 10^7/\text{cm}^3$, and $[O_2] = 7.3 \times 10^5/\text{cm}^3$, equations (8) through (11) yield ion densities of $[O^+] = 2.8 \times 10^6/\text{cm}^3$, $[NO^+] = 120/\text{cm}^3$, and $[O_2^+] = 240/\text{cm}^3$. The electron density is approximately equal to the density of O^+ , and this value is consistent with peak daytime electron densities $\sim 10^6/\text{cm}^3$ measured by the Langmuir probe aboard the PDP.

The velocity distributions of the ambient ions can be modeled by assuming Maxwellian velocity distributions of the form

$$f_i(\vec{v}) = n_i \left(\frac{m_i}{2\pi kT_i} \right)^{3/2} \exp \left[- \frac{m_i (\vec{v} - \vec{v}_{sc})^2}{2kT_i} \right] \quad (12)$$

The results of such modeling are shown in Figure 9. In that figure, the V axis is chosen so that it is parallel to \vec{v}_{sc} , and the ion densities are from the steady-state solution of equations (8) through (11). An ion temperature of 1000 °K is assumed. The distributions

peak at $V = -V_{SC}$. By applying equation (1), the differential flux due to these ions can be computed. The total flux, $j'(E)$, is shown in Figure 10 for the direction opposite to the vector \vec{v}_{SC} . This flux peaks at 5 eV corresponding to the orbital ram energy of the dominant species, O^+ . Fluxes at energies greater than 10 eV are due primarily to NO^+ and O_2^+ which have ram energies of approximately 10 eV.

Orbiter Gas Cloud and Ion Pick-Up

The Orbiter releases gases in several different ways as it flies through the ionosphere. Water, which is produced as a byproduct of the generation of electricity, is periodically dumped, and thrusters are fired frequently to change or correct the Orbiter attitude. The thrusters rely on a reaction between N_2O_4 and MMH (monomethyl hydrazine). This reaction is predicted to result in a complex set of products which include H_2O , N_2 , CO_2 , H_2 , H , and $MMH-NO_3$ [8]. In addition to these sources, outgassing from Orbiter surfaces and leakage from pressurized systems probably occur as well.

With the exception of the thrusters, these gases are released at a temperature approximately equal to the temperature of the Orbiter surface, about 300 °K, so that the thermal speed of the gas, C , is small compared to V_{SC} . The result is a cloud of gas which, in the reference frame of the Orbiter, expands slowly with a speed approximately equal to C . Thruster gases, on the other hand, are emitted with a high velocity relative to the Orbiter. Thruster firings have been observed on several shuttle flights by neutral mass spectrometers

and by plasma instruments, and the effects of the thrusters are seen to dissipate on a time scale on the order of seconds or less [8,9]. At times when the thrusters are inactive, neutral gases and ions which are not usually found in the upper atmosphere are still observed. The commonly observed species include H_2O , He, H_2O^+ , and H_3O^+ [10,11,12].

Gases co-orbiting with the Orbiter are subject to collisions with atmospheric gases, reactions with ionospheric ions, and ionization by solar ultraviolet radiation or by the impact of energetic photoelectrons. Collisions with the atmospheric constituents scatter and thermalize the molecules released from the Orbiter so that a trail of contaminants is left behind the spacecraft. Molecules which are ionized produce a distinctive velocity-space distribution, and can be detected by the Lepedea.

Consider the situation shown in Figure 11. A neutral molecule of mass m_1 moves in the X-Z plane with a velocity equal to \vec{v} . There is a magnetic field \vec{B} directed parallel to Z, and the components of \vec{v} perpendicular to \vec{B} and parallel to \vec{B} are $V_{\perp} = V \sin(\alpha)$ and $V_{\parallel} = V \cos(\alpha)$. The molecule is unaffected by the magnetic field, and has a trajectory which is a straight line as shown in Figures 11(a) and 11(b). At a time $t = t_0$ when the molecule is at a point A, the molecule is ionized by charge exchange or by absorbing an energetic photon, processes which have little effect on the momentum of the molecule. The newly formed ion experiences a Lorentz force $\vec{F} = q \vec{v} \times \vec{B}$, where q is the charge of the ion. The subsequent ion velocity, as a function of time, is given by

$$\vec{V}_1 = V_{\perp} \cos[\omega(t - t_0)]\hat{x} + V_{\perp} \sin[\omega(t - t_0)]\hat{y} + V_{\parallel}\hat{z} \quad , \quad (13)$$

where \hat{x} , \hat{y} , and \hat{z} are unit vectors in the X, Y, and Z directions. The ion motion is a combination of translation parallel to \vec{B} and gyration perpendicular to \vec{B} , resulting in a helical trajectory as shown in Figures 11(c) and 11(d). The radius of the helix is given by $R_g = m_i V_{\perp} / qB$ and the frequency of the gyration by $\omega_g = qB / m_i$.

Now consider a cloud of molecules co-orbiting with the Orbiter, as shown in Figure 12. If these molecules have thermal velocities which are small compared to V_{sc} , then in the rest frame of the ionosphere each molecule has a velocity given approximately by $\vec{v} = \vec{v}_{sc}$. The components parallel to and perpendicular to the Earth's magnetic field are $V_{\parallel} = V_{sc} \cos(\alpha)$ and $V_{\perp} = V_{sc} \sin(\alpha)$. A molecule which is ionized at $t = t_0$ will have a velocity given by

$$\begin{aligned} \vec{V}_1 = & V_{sc} \sin(\alpha) \cos[\omega(t - t_0)]\hat{x} + V_{sc} \sin(\alpha) \\ & \times \sin[\omega(t - t_0)]\hat{y} + V_{sc} \cos(\alpha)\hat{z} \quad . \end{aligned} \quad (14)$$

In the rest frame of the spacecraft the velocity is equal to

$$\vec{V}'_1 = \vec{V}_1 - \vec{v}_{sc} \quad ,$$

so that

$$\begin{aligned} \vec{v}'_i &= V_{sc} \sin(\alpha) \{ \cos[\omega(t - t_0)] - 1 \} \hat{x} \\ &+ V_{sc} \sin(\alpha) \sin[\omega(t - t_0)] \hat{y} \quad . \end{aligned} \quad (15)$$

In velocity space, equation (15) describes a circle of radius $v_{\perp} = V_{sc} \sin(\alpha)$. This circle lies in a plane perpendicular to \vec{B} and is centered at $v_x = -v_{\perp}$ as shown in Figure 13. The ion velocity ranges from zero to $-2 V_{sc} \sin(\alpha) \hat{x}$ resulting in a kinetic energy, $1/2 m_i v_i'^2$, which ranges between zero and $2 m_i V_{sc}^2 \sin^2(\alpha)$. The time average of this velocity is

$$\langle \vec{v}'_i \rangle_t = -v_{sc} \sin(\alpha) \hat{x} \quad ,$$

which is equal to the component of $-\vec{v}_{sc}$ projected into the plane perpendicular to \vec{B} . To an observer on the spacecraft, the ion appears to gyrate about a center which moves away from the spacecraft with a velocity equal to $\langle \vec{v}'_i \rangle_t$. If \vec{v}_{sc} and \vec{B} are perpendicular so that $\alpha = 90$ degrees, then $\langle \vec{v}'_i \rangle_t = -\vec{v}_{sc}$, and the center of gyration moves past the spacecraft with the same velocity as the ambient ionospheric ions. If $\alpha \neq 90$ degrees, then the velocities of flow of the ambient ions and the ions created from the co-orbiting gas cloud are not the same. For the case where $\alpha = 0$ degrees, the Lorentz force on the newly created ions is zero, so that these ions continue to co-orbit with the spacecraft until colliding with atmospheric gases.

If many molecules are ionized then, in the absence of other forces or collective effects, the resulting ion velocity distribution is ring shaped with a diameter equal to $2 V_{sc} \sin(\alpha)$. The ring lies in the plane perpendicular to \vec{B} and is centered at $V_x = -V_{sc} \sin(\alpha)$. In this discussion, the finite temperature of the contaminant gas has been neglected. A finite thermal spread in velocities would tend to give the ring a finite width. Also ignored are collective plasma effects resulting in waves which would alter the ion velocity distributions.

The ionization of a neutral gas moving transverse to a magnetic field is a process known as "ion pick-up" [13]. Velocity distributions resulting from this process have been observed in the solar wind as it interacts with cometary atmospheres [14,15] and helium of interstellar origin [16]. In these cases, however, the ions appear to have been scattered both in energy and in direction so that the ion velocity-space distributions form either a sphere or a spherical shell rather than a ring.

CHAPTER III
OBSERVATIONS

Figure 14 is a plot of the differential ion flux from the direction of orbital motion, i.e., along $-\vec{v}_{SC}$, on August 1 of 1985 at 0208 UT. At this time the PDP is at a distance of 280 m from the Orbiter, and the angle between \vec{B} and \vec{v}_{SC} is 86 degrees. The spectrum shown in Figure 14 peaks at an energy-per-charge < 5 V. This peak saturates the ion detector in which it is observed and the fluxes for this peak are derived from the electron count rates as discussed in Chapter I. A secondary peak is observed at an energy-per-charge ≈ 18 V, while between 20 V and 60 V the spectrum gradually decreases, and at 60 V drops sharply by almost two orders of magnitude.

The low energy peak is due to ambient ionospheric ions that flow past the spacecraft with a velocity equal to $-\vec{v}_{SC}$, as discussed in Chapter II. These ions are expected to have energies approximately equal to $1/2 m_i v_{SC}^2$. For atomic oxygen ions this corresponds to an energy of 5 eV which is consistent with the observed energy of the peak. Because this ion distribution is so sharply peaked, it cannot be properly resolved by the Lepedea so it is not possible to make estimates of either the density or the temperature of these thermal ions from the observations.

For singly charged ions, the higher energy peak is at an energy = 18 eV. This energy is somewhat lower than the maximum energy of water-group ions (i.e., OH^+ , H_2O^+ , H_3O^+) picked up from a cloud of gases moving with the Orbiter. The maximum energy of H_2O^+ picked up from such a cloud is 23 eV, 22 percent higher than the energy of the observed peak. Water and water ions, however, are observed to be the predominant contaminants in the near vicinity of the Orbiter [10,11], and H_2O^+ was observed throughout the free flight by the ion mass spectrometer aboard the PDP [12]. In addition, the velocity-space contours of the ion velocity distribution, shown in Figures 15 and 16 and discussed below, indicate that these ions are pick-up ions. The contours show that the peak at 18 V is actually a cross section through an extended ring-like distribution rather a single localized peak. This kind of distribution is consistent with pick-up ions, but not with ambient ionospheric ions which have a distribution that forms a single well-defined peak. For these reasons, the secondary maximum observed at 18 V is interpreted as water ions gyrating about Earth's magnetic field with a speed approximately equal to the orbital speed of the spacecraft. The discrepancy between the observed energy of these ions and the expected energy may be due to the mechanism by which neutral water is ionized, or may be caused by collective plasma processes after the ions are formed.

Neutral water molecules in the vicinity of the Orbiter are subject to charge exchange with ionospheric O^+ resulting in H_2O^+ ions and neutral OI . As will be shown in Chapter IV, this process is the

dominant mechanism for ionization of H_2O at the altitude of the Orbiter. Charge exchange reactions generally proceed with little exchange of momentum between the interacting particles, however, some momentum transfer can occur [17]. The fact that the ions observed by the Lepedea have an energy somewhat lower than expected may be an indication that some momentum transfer does occur or that some of the kinetic energy of the H_2O molecule is converted to internal energy during the charge exchange process. An alternative explanation is that the H_2O^+ ions lose energy through wave-particle interactions. The spectrum of Figure 14 clearly shows a multiply peaked distribution, and such distributions are known to be unstable to the generation of plasma waves. An instability arising from this distribution could alter the velocity distribution of the plasma and might be the reason why the H_2O^+ ions are observed at an energy which is lower than the energy predicted by the simple arguments presented in Chapter II.

Ions with energy greater than 20 eV are also shown in Figure 14. The broad plateau-like region between 20 V and 60 V is also a cross section through an extended distribution, and is probably due to the pick-up of ions with masses greater than 18 AMU. It is interesting to note that CO_2 , which is predicted to be one of the contaminants produced by thrusters, would have a maximum pick-up energy of 55 eV, which corresponds closely to the cut-off energy of the spectrum of Figure 14.

Figure 15 displays contours of constant $f(\vec{v})$ at 0208 UT in the velocity-space plane containing V_x and V_y . This plane is

perpendicular to the magnetic field which lies along the V_z axis. The projection of \vec{v}_{sc} into this plane lies along the V_x axis, and for this case \vec{v}_{sc} is out of the plane by only 4 degrees. To calculate \vec{v} and $f(\vec{v})$, a mass of 16 AMU corresponding to the mass of O^+ ions is assumed. For water ions, which have a mass of 18 AMU, the contours are approximately accurate. For more massive ions, however, the contours and velocities should be recomputed. The outermost contour in Figure 15, which crosses the V_x axis at -2.9×10^6 cm/sec, corresponds to $f = 10^{-19}$ sec³/cm⁶. Successive interior contours increase in value by factors of 10. The maximum in f near $V_x = -0.8 \times 10^6$ cm/sec is the signature of the ambient ionospheric ions. The maximum seen in the energy spectrum of Figure 14 at 18 V is represented in Figure 15 by the contour which crosses V_x at -1.5×10^6 cm/sec. This contour and adjacent contours are nearly circular and similar in placement and shape to the velocity-space trajectory of a single ion picked up by a magnetic field (Figure 13). The low-energy threshold of the Lepedea is 2 V corresponding to a speed of 0.5×10^6 cm/sec, so the region near the origin where these circular contours would be expected to close is not accessible to observation. To demonstrate that the distribution is ring-like rather than spherical, it is necessary to look at the distribution in a plane perpendicular to the plane of Figure 15.

Figure 16 is a second contour plot, also at 0208 UT, but for the plane containing V_x and V_z . The magnetic field is parallel to the V_z axis, and this plane is perpendicular to the plane of Figure 15.

From this figure and Figure 15, it is clear that the extent of the distribution parallel to \vec{B} is much less than in the direction perpendicular to \vec{B} . With the exception of the three innermost contours near $V_x = -0.8 \times 10^6$ cm/sec that are due to the ionospheric ions, the velocity-space contours show a broad distribution that occupies a ring-like or disk-like region of velocity space, with the plane of the disk lying perpendicular to the magnetic field. As discussed in Chapter II, this is consistent with the type of distribution expected for pick-up ions. For the distribution shown in Figures 15 and 16, however, the ring-like nature of the pick-up ion distribution is partially obscured by the ambient ions which fill the center of the ring.

When \vec{B} and \vec{V}_{SC} are not perpendicular, the plane of the ring remains perpendicular to \vec{B} , however the diameter of the ring, which is proportional to $\sin(\alpha)$, decreases. The ambient ionospheric ions, on the other hand, always lie in a direction opposite to \vec{V}_{SC} , so that in general they do not lie in the plane of the ring. A distribution that demonstrates this behavior is observed at 0237 UT when \vec{B} and \vec{V}_{SC} are at an angle of 125 degrees.

Figure 17 shows the differential ion flux along the $-V_x$ axis at 0237 UT. At this time the angle between the V_x axis and \vec{V}_{SC} is equal to 35 degrees. In this figure the low-energy peak, seen in Figure 14 at an energy-per-charge < 5 V, is absent. This is as expected since that peak is due to ambient ionospheric ions which have velocities approximately equal to $-\vec{V}_{SC}$, and the vector \vec{V}_{SC} no longer lies along the V_x axis. The higher energy peak is still present, but has

decreased in energy to an energy-per-charge of 12 V. This peak is a cross section through the ring, and this decrease in energy is consistent with the expectation that the diameter of the ring should shrink as $\sin(\alpha)$ decreases.

Contours of constant $f(\vec{v})$ are shown in Figure 18 for the plane perpendicular to \vec{B} . As in Figure 15, the contours are ring-like, however in this case, the distribution has a smaller diameter. Also, the distribution decreases near $v_x = -0.8 \times 10^6$ cm/sec due to the fact that the distribution of ambient ionospheric ions is no longer centered in this plane. The two innermost contours in Figure 18 correspond to the same value, $f = 10^{-16}$ sec³/cm⁶, and the region of velocity space interior to the innermost contour is a slight depression in $f(\vec{v})$ rather than a peak. This is shown more clearly in Figure 19 which is a cross section through both the ring and the distribution of ionospheric ions.

Figure 19 displays the contours in the v_x, v_z plane. The dashed line in this figure is parallel to \vec{v}_{sc} . It is clear from this figure that the ambient ions have been "lifted" from the plane of the ring. The ionospheric ions lie along the direction opposite to \vec{v}_{sc} while the rest of the distribution, which is due to pick-up, remains in the plane perpendicular to \vec{B} . Again, this is as expected and helps confirm the identification of the separate pick-up ion and ambient ion distributions.

Distributions similar to those discussed above were observed throughout the free flight, indicating that the contaminant ions reach

at least as far as the maximum distance of the PDP from the Orbiter, 400 m. The essentially ring-like nature of the pick-up ion distributions indicates that these ions follow trajectories which are generally consistent with the single-particle motion of ions created from a cloud of gas moving with the Orbiter. The energy at which the contaminant distribution peaks is somewhat lower than the energy expected of water ions formed from such a cloud. This may be due to the charge-exchange process through which the ions are formed, or to an instability associated with the ion velocity distribution. The identification of these ions as water ions is consistent with measurements made by the ion mass spectrometer on the PDP and with observations of neutral H_2O and H_2O^+ ions on other Shuttle flights. Heavier ions appear to be present as well, but in lower concentrations than H_2O^+ . The density of heavy ions is estimated to be less than ten percent of the density of H_2O^+ . The distributions have a finite spread both in energy and in pitch angle, α . These features may be due to the finite temperature of the source cloud, or they may indicate that the ions are scattered by either plasma waves or collisions. However, it is clear that scattering has not progressed to such an extent that the ion distributions have become isotropic, forming a spherical shell or filled sphere in velocity space.

The observed pick-up ion distributions can be integrated numerically to obtain a quantitative estimate of the density of these ions. To determine the density of the pick-up ions, it is necessary to remove the contribution from the ionospheric ions. Also, part of

the pick-up distribution lies below the low-energy threshold of the detectors, and it is also necessary to account for this unobserved portion of the distribution. The ionospheric ions are eliminated by removing from the integration a spherical region of velocity space centered at the velocity of the ambient-ion peak. The diameter of this sphere is chosen to be large enough to remove the bulk of the ambient ions, but not so large as to include a significant part of the pick-up distribution. The unobserved part of the pick-up distribution is accounted for in the following way. Rather than attempt to integrate the entire distribution, only that part which is at $V_x < -V_{sc} \sin(\alpha)$ is included in the integration. This accounts for half of the ring, and the resulting density is multiplied by a factor of two to account for the rest. This procedure could lead to a significant error if a large fraction of the pick-up ions are bunched at a given phase rather than spread out gyrotropically about the ring. Bunches of this sort, however, are not clearly observed in the data, and therefore do not appear to be significant for the distributions observed during the free flight. The pick-up densities calculated in this way at 0208 UT and 0237 UT are $490/\text{cm}^3$ and $210/\text{cm}^3$.

CHAPTER IV

MODELING

A number of simplifying assumptions are made about the processes affecting the contaminant molecules and ions surrounding the Orbiter. These assumptions are incorporated into a model which predicts spatial and temporal variations in the density of the contaminant ions at the position of the PDP. The rate at which the Orbiter releases neutral gas is a free parameter in this model, and an estimate of this rate is obtained by normalizing the modeled pick-up densities to the densities measured by the Lepedea.

The Orbiter's Gas Cloud

In order to model the pick-up of ions it is first necessary to develop a model of the cloud of gases which is their source. To simplify the chemistry, only H_2O molecules are included in this model. As discussed in Chapter III, water and water ions have been observed to be the dominant contaminant species near the Orbiter, and the energy spectrum of ions observed by the Lepedea is consistent with these observations. Therefore, it is expected that the major features of the gas and ion clouds can be reproduced by considering H_2O to be the only molecule released. The water is assumed to leave the Orbiter with a temperature of 300 °K, the approximate temperature of the

Orbiter surfaces. The density of the resulting water cloud is assumed to be low enough that collisions between the water molecules are unimportant. The shape of the Orbiter is fairly complicated, and the actual source of the water is unknown. To simplify, the contaminant cloud is modeled as radial flow from a spherically symmetric source with a radius $R_0 = 10$ m, the approximate linear dimension of the Orbiter. The gas expands radially with a speed relative to the Orbiter of $C = 525$ m/sec corresponding to the thermal speed of H_2O at 300 °K.

The cloud is shaped by collisions with the ambient atmospheric gases, predominantly OI. The mean free path for such collisions is $\lambda = 1/(n_g \sigma)$, where n_g is the atmospheric density, and σ is the cross section for the collisions. The cross section for collisions between OI and H_2O is not known but can be estimated assuming diameters of 4.6×10^{-8} cm for H_2O and 2.6×10^{-8} cm for OI [17], where the diameter of OI is assumed to be equal to the diameter of Ne. Using these diameters, and assuming hard-sphere collisions leads to an estimate of $\sigma = 4 \times 10^{-15}$ cm². Since $C \ll V_{sc}$, the water molecules have a velocity relative to the atmosphere approximately equal to \vec{v}_{sc} , and the mean collision time is given approximately by $\tau = \lambda/V_{sc}$. Relative to the Orbiter, then, these gas molecules travel a distance $d = C\tau = C\lambda/V_{sc}$ before colliding with the atmosphere. The parameter d is an "effective" mean free path which is also a measure of the scale of the cloud. The effect of collisions is to transfer momentum from the atmospheric gases to the water. Assuming hard-sphere elastic

collisions, approximately 90 percent of all such collisions result in H₂O molecules with speeds > 5 C relative to the Orbiter. Therefore, these molecules are rapidly scattered away from the spacecraft. The density of contaminant molecules that have not suffered collisions can be derived in an approximate way from the equation of continuity by assuming that losses are proportional to the flux of atomic oxygen molecules through the cloud and that the flux of atomic oxygen is unperturbed by the collisions. This approximation is valid so long as the mean free path for collisions in the cloud remains greater than the dimension of the cloud. The equation of continuity may be written

$$\frac{\partial n}{\partial t} + \vec{\nabla} \cdot (n\vec{C}) = L \quad , \quad (16)$$

where L represents the losses due to collisions, n is the density of H₂O, and \vec{C} is the radial velocity of expansion of the cloud in a frame of reference centered on and moving with the Orbiter. The loss term L may be written

$$L = - nV_{sc}n_a\sigma = - \frac{nV_{sc}}{\lambda} \quad .$$

In spherical coordinates, and assuming steady-state conditions so that $\partial n/\partial t = 0$, equation (16) may be written as

$$\frac{1}{r^2} \frac{\partial}{\partial r} (r^2 n C) = - \frac{n V_{sc}}{\lambda} .$$

The derivatives on the left-hand side of this equation are evaluated and the equation rearranged algebraically to yield

$$\frac{1}{n} \frac{\partial n}{\partial r} = - \frac{2}{r} - \frac{V_{sc}}{\lambda C} .$$

The solution may be written

$$n(r) = n(R_0) \frac{R_0^2}{r^2} \exp\left[- \frac{(r - R_0)}{d}\right] , \quad (17)$$

where $d = C\lambda/V_{sc}$ is the "effective" mean free path which has already been predicted through qualitative arguments. This equation is valid for $r > R_0$, $C \ll V_{sc}$, and for a cloud of water that does not significantly affect the flow of OI through the cloud. It can be seen from equation (17) that if there are no collisions with the atmosphere, then d becomes infinite and the density of water within the cloud varies as $1/r^2$, a result which can be obtained directly by setting the loss term, L , in equation (16) to zero. The constant $n(R_0)$ may be rewritten in terms of the rate at which gas escapes the spherical surface at R_0 . This rate, \dot{N} , is given by

$$\dot{N} = 4\pi R_0^2 n(R_0) C \quad .$$

Equation (17) is used to model the H₂O cloud from which H₂O⁺ ions are created. The goal of the model is to account for the H₂O⁺ ion densities observed by the PDP. Water molecules that have collided with the atmosphere are scattered away from the spacecraft. Since these molecules have speeds relative to the spacecraft which are much greater than C, they disperse rapidly. Therefore, the principal contribution to the distribution of pick-up ions observed by the PDP is expected to be water molecules that have not yet suffered collisions. The validity of equation (17) is probably somewhat better ahead of the Orbiter than behind, since collisions generally scatter the H₂O into the region behind the Orbiter. The actual density of water within the cloud, however, is probably no greater than it would be in a collisionless cloud, and during the PDP free flight the density predicted by equation (17) varied from the density within a collisionless cloud by no more than a factor of two.

Ionization and Losses

Possible sources for ionization of H₂O at Orbiter altitudes include photoionization by solar ultraviolet radiation, ionization caused by the impact of energetic photoelectrons, and charge exchange with O⁺ ions through the reaction



Momentum transfer during the charge exchange process is small [15], so that an H_2O^+ ion created in this way initially has a velocity about the same as the neutral H_2O molecule. Of these three processes, reaction (18) dominates and the other two processes can be neglected by comparison. To see that this is so, it is possible to estimate the ionization rates for photoionization and electron impact ionization. The ionization potential of H_2O is 12.6 eV which corresponds to a photon wavelength of 986 Å. The solar flux between 2 Å and 1000 Å for low-average solar conditions can be computed from the tables in reference [5] to be $< 5 \times 10^{10}/\text{cm}^2 \text{ sec}$. The photoionization cross section between 400 Å and 1000 Å has been measured by Wainfan et al. [18] to be $< 2.5 \times 10^{-17} \text{ cm}^2$. If it is assumed that this represents an upper limit to the cross section for the entire range of wavelengths then the photoionization rate is $< 10^{-6}/\text{sec}$. The rate for ionization of H_2O by electron impact is calculated using the observed spectrum of energetic photoelectrons and the measured cross section for this process [19]. For the free flight this rate is calculated to be less than $1.5 \times 10^{-8}/\text{sec}$, about the same as the rate for electron impact ionization of OI. The cross section for charge exchange between H_2O and O^+ for the 5 eV energy of O^+ ions relative to the cloud appears uncertain. Measured cross sections for this reaction range from $0.6 \times 10^{-15} \text{ cm}^2$ to $2.6 \times 10^{-15} \text{ cm}^2$ [20,21]. We adopt the cross section measured by Turner and Rutherford [21] which is equal to $2.6 \times 10^{-15} \text{ cm}^2$. This value is a factor of two lower than the cross section for charge exchange for H_2^+ incident on H_2O at an energy of

30 eV [22]. For a relative velocity of 7.8×10^5 cm/sec, this cross section leads to a reaction rate $\gamma_3 = 2 \times 10^{-9}$ cm³/sec. If it is assumed that this value is a reasonable estimate of the reaction rate for reaction (18), then for typical ionospheric O^+ densities ranging from 10^4 to 10^6 /cm³, the rate for ionization of H_2O by charge transfer with O^+ can be estimated to be between 2×10^{-5} and 2×10^{-3} /sec, much faster than the estimated rates for either photoionization or electron impact ionization.

Water ions can be lost through dissociative recombination with electrons



or through an ion-molecule reaction with neutral H_2O



The H_3O^+ ions resulting from reaction (20) may recombine with electrons



The reaction rates for reactions (19) and (21) are $\alpha_3 = 1.7 \times 10^{-7}$ cm³/sec and $\alpha_4 = 1.9 \times 10^{-7}$ cm³/sec, respectively [23]. For

reaction (20), the kinetic energy of the H_2O^+ relative to the H_2O cloud ranges from zero to approximately 23 eV, due to the fact that these ions are gyrating about the magnetic field. The rate used in the model is the rate at 300 °K which is $\gamma_4 = 1.7 \times 10^{-9} \text{ cm}^3/\text{sec}$ [24]. The reactions involving H_2O , H_2O^+ , and H_3O^+ that are included in the model are summarized in Table 2.

Reactions (19) through (21) lead to a pair of differential equations for the concentrations of H_2O^+ and H_3O^+ . These equations are

$$\begin{aligned} \frac{\partial}{\partial t} [\text{H}_2\text{O}^+] &= \gamma_3[\text{H}_2\text{O}][\text{O}^+] - \gamma_4[\text{H}_2\text{O}^+][\text{H}_2\text{O}] \\ &\quad - \alpha_3[\text{H}_2\text{O}^+][\text{e}^-] \end{aligned} \quad (22)$$

$$\frac{\partial}{\partial t} [\text{H}_3\text{O}^+] = \gamma_4[\text{H}_2\text{O}^+][\text{H}_2\text{O}] - \alpha_4[\text{H}_3\text{O}^+][\text{e}^-] \quad (23)$$

Equations (22) and (23) are solved numerically with a fifth-order Runge-Kutta routine. As discussed in Chapter II, the pick-up ions leave the water cloud with a time-averaged velocity equal to $-\vec{v}_\perp$. To account for this motion the equations are solved in a reference frame that is at rest with respect to the instantaneous center of gyration of the pick-up ions.

Consider the geometry shown in Figure 20. The coordinate system used in the model is one in which the V axis points along \vec{v}_{sc} and the vector \vec{R} from the Orbiter to the PDP lies in the plane defined

by V and W. Integration of equations (22) and (23) is performed at the point P which, sliding along the field line \vec{B} with velocity $\vec{v}_\parallel = \vec{v}_{sc} \cdot \vec{B}/B$, intercepts the PDP at time $t = t_0$. The density of H_2O at P is found from equation (17) with $r(t) = |\vec{R} + \vec{v}_\perp(t_0 - t)|$. In practice, the integration is started at a time $t = 0$ when P is sufficiently far from the center of the water cloud that the density of H_2O at P is approximately zero. The fact that the ions have a finite radius of gyration of about 30 m is neglected.

CHAPTER V
MODEL RESULTS

Pick-up ion densities measured during the free flight and densities calculated from the model are shown in Figure 21. Also shown in this figure are the angle, θ , between \vec{R} and \vec{V}_{sc} and the distance, R , between the two spacecraft. The angle θ is an indication of whether the PDP is ahead of or behind the Orbiter. The Orbiter's thrusters are not fired during any of the density measurements shown in Figure 21. Most of the calculations are performed assuming that the density of O^+ is equal to the density of electrons measured with the Langmuir probe, however, between 0232 and 0250 UT and between 0405 and 0422 UT reliable Langmuir probe sweeps are not available and the O^+ density is assumed to be $10^4/\text{cm}^3$. Poor agreement between the model and the data for the first of these intervals may be due to O^+ densities which are higher than have been assumed. The density of H_2O at 10 m from the Orbiter is a free parameter in the model and has been chosen by normalizing the model results to the data for the peak near 0350 UT. This normalization yields a density of H_2O at R_0 equal to $3.8 \times 10^{10}/\text{cm}^3$ and a corresponding water release rate of $\dot{N} = 2.5 \times 10^{22}/\text{cm}^3 \text{ sec}$. If this rate is constant for the entire eight-day mission, a total of 500 kg of water is released. The integrated column density for the cloud is $\approx 4 \times 10^{13}/\text{cm}^2$. This can be compared

to maximum column densities inferred from neutral mass spectrometer measurements from within the Orbiter's bay during the STS-2, STS-3, and STS-4 missions [25]. These column densities range from 1.5×10^{11} to $3.2 \times 10^{13}/\text{cm}^2$. For these flights, the measured water densities are largest at the beginning of the flight, and decrease with a time constant of approximately 10 hours.

It should be noted that the density of the neutral water cloud inferred from the model is inversely proportional to the cross section for charge exchange between O^+ and H_2O . If the actual cross section is a factor of five lower than the value estimated in Chapter IV, then the density of H_2O inferred from the model would be a factor of five higher than the estimate discussed above.

Because the water density near the Orbiter is so high, approximately two orders of magnitude greater than n_a at R_0 , the assumption that the fluxes of OI and O^+ through the cloud are unperturbed is probably not correct for distances from the Orbiter < 50 m, or in the region directly behind the Orbiter. Directly behind the Orbiter these assumptions are not satisfied in any case because the Orbiter itself obstructs the flow and is known to produce a plasma wake [26]. Between 0420 UT and 0500 UT the PDP traversed the region directly behind the Orbiter, and the divergence of modeled and measured densities during this time may be due to the wake of the Orbiter or to a depletion of O^+ near the dense center of the cloud. Between 0115 and 0130 UT, however, the PDP was also in this near-downstream region and the agreement during this time period appears to be quite good. The

fit to the model is also poor between 0310 and 0330 UT. This may be due to a variation in the water release rate or to difficulties integrating the observed distributions to obtain the density. During this time period the angle α between \vec{B} and \vec{V}_{SC} becomes relatively small, ranging from 30 to 60 degrees. When this occurs it is difficult to remove the ambient ions from the integration without removing a significant part of the pick-up ion distribution as well.

Despite the discrepancies at the times mentioned above, the modeled and observed densities are in good qualitative agreement, and for some portions of the free flight the model provides a good quantitative fit to the data as well. We note that the agreement is also good near the first and second sunrise of the free flight even though a variation in the rate of release of water might be expected at these times, when Orbiter surfaces are suddenly exposed to sunlight.

As can be seen in Figure 21, the variation in density of the pick-up ions ranges over more than two orders of magnitude. Much of this is due to variations in the ionospheric plasma density, since the rate of pick-up is proportional to $[O^+]$. The position of the PDP relative to the spacecraft, however, is also important. In Figure 22 the calculated densities of the H_2O cloud and of H_2O^+ and H_3O^+ pick-up ions are shown along an axis parallel to the V axis of Figure 20 but displaced 50 m from the center of the cloud. For this calculation, \vec{B} and \vec{V}_{SC} are taken to be perpendicular and typical daytime densities of $[OI] = 2.3 \times 10^8/cm^3$ and $[O^+] = 4.3 \times 10^5/cm^3$ are assumed. The scale

length, d , of the H_2O cloud is equal to 714 m. In the region ahead of the Orbiter the H_2O^+ density generally follows the density of H_2O , but is five orders of magnitude lower. The formation of H_3O^+ is proportional to the densities of H_2O^+ and H_2O , so that $[H_3O^+]$ becomes significant only near the center of the cloud where $[H_2O]$ and $[H_2O^+]$ are relatively large. Behind the Orbiter $[H_2O^+]$ and $[H_3O^+]$ remain approximately constant. This happens because the ions are transported downstream with a velocity equal to $-\vec{v}_{SC}$, and are many kilometers behind the spacecraft before recombination occurs.

The density of the H_2O cloud falls off as

$$\frac{1}{r^2} \exp\left[-\frac{(r - R_0)}{d}\right],$$

where d is proportional to $1/(n_a \sigma)$. Therefore, changes in n_a , the atmospheric density, affect the density of the neutral water cloud and hence the density of the pick-up ions as well. Figure 23 is similar to Figure 22, but is calculated for an atmospheric density five times higher than the density used for the calculation of Figure 22. This density would be observed at an altitude of 270 km, 50 km lower than the altitude of the free flight, during moderate solar conditions. In this case, the scale length of the water cloud is only 143 m, and the density of water ions falls below $1/cm^3$ at a distance approximately 700 m upstream from the Orbiter.

The dependence of the pick-up densities on the angle between \vec{B} and \vec{V}_{SC} is illustrated in Figure 24. This figure shows a calculation of $[H_2O^+]$ and $[H_3O^+]$ along the same axis as in Figures 22 and 23, but for the case where the angle α between \vec{B} and \vec{V}_{SC} is equal to 60 degrees. The densities of OI and O^+ are the same as in Figure 22. Upstream, the pick-up densities are approximately the same as for the case of Figure 22. However, behind the Orbiter the ion density drops rapidly as a consequence of the transport of the pick-up ions along the magnetic field. This transport speed is equal to $V_{SC} \cos(\alpha)$, so the further α is from 90 degrees, the higher the speed of transport. Limiting cases of $\alpha = 0^\circ$ and $\alpha = 180^\circ$ would result in pick-up ions which flow along the field with speed V_{SC} . In these cases, the ions would co-orbit with the spacecraft and would be removed only by recombination with electrons or collisions with the atmosphere. For the Spacelab-2 mission, $30^\circ < \alpha < 150^\circ$, so these cases are not observed.

Table 1. Ionospheric Reactions

Reaction	Rate
$O + h\nu \rightarrow O^+ + e^-$	$I_\nu = 1.7 \times 10^{-7}/\text{sec}$
$O + e^- \rightarrow O^+ + 2e^-$	$I_e = 2 \times 10^{-8}/\text{sec}$
$N_2 + O^+ \rightarrow NO^+ + N$	$\gamma_1 = 1.2 \times 10^{-12}(300/T) \text{ cm}^3/\text{sec}$
$O_2 + O^+ \rightarrow O_2^+ + O$	$\gamma_2 = 2 \times 10^{-11}(300/T)^{1/2} \text{ cm}^3/\text{sec}$
$NO^+ + e^- \rightarrow N + O$	$\alpha_3 = 4.2 \times 10^{-7}(300/T_e) \text{ cm}^3/\text{sec}$
$O_2^+ + e^- \rightarrow O + O$	$\alpha_2 = 2.2 \times 10^{-7}(300/T_e)^{(0.7 \text{ to } 1.0)} \text{ cm}^3/\text{sec}$

Note: The symbols T and T_e in the expressions for the rates refer to the temperatures of the gas and the electrons, respectively.

Table 2. Model Reactions

Reaction	Rate
$\text{H}_2\text{O} + \text{O}^+ \rightarrow \text{H}_2\text{O}^+ + \text{O}$	$\gamma_3 = 5 \times 10^{-9} \text{ cm}^3/\text{sec}$
$\text{H}_2\text{O}^+ + \text{e}^- \rightarrow \text{OH} + \text{H}$	$\alpha_3 = 1.7 \times 10^{-7} \text{ cm}^3/\text{sec}$
$\text{H}_2\text{O}^+ + \text{H}_2\text{O} \rightarrow \text{H}_3\text{O}^+ + \text{OH}$	$\gamma_4 = 1.7 \times 10^{-9} \text{ cm}^3/\text{sec}$
$\text{H}_3\text{O}^+ + \text{e}^- \rightarrow \text{products}$	$\alpha_4 = 1.9 \times 10^{-7} \text{ cm}^3/\text{sec}$

D-386-644-1

PDP BOOMS DEPLOYED CONFIGURATION

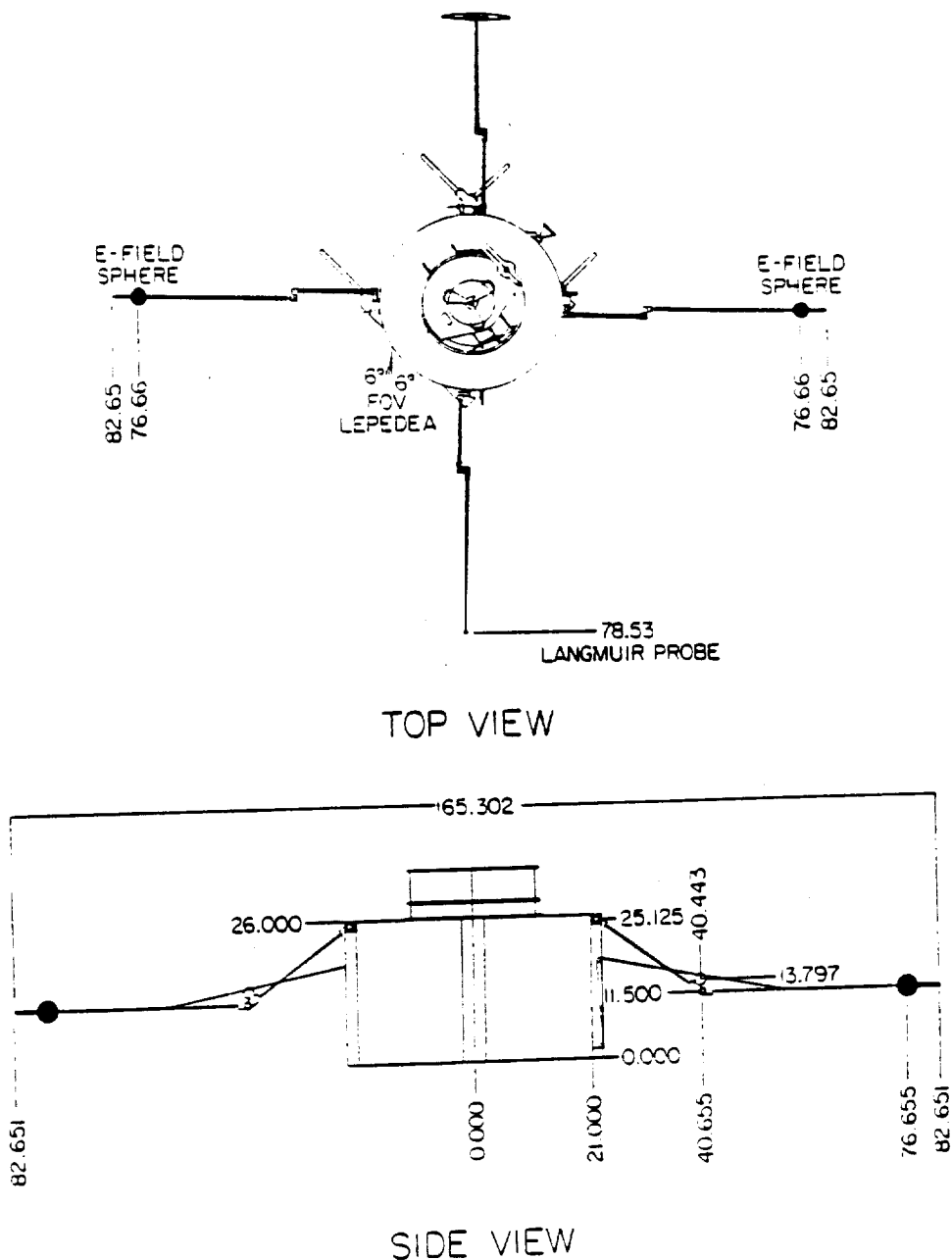


Figure 1. Top and side views of the PDP with the booms deployed as in free flight. Distances are in inches.

A-G87-195

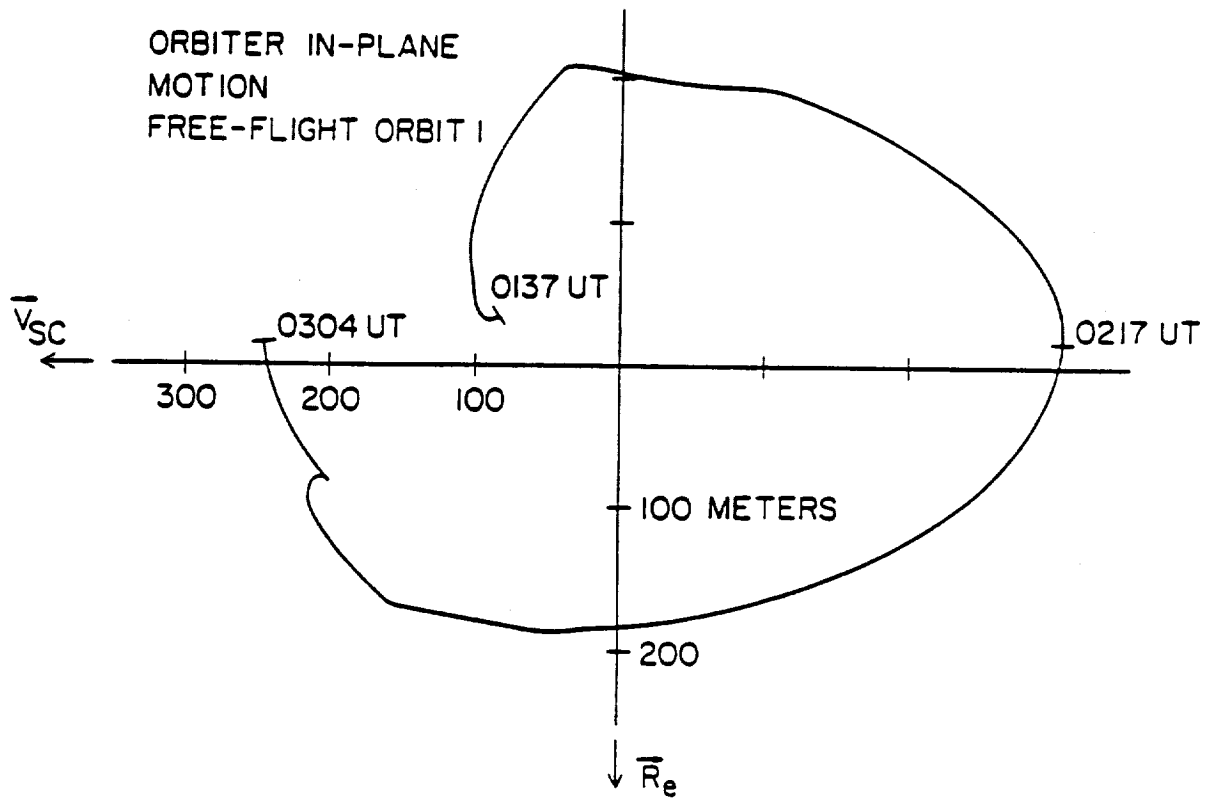


Figure 2. Orbital-plane motion of the Orbiter relative to the PDP between 0137 and 0304 UT.

A-G87-196

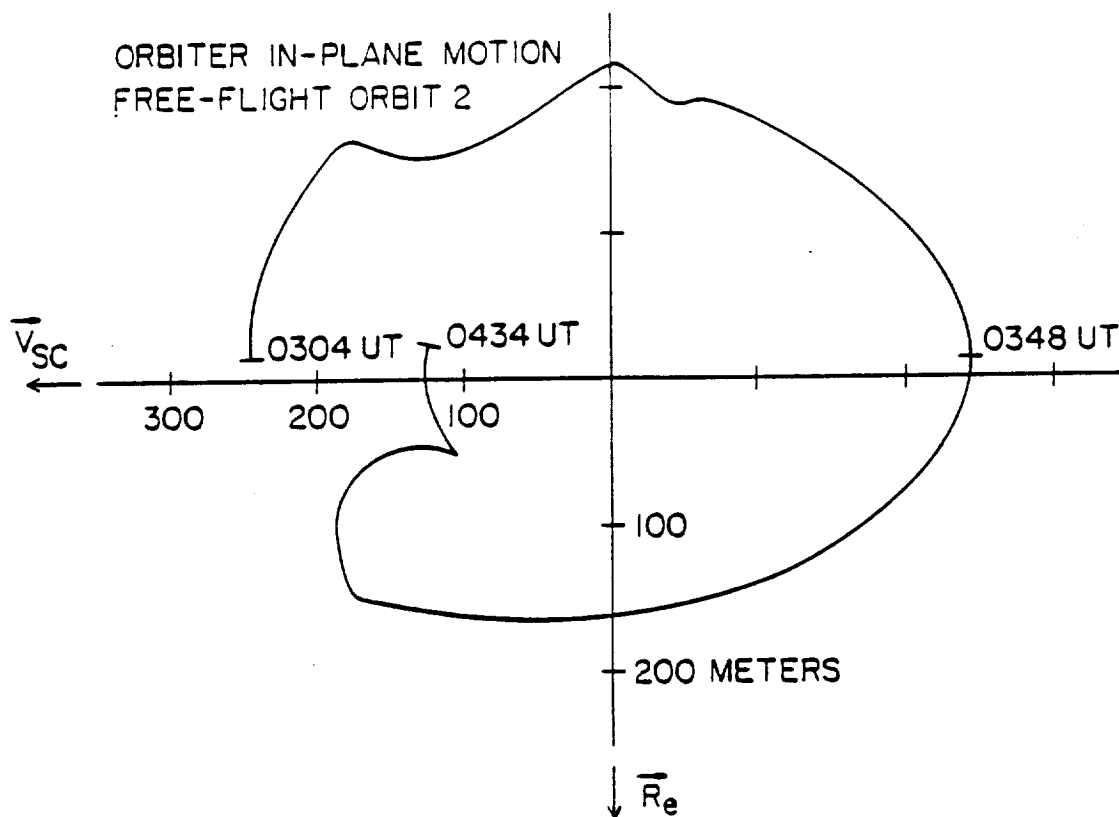


Figure 3. Orbital-plane motion of the Orbiter relative to the PDP between 0304 and 0434 UT.

A-G87-214

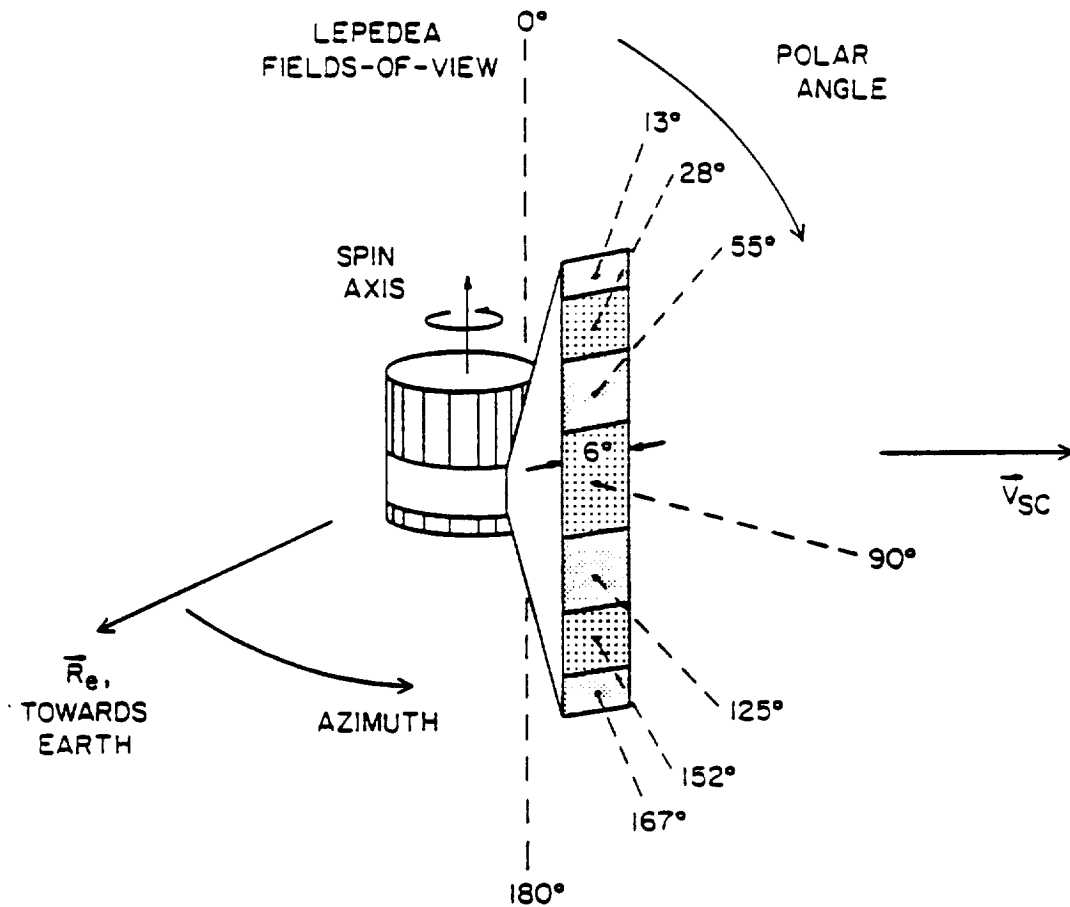


Figure 4. Relative orientations of \vec{R}_e , \vec{V}_{sc} , the PDP spin axis, and the fields-of-view of the Lepedeo (adapted from Frank [2]).

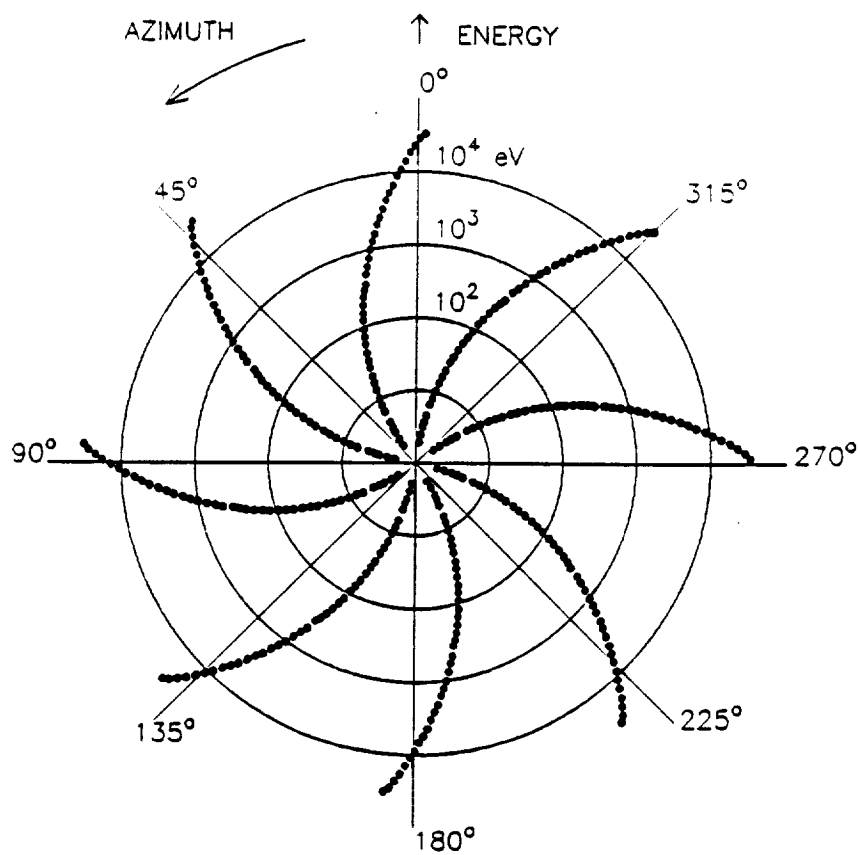


Figure 5. Polar plot showing the azimuth angles of samples from the Lepedeidae during eight consecutive energy sweeps for a spin period of 13.1 sec. Radial distance is proportional to the logarithm of the energy of the sample.

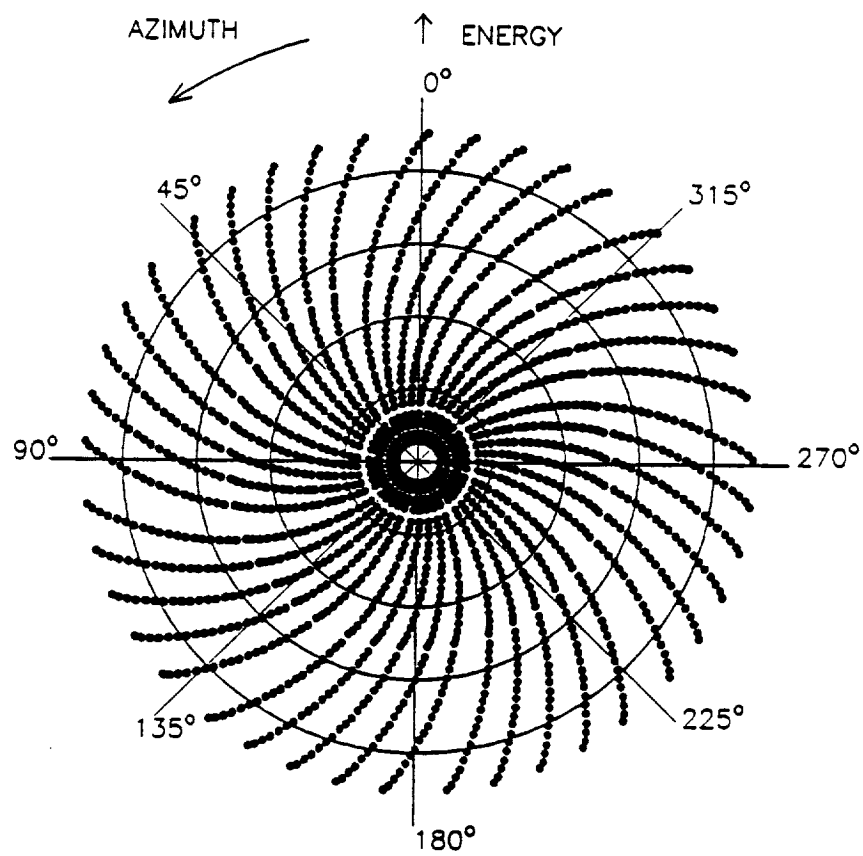


Figure 6. Same as Figure 5 except that 41 consecutive energy sweeps are shown.

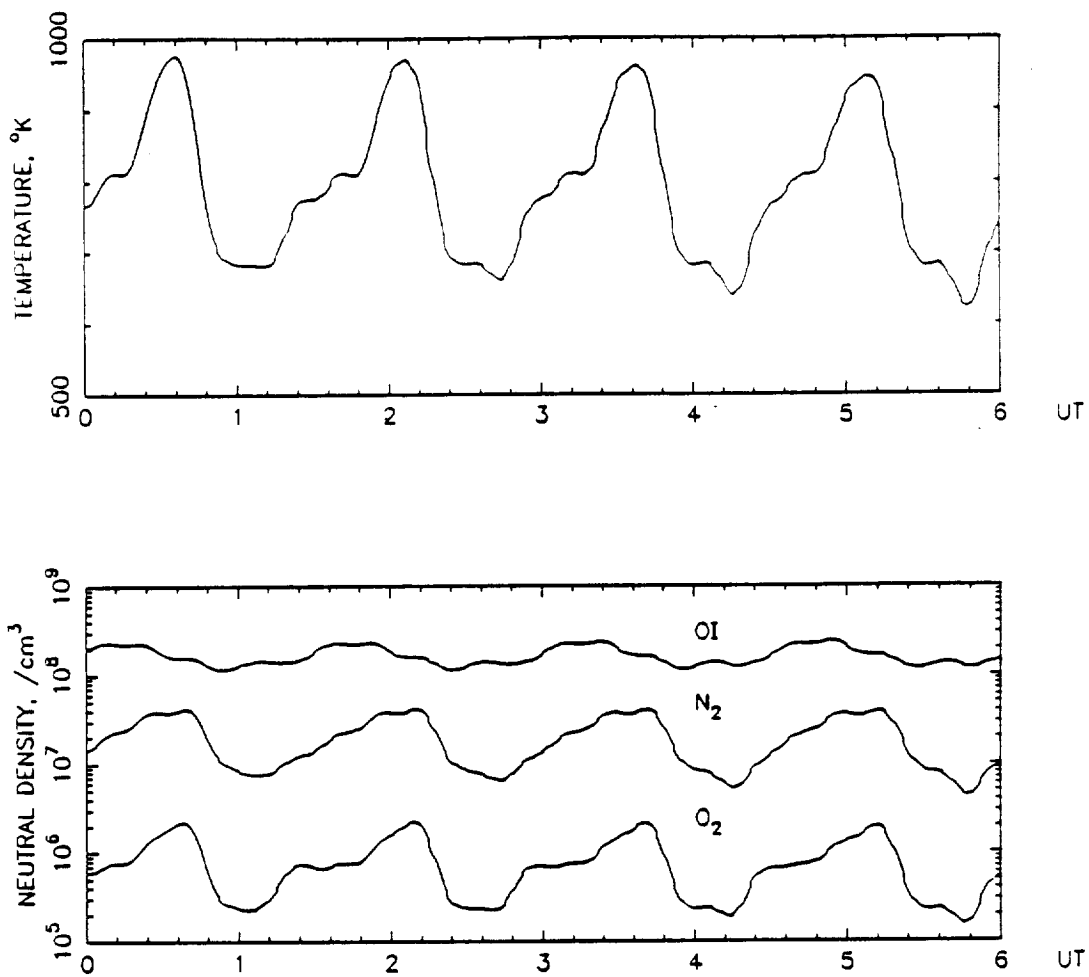


Figure 7. Atmospheric temperature and densities at the position of the spacecraft during the free flight. Calculated from the MSIS-83 atmospheric model (Hedin [4]).

A-G87-410

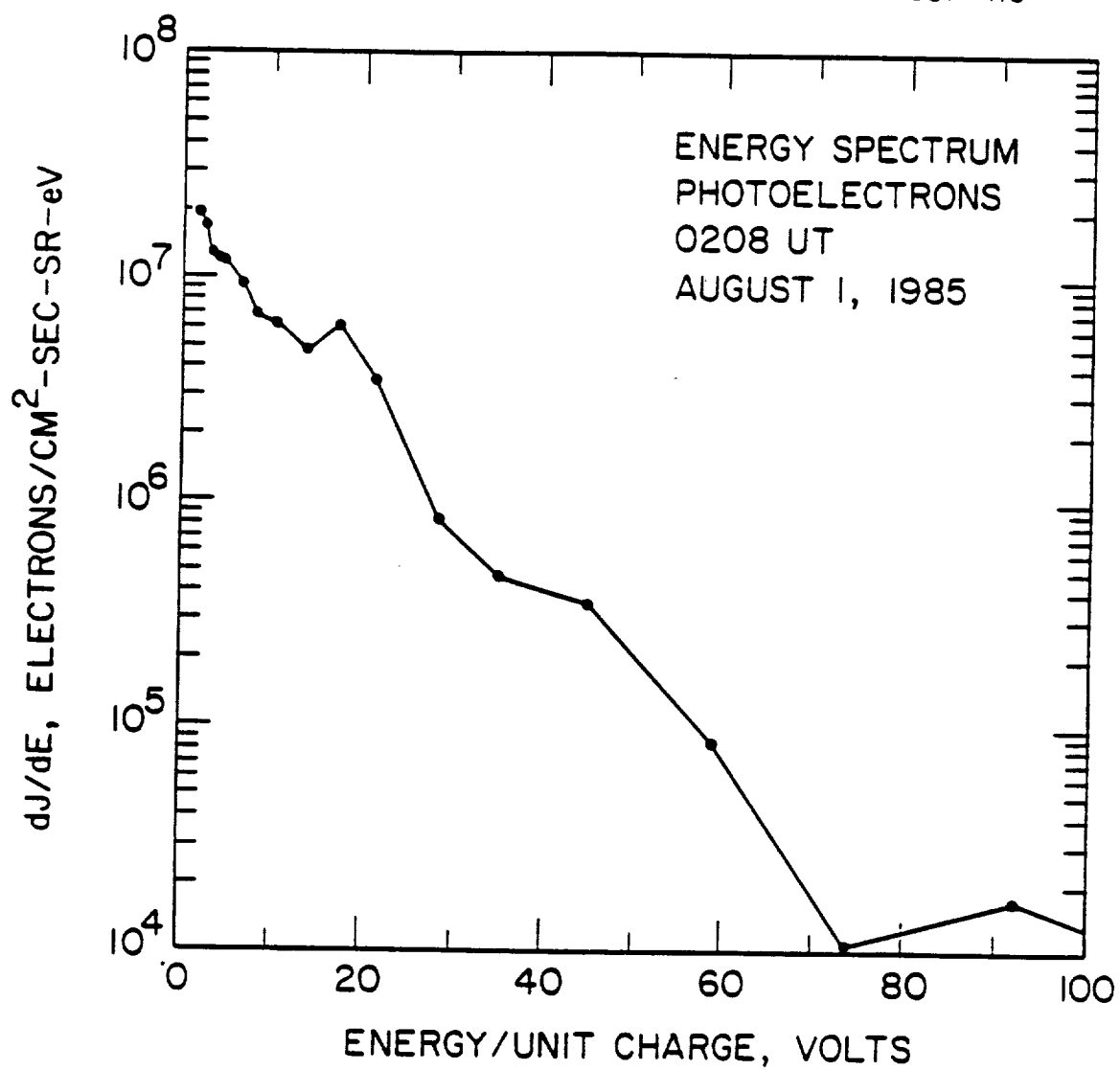


Figure 8. The energy spectrum of photoelectrons observed at 0208 UT.

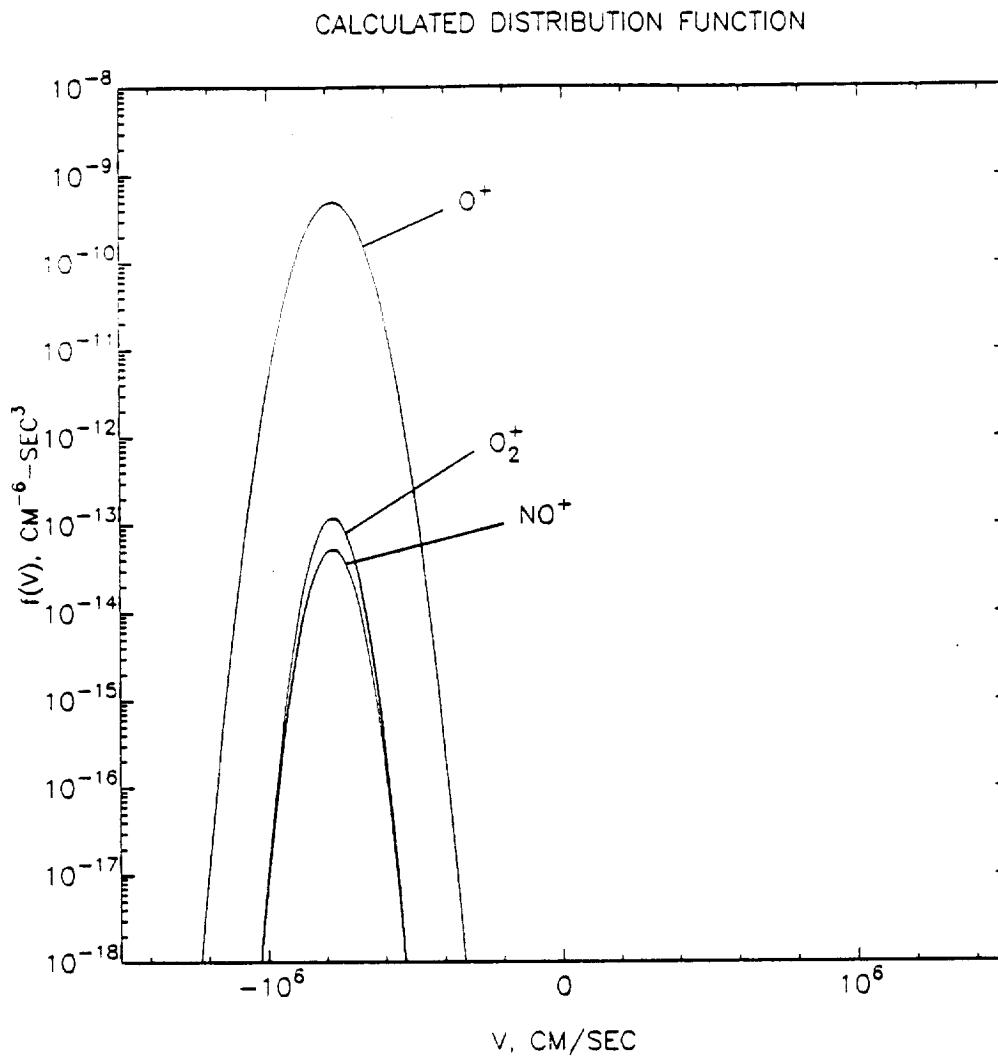


Figure 9. Calculated ion distributions in a reference frame moving with velocity $V = 7.8 \times 10^3$ m/sec with respect to the rest frame of the ions.

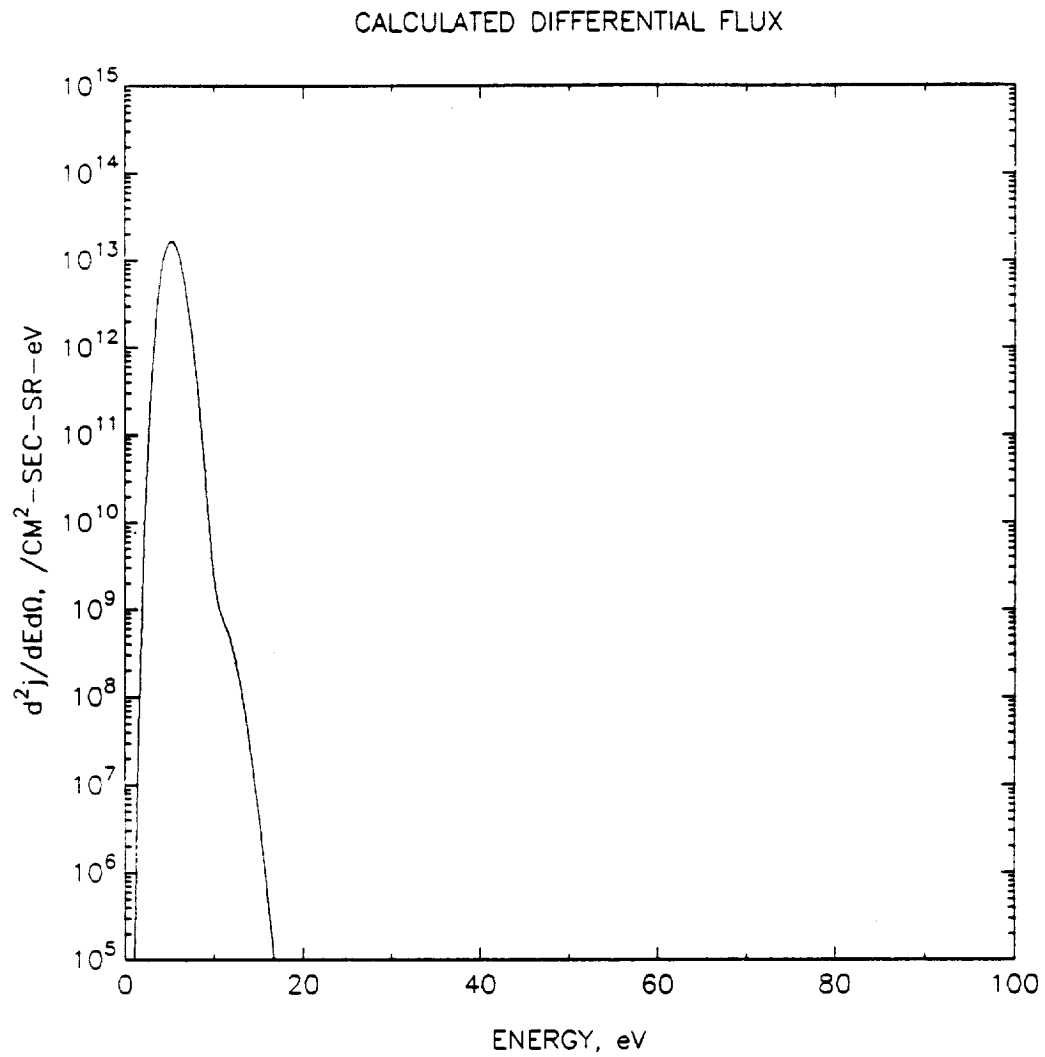
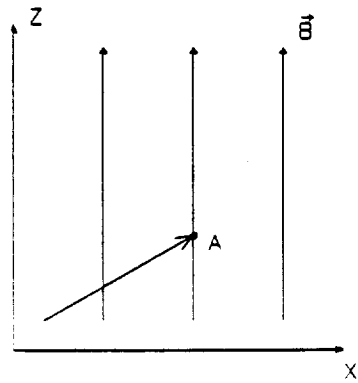
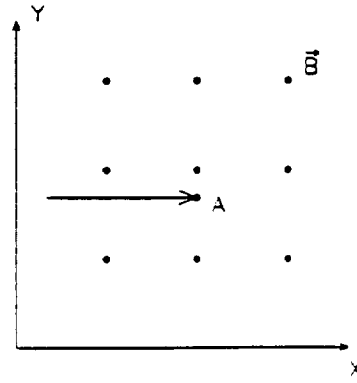


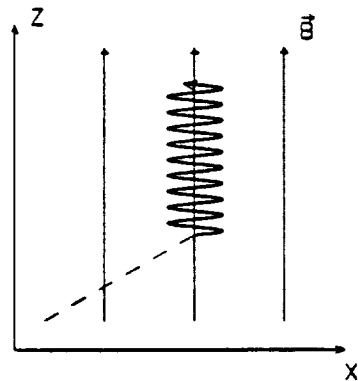
Figure 10. Energy spectrum calculated for the distributions of Figure 9.



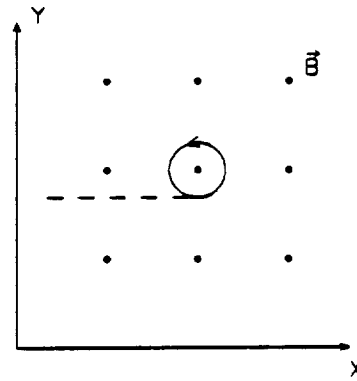
(a)



(b)



(c)



(d)

Figure 11. Motion of a particle in a magnetic field before and after ionization. The particle is ionized at point A. (a) Trajectory of the particle in the X, Z plane before ionization. (b) Trajectory of the particle in the X, Y plane before ionization. (c) Trajectory of the particle in the X, Z plane after ionization. (d) Trajectory of the particle in the X, Y plane after ionization.

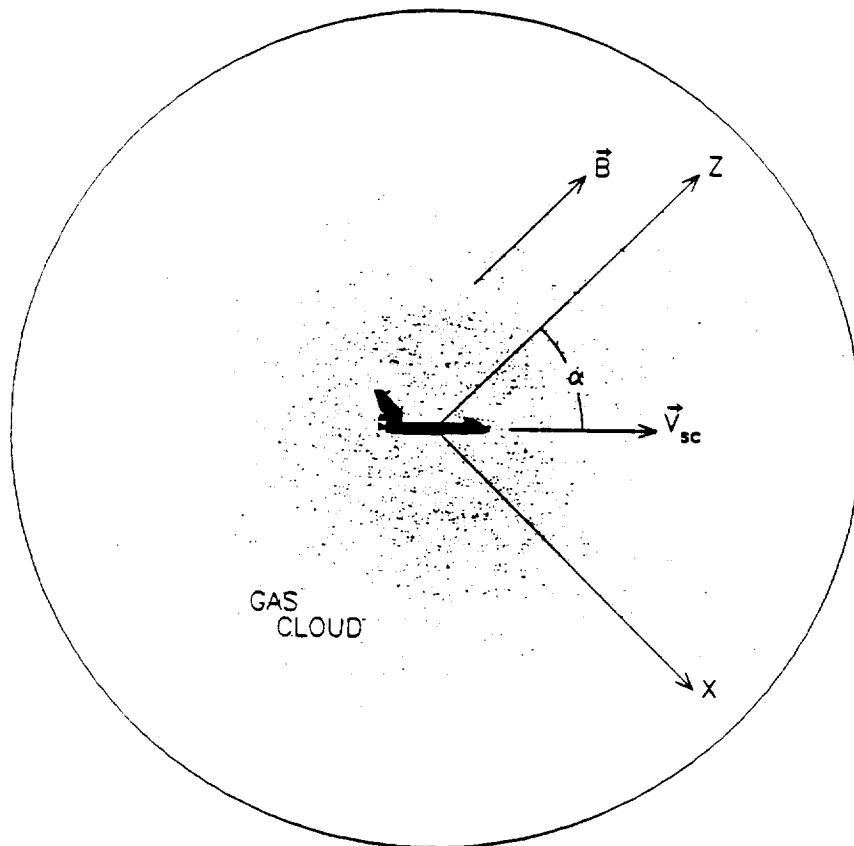


Figure 12. Coordinates used to describe pick-up of ions from a cloud of gases co-orbiting with the Orbiter.

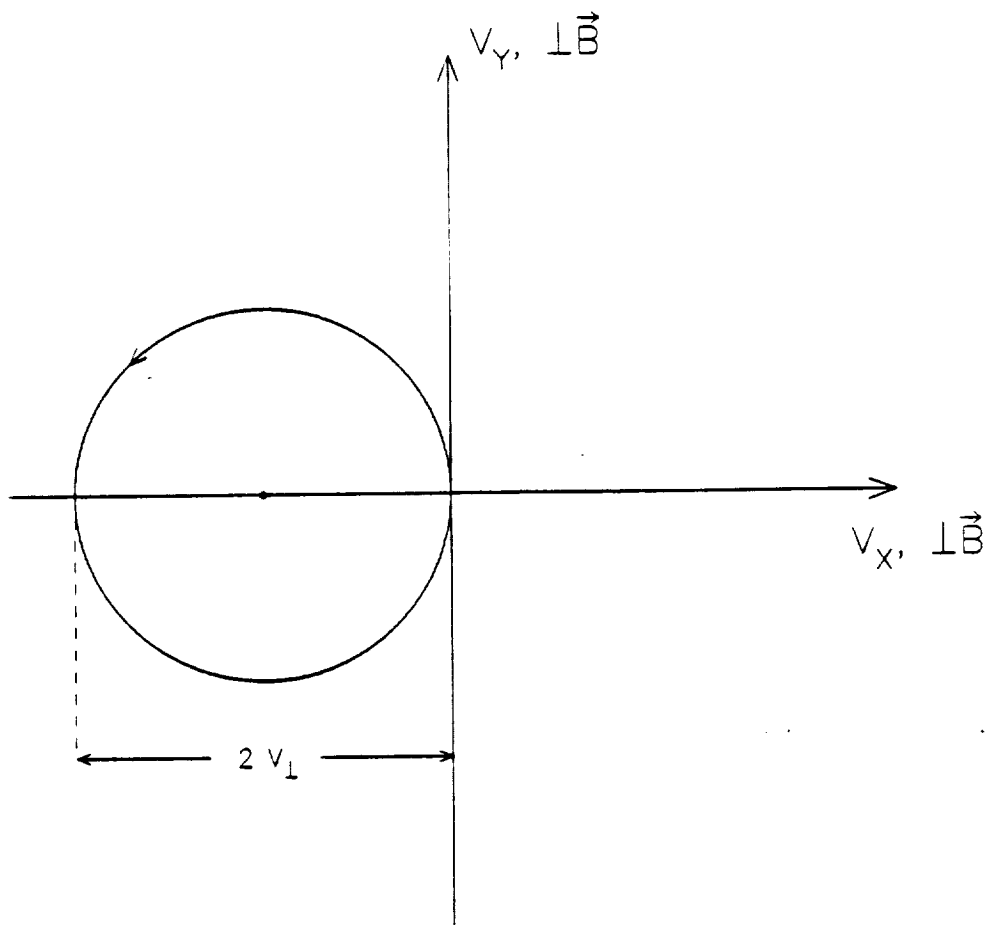


Figure 13. The velocity-space trajectory of a single pick-up ion. The magnetic field is out of the plane of the figure. The ion speed ranges from zero to $2 v_{\perp}$.

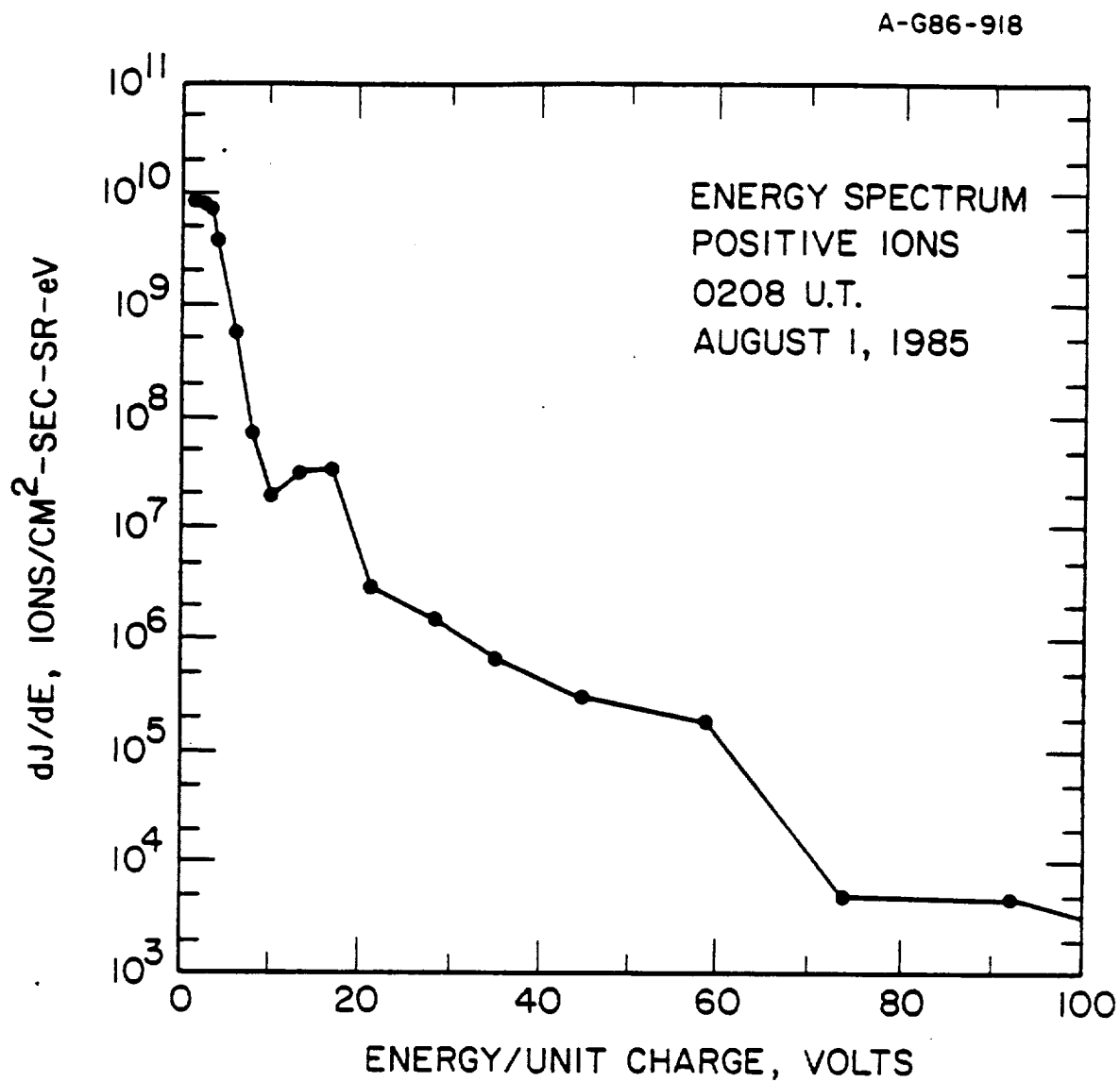


Figure 14. The energy spectrum of positive ions observed by the Lepedea at 0208 UT in the direction of orbital motion.

A-G86-920

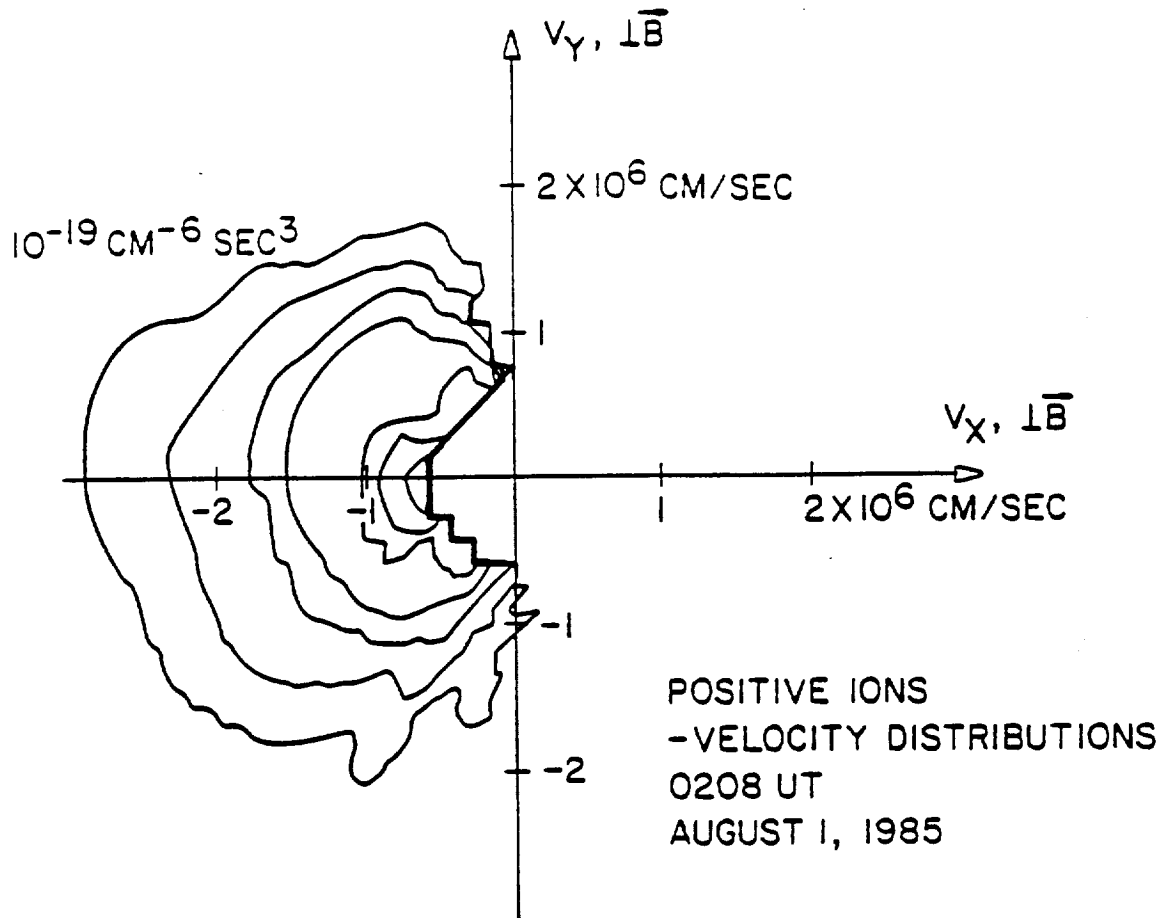


Figure 15. Contours of constant $f(\vec{v})$ at 0208 UT in the V_x, V_y plane. Both V_x and V_y are perpendicular to \vec{B} . The projection of \vec{v}_{sc} into the plane is along V_x . At this time, \vec{v}_{sc} and \vec{B} are at an angle of 86° . The outermost contour is for $f = 10^{-19} \text{ sec}^3/\text{cm}^6$. Contours interior to this increase by factors of ten.

A-G86-921

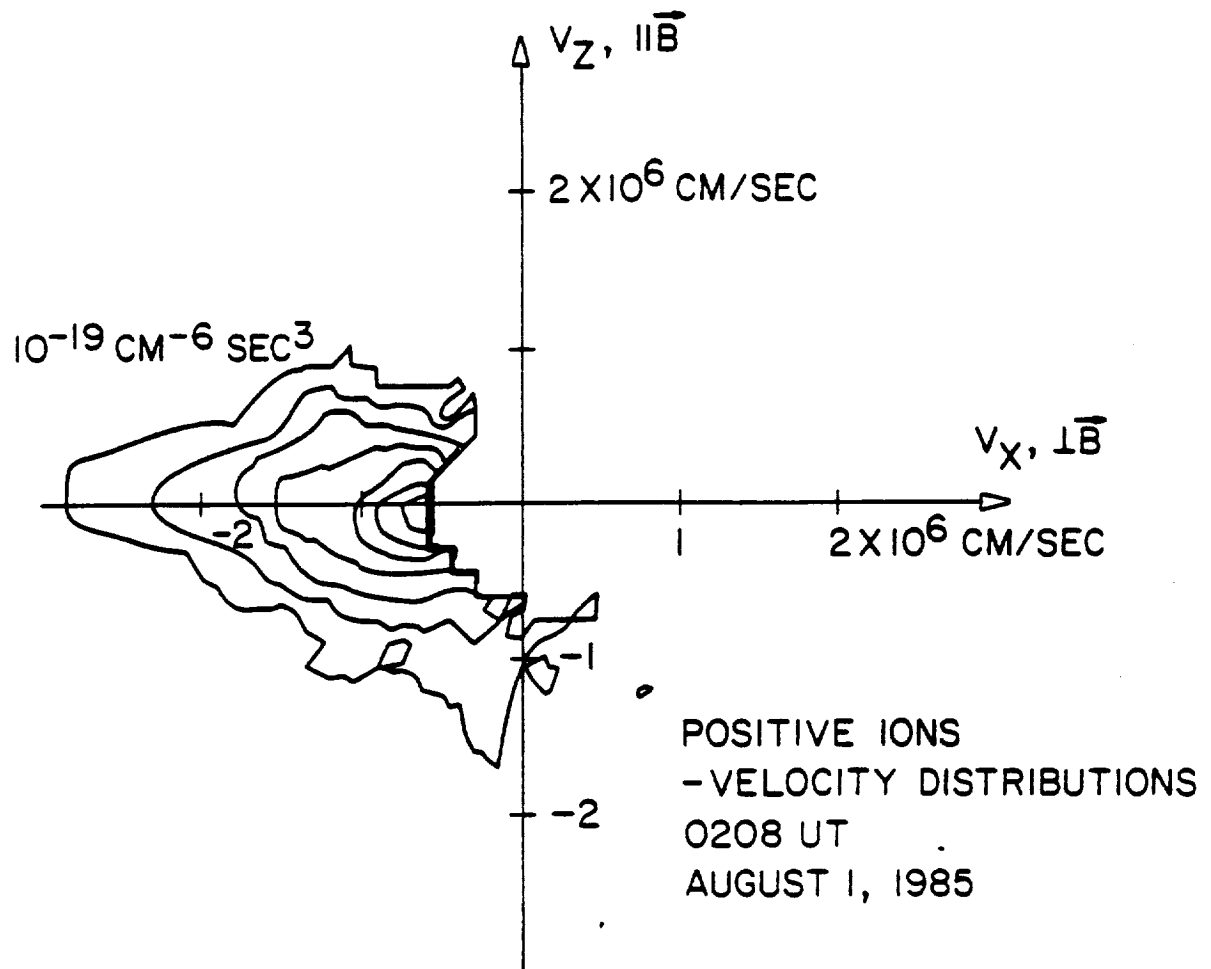


Figure 16. Contours of constant $f(\vec{v})$ at 0208 UT in a plane perpendicular to the plane of Figure 15. The magnetic field is parallel to the V_z axis.

A-G87-194

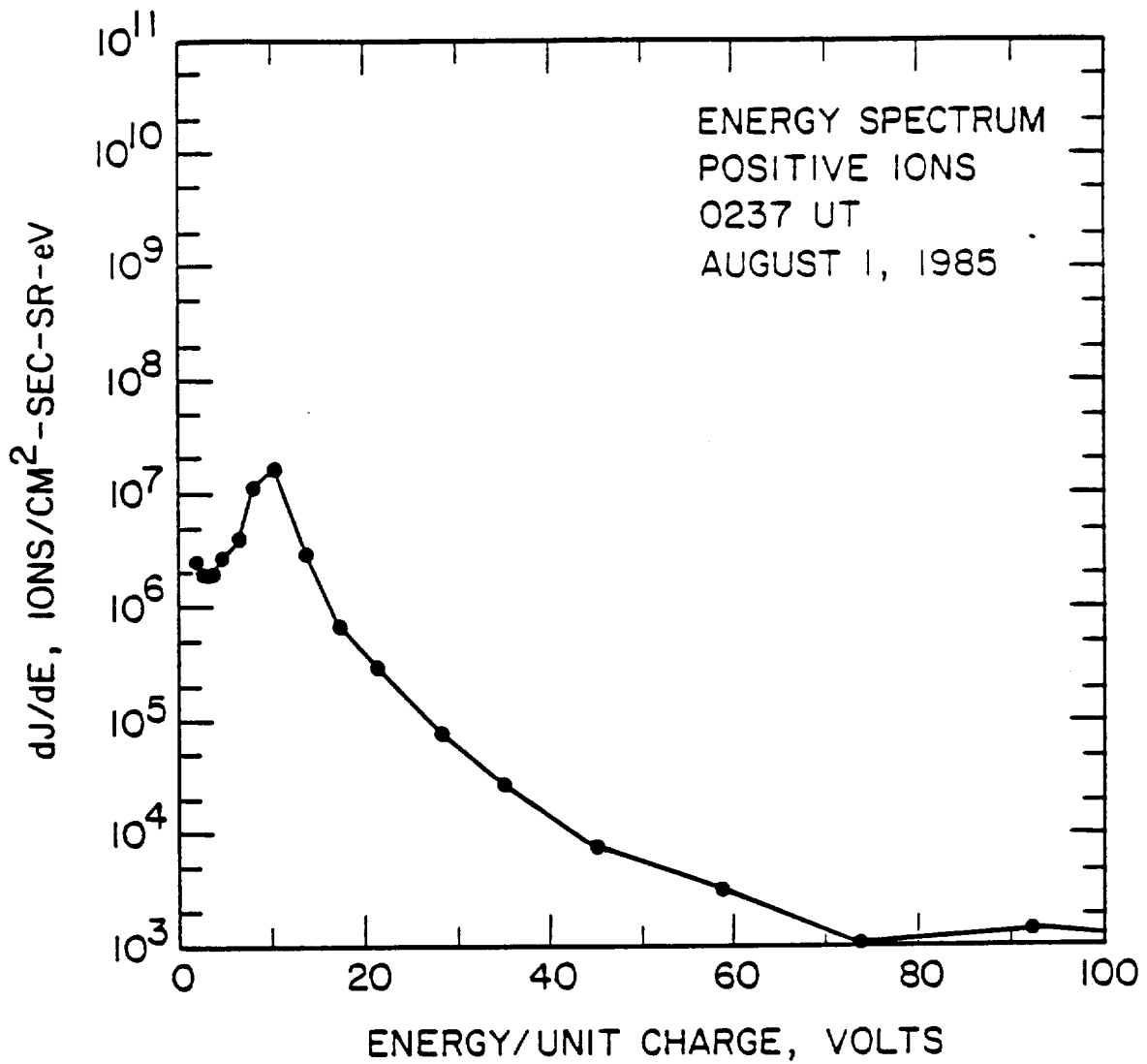


Figure 17. Energy spectrum of positive ions at 0237 UT in the direction of V_x .

A-G87-197

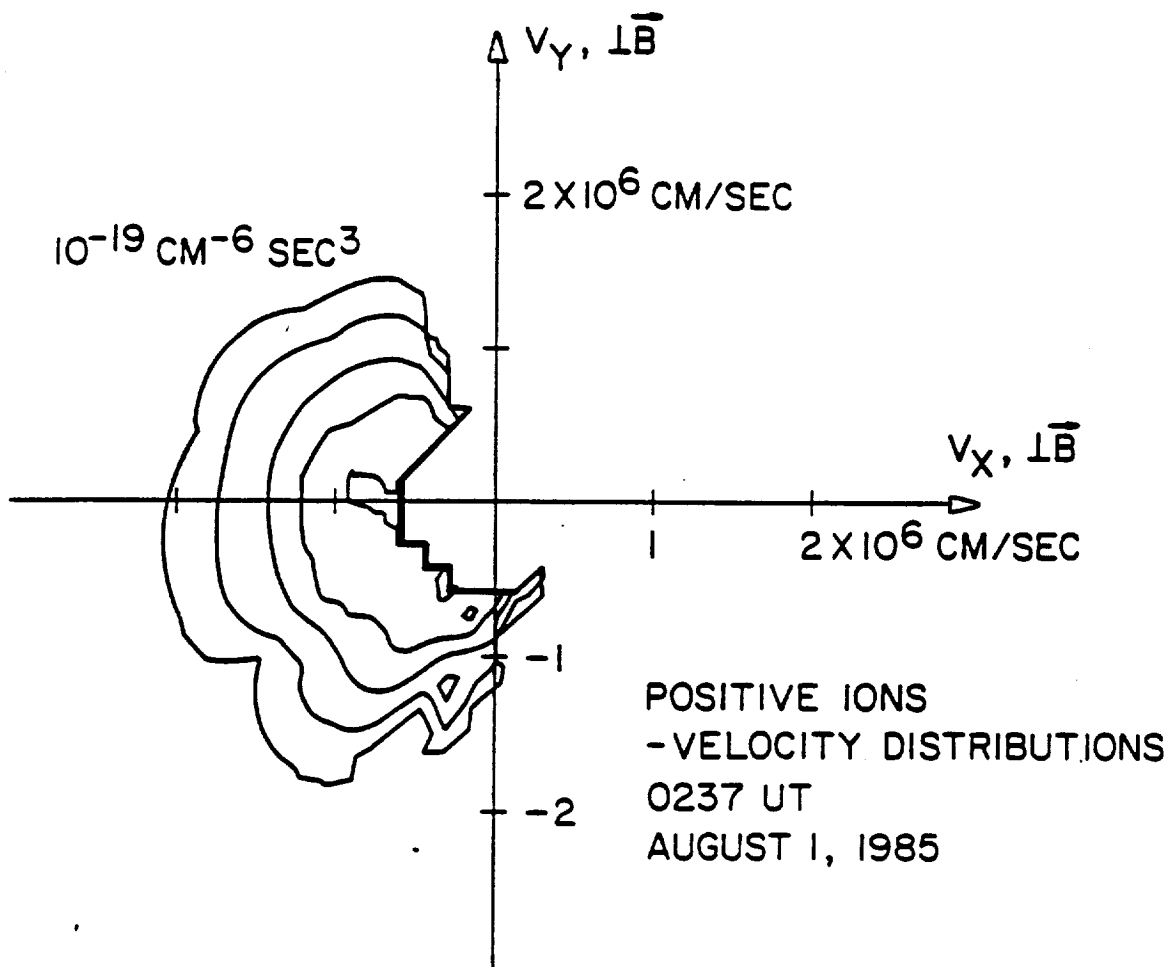


Figure 18. Contours of constant $f(\vec{v})$ in the V_x, V_y plane at 0237 UT.

A-G87-198

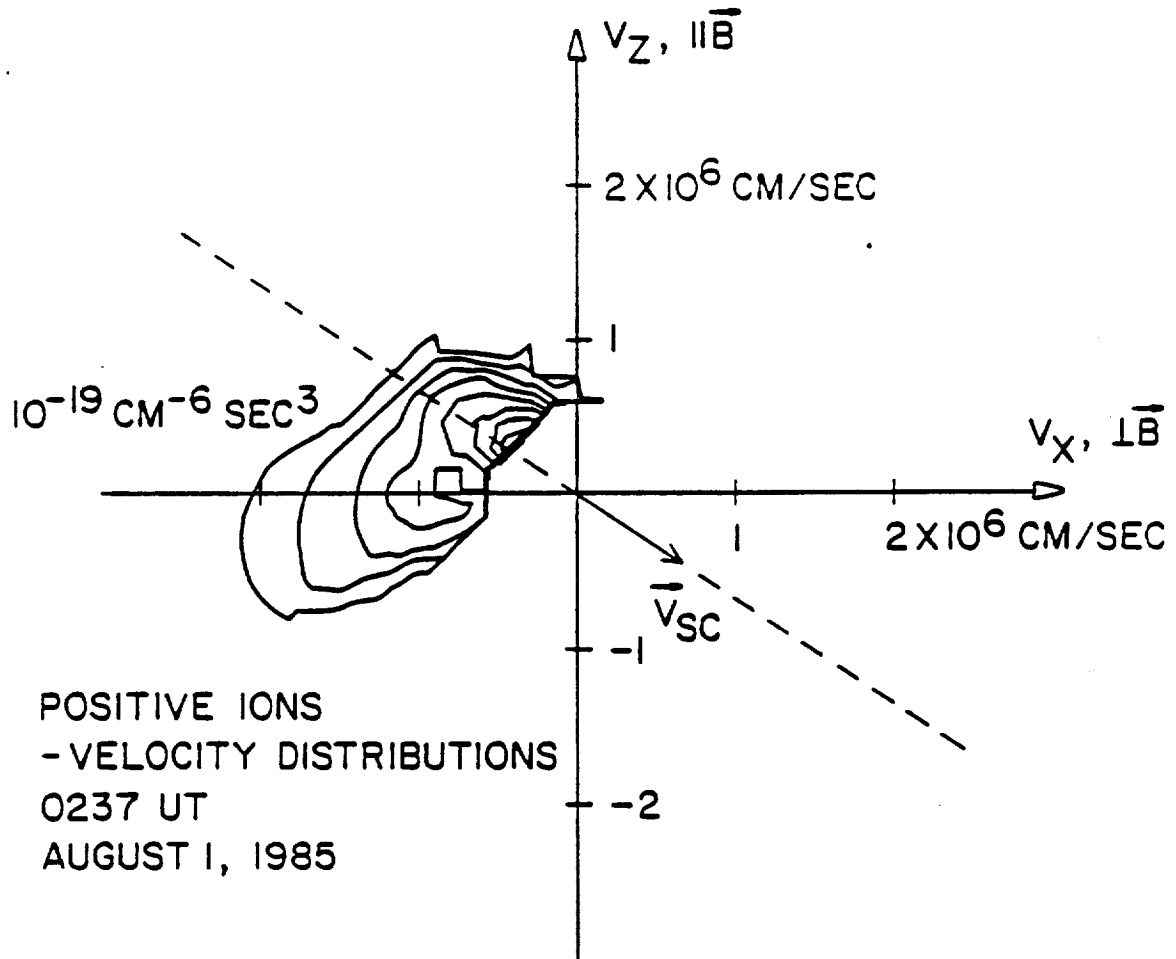


Figure 19. Contours of constant $f(\vec{v})$ in the V_x, V_z plane at 0237 UT. The direction of orbital motion is indicated by the dashed line and the arrow marked \vec{v}_{sc} .

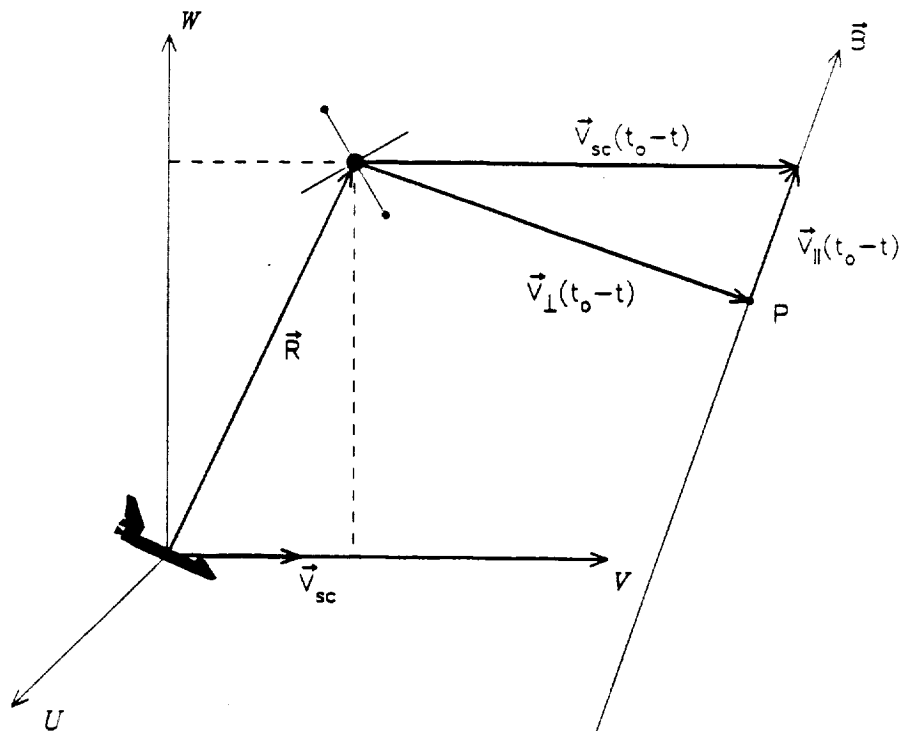


Figure 20. The coordinate system used to integrate equations (22) and (23). The integration is performed at the point P on the field line \vec{B} . The point P moves along \vec{B} with a velocity equal to $\vec{V}_{||}$. Magnetic field lines sweep past the Orbiter with velocity $-\vec{V}_{sc}$. The PDP lies in the U, V plane at a distance R from the Orbiter.

A-G86-922

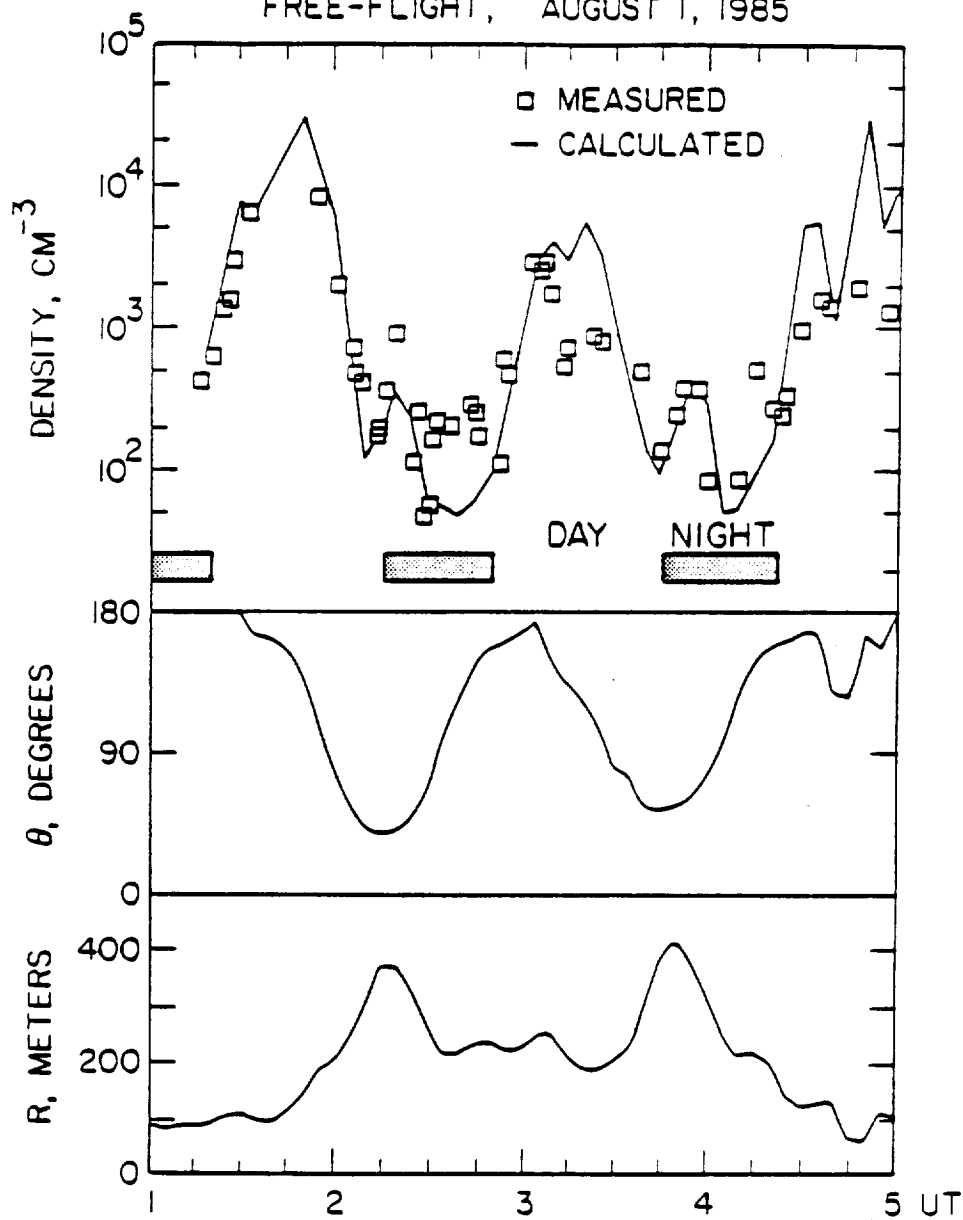
 H_2O^+ DENSITIES OBSERVED DURING
FREE-FLIGHT, AUGUST 1, 1985

Figure 21. Comparison of observed and calculated pick-up ion densities during the free flight. The lower panels show the angle θ between \vec{R} and \vec{V}_{SC} , and the distance R between the PDP and the Orbiter.

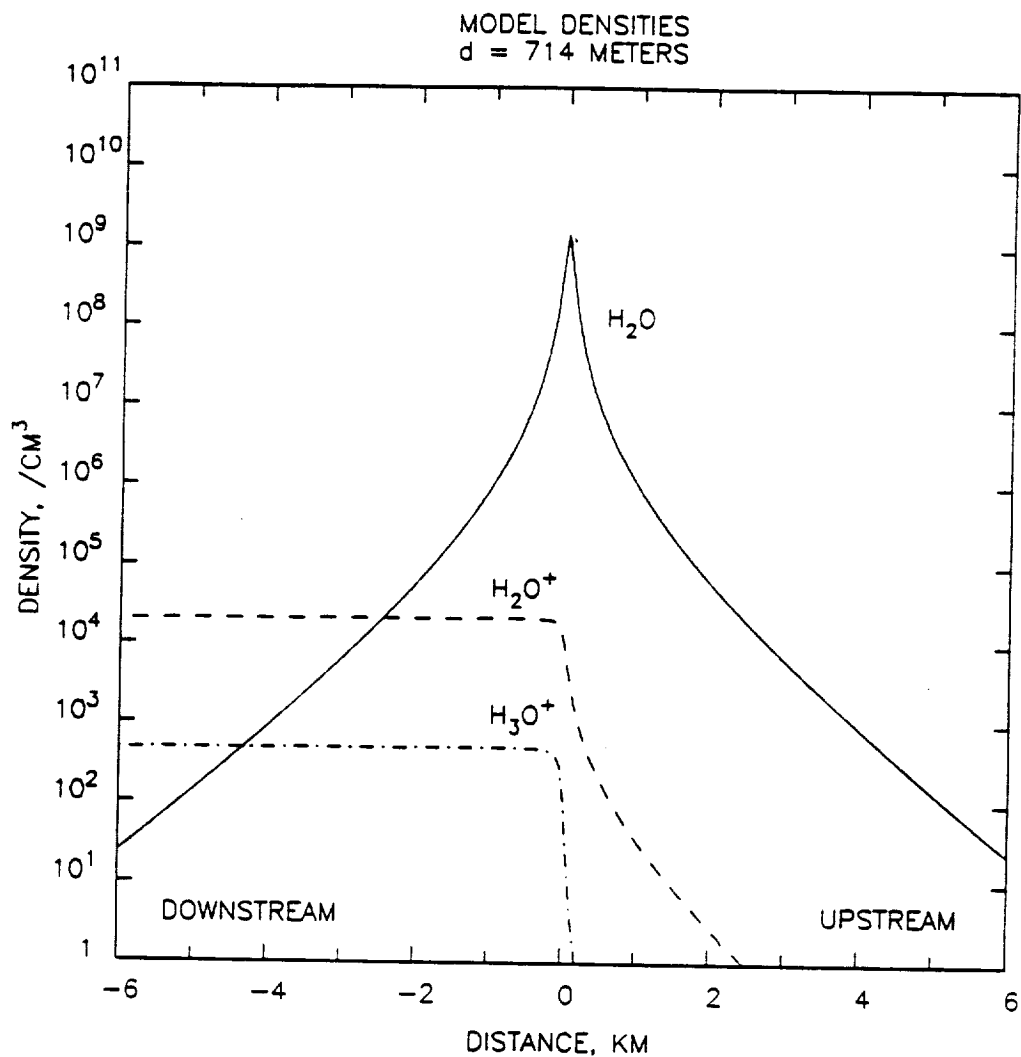


Figure 22. Calculated H_2O , H_2O^+ , and H_3O^+ densities along a line which is parallel to the V axis of Figure 20 and which passes within 50 m of the center of the water cloud. Parameters used in the calculation are discussed in the text. The angle between \vec{B} and \vec{V}_{sc} is 90° .

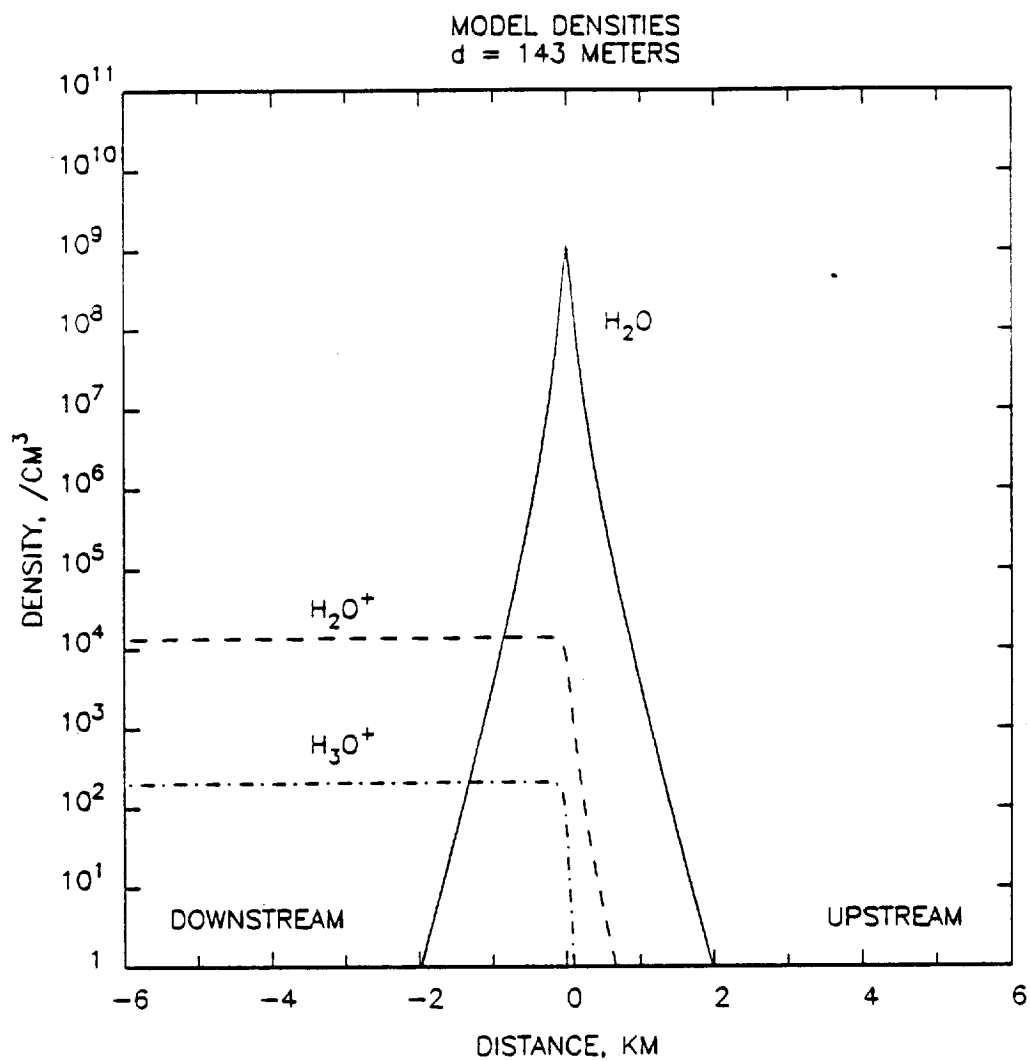


Figure 23. Same as Figure 22 but calculated for an atmospheric density five times higher than the density of Figure 22.

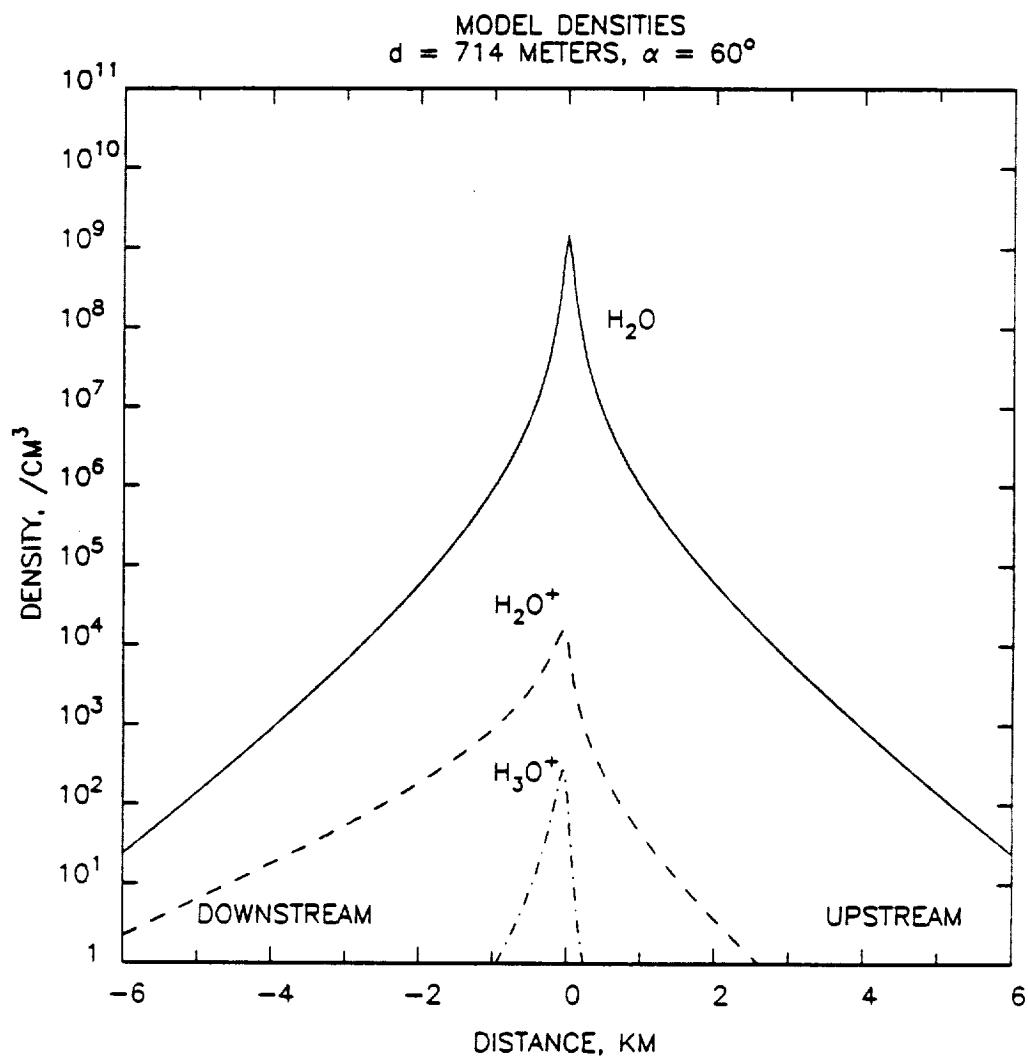


Figure 24. Same as Figure 22 but for an angle between \vec{B} and \vec{V}_{sc} of 60° .

REFERENCES

- [1] S. D. Shawhan, G. B. Murphy, and J. S. Pickett, "Plasma Diagnostics Package Initial Assessment of the Shuttle Orbiter Plasma Environment," J. Spacecr. Rockets, 21, 387, 1984.
- [2] L. A. Frank, D. M. Yeager, H. D. Owens, K. L. Ackerson, and M. R. English, "Quadr spherical LEPEDAS for ISEE's-1 and -2 Plasma Measurements," IEEE Trans. Geosci. Electron., 3, 221, 1978.
- [3] F. F. Chen, Introduction of Plasma Physics and Controlled Nuclear Fusion, 2nd ed., Vol. 1 (Plenum Press, New York, 1984).
- [4] A. E. Hedin, "A Revised Thermospheric Model Based on Mass Spectrometer and Incoherent Scatter Data," J. Geophys. Res., 88, 10,170, 1983.
- [5] P. M. Banks and G. Kockarts, Aeronomy, Part A (Academic Press, New York, 1973).
- [6] E. Brook, M. F. A. Harrison, and A. C. H. Smith, "Measurements of the Electron Impact Ionisation Cross Sections of He, C, O, and N Atoms", J. Phys. B, 11, 3115, 1978.
- [7] A. Dalgarno, "Charged Particles in the Upper Atmosphere," Ann. Geophys., 17, 16, 1961.
- [8] J. S. Pickett, G. B. Murphy, W. S. Kurth, C. K. Goertz, and S. D. Shawhan, "Effects of Chemical Releases by the STS 3 Orbiter on the Ionosphere," J. Geophys. Res., 90, 3487, 1985.
- [9] E. Wulf and U. von Zahn, "The Shuttle Environment: Effects of Thruster Firings on Gas Density and Composition in the Payload Bay," J. Geophys. Res., 91, 3270, 1986.
- [10] R. Narcisi, E. Trzcinski, G. Frederico, L. Wlodyka, and D. Delorey, "The Gaseous and Plasma Environment around the Space Shuttle," AIAA Paper 83-2659, 1983.
- [11] D. E. Hunton and J. M. Calo, "Low Energy Ions in the Shuttle Environment: Evidence for Strong Ambient-Contaminant Interactions," Planet. Space Sci., 33, 945, 1985.

- [12] J. M. Grebowsky, H. A. Taylor, M. W. Pharo, and N. Reese, "Thermal Ion Perturbations Observed in the Vicinity of the Space Shuttle," Planet. Space Sci., 35, 501, 1987.
- [13] C. K. Goertz, "Io's Interaction with the Plasma Torus," J. Geophys. Res., 85, 2949, 1980.
- [14] F. M. Ipavich, A. B. Galvin, G. Gloecker, D. Hovestadt, B. Klecker, and M. Scholer, "Comet Giacobini-Zinner: In Situ Observation of Energetic Heavy Ions," Science, 232, 366, 1986.
- [15] T. Mukai, W. Miyake, T. Terasawa, M. Kitayama, and K. Hirao, "Plasma Observation by Suisei of Solar-Wind Interaction with Comet Halley," Nature, 321, 299, 1986.
- [16] E. Möbius, D. Hovestadt, B. Klecker, M. Scholer, G. Gloecker, and F. M. Ipavich, "Direct Observation of He⁺ Pick-Up Ions of Interstellar Origin in the Solar Wind," Nature, 318, 1985.
- [17] E. W. McDaniel, Collision Phenomenon in Ionized Gases (John Wiley and Sons, New York, 1964).
- [18] N. Wainfan, W. C. Walker, and G. L. Weissler, "Photoionization Efficiencies and Cross Sections in O₂, N₂, A, H₂O, H₂, and CH₄," Phys. Rev., 99, 542, 1955.
- [19] T. D. Mark and F. Egger, "Cross-Section for Single Ionization of H₂O and D₂O by Electron Impact from Threshold up to 170 eV," Int. J. Mass Spectrom. Ion Phys., 20, 89, 1976.
- [20] E. Murad and S. T. F. Lai, "Some Charge Exchange Reactions Involving H₂O," Chem. Phys. Lett., 5, 427, 1986.
- [21] B. R. Turner and J. A. Rutherford, "Charge Transfer and Ion-Atom Interchange of Water Vapor Ions," J. Geophys. Res., 73, 6751, 1968.
- [22] M. A. Coplan and K. W. Ogilvie, "Charge Exchange for H⁺ and H₂⁺ in H₂O, CO₂, and NH₃⁺," J. Chem. Phys., 52, 4154, 1970.
- [23] G. W. Sjolander and E. P. Szuszczewicz, "Chemically Depleted F₂ Ion Composition: Measurements and Theory," J. Geophys. Res., 84, 4393, 1979.
- [24] D. L. Albritton, "Ion-Neutral Reaction-Rate Constants Measured in Flow Reactors through 1977," At. Data Nucl. Data Tables, 22, 1, 1978.

- [25] G. R. Carignan and E. R. Miller, "STS-2, -3, -4 Induced Environment Contamination Monitor (IECM) Summary Report, NASA Technical Memorandum TM-82524, 1983.
- [26] G. B. Murphy, J. S. Pickett, N. D'Angelo, and W. S. Kurth, "Measurements of Plasma Parameters in the Vicinity of the Space Shuttle," Planet. Space Sci., **34**, 993, 1986.

THE LARGE SCALE WAKE STRUCTURE
OF THE SHUTTLE ORBITER: PLASMA
DENSITY, TEMPERATURE, AND TURBULENCE

by

Alan C. Tribble

A thesis submitted in partial fulfillment
of the requirements for the Doctor of
Philosophy degree in Physics
in the Graduate College of
The University of Iowa

May 1988

Thesis supervisor: Professor Nicola D'Angelo

Graduate College
The University of Iowa
Iowa City, Iowa

CERTIFICATE OF APPROVAL

PH.D. THESIS

This is to certify that the Ph.D. thesis of

Alan C. Tribble

has been approved by the Examining Committee
for the thesis requirement for the Doctor of
Philosophy degree in Physics at the May 1988
graduation.

Thesis committee:

Nicola D'Angelo

Thesis supervisor

D. R. Ahl

Member

Kurt Elmgren

Member

Sam Gammott

Member

Robert H. Merlino

Member

ACKNOWLEDGEMENTS

There are a number of people who deserve special recognition and thanks for their help in the preparation of this manuscript. First and foremost I must express my gratitude to my advisor, Nicola D'Angelo, for his insight into many of the problems that were encountered and for his helpful critiques of the resulting presentations. At the same time I cannot underestimate the assistance rendered to me by Gerald Murphy and Jolene Pickett. Being able to rely upon their experience with the Langmuir probe made this job much easier. The other members of my committee, Dr.'s Andersen, Gurnett, Longrenn, and Merlino, all warrant acknowledgement for their comments and advice.

In addition to those just mentioned I also owe my gratitude to Alice Shank, for help with the word processing program, and to John Birkbeck for drafting the numerous figures used in this dissertation. Lastly, I thank my fiancee, Beth Gunion, for her patience and support during the many months it took to finish the research presented here. Maybe I will get to return the favor some day.

This work was supported by grant NAG3-449 from the NASA Lewis Research Center, contract NAS8-32807 from the NASA Marshall Space Flight Center, and grant NGT-50402 from NASA headquarters.

ABSTRACT

The large scale plasma wake structure of the shuttle orbiter is studied using a Langmuir probe on a smaller ionospheric satellite. This satellite, the University of Iowa's Plasma Diagnostics Package (PDP), was flown on shuttle mission STS-51F from 29 July to 6 August 1985. The PDP was carried in the shuttle's payload bay, but during certain times throughout the mission it was placed on the arm of the shuttle, the Remote Manipulator System (RMS), or ejected as a free-flying satellite, so that both the near and far wake of the orbiter could be studied. The resulting data on the electron temperature, electron density, and fluctuations in the electron density in the orbiters wake provide the first in situ observations of the large scale wake of the orbiter. The density profile suggests the possibility of converging ion streams in the orbiters wake and the temperature profile indicates enhanced electron temperatures at distances as great as 250 m downstream from the orbiter. The region of density depletion and temperature enhancement are bounded by the orbiter's Mach cone. The turbulence data indicates an enhancement of about 10 dB on the order of the ion plasma frequency along the Mach cone with no appreciable increase in turbulence detected directly on the wake axis.

TABLE OF CONTENTS

	Page
LIST OF TABLES	v
LIST OF FIGURES	vi
CHAPTER	
I. INTRODUCTION	1
II. REVIEW OF PLASMA WAKES	4
An Obstacle in a Plasma	4
Plasma Expansion into a Vacuum	8
Factors Influencing Wake Phenomena	10
Summary	11
III. THE EXPERIMENT	12
Equipment	12
Procedure	14
The Ambient Ionosphere	16
IV. THE NEAR WAKE	17
Plasma Density and Temperature	17
Plasma Turbulence	19
V. THE MID AND FAR WAKE	23
Plasma Density and Temperature	23
Plasma Turbulence	25
VI. SUMMARY AND CONCLUSIONS	29
APPENDIX A: DERIVATION OF LANGMUIR PROBE EQUATIONS	33
APPENDIX B: THE WAKE OF THE PDP	39
REFERENCES	124

LIST OF TABLES

Tables	Page
1. Langmuir Probe Performance Characteristics	41
2. Spectrum Analyzer Performance Characteristics	42
3. Ionospheric Plasma Characteristics	43

LIST OF FIGURES

Figure	Page
1. An idealized view of the plasma wake of an object in a flowing plasma.	44
2. Plasma Expansion into a vacuum.	45
3. The Plasma Diagnostics Package.	46
4. XPOP roll, the procedure used to study the near wake of the orbiter.	47
5. In plane distance between the orbiter and the PDP, 00:00 - 01:30. .	48
6. In plane distance between the orbiter and the PDP, 01:30 - 03:00. .	49
7. In plane distance between the orbiter and the PDP, 03:00 - 04:30. .	50
8. In plane distance between the orbiter and the PDP, 04:30 - 06:00. .	51
9. Ambient ionospheric characteristics, 01:30 - 03:00.	52
10. Ambient ionospheric characteristics, 03:00 - 04:30.	53
11. A comparison of the electron density calculated from the Langmuir curves (top) with that calculated from the 0-1 Hz data (bottom). .	54
12. Electron density depletions during near wake transit one.	55
13. Electron temperature enhancements during near wake transit one. .	56
14. Electron density depletions during near wake transit two.	57
15. Electron temperature enhancements during near wake transit two. .	58
16. Electron density depletions during near wake transit three.	59
17. 1-6 Hz data during near wake transit one.	60

18. 6-40 Hz data during near wake transit one.	61
19. 6-40 Hz data during near wake transit two.	62
20. 6-40 Hz data during near wake transit three.	63
21. 0-40 Hz FFT data corresponding to orbiter phase angles 124° – 136°.	64
22. 0-40 Hz FFT data corresponding to orbiter phase angles 137° – 149°.	65
23. 0-40 Hz FFT data corresponding to orbiter phase angles 150° – 162°.	66
24. 0-40 Hz FFT data corresponding to orbiter phase angles 163° – 175°.	67
25. 0-40 Hz FFT data corresponding to orbiter phase angles 175° – 187°.	68
26. Near wake transit one spectral density data corresponding to orbiter phase angle 159°.	69
27. Near wake transit one spectral density data corresponding to orbiter phase angle 164°.	70
28. Near wake transit one spectral density data corresponding to orbiter phase angle 167°.	71
29. Near wake transit one spectral density data corresponding to orbiter phase angle 175°.	72
30. Near wake transit one spectral density data corresponding to orbiter phase angle 180°.	73
31. Near wake transit one spectral density data corresponding to orbiter phase angle 185°.	74
32. Near wake transit one spectral density data corresponding to orbiter phase angle 190°.	75
33. Near wake transit one spectral density data corresponding to orbiter phase angle 198°.	76
34. Near wake transit one spectral density data corresponding to orbiter phase angle 206°.	77

35. Mid and Far wake transits.	78
36. Spatial relationship between the orbiter and the PDP during backaway.	79
37. Electron density depletions during backaway.	80
38. Electron temperature enhancements during backaway.	81
39. Spatial relationship between the orbiter and the PDP during far wake transit one.	82
40. Electron density depletions during far wake transit one.	83
41. Electron temperature enhancements during far wake transit one. ...	84
42. Spatial relationship between the orbiter and the PDP during far wake transit two.	85
43. Electron density depletions during far wake transit two.	86
44. Electron temperature enhancements during far wake transit two. ...	87
45. Spatial relationship between the orbiter and the PDP during far wake transit three.	88
46. Electron density depletions during far wake transit three.	89
47. Electron temperature enhancements during far wake transit three. ..	90
48. Spatial relationship between the orbiter and the PDP during far wake transit four.	91
49. Electron density depletions during far wake transit four.	92
50. Electron temperature enhancements during far wake transit four. ...	93
51. Electron density depletions in the wake of the shuttle orbiter for constant values of N_w/N_a	94
52. Electron density depletions in the wake of the shuttle orbiter for constant values of Z/R	95

53. Electron temperature enhancements in the wake of the shuttle orbiter.	96
54. 6-40 Hz data during backaway.	97
55. 6-40 Hz data during far wake transit one.	98
56. 6-40 Hz data during far wake transit two.	99
57. 6-40 Hz data during far wake transit three.	100
58. 6-40 Hz data during far wake transit four.	101
59. 0-40 Hz FFT data obtained on the wake axis 35 m downstream from the orbiter.	102
60. 0-40 Hz FFT data obtained on the wake axis 120 m downstream from the orbiter.	103
61. 0-40 Hz FFT data obtained on the Mach cone 200 m downstream from the orbiter.	104
62. 0-40 Hz FFT data obtained just outside the Mach cone 20 m downstream from the orbiter.	105
63. 0-40 Hz FFT data obtained just outside the Mach cone 90 m downstream from the orbiter.	106
64. The locations where Langmuir probe spectrum analyzer data is available during wake studies.	107
65. Ambient ionospheric conditions as measured by the spectrum analyzer.	108
66. Spectral density of $\Delta N/N$ at location I.	109
67. Spectral density of $\Delta N/N$ at location II.	110
68. Spectral density of $\Delta N/N$ at location III.	111
69. Spectral density of $\Delta N/N$ at location IV.	112

70. Spectral density of $\Delta N/N$ at location V.	113
71. Spectral density of $\Delta N/N$ at location VI.	114
72. Spectral density of $\Delta N/N$ at location VII.	115
73. Spectral density of $\Delta N/N$ at location VIII.	116
74. Spectral density of $\Delta N/N$ at location IX.	117
75. Spectral density of $\Delta N/N$ at location X.	118
76. Spectral density of $\Delta N/N$ at location XI.	119
77. Spectral density of $\Delta N/N$ at location XII.	120
78. A typical Langmuir probe sweep showing the values of N_o , I, and 'slope' needed to calculate N_e , T_e , and V_p	121
79. Electron density depletions in the wake of the PDP.	122
80. Electron temperature enhancements in the wake of the PDP.	123

CHAPTER I

INTRODUCTION

The phenomena involved in the expansion of a plasma into a vacuum are of fundamental importance to many areas of plasma physics. This expansion process is qualitatively similar to many naturally occurring processes in the solar system, as well as certain processes in laser fusion. The distribution of charged particles and electric fields in the wake of an object moving supersonically in a plasma is an example of the expansion of a plasma into a void (vacuum) or into a more tenuous plasma. One specific problem of particular interest is the structure of the wake of a satellite as it moves through the Earth's ionosphere. Here the interaction takes place in a flow regime that is both supersonic and sub-Alfvénic. This suggests application to the motion of natural satellites, such as Io and Titan, orbiting their parent planets in the outer solar system. As listed by Martin [1], the interaction of the plasma with the satellite is important in that:

1. The charged particles will contribute to the drag of the body as it moves through the plasma.
2. The disturbance produced by the body must be known if diagnostic and measuring instruments are to be placed on board a vehicle.

3. The redistribution of charged particles and the potentials and screening sheaths will have an effect upon any radio-frequency antennae, aeri-als, and probes which are mounted on the vehicle.
4. The disturbed wake of the body will be of interest to radar detection and tracking applications.
5. The design of shields for protection against high energy particles, and their radiation, will have to take the disturbed conditions into account.
6. The excitation of plasma waves and other propagating disturbances will be influenced by the changes caused by the vehicle.

Some in situ observational attempts have been made to study these interactions, Samir and Wrenn [2], Samir and Willmore [3], Henderson and Samir [4], however, as reported by Samir [5], and Stone and Samir [6] the available in situ data is meager, fragmentary and applicable only to the very near wake zone.

The object of this dissertation is to obtain a better understanding of the physical processes responsible for the phenomena that are associated with the plasma wake of a large object, in this case the shuttle orbiter. This will be accomplished by examining data collected by a Langmuir probe on The University of Iowa's Plasma Diagnostics Package (PDP). From 30 July to 6 August 1985 the PDP was flown as part of the Spacelab-2 payload on space shuttle flight STS-51F. During this time the shuttle orbiter executed a series of maneuvers designed to allow the PDP to make extensive studies of plasma parameters in both the near and far wake zones. This was the first study of its kind and has produced the only in situ data on the mid and far orbiter wake that is available at this time.

We should note that the Spacelab-2 mission was actually the second shuttle flight for the PDP. The PDP was first flown on the STS-3 mission as part of the first Office of Space Sciences (OSS) payload in March of 1982. That mission yielded some of the first measurements of plasma parameters near the shuttle orbiter, Murphy et al. [7] and Raitt et al. [8]. The OSS-1 mission provided investigators with a general idea of what conditions were like in the vicinity of the orbiter and led to a much more comprehensive study of the orbiters wake during the Spacelab-2 mission.

This dissertation will begin with a review of plasma wakes, Chapter II. The object of this review is two-fold. It will afford us with an idea of the type of phenomena we can expect to see in the wake of an object, such as the shuttle orbiter, and it will also indicate the areas where this study can be expected to make significant contributions. Chapter III will describe the experimental wake studies conducted during Spacelab-2, Chapter's IV and V will present the data, and Chapter VI will summarize our results.

CHAPTER II

REVIEW OF PLASMA WAKES

An Obstacle in a Plasma

When an obstacle is placed in a plasma it will be subjected to a current due to the electrons and ions that are striking it. If there is an imbalance between the electron current and the ion current the obstacle will begin to charge. This charging will continue until the obstacle reaches an electrical potential that will cause the ion flux to balance the electron flux. When this occurs the obstacle is said to be charged to the floating potential, ϕ_{fl} . The equation that describes this is

$$I_{ion} - I_{electron} = 0, \quad (1)$$

where I_{ion} is the sum of the ion currents and $I_{electron}$ is the sum of the electron currents. In the example that follows we will use the word 'ram' to refer to the region within 90° of the spacecraft velocity vector, while 'wake' will refer to the region within 90° of the vector antiparallel to the spacecraft velocity vector.

Measurements taken at the altitude of the Spacelab-2 mission, 340 km, indicate a typical electron density given by $n_e = 1 \times 10^{-5} \text{ cm}^{-3}$ and an electron temperature of $T_e = 2500 \text{ K}$. This will be examined in more detail in the next chapter. Assuming these to be the nominal values for n_e and T_e and that $n_e \approx n_i$,

$T_e \approx T_i$, as is typical of ionospheric plasmas, we find the ion and electron thermal velocities to be 1.1 km/s and 180 km/s, respectively. Since the velocity of the orbiter, v_o , was 7.7 km/s we are in the regime where $v_{i,th} \ll v_o \ll v_{e,th}$. Under these conditions the ion current to an ionospheric satellite will consist of the ions that are 'rammed' out by the the spacecraft's orbital motion. The equation describing this is

$$I_{i,sc} = A_i e n_i v_o, \quad (2)$$

where A_i is the cross sectional area that is swept out by the spacecraft, n_i is the ambient ion density, and v_o the satellite orbital velocity.

Since the thermal velocity of the electrons is greater than than the orbital velocity of our satellite all surfaces of the satellite will collect electron current, not just the ram side. We assume that the electrons have a Maxwellian velocity distribution given by

$$f_e(v) = n_e \left(\frac{m_e}{2\pi k T_e} \right)^{3/2} \exp\left(\frac{-m_e v^2}{2k T_e} \right). \quad (3)$$

The electron current to a satellite at a potential V less than the plasma potential, and measured relative to the plasma potential, consists of those electrons with energies greater than $|eV|$ that strike the satellite, and is given by

$$I_{e,sc} = A_e e n_e \left(\frac{k T_e}{2\pi m_e} \right)^{1/2} \exp\left(\frac{eV}{k T_e} \right), \quad (4)$$

where A_e is the surface area of the satellite, T_e is the electron temperature, k is Boltzmann's constant, n_e is the electron density, and m_e is the electron mass. Combining equations (2), (4), and (1) we find that the floating potential is given by

$$\phi_{fl} = \frac{kT_e}{e} \ln \left(\frac{A_i e n_i v_o}{A_e e n_e \left(\frac{kT_e}{2\pi m_e} \right)^{1/2}} \right). \quad (5)$$

The value of the floating potential that we would calculate from this equation for the PDP is -0.86 volts, Tribble et al. [9]. This derivation has ignored the possibility of photoemission of electrons and a number of other factors that may add small corrections to equation (5). These corrections, which are not expected to have an impact on measurements to be presented in this dissertation, are adequately discussed by Kasha [10].

The potential on the body, ϕ_{fl} , is one of two parameters that play an important role in the formation of a plasma wake. The second parameter is known as the space charge field. The space charge field is the electric field that arises because of the differing thermal velocities of the ions and electrons. Since we are in a regime where $v_{i,th} \ll v_o \ll v_{e,th}$ the electrons will be able to fill in the wake of our obstacle quite easily. The ions, having much slower thermal speeds, will not be able to reach the area in the very near wake of the obstacle and a charge separation will result giving rise to the space charge field. The relative abundance of electrons in the near wake of the satellite will be responsible for causing that region to be a region of negative potential. This negative potential

will then act as a barrier to additional electrons and the near wake of the satellite will be characterized by an unequal depletion of both ions and electrons. Samir, Maier, and Troy [11].

It is appropriate to mention that electron temperature enhancements are usually observed in these regions of negative potential. Samir and Wrenn [12], Illiano and Storey [13], and Troy, Maier, and Samir [14] report that these enhancements are typically on the order of 50 -100%, but can sometimes be higher. Samir, Brace, and Brinton [15] report that the magnitude of the enhancement is dependent upon the size of the object and the ambient temperature but not upon the plasma density. Morgan, Chan, and Allen [16] report that the enhancement depends on the ratio of the ion energy to the electrical potential energy of the object. The mechanism for production of this temperature enhancement is not agreed upon in the literature. Two explanations have been offered to account for this effect. One is that a wave-particle interaction may take place in the potential well behind the object. This interaction may apply a filtering mechanism to the electrons that leave the well and result in a population of hotter electrons close to the spacecraft. Alternatively, one may infer the possibility of a heating mechanism related to stream interactions and/or instabilities correlated with plasma oscillations in the near wake, Samir and Wrenn [12].

A simple sketch of the wake, as depicted by Fournier and Pigache [17] and Martin [1], is seen in Figure 1. Because of the electric field due to the body potential, ions passing near the body will be deflected towards the wake axis. These deflected ions may produce an ion density peak in the wake. The

location of the peak, z_{near} , and the deflection angle, θ_D , are both dependent upon the body potential, ϕ_{fl} . Several investigations into the properties and dependencies of these ion density peaks have been carried out. Worthy of special note are the studies by Taylor [18,19], Skvortsov and Nosachev [20,21], Schmitt [22], Bogaschenko et al. [23], Stone, Oran, and Samir [24], and Merlino and D'Angelo [25], in addition to those previously mentioned.

After the ion streams pass the edge of the body they will continue to be accelerated by the space charge field. The transverse velocity acquired by these ions is on the order of the ion acoustic speed. In the far wake of the object we may detect a wave-like disturbance propagating at about the Mach angle $\theta_m = \sin^{-1}(1/M)$. It can easily be seen that this transverse ion acceleration is similar to the process of plasma expansion into a vacuum, which is the subject of the next section.

Plasma Expansion into a Vacuum

Consider a semi-infinite plasma confined to the region $x \leq 0$ at $t = 0$, Figure 2 a). If the plasma is allowed to expand into the vacuum, the region $x > 0$, how will the density and velocity distribution evolve? As the expansion begins the electrons will enter the vacuum first, because of their higher thermal velocities. This is the charge separation mentioned earlier. The space charge field will accelerate the ions and an 'expansion front' will move into the vacuum. To compensate for this a region of decreased plasma density, a 'rarefaction wave', will move into the ambient plasma. The ion acceleration has been studied by

Gurevich, Pariškaya, and Pitaevskiĭ [26], who report that it is the ions nearest the interface that will attain the highest velocities. Since the rarefaction wave is the result of ion motion it can be expected to travel at the ion acoustic velocity.

A numerical simulation by Singh et al. [27] reports that this plasma expansion can account for the electron temperature enhancements mentioned earlier. The picture they present is that as the ambient plasma expands into the vacuum it is the electrons with highest thermal velocities that arrive in the vacuum first. Then, as time elapses progressively slower electrons will stream into the void. The electric potential in the void will grow more negative as the electrons fill in the region. This negative potential slows down the electrons that have yet to arrive. As a result, electrons that are already in the region of negative potential, the electrons in the tail of the original Maxwellian distribution, will account for the majority of electrons seen there. Consequently, we will detect a warm electron population with a thermal spread in the velocity distribution about a factor of 2 larger than the thermal spread in the ambient plasma.

As summarized by Samir, Wright, and Stone [28], the phenomena we may expect to see in the wake of an object in a plasma are as follows:

1. Ions are accelerated to high energies.
2. A rarefaction wave is created which propagates into the ambient plasma.
3. An ion front (shock) moves into the vacuum region.
4. Excitation of instabilities and plasma waves over certain volumes in space take place.

5. Strong (or jump) discontinuities in the plasma occur at the expansion front.

In the next section we will examine how some of the phenomena seen in the wake are dependent upon the plasma and upon the object being studied.

Factors Influencing Wake Phenomena

In order to understand the specific case of a satellite in the ionosphere we need to first understand how the properties associated with a plasma wake are dependent upon both the size and shape of the object and upon the plasma being studied. That is, how do the values of the plasma density and temperature, the satellite floating potential, and the ratio of object size to Debye length affect the wake structure. Let's first examine the effect of body size on wake structure. As reported by Martin [1] the ratio of body size to Debye length plays an important role. In the situation where $R_o < \lambda_D$ the wake will be dominated by the ion deflection effects that are controlled by the potential on the object. If we move to the region where $R_o > \lambda_D$ we find that the body potential loses much of its influence upon the ion trajectories and the wake is controlled mostly by the space charge field. The reason for this is fairly straightforward to understand. Consider a disk 1 cm in diameter in a streaming plasma with a Debye length of 1 cm. Obviously, a sizeable fraction of the ions found in the objects wake must have passed within one Debye length of the object. In contrast, if the disk was 10 m in diameter, then the fraction of ions in its wake that had passed within one Debye length of its edge would be negligible. The shape of the object will

also play an important role in determining wake features. As reported by Oran, Stone, and Samir [29], the cross sectional area is actually more important than the overall size. A highly symmetrical object would be expected to give rise to a highly symmetrical wake with sharp wake features, whereas the converse would be true for an asymmetrical object.

Changing the ratio of T_e/T_i may also have a noticeable effect on some wake features. Könemann [30] reports that in isothermal plasmas no sharp wake features can be expected, because the appropriate waves are heavily damped and other features are smoothed by the thermal motion of the ions. Effects associated with varying the value of the body potential, ϕ_{f1} , have already been discussed.

Summary

We can now summarize some of the results that we would expect to see in the wake of an object like the shuttle orbiter. First, since we are in the realm where $R \gg \lambda_D$ we would not expect to see effects due to deflected streams of ions, as seen in Figure 1. Rather we would expect to see only those effects related to the space charge field, i.e., wake disturbances that propagate outward at the Mach angle. Second, since the ionosphere satisfies the condition $T_i \approx T_e$ we would expect most of the waves in the wake of the orbiter to be heavily damped. Finally, the fact that the orbiter presents a highly asymmetrical cross section to plasma flow indicates that we will not expect any 'sharp' wake features and the regions of density depletion, temperature enhancements, and turbulence would be spatially 'smoothed'.

CHAPTER III

THE EXPERIMENT

Equipment

The data that will be presented in this dissertation was collected by a University of Iowa satellite the Plasma Diagnostics Package (PDP), Figure 3. The PDP was composed of 14 instruments designed to make measurements of magnetic and electric fields, particle distributions, radio waves, plasma composition, as well as plasma density, temperature, and turbulence. In particular, we will be examining data collected by a Langmuir probe on the PDP, which was mounted on one of the PDP's extendable booms. The Langmuir probe consisted of a 3 cm diameter gold-plated sphere and supporting electronics. The probe was used to measure plasma densities from 10^3 to 10^7 electrons/cm³, plasma temperatures from about 1000 K to 5000 K, and density fluctuations in the frequency range 30 Hz to 178 kHz.

The electronics that control the probe's operation alternate between two different modes, one complete cycle requiring 12.8 seconds. The first is an 11.8 second 'lock' mode. During this time the Langmuir probe is biased at +10 volts, relative to the PDP chassis, and is used to measure electron density fluctuations. The current to the probe is sampled at a rate of 120 Hz. The data is passed through three filters, 1 Hz low pass, 1-6 Hz bandpass, and 6 - 40 Hz bandpass,

with sampling rates of 5 Hz, 20 Hz, and 120 Hz respectively. A fourth filter, 30 Hz high pass, routes the output to a wideband receiver and spectrum analyzer which can look at details of the current fluctuations up to a frequency of 178 kHz.

The 'lock' mode is followed by a 1.0 second 'sweep' mode where the bias voltage on the probe is swept from +10 volts to -5 volts in discrete steps of 0.125 volts and then returned to +10 volts. During the sweep mode the data collected by the Langmuir probe is sent through a 0-50 Hz low pass filter and can be used to determine the electron temperature, electron density, and plasma potential. A derivation of the appropriate equations is given in Appendix A. The data we obtain from the probe therefore consists of one measurement of electron density, temperature, and plasma potential every 12.8 seconds, in addition to the 11.8 seconds of density fluctuation data. Experience has shown that when the Langmuir probe is in the lock mode the output from the 1 Hz low pass filter, which is essentially the DC current to the probe, can be used as a good approximation to the electron density. This will be justified in the section on the ambient ionosphere. The performance characteristics of the probe are listed in Table 1.

It is also possible to perform a spectral analysis on the 0-40 Hz data that we have just described. To do this we first create a data file containing the 11.8 seconds worth of lock mode data. We then apply a cosine weighting function to the first and last 10% of the data, Bingham et al. [31], and set any bad or missing data to zero. By taking the Fast Fourier Transform (FFT) of these data we are

able to look at the spectral density. The output from this FFT is given in units of dB ($\delta N/N$) and is calibrated to have a minimum of 0.01% and a maximum of 2.7%. We will look at the dB average ($20 \times \log(\text{data})$) and the peak values over the range -80 to -31.37 dB.

Finally, we will give examples of the spectral density obtained by routing the Langmuir probe data through a spectrum analyzer. The spectrum analyzer consists of 16 channels. The output from each channel is an amplitude spectrum given in units of dB $\left(\frac{\delta N/N}{\sqrt{Hz}}\right)$, found from the relation ($20 \times \log(V_{rms})$). Table 2 shows the channels, their bandwidths, their saturation levels and the appropriate multiplying factors (see below). Subsequent to the mission four of the channels were found to contain bad data, these are the channels that are not reported in Table 2. Note that the saturation $\delta N/N$ has been multiplied by the square root of 2 since we wanted peak values rather than RMS values. The multiplying factor is formed by dividing saturation $\delta N/N$ by the square root of the bandwidth.

Procedure

The data used to study the wake of the orbiter was obtained during two separate maneuvers designed to allow the PDP to study both the near and far wake of the orbiter. The first maneuver, designed for near wake studies, involved placing the PDP on the RMS a distance of 10.53 m above the center of the payload bay with the booms partially extended. By keeping the x-axis of the orbiter perpendicular to the orbital plane rolling the orbiter at a rate of 1° per second would move the PDP alternatively into and out of the orbiter's wake,

Figure 4. This maneuver is referred to as XPOP roll. At this same time, the RMS could be rotated at the same rate so that the orientation of the PDP, relative to plasma flow, remained unchanged. In the plane of rotation the biggest obstacles to plasma flow were the orbiter's payload bay doors, which were 10.35 m wide. Consequently, if we define Z to be the width of our obstacle, 10.35 m, and R to be our downstream distance, 10.53 m, the XPOP roll maneuver occurred at a characteristic ratio of $Z/R \approx 1$.

For a period of 6 hours the PDP was released as a free-flying satellite in order to allow the PDP to study the mid and far wake of the orbiter. During this time the booms seen in Figure 3 were extended to their full length. After release from the orbiter the PDP was spin stabilized with an inertial spin period of 13.06 seconds. The plane of PDP rotation was coincident with the orbital plane. During this period of six hours the orbiter executed a series of maneuvers around the PDP designed to allow the PDP to study the wake of the orbiter. Also, on four occasions the PDP and the orbiter were aligned on approximately the same magnetic field line which allowed for a study of flux tube events. The distance from the orbiter to the PDP, in a non-inertial coordinate system using the orbiter as its origin, is shown in Figures 5 - 8. Here the largest obstacle to plasma flow is the body of the orbiter itself, with a length of 35.56 m. The data obtained during this six hours of free flight represents the only in situ observations on the mid and far wake of the shuttle orbiter.

The Ambient Ionosphere

It is appropriate to discuss the characteristics of the ambient ionosphere. The plasma in the Earth's ionosphere arises due to the ionizing effect of the sun's UV radiation striking the neutral gases found there. At the altitude of the Spacelab 2 mission the ionization is 1 - 2% of the neutral gas, with the major constituent being atomic oxygen. Data obtained by the Langmuir probe on the PDP during the period of free flight just described is illustrated in Figures 9 and 10. These data correspond to the times when the distance between the PDP and the orbiter were those given in Figures 6 and 7, respectively. The apparent data drop outs that occur with a periodicity of approximately 9.5 minutes are an indirect result of the operation of another PDP instrument, the LEPEDEA, and are described in more detail by Tribble et al. [9]. For the remainder of this dissertation we will remove any visible perturbations in the data that we can associate with the LEPEDEA so that it will not have an affect on the results we present. At this point we can compare the 0-1 Hz data with the results from the Langmuir probe sweep mode. Earlier we had mentioned that the 0-1 Hz data could be used as our approximation to electron density. This agreement is confirmed in Figure 11. We will use the 0-1 Hz data as our estimate of the electron density in the succeeding chapters since it is sampled at a rate of 5 Hz and not once every 12.8 seconds as is the sweep mode data.

As we can see from Figures 9 and 10, the data we measure agree with the assumptions used in Chapter II. A listing of some of the plasma parameters associated with the ionospheric plasma are given in Table 3.

CHAPTER IV

THE NEAR WAKE

Plasma Density and Temperature

Our discussion of the near wake of the orbiter will center around data taken during XPOP roll. Since the rotation rate of the orbiter was one degree per second we will present the data in terms of an orbiter phase angle, which we define as the angle, in the orbiters' yz plane, between the velocity vector of the orbiter and the vector that points from the center of mass of the orbiter to the center of the PDP.

Measurements of the plasma density and temperature found during the first transit of the orbiters' near wake are shown in Figure 12. Unlike the remaining wake transits, during the first near wake transit the RMS was kept fixed. Two things should be noted about this data. First, the apparent density enhancement at a phase angle of 180° is associated with a thruster firing. Second, the wake of the orbiter appears to be centered around a phase angle of about 185° and not 180° as we might expect. This 5° offset occurs because the physical displacement of the Langmuir probe from the center of the PDP was such that the Langmuir probe did not arrive at the center of the orbiter's wake until the orbiter phase angle was approximately 185° .

If we assume that the ambient plasma conditions can be given by a straight line fit between the data collected at a phase angle of 130° and that collected at 230° we can calculate the density depletions and temperature enhancements in the wake as shown in Figures 12 and 13, respectively. During the maneuver known as XPOP roll we have data on 8 transits of the orbiters wake. The value of the electron density obtained when on wake axis, i.e. when the orbiter phase angle was 180° , was always below the minimum sensitivity of the instrument. But, by interpolating as in Figure 12 we can infer that on the wake axis at a distance of 10 meters behind the orbiter the electron density is approximately 0.1% of its ambient value, while the electron temperature shows an enhancement on the order of 300-500%. The value for the Mach angle calculated for these conditions is approximately 43° . If we allow for the 5° offset due to the physical displacement of the Langmuir probe boom we would expect the Langmuir probe to enter the Mach cone when the orbiter phase angle was 142° and exit it when the phase angle was 228° . This is in excellent agreement with the data. For completeness data on the succeeding two wake transits are shown in Figures 14 through 16. The electron temperature data for the third wake transit is not presented because, as can be seen from Figure 16, there are too few data points available to allow an accurate interpretation of temperature enhancements.

Plasma Turbulence

We can now proceed with an examination of the plasma turbulence in the orbiter's wake. As mentioned in Chapter II, the output from the Langmuir

probe circuitry is broken up into three channels representing the 0-1 Hz, 1-6 Hz, and 6-40 Hz components, respectively. The 1-6 Hz data obtained for near wake transit one is shown in Figure 17, while the 6-40 Hz data is shown in Figure 18. The 1-6 Hz data indicate that there are few, if any, wake effects visible in this frequency range. This data is reproducible throughout XPOP roll. The 6-40 Hz data on the other hand, indicate there is a great deal of turbulence in this frequency range that is associated with the wake of the orbiter. In addition to the wake structure, Figure 18 indicates the effects of thruster firings at 130° and 230° . Also, the effects of the LEPEDA are visible when that instrument points into the ram of the plasma flow, phase angles 250° to 270° . The 6-40 Hz data obtained during the two successive wake transits are shown in Figures 19 and 20. Again increases in turbulence which are associated with thruster firings are visible in Figure 20 at a phase angle of approximately 130° . Recall that during near wake transit one there was a thruster firing at an orbiter phase angle of about 180° . We believe that this is the explanation for the fact that turbulence is seen throughout near wake transit one, while transits two and three indicate a decrease in turbulence when directly on the wake axis. These data support the conclusion that we encounter turbulence as we cross the orbiter's Mach cone. This turbulence then decreases to a level below that associated with the ambient ionosphere when directly on wake axis.

A brief aside is in order here to discuss the Langmuir probe circuitry. Recall from Figure 12 that the measurements of electron density when on the wake axis were below the minimum sensitivity of the instrument. We have examined

the possibility that the decrease in turbulence seen when crossing the wake axis was due to instrumental effects. However, the gain of the 6-40 Hz channel is a factor of 154 greater than the gain of the 0-1 Hz channel. We believe that the decrease in current to the probe, when on the wake axis, would not in itself be sufficient to account for the decrease in turbulence.

We can carry our analysis one step further by performing a Fast Fourier Transform (FFT) on the 0-40 Hz data. Recall that the FFT calculation utilizes 11.8 seconds of data to produce one graph. Since this corresponds to an 11.8° arc through the wake this will limit our spatial resolution. We should also mention that an examination of the FFT data does not indicate any effects that we can associate with the effect of the LEPEDEA.

FFT Data obtained during near wake transit one is presented in Figures 21 through 25. The starting and ending values of the orbiter phase angle that correspond to each graph can be calculated by adding the decimal seconds of the starting and ending time of each graph to 120° . For example, Figure 21, which begins at 04 seconds and ends at 16 seconds, represents data obtained between an orbiter phase angle of 124° and 136° . The conditions indicated by Figure 21, taken just outside of the orbiter's Mach cone, are equivalent to those encountered in the ambient ionosphere. Immediately after crossing the Mach cone, Figure 22, the basic shape of the signature remains the same but the spectral density is shifted downward by about 20 dB. When we reach a phase angle of about 150° , Figure 23, the spectral density of the lowest frequency components, 0 - 1 Hz, are about the same, -50 dB, but the spectral density of the higher frequency

components, 2 - 40 Hz, has increased from -80 dB to -65 dB. This is the increase seen previously in the 6-40 Hz data of Figure 18. This leveling of the spectral density increases as the phase angle progresses to 143° , Figure 24. The data obtained when crossing the wake axis, Figure 25, is essentially the same as that seen in Figure 24 except for an increase in spectral density in the 0-5 Hz range. This particular increase is most likely the result of the thruster firing reported earlier that occurred at a phase angle of 180° . The data pertaining to the two subsequent wake axis crossings, Figures 21 and 22, are identical to that seen in Figure 25 except for the increase in the 0-5 Hz range. As the PDP exits the orbiters wake Figures 21 - 25 are essentially repeated in reverse order, confirming the geometrical symmetry that we would expect.

We will now examine the spectral analyzer data which examines details of density fluctuations from 30 Hz to 178 kHz. These data are sampled once every 6.83 minutes for a period of 51.2 seconds at a stretch. The only spectral analyzer data that are available during a near wake transit is that of near wake transit five. The density, temperature, and turbulence data for near wake transit five are quite similar to those presented for near wake transits one through three previously given.

The spectrum analyzer data corresponding to an orbiter phase angle of 159° are given in Figure 26. There appears to be a fairly sharp drop off in spectral density of $\Delta N/N$ past a frequency of 10,000 Hz. This frequency is on the order of the ion plasma frequency, 39,000 Hz. Recall that the Langmuir probe would cross the orbiter's Mach cone at phase angles of 142° and 225° , so

we are well within this range. The data corresponding to a phase angle of 164° is shown in Figure 27. It is fairly similar to that given in Figure 26 in that there is a sharp drop off in the spectral density of $\Delta N/N$ at 10,000 Hz. However, Figure 29 indicates a drop in the spectral density for the frequency range 31 - 200 Hz and an increase for the 200 - 10,000 Hz range. This trend is continued in the next graph, corresponding to a phase angle of 167° , Figure 28. Figure 29, corresponding to a phase angle of 175° , indicates a return to the conditions of Figure 28. This is repeated when the PDP is directly on the orbiter's wake axis, Figure 30.

The same shift, from a spectral density of about -80 dB to -90 dB in the frequency range of 31 - 200 Hz is observed as the PDP continues in its transit of the orbiter's wake. Figures 30 and 31 indicate a spectral density of about -80 dB for this frequency range, while Figure 32, orbiter phase angle 190° , shows the spectral density here depressed by about 10 dB in comparison to the spectral density at 1000 Hz. The conditions return to those originally seen in Figure 26 for phase angles of 198° and 206° , see Figures 33 and 34.

CHAPTER V

THE MID AND FAR WAKE

Plasma Density and Temperature

We have a number of opportunities to view cross sections of data taken downstream from the orbiter during the six hours of free flight. The spatial location of the PDP during the times best suited for wake studies can be culled from Figures 5 - 8, and is given in Figure 35. The first data set that we will examine was taken just after the PDP was released from the orbiter. This maneuver, which we refer to as backaway, is illustrated in Figure 36. The electron density dependence seen during this time is illustrated in Figure 37. The dashed line in Figure 37 a) represents the value associated with the ambient ionosphere. Note that the enhancements seen from 11:45 to 12:00 minutes are associated with a series of thruster firings. The ambient data was obtained at the same local time 1.5 hours later in the mission when the PDP was not in the wake of the orbiter. Similarly, the electron temperature dependence is shown in Figure 38. Note that two symbols are used to indicate the values obtained for the electron temperature. Due to the rotation of the PDP some data points were obtained when the Langmuir probe was in the wake of the PDP and may show effects associated with the PDP's wake. A box is used for these points while an asterisk is used for data points taken when the Langmuir probe was not in the wake of

the PDP. The wake of the PDP is discussed in Appendix B. During backaway the electron density increases exponentially from a low value of approximately 5% of the ambient density as the distance between the PDP and the orbiter increases, while the electron temperature shows an initial enhancement of approximately 100%, which decreases linearly as distance increases.

The first far wake transit is illustrated in Figure 39. The electron density and electron temperature dependencies for this time are given in Figures 40 and 41. Again, the values shown in Figures 40 b) and 41 b) have used a straight line fit between the unperturbed ambient conditions. Data for wake transit two is given in Figures 42 through 44, wake transit three is shown in Figures 45 through 47, and wake transit four is given in Figures 48 through 50.

It is possible to combine the values obtained from each wake transit into one graph that describes the density depletions measured in the wake of the orbiter, Figure 51. This plot is quite significant in that it represents the first such contour model obtained from in situ data. Also of significance is the fact that the lines associated with the value of N_w/N_a cross approximately 100 m downstream from the orbiter. This may suggest the possibility of crossing streams of ions as measured by Merlino and D'Angelo [25]. The work by Murphy et al., [32], indicates values for the maximum electron density depletion on the wake axis that are slightly different than the values that would be calculated from the data in this dissertation. The difference arises because Murphy assumes an ambient model that allows for slight ionospheric variations over the 4-5 minutes necessary for wake transit. Values for $n_{e,wake}/n_{e,ambient}$ measured by both methods agree

to within the errors of the experiment. In order to compare our results with laboratory observations the data in Figure 51 were used to obtain a graph of density depletions for constant values of Z/R . That is, at fixed distances downstream of the orbiter, measured along the orbiters' z-axis, the value of N_w/N_a that would be encountered at various transverse locations, measured along the orbiters' x-axis, were interpolated from Figure 51. These results are presented in Figure 52.

Our efforts to obtain a similar graph for the electron temperature enhancements were somewhat complicated. As is seen in Figures 44, 47, and 50, some of the temperature data taken inside of the orbiters Mach cone happen to coincide with times when the Langmuir probe was in the wake of the PDP. For this reason we have avoided the use of any data points taken in the wake of the PDP in our attempt to obtain a contour map of the temperature dependence in the wake of the orbiter. The remaining data are not sufficient to obtain an accurate map, but they do indicate a distinct temperature gradient as illustrated in Figure 53.

Plasma Turbulence

Due to the problem with the LEPEDEA, Tribble et al., [9], the 1-6 Hz data is completely unusable during free flight. The 6-40 Hz data is somewhat perturbed, but the majority of these perturbations can be removed from the data. The 6-40 Hz data obtained during backaway is seen in Figure 54. These data indicate that the majority of the turbulence in this frequency range that is seen on axis as we move away from the orbiter is confined to the first 2.5 minutes

of backaway, or a distance of 25 m downstream. The large enhancements seen between 11.75 and 12.0 minutes and the smaller enhancements seen at approximately 14.9 minutes, 16.1 minutes, 16.5 minutes, etc., are all associated with thruster firings. If we move to an examination of the far wake transit one data, Figure 55, we see that there are no large structures that we can associate with the orbiter wake. A very slight enhancement is visible at about 02:58:30, between 03:01 and 03:06, and again between 03:08 and 03:09. The interval 03:01 - 03:06 corresponds to the times when the PDP is inside the orbiter's Mach cone. The times 02:58:30 and 03:08 - 03:09 are times when the LEPEDA is in ram. Even though we have removed a majority of the data that show the effects of this problem, some perturbations are still visible in the data when the LEPEDA is in ram. The data corresponding to far wake transit two, Figure 56, indicate a larger enhancement centered at about 04:33:15 and a number of smaller enhancements noticeable throughout this interval. In Figure 56, the PDP was inside of the orbiter's Mach cone from 04:30 to 04:34. Again in far wake transit three, Figure 57, there are a number of sharp, short lived enhancements that we associate with thruster firings. But as in Figure 56 there are no large enhancements to associate with the Mach cone crossings at 04:47 and 04:51. The final far wake transit data are shown in Figure 58, which again shows no large enhancements linked to the Mach cone crossings at 04:58 and 05:03.

The 6-40 Hz data did not indicate any large increases in turbulence that we can associate with the wake of the orbiter. We shall next turn to an examination of the FFT of the 0-40 Hz data. First we will examine data obtained during

backaway 35 m downstream of the orbiter, Figure 59. These data do not differ appreciably from that seen in the ambient ionosphere. Data obtained 120 m downstream, about 20 m past the wake 'crossing point' seen in Figure 51, is presented in Figure 60. These data both indicate a similar drop in spectral density at the higher frequencies. Data taken along the orbiter's Mach cone 200 m downstream are presented in Figure 61. In comparison to the 2 previous figures we see a drop in spectral density on the order of 15 - 20 dB at the higher frequencies. Data taken just outside the orbiter's Mach cone at distances of 20 m and 90 m downstream from the orbiter are shown in Figures 62 and 63, respectively. These bear the general shape of the data obtained on the wake axis, but they also exhibit more rapid variations in spectral density as frequency increases.

The data just presented was chosen so that the LEPEDEA would be facing the wake of the PDP during most of the 11.8 second period covered by the graph. In this manner we have attempted to minimize its effect. However, we previously mentioned that the 1-6 Hz data was completely unusable due to this problem and that the 6-40 Hz data was noticeably perturbed. These perturbations were not removed by the algorithms that computes the FFT of the data. However, by comparing the free flight data with data taken from the RMS or payload bay were are unable to detect any significant differences that we can attribute to either the wake of the PDP or the LEPEDEA.

Due to the different sampling schedule of the spectral analyzer we did not have as many data points available to us as we did for the FFT data. The

locations where we do have spectral analyzer data available to us are shown in Figure 64. The roman numerals will be used to reference the individual data points. For the sake of comparison we will first present data obtained in the ambient ionosphere, Figure 65. Recall the turbulence seen in the very near wake of the orbiter in the 6-40 Hz data. Again, when in the very near wake at location I of Figure 65 we see that the measurements of the turbulence show enhancements, Figure 66. However, the data taken 50 m further downstream, at location II, do not indicate such enhancements, Figure 68. An examination of data obtained on the orbiter's Mach cone at a distance of 250 m, location III, indicates an enhancement of approximately 5 dB at a frequency of 10,000 Hz, Figure 69. This enhancement disappears on wake center, IV, Figure 69, but seems to reappear at the opposite side of the Mach cone, V, Figure 70. Just inside the orbiter's Mach cone at a distance of 150 m downstream, VI, we see an enhancement of approximately 15 dB at a frequency of approximately 20,000 Hz, Figure 71. Again, even at the closer distance, III, the enhancement is not visible on axis, Figure 72. Data obtained at the 5 remaining locations is presented in Figures 73 - 77.

CHAPTER VI

SUMMARY AND CONCLUSIONS

Having completed our analysis of the data we can now present the description of the wake of the orbiter as inferred from the in situ observations. The very near wake of the orbiter, $Z/R \approx 1$, is a region of electron density depletion and temperature enhancement bounded by the orbiter's Mach cone. The electron density measured on the wake axis is 10^{-3} of the ambient value, while the temperatures measured there are increased by a factor of 3 - 5 over ambient conditions. The turbulence in the 6-40 Hz range exhibits a change from a fraction of a percent to over three percent as the PDP entered the orbiter's Mach cone. This turbulence decreased to a level slightly below that associated with the ambient ionosphere when the PDP was within $2^\circ - 3^\circ$ of the orbiter's wake center. The FFT of the low frequency data indicated an overall decrease in the spectral density when crossing the Mach cone and a flattening of the spectral density signature when on the wake axis.

The spectral density of $\Delta N/N$ in the near wake decreased significantly for frequencies higher than $f_{p,i}$ at all times. The turbulence that we associate with crossing the orbiter's Mach cones exhibited an increase in the spectral density for frequencies below about 200 Hz. When in the quieter wake region there was a decrease in the spectral density of these lower frequencies and a slight increase

for frequencies between 200 Hz and 10,000 Hz. When directly on the wake axis, the spectral density at the lowest frequencies was about -80 dB and decayed exponentially as the frequency increased to a spectral density of about -95 dB at a frequency of 10,000 Hz.

In the far wake of the orbiter, the electron density depletion data, Figure 51, indicates a 'crossing point', a region where the electron density on the wake axis was less both upstream of this point and downstream of it. It is important to note that the first far wake transit was at times as much as 15 m out of the orbital plane. Therefore, the density depletions indicated by this farthest wake transit might have indicated densities as low as $0.5 N_a$ had this transit been completely in plane. In any case, the significance of Figure 51 is that it shows conclusively that the density depletions behind the orbiter extend to a distance of several hundred meters behind the orbiter, perhaps even as far as a kilometer. Similarly, the electron temperature enhancements shown in Figure 53 extend equally far downstream.

The 6-40 Hz data indicate that the region of maximum turbulence is confined to a region on the order of the size of the orbiter itself, 35 m. The fact that there is no minimum on the orbiter's axis seen after release from the orbiter may indicate that the turbulence associated with the Mach cones during XPOP roll converges approximately 15 m downstream of the orbiter. It is difficult to find low frequency turbulence that we associate with the far wake of the orbiter, but the effects of thruster firings are readily visible as far as 250 m downstream. The FFT data support the conclusion that there is a decrease in the overall spectral

density when crossing the orbiter's Mach cone and a slight increase when at the 'crossing point' just mentioned.

The spectral density of $\Delta N/N$ is largest in the near wake, a further confirmation of the fact that the majority of the turbulence is confined to a region on the order of the size of the orbiter. The spectral density is essentially constant along the wake axis both before and after the 'crossing point', however this point exhibits a slight increase in the lower frequency spectral density. The spectrum analyzer data indicate that there are ion plasma waves, excited by the passage of the orbiter, that travel outward at the ion acoustic velocity. Since these ion plasma waves were not observed during XPOP roll this data is consistent with the picture seen in Figure 1. That is, the region of turbulence that expands at the Mach angle originates some distance downstream of the obstacle. Since the signature of these waves can vary by 5 - 10 dB, depending on the location of the sample, it would support the statement that waves in the wake of a large obstacle are heavily damped, [30].

Having completed our analysis we find that our results are in agreement with what was expected in Chapter II. Our results are summarized as follows:

1. The electron density depletions and temperature enhancements associated with the wake of the orbiter extend to distances on the order of 1 km behind the orbiter.
2. There is a great deal of low frequency turbulence confined to the near wake, ≈ 35 m, region downstream of the orbiter.

3. The regions of greatest turbulence in the orbiter's wake have essentially a constant spectral density in the 0-40 Hz range.
4. There are ion plasma waves generated in the wake of the orbiter that are traveling at the ion acoustic speed.

APPENDIX A

DERIVATION OF LANGMUIR PROBE EQUATIONS

During the sweep mode the current that is collected by the Langmuir probe is sent through a 0-50 Hz low pass filter and can be used to determine electron density, temperature, and the plasma potential. From elementary plasma physics we know the effect of introducing an object that is charged to a potential, such as a point charge or a probe, into a plasma. If we make the assumption that the mobility of the ions can be neglected in comparison to the mobility of the electrons then the potential around a test charge q is given by

$$V(r) = \frac{q}{r} \exp\left(\frac{-r}{\lambda_e}\right), \quad (\text{A.1})$$

where

$$\lambda_e = \left(\frac{T_e}{4\pi n_o e^2}\right), \quad (\text{A.2})$$

T_e is the electron temperature and λ_e is the Debye length for electrons. Because the potential falls off so rapidly as r increases electrons and ions further than one Debye length away from the probe will be virtually unaffected by the probe's presence. If we apply a large positive bias to the probe we can expect to attract all of the electrons and repel all of the ions within one Debye length of the probe.

Then, as shown, for example, by Huddleston and Leonard [33], we can compute the current collected by the probe in the following manner. If the radius of the probe is much larger than the Debye length, we may assume that all of the particles passing within one Debye length of the probe, through thermal motions for example, will hit the probe. If the probe is perfectly absorbing, then the current collected by the probe will be

$$I = J_r A_s, \quad (A.3)$$

where J_r is the random current flux and A_s is the surface area of the sheath one Debye length away from the probe. Since the radius of the probe is assumed to be much larger than the Debye length we can approximate the area of the sheath by the surface area of the probe. We now have

$$A_s = 4\pi r^2. \quad (A.4)$$

By definition,

$$J_r = Q_s \times (\text{number of particles hitting the probe/unit time}). \quad (A.5)$$

Q_s refers to the charge of each species present in the plasma, a sum over each species in the plasma is implied. To determine the quantity in parenthesis we can look at a differential volume element located at the edge of the sheath farthest from the probe. The particles here are far enough away from the probe that

we only need consider their thermal motions. Therefore, half of the particles in this volume element would be entering the Debye sheath, half would be leaving it. We conclude that the number of particles entering the sheath per unit time, i.e. the number of particles that will eventually impact the probe, is $(N_s/2)A_s v_s$, where N_s is the density of each species in the plasma and v_s is their velocity. This tells us that

$$J_r = \frac{Q_s N_s A_s v_s}{2} \quad (A.6)$$

If we assume each plasma species has a Maxwellian velocity distribution then

$$P(v) = 4 \left(\frac{M_s}{2\pi k T_s} \right)^{3/2} v^2 \exp \left(\frac{-M_s v}{2k T_s} \right) \quad (A.7)$$

is the probability that a given particle will have its velocity between v and $v + dv$. The average magnitude of the velocity is given by

$$\langle v_s \rangle = \int_{-\infty}^{+\infty} v_s P(v_s) dv_s = 2 \left(\frac{2k T_s}{\pi M_s} \right)^{1/2} \quad (A.8)$$

The direction of the velocity vector, for the particles entering the sheath, will be randomly distributed over 180° . Therefore, we can define the vector so that the component of velocity directed at the probe is given by $v_s \cos \theta$. When we integrate over the factor $\cos \theta$ to find the average component of velocity in the direction of the probe we pick up a factor of $1/2$, which cancels a factor of 2 in the previous expression for v_s . Therefore, when we combine this definition of v_s with the definition of J_r , we find that the current collected by the probe is

$$I = Q_s(4\pi r^2) \frac{N_s}{2} \left(\frac{2kT_s}{\pi M_s} \right)^{1/2} \quad (A.9)$$

Again, there is an implied sum over all the species present in the plasma. If we apply a large positive bias voltage to the probe we may assume that only electrons will contribute to the current collected, that is, the ion current will be negligible. Therefore, the value of the electron current, before the probe saturates, is given by

$$I = -e(4\pi r^2) \frac{N_e}{2} \left(\frac{2kT_e}{\pi M_e} \right)^{1/2} \quad (A.10)$$

This equation is dependent upon both density and temperature. However, we can make use of the Boltzmann relation from statistical mechanics. In the presence of a potential, in this case the probe, the density is given by

$$N_e = N_o \exp \left(\frac{-eV}{kT_e} \right) \quad (A.11)$$

Plugging this into the previous equation gives

$$I = -e(4\pi r^2) \frac{N_o}{2} \left(\frac{2kT_e}{\pi M_e} \right)^{1/2} \exp \left(\frac{-eV}{kT_e} \right) \quad (A.12)$$

Now we have an equation involving the electron temperature and the probe bias voltage V . Taking the natural log of both sides of this equation gives

$$\ln I = C + (C' \ln T_e) + \left(\frac{-e}{kT_e} \right) V \quad (A.13)$$

where both C and C' are constants depending on the radius of the probe, the mass of the electron, and so on. The term proportional to $\ln T_e$ will vary much slower than $1/T_e$, therefore we may approximate the $\ln T_e$ term as a constant. The equation becomes

$$\ln I = C'' + \left(\frac{-e}{kT_e} \right) V. \quad (\text{A.14})$$

If we graph $\ln I$ vs V , before the probe saturates, the slope will be given by $(-e/kT_e)$. This gives us an expression for T_e ,

$$T_e = \frac{-e}{k \text{ slope}}. \quad (\text{A.15})$$

Once we have T_e we can plug this into the expression for I , equation A.10, and deduce an expression for N_e , which is

$$N_e = \frac{-2I}{e(4\pi r^2)} \left(\frac{\pi M_e}{2kT_e} \right)^{1/2}, \quad (\text{A.16})$$

Consequently, we find that the Langmuir probe can indeed give us temperature. If we define the plasma potential as the bias voltage at which the electron density and the probe saturates, a graph of $\ln I$ vs V will also give us the plasma potential. A typical sweep is shown in Figure 78. Note that the value of I that we use in the determination of N_e is chosen so that V is as positive as possible without saturating the probe. This completes our discussion of the equations governing the operation of the Langmuir probe. For a more in depth discussion of probe characteristics under specific plasma conditions see the works by Parrot et al.

[34], Rubinstein and Laframboise [35], Szuszczewicz and Takacs [36], or Makita and Kuriki [37].

APPENDIX B

THE WAKE OF THE PDP

There are times during free flight when the Langmuir probe passes through the wake of the PDP. It is important to understand what effect this may have on the data collected by the probe. Measurements of the electron density depletions in the wake of the PDP are presented in Figure 79 where the PDP phase angle is defined analogously to the orbiter phase angle defined previously. That is, the PDP phase angle is defined as the angle between the PDP's velocity vector and the vector that points from the center of the PDP to the Langmuir probe. Figure 79 seems to indicate that the wake of the PDP is centered around a phase angle of 190° and not the 180° that we might expect. We believe that this ten degree offset arises from uncertainties associated with the calculation of the PDP phase angle and is not indicative of an asymmetric wake.

The data in Figure 79 indicate a density depletion on the order of 30 - 40% of the ambient values when directly in the wake of the PDP. These data also confirm that the density depletions in the wake of the PDP are bounded by the orbiter's Mach cone. Figure 79 represents data collected during four complete rotations by the PDP, so we can conclude that the wake structure is quite stable.

Data pertaining to temperature enhancements in the wake of the PDP are presented in Figure 80. The asterisks are used to indicate data points taken

when the Langmuir probe was outside of the PDP's Mach cone, while the boxes indicate that the probe was inside the Mach cone. We conclude that the wake of the PDP is characterized by a temperature enhancement on the order of 75%, in agreement with previous studies, [12 - 16].

TABLE 1.
Langmuir Probe Performance Characteristics

Current Sensor	$0.1\mu a - 1ma$
T_e	800 - 5000 K
n_e	$10^3 - 10^7 cm^{-3}$
$\Delta N/N$	
≤ 1 Hz	1.8% - 460%
1 - 6 Hz	0.12% - 30%
6 - 40 Hz	0.012% - 3%
≥ 30 Hz (spectrum analyzer)	-30 dB $\Delta N/N$ to -80 dB $\Delta N/N$

TABLE 2.
Spectrum Analyzer Performance Characteristics

Channel	Center Freq. (kHz)	Saturation $\Delta N/N$	Saturation Input (V)	Bandwidth (Hz)	Mult. Factor
0	0.0355	0.113	0.5012	16.1	0.05639822
1	0.0633	0.057	0.2512	21.5	0.04880926
2	0.1200	0.090	0.3981	34.9	0.03830448
3	0.2000	—	—	—	—
4	0.3110	0.226	1.0000	89.1	0.02397155
5	0.5620	—	—	—	—
6	1.0000	0.226	1.0000	353.0	0.01204336
7	1.7800	—	—	—	—
8	3.1100	0.113	0.5012	907.0	0.00751406
9	5.6200	—	—	—	—
10	10.0000	0.113	0.5012	2,050.0	0.00499806
11	16.5000	0.226	1.0000	2,780.0	0.00429158
12	31.1000	0.226	1.0000	3,550.0	0.00379771
13	56.2000	0.226	1.0000	7,110.0	0.00268349
14	100.0000	0.226	1.0000	11,300.0	0.00212861
15	178.0000	0.180	0.7943	12,200.0	0.00204878

TABLE 3.
Ionospheric Plasma Characteristics

Parameter	Symbol and Value
Electron/Ion density	$n_e \approx n_i \approx 1 \times 10^5 \text{ cm}^{-3}$
Electron/Ion temperature	$T_e \approx T_i \approx 2500 \text{ K}$
Orbital velocity	$v_o = 7.7 \text{ km/s}$
Earth's magnetic field strength	$B_E \approx 5 \times 10^{-5} \text{ T}$
Thermal electron velocity	$v_{e,th} = \left(\frac{2kT_e}{m_e} \right)^{1/2} \approx 180 \text{ km/s}$
Thermal ion velocity	$v_{i,th} = \left(\frac{2kT_i}{m_i} \right)^{1/2} \approx 1.1 \text{ km/s}$
Electron plasma frequency	$f_{p,e} = \frac{1}{2\pi} \left(\frac{4\pi n_e e^2}{m_e} \right)^{1/2} = 440 \text{ kHz}$
Ion plasma frequency	$f_{p,i} = \frac{1}{2\pi} \left(\frac{4\pi n_i e^2}{m_i} \right)^{1/2} = 39 \text{ kHz}$
Electron gyrofrequency	$\Omega_e = \left(\frac{eB_e}{m_e c} \right) = 3.5 \times 10^{-2} \text{ s}$
Ion gyrofrequency	$\Omega_i = \left(\frac{eB_e}{m_i c} \right) = 1.0 \times 10^{-6} \text{ s}$
Electron Larmor radius	$R_{e,L} = \left(\frac{m_e v_{e,th}}{eB_E} \right) = 2 \text{ m}$
Ion Larmor radius	$R_{i,L} = \left(\frac{m_i v_{i,th}}{eB_E} \right) = 46 \text{ m}$
Electron Debye length	$\lambda_{e,D} = \left(\frac{T_e}{4\pi n_e e^2} \right) = 1 \text{ cm}$
Ion acoustic speed	$C_s = \left(\frac{kT_e + 3kT_i}{m_i} \right)^{1/2} = 1.6 \text{ km/s}$
Mach number	$M = \left(\frac{v_o}{C_s} \right) = 3.85$
Mach angle	$\theta_m = \tan^{-1} M = 14.5^\circ$

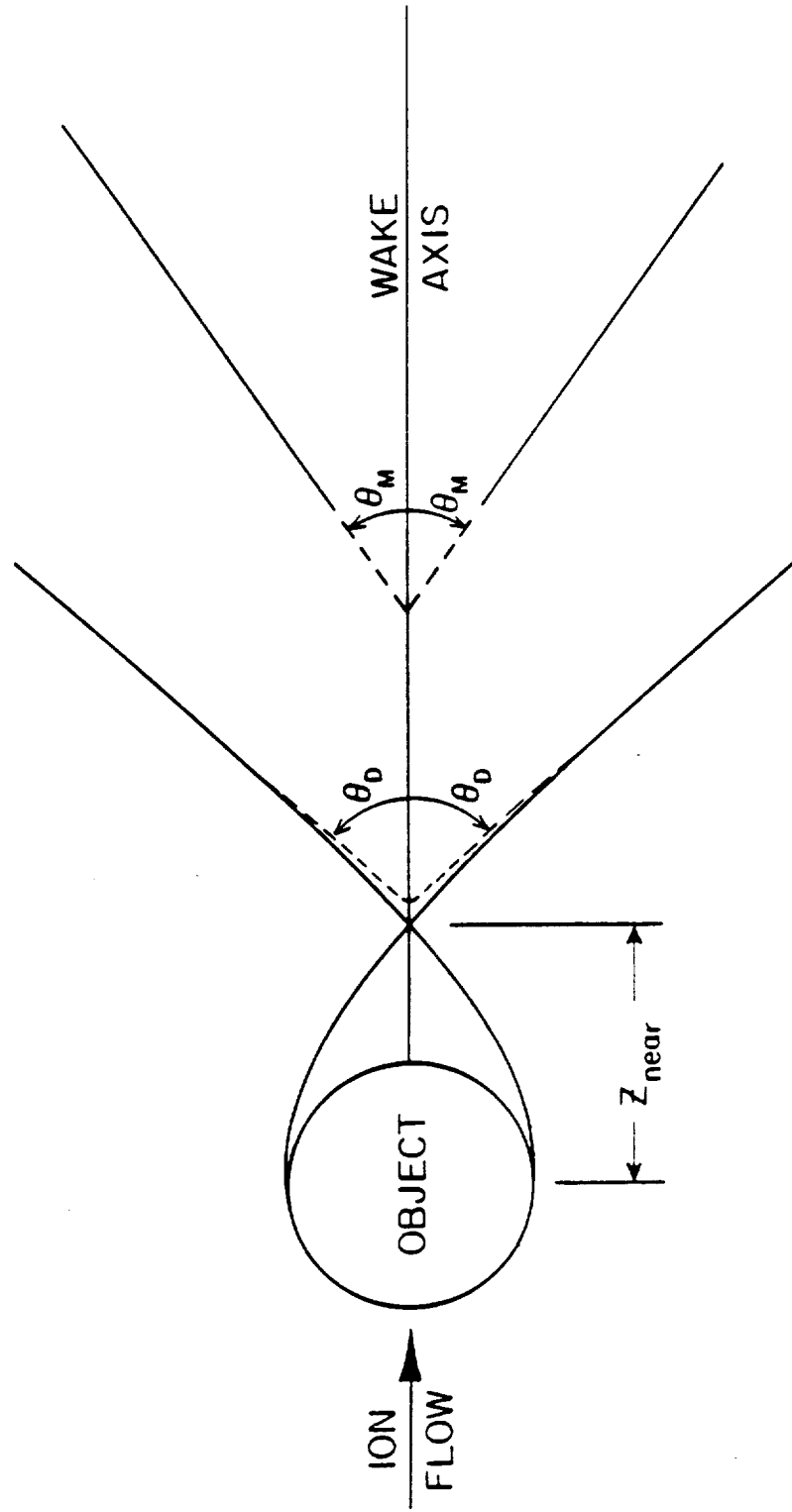


Figure 1. An idealized view of the plasma wake of an object in a flowing plasma.

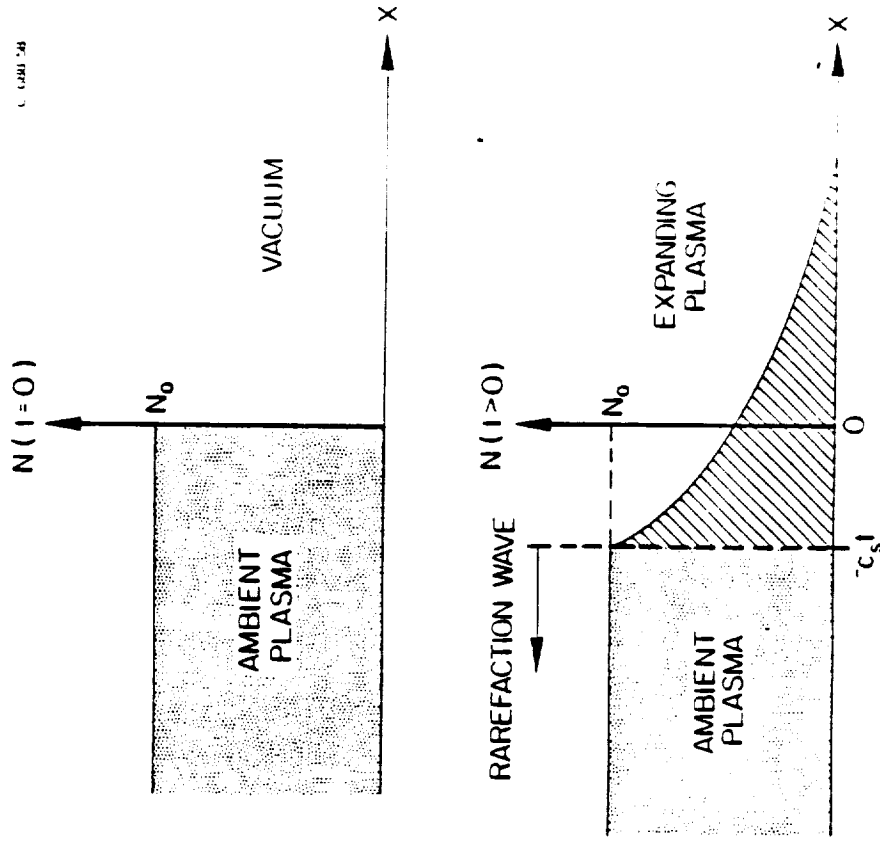
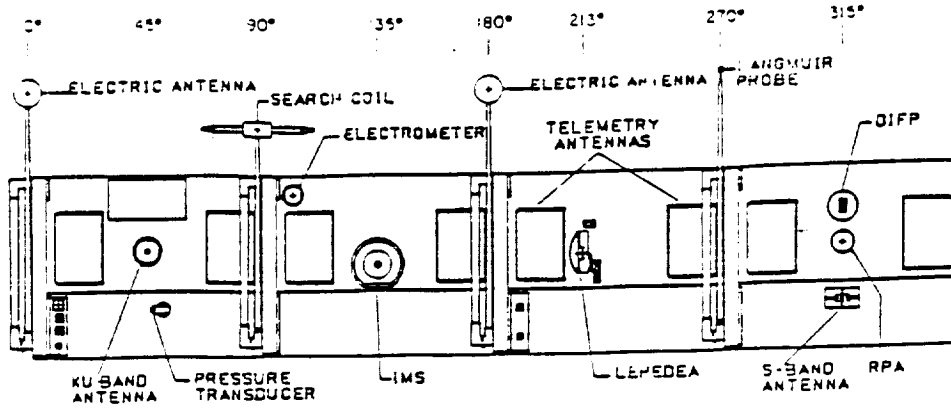


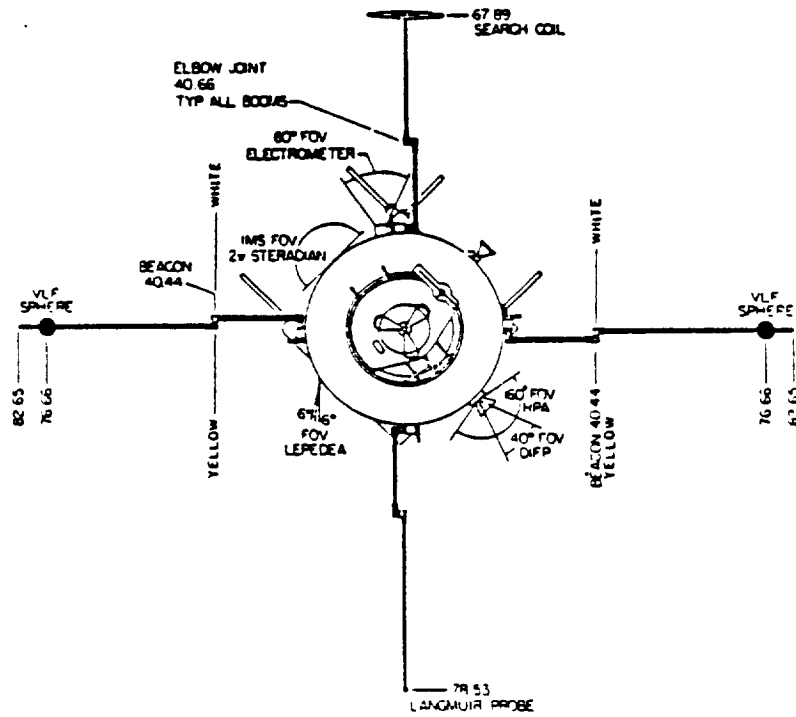
Figure 2. Plasma Expansion into a vacuum.

8-685-947

PDP SENSOR LOCATIONS



PDP "UNROLLED" SIDE VIEW
(BOOMS STOWED)



PDP TOP DOWN VIEW
(BOOMS DEPLOYED)

Figure 3. The Plasma Diagnostics Package.

ORIGINAL PAGE IS
OF POOR QUALITY

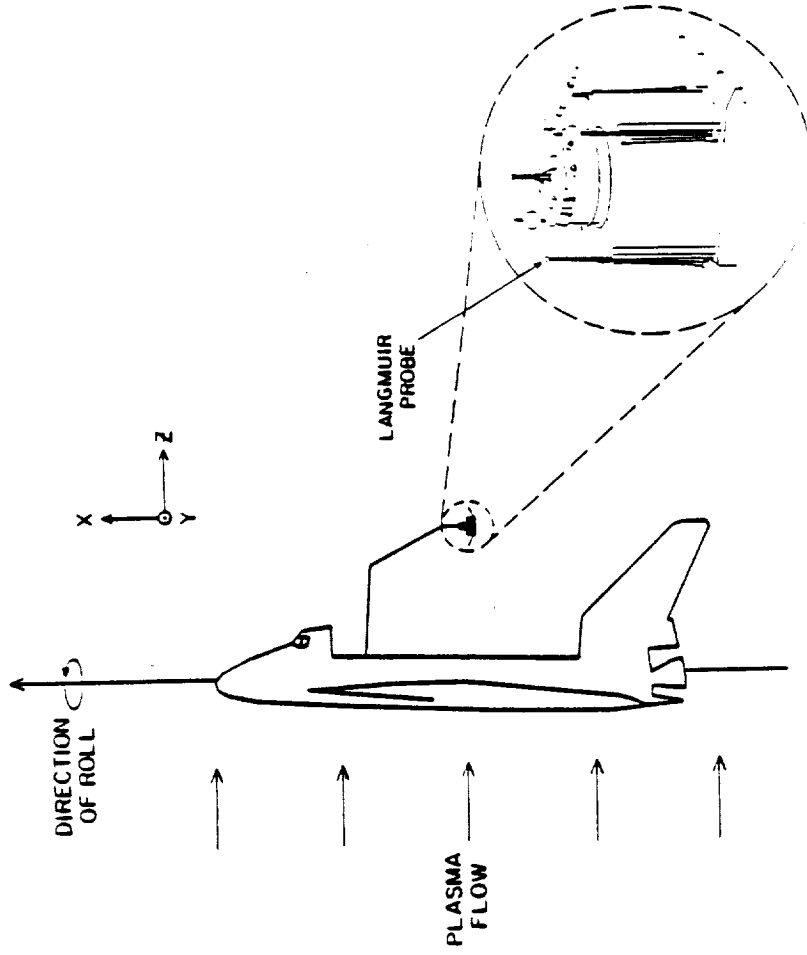


Figure 4. XPOP roll, the procedure used to study the near wake of the orbiter.

A-G88-135

IN PLANE DISTANCE: 0000-0130

1 AUGUST 1985

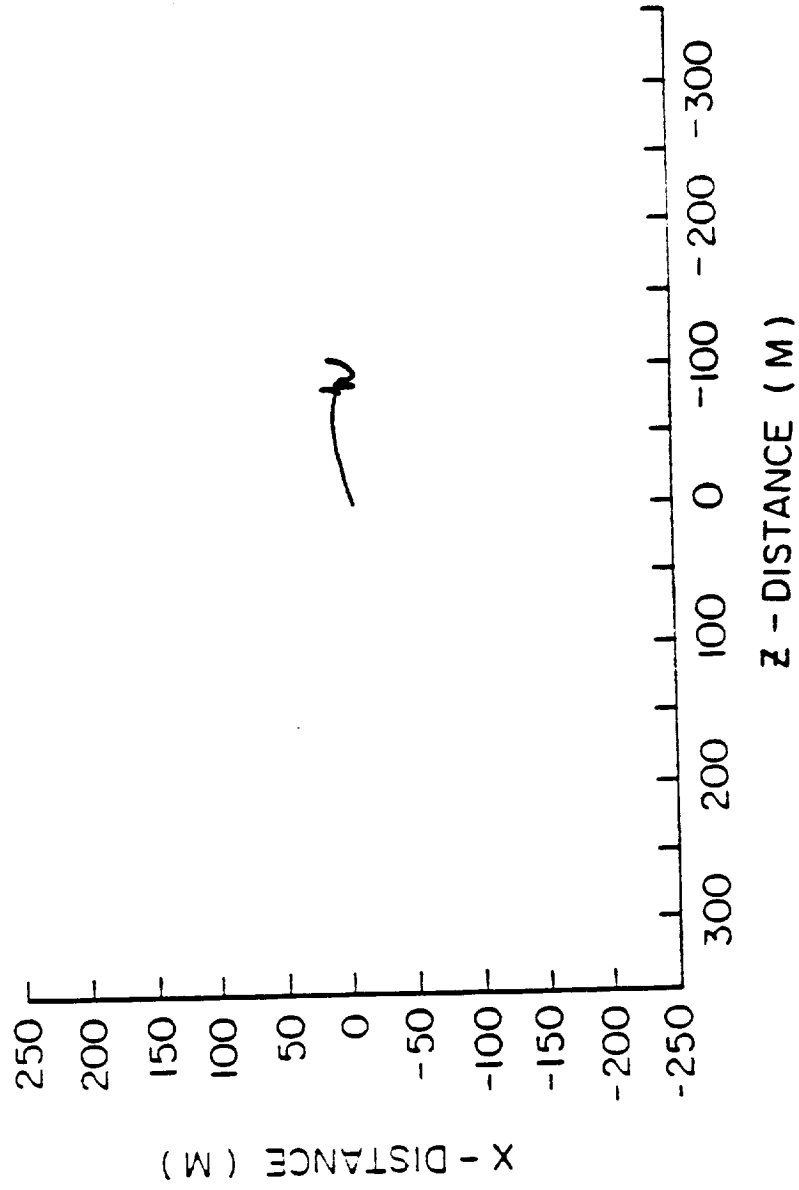


Figure 5. In plane distance between the orbiter and the PDP, 00:00 - 01:30.

A - 688 - 136

IN PLANE DISTANCE: 0130 - 0300

1 AUGUST 1985

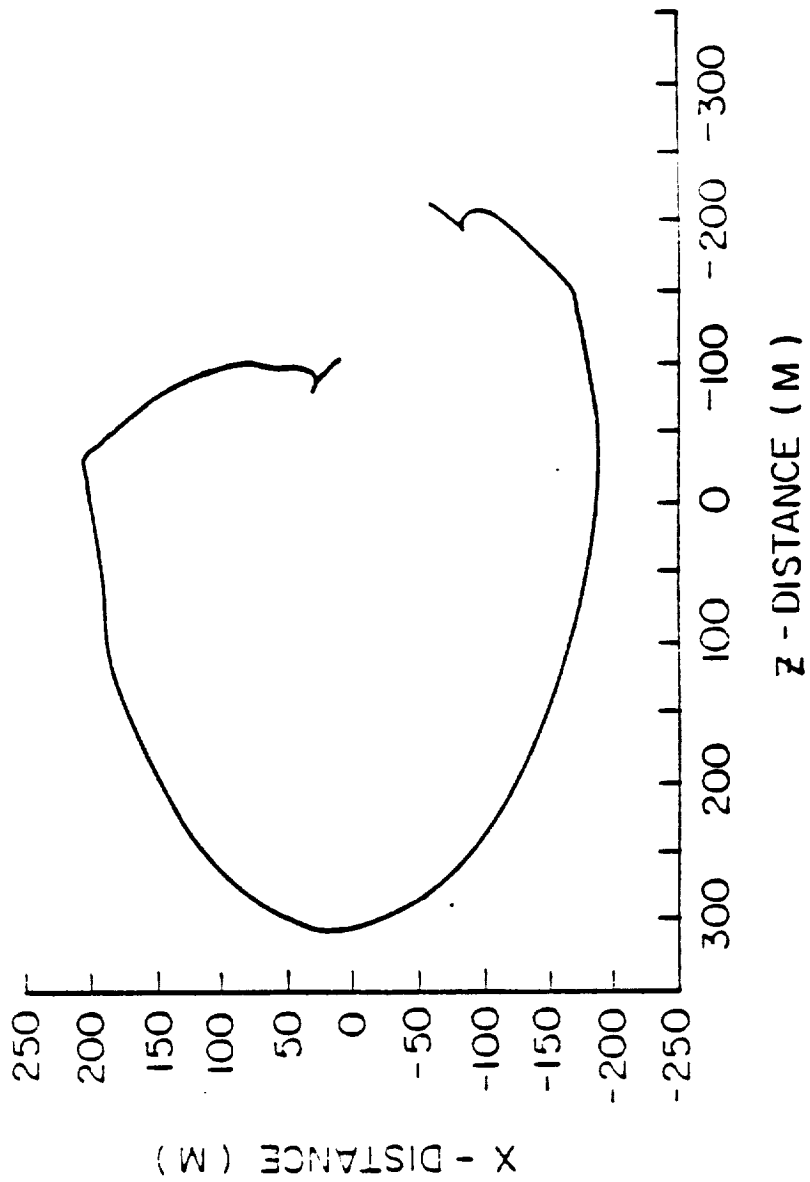


Figure 6. In plane distance between the orbiter and the PDP, 01:30 - 03:00.

A-G88-133

IN PLANE DISTANCE: 0300-0430

1 AUGUST 1985

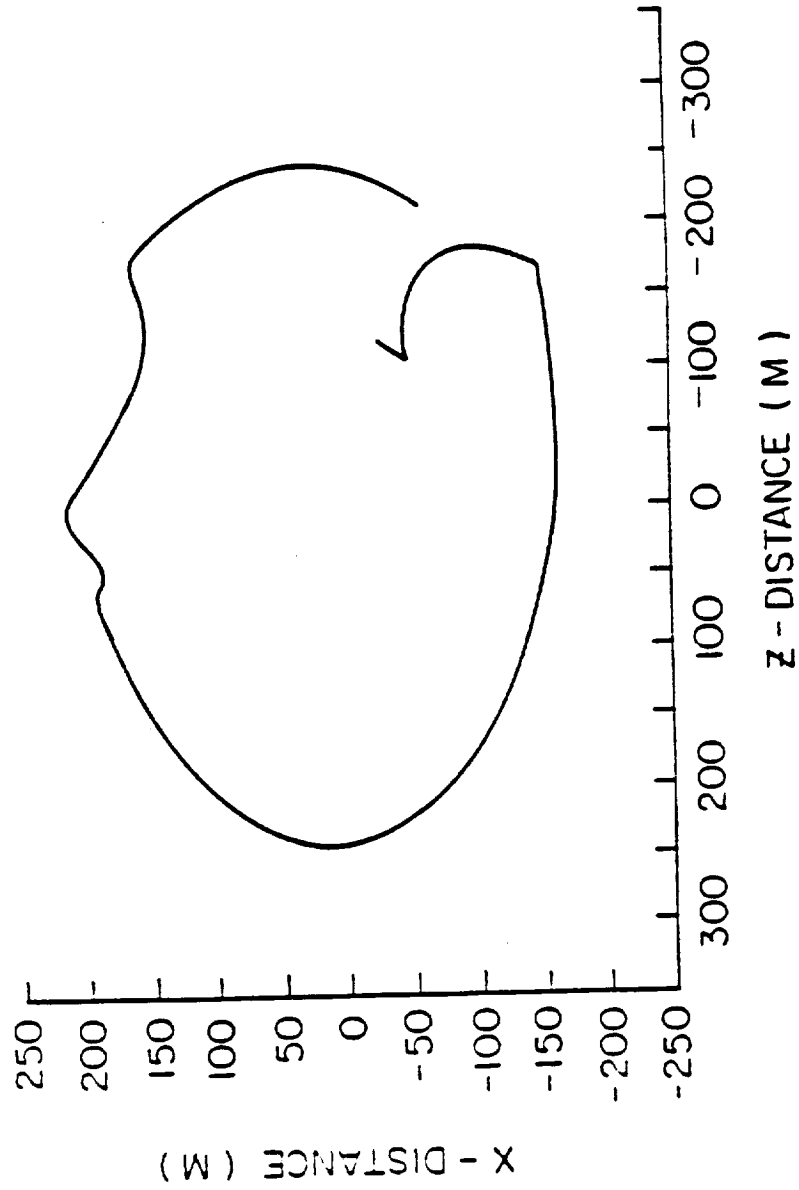


Figure 7. In plane distance between the orbiter and the PDP, 03:00 - 04:30.

A-688-134

IN PLANE DISTANCE: 0430-0600

1 AUGUST 1985

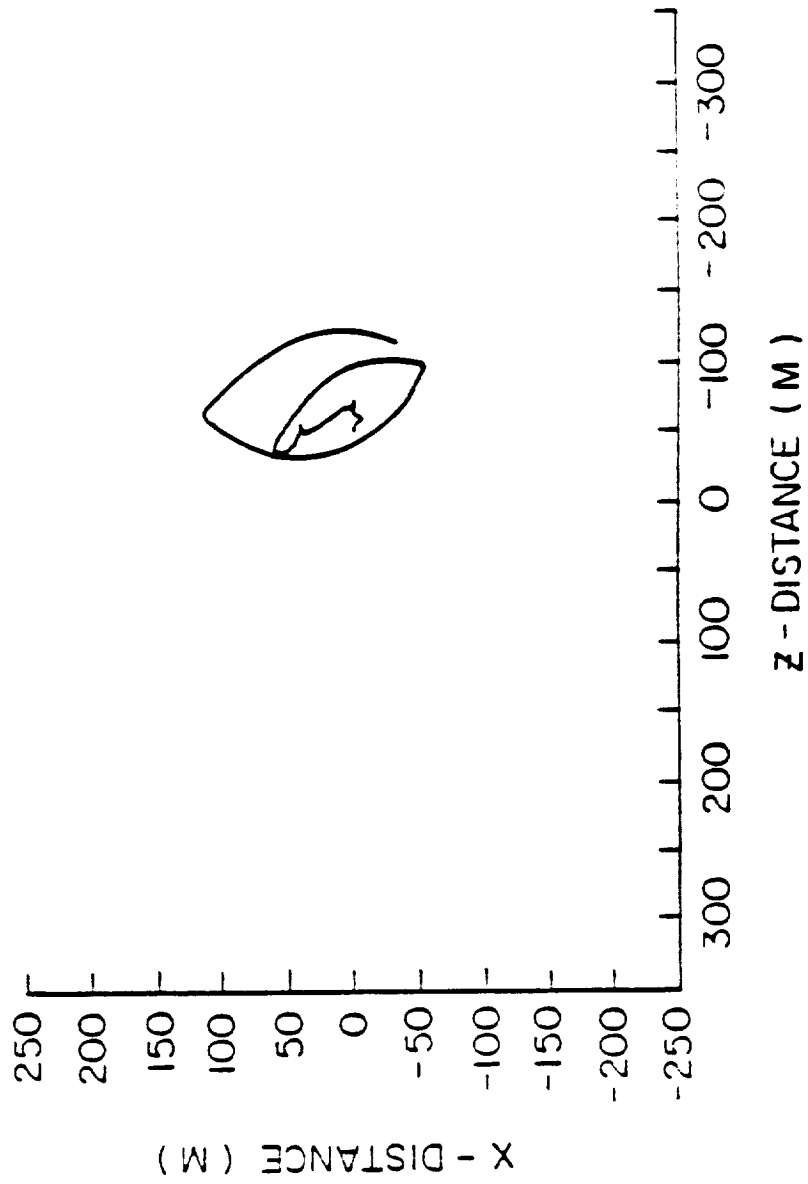


Figure 8. In plane distance between the orbiter and the PDP, 01:30 - 06:00.

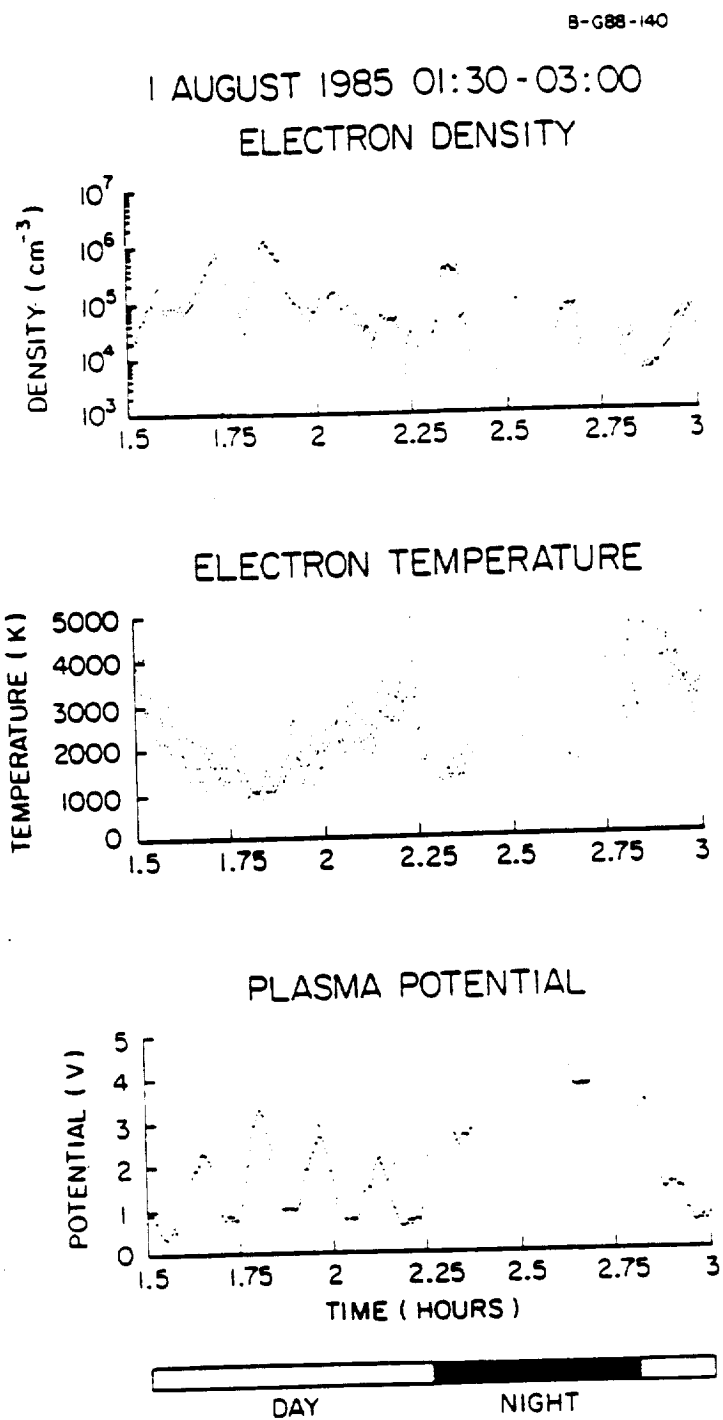
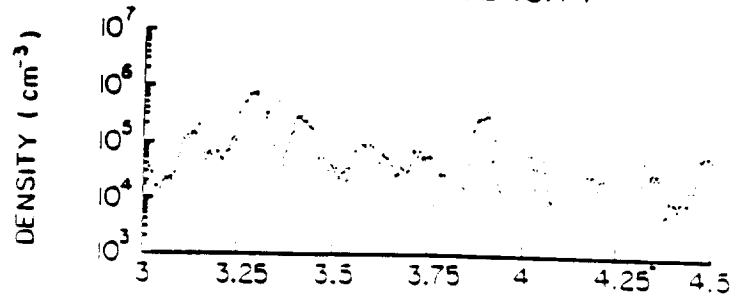


Figure 9. Ambient ionospheric characteristics, 01:30 - 03:00.

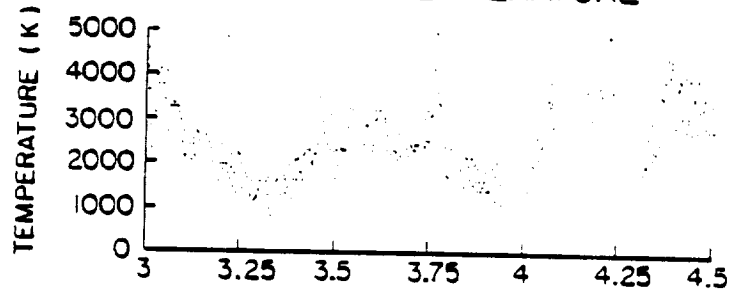
B-G88-139-1

1 AUGUST 1985 03:00-04:30

ELECTRON DENSITY



ELECTRON TEMPERATURE



PLASMA POTENTIAL

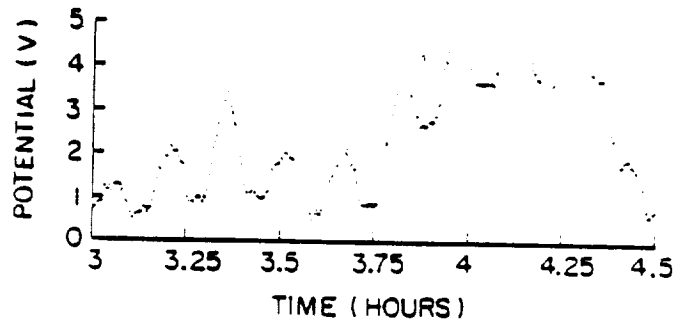


Figure 10. Ambient ionospheric characteristics, 03:00 - 04:30.

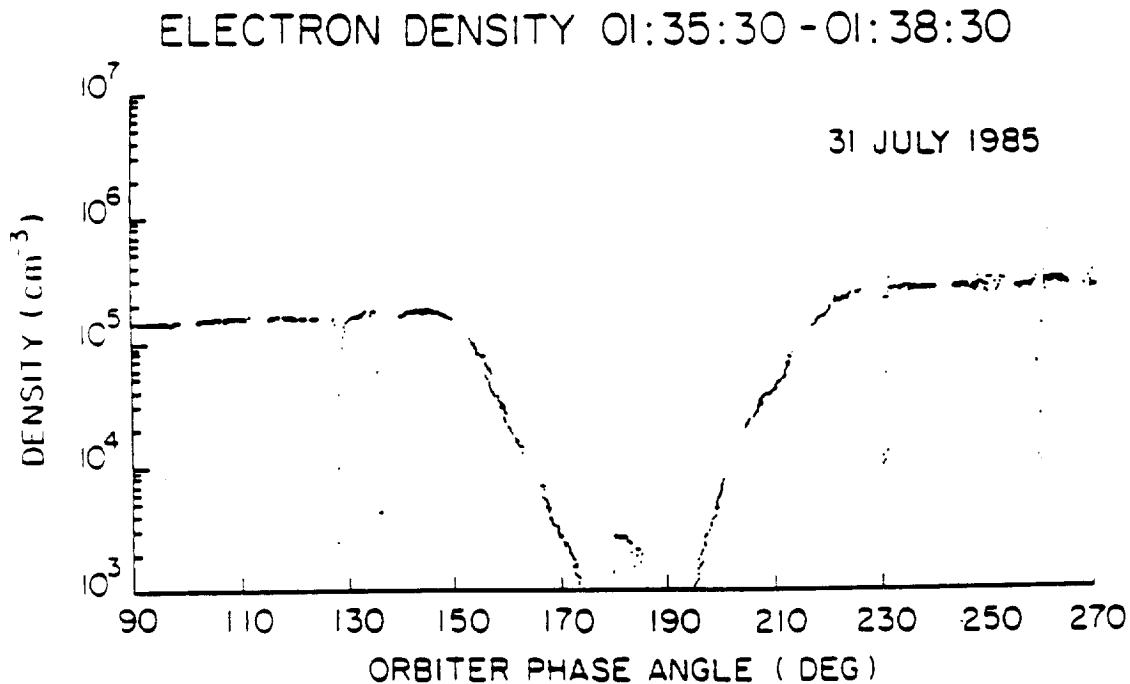
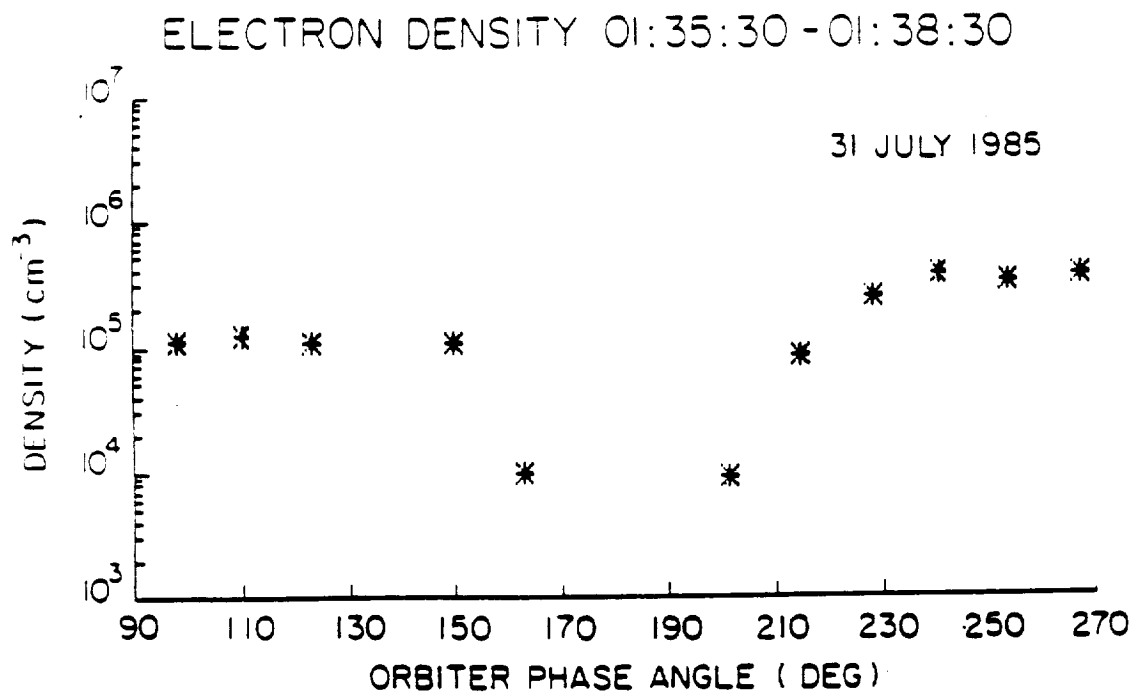


Figure 11. A comparison of the electron density calculated from the Langmuir curves (top) with that calculated from the 0-1 Hz data (bottom).

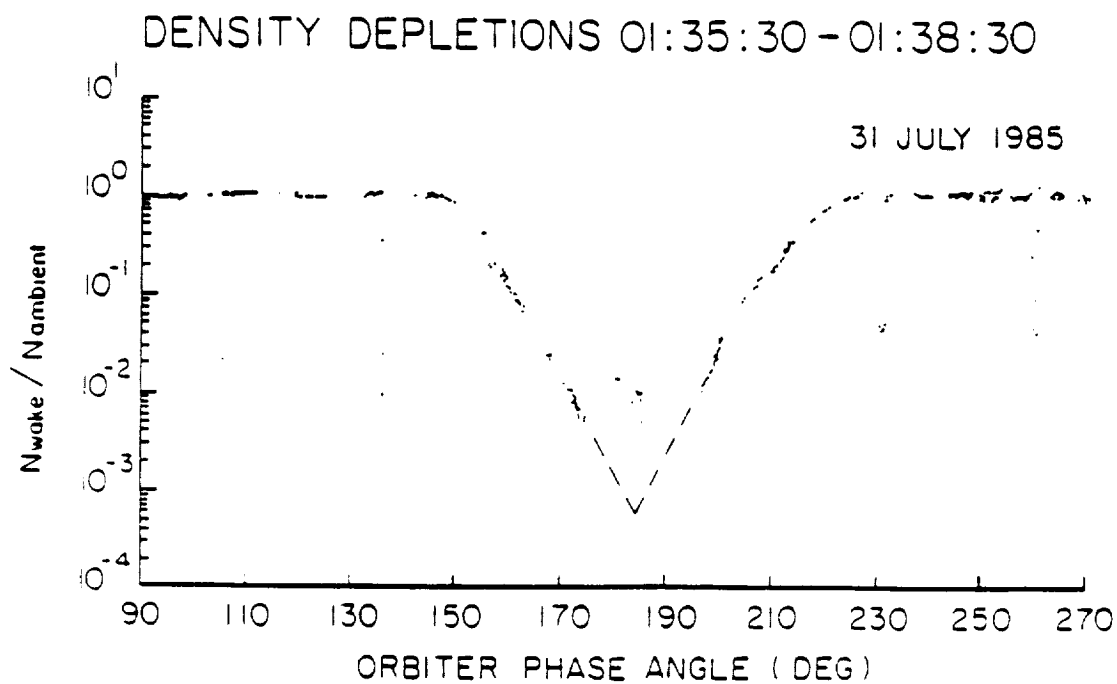
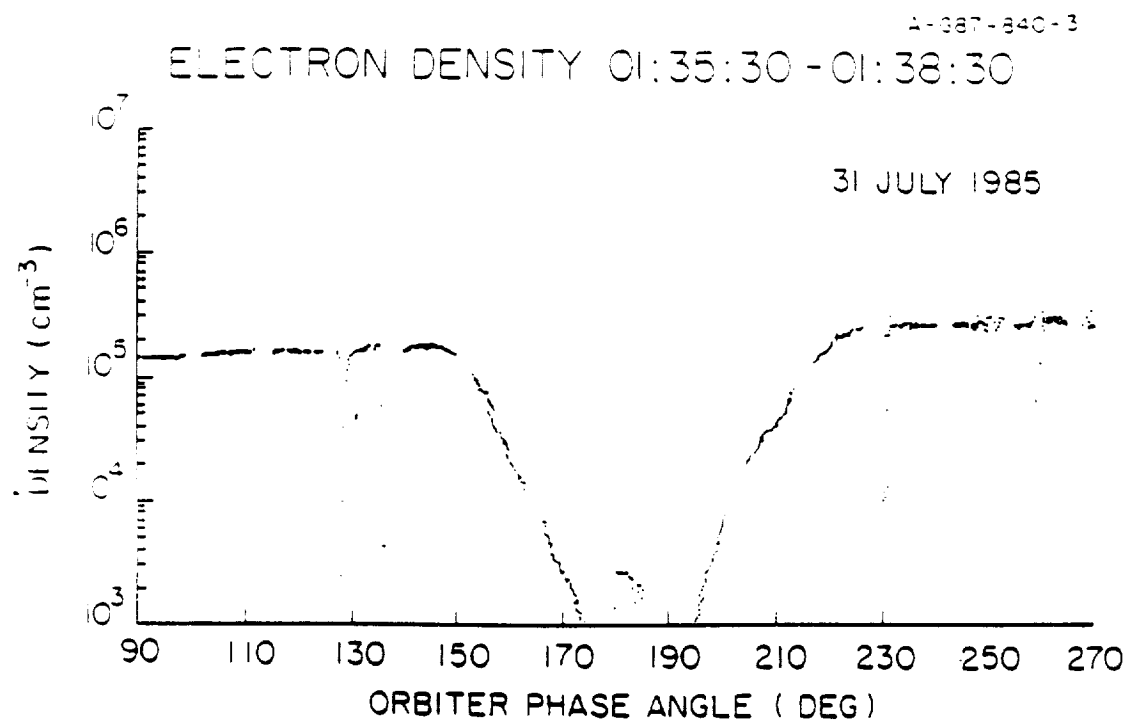


Figure 12. Electron density depletions during near wake transit one.

A-G87-837-3

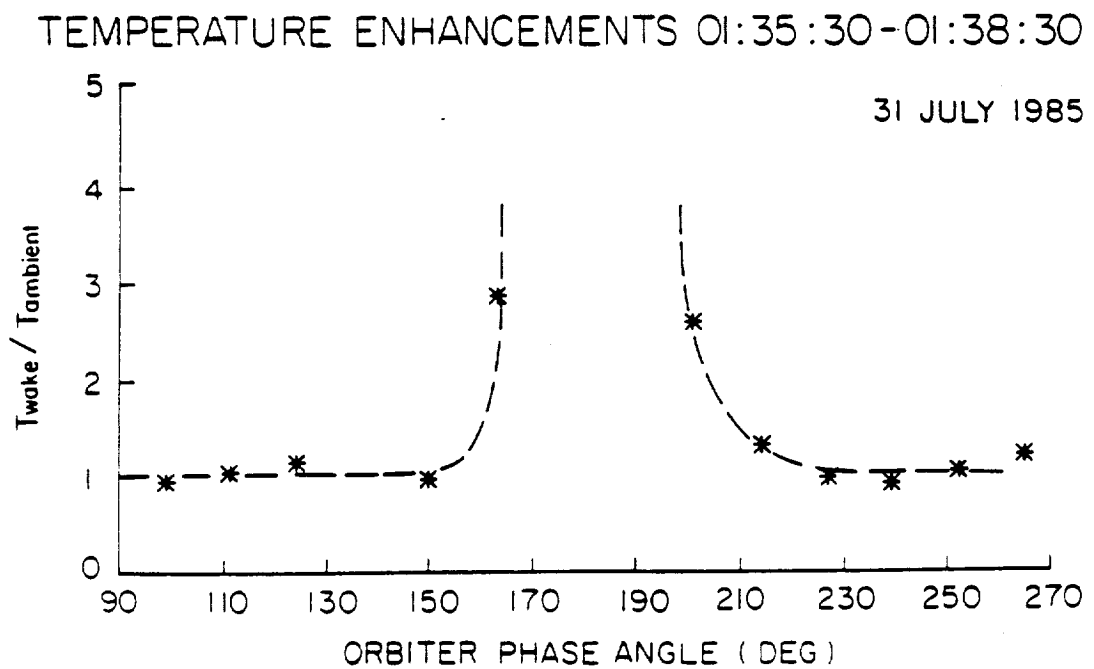
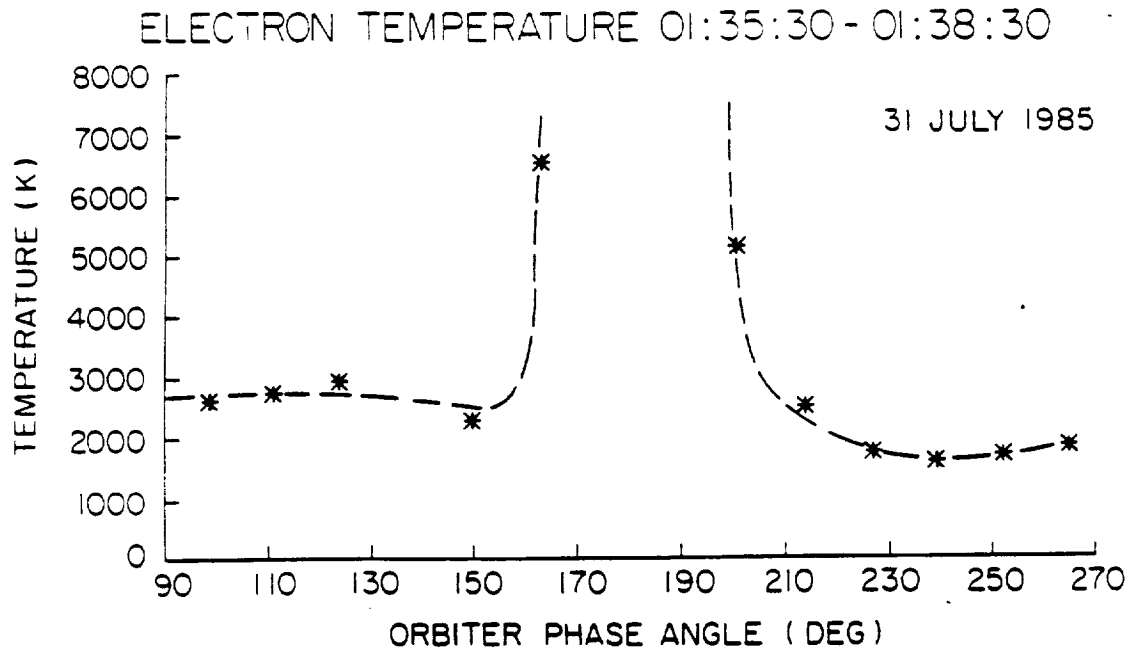


Figure 13. Electron temperature enhancements during near wake transit one.

A-387-341

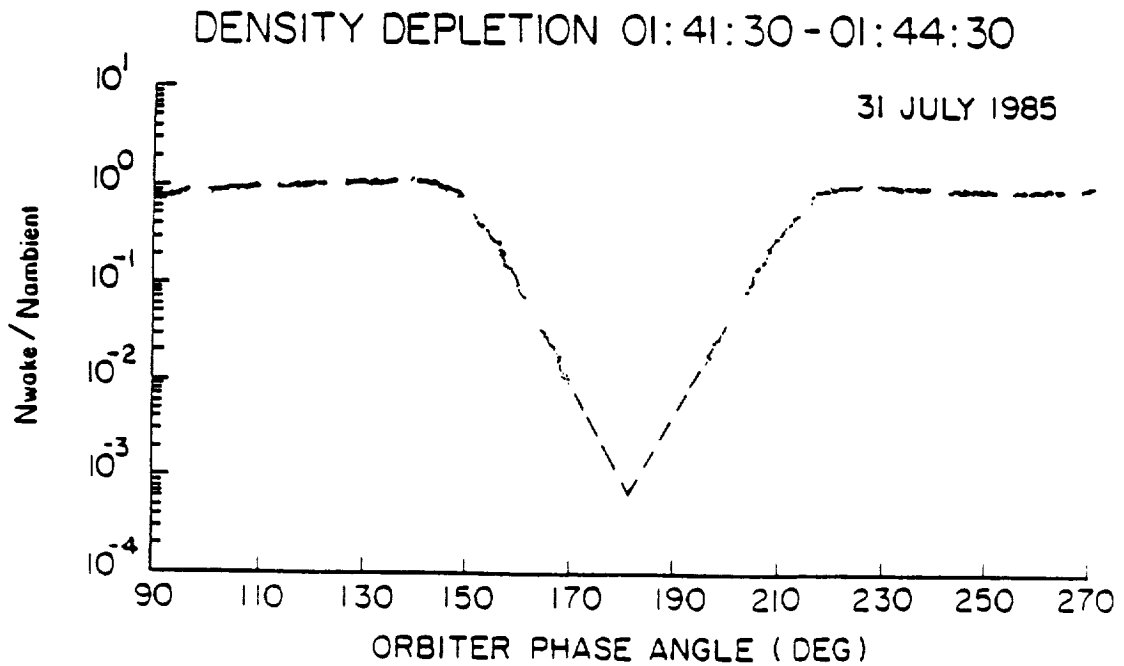
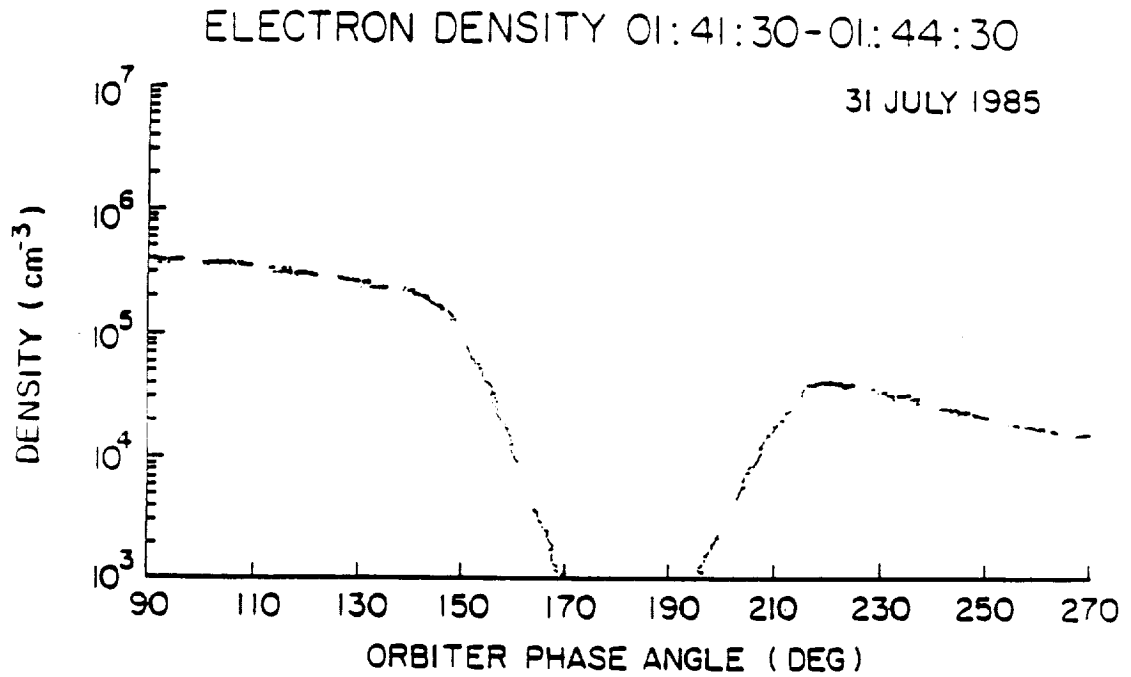


Figure 14. Electron density depletions during near wake transit two.

A-687-838-2

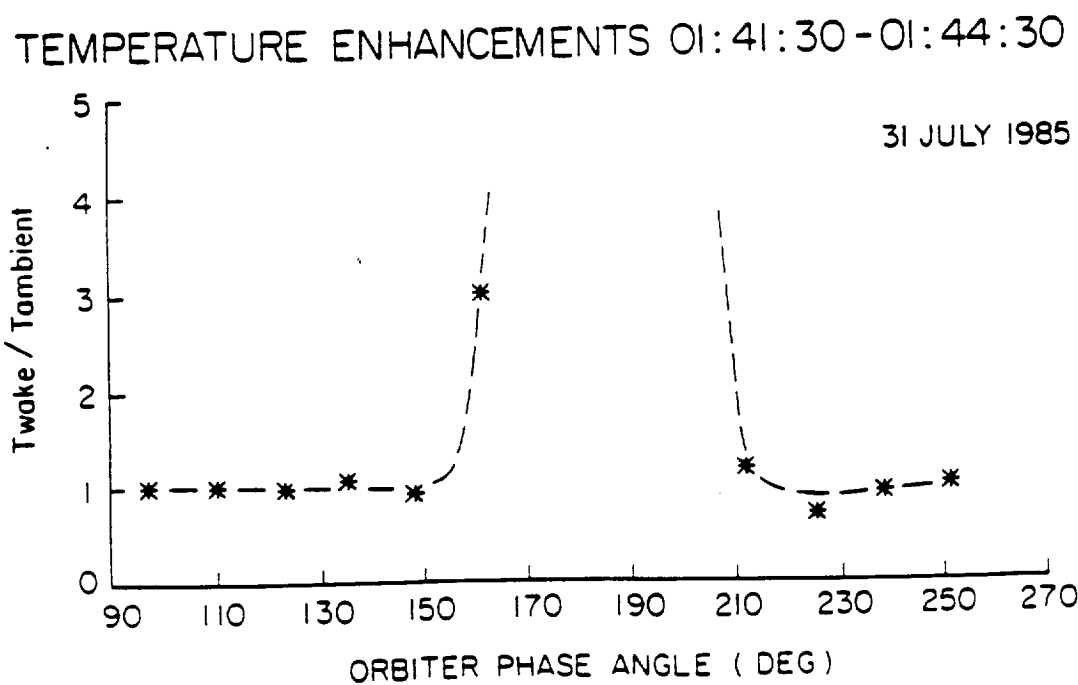
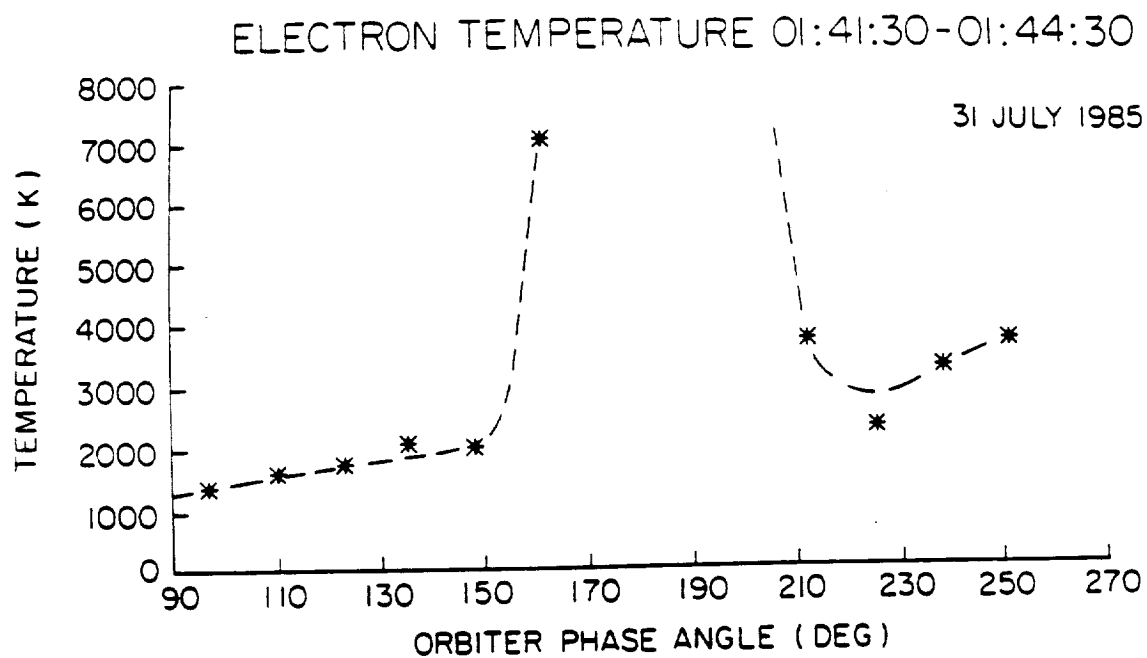
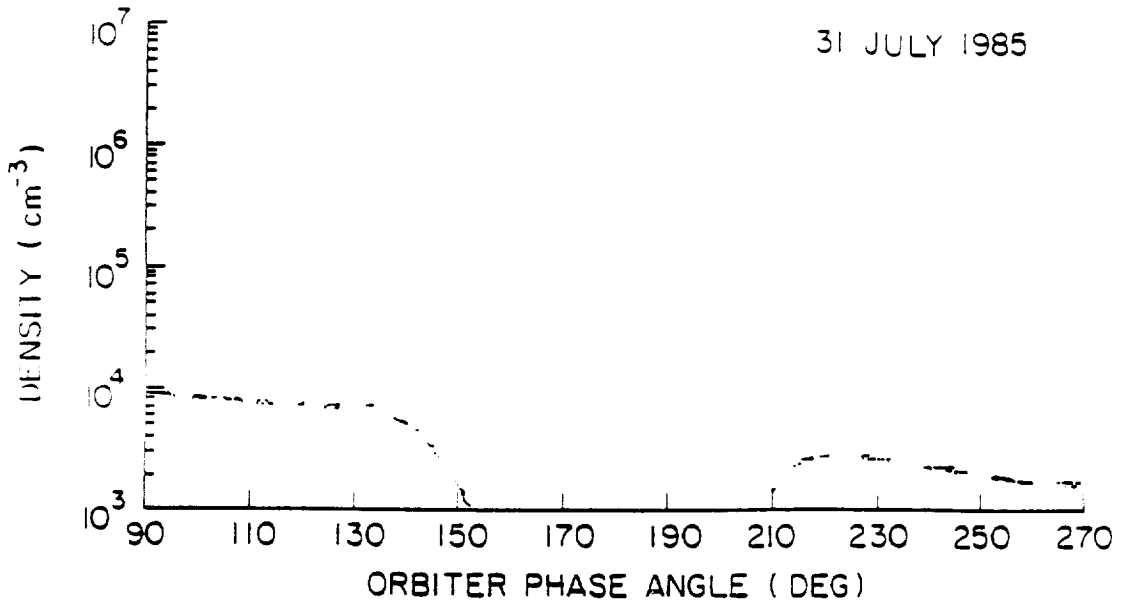


Figure 15. Electron temperature enhancements during near wake transit two.

A-387-839

ELECTRON DENSITY 01:47:30-01:50:30

31 JULY 1985



DENSITY DEPLETIONS 01:47:30-01:50:30

31 JULY 1985

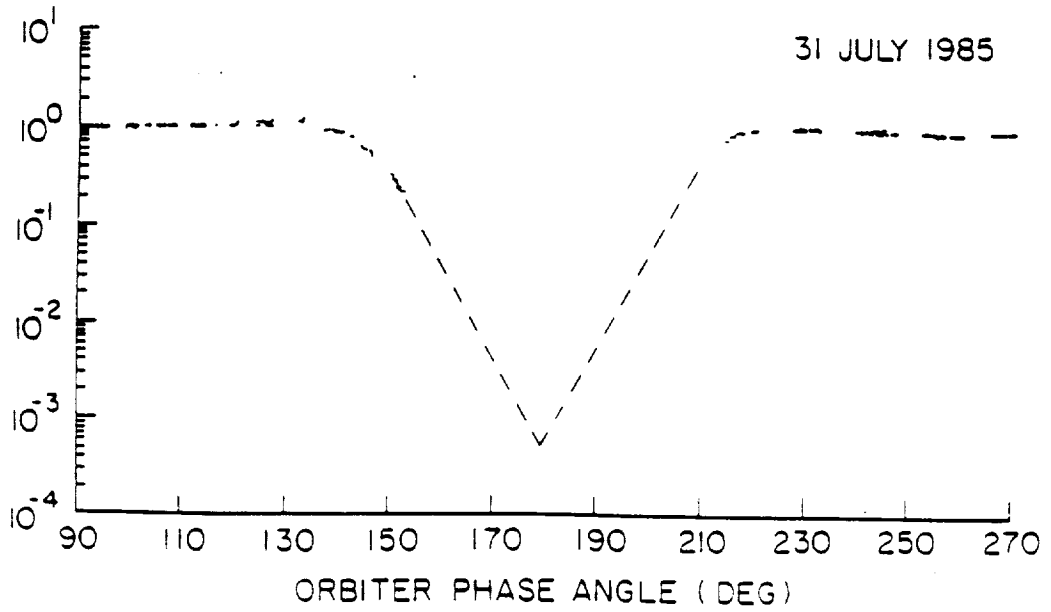
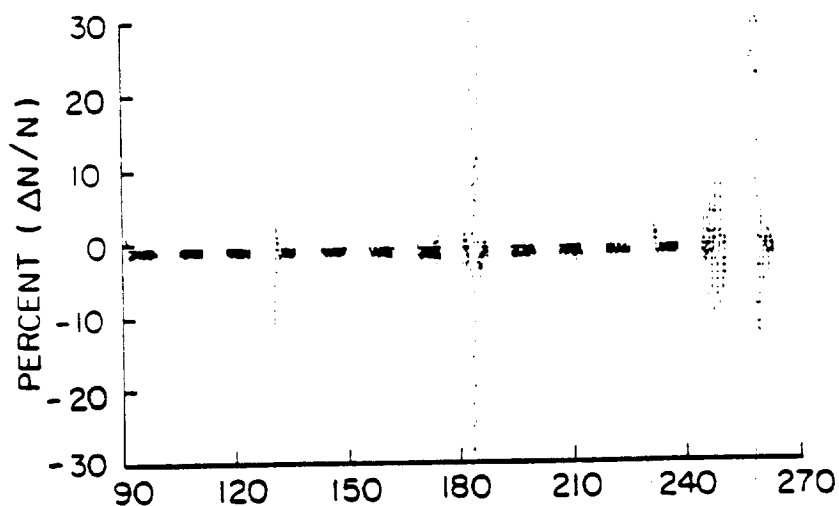


Figure 16. Electron density depletions during near wake transit three.

B-G88-137

1-6 Hz DATA 01:35:30 - 01:38:30



RMS VALUES 01:35:30 - 01:38:30

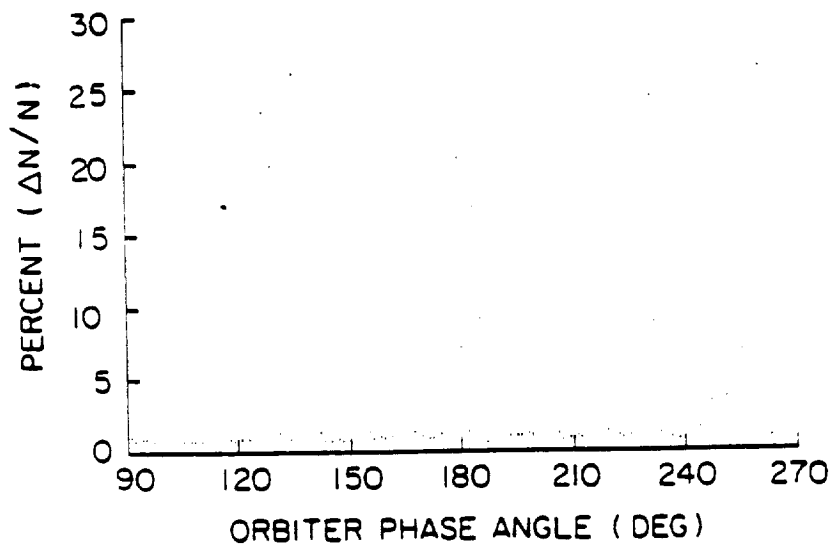
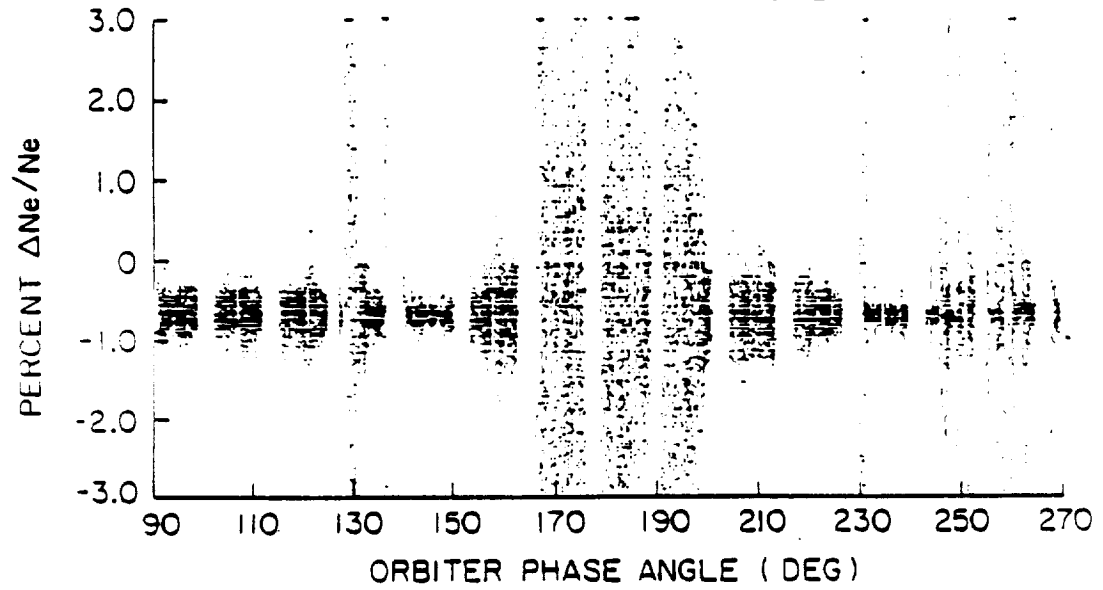


Figure 17. 1-6 Hz data during near wake transit one.

A-87-834

6-40 Hz DATA 01:35:30 - 01:38:30

31 JULY 1985



RMS VALUES 01:35:30 - 01:38:30

31 JULY 1985

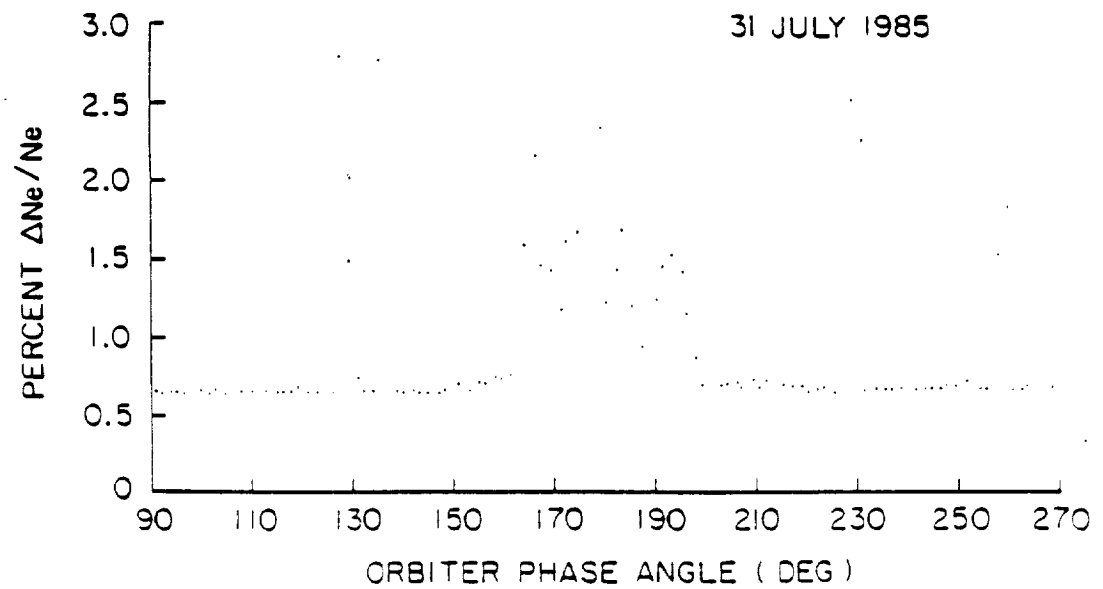


Figure 18. 6-40 Hz data during near wake transit one.

ORIGINAL PAGE IS
OF POOR QUALITY

A-G87-835

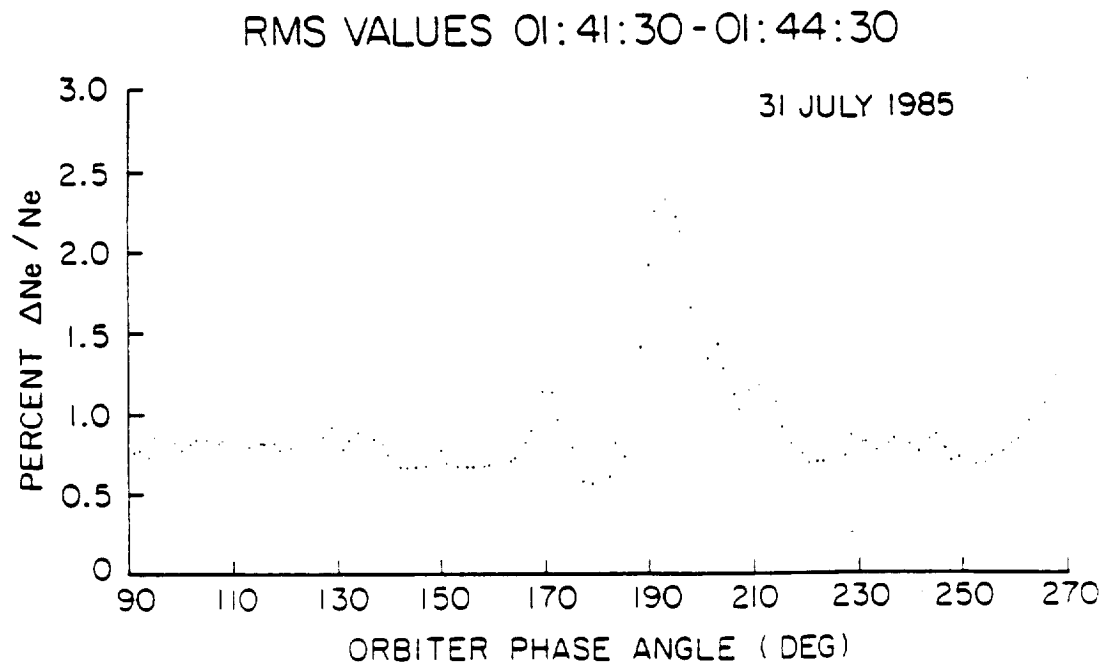
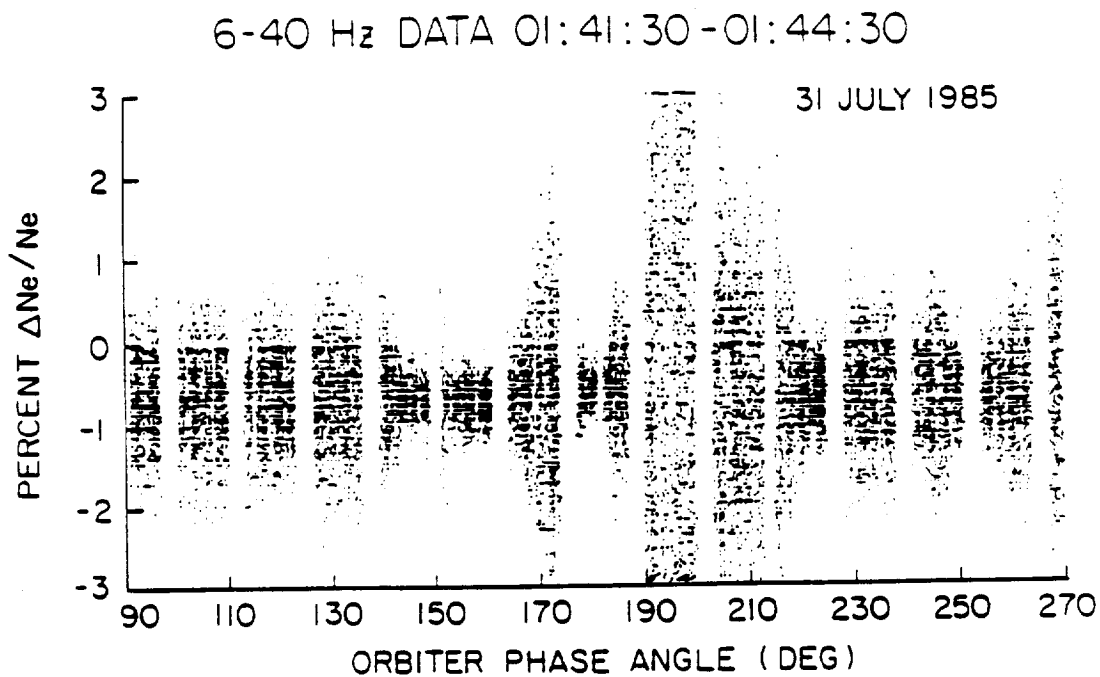
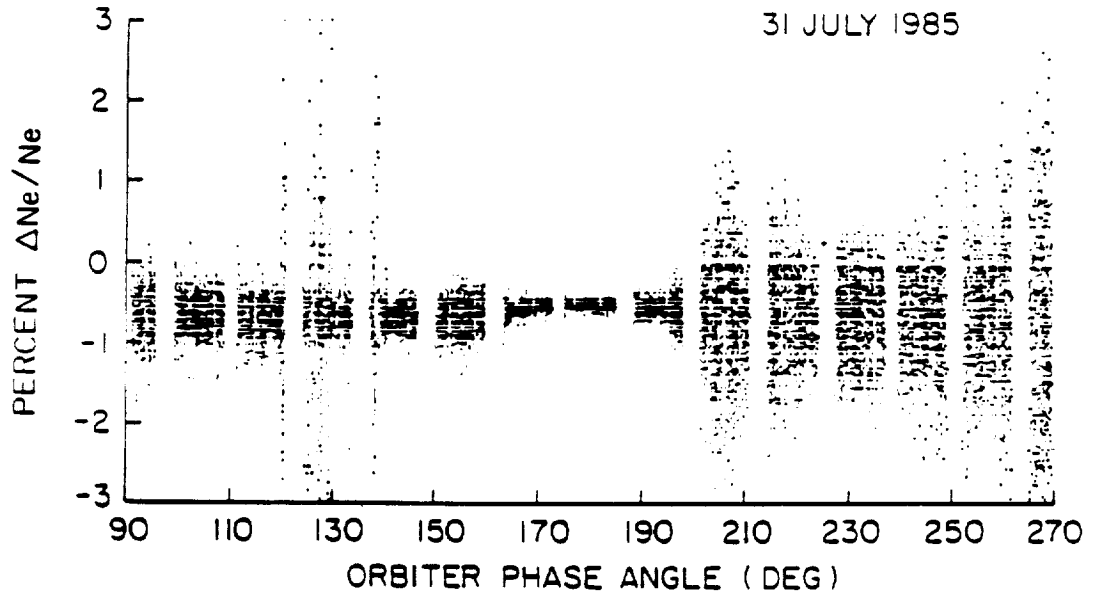


Figure 19. 6-40 Hz data during near wake transit two.

ORIGINAL PAGE IS
OF POOR QUALITY

A-687-836

6-40 Hz DATA 01:47:30 - 01:50:30



RMS VALUES 01:47:30 - 01:50:30

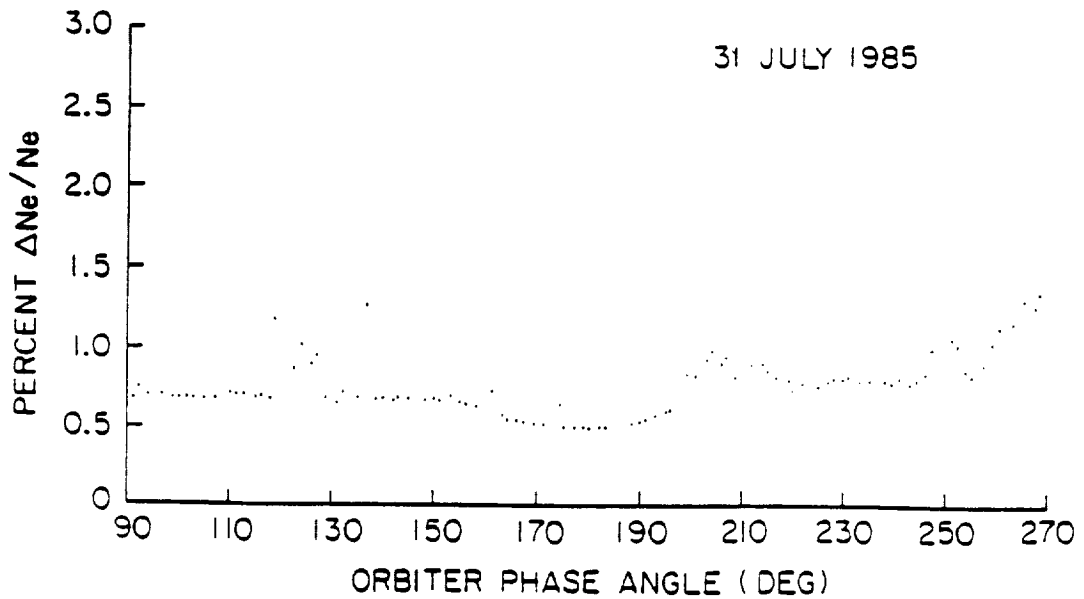


Figure 20. 6-40 Hz data during near wake transit three.

ORIGINAL PAGE IS
OF POOR QUALITY

SPECTRAL ANALYSIS: 0-40 Hz DATA
31 JULY 1985 01:36:04 - 01:36:16

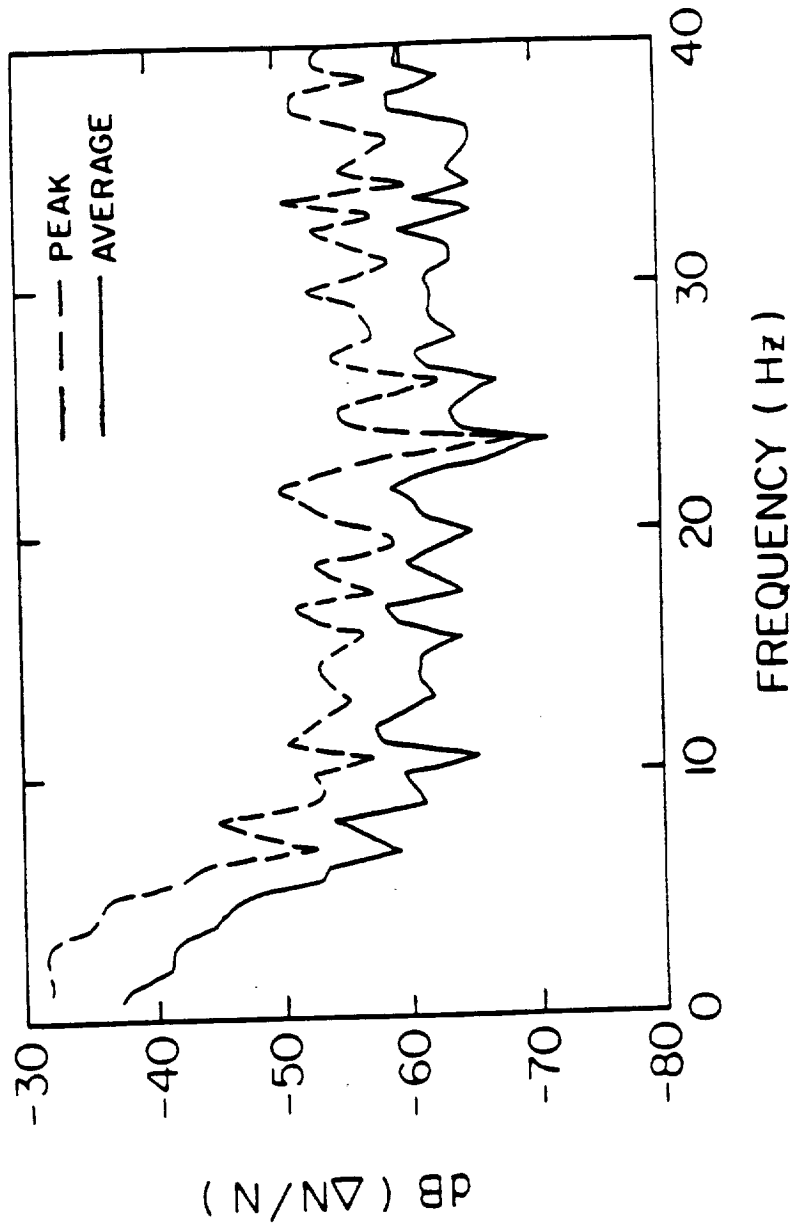


Figure 21. 0-40 Hz FFT data corresponding to orbiter phase angles $124^\circ - 136^\circ$.

A - 688 - 175

SPECTRAL ANALYSIS: 0-40 Hz DATA
31 JULY 1985 01:36:17 - 01:36:29

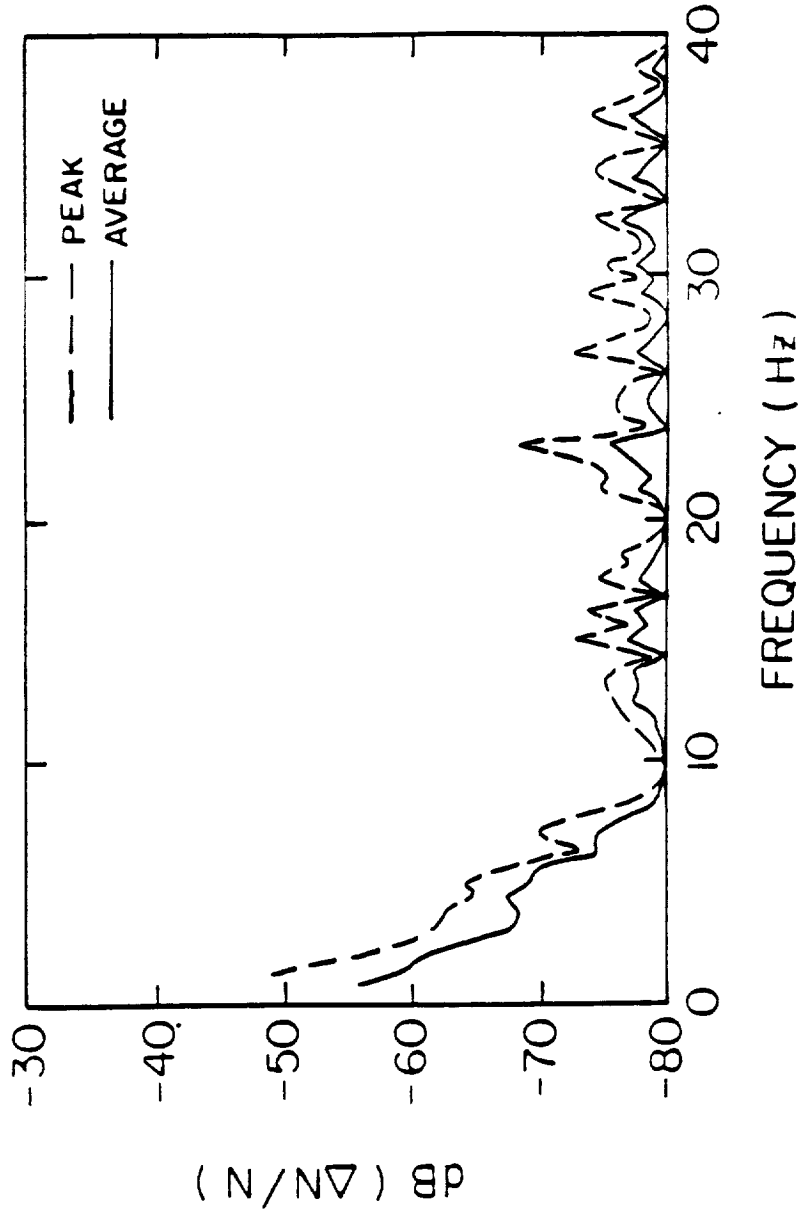


Figure 22. 0-40 Hz FFT data corresponding to orbiter phase angles 137° - 149°.

A-G88-176

SPECTRAL ANALYSIS: 0-40 Hz DATA
31 JULY 1985 01:36:30 - 01:36:42

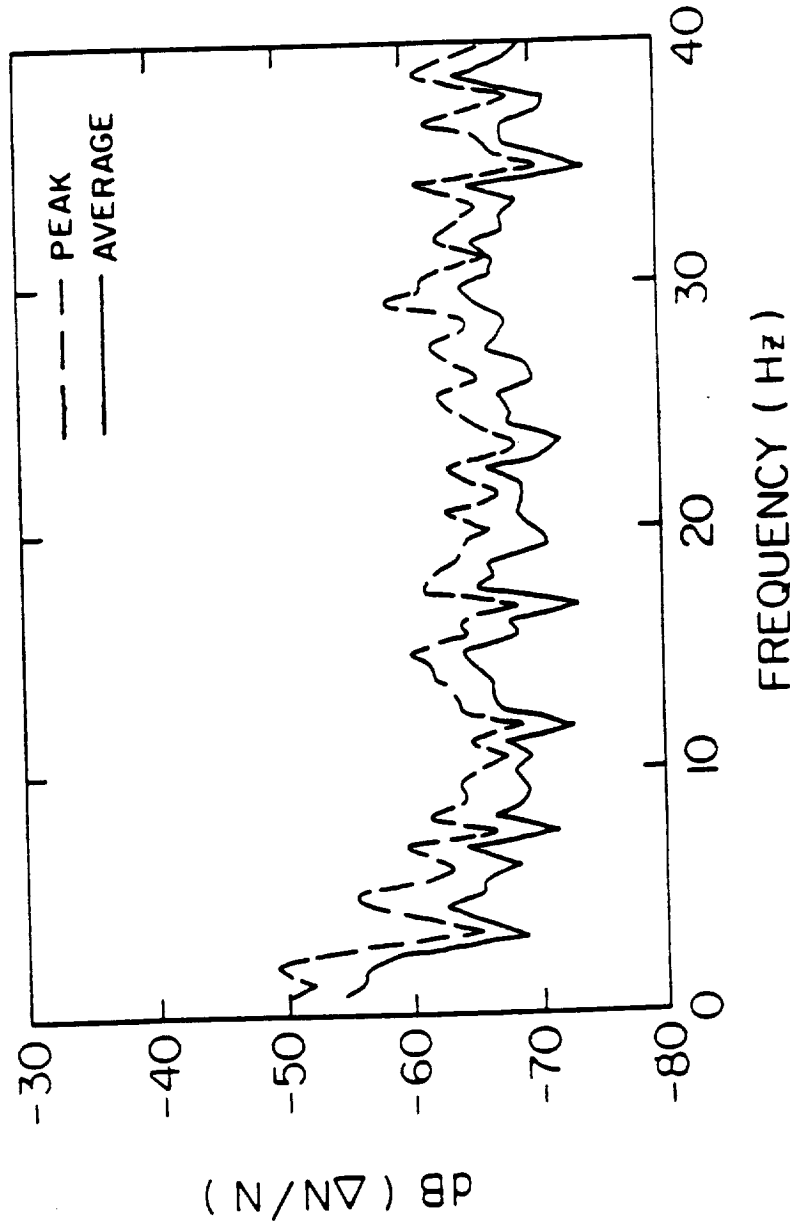


Figure 23. 0-40 Hz FFT data corresponding to orbiter phase angles $150^\circ - 162^\circ$.

A-688-177

SPECTRAL ANALYSIS: 0-40 Hz DATA
31 JULY 1985 01:36:43 - 01:36:55

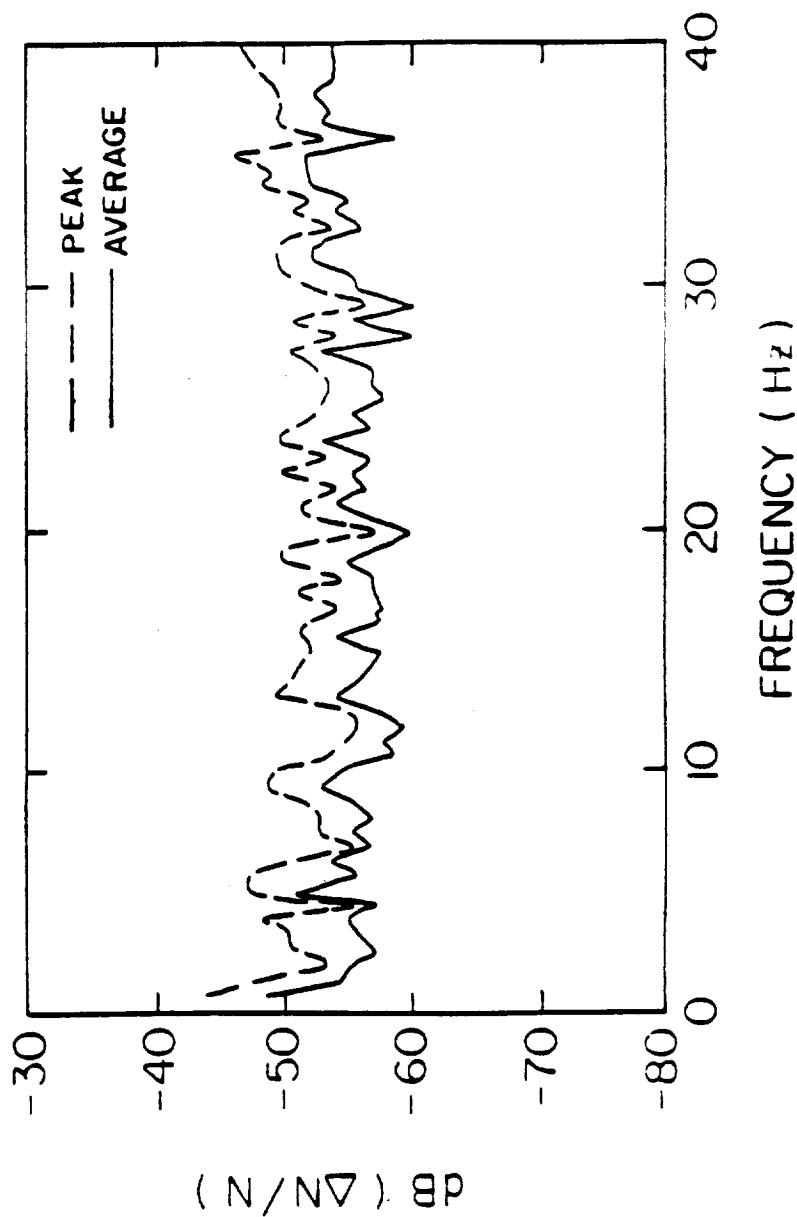


Figure 24. 0-40 Hz FFT data corresponding to orbiter phase angles $163^\circ - 175^\circ$.

A - G88 - 178

SPECTRAL ANALYSIS: 0-40 Hz DATA
31 JULY 1985 01:36:55 - 01:37:07

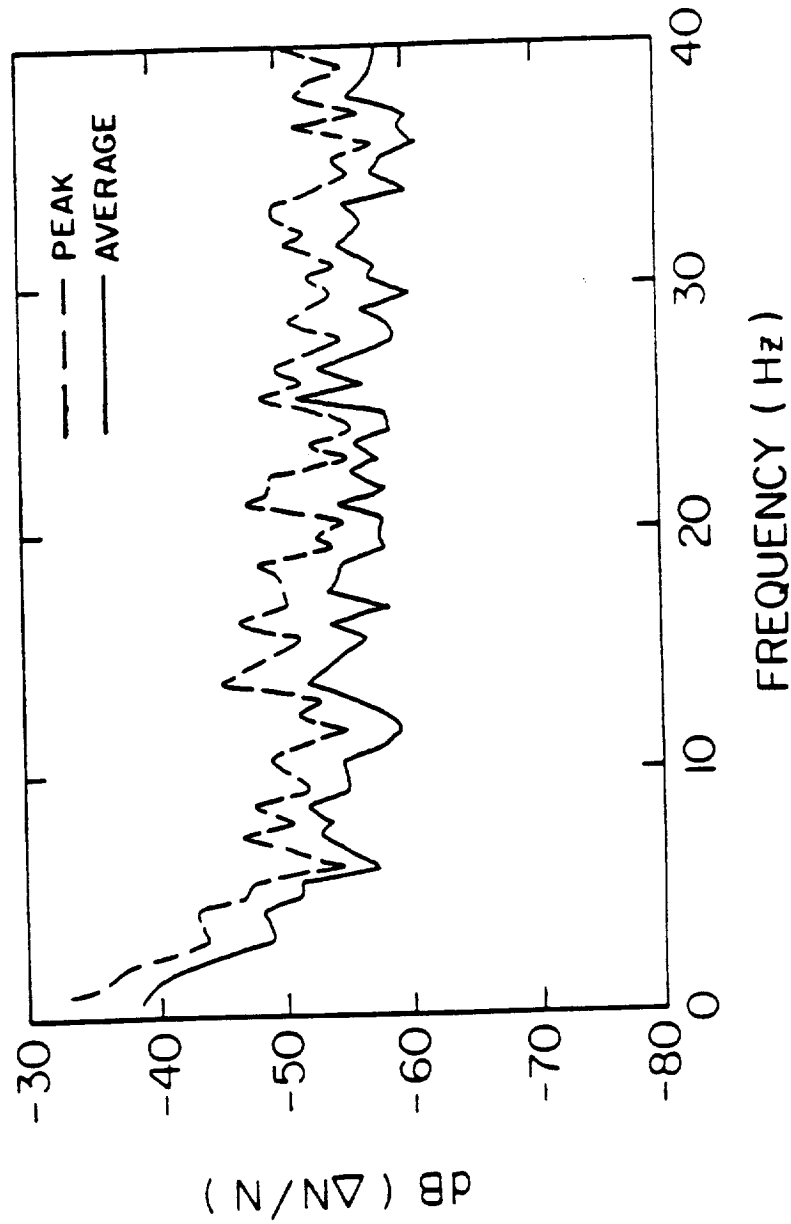


Figure 25. 0-40 Hz FFT data corresponding to orbiter phase angles 175° - 187°.

SPECTRUM ANALYZER DATA

31 JULY 1985 02:00:39

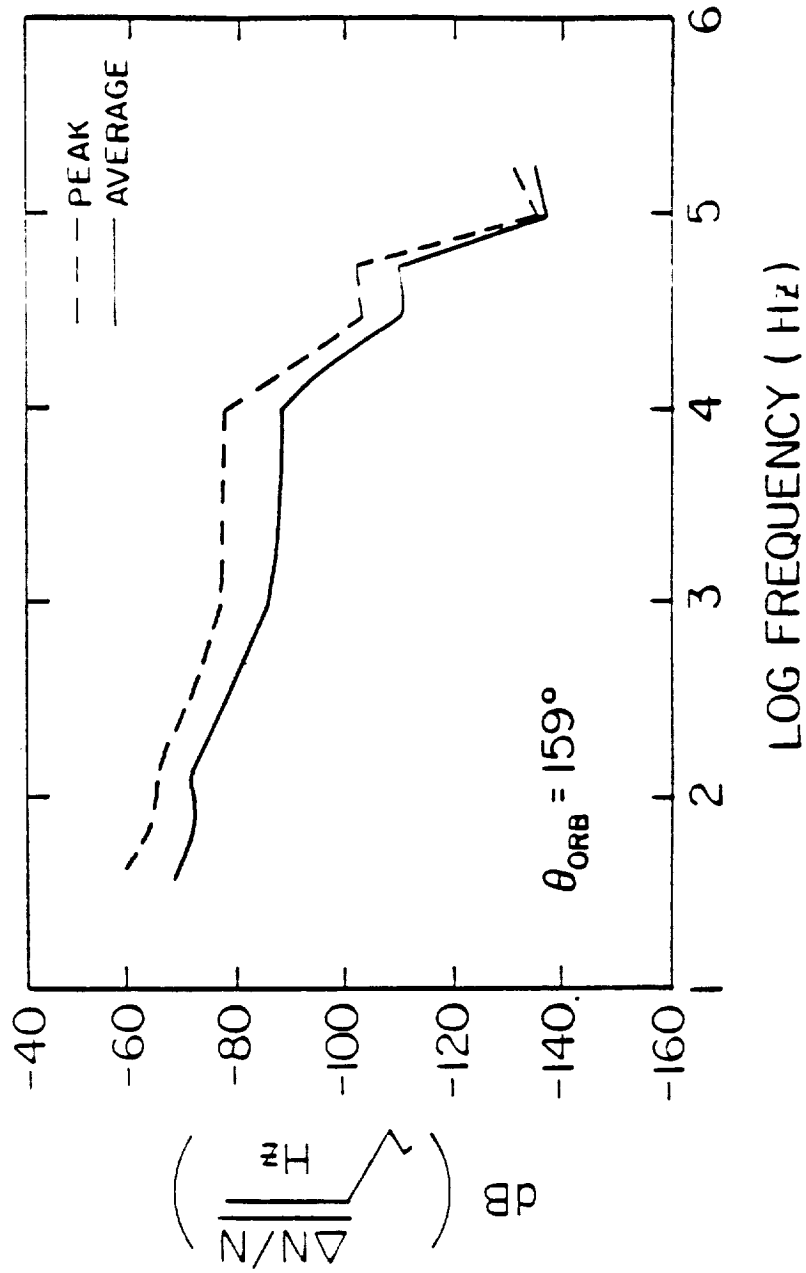


Figure 26. Near wake transit one spectral density data corresponding to orbiter phase angle 159°.

SPECTRUM ANALYZER DATA

31 JULY 1985 02:00:44

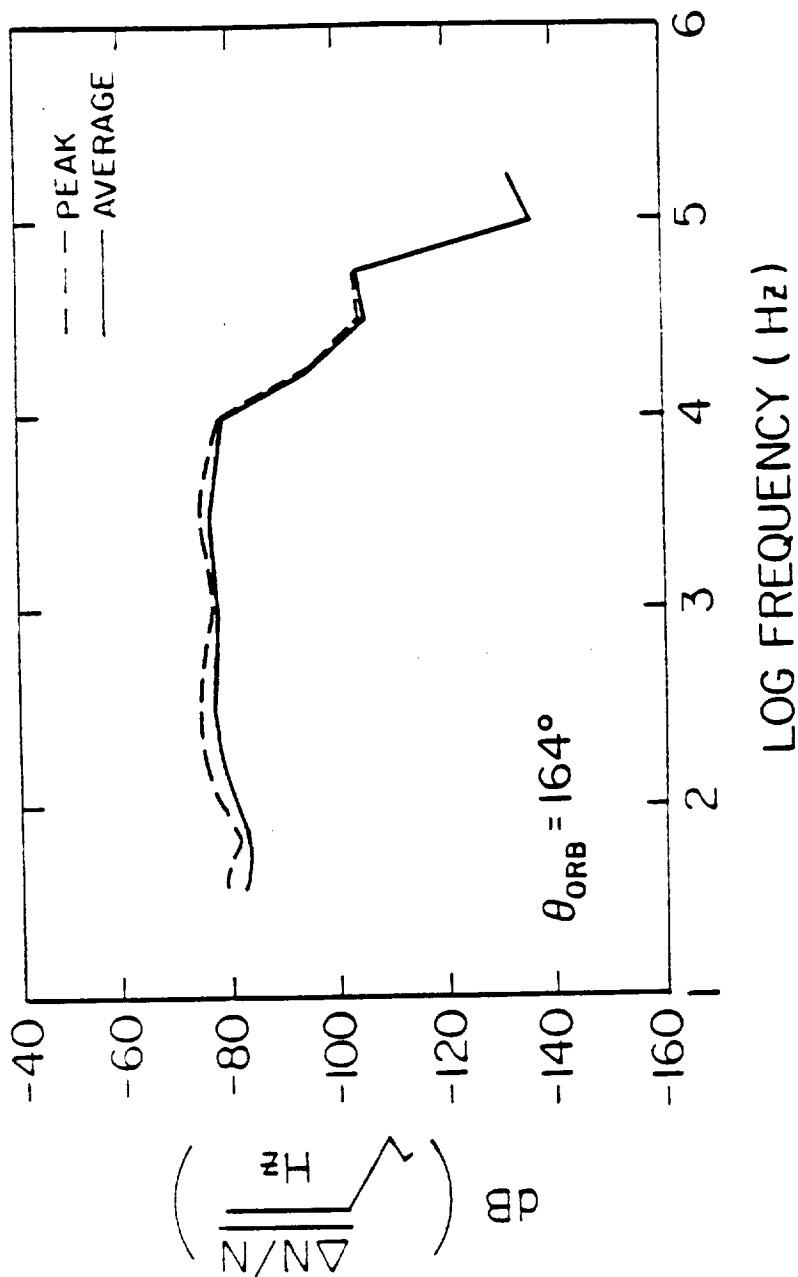


Figure 27. Near wake transit one spectral density data corresponding to orbiter phase angle 164°.

SPECTRUM ANALYZER DATA

31 JULY 1985 02:00:47

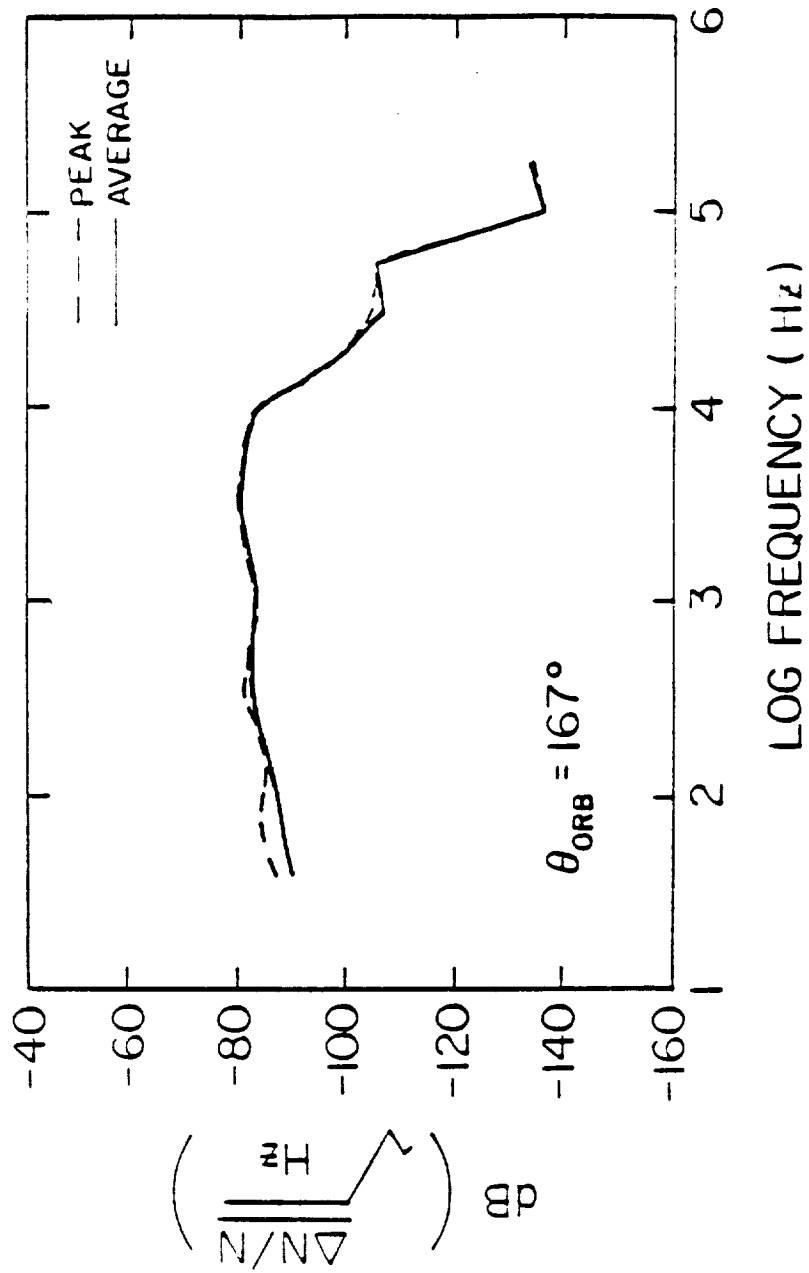


Figure 28. Near wake transit one spectral density data corresponding to orbiter phase angle 167°.

SPECTRUM ANALYZER DATA

31 JULY 1985 02:00:55

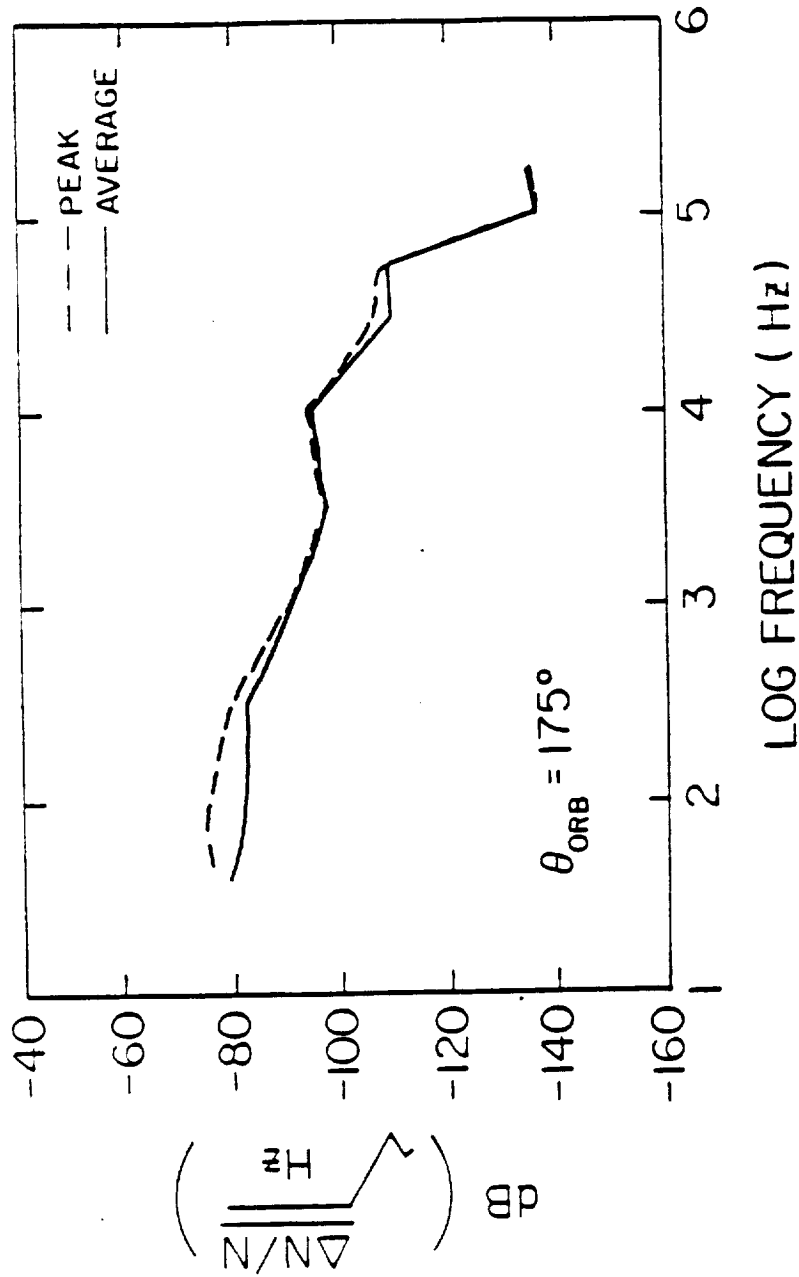


Figure 29. Near wake transit one spectral density data corresponding to orbiter phase angle 175°.

SPECTRUM ANALYZER DATA

31 JULY 1985 02:01:05

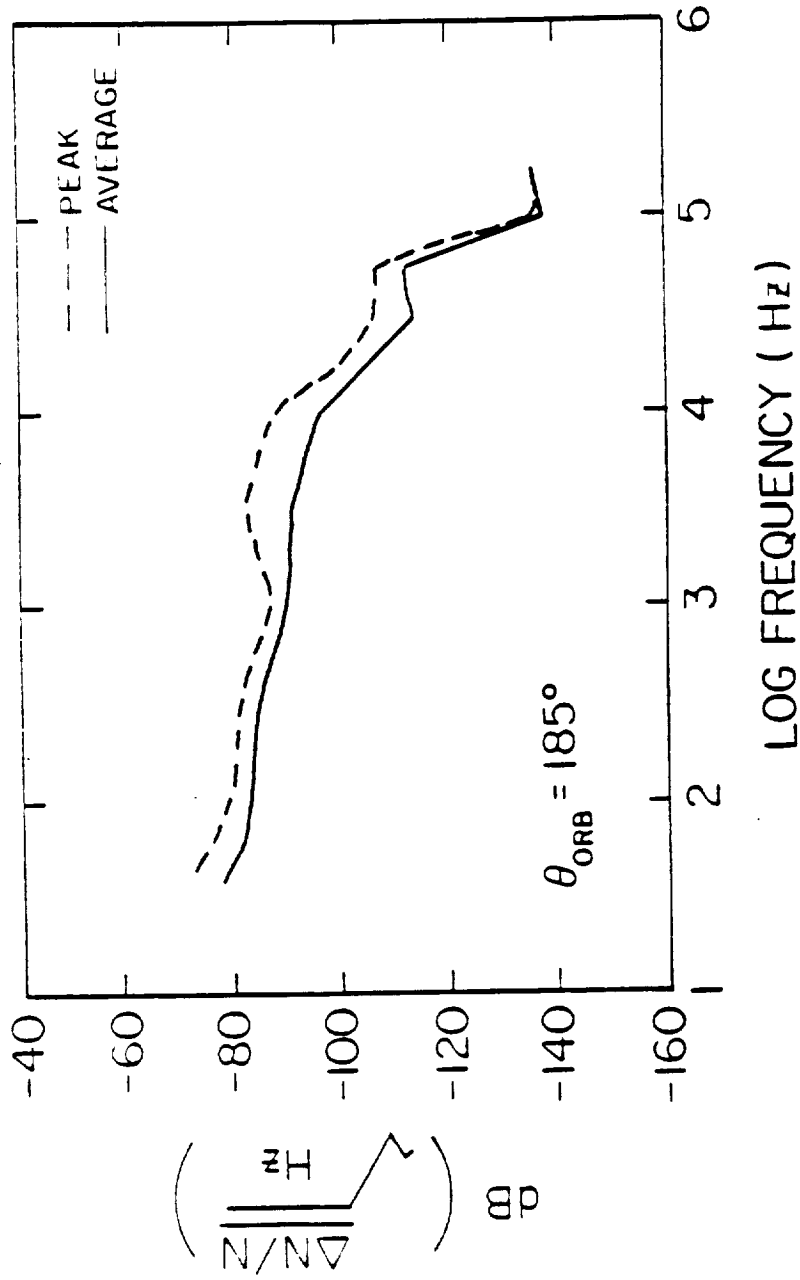


Figure 31. Near wake transit one spectral density data corresponding to orbiter phase angle 185°.

SPECTRUM ANALYZER DATA

31 JULY 1985 02:01:10

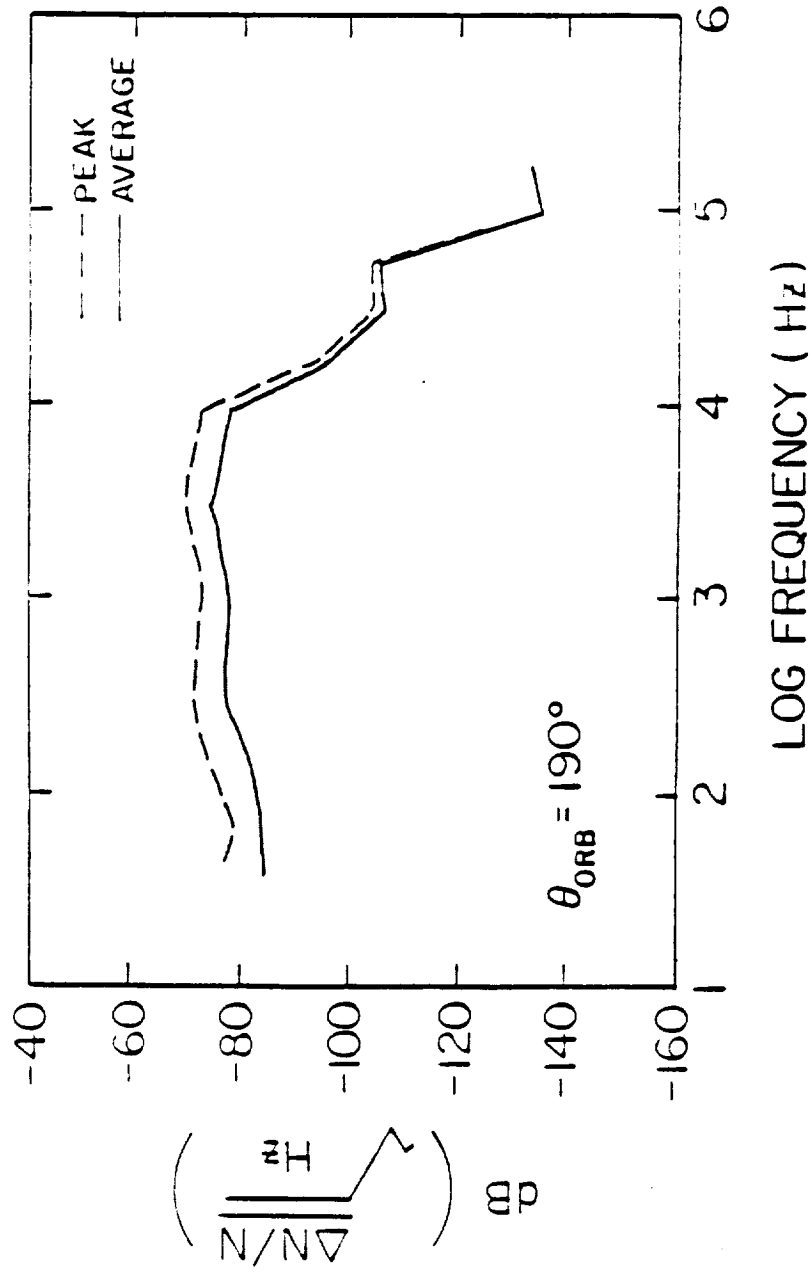


Figure 32. Near wake transit one spectral density data corresponding to orbiter phase angle 190°.

SPECTRUM ANALYZER DATA
31 JULY 1985 02:01:18

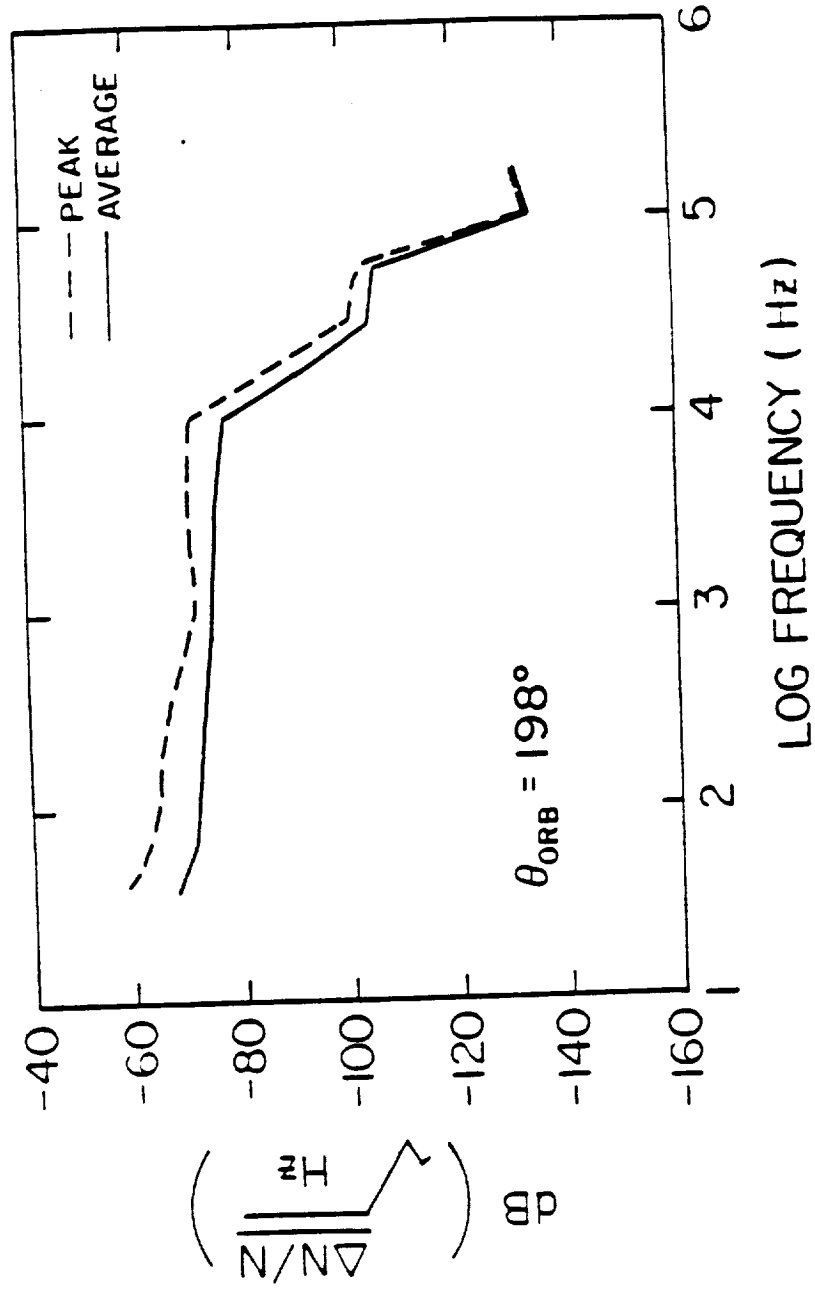


Figure 33. Near wake transit one spectral density data corresponding to orbiter phase angle 198°.

SPECTRUM ANALYZER DATA
31 JULY 1985 02:01:26

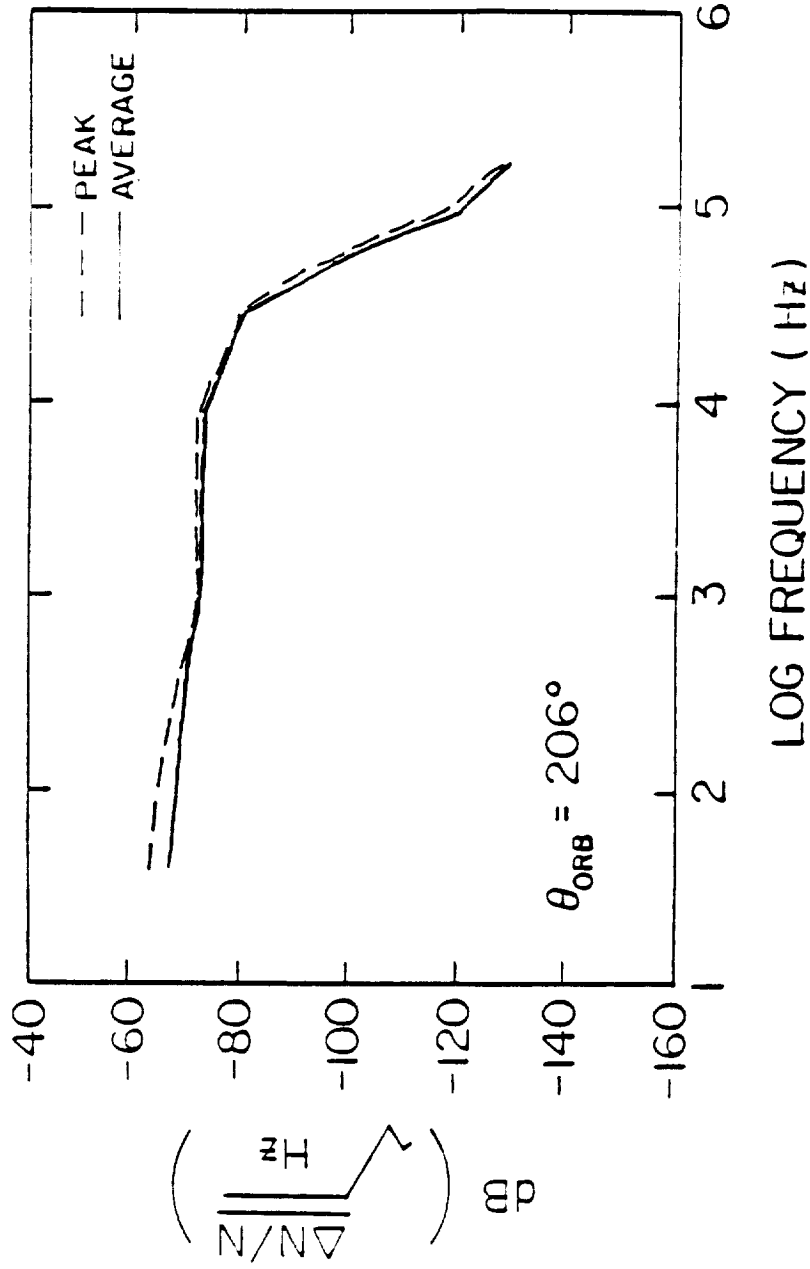


Figure 34. Near wake transit one spectral density data corresponding to orbiter phase angle 206°.

MID AND FAR WAKE TRANSITS

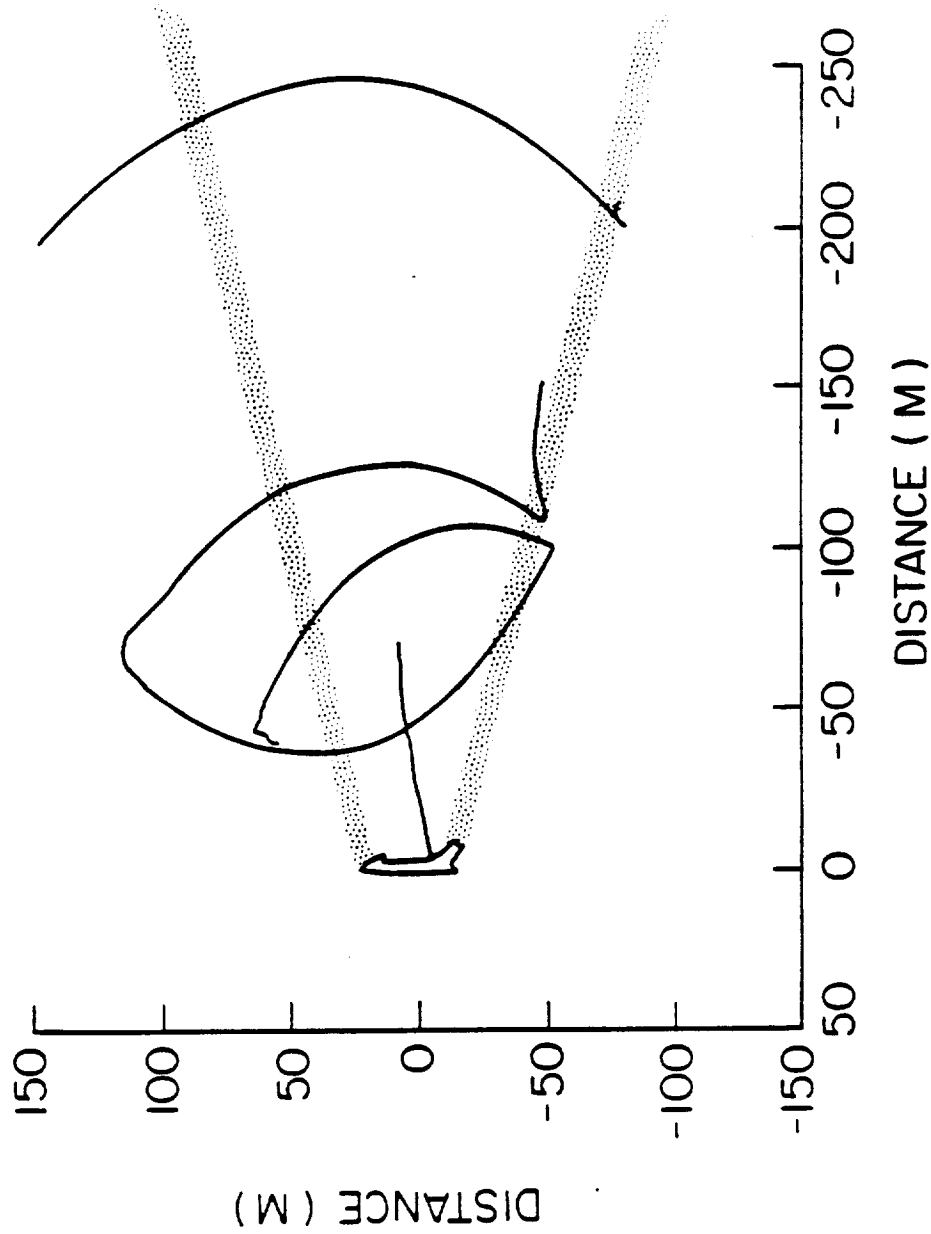
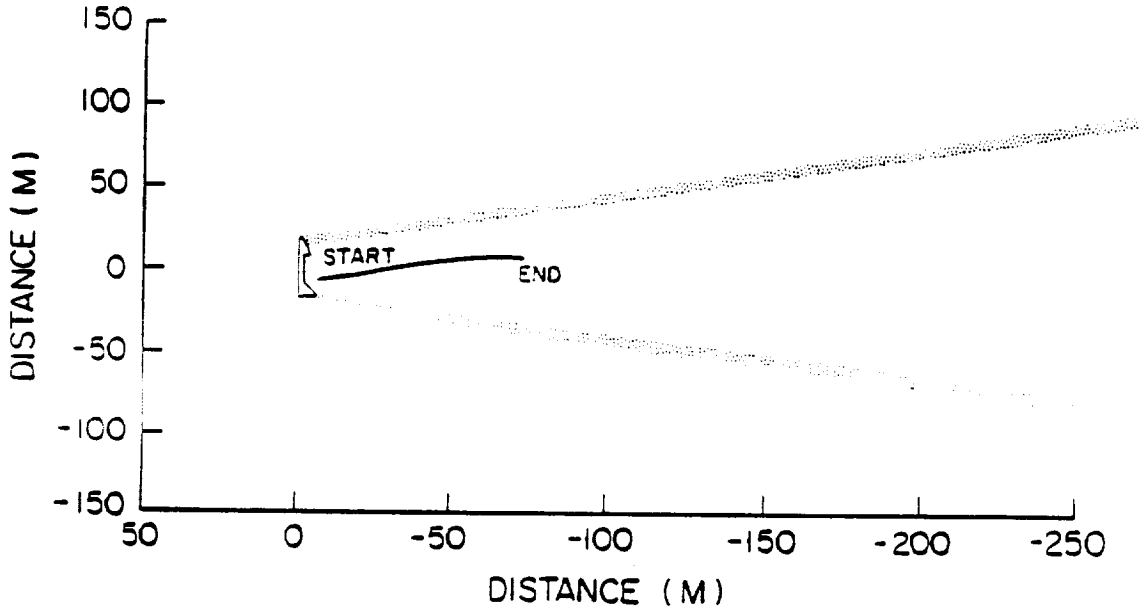


Figure 35. Mid and Far wake transits.

A-687-795

IN PLANE DISTANCE 00:11-00:20



OUT OF PLANE DISTANCE 00:11-00:20

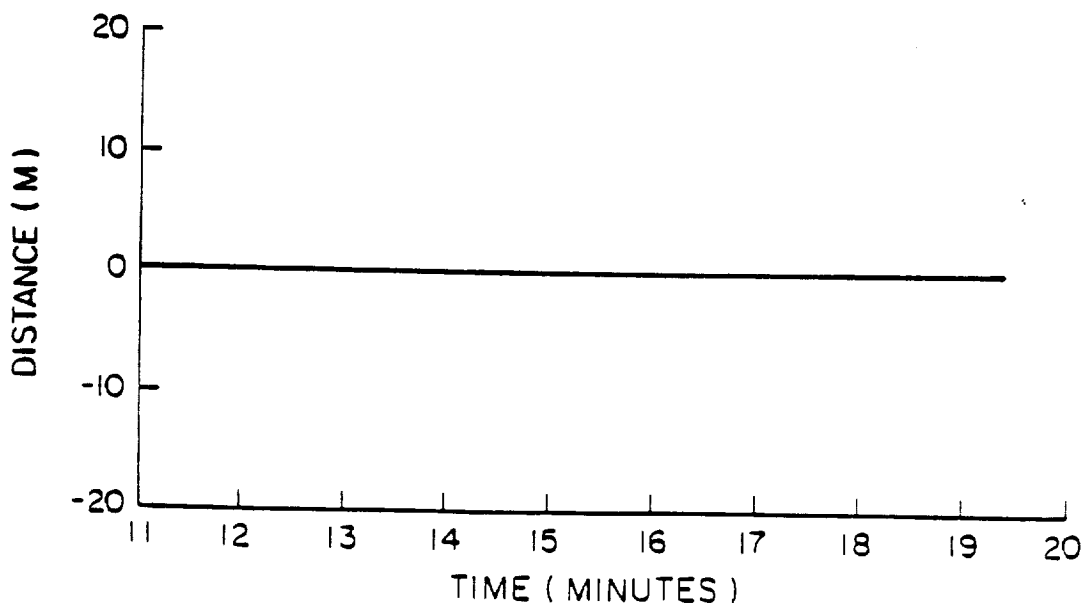


Figure 36. Spatial relationship between the orbiter and the PDP during backaway.

A-587-789

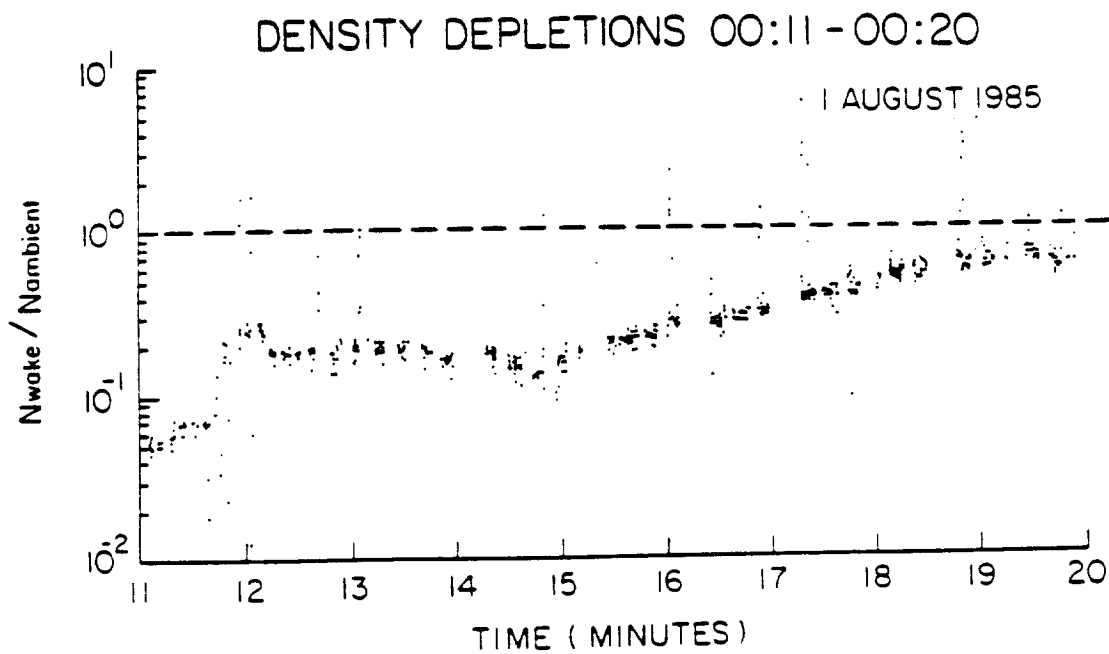
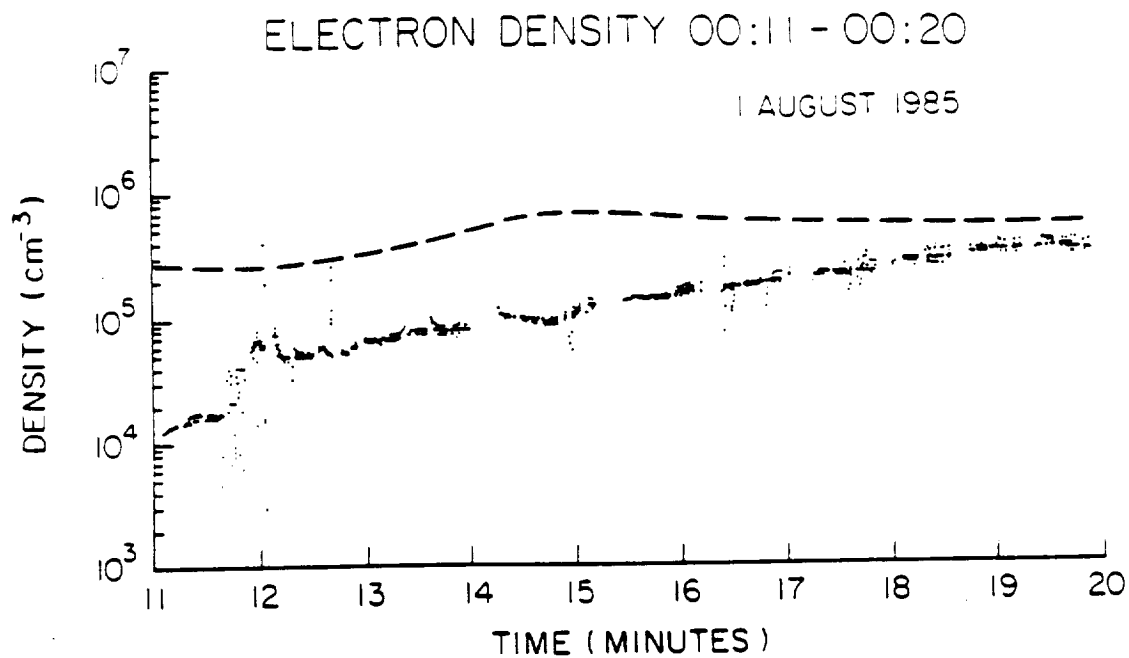


Figure 37. Electron density depletions during backaway.

A-687-801

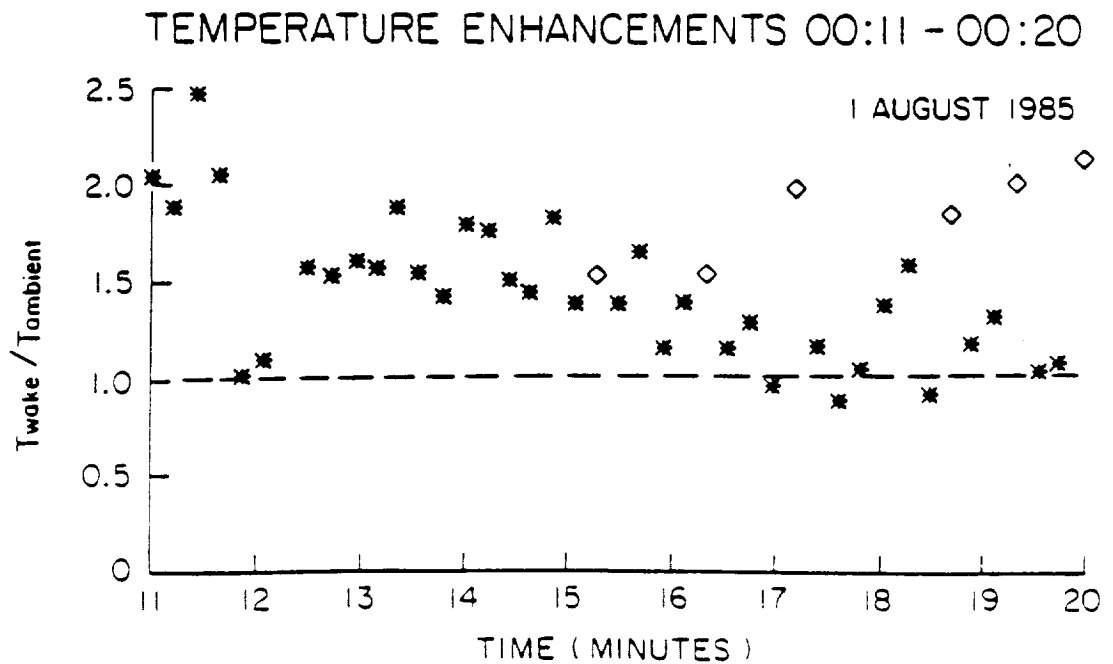
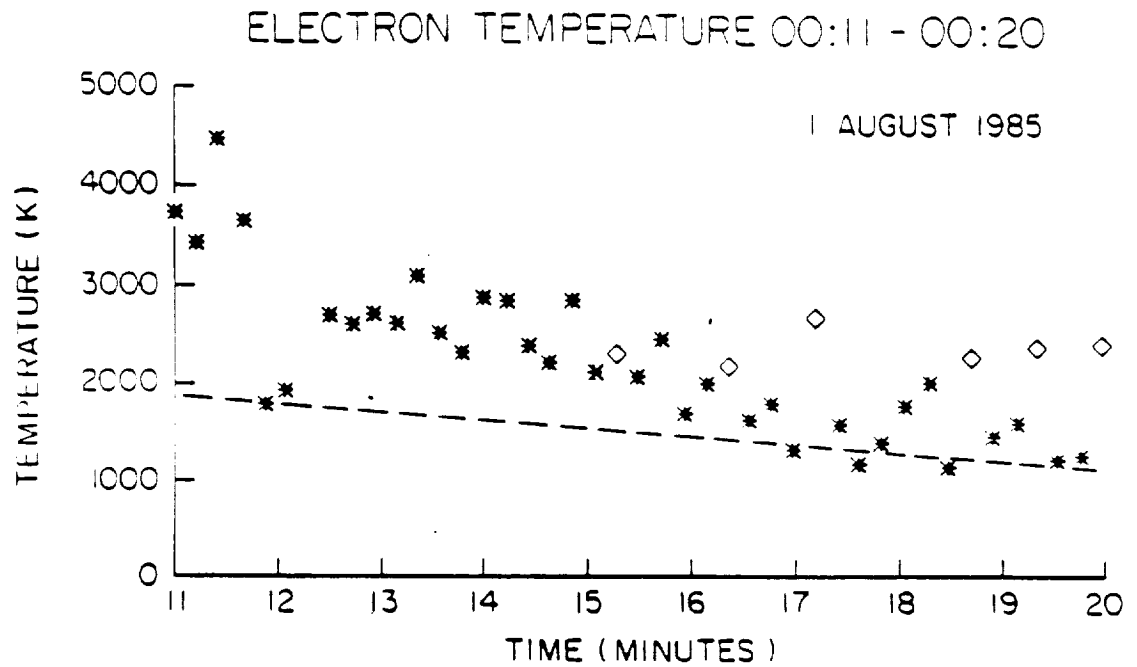
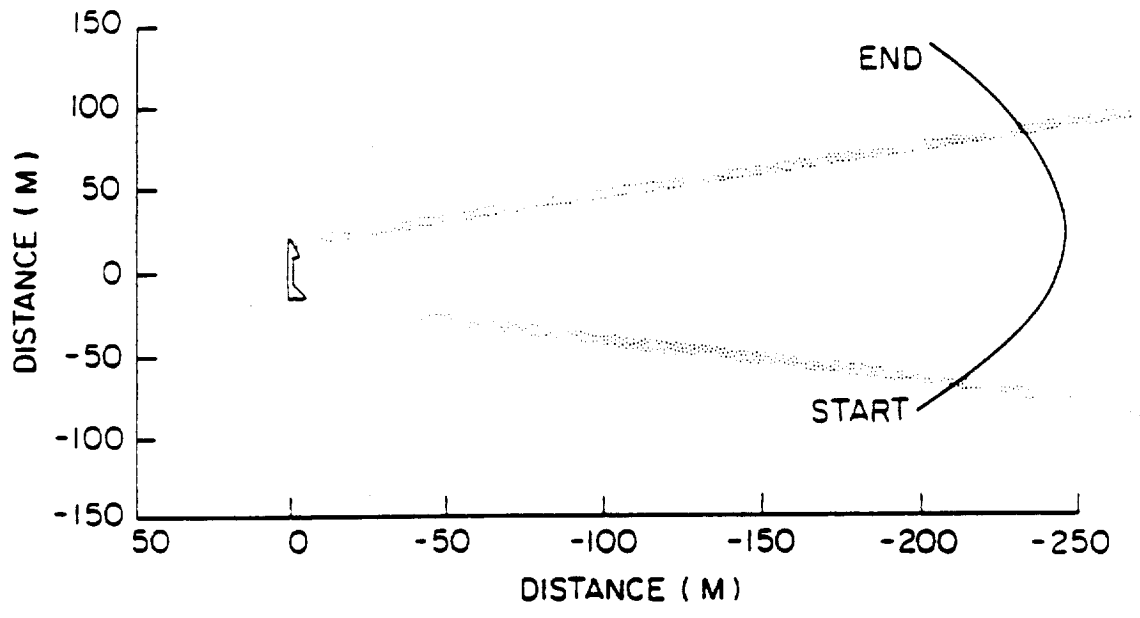


Figure 38. Electron temperature enhancements during backaway.

IN PLANE DISTANCE 02:58-03:10



OUT OF PLANE DISTANCE 02:58-03:10

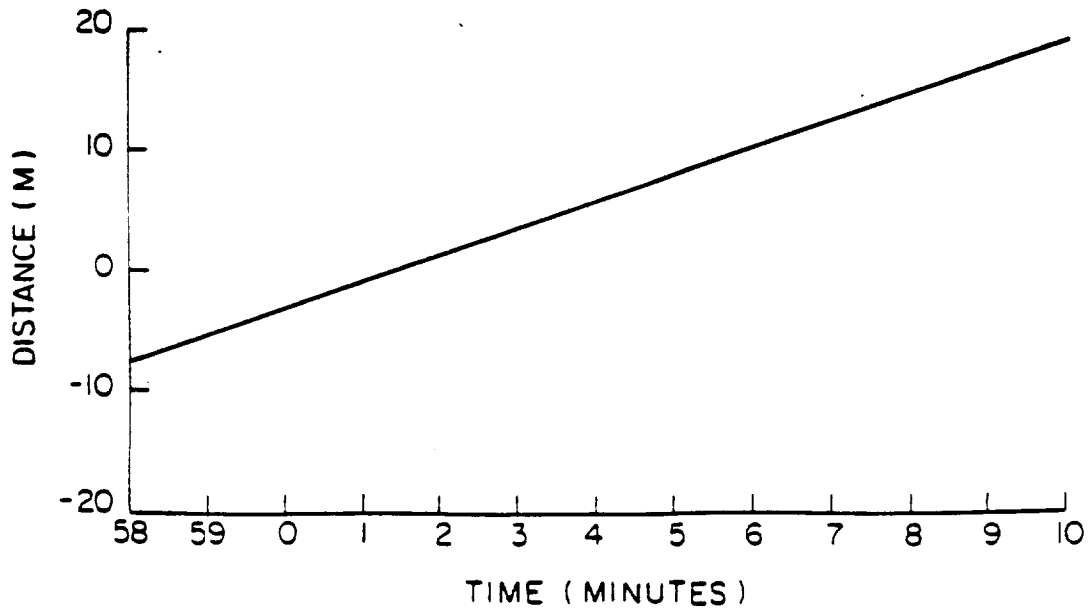


Figure 39. Spatial relationship between the orbiter and the PDP during far wake transit one.

A-687-793

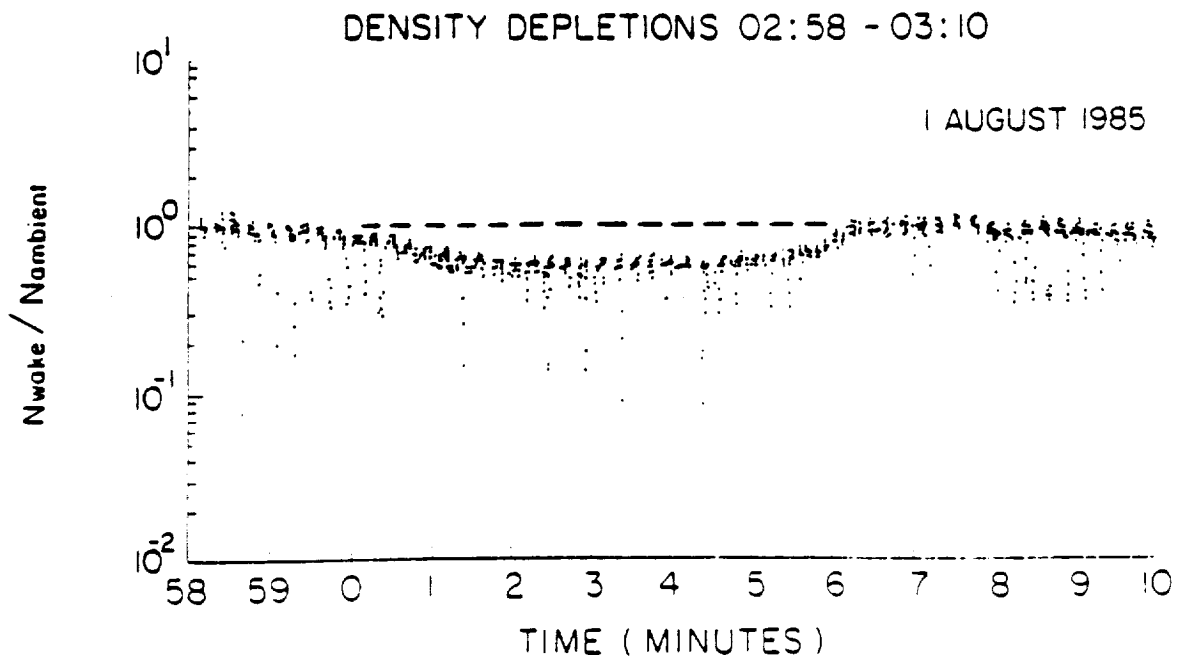
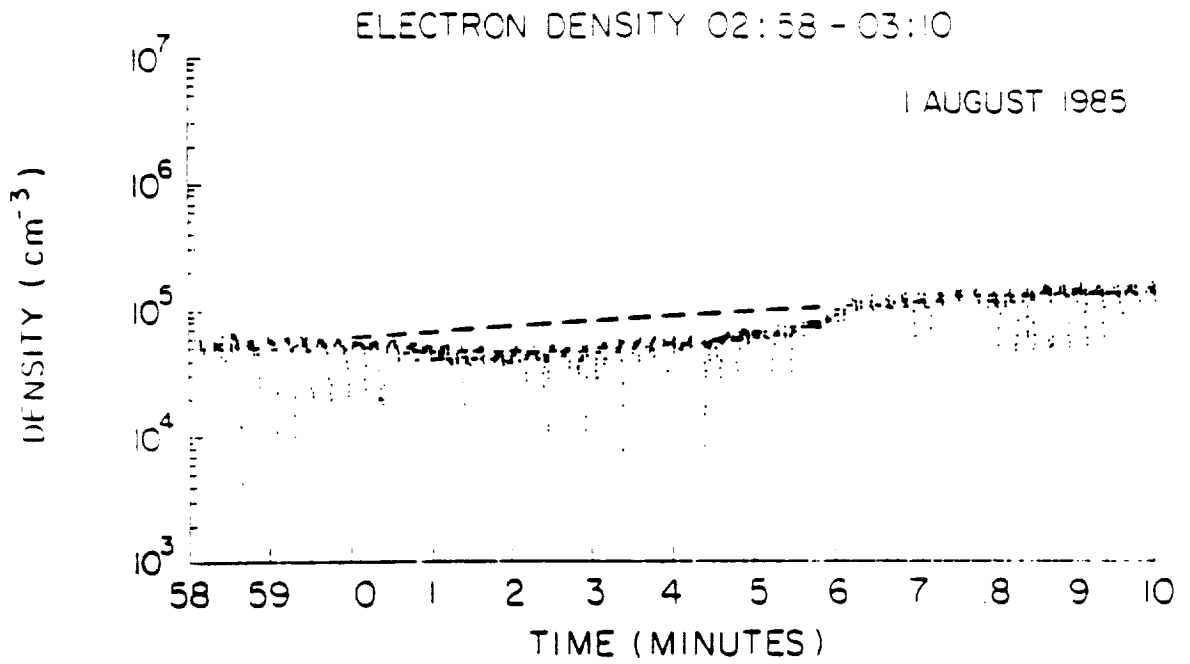


Figure 40. Electron density depletions during far wake transit one.

A-587-802-1

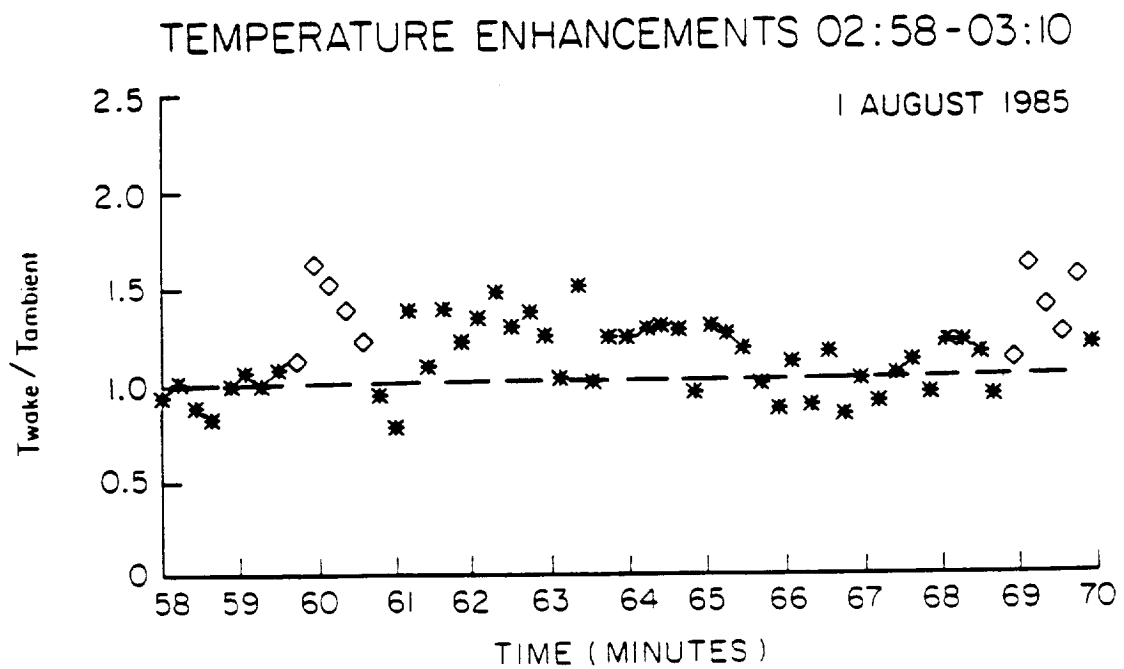
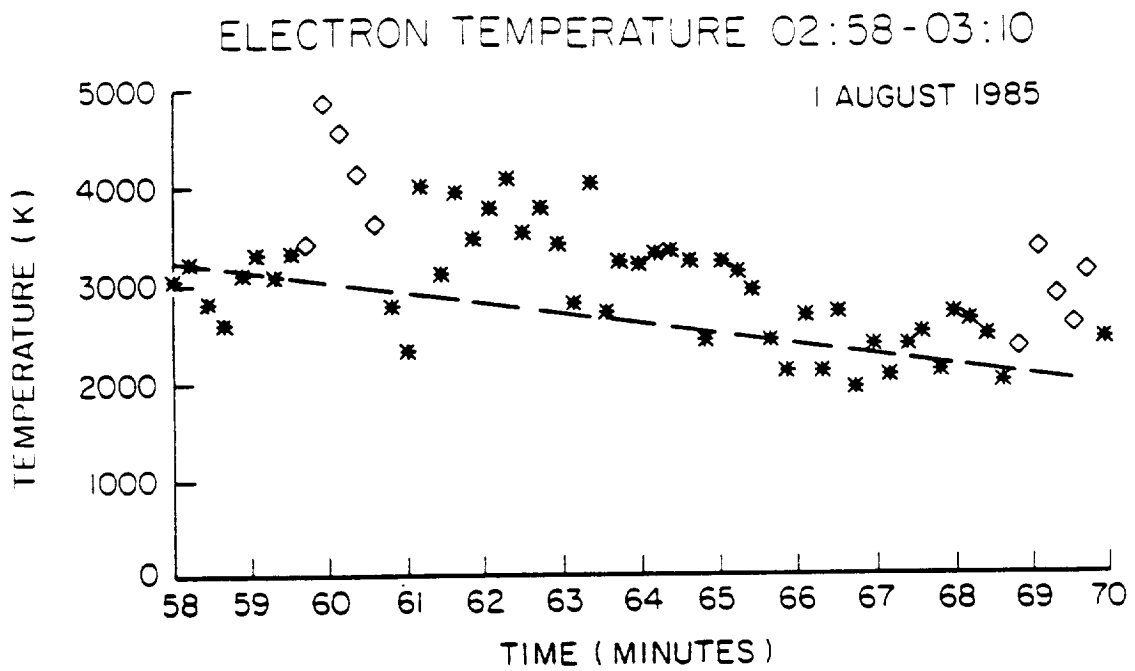


Figure 41. Electron temperature enhancements during far wake transit one.

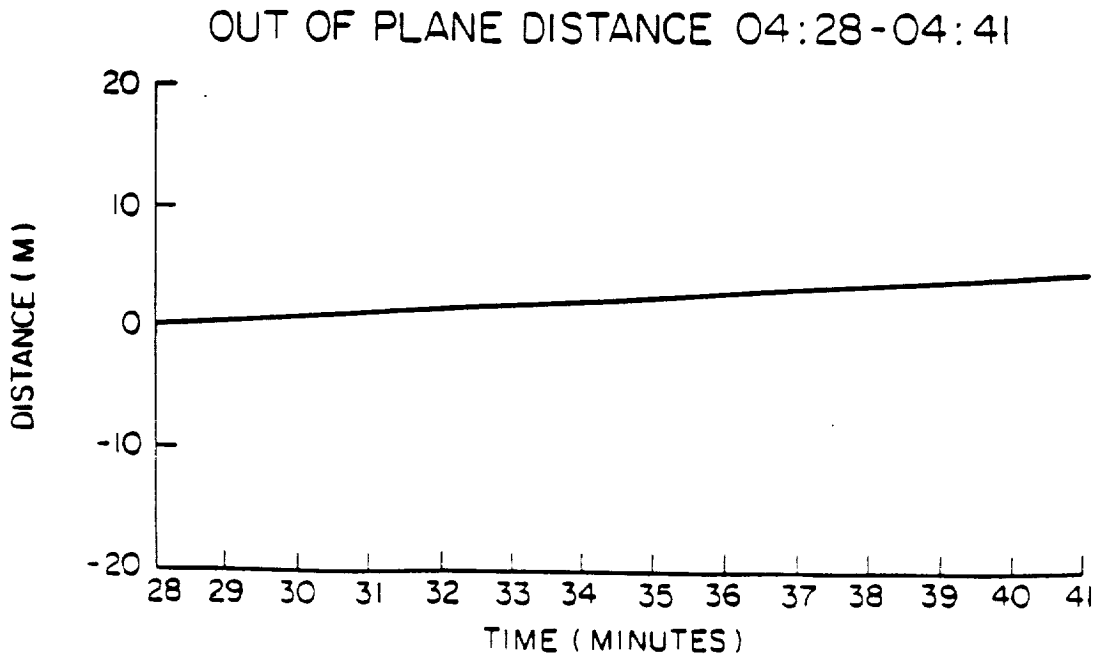
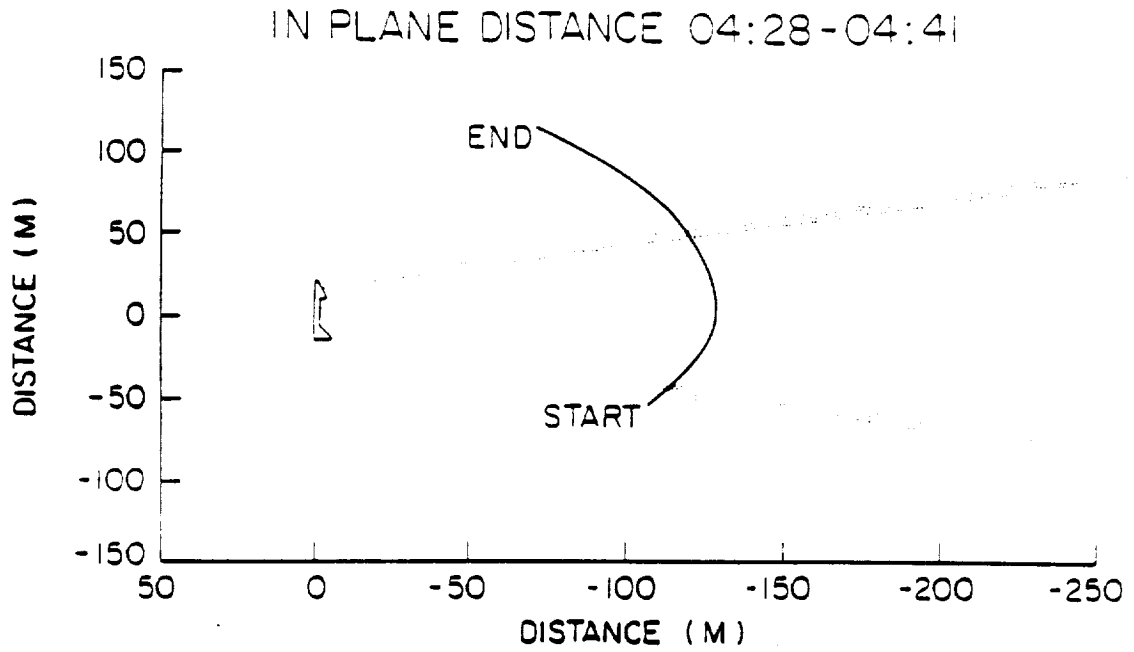


Figure 42. Spatial relationship between the orbiter and the PDP during far wake transit two.

A-G87-790

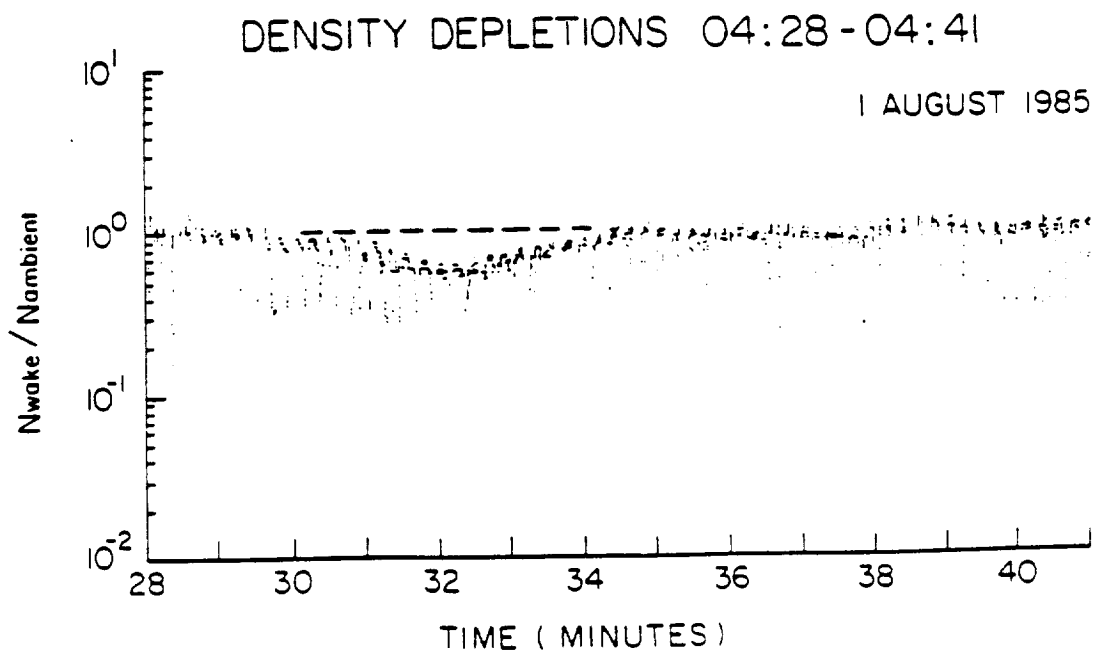
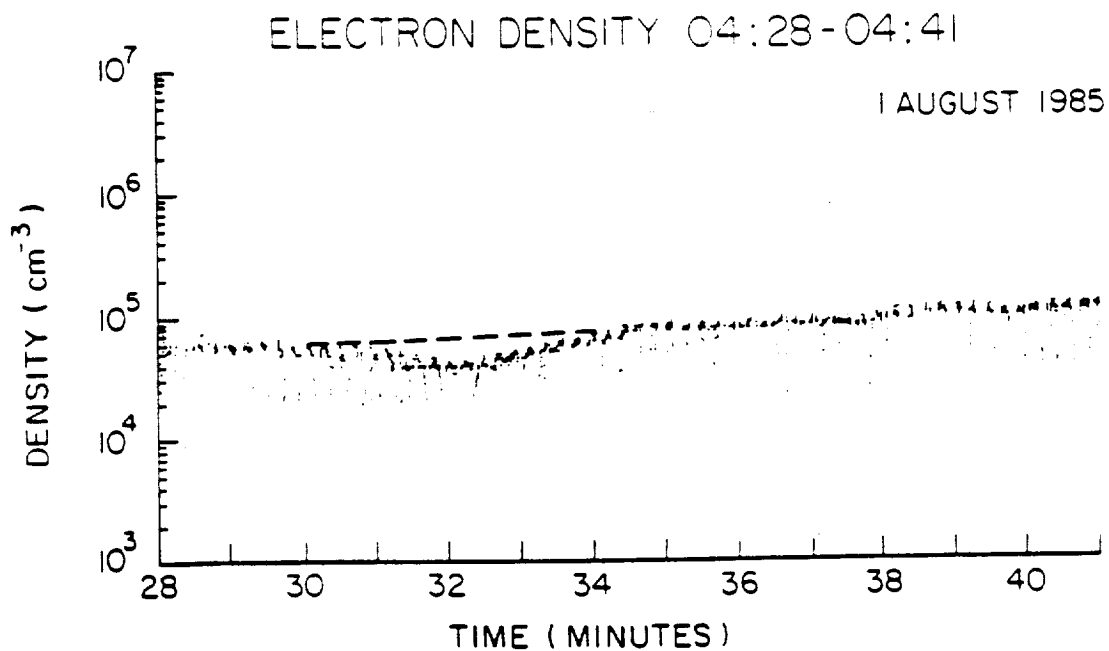


Figure 43. Electron density depletions during far wake transit two.

A-687-803-1

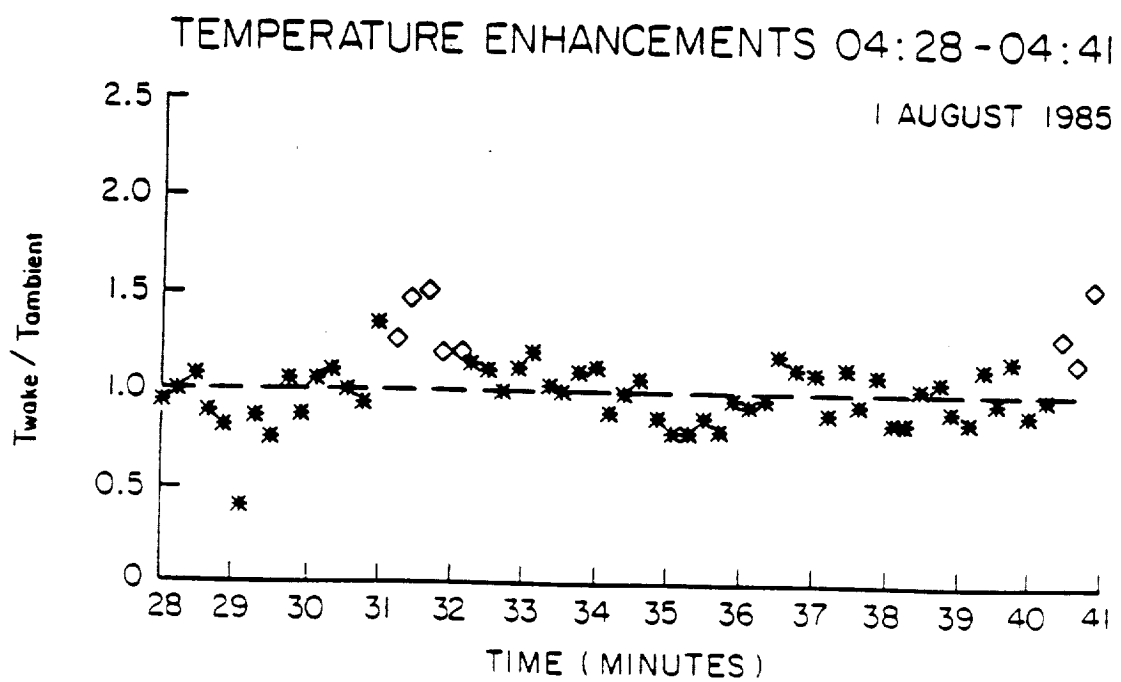
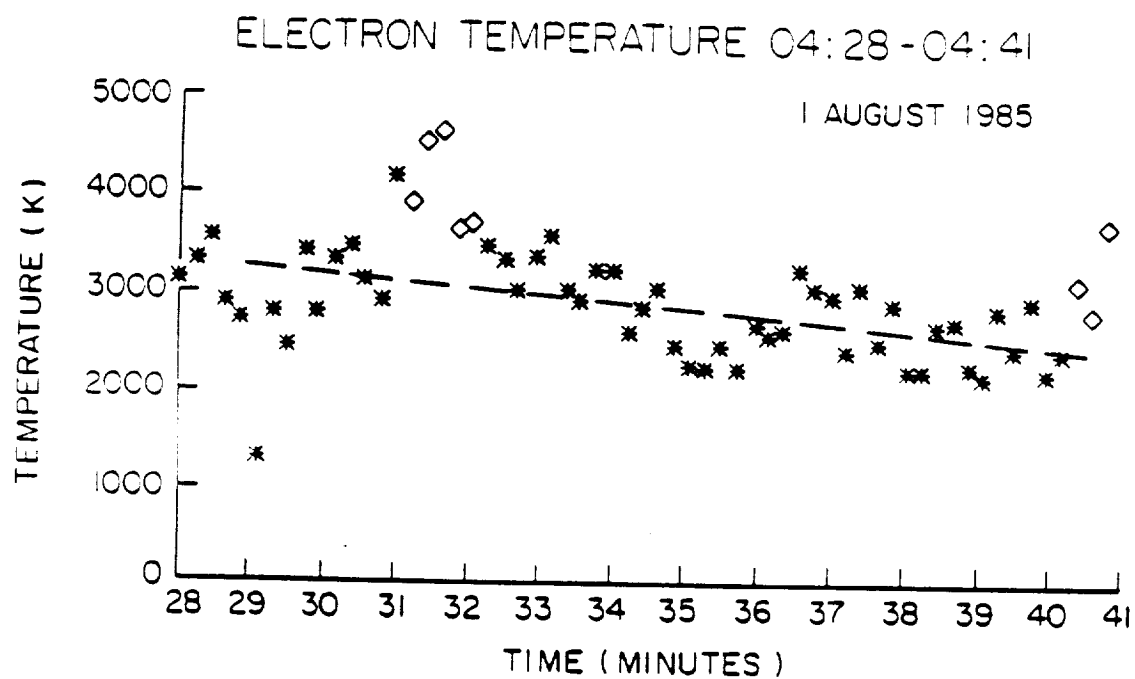


Figure 44. Electron temperature enhancements during far wake transit two.

A-G87-788

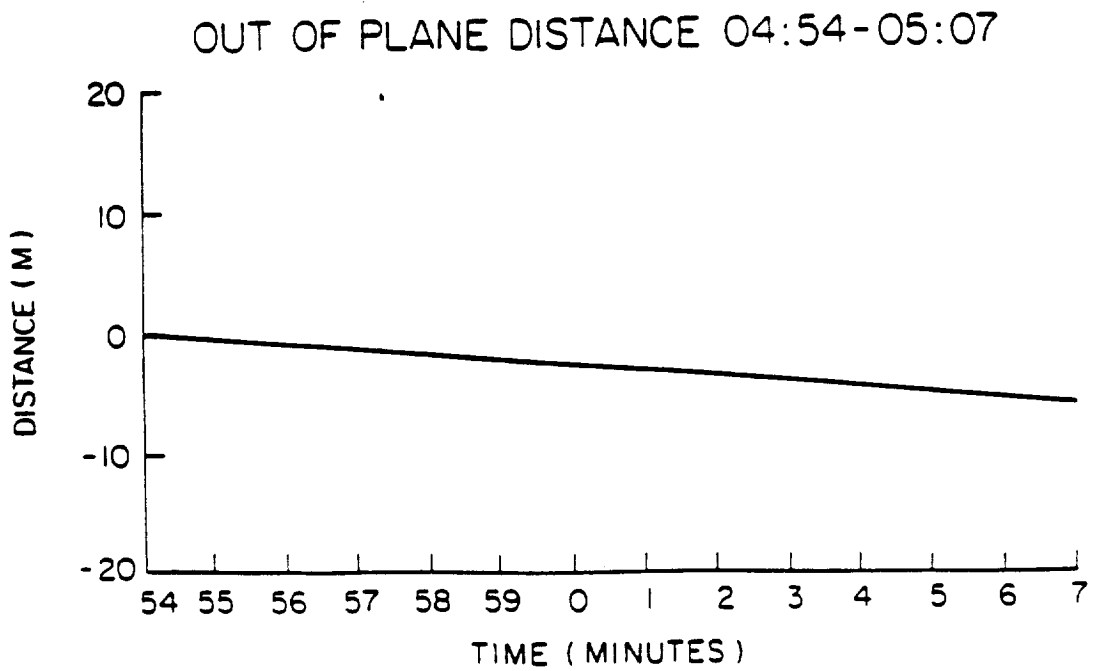
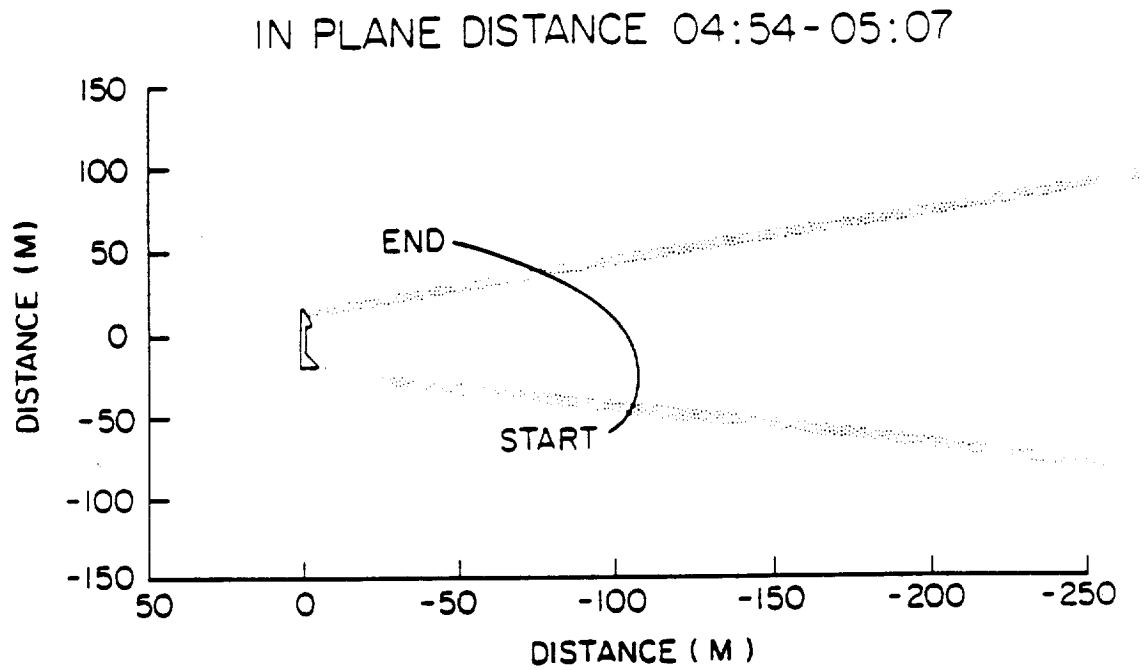
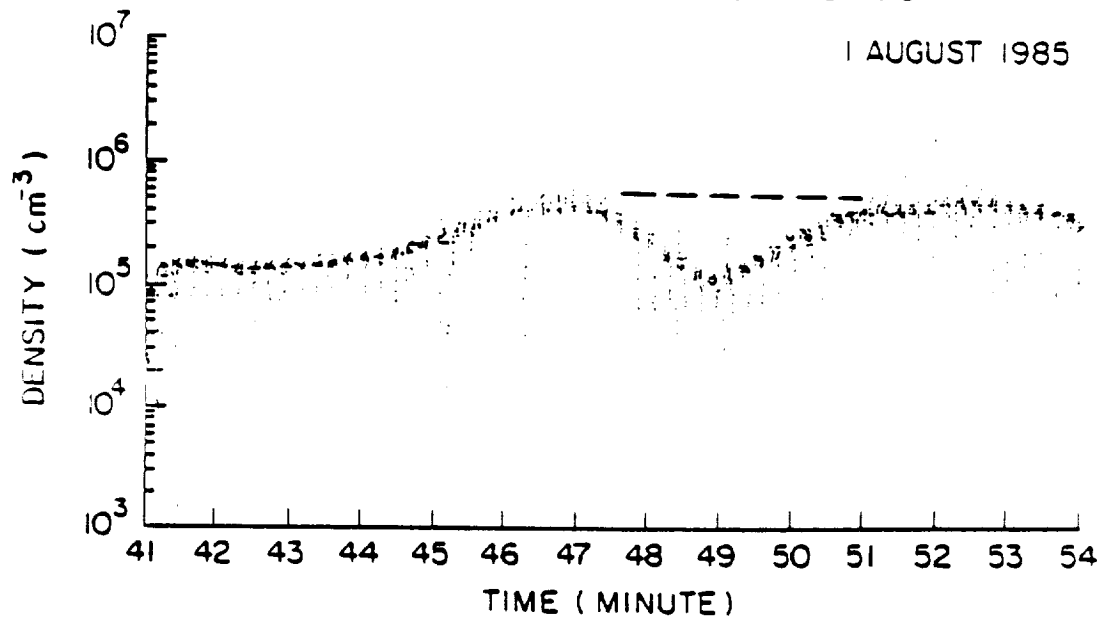


Figure 45. Spatial relationship between the orbiter and the PDP during far wake transit three.

A-687-792

ELECTRON DENSITY 04:41-04:54

1 AUGUST 1985



DENSITY DEPLETIONS 04:41-04:54

1 AUGUST 1985

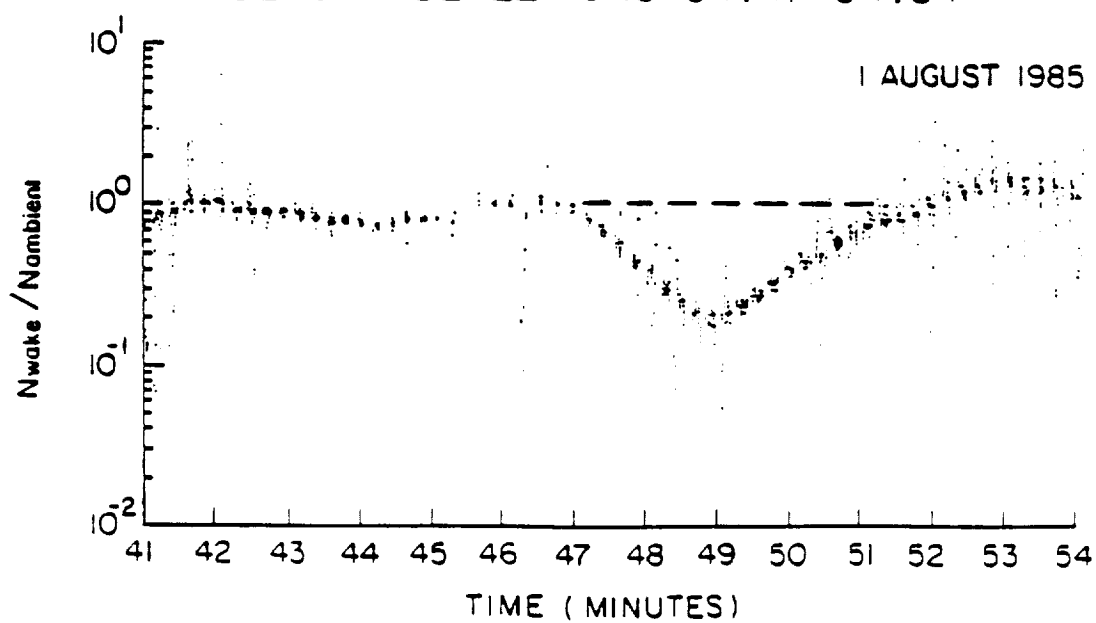


Figure 46. Electron density depletions during far wake transit three.

A-G87-804 -1

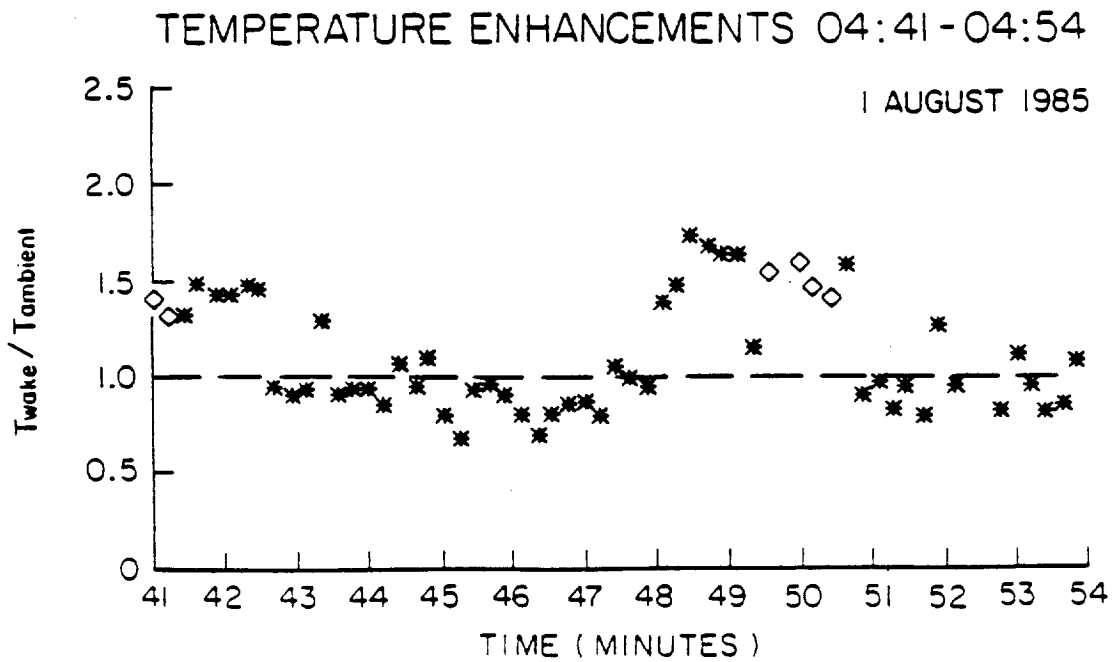
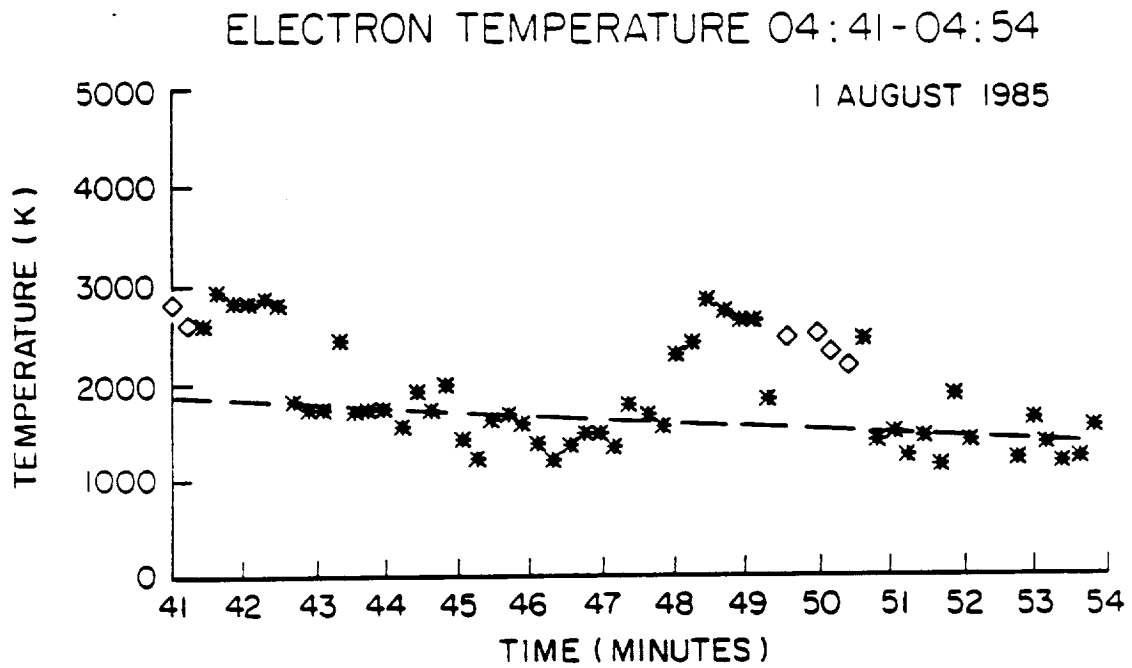


Figure 47. Electron temperature enhancements during far wake transit three.

A-G87-797

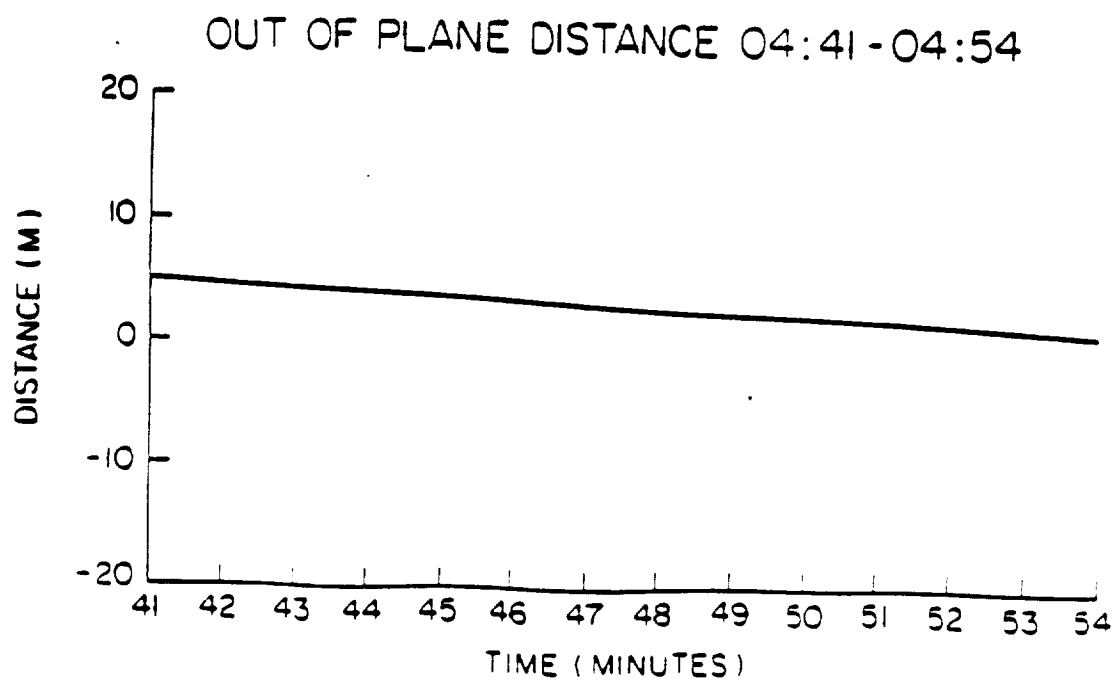
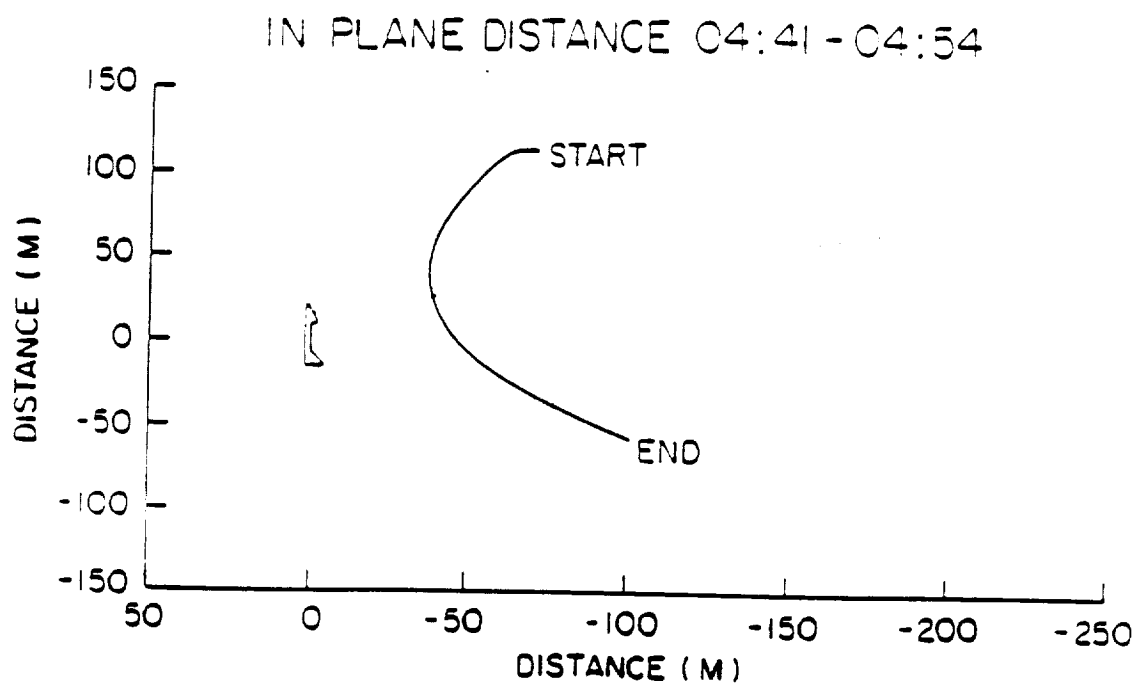
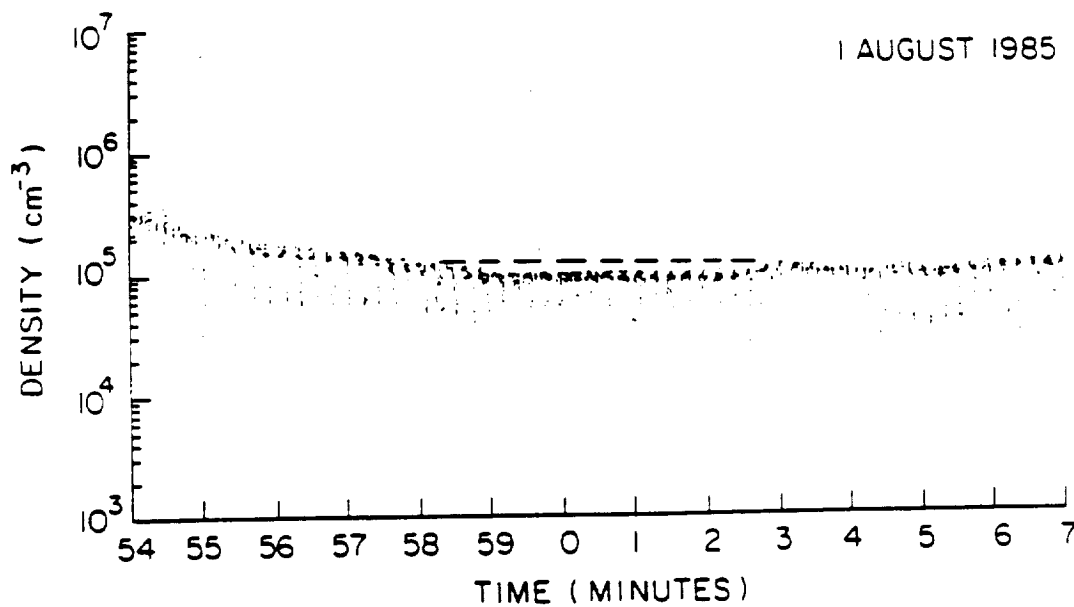


Figure 48. Spatial relationship between the orbiter and the PDP during far wake transit four.

A-G87-791

ELECTRON DENSITY 04:54-05:07

1 AUGUST 1985



DENSITY DEPLETIONS 04:54-05:07

1 AUGUST 1985

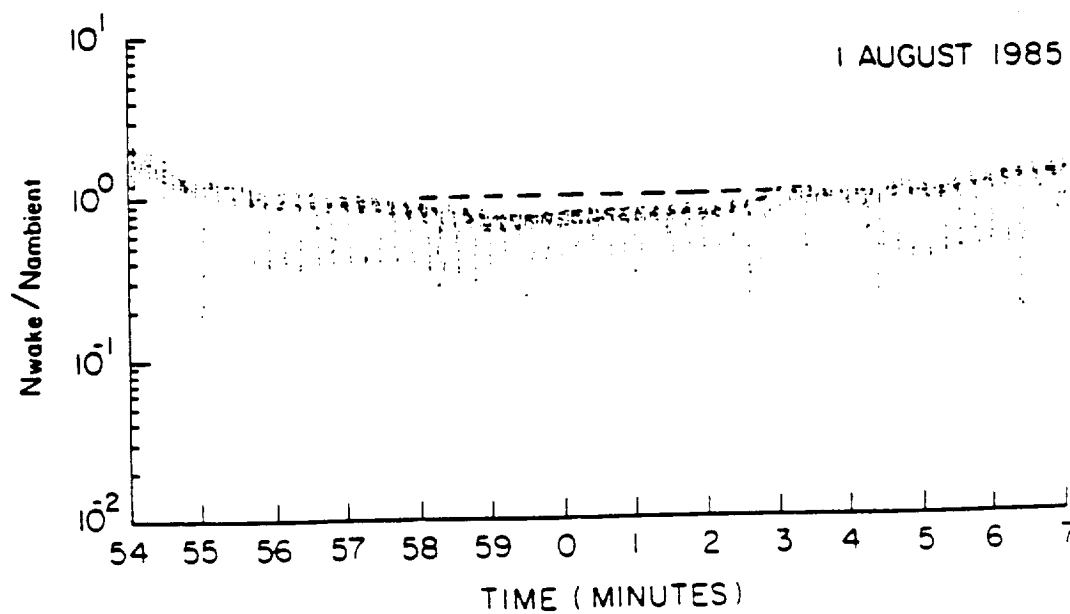


Figure 49. Electron density depletions during far wake transit four.

A-27-305

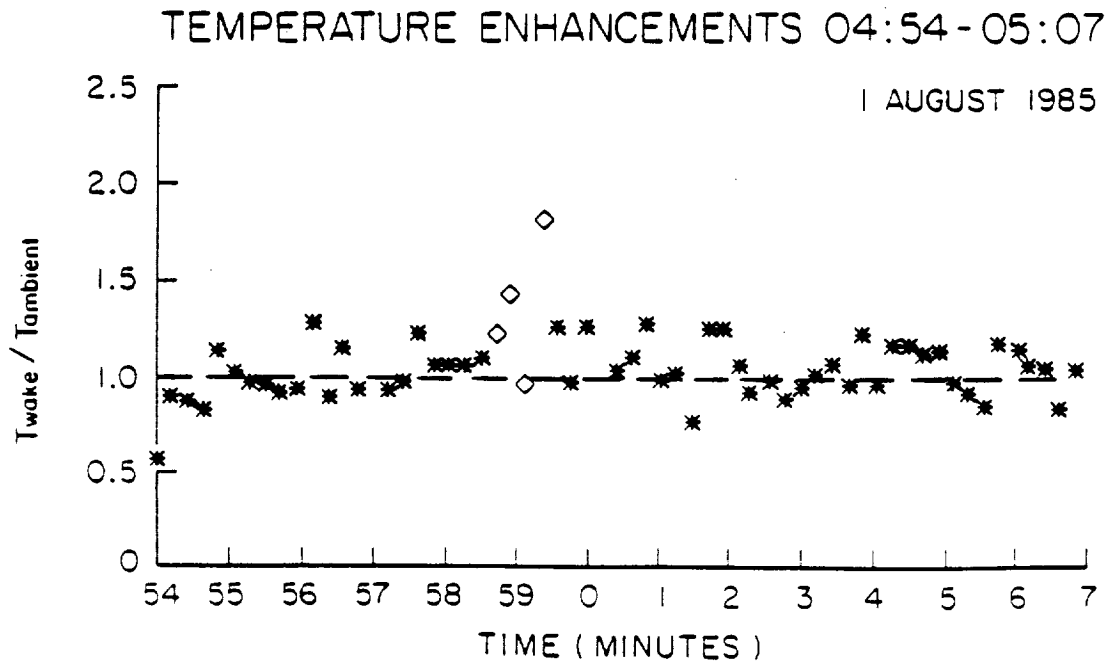
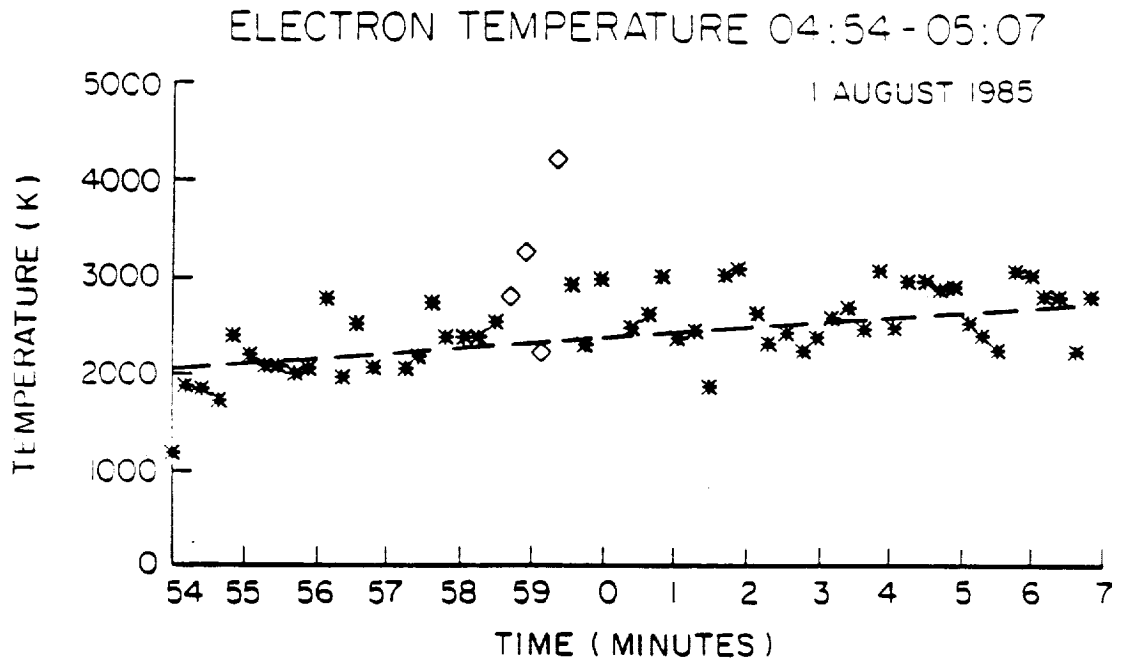


Figure 50. Electron temperature enhancements during far wake transit four.

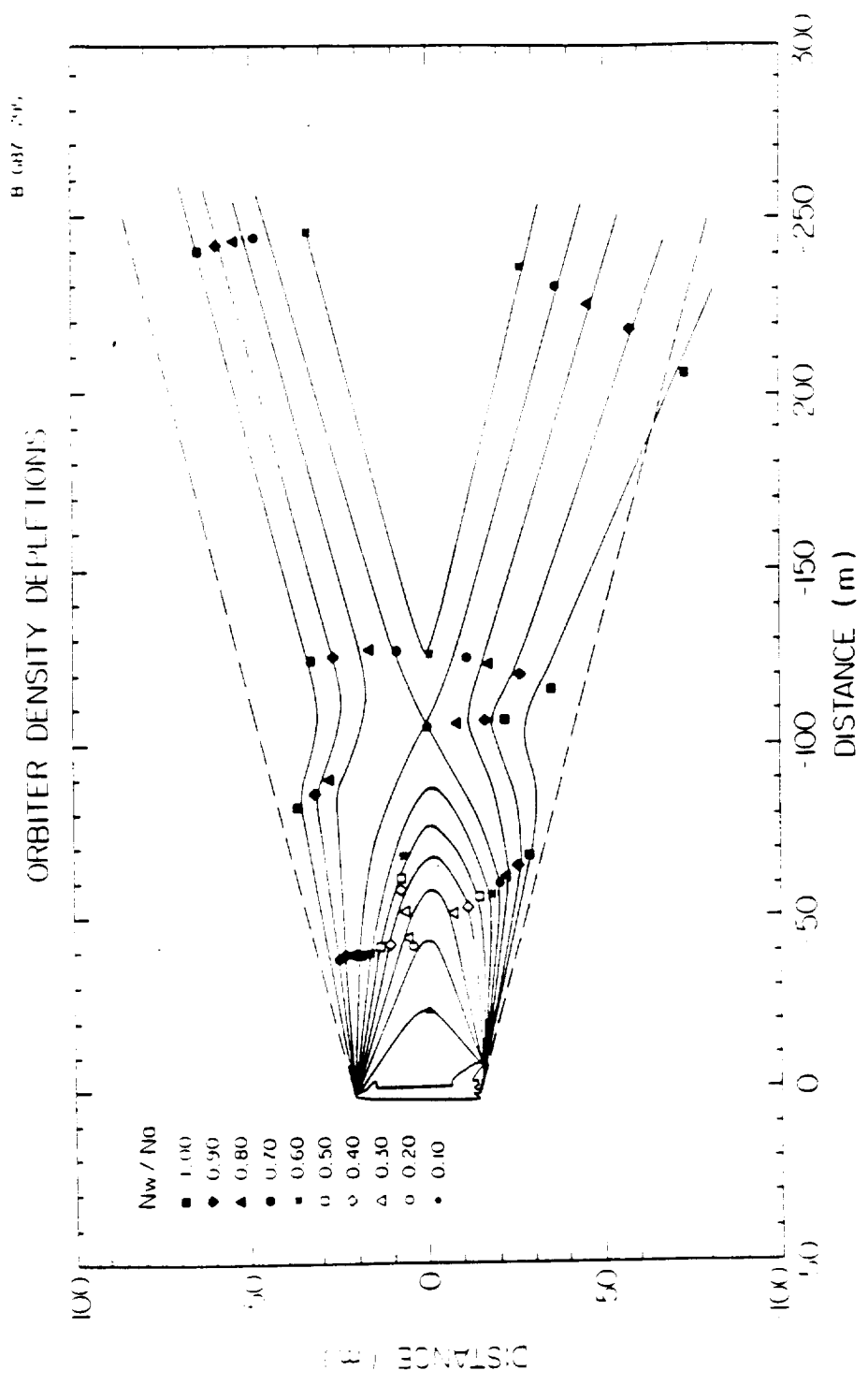


Figure 51. Electron density depletions in the wake of the shuttle orbiter for constant values of N_w/N_0 .

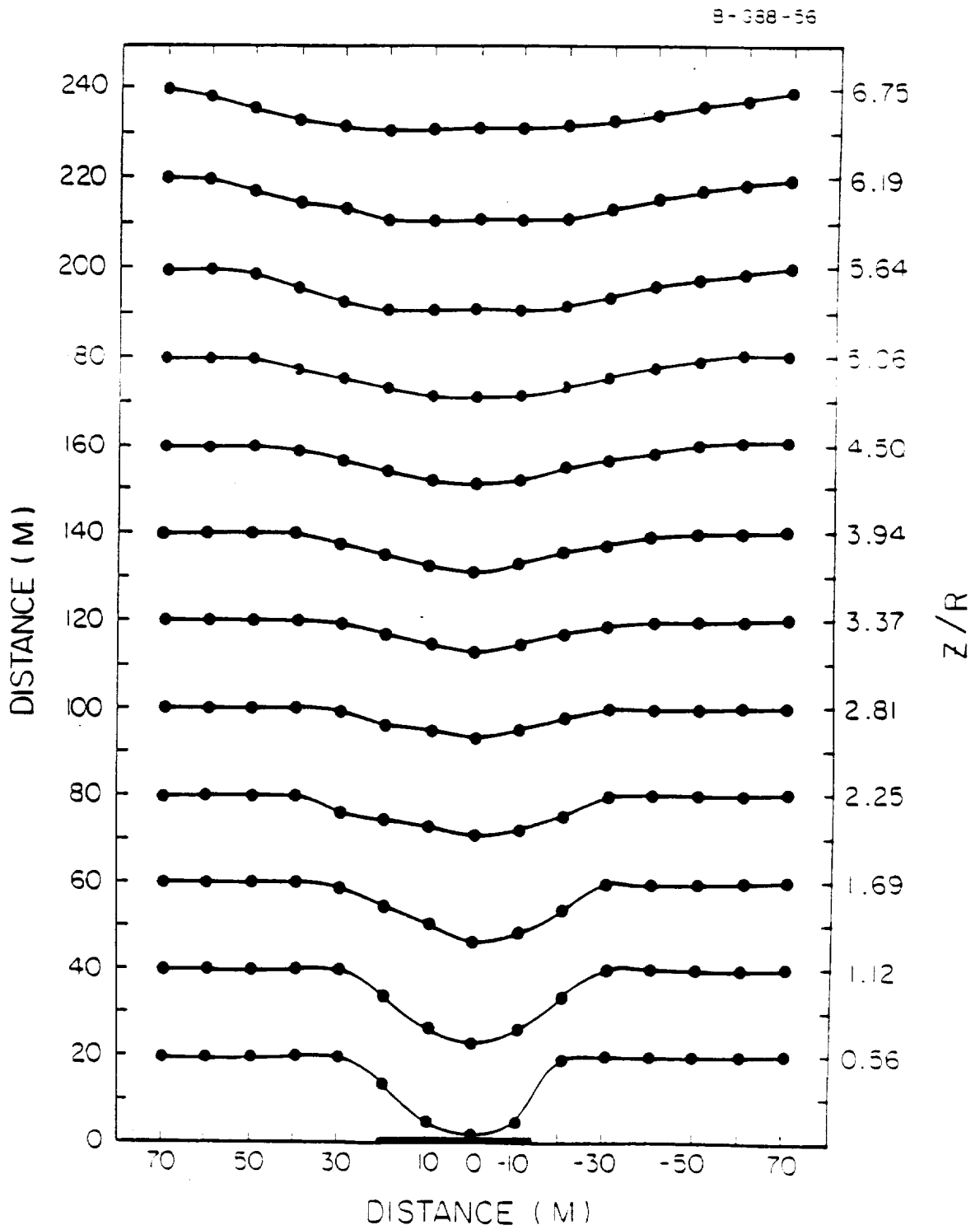


Figure 52. Electron density depletions in the wake of the shuttle orbiter for constant values of Z/R.

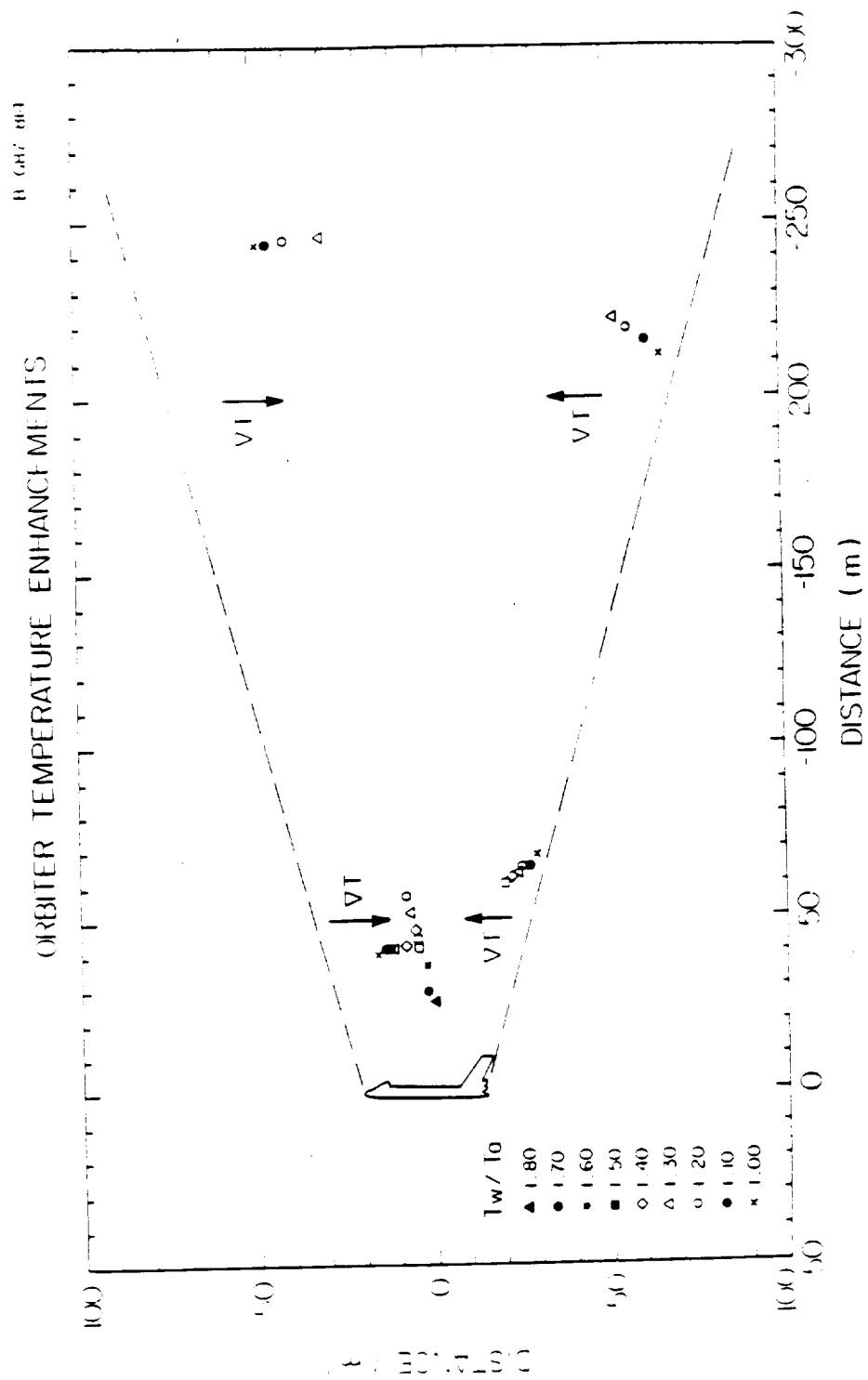


Figure 53. Electron temperature enhancements in the wake of the shuttle orbiter.

8-088-24

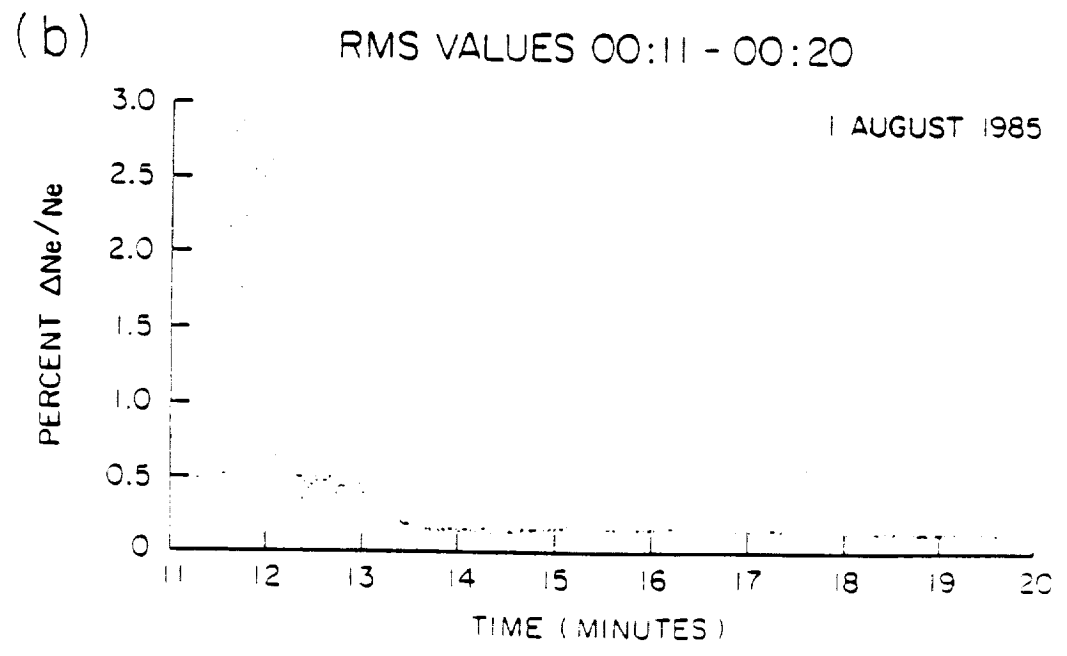
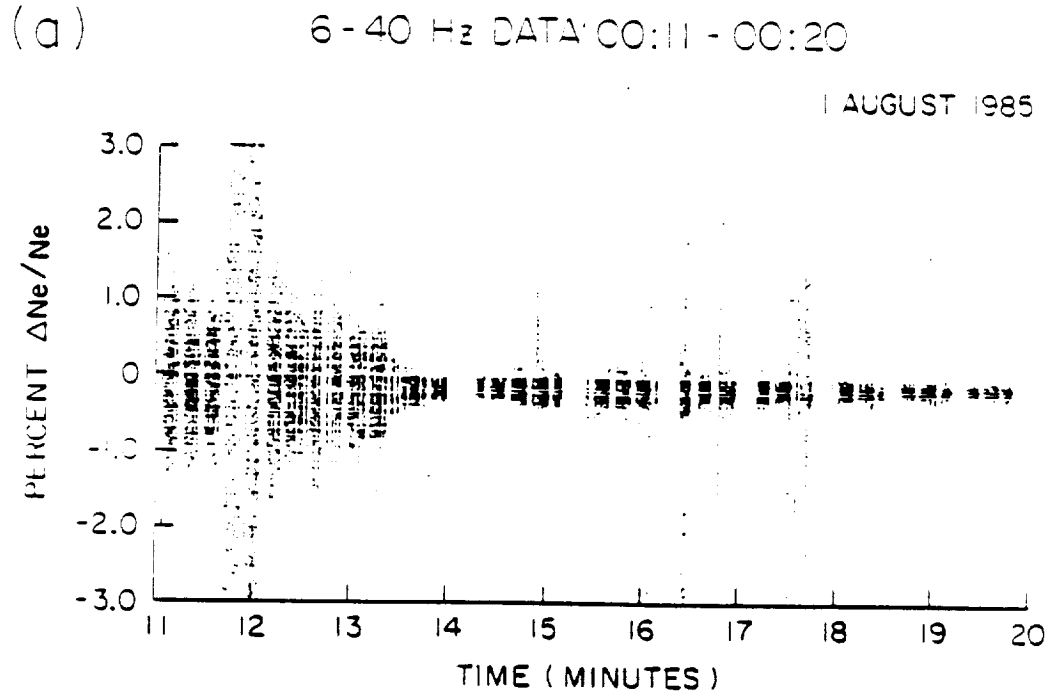


Figure 54. 6-40 Hz data during backaway.

B-G88-25

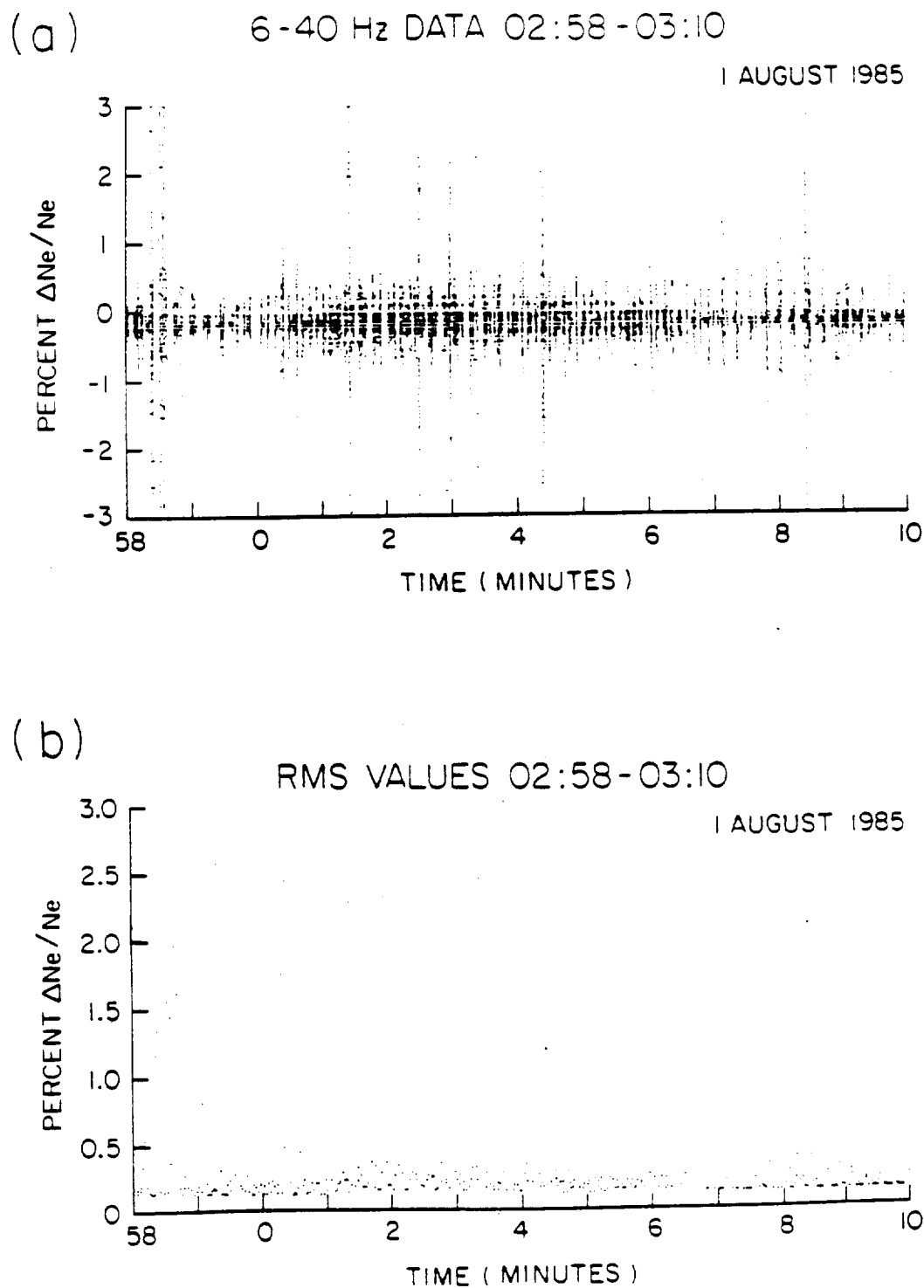


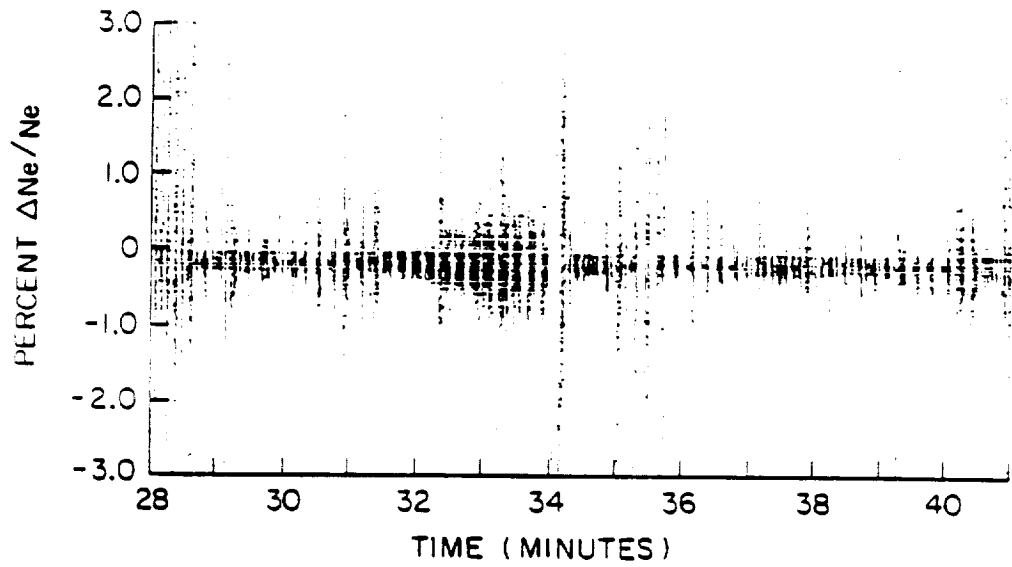
Figure 55. 6-40 Hz data during far wake transit one.

B-388-26

(a)

6-40 Hz DATA 04:28-04:41

1 AUGUST 1985



(b)

RMS VALUES 04:28-04:41

1 AUGUST 1985

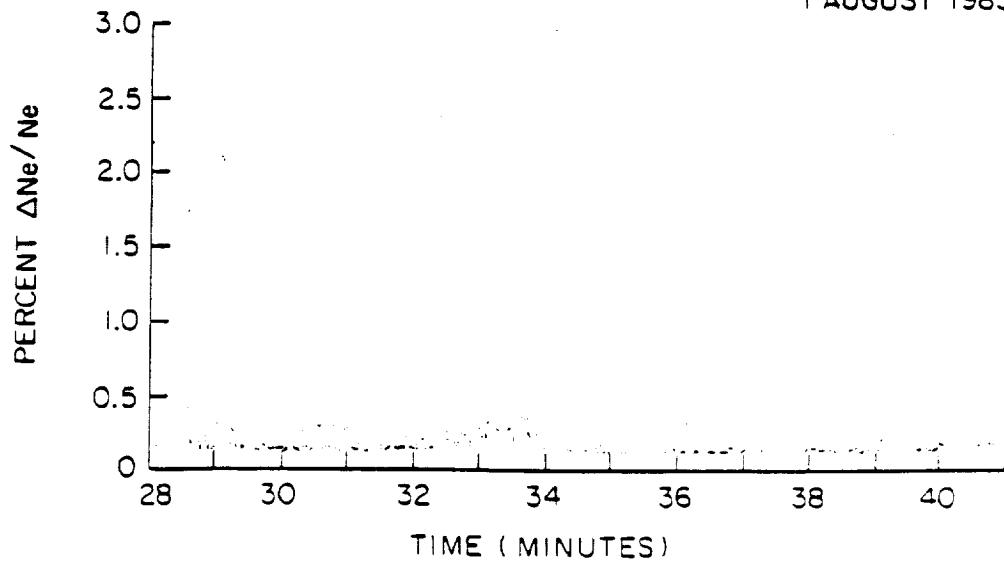


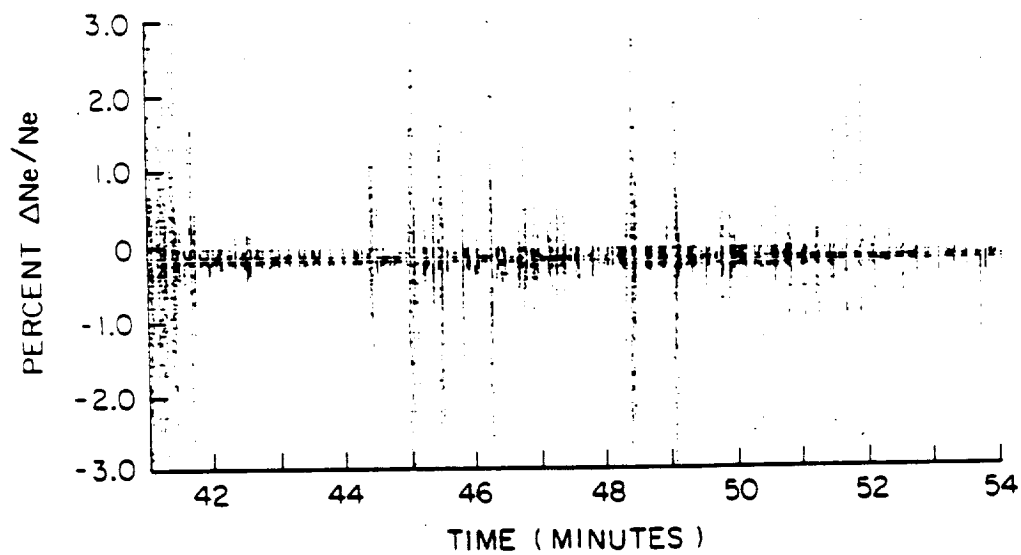
Figure 56. 6-40 Hz data during far wake transit two.

B-G88-27

(a)

6-40 Hz DATA 04:41-04:54

1 AUGUST 1985



(b)

RMS VALUES 04:41-04:54

1 AUGUST 1985

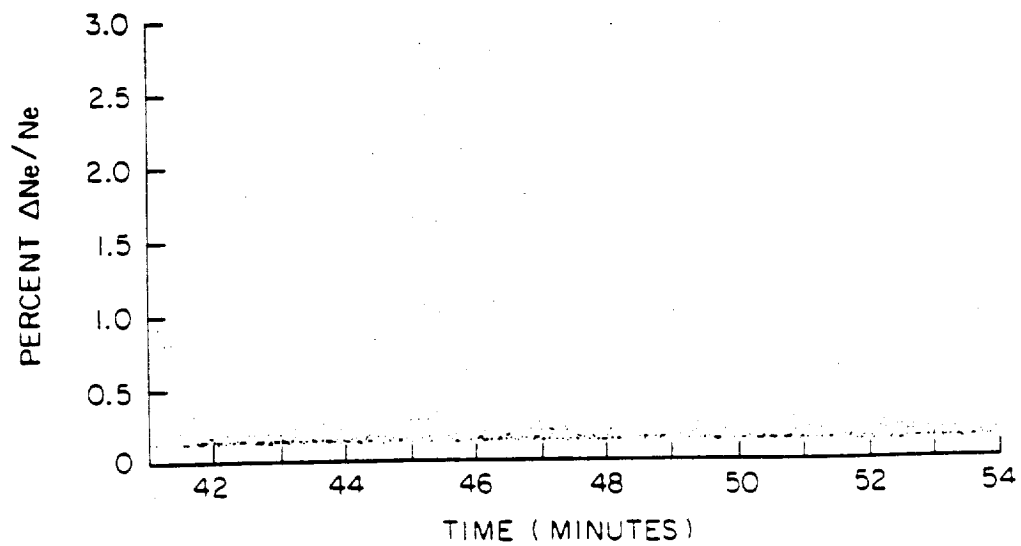


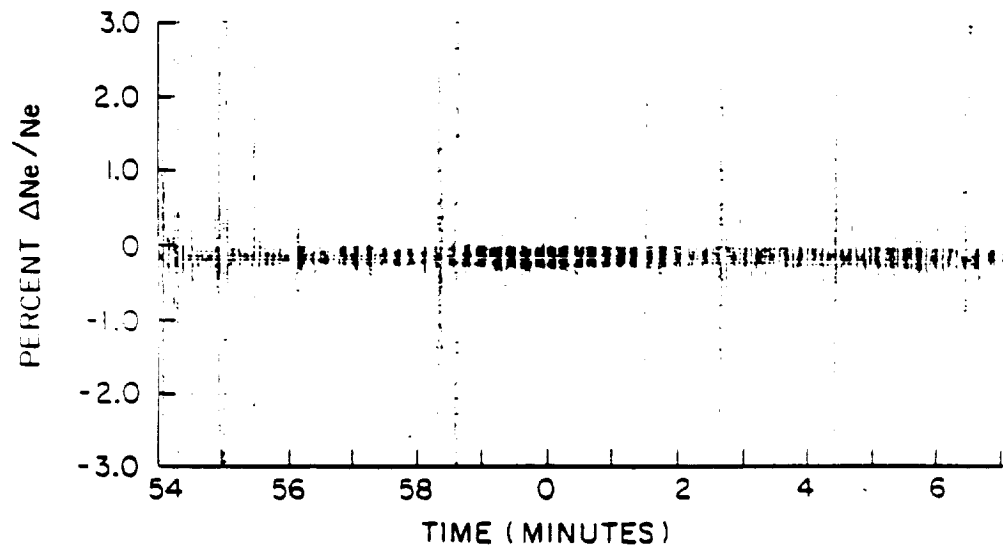
Figure 57. 6-40 Hz data during far wake transit three.

B-588-28

(a)

6-40 Hz DATA 04:54 - 05:07

1 AUGUST 1985



(b)

RMS VALUES 04:54 - 05:07

1 AUGUST 1985

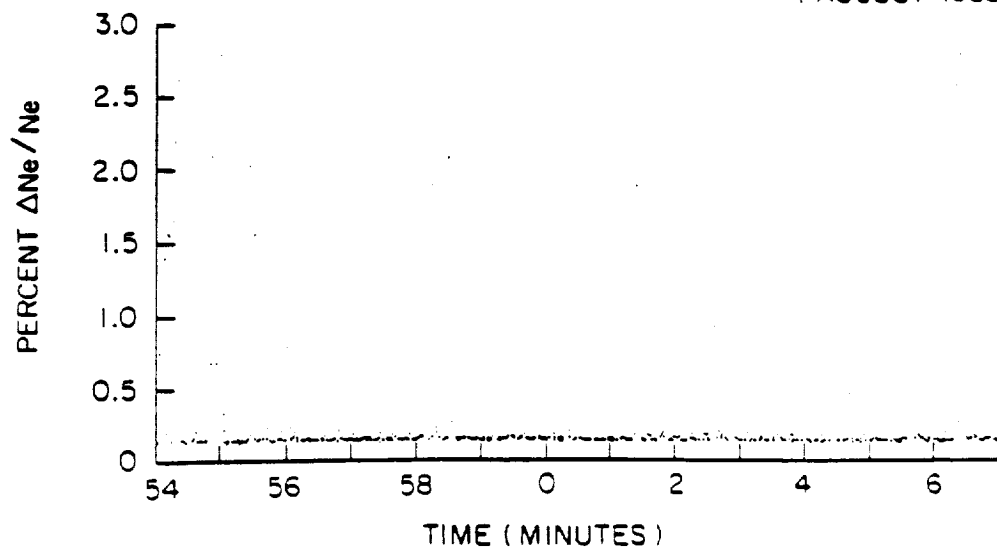


Figure 58. 6-40 Hz data during far wake transit four.

A - G88 - 180

SPECTRAL ANALYSIS: 0-40 Hz DATA
1 AUGUST 1985 00:15:03 - 00:15:15

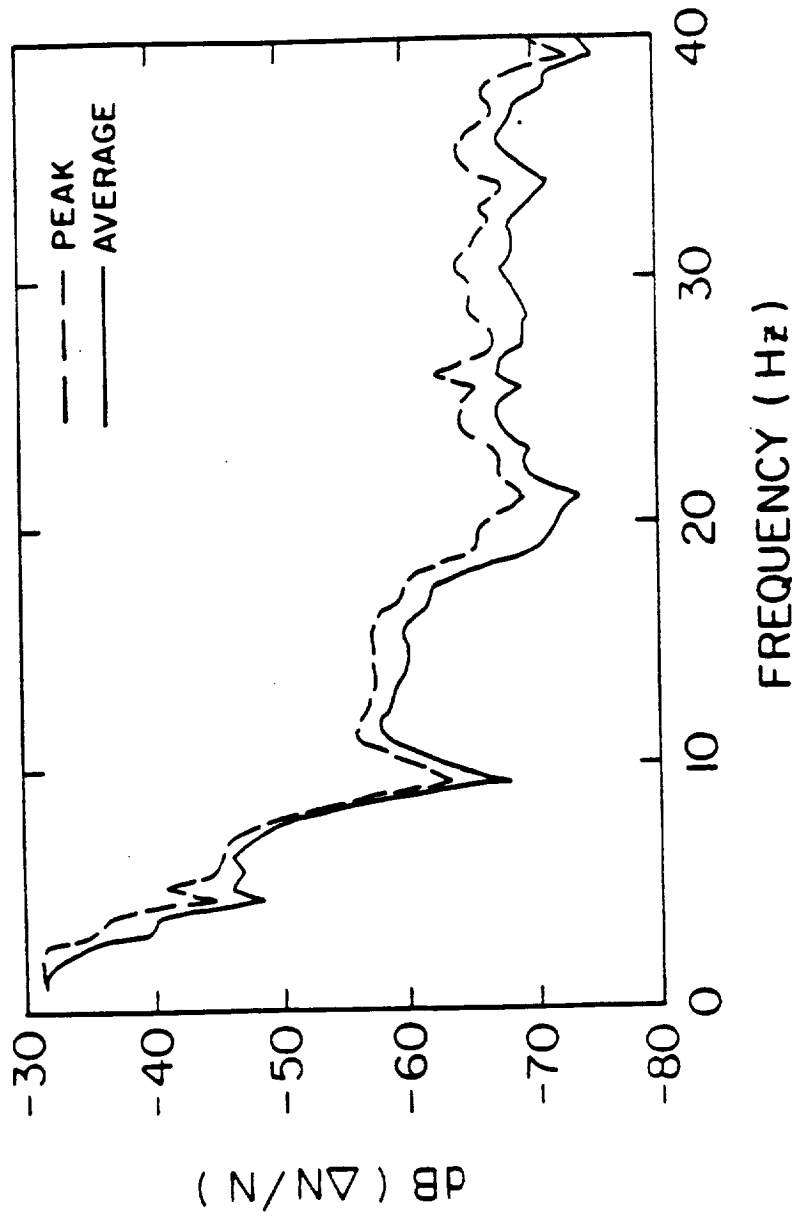


Figure 59. 0-40 Hz FFT data obtained on the wake axis 35 m downstream from the orbiter.

A - G88 - 181

SPECTRAL ANALYSIS: 0-40 Hz DATA
1 AUGUST 1985 04:28:04 - 04:28:16

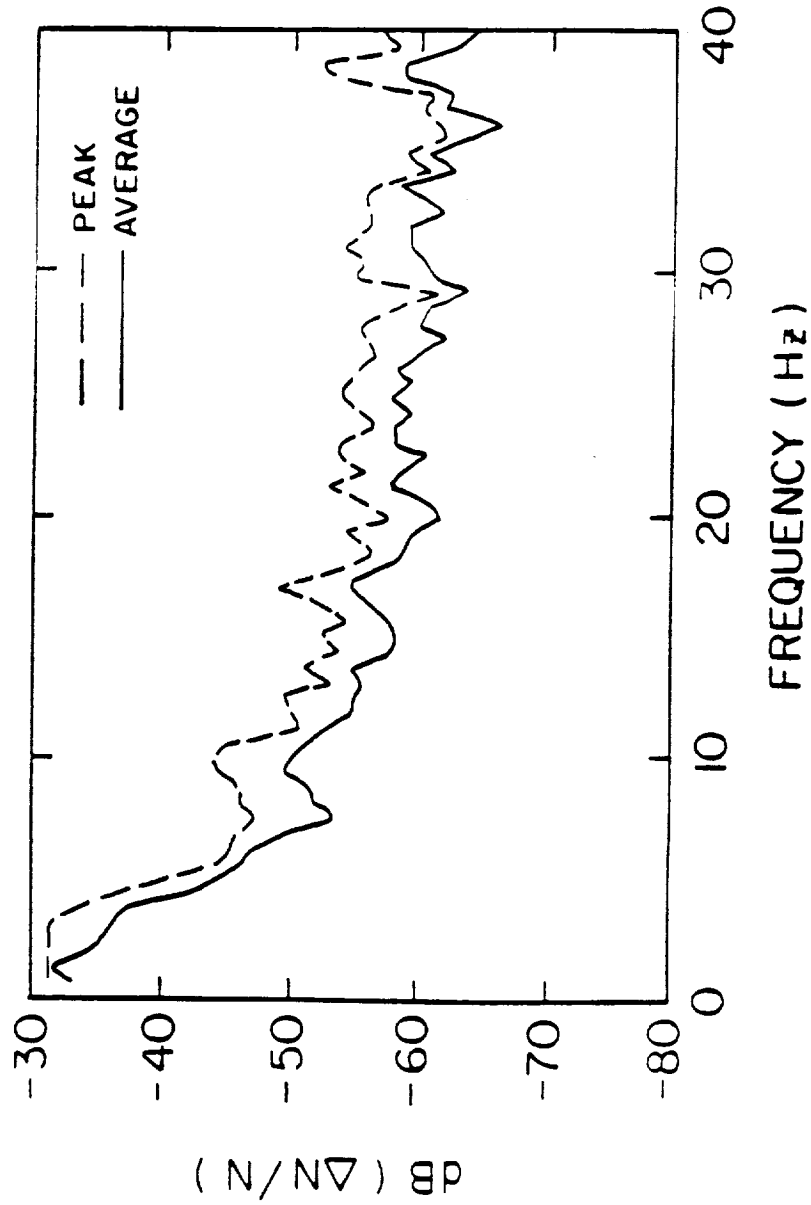


Figure 60. 0-40 Hz FFT data obtained on the wake axis 120 m downstream from the orbiter.

SPECTRAL ANALYSIS: 0-40 Hz DATA
1 AUGUST 1985 02:56:07 - 02:56:19

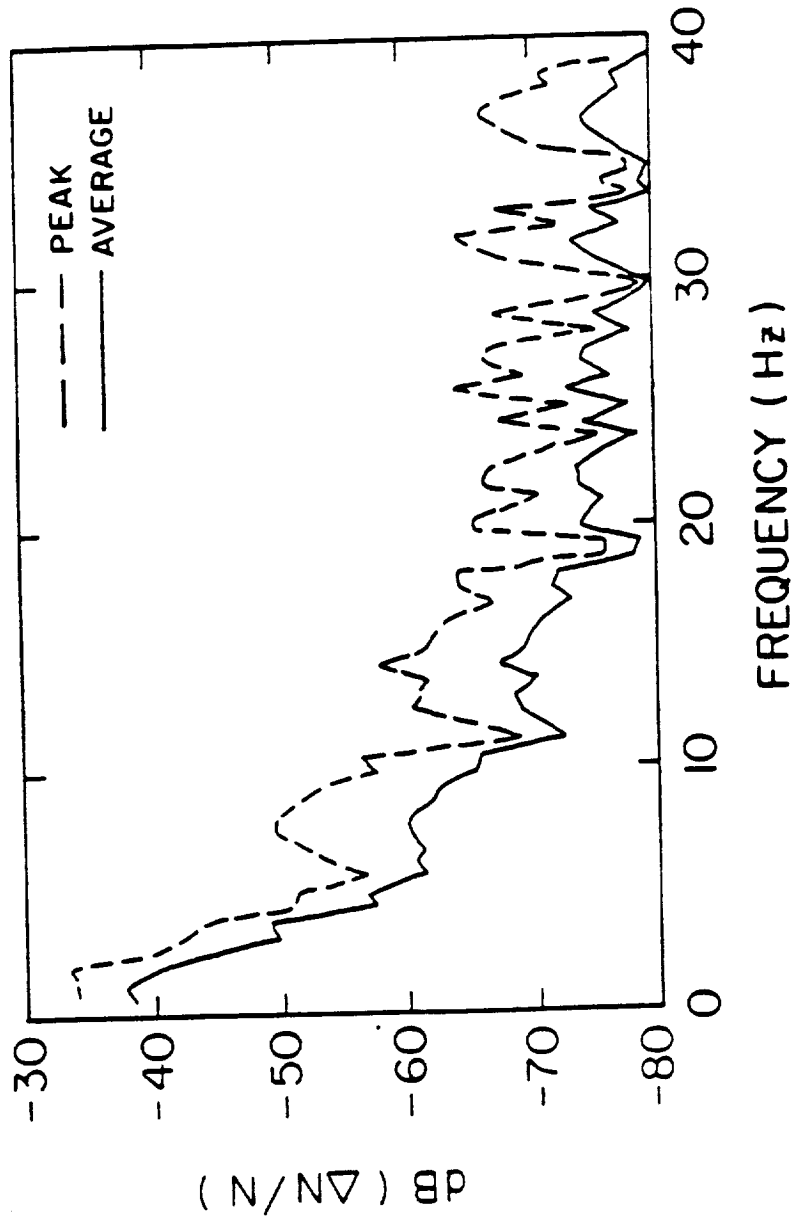


Figure 61. 0-40 Hz FFT data obtained on the Mach cone 200 m downstream from the orbiter.

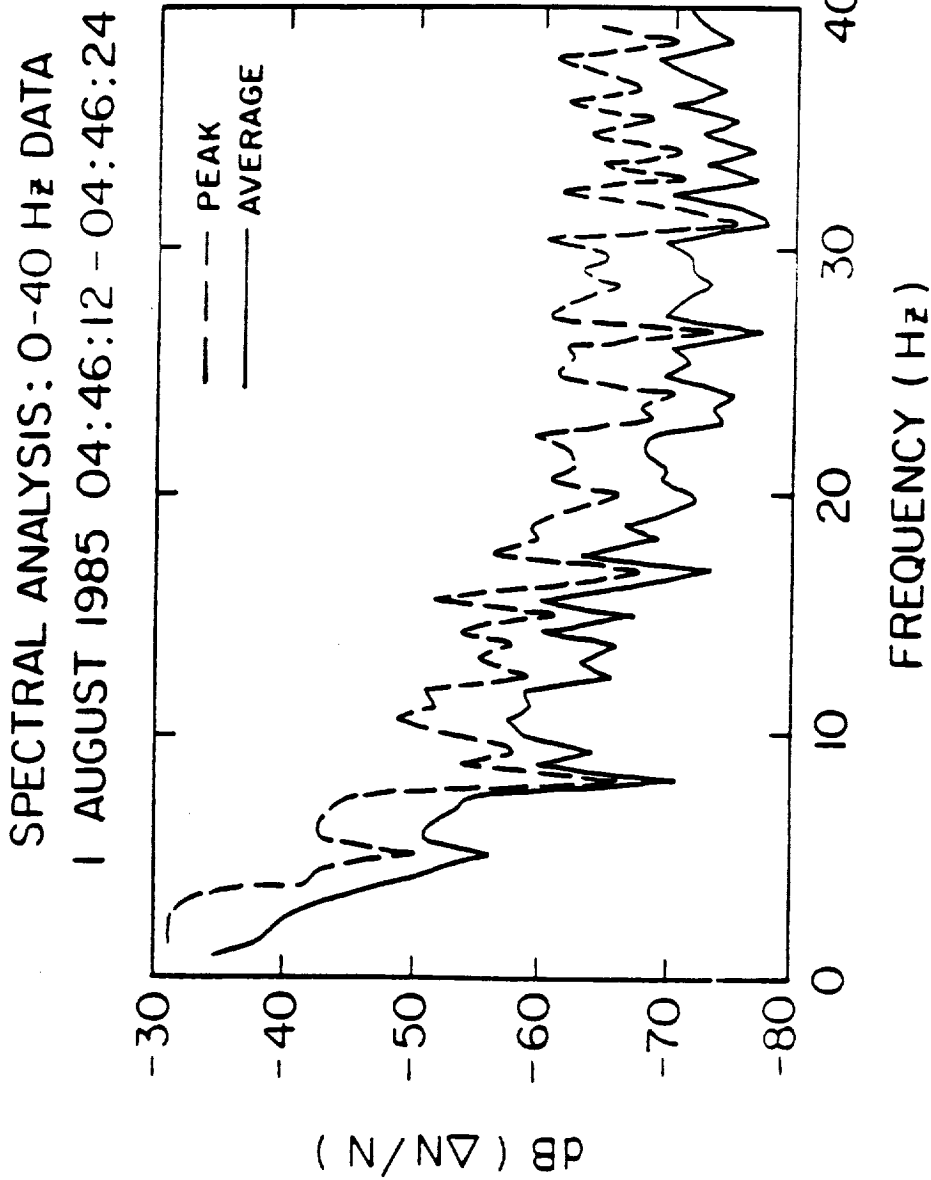


Figure 62. 0-40 Hz FFT data obtained just outside the Mach cone 20 m downstream from the orbiter.

SPECTRAL ANALYSIS: 0-40 Hz DATA
1 AUGUST 1985 04:37:02 - 04:37:14

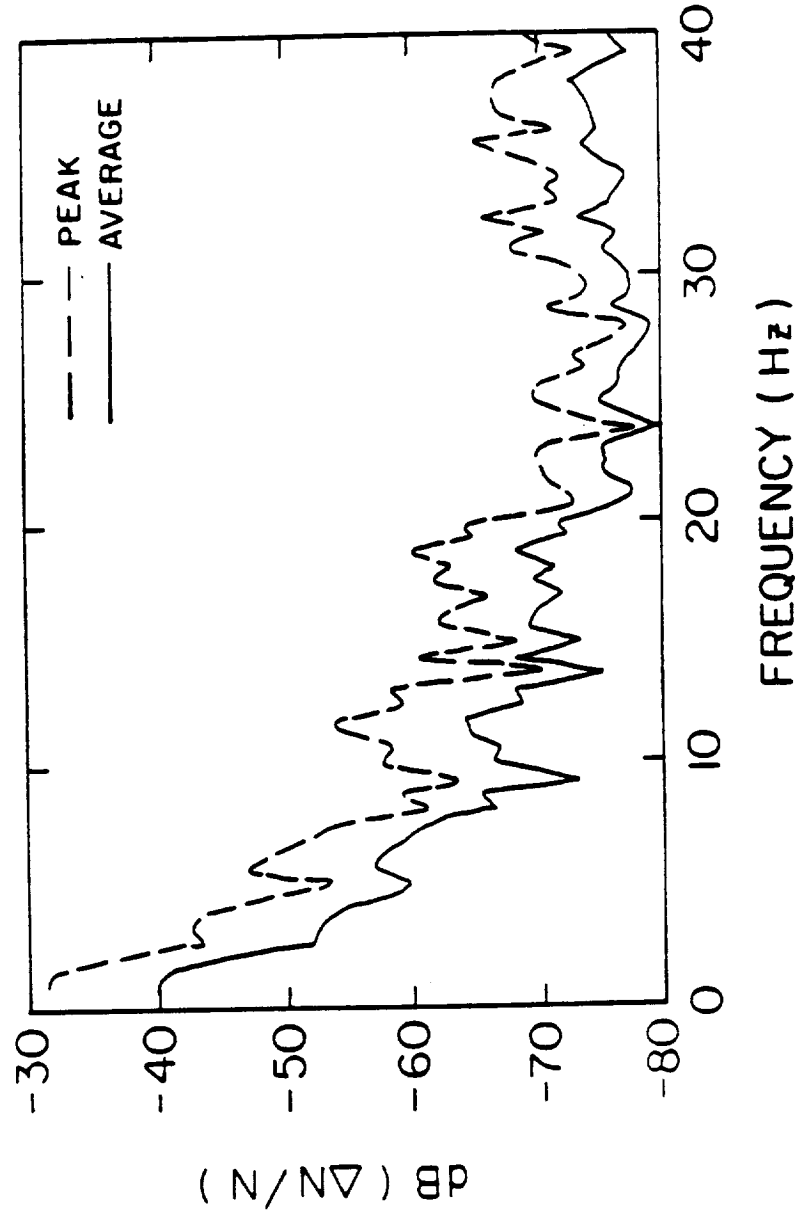


Figure 63. 0-40 Hz FFT data obtained just outside the Mach cone 90 m downstream from the orbiter.

AVAILABLE SPECTRUM ANALYZER DATA

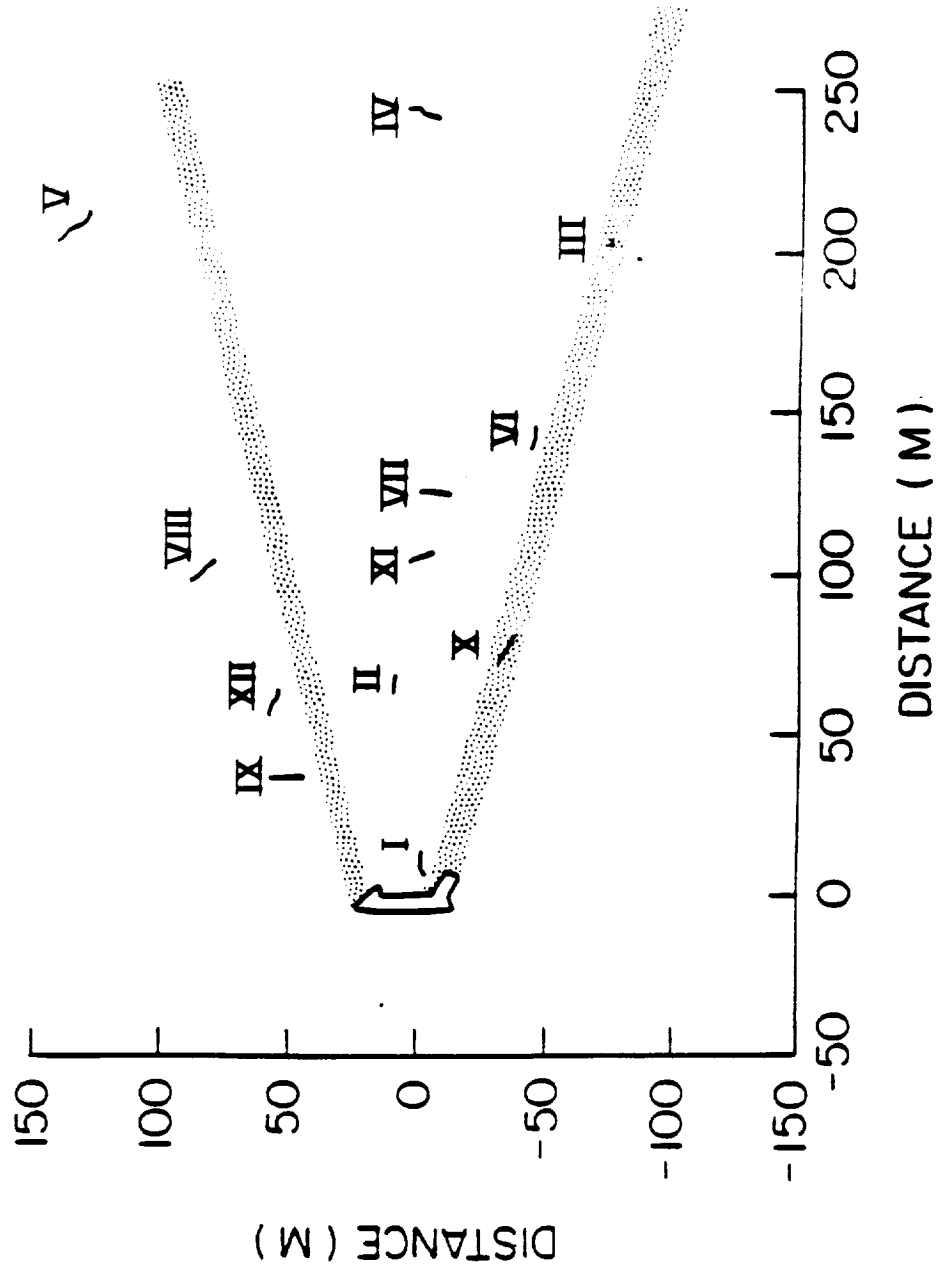


Figure 64. The locations where Langmuir probe spectrum analyzer data is available during wake studies.

A-G88-163

SPECTRUM ANALYZER DATA

1 AUGUST 1985 03:16:14

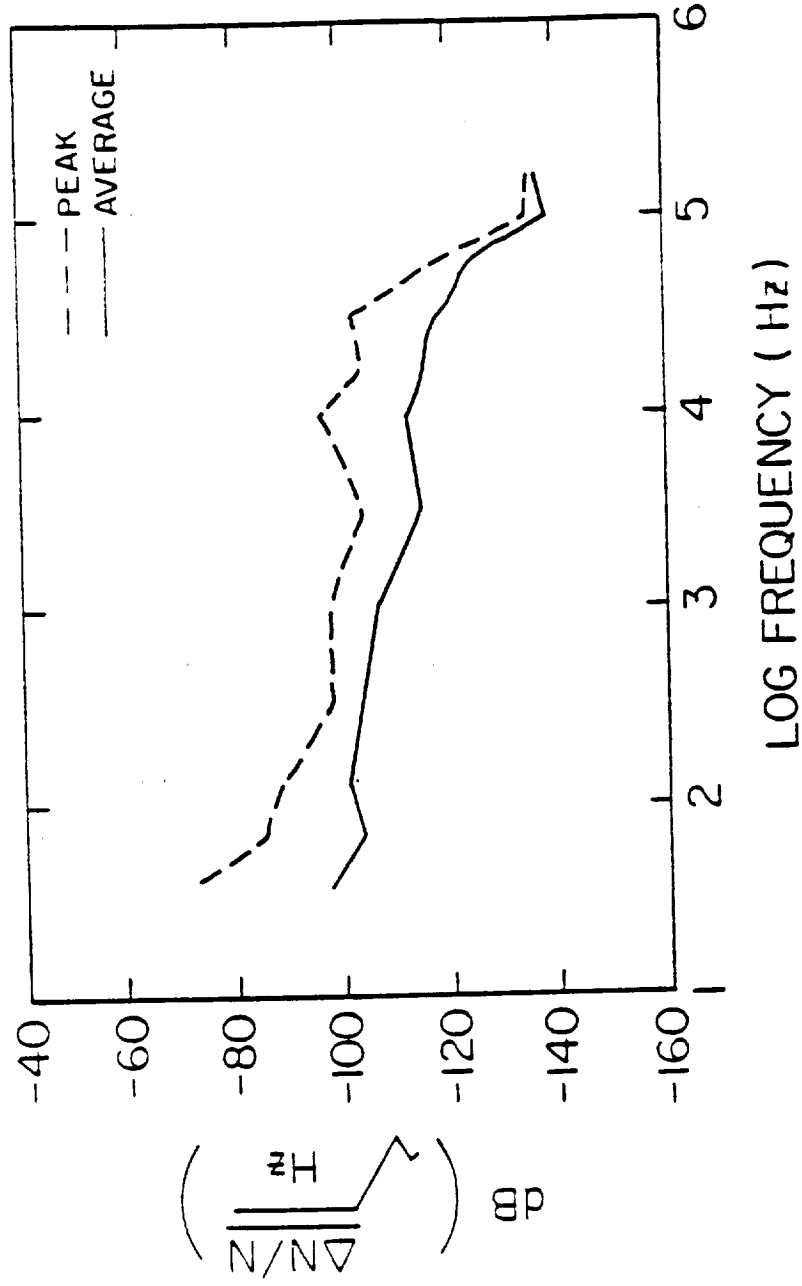


Figure 65. Ambient ionospheric conditions as measured by the spectrum analyzer.

SPECTRUM ANALYZER DATA

1 AUGUST 1985 00:11:56

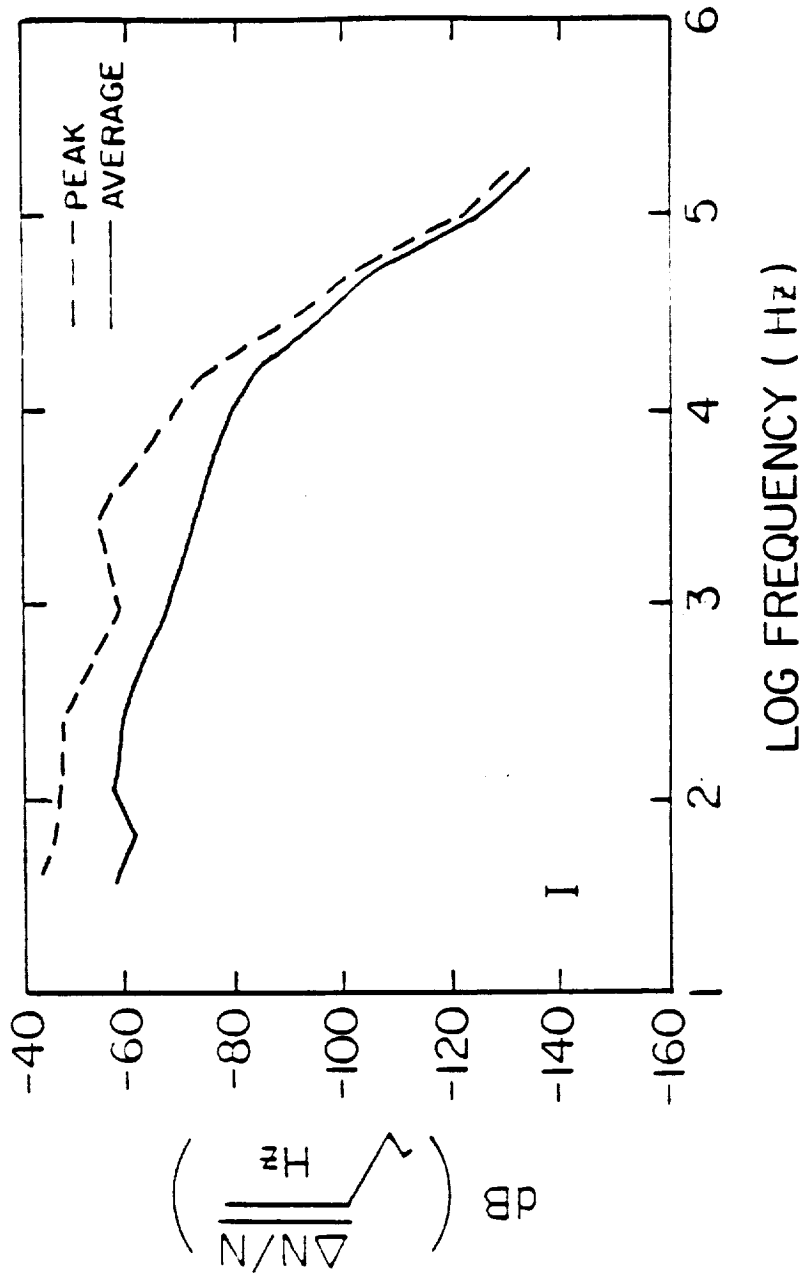


Figure 66. Spectral density of $\Delta N/N$ at location I.

A-G88-152

SPECTRUM ANALYZER DATA

1 AUGUST 1985 00:18:45

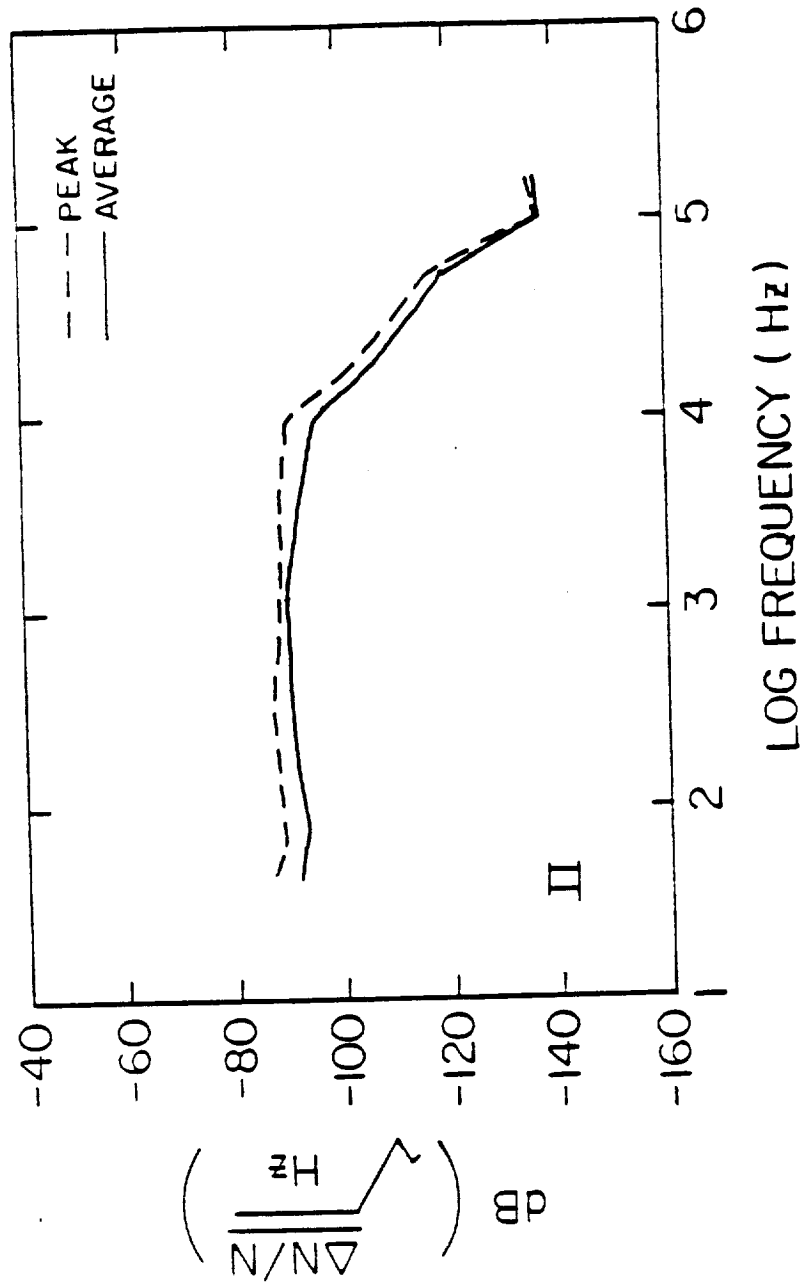


Figure 67. Spectral density of $\Delta N/N$ at location II.

SPECTRUM ANALYZER DATA

1 AUGUST 1985 02:55:51

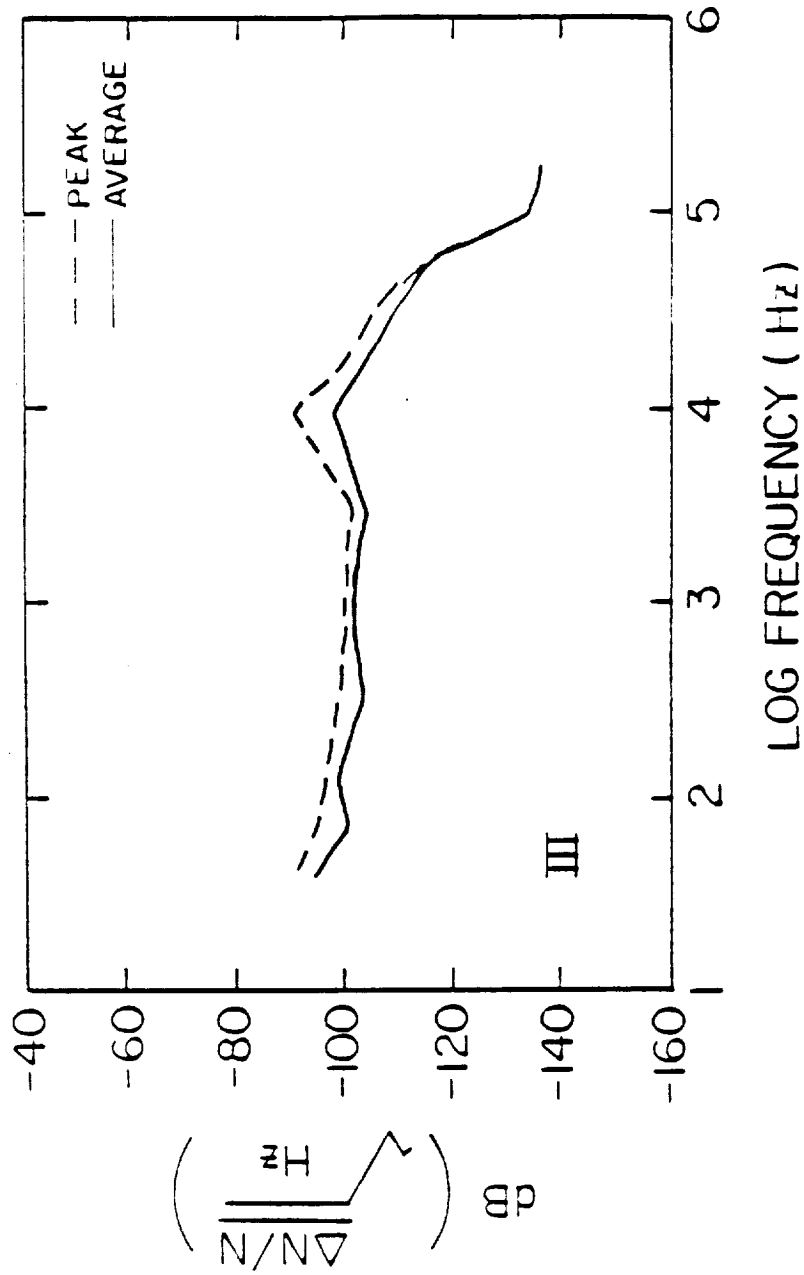


Figure 68. Spectral density of $\Delta N/N$ at location III.

A-G88-154

SPECTRUM ANALYZER DATA

1 AUGUST 1985 03:02:38

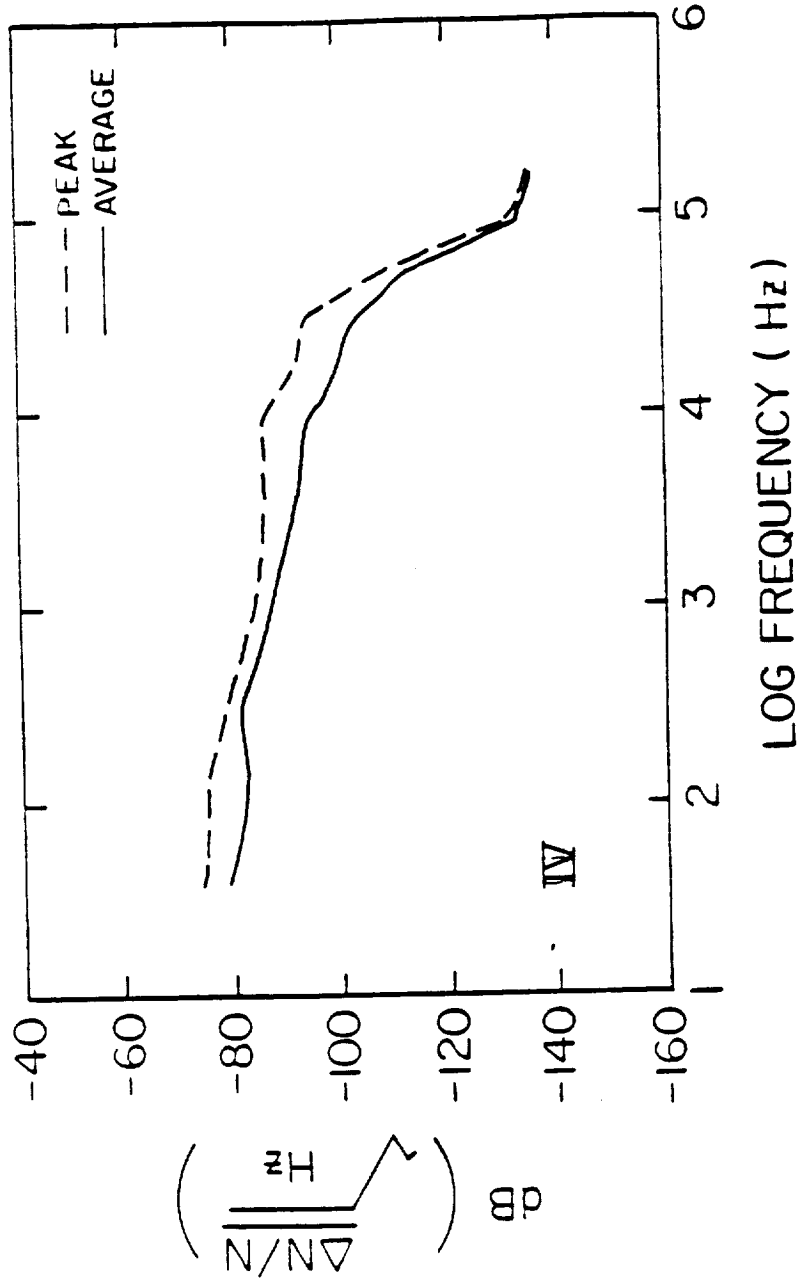


Figure 69. Spectral density of $\Delta N/N$ at location IV.

SPECTRUM ANALYZER DATA

1 AUGUST 1985 03:09:24

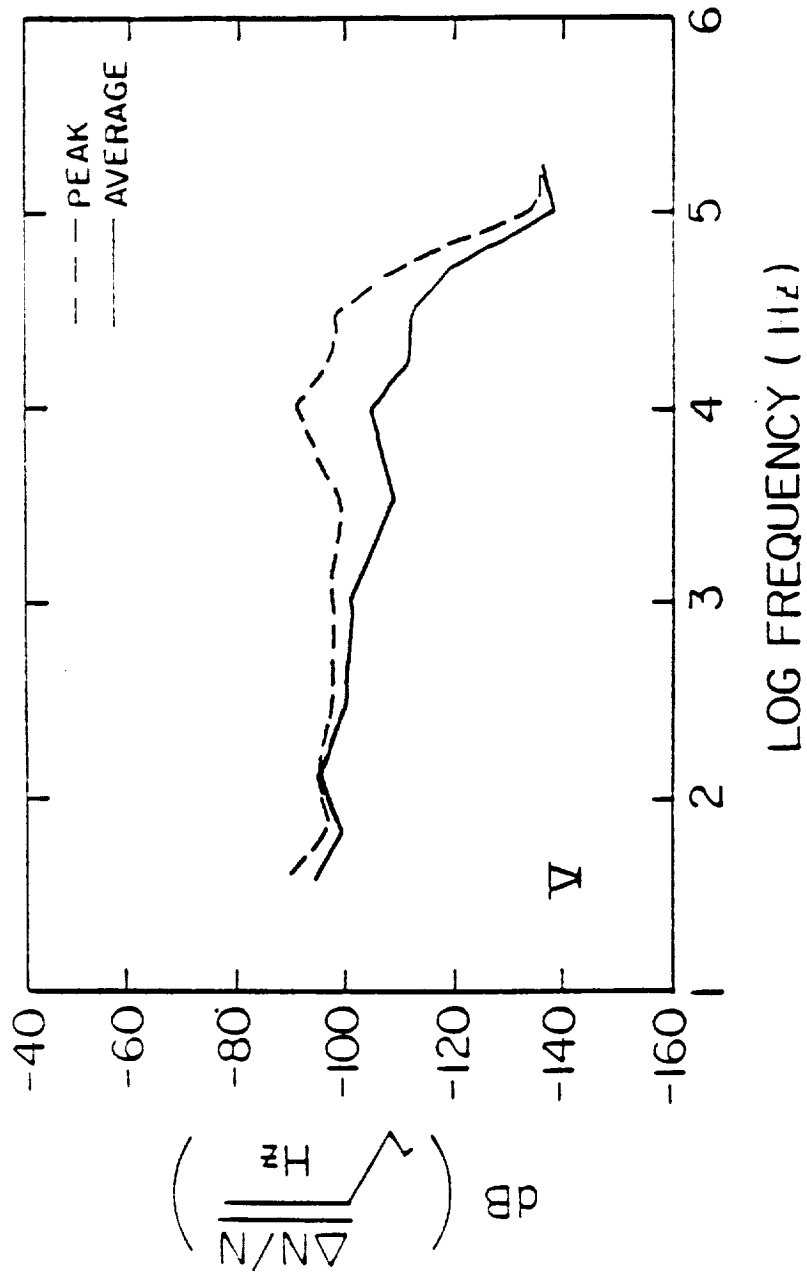


Figure 70. Spectral density of $\Delta N/N$ at location V.

A - G88 - 156

SPECTRUM ANALYZER DATA

1 AUGUST 1985 04:24:34

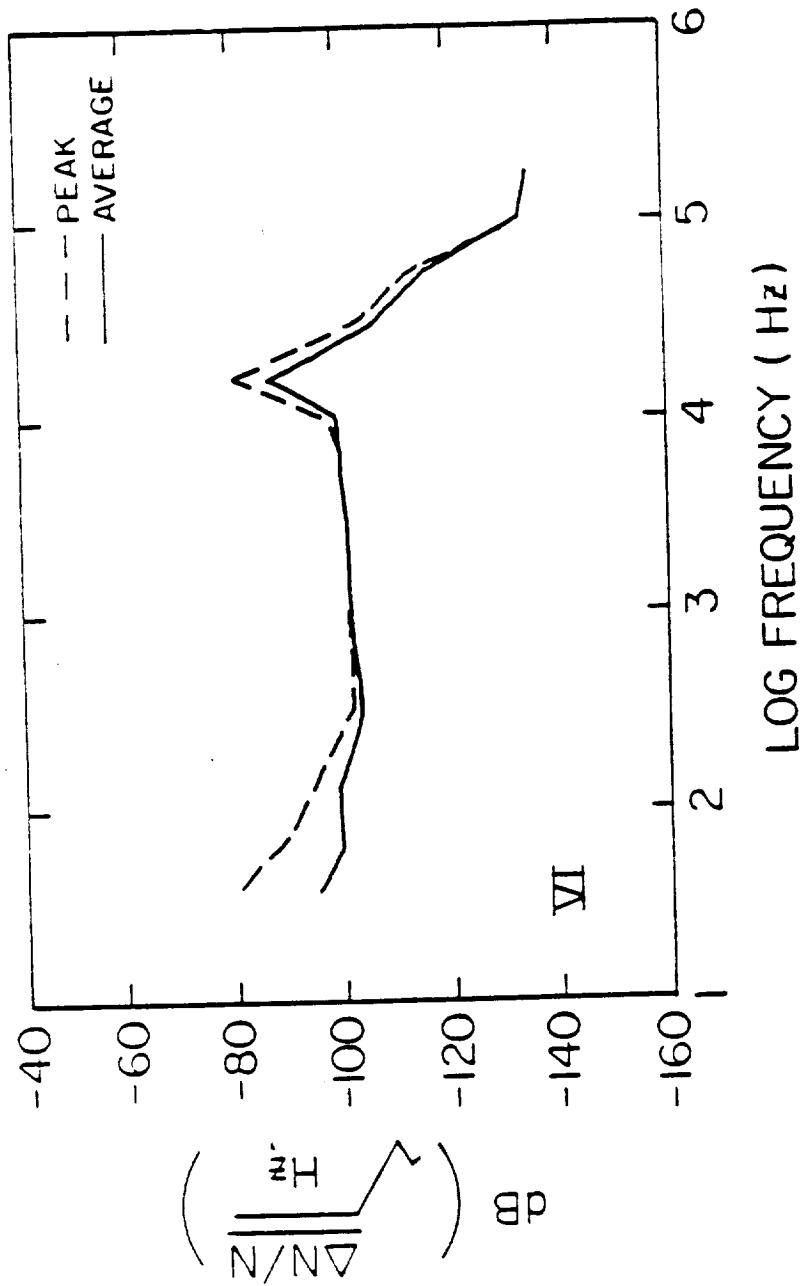


Figure 71. Spectral density of $\Delta N/N$ at location VI.

SPECTRUM ANALYZER DATA

1 AUGUST 1985 04:31:19

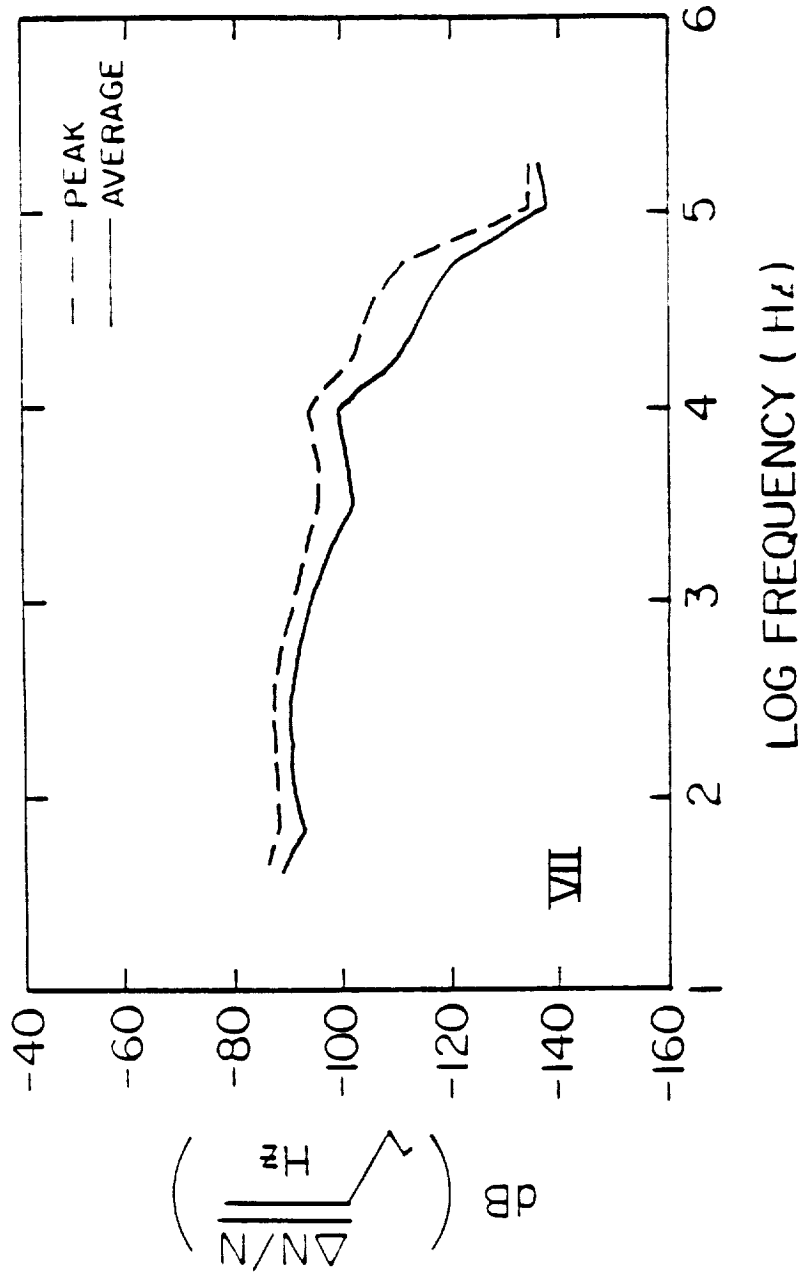


Figure 72. Spectral density of $\Delta N/N$ at location VII.

SPECTRUM ANALYZER DATA
1 AUGUST 1985 04:38:17

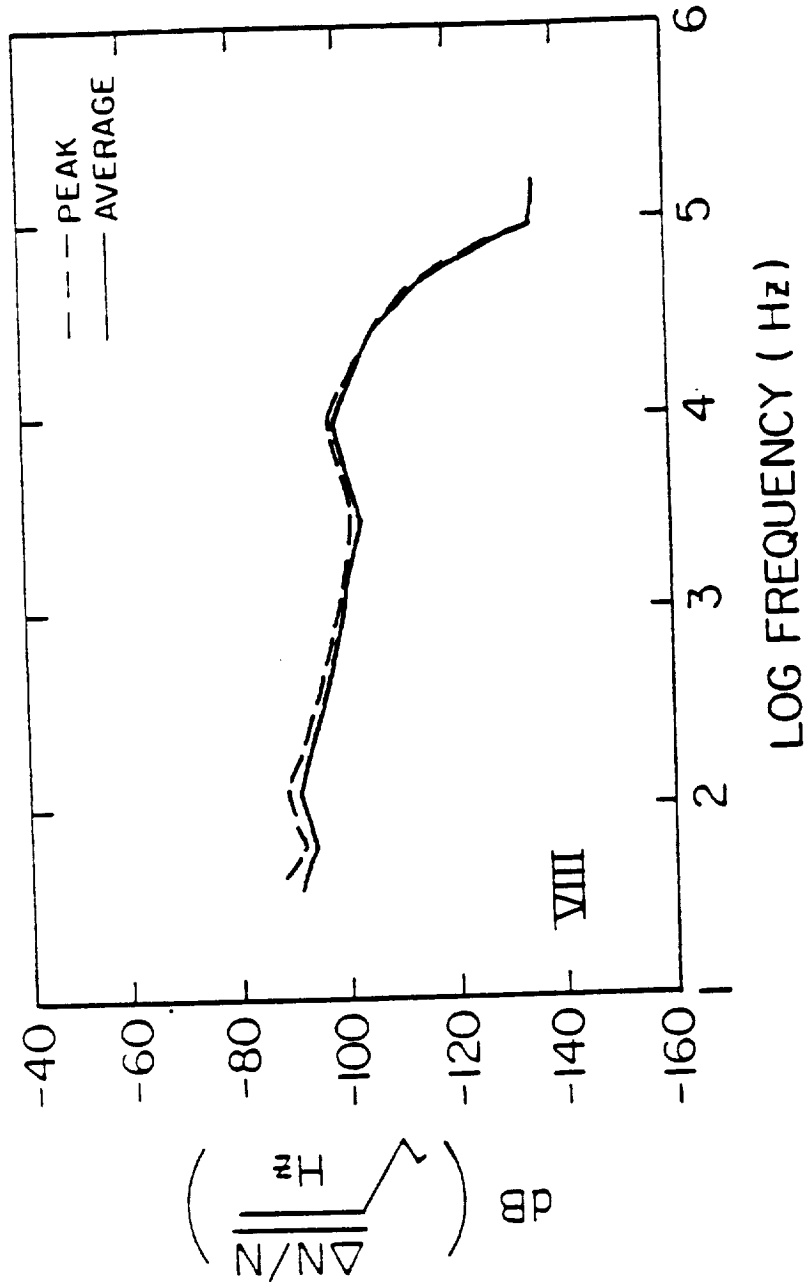


Figure 73. Spectral density of $\Delta N/N$ at location VIII.

SPECTRUM ANALYZER DATA

1 AUGUST 1985 04:45:18

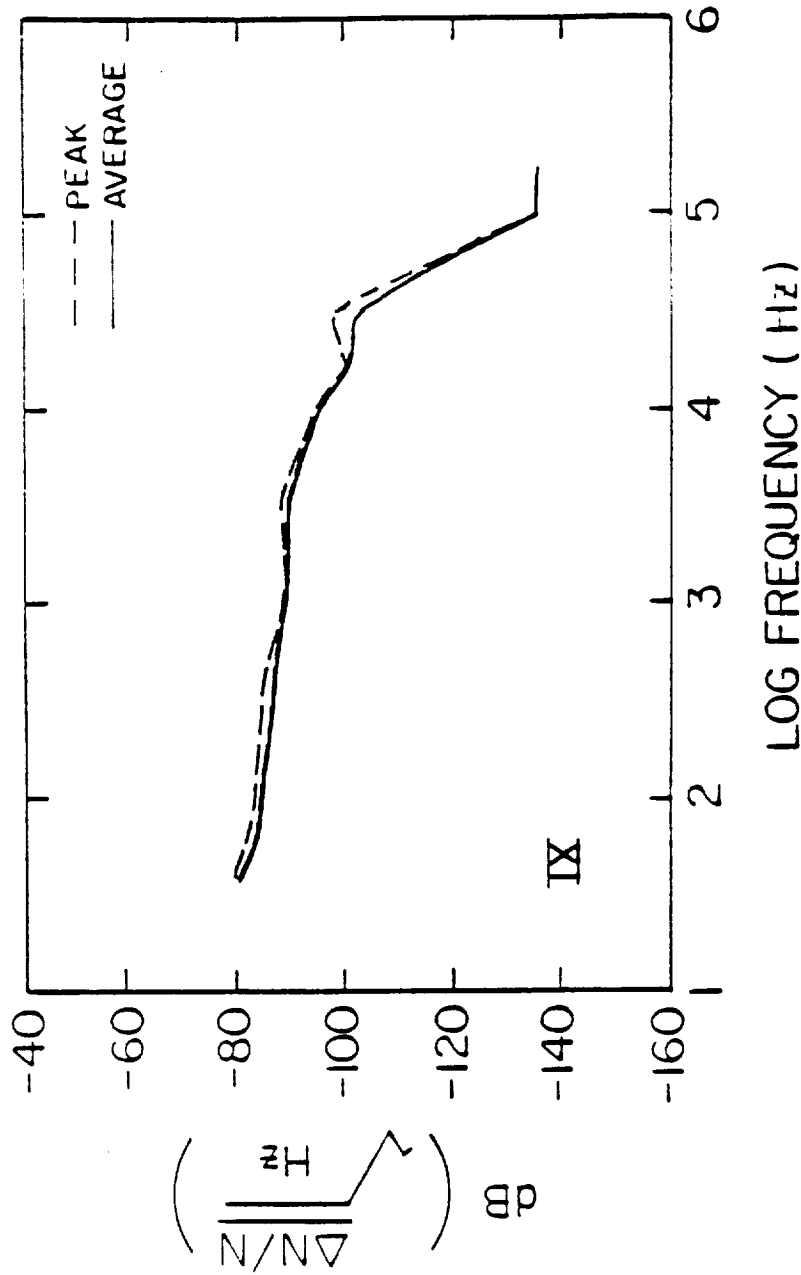


Figure 74. Spectral density of $\Delta N/N$ at location IX.

A-G88-160

SPECTRUM ANALYZER DATA

1 AUGUST 1985 04:51:50

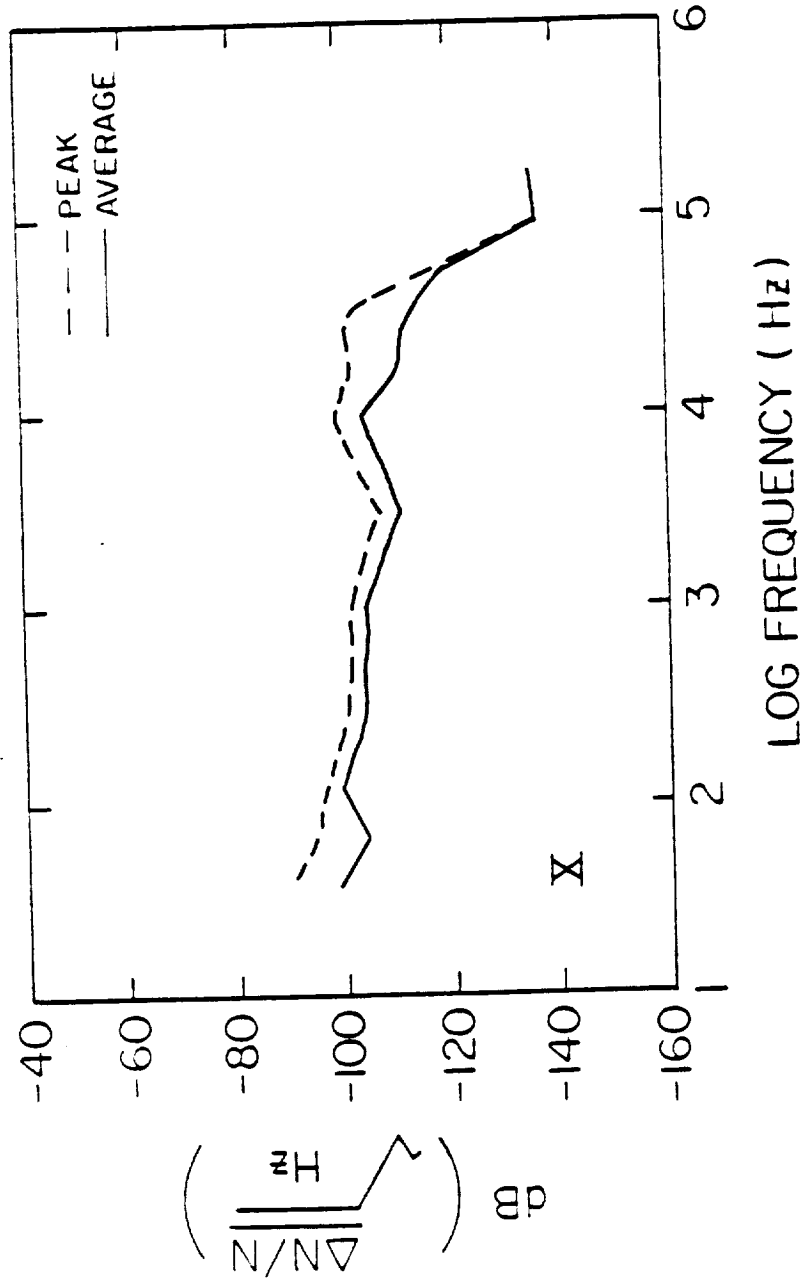


Figure 75. Spectral density of $\Delta N/N$ at location X.

A-G88-161

SPECTRUM ANALYZER DATA

1 AUGUST 1985 04:58:38

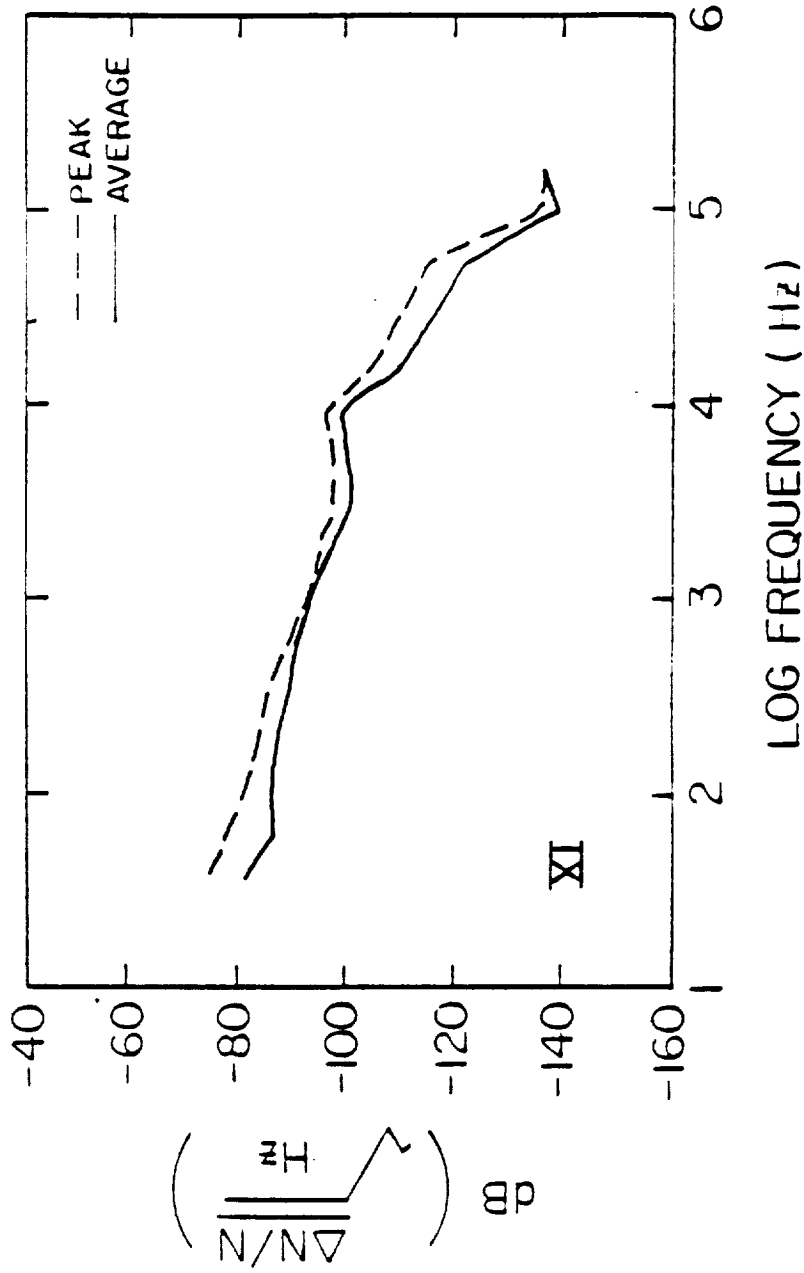


Figure 76. Spectral density of $\Delta N/N$ at location XI.

A-688-162

SPECTRUM ANALYZER DATA

1 AUGUST 1985 05:05:35

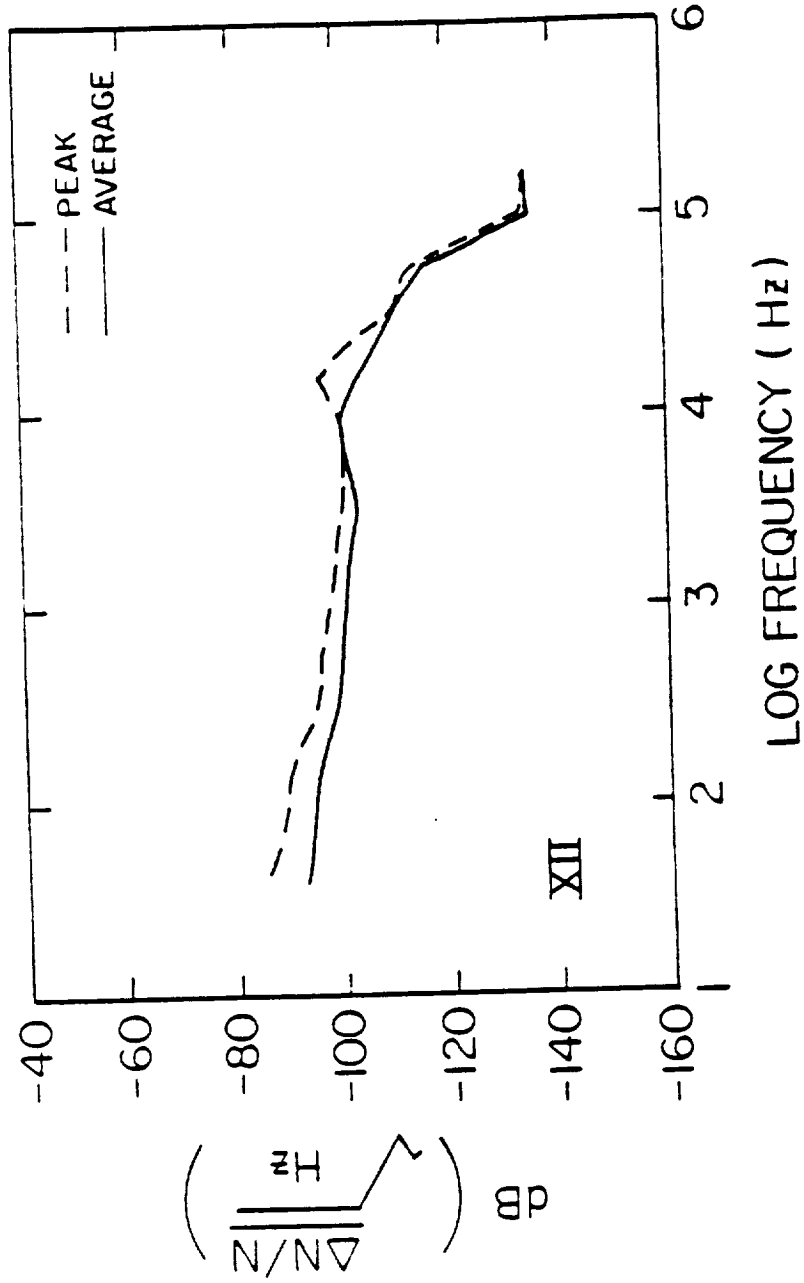


Figure 77. Spectral density of $\Delta N/N$ at location XII.

LANGMUIR PROBE SWEEP DATA

2 AUGUST 1985
06:33:59

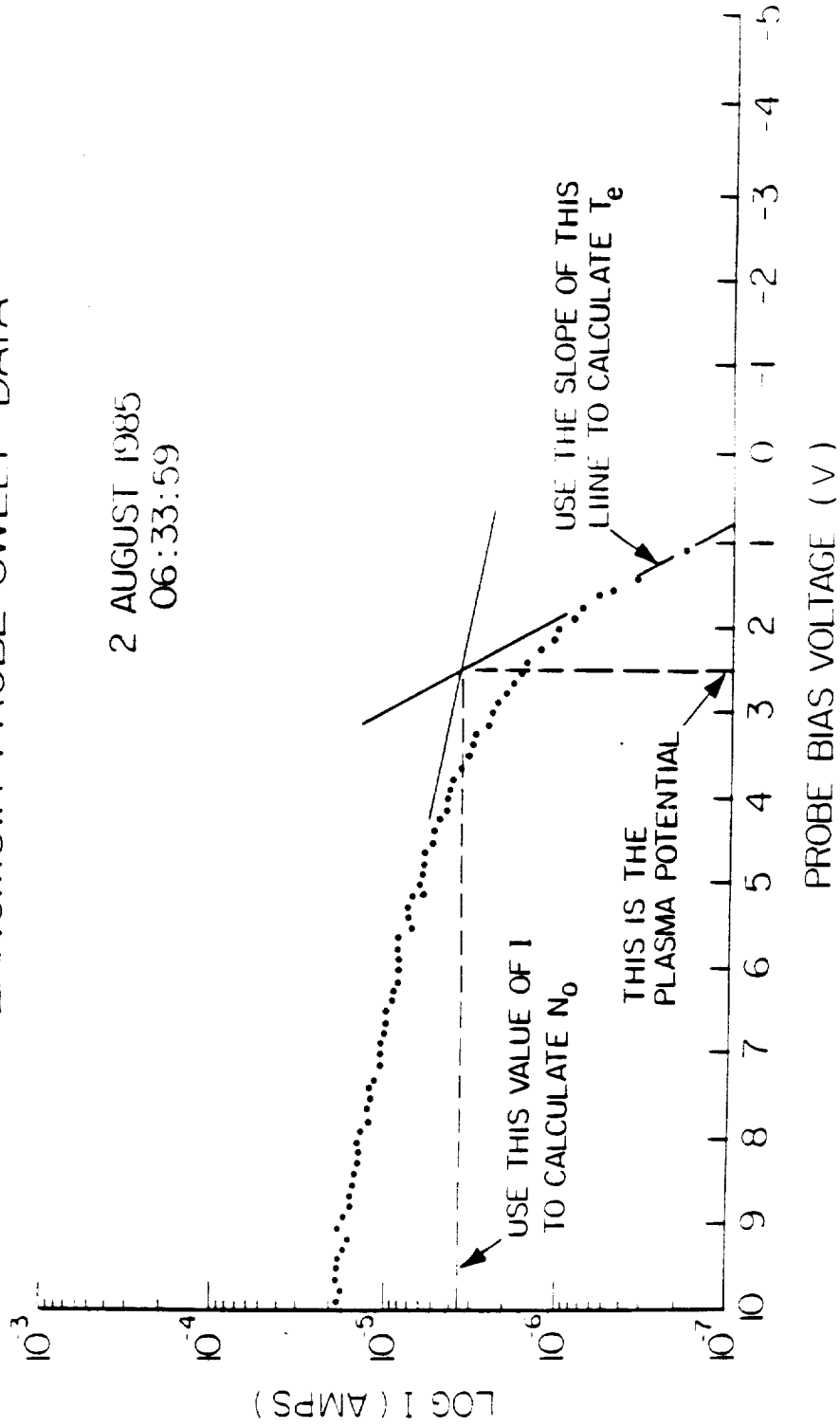


Figure 78. A typical Langmuir probe sweep showing the values of N_0 , I , and 'slope' needed to calculate N_e , T_e , and V_p .

A-G87-876-3

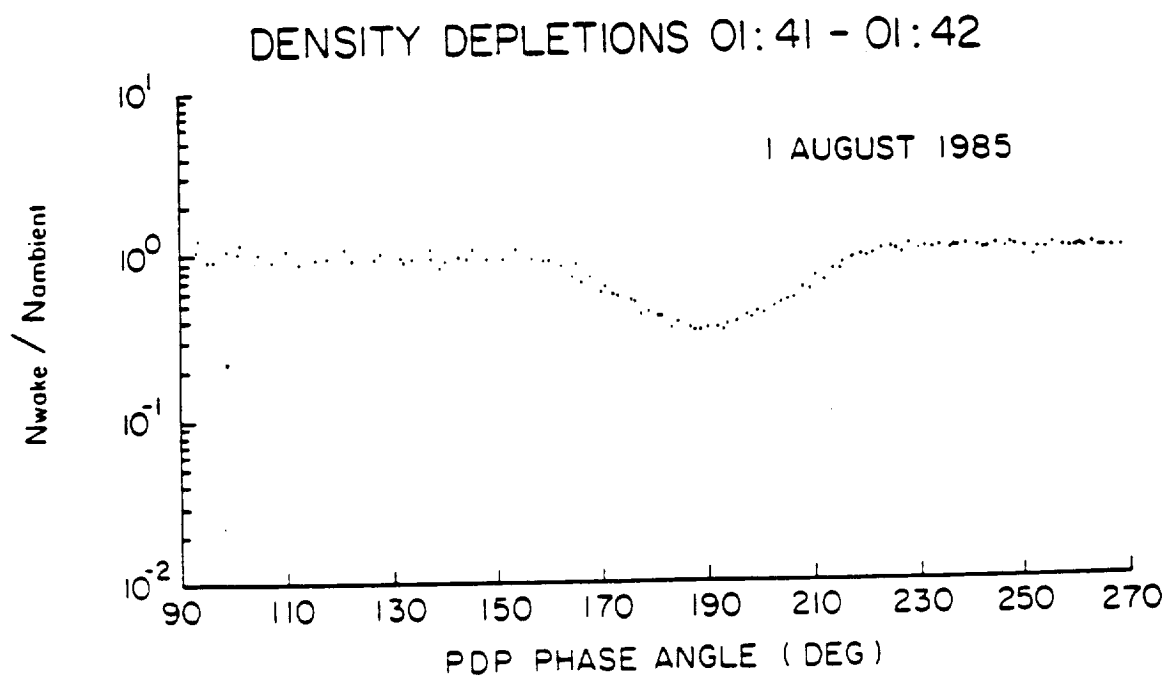
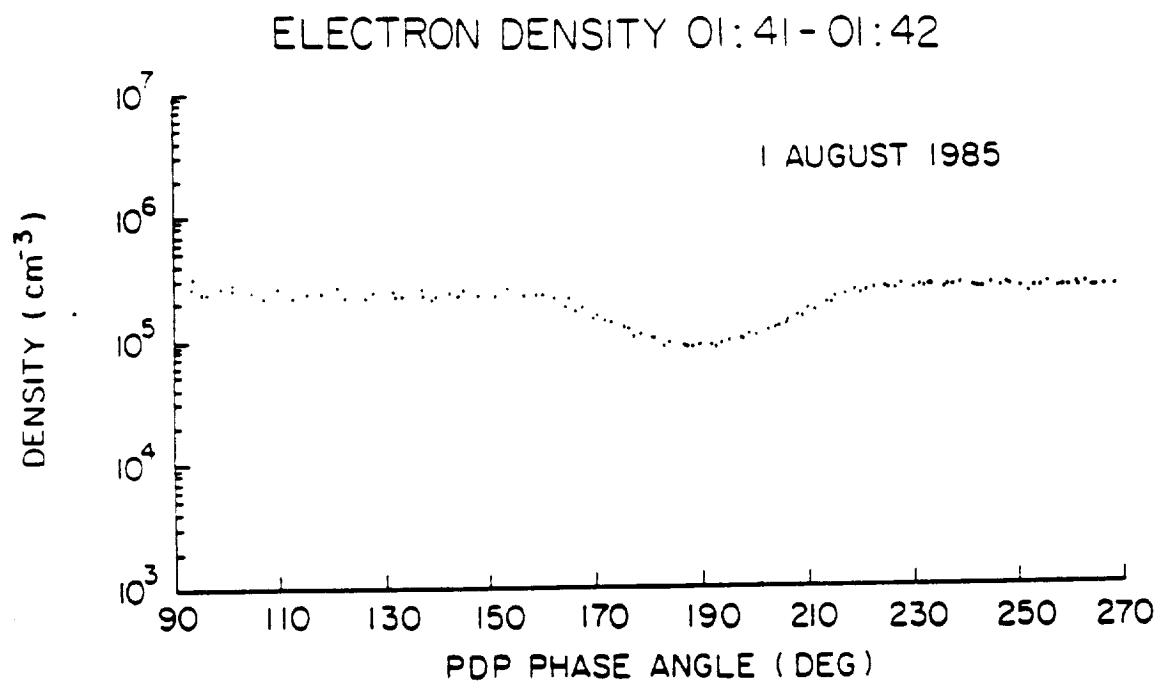


Figure 79. Electron density depletions in the wake of the PDP.

A-G87-877-3

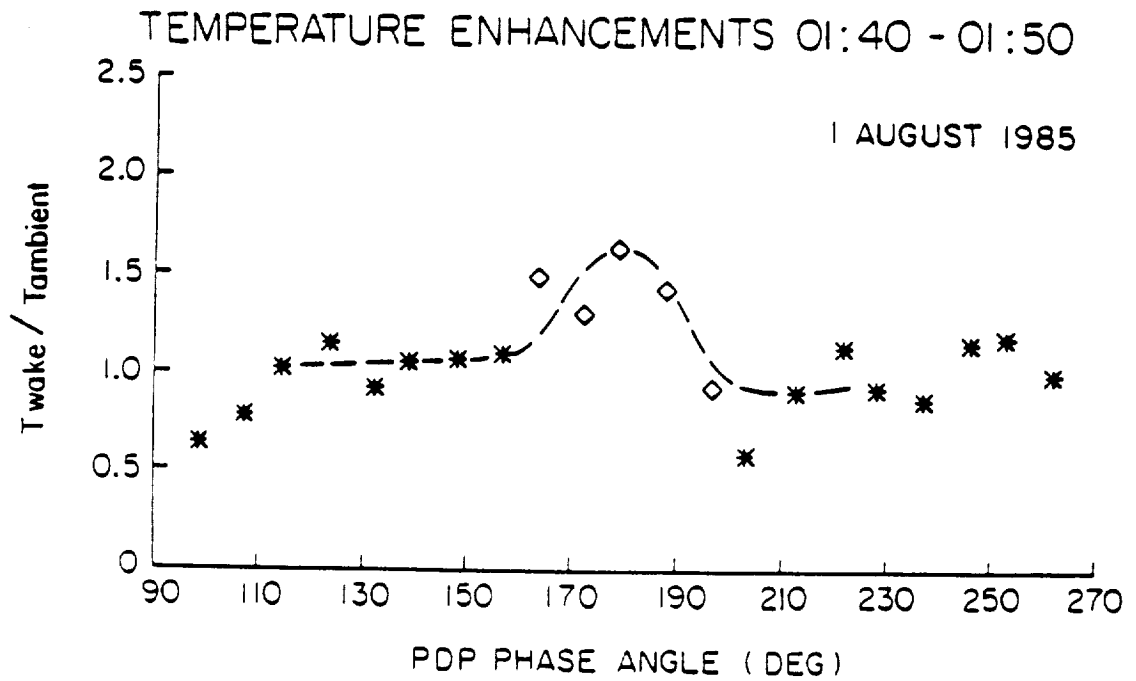
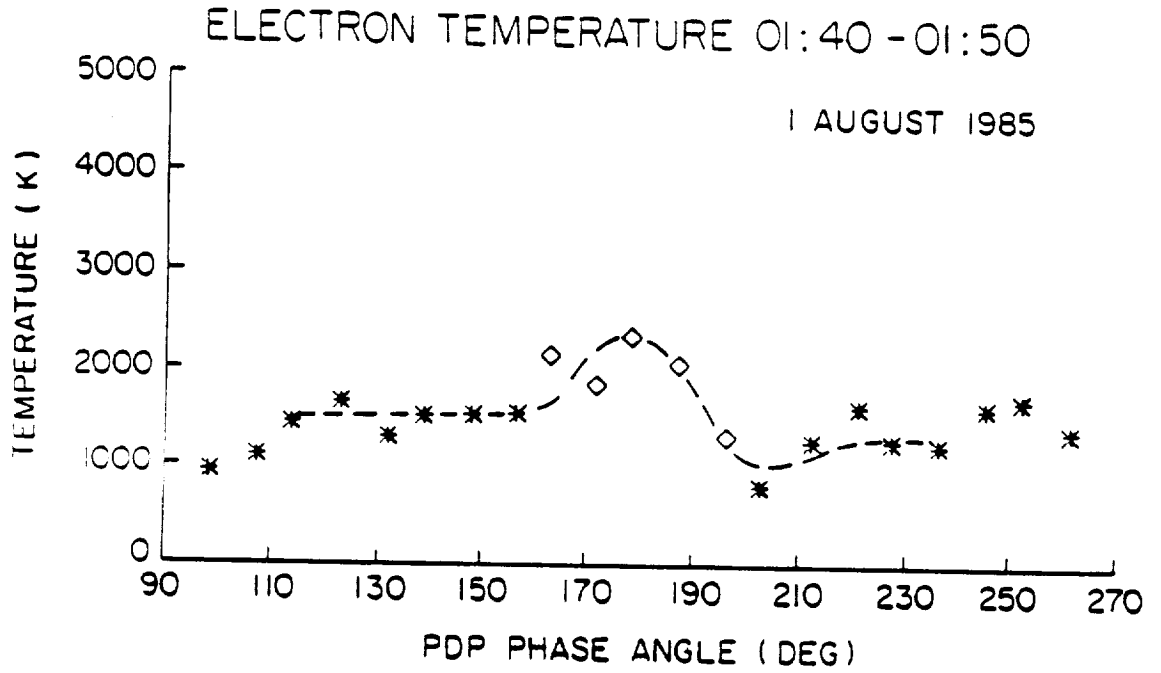


Figure 80. Electron temperature enhancements in the wake of the PDP.

REFERENCES

1. Martin, Anthony R., "Numerical Solutions to the Problem of Charged Particle Flow Around an Ionospheric Spacecraft," *Planet. Space Sci.*, Vol. 22, 121 (1974).
2. Samir, U., and G. L. Wrenn, "The Dependence of Charge and Potential Distribution Around a Spacecraft on Ionic Composition," *Planet. Space Sci.*, Vol. 17, 693 (1969).
3. Samir, U., and A. P. Willmore, "The Distribution of Charged Particles Near a Moving Spacecraft," *Planet. Space Sci.*, Vol. 13, 285 (1965).
4. Henderson, C. L., and U. Samir, "Observations of the Disturbed Region Around an Ionospheric Spacecraft," *Planet. Space Sci.*, Vol. 15, 1499 (1967).
5. Samir, Uri, "Bodies in Flowing Plasmas: Spacecraft Measurements," *Adv. Space Res.*, Vol. 1, 373 (1981).
6. Stone, N. H., and U. Samir, "Bodies in Flowing Plasmas: Laboratory Studies," *Adv. Space Res.*, Vol. 1, 361 (1981).
7. Murphy, G., J. Pickett, N. D'Angelo, and W. S. Kurth, "Measurements of Plasma Parameters in the Vicinity of the Space Shuttle," *Planet. Space Sci.*, Vol. 34, 993, 1986.
8. Raitt, W. J., D. E. Siskind, P. M. Banks, and P. R. Williamson, "Measurements of the Thermal Plasma Environment of the Space Shuttle," *Planet. Space Sci.*, Vol. 32, 457 (1984).
9. Tribble, A. C., N. D'Angelo, G. Murphy, J. Pickett, and J. Steinberg, "Exposed High-Voltage Source Effect on the Potential of an Ionospheric Satellite," *J. Spacecraft Rockets*, [in press].
10. M. A. Kasha, The Ionosphere and Its Interaction With Satellites, Gordon and Breach, Science Publishers, New York, 1965.
11. Samir, U., E. J. Maier, and B. E. Troy, Jr., "The Angular Distribution of Ion Flux Around an Ionospheric Satellite," *J. Atmos. Terres. Phys.*, Vol. 35, 513 (1973).

12. Samir, U., and G. L. Wrenn, "Experimental Evidence of an Electron Temperature Enhancement in the Wake of an Ionospheric Satellite." *Planet. Space Sci.*, Vol. 20, 899 (1972).
13. Illiano, J. M., and L. R. O. Storey, "Apparent Enhancement of Electron Temperature in the Wake of a Spherical Probe in a Flowing Plasma," *Planet. Space Sci.*, Vol. 22, 873 (1974).
14. Troy, B. E., Jr., E. J. Maier, and U. Samir, "Electron Temperatures in the Wake of an Ionospheric Satellite," *J. Geophys. Res.*, Vol. 80, 993 (1975).
15. Samir, U., L. H. Brace, and H. C. Brinton, "About the Influence of Electron Temperature and Relative Ionic Composition on Ion Depletion in the Wake of the AE-C Satellite," *Geophys. Res. Lett.*, Vol. 6, 101 (1979).
16. Morgan, M. A., C. Chan, and R. C. Allen, "A Laboratory Study of the Electron Temperature in the Near Wake of a Conducting Body," *Geophys. Res. Lett.*, Vol. 14, 1170 (1987).
17. Fournier, G., and D. Pigache, "Wakes in Collisionless Plasma," *Phys. Fluids*, Vol. 18, 1443 (1975).
18. J. C. Taylor, "Disturbance of a Rarefied Plasma by a Supersonic Body on the Basis of the Poisson-Vlasov Equations-I, The Heuristic Method," *Planet. Space Sci.*, Vol. 15 155 (1967).
19. J. C. Taylor, "Disturbance of a Rarefied Plasma by a Supersonic Body on the Basis of the Poisson-Vlasov Equations-II, Formal Method," *Planet. Space Sci.*, Vol. 15 463 (1967).
20. Skvortsov, V. V., and L. V. Nosachev, "The Structure of the Trail Behind a Spherical Model in a Stream of Rarefied Plasma," *Cosmic Res.*, Vol. 6, 191 (1968).
21. Skvortsov, V. V., and L. V. Nosachev, "Some Results on Disturbances Introduced by Extraneous Bodies into a Stream of Rarefied Plasma," *Cosmic Res.*, Vol. 6, 718 (1968).
22. J. P. M. Schmitt, "Wake Past an Obstacle in a Magnetized Plasma Flow," *J. Plasma Physics*, Vol. 15, 677 (1973).
23. Bogashchenko, I. A., A. V. Gurevich, R. A. Salimov, and Yu. I. Éydel'man, "Flow of Rarefied Plasma Around a Body," *Soviet Physics JETP*, Vol. 32, 841 (1971).
24. Stone, N. H., W. A. Oran, and U. Samir, "Collisionless Plasma Flow Over A Conducting Sphere," *Planet. Space Sci.*, Vol. 20, 1787 (1972).

25. Merlino, R. L., and N. D'Angelo, "The Interaction of a Conducting Object With a Supersonic Plasma Flow: Ion Deflection Near a Negatively Charged Obstacle," *J. Plasma Physics*, Vol. 37, 185 (1987).
26. Gurevich, A. V., L. V. Pariiskaya, and L. P. Pitaevskii, "Ion Acceleration Upon Expansion of a Rarefied Plasma," *Soviet Physics JETP*, Vol. 36, 274 (1973).
27. Singh, N., U. Samir, K. H. Wright, Jr., and N. H. Stone, "A Possible Explanation of the Electron Temperature Enhancement in the Wake of a Satellite," *J. Geophys. Res.*, Vol. 92, 6100 (1987).
28. Samir, U., K. H. Wright, Jr., and N. H. Stone, "The Expansion of a Plasma Into a Vacuum: Basic Phenomena and Processes and Applications to Space Plasma Physics," *Rev. Geophys. Space Phys.*, Vol. 21, 1631 (1983).
29. Oran, W. A., N. H. Stone, and U. Samir, "The Effects of Body Geometry on the Structure in the Near Wake Zone of Bodies in a Flowing Plasma," *J. Geophys. Res.*, Vol. 80, 207 (1975).
30. B. Könemann, "The Collisionless Flow of Unmagnetized Plasmas Around Bodies," *J. Plasma Physics*, Vol. 20, 17 (1978).
31. Bingham, G., et al., *Modern Techniques of Power Spectrum Estimation*, *IEEE Trans.*, AU-15 2, 56, 1967.
32. Murphy, G. B., D. L. Reasoner, A. Tribble, N. D'Angelo, J. S. Pickett, W. S. Kurth, "The Plasma Wake of the Shuttle Orbiter," *J. Geophys. Res.*, submitted December 1987.
33. Huddleston, R. H., and S. L. Leonard (Eds.), Plasma Diagnostic Techniques, Academic Press, New York, 1965.
34. Parrot, M. J. M., L. R. O. Storey, L. W. Parker, and J. G. Laframboise, "Theory of Cylindrical and Spherical Langmuir Probes in the Limit of Vanishing Debye Number," *Phys. Fluids*, Vol. 25, 2388 (1982).
35. Rubinstein, J., and J. G. Laframboise, "Theory of a Spherical Probe in a Collisionless Magnetoplasma," *Phys. Fluids*, Vol. 25, 1174 (1982).
36. Szuszczewicz, E. P., and P. Z. Takacs, "Magnetosheath Effects on Cylindrical Langmuir Probes," *Phys. Fluids*, Vol. 22, 2424 (1979).
37. Makita, H., and K. Kuriki, "Current Collection by Spherical Langmuir Probes Drifting in a Collisionless Plasma," *Phys. Fluids*, Vol. 21, 1279 (1978).



QUASI-STATIC ELECTRIC FIELD MEASUREMENTS
MADE WITH THE PLASMA DIAGNOSTICS PACKAGE
IN FREE FLIGHT DURING SPACELAB-2

by

John Tyree Steinberg

An Abstract

Of a thesis submitted in partial fulfillment
of the requirements for the Doctor of
Philosophy degree in Physics
in the Graduate College of
The University of Iowa

May 1988

Thesis supervisor: Professor Donald A. Gurnett

ABSTRACT

As part of the Spacelab-2 mission the Plasma Diagnostics Package (PDP) was released from the shuttle as a free flying satellite. The shuttle performed maneuvers around the PDP in order that the ionospheric plasma around the shuttle might be studied. One objective of the PDP was to measure quasi-static electric fields in the vicinity of the shuttle. During most of the free flight, the measured electric field was comparable to the induced electric field due to the orbital motion of the spacecraft. The difference between the measured field and the motional field was typically on the order of the uncertainty of measurement. At certain times, when the shuttle thrusters were operating, decreases in the motional electric field by 10% to 20% were observed. The decreases are explained by the generation of an Alfvén wave from pickup current. An estimate of the electric field associated with Alfvén wave excitation agrees with the decreases observed at times of thruster firings. The Alfvén wave model predicts that large changes in the electric field should occur only at times of large neutral gas releases from the shuttle. The decreases in the electric field occur in the region of the thruster plume, as well as along the magnetic flux tubes passing through the plume.

During times when an electron beam was ejected from the shuttle, large signals were also recorded. These large signals were probably

not due to ambient electric fields, but can be attributed to three causes: differences in fluxes of streaming electrons to the two probes due to shadowing by the PDP chassis, depressions in the plasma density caused by the PDP wake, and spatial gradients in the fluxes of energetic electrons reaching the probes. Energetic electrons were found in a region 20 m wide and up to at least 170 m downstream from the electron beam. At 80 or more meters downstream from the beam, the energetic electrons had a preferential direction of motion opposite to the beam injection direction.

Abstract approved: Donald A. Hunt
Thesis supervisor

Professor, Physics and Astronomy
Title and department

May 4, 1988
Date

QUASI-STATIC ELECTRIC FIELD MEASUREMENTS
MADE WITH THE PLASMA DIAGNOSTICS PACKAGE
IN FREE FLIGHT DURING SPACELAB-2

by

John Tyree Steinberg

A thesis submitted in partial fulfillment
of the requirements for the Doctor of
Philosophy degree in Physics
in the Graduate College of
The University of Iowa

May 1988

Thesis supervisor: Professor Donald A. Gurnett

Graduate College
The University of Iowa
Iowa City, Iowa

CERTIFICATE OF APPROVAL

PH.D. THESIS

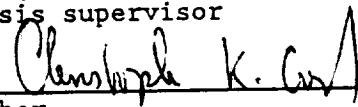
This is to certify that the Ph.D. thesis of

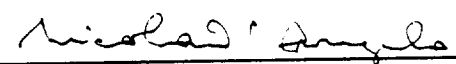
John Tyree Steinberg

has been approved by the Examining Committee
for the thesis requirement for the Doctor of
Philosophy degree in Physics at the May 1988
graduation.

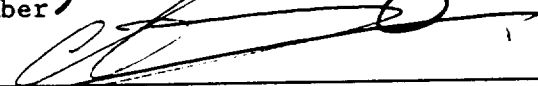
Thesis committee:


Thesis supervisor


Member


Member


Member


Member

ACKNOWLEDGEMENTS

I thank my graduate advisor, Dr. Donald A. Gurnett, for the support and guidance he has given me on this work. I also thank the following professors for their assistance: Dr. Nicola D'Angelo, Dr. Christoph K. Goertz, and Dr. Karl Lonngren. The following people, who have helped me on this work numerous times, have my gratitude: Terrance Averkamp, Scott Boardsen, William Farrell, Larry Granroth, Robert Lane, Gerald Murphy, William Paterson, Jolene Pickett, and Alan Tribble. Thanks also to John Birkbeck for his fine drafting. I am especially grateful to Kathy Kurth, and her able assistant, Tami Thompson, for taking the stacks of scrawled writings and the floppy disks I gave them, waving their magic wands over them, and transforming them into this thesis manuscript.

I thank my wife, Kati, for her constant faith in me. This thesis is dedicated to my father, the late Alvin Steinberg.

The research was supported by NASA through contract NAS8-32807 with Marshall Space Flight Center, contract NAG3-449 with NASA Lewis Research Center, and grant NGL 16-001-043 with NASA Headquarters.

ABSTRACT

As part of the Spacelab-2 mission the Plasma Diagnostics Package (PDP) was released from the shuttle as a free flying satellite. The shuttle performed maneuvers around the PDP in order that the ionospheric plasma around the shuttle might be studied. One objective of the PDP was to measure quasi-static electric fields in the vicinity of the shuttle. During most of the free flight, the measured electric field was comparable to the induced electric field due to the orbital motion of the spacecraft. The difference between the measured field and the motional field was typically on the order of the uncertainty of measurement. At certain times, when the shuttle thrusters were operating, decreases in the motional electric field by 10% to 20% were observed. The decreases are explained by the generation of an Alfvén wave from pickup current. An estimate of the electric field associated with Alfvén wave excitation agrees with the decreases observed at times of thruster firings. The Alfvén wave model predicts that large changes in the electric field should occur only at times of large neutral gas releases from the shuttle. The decreases in the electric field occur in the region of the thruster plume, as well as along the magnetic flux tubes passing through the plume.

During times when an electron beam was ejected from the shuttle, large signals were also recorded. These large signals were probably

not due to ambient electric fields, but can be attributed to three causes: differences in fluxes of streaming electrons to the two probes due to shadowing by the PDP chassis, depressions in the plasma density caused by the PDP wake, and spatial gradients in the fluxes of energetic electrons reaching the probes. Energetic electrons were found in a region 20 m wide and up to at least 170 m downstream from the electron beam. At 80 or more meters downstream from the beam, the energetic electrons had a preferential direction of motion opposite to the beam injection direction.

TABLE OF CONTENTS

	Page
LIST OF TABLES	vi
LIST OF FIGURES	vii
CHAPTER	
I. INTRODUCTION	1
II. INSTRUMENTATION	7
III. DATA ANALYSIS	9
IV. GENERAL RESULTS	13
V. THRUSTER RELATED EFFECTS	18
A. Observations	18
B. Discussion	19
VI. ELECTRON BEAM RELATED EFFECTS	42
A. Observations	42
B. Discussion	46
VII. CONCLUSION	61
REFERENCES	131

LIST OF TABLES

Table	Page
1.	Instrument parameters and dynamic ranges. 64
2.	Correlation coefficient between $E_{V \times B} / \vec{V} \times \vec{B} $ and the emission rate of thrusters, and the probability of obtaining a correlation coefficient greater than or equal to the value calculated if the measurements are randomly distributed. 65
3.	Parallel conductivity σ_{\parallel} , Pedersen conductivity σ_p , and Hall conductivity σ_h for different neutral densities n_n , assuming an ambient plasma density $n_e = 10^5 \text{ cm}^{-3}$ and magnetic field $B = 0.25$ gauss. 66
4.	Electric field screening determined from Alfvén wave model. 67
5.	Electric field screening determined from Alfvén wave model. 68
6.	Beam Parameters, Sunlight Conditions, PDP Orientation 69
7.	Parameters Used In Evaluation of Equation 25 70

LIST OF FIGURES

Figure		Page
1.	Measurements made with the PDP during the STS-3 mission. The plot labeled -SC POT is the average potential of the electric probes of the PDP relative to the shuttle potential. The potential changes at times of thruster operations [Shawhan et al., 1984]	71
2.	The Plasma Diagnostics Package. Dimensions are given in meters.	73
3.	Average potential measurements showing a variation at the spacecraft spin period. Arrows indicate the times when the aperture of the Lepedea faced directly into the ram direction.	75
4.	A segment of the electric field signal showing the contamination of the signal by a common mode signal related to the operation of the Lepedea, and the passage of the probes through the spacecraft wake.	77
5.	The portion of the electric field signal remaining after segments of the signal known to be contaminated are removed.	79

6.	Dots indicate measurements of the magnitude of the electric field in the spacecraft spin plane. The solid line indicates the projection of $\vec{V} \times \vec{B}$ in the spin plane.	81
7.	The RMS error of the sampled electric field values with respect to the least square's fit to a sinusoidal function.	83
8.	The component of the electric field along the direction of the velocity vector projected into a plane perpendicular to the magnetic field.	85
9.	Dots indicate measurements of the component of the electric field along the direction of $\vec{V} \times \vec{B}$. The solid line indicates $\vec{V} \times \vec{B}$	87
10.	The ratio of the component of the electric field along the direction of $\vec{V} \times \vec{B}$ to the magnitude of $\vec{V} \times \vec{B}$	89
11.	Electric field measurements during interval 1 when the high gain was not saturated. Dotted line is the component in the direction of $\vec{V} \times \vec{B}$. The motional field $\vec{V} \times \vec{B}$ has been subtracted from the measured field. Solid line is the component in the direction of V_{\perp} , the velocity projected into the plane perpendicular to the magnetic field.	91

12. Electric field measurements during interval 2 when the high gain was not saturated. Dotted line is the component in the direction of $\vec{V} \times \vec{B}$. The motional field $\vec{V} \times \vec{B}$ has been subtracted from the measured field. Solid line is the component in the direction of V_{\perp} , the velocity projected into the plane perpendicular to the magnetic field. 93
13. Electric field measurements during intervals 3 and 4 when the high gain was not saturated. Dotted line is the component in the direction of $\vec{V} \times \vec{B}$. The motional field $\vec{V} \times \vec{B}$ has been subtracted from the measured field. Solid line is the component in the direction of V_{\perp} , the velocity projected into the plane perpendicular to the magnetic field. 95
14. Upper plot shows the ratio $|V_{\times B}|/|\vec{V} \times \vec{B}|$.
Lower plot shows the thruster emission rate. 97
15. Upper plot shows the ratio $|V_{\times B}|/|\vec{V} \times \vec{B}|$.
Lower plot shows the thruster emission rate. 99
16. Upper plot shows the ratio $|V_{\times B}|/|\vec{V} \times \vec{B}|$.
Lower plot shows the thruster emission rate. 101

17.	<p>The ratio $E_{V_{xB}}/ \vec{V}_{xB}$ versus the thruster emission rate averaged over 13 seconds. Points from all 4 time intervals are included. 103</p>
18.	<p>Measurements of $E_{V_{xB}}/ \vec{V}_{xB}$ are segregated into bins having comparable numbers of measurements, and averaged. The vertical lines show the boundaries of each bin. The error bars indicate the standard deviation of the mean in each bin. 105</p>
19.	<p>The ratio $E_{V_{xB}}/ \vec{V}_{xB}$ versus the thruster emission rate averaged over 13 seconds. Points from all four time intervals are included. Times when the electron beam generator was operating are excluded. 107</p>
20.	<p>Measurements of $E_{V_{xB}}/ \vec{V}_{xB}$ are segregated into bins having comparable numbers of measurements, and averaged. The vertical lines show the boundaries of each bin. The error bars indicate the standard deviation of the mean in each bin. Times when the electron beam generator was operating are excluded. 109</p>
21.	<p>Directions of x, y, z coordinates. 111</p>
22.	<p>Alfvén wave disturbance generated by a current source moving through a magnetized plasma. The electric field E_2 between the current wings</p>

	is of lower magnitude than the motional field	
	$E_1 = \vec{V} \times \vec{B}$	113
23.	Alfvén wave disturbance generated by a current source moving through a magnetized plasma. The electric field E_2 between the current wings is of lower magnitude than the motional field	
	$E_1 = \vec{V} \times \vec{B}$	115
24.	Large differential voltage signals associated with times of the electron beam generator operation. . .	117
25.	Dashed lines indicate the trajectory of PDP in the plane perpendicular to \vec{B} during times of electron beam generator operation. The trajectories for events 1 through 5 are shown as solid segments. The origin represents the position of the magnetic field line on which the beam lies. V_{\perp} is the component of velocity perpendicular to \vec{B}	119
26.	Average potential measurements during times when large electric field signals were detected.	121
27.	Solution of Equation 25 using values from Table 6. Model of floating potential as a function of energetic electron current. Antenna probe and PDP chassis have different floating potentials because of their different current collecting surface areas.	123

28. The PDP with the spin plane corresponding to the plane of the page. Energetic electrons move along the field lines. As the PDP spins, the antenna periodically becomes aligned with the magnetic field, and one probe is shielded from the electron flux. The probe also passes through the PDP wake. 125
29. The PDP viewed with the spin axis in the plane of the page. The angle θ of the magnetic field to the spin plane is shown. If θ is small, then particles moving along field lines can be shadowed from one probe. 127
30. Vectors indicating the direction of the gradient in energetic electron flux along the trajectory of the PDP. Note that the beam will have a finite width, and the location of the beam center shown is accurate only to within a few meters. 129

CHAPTER I

INTRODUCTION

As part of the Spacelab-2 mission, which was launched on July 29, 1985, a spacecraft called the Plasma Diagnostics Package (PDP) was released from the space shuttle to survey the plasma environment around the orbiter. The PDP, which consisted of a scientific instrument package containing 14 instruments, was designed and constructed at the University of Iowa, and is described by Shawhan et al. [1982]. The PDP was in free flight for roughly six hours, during which time the shuttle was maneuvered to performed two complete fly-arounds of the PDP. The fly-arounds allowed the PDP to make measurements both upstream and downstream from the shuttle at distances up to 400 meters. The fly-arounds also included four magnetic conjunctions during which the shuttle was targeted to pass through the magnetic field line passing through the PDP. At various times an electron beam was ejected from the shuttle so that the effects in the plasma might be studied. The electron beam generator, flown as part of the Vehicle Charging and Potential (VCAP) experiment provided by Stanford University and Utah State University, is described by Banks et al. [1987]. The PDP and the electron beam generator were previously flown on the STS-3 flight [Shawhan et al., 1984a]. The PDP carried instrumentation which made

differential voltage measurements between two floating probes in order to measure quasi-static electric fields. This thesis reports on efforts to measure the quasi-static electric fields in the plasma with the PDP during the free flight. The discussion is divided into two main topics: measurements of perturbations in the electric field associated with operation of the shuttle thrusters, and measurements of large differential voltages between the double probes at times of electron beam operations.

In situ measurements of the plasma environment around the space shuttle have shown that the plasma differs significantly from that expected for an ambient ionospheric plasma. Some of the plasma measurements which have been performed from the shuttle are reported in the papers by Stone et al. [1983], Raitt et al. [1984], Shawhan et al. [1984b], Pickett et al. [1985], Hunten and Calo [1985], Murphy et al. [1986], Reasoner et al. [1986], Stone et al. [1986], Grebowsky et al. [1987a], and Grebowsky et al. [1987b]. A review of the ion and neutral particle measurements on shuttle flights STS-2 through STS-4 is given by Green et al. [1985]. The plasma around the shuttle is characterized by the induced effects of neutral gases released from the orbiter. Neutral gases are released from the shuttle by outgassing of shuttle surfaces, orbiter water dumps, flash evaporator system releases, and thruster operations. Charge exchange reactions between the neutral particles of shuttle origin and the ambient plasma particles lead to the creation of molecular ions which are not naturally present at

shuttle altitudes, or that do not generally occur in the concentrations measured around the shuttle. The principal contaminant neutral species is H_2O , although the thruster emissions also include significant amounts N_2 , H_2 , and CO , plus lesser amounts of a few other species. The contaminant molecular ions identified in the region around the shuttle include H_2O^+ , H_3O^+ , NO^+ , OH^+ , N_2^+ , N^+ , and O_2^+ . Some of the ions measured near the shuttle are found to have drift velocities with respect to the shuttle less than the orbital velocity [Hunten and Calo, 1985], thus suggesting that some plasma moves with the shuttle.

In this thesis, the effect of the interaction between shuttle derived neutrals and ambient plasma on the quasi-static electric field near the shuttle is considered. The motion of the orbiting shuttle through the earth's magnetic field \vec{B} induces an electric field in the reference frame of the shuttle equal to $\vec{V} \times \vec{B}$, where \vec{V} is the velocity vector of the shuttle relative to the ionospheric plasma, which is assumed to co-rotate with the earth. However, plasma processes may alter the electric field. Katz et al. [1984] point out that if a cloud of plasma drifts with the shuttle, the plasma cloud would polarize and partially or completely screen out the motional electric field. Pickett et al. [1985] suggest that if ions formed by charge exchange reactions do not drift with the shuttle, but rather are picked-up by the ionospheric plasma flow, then the motion of the pickup ions may cause partial screening out of the motional electric field. The effect

of pickup ions on the electric field will be considered further in a later section of this thesis.

Measurements of the electric field around the shuttle made using probes attached to the shuttle orbiter have previously been reported. Smiddy et al. [1983] measured electric fields by measuring the differential voltage between two spherical probes mounted 1.6 m apart in the bay of the orbiter. Their measurements showed no discernible changes in the motional $\vec{V} \times \vec{B}$ electric field during thruster firings or water dumps. Other indications of the electric field around the shuttle are given by the measurements of Shawhan et al. [1984b] and of Raitt et al. [1984]. Both groups measured the floating potential of a probe attached to the orbiter. Since the main engine nozzles are the only exposed conducting surfaces of the orbiter, the measurements were compared to $(\vec{V} \times \vec{B}) \cdot \vec{L}$, where \vec{L} is the vector from the probe to the center of the main engine nozzles. Both groups claim that $(\vec{V} \times \vec{B}) \cdot \vec{L}$ provides a good first-order model of the data, indicating that the motional electric field is screened to only a small degree. However, the Shawhan et al. results show reductions in the measured potential at times of thruster operations (Figure 1). This suggests that at times of large gas releases such as those associated with thruster firings, the electric field may be partially screened.

Whereas the previous electric field measurements were made from probes attached to the orbiter, this thesis discusses measurements made with the PDP while it was released as a free-flying satellite. During

the free flight there were no water dumps, and no flash evaporator system operations were performed. The only chemical releases were the outgassing from the shuttle surfaces, and thruster firings. Except for perturbations related to electron beam operations, the only perturbations to the motional electric field detected with the PDP were associated with thruster firings.

In addition to study of the interaction of the ionospheric plasma with neutral gases released from the shuttle, the Spacelab-2 mission provided opportunity to study the interaction of an electron beam with the ionospheric plasma. Prior to shuttle flights, several electron beam experiments were performed in plasma chambers and from rockets. Some of these experiments included electric field measurements. Using the same PDP and electron beam generator later flown onboard Spacelab-2, quasi-static electric fields of the order of a few volts/m were measured within a few meters of the beam in a large plasma chamber at Johnson Space Flight Center [Shawhan, 1982]. Denig [1982] questioned the reliability of these measurements because of the possibility of differential charging on the measuring probes, and because the fields seemed too large to be sustained in the given apparatus. Kellogg et al. [1982] also reported measuring fields of a few volts/m in a similar chamber test. Measurements of the quasi-static electric fields have also been reported in association with electron beams emitted from rockets in the ionosphere. In the Polar 5 experiment, fields on the order of 0.1 volts/m were detected

over 100 meters away from the beam source [Jacobsen and Maynard, 1978]. During the Echo 6 experiment, Winckler and Erickson [1986] measured fields on the order of 0.2 volts/m at a distance of 40 meters from the flux tube on which the beam was expected to be centered. All the measurements mentioned here involved differential voltage measurements using floating probes. Considering the chamber and rocket experiments, on the Spacelab-2 mission we expected to detect fields on the order of 1 volt/m associated with the electron beam.

The electron beam generator was operated at various times throughout the free flight, both in a steady (DC) mode, and in a pulsed mode. During several of these times, signals on the order of 1 volt/m were detected by the quasi-static electric field instrument. In this thesis the large signals obtained in association with the electron beam firings are described and the origin of the signals is discussed.

Understanding the plasma environment around the shuttle is of interest for planning other scientific experiments to be performed from the shuttle, and for designing other large objects to be placed in low earth orbit. The interaction of the gas around the shuttle with the ambient plasma is also interesting because of its analogy to other important problems in space plasma physics, such as the interaction between comets and the solar wind, Io and the Jovian magnetosphere, or Titan and the Saturnian magnetosphere. Understanding beam plasma interactions is of interest as electron beam experiments continue to be performed in the ionosphere.

CHAPTER II

INSTRUMENTATION

Quasi-static electric field measurements were made on the PDP by measuring potentials using two conducting spheres, both at floating potential, mounted on insulated booms on opposite sides of the spacecraft. The sphere-to-sphere separation was 3.89 meters, and the diameter of the spheres was 10.2 cm. A diagram of the PDP, showing the dimensions of the main chassis and the locations of spherical probes, which are labeled sphere 1 and sphere 2, is presented in Figure 2. Two types of measurements were made: the differential voltage, V_{diff} , between the two probes was measured at both a high gain and a low gain, and the average voltage, V_{ave} , of the two probes relative to the PDP chassis was measured at a fixed gain. The following relations describe the two measurements:

$$V_{diff} = V_2 - V_1$$

$$V_{ave} = (V_2 + V_1)/2$$

where V_1 and V_2 are respectively the potentials of sphere 1 and sphere 2 relative to the PDP chassis. Typically the quantity V_{diff}/L , where L is the antenna length, is interpreted as a measurement of the electric

field. The basic instrument parameters and dynamic ranges are given in Table 1. Since the floating potential of an object in a plasma is dependent on the surface materials, it is also important to describe the surface properties of the spacecraft and spheres. The PDP chassis was covered with a teflon-coated fiberglass cloth which in turn was covered with an aluminum mesh to provide a uniform conducting surface. Potential measurements were referenced to the aluminum mesh. The spherical antenna probes were coated with a conducting graphite-epoxy paint.

After release from the shuttle, the PDP was made to spin by the action of an inertia wheel within the PDP. When spinning at its maximum rate, the spacecraft had a spin period of 13.1 seconds. The spin axis was oriented approximately perpendicular to the orbital plane. Thus, the spacecraft velocity vector lay approximately in the PDP spin plane.

The electron beam generator was mounted in the shuttle payload bay. A beam was produced by accelerating electrons emitted from a heated tungsten wire filament through a 1 kilovolt potential. The generator operated at beam currents of either 50 ma or 100 ma, and could produce either a steady or a pulsed beam. The beam was pulsed at frequencies up to 800 kHz.

CHAPTER III
DATA ANALYSIS

From the electric field signal (V_{diff}/L), one can obtain a measurement of the electric field in the spacecraft spin plane. The complete electric field vector was evaluated by first determining the electric field in the spin plane, and then using the assumption that $\vec{E} \cdot \vec{B} = 0$ to find the component of \vec{E} along the spin axis. The magnetic field was determined from a multipole model of the earth's magnetic field. In the region of the ionosphere where the Spacelab-2 mission was flown, the parallel conductivity is generally much greater than the perpendicular conductivity, so the assumption that the parallel electric field is zero is reasonable. A discussion of the determination of the electric field in the spin plane follows.

Upon initial release from the shuttle, the PDP was not spinning. After release, the inertia wheel inside the PDP was activated and the PDP began to spin, attaining a spin period of 13.1 seconds after 73 minutes. The spin rate of the inertia wheel was gradually reduced starting at about 53 minutes before the end of the free flight, so that the PDP was not spinning when the spacecraft was retrieved. When the PDP was rotating, the potential difference between the spheres was expected to vary sinusoidally, with the spin period. A measurement of

the electric field vector in the spin plane, \vec{E}_s , was obtained by using a least square's fit method to fit a 13.1-second segment of the electric field signal to the function

$$F(t) = F_1 + F_2 \cos(2\pi t/T - \Phi) \quad (1)$$

where T is the spin period in seconds, and F_1 , F_2 , and Φ are parameters determined by the fit procedure. Measurements of the electric field were made for all times when the PDP spin period was 15 seconds or less. During these times the PDP was no closer than 50 meters from the shuttle.

As part of the fitting procedure, it was found to be necessary to remove certain contaminating signals. The contaminating signals were found to be related to the operation of the Low Energy Proton and Electron Differential Energy Analyzer (Lepedea) on the PDP. As Tribble et al. [1987] report, the operation of the Lepedea resulted in changes in the spacecraft potential. The Lepedea utilized a current collecting plate whose voltage jumped to +2 kilovolts every 1.6 seconds. The plate collected a large thermal electron current, and the PDP potential decreased by several volts, typically recovering its original value within 0.8 seconds. The average potential V_{ave} of the probes was sampled every 1.6 seconds and always 0.166 seconds after the voltage on the Lepedea current collecting plate jumped to 2 kilovolts. Thus, V_{ave} was sampled at a time when the PDP potential was lower than when

Lepedea was not collecting current. Or equivalently, the average potential of the probes relative to the PDP at the sample time was higher than when Lepedea was not collecting current. The degree of charging of the spacecraft was less when the Lepedea aperture faced the spacecraft wake, than when the aperture faced the ram direction. The V_{ave} potential signal was spin modulated because of this effect, as can be seen in Figure 3. For the V_{diff} measurement, a large negative potential on the PDP was equivalent to a large positive common mode signal on the probes. Because of limitations in the common mode rejection, the V_{diff} signal was contaminated whenever the PDP potential exceeded several volts negative. An example of the contaminating signal is shown in Figure 4. In order to remove this contaminating signal, 0.8 seconds of the signal was removed every 1.6 seconds. This process significantly degraded the accuracy and resolution of the electric field measurement, but was unavoidable due to the contaminating signal from the Lepedea.

In addition to the contamination from the Lepedea, times when one probe was in the PDP spacecraft wake were also removed from the signal. Examination of the electric field signal shows that during much of the free flight, the signal deviated from a sine wave whenever one of the probes passed through the PDP wake. An example is shown in Figure 4. In the spacecraft wake, the plasma density is lower than the ambient density, and the electron temperature is higher. Whenever the plasma environment differs between the two probes, differential voltage

measurements on floating probes do not give a reliable measure of the electric field. The antenna probe is typically within the Mach cone extending downstream from the PDP when the angle of the antenna to the velocity vector is less than 26° . In order to be sure to remove the effects of the spacecraft wake, the electric field signal was removed if the angle between the antenna and the velocity vector was less than 35° . This turns out to be a segment of the signal lasting 2.5 seconds. Figure 5 shows the signal remaining after the various known contaminating signals were removed.

Measurements of the electric field in the spin plane were made every 5 seconds, by sliding the 13.1-second sample of the signal used in the fit procedure along in 5-second intervals. That is, each measurement contains 8.1 seconds of the signal used in the previous measurement. In order to estimate the uncertainty of E_s for each measurement, the following goodness of fit parameter was calculated:

$$X = \left[\frac{\sum (F(t_i) - x_i)^2}{(N - 3)} \right]^{1/2} / F_2 \quad (2)$$

The parameter X is derived from the chi square parameter normally used in statistical analysis, by scaling chi square to the sine wave magnitude F_2 , so as to obtain a dimensionless parameter. Small values of X (less than about 0.1) indicate that fitted function $F(t)$ represents the data well.

CHAPTER IV
GENERAL RESULTS

The magnitude of the measured electric field in the PDP spin plane was usually on the order of the component of $\vec{V} \times \vec{B}$ in the spin plane, which ranged from 0.04 volts/m to 0.16 volts/m. Exceptions occurred during the following five time intervals when the electron beam was operating, and V_{diff}/L signals from 0.5 volts/m to 2 volts/m were detected.

GMT 213 00:46:10 - 00:49:15

GMT 213 01:19:25 - 01:20:20

GMT 213 02:47:30 - 02:50:45

GMT 213 03:33:25 - 03:34:25

GMT 213 04:11:10 - 04:12:00

The signals during these intervals will be discussed in Section VI. Measured values of the electric field magnitude in the spin plane, for all times excluding the above five intervals, are shown in Figure 6. The line in the figure represents the spin plane component of $\vec{V} \times \vec{B}$. The magnitude of the measured field is generally within about 10% of the motional field. Figure 7 displays the uncertainty of measurement as determined from Equation 2.

After the electric field in the spin plane \vec{E}_s was measured, the electric field vector \vec{E} was determined as described in the previous section. The electric field vector was resolved into two components which lie in a plane perpendicular to the magnetic field. One component, E_v , is along the direction of the velocity vector projected into the plane perpendicular to the magnetic field. The other component, $E_{v \times B}$, is along the direction of the motional field, $\vec{v} \times \vec{B}$. Figure 8 shows the measured values of E_v . Comparing Figures 7 and 8 one finds that the E_v component is of the order of magnitude of the uncertainty of measurement. Measured values of $E_{v \times B}$ are plotted as points in Figure 9. The line in the Figure 9 represents $|\vec{v} \times \vec{B}|$.

The measured values of $E_{v \times B}$ are considered further in Figure 10, where the ratio $E_{v \times B}/|\vec{v} \times \vec{B}|$ is plotted. If $E_{v \times B}/|\vec{v} \times \vec{B}|$ is 1, then only the motional field is measured. If $E_{v \times B}/|\vec{v} \times \vec{B}|$ is less than 1, then the motional field is possibly being screened in the region near the shuttle. Values of $E_{v \times B}/|\vec{v} \times \vec{B}|$ less than 1 were recorded during the free flight, although at no time was the magnitude of the measured electric field less than 0.5 times $|\vec{v} \times \vec{B}|$. Values of $E_{v \times B}/|\vec{v} \times \vec{B}|$ greater than 1 were not expected, as they imply plasma flow past the spacecraft at speeds greater than the orbital speed. Yet values greater than 1 were recorded at times. Only during the five times listed at the beginning of this section, when operation of the electron beam generator on board the shuttle lead to large electric field signals, was $E_{v \times B}/|\vec{v} \times \vec{B}|$ greater than 1.3. The measurements for these

five times, which are not included in Figure 10, will be discussed in Section VI. Figure 10 also shows that at other times the measured value of $E_{VxB}/|\vec{V} \times \vec{B}|$ was greater than 1. Possible reasons for this are considered next.

The times when $E_{VxB}/|\vec{V} \times \vec{B}|$ stayed consistently greater than 1 occurred primarily when the PDP was on the day side of the orbit. One can see this by comparing the times for dawn and dusk listed below to Figure 10.

<u>Dawn</u>	<u>Dusk</u>
GMT 212 23:49	GMT 213 00:44
GMT 213 01:20	GMT 213 02:15
GMT 213 02:50	GMT 213 03:45
GMT 213 04:21	GMT 213 05:16

At all times on the dayside of the orbit, the angle of the PDP spin plane to the Sun was such that one probe passed through the spacecraft shadow as the PDP rotated. A shadow on the probe can affect the electric field measurements in the following manner. While in the shadow, the probe does not emit photoelectrons, and thus the probe's floating potential is lower than if it were not in a shadow. The resulting effect on the measurement would be an apparent, but not real, electric field in the anti-Sunward direction. If $\vec{V} \times \vec{B}$ were also in the anti-Sunward direction, then the apparent electric field due to the photoelectric emission would add to the motional $\vec{V} \times \vec{B}$ field leading to values of $E_{VxB}/|\vec{V} \times \vec{B}|$ greater than one. However, on the day side of

the orbit, $\vec{V} \times \vec{B}$ as projected onto the spin plane was directed anti-Sunward at times and Sunward at other times. Thus, even though the values of $E_{V \times B} / |\vec{V} \times \vec{B}|$ greater than 1 were recorded mainly on the day side of the orbit, the values are not explained by photoelectric emission from the probes.

Whereas the magnitude of the measured electric field in the spin plane varied between 0.03 volts/m and 0.16 volts/m, signals larger than 0.064 volts/m were out of the range of the high gain, as can be seen by referring to Table 1. The times when $E_{V \times B} / |\vec{V} \times \vec{B}|$ stayed consistently greater than 1 occurred primarily when the electric field in the spin plane was greater than 0.064 volts/m, and the low gain was used. Thus, the values of $E_{V \times B} / |\vec{V} \times \vec{B}|$ greater than 1 are probably related to the inaccuracy inherent the low gain data.

The resolution of the low gain circuitry (the size of one digitizing step) was 0.017 volts/m. Thus, the resolution of the low gain was on the order of 10% of $|\vec{V} \times \vec{B}|$. So, for those times when the electric field was out of the range of the high gain, the difference between the measured signal and $|\vec{V} \times \vec{B}|$ was typically on the order of the uncertainty of measurement. In order to measure precisely the small differences between the electric field in the plasma and the motional electric field, times when the measured signal in the spin plane was less than 0.064 volts/m were considered. At those times, the high gain can be used, and the resolution of the measurement is 0.51 millivolts/m. During the free flight, the measured signal was within

the range of the high gain for the following four time intervals.

- (1) GMT 213 01:03:20 - 01:18:00
- (2) GMT 213 02:30:00 - 02:47:00
- (3) GMT 213 04:02:00 - 04:11:00
- (4) GMT 213 04:12:25 - 04:19:56

The nature of the measured electric field during these time intervals will be discussed in Section V.

CHAPTER V
THRUSTER RELATED EFFECTS

A. Observations

The four time intervals when the measured signal was within the range of the high gain are listed in the previous section. In this section the nature of the measured signal during these intervals will be addressed. During interval 1, the PDP was located directly downstream from the shuttle, between 85 and 89 meters away. For interval 2, the PDP was located generally above the shuttle, between 212 and 256 meters away. During this interval, the PDP passed within 20 m of the magnetic flux tube passing through the shuttle, moving from upstream to downstream of the flux tube. During interval 3 the PDP was generally located above the shuttle, between 216 and 297 meters away. The PDP was upstream of the magnetic flux tube passing through the shuttle. At the end of this interval, the PDP approached to within 10 meters of the flux tube passing through the shuttle. During interval 4 the PDP was located above the shuttle, between 199 and 229 meters away. At that time the PDP was downstream from the magnetic flux tube passing through the shuttle.

In Figures 11, 12, and 13 the components E_v and $E_{v \times B}$ of the measured electric field are plotted. The motional field has been

subtracted from the measured electric field in these plots, so that a value of zero corresponds to a measured electric field equal to the motional field. Study of the measurements made during all four time intervals shows that deviations of the measured electric field from the predicted motional electric field occur primarily in the component E_{VxB} , and occur as decreases in the motional field. The ratio $E_{VxB}/|\vec{V} \times \vec{B}|$ during all four time intervals is shown in Figures 14, 15, and 16. These plots show that the motional field is reduced at times by 10% or more. Also shown in Figures 14, 15, and 16 is the total gas emission rate of all thrusters operating during the given interval. Inspection of these plots indicates a possible relation between the firing of the thrusters and the diminutions of E_{VxB} .

B. Discussion

In order to investigate the relationship between changes in E_{VxB} and thruster firings, the linear correlation coefficient between the ratio $E_{VxB}/|\vec{V} \times \vec{B}|$ and the thruster emission rate in grams/s was calculated. Because each measurement of the electric field uses 13.1 seconds of data, the thruster emissions were averaged over a comparable time period, 13.0 seconds, before evaluating the correlation coefficient. The correlation was evaluated using the total emission rate from all the 44 thrusters on the shuttle, and for the emission rate from a sum of those thrusters that should be more or less pointed at the PDP. Throughout the PDP free flight, except during a portion of interval 1, the shuttle was maintained in an orientation such that the

shuttle bay was pointed toward the PDP within about 10° . Therefore the 9 thrusters which are directed "up," corresponding to the direction "up" out of the bay, were generally directed toward the PDP. A diagram showing the location and emission direction of the shuttle thrusters can be found in Murphy et al. [1983]. To aid in the interpretation of the correlation coefficients, we evaluated a second parameter: the probability of obtaining a correlation coefficient equal to or larger than the calculated coefficient, if the values are actually randomly distributed, given the size of the sample [Bevington, 1969]. The results are listed in Table 2. For time intervals 1, 2, and 4, the magnitude of the correlation between the ratio $E_{V_{xB}}/|\vec{V} \times \vec{B}|$ and the sum of all thruster activity ranges from 0.30 to 0.44, and in each case is much larger than would be likely if the two quantities were randomly distributed. Thus, the ratio $E_{V_{xB}}/|\vec{V} \times \vec{B}|$ appears to be anti-correlated to thruster activity.

The inverse relationship between the ratio $E_{V_{xB}}/|\vec{V} \times \vec{B}|$ and thruster activity is indicated in Figure 17, where the measurements for all four time intervals are combined and plotted together. As in the determination of correlation coefficients, the thruster emissions are averaged over 13 seconds. In Figure 18 the measurements are separated into bins having similar numbers of measurements, and the average of the ratio $E_{V_{xB}}/|\vec{V} \times \vec{B}|$ in each bin is plotted. The error bars indicate the standard deviation of the mean of each bin. Figure 18 indicates that $E_{V_{xB}}/|\vec{V} \times \vec{B}|$ decreases as the average thruster emission rate

increases. It must be noted that during parts of the time intervals we are considering, the electron beam generator on board the shuttle was operating. During interval 2 the beam generator was turned on from 02:31:38 until 02:37:46. The beam generator was also turned for the period from 04:11:03 until 04:18:24, which overlaps intervals 3 and 4. In order to determine if the diminutions in the electric field are actually related only to the electron beam operation, and not to thruster operation, the ratio $E_{V \times B} / |\vec{V} \times \vec{B}|$ was plotted versus thruster activity in Figure 19 for those times when there was no electron beam operation. In Figure 20 the measurements are separated into bins having similar numbers of measurements, and the average of the ratio $E_{V \times B} / |\vec{V} \times \vec{B}|$ in each bin is plotted. Examination of the plot shows that, although, for thruster emission rates of less than 100 grams/sec the electric field is not significantly altered, for thruster emission rates greater than 100 grams/sec, the electric field is reduced.

In order to explain the relationship between the thruster firings and the electric field measurements, the thruster-induced effects which might reduce the validity of the measurements are considered. One such effect would be a large reduction in the plasma density. A large release on neutral gas can deplete the plasma density in a two-step process [Mendillo and Forbes, 1978]. First, the molecular neutral particles undergo charge exchange reactions with ionospheric O^+ ions. Then, the newly produced molecular ions recombine with electrons, doing so more readily than the ambient atomic ions. Recombination is more

favorable for molecular ions since only a two-body collision is required, whereas for atomic ions a three-body collision is necessary. If the plasma density becomes too low, then the probe sheath resistance becomes comparable to the input resistance of the differential voltage measurement circuitry. The measured signal is then less than the actual electric field. The probe sheath resistance can be estimated in the following manner. The potential of a probe in a plasma is given by [Kasha, 1969]

$$\Phi = -U_e \ln[(I - I_i)/I_e] \quad , \quad (3)$$

where U_e is the electron temperature in electron volts, I is the total current to the probe, I_i is the total ion current collected by the probe, and I_e is the electron current gathered by a probe at the plasma potential. The sheath resistance for a floating probe is given by

$$R_s = (d\Phi/dI) \Big|_{I=0} = \frac{U_e}{I_i} \quad (4)$$

Because the orbital velocity is greater than the ion thermal speed, the ion current is determined by the sweeping up of ions as the probe moves through the plasma. The expression for the ion current is

$$I_i = n_e A e V_{sc} \quad , \quad (5)$$

where n_e is the plasma density, A is the probe cross sectional area, and V_{sc} is the orbital velocity. With $U_e = 0.2$ volts, $A = 82 \text{ cm}^2$, $V_{sc} = 7.8 \text{ km/s}$, and $n_e = 10^2 \text{ cm}^{-3}$, the sheath resistance is found to be 2.0×10^8 ohms. In contrast, the input resistance of the differential voltage measurement circuitry is greater than 10^{10} ohms. So for plasma densities greater than 10^2 cm^{-3} , the probe sheath resistance is not of concern. Although the Langmuir probe instrument on the PDP detected reductions in the plasma density at the times of the thruster firings studied in this paper, the measured density did not become as low as 10^2 cm^{-3} [personal communication, A.C. Tribble].

Another effect that might call into question the validity of the measurements is the possible deposition of thruster emission products on the probes. A deposit might form a resistive layer on a probe. If both probes are coated with deposit symmetrically, then the measurement will only be affected if the resistance of the layer is comparable to the instrument input resistance. If a deposit forms on the probes differentially, then the measured signal could be either larger or smaller than the actual electric field. The measured electric field is observed primarily to decrease at the times of thruster operations. The perturbations in the electric field do not last significantly longer than the thruster firing. Also the Langmuir probe measurements of the density depletions last only about as long as the thruster firing [personal communication, A.C. Tribble]. Thus, if deposits are formed on the probe, they apparently do not persist. However, if the

perturbations in the electric field are due to deposits on the probes, then the correlations calculated in Table 2 should be larger for the case where only thrusters directed toward the PDP are considered. For intervals 2 and 4, the correlation is in fact larger when all thrusters are considered. Thus, it seems to be unlikely that the decreases in measured electric field are due to deposits on the probe.

Having considered some possible sources of error in measurement, and argued that they are not important, changes in the plasma caused by the thruster operation are considered which would affect the electric field. The introduction of a large concentration of neutrals will alter the conductivity in the plasma by increasing the collision frequencies for ions and electrons. If the region of the thruster plume is a region of higher conductivity than the surrounding plasma, then it is possible that the motional electric field is screened out in the region of the plume. The collision frequencies, parallel conductivity, Pedersen conductivity, and Hall conductivity are calculated here from relations given by Hanson [1965]. The results are shown in Table 3. A reasonable value for the ambient neutral density is $3 \times 10^8 \text{ cm}^{-3}$. From a model of the thruster plume [Hoffman and Hetrick, 1982], it is estimated that the density of neutrals from the thruster 100 m away from the shuttle is approximately 10^{12} cm^{-3} . From Table 3 one can see that if the neutral density is increased from $3 \times 10^8 \text{ cm}^{-3}$ to 10^{12} cm^{-3} , the Pedersen conductivity does not change by a very large amount. A larger change can be found in the Hall

conductivity, which becomes comparable to the Pedersen conductivity. However, a large Hall current leads to a polarization field with a component along the direction of $\vec{E} \times \vec{B}$, and this is not observed in the measured electric field.

The above evaluation of the conductivity does not consider an important source of current: the current due to the motion of the newly formed ions after a charge exchange reaction. The newly formed pickup ions move in such a way as to produce a current in the direction of the motional electric field [Goertz, 1980]. Consider a water molecule that is initially stationary with respect to the shuttle. If the H_2O molecule undergoes a charge exchange reaction, then an H_2O^+ ion is formed which is initially at rest with respect to the shuttle. In the frame of the H_2O^+ ion there is an electric field equal to $\vec{V} \times \vec{B}$. The ion will begin to move on a cycloid trajectory, drifting in the $\vec{E} \times \vec{B}$ direction. In addition, the guiding center of the ion is displaced in the direction of $\vec{V} \times \vec{B}$ by one cyclotron radius. The current is given by

$$\vec{J} = \sum \left\{ q_s \frac{dn_s}{dt} r_{cs} \frac{E}{|\vec{E}|} \right\} \quad (6)$$

$$= \sum \left\{ \frac{dn_s}{dt} m_s \frac{\vec{E}}{|\vec{B}|^2} \right\}$$

where q_s is the ion charge, n_s is the ion density, r_{cs} is the ion cyclotron radius, m_s is the ion mass, and the sum is over all product ion species. Even if the pickup ions undergo collisions at a rate greater than the cyclotron frequency, there will still be a pickup current, since the particles are still on average displaced in the direction of $\vec{V} \times \vec{B}$.

The thruster emissions are not initially stationary with respect to the shuttle. In fact, the exit velocity is about 3.5 km/s [Pickett et al., 1985]. Therefore, the trajectory of a pickup ion must be considered more carefully than previously stated. Consider the motion of a newly formed ion that has an initial velocity relative to the shuttle. The coordinates used here are represented in Figure 21. The shuttle velocity vector \vec{V} is along the +y direction, the magnetic field is along the +z direction, and $\vec{V} \times \vec{B}$ is along the +x direction. At time $t = 0$, the ion is located at position $x = 0$ and $y = 0$, and has velocity V_{x0} and V_{y0} . Given the electric field $\vec{E} = \vec{V} \times \vec{B}$, the time averaged value of x is

$$\langle x \rangle = \frac{V_{y0} + E/B}{f_c} \quad (7)$$

Thus, the pickup ion will be displaced in the direction of $\vec{V} \times \vec{B}$, as long as $V_{y0} > -E/B$. The pickup ion may be displaced in the $-\vec{V} \times \vec{B}$ direction if the thrusters fire directly downstream, and E/B is less

than 3.5 km/s. For the observations presented here, E/B is always greater than 3.5 km/s, except from 04:02 until 04:08 during interval 3. During every other time considered here, pickup ions associated with thruster emissions should move in such a way as to produce a current.

With pickup current occurring within the thruster plume, the situation is that of a current source moving through a background plasma. In this situation, an Alfvén wave is generated. The topic was addressed originally by Drell et al. [1965] with application to conducting satellites in the ionosphere. The topic has also been treated with respect to Jupiter's moon, Io, by Goertz [1980] and Neubauer [1980], for example. The general picture is shown in Figures 22 and 23.

The Alfvén wave system shown in Figures 22 and 23 can be understood as follows. The current course causes a disturbance in the magnetic field, the electric field, and the plasma flow velocity. This disturbance propagates away from the current source along magnetic field lines as a shear Alfvén wave. The perpendicular current in the current source is closed by currents along the magnetic field lines, which in turn are closed by a polarization current in the propagating Alfvén wave front. The sheets of parallel current, which connect to each side of the current source, are referred to as Alfvén wings. Momentum is transferred from the moving current course to the plasma by the Alfvén wave. As the Alfvén wave front propagates along the field lines, the plasma behind the wave front, which is the plasma between

the Alfvén wings, is accelerated to convect with the current source. Because of the change in the plasma flow, the electric field in the region between the Alfvén wings (E_2 in Figures 22 and 23) is reduced from the motional electric field (E_1 in Figures 22 and 23). The electric field between the Alfvén wings is the same as the electric field within the current source region.

In order for an Alfvén wave, which is a magnetohydrodynamic wave, to be generated by the thruster plume, the plume must be much larger than the ion cyclotron radius. For a magnetic field of 0.25 gauss, atomic oxygen ions of energy 0.2 eV, a reasonable value for the thermal energy, will have larmor radius of 10 meters. The thruster plume extends over a comparably larger distance of a few hundred meters.

The plasma in the thruster plume convects with the current source as long as a current is driven through the source. If the thrusters are fired continuously, then the pickup current will be continuous. However, the thrusters firings are of finite duration. When a cloud of ionized gas is moving through a background plasma, momentum will be transferred from the cloud to the plasma by the Alfvén wave until the cloud comes to rest with respect to the background plasma. Scholer [1970] shows that the time scale for the cloud coming to rest with respect to the background plasma is given by

$$\tau = \frac{\mu_0 \rho \Delta z V_a}{2B^2} \quad (8)$$

where ρ is the mass density of the ionized gas cloud, Δz is the thickness of the cloud in the \vec{B} direction, and V_a is the Alfvén speed. The quantity τ is then the time for the Alfvén wave front to move over a volume of ambient plasma of mass comparable to the mass of the plasma cloud. Using the following representative values for the shuttle environment: $B = 0.25$ gauss, $\rho = 3.0 \times 10^{-15}$ kg/m³, $V_a = 4 \times 10^5$ m/s, and $\Delta z = 100$ m, the time for the cloud to be picked up by the ambient flow is $\tau = 1.2 \times 10^{-4}$ sec. Because this time is so short, the perturbation in the electric field will only be present as long as the contaminating neutral gas is being released. When the source is removed, or when the thruster firing ends, the current source is turned off. The pickup ions formed are then immediately convected away with the ambient plasma.

An expression for the electric field in the perturbed region is obtained in the following manner. The force on the plasma in the region of the Alfvén wave front is expressed as

$$\vec{J} \times \vec{B} = \rho \frac{d\vec{u}}{dt} \quad , \quad (9)$$

where ρ is the plasma mass density, and \vec{u} is the plasma flow velocity. Using the coordinates shown in Figure 21, the relation becomes

$$J_{\perp} B_0 = \rho \frac{dU_y}{dt} \quad (10)$$

Given that the Alfvén wave front propagates at speed V_a , the change in plasma flow velocity can be expressed as

$$\frac{dU_y}{dt} = V_a \frac{dU_y}{dz} \quad (11)$$

Combining equations 10 and 11, and noting that $U_y = E_x/B_0$, the current in the wave front J_{\perp} can be expressed as

$$J_{\perp} = (\mu_0 V_a)^{-1} \frac{dE_x}{dz} \quad (12)$$

The Alfvén conductance Σ_a is defined as $\Sigma_a = (\mu_0 V_a)^{-1}$. For convenience, we integrate the current over the thickness of the Alfvén wave front, and write the relation in terms of the height integrated current J'_{\perp}

$$J'_{\perp} = \Sigma_a (E_1 - E_2) \quad (13)$$

where E_1 is the electric field in the undisturbed plasma, and E_2 is the field in the region of the current source and between the Alfvén wings. If the conductance within the region of pickup is called Σ_{pu} , then the current in that region can be written as

$$J'_1 = \Sigma_{pu} E_2 \quad (14)$$

Equating Equations 13 and 14, one obtains a relation between the motional electric field and the perturbation electric field

$$E_2/E_1 = \Sigma_a / (\Sigma_a + \Sigma_{pu}) \quad (15)$$

To determine the change in the electric field, Σ_{pu} must be estimated. From Equation 6, the pickup conductivity is seen to be

$$\sigma_{pu} = \Sigma \left[\frac{dn_s}{dt} m_s \right] / B_o^2, \quad (16)$$

and thus the pickup conductance is

$$\Sigma_{pu} = \int \sigma_{pu} dz \quad (17)$$

The pickup ion production rate is expressed as

$$\frac{dn_s}{dt} = k_s [O^+] [M_s] \quad (18)$$

where k_s is the reaction rate constant, and $[M_s]$ is the density of the molecular species. The electric field can now be determined from Equations 15, 16, 17, and 18.

First consider the prediction of this model for times when no thrusters are firing. Since significant screening of the motional field is observed mainly during thruster firings, the model should predict no change in the electric field. An approximation for Σ_{pu} during times of no thruster firings is needed. It is assumed that H_2O^+ is the only important contaminant ion. In assigning values to parameters in Equation 18, the highest expected values are chosen, so as to estimate the maximum change in electric field at times without thruster firings. The ambient plasma density, $[O^+]$, is estimated to be 10^6 cm^{-3} , which is on the order of the upper range of densities measured by the Langmuir probe during the mission [personal communication A.C. Tribble]. During the STS-3 mission, the PDP detected neutral pressures in the near shuttle region on the order of 10^{-6} torr, which is an order of magnitude larger than the expected ambient pressure [Shawhan et al. 1984b]. Since 10^{-6} torr corresponds to approximately 10^{10} cm^{-3} , the water density, $[H_2O]$, is estimated to be 10^{10} cm^{-3} . The rate constant used is $k = 1.95 \times 10^{-9} \text{ cm}^3/\text{s}$ [Turner and Rutherford, 1968]. A lower value of the rate constant, $k = 3.9 \times 10^{-10} \text{ cm}^3/\text{s}$ was reported by Murad and Lai [1986]. For the present calculation, we want to find an upper limit to the electric field perturbation, so the larger value of the rate constant is used. Assuming a cloud with a diameter on the order of 200 m (a probable overestimate), the result is $\Sigma_{pu} = 0.19 \text{ ohm}^{-1}$. Using $B = 0.25$ gauss, the Alfvén conductance is $\Sigma_a = 5.82 \text{ ohm}^{-1}$. Thus,

from Equation 15, $E_2/E_1 = 0.97$; the estimated change in the electric field for this case is small, and the actual change in electric field is expected to be smaller.

Next, the electric field during a thruster firing is estimated. First, the pickup conductivity within the thruster plume must be determined. The thruster emissions include a number of molecular species which can undergo charge exchange reactions with O^+ . However, here we consider only the following reactions:



and



The H_2O and N_2 make up 63% of the molecules in the thruster emission. Also, H_2O and NO have lower ionization potentials than O , making the above reactions favorable. The other molecules likely to undergo charge exchange reactions all have ionization potentials greater than O , making their reactions less likely. Inclusion of other charge exchange reactions between thruster molecules and ambient plasma particles would lead to a larger pickup conductivity. So, by considering only 2 reactions, we are underestimating the pickup current. However, the correct order of magnitude should be obtained.

The concentration of neutrals in the thruster plume is determined from the relation

$$[M_s] = \frac{f_s (6.02 \times 10^{23}) Y}{M_{th} V_{th}}, \quad (21)$$

where f_s is the mole fraction of the neutral molecule, M_{th} is the mass of one mole of thruster emission, V_{th} is the thruster emission speed, and Y is the mass flux of thruster emissions given by [Hoffman and Hetrick, 1982]

$$Y(r, \theta) = [1351.0/r^2] [\cos(0.0126\theta)]^{10} \text{ g/cm}^2/\text{s} \quad [0^\circ \leq \theta \leq 64^\circ] \quad (22)$$

$$Y(r, \theta) = [35.0/r^2] e^{-0.084(\theta-64^\circ)} \text{ g/cm}^2/\text{s} \quad [64^\circ \leq \theta \leq 180^\circ]$$

In the above expression, r is the distance from the thruster, and θ is the angle from the center line of the thruster nozzle. With Equations 16, 18, 21 and 22, Equation 17 is integrated numerically over the thruster plume.

Some values for the pickup conductance, obtained by integrating Equation 17, and the corresponding values of $E_{V \times B} / |\vec{V} \times \vec{B}|$, are shown in Tables 4 and 5. The calculations are performed using both values of the rate constant given earlier for Equation 19. The higher value of the rate constant is used for Table 4, and the lower value is used for

Table 5. The rate constant used for Equation 20 is $k = 3 \times 10^{-10} \text{ cm}^3/\text{s}$ [McFarland et al., 1973]. For the cases presented, the integration is performed along a magnetic field line which intersects the centerline of the thruster nozzle at a distance of 100m from the nozzle. Results are shown for thruster injections at various angles to the magnetic field. Also, calculation results are shown for different values of the magnetic field strength and ambient plasma density. The magnetic field strengths and plasma densities used are typical of the F-region of the ionosphere. The model results in Tables 4 and 5 for the electric field values are of the same order of magnitude as the measured values shown in Figures 11-16. For example, given the representative values $n_e = 10^5 \text{ cm}^{-3}$ and $B = 0.5 \text{ gauss}$, the computed value of $E_{\vec{v} \times \vec{B}} / |\vec{v} \times \vec{B}|$ in Table 5 varies from 0.96 for a thruster injection angle of 90° , to 0.47 for a thruster injection angle of 2° . Thus the model can account for the measured values.

The results in Tables 4 and 5 indicate that the electric field screening is stronger for higher ambient plasma densities, for weaker magnetic field strengths, and for smaller thruster injection angles to the magnetic field. These dependences are understood simply as follows. If the ambient plasma density is higher, the rate of pickup ion production is greater, so the pickup current is larger. For weaker magnetic fields, the Larmor radius of the pickup ion is larger; thus, the pickup ion is displaced a greater distance and the pickup current is larger. If the thruster injection angle is small, (injection is

along the magnetic field) then the integrated pickup current along the magnetic flux tube will be much larger than if the thruster injection angle is large (injection is perpendicular to the magnetic field).

The electric field at the PDP is reduced under either one of the following conditions: 1.) the PDP is within the thruster plume where the pickup process is taking place; or 2.) the PDP is on a magnetic field line which passes through the region of the thruster plume where the pickup process is taking place. The thrusters do not have to be firing directly toward the PDP. Thus, it is not surprising that the correlation coefficient did not improve when we considered only thrusters firing generally toward the PDP, instead of all the thrusters [see Table 2]. However, by including all thrusters, we included thruster firings which do not satisfy either of the above conditions, and thus are not related to changes in the electric field.

The screening of electric field will last only for the duration of the thruster operation, which can be a very short time; the thrusters have a minimum on-time of about 80 milliseconds. Further, recall that each measurement of the electric field requires 13.1 seconds. Thus, a change in the electric field will only be noticed during times when thrusters are fired continuously over a period of more than a second. Recall that in Figures 18 and 20, the average thruster emission rate for 13.0 seconds was plotted. The actual thruster emission rate for the primary thrusters is 1419 grams/second/engine. A 13.0-second averaged thruster emission rate of 100 grams/sec could correspond to a

single thruster firing lasting 0.92 seconds. Thus, the ratio $E_{V \times B} / |\vec{V} \times \vec{B}|$ in Figures 18 and 20 should be lower mainly for thruster emission rates above 100 grams/sec. If the electric field was screened for only a few seconds, then the measured reduction in the field will be less than the actual reduction, because the measurement is an average value of the field over 13.1 seconds. Also, recall that in the data reduction, certain segments of the measured signal up to 2.5 seconds long were removed. Thus, for a thruster firing lasting less than 2.5 seconds, its effect on the electric field may be completely missed in the measurement. Given the above considerations, it is not surprising that the thruster firings and the electric field measurements do not appear to be perfectly correlated.

As mentioned earlier in this section, the observations considered have included time periods when the electron beam generator on the shuttle was operating. The relationship of the electron beam to screening of the electric field has not yet been discussed. When the beam is emitted from the shuttle, there is a return current to the shuttle. A perpendicular current is then driven through the shuttle, and the possibility that this current generates an Alfvén wave should be considered. Alfvén wings might form on opposite sides of the shuttle vehicle. For the Alfvén wave model to be an appropriate description, the separation of the Alfvén wings should be greater than two ion Larmor radii for typical ions. A thermal O^+ ion has a Larmor radius on the order of 10m. The largest shuttle dimension is the nose

to tail length of 37m. So the condition that the Alfvén wings be separated by more than two Larmor radii might only barely be met. The thruster plume, in contrast, spreads out over several hundred meters. We point out also that the predicted total current associated with the pickup ions at the time of a thruster firing is typically several times larger than the beam current. The electron beam generator normally operated at 100ma. The total current associated with the pickup ions is estimated as follows. The height integrated current density, J'_{\perp} in Equation 13 is approximated by

$$J'_{\perp} = I/L \quad (23)$$

where I is the total current and L is the size of the thruster cloud along the direction of the velocity flow. Equation 13 becomes

$$I = L \Sigma_a (E_1 - E_2) \quad (24)$$

Reasonable approximations for L and $(E_1 - E_2)$ are $L = 100\text{m}$ and $(E_1 - E_2) = 0.01$ volts/m. Values for the Alfvén conductance Σ_a range from 0.3 mhos to 7.3 mhos, which yields total currents ranging from 290 ma to 7.3 amps. Thus, the pickup current may be more important than the beam current. Under certain conditions, the beam current may enhance the current associated with the pickup ions. The beam will also have other important affects on the plasma which will complicate the

physical picture. For example, the electron beam will cause ionization through impacts, which can produce pickup ions. Plasma heating will occur in regions disturbed by the electron beam. A complete physical description of the case when thrusters operate and the electron beam generator is operating is quite complicated, and will require a more detailed analysis than attempted here. However, for electric field screening, the thruster effects are more important than the beam effects.

The measurements have several other features which are not fully explained. For example, in Figures 14, 15 and 16 the measurements appear to have a periodicity of about 1 minute. This periodicity has been investigated, but no cause for variation of the signal at this frequency has been determined. Also, in some cases the measured reductions in the motional electric field are not simultaneous with thruster firings as the model suggests they will be. Instead, the reduction is found up to one minute after a thruster firing. Additionally, note that the discussion thus far has emphasized the reduction in the electric field in the region between the Alfvén wings, but in the region immediately outside the Alfvén wings the electric field will be enhanced. Although reductions in the electric field associated with thruster firings are observed, significant enhancements of the field are not observed. Failure to observe enhanced electric fields indicates that the PDP was never outside the Alfvén wings. The measurements presented were made at distances up to 300 meters away

from the shuttle, so the region of plasma influenced by the thruster plume likely extends to 300 meters. Typically, several thrusters pointing in different directions are fired at once, so that pickup current is produced in an extended region of several overlapping plumes. Thus, the region of space influenced by the thruster plumes is known to be quite large, but a complete understanding of the extent of the thruster plume requires further study.

In summary the following conclusions are drawn from analysis of the time intervals where the measured signal was within the range of the high gain. Partial screening of the motional electric field was observed at distances over 200 meters away from the shuttle. The screening of the field, which was on the order of 10% to 20%, occurred primarily when the shuttle thrusters were operating. The changes in the electric field are explained by the generation of an Alfvén wave from pickup current, as suggested by Pickett et al. [1985]. An estimate of the electric field associated with an Alfvén wave is in agreement with the measurements at times of thruster firings. Further, the model predicts that the pickup current is sufficient to produce a large change in the electric field only at times of large releases of neutral gas from the shuttle. The effect occurs in the region of the thruster plume, as well as along the magnetic flux tubes passing through the plume. Thus, perturbations in the electric field can be detected far from the shuttle. The screening of the field lasts only for the duration of the thruster firing, and thus was not detectable

with the PDP unless many thruster firings occurred over a period of several seconds.

CHAPTER VI
ELECTRON BEAM RELATED EFFECTS

A. Observations

At five times during the free flight when the electron beam generator was operating, electric field signals were recorded that were significantly larger than $|\vec{V} \times \vec{B}|$. The five time intervals are listed in section IV. The cause of these large signals is discussed in this section.

The signals for the five events are shown in Figure 24, and the events are numbered 1 through 5. At no other times during the PDP free flight were signals this large recorded. Of these five events, the beam was operated in a steady mode for three events, and in a pulsed mode for two events. The beam injection pitch angle varied widely among these events. Table 6 lists the beam operation mode, injection pitch angle, beam current, and several other important parameters.

In addition to the basic periodicity due to the spinning of the spacecraft, the V_{diff} signals in Figure 24 have a number of unusual features. During event 1 the instrument saturates. Thus, the difference voltage on the probes is greater than 8 volts, which corresponds to an inferred electric field strength in the spin plane greater than 2 volts/m. Event 2 has a "spiky" character, and events 3,

4, and 5 all show a "double peak" character. At the end of event 3 (around 00:49), there is an apparent higher frequency structure to the signal. This structure is associated with the pulsing of the electron beam. Note that as long as the beam pulse frequency is much greater than the V_{diff} sample rate, then no effect of the pulsing should be apparent in the V_{diff} signal. Such is the case for event 2, where the beam was pulsed at 1.2 kHz. However, during event 3 the beam pulse frequency was lowered in steps from 600 Hz down to frequencies near the V_{diff} sample frequency of 20 Hz. The apparent higher frequency structure is the result of a beating effect that occurs between the beam pulse rate and the V_{diff} sample rate.

In order to understand the origin of the large signals, the phase angle of the spinning PDP was investigated. Arrows are plotted in Figure 24 at the top of the graph to indicate times when the electric antenna was aligned with the spacecraft velocity vector. Recall that the velocity vector lay approximately in the PDP spin plane. Arrows are plotted in Figure 24 at the bottom of the graph to indicate times when the antenna was aligned with the magnetic field projected onto the spin plane. In general, the magnetic field vector did not lie exactly in the spin plane, but made an angle of between 10° and 24° with the spin plane. The angle for each event is given in Table 6. Inspection of Figure 24 reveals that for cases 2, 3, 4, and 5 a voltage peak occurs when the antenna is aligned with the spacecraft velocity vector,

and for cases 3, 4, and 5 a second peak occurs when the antenna is aligned parallel to the magnetic field projected onto the spin plane.

Figure 25 shows the trajectory of the PDP in a plane perpendicular to the magnetic field during all times that the electron beam generator was operating. The direction V_{\perp} indicated in the figure is along the component of the velocity perpendicular to \vec{B} . The origin represents the position of the magnetic field line on which the electron beam should be centered. The beam is assumed to lie on a magnetic field line which intersects the electron beam generator, and the field is determined from a multipole model of the Earth's magnetic field. Although the beam is shown in Figure 25 only as a point, the beam electrons will have a cyclotron motion about the magnetic field. The injection pitch angles are listed in Table 6. The pitch angles are relatively small (less than 10°) for events 1 and 2 and large (greater than 30°) for events 3, 4, and 5. The beam also has some spreading due to beam divergence, space charge repulsion of the beam electrons, and beam instability. The actual width of the beam is unknown; however, previous beam experiments indicate that the cyclotron radius of a beam electron with pitch angle 90° is a reasonable approximation for the beam radius. For a 1 keV electron in a magnetic field of 0.25 - 0.5 gauss, the cyclotron radius is approximately 2-4 meters.

The trajectories during the five large events are shown in Figure 25 as solid segments, and the trajectories during times when the beam generator was operating but the measured differential voltages as small

(i.e., approximately equal to $|(\vec{V} \times \vec{B}) \cdot \vec{L}|$, are shown by the dashed lines. During events 1 and 2, the length of time the electron beam generator was turned on was longer than the length of time large signals were recorded, indicating that the spatial region over which large signals occur is limited. For each of events 3, 4, and 5, large signals were recorded for the entire period the beam generator was on. Note that events 1 through 5 occur at times when the PDP was in a region downstream of the flux tube carrying the electron beam. Except briefly during event 1, the perpendicular distance from the PDP to the flux tube of the electron beam was much greater than the 2 to 4 meter predicted beam radius, so that the PDP was well outside of the region of the primary beam. Events 1 and 2 occur when the PDP was closest to the flux tube of the electron beam, and are the largest in magnitude.

The average potential V_{ave} measurements for events 1 through 5 are shown in Figure 26. The largest changes in the average potential measurements associated with the electron beam are seen during events 1 and 2, where the average potential measurements of the probes goes from positive values of +2 to +4 volts to negative values of -2 to -4 volts. The spin period variation of the signal discussed in Section III can be seen in the graphs for events 1 and 2 during the times before and after the large negative excursions of the signal. During events 3, 4, and 5, the average potential does not change by a large amount, but the smooth spin period variation of the signal is disrupted.

B. Discussion

Because the determination of the quasi-static electric field with the PDP is based on measurements of the differential voltage between two floating probes, the results can be affected by energetic beam electrons striking the probes. It is easily shown that a small flux of energetic electrons may alter the floating potential of the probes by a large amount [Fahleson, 1967]. Arnoldy and Winckler [1981] reported a population of energetic electrons in the region around an electron beam, causing the floating potential of the Echo 3 rocket to become several volts negative. A similar observation was made on Echo 6 [Winckler et al. 1984]. Thus we expect to find that the PDP potential is affected by energetic electrons around the beam. In fact, during each of events 1 through 5 discussed here, the Lepedea on the PDP detected energetic electrons at energies nearly up to the beam energy [W. R. Paterson, personal communication, 1987]. Further, data from the PDP Langmuir probe seems to indicate that the PDP charged to at least -4.3 volts during event 2, and to at least -7.6 volts during event 1 [A. C. Tribble, personal communication, 1987]. Therefore there is reason to suspect that the probes also charged. If the charging is different for the two probes, then V_{diff}/L cannot be safely interpreted as a good measure of the electric field.

To determine the possible effect on our measurements, a simple calculation of the floating potential is performed. This is done by considering the balance of currents to the object of concern (see for

example Kasha, 1969). The possible current sources are: (1) thermal (background) electrons, (2) thermal (background) ions swept up by the motion of the spacecraft, (3) energetic electrons (energies $\gg kT_e$), (4) energetic ions (energies $\gg 5.0$ eV, the ramming energy), (5) secondary electron emission, and (6) photoelectron emission. Measurements made with the Lepedea indicate that the current from energetic ions is much less than that from the ramming ions [W. R. Paterson, personal communication, 1987], so this current can be neglected. The maximum secondary electron yields for aluminum (PDP surface material) and graphite (probe surface material), are 1.0 secondaries/primary for 300 eV primaries [Whetten, 1985]. Thus, secondary production would reduce the negative charging effect of the energetic electrons by some fraction. Photoemission would also reduce the negative charging. But since we wish to obtain a worst case estimate of the spacecraft potential, both secondary production and photoemission are neglected. Consider then the following current balance equation for an object at potential $V < 0$

$$A_x n_e u_{sc} (1 - eV/E_i) - A_s n_e (kT_e/2\pi m_e)^{1/2} \exp(eV/kT_e) - A_s J_b = 0 \quad (25)$$

The first term in the above equation includes the ion current due to the sweeping up of the ionospheric ions by the spacecraft motion plus some effect of the attraction of ions to the negatively charged object. The second term is the electron current from the thermal electrons.

The third term is the current to the object due to energetic electrons. The variables in the Equation 25 are identified in Table 7. Note that Equation 25 differs from the expression for probe potential used in Section IV (Equation 3), in which the energetic electron current and the attraction of ions to the negatively charged object were neglected.

Using the representative parameters given in Table 7, Equation 25 was solved numerically for various values of J_b and n_e . The floating potential was determined from Equation 25 for both the spherical probes and for the PDP chassis. The current collecting area of the PDP was taken to be its surface area. Unfortunately, the current collecting properties of the spacecraft body are complicated, and this estimate is to be taken only as a rough approximation. The solution for the floating potential as a function of the energetic electron current density is plotted in Figure 27. Measurements from the Lepedea during beam event 1 indicate J_b was as high as 4×10^{-4} amp/m² [W. R. Paterson and L. A. Frank, personal communication, 1987]. The Langmuir probe measurements indicate that during event 1, n_e was of the order of 10^{11} m⁻³ [A. C. Tribble, personal communication, 1987]. From Figure 27 one can see that under the conditions of event 1 the PDP floating potential could easily be lower than -10 volts. This is consistent with the Langmuir probe observation mentioned previously which show that the PDP charged to at least -7.6 volts during event 1. More importantly for the V_{diff} measurements, under the conditions of event 1 differences in J_b on the order of 10^{-5} amp/m² lead to floating

potential differences on the probes of several volts. During events 2, 3, 4, and 5 the Langmuir probe measurements indicate that n_e was on the order of 10^{10} m^{-3} [A. C. Tribble, personal communication, 1987]. For this lower ambient density, Figure 27 shows that differences in J_b on the order of 10^{-6} amp/m^2 lead to floating potential differences on the probes of several volts. Figure 27 also shows that for a fixed value of J_b , small differences in the ambient plasma density lead to floating potential differences of several volts.

Using the differential voltage between the probes to infer electric field values can produce erroneous results if the two antenna probes receive different amounts of current from any of the various current sources. Current differences can occur if one of the probes is shielded by the PDP chassis from a current source, or if the plasma environment is nonuniform over the length of the antenna. During events 2, 3, 4, and 5 the peaks in the electric field data are associated with special orientations of the antenna, and therefore can be primarily attributed to shadowing of one probe. A shadowing effect was observed by Winckler et al. [1984] during the Echo 6 experiment. In that experiment, large signals at the payload spin frequency were attributed to shadowing of one probe from a magnetic field aligned plasma flow. At the time, the electric probes were stowed in the payload body. During events 3, 4, and 5 the "double peak" character of the signals indicates that two different shadowing effects are occurring. Each effect is discussed separately below.

For events 3, 4, and 5 one finds a voltage peak, and therefore a probable shadowing of one probe, when the antenna is aligned with the magnetic field. Because the local ion larmor radius is much larger than the PDP, a shadowing along field lines suggests a shadowing of electrons. We explain the signal peak in the following manner. For events 3, 4, and 5 the beam was injected in the direction of \vec{B} . At the time when the antenna was aligned with \vec{B} , the probe on the boom pointing in the direction of \vec{B} was at a lower potential than the probe on the boom pointing in the direction of $-\vec{B}$. Thus, we conclude that some energetic electrons are moving in the direction of $-\vec{B}$, and one probe is shielded from them. So, for the three events when the PDP is 80 or more meters from the beam, the energetic electrons have a preferred direction, which is opposite to the injection direction. This explanation is consistent with the report by the Lepedea group of a secondary electron beam in the shuttle wake [Frank et al., 1987]. The shadowing of one probe from electrons moving down the field lines is pictured in Figure 28. Consideration of Figure 29. shows that if the angle θ of the magnetic field to the spacecraft spin plane is too large, then shadowing along the field lines will not occur. The range of angles where shadowing is possible is $\theta < 20.4^\circ$. Referring to the values of θ listed in Table 6, one finds that shadowing along field lines is possible for events 2, 3, 4, and 5.

The energetic electrons moving down the field lines and charging the probes in events 3, 4, and 5, may be attributed to reflection of

beam electrons by collisions with atmospheric neutrals, or to a beam plasma interaction. First, consider reflection of electrons by collisions. Given the distance of the PDP downstream from the beam for these events, and the spacecraft velocity, one can determine the time of flight for the energetic electrons to be around 10 to 20 msec. For 1 keV electrons, the corresponding total distance traveled is about 200 to 400 km. For comparison, the mean free path of electrons for collisions with oxygen atoms can be roughly estimated by $\lambda = 1/(n_n \sigma)$, where n_n is the atomic oxygen density and σ is the collision cross section. We use a value for σ of $7 \times 10^{-16} \text{ cm}^2$, the total scattering cross section for 100 eV electrons measured by Sunshine et al. [1967]. At an altitude of 300 km, n_n is approximately 10^8 cm^{-3} [Johnson, 1965], which yields a mean free path $\lambda \approx 140 \text{ km}$. Because the atomic oxygen density is larger at lower altitude, λ will become shorter at lower altitudes. Thus, for events 1 and 3 where the beam was injected downward, it is quite reasonable that electrons reflected by collisions with neutrals could reach the PDP. Since the atomic oxygen density is smaller at higher altitudes, λ becomes longer at higher altitudes. At an altitude of 400 km, n_n is approximately 10^7 cm^{-3} , which yields $\lambda \approx 1400 \text{ km}$. For events 2, 4, and 5 where the beam was injected upward, it may seem unlikely that the PDP could be affected by reflected electrons. However, it is not necessary that most of the beam particles be reflected. The solution of Equation 25 showed that the measured signals are explained by differential energetic electron

currents of the order of 10^{-6} amp/m², and this current can result from only a small percentage of beam particles being reflected. An alternative explanation is considered by Wilhelm et al. [1985]. In the SCEX experiment, Wilhelm et al. measured energetic electrons in the region downstream of an electron beam. They discuss the possibility that the energetic electrons are the product of a beam plasma interaction. Both explanations are possible, and without a further, more detailed analysis we cannot say which is correct.

A different shadowing effect occurs for events 2, 3, 4, and 5 when the antenna is aligned with the velocity vector. Because the local ion thermal speed is less than the spacecraft velocity, ions are swept up by the spacecraft motion. The electron thermal velocity is much greater than spacecraft velocity, so the electrons are not swept up. However, because quasineutrality must be maintained, both the ion and the electron densities are reduced behind the spacecraft, forming a plasma wake. The sweeping of the antenna through the wake as the PDP spins is indicated in Figure 28. Because the velocity vector lay in the PDP spin plane as shown, the antenna always passed through the wake region. In order to estimate the plasma density in the wake at the location of the antenna probe, we use the self-similar solution for the expansion of a plasma into a vacuum as shown by Samir et al. [1983] and Singh and Schunk [1982]. In the standard treatment one assumes initially a plasma of density N_0 for the region $x < 0$, and a vacuum for the region $x > 0$. At time $t = 0$ the plasma is allowed to expand into

the vacuum region. The solution for the density at later times is given by

$$N = N_0 \exp[-(x/(S_0 \tau) + 1)] \quad (26)$$

where S_0 is the ion sound speed. To obtain from Equation 24 an estimate of the density at the probe when the probe is in the wake, we take for x the radius of the PDP, $x = 0.53$ m, and for τ the time for the ionospheric plasma to flow a distance of half of the antenna length relative to the PDP, $\tau = 2.5 \times 10^{-4}$ sec. Assuming an electron temperature of 0.2 eV, and assuming ions are atomic oxygen, the ion sound speed is estimated to be about 1.4×10^3 m/s, yielding a wake density

$$N = 0.08 N_0 \quad (27)$$

This solution corresponds to the expansion of the plasma in one direction only. The wake fills in from all directions, so we expect the density in the wake at the location of the antenna probe to be greater than $0.08 N_0$, but less than N_0 . Examination of Figure 27 shows that if both probes receive the same amount of energetic electron current, but one probe is in the wake where the density is lower, then the probe in the wake will be several volts lower in potential than the

probe upstream. This explanation is consistent with the observed signals.

Event 1 does not lend itself to explanation in terms of probe shadowing, as the other events do. The angle θ between the magnetic field and the spin plane (see Table 6) is greater than 20.4° , so that probes are not shadowed along field lines. Figure 24 shows that the peaks in voltage are not consistently centered about the times the antenna is aligned with the velocity vector or the magnetic field. The peaks are also broader than expected if due only to a shielding effect. Thus the signal is due either to only a gradient in the fluxes of energetic electrons reaching the probes, or both a gradient in fluxes of energetic electrons and an electric field. We cannot rule out the possibility that we have measured the electric field. However, because the entire region where energetic electrons are observed is only 20 meters wide (refer to Figure 25), gradients over the antenna length are expected. As will be discussed below, we consider it likely that the electric field measurement in event 1 is caused mainly by a gradient in energetic electron fluxes.

In order to investigate the possible interpretation of the large signals associated with event 1, the V_{diff} signals were analyzed as follows. Due to the spacecraft rotation, the V_{diff} signal varies sinusoidally with the PDP spin period of 13.1 seconds, and it is assumed that V_{diff} attains peak value when the antenna is aligned with the direction of strongest gradient in the energetic electron flux.

The direction and relative magnitude of the gradient is then obtained by using a least squares method to fit a 13.1-second segment of the V_{diff} signal to the function $F(t)$ defined in Equation 1 in Section III. If the signal is interpreted as a measure of the gradient of the energetic electron flux, then the constant F_2 gives the magnitude of the gradient and ϕ gives the direction of the gradient in the spin plane. It is not expected that the energetic electron flux varies much along the direction of \vec{B} , so it is assumed that the gradient lies in the plane perpendicular to \vec{B} and that the component of the gradient projected onto the PDP spin plane has been measured. Using this assumption, the magnitude of the gradient vector in the plane perpendicular to \vec{B} was determined. In order to establish a "goodness of fit" of the curve performed for each measurement, the test variable X , defined in Equation 2 in Section III was calculated. Measurements were retained if $X < 0.25$, corresponding roughly to 25% error.

The vectors obtained by the above analysis are shown in Figure 30. The vectors are plotted along the trajectory of the PDP relative to the electron beam where the coordinate directions are the same as in Figure 25. The V_{diff} signals first become larger than $|(\vec{V} \times \vec{B}) \cdot \vec{L}|$, and the gradient in the energetic electron flux first becomes significant when the PDP is about 10 meters away from a line extending directly downstream from the center of the beam. The V_{diff} signal, and thus the gradient in the electron flux, becomes larger as the PDP gets closer to this line. The gradient vectors tend to point toward the line. The

indicated picture is that of a region of energetic electrons downstream from the primary electron beam. The region is not homogeneous but rather the electron flux increases as the PDP approaches the line extending directly downstream from the primary beam.

The presence of a gradient in energetic electron flux can account for the large magnitude (larger than 8 volts) of the V_{diff} signals during event 1. If the magnitude of the gradient in J_b is estimated from the Lepedea measurements, then the V_{diff} signal that would result from such a gradient can be estimated. As stated previously, the Lepedea measured a peak value of J_b of about 4×10^{-4} amp/m². We assume that the flux of energetic electrons is peaked on a line extending directly downstream from the center of the beam, and is symmetric about that line. Since the region where large signals are detected is about 20 meters wide, the spatial gradient $\Delta J_b / \Delta x$ is approximately $(4 \times 10^{-4} \text{ amp/m}^2) / (10\text{m}) = 4 \times 10^{-5}$ amp/m. The resulting V_{diff} can be estimated by

$$V_{diff} = (\Delta J_b / \Delta x) (\Delta V / \Delta J_b) (L \sin \theta) \quad (28)$$

where the quantity $\Delta V / \Delta J_b$ must be determined from Figure 27, L is the antenna length, and θ is the angle of \vec{B} to the spin plane. For $n_e = 10^{11} \text{ m}^{-3}$ and $J_b > 4 \times 10^{-5} \text{ amp/m}^2$, $\Delta V / \Delta J_b$ is -1.6×10^5 volts/amp/m². The antenna length is 3.89m (see Table 1) and θ is about 23° (see Table 6). Using Equation 28 with the given values, we obtain

$V_{diff} \approx 9.7$ volts. Thus, a gradient in the energetic electron flux of the magnitude indicated by the Lepedea measurements could possibly produce the V_{diff} signals recorded during event 1.

Even though the energetic electron flux is expected to be symmetric about the line extending directly downstream from the electron beam, the electric field signals during event 1 do not indicate a reversal of the gradient as this line is crossed. The reason for a lack of a reversal is not completely understood. However, at the time the PDP crossed the line extending directly downstream from the expected beam center, the PDP was within about 3 meters of the beam center. The electron beam width is expected to be on the order of about 3 meters. Thus, the PDP was possibly in a region containing both backscattered beam electrons and primary beam electrons. Within such close proximity of the beam center, the description of the plasma becomes more complicated than further away from the beam center. The failure to detect a reversal in the electric field signal is probably due to effects of the primary beam, given the small distance between the PDP and the primary beam at the time the PDP crossed the line extending directly downstream from the beam center.

Analysis of all five events suggests that energetic electrons are found in a region about 20 meters wide extending up to 170 meters downstream from the injected electron beam. Consideration of event 1 indicates that very close to the beam, there is a large spatial gradient in the energetic electron flux: the flux increases as one

approaches the line extending directly downstream from the center of the beam. For events 3, 4, and 5, in which the PDP was 80 or more meters away from the beam, the signals are explained by the presence of energetic electrons having a preferential direction of motion along the magnetic field line, but in a direction opposite to the beam injection.

Although the main features of the electric field signals during events 1 through 5 are understood in terms of the discussion given above, some features remain unexplained. For example, the voltage peaks during event 4 are bumps on a signal that is otherwise sinusoidal. The peaks in event 4 are explained by alignment of the antenna with the magnetic field or with the velocity vector in the presence of energetic electrons. However, the electric field signal for event 4 shown in Figure 24 would also provide a reasonably good fit to the function in Equation 1. Yet, since the shadowing effects are apparent in the measurements, a fit of the signal to Equation 1 would be difficult to interpret. It is not clear why event 4 has a more sinusoidal character than events 3 or 5. Similarly, the large peaks in the signal during event 2 can be attributed to alignment of the antenna with the velocity vector in the presence of energetic electrons, but the signal remains $> |(\vec{V} \times \vec{B}) \cdot \vec{L}|$ when the probes are not in the spacecraft wake.

Finally, the average potential measurements are considered. The measurements show that during periods of no beam operation, the average probe floating potential was several volts higher than the PDP chassis

floating potential. The solution of Equation 25 (see Figure 27) indicates that the probes should float to a potential which is much less than a volt higher than the PDP potential. During events 1 and 2 the average probe floating potential became lower than the PDP potential. The solution of Equation 25 indicates that the average probe floating potential should always be higher than the PDP chassis potential. The reasons for these discrepancies are not clear. However, it is probable that explanation involves the properties of the PDP surface materials. In solving Equation 25 for the PDP potential, it was assumed that the PDP had a uniformly conducting surface. However the potential of the aluminum mesh on the PDP surface may be influenced by the fiberglass cloth which underlies it. The fiberglass cloth may have charged to a different potential than the aluminum mesh. Katz and Davis [1987] analyzed some of the effects of the fiberglass cloth-aluminum mesh arrangement for the case of the PDP attached to the shuttle. The ultimate effect on the mesh potential when the PDP was in free flight is uncertain.

In summary, analysis of the large signals seen at times of electron beam operations leads to the following conclusions. The large signals measured by the PDP quasi-static electric field instrument during electron beam operation can primarily be attributed to three causes. First, at times when the electric antenna is aligned with the projection of the magnetic field into the spin plane, the spacecraft body shields one probe from energetic electrons moving along the

magnetic field lines. The two probes receive different amounts of electron current, thereby causing large signals. Second, at times when energetic electrons are reaching both probes, but one probe is in the PDP wake, the wake produces asymmetries in the plasma density at the two probes, thereby causing large signals. Finally, spatial gradients in the energetic electron current to the two probes, thereby causing large signals. When the electron beam generator is operating, energetic electrons are found in a region about 20 meters wide and up to 170 meters downstream from the injected electron beam. Because the region is so narrow, the spatial gradients are significant even over the length of the PDP antenna. For events 80 or more meters away from the beam, the electric field results are explained by the presence of energetic electrons having a preferential motion back down the magnetic field line on which the beam was injected.

CHAPTER VII

CONCLUSION

The electric field measured with the PDP in free flight during the Spacelab-2 mission was generally on the order of the motional field $\vec{V} \times \vec{B}$. Much of the time, the difference between the measured field and the motional field was within the measurement uncertainty. At a few times when the signal was within the range of the instrument high gain, partial screening of the motional field was observed. The screening of the field during these times was associated with operation of the shuttle thrusters. Signals much larger than $\vec{V} \times \vec{B}$ were observed five times when the electron beam generator on board the shuttle was operating.

Partial screening of the motional electric field associated with thruster operations can be explained by the generation of an Alfvén wave from pickup current, as suggested by Pickett et al. [1985]. An estimate of the electric field associated with an Alfvén wave is in agreement with the measurements at times of thruster firings. This model predicts that that the pickup current is sufficient to produce a large change in the electric field only at times of large releases of neutral gas from the shuttle. Though the shuttle is constantly

outgassing, screening of the electric field is not significant except during a large gas release.

The large signals detected at times of electron beam operation are not representative of ambient electric fields. Rather they can be attributed to three causes: differences in fluxes of energetic electrons to the two probes due to shadowing by the PDP chassis, depressions in the plasma density caused by the PDP wake, and spatial gradients in the fluxes of energetic electrons reaching the measurement probes.

On the Spacelab-2 mission, it was demonstrated that it is possible to carry out detailed studies of electron beam effects from the shuttle. Further, it should be possible to obtain a good map of the electric field near an electron beam. However, our experience indicates that double probe floating potential measurements are not reliable in the region near the beam. The floating potential of an object in a region of energetic electrons can be many times kT_e/e more negative than the plasma potential. A small difference in energetic electron current collected by each probe of a double probe system can then lead to differential voltages much higher than those due to any electric field in the plasma. Reliable potential measurements near a beam probably require biased probes, such as described by Fahleson [1965], or emissive probes such as described by Bettinger [1965]. These active potential measurements are not as sensitive to energetic electrons. An example of a biased probe system is found on the ISEE-1

spacecraft [Mozer et al., 1978]. In general, though, active potential measurements have not been used much because of the appealing simplicity of floating potential measurements. However, for future spacecraft electron beam experiments, active instead of passive potential measurements will have to be considered.

Table 1. Instrument parameters and dynamic ranges

Electric field high gain range	± 0.064 volts/m
Electric field high gain precision	± 0.51 millivolts/m
Electric field low gain range	± 2.0 volts/m
Electric field low gain precision	± 0.017 volts/m
Electric field sample rate	20.0 samples/second
Average potential range	± 8.0 volts
Average potential sample interval	1.6 seconds/sample
Spherical probe separation	3.89 meters
Spherical probe diameter	10.2 cm

Table 2. Correlation coefficient between $|E_{\vec{v} \times \vec{B}}|/|\vec{V} \times \vec{B}|$ and the emission rate of thrusters, and the probability of obtaining a correlation coefficient greater than or equal to the value calculated if the measurements are randomly distributed

time interval	213 01:03:20	213 02:30:00	213 04:02:00	213 04:12:25
GMT	- 01:18:00	- 02:47:00	- 04:11:00	- 04:19:56
correlation coefficient, all thrusters	-0.31633	-0.37168	0.05206	-0.44041
probability of correlation, all thrusters	2.98×10^{-5}	2.17×10^{-6}	0.593	1.63×10^{-5}
correlation coefficient, thrusters directed toward PDP		-0.29937	0.13804	-0.43155
probability of correlation, thrusters directed toward PDP		1.87×10^{-5}	0.154	2.40×10^{-5}

Table 3. Parallel conductivity σ_{\parallel} , Pedersen conductivity σ_p , and Hall conductivity σ_h for different neutral densities n_n , assuming an ambient plasma density $n_e = 10^5 \text{ cm}^{-3}$ and magnetic field $B = 0.25 \text{ gauss}$

$n_n (\text{cm}^{-3})$	$f_e (\text{Hz})$	$f_i (\text{Hz})$	$\sigma_{\parallel} (\Omega^{-1} \text{m}^{-1})$	$\sigma_p (\Omega^{-1} \text{m}^{-1})$	$\sigma_h (\Omega^{-1} \text{m}^{-1})$
3×10^8	57.8	3.1	50.0	1.3×10^{-5}	-2.8×10^{-7}
10^{11}	2.6×10^3	10^3	1.1	9.4×10^{-5}	-6.3×10^{-4}
10^{12}	2.6×10^4	10^4	0.11	1.3×10^{-5}	-6.3×10^{-4}
10^{13}	2.6×10^5	10^5	1.1×10^{-2}	3.9×10^{-5}	-6.4×10^{-4}
10^{14}	2.6×10^6	10^6	1.1×10^{-3}	2.8×10^{-4}	-4.7×10^{-4}

Table 4. Electric field screening determined from Alfvén wave model. Reaction rate constant used for $H_2O + O^+$ reaction was $1.95 \times 10^{-9} \text{ cm}^3/\text{s}$

thruster injection angle degrees	plasma density cm^{-3}	B field gauss	$\Sigma_{pu} \text{ ohms}^{-1}$	$\Sigma_a \text{ ohms}^{-1}$	$E_{VxB}/IV \times BI$
2.0	1.0×10^4	0.25	1.3340	0.5812	0.3035
2.0	1.0×10^5	0.25	13.3400	1.8379	0.1211
2.0	1.0×10^6	0.25	133.3999	5.8119	0.0417
2.0	1.0×10^4	0.50	0.3335	0.2906	0.4656
2.0	1.0×10^5	0.50	3.3350	0.9189	0.2160
2.0	1.0×10^6	0.50	33.3500	2.9059	0.0802
45.0	1.0×10^4	0.25	0.0655	0.5812	0.8987
45.0	1.0×10^5	0.25	0.6554	1.8379	0.7371
45.0	1.0×10^6	0.25	6.5545	5.8119	0.4700
45.0	1.0×10^4	0.50	0.0164	0.2906	0.9466
45.0	1.0×10^5	0.50	0.1639	0.9189	0.8487
45.0	1.0×10^6	0.50	1.6386	2.9059	0.6394
90.0	1.0×10^4	0.25	0.0467	0.5812	0.9256
90.0	1.0×10^5	0.25	0.4672	1.8379	0.7973
90.0	1.0×10^6	0.25	4.6723	5.8119	0.5543
90.0	1.0×10^4	0.50	0.0117	0.2906	0.9614
90.0	1.0×10^5	0.50	0.1168	0.9189	0.8872
90.0	1.0×10^6	0.50	1.1681	2.9059	0.7133

Table 5. Electric field screening determined from Alfvén wave model. Reaction rate constant used for $H_2O + O^+$ reaction was $3.9 \times 10^{-10} \text{ cm}^3/\text{s}$

thruster injection angle degrees	plasma density cm^{-3}	B field gauss	Σ_{pu} ohms-1	Σ_a ohms-1	$E_{V \times B} / V \times B $
2.0	1.0×10^4	0.25	0.4728	0.5812	0.5514
2.0	1.0×10^5	0.25	4.7281	1.8379	0.2799
2.0	1.0×10^6	0.25	47.2807	5.8119	0.1095
2.0	1.0×10^4	0.50	0.1182	0.2906	0.7109
2.0	1.0×10^5	0.50	1.1820	0.9189	0.4374
2.0	1.0×10^6	0.50	11.8202	2.9059	0.1973
45.0	1.0×10^4	0.25	0.0232	0.5812	0.9616
45.0	1.0×10^5	0.25	0.2323	1.8379	0.8878
45.0	1.0×10^6	0.25	2.3231	5.8119	0.7144
45.0	1.0×10^4	0.50	0.0058	0.2906	0.9804
45.0	1.0×10^5	0.50	0.0581	0.9189	0.9406
45.0	1.0×10^6	0.50	0.5808	2.9059	0.8334
90.0	1.0×10^4	0.25	0.0166	0.5812	0.9723
90.0	1.0×10^5	0.25	0.1656	1.8379	0.9173
90.0	1.0×10^6	0.25	1.6560	5.8119	0.7782
90.0	1.0×10^4	0.50	0.0041	0.2906	0.9860
90.0	1.0×10^5	0.50	0.0414	0.9189	0.9569
90.0	1.0×10^6	0.50	0.4140	2.9059	0.8753

Table 6. Beam parameters, Sunlight conditions, PDP orientation

Event	1	2	3	4	5
Distance from PDP to shuttle	206m	218m	93m	90m	235m
Distance from PDP to Flux Tube of Beam	26-3m	9-40m	87m	84m	143m
θ - Angle of B to Spin Plane	22.9° -23.6°	15.4° -15.7°	15.1° -19.4°	10.8° -12.1°	15.4° -16.6°
Day/Night	day	night	night	night -sunrise	night -sunrise
Beam Current	50 ma	100 ma	100 ma	100 ma	100 ma
Beam Injection Direction	down	down	down	up	up
Beam Injection Pitch Angle	<7.5°	2.4°-10°	54°-70°	68°-69°	38°-45°
Beam Mode	DC	1.2 kHz	54s DC 115s pulsed 600 Hz stepped down to 10 Hz	DC	DC

Table 7. Parameters used in evaluation of Equation 25

U_{sc} spacecraft velocity	7.8×10^3 km/s
Ax cross sectional area for ion collection: PDP	0.869 m ²
probe	8.11×10^{-3} m ²
As total surface area: PDP	4.52 m ²
probe	3.24×10^{-2} m ²
Ei ion energy in spacecraft reference frame	5.08 eV
T_e electron temperature	0.2 eV
n_e plasma density	5.0×10^{11} m ⁻³
J_b current density of energetic electrons	$0-5.5 \times 10^{-4}$ amp/m ²

Figure 1. Measurements made with the PDP during the STS-3 mission. The plot labeled -SC POT is the average potential of the electric probes of the PDP relative to the shuttle potential. The potential changes at times of thruster operations [Shawhan et al., 1984].

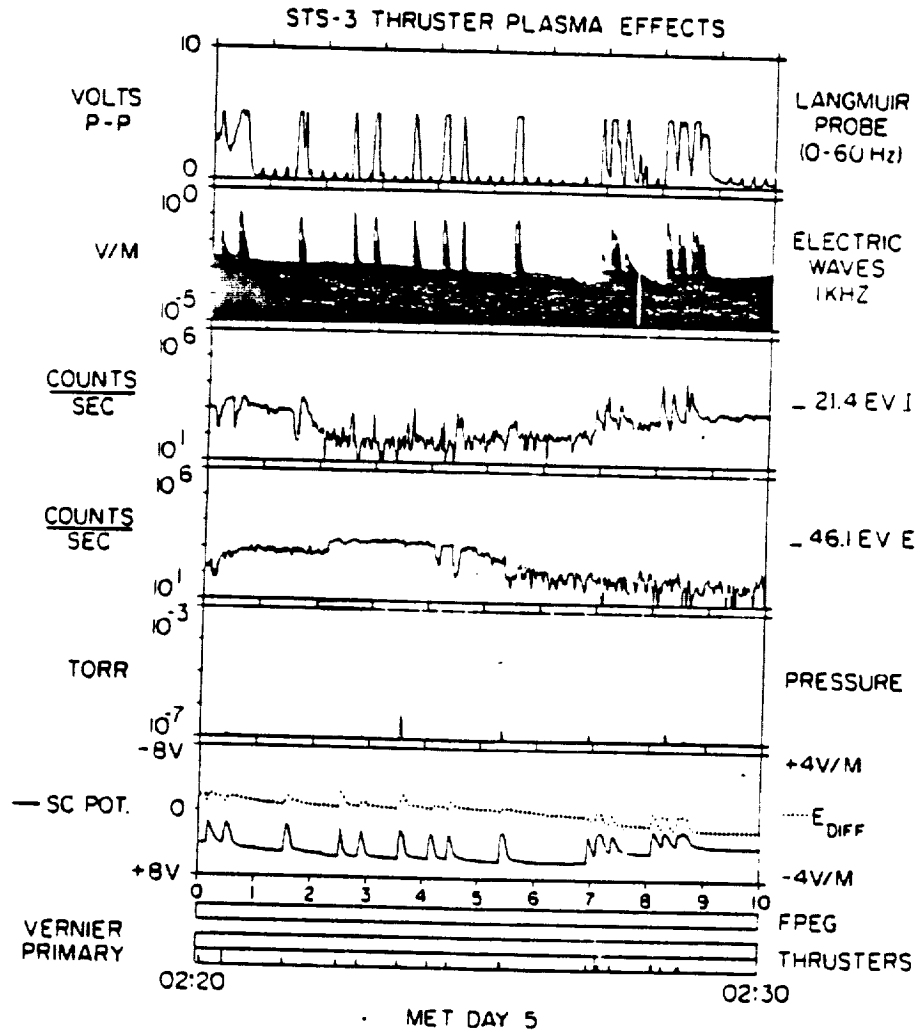


Figure 2. The Plasma Diagnostics Package. Dimensions are given in meters.

C-G87-683-1

PDP CONFIGURATION

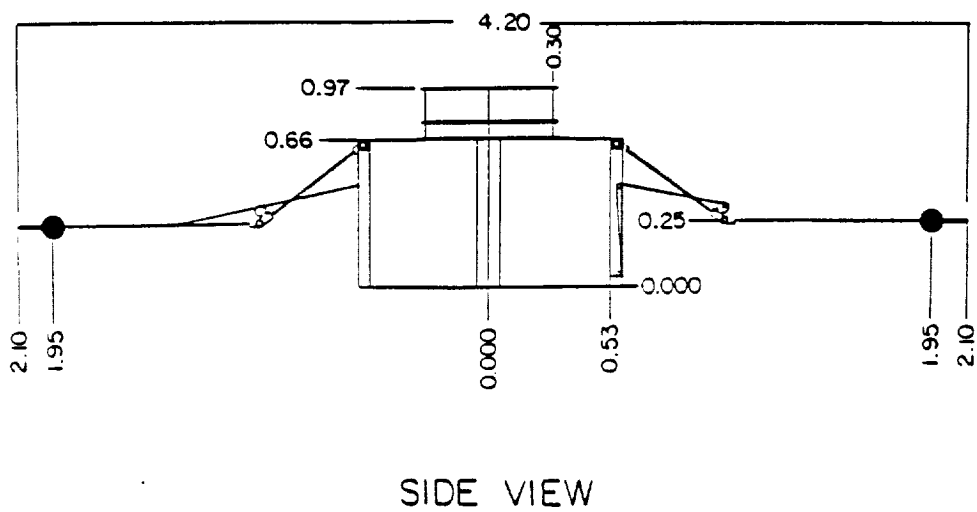
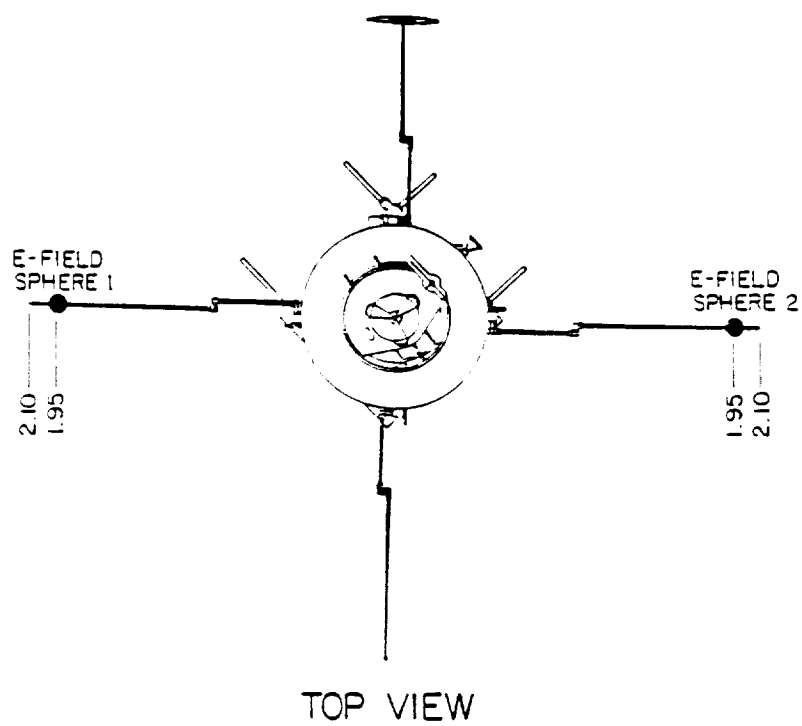
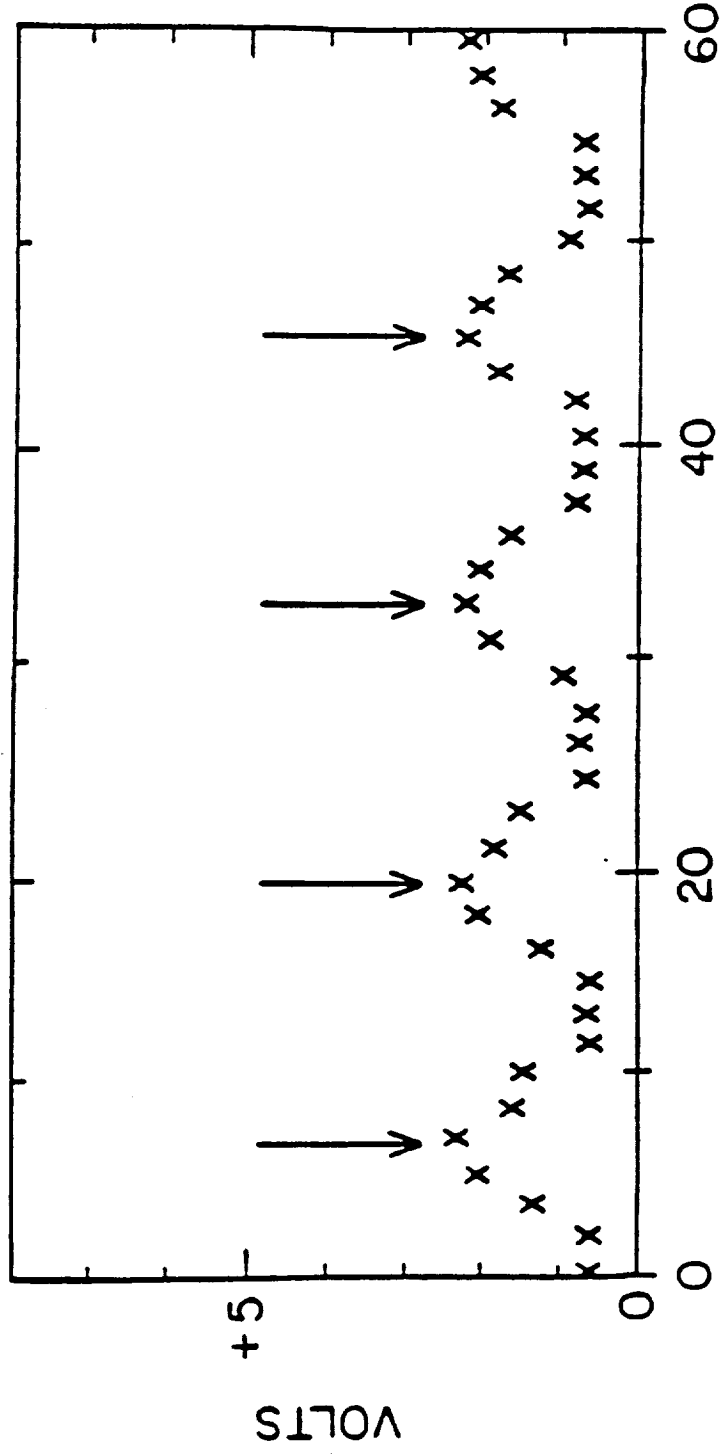


Figure 3. Average potential measurements showing a variation at the spacecraft spin period. Arrows indicate the times when the aperture of the Lepedea faced directly into the ram direction.

A - G86 - 643

AVERAGE DC POTENTIAL



TIME, IN SECONDS, STARTING DAY 213, 01:39:00

Figure 4. A segment of the electric field signal showing the contamination of the signal by a common mode signal related to the operation of the Lepedea, and the passage of the probes through the spacecraft wake.

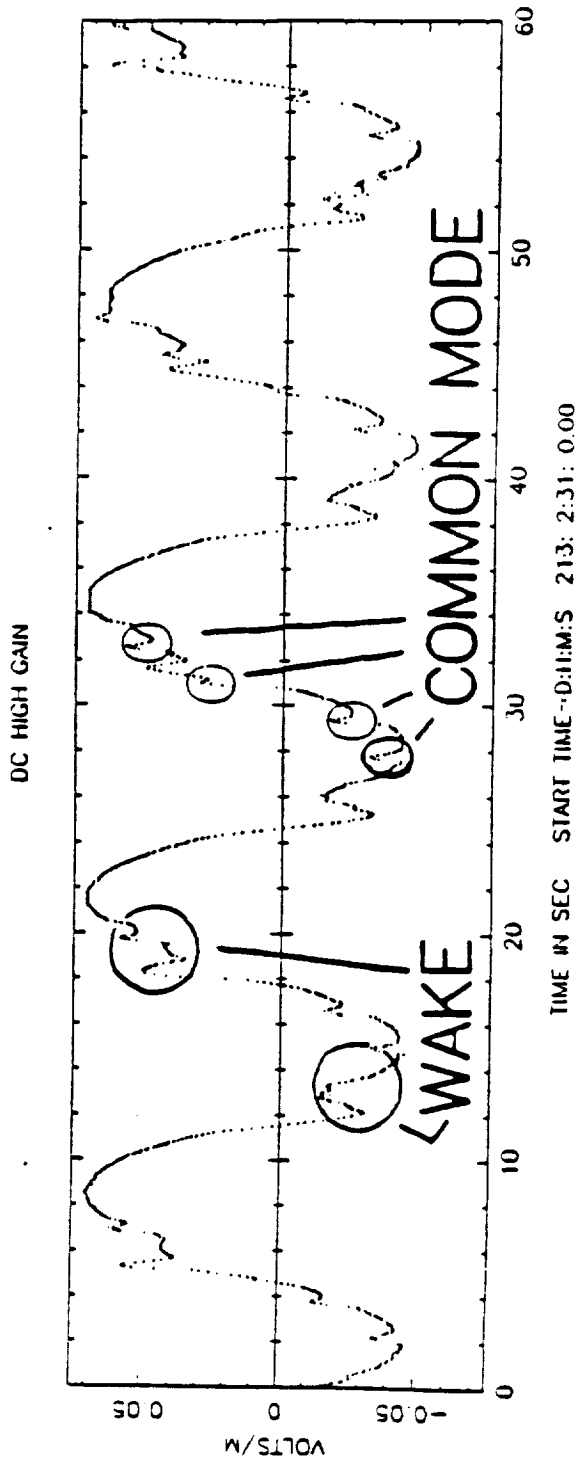


Figure 5. The portion of the electric field signal remaining after segments of the signal known to be contaminated are removed.

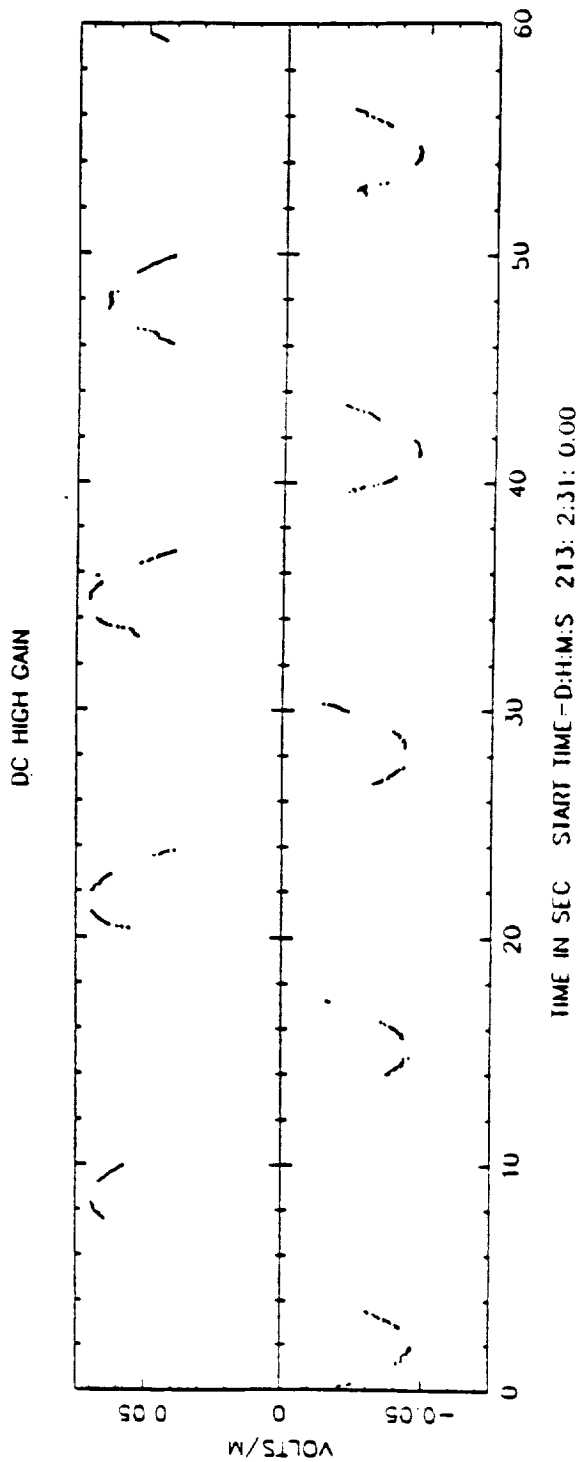


Figure 6. Dots indicate measurements of the magnitude of the electric field in the spacecraft spin plane. The solid line indicates the projection of $\vec{V} \times \vec{B}$ in the spin plane.

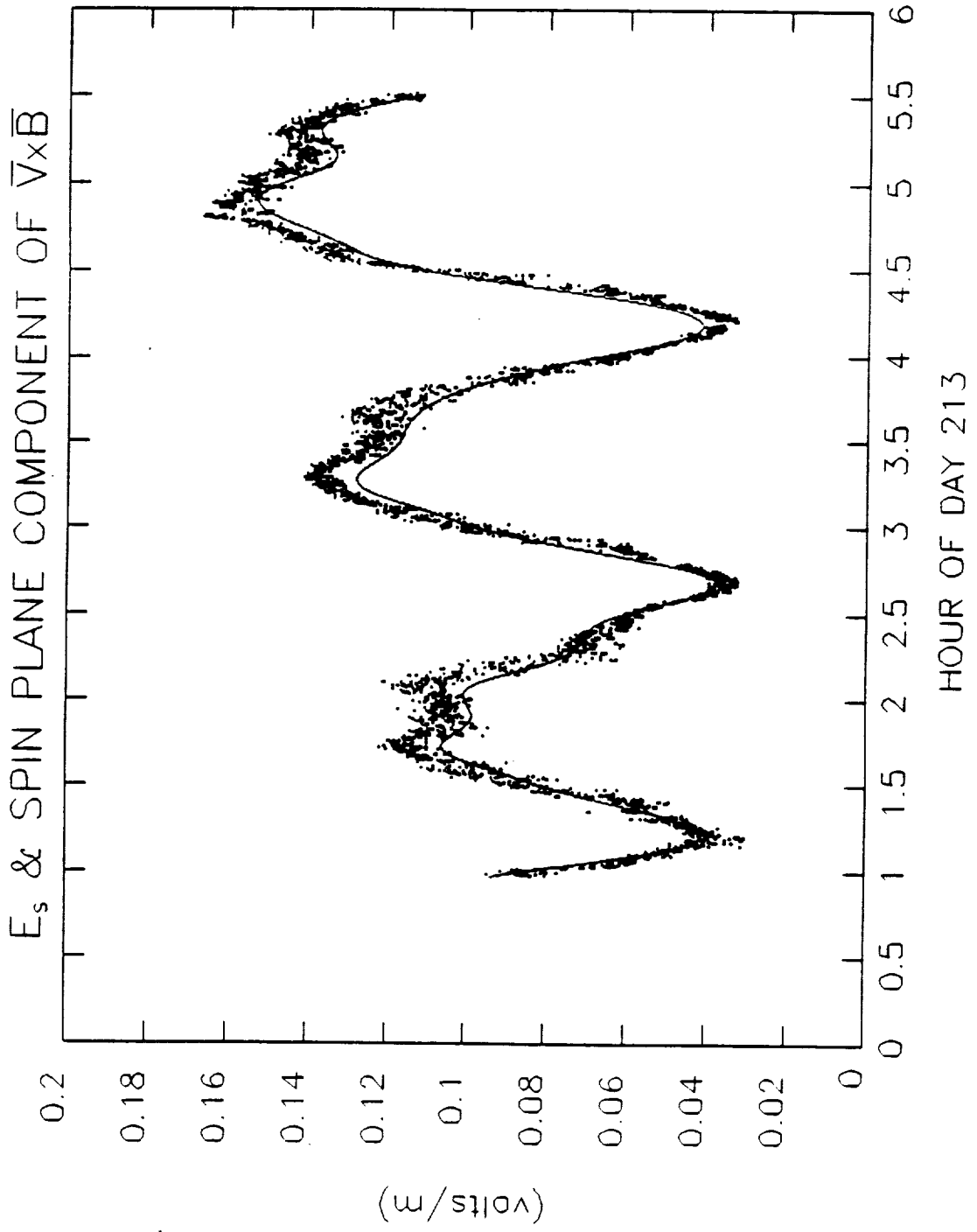


Figure 7. The RMS error of the sampled electric field values with respect to the least square's fit to a sinusoidal function.

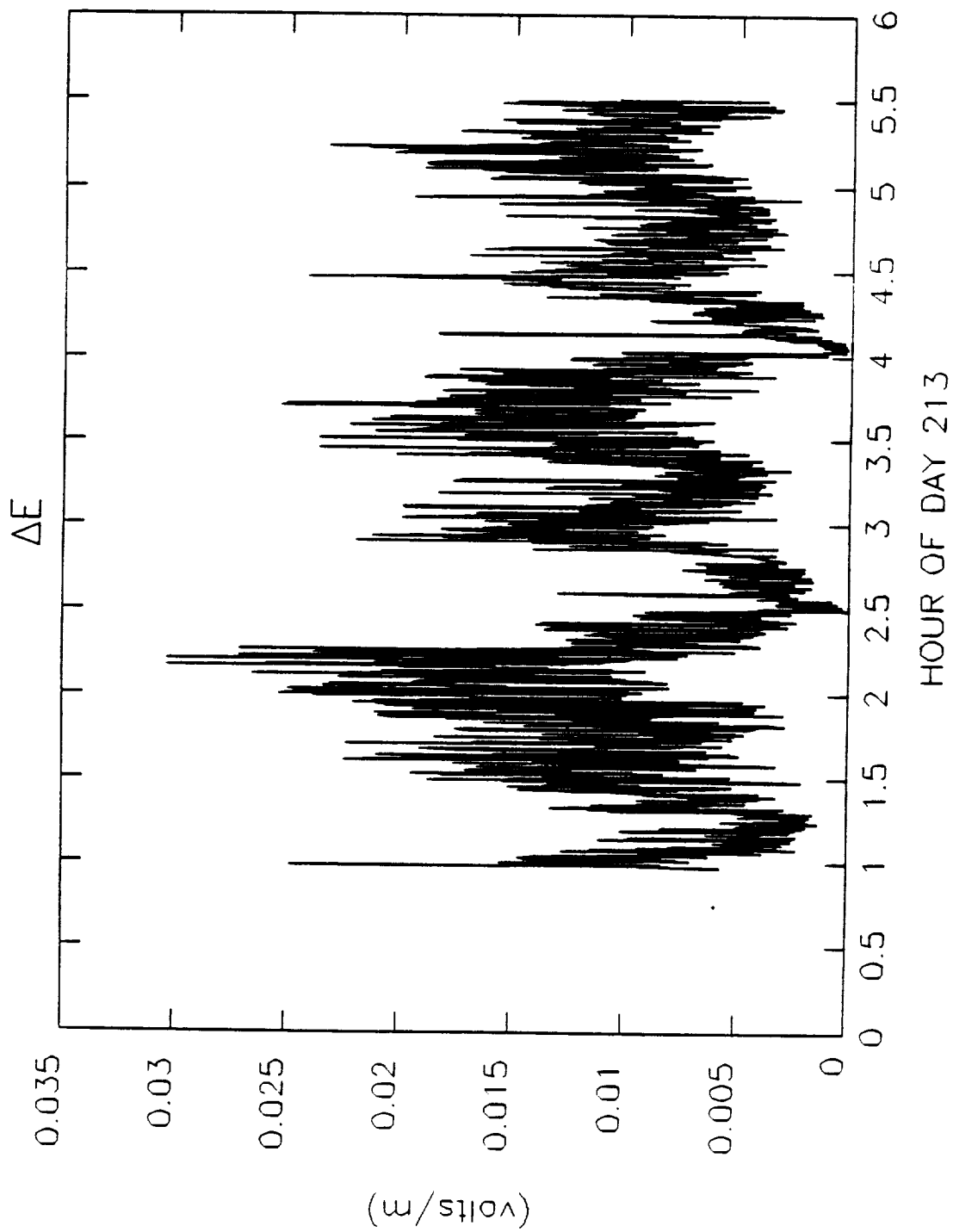


Figure 8. The component of the electric field along the direction of the velocity vector projected into a plane perpendicular to the magnetic field.

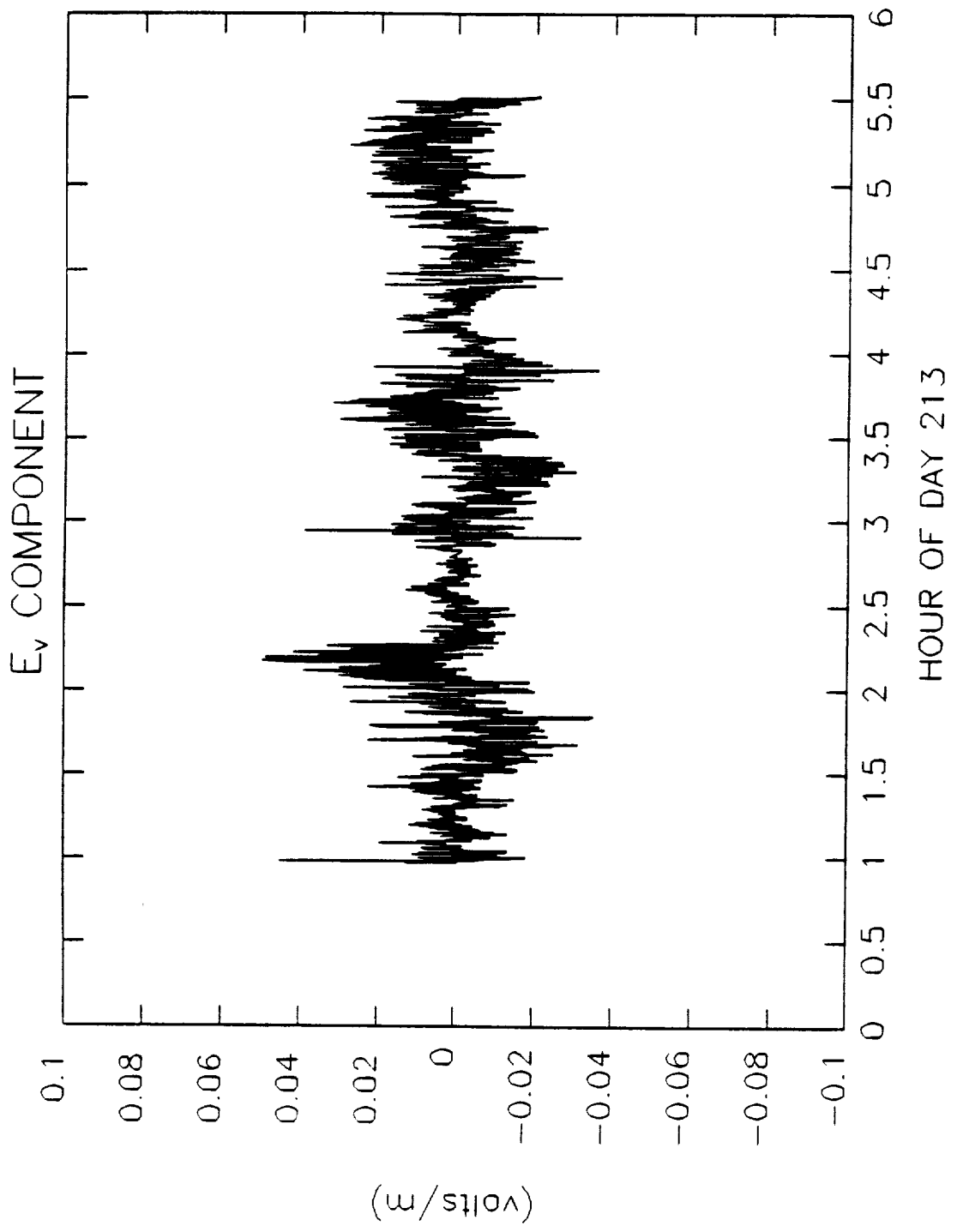


Figure 9. Dots indicate measurements of the component of the electric field along the direction of $\vec{V} \times \vec{B}$. The solid line indicates $\vec{V} \times \vec{B}$.

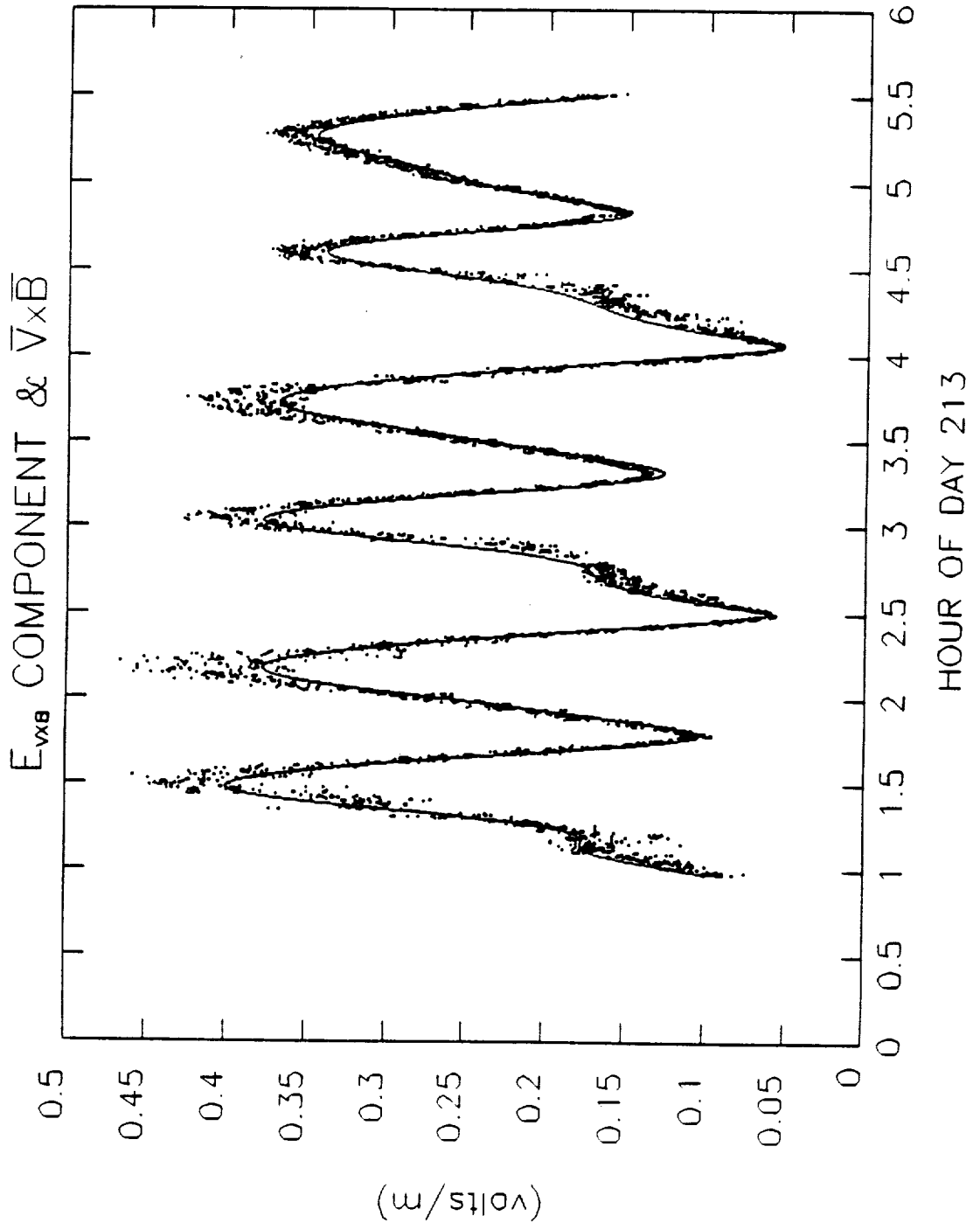


Figure 10. The ratio of the component of the electric field along the direction of $\vec{V} \times \vec{B}$ to the magnitude of $\vec{V} \times \vec{B}$.

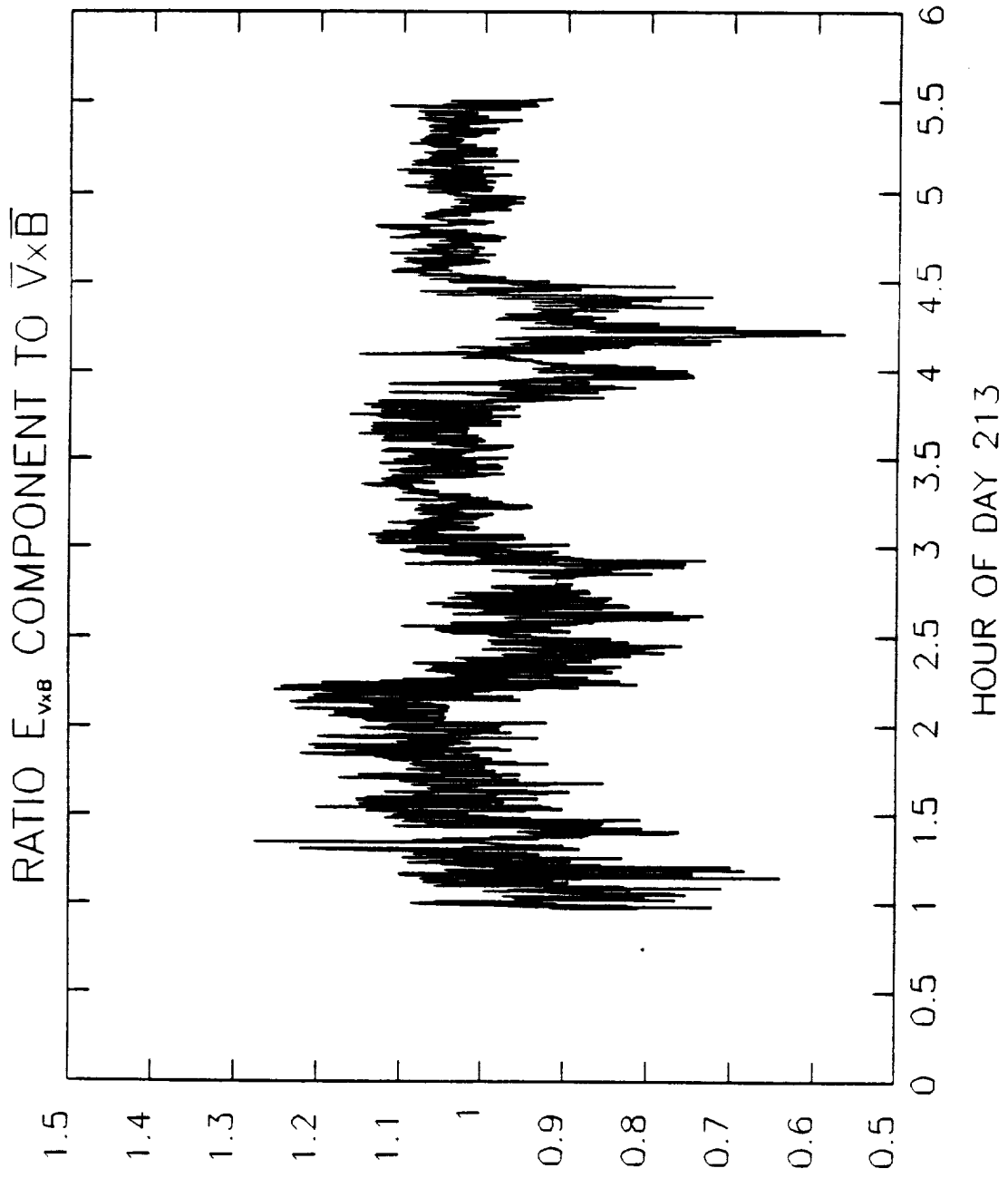


Figure 11. Electric field measurements during interval 1 when the high gain was not saturated. Dotted line is the component in the direction of $\vec{V} \times \vec{B}$. The motional field $\vec{V} \times \vec{B}$ has been subtracted from the measured field. Solid line is the component in the direction of V_{\perp} , the velocity projected into the plane perpendicular to the magnetic field.

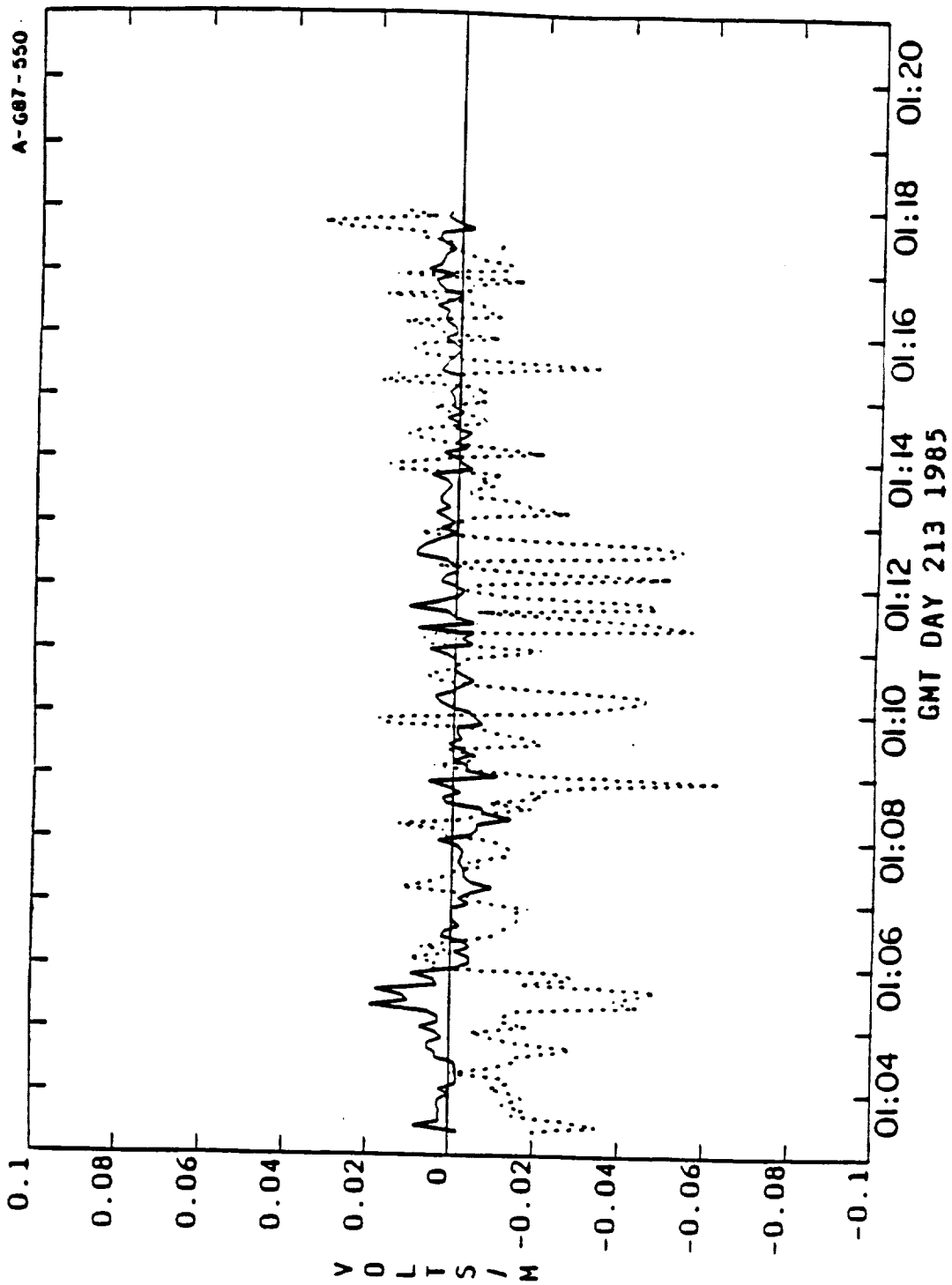


Figure 12. Electric field measurements during interval 2 when the high gain was not saturated. Dotted line is the component in the direction of $\vec{V} \times \vec{B}$. The motional field $\vec{V} \times \vec{B}$ has been subtracted from the measured field. Solid line is the component in the direction of V_{\perp} , the velocity projected into the plane perpendicular to the magnetic field.

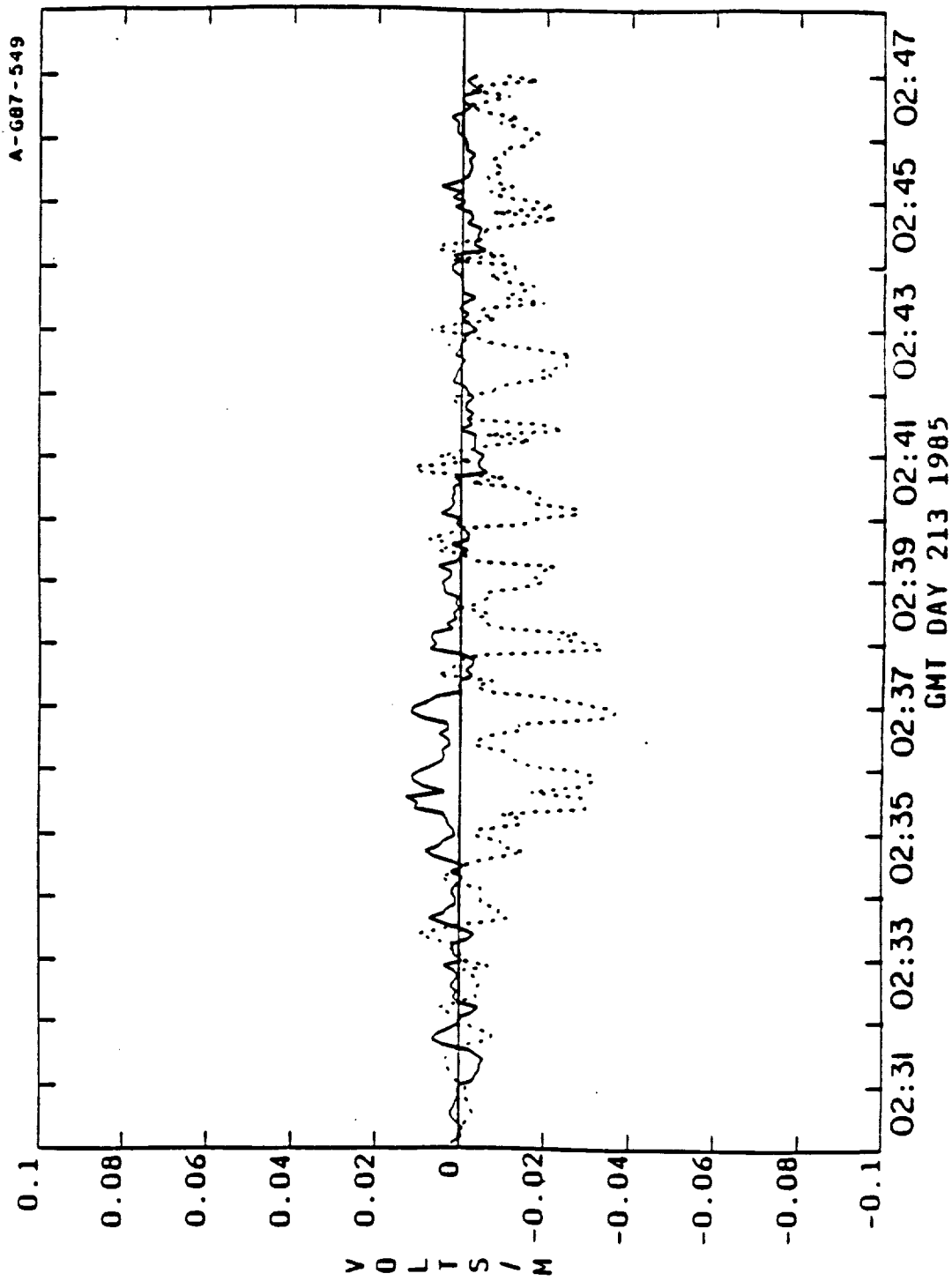


Figure 13. Electric field measurements during intervals 3 and 4 when the high gain was not saturated. Dotted line is the component in the direction of $\vec{V} \times \vec{B}$. The motional field $\vec{V} \times \vec{B}$ has been subtracted from the measured field. Solid line is the component in the direction of V_{\perp} , the velocity projected into the plane perpendicular to the magnetic field.

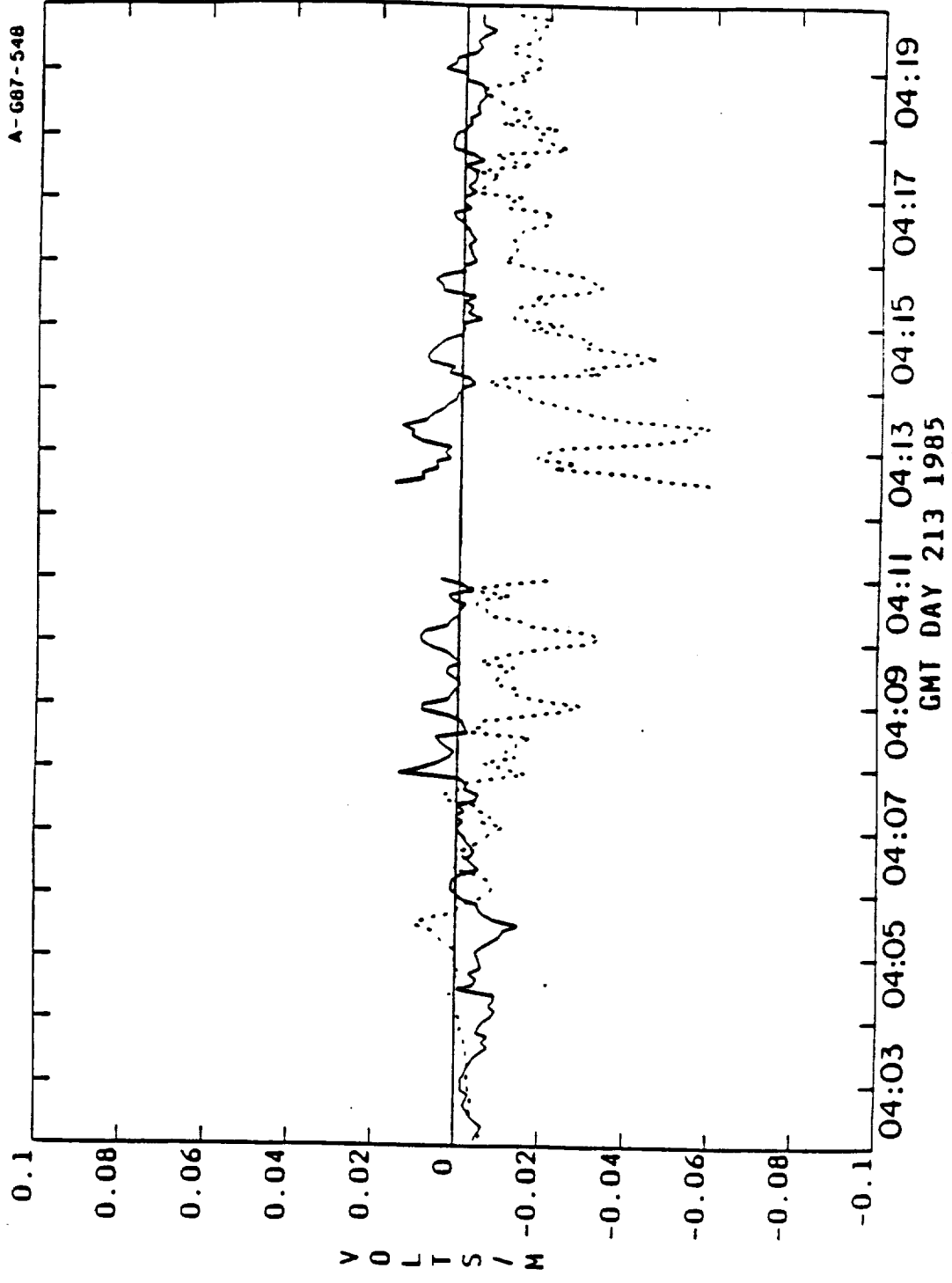


Figure 14. Upper plot shows the ratio $E_{V \times B} / |\vec{V} \times \vec{B}|$. Lower plot shows the thruster emission rate.

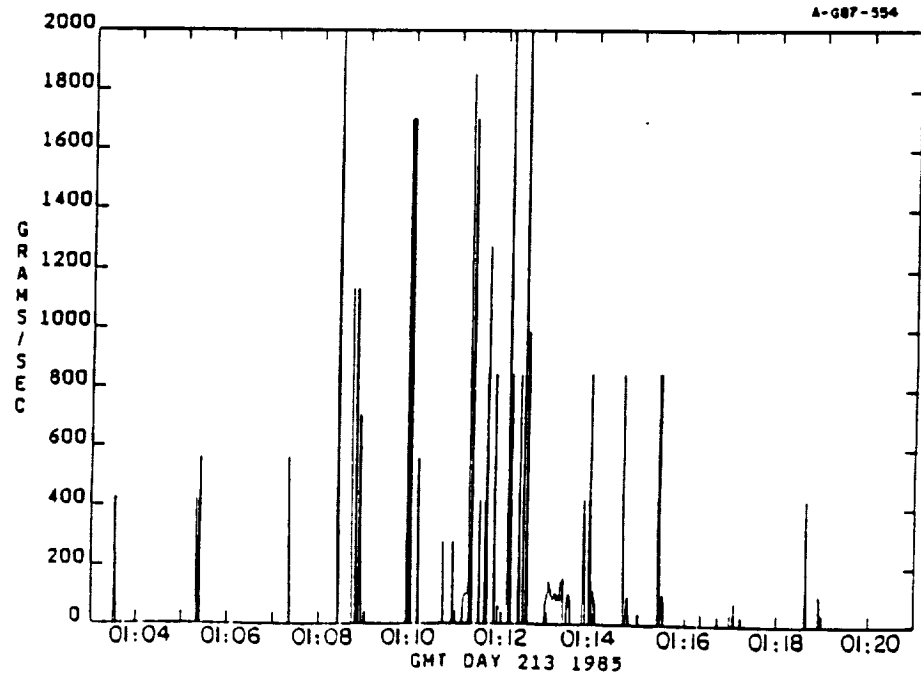
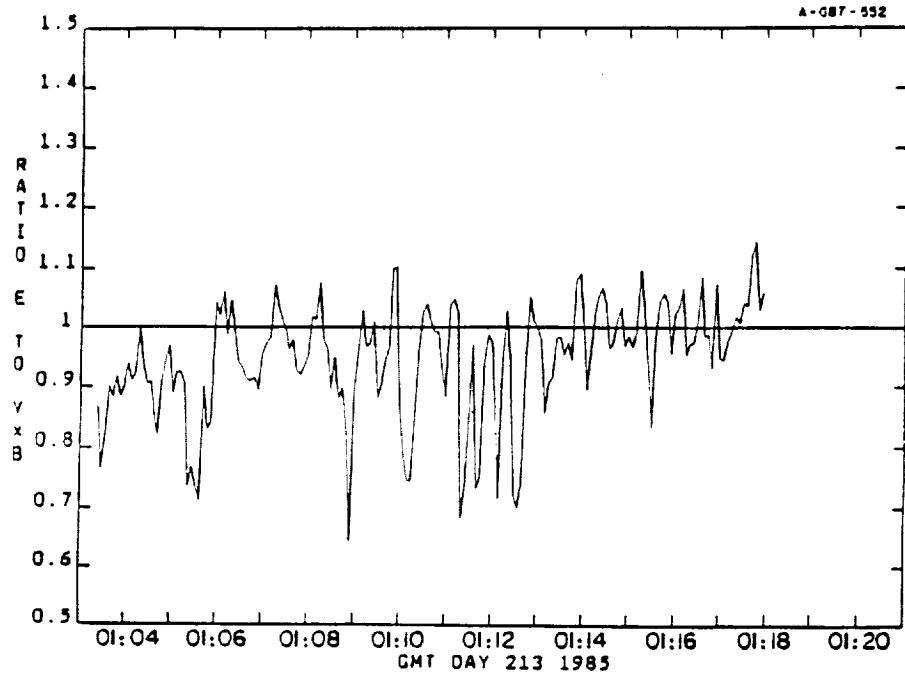


Figure 15. Upper plot shows the ratio $E_{VxB}/|\vec{V} \times \vec{B}|$. Lower plot shows the thruster emission rate.

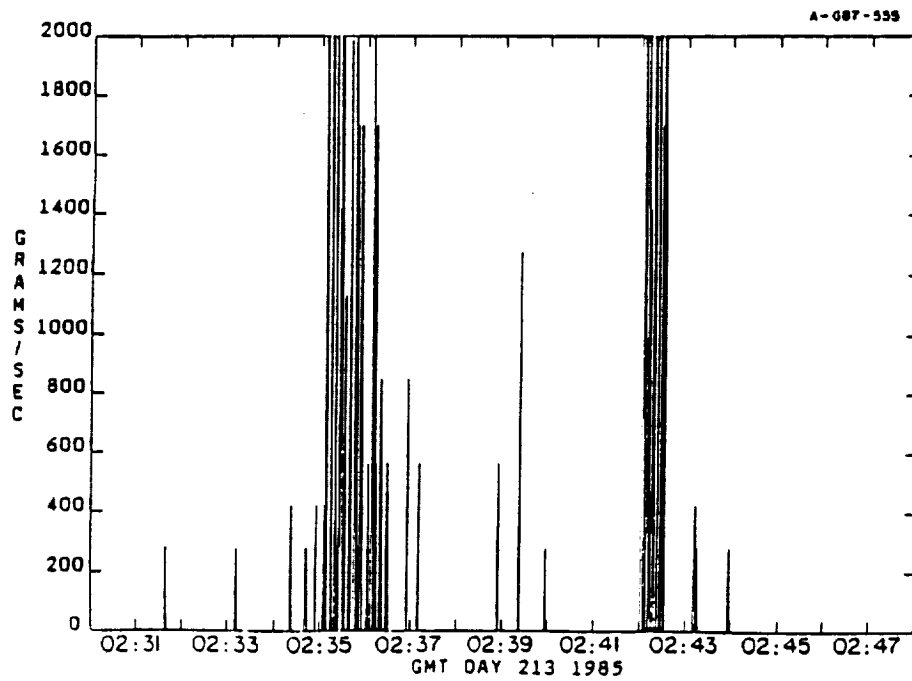
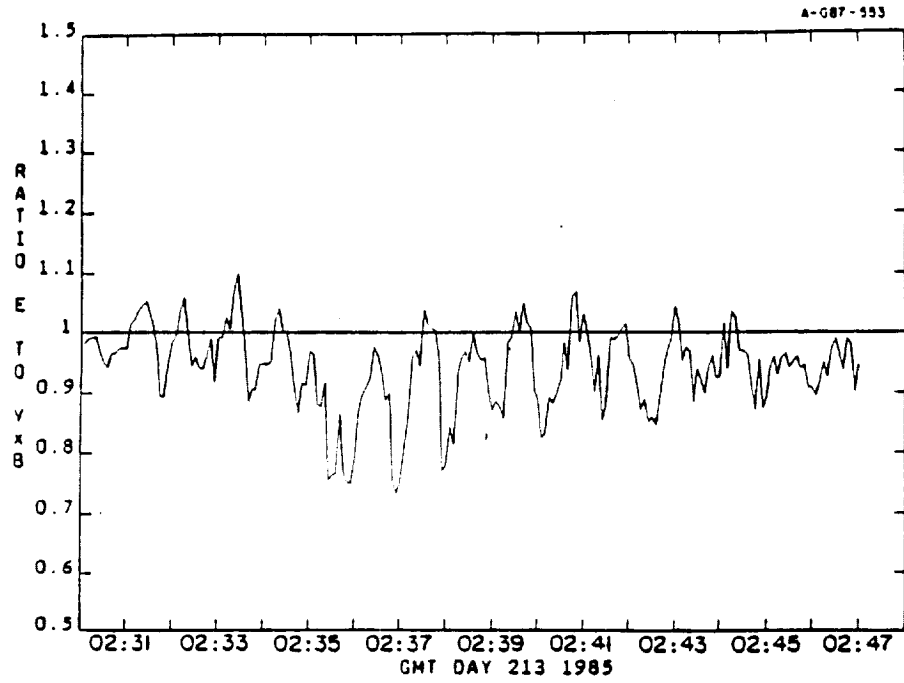


Figure 16. Upper plot shows the ratio $E_{VxB}/|\vec{V} \times \vec{B}|$. Lower plot shows the thruster emission rate.

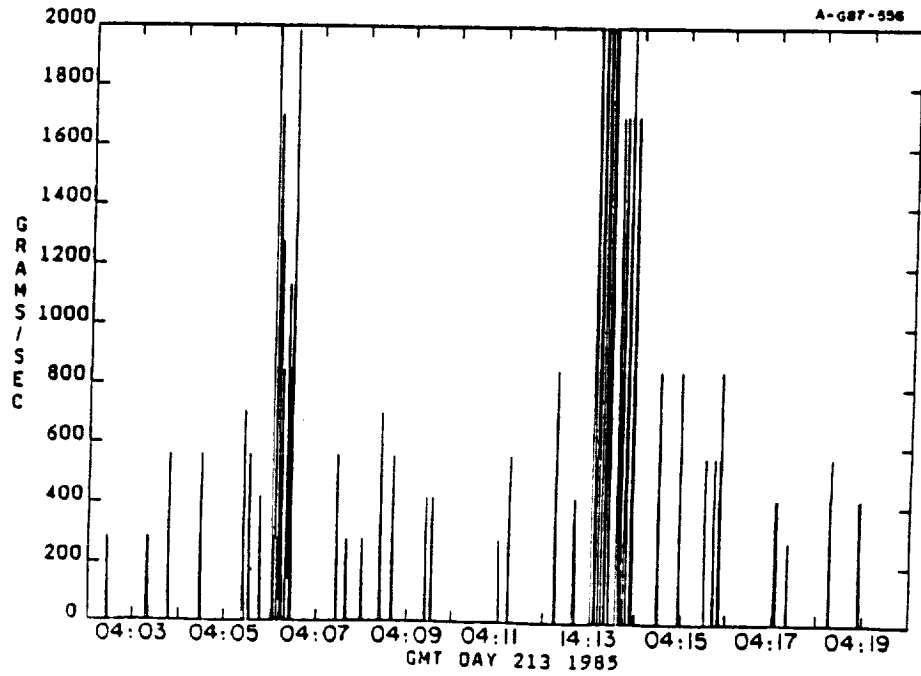
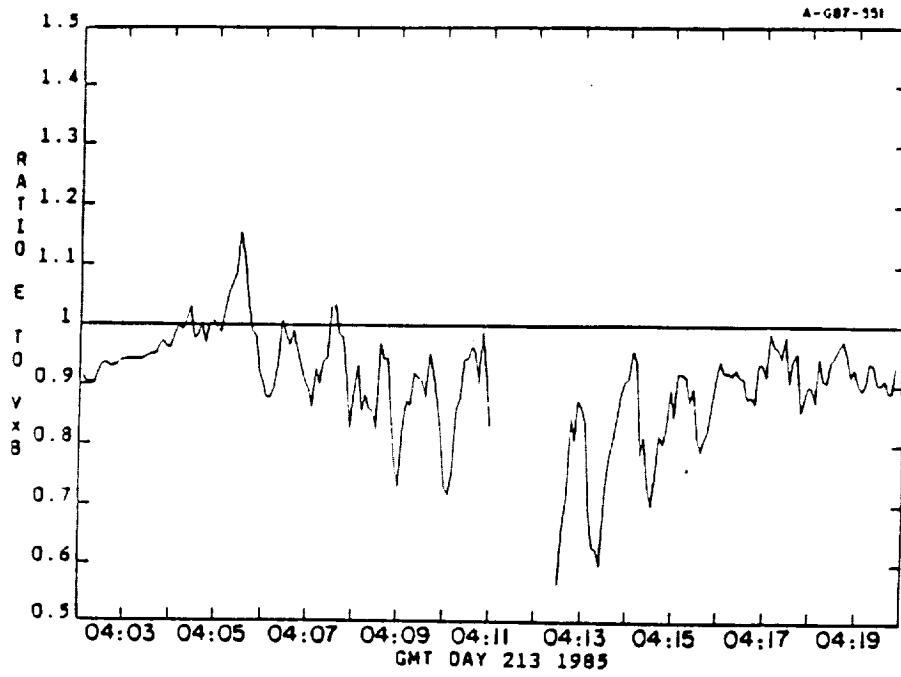


Figure 17. The ratio $E_{VxB}/|\vec{VxB}|$ versus the thruster emission rate averaged over 13 seconds. Points from all 4 time intervals are included.

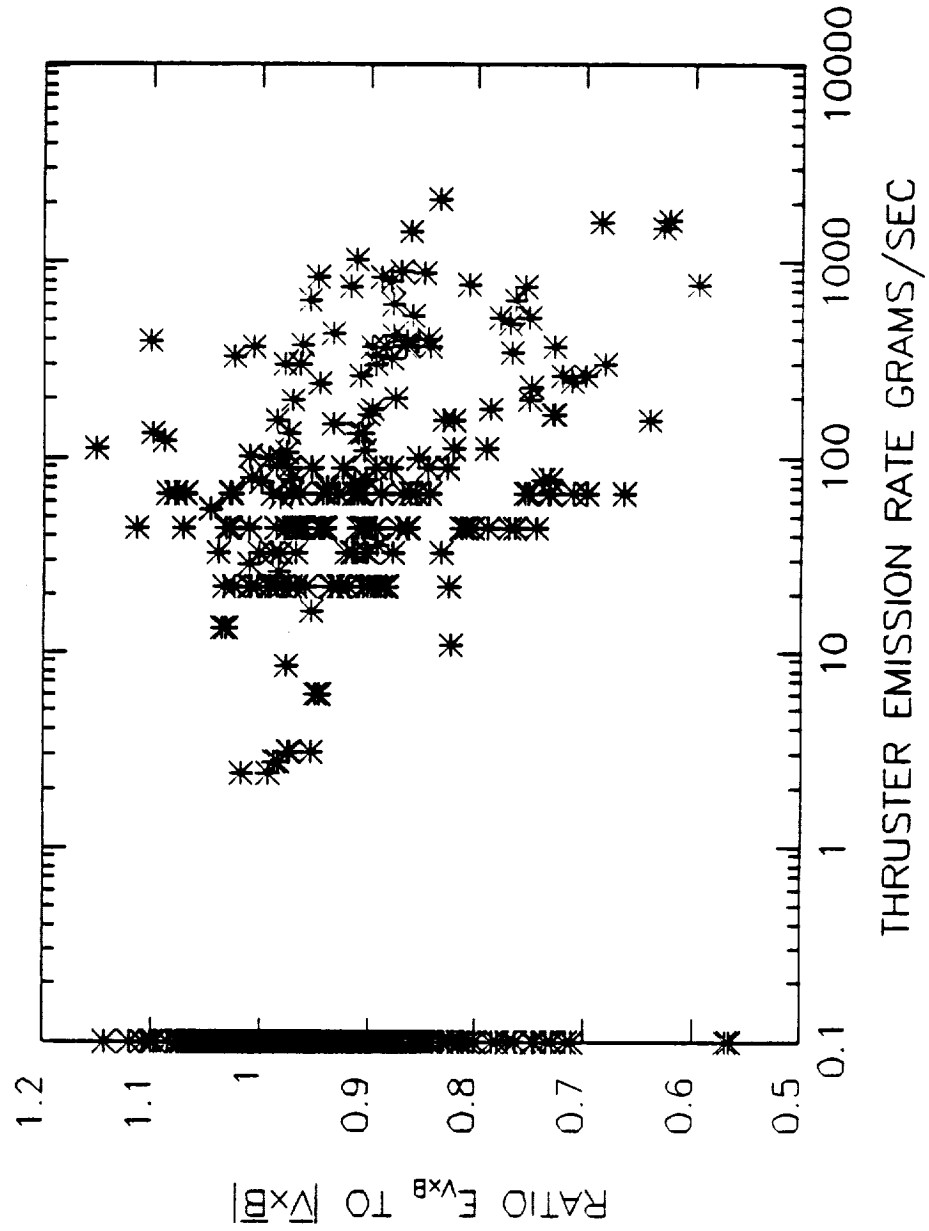


Figure 18. Measurements of $E_{\vec{v} \times \vec{B}} / |\vec{v} \times \vec{B}|$ are segregated into bins having comparable numbers of measurements, and averaged. The vertical lines show the boundaries of each bin. The error bars indicate the standard deviation of the mean in each bin.

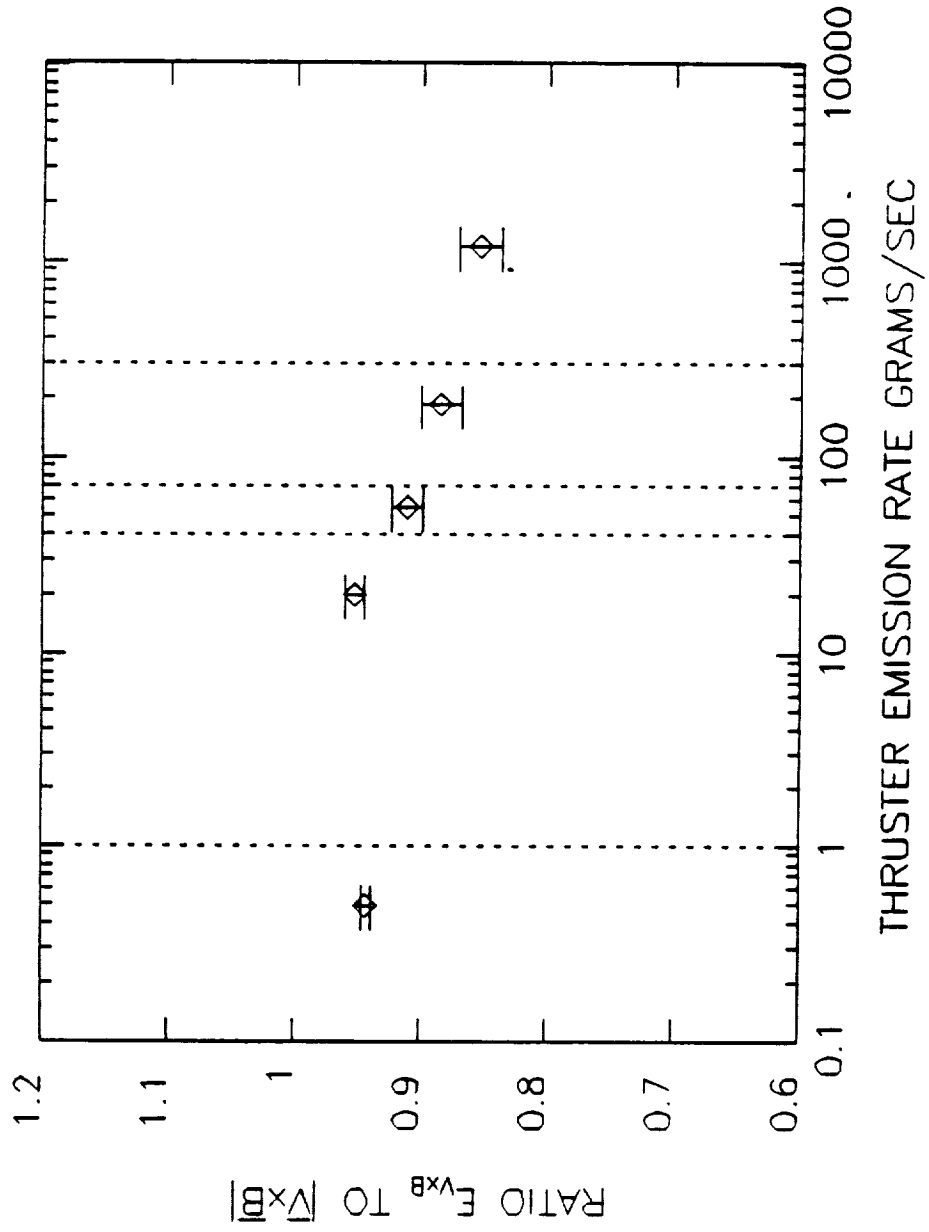


Figure 19. The ratio $E_{V \times B} / |\vec{V} \times \vec{B}|$ versus the thruster emission rate averaged over 13 seconds. Points from all four time intervals are included. Times when the electron beam generator was operating are excluded.

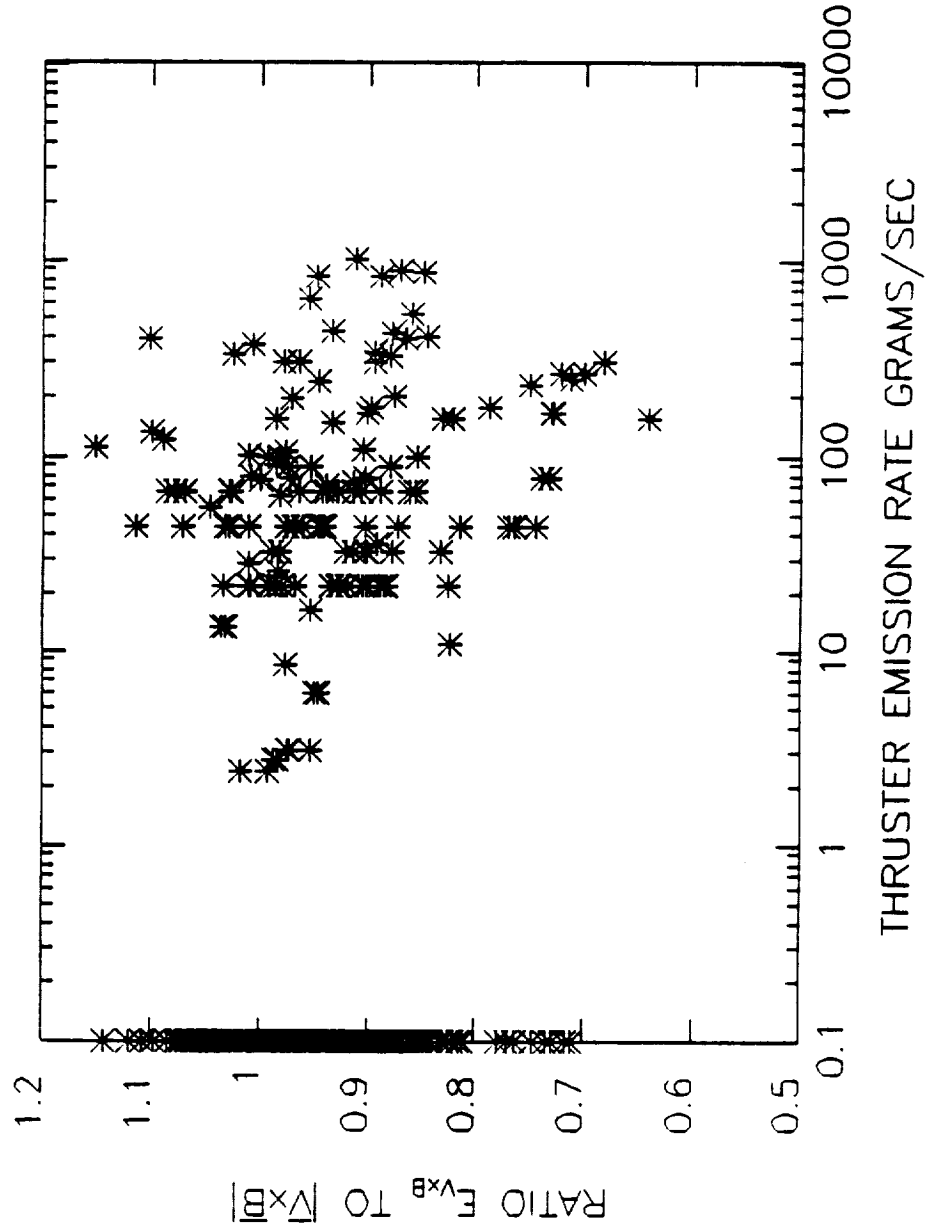


Figure 20. Measurements of $E_{VxB}/|\vec{V} \times \vec{B}|$ are segregated into bins having comparable numbers of measurements, and averaged. The vertical lines show the boundaries of each bin. The error bars indicate the standard deviation of the mean in each bin. Times when the electron beam generator was operating are excluded.

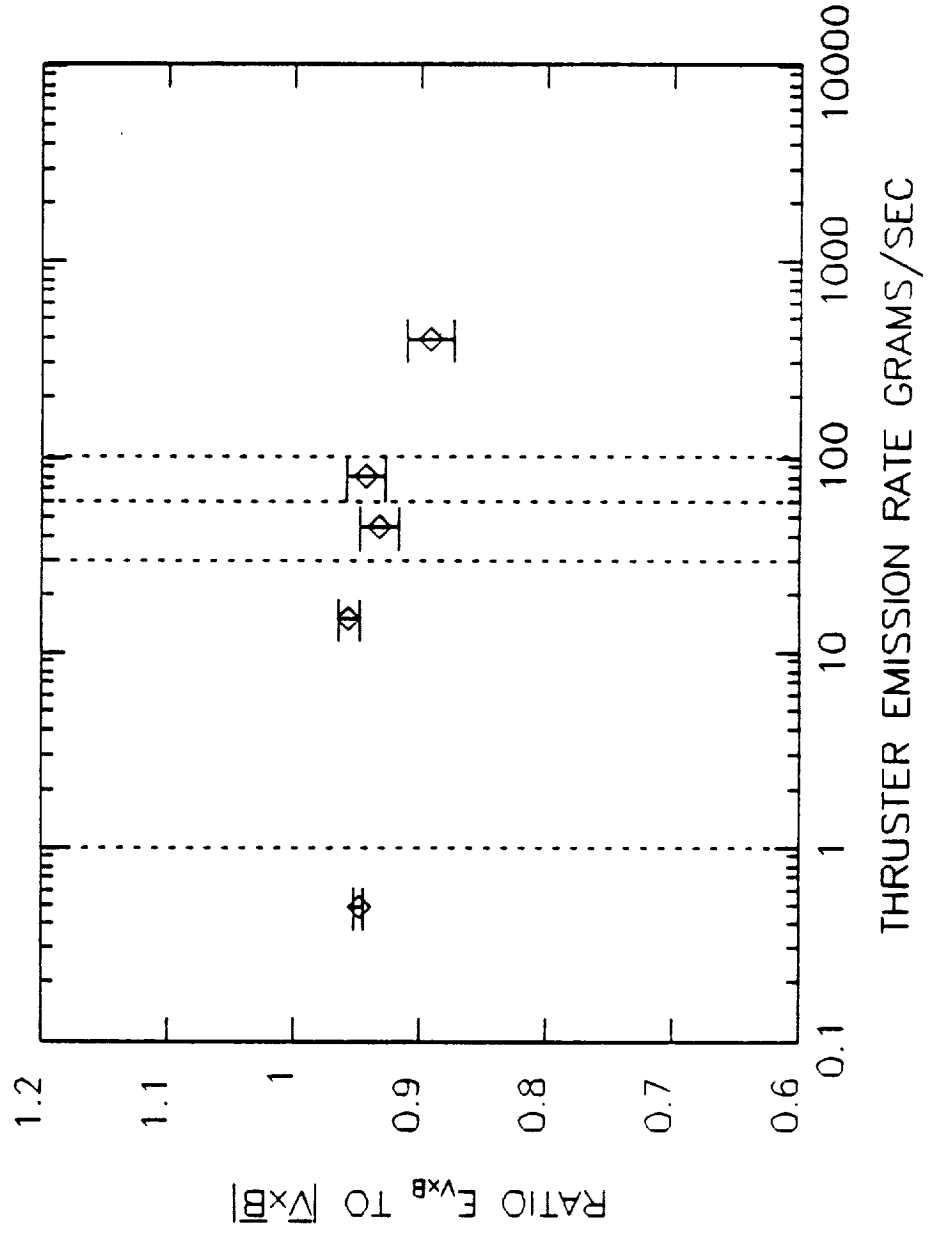


Figure 21. Directions of x, y, z coordinates.

8-687-558

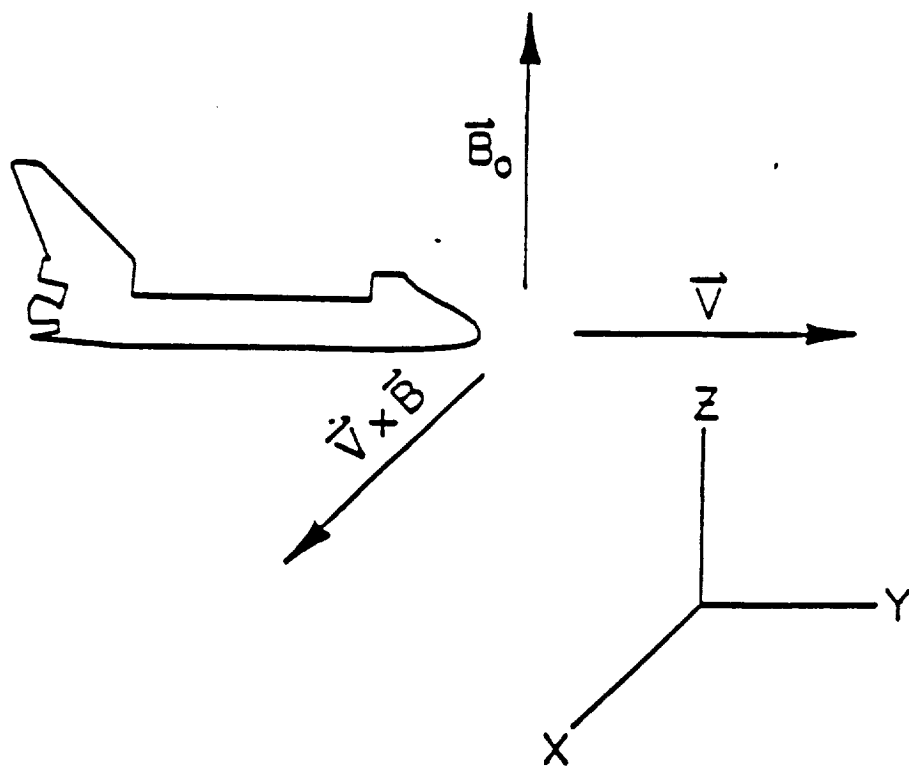


Figure 22. Alfvén wave disturbance generated by a current source moving through a magnetized plasma. The electric field E_2 between the current wings is of lower magnitude than the motional field $E_1 = \vec{V} \times \vec{B}$.

8-G87-325

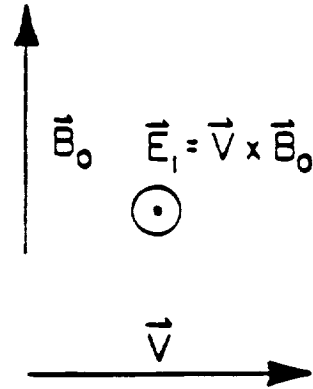
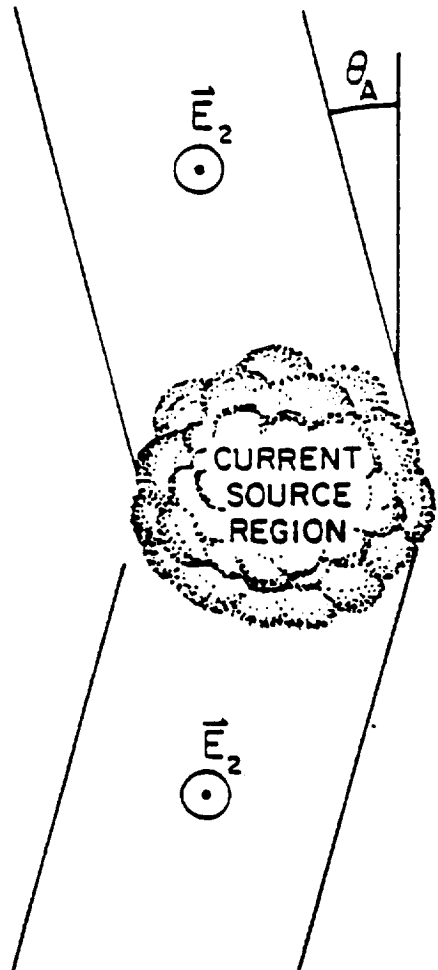


Figure 23. Alfvén wave disturbance generated by a current source moving through a magnetized plasma. The electric field E_2 between the current wings is of lower magnitude than the motional field $E_1 = \vec{V} \times \vec{B}$.

D-G88-72

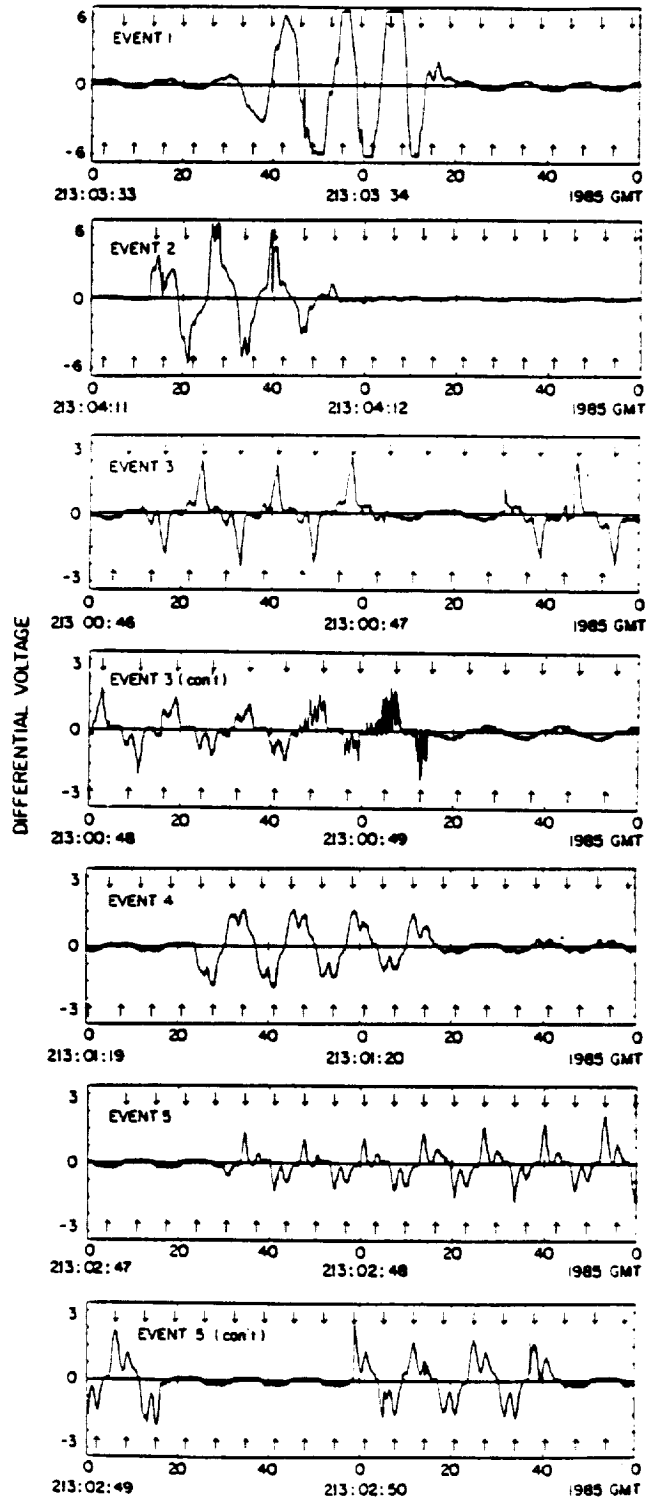


Figure 25. Dashed lines indicate the trajectory of PDP in the plane perpendicular to \vec{B} during times of electron beam generator operation. The trajectories for events 1 through 5 are shown as solid segments. The origin represents the position of the magnetic field line on which the beam lies. v_{\perp} is the component of velocity perpendicular to \vec{B} .

B-G86-832

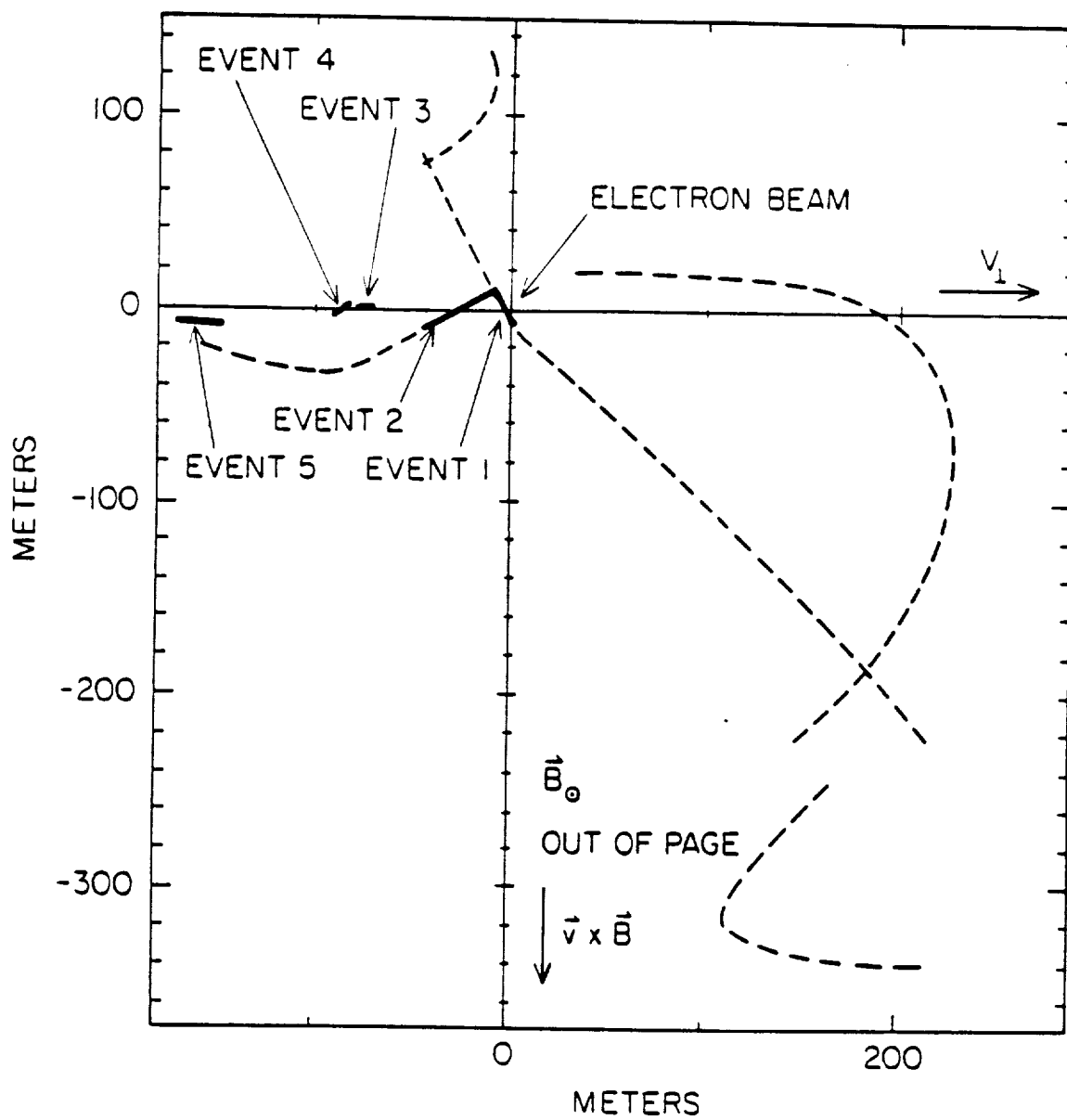


Figure 26. Average potential measurements during times when large electric field signals were detected.

D-687-715-2

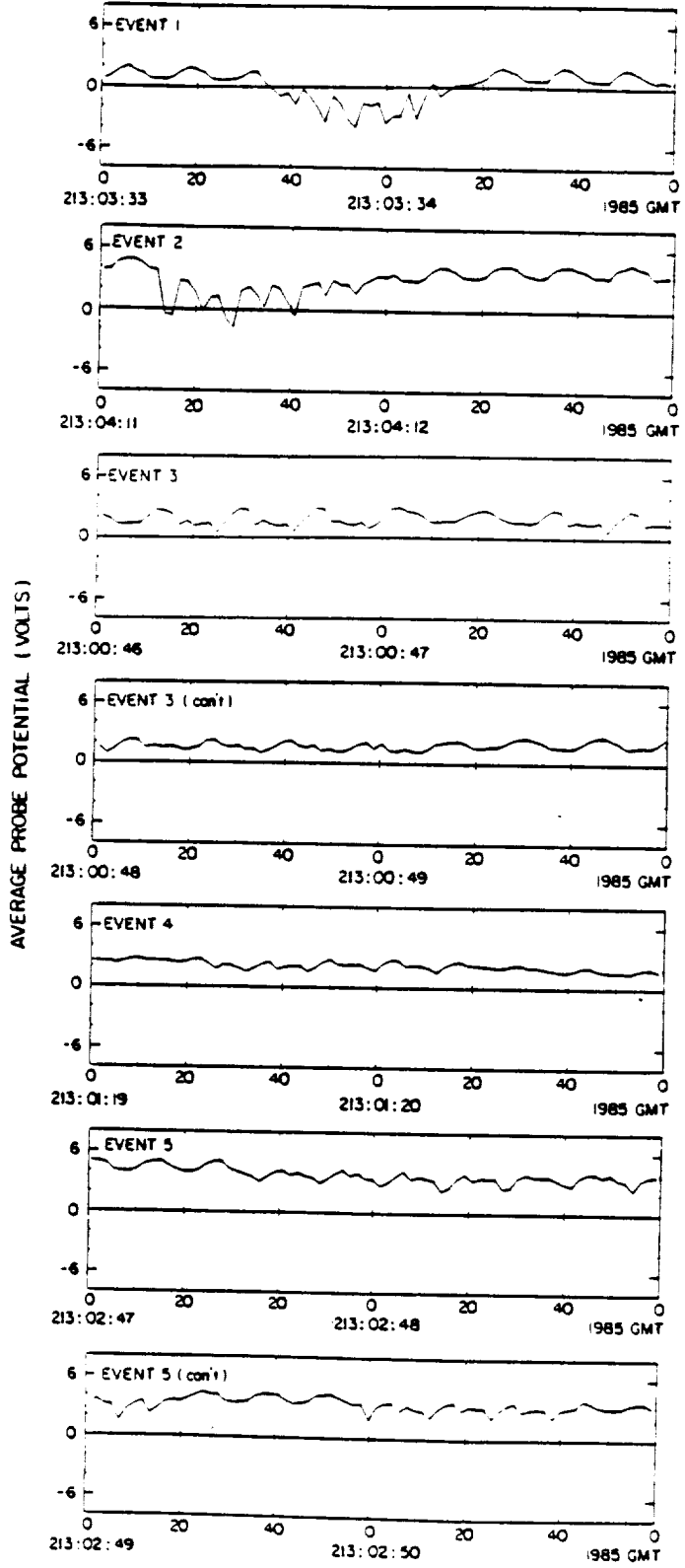


Figure 27. Solution of Equation 25 using values from Table 6.
Model of floating potential as a function of energetic
electron current. Antenna probe and PDP chassis have
different floating potentials because of their different
current collecting surface areas.

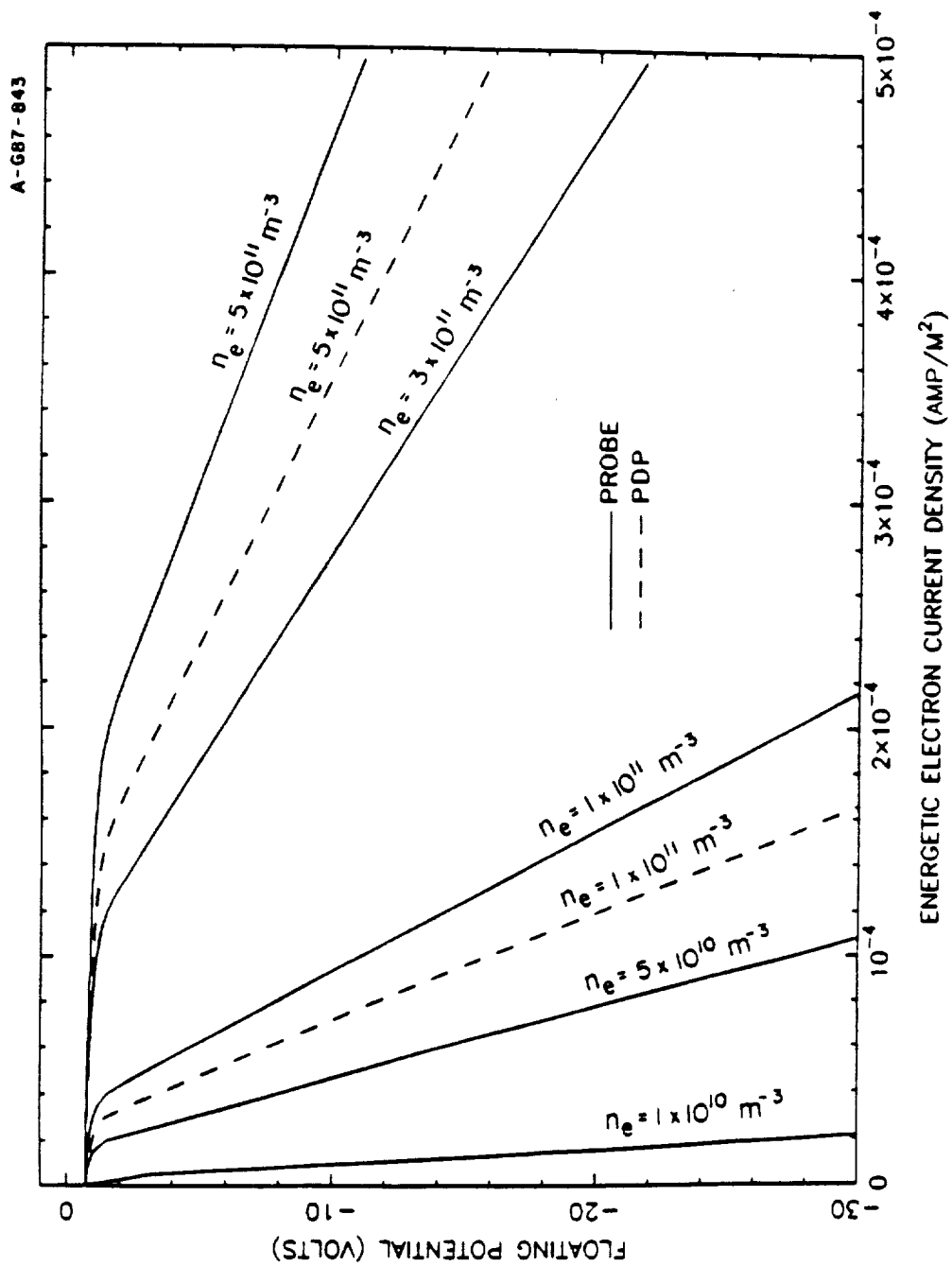


Figure 28. The PDP with the spin plane corresponding to the plane of the page. Energetic electrons move along the field lines. As the PDP spins, the antenna periodically becomes aligned with the magnetic field, and one probe is shielded from the electron flux. The probe also passes through the PDP wake.

A-G87-681

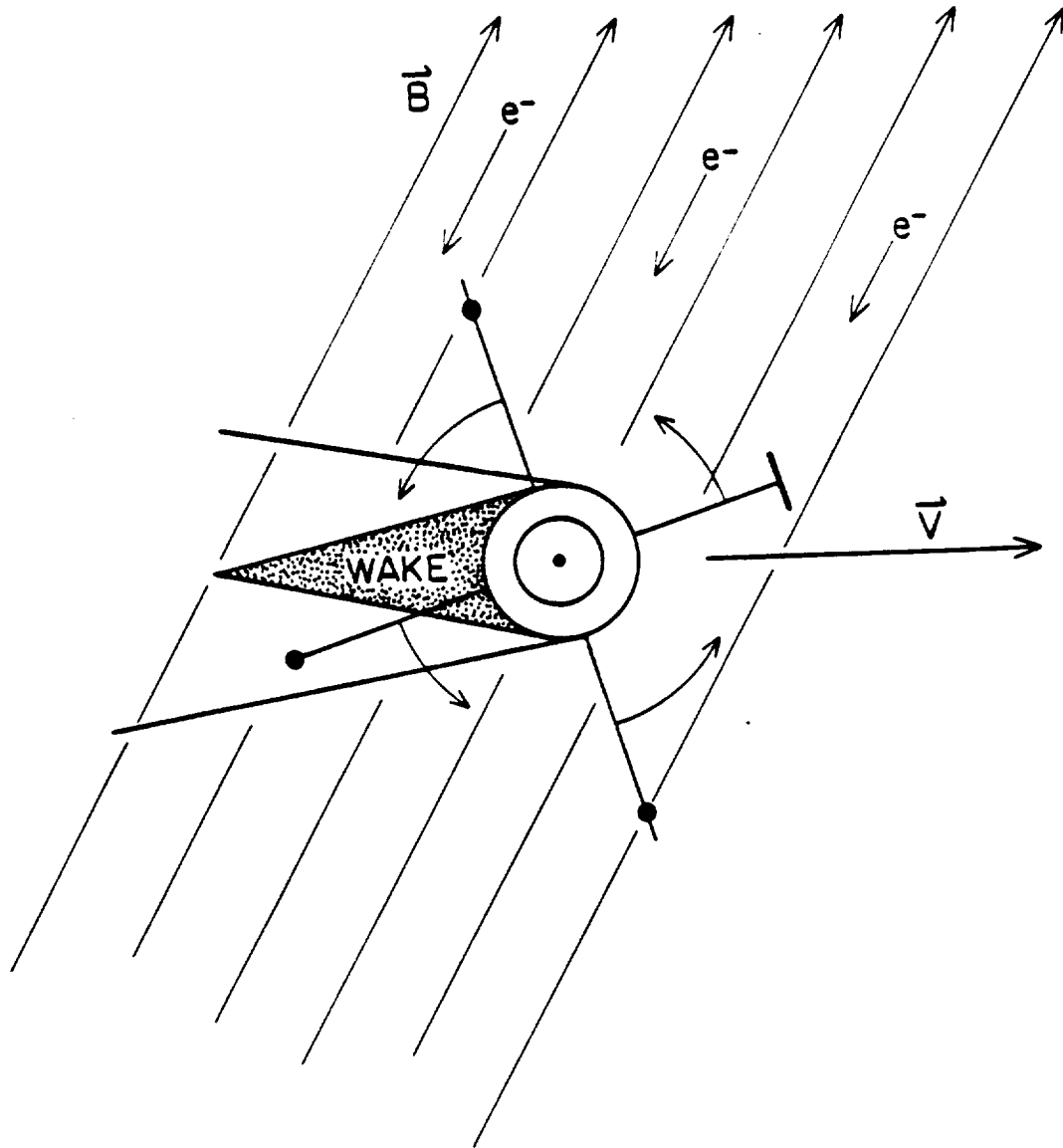


Figure 29. The PDP viewed with the spin axis in the plane of the page. The angle θ of the magnetic field to the spin plane is shown. If θ is small, then particles moving along field lines can be shadowed from one probe.

A-G87-682

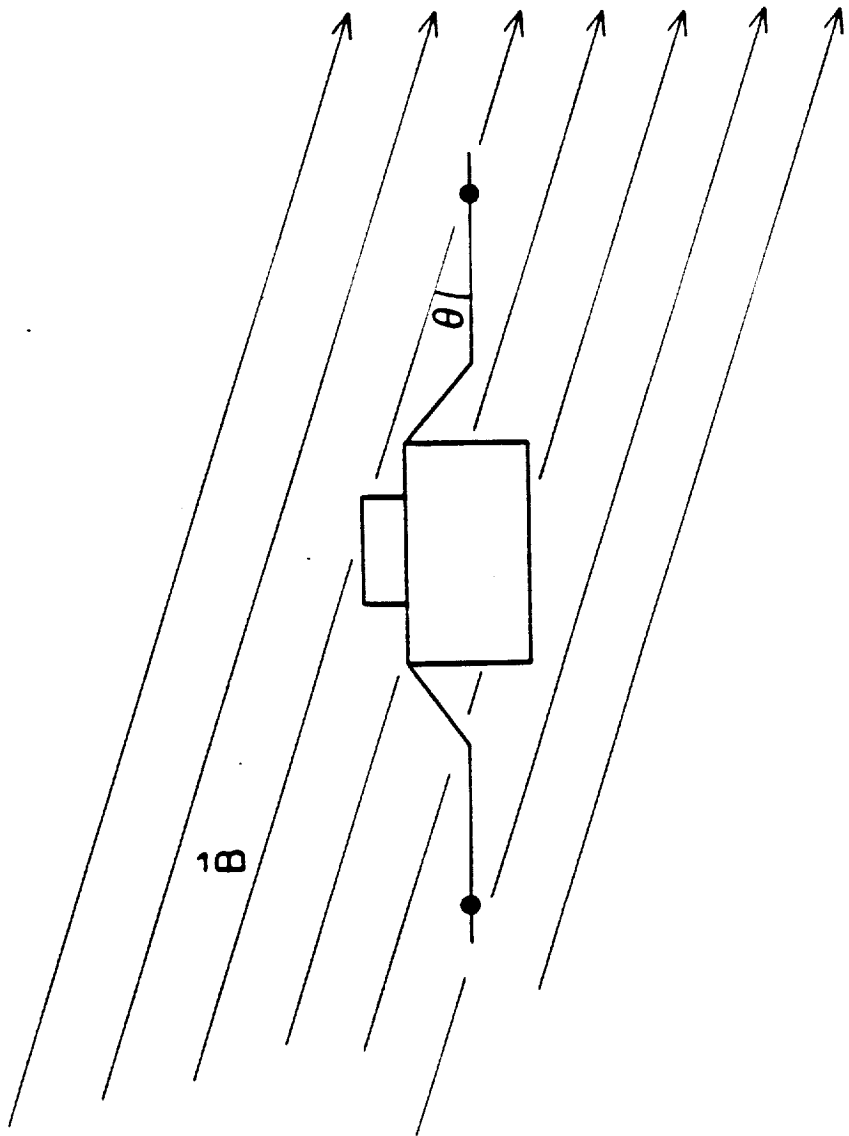
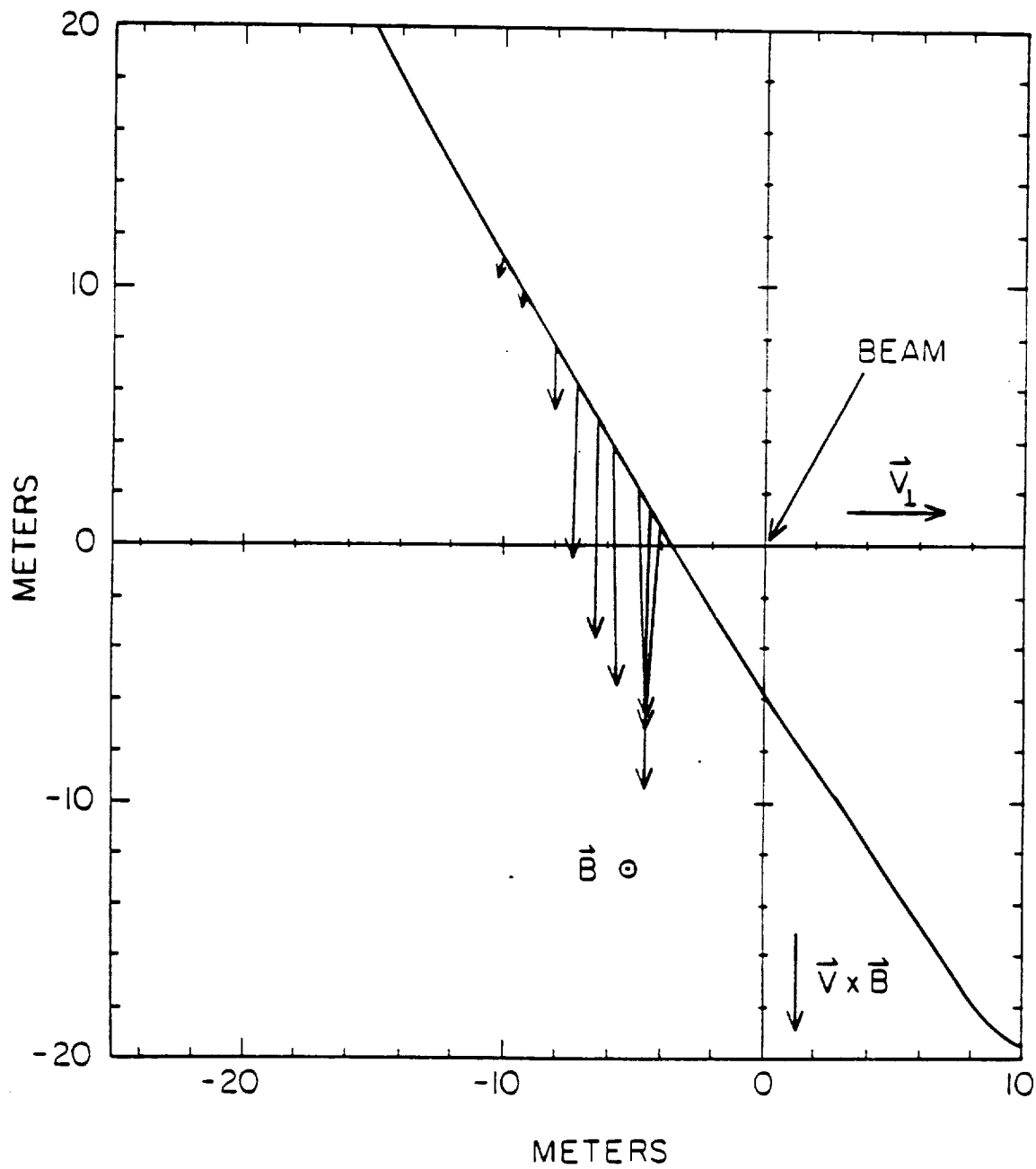


Figure 30. Vectors showing the gradient in energetic electron flux along the trajectory of the PDP. Note that the beam will have a finite width, and the location of the beam center shown is accurate only to within a few meters.

B-G86-831



REFERENCES

- Arnoldy, Roger L., and John R. Winckler, The hot plasma environment and floating potentials of an electron beam-emitting rocket in the ionosphere, J. Geophys. Res., 86, 575-584, 1981.
- Banks, P. M., W. J. Raitt, A. B. White, R. I. Bush, and P. R. Williamson, Results from the Vehicle Charging and Potential Experiment on STS-3, J. Spacecraft and Rockets, 28, 138-149, 1987.
- Bettinger, Richard T., An in situ probe system for measurement of ionospheric parameters, in Interactions of Space Vehicles With an Ionized Atmosphere, ed. S. F. Singer, 163-270, Pergamon Press, New York, 1965.
- Bevington, Philip R., Data Reduction and Error Analysis for the Physical Sciences, McGraw-Hill Book Company, New York, 1969.
- Denig, W. F., Wave and particle observations associated with the beam plasma discharge in a space simulation chamber, Ph.D. Thesis, Utah State University, 1982.
- Drell, S. D., Foley, H. M., Ruderman, M. A., Drag and propulsion of large satellites in the ionosphere: An Alfvén propulsion engine in space, J. Geophys. Res., 70, 3131-3145, 1965.
- Fahleson, U., Theory of electric field measurements conducted in the magnetosphere with electric probes, Space Science Reviews, 7, 238-262, 1967.
- Frank, L. A., D. A. Gurnett, M. Ashour-Abdalla, W. R. Paterson, W. S. Kurth, N. Omid, P. M. Banks, and W. J. Raitt, The secondary electron beams and plasma waves associated with electron beam injection in space (abstract), Bulletin American Physical Society, 32, 1823, 1987.
- Goertz, C. K., Io's interaction with the plasma torus, J. Geophys. Res., 85, 2949-2956, 1980.

- Grebowsky, J. M., H. A. Taylor, and W. M. Pharo III, Thermal ion perturbations in the vicinity of the space shuttle, Planet. Space Sci., 35, 501-513, 1987a.
- Grebowsky, J. M., H. A. Taylor, and W. M. Pharo III, Thermal ion complexities observed within the Spacelab 2 bay, Planet. Space Sci., 35, 1463-1469, 1987b.
- Green, B. D., G. E. Caledonia, and T. D. Wilkerson, The shuttle environment: Gases, particles, and glow, J. Spacecraft and Rockets, 22, 500-511, 1985.
- Hanson, W.B., Structure of the ionosphere, in Satellite Environment Handbook, Second Edition, ed. Francis S. Johnson, Stanford University Press, Stanford, California, 1965.
- Hoffman, R. J., and M. A. Hetreck, Jr., Plume contamination effects prediction: Contam III Computer Program, Tech. Rep. AFRPL TR82-033, Air Force Rocket Propul. Lab., Edwards AFB, Calif., 1982.
- Hunten, D.E., and J. M. Calo, Low energy ions in the shuttle environment: Evidence for strong ambient-containment interactions, Planet. and Space Sci., 33, 945-951, 1985.
- Jacobsen, T. A., and N. C. Maynard, Polar 5 - An electron accelerator experiment within an aurora. 3. Evidence for significant spacecraft charging by an electron accelerator at ionospheric altitude, Planet. Space Sci., 28, 291-307, 1978.
- Johnson, Francis S., Structure of the upper atmosphere, in Satellite Environment Handbook, Second Edition, ed. Francis S. Johnson, 3-20, Stanford University Press, Stanford, California, 1965.
- Kasha, Michael A., The Ionosphere and Its Interaction With Satellites, Gordon and Breach, Science Publishers, New York, 1969.
- Katz, I., D. E. Parks, D. L. Cooke, and J. A. Lilley, Jr., Polarization of spacecraft generated plasma clouds, Geophys. Res. Lett., 11, 1115-1116, 1984.
- Katz, I., and V. A. Davis, Ram ion scattering caused by space shuttle VxB induced differential charging, J. Geophys. Res., 92, 8787-8791, 1987.

- Kellogg, P. J., H. R. Anderson, W. Bernstein, T. J. Hallinan, R. H. Holzworth, R. J. Jost, H. Leinbach, and E. P. Szuszczewicz, Laboratory simulation of injection particle beams in the ionosphere, in Artificial Particle Beams in Space Plasma Studies, ed. by B. Grandel, pg. 289, Plenum Press, New York, 1982.
- McFarland, M., D. L. Albritton, F. C. Fehsenfeld, E. E. Ferguson, and A. L. Schmeltekopf, Flow-drift technique for ion mobility and ion-molecule reaction rate constant measurements, II, Positive ion reactions of N^+ , O^+ , and H_2^+ with O_2 and O^+ with N_2 from thermal to $\sim 2eV$, J. Chem. Phys., 59, 6620, 1973.
- Mendillo, Michael, and Jeffrey M. Forbes, Artificially created holes in the ionosphere, J. Geophys. Res., 83, 151-162, 1978.
- Mozer, F. S., R. B. Torbert, U. V. Fehleson, C. G. Falthammer, A. Gonfalalone, and A. Pedersen, Measurements of quasistatic and low-frequency electric fields with spherical double probes on the ISEE-1 spacecraft, IEEE Trans. Geosci. Elect., GE-16, 258-261, 1978.
- Murad, Edmond, and S. T. F. Lai, Some charge exchange reactions involving H_2O , Chem. Phys. Lett., 126, 427-429, 1986.
- Murphy, G., J. Pickett, N. D'Angelo, and W. S. Kurth, Measurement of plasma parameters in the vicinity of the space shuttle, Planet. Space Sci., 34, 993-1004, 1986.
- Murphy, Gerald B., Stanley D. Shawhan, and Jolene S. Pickett, Perturbations to the plasma environment induced by the orbiter's maneuvering thrusters, AIAA 83-2599, 1983, AIAA Shuttle Environment and Operations Meeting, Oct. 31 - Nov. 2, 1983, Washington D.C.
- Neubauer, F. M., Nonlinear standing Alfvén current system at I_0 : Theory, J. Geophys. Res., 85, 1171-1178, 1980.
- Pickett, J. S., G. B. Murphy, W. S. Kurth, C. K. Goertz, S. D. Shawhan, Effects of chemical releases by the STS-3 orbiter in the ionosphere, J. Geophys. Res., 90, 3487-3497, 1985.
- Raitt, W. J., D. E. Siskind, P. M. Banks, P. R. Williamson, Measurements of the thermal plasma environment of the space shuttle, Planet. Space Sci., 32, 447-467, 1984

- Reasoner, David L., Stanley D. Shawhan, and Gerald Murphy, Plasma Diagnostics Package measurements of ionospheric ions and shuttle induced perturbations, J. Geophys. Res., 91, 13,463-13,471, 1986.
- Samir, U., K. H. Wright, Jr., and N. H. Stone, The expansion of a plasma into a vacuum: Basic phenomena and processes and application to space plasma physics, Rev. Geophys. and Space Phys., 21, 1631, 1983.
- Scholer, M., On the motion of artificial ion clouds in the magnetosphere, Planet. Space Sci., 18, 977-1004, 1970.
- Shawhan, S.D., Description of the Plasma Diagnostics Package (PDP) for the OSS-1 shuttle mission and JSC chamber test in conjunction with the Fast Pulse Electron Gun (FPEG), Artificial Particle Beams In Space Studies, ed. by B. Grandel, 419-430, Plenum, N. York, 1982.
- Shawhan, S. D., G. B. Murphy, P. M. Banks, P. R. Williamson and W. J. Raitt, Wave emissions from dc and modulated electron beams on STS-3, Radio Science, 19, 471-486, 1984a.
- Shawhan, S. D., G. B. Murphy, and J. S. Pickett, Plasma Diagnostics Package initial assessment of the shuttle orbiter plasma environment, J. Spacecraft and Rockets, 21, 387-391, 1984b.
- Singh, N., and R. W. Schunk, Numerical calculations relevant to the initial expansion of the polar wind, J. Geophys. Res., 87, 9154, 1982.
- Smiddy, M., W. P. Sullivan, D. Girouard, and P. J. Anderson, Observation of electric fields, electron densities and temperature from the space shuttle, AIAA 83-2625, 1983, AIAA Shuttle Environment and Operations Meeting 1983, Washington D.C.
- Steinberg, J. T., D. A. Gurnett, P. M. Banks, and W. J. Raitt, Quasi-static electric field measurements near the electron beam on Spacelab-2, submitted to J. Geophys. Res., 1987.
- Stone, N. H., U. Samir, K. H. Wright, Jr., D. L. Reasoner, and S. D. Shawhan, Multiple ion streams in the near vicinity of the space shuttle, Geophys. Res. Lett., 10, 1215-1218, 1983.
- Stone, N. H., K. H. Wright, Jr., K. S. Hwang, U. Samir, G. B. Murphy, and S. D. Shawhan, Further observations of space shuttle plasma-electrodynamic effects from OSS-1/STS-3, Geophys. Res. Lett., 13, 217-220, 1986.

- Sunshine, Gabriel, Bertand B. Aubrey, and Benjamin Bederson, Absolute measurements of total cross sections for the scattering of low-energy electrons by atomic and molecular oxygen, Phys. Res., 154, 1-8, 1967.
- Tribble, A. C., N. D'Angelo, G. Murphy, J. Pickett, and J. T. Steinberg, Effect of an exposed High-Voltage Source on the potential of an ionospheric satellite released from the shuttle orbiter, to be submitted to J. Spacecraft and Rockets, 1986.
- Turner, B. R., and J. A. Rutherford, Charge transfer and Ion-atom interchange reactions of water vapor ions, J. Geophys. Res., 73, 6751-6758, 1968.
- Whetten, N. R., Secondary electron emission, in CRC Handbook of Chemistry and Physics, 65th Edition CRC Press, Inc., Boca Raton, Florida, 1985.
- Wilhelm, Klaus, Willian Bernstein, Paul J. Kellog, and Brian A. Whalen, Fast magnetospheric echoes of energetic electron beams, J. Geophys. Res., 90, 491-504, 1985.
- Winckler, J. R., J. E. Steffen, P. R. Malcolm, K. N. Erickson, Y. Abe, and R. L. Swanson, Ion resonances and ELF wave production by an electron beam injected into the ionosphere: Echo 6, J. Geophys. Res., 89, 7565-7571, 1984.
- Winckler, J. R., and K. N. Erickson, Plasma heating, plasma flow and wave production around an electron beam injected into the ionosphere, JPL Symposium on Space Technology Plasma Issues in 2001, ed. by Henry Garrett, Joan Feynman, Stephen Gabriel, pg. 295-306, JPL Publication 86-49, Oct. 1, 1986.

